

Edited by

E. Batista
P. Vellasco
L. de Lima

VOLUME 1

Proceedings of

International Colloquium Stability and Ductility of Steel Structures





www.EngineeringEBooksPdf.com



SDSS'Rio 2010

International Colloquium

Stability and Ductility of Steel Structures

www.EngineeringEBooksPdf.com

First published in Brazil in 2010 by Federal University of Rio de Janeiro and State University of Rio de Janeiro

All rights reserved. No part of this book may be reproduced or transmitted in any form or by any means, electronic or mechanical, including photocopying, recording or by any information storage and retrieval system, without permission in writing from the publisher.

International Colloquium on Stability and Ductility of Steel Structures, SDSS'Rio 2010

ISBN: 978-85-285-0137-7

Graphic Art Production: Angela Jaconniani and Lucia Lopes

Printed and Bound by: J. Sholna Reproduções Gráficas Ltda.

Distribution:
Federal University of Rio de Janeiro and State University of Rio de Janeiro
Telephone: (+55 21) 2562-8474 and (+55 21) 2334-0469
E-mail: batista@coc.ufrj.br ; pvellasco@globo.com and luciano@eng.uerj.br

Editors: Eduardo de M. Batista, Pedro C. G. da S. Vellasco and Luciano R. O. de Lima

www.EngineeringEBooksPdf.com



SDSS'Rio 2010

International Colloquium

Stability and Ductility of Steel Structures

RIO DE JANEIRO - BRAZIL

08 - 10 SEPTEMBER 2010

ORGANISATION

Federal University of Rio de Janeiro, UFRJ
State University of Rio de Janeiro, UERJ
Structural Stability Research Council, SSRC

EDITORS

Eduardo de M. Batista
Pedro C. G. da S. Vellasco
Luciano R. O. de Lima

SPONSORS

UFRJ
Universidade Federal
do Rio de Janeiro

UERJ
Universidade do Estado do Rio de Janeiro

COPPE
UFRJ

FAPERJ
Fundação Carlos Chagas Filho de Amparo
à Pesquisa do Estado do Rio de Janeiro

CNPq
Conselho Nacional de Desenvolvimento
Científico e Tecnológico

CAPES

CBCA
Centro Brasileiro da Construção em Aço

www.EngineeringEBooksPdf.com

SCIENTIFIC COMMITTEE

S.A.L. Andrade - Brazil
R. Azoubel - Brazil
E.M. Batista - Brazil
R. Battista - Brazil
E. Bayo - Spain
D. Beg - Slovenia
F. Bijlaard - Netherlands
R. Bjorhovde - USA
M.A. Bradford - Australia
I. Burges - UK
D. Camotim - Portugal
P.J.S. Cruz - Portugal
J.B. Davison - UK
R. Driver - Canada
D. Dubina - Romania
L. Dunai - Hungary
W.S. Easterling - USA
R.H. Fakury - Brazil
J.M. Franssen - Belgium
T. Galambos - USA
P.B. Gonçalves - Brazil
R. Greiner - Austria
G. Hancock - Australia
J.-P. Jaspart - Belgium
V. Kodur - USA
U. Kuhlmann - Germany
R. LaBoube - USA
D. Lam - UK
A. Landesmann - Brazil
R. Landolfo - Italy
J.R. Liew - Singapore
L.R.O. Lima - Brazil
J. Lindner - Germany
M. Mahendran - Australia
R. Maquoi - Belgium
F. Mazzolani - Italy
E. Mirambel - Spain
J.R. Muzeau - France
D.A. Nethercot - UK
L.C. Neves - Portugal
J. Packer - Canada
G. Parke - UK M. Pfeil - Brazil
R. Plank - UK
A. Plumier - Belgium
K.J. Rasmussen - Australia
P.V. Real - Portugal
J.P.C. Rodrigues - Portugal
B. Schafer - USA
J.G.S. Silva - Brazil
L.S. Silva - Portugal
N. Silvestre - Portugal
M. Skaloud - Czech Rep.
H. Snijder - Netherlands
R. Souza - Brazil
B. Uy - Australia
P.C.G.S. Vellasco - Brazil
A. Wadee - UK
F. Wald - Czech Rep.
B. Young - Hong Kong
R. Ziemian - USA

ORGANIZING COMMITTEE

Alexandre Landesmann - UFRJ
Arlene Maria Sarmanho Freitas - UFOP
Eduardo de Miranda Batista - UFRJ
Francisco Carlos Rodrigues - UFMG
José Guilherme S. da Silva - UERJ
Leandro Palermo Junior - UNICAMP
Luciano Rodrigues Ornelas de Lima - UERJ
Luciano Mendes Bezerra - UNB
Maximiliano Malite - USP / SC
Michele Schubert Pfeil - UFRJ
Pedro Colmar G. da Silva Vellasco - UERJ
Remo Magalhães de Souza - UFPA
Ronaldo Carvalho Battista - UFRJ
Sebastião A. L. de Andrade - PUC-RJ/UERJ
Zacarias M. Chamberlain Pravia - FUPF

www.EngineeringEBooksPdf.com

SDSS'Rio 2010 STABILITY AND DUCTILITY OF STEEL STRUCTURES
E. Batista, P. Vellasco, L. de Lima (Eds.)
Rio de Janeiro, Brazil, September 8 - 10, 2010

PREFACE

The Stability and Ductility of Steel Structures, SDSS, is a series of international conferences that followed the original Structural Stability Research Council (SSRC) International Colloquia. This series of conferences started in 1972 and their previous editions took place in several different cities and countries, the last three were held in Timisoara, Romania (1999), in Budapest, Hungary (2002) and in Lisbon, Portugal (2006). The SDSS conferences are intended to summarize the progress in theoretical, numerical and experimental research concerning the analysis and design of steel structures, with particular emphasis addressed to topics related to stability and ductility aspects. Special attention is always paid to new concepts and procedures and also to the background, development and application of rules and recommendations either appearing in recently published Codes and Specifications or about to be included in their upcoming versions.

The present Proceedings of the International Colloquium on Stability and Ductility of Steel Structures SDSS'Rio 2010 contains 130 peer-reviewed selected papers and eight invited keynote lectures presented during the conference in Rio de Janeiro, September 8-10, 2010. The opening chapter is addressed to the keynote lectures while following include all the full papers sorted according to the conference themes sessions.

The editors address their profound acknowledgements to those that supported the innumerous tasks of organization which were developed during the last two years in order to prepare with success the SDSS'Rio 2010. This conference is the result of the enthusiasm and dedication of these individuals. Special thanks are due to the conference sponsors UFRJ, UERJ, COPPE, FAPERJ, CNPq, CAPES and CBCA.

We are indebted to the authors of keynote lectures and selected papers which conferred the high standard of their contributions included in this book as well as the quality of the oral presentations during the conference. Their effort to present their research results were very much appreciated and can be confirmed in the following pages of this book.

The editors gratefully thank the members of the Organizing and the Scientific Committees that supported the extensive work of reviewing the submitted papers. SDSS'Rio 2010 scientific standard is the result of this highly qualified work.

Finally, one last word of appreciation for the support provided by the staff of the Civil Engineering Program of COPPE-UFRJ, the visual design professionals from COPPE that developed the visual program of the conference and the professionals from COPPE that supported the computational facilities that enabled the organization of the conference.

Rio de Janeiro, September 2010

Eduardo Batista
Pedro Vellasco
Luciano de Lima

www.EngineeringEBooksPdf.com

www.EngineeringEBooksPdf.com

CONTENTS

VOLUME 1

PREFACE **v**

1. SDSS HISTORICAL BACKGROUND **1**

How all of it started - some reminiscences about the first international colloquia in the stability series 3
M. Škaloud

2. KEYNOTE LECTURES **7**

Some issues for column stability criteria 9
Reidar Bjorhovde

The effect of edge support on tensile membrane action of composite slabs in fire 21
Anthony K. Abu and Ian W. Burgess

Latest developments in the GBT analysis of thin-walled steel structures 33
Dinar Camotim, Cilmar Basaglia, Rui Bebiano, Rodrigo Gonçalves and Nuno Silvestre

Dual-steel frames for multistory buildings in seismic areas 59
D. Dubina

Advanced stability analysis of regular stiffened plates and complex plated elements 81
László G. Vigh and László Dunai

Direct strength design of cold-formed sections for shear and combined actions 101
Cao Hung Pham and Gregory J Hancock

Manufacturing specifications for hollow sections in 2010 115
Jeffrey A. Packer

Numerical study on stainless steel beam-columns with transverse loading 123
N. Lopes, P. Vila Real and L. Simões da Silva

3. BRIDGES AND FOOTBRIDGES **131**

Improved cross frame connection details for steel bridges with skewed supports 133
Craig Quadrato, Anthony Battistini, Todd A. Helwig, Karl Frank and Michael Engelhardt

Flange thirkness transitions of bridge griders-buckling behaviour in global bending 141
A. Lechner, A. Taras and R. Greiner

A visco-elastic sandwich solution for orthotropic decks of steel bridges 149
Ronaldo C. Battista, Emerson F. dos Santos, Raimundo Vasconcelos and Michèle S. Pfeil

www.EngineeringEBooksPdf.com

Elegance and economy - a new viaduct over the river Llobregat 157
Peter Tanner, Juan L. Bellod and David Sanz

Design of beam-to-beam butt-plate joints in composite bridges 165
A. Lachal, S.S. Kaing and S. Guezouli

4. CONNECTIONS **173**

Experimental analysis of composite connections using slab made by precast joist with lattice and bricks 175
William Bessa, Roberto M. Gonçalves, Carlo A. Castiglioni and Luis Calado

Response of end-plate joints under combined forces 183
N. Baldassino, A. Bignardi and R. Zandonini

Influence of member components on the structural performance of beam-to-column joints of pitched roof portal frames with class 3 and 4 sections 191
I. Mircea Cristutiu, Dan Dubina

Application of Eurocode 3 to steel connections with four bolts per horizontal row 199
J.-F. Demonceau, K. Weynand, J.-P. Jaspart and C. Müller

A new hybrid testing procedure of the low cycle fatigue behaviour for structural elements and connections 207
Carlo Andrea Castiglioni, Alberto Drei and Roberto Goncalves

Proposal of a three-dimensional semi-rigid composite joint: tests and finite element models 215
Beatriz Gil, Rufino Goñi and Eduardo Bayo

Strength and ductility of bolted T-stub macro-components under monotonic and cyclic loading 223
Nicolae Muntean, Daniel Grecea, Adrian Dogariu and Dan Dubina

Prediction of the cyclic behaviour of moment resistant beam-to-column joints of composite structural elements 231
Nauzika Kovács, László Dunai and Luís Calado

Numerical modeling of joint ductility in steel and steel-concrete composite frames 239
Leslaw Kwasniewski and Marian Gizejowski

Influence of chord axial loading on the stiffness and resistance of welded “T” joints of SHS members 247
Rui M. M. P. de Matos, Luís F. Costa-Neves and Luciano R. O. de Lima

Experimental studies of behaviour of composite beam-column flush end plate connections subjected seismic loading 255
Olivia Mirza and Brian Uy

Modelling connections of moment resisting steel frames for seismic analysis 263
L. Mota, A. T. da Silva, C. Rebelo, L. Simões da Silva and Luciano R. O. de Lima

Influence of local plastic buckling of joint on carrying capacity of a thin-walled truss 271
H. Pasternak, G. Kubieniec and V. Bachmann

www.EngineeringEBooksPdf.com

Numerical analysis of endplate beam-to-column joints under bending and axial force 279
Monique C. Rodrigues, Luciano R. O. de Lima, Sebastião A. L. de Andrade, Pedro C. G. da S. Vellasco and José G. S. da Silva

Loss of preload in bolted connections due to embedding and self loosening 287
Roland Friede and Jörg Lange

Plastic resistance of L-stubs joints subjected to tensile forces 295
M.Couchaux, I.Ryan and M.Hjiaj

Composite beam modelling at real scale including beam-to-beam joint 303
S. Guezouli and A. Lachal

Resistance of laser made t RHS joints under compression load 311
Jerzy K. Szlendak

Cold-formed steel and concrete composite beams: study of beam-to-column connection and region of hogging bending 319
Mairal R. and Malite M.

Shear bolted connections: numerical model for a ductile component, the plate-bolt in bearing 327
J. Henriques, L. Ly, J.-P. Jaspart and L. Simões da Silva

5. DYNAMIC BEHAVIOR AND ANALYSIS 335

Considerations on the design, analysis and performances of eccentrically braced composite frames under seismic action 337
Hervé Degée, Nicolas Lebrun and André Plumier

Effect of the loading modelling, human heel impact and structural damping on the dynamic response of composite footbriges 345
José Guilherme S. da Silva, Francisco J. da C. P. Soeiro, Pedro C. G. da S. Vellasco, Luciano R. O. de Lima and Nelson L. de A. Lima

Structural damage assessment using the differential evolution and the ant colony optimization techniques 353
Genasil F. dos Santos, José Guilherme S. da Silva and Francisco J. da C. P. Soeiro

Free and forced nonlinear vibrations of steel frames with semi-rigid connections 361
Andréa R.D. Silva, Ricardo A.M. Silveira, Alexandre S. Galvão and Paulo B. Gonçalves

Static and dynamic behavior of lens-type shear panel dampers for highway bridge bearing 369
Tatsumasa Takaku, Feng Chen, Takashi Harada, Masayuki Ishiyama, Nobuhiro Yamazaki, Tetsuhiko Aoki and Yuhshi Fukumoto

Elasto-plastic buckling behavior of H-shaped beam with large depth-thickness ratio under cyclic loading 377
Tao Wang and Kikuo Ikarashi

Analytical studies of a full-scale steel building shaken to collapse 385
Keh-Chyuan Tsai, Yi-Jer Yu and Yuan-Tao Weng

www.EngineeringEBooksPdf.com

Robustness of steel and composite buildings under impact loading 393
Ludivine Comeliau, Jean-François Demonceau and Jean-Pierre Jaspart

Design of steel frames of dissipative shear walls 401
C. Neagu, F. Dinu and D. Dubina

Effects of wind on a 3 dimensional steel structure for the central corridor roof (central spine) at TCS campus at Siruseri, Chennai (India) - a case study 409
T. S. Gururaj and Nagaraja M. Thontalapura

Influence of system uncertainties on structural damage identification through ambient vibrations of steel structures 417
Leandro Fadel Miguel, Letícia Fadel Miguel, Jorge D. Riera, Marta G. Amani and Raúl O. Curadelli

Non-linear dynamic analysis of stayed steel columns 423
Ricardo R. de Araujo, José G. S. da Silva, Pedro C. G. da S. Vellasco, Sebastião A. L. de Andrade, Luciano R. O. de Lima and Luis A. P. Simões da Silva

6. FIRE ENGINEERING **431**

Interaction diagrams for design of concrete-filled tubular columns under fire 433
Rodrigo B. Caldas, João Batista M. Sousa Jr. and Ricardo H. Fakury

Ductility of simple steel connections in fire 441
J. Buick Davison, Ian W. Burgess, Roger J. Plank, Hongxia Yu and Ying Hu

Methodology for reliability-based design of steel members exposed to fire 449
Shahid Iqbal and Ronald S. Harichandran

Capacity reduction and fire load factors for steel columns exposed to fire 457
Shahid Iqbal and Ronald S. Harichandran

Stability of steel columns subjected to fire 465
Markus Knobloch, Diego Somaini, Jacqueline Pauli and Mario Fontana

Fire behavior of concrete-filled steel circular hollow section columns with massive steel core 473
Martin Neuenschwander, Markus Knobloch and Mario Fontana

Buckling of concrete filled steel hollow columns in case of fire 481
Tiago A. C. Pires, João P. C. Rodrigues and J. Jéfferson Rêgo Silva

Buckling of steel and composite steel and concrete columns in case of fire 489
Antonio M. Correia and João Paulo C. Rodrigues

A coupled fluid-thermal-mechanical analysis of composite structures under fire conditions 497
Julio Cesar Gonçalves da Silva and Alexandre Landesmann

Behaviour of composite floor beam with web openings at high temperatures 505
V.Y. Bernice Wong, Ian W. Burgess and Roger J. Plank

To shear resistance of castellated beam exposed to fire 513
F. Wald, A. Pelouchová, J. Chlouba and M. Strejček

www.EngineeringEBooksPdf.com

Numerical analysis of steel columns considering the walls on fire condition 521
Jonas B. Dorr, Jorge M. Neto and Maximiliano Malite

On the strength and DSM design of cold-formed steel columns failing distortionally under fire conditions 529
Alexandre Landesmann, Dinar Camotim

VOLUME 2

7. MEMBERS' BEHAVIOR: TENSION, COMPRESSION, BEAMS, BEAM-COLUMNS 537

The collapse load in submarine pipelines under compressive load and internal pressure 539
Luciano M. Bezerra and Ramon S. Y. C. Silva

Stability analysis of 3D frames using a mixed co-rotational formulation 547
Rabe Alsafadie, Mohammed Hjiaj and Jean-Marc Battini

Plastic collapse mechanisms in compressed elliptical hollow sections 555
Aimar Insausti and Leroy Gardner

Collapse of a steel structure as a result of local buckling 563
Heiko Merle and Jörg Lange

Strength and ductility of steel beams with flange holes 571
K.S. Sivakumaran, P. Arasaratnam and M. Tait

Residual stress measurements in roller bent he 100b sections 579
R.C. Spoorenberg, H.H. Snijder and J.C.D. Hoenderkamp

Lateral torsional buckling of space structures with I-beams - structural behavior and calculation 587
Richard Stroetmann

Analytical derivation of a generalized-slenderness formula for in-plane beam-column design and comparison with interaction-concept formulae 595
Andreas Taras and Richard Greiner

Load bearing capacity of bracing members with almost centric joints 603
Harald Unterweger

Finite element modeling of angle bracing member behavior in experimentally tested sub-frame specimens 611
Anna M. Barszcz, Marian A. Gizejowski and Wael A. Salah Khalil

Influence of splices on the stability behaviour of columns and frames 619
Pedro D. Simão, Ana M. Girão Coelho and Frans S. K. Bijlaard

Further results on the application of the extrapolation techniques 627
Tadeh Zirakian

Elastic lateral-distortional buckling of singly symmetric i-beams: the 2005 AISC specification 635
Tadeh Zirakian and Jian Zhang

www.EngineeringEBooksPdf.com

System stability design criteria for aluminum structures 641
Ronald D. Ziemian and J. Randolph Kissell

Advanced nonlinear investigations of a 50 m span frame case study: the steel structure of the ice rink, city of Targus-Mureş, Romania 649
Zsolt Nagy and I. Mircea Cristutiu

Local post-buckling behaviour of elliptical tubes 657
Nuno Silvestre and Leroy Gardner

Plastic design of stainless steel structures 665
Marios Theofanous and Leroy Gardner

Inelastic behaviour of partially restrained steel frames 673
Renata G. L. da Silva and Armando C. C. Lavall

Robust design – alternate load path method as design strategy 681
Lars Roelle and Ulrike Kuhlmann

Use of eigenvalue analysis for different levels of stability design 689
Jozsef Szalai

The non-destructive measurement of residual stresses in stainless steel roll formed sections 697
Rachel B. Cruise and Anna M. Paradowska

Influence of flange-to-web connection on the patch load resistance of I beams 705
László G. Vigh

Further studies on the lateral-torsional buckling of steel web-tapered beam-columns: analytical studies 713
Gabriel A Jimenez

Lateral buckling of continuous steel beams with hinges 721
Peter Osterrieder, Stefan Richter and Matthias Friedrich

8. PLATED STRUCTURES AND BOX GIRDERS 729

The interaction behaviour of steel plated structures under transverse loading, bending moment and shear force 731
Benjamin Braun and Ulrike Kuhlmann

Hybrid steel plate girders subjected to patch loading 739
Rolando Chacon, Enrique Mirambell and Esther Real

Numerical and experimental research in tapered steel plate girders subjected to shear 747
E. Real, A. Bedynek and E. Mirambell

Shear strength of steel plates with reinforced opening 755
Bo Chen and K.S. Sivakumaran

Crack initiation under static loads including the influence of residiual welding stresses 763
Michael Volz and Helmut Saal

www.EngineeringEBooksPdf.com

The fatigue and serviceability limit states of the webs of steel girders subjected to repeated loading 771
M. Škaloud and M. Zörnerová

Imperfections in steel plated structures and their impact on ultimate strength 779
J.Kala, M.Škaloud, J.Melcher and Z.Kala

Imperfection sensitivity analysis of longitudinally stiffened plated girders subjected to bending-shear interaction 787
F. Sinur and D. Beg

9. SHELLS **795**

Influence of geometry on the dynamic buckling and bifurcations of cylindrical shells 797
Zenon N. del Prado and Paulo B. Gonçalves

Buckling of a shallow rectangular bimetallic shell subjected to outer loads and temperature 805
M. Jakomin and F. Kosel

A geometry based method for the stability analysis of plates 813
Hesham Ahmed, John Durodola and Robert G. Beale

Critical loads and stability of an open elastic-plastic cylindrical shell with the core of variable stiffness 821
Jerzy Zielnica

10. STEEL-CONCRETE COMPOSITE MEMBERS AND STRUCTURES **829**

Ductile response of composite steel and concrete frames 831
Luigi Di Sarno

Stability and ductility of castellated composite beams subjected to hogging bending 839
Marian A. Gizejowski and Wael A. Salah Khalil

Shear connection in steel and concrete composite trusses 847
Josef Machacek and Martin Cudejko

Steel and concrete composite building structures – an economical approach 855
Catarina Costa, Luís F. Costa-Neves and Luciano R. O. de Lima

Behavior of steel-concrete composite beams with flexible shear connectors 863
Gilson Queiroz, Francisco C. Rodrigues, Sebastião S. Pereira, Michèle S. Pfeil, Cláudia G. Oliveira and Luciene A. C. da Mata

Influence of the friction at the support in the longitudinal shear strength of composite slab 871
A. C. C. Lavall, R. S. Costa and F. C. Rodrigues

A parametric analysis of composite beams with t-perfobond shear connectors 879
Juliana da C. Vianna, Sebastião A. L. de Andrade, Pedro C. G. da S. Vellasco and Luís F. da C. Neves

www.EngineeringEBooksPdf.com

FE modelling of slender concrete-filled stainless steel tubular columns under axial compression 887
Zhong Tao, Brian Uy and Lin-Hai Han

Buckling resistance of steel-concrete columns composed of high-strength materials 895
Marcela Karmazínová and Jindrich J. Melcher

11. THIN-WALLED CONSTRUCTION AND COLD-FORMED MEMBERS 903

Effects of distortion on the shear stiffness of rack structures 905
Sambasiva R. Sajja, Robert G. Beale and Michael H.R. Godley

Buckling, post-buckling, collapse and design of two-span cold-formed steel beams 913
Cilmar Basaglia and Dinar Camotim

Experimental and numerical investigation of polyurethane sandwich panels 921
I. Vayas, M.-E. Dasiou and X. A. Lignos

Imperfections' sensitivity analysis of pitched roof cold-formed steel portal frames 929
Dan Dubina, Viorel Ungureanu, Zsolt Nagy, Luis Nunes and Paul Pernes

Ultimate limit strength of perforated cold-formed steels sections 937
Andrei Crisan, Viorel Ungureanu and Dan Dubina

On the use of cold-formed thin walled members for vertical addition of existing masonry buildings 945
G. Di Lorenzo, A. Formisano, R. Landolfo, F. M. Mazzolani and G. Terracciano

Theoretical analysis of perforated rack columns 953
Arlene M. S. Freitas, Marcílio S. R. Freitas and Flávio T. Souza

Optimization of cold-formed steel channel using the direct strenght method and finite strip method 961
Gladimir de Campos Grigoletti, Ignacio Iturrioz, Gustavo Mezzomo and Zacarias Martin Chamberlain Pravia

Experimental investigation of high strength cold-formed supacee sections in shear 969
Cao Hung Pham and Gregory J. Hancock

Effective design of cold-formed thin-walled channel beams with bent edges of flanges 977
Ewa Magnucka-Blandzi and Krzysztof Magnucki

Lateral buckling of steel sigma-cross-section beams with web holes 985
Jindrich J. Melcher and Marcela Karmazínová

Load-bearing capacity of perforated trapezoidal sheeting 993
Thomas Misiek and Helmut Saal

Trapezoidal sheeting made of stainless steel – two amendments to complete the design codes 1001
Thomas Misiek, Helmut Krüger, Karsten Kathage and Thomas Ummenhofer

Pull-trough resistance of tensile-loaded screw-fastenings of thin-walled sheeting and sandwich panels 1009
Thomas Misiek, Saskia Käpplein and Karsten Kathage

www.EngineeringEBooksPdf.com

The cold work of forming effect in steel structural members 1017
Tian Gao and Cristopher D. Moen

Finite element analysis of high strength cold-formed supacee sections in shear 1025
Cao Hung Pham and Gregory J. Hancock

Classification of stability failure modes of sandwich panels under compression loading: global and local buckling, crippling at support line 1033
Saskia Käpplein and Thomas Ummenhofer

Strength estimation of end failures in corrugated steel shear diaphragms 1043
Nobutaka Shimizu and Kikuo Ikarashi

Plate buckling according to Eurocode 3. Comparison of the effective width method and the reduced stress method 1051
Jose M. Simon-Talero and Ana Caballero

DSM design of lipped channel columns undergoing local/distortional/global mode interaction 1061
Nuno Silvestre, Pedro B. Dinis, Dinar Camotim and Eduardo M. Batista

Bracing stiffness and strength in sheathed cold-formed steel stud walls 1069
Luiz C. M. Vieira Jr. and Benjamin W. Schafer

Shear behaviour of trapezoidal sheeting without shear panel construction 1077
J. Lindner and F. Seidel

Thin beam static stability analysis by an improved numerical method 1085
A. Khelil

Investigation of the test method for distortional buckling of compressed pallet rack members 1093
Miquel Casafont, Magdalena Pastor, Francesc Roure and Teoman Peköz

Behaviour of expanded metal panels under shear loading 1101
Phung Ngoc Dung and André Plumier

Analysis of contact buckling in built-up cold-formed steel beams assembled by laser welding 1109
F. Portioli, O. Mammana, G. Di Lorenzo and R. Landolfo

Cross-sectional stability of structural steel 1117
Mina S. Seif and Benjamin W. Schafer

Influence of holes on the behaviour of cold-formed steel sections under compression 1125
M.M. Pastor, M. Casafont, F. Roure, J. Bonada and J. Noguera

Applications of pure and combined buckling mode calculation of thin-walled members using the finite element method 1133
Gustavo P. Mezzomo, Ignacio Iturrioz and Gladimir de C. Grigoletti

Post-buckling behaviour and strength of angle columns 1141
Pedro B. Dinis, Dinar Camotim and Nuno Silvestre

Experimental study on cold-formed steel lipped channel columns undergoing local-distortional-global interaction 1151
Eliane S. Santos, Eduardo M. Batista and Dinar Camotim

www.EngineeringEBooksPdf.com

12. TRUSSES, TOWERS AND MASTS **1159**

Stability bracing requirements of trusses 1161
Rangsan Wongjeeraphat and Todd A. Helwig

Theoretical and experimental analysis of steel space-truss with stamped connection 1169
Cleirton A. S. Freitas, Luciano M. Bezerra and Ramon S. Y. Silva

Real scale experimental analyses of circular hollow section multi-planar steel trusses 1177
Rodrigo C. Vieira, João A. V. Requena, Newton de O. P. Junior and Afonso H. M. de Araújo

Natural period of steel chimneys 1185
Aleksander Kozlowski, Andrzej Wojnar and Leonard Ziemianski

Dynamic response of conical and spherical shell structures subjected to blast pressure 1193
Tomasz Kubiak, Zbigniew Kolakowski, Katarzyna Kowal-Michalska, Radoslaw Mania and Jacek Swiniarski

AUTHOR INDEX

Volume 1 **537**

Volume 2 **1201**

www.EngineeringEBooksPdf.com

1. SDSS HISTORICAL BACKGROUND

www.EngineeringEBooksPdf.com

www.EngineeringEBooksPdf.com

SDSS'Rio 2010 STABILITY AND DUCTILITY OF STEEL STRUCTURES
E. Batista, P. Vellasco, L. de Lima (Eds.)
Rio de Janeiro, Brazil, September 8 - 10, 2010

HOW ALL OF IT STARTED – SOME REMINISCENCES ABOUT THE FIRST INTERNATIONAL COLLOQUIA IN THE STABILITY SERIES

M. Škaloud*

*Institute of Theoretical and Applied Mechanics, Czech Academy of Sciences, Prague
e-mail: skaloud@itam.cas.cz

Keywords: Stability, First International Colloquia, Reminiscences.

Abstract: The author, who during the period 1977 – 2002 was linked with the preparation of five international stability colloquia, gives some brief information about all of them. He starts with the first one, organised jointly by Prof. Otto Halász and himself in 1977 and held at Balatonfured; and then briefly reports about four subsequent colloquia, prepared jointly with Prof. Miklos Iványi and held in Tihányi and Budapest in 1986, 1990, 1995 and 2002.. For each of them he presents historical background, some technical information and personal reminiscences.

The author is grateful to Profs Eduardo Batista and Pedro Vellasco, the main organisers of the Rio de Janeiro International Colloquium „ Stability and Ductility of Steel Structures" for enabling him to write a few sentences in regard to the history of the preceding five international stability colloquia held in Central Europe. It was a privilege and pleasure for the author of this short contribution to be linked with the preparation of all of them.

The whole story started in the middle of the seventies, in 1975 to put it more accurately, when Prof. Otto Halász, then Head of the Department of Steel Structures and Dean of the Faculty of Civil Engineering of Budapest University, and most importantly an excellent expert on steel construction and a very good man, invited the author to organise with him an international stability colloquium. After some discussion it was decided, account taken of the fact that Prof. Halász was then Dean of the Civil Engineering Faculty and held other important functions at Budapest University and was consequently able to provide adequate support for the colloquium, to hold the colloquium in Budapest. The author agreed and so Prof. .Halász became chairman and the author vice-chairman of the scientific committee for the event.

Of course, we knew that our colloquium was not going to be the first international stability conference and were aware of the fact that similar colloquia would take place in Tokyo, Liege and Washington before our event, all of them being organised under the sponsorship of the International Association for Bridge and Structural Engineering, the European Convention for Constructional Steelwork, and the United States Structural Stability Research Council. All of these conferences were attributed the adjective „regional", and Otto Halász and the author just wanted to organise another regional stability colloquium, this time in Central Europe.

Our conference was then held at Balatonfured in October 1977 and proved to be a success, with practically all of the stars in the sky of stability research attending it. So the event significantly surpassed the character of a regional colloquium and became a real international conference. 56 contributions were presented there, which were divided into the following sessions: (i) Stability problems in national specifications (4 contributions), (ii) Compressed members (6 contributions), (iii) Frames (9 contributions), (iv) Lateral buckling (4 contributions), (v) Plate and box girders (11 contributions), (vi) Shells (7 contributions), (vii) Special problem (8 contributions), and (viii) Experimental research (7 contributions). The success of the conference was also supported by its beautiful setting, i.e. by the pretty

www.EngineeringEBooksPdf.com

shores of the Balaton Lake, which looked particularly attractive in the sunshine of the second half of October 1977.

Given the success of this colloquium, Otto Halász and the author decided to repeat it in the middle of the eighties, and in October 1985 the writer spent two days in the flat of Prof. Halász, during which they performed an important part of the preparatory work for this Stability Colloquium No 2. Otto Halász was then already seriously ill, but still very active and enthusiastic about the Colloquium. It was decided that the author should again come to Budapest in February so that they could put a finishing touch to the preparation of the event. Consequently at the beginning of February the writer telephoned Otto Halász´s flat and was told by him that he was going to be transported to hospital for several days and that they should fix up the author´s visit to Budapest thereafter , ie. in a week or so later on. But this thereafter did not come; never thereafter had the writer the pleasure of talking to Otto Halász any more, since a few days after that they phoned him from Budapest (it was Dr Veröci, senior member of Prof. Halász´s staff, who called) to let him know that Prof. Halász had died. They also posed the question of what should be done about the International Stability Conference under preparation.

So the author travelled to Budapest, met Prof. Miklos Iványi, who was then Head of the Department of Steel Structures, and his colleagues. It was decided that the preparations for the Stability Colloquium No 2 should go on. Prof. Iványi became chairman of the Scientific Committee of the Colloquium and the author retained the job of vice-chairman. They were very significantly supported by the staff of the Department of Steel Structures, by Prof. Dunai, Dr Veroci, Dr Hegedus and others. And also by the whole Budapest University of Technology and Economics, and most helpful was also international support which we received from the US Structural Stability Research Council (Prof. T.V.Galambos, one of the leading members of SSRC, was invited to be Honorary Chairman of the Scientific Committee of the Colloquium) and the International Association for Bridge and Structural Engineering. The writer of this short contribution is very grateful to all of the aforesaid.

Together, proceeding hand in hand, we organised four international stability colloquia - in Tihányi in 1986 and in Budapest in 1990, 1995 and 2002.. And the author would like to pay his tribute to Miklos Iványi and the other members of Budapest Department of Steel Structures, who had most of the work on their shoulders. We hope that it can be said that these colloquia were useful and successful; we hope that we can say that these colloquia surpassed the modest wish we had with Otto Halász, i.e. to organise a regional stability conference, and that we can say that they became real world-wide events, with members of their scientific committees, general reporters, chairmen of conference sessions, and authors of conference contributions coming from all continents. Later also the framework of the conferences was extended and they became colloquia on the stability and ductility of steel structures.

It should also be mentioned at this juncture that the last in the series, i.e. the colloquium held in 2002, was organised as a Professor Otto Halász memorial session; by which we desired to express our esteem to the man who was the main organiser of the first conference in the whole series.

100 contributions, written by European, American, Japanese and Australian authors, were presented at this colloquium, and they were divided into the following sessions: (i) Compressed members and beams (16 papers), (ii) Cold-formed members (13 papers), (iii) Frames (11 papers), (iv) Ductility problems (6 papers), (v) Plated structures (11 papers), (vi) Shells (5 papers), (vii) Bridges and special problems) (9 papers), (viii) Composite structures (4 papers), (ix) Earthquake and fire (16 papers), and (x) general concepts (9 papers). To appreciate the important role of the Hungarian Academy of Sciences in the preparation of the Colloquium, one of its distinguished members, Prof. J. Szabo, was invited to be Honorary Chairman of the Scientific Committee.

But the writer of this short contribution would also like to pay tribute to a great number of excellent scientists and engineers, coming from all parts of the globe, who were members of the international scientific committees of the colloquia, general reporters and chairmen of their sessions, and authors of papers and contributors to conference discussions. It is also their merit that the colloquia proved to be a success.

www.EngineeringEBooksPdf.com

Dear colleagues, it was a privilege and pleasure for me to cooperate with you. And many thanks for this cooperation of yours. My desire once more to thank you is one of the reasons for my writing this short paper.

Once the series of the five international stability colloquia described above was completed, the question arose of how to continue, i.e. at what venue and with what new organisers to continue. And in this respect we were fortunate, and it was a pleasure for the author to see it, that this continuation should get into the skilful hands of (i) Prof. Dinar Camotim and (ii) Prof. Eduardo Batista and Prof. Pedro Vellasco, who in addition to being first-class researchers in the domain of stability are also very good organisers. Prof. Camotim, although most of the preparatory work was only on his shoulders, did excellent work in organising the 2006 Lisbon "edition" of the colloquia, and it is certain that our Rio de Janeiro colleagues, Profs Batista and Vellasco, will do the same in the case of the Rio de Janeiro Stability and Ductility Conference. Good luck and best wishes.

www.EngineeringEBooksPdf.com

www.EngineeringEBooksPdf.com

2. KEYNOTE LECTURES

www.EngineeringEBooksPdf.com

www.EngineeringEBooksPdf.com

SDSS'Rio 2010 STABILITY AND DUCTILITY OF STEEL STRUCTURES
E. Batista, P. Vellasco, L. de Lima (Eds.)
Rio de Janeiro, Brazil, September 8 - 10, 2010

SOME ISSUES FOR COLUMN STABILITY CRITERIA

Reidar Bjorhovde*

* The Bjorhovde Group, Tucson, Arizona, USA
rbj@bjorhovde.com

Keywords: Columns, Stability, Steel Structures, Design Criteria, Limit States, Codes.

Abstract. *The strength and stability of columns have been the subjects of numerous studies since the original work of Euler in 1744 and 1759. Elastic buckling of perfectly straight columns was examined during the 19th century, with landmark theories developed by Engesser and Considère. Several series of column tests were conducted to establish the correlation between theory and physical behavior. Research in the 20th century examined the influence of material and member imperfections, including the tangent modulus study of Shanley. These efforts provided the resolution of the effects of material non-linearity, residual stress and out-of-straightness. The definitive solutions were developed in the 1970-s, when modeling and numerical procedures allowed all nonlinear effects to be included. Since that time reliability and probabilistic solutions have provided state-of-the-art limit states criteria for steel columns. Such approaches are now the bases for columns in all advanced design codes in the world.*

1 INTRODUCTION

The strength and behavior of columns is one of the longest lasting, continuous research endeavors in structural engineering. From the classical studies of Euler, Tredgold, Tetmajer, Engesser, Considère, von Kármán, Salmon, Shanley, Beedle and others until today [1], the level of knowledge has advanced from understanding the characteristics of the straight, elastic member to the current treatment of columns with all forms of nonlinearities. The columns are now analyzed and designed as structural members that interact with and are affected by the other members and the connections and indeed the entire structure. The advancement has closely paralleled the evolution of testing and computational tools.

The most significant developments have taken place since the late 1960-s, and this was only possible because of the advent of computers. For example, the solution of the general inelastic flexural buckling problem dates from that time, and studies of the influence of end restraint on inelastic columns were only finalized in the late 1990-s [2]. In brief, the solution of two- and three-dimensional inelastic stability problems with randomly variable column strength parameters was far too complex for the traditional closed-form techniques. Numerical solutions were the only option, and advances in testing equipment and measurement tools have allowed for close agreement between tests and theory.

A variety of column strength formulas have been developed over the years, being based on theoretical models or the results of column tests or combinations thereof. Some of these have appeared in design codes, but most have not survived the tests of time and usefulness. However, even the most advanced of some of these approaches have suffered from certain drawbacks, whether due to complexity in formulation, limited applicability or consistency for all types of members and steel types, or any number of other reasons.

At this time, however, the states-of-the-art of computation and testing have progressed so far that accuracy in modeling and realism in testing make it possible to expand the design criteria to take into account a number of additional features. For example, two- and three-dimensional response characteristics are incorporated into some of the advanced software that is available, as is improved correlation and interaction between the column and the surrounding structure. Thus, connection restraint

www.EngineeringEBooksPdf.com

is now built into some modeling schemes, and overall structural reliability has become a realistic feature of several international codes [3, 4, 5].

Technical advances have significantly shortened the time lag between research results availability and code adoption. In some respects this is a desirable development; it also has certain disadvantages. This is particularly because too rapid acceptance may cause some, if not all, practical needs and implications to be overlooked. Contradictory as this may sound, it is nevertheless a fact that design criteria need a certain period of thought and practical maturation before they are adopted by a design standard. As an example (although not a stability consideration), the early incorporation of the initial block shear provisions into the AISC Specification in 1978 led to a great number of difficulties. Since that time a number of researchers have advanced proposals for correct representation of limit states and improved design accuracy. However, changes continue to be developed, including in the AISC Specification that was recently adopted [3].

For the case of steel columns, the current level of knowledge reflects the fact that much effort has been devoted to evaluating practical applications of the strength and performance data that are available [2, 6, 7, 8, 9]. It is a matter of record that the present amount of data and other information significantly exceeds the size of the data base that was used to establish earlier column formulas. Improvements therefore can and have been made on the basis of factual results, with continuing improvements through earlier and current code editions [2, 3, 4, 5].

2 ELEMENTARY AND ADVANCED STABILITY CONCEPTS

The basic mechanistic column models can be categorized as follows, in ascending order of accuracy and complexity:

(i) Individual pinned-end column, perfectly straight, elastic material

(ii) Individual pinned-end column, initially curved, elastic or inelastic material, elastic or inelastic structural response, incorporating residual stress, for example.

(iii) Individual column with restrained ends, initially curved, inelastic material and/or response, incorporating end restraint developed by members that frame into the column, for example. Random behavior of the column strength parameters can be included, for complete reliability analysis.

(iv) The column is no longer an individual element, but part of a planar subassemblage. This consists of the member itself with all its material and geometric imperfections, and at least the immediately adjacent columns in the frame. End restraint effects may be taken into account by using the properties of the actual connections, although the original model used rigid joints [10].

(v) The column is one of the elements of the original planar structure, including all of the individual performance parameters. The overall influence of framed and leaning columns is accounted for by this model.

(vi) The column is part of a three-dimensional subassemblage which incorporates end restraint, initial curvature and inelastic response characteristics. The ultimate limit state may be flexural buckling about any axis, or flexural-torsional buckling.

(vii) The column is one of the elements of a three-dimensional frame. The model incorporates all conceivable strength and stiffness parameters, including the influence of leaning columns.

It is understood that any of the mechanistic models may treat the column strength parameters as deterministic or probabilistic. In the latter case, the evaluation of the column stability will also incorporate the reliability aspects of the member and at least the subassemblage; the complete frame may be used in lieu of the subassemblage. In a limit states code format, this is required.

www.EngineeringEBooksPdf.com

Model (i) was used by Euler for his classical solution. It was also that of the Engesser and Considère tangent modulus (and double modulus) solution. Model (ii) was the state-of-the-art in the early 1970-s [1, 2, 7, 11]. Figure 1 illustrates the basic load-deflection characteristics of the inelastic column models, including the tangent modulus response of the perfectly straight column. Various forms of Model (iii) were developed through an intensive, international research effort in the 1980-s that led to realistic modeling and quantification of the restraint effects, including criteria for code implementation and design [12, 13, 14, 15, 16].

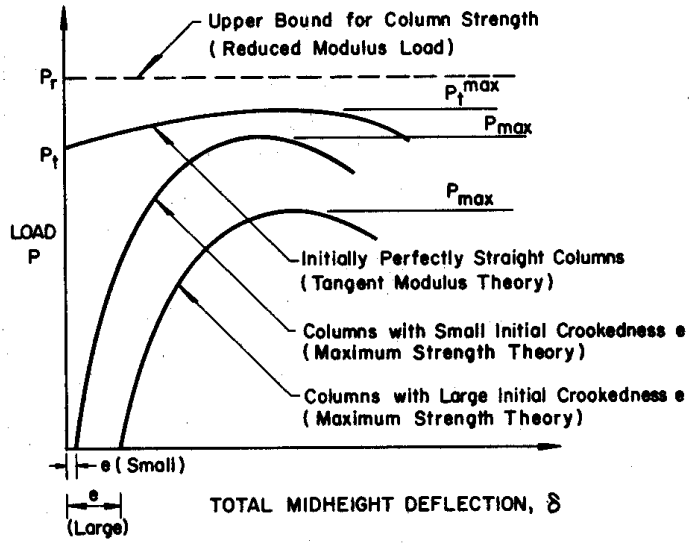


Figure 1: Load-Deflection Curves for Inelastic Columns

Common to Models (ii) through (iv) is the fact that they provide detailed theoretical solutions for the column strength, and the influence of the strength parameters is covered explicitly. Notwithstanding the limitations, the results are not subject to the random variations that are associated with physical tests. The sources, but not the magnitudes of the test variations are largely known, and emphasize the need for a very large body of test data if such are to serve as the sole basis for the design criteria [7, 17, 18]. This is further emphasized by the approximately 100 full scale column test results that are illustrated in Fig. 2. Only an accurate mechanistic model, whose performance can be verified by comparisons with the test results, is capable of giving the kind of rational design criteria which will not be at the mercy of new test data at any time.

A much better approach than the test-based criterion would have been to use multiple column curves, as proposed in the early 1970s [6, 7, 9, 19]. The curves developed for the United States are shown in Fig. 3, labeled as Curves 1 through 3 and 1P through 3P [7, 9], where the first set used an out-of-straightness of 1/1000 of the member length and the second set was based on the probabilistically-based out-of-straightness of 1/1500 (actually, 1/1470, which was the mathematical mean on the basis of the shape of the probability density function for the out-of-straightness [7]). Curve 2P is the single curve that has been used by AISC for its limit states code (LRFD) since 1986, specifically because of the maximum strength basis and the use of the mean crookedness, rounded off to 1/1500.

The Canadian steel design standard CSA S16-1 has used two curves for several years [5]. The current Eurocode 3 [4] has five curves, as originally proposed by Beer and Schulz [6]; these are shown in Fig. 4, where the current, single AISC column curve also is included for comparison purposes [3]. As

www.EngineeringEBooksPdf.com

should be expected, the curves are all fairly close, with the AISC very close to EC3 curves a and b for most of the slenderness ratio range. For very large slenderness ratios the EC3 a_0 curve and the AISC curve overlap, as they should, since elastic buckling governs for columns of this type. The yield stress of the steel does not play a role in this slenderness range.

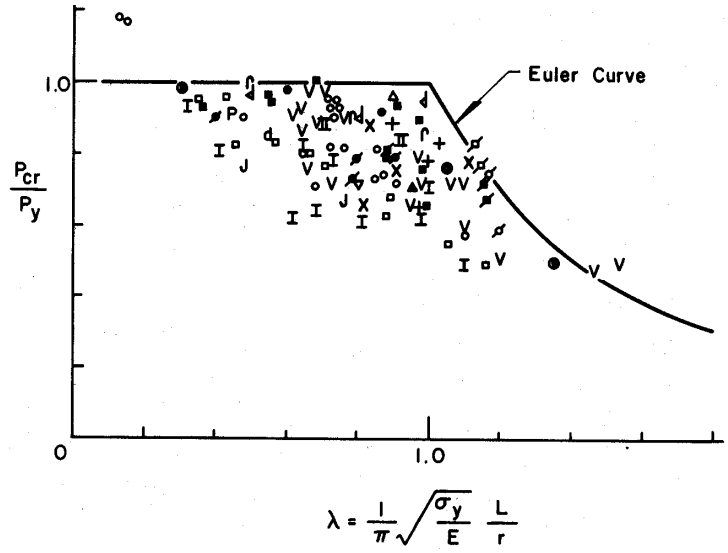


Figure 2: Approximately 100 Full-Scale Column Test Results for a Variety of Shapes, Steel Grades and Fabrication Methods

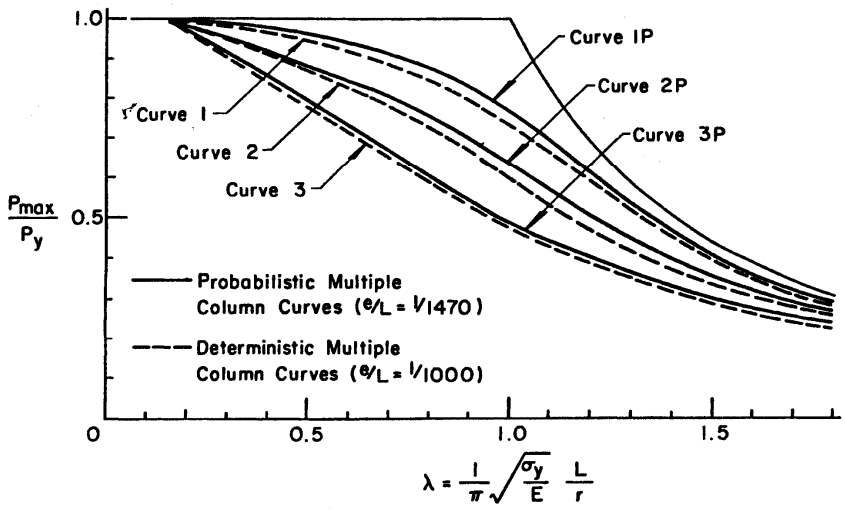


Figure 3: Proposed American Multiple Column Curves, Including the Current AISC Curve = Curve 2P

Models (iv) through (vii) reflect progressively more accurate, but also significantly more complex approaches to the evaluation of the stability of columns as parts of frameworks. In its original form,

www.EngineeringEBooksPdf.com

Model (iv) was developed as an idealized, elastic buckling solution for a three-story column, with beams framing into it with rigid connections [10, 20]. Using a slope-deflection analysis, the characteristic equation for the stability of the column as part of the subassemblage was obtained for the sway and non-sway cases. This led to the development of the well-known effective length (K-factor) alignment charts (= nomograms), which have been used extensively for years. At this time, however, due to advanced analysis techniques and much better computation software and facilities, elastic and inelastic second order procedures have made the use of the K-factor un-necessary, indeed undesirable. However, many engineers prefer the older method, since they are familiar with the approach and the solution is acceptable for many types of structures.

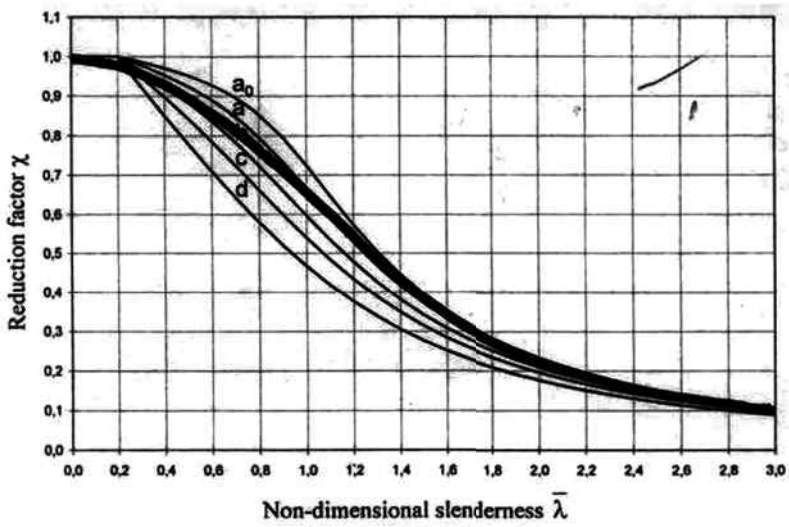


Figure 4: The Five Column Curves of Eurocode 3 and the AISC Column Curve

However, major assumptions were made for the effective length solutions, which is one of the reasons researchers and advanced designers have been questioning their use in practice. For example, Yura [21] modified the elastic treatment to take into account inelastic buckling; this led to the concept of the inelastic K-factor. Combined with the restraining effects of columns and the appropriate stiffness of beams and the far end support conditions, Johnston [22] formulated a much-improved solution for columns in frames, and Yura expanded on this approach. This was subsequently enhanced very significantly by Hellesland and Bjorhovde [23, 24].

Last, but by no means least, Yura [21] defined the concept of leaning columns, and provided a solution that considered their influence on the overall stability of the frame. This has become increasingly important as a result of refinements of structural analysis techniques. The advent of limit states design (LRFD) has also played a major role. Contemporary codes take these influences explicitly into account through the so-called Direct Analysis Method [3].

In the last several years, a number of studies have addressed the issue of using realistic connection restraint characteristics in the assessment of column stability. Some of this has been reflected in the criteria for the strength of individual columns, as indicated for Models (iv) through (vii). However, a major body of work has been devoted to incorporating such properties into the stability of columns in frame subassemblages. Numerous studies have offered improved understanding of the buckling mechanisms as well as how the end restraint concept may be implemented in practice. The advantage of

www.EngineeringEBooksPdf.com

this approach is that it ties directly into what has been common practice for years, with well-defined physical modifications of known and accepted methods.

Models (vi) and (vii) essentially expand the principles of Model (v), to incorporate the entire planar frame into the stability analysis. Beam-to-column connections are treated as rigid or pinned, or the actual moment-rotation response is used. The latter reflects the characteristics of semi-rigid (Type PR) connections, emphasizing the fact that realistic joints may exhibit elastic initial response, but the moment-rotation curve will sooner or later become non-linear. Having developed the mechanistic concepts through Models (ii) through (v), arriving at a complete frame solution basically requires only additional computational capacity. However, the word "only" can be misleading. This is especially true if PR connections are used, and/or if three-dimensional response is to be included.

For almost all structural types, and notably those with substantial gravity and/or lateral load from wind or seismic action, it is essential to account for second order effects. This applies whether the frame is braced or unbraced, although the latter tends to be much more affected. The original research work and the solution for these P-Delta effects were provided by P. F. Adams while he was a Ph.D. student at Lehigh University. Details of the historical development have been detailed by Galambos [11].

Significant advances have been made over the last few years towards practical analysis and design methods for PR frames. All major international design codes give provisions for such designs, but actual use continues to be limited. This is mostly because commercial PR analysis and design software is missing, but connection modeling is also a major issue. Data bases for certain types of connections have been developed [25, 26], but the real problem lies with the fact that it is nearly impossible to use actual test data in practical designs. The approach that appears to offer the most useful procedure is based on a classification system for the connections, focusing on the key characteristics of the moment-rotation behavior [4, 27].

Many designers still prefer to use elastic methods of analysis and design, and there are a number of software packages for such work. However, researchers and advanced designers now have transitioned to complete inelastic analysis. State-of-the-art standards have adopted such procedures [3, 4, 5], especially when seismic response has to be taken into account [28].

In a major development towards inelastic design, Appendix 1 of the new AISC Specification [3] contains a comprehensive section on this approach. Several studies have already examined the proposed procedure, and although the method is complex and likely will only be used by very advanced designers, the method offers a clear view of where design is headed [29, 30, 31, 32]. Most importantly, the 2010 AISC stability provisions represent a major improvement that will make for an all-inclusive approach [3].

The preceding has given an overview of the history and status of the stability treatment of individual columns and of columns as parts of frameworks. The contemporary approach is the evaluation of the complete structure, but by necessity most of the strength criteria have been and will continue to be based on individual members. Therefore, the better the data base for structural elements, the better will be the design procedure and the easier will be the eventual transition to the full structure.

3 MECHANISTIC VERSUS EMPIRICAL MODELING

The preceding has demonstrated that much has been done to develop mechanistic column response models. Further, over the years a substantial number of column tests have been conducted, in some cases only to verify theoretical solutions. In other projects, however, series of tests have been carefully planned and executed, to cover all column strength variables, with the specific aim of arriving at experimentally based design criteria. Well-known historical examples of the latter are the column tests of Tetmajer and von Kármán [1]. Among the more recent tests are the series of the European Convention for Constructional Steelwork (ECCS) [33, 34]. These were carried out to verify and supplement the theoretical studies of Beer and Schulz [6] in arriving at the ECCS, now the Eurocode 3 column curves, as shown in Fig. 3 [4].

www.EngineeringEBooksPdf.com

Both of the fundamental approaches that have been described in the preceding have been used to develop column design curves and other criteria. In addition, a number of studies have aimed at devising mathematically simple equations and curves that approximate those with an engineering theory background but otherwise offer no physical interpretation. The work of Rondal and Maquoi [35] and Rotter [36] are the most comprehensive of these efforts. Loov [37] provided an elegant simplification into a single equation for the two Canadian column curves which were SSRC Curves 1 and 2 [5, 7, 9, 19].

The most significant benefit of using mechanics-based column curves is their predictability and their ability to replicate test results. In addition, a model that offers a clear physical illustration and solid grounding in mechanics has a definite advantage. In other words, given the material properties and other relevant member data, such column curves can be used to predict the outcome of physical tests. The more column strength parameters that are incorporated into the model, the closer will be the magnitudes of the theoretical and physical strengths. Thus, column models (ii) through (iv) are generally capable of producing results that are within 5 percent of the test results [2, 7, 9, 11, 36].

Many such column curves have been developed over the years. For example, the formula of the Column Research Council (CRC), the CRC Curve [22], was used for many years as the basis for the AISC allowable stress design specification. It reflected the tangent modulus solution for a perfectly straight column with residual stress. The two sets of the three SSRC Curves (Curves 1 to 3 and Curves 1P to 3P), as shown in Fig. 3, were maximum strength solutions, taking into account residual stress as well as out-of-straightness [7]. SSRC 1P to 3P also incorporated the random nature of the column strength parameters; these were a perfect fit for a limit states design code. This was accomplished for the US in the 1970s and early 1980s [2, 7, 9, 11, 19, 30] and for Europe in the 1970s to 1990s [4, 6, 33, 34]. The Canadian steel design standard adopted SSRC Curve 2 in 1974; subsequently SSRC Curve 1 was added, such that this standard has used two column curves since 1989 [5]. SSRC Curve 2P has been the column curve for the AISC Specification since 1986 [3]. Finally, Fig. 5 shows the column curve selection table that was developed for use with the SSRC multiple column curves [7, 9]; this would have been part of the code if AISC had chosen to use several curves in lieu of a single one. For reasons of simplicity, AISC chose to use the one curve.

Fabrication Details		Axis	Specified Minimum Yield Stress of Steel (ksi)				
			≤ 36	37 to 49	50 to 59	60 to 89	≥ 90**
Hot-rolled W-shapes	Light and medium W-shapes	Major	2	2	1	1	1
		Minor	2	2	2	1	1
	Heavy W-shapes (flange over 2 in.)	Major	3	2	2	2	2
		Minor	3	3	2	2	2
Welded Built-up H-shapes	Flame-cut plates	Major	2	2	2	1	1
		Minor	2	2	2	2	1
	Universal mill plates	Major	3	3	2	2	2
		Minor	3	3	3	2	2
Welded Box Shapes	Flame-cut and universal mill plates	Major	2	2	2	1	1
		Minor	2	2	2	1	1
Square and Rectangular Tubes	Cold-formed	Major	N/A	2	2	2	2
		Minor	N/A	2	2	2	2
	Hot-formed and cold-formed heat-treated	Major	1	1	1	1	1
		Minor	1	1	1	1	1
Circular Tubes	Cold-formed	N/A	2	2	2	2	2
	Hot-formed	N/A	1	1	1	1	1
All Stress-relieved Shapes		Major and Minor	1	1	1	1	1

Figure 5: The SSRC Column Curve Selection Table [2, 7, 9, 38]

www.EngineeringEBooksPdf.com

The major drawback of the test-based approach is that without a mechanistic base, any new test results would have to be incorporated into the data base for the design curve. This would require a full analysis of the expanded data base, to determine whether resistance factor changes would be needed. This might also lead to changes in the curve itself. Most importantly, such changes would have to be made any time new steel grades or products were developed by the industry. Apart from the impractical aspect of having a basic design curve change every so often, and then only due to certain test data, the real problem is rooted in the fact that test results are highly subject to interpretation. In other words, due to the many factors that influence the column strength, the outcome of an experiment is not always clearly understood, much less properly interpreted. Some of the parameters are not easily quantified, there is a certain amount of interaction between others, and yet others may not have been recognized as playing a role.

On this background, it is clear that a proper and reliable column strength criterion is one that gives excellent correlation between tests and theory, and that takes all major strength parameters explicitly into account. Such can only be achieved with an accurate and robust mechanistic model.

4 SOME COLUMN STRENGTH CONSIDERATIONS

Due to the complexity of the inelastic flexural buckling problem, all of the primary strength parameters were not included in the analyses until adequate computational tools were available. Previously, closed-form solutions were always sought. As a result, it was feasible to take into account the presence of residual stresses, but initial crookedness could only be considered through stress-based analyses. For example, the secant formula did this by an elastic flexural analysis which limited the maximum stress in the cross section to the yield level [1]. Similar attempts were made to include restraint effects.

The following gives a condensed review of the evolution of column modeling through the stages of parameter incorporation.

4.1 Influence of residual stress

Very well known and documented, through extensive tests and analyses, residual stress is one of the main column strength parameters. Residual stress data are available for a variety of shapes, plates, sizes, grades of steel and manufacturing practices, including the influence of welding, flame cutting and cold straightening [2, 11, 19, 38]. Some limitations still exist for the very heavy shapes, although additional measurement and computation results are becoming available [9].

Column formulas around the world have incorporated the influence of residual stress since the 1950s. The initial applications were all based on tangent modulus formulations [1, 22], and some were still using such criteria until a few years ago, like cold-formed members.

4.2 Out-of-straightness effects

Crookedness was early recognized as a major factor in the column strength equation, but the difficulty of obtaining closed form solutions prevented it from being adopted into design codes. The most common approach was to use a variable factor of safety to account for the effects of the crookedness. This solution was chosen by a number of design standards. For example, the old AISC allowable stress design criteria used a factor of safety that varied from 1.67 to 1.92, covering the combined effects of out-of-straightness, load eccentricity and so on.

Current limit states design criteria [3, 4, 5] cover the crookedness effects explicitly by using the maximum strength as the basic criterion. This was made feasible when computer technology allowed for numerical solutions of the inelastic load-deflection column problem. Some standards have focused on the maximum value of the out-of-straightness; depending on the type of cross section and manufacturing method, this is commonly around 1/1000 of the member length. The Canadian [5] and the European [4] codes have chosen this approach. The LRFD criteria of AISC use the mean value of 1/1500 of the length, on the premise that in the first order, second moment approach to limit states design, all

www.EngineeringEBooksPdf.com

parameters use the mean as the key central tendency. The value of 1/1500 is based on probabilistic evaluations of the out-of-straightness effects [7].

4.3 Straightening effects

Much of the residual stress data that has been mentioned represent those of hot-rolled and welded built-up shapes, mostly of the wide-flange or H- or I-type. However, it has been common practice for years in steel mills to straighten the shapes to meet tolerance requirements. The straightening is done at room (ambient) temperature, and is referred to as cold-straightening. The process is either continuous (rotary straightening) or point-applied (gag straightening). Small to medium size shapes are usually rotary straightened; heavier shapes are gag-straightened. But it is known that rotary cold-straightening has a significant influence on the magnitudes and distribution of the residual stresses in a shape; this is not so for gag-straightened shapes [2].

Tests results are limited, as are theoretical evaluations, but it is known that rotary straightening will lower the peak values of the residual stresses within a shape. Most importantly, the compressive residual stress maxima will be reduced. As a result, the axial compressive strength of a rotary straightened shape will be higher than that of an unstraightened shape. This effect is more pronounced for small to medium size shapes. Gag straightening does not produce such an effect, since the residual stress distribution is only affected in a areas close to the gag load application point [39, 40].

Although current column models are capable of incorporating cold-straightening effects, the lack of a large body of cohesive, carefully developed residual stress data has prevented design standards from taking advantage of the benefit. Further research is clearly needed.

4.4 Some other considerations

Overall frame stability and methods of taking actual connection characteristics into account continue to be studied today. This is reflected in part by the six international steel connection workshops that have been arranged since 1987. The first such workshop addressed the great variety of connections and how their properties could be built into frame analysis and stability considerations [15]. The use and design of frames with semi-rigid (PR) connections continue to be the subject of several international research projects, and a large number of papers continue to address the subject [for example: 27, 31, 32, 41, 42, 43].

5 STRUCTURAL SAFETY, STRENGTH AND ECONOMY

In engineering terms, safety is the issue of overriding concern, but strength is generally much easier to address. Design criteria have therefore tended to focus on achieving adequate safety by setting the strength requirements sufficiently high. Albeit an admirable goal, the lack of attention to the variability of the strength parameters have typically led to highly variable factors of safety in allowable stress design. The old AISC ASD criteria offer a good example, where the theoretical column safety for a range of member types and sizes would be from 1.67 to 1.92, but the actual safety margins varied from 1.4 to 2.5 [8].

Economy, on the other hand, is an elusive concept. It is possible to estimate structural costs by considering the amount of steel and other materials that are used. However, this does not address fabrication and construction costs, for instance, and these can vary substantially from one area to another. For the designer, therefore, the key issue is to concentrate on providing as accurate calculations as possible, and this is helped by accurate design requirements. In other words, the more of the strength and stiffness parameters that are taken into account in the code, the better will be the resulting structure. On the other hand, selecting member and connection sizes and details based strictly on minute numerical differences is likely to prove costly. A balance has to be struck between the numerical and the practical demands, to ensure improved economy of construction.

In the evolution of the column stability criteria, it is a fact that more and more of the important strength parameters have been incorporated into the code equations. The column curves of today reflect residual stress and out-of-straightness through the maximum strength concept, and the limit state format

www.EngineeringEBooksPdf.com

allows for the random variability of these and other factors of influence. Safety is therefore achieved in the best possible fashion. Future refinements of the column criteria therefore should only be regarded in conjunction with the improvements that are being contemplated for the overall design of the frame. That is clearly the direction that must be pursued for the future.

6 SUMMARY

A comprehensive review has been provided of the development of the column stability criteria as they have appeared in research studies and design codes for the past 50 years. It has been demonstrated that through improved analytical and experimental techniques, all of the major strength parameters are now explicitly accounted for in the primary design codes of the world. The advantages of mechanics-based formulations of the design criteria are explained in detail, offering the rationale for code development that is not subject to short term practice and market variations.

REFERENCES

[1] Johnston, B.G., "Column Buckling Theory: Historical Highlights", *Journal of the Structural Division*, ASCE, **107**(ST4), 649-670, 1981.

[2] Ziemian, R.D. (ed.), *Guide to Stability Design Criteria for Metal Structures*, 6th Ed., John Wiley & Sons, New York, NY, 2010.

[3] American Institute of Steel Construction (AISC), *Specification for Structural Steel Buildings,* ANSI/AISC Standard No. 360-10, AISC, Chicago, IL, 2010.

[4] Comité Européen de Normalisation (CEN), *Eurocode 3 – Design of Steel Structures,* Standard No. 1993-1, CEN, Brussels, Belgium, 2005.

[5] Canadian Standards Association (CSA), *Steel Structures for Buildings,* CSA Standard No. S16-01, CSA, Mississauga, Ontario, Canada, 2009.

[6] Beer, H. and Schulz, G., "Theoretical Bases for the European Buckling Curves", *Construction Métallique,* **7**(3), 37-55, 1970 (in French).

[7] Bjorhovde, R.,"Deterministic and Probabilistic Approaches to the Strength of Steel Columns", Ph.D. Dissertation, Lehigh University, Bethlehem, PA, 1972.

[8] Bjorhovde, R., "The Safety of Steel Columns", *Journal of the Structural Division,* ASCE, **104**(ST3), 463-477, 1978.

[9] Bjorhovde, R., "Columns: From Theory to Practice", *Engineering Journal,* AISC, **25**(1), 21-34, 1988.

[10] Galambos, T.V. and Surovek, A.E., *Structural Stability of Steel – Concepts and Applications for Structural Engineers,* John Wiley & Sons, New York, NY, 2008.

[11] Galambos, T.V. (ed.), *Guide to Stability Design Criteria for Metal Structures,* 4th Ed., John Wiley & Sons, New York, NY, 1988.

[12] Jones, S.W., Kirby, P.A. and Nethercot, D.A., "Effect of Semi-Rigid Connections on Steel Column Strength", *Journal of Constructional Steel Research,* **1**(1), 35-46, 1980.

[13] Sugimoto, H. and Chen, W.-F., "Small End Restraint Effects on Strength of H-Columns", *Journal of the Structural Division,* ASCE, **108**(ST3), 661-681, 1982.

[14] Bjorhovde, R., "Effect of End Restraint on Column Strength – Practical Applications", *Engineering Journal,* AISC, **20**(1), 1-13, 1984.

[15] Bjorhovde, R., Brozzetti, J. and Colson, A. (eds.), *Connections in Steel Structures: Behaviour, Strength and Design,* Elsevier Applied Science, London, England, 1988.

www.EngineeringEBooksPdf.com

[16] Bjorhovde, R., Colson, A., Haaijer, G. and Stark, J.W.B. (eds.), *Connections in Steel Structures II,* AISC, Chicago, IL, 1992.

[17] Fukumoto, Y. and Itoh, Y., "Evaluation of Multiple Column Curves from the Experimental Data Base Approach", *Journal of Constructional Steel Research,* **3**(3), 2-19, 1983.

[18] Hall, D.H., "Proposed Steel Column Design Criteria", *Journal of Structural Engineering*, ASCE, **109**(9), 2086-2096, 1983.

[19] Johnston, B.G. (ed.), *Guide to Stability Design Criteria for Metal Structures*, 3rd Ed., John Wiley & Sons, New York, NY, 1976.

[20] Julian, O.G. and Lawrence, L.S., "Notes on S & L Nomograms for Determination of Effective Lengths", Unpublished Report, Jackson & Moreland Engineers, Boston, MA, 1959.

[21] Yura, J.A., "The Effective Length of Columns in Unbraced Frames", *Engineering Journal,* AISC, **8**(2), 37-42, 1971.

[22] Johnston, B.G. (ed.), *Guide to Stability Design Criteria for Metal Structures*, 2nd Ed., John Wiley & Sons, New York, NY, 1966.

[23] Hellesland, J. and Bjorhovde, R., "Restraint Demand Factors and Effective Lengths of Braced Columns", *Journal of Structural Engineering*, ASCE, **122**(10), 1216-1224, 1996.

[24] Hellesland, J. and Bjorhovde, R., "Improved Frame Stability Analysis with Effective Lengths", *Journal of Structural Engineering*, ASCE, **122**(11), 1275-1283, 1996.

[25] Nethercot, D.A., "Steel Beam-to-Column Connections – A Review of Test Data and Their Applicability to the Evaluation of the Joint Behaviour of the Performance of Steel Frames", CIRIA, London, England, 1985.

[26] Kishi, N. and Chen, W.-F., "Data Base of Steel Beam-to-Column Connections", Vols. I and II, Structural Engineering Report No. CE-STR-86-26, Purdue University, West Lafayette, IN, 1986.

[27] Bjorhovde, R., Colson, A. and Brozzetti, J., "Classification System for Beam-to-Column Connections", *Journal of Structural Engineering,* ASCE, **116**(11), 3063-3080, 1990.

[28] American Institute of Steel Construction (AISC), *Seismic Provisions for Structural Steel Buildings*, ANSI/AISC Standard No. 341-10, AISC, Chicago, IL.

[29] White, D.W. and Hajjar, J.F., "Buckling Models and Stability Design of Steel Frames: A Unified Approach", *Journal of Constructional Steel Research*, **42**(3), 171-207, 1997.

[30] White, D.W. and Hajjar, J.F., "Design of Steel Frames without Consideration of Effective Lengths", *Engineering Structures,* **19**(10), 797-810, 1997.

[31] Surovek, A.E., White, D.W. and Leon, R.T., "Direct Analysis for Design Evaluation and Design of Partially Restrained Steel Framing Systems", *Journal of Structural Engineering*, ASCE, **131**(9), 1376-1389, 2005.

[32] White, D.W. and Goverdhan, A.V., "Design of PR Frames Using the AISC Direct Analysis Method", in [41], *Bjorhovde et al. (2008)*, 255-264, 2008.

[33] Sfintesco, D., "Experimental Basis for the European Column Curves", *Construction Métallique*, **7**(3), 1970 (in French).

[34] Jacquet, J., "Column Buckling Tests and Their Statistical Evaluation", *Construction Métallique*, **7**(3), 1970 (in French).

[35] Rondal, J. and Maquoi, R., "Single Equation for SSRC Column Strength Curves", *Journal of the Structural Division,* ASCE, **105**(ST1), 247-250, 1979.

[36] Rotter, J.M., "Multiple Column Curves by Modifying Factors", *Journal of the Structural Division,* ASCE, **108**(ST7), 1665-1669, 1982.

www.EngineeringEBooksPdf.com

[37] Loov, R., "A Simple Equation for Axially Loaded Steel Column Design Curves", *Canadian Journal of Civil Engineering,* **23**(1), 272-276, 1996.

[38] Galambos, T.V. (ed.), *Guide to Stability Design Criteria for Metal Structures*, 5th Ed., John Wiley & Sons, New York, NY, 1998.

[39] Brozzetti, J., Alpsten, G.A. and Tall, L., "Residual Stresses in a Heavy Rolled Shape 14WF730", Fritz Engineering Laboratory Report No. 337.1, Lehigh University, Bethlehem, PA, 1970.

[40] Aschendorff, K.K., Bernard, A., Bucak, Ö., Mang, F. and Plumier, A., "Buckling Tests on Heavy Rolled I-Shapes in St 37 and St 52, and in St E 460 with Standard Sizes", *Der Bauingenieur*, **58**, 261-268, 1983 (in German).

[41] Bjorhovde, R., Bijlaard, F.S.K. and Geschwindner, L.F. (eds.), *Connections in Steel Structures VI*, AISC, Chicago, IL, 2008.

[42] Deierlein, G.G., "An Inelastic Analysis and Design System for Steel Frames with Partially Restrained Connections", in [16], *Bjorhovde et al. (1992),* 408-417, 1992.

[43] Christopher, J.E. and Bjorhovde, R., "Semi-Rigid Frame Design Methods for Practicing Engineers", *Engineering Journal*, AISC, **36**(1), 12-28, 1999.

www.EngineeringEBooksPdf.com

SDSS'Rio 2010 STABILITY AND DUCTILITY OF STEEL STRUCTURES
E. Batista, P. Vellasco, L. de Lima (Eds.)
Rio de Janeiro, Brazil, September 8 - 10, 2010

THE EFFECT OF EDGE SUPPORT ON TENSILE MEMBRANE ACTION OF COMPOSITE SLABS IN FIRE

Anthony K. Abu* and Ian W. Burgess**

* Department of Civil & Natural Resources Engineering, University of Canterbury, New Zealand
e-mail: tony.abu@canterbury.ac.nz

** Department of Civil & Structural Engineering, University of Sheffield, United Kingdom
e-mail: Ian.Burgess@sheffield.ac.uk

Keywords: edge beam failure, fire, reinforcement ratios, slab panels, tensile membrane action.

Abstract. *The Bailey-BRE Method is a simplified design approach that facilitates the use of a tensile membrane action design philosophy for composite floors under fire conditions. The method requires the division of a composite floor into rectangular slab panels, composed of parallel unprotected composite beams in their interior parts, supported vertically by protected composite edge beams. Enhanced slab capacities are obtained after the unprotected beams have lost significant strength, by allowing large deflections of the slab in biaxial bending. The use of tensile membrane action generates significant cost savings in composite structures, as a large number of floor beams can be left unprotected. However, the protected beams which provide vertical support to the edges of panels lose strength under the combined effects of thermal degradation and the increased loading due to biaxial bending, and this has the potential to cause panels to lose structural stability altogether. It is therefore imperative to investigate what constitutes adequate vertical support and the detrimental effects of inadequate vertical support on tensile membrane action of composite slabs in fire. This paper reports on a study of this effect, and puts forward some simple recommendations to avoid loss of stability of composite floors designed by this method.*

1 INTRODUCTION

Improved understanding of real structural behaviour under fire conditions in recent years has resulted in the increased use of performance-based design methods to ensure the fire resistance of steel structures. Traditional methods, in which all exposed steelwork is protected in the aftermath of normal limit-state design which ignores the fire case, are being replaced by performance-based alternatives, which ensure structural stability and in many cases offer considerable savings. In particular, it has been observed that, if composite floors are allowed to undergo large vertical displacements in biaxial bending during heating by fire, they can achieve load-bearing capacities several times greater than their traditional yield-line capacities, through a mechanism known as tensile membrane action [1]. This mechanism produces increased load-bearing capacity, particularly in thin slabs undergoing large vertical displacements. It is characterised by a large area of radial tension in the central area of a slab which induces an equilibrating peripheral ring of compression. The conditions necessary for this mechanism to be effective are two-way bending of the slab and vertical support along all of its edges. Due to its self-equilibrating nature, horizontal edge restraint is not required for the mobilisation of tensile membrane action, in contrast to the catenary tension which can occur in one-way bending.

To optimise composite floors to take advantage of this enhanced load capacity in structural fire engineering design, a composite floor is divided into a number of fire-resisting rectangular areas, preferably of low aspect ratio, called slab panels. Each of these comprises one or more parallel unprotected composite beams in the interior part of the panel, with edges whose role is primarily to resist

www.EngineeringEBooksPdf.com

vertical deflection. This vertical support is usually provided by thermally-protected primary and secondary composite beams along all four edges, and these are generally directly supported by columns on the building's main gridlines, as shown in Figure 1. Composite slabs are usually reinforced with light meshes (typically with steel areas between 142mm^2/m and 393mm^2/m) whose normal role is to control cracking during construction. In fire the unprotected beams lose strength and stiffness rapidly, and their loads are then borne by the composite slab, which undergoes two-way bending and increases its load capacity as its deflections increase.

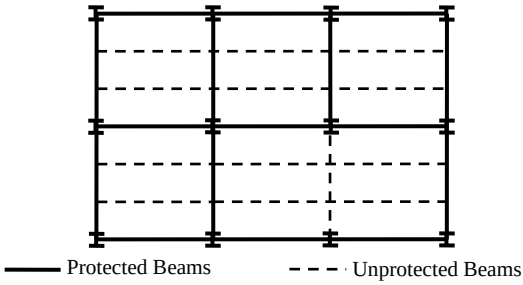


Figure1: Typical slab panels

At large deflections and high temperatures, a slab panel's capacity is dependent on the tensile capacity of the reinforcement, provided that adequate vertical support is available at its boundary. The merits of incorporating tensile membrane action into structural fire engineering design have prompted the development of several software packages to help quantify slab capacities in fire. Tensile membrane action, as a part of whole-structure behaviour at high temperatures, can be modelled in a three-dimensional framework with sophisticated finite element software, such as *Vulcan* [2]-[3], TNO DIANA, SAFIR and ABAQUS, which incorporate geometrically nonlinear effects of structures as well as nonlinear material behaviour. Although such finite element simulations provide useful information on complete load-deformation behaviour and stress development at elevated temperatures, they can be very costly processes in computational effort and in runtimes. Simpler performance-based methods, such as the Bailey-BRE membrane action method [1] or the New Zealand Slab Panel Method [4] (which can easily be set up as a spreadsheet), are often preferred for routine design. However, there have been some suspicions that the simplifications applied in these approaches can lead to unrealistic or over-conservative designs.

In order to assess their efficiency as tools for preliminary investigations, there is an implicit need to determine the limitations of these simplified methods. The reliance of the Bailey-BRE method on the determination of enhancements to the traditional yield-line capacity of the slab, the assumption of continuous vertical support throughout the duration of a fire, and the detrimental effects of structural failure of the edge beams are some of the issues that need to be addressed. The study reported here initially examined the credibility of the Bailey-BRE method through the use of a finite element study, with the aim of establishing slab panel capacities as a function of the amount of reinforcement within a panel and the degree of vertical support available along the slab panel boundary.

2 THE BAILEY-BRE METHOD & TSLAB

Tensile membrane action (TMA) was observed as a primary load-bearing mechanism of composite slabs in fire after a series of full-scale fire tests in the United Kingdom in the 1990s [5]. The Bailey-BRE method was developed in order to simplify the process of incorporating the rather complex mechanics of TMA into routine design of composite slabs in fire. The method divides a composite floor into several rectangular slab panels of low aspect ratio. Based on a conservative assumption that the light slab reinforcement will fracture in hogging over protected beams when the composite slabs are continuous, the

www.EngineeringEBooksPdf.com

Bailey-BRE method [1, 6] treats each slab panel as isolated in the sense that it is horizontally unrestrained, but as vertically supported along its edges (see Figure 2). Each of these panels is composed internally of simply supported unprotected composite beams, spanning in only one direction. With increasing exposure to elevated temperatures, the formation of plastic hinges in the unprotected beams re-distributes their loads to the biaxially bending slab, undergoing large vertical deflections. By employing rigid-plastic theory with large change of geometry, the additional slab resistance provided by tensile membrane action is calculated as an enhancement to the small-deflection yield-line slab capacity; the enhancement increases with increasing slab deflection. Failure of the integrity of the slab as a separating element is determined by the eventual formation of a full-depth tension crack across the shorter span of the slab; in highly-reinforced slabs there may alternatively be a compressive failure of concrete at the corners.

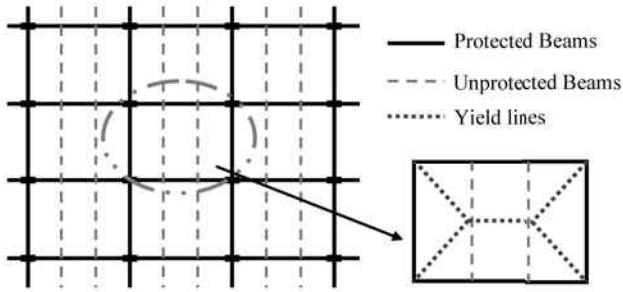


Figure 2: Schematic diagram of the Bailey-BRE Method

The protected beams around the edges of slab panels are assessed as isolated beams under their increased load ratios due to load-shedding from the unprotected beams. The method conservatively ignores any contribution of the tensile strength of concrete to the capacity of the slab, and does not provide any additional information on the state of the protected boundary beams, apart from the assumption that they remain vertically undeflected throughout a fire. The procedure, developed as an extension of the principles of the ambient-temperature behaviour to the elevated-temperature phase, assumes that yield-lines formed at small deflections are maintained at elevated temperatures [1]. However, subsequent research has shown that at elevated temperatures the differential thermal expansion through the depth of the slab thickness induces deflections sufficient to induce tensile membrane action, and that yield line patterns form in the plane of the slab when significant reductions in material strength have occurred and failure is imminent [7]-[8].

To facilitate the use of the Bailey-BRE method in the United Kingdom, a design guide [5] and the spreadsheet-based software TSLAB have been produced. Using the generic version of Bailey-BRE, a particular slab panel arrangement (a vertically-supported rectangular reinforced-concrete slab incorporating unprotected secondary beams) can be optimised for a given fire limit state, based on an allowable vertical deflection limit, expressions for which are shown in Equations 1 and 2. This limit is based on the mechanical strain allowed in the reinforcement at yield combined with thermal bowing in the slab under an assumed linear temperature gradient. In these equations, α is the coefficient of thermal expansion; T_2 and T_1 are the bottom and top surface temperatures of the slab respectively; h is the average depth of the concrete slab; l and L are the shorter and longer spans of the slab panel and f_y and E are respectively the yield strength and Young's modulus of the reinforcing steel at ambient temperature.

$$v = \frac{\alpha(T_2 - T_1)l^2}{19.2h} + \sqrt{\frac{0.5 f_y}{E}_{t=20^\circ C} \times \frac{3L^2}{8}} \qquad (1)$$

www.EngineeringEBooksPdf.com

$$v \leq \frac{\alpha(T_2 - T_1)l^2}{19.2h} + \frac{l}{30} \quad (2)$$

TSLAB begins by performing thermal analyses on the unprotected intermediate beam and the composite slab. Then, using the temperatures of the individual components and an allowable vertical deflection criterion, it calculates the total capacity of the simply-supported slab panel model by summation of the residual capacity of the unprotected beams and the enhanced slab capacity. This capacity is then checked against the applied load at the Fire Limit State. If the capacity of the panel is found to be below the applied load at the fire limit state. This determines whether either the capacity of the internal beams or the reinforcement mesh size needs to be increased.

The Bailey-BRE method has previously been compared with fundamental approaches based on finite element analyses. An investigation by Huang *et al.* [9] into the effects of a panel's horizontal edge support conditions revealed that the Bailey-BRE method correlated very closely with a hinge-supported slab (allowing no pull-in at the edges), although it had been developed on the basis of simple supports. Another investigation into the effects of increased reinforcement ratios on slab panel capacity showed that only a marginal increase in slab panel resistance was observed in finite element models with an aspect ratio of 1.0, while disproportionately large increases in strength were observed in the Bailey-BRE models [10, 11]. It was also observed that the finite element models compared closely with the Bailey approach when high reinforcement ratios were used in slabs of aspect ratio 2.0. The observations led Foster [7] and Bailey and Toh [6] to perform experimental tests on small-scale slabs at ambient and elevated temperatures. They examined slabs with various reinforcement ratios with varying rebar ductilities. The experiments showed that high reinforcement ratios could cause compressive failure of concrete in the slab corners, and the Bailey method was modified accordingly [6]. The Bailey-BRE method determines its slab capacities by calculating the enhancements to the theoretical yield-line capacity provided by large deflections. This suggests that increasing reinforcement diameter increases the capacity of the slabs, since the yield-line capacities will themselves be considerably increased. Therefore, with a given enhancement from large deflections, a considerable slab capacity can be obtained by applying modest increases in reinforcement area. Composite slabs are normally lightly reinforced to control cracking during construction, and therefore, may fail in compression if they are over-reinforced.

In practice, slab panel vertical support is achieved by protecting the beams around the perimeter of each panel. The assumption of continuous vertical restraint at all times during a fire must therefore be unrealistic. During the fire, the combination of imposed loads, together with loss of strength and stiffness of the perimeter beams, will progressively induce vertical displacements which will reduce curvatures in at least one direction, affecting the generation of tensile membrane action. Eventually the reduction of strength of the supporting beams will allow the formation of a single-curvature slab-bending (folding) mechanism. The slab panel will then impose horizontal tying-force components on its connections, in addition to the vertical forces for which they are designed. Depending on the location of the panel, this may lead either to pull-in of columns or to connection failure, both of which are real structural resistance failures, in contrast to the compartment integrity failure which is used as the normal limiting condition. The potential for these additional modes of failure has led to the series of finite element studies reported here, into the effects of reinforcement and slab panel vertical support on composite slab behaviour in fire.

3 SLAB PANEL ANALYSES

The three slab panel layouts shown in Figure 3 were used for the structural analyses. The 9m x 6m, 9m x 9m and 9m x 12m panels were designed for 60 minutes' standard fire resistance, assuming normal-weight concrete of cube strength 40MPa and a characteristic imposed load on the slab of 5.0kN/m^2, plus 1.7kN/m^2 for ceilings and services. Using the trapezoidal slab profile shown in Figure 4, the requirements of SCI P-288 [5] and the slab specifications given in Table 1, the floor beams were designed according to BS5950-3 [12] and BS5950-8 [13], assuming full composite action between steel and concrete and simple support to all beams, in line with common UK engineering practice. The "Office"

www.EngineeringEBooksPdf.com

usage class was assumed, so that the partial safety factors applied were 1.4 (dead) and 1.6 (imposed) for ULS and 1.0 and 0.5 for FLS. The assumed uniform cross-section temperatures of the protected beams were limited to 550°C at 60 minutes. The ambient- and elevated-temperature designs resulted in specification of the steel beam sizes shown in Table 2.

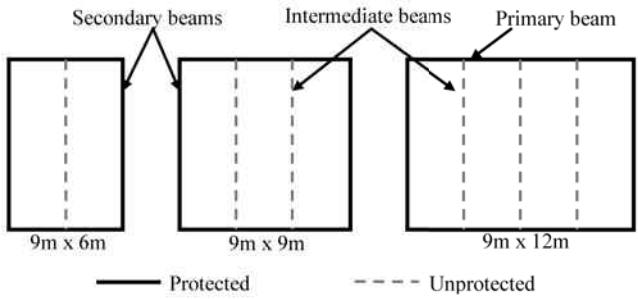


Figure 3: Slab Panel Sizes

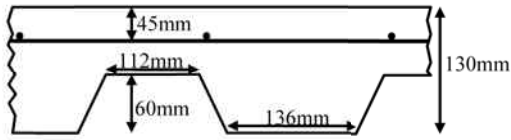


Figure 4: Concrete slab cross-section

Table 1: Slab panel requirements (R60)

Slab Panel size	9m x 6m	9m x 9m	9m x 12m
Dead load (kN/m^2)	4.33	4.33	4.33
Live load (kN/m^2)	5.0	5.0	5.0
Additional load (kN)	14	37	49
Beam design factor	0.77	1.00	0.83
Min. Mesh size	A193	A193	A252

Table 2: Protected beam design data (R60)

Slab Panel Size	Beam Type	Beam Section	Load Ratio	Limiting Temperature	Temperature at 60 minutes
9m x 6m	Secondary	356 x 171 x 57 UB	0.426	636°C	548°C
	Primary	406 x 378 x 60 UB	0.452	627°C	549°C
9m x 9m	Secondary	356 x 171 x 67 UB	0.442	630°C	550°C
	Primary	533 x 210 x 101 UB	0.446	629°C	548°C
9m x 12m	Secondary	406 x 178 x 67 UB	0.447	629°C	548°C
	Primary	610 x 305 x 179 UB	0.471	620°C	547°C

The assessment in this paper is presented as a comparison between the Bailey-BRE method and *Vulcan* finite element analysis. Both the Bailey-BRE Method and TSLAB implicitly assume that the edges of a slab panel do not deflect vertically. The progressive loss of strength of the intermediate unprotected beams is captured by a reduction in the steel yield stress with temperature. The reduced capacity of the unprotected composite beams is deducted from the total applied load at the fire limit state

www.EngineeringEBooksPdf.com

to determine the load which needs to be carried by TMA, and by implication the vertical displacement required by the reinforced concrete slab (whose yield-line capacity also reduces with temperature) to generate sufficient enhancement to carry this load. The required displacement is then limited by applying Equations 1 and 2. The *Vulcan* finite element analysis, on the other hand, properly models the behaviour of protected edge beams, with full vertical support available only at the corners of each panel. *Vulcan* is a three-dimensional geometrically-nonlinear specialised finite element program which also considers nonlinear elevated-temperature material behaviour [2, 3] capable of modelling both membrane and bending effects in slabs and beams.

The analyses were initially performed with the standard isotropic reinforcing mesh sizes A142, A193, A252 and A393. These are respectively composed of 6mm-, 7mm-, 8mm- and 10mm-diameter bars of 500N/mm^2 yield strength at 200mm spacing in either direction. The structural properties of the two models were selected to be consistent with the assumptions of the Bailey-BRE Method [1, 6]. The required vertical displacements of the Bailey-BRE approach and the central vertical deflections of the *Vulcan* analyses have been compared with the TSLAB, BRE and Standard Fire Test (l/20) deflection limits. The results are also compared with a simple slab panel failure mechanism [8] in Figure 5. This mechanism determines the time at which the slab panel loses tensile membrane action, and goes into single-curvature bending. Using a plastic energy-work balance equation, it predicts when the parallel arrangements of primary or secondary (unprotected intermediate and protected secondary) composite beams simultaneously lose their ability to carry the applied fire limit state load due to their temperature-induced strength reductions.

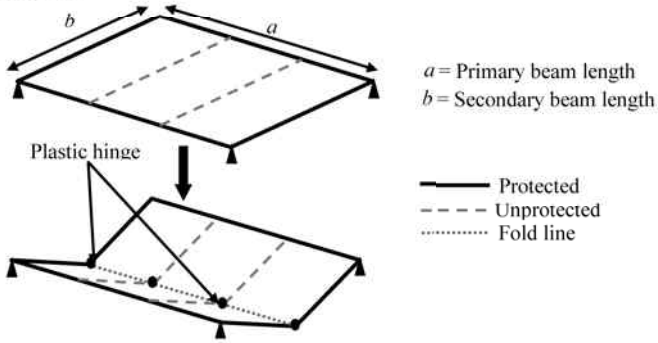


Figure 5: Slab panel failure mechanism

The expressions for failure of either primary or secondary beams are shown in Equations (3) and (4) respectively as:

Primary beam failure

$$\frac{wab}{2} - \frac{4\sum M_p}{a} \geq 0 \tag{3}$$

Secondary beam failure

$$\frac{wab}{2} - \left(\frac{4\sum M_s}{b} + \frac{4\sum M_u}{b} \right) \geq 0 \tag{4}$$

In the equations above a and b are the lengths of the primary and secondary beams; w is the applied fire limit state floor loading and M_u, M_s and M_p are the temperature-dependent capacities of the unprotected, protected secondary and protected primary composite beams, respectively, at the temperatures corresponding to any given time.

www.EngineeringEBooksPdf.com

The observations from these early analyses led to a more detailed investigation of the combined effects of edge-beam stability and the reinforcement ratios on slab panel failure in fire. For like-against-like comparison of the Bailey-BRE Method and *Vulcan* analyses, the temperature profile of slab panels which is used by TSLAB was adopted. The unprotected intermediate beam temperatures from TSLAB were applied directly to the two models. TSLAB generates weighted mean temperatures of the slab top surface, bottom surface and reinforcement. These were applied directly to the Bailey-BRE models. The same could not be assumed for the *Vulcan* analyses, as fictitious temperatures had to be assumed for the other layers in the slab's cross-section. These assumptions could potentially adversely influence both thermal and stress-related strains in the model. Thus, following the earlier research [8], a one-dimensional thermal analysis of the average depth of the profiled slab (100mm) was performed with the software FPRCBC-T [14]. The temperatures generated in this way correlated very closely with those from TSLAB, and were applied in the analyses.

4 RESULTS

The results of the comparative analyses shown in Figures 6-8 show slab panel deflections for different reinforcement mesh sizes. For ease of comparison, the A142-reinforced panels are shown as dotted lines, while those reinforced with A193, A252 and A393 are shown as dashed, solid and chain-dot lines respectively. For clarity the two slab panel types are shown on separate graphs ('a' and 'b') for the Bailey-BRE Method and the *Vulcan* analyses, respectively. These differ, in that graphs 'a' show the vertical displacements required by the Bailey-BRE Method and 'b' show actual vertical deflections from the *Vulcan* analyses. The limiting deflections and the times at which plastic folding of the slab, including the protected edge beams, takes place are also shown. Regardless of the layout of a panel, it was observed that the single-curvature fold line always occurred first across secondary beams; the associated collapse times are indicated by the vertical lines in the figures. The temperatures of the various intermediate and protected secondary beams at failure are shown in Table 3 for the three slab panel layouts. Apart from the 9m x 6m panel it can be seen that failure occurred when the protected secondary beams were below their own limiting temperatures (see Table 2).

Table 3: Slab panel failure times and corresponding secondary beam temperatures (R60)

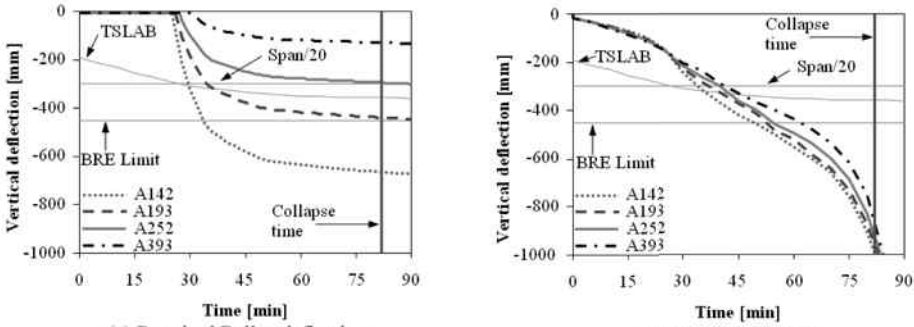
Slab Panel	Failure time	Intermediate beam temperature	Secondary beam temperature
9m x 6m	82min	983°c	663°c
9m x 9m	73min	963°c	621°c
9m x 12m	68min	952°c	594°c

4.1 Slab panel analyses

SCI P-288 [5] specifies A193 as the minimum reinforcing mesh required for 60 minutes' fire resistance. Figure 6a shows the required Bailey-BRE displacements together with the deflection limits and the slab panel collapse time. A193 mesh satisfies the BRE limit, but is inadequate for 60 minutes' fire resistance according to TSLAB. A252 and A393 satisfy all deflection criteria. It should be noted that there is no indication of failure of the panels according to Bailey-BRE, even when the collapse time is approached. This is partly due to the behaviour of the edge beams being neglected; runaway failure of Bailey-BRE panels is only evident in the required deflections when the reinforcement has lost significant strength. *Vulcan* deflections are shown in Figure 6b, and it can be seen that the panel with A393 mesh just satisfies the BRE limiting deflection at 60 minutes. It can also be seen that the deflections of the various *Vulcan* analyses converge at the 'collapse time' (82min) given by the simple slab panel folding mechanism. This clearly indicates the loss of bending capacity of the protected secondary beams. Comparing Figures 6a and 6b, the Bailey-BRE Method predicts substantial enhancement of the panel fire resistance with increasing reinforcement mesh size, while *Vulcan* shows a marginal increase. The Bailey-

www.EngineeringEBooksPdf.com

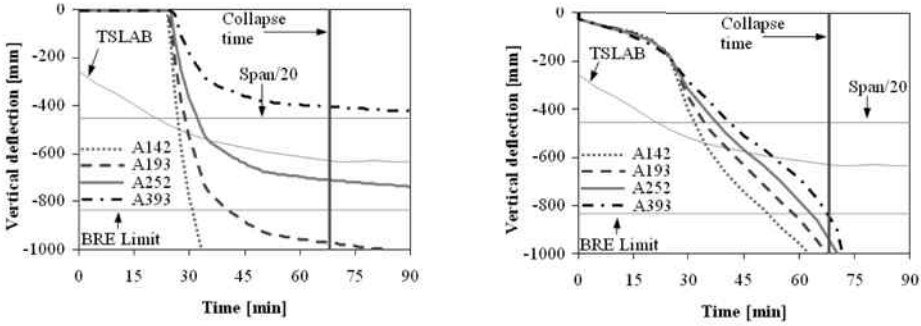
BRE approach is also found to be conservative with A142 and A193 and unconservative with the larger mesh sizes.



(a) Required Bailey deflections (b) *Vulcan* deflections

Figure 6: 9m x 6m Slab Panel results

In the 9m x 6m slab panel the secondary beams were longer than the primary beams, but in the 9m x 12m layout this is reversed. However, the large overall size of the 9m x 12m panel requires its minimum mesh size to be A252 [5]. From the required displacement plots in Figure 7a, A252 satisfies a 60-minute fire resistance requirement with respect to the Bailey-BRE limit. It is observed that increasing the mesh size from A252 to A393 results in an increase in the slab panel capacity from about 37min to over 90min, according to the TSLAB deflection limit. The same cannot be said for the *Vulcan* results (Figure 7b), which show very little increase in capacity with larger meshes.



(a) Required Bailey deflections (b) *Vulcan* deflections

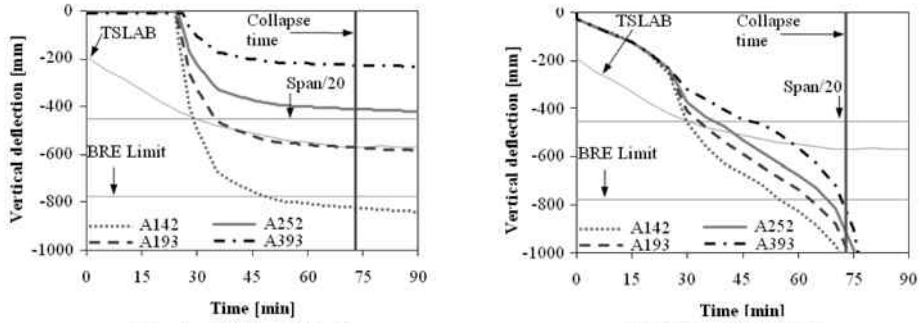
Figure 7: 9m x 12m Slab Panel results

It is shown that A252 and A393 meshes meet the fire resistance requirement at 60 minutes with respect to the BRE limiting deflection. It is also observed that the *Vulcan* deflections appear to converge on the slab panel folding collapse time of 68min. At failure, the protected secondary beams are at 594°C, which is considerably below their limiting temperature. In this study, sufficient protection was applied to all protected beams to ensure that their common design temperature (at 60 minutes) was limited to 550°C. Typically, each gridline beam would be protected to achieve a temperature just below its critical temperature at the required fire resistance time, in order to save cost. Since these temperatures would all be above 550°C this would potentially cause structural failure of the panel earlier than 68min.

Figure 8 shows results for the 9m x 9m slab panel, plotted together with the edge beam folding collapse mechanism and the three deflection criteria. The discrepancy between the Bailey-BRE limit and

www.EngineeringEBooksPdf.com

TSLAB is evident once again; the recommended minimum reinforcement for 60 minutes' fire resistance, A193, is adequate with respect to the BRE limit, but fails with the TSLAB limit. As reported for the other panel layouts, an increase in mesh size results in a disproportionately large increase in the Bailey-BRE panel resistance (Figure 8a) while *Vulcan* shows a much more modest increase. Failure of the protected secondary beams at 73min limits any contribution the reinforcement might have made to the panel's capacity.



(a) Required Bailey deflections

(b) *Vulcan* deflections

Figure 8: 9m x 9m Slab Panel results

The comparisons shown in Figures 6-8 show that the finite element method indicates marginal increases in slab panel capacity with increasing reinforcement size. The Bailey-BRE method, on the other hand, shows huge gains in slab panel resistance with larger mesh sizes. This is true even when the comparison is made in terms of the relative displacements given by the finite element analyses, although this has not been plotted here. Results for the 9m x 6m and 9m x 9m slab panels have shown that the Bailey-BRE method is conservative with the lower reinforcement sizes, while higher mesh sizes cause an overestimate of slab panel capacities. The 9m x 12m panel, however, requires higher reinforcement sizes. The *Vulcan* results show that slab panel capacity is affected much more directly by geometry than by reinforcement area. There is a need to incorporate the effect of edge beams into the simplified Bailey-BRE analysis, and so the results of a more detailed study of the effect of reinforcement area relative to slab panel failure are now presented.

3.2 Effects of reinforcement ratios

The comparison in the previous section showed that the Bailey-BRE Method can predict very high increases of slab panel capacity from small changes in reinforcement area, while *Vulcan* on the other hand indicates only marginal increases. Ignoring the structural response of the protected secondary beams seems to be the key to this over-optimistic prediction by the Bailey-BRE Method. Therefore, to investigate the real contribution of reinforcement ratios, structural failure of the panel as a whole by plastic folding has been incorporated as a further limit on the Bailey-BRE deflection range. Fictitious intermediate reinforcement sizes have been used in addition to the standard meshes, in order to investigate in a more continuous fashion the effects of increasing reinforcement area on slab panel resistance. The range of reinforcement area is maintained between 142mm^2/m and 393mm^2/m, with additional areas of 166, 221, 284, 318 and 354 (mm^2/m). The investigation in this section examines failure times of the slab panel with respect to the three deflection criteria (TSLAB, BRE Limit and Span/20) normalised with respect to the time to creation of a panel folding mechanism, since this is a real structural collapse of the entire slab panel. Results for the 9m x 6m, 9m x 12m and 9m x 9m panels are shown in Figure 9. The lightly-shaded solid curves show results from the Bailey-BRE Method. Those from *Vulcan* are shown as darker solid curves. The dotted, solid and dashed lines refer respectively to failure times with respect to the (short span/20) criterion, the TSLAB deflection limit and the BRE limit.

www.EngineeringEBooksPdf.com

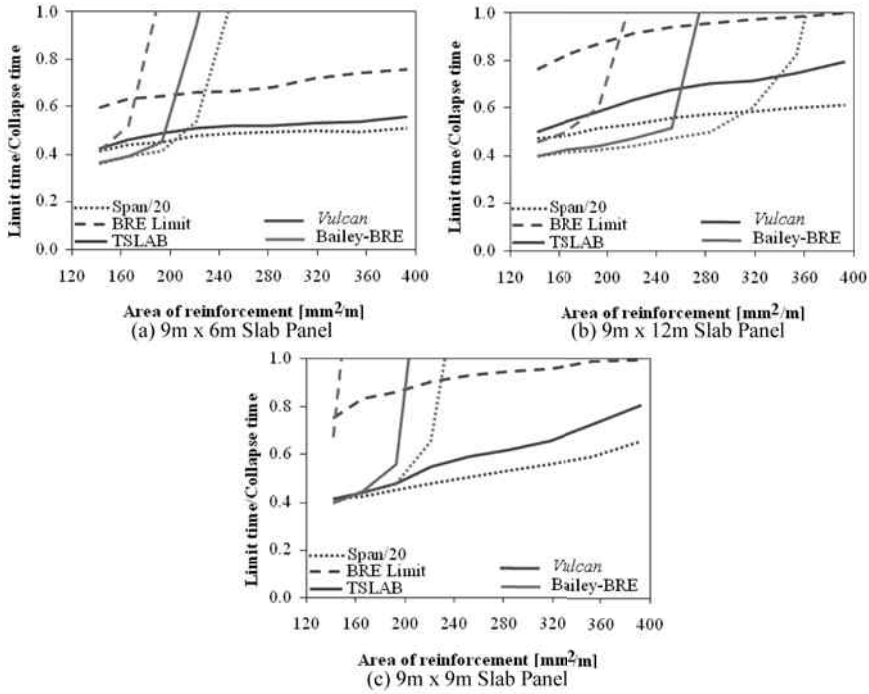


Figure 9: Normalised slab panel failure times

The comparisons in Figure 9 further confirm that the Bailey-BRE Method is conservative for the lower areas of reinforcement, but is unconservative otherwise. The method depends on the calculation of an enhancement to the small-deflection yield-line capacity which increases with increasing reinforcement size. Disproportionately higher slab capacities are obtained with higher reinforcement ratios, without adequate consideration of the capacity of the protected edge beams. The results show that the finite element analyses give a more logical indication of the contribution of the reinforcement area to slab panel capacity. The *Vulcan* 60-minute analyses show a steady increase in slab resistance with increasing reinforcement area, as they realistically consider the behaviour of edge beams and the failure properties of concrete and reinforcement.

3.3 Other Slab Panel failure mechanisms

In practice, slab panels are usually continuous over at least two supports. Continuity should provide higher slab panel resistance in fire. However, depending on the extent of the fire scenario in the building and the lightness of the reinforcement used in composite floor construction, this continuity could be lost, or significantly higher loads could be imposed on a protected perimeter beam between two adjacent slab panels. Coupled with thermal degradation of mechanical properties, these beams can experience fairly large deflections, and may collapse. Therefore it is prudent to examine the possible collapse mechanisms which could develop in these slab panels, so that they can be monitored in designs which employ the Bailey-BRE method or similar simplified methods, in order to ensure that each panel can develop its full tensile membrane capacity and not fail by the loss of the support from its protected beams. An examination of all possible scenarios offers the possibility of selecting the mechanism which requires the least plastic energy. A discussion of possible collapse scenarios is therefore provided in this section.

www.EngineeringEBooksPdf.com

Figure 10 shows some potential slab panel folding failure mechanisms:

- The simple folding mechanism discussed earlier is shown as Mechanism 1. This applies to the isolated panel shown, which of course could represent panels whose rebar has fractured across their support beams.
- Collapse Mechanisms 2a and 2b can occur when multiple slab panels are exposed to a fully developed fire. These are essentially the same as Mechanism 1, but with additional hogging fold-lines along the assumed-undeflected support beams.
- Mechanism 3 is typical for an edge slab panel, in which the beam at the edge could be considerably lighter than those in the interior parts, and does not benefit from continuity. However this could have catenary support from adjacent floor panels.
- For corner slab panels, a mechanism of the general type shown as Collapse Mechanism 4 could be appropriate, although the exact location and alignment of the sagging fold line would depend on the least-energy mechanism.

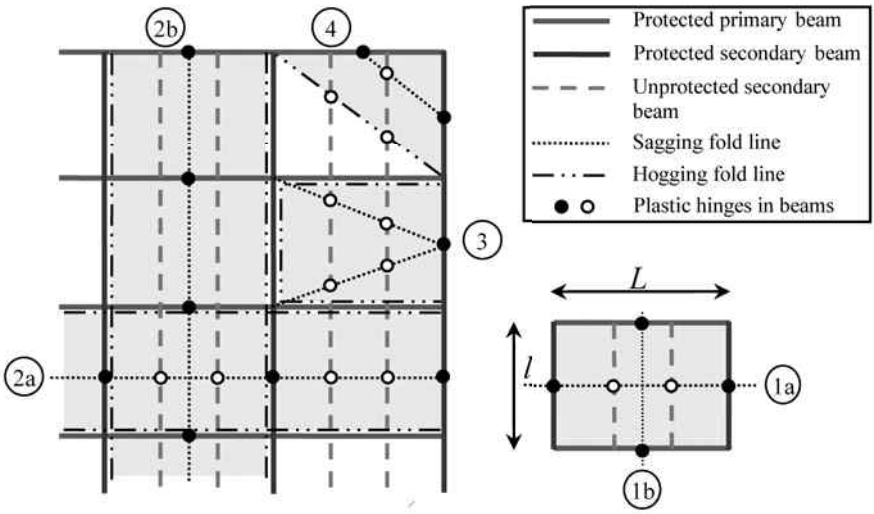


Figure 10: Potential Slab Panel Failure Mechanisms

Incorporating such folding mechanisms into the simplified approaches will help make them more robust for design by providing the resistance limits that these methods currently lack.

4 CONCLUSIONS

Both the original Bailey-BRE Method and TSLAB have based their acceptance criteria for fire resistance on the compartmentation integrity criterion, which is one of the three criteria which have to be satisfied, either in standard testing or in fire resistance design. This is almost certainly the key criterion when ideal conditions of vertical slab-panel support are maintained, and the deflection limits used appear justifiable for the prescribed mode of failure due to the occurrence of a single tension fracture across the slab's shorter span. However the results of these studies show that, since overall structural stability ("resistance" in Eurocode jargon), is not included in the method, its predictions can lose their conservatism with higher reinforcement ratios. The method's reliance on calculating the deflection required to enhance the traditional yield-line capacity without considering the stability of the edge beams results in very optimistic predictions of slab panel resistance with larger mesh sizes. The finite element analyses, on the other hand, show that, given the load redistribution which takes place, and the effects of

www.EngineeringEBooksPdf.com

aspect ratios and edge beam deflections, only marginal increases in slab panel capacity are obtained with increasing reinforcement size, and the slab panel eventually fails by overall folding. Further analyses of the effect of reinforcement area on slab panel capacity has revealed that, for small-sized panels, and for lower fire resistance requirements, increases in reinforcement area does not significantly increase the capacity. Larger mesh sizes are required for large panels, and higher reinforcement ratios are also required for longer fire resistance times to resist the large initial thermal bending which takes place. In terms of membrane-action enhancement, however, there is little influence from increasing the mesh size. The simple edge beam collapse mechanism has been found to give accurate predictions of runaway failure of slab panels. Including this mechanism in the Bailey-BRE Method would therefore make its design predictions more realistic, at least for slabs of certain sizes and aspect ratios.

REFERENCES

[1] Bailey, C.G., *Design of Steel Structures with Composite Slabs at the Fire Limit State, Final Report No. 81415, prepared for DETR and SCI*, The Building Research Establishment, Garston, UK. 2000

[2] Huang, Z., Burgess I.W. and Plank R.J., "Modelling membrane action of concrete slabs in composite slabs in fire. I: Theoretical Development", *ASCE Journal of Structural Engineering*, **129** (8), 1093-1102, 2003

[3] Huang, Z., Burgess, I.W. and Plank, R.J., "3D Modelling of Beam-Columns with General Cross-Sections in Fire", Paper S6-5, *Third International Workshop on Structures in Fire*, Ottawa, Canada, 323-334, 2004

[4] Clifton, C., "Design of multi-storey steel framed buildings with unprotected secondary beams or joists for dependable inelastic response in severe fires." *Steel Design and Construction Bulletin* **60**, New Zealand Heavy Engineering Research Association (HERA), 1-58, 2001

[5] Newman, G.M., Robinson, J.T. and Bailey, C.G., *Fire Safe Design: A New Approach to Multi-Storey Steel-Framed Buildings*, Second Edition, SCI Publication P288, The Steel Construction Institute, UK, 2006

[6] Bailey, C.G. and Toh, W.S., "Behaviour of concrete floor slabs at ambient and elevated temperatures" *Fire Safety Journal*, **42**, 425-436, 2007

[7] Foster, S.J., *Tensile Membrane Action of Reinforced Concrete Slabs at Ambient and Elevated Temperatures*, PhD thesis, University of Sheffield, 2006

[8] Abu, A.K., *Behaviour of Composite Floor Systems in Fire*, PhD thesis, University of Sheffield, 2009

[9] Huang, Z., Burgess, I.W. and Plank, R.J., "The Influence of Tensile Membrane Action on the Behaviour of Composite Steel-Framed Buildings in Fire", *Proc. ASCE Structures Congress*, Washington DC, 2001

[10] Huang, Z., Burgess, I.W., Plank, R.J. & Bailey, C.G., "Strategies for Fire Protection of Large Composite Buildings", *Proc. Interflam 2001*, 395-406, 2001

[11] Huang, Z., Burgess, I.W., Plank, R.J. and Bailey, C.G., "Comparison of BRE Simple Design Method for Composite Floor Slabs in Fire with Non-Linear FE Modelling", *Fire and Materials*, **28** (2-4), 127-138, 2004

[12] British Standards Institute. *Structural use of steelwork in building – Part 3: Design in composite construction*, British Standards Institute, UK, 1990

[13] British Standards Institute. *Structural use of steelwork in building – Part 8: Code of practice for fire resistant design*, British Standards Institute, UK, 2003

[14] Huang, Z., Platten, A. and Roberts, J., "Non-linear Finite Element Model to Predict Temperature Histories within Reinforced Concrete in Fires", *Building and Environment*, **31**(2), 109-118, 1996.

www.EngineeringEBooksPdf.com

SDSS'Rio 2010 STABILITY AND DUCTILITY OF STEEL STRUCTURES
E. Batista, P. Vellasco, L. de Lima (Eds.)
Rio de Janeiro, Brazil, September 8 - 10, 2010

LATEST DEVELOPMENTS IN THE GBT ANALYSIS OF THIN-WALLED STEEL STRUCTURES

Dinar Camotim*, Cilmar Basaglia*, Rui Bebiano, Rodrigo Gonçalves*** and Nuno Silvestre***

* Department of Civil Engineering and Architecture, ICIST/IST, Technical University of Lisbon, Portugal
e-mails: dcamotim@civil.ist.utl.pt, cbasaglia@civil.ist.utl.pt, nunos@civil.ist.utl.pt

** EST Barreiro, Polytechnical Institute of Setúbal, Barreiro, Portugal
e-mail: rui.bebiano@estbarreiro.ips.pt

*** Department of Civil Engineering, UNIC, Universidade Nova de Lisboa, Caparica, Portugal
e-mail: rodrigo.goncalves@fct.unl.pt

Keywords: Generalised Beam Theory (GBT), Thin-walled steel structures, First-order analysis, Buckling analysis, Post-buckling analysis, Vibration analysis, Dynamic analysis.

Abstract. *This work presents a state-of-the-art report of the most recent developments concerning formulations, numerical implementations and applications of Generalised Beam Theory (GBT) to analyse the structural response of thin-walled steel members and frames. After a brief overview of the cross-section analysis, one addresses new findings dealing with the use of GBT to assess the (i) first-order behaviour of steel-concrete composite bridge decks, (ii) buckling and post-buckling behaviour of members and frames with arbitrary loading and support conditions, (iii) vibration behaviour of load-free and loaded open-section members and (iv) dynamic behaviour of members subjected to periodic and moving loads. In order to illustrate the unique features and show the potential of the GBT approach, several numerical results are presented and discussed. For validation purposes, most of these results are compared with values yielded by shell finite element analyses, performed in the codes ADINA, ABAQUS and ANSYS.*

1 INTRODUCTION

Generalised Beam Theory (GBT) may be viewed as an extension of Vlasov's classical thin-walled bar theory that includes cross-section deformations (wall bending and distortion), thus combining the advantages of a one-dimensional formulation with the capability of folded-plate theory. It has been amply shown that GBT constitutes a rather powerful, elegant and clarifying method of structural analysis for prismatic thin-walled member and structures. Indeed the GBT approach offers possibilities not available when other numerical techniques, such as finite strip or (mostly) shell finite element analyses, are employed. This is due to the GBT unique features, which make it possible to decompose a member/frame deformed configuration or buckling/vibration mode into a linear combination of structurally meaningful "modal contributions". Such modal decomposition requires the identification of cross-section *deformation modes*, which is achieved through the performance of a special discretisation-and-orthogonalisation procedure designated as *cross-section analysis* – the "trademark" of GBT.

The pioneering work that led to the development of the GBT approach to perform structural analysis must be credited to Schardt [1], who subsequently was also responsible, together with his collaborators at the University of Darmsdadt, for the growth of GBT during about four decades. Another important contribution was due to Davies and co-workers [2-3], who (i) extensively employed GBT to investigate the local and global buckling behaviour of cold-formed steel profiles, and (ii) contributed decisively to disseminate it amongst the English-speaking technical-scientific community (the vast majority of the work carried out by Schardt *et al.* was only published in German). By the end of the last millennium, GBT was primarily used to perform elastic first-order and buckling analyses of thin-walled steel members with unbranched open cross-sections, namely cold-formed steel profiles (even if other structural analyses and cross-section shapes could already be handled by GBT [4]).

www.EngineeringEBooksPdf.com

In the last decade, a research team at IST (Technical University of Lisbon) has devoted a very significant amount of research work to the development, numerical implementation, application and worldwide dissemination of novel GBT formulations that considerably broaden the scope of this theory, by enabling the performance of several additional analyses and covering a wider range of structural systems [5-7]. In particular, it is now possible to carry out (i) first-order, buckling, post-buckling, vibration and dynamic analyses of metal and FRP members with open and closed cross-sections, and (ii) first-order, buckling and post-buckling analyses of thin-walled steel frames.

The aim of this work is to report and provide a unified view on the most recent advances concerning the use of GBT analyses to assess the structural response of thin-walled steel members and frames. Besides presenting a brief (but insightful) overview of the fundamental concepts and main procedures involved in the performance of a GBT cross-section analysis, it (i) provides an account, illustrates the application and show the capabilities of several formulations that were developed and numerical implemented (beam finite elements) in the last couple of years, and also (ii) addresses the research work dealing with GBT that is currently under way. Due to space limitations and the large amount of material available, it is only possible to include a brief description of the new developments, followed by the presentation and discussion of illustrative numerical results – however, all the key references are provided, where the interested reader may find detailed accounts of all the work reported here. In particular, this paper is concerned with GBT formulations that can be applied to analyse the (i) first-order behaviour of steel-concrete composite bridge decks, (ii) buckling and post-buckling behaviour of members and frames exhibiting arbitrary loading and support conditions, (iii) vibration behaviour of load-free and loaded open-section members and (iv) dynamic behaviour of members subjected to periodic and moving loads. For the sake of validation and numerical efficiency assessment, most of the GBT-based results presented are compared with values yielded by shell finite element analyses carried out in commercial codes, namely ADINA [8], ABAQUS [9] and ANSYS [10].

2 CROSS-SECTION ANALYSIS

In order to obtain a displacement field representation compatible with the classical beam theory, GBT adopts the variable separation

$$u(x,s) = u_k(s)\phi_{k,x}(x) \qquad v(x,s) = v_k(s)\phi_k(x) \qquad w(x,s) = w_k(s)\phi_k(x) \quad , \quad (1)$$

where (i) x and s denote coordinates along the member length and cross-section mid-line, (ii) $u_k(s)$, $v_k(s)$ and $w_k(s)$ are functions providing the longitudinal, transverse membrane and transverse flexural displacements characterising deformation mode k, (iii) $(.)_{,x} \equiv d(.)/dx$, (iv) the summation convention applies to subscript k and (v) $\phi_k(x)$ are mode amplitude functions defined along the member (or finite element) length.

Before carrying out a GBT structural analysis (*e.g.*, a first-order, post-buckling or vibration analysis) of a given thin-walled system (member or frame), one must begin by performing *cross-section analyses*, which provide the corresponding member "deformation modes" (*i.e.*, the functions $u_k(s)$, $v_k(s)$ and $w_k(s)$ appearing in eq. (1), which are the "essence" and "trademark" of GBT) and associated modal mechanical properties. This is achieved by means of specific discretisation-and-orthogonalisation procedures that vary with the cross-section type and were sequentially developed and reported in detail by (i) Silvestre and Camotim [11], Dinis *et al.* [12], Gonçalves *et al.* [13] and Silvestre [14, 15], in the context of buckling analysis, and by (ii) Silvestre and Camotim [16], for post-buckling analysis – it still worth noting the very recent work by Gonçalves *et al.* [17], which provides a very insightful and complete account on the determination of deformation modes in polygonal cross-sections.

In polygonal cross-sections (*i.e.*, excluding the circular and elliptical tubes investigated by Silvestre [14, 15]), it is possible to identify *two* main groups of deformation modes, involving (i) *conventional* (those originally considered by Schardt [1]) and (ii) *non-conventional* modes – the latter comprise *membrane shear*, *warping shear* and *transverse extension* modes. The main features of these various deformation mode sets are the following:

(i) The *conventional* modes, which are based on the null membrane shear strain and transverse extension assumptions, constitute the core of GBT and can still be subdivided into (i_1) *global* (cross-section in-plane rigid-body motions: axial extension, major/minor axis bending and torsion), (i_2) *distortional* and (i_3) *local* modes – the last two categories involve cross-section in-plane deformation (distortion and/or wall bending).

(ii) The *membrane shear* modes account for the membrane shear deformation occurring in walls belonging to

www.EngineeringEBooksPdf.com

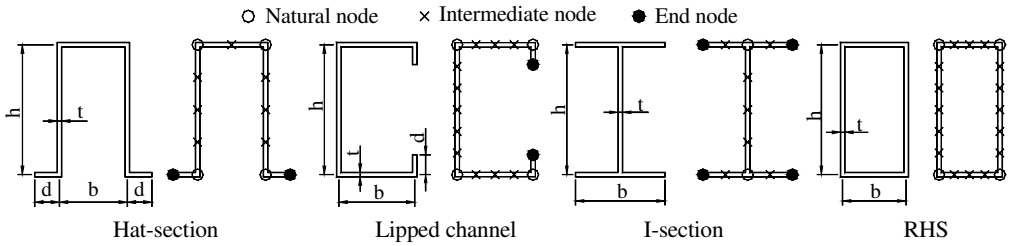
closed cells. They are obtained through the sequential imposition of unit membrane shear strains at each closed-cell wall ($\gamma^M=v_{,x}+u_{,s}=1$), while keeping null values at all the remaining (closed-section and open-branch) walls.

(iii) The *warping shear* modes make it possible to capture the *non-linear* variation of the warping displacements along the cross-section wall mid-lines. They are obtained by imposing unit warping displacements $u(s)$ and null membrane transverse displacements $v(s)$ at each (natural and intermediate) node – this procedure automatically implies null flexural displacements $w(s)$, *i.e.*, one has only $u(s)\neq 0$.

(iv) The *transverse extension* modes involve only in-plane displacements (*i.e.*, $u(s)=0$) and account for the cross-section deformation due to the wall membrane transverse extensions. They are obtained through the imposition of unit membrane transverse displacements $v(s)$ and null warping displacements $u(s)$ at each node – flexural transverse displacements $w(s)$, uniform along each wall mid-line, may be required to ensure transverse displacement compatibility at the natural nodes.

Non-conventional deformation modes were already included in recent GBT-based investigations. For instance, (i) Gonçalves and Camotim [18] considered warping shear modes to analyse the shear lag effects in twin-box girder bridges, (ii) Silvestre and Camotim [19] used warping shear and transverse extension modes to study the post-buckling behaviour of cold-formed steel lipped channel members, and (iii) Dinis *et al.* [20] utilised membrane shear modes to assess the buckling behaviour of cold-formed steel hollow-flange channel beams.

Figure 1 shows the geometries (shapes and dimensions) and possible GBT discretisations of most of the thin-walled member cross-sections dealt with in this work. Figures 2 to 5 depict the main features of the corresponding deformation modes that are more relevant for the analyses carried out in the paper (*i.e.*, those with significant contributions to the member buckling/vibration mode shapes or first-order/post-buckling deformed configurations).



Designation	Shape	Young's modulus (GPa)	Web *h* (*mm*)	Flange *b* (*mm*)	Lip *d* (*mm*)	Thickness *t* (*mm*)
HS120×60×2.0	Hat-section	210	120	60	20	2.0
C100×40×1.0		210	100	40	20	1.0
C100×60×1.0	Lipped	205	100	60	5	1.0
C100×100×2.0	Channel	200	100	100	20	2.0
C202×75×2.3		205	202	75	20	2.3
I300×150×5.0	I-section	205	300	150	-	5.0
RHS200×75×3.0	RHS	205	200	75	-	3.0

Note: All the steel members dealt with in this work have mass density $\rho=7.85 g/cm^3$ and Poisson's ratio $\nu=0.3$.

Figure 1: Hat-section, lipped channel, I-section and RHS dimensions and possible GBT discretisations.

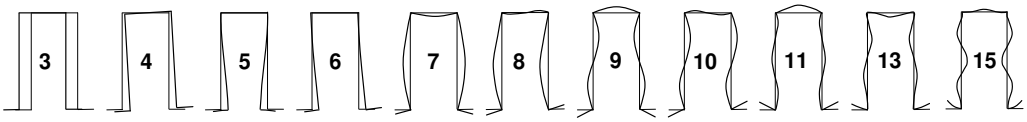


Figure 2: Main features of the most relevant hat-section deformation modes.

www.EngineeringEBooksPdf.com

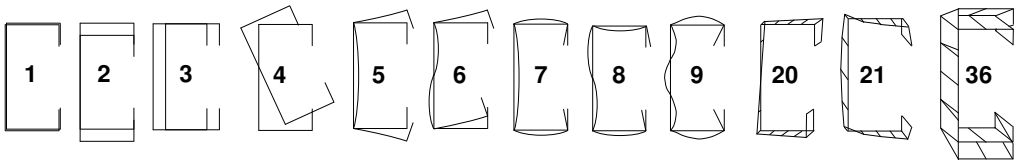


Figure 3: Main features of the most relevant lipped channel deformation modes.

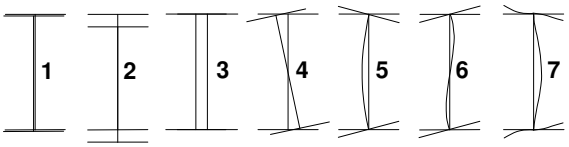


Figure 4: Main features of the most relevant I-section deformation modes.

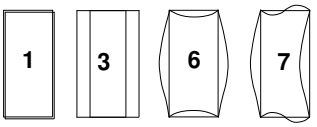


Figure 5: Main features of the most relevant RHS deformation modes.

3 FIRST-ORDER ANALYSIS

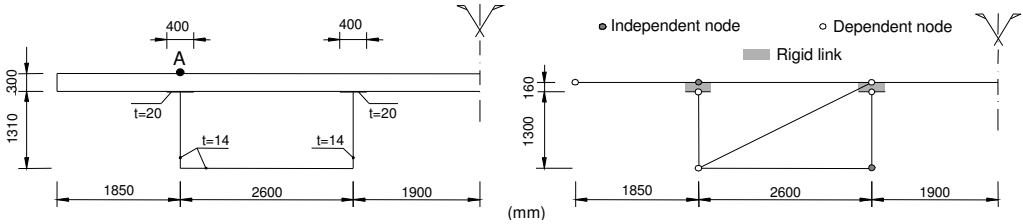
In the context of member first-order (geometrically linear) analysis, the GBT system of equilibrium equations (one per deformation mode), expressed in terms of the modal amplitude functions $\phi_k(x)$, is given by

$$C_{ik}\phi_{k,xxxx} - D_{ik}\phi_{k,xx} + B_{ik}\phi_k = q_h \quad , \quad (2)$$

where (i) q_h are the modal applied loads and (ii) C_{ik}, D_{ik} and B_{ik} are cross-section modal mechanical properties, defined in [11, 18] – while C_{ik} and D_{ik} concern the warping displacements and torsional rotations, B_{ik} stem from local deformations (wall bending and distortion).

Gonçalves and Camotim [18] have recently employed a novel GBT-based approach to analyse the first-order behaviour of steel-concrete composite beams and bridges (i) acted by eccentric vertical loads, causing bending and torsion, and (ii) having cross-sections that combine closed cells with open branches and exhibit displacement constraints to model box diaphragms. In order to illustrate this approach, let us consider the first-order behaviour of the simply supported (pinned end sections that may warp freely) steel-concrete composite twin-box girder bridge with (i) the cross-section geometry and dimensions given in figure 6(a), (ii) a 20m span and (iii) the material properties *E=37GPa*, *v=0.1* (C50/60 concrete deck) and *E=210GPa*, *v=0.3* (steel girders). The loading consists of a mid-span vertical force applied at point *A* (see fig. 6(a)), causing combined bending and torsion in the bridge – due to symmetry, only half of the bridge is analysed.

Concerning the cross-section analysis, the main challenge is to identify deformation modes that can easily accommodate the presence of box diaphragms at the bridge piers and/or along its span. This challenge is met by means of the auxiliary system depicted in figure 6(b), in which (i) the diaphragm constraint is modelled by a single cross-link (all walls are assumed inextensible) and (ii) rigid links fill the gap between the mid-lines of the concrete slab and steel girder top flanges. Then, the cross-section analysis leads to the following *13* deformation modes:



(a) (b)

Figure 6: Bridge cross-section (a) geometry and (b) GBT discretisation.

www.EngineeringEBooksPdf.com

(i) *5* modes calculated assuming $u_x+v_x=0$ (**1-5**: axial extension, major/minor axis bending torsion and distortion) – see figure 7. The torsion mode (**4**) involves the combination with a closed-cell "shear flow" mode [17].

(ii) *2* modes due to the imposition a unit elongation at each cross-links: symmetric (**6**) and anti-symmetric (**7**) cross-link-induced distortion – see figure 7.

(iii) *6* membrane shear modes stemming from the imposition of unit membrane shear strains in each of the *6* steel closed-cell walls (**8-13** – see fig. 8) – the concrete deck is assumed rigid and rigidly attached to the top flanges.

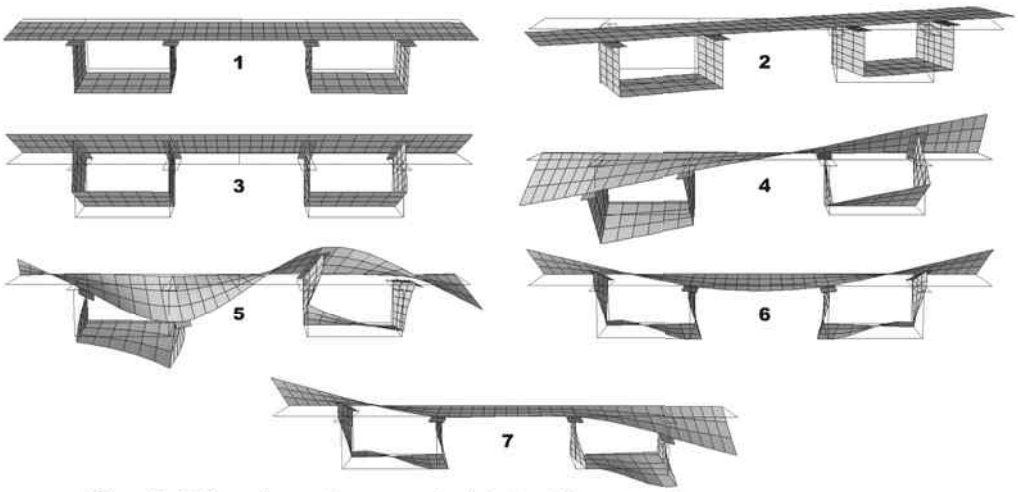


Figure 7: Deformation modes: conventional (**1-5**) and due to cross-link induced distortion (**6-7**).

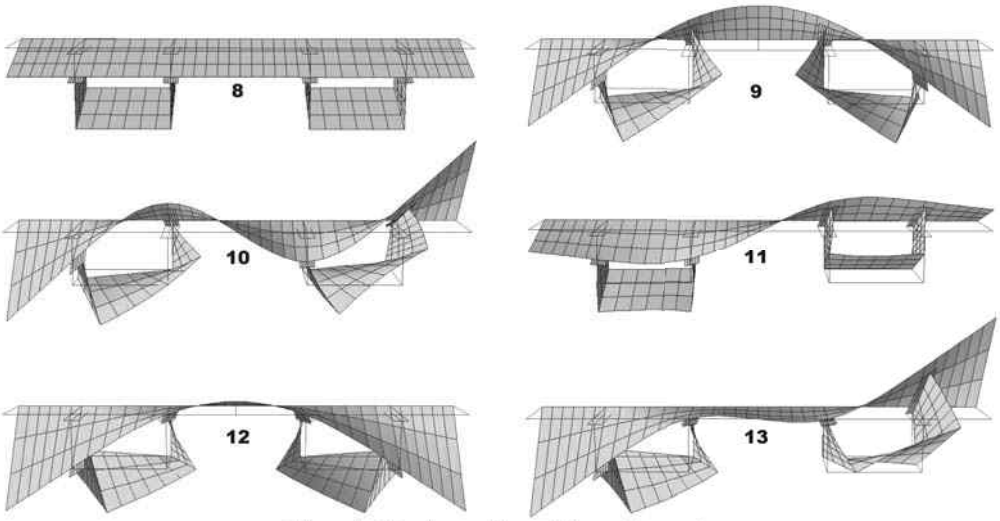


Figure 8: Membrane shear deformation modes.

Figures 9 and 10 show the deformed configurations of one half of the bridge with diaphragms located (i) at the piers and (ii) at the piers and mid-span – these configurations were yielded by (i) GBT-based beam finite element analyses (*3* equal-length elements) and (ii) ADINA shell finite element analyses (*4*-node element mesh). On the other hand, figures 11(a)-(b) and 12(a)-(b) show the variation of the vertical displacement (i) with the beam finite element number (at mid-span) and (ii) along the length (GBT values with *3* elements) for the two bridge configurations.

www.EngineeringEBooksPdf.com

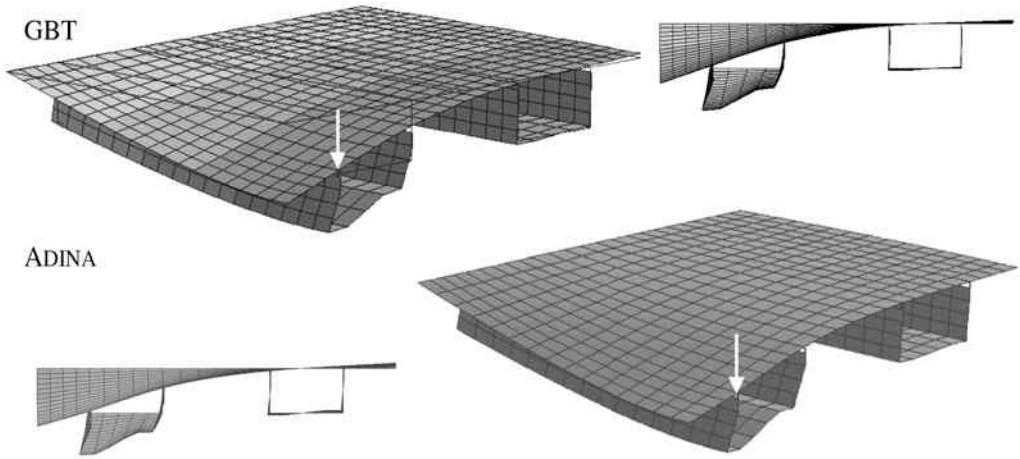


Figure 9: Deformed configurations of half of the bridge (diaphragms at the piers) ($\times 10^5$).

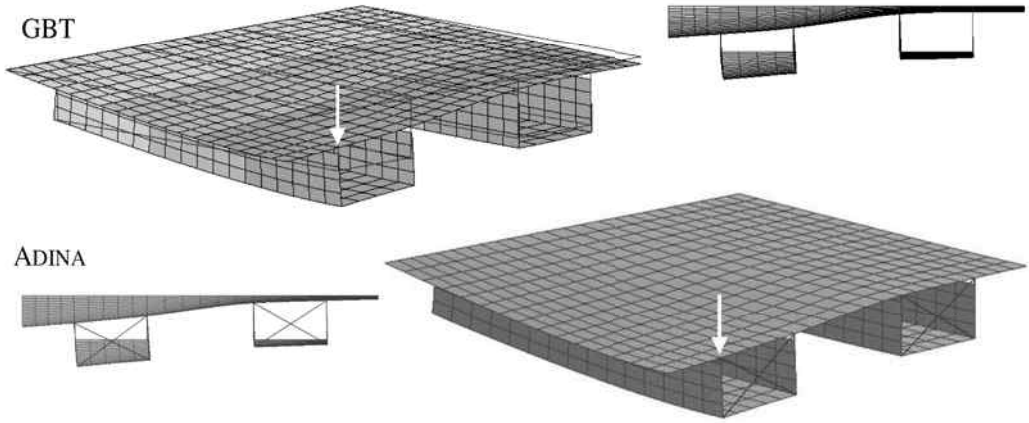


Figure 10: Deformed configurations of half of the bridge (diaphragms at piers and mid-span) ($\times 10^5$).

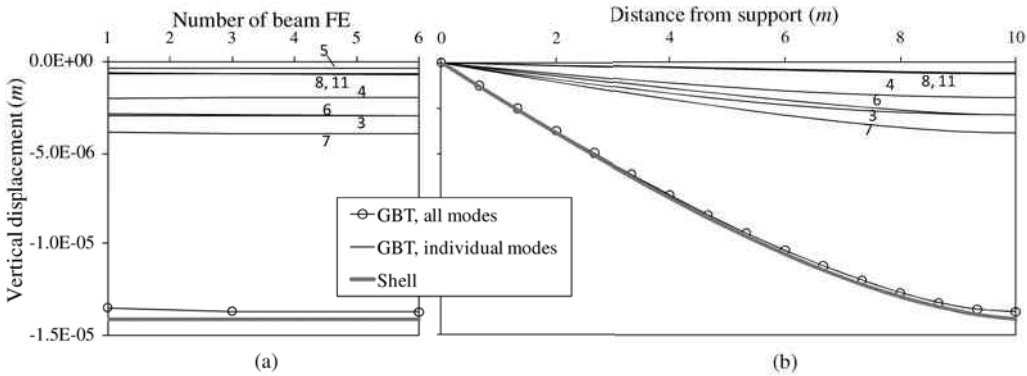


Figure 11: Variation of the vertical displacements (a) with the beam finite element number (at mid-span – point *A*) and (b) along the beam length (longitudinal line passing in *A*) – bridge with diaphragms at the piers.

www.EngineeringEBooksPdf.com

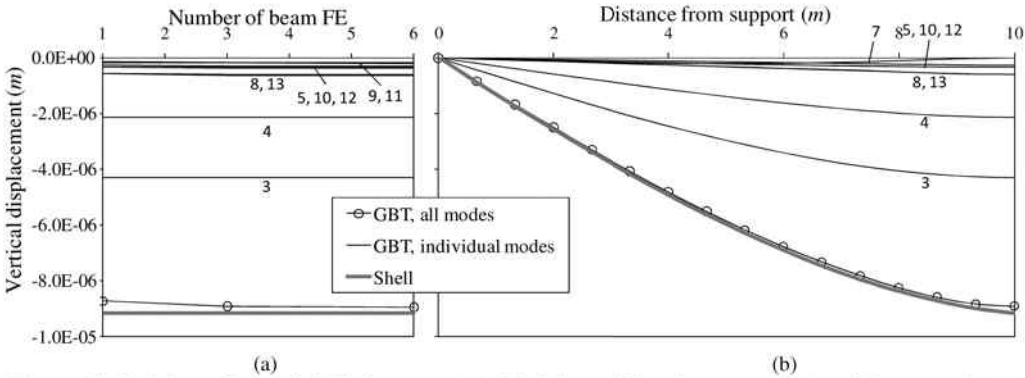


Figure 12: Variation of the vertical displacements (a) with the beam finite element number (at mid-span – point *A*) and (b) along the beam length (longitudinal line passing in *A*) – bridge with diaphragms at the piers and mid-span.

One notices that the GBT-based and ADINA results virtually coincide, even for a discretisation involving as little as *3* beam finite element – for this discretisation, displacement differences of *3.0%* (diaphragms at the piers) and *2.5%* (diaphragms at the piers and mid-span). Moreover, the GBT modal participations, shown in figures 11 and 12, provide valuable insight into the mechanics of the bridge structural response – no such detailed and structurally meaningful information can be extracted from the shell finite element results.

The GBT analysis may also account for the shear lag effects, by incorporating deformation modes associated with the non-linear variation of the warping displacements along cross-section wall mid-lines (warping shear modes) [18]. In this case, the deformation modes included in the analysis concerned the bottom flanges and consisted of single half-wave sinusoidal warping functions – modes **14** and **15** in figure 13(a). Figure 13(b) shows the normal stress distributions at the mid-span loaded cross-section half for the two bridge configurations – results yielded by (i) GBT analyses (*3* beam finite elements) including modes **1**-**13** and **1**-**15**, and (ii) the previous ADINA analysis. It is clear that including the "shear lag modes" makes it possible to capture the non-linearity of the lower flange stress distribution. Moreover, the GBT stresses match quite accurately the ADINA ones, even if one peak stress (*78.6kPa* – bottom right corner) is underestimated by about *17%* – additional deformation modes, namely *local* ones, would be required to obtain a more accurate peak stress.

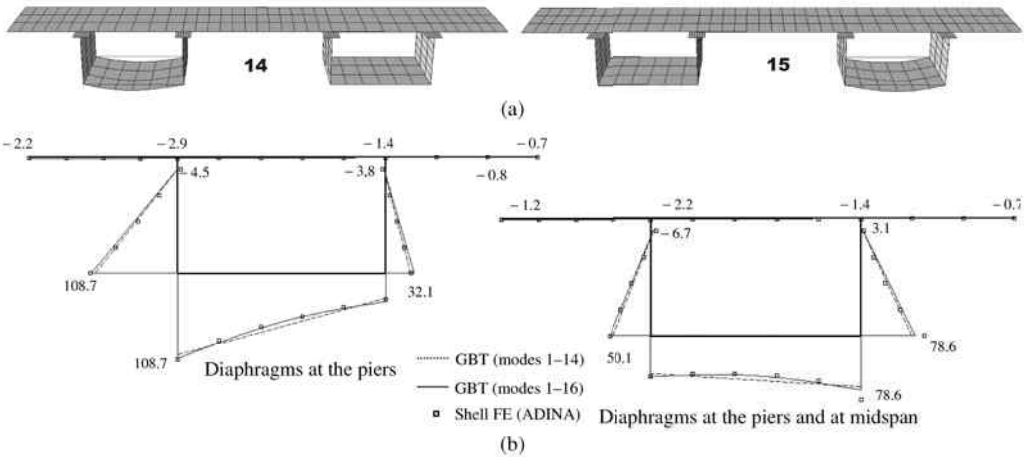


Figure 13: (a) Single half-wave shear lag deformation modes and (b) normal stress distributions (*kPa*) at the mid-span loaded cross-section half for the two bridge configurations (stress values indicated from the ADINA analysis).

www.EngineeringEBooksPdf.com

4 BUCKLING ANALYSIS

The GBT system of equilibrium equations governing the member or frame buckling behaviour is given by

$$C_{ik}\phi_{k,xxxx} - D_{ik}\phi_{k,xx} + B_{ik}\phi_k - \lambda\left[X^{\sigma}_{jik}\left(W^0_j\phi_{k,x}\right)_{,x} - X^{\tau}_{jki}\left(W^0_{j,x}\phi_k\right)_{,x} + W^0_{j,x}X^{\tau}_{jik}\phi_{k,x}\right] = 0 \quad , \quad (3)$$

where (i) λ is the load parameter and (ii) X^{σ}_{jik} and X^{τ}_{jik} are geometric stiffness components associated with the pre-buckling normal stress resultants W^0_j and shear stresses due to the longitudinal stress gradients, all defined in [21].

Concerning the buckling analysis of isolated members, Bebiano *et al.* [21] developed a GBT-based beam finite element formulation capable of analysing single-span beams with standard support conditions (*i.e.*, free, pinned or fixed end sections) acted by transverse loadings associated with major and/or minor axis bending. This formulation incorporates the geometric stiffness reduction due to non-uniform compression and/or major/minor axis bending, causing longitudinal normal stress gradients and shear stresses (varying bending moments). Soon after, Camotim *et al.* [22] extended the above GBT-based beam finite element, making it possible to assess the local, distortional and global buckling behaviour of thin-walled members with a wide variety of loading and support conditions, including intermediate and/or localised supports (simulating bracing systems or connectors). In order to incorporate these non-standard support conditions into the analysis, the system (3) must be solved subjected to *constraint conditions* that (i) vary from case to case and (ii) are expressed as linear combinations of the appropriate set of modal degrees of freedom (d.o.f.). A little later, Silva *et al.* [23] further improved the GBT buckling analysis capabilities, by incorporating into the beam finite element formulation geometric stiffness associated with *transverse* normal stresses, a feature enabling the capture of effects related to (i) patch loading (concentrated loads) and/or (ii) the application of transverse loads away from the cross-section shear centre (*e.g.*, loads applied at channel or I-beam top flanges).

As far as thin-walled frames are concerned, the major difficulties in applying GBT (or any other beam model) lie in the appropriate treatment of the joints, which involves the simultaneous consideration of (i) the warping transmission due to torsion and/or distortion and (ii) the compatibility between the transverse (membrane and flexural) displacements of the connected member end sections – moreover, it also convenient to be able to simulate the connections/restraints stemming from the presence of bracing systems. To overcome these difficulties, a GBT-based beam finite element approach was developed and numerically implemented. This approach makes it possible to assess the buckling behaviour of thin-walled plane and space frames (i) built from RHS or open cross-section members, (ii) having localised supports stemming bracing systems, (iii) exhibiting various joint configurations and (iv) acted by loadings causing non-uniform internal force and moment diagrams. This work is mostly due to Basaglia [24] and a fairly complete state-of-the-art report was recently published by Camotim *et al.* [7].

4.1 Illustrative examples

In this sub-section, numerical results concerning the buckling behaviour of (i) hat-section cantilevers [23], (ii) a cold-formed RHS portal frame [25] and (iii) a restrained space frame [26] are presented and discussed. For validation purposes, most GBT-based critical buckling loadings and mode shapes are compared with values yielded by shell finite element analyses carried out in ABAQUS [9] or ANSYS [10] – the cantilevers and frames are discretised into refined S9R5 (ABAQUS) and SHELL181 (ANSYS) element meshes, respectively.

4.1.1 Hat-section cantilevers

One analyses the buckling behaviour of HS120×60×2.0 cantilevers acted by two identical transverse point loads applied at either the end-section web-flange or web-lip corners – Q is the total applied load. The main objective is to assess the influence of the load position on the cantilever critical buckling moment (M_{cr}=Q_{cr}.L) and mode shape. Figures 14(a)-(b) and 15 show, for the two loadings considered, (i) $M_{cr}(L)$ buckling curves, (ii) the corresponding GBT modal participations diagrams and (iii) the GBT-based critical buckling mode shapes concerning cantilevers with three lengths. The observation of these buckling results prompts the following remarks:

(i) There is an excellent agreement between all the GBT and ABAQUS critical moments – differences below *4%*.

(ii) There is a clear difference between the cantilever critical buckling moments and mode shapes associated with the top and bottom loadings. Concerning the M_{cr} values, those corresponding to bottom loading may exceed by more than *300%* their top loading counterparts (see fig. 14(a)). In both cases, the critical buckling modes include

www.EngineeringEBooksPdf.com

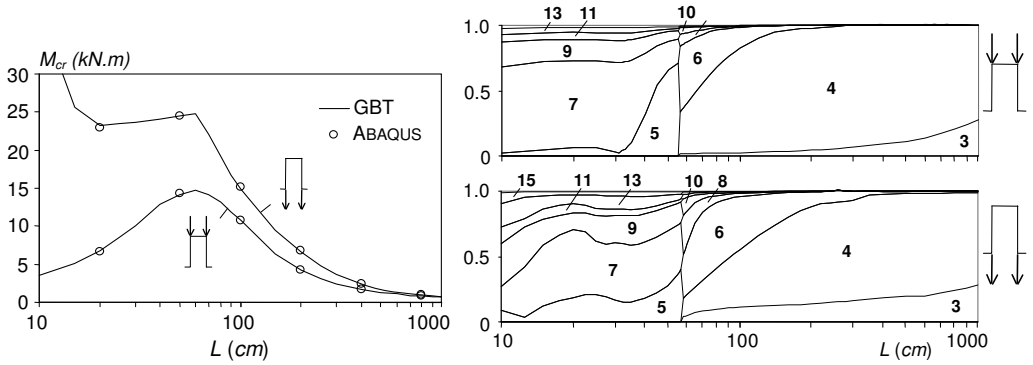


Figure 14: Hat-section cantilevers: (a) $M_{cr}(L)$ buckling curves and (b) GBT modal participation diagrams concerting the two position of the tip point loads.

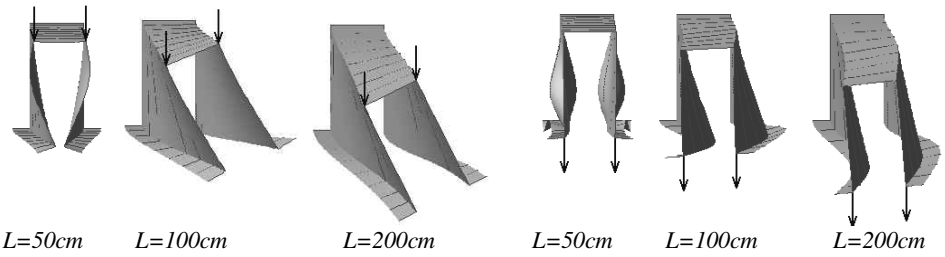


Figure 15: Hat-section cantilevers: GBT-based critical buckling mode shapes for three lengths and the two loadings under consideration.

relevant contributions from global, distortional and local deformation modes, as shown in figures 14(b) and 15 – they combine (ii_1) symmetric distortional (**5**) and local (**7**, **9**, **11**, **13**, **15**) modes, for $L<55$ *cm*, or (ii_2) anti-symmetric global (**3**, **4**), distortional (**6**) and local (**8**, **10**) modes, for $L>55$ *cm*.

(iii) Figure 15 shows the critical buckling modes of three cantilevers ($L=50$ *cm*, $L=100$ *cm* and $L=200$ *cm*) under top and bottom loading. In order to illustrate the statements made in the previous item, consider the $L=100$ *cm*, for which one has (iii_1) $M_{cr}=10.67$ *kN.m* and *14.84 kN.m* (*39%* increase), and (iii_2) the "replacement" of contribution of torsion (mode **4** – *80.2-43.9%* decrease) by those of distortion and minor axis bending (modes **6** and **3** – *15.9-40.5%* and *2.4-11.2%* increases) – see figures 14(a)-(b).

4.1.2 RHS plane frame

Next, one investigates the buckling behaviour of the symmetric portal frame depicted in figure 16, (i) formed by three orthogonal RHS200×75×3.0 members (*A*, *B*, *C* – frame in-plane behaviour corresponding to minor axis bending), (ii) with fixed column bases and (iii) subjected only to axial compression (equal loads *P* applied at the joints). Figure 17 provides ANSYS and GBT-based 3D representations of the buckled frame joint region – note that the GBT view is obtained from a *beam* finite element analysis. Figure 18 displays, for each frame member, the amplitude functions of the two deformation modes that participate in the frame critical buckling mode. The comparison between the buckling results yielded by the two numerical models leads to the following comments:

(i) The two critical loads obtained virtually coincide: $P_{cr.GBT}=370.3kN$ and $P_{cr.ANSYS}=381.3kN$ (*2.9%* difference). However, note the disparity between the d.o.f. numbers: *648* (GBT – *80* finite elements) and *22600* (ANSYS).

(ii) There is also a close agreement between the GBT modal amplitude functions and the ANSYS buckling mode shape – they providing different representations of a well defined local buckling mode. However, it can easily be argued that the GBT result enables a better quantitative and qualitative grasp of the frame buckling mechanics.

www.EngineeringEBooksPdf.com

(iii) The frame critical buckling mode is anti-symmetric and involves the three members: it exhibits *12* half-waves in each column and *6 half-waves* in the beam. Only the local deformation modes **6** and **7** have visible contributions to the frame critical buckling mode, with a clear dominance of mode **6** (note that the mode **7** contribution is amplified ten times). The more relevant (local) deformations occur in the column central regions and, as expected, the beam deformations are noticeably smaller.

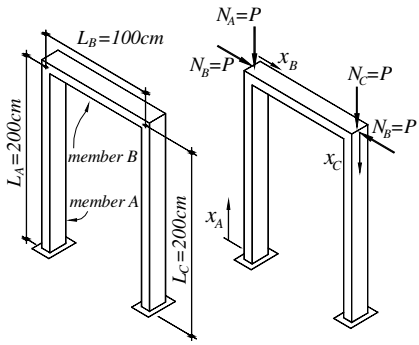


Figure 16: RHS portal frame geometry, loading and support conditions.

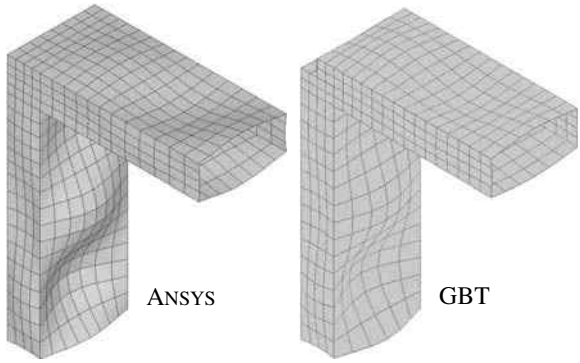


Figure 17: ANSYS and GBT views of the buckled frame joint region.

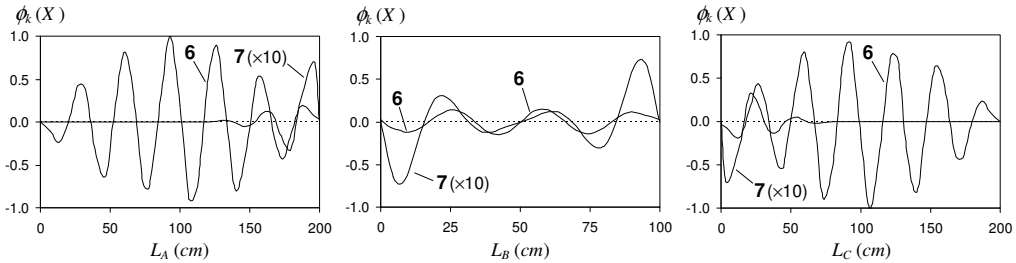


Figure 18: RHS portal frame – member modal amplitude functions $\phi_k(X)$.

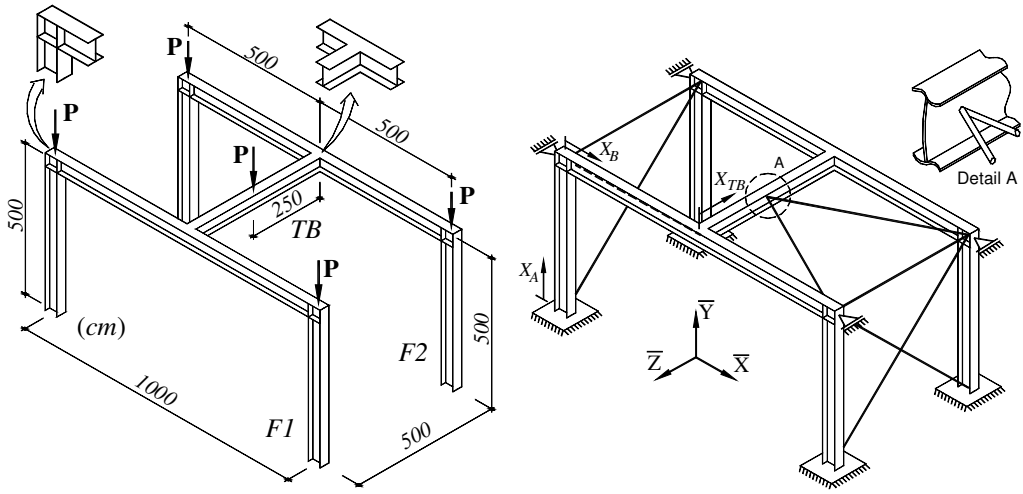
4.1.3 I-section space frame

Finally, the buckling analysis of the symmetric space frame depicted in figure 19(a) is presented and discussed. This frame (i) comprises two portal frames (*F1* and *F2*) joined by a transverse beam (*TB*), all built from I300×150×5.0 members, and (ii) is acted by five equal vertical loads (*P*) applied at the four column tops and at the centroid of the transverse beam mid-span cross-section. All column-to-beam joints are box-stiffened (web continuity) and the beam-to-beam ones exhibit flange continuity. Moreover, (i) the column bases are fixed, (ii) the transverse displacement along $\overline{X}$ is prevented at all column-to-beam joints (see fig. 19(b)) and at the *TB* mid-span cross-section, and (iii) the displacement along $\overline{Z}$ is prevented at all column-to-beam joints ("rigid" diagonal and transversal tie-rods, connected to I-section mid-web point – see also fig. 19(b)).

Figures 20(a) and 20(b) show (i) the GBT modal amplitude functions for column *A* and beams *B* and *TB*, and (ii) a 3D view of the frame critical buckling mode shape, yielded by the ANSYS shell finite element analysis (tie-rod modelled with a *6cm* and BEAM189 elements). As before, the GBT analysis requires only a small fraction of the d.o.f. involved in its ANSYS counterpart: *1030* (*80* beam elements – *8* per column and *16* per beam) versus *25000*. The following conclusions can be drawn from the comparison between these two sets of frame buckling results:

(i) The GBT and ANSYS critical loads are again extremely close: $P_{cr.GBT}=161.83kN$ and $P_{cr.ANSYS}=159.11kN$ (*1.71%* difference). Moreover, there is an excellent correlation between the ANSYS buckling mode shape and the GBT modal amplitude functions. This assessment can by further (and amply) confirmed by looking at figure 20(c), providing ANSYS and GBT 3D views of the buckled *TB* mid-span region.

www.EngineeringEBooksPdf.com



(a) (b)

Figure 19: Space frame (a) geometry and loading, and (b) support conditions and transverse beam bracing detail.

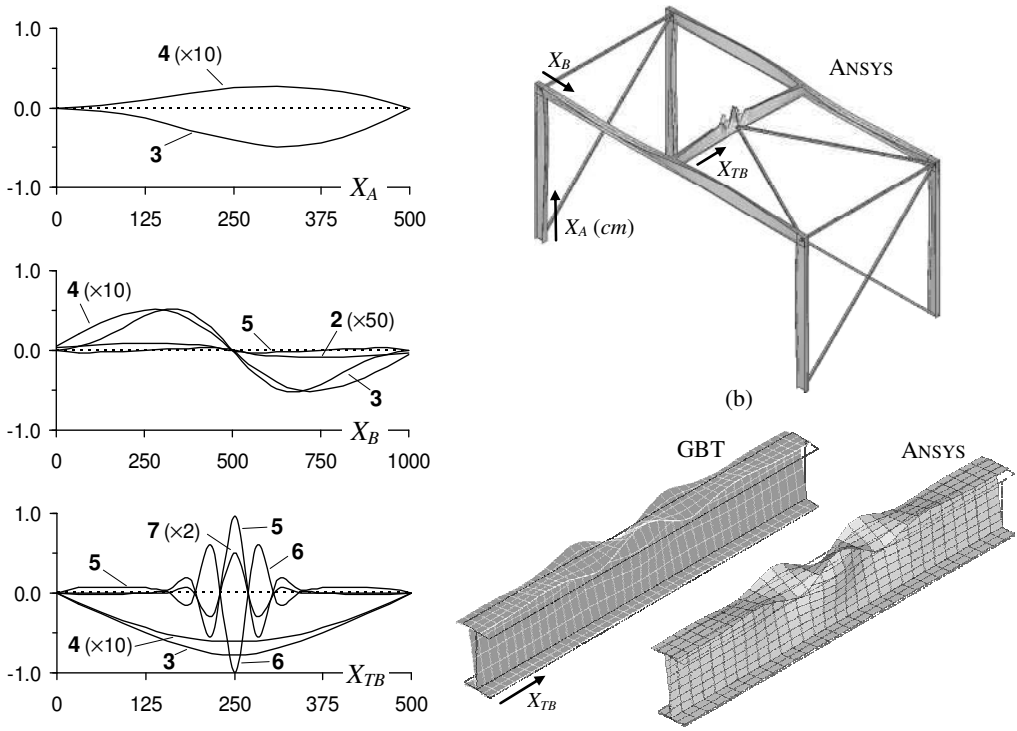


Figure 20: (a) GBT and (b) ANSYS space frame critical buckling mode representations, and (c) *TB* mid-span region buckled shapes.

www.EngineeringEBooksPdf.com

(ii) The frame critical buckling mode is triggered by the *TB* and combines participations from global (**3**, **4**) and local (**5**, **6, 7**) deformation modes. While the latter occur mainly in the beam mid-span region (higher bending moments), the influence of the former is felt along the whole beam length – due to small wall thickness, the occurrence of local buckling hamper the bracing system efficiency in preventing lateral-torsional buckling.

(iii) The portal frame members experience mostly lateral-torsional buckling (maximum values near the beam 1/4 and 3/4-span cross-sections) – in the beams, there are also minute contributions from modes **2** and **5**.

5 POST-BUCKLING ANALYSIS

The determination of a member/frame post-buckling behaviour involves solving the one-dimensional problem governed by the system of non-linear differential equilibrium equations

$$C_{kh}(\phi_k-\bar{\phi}_k)_{,xxxx}-D_{kh}(\phi_k-\bar{\phi}_k)_{,xx}+B_{kh}(\phi_k-\bar{\phi}_k)-C_{kh}(\phi_k-\bar{\phi}_k)_{,xxxx}+\tfrac{1}{2}C_{hjk}(\phi_{k,x}\phi_{j,x}-\bar{\phi}_{k,x}\bar{\phi}_{j,x})_{,xx}+ \\ +\tfrac{1}{2}C_{kijh}(\phi_{k,x}\phi_{i,x}\phi_{j,x}-\bar{\phi}_{k,x}\bar{\phi}_{i,x}\phi_{j,x})_{,x}+h.o.t.=q_h \quad , \quad (4)$$

where the bar identifies the modal amplitude functions defining the initial geometrical imperfections. While the second-order tensor components (C_{kh}, D_{kh}, B_{kh}) characterise the member linear (first-order) behaviour, the third (C_{kijh}, etc.), fourth (C_{kijh}, etc.) and higher-order (*h.o.t.*, not shown in (4)) ones are associated with its geometrically non-linear behaviour – all these tensor components are given in [16, 27].

In isolated members, the solution of the non-linear system (4) can be obtained by means of a GBT-based beam finite element formulation developed and implemented by Silvestre and Camotim [16], in the context of unbranched open-section members, and recently extended by Basaglia *et al.* [27] to cover members with arbitrary open cross-sections (*i.e.*, including also branched ones) and allow for the consideration of non-standard support conditions, such as localised displacement restraints (*e.g.*, those stemming from bracing) or intermediate supports.

The most recent GBT developments are due to Basaglia *et al.* [28, 29] and concern a geometrically non-linear GBT formulation applicable to assess the local, distortional and global post-buckling behaviour of thin-walled frames. It incorporates arbitrary initial geometrical imperfections (expressed in *modal* form) and is able to handle the kinematics of joints connecting two non-aligned members, namely those associated with the compatibility between the connected cross-section warping (due to axial extension, bending, torsion, distortion and/or shear) and transverse (due to overall flexure, wall bending and transverse extension) displacements and rotations. As in the case of isolated members, the numerical solution of the discretised system of non-linear algebraic equilibrium equations is obtained by means of an incremental-iterative technique based on Newton-Raphson's method and adopting either a load or a displacement control strategy.

5.1 Illustrative examples

This sub-section includes numerical results concerning the post-buckling behaviours of (i) a laterally restrained lipped channel beam [30] and (ii) a symmetric portal frame [28], both containing critical-mode initial geometrical imperfections. As before, the GBT beam finite element results are compared with values yielded by shell finite element analyses – in this case, carried out in ANSYS and adopting discretisations into SHELL181 element meshes.

5.1.1 Laterally restrained lipped channel beam

The beam analysed is simply supported, has length $L=200cm$, exhibits a C202×75×2.3 cross-section, is acted by a uniformly distributed load q applied at the shear centre axis and is laterally restrained by means of two pairs of rigid supports located at the web-flange corners (see detail in fig. 21) of its 1/3 and 2/3-span cross-sections.

The first step consists of determining the beam buckling behaviour. Figure 21 provides representations of the beam critical buckling mode provided by the ANSYS (3D view) and GBT (modal amplitude functions $\phi_k(x)$) analyses – the corresponding buckling loads are $q_{cr,ANSYS}=0.664\ kN/cm$ and $q_{cr,GBT}=0.671\ kN/cm$ (*1.05%* difference). It is also worth noting that, due to the lateral restraints, only distortional (**5**+**6**) and local (**7**+**8**) deformation modes have perceptible contributions to the beam buckling mode – as expected, the maximum participations of these modes occur in the beam mid-span region.

www.EngineeringEBooksPdf.com

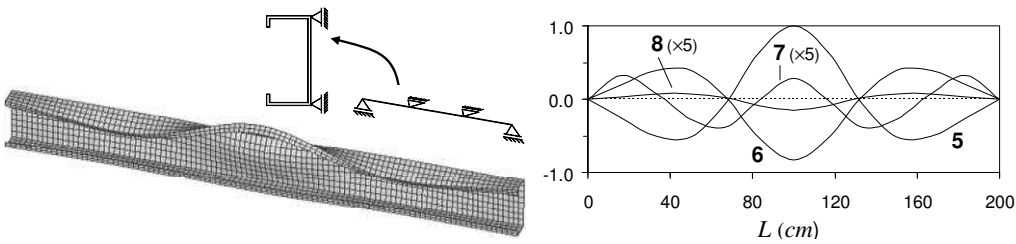


Figure 21: ANSYS and GBT representations of the restrained beam critical buckling mode shape.

The post-buckling analysis performed involves a beam containing critical-mode initial imperfections with amplitude $v_0 = -0.02cm$, where v is the mid-span flange-lip corner vertical displacement – see fig. 22(a). Figure 22(a) shows the equilibrium paths (q vs. v) yielded by the shell (ANSYS) and beam (GBT) finite element analyses. The modal participation diagram of figure 22(b) provides information about the evolution of the "relative participations" of the various GBT deformation modes to the beam deformed mid-span cross-section along the post-buckling equilibrium path. After observing these post-buckling results, one is led to the following conclusions:

(i) A virtually "exact" beam post-buckling equilibrium path is provided by a GBT analysis that includes only deformation modes **1+2+5-8+20+21+36** – for $v<5.0cm$, the differences between the GBT and ANSYS equilibrium paths are always below *3.5%*. Moreover, note that the GBT analyses involve only a small fraction of the number of degrees of freedom required by the ANSYS ones: *168* against over *12500*.

(ii) Major axis flexure (mode **2**) governs the early loading stages and is progressively "replaced" by distortional (modes **5**+**6**) and local (**7**) deformation as the applied load increases.

(iii) The modal participation diagram shows that the contributions of modes **5** and **6-8** decrease until they reach null values, for $q=0.107\,kN/cm$ and $q=0.278kN/cm$, and then gradually increase again. This fact stems from the predominance of major axis flexure (mode **2**), which "forces" modes **5-8** to invert their amplitude signs – *i.e.*, forces the upper flange-lip assembly to move downwards (the initial imperfection made it move upwards).

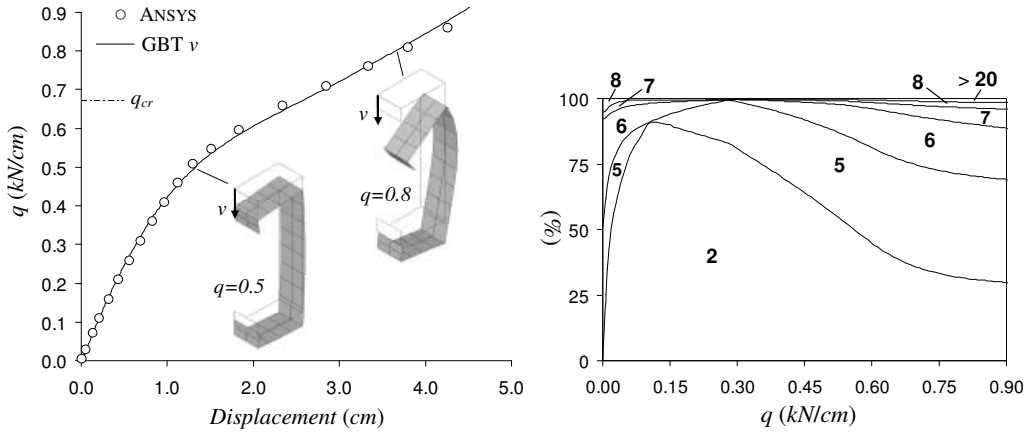


Figure 22: Restrained beam (a) post-buckling equilibrium paths and two mid-span cross-section deformed configurations (ANSYS – ×2), and (b) modal participation diagram concerning the mid-span cross-section.

Figure 23 shows the beam deformed configuration and longitudinal normal stress distribution for $q=0.5kN/cm$, both yielded by the GBT analysis. Note that (i) there is an excellent correlation between the ANSYS and GBT-based mid-span cross-section deformed configuration (see fig. 22(a)), and (ii) high compressive and tensile stresses occur at the beam central third-length, involving the whole width of the top and bottom flanges, respectively.

www.EngineeringEBooksPdf.com

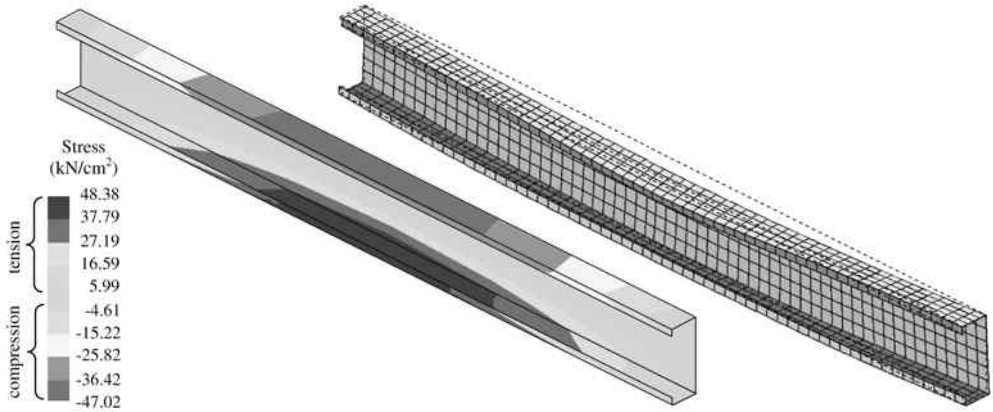


Figure 23: Restrained beam GBT 3D deformed configuration and normal stresses (q=0.5 kN/cm).

5.1.2 Lipped channel portal frame

Finally, one presents the analysis of post-buckling behaviour of the symmetric portal frame depicted in figure 24, which (i) is formed by three equal length (L=70cm) C100×60×1.0 members (columns A + C, and beam B), (ii) has fixed column bases and unstiffened joints with flange continuity, and (iii) is subjected exclusively to uniform axial compression (N_A=N_C=P and N_B=1.2P). Note that this (unrealistic) frame geometry was carefully selected to ensure a high susceptibility to both local and distortional deformations/buckling.

Figure 25 shows the results of the frame buckling analysis: ANSYS (3D view) and GBT (modal amplitude functions in column A and beam B) representations of the critical buckling mode shape, which correspond to $P_{cr,ANSYS}$=14.68kN and $P_{cr,GBT}$=14.34kN (2.32% difference). The frame buckles in "mixed" local-distortional mode that (i) involves the three members and (ii) includes contributions from deformation modes **5** (distortional) and **7+9** (local) – although mode **5** is highly dominant (75.3%), with the maximum values occurring at the beam B mid-span region, there are also non-negligible contributions from modes **7** and **9** in the joint vicinities.

Figure 26 shows post-buckling equilibrium paths involving the transverse displacements ($v_{\bar{Y}}$) of (i) the member A and B mid-span flange-lip corners (points R_1 and R_3) and (ii) the intersection of the flange-lip longitudinal edges at

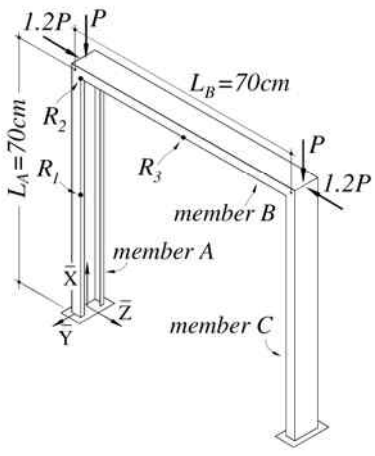


Figure 24: Symmetric portal frame: geometry and loading.

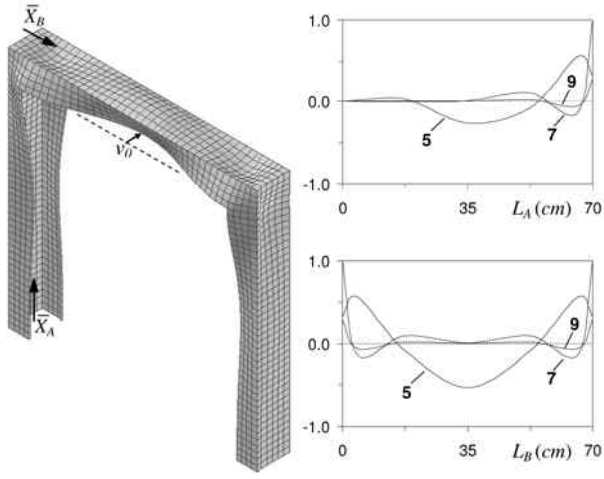


Figure 25: Frame critical buckling mode: 3D view (ANSYS) and column A and beam B modal amplitude functions (GBT).

www.EngineeringEBooksPdf.com

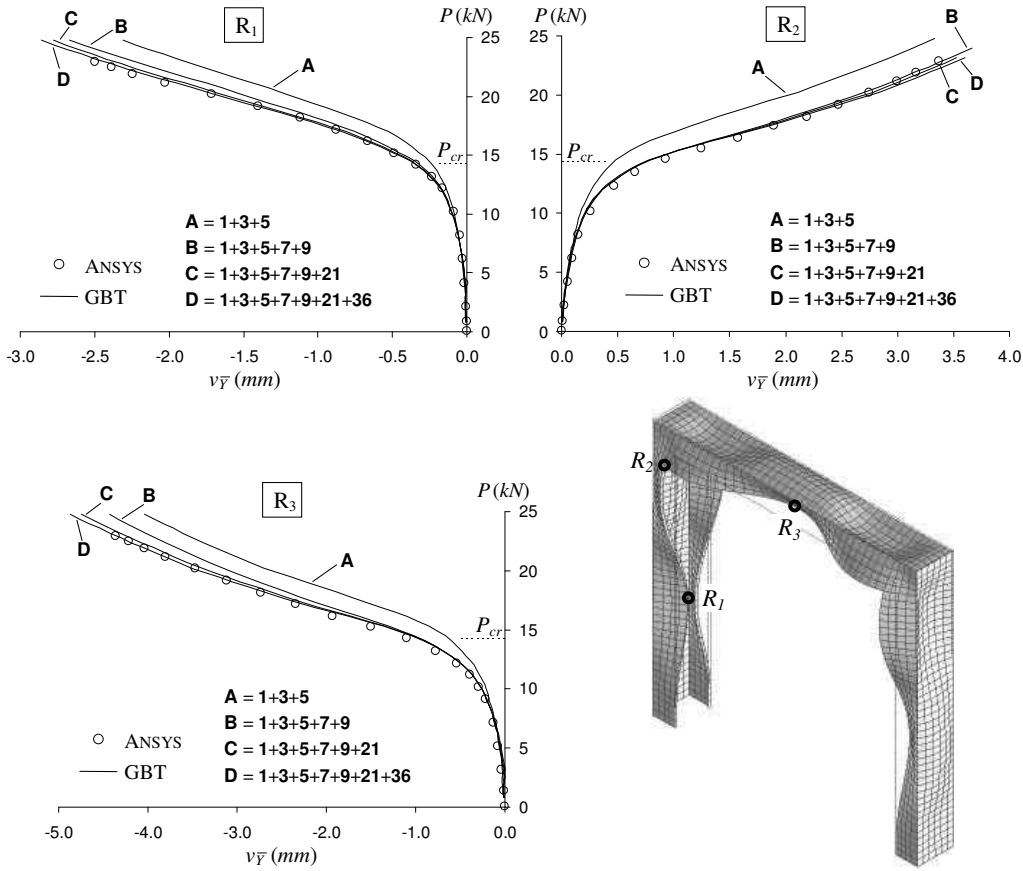


Figure 26: Frame equilibrium paths P vs. $v_{\bar{Y}}$ (points R_1, R_2, R_3) and ANSYS deformed configuration (P=23kN).

the joint (point R_2) – this figure also includes the ANSYS deformed configuration at P=23kN. The frame contains critical-mode initial geometrical imperfections with amplitude v_0=−0.15mm (v_0 is the beam initial $v_{\bar{Y}}$ value – *inward* flange-lip motions). Note that the GBT results presented were obtained with four different deformation mode sets. After comparing these beam (GBT) and shell (ANSYS) finite element post-buckling results, one concludes that:

(i) The "simpler" GBT analysis (only modes **1**+**3**+**5**) provides $V_{\bar{Y}}$ values that are very accurate up to $P\cong 10kN$ (*i.e.*, $P/P_{cr}\cong 0.7$). The accuracy is gradually eroded as P increases, particularly in the beam – *e.g.*, for $P=P_{cr}$ the GBT $V_{\bar{Y}}$ values may underestimate the "exact" (ANSYS) ones by as much as *40%*.

(ii) The sole addition of the local modes **7**+**9** leads to accurate results up to about $P=P_{cr}$. At more advanced post-buckling stages, the GBT model becomes stiffer than the ANSYS one – *e.g.*, for P=23kN (*i.e.*, P/P_{cr}=1.6) GBT provides a $V_{\bar{Y}}$ value at point R_3 that is *10%* above the "exact" one.

(iii) Further adding the warping shear mode **21** considerably improves the accuracy of the results, as the differences between the GBT and ANSYS values become quite small over the whole applied load range – the maximum discrepancy concerns point R_1 (column *A*), where the "exact" $V_{\bar{Y}}$ values is underestimated by *4.5%*.

(iv) Finally, including the transverse extension mode **36** in the analysis leads to virtually coincident GBT and ANSYS post-buckling equilibrium paths – even if the maximum difference is almost the same (*4.0%* for point R_2 and $P=1.6P_{cr}$), there is clear improvement in accuracy brought about by the inclusion of this mode.

(v) Given the similarity between the frame (v_1) critical buckling mode shape, displayed in figure 25, and (v_2) deformed configuration, shown in figure 26, one may conclude it that the frame retains (at least qualitatively) its

www.EngineeringEBooksPdf.com

buckling deformation pattern throughout the whole post-buckling range (up until $P=1.6P_{cr}$).

(vi) Lastly, note once more the very high computational efficiency of the GBT approach: its more "heavy" implementation (*7* deformation modes and *24* beam finite elements – *8* per member) involves *346* degrees of freedom, against the more than *12500* required to perform a similarly accurate ANSYS analysis.

6 VIBRATION ANALYSIS

The system of differential equations to analyse the vibration behaviour of load-free or non-uniformly loaded isotropic members reads

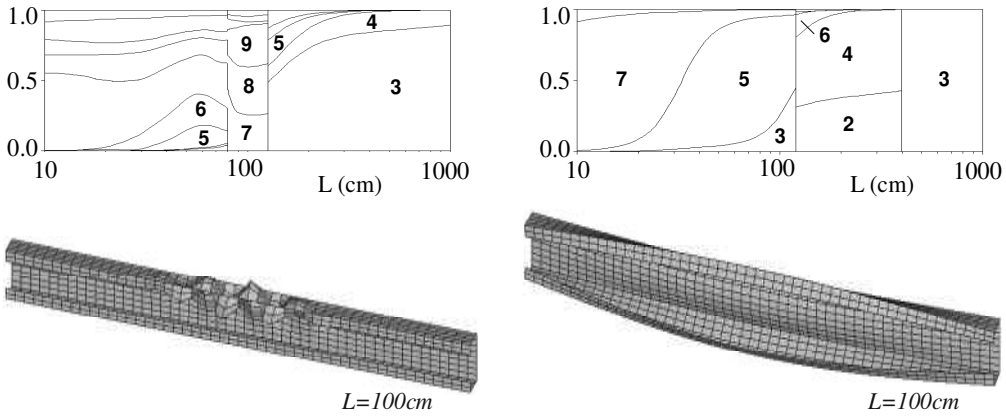
$$\begin{aligned} &C_{ik}\phi_{k,xxxx} - D_{ik}\phi_{k,xx} + B_{ik}\phi_k - \omega^2\left(R_{ik}\phi_k - Q_{ik}\phi_{k,xx}\right) - \\ &- X_{jik}\left(W_j^0\phi_{k,x}\right)_{,x} + X_{jki}^{\tau}\left(W_{j,x}^0\phi_k\right)_{,x} - W_{j,x}^0 X_{jik}^{\tau}\phi_{k,x} = 0 \end{aligned} \quad , \quad (5)$$

where (i) ω are the member *natural frequencies* and (ii) R_{ik} and Q_{ik} are mass components that are given in [31] and account for the influence of the inertia forces on the *out-of-plane* and *in-plane* cross-section displacements – these tensor components include both translational and rotational inertia forces. The solution of this eigenvalue problem is again obtained by means of a GBT-based beam finite element, developed and implemented by Bebiano *et al.* [31], who then employed it to analyse the vibration behaviour of simply supported C100×40×1.0 beams subjected to a uniformly distributed transverse load applied along the shear centre axis – maximum bending moment M, taken as a fraction α of its critical value ($M=\alpha M_{cr}$). The most important aspects of this analysis are presented next.

When investigating the vibration behaviour of a loaded member, it is necessary to begin by studying its buckling and free vibration behaviours. Figures 27(a)-(b) show the corresponding GBT modal participation diagrams composition for beam lengths in the range *10<L<1000cm*, and also the ANSYS critical buckling and fundamental vibration mode shapes of the *L=100cm*. These buckling and vibration results show that:

(i) For *10 <L<80cm*, the beam critical buckling basically combine the local modes **7**-**10**, even if non-negligible participations of the distortional modes **5** and **6** appear for *L>30cm* and grow steadily up to *L≈80cm*. Inside the *80<L<130cm* range modes **7**-**9** govern and for *L>130cm* modes **3**+**4** are clearly predominant.

(ii) The fundamental vibration mode shape is predominantly (ii$_1$) *local* (mode **7**) for *L<25cm*, (ii$_2$) *distortional* (mode **5**, but relevant contributions from modes **3** and **7**) for *25<L<120cm*, (ii$_3$) *flexural-torsional-distortional* (modes **2**, **4** and **6**), for *120<L<400cm*, and (ii$_4$) *purely flexural* (mode **3**), for *L>400cm*.



(a) (b)

Figure 27: Beam (a) critical buckling (uniformly distributed load) and (b) fundamental free vibration modes.

The curves in figure 28(a) provide the variation of the fundamental frequencies $\omega_{f,0}$ ($\alpha=0$ – load-free member) and $\omega_{f,\alpha}$ ($\alpha\neq0$ – members with eight M levels) with L. Moreover, figure 28(b) shows the modal participation

www.EngineeringEBooksPdf.com

diagrams of beams with three of those α values. The observation of these results prompts the following remarks:

(i) The load only causes noticeable fundamental frequency drops for $\alpha \geq 0.25$. Within the $0.5 < \alpha < 0.95$ range, the frequency drop rate increases significantly. Moreover, for $\alpha \geq 0.90$ the curves no longer decrease monotonically – they exhibit more or less pronounced upward branches at short-to-intermediate length ranges.

(ii) Severe fundamental frequency drops (*88%* and *86%*) occur for $110 \leq L \leq 145cm$ – within this length range, the vibration mode changes abruptly from (ii_1) local (**7**-**9**) with *25* half-waves to (ii_2) flexural-torsional-distortional (**3**-**6**) with a single half-wave, *i.e.*, a much more flexible configuration. In order to confirm this particular behaviour, the three ANSYS values included in figure 28(a) were determined – an excellent agreement was found, both in frequency values and vibration mode shapes (not shown here).

(iii) The comparison between the modal participation diagrams for $\alpha=0$ (see fig. 27(b)) and $\alpha=0.1$ shows that, unlike the ω_α value, the fundamental vibration mode shape may be considerably altered by the presence of even quite small applied moments – in fact, either the distortional mode **6** joins modes **5**+**7** (intermediate beams) or the global mode **3** join modes **2**+**4** (longer beams – they are totally separated for $\alpha=0$).

(iv) Inside the $0.1<\alpha<0.95$ range, (iv_1) modes **8**-**10** gradually replace mode **7** (short beams), (iv_2) the contributions of modes **5** and **6** become closer (intermediate beams) and (iv_3) the relevance of mode **2** gradually fades (longer beams). Finally, for $\alpha>0.95$ the vibration mode shapes change quite drastically, approaching their critical buckling mode counterparts – indeed, for $\alpha=0.999$ the beam fundamental vibration and critical buckling modes virtually coincide throughout the whole length range, as attested by the comparison with figure 27(a).

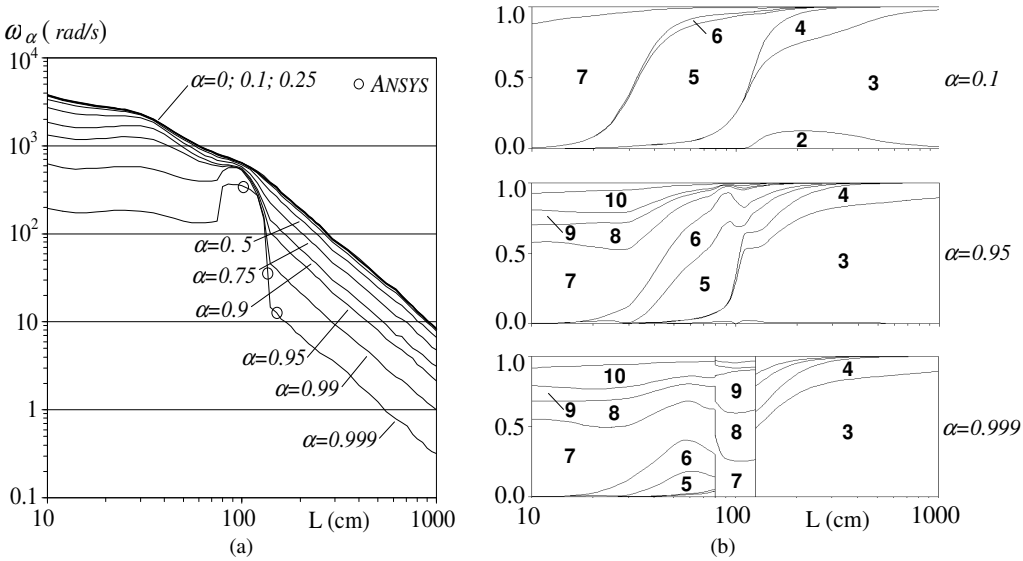


Figure 28: Variation of the fundamental (a) frequency ω_α and (b) vibration mode participation diagram with L ($\alpha=0.0$, *0.95* and *0.999*).

7 DYNAMIC ANALYSIS

Quite recently, Bebiano *et al.* [32] and Bebiano [33] developed a GBT formulation to analyse the local, distortional and global dynamic behaviour of open-section thin-walled members, which combines (i) the GBT modal discretisation with (ii) the classical Vibration Mode Superposition Principle (*e.g.*, [34]. This approach yields an original "doubly modal" displacement field representation that provides in-depth insight on the mechanics involved in the member dynamic response. The main concepts and procedures associated with this GBT formulation are briefly described and commented next:

(i) The system of GBT differential equilibrium equations describing the member dynamic behaviour is written as

www.EngineeringEBooksPdf.com

$$C_{ik}\zeta_{k,xxxx} - D_{ik}\zeta_{k,xx} + B_{ik}\zeta_k - Q_{ik}\zeta_{k,xxtt} + R_{ik}\zeta_{k,tt} - q_i\varphi = 0 \quad , \quad (6)$$

where (i) $\zeta_k(x,t)$ are mode amplitude functions varying along the member axis and with time t, (ii) q_i is the load resultant acting at a cross-section (obtained through the integration over its mid-line) and (iii) function $\varphi(x,t)$ describes the variation of this load resultant with the cross-section location and time.

(ii) The first step of solving (6) by means of the Vibration Mode Superposition Principle consists of determining the member (free) vibration mode shapes, which are the solution of the vibration eigenvalue problem defined by

$$C_{ik}\phi_{kj,xxxx} - D_{ik}\phi_{kj,xx} + B_{ik}\phi_{kj} - \omega_j^2(R_{ik}\phi_{kj} - Q_{ik}\phi_{kj,xx}) = 0 \quad , \quad (7)$$

where function $\phi_{kj}(x)$ provides the amplitude of the contribution of deformation mode k to the member vibration mode j, corresponding to the natural frequency ω_j. The solution of (7) may be obtained (ii_1) analytically, for pinned members, or (ii_2) numerically (GBT-based finite element), for members with other support conditions.

(iii) Then, the above vibration mode shapes are used as *coordinates* to represent the member dynamic response, *i.e.*, the solution of (6) – $\zeta(x, t)$. This solution is expressed as a linear combination of components of the form

$$\zeta_k(x,t) = \phi_{kj}(x)Y_j(t) \quad , \quad (8)$$

where (iii_1) function $Y_j(t)$ describes the time evolution of the component akin to vibration mode j and (iii_2) j varies between *1* and the number of vibration modes incorporated in the dynamic analysis (n_v). The number and nature of such components depends on the particular GBT cross-section discretisation adopted and also on which subset of n_d deformation modes are considered in the analysis.

(iv) In order to determine the n_v functions $Y_j(t)$, thus completely characterising the member dynamic response, it is necessary to solve the differential equation system

$$Y_{j,tt}(t) + \omega_j^2 Y_j(t) = \varphi_j^*(t) \quad , \quad (9)$$

where $\varphi_j^*(t)$ is the generalised load associated with the (vibration) modal coordinate j, whose determination depends on whether the vibration eigenvalue problem (7) is solved analytically or numerically. This system comprises n_v uncoupled equations and, for most loadings, can be solved by means of standard analytical or numerical methods available in the literature.

(v) The member displacement field can finally be expressed as a product of functions of (x,s) and t – one has

$$u(x,s,t) = \{\ [\Phi]_x\ ]\{Y\} \qquad v(x,s,t) = \{\ [\Phi]\}\{Y\} \qquad w(x,s,t) = \{\ [\Phi]\}\{Y\} \quad , \quad (10)$$

where (v_1) the $1{\times}n_d$ vectors $\{\mathbf{u}\}$, $\{\mathbf{v}\}$ and $\{\mathbf{w}\}$ contain the GBT deformation mode shapes $u_k(s)$, $v_k(s)$ and $w_k(s)$, (v_2) the $n_d{\times}n_v$ matrix $[\Phi]$ components $\phi_{kj}(x)$ are longitudinal amplitude functions providing the contributions of each GBT deformation mode to each vibration mode, and (v_3) the $n_v{\times}1$ vector $\{Y\}$ comprises the vibration mode evolution functions $Y_j(t)$**.** Since (10) involves both GBT deformation modes and vibration modes, it may be viewed as a *doubly modal* representation of the member dynamic response. It is possible to identify the individual contribution of a given (v_1) deformation mode (participating in several vibration modes) or (v_2) vibration mode (involving several deformation modes) to the member overall dynamic response.

7.1 Illustrative examples: lipped channel beams

One analyses the dynamic behaviour of a simply supported (locally and globally pinned end section that may warp freely) C100×100×2.0 steel beam with length $L=100cm$ and acted by (i) a uniformly distributed transverse load $q_z=0.01kN/cm^2$, applied on the web with a periodic (sinusoidal) time variation, and (ii) a point transverse load $Q_z=1.0kN$, moving longitudinally (constant speed c) along the beam mid-web segment – see figures 29(a)-(b). The time-dependencies of these loads are described by the functions $\varphi(t)=\sin(\Omega t)$ and $\varphi(x,t)=\delta(x-ct)$, where (i) Ω is the angular frequency and (ii) δ is the Dirac delta function.

7.1.1 Preliminary vibration analysis

Table 1 presents the results of the lipped channel beam free vibration analysis, required to assess the beam dynamic response by means of the Mode Superposition Principle. It includes information concerning the first *10*

www.EngineeringEBooksPdf.com

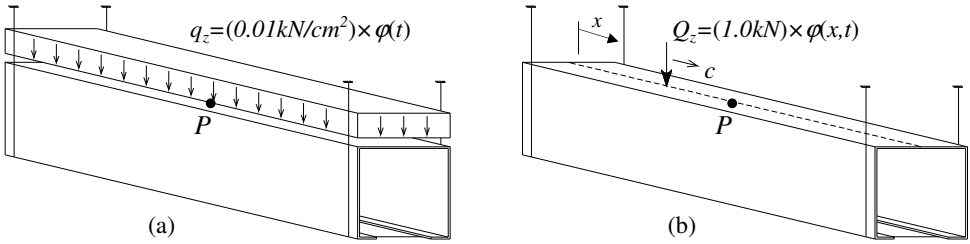


Figure 29: Lipped channel dynamic loadings: (a) uniformly distributed load and (b) moving point load.

vibration modes, namely (i) the natural (angular) frequency values ω_j, obtained by means of GBT and ANSYS (shell finite element) analyses, (ii) the relative differences $\Delta(\%)$ between them, (iii) the number of longitudinal half-waves n_j and (iv) the modal participation factors $mp_k(\%)$. Due to the symmetry of the loadings (with respect to the member major plane), only *symmetric* (odd-numbered) deformation modes were included in the GBT analysis, which implies that the vibration mode orders are different in the GBT and ANSYS analyses (see the first and third columns of table 1) – the latter yields both symmetric (odd-numbered) and anti-symmetric (even-numbered) vibration mode shapes. Note also that, when analysing the beam acted by the uniformly distributed transverse load, only the vibration modes with *odd* half-wave numbers (*i.e.*, longitudinally symmetric) need to be considered: the ***1st***, ***3rd***, ***4th***, ***6th***, ***8th*** and ***10th*** (GBT) vibration modes, whose mid-span cross-section deformed configurations are shown in figure 30.

Table 1 shows that the ω_j values yielded by the GBT (*8* d.o.f.) and ANSYS (*6341* d.o.f.) analyses are almost identical – the higher differences concern the ***3rd*** and ***4th*** (GBT) vibration modes and are equal to *3.11%* and *1.49%*. In spite of these small Δ values, it will be shown later that, in the particular cases dealt with here, the ω_j difference has a non-negligible impact on the beam dynamic response.

Table 1: GBT and ANSYS beam free vibration analysis – ten first natural frequencies and vibration modes.

GBT		ANSYS		n_j	$\Delta(\%)$	Modal Participations (%)							
Mode	ω_j (*rad/s*)	Mode	ω_j (*rad/s*)			mp_3	mp_5	mp_7	mp_9	mp_{11}	mp_{13}	mp_{15}	mp_{17}
1st	582.8	*1st*	582.2	1	0.11	0.58	98.15	1.01	0.22	0.02	0.02	0.00	0.00
2nd	1307.3	*3rd*	1297.2	2	0.77	0.18	93.4	5.24	0.99	0.06	0.10	0.02	0.01
3rd	1871.2	*6th*	1814.8	1	3.11	53.61	32.61	5.34	7.54	0.55	0.26	0.06	0.02
4th	2436.4	*7th*	2400.6	3	1.49	0.14	73.42	23.35	2.46	0.1	0.43	0.06	0.03
5th	3219.0	*9th*	3180.1	4	1.23	0.11	41.82	54.7	1.28	1.09	0.85	0.10	0.05
6th	3557.7	*10th*	3549.3	1	0.24	5.89	45.00	47.24	0.93	0.20	0.60	0.12	0.03
7th	3660.5	*11th*	3642.8	2	0.49	1.47	47.56	42.64	7.17	0.66	0.38	0.08	0.04
8th	3681.4	*12th*	3646.2	5	0.96	0.07	22.04	72.47	1.52	2.39	1.32	0.13	0.06
9th	4097.3	*16th*	4061.4	6	0.88	0.04	12.57	77.85	3.95	3.52	1.81	0.17	0.08
10th	4260.4	*17th*	4227.7	3	0.77	0.27	52.82	33.34	11.91	0.89	0.58	0.12	0.06

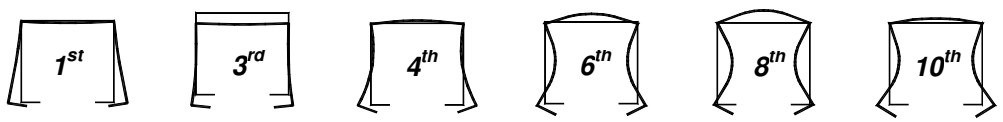


Figure 30: Mid-span cross-section deformed configurations of the ***1st***, ***3rd***, ***4th***, ***6th***, ***8th*** and ***10th*** vibration modes.

www.EngineeringEBooksPdf.com

7.1.2 Dynamic response: periodic (sinusoidal) uniformly distributed load

The transverse displacement of the beam mid-web point P (see fig. 29(a)), obtained through the superposition of its modal contributions, exhibits a sinusoidal time variation and is given by

$$w_P(t) = w_P^M \sin(\Omega t - \theta) \quad , \quad (11)$$

where w_P^M and θ are the response amplitude and phase delay. Figures 31(a)-(b) show the corresponding $w_P^*-\Omega$ and $\theta-\Omega$ curves for the frequency range $0 \leq \Omega \leq 4000 rad/s$ – $w_P^* = w_P^M / w_P^0$ is the w_P dynamic magnification factor and $w_P^0 = 0.178 cm$ is the *static* displacement value. Curves obtained by means of GBT and ANSYS analyses are presented, and it is possible to observe the near coincidence between them. On the other hand, figure 32 provides the individual contributions to the $w_P^*-\Omega$ curve of the (i) **1st**, **3rd** and **6th** vibration modes, and (ii) GBT deformation modes **3**, **5** and **7**. The observation of the results presented in figures 31(a)-(b) and 32 prompts the following remarks:

(i) The $w_P^*-\Omega$ curve exhibits several well defined "peaks" (P_1-P_5 – w_P^* tends to infinity) and "dips" (P'_1-P'_4 – w_P^* tends to zero), corresponding to (i_1) *resonance* with the beam natural vibration modes and (i_2) *anti-resonance*, due to the cancellation of vibration mode contributions (in counter-phase).

(ii) The absence of a dip between P_2 and P_3, "compensated" by the existence of two consecutive ones between P_3 and P_4 (P'_2 and P'_3), is due to the negative amplitude of the **4th** vibration mode contribution (proportional to $-\sin(\Omega t-\theta)$). This means that the contributions of the **4th** and **6th** vibration modes, associated with the resonance frequencies of P_3 and P_4, are in phase with the dynamic load and, thus, P'_2 and P'_3 correspond to cancellations between the (ii_1) **3rd** and **4th**, and (ii_2) **3rd** and **6th** vibration mode contributions. Finally, one last word to mention that, as expected, one has $w_P(t) \equiv w_P^0$ (*i.e.*, $w_P^* = 1$) for $\Omega = 0$ – *i.e.*, when the load acts *statically*.

(iii) Figure 31(b) depicts the typical variation of the response phase delay θ with the loading frequency Ω. Generally speaking, in the vicinity of a given *resonance frequency* ω_j one has (iii_1) $\theta = 0$ for $\Omega < \omega_j$ (in phase), (iii_2) $\theta = \pi$ for $\Omega > \omega_j$ (in counter-phase) and (iii_3) again $\theta = 0$ for Ω higher than the corresponding *anti-resonance frequency* that usually follows. The exception to this behaviour stems from the negative contribution of the **4th** vibration mode: for $\Omega > \omega_3$, θ rises initially from 0 up to π, then rises again from π to 2π and, finally falls back to $\theta = 0$ after the two consecutive anti-resonance frequencies.

(iv) There is an excellent qualitative agreement between the GBT and ANSYS $w_P^*-\Omega$ curves. Quantitatively speaking, such an excellent agreement is slightly "soiled" by a visible horizontal mismatch between the P_2 peaks, due to the *3.11%* difference between the ω_3 values yielded by the two approaches (see table 1). Since the **3rd** vibration mode (associated with the P_2 peak) involves significant minor axis flexure, the above difference stems most likely from *shear lag* effects (not included in the GBT formulation employed).

(iv) Figure 32(a) shows the (expected) *regular* variation of the **1st**, **3rd** and **6th** vibration mode contributions to the beam response with Ω. Each curve has a single peak, for $\Omega = \omega_j$, and then decays asymptotically to zero as $\Omega \rightarrow \infty$. The variation of the deformation mode **3**, **5** and **7** contributions, displayed in figure 32(b), are clearly *irregular*, due to the fact that more than one vibration mode is involved in each of them. Since they characterise

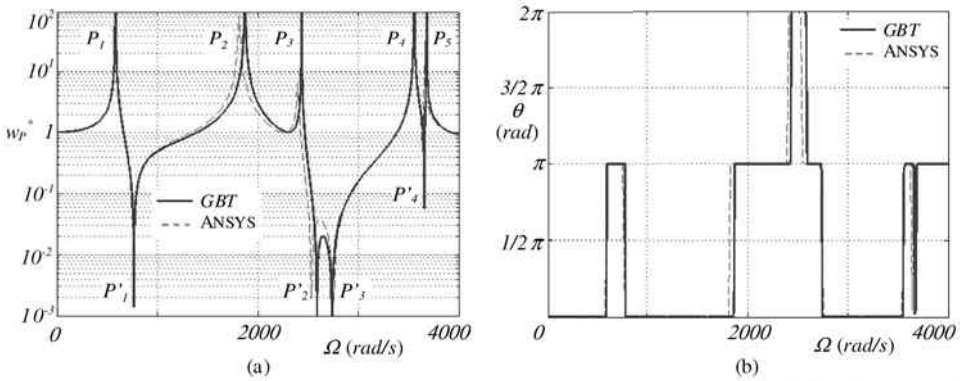


Figure 31: Variation of (a) w_P^* (magnification factor) and (b) θ (phase delay angle) with Ω ($0 \leq \Omega \leq 4000 rad/s$).

www.EngineeringEBooksPdf.com

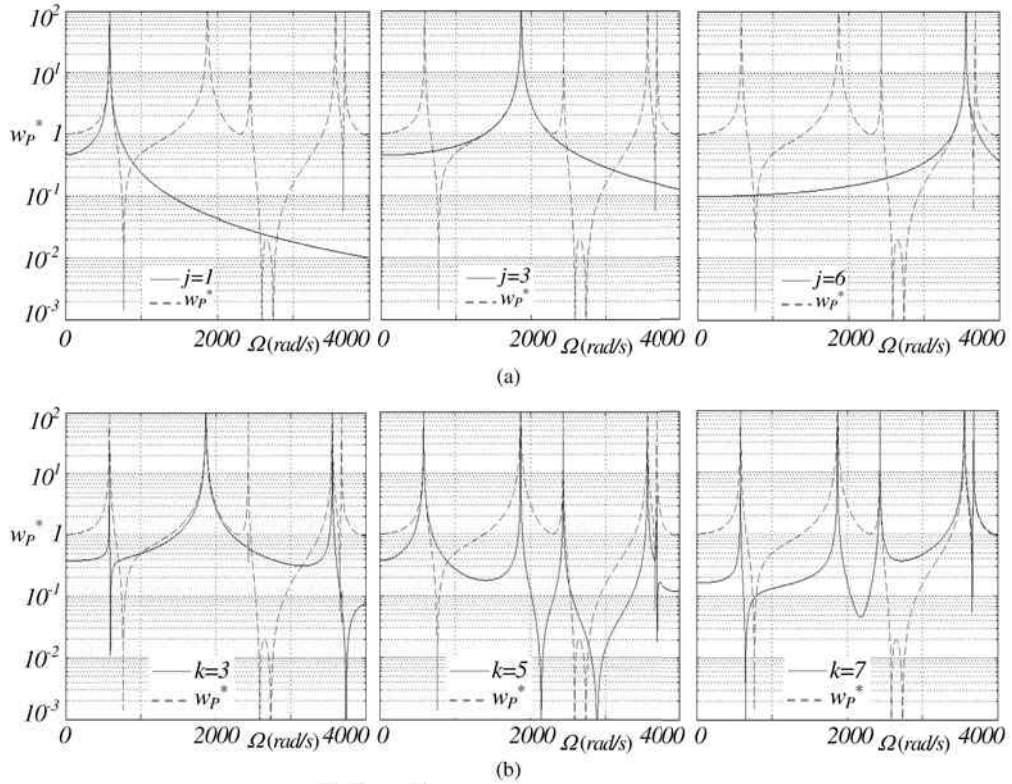


Figure 32: Contributions of the (a) **1st**, **3rd** and **6th** vibration modes and (b) GBT modes **3**, **5** and **7** to the w_P^*–Ω curve.

a specific structural behaviour (minor axis flexure, symmetric distortion or wall bending), several peaks may occur (when Ω equals a "participated" natural frequency), as well as dips (cancellation points). If a deformation mode k is very predominant in a vibration mode j, its contribution to w_P^* is close to the total value for $\Omega \approx \omega_j$ – *e.g.*, the contribution of mode **5** (predominant in the **1st** vibration mode) in the vicinity of peak P_1.

7.1.3 Dynamic response: moving point load

The results presented consist of static and dynamic *influence lines* concerning the vertical displacement of point P (mid-span cross-section mid-web point – see fig. 29(b)). The beam response is again determined by superposing the vibration modes and the aim is to (i) assess the dynamic effects and (ii) investigate how the local (cross-section) deformations influence these effects. This last goal is achieved by performing two GBT analyses, (i) one including only deformation mode **3** (minor axis flexure) and (ii) the other involving all odd-numbered modes **3-17** (n_d=8).

Figure 33(a) show two static influence lines $A_P = w_P / w_P^{max}$ vs. x/L, where (i) $w_P^{max} \approx 0.102cm$ is the maximum displacement, corresponding to the point load acting at mid-span, and (ii) w_P is the displacement caused by the point load acting at cross-section located at a distance x from the beam left support. The two GBT-based curves concern (i) the total displacement (odd-numbered modes **3-17**) and (ii) only the flexural displacement (mode **3**) – they are compared with ANSYS shell finite element values and values yielded by classical beam flexural theory (BFT), respectively. Figure 33(b) provides the modal decomposition of the total displacement curve. One observes that:

(i) While the A_P concerning the total displacement varies quite drastically for $3/8 \leq x/L \leq 5/8$, its flexural counterpart behaves quite "smoothly" and reaches a maximum for $A_P \approx 0.104$ – this means that local deformations account for nearly 90% of A_P. Note also the very good agreement between the GBT results and the ANSYS and BFT values – maximum differences of 4% and 0.1%, respectively (occurring at mid-span).

www.EngineeringEBooksPdf.com

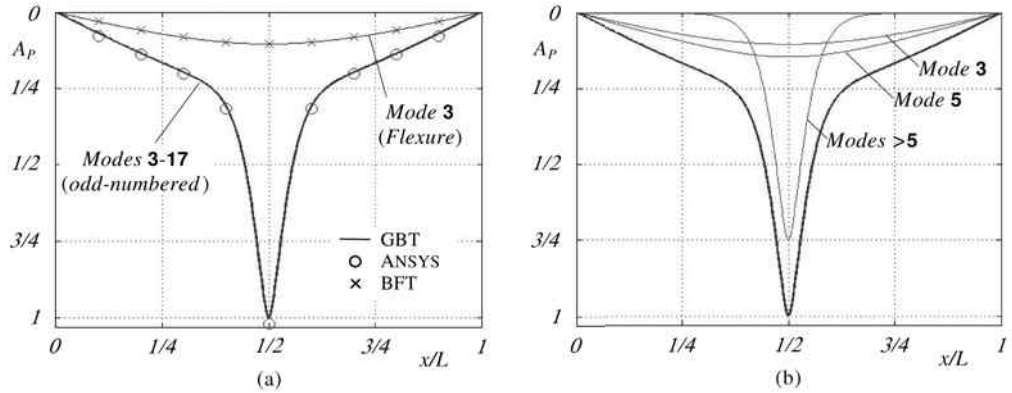


Figure 33: Beam static influence lines A_P vs. x/L (total and flexural displacement) concerning a point load: (a) comparison between GBT, ANSYS and BFT values, and (b) GBT modal decomposition (total displacement).

(ii) The drastic mid-span displacement increase for $3/8 \leq x/L \leq 5/8$ is due to *local deformations* (modes **> 5**, mostly modes **7** and **9**). Indeed, while the contributions of modes **3** (flexure) and **5** (distortion) span the whole x/L range, the local mode ones are practically null outside the $3/8 \leq x/L \leq 5/8$ range. Note also that the contributions of modes **3** and **5** are of the same order of magnitude, even if the latter is always a bit higher.

Figures 34(a)-(b) depict the *dynamic* influence lines w_P^* vs. x/L, where $w_P^* = w_P / w_P^0$ and $w_P^0 \approx 0.102cm$ is the maximum static displacement) due to the moving point load, for (i) both flexural (Euler-Bernoulli) and total displacements, and (ii) various crossing frequencies $f = c/L$ ($f=0$ corresponds to the static influence lines shown in fig. 33(a)). It is worth noting that the free vibration behaviour taking place after the load has left the beam has not been considered (*i.e.*, the influences lines concern only the load *acting on* the bridge). All the influence lines were obtained by means of GBT analyses including (i) the odd-numbered deformation modes **3-17** and (ii) the first *10* vibration modes, characterised in table 1 – note that longitudinal symmetry no longer exists. For validation purposes, figure 34(b) also includes an influence line, concerning $f = 250\ s^{-1}$, that was obtained by means of an ANSYS shell finite element analysis – the moving load was modelled through the application of successive rectangular impulsive nodal loads along the beam "crossed path". These dynamic results lead to the following comments:

(i) The flexural dynamic influence lines exhibit the well-known evolution (*e.g.*, [35]): w_P^* vs. x/L (i_1) "oscillates" closely (small amplitude differences) about the static influence line, for low crossing speeds (*e.g.*,

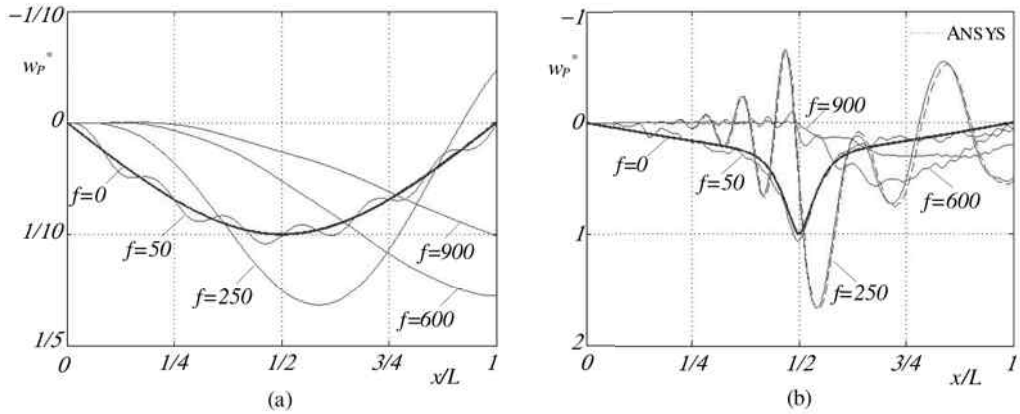


Figure 34: Beam dynamic influence lines w_P^* vs. x/L for crossing frequencies $f = 0, 50, 250, 600, 900\ s^{-1}$: (a) flexural and (b) total displacements (different vertical scales).

www.EngineeringEBooksPdf.com

f=50 s^{-1}), (ii) is "smooth" and exhibits a much higher maximum value when the load is well within the beam span, for intermediate speeds (*e.g.*, f=250 s^{-1}), and (iii) is again "smooth" but exhibits its maximum value when the load leaves the beam, for high speeds (*e.g.*, f >600 s^{-1}). In the latter case, the maximum displacement drops as f increases (recall that the free vibration behaviour occurring after the load exit was neglected) – f≈600 s^{-1} may be viewed as a "critical crossing speed", in the sense that the maximum displacement occurs exactly when the load is about to leave the beam. Note also the *slower* beam response as f increases – w_P^* remains practically null up to progressively higher x/L values.

(ii) Due to the presence of distortional and (mostly) local deformation, the total deformation dynamic influence lines are much more irregular than their flexural counterparts. Nevertheless, they display similar qualitative features, even if the amplification levels are now much higher (note the different vertical scales in figs. 34(a) and 34(b)) – this fact provides clear evidence of the relevance of the cross-section in-plane deformation. Finally, note the virtual coincidence between the GBT and ANSYS f=250 s^{-1} influence lines.

8 CONCLUDING REMARKS AND FUTURE DEVELOPMENTS

This paper presented a state-of-the-art report on the most recent developments concerning formulations, numerical implementations and applications of GBT to analyse the structural response of thin-walled steel members and frames. Following an overview of the fundamental concepts and main procedures involved in the performance of the cross-section analysis, a unified view of the research activity recently carried out at IST (Technical University of Lisbon) was provided, namely by presenting brief accounts and illustrative examples for the various GBT formulations and numerical implemented (beam finite elements) developed in the last couple of years. In particular, the numerical results presented and discussed, aimed at showing the capabilities (numerical efficiency and structural clarity) of the novel GBT approaches, concern the local, distortional and/or global:

(i) First-order behaviour of steel-concrete composite beams and bridge decks (i_1) with cross-sections that combine closed cells with open branches and may include diaphragms (displacement restraints), and (i_2) acted by eccentric vertical loads. Shear lag effects were also taken into account, through the incorporation of specific deformation modes associated with non-linear (sinusoidal) warping along the steel flanges.

(ii) Buckling behaviour of members and frames subjected to complex loadings (namely those causing non-uniform internal force and moment diagrams) and exhibiting non-standard end and localised support conditions (*e.g.*, those modelling displacement restraints associated with bracing systems). Frames built from RHS members were also analysed (but subjected loadings causing only member axial compression).

(iii) Post-buckling behaviour of open-section beams subjected to non-uniform bending, exhibiting localised support conditions and containing critical-mode initial geometrical imperfections.

(iv) Post-buckling behaviour of frames built from open-section profiles, subjected to simple loadings (member axial compression only), exhibiting standard end support conditions (pinned, fixed or free end sections) and also containing critical-mode initial geometrical imperfections.

(v) Vibration behaviour of open-section members subjected to non-uniform internal force and moment diagrams and exhibiting standard end support conditions.

(vi) Dynamic behaviour of open-section members subjected to various loadings, such as a periodic uniformly distributed load or a point load moving along the member span.

For validation and computational efficiency assessment purposes, most the above GBT-based numerical results were compared with values yielded by shell finite element analyses performed in commercial codes (ADINA, ABAQUS and ANSYS). Despite the huge disparity between the numbers of degrees of freedom involved in the two analyses (orders of magnitude apart), an excellent agreement was invariably found. Moreover, the unique modal features of GBT make it possible to acquire in-depth insight on the mechanics of the structural problems investigated and, in some cases, unveil and/or shed new light on interesting phenomena. One must also stress the fact that *one-dimensional* beam models (but including folded-plate theory concepts) are able to provide accurate solutions for various 3D problems involving cross-section in- and out-of-plane deformations of prismatic thin-walled members and frames. For instance, it was possible to investigate in this paper aspects related to the:

(i) Influence of diaphragms located in specific composite bridge deck cross-sections.

www.EngineeringEBooksPdf.com

(ii) Influence of the load position on the cantilever local, distortional and global buckling behaviour.
(iii) Buckling and post-buckling behaviour of members and frames with localised displacement restraints.
(iv) Relevance of including local deformations in the dynamic analysis of thin-walled members.

At this stage, it is also worth mentioning the recent development of a *preliminary version* of a GBT-based code to perform buckling and free vibration analyses of open-section single-span thin-walled members with various end support conditions and acted by non-uniform axial compression and/or bending moment diagrams. This code is designated GBTUL1.0β [36] and can be freely downloaded from a TU Lisbon web page [37].

Before closing the paper, it is worth devoting a few words to mention work either currently under way or planned for the near future, concerning the development/implementation, application and dissemination of GBT formulations. It aims at covering the following (more or less specific) topics:

(i) Local, distortional and global dynamic behaviour of high-speed railway bridge decks – some results have already been reported [38].
(ii) First-order and buckling behaviour of steel-concrete composite structures including an improved concrete material modelling, namely by taking into account the non-linear effects due to cracking.
(iii) Buckling behaviour of plane and space frames acted by transverse loadings applied, taking into account (iv_1) localised effects associated patch loading and/or (iv_2) destabilising/stabilising effects stemming from the location of the load point of application within the cross-section (with respect to the shear centre).
(iv) Local, distortional and global post-buckling behaviour of plane and space frames built from open and closed-section members and exhibiting arbitrary loading and support conditions.
(v) Vibration and dynamic behaviour of plane and space thin-walled frames.
(vi) First-order, buckling and post-buckling behaviour of elastic-plastic thin-walled steel members and frames – in particular, the first step of this research effort will consist of trying to develop a "spatial plastic hinge approach".

Finally, one last word to inform that an upgraded version of the code GBTUL1.0β [36, 37] will be made available in the near future. Besides correcting the bugs detected in the preliminary version, this second version will (i) have a friendlier graphical interface and (ii) cover members with arbitrary polygonal cross-sections, namely those combining closed cells with open branches. Moreover, the development of user-friendly and easy-to-use GBT-based numerical tools to analyse the fist-order and buckling behaviour of open and closed-section thin-walled steel frames is also planned for the not too distant future.

ACKNOWLEDGEMENTS

The second author gratefully acknowledges the financial support of "*Fundação para a Ciência e Tecnologia*" (FCT – Portugal), through the post-doctoral scholarship nº SFRH/BPD/62904/2009.

REFERENCES

[1] Schardt R., *Verallgemeinerte Technische Biegetheorie*, Springer-Verlag, Berlin, 1989. (German)

[2] Davies J.M. and Leach P., "First-order generalised beam theory", *Journal of Constructional Steel Research*, **31**(2-3), 187-220, 1994.

[3] Davies J.M., Leach P. and Heinz D., "Second-order generalised beam theory", *Journal of Constructional Steel Research*, **31**(2-3), 221-241, 1994.

[4] Schardt C., *Bibliographie zur VTB – Bibliograpy of the Generalized BeamTheory*, http://www.vtb.info/, 2001.

[5] Camotim D., Silvestre N., Gonçalves R. and Dinis P.B., "GBT analysis of thin-walled members: new formulations and applications", *Thin-Walled Structures: Recent Advances and Future Trends in Thin-Walled Structures Technology* (Loughborough, 25/6), J. Loughlan (ed.), Canopus Publishing, Bath, 137-168, 2004.

[6] Camotim D., Silvestre N., Gonçalves R. and Dinis P.B., "GBT-based structural analysis of thin-walled members: overview, recent progress and future developments", *Advances in Engineering Structures, Mechanics and Construction* (Waterloo, 14-17/5), M. Pandey, W.C. Xie, L. Xu (eds.), Springer, Dordrecht, 187-204, 2006.

www.EngineeringEBooksPdf.com

[7] Camotim D., Basaglia C. and Silvestre N., "GBT buckling analysis of thin-walled steel frames: A state-of-the-art report", *Thin-Walled Structures*, 2010, in press.

[8] Bathe K.J., *ADINA System*, ADINA R&D Inc., 2003.

[9] Simulia Inc. *ABAQUS Standard*, version 6.7-5, 2008.

[10] Swanson Analysis Systems Inc., *ANSYS Reference Manual*, version 8.1, 2004.

[11] Silvestre N. and Camotim D., "First-order generalised beam theory for arbitrary orthotropic materials", *Thin-Walled Structures*, **40**(9), 755-789, 2002.

[12] Dinis P.B., Camotim D. and Silvestre N., "GBT formulation to analyse the buckling behaviour of thin-walled members with arbitrarily 'branched' open cross-sections", *Thin-Walled Structures*, **44**(1), 20-38, 2006

[13] Gonçalves R., Dinis P.B. and Camotim D., "GBT formulation to analyse the first-order and buckling behaviour of thin-walled members with arbitrary cross-sections", *Thin-Walled Structures*, **47**(5), 583-600, 2009.

[14] Silvestre N., "Generalised beam theory to analyse the buckling behaviour of circular cylindrical shell and tubes", *Thin-Walled Structures*, **45**(2), 185-198, 2007.

[15] Silvestre N., "Buckling behaviour of elliptical cylindrical shells and tubes under compression", *International Journal of Solids and Structures*, **45**(16), 4427-4447, 2008.

[16] Silvestre N. and Camotim D., "Non-linear generalised beam theory for cold-formed steel members", *International Journal of Structural Stability and Dynamics*, **3**(4)**,** 461-490, 2003.

[17] Gonçalves R., Ritto Corrêa M. and Camotim D., "A new approach to the calculation of cross-section deformation modes in the framework of generalised beam theory", *Computational Mechanics*, accepted for publication, 2010.

[18] Gonçalves R. and Camotim D., "Steel-concrete composite bridge analysis using generalised beam theory", *Steel & Composite Structures*, accepted for publication, 2010.

[19] Silvestre N. and Camotim D., "Local-plate and distortional post-buckling behavior of cold-formed steel lipped channel columns with intermediate stiffeners", *Journal of Structural Engineering* (ASCE), **132**(4), 529-540, 2006.

[20] Dinis P.B., Gonçalves R. and Camotim D., "On the local and global buckling behaviour of cold-formed steel hollow-flange channel beams", *Proceedings of 5th International Conference on Thin-Walled Structures* (ICTWS 2008 – Brisbane, 18-20/6), M. Mahendran (ed.), 425-432, 2008.

[21] Bebiano R., Silvestre N. and Camotim D., "Local and global vibration of thin-walled members subjected to compression and non-uniform bending", *Journal of Sound and Vibration*, **315**(3), 509-535, 2008.

[22] Camotim D., Silvestre N., Basaglia C. and Bebiano R., "GBT-based buckling analysis of thin-walled members with non-standard support conditions", *Thin-Walled Structures*, **46**(7-9), 800-815, 2008.

[23] Silva N.F., Camotim D. and Silvestre N., "Generalized beam theory formulation capable of capturing localized web buckling and load application effects", *Proceedings of 19th Specialty Conference on Cold-Formed Steel Structures*, (St. Louis, 14-16/10)**,** R. LaBoube, W.-W. Yu (eds.), 33-59, 2008.

[24] Basaglia C., *Non-Linear Analysis of Thin-Walled Steel Members and Frames Using Generalised Beam Theory*, Ph.D. Thesis, IST, Technical University of Lisbon, 2010. (Portuguese)

[25] Basaglia C. and Camotim D., "Buckling analysis of cold-formed RHS frames using generalised beam theory", *Proceedings of 13th International Symposium on Tubular Strucutures* (Hong Kong, 15-17/12), in press, 2010.

[26] Basaglia C., Camotim D. and Silvestre N., "Buckling behaviour of locally and globally braced thin-walled steel frames", *Proceedings of 6th International Conference on Advances in Steel Structures* (ICASS'09 – Hong Kong, 16-18/12), S.L. Chan (ed.), 891-890, 2009.

[27] Basaglia C., Camotim D and Silvestre N., "Non-linear GBT formulation for open-section thin-walled members with arbitrary support conditions", *Proceedings of 12th International Conference on Civil, Structural*

www.EngineeringEBooksPdf.com

and Environmental Engineering Computing (CC 2009 – Funchal, 1-4/9), B. Topping *et al.* (eds), Civil-Comp Press, 21, 2009. (full paper in CD-ROM Proceedings)

[28] Basaglia C., Camotim D. and Silvestre N., "Non-linear GBT for thin-walled steel frames: formulation, implementation and application", *Proceedings of SSRC Annual Stability Conference* (Orlando, 12-15/5), 461-480, 2010.

[29] Basaglia C., Camotim D. and Silvestre N., "Local, distortional and global post-buckling analysis of frames using generalised beam theory", *Proceedings of 10th International Conference on Computational Structures Technology* (CST 2010 – Valencia, 14-17/9), in press, 2010.

[30] Basaglia C., Camotim D. and Silvestre N., "Non-linear GBT formulation for open-section thin-walled members with arbitrary support conditions", *submitted for publication,* 2009.

[31] Bebiano R., Silvestre N. and Camotim D., "Local and global vibration of thin-walled members subjected to compression and non-uniform bending", *Journal of Sound and Vibration*, **315**(3), 509-535, 2008.

[32] Bebiano R., Silvestre N., and Camotim D., "GBT-based dynamic analysis of thin-walled members", *Proceedings of 5th International Conference on Thin-Walled Structures* (ICTWS 2008 – Brisbane, 18-20/6), M. Mahendran (ed.), 1197-1210, 2008.

[33] Bebiano R., *Stability and Dynamics of Thin-Walled Members: Application of Generalised Beam Theory*, Ph.D. Thesis, IST, Technical University of Lisbon, 2010.

[34] Clough R.W. and Penzien J., *Dynamics of Structures* (2nd ed.), McGraw-Hill, New-York, 1993.

[35] Frýba L., *Vibration of Solids and Structures under Moving Loads* (3rd ed.), Thomas Telford, London, 1999.

[36] Bebiano R., Silvestre N. and Camotim D., "GBTUL – a code for the buckling analysis of cold-formed steel members", *Proceedings of 19th International Specialty Conference on Recent Research and Developments in Cold-Formed Steel Design and Construction* (St. Louis, 14-15/10), R. LaBoube, W.-W. Yu (eds.), 61-79, 2008.

[37] Bebiano R., Silvestre N. and Camotim D., *GBTUL 1.0β - Code for Buckling and Vibration Analysis of Thin-Walled Members*, freely available at http://www.civil.ist.utl.pt/gbt, 2008.

[38] Bebiano R., Silvestre N. and Camotim D., "Generalized beam theory-based local and global dynamic analysis of high-speed railway bridge decks", *Proceedings of 12th International Conference on Civil, Structural and Environmental Engineering Computing* (CC 2009 –Funchal, 1-4/9), B.H.V Topping *et al.* (eds.), Civil-Comp Press, 12, 2009. (full paper in CD-ROM Proceedings)

www.EngineeringEBooksPdf.com

SDSS'Rio 2010 STABILITY AND DUCTILITY OF STEEL STRUCTURES
E. Batista, P. Vellasco, L. de Lima (Eds.)
Rio de Janeiro, Brazil, September 8 - 10, 2010

DUAL-STEEL FRAMES FOR MULTISTORY BUILDINGS IN SEISMIC AREAS

D. Dubina*,**

* The "Politehnica" University of Timisoara, 1 Ioan Curea, 300224 Timisoara, Romania
e-mail: dan.dubina@ct.upt.ro
** Romanian Academy, Timisoara Branch, 24 Mihai Viteazul, 300223 Timisoara, Romania

Keywords: Dual steel, High strength steel, Ductility.

Abstract. *Seismic resistant building frames designed as dissipative structures must allow for plastic deformations to develop in specific members, whose behavior has to be predicted by proper design. Members designed to remain elastic during earthquake, such as columns, are responsible for robustness of the structure and prevention the collapse, being characterized by high strength demands. Consequently, a framing solution obtained by combining HSS and MCS, is natural. The robustness of structures to severe seismic action is ensured by their global performance, in terms of ductility, stiffness and strength, e.g. the "plastic" members of MCS – (S235 to S355) will dissipate the seismic energy, acting like "structural fuses", while the "elastic" members (HSS - S460 to S690), provided with adequate overstrength, will have the capacity to carry the supplementary stresses, following the redistribution of forces after appearance of plastic hinges. Such a structure is termed dual-steel structure. When braced frames of removable MCS dissipative members are used, such as the links in EBF , Buckling Restrained Braces in CBF or Shear Walls in MRF systems, the elastic HSS part of the structure has a beneficial restoring effect after earthquake enabling to replace the "fuses" .Dual-steel approach can be considered for beam-to column connections, too, on the same philosophy related to the role of ductile and brittle components. The paper summarizes the numerical and experimental results obtained on this subject in the Department of Steel Structures and Structural Mechanics at the Politehnica University of Timisoara.*

1 INTRODUCTION

Multi-storey steel buildings are assigned to one of the following structural types, depending to the behavior of their lateral force resisting systems [1]:
- moment resisting frames (MRF), in which the horizontal forces are mainly resisted by members acting essentially in flexural mode; for such structures the performance of MR joints is crucial;
- frames with concentric bracings (CBF), in which the horizontal forces are mainly resisted by members subjected to axial forces;
- frames with eccentric bracings (EBF), in which the horizontal forces are mainly resisted by axially loaded members, but where the eccentricity of the layout is such that energy can be dissipated in seismic links by means of either cyclic bending or cyclic shear;
- moment resisting frames combined with dissipative shear walls (SW), which resist lateral forces by shear.

Ussualy, current building frames are Dual-Structures (DS) obtained by combination of a MRF with one of the lateral resisting systems, eg. MRF + CBF, MRF + EBF, MRF + SW.

Each of these structural systems dissipates a part of the seismic energy imparted in the structure through plastic deformations in the dissipative zones of the ductile members (i.e. beams in MRF, links in EBF or braces in CBF). The other members should remain in the linear range of response because nonlinear response is not feasible (i.e. columns). In order to avoid the development of plastic hinges in

www.EngineeringEBooksPdf.com

these non-dissipative members, they must be provided with sufficient overstrength. To ensure this overstrength, European seismic design code EN1998, amplifies the design forces and moments by a multiplier equal to $1,1\gamma ov$, where 1.1 takes into account for stress hardening, γ_{ov} is the overstrength factor and Ω is the ratio between the plastic resistance and the design value of the force in the dissipative member. In case of HSS structures, the values of factors composing this multiplier need to be very carefully analyzed. For some structural configurations (i.e. CBFs), the Ω factor may result considerably high, due to the fact that other non-seismic combinations (e.g. wind load) could be critical. A similar approach is also used in the AISC 2005 [2], where this factor may reach a value of 3 for some structural types. Even though, the verification of the non-dissipative members using such amplified forces do not guarantee they will behave entirely in the elastic range.

In order to get an economic design of the structure is necessary to keep the stresses quite low in the "dissipative" members using lower yield steel, and therefore to reduce the demand in the "non-dissipative" members, made by higher yield strength steel but still current. Such a solution has been recently applied to the design of a 26 story steel building frame in Bucharest, where lower yield strength steel S235 was used for the dissipative braces in the CBFs, while the other members were of S355 [3]. If this option is not possible, the alternative is to increase the strength of the non-dissipative members by using heavier sections or by using higher yield strength steel. For MRF structures, first option is recommended, as this will lead to an increase of the stiffness, which in many cases is critical in the seismic design, but for braced structures or for dual structures, this will lead to a stress concentration in the non-dissipative members (i.e. columns). For these structures, the adoption of high strength steel in the non-dissipative members (e.g. to remain in elastic range during the earthquake) seems to be more likely. However, previous results obtained by Dubina et al [4] have shown that for MRF structures, strengthening of columns by using HSS may be effective to avoid column failure in case of "near-collapse" state. This may also improve robustness of structure in case of other extreme loads (e.g. impact, blast). In case of such Dual Steel Frames, particular care is needed for the proper location and seizing of member sections of different materials, as well as for their connections. The design target is to obtain a dissipative structure, composed by "plastic" and "elastic" members, able to form a full global plastic mechanism at the failure, in which the history of occurrence of plastic hinges in ductile members can be reliable controlled by design procedures. To sustain these assumptions, a numerical study developed on DS of *conventional* CBF and EBF and on *non-conventional* braced systems, e.g. EBF of bolted removable links, CBF of Buckling Restrained Braces (BRB) and MRF of Steel Plate Shear Walls (SPSW), is presented. These so called "non-conventional" systems use dissipative components made by Mild Carbon Steel (MCS), which act as "seismic fuses" and are sacrificial member, which after a strong earthquake can be replaced.

2 SEISMIC PERFORMANCE OF DUAL STEEL FRAMES

2.1 Dual steel frames' modeling and design

Four building frame typologies of eight and sixteen story, respectively, are considered [5]. The four lateral load resisting systems are: Eccentrically Braced Frames (EBF), Centrically V Braced Frames (CBF), Buckling Restrained Braced Frames (BRB) and Shear Walls (SW) (Figure 1). They are made by European H-shaped profiles. EBF, CBF and BRB systems have three bays of 6m. SW system has exterior moment frames bays of 5.0m, interior moment frame bay of 3.0m and shear wall bays of 2.5m. All structures have equal storey heights of 3.5m. Each building structure use different combinations of Mild Carbon Steel S235 and High Strength Steel S460. The design was carried out according to EN1993-1 [6], EN1998-1 and P100-1/2006 (Romanian seismic design code, aligned to EN1998-1) [7]. A 4 kN/m^2 dead load on the typical floor and 3.5kN/m^2 for the roof were considered, while the live load amounts 2.0kN/m^2. The buildings are located in a moderate to high risk seismic area (i.e. the Romanian capital, Bucharest), which is characterized by a design peak ground acceleration for a returning period of 100 years equal to 0.24g and soft soil conditions, with T_c=1.6sec. It is noteworthy the long corner period of

www.EngineeringEBooksPdf.com

the soil, which in this case may affect flexible structures. In such a case, there is a large demand in terms of plastic deformation capacity for dissipativelly designed components, while it is very difficult to keep elastic the non-dissipative ones. For serviceability check, the returning period is 30 years (peak ground acceleration equal to 0.12g), while for collapse prevention it is 475 years (peak ground acceleration equal to 0.36g) (P100-1, 2006). Interstory drift limitation of 0.008 of the storey height was considered for the serviceability verifications.

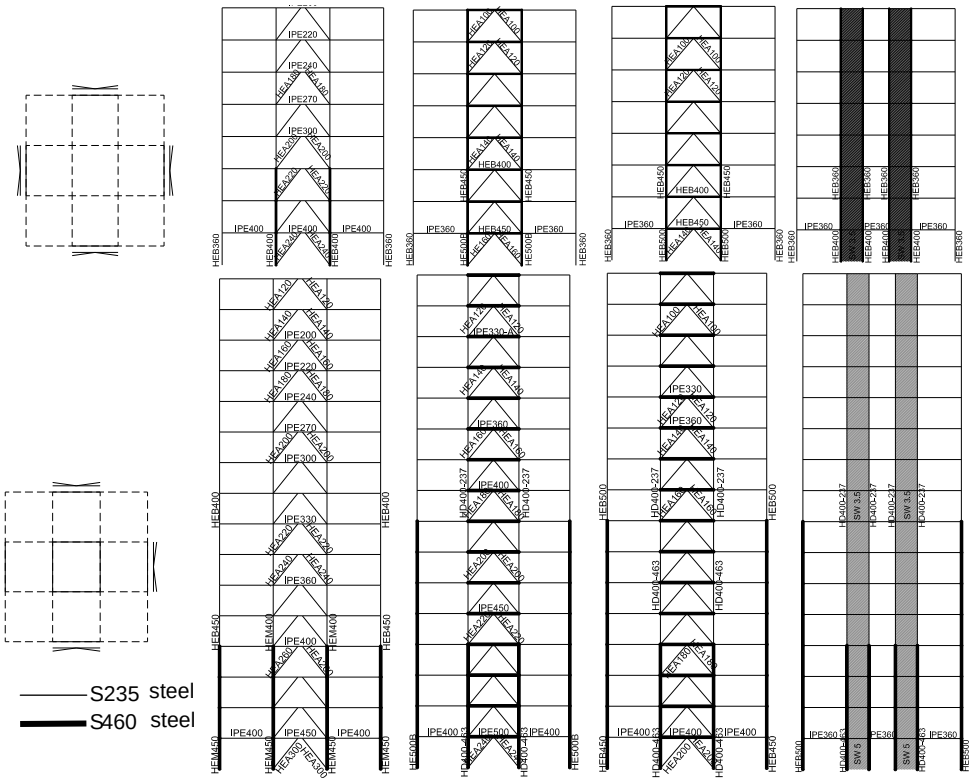


Figure 1. Frame systems: (a) plan view and elevation of EBF8, CBF8, BRB8 and SW8 structures; (b) plan view and elevation of EBF16, CBF16, BRB16 and SW16 structures

According to EN1998-1, the maximum value of the reduction factor q for dual frame systems of moment frames and eccentrically braced frames (MRF+EBF) is equal to 6. For dual frame systems made from moment frames and centrically braced frames (MRF+CBF), q factor amounts 4.8. For dual frame systems of moment frames and buckling restrained braces (MRF+BRB) and moment frames and shear walls (MRF+SW), EN1998-1 does not provide any recommendations regarding the q factor. For these structural systems, AISC 2005 provisions were taken as guidance. According to the later code, the reduction factor for MRF+BRB systems and MRF+SW is similar to that of special moment frames. Concluding, the design was based on a q factor equal to 6, excepting the MRF+CBF, which was designed for q equal to 4.8. For designing the non-dissipative members, EN1998-1 and P100-1/2006 amplifies the design seismic action by a multiplicative factor $1.1\gamma_{ov}\,\Omega$, where γ_{ov} is equal to 1.25. Unlike EN1998-1, which considers Ω as the minimum value of Ω_i among all dissipative members, Romanian code P100-1/2006 suggests the use of maximum value. A similar approach is also employed in AISC 2005, where the multiplicative factor $1.1\gamma_{ov}\Omega$ is replaced by a unique factor Ω_0, called the overstrength factor. AISC

www.EngineeringEBooksPdf.com

2005 and P100-1/2006 also contain values of multiplicative factors to be used in design, which ranges between 2.0 and 2.5. Table 1 presents the multiplicative factors for each structural system obtained by calculation. The overstrength factors Ω range between 1.90 and 2.90 for eight story structures and between 1.70 and 2.90 for sixteen story structures. For the eight-story building, two exterior bays of braces or shear walls on each exterior frames were necessary. For sixteen story building, the larger demand in lateral resisting capacity leads to braces or shear walls in all for bays.

The four structural systems were designed for similar base shear force capacities, with the exception of EBF, which were designed for lower capacities. The first mode periods for eight and sixteen story structures are presented in Table 1. It may be seen the four structural systems amount almost identical the first-mode periods.

Table 1. First mode periods and multiplicative factors for the structures

Structure	EBF8	CBF8	BRB8	SW8
1.1γov Ω	2.2	2.2	1.9	2.9
Period, [sec]	0.92	0.97	0.97	1.00
Structure	EBF16	CBF16	BRB16	SW16
1.1γov Ω	2.9	1.7	2.1	2.5
Period, [sec]	1.79	1.53	1.61	1.61

Beams and columns were modelled with plastic hinges located at both ends. In order to take into account the buckling of the diagonals in compression, the post buckling resistance of the brace in compression was set 0.2Nb,Rd (Figure 2.a), where Afy is the tensile yield resistance and $N_{b,Rd}$ is the buckling resistance for compression [8]. For the braces of the BRB systems, similar behaviour in tension and compression was adopted, as the buckling in compression is prevented (Figure 2.b). The inelastic shear link element model used for the EBF systems was based on the proposal of Ricles and Popov [9]. As the original model consisted in four linear branches, it was adapted to the trilinear envelope curve available in SAP2000 [10]. A rigid plastic behaviour was adopted till the attainment of the shear plastic capacity.

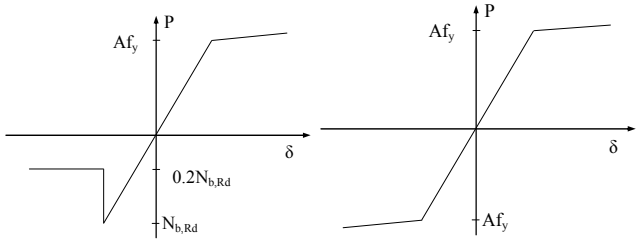


Figure 2. Response of bracing members: a) conventional brace; b) buckling restrained brace

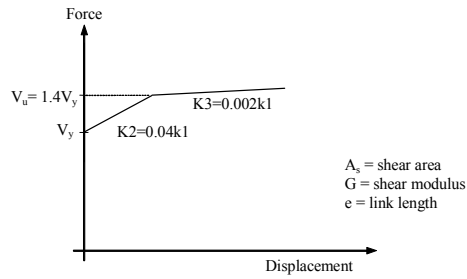


Figure 3. Force – displacement relationships for shear link element

www.EngineeringEBooksPdf.com

For the shear wall structures (SW), non-compact shear walls, with the slenderness ratio h/tw larger than λp but smaller than λr were selected (Figure 4) [11], where k_v is given by:

$$kv = 5 + \frac{5}{(a/h)^2}$$
$$= 5 \text{ when } a/h > 3.0 \text{ or } a/h > \left[260/\left(h/t_w\right)\right]^2 \quad (1)$$

where a is the distance between tension fields

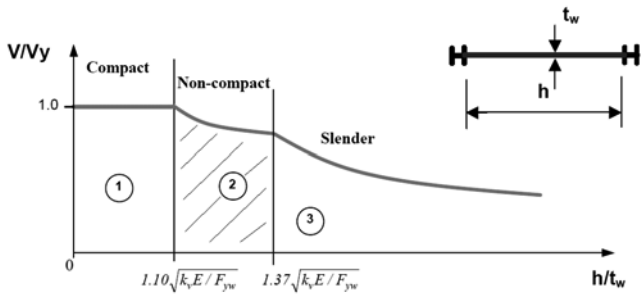


Figure 4. The regions of behaviour of the steel shear walls

The walls framed within this category are expected to buckle, while some shear yielding has already taken place. In this case, the story shear is resisted by the horizontal components of the tension and compression diagonal forces. In order to model the steel shear walls, Thorburn et al. [12], replaced the steel plates by a series of truss members (strips), parallel to tension fields (Figure 5). In this model, the infill steel plate is modelled as a series of tension–only strips oriented at the same angle of inclination, α, as the tension field. Studies have shown that ten strips per panel adequately represent the tension field action developed in the plate. Driver et al. [13] noted that there were certain phenomena present in steel plate shear wall behaviour that are not captured by the strip model. In their study, a compression strut oriented in the opposite diagonal direction to that of the tension strips was introduced. Moreover, a discrete axial hinge that includes the effects of deterioration was provided only for the two tension strips that intersect the frame closest to the opposite corners of the steel plate shear wall panel, as shown in Figure 5. The equation for the area of the compression strut is as follows:

$$A = \frac{tL\sin^2 2\alpha}{2\sin\phi\sin 2\phi} \quad (2)$$

where

-ϕ is the acute angle of the brace with respect to the column;

- L is the centre-to-centre distance of columns;

-α is the angle of inclination of the average principle tensile stresses in the infill plate with respect to the boundary column;

- t is the infill plate thickness.

The equation for ϕ is as follows:

$$\tan\phi = \sqrt[4]{\frac{1 + tL/2A_c}{1 + th\left(1/A_b + h^3/360I_cL\right)}} \quad (3)$$

The width and spacing of the pin-ended tension and deterioration strips for each panel, based on ten strips per panel, were calculated to determine the area of each strip. The area calculated for the

www.EngineeringEBooksPdf.com

compression strut is equally distributed among the tension strips. Figure 6 presents the typical behaviour for axial tension strip hinge, compression strut hinge and deterioration strip hinge.

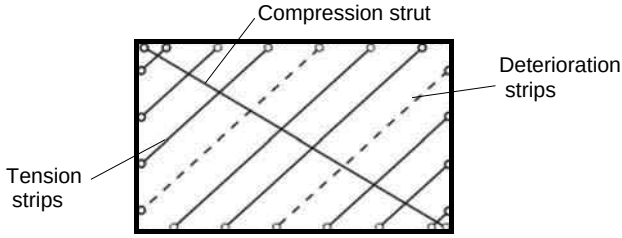


Figure 5. Strip model

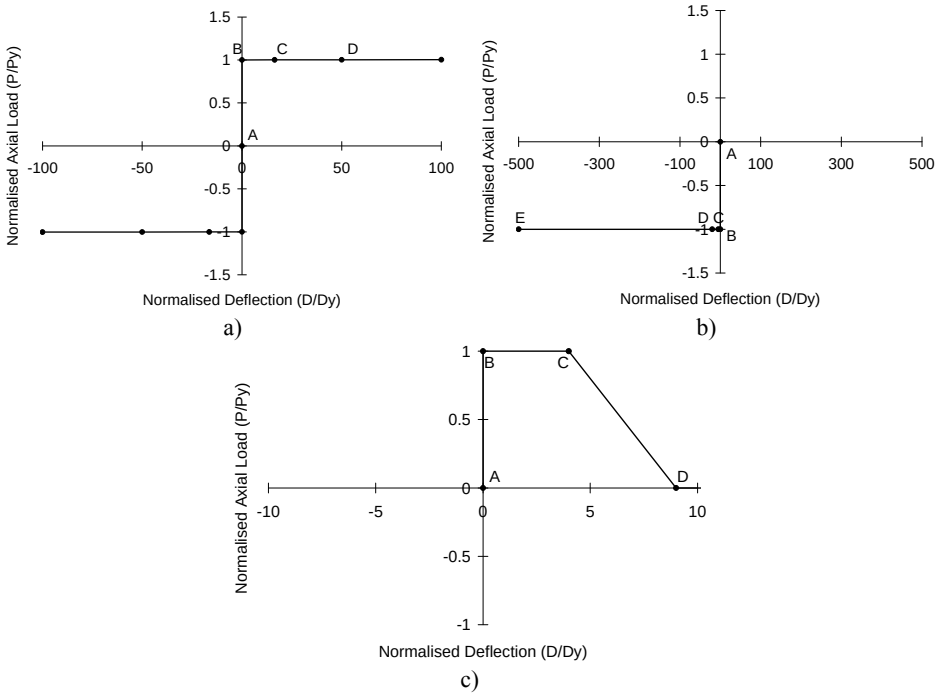


Figure 6. Axial hinge definitions: a) tension strip (infill plate); b) compression strut; c) deterioration hinge

2.2 Performance Based Evaluation

The nonlinear response of the structures was analysed using the N2 method [14]. This method combines the push-over analysis of a multi-degree of freedom model (MDOF) with the response spectrum analysis of a single degree of freedom system (SDOF). The elastic acceleration response spectrum was determined according to Romanian seismic code P100-1/2006, for a peak ground acceleration of 0.24g. The lateral force, used in the push-over analysis, has a "uniform" pattern and is proportional to mass, regardless of elevation (uniform response acceleration). The non-linear analysis was performed with SAP2000 computer program. Table 2 shows the values of target displacement, D_t, for the studied frames, calculated using N2 method.

www.EngineeringEBooksPdf.com

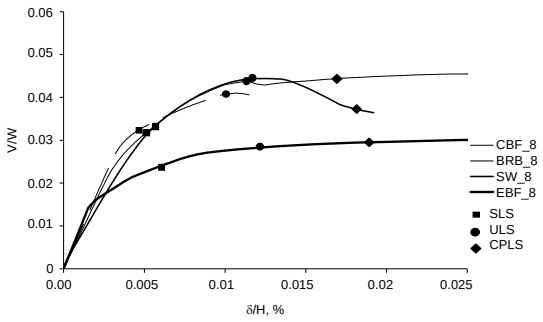
Table 2. Target displacement, D_t, for the MDOF systems for ULS

Structure	EBF8	CBF8	BRB8	SW8
D_t, [m]	0.34	0.29	0.31	0.32
Structure	EBF16	CBF16	BRB16	SW16
D_t, [m]	0.64	0.49	0.53	0.62

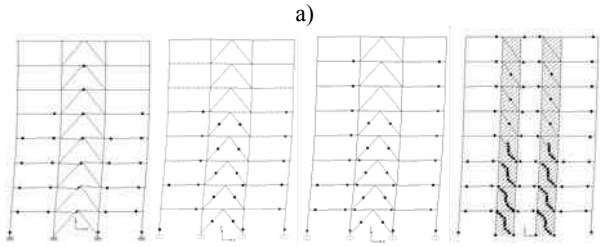
Three performance levels were considered: serviceability limit state (SLS), ultimate limit state (ULS) and collapse prevention (CPLS) limit state. Intensity of earthquake action at the ULS is equal to the design one (intensity factor $\lambda = 1.0$). Ground motion intensity at the SLS is reduced to $\lambda = 0.5$ (similar to $\nu = 0.5$ in EN 1998-1), while for the CPLS limit state was increased to $\lambda = 1.5$ [8]. Based on [8], the following acceptance criteria were considered in the study:

- link deformations at SLS, ULS and CPLS are γ_u=0.005rad, γ_u=0.11rad and γ_u=0.14rad.
- for conventional braces in compression (except EBF braces), plastic deformations at SLS, ULS and CPLS are $0.25\Delta_c$, $5\Delta_c$ and $7\Delta_c$, where Δ_c is the axial deformation at expected buckling load.
- for conventional braces in tension (except EBF braces), plastic deformations at SLS, ULS and CPLS are $0.25\Delta_t$, $7\Delta_t$ and $9\Delta_t$, where Δ_t is the axial deformation at expected tensile yielding load.
- for beams in flexure, the plastic rotation at ULS and CPLS are $6\theta_y$ and $8\theta_y$, where θ_y is the yield rotation
- for columns in flexure, the plastic rotation at ULS and CPLS are $5\theta_y$ and $6.5\theta_y$, where θ_y is the yield rotation

The performance is assessed by comparing the capacity of the structure, obtained from the push-over analysis, with the seismic demand expressed by the target displacement. Pushover curves for the EBF, CBF, BRB and SW structures and the occurrence of plastic hinges up to the target point are shown in Figure 6 and Figure 7. Table 3 presents the interstory drift demands for SLS and Table 4 presents the plastic deformations demand in members for the SLS, ULS and CPLS.



a)



b)

Figure 6. Pushover curves (normalized base shear vs. normalized top displacement) for eight story buildings a) and plastic hinges at ULS for EBF8, CBF8, BRB8 and SW8 structures b)

www.EngineeringEBooksPdf.com

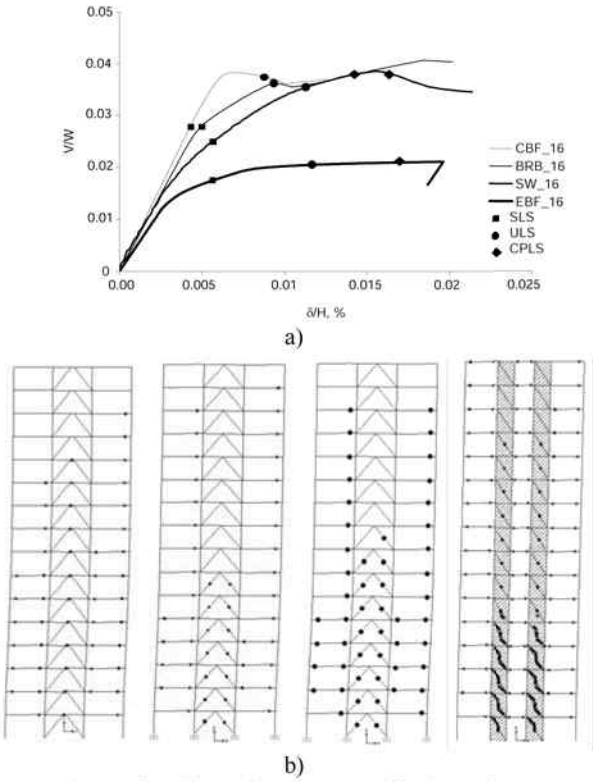


Figure 7. Pushover curves (normalized base shear vs. normalized top displacement) for sixteen story buildings a) and plastic hinges at ULS for EBF16, CBF16, BRB16 and SW16 structures b)

Table 3. Interstory drift demands for SLS

Structure	EBF8	CBF8	BRB8	SW8
δ/H_s, %	0.008	0.007	0.008	0.007
Structure	EBF16	CBF16	BRB16	SW16
δ/H_s, %	0.008	0.005	0.006	0.007

First of all, before detailing the comparative analysis of studied frames, it is important to observe that no plastic hinges occur in columns for 15 story frames, even for CPLS, excepting conventional CBF system. For 8 story frames, practically no plastic hinges appear in columns up to ULS (the values of plastic hinge deformation demands in Table 4 are very low), which is for sure that, with plastic deformation recor4ded for CPLS stage, the frames are safely standing up, but again, excepting CBF system.

In comparison with the centrically braced structures (using conventional braces CBF and buckling restrained braces BRB), the ones using eccentrically braces (EBF) and shear walls (SW) are characterised by lower stiffness. Base shear force capacity is very similar for CBF, BRB and SW structures, implying similar design strength under seismic action. Lower base shear force capacities are recorded for EBF structures. Displacements demands for SLS are lower then the interstorey drift limitation of $0.008H_s$ used in design (Table 3). Structures designed using the dissipative approach, may experience structural damage even under moderate (SLS) earthquake. This is clearly seen in Table 4, where plastic

www.EngineeringEBooksPdf.com

deformation demands in members are presented. Plastic deformations in dissipative members indicate a moderate damage to the structure at SLS.

All structures satisfy the criteria for ULS. Plastic deformation demands in beams are more severe for EBF and SW compared to CBF and BRB, and plastic mechanisms develop almost on entire height of the structures. Shear wall frames show a very good ductility, comparable to eccentrically braced ones, but also providing a higher stiffness. For sixteen story buildings, no plastic hinges are recorded in the columns, while for eight story buildings plastic hinges are recorded at the bottom part of the first story columns. This shows that in case of higher buildings, when the contribution of the gravity loads (i.e. dead loads, live loads) is lower, the Ω factor is more effective in design of non-dissipative members. Dissipation capacity shown by the structures confirms the reduction factors q used in design. Ductility of EBF, BRB and SW structures is similar to that of MRF, while CBF proved to be less ductile.

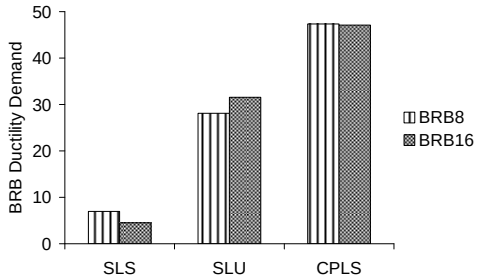


Figure 8. Ductility Demand Ratios for the buckling restrained braces

Table 4: Plastic deformation demands in members at SLS (λ= 0.5), ULS (λ = 1.0) and CPLS (λ = 1.5)

	beams				columns				links	braces	
	[rad]				[rad]				[rad]		
	EBF8	CBF8	BRB8	SW8	EBF8	CBF8	BRB8	SW8	EBF8	CBF8	BRB8
SLS	0.004	0.0013	0.0012	0.005	-	-	-	-	0.04	0.001	0.003
ULS	0.018	0.016	0.016	0.016	0.006	0.002	0.002	0.004	0.1	0.043	0.0034
CPLS	0.027	PF*	0.035	0.038	0.01	PF*	0.03	0.033	0.15	PF*	0.094
	EBF15	CBF15	BRB15	SW15	EBF15	CBF15	BRB15	SW15	EBF15	CBF15	BRB15
SLS	0.007	0.0004	0.007	0.007	-	-	-	-	0.037	-	0.0038
ULS	0.021	0.013	0.015	0.017	-	-	-	-	0.11	0.044	0.028
CPLS	0.033	PF*	0.028	0.027	-	PF*	-	-	0.165	PF*	0.067

** PF – premature failure following the buckling of braces*

Structures perform well till the attainment of the target displacement at CPLS, excepting CBF systems, which fail prematurely, mainly due to the failure of the braces in compression. When conventional braces are replaced by BRBs, the performance is improved and the performance level of collapse prevention is reached.

In case of EBF structures, plastic rotation demands in links exceed the rotation capacity. However, experimental tests on such elements have shown that in case of very short links, plastic rotation capacity may reach 0.17-0.20 rad [15]. The ductility demands in the buckling restrained braces are plotted in Figure 8. Experimental investigation on such type of members has shown the ductility of braces may exceed 25-30, depending on the material properties [16].

www.EngineeringEBooksPdf.com

3. DUAL STEEL ECCENTRICALLY BRACED FRAMES OF REMOVABLE LINKS: PERFORMANCE AND RECENTERING CAPACITY

3.1 Removable link concept

As stated in Introduction, there are many possible solutions for structures with removable dissipative members. Application of this principle to eccentrically braced frames (EBFs), where links act as dissipative fuses, is presented in Figure 9 [17], [15]. The connection of the link to the beam is realized by a flush end-plate and high-strength friction grip bolts. In order to isolate inelastic deformations in removable dissipative elements only, these elements may be realised using lower yield steel. A similar effect can be obtained by using high strength steel in non-dissipative elements. The main advantage over special dissipative devices is the fact that removable links can be designed using methods readily available to structural engineers and can be fabricated and erected using standard procedures.

Bolted links for eccentrically braced frames were previously investigated by [18], [19] and [20].

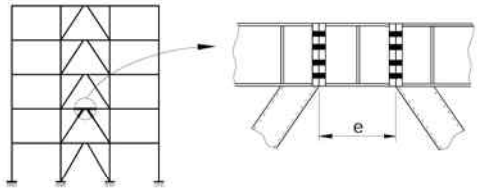
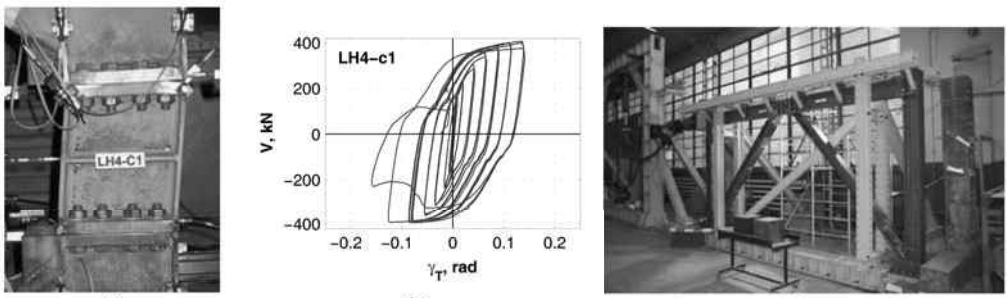


Figure 9. The bolted link concept

Two series of experimental tests on removable link assemblies were carried out at the "Politehnica" University of Timisoara in order to determine cyclic performance of bolted links and to check the feasibility of the removable link solution [17], [15]. The first series of tests was realised on isolated links (see Figure 10a-b), while the second one on full-scale model of a single bay and single storey eccentrically braced frame with removable link (see Figure 10c). Tests on links showed an important influence of the connection on the total response of the bolted link, in terms of stiffness, strength and overall hysteretic response. Shorter links were found to be suitable for the bolted solution, as plastic deformations were constrained to the link, while the connection response was almost elastic, allowing for an easy replacement of the damaged link. At the frame level, the experimental tests showed that the removable link solution is feasible. Inelastic deformations were constrained to the removable links alone, all other frame members and connections remaining in the elastic range. Additionally, it was possible to replace the damaged removable links with new elements.



(a) (b) (c)

Figure 10. Experimental test on removable bolted link – LH4-c1 specimen (a); force-deformation relationship V-γT of the same specimen (b) and tests on full-scale frame with bolted links (c)

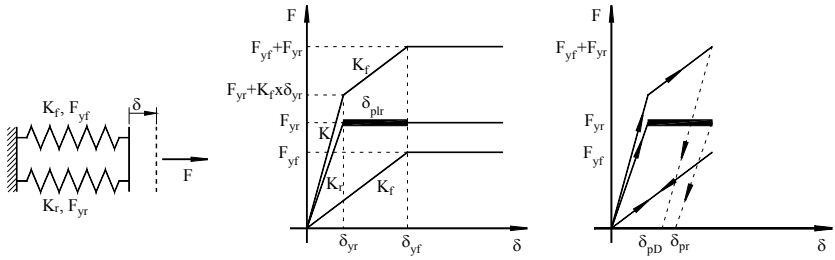
www.EngineeringEBooksPdf.com

For a system containing removable dissipative elements to be efficient, it must fulfil to requirements. The first one consists in isolating inelastic to removable elements only, assuring an easy repair of the damaged structure. Capacity design rules incorporated in modern design codes can be used in order to attain this objective. The second requirement is related to the possibility to replace damaged dissipative elements that can be difficult to realise if the structure has experienced large permanent deformations.

Several researchers investigated seismic performance of dual systems, consisting of rigid and flexible subsystems. According to these studies, the potential benefits of dual structural configurations may be summarised as follows:

- Efficient earthquake resistance due to prevention of excessive development of drifts in the flexible subsystem, and dissipation of seismic energy in the rigid subsystem by plastic deformations.
- Alternative load path to seismic loading provided by the secondary subsystem (the flexible one) in the case of failure of the primary subsystem (the rigid one)

In order to analyse the factors controlling the two requirements for structures with removable dissipative members (e.g. isolation of damage and limitation of permanent drifts), it is useful to consider a simple dual system consisting of two inelastic springs connected in parallel (see Figure 11a).



(a) (b) (c)

Figure 11. Simplified model of a generalized dual system

Provided that the flexible subsystem is not very weak, plastic deformations appear first in the rigid subsystem. Therefore, an efficient dual system must be realised by combining a rigid and ductile subsystem, with a flexible subsystem. In order to maximize system performance, plastic deformations in the flexible subsystem should be avoided. At the limit, when the yield force F_{yf} and yield displacement δ_{yf} are attained in the flexible subsystem, the rigid subsystem experiences the yield force Fyr and the total displacement $\delta_{yr} + \delta_{plr}$ (see Figure 11b). Equating the two displacements:

$$\delta_{yf} = \delta_{yr} + \delta_{plr}$$

and considering the relationship between force and deformation:

$$F = k \cdot \delta$$

it can be shown that

$$\mu_D = \frac{\delta_{yr} + \delta_{plr}}{\delta_{yr}} = \frac{\delta_{yf}}{\delta_{yr}} = \frac{F_{yf}}{F_{yr}} \cdot \frac{K_{yr}}{K_{yf}}$$

The notation μD represents the "useful" ductility of the rigid subsystem, for which the flexible subsystem still responds in the elastic range. It can be observed that there are two factors that need to be considered in order to obtain a ductile dual system with plastic deformations isolated in the rigid subsystem alone. The first one is the ratio between the yield strength of the flexible and rigid subsystems (F_{yf}/F_{yr}), while the second one is the ratio between the stiffness of the rigid subsystem and the one of the flexible subsystem. The larger are these two factors, the larger is the "useful" ductility μ_D of the dual system.

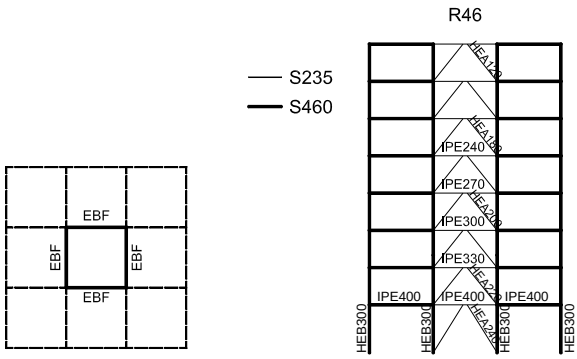
www.EngineeringEBooksPdf.com

The second objective, of limitation of permanent deformations, is not easily attainable. Though the dual configuration is results in smaller permanent drifts δ_{pD} in comparison with permanent deformations of the rigid system alone δ_{pr} (see Figure 11c), they are not eliminated completely after unloading. However, permanent deformations can be eliminated if the rigid subsystem is realised to be removable. Once it is replaced after the system experienced inelastic deformations, the flexible subsystem alone provides the necessary stiffness and strength to the system. If the flexible subsystem is still in the elastic range, it will return the system to the initial position, implying zero permanent deformations.

Considering the above, practical implementation of the concept of removable dissipative elements and dual systems can be obtained by combining eccentrically braced frames with removable links (the rigid subsystem) and moment-resisting frames (flexible subsystem).

3.2 Evaluation of performance of EBFs with removable links

In order to assess seismic performance of eccentrically braced frames with removable links, a medium rise structure was investigated as a case study. The building has 3x3 bays of 6 m each, and 8 storeys (see Figure 12).



(a) (b)

Figure 12. Structural layout: (a) plan view; (b) elevation dual frame R46

All storeys are 3.5 m, except the first one, which equals 4.5 m. The design was carried out according to EN 1993, EN 1998 (2004) and P100-1/2006. A 4 kN/m^2 dead load on the typical floor and 3.5 kN/m^2 for the roof were considered, while the live load amounted 2.0 kN/m^2. The building location is again Bucharest (PGA = 0.24g, T_C=1.6 sec). A behaviour factor q=6, and an interstory drift limitation of 0.008 of the storey height were considered in design. Columns are of fixed base and rigid beam to column connections were assumed.

The Moment Resisting (MR) part of the frame DS (e.g. the “elastic” one) is realised of S460 steel, while the EBF part (e.g. the “plastic” one), including the removable link is of S235.

Experimental results showed that for very short links the flush end plate connection remained essentially elastic. For these links the strength was governed by the shear strength of the link, and the cyclic response was not affected by strength and stiffness degradation in the connection like for longer links. For the numerical investigation, very short links were used, with e=400mm, characterised by negligible influence of connection on cyclic response of the removable link. Therefore, only the stiffness of the removable link was considered to be affected by the flexibility of the bolted link-beam connection. Based on experimental tests, an equivalent stiffness of 0.25 of the theoretical shear stiffness of continuous links was considered for bolted links. In order to reduce inelastic deformations in members outside links, higher steel grade was used in these members.

Inelastic analysis of the frames was realised using DRAIN-3DX computer program. Beams, columns and braces were modelled with fibre hinge beam-column elements, with plastic zones located at the ends.

www.EngineeringEBooksPdf.com

Nominal steel characteristics were used. Elastic-perfectly plastic behaviour was assumed, without strength and stiffness degradation. Buckling of braces was not considered explicitly in the model due to the limitations of the inelastic beam-column element available in the program. However, compression force demand in braces was checked against buckling strength of braces, computed according to EN 1993-1-1 provisions using nominal material characteristics and a buckling length equal to 0.8 times the clear length of the brace, corresponding to braces welded directly to the column and beam.

The inelastic shear link element model was based on the one proposed by Ricles and Popov [9]. As the original model consisted in four linear branches, it was adapted to the trilinear envelope curve available in Drain-3dx. It consists of an initial elastic response up to yield force, followed by a strain hardening range with a stiffness of 4% from the initial one up to a force 1.4 times the yield one, with a strain hardening behaviour afterwards at the 0.2% of the initial stiffness.

A set of seven ground motions were used. Spectral characteristics of the ground motions were modified by scaling Fourier amplitudes to match the target elastic spectrum from P100-1/2006, see Figure 13. This results in a group of semiartificial records representative to the seismic source affecting the building site and soft soil conditions in Bucharest. The procedure was based on the SIMQKE-1 program [21].

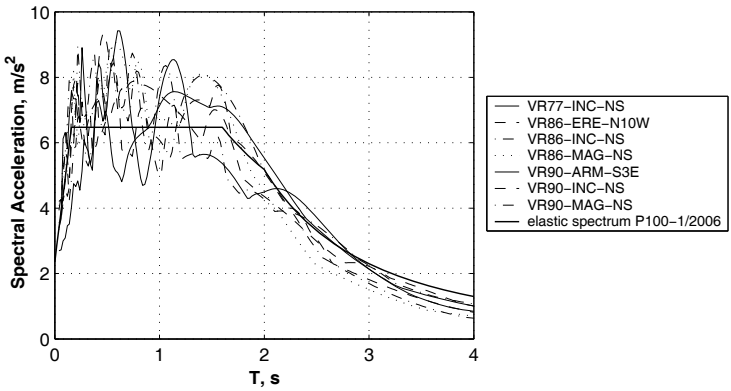


Figure 13. Elastic response spectra of semiartificial records and P100-1/2006 elastic spectrum.

In order to assess structural performance, an incremental dynamic analysis (IDA) was performed. Three performance levels were considered: serviceability limit state (SLS), ultimate limit state (ULS), and collapse prevention (CPLS) limit state. Intensity of earthquake action at the ULS was equal to the design one (intensity factor $\lambda = 1.0$). Ground motion intensity at the SLS was reduced to $\lambda = 0.5$ (according to $\nu = 0.5$ in EN 1998-1), while for the CPLS limit state was increased to $\lambda = 1.5$ (according to FEMA 356). Based on experimental results and FEMA 356 provisions, ultimate link deformations at ULS and CPLS were γ_u=0.11 rad and γ_u=0.14 rad, respectively.

Results of IDA are synthetically presented in Figure 14, in terms of maximum transient interstorey drift ratio (IDR) and maximum permanent IDR. The benefit of HSS for the structure with removable links (R46) is clearly identified in Figure 14b, giving the lowest values of permanent drifts up to intensity factors of $\lambda = 1.0$ - 1.2. Low permanent drifts allow easier replacement of damaged removable links. Maximum plastic deformation demands in members at SLS, ULS and CPLS are presented in Table 5. Structures designed using the dissipative approach, may experience structural damage even under moderate (SLS) earthquake. This can be seen in Figure 15, where plastic deformation demands in members are represented. One observes the plastic deformations outside the link are completely avoided for SLS stage, negligible for ULS and reduced for CPLS, so *quod erat demonstrandum*.

www.EngineeringEBooksPdf.com

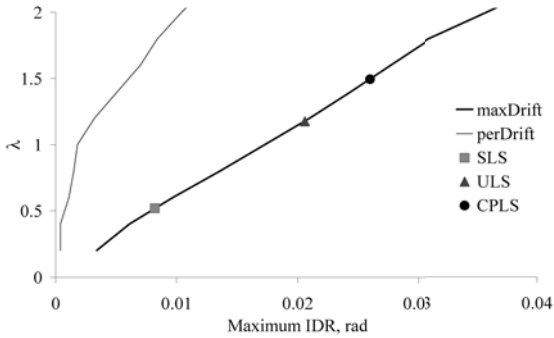


Figure 14. IDA curves: maximum and permanent drift vs. acceleration multiplier, average of all records

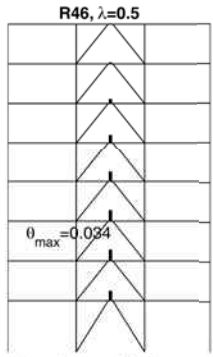


Figure 15. Plastic deformation demands in members at SLS ($\lambda = 0.5$) for the R46 structure, average of all records

Table 5. Plastic deformation demands in members at SLS ($\lambda = 0.5$), ULS ($\lambda = 1.0$) and CPLS ($\lambda = 1.5$) for the R46 structures, average of all records, [in rad]

	links	beams	columns
SLS	0.036	-	-
ULS	0.092	0.004	0.002
CPLS	0.145	0.014	0.008

3.3 Recentering capacity: study case

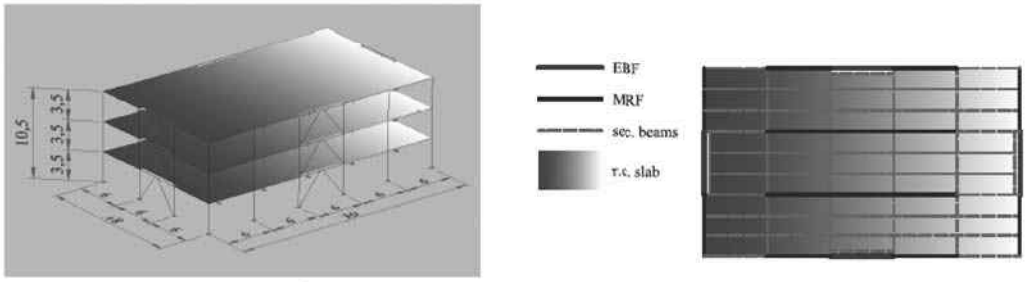
The main advantage of using removable dissipative members in dual-steel structures is to take benefit from possibility to replace those members after they consumed their fuse role. On this purpose, it is important to size correctly the structural components on the aim to keep small the residual drift and ensure the recentering of the structure after the earthquake. A case study will used in order to provide evidence of the advantages of using removable links associated with HSS components in the elastic part of the dual framing.

In order to check the level of permanent forces and deformations, the test structure was designed according to EN 1993-1-1 and EN 1998-1 for typical gravity loadings and a peak ground acceleration of 0.24g, corresponding to soil conditions in Bucharest (Figure 16). A nonlinear time-history analysis was then performed on the test structure under the NS component of the Vrancea '77 ground motion record,

www.EngineeringEBooksPdf.com

scaled in order to correspond to attainment of ultimate shear deformation in links (0.1 rad). Results from Table 6 present the normalized interstory drift, link shear displacements and vertical relative displacements of the link ends along the building stories. In Table 7 the bending moment and shear force in the links are presented. In order to mark the residual (or permanent) deformations and stresses in the links, both maximum values and permanent values at the end of the analysis are presented.

Values of permanent deformations and lateral displacements in the structure are very small, compared to maximum values recorded during analysis. Thus, the maximum permanent interstorey drift amounts only to 5.5% of the maximum one, while permanent shear deformation amounts to 6.6% of the maximum plastic rotation. The residual vertical displacement between link ends is 2.7 mm only, which shows a very small residual plastic deformation in the link. Residual stresses are also low, bending moment amounts 9.7% of the maximum one, while shear force is just 1.8% of the maximum one. Based on these reduced values of residual stresses, it can be anticipated that the replacement of the damaged links is feasible, even without relaxing completely the links in shear by the flame cutting of the link web. As the beams outside the links remain elastic, the initial position can be completely regained after the damaged links are dismantled. Though this analysis was performed for a single seismic record, but which is very demanding, the results show that in many cases the flame cutting could be avoided. This research is part of an ongoing SERIES Project, "DUAREM". Within this project, the full scale structure will be tested pseudo-dynamically at JRC Ispra.



a) b)

Figure 16. General view (a) and plan layout (b) of the structure.

Table 6. Values of interstorey drift and link rotation along the stories

	Relative interstorey drift [%Hs]		Links ends vertical displacement [mm]		Plastic rotation in links [rad]	
	maximum	permanent	maximum	permanent	maximum	permanent
1st storey	0.82	0.045	40	2.7	0.10	0.0068
2nd storey	0.61	0.029	26.1	1.6	0.06	0.004
3rd storey	0.17	0.0008	7.8	0	0.019	0

Table 7. Values of bending moment and shear forces in links, along the stories

	Bending moment in links, ML, [kNm]		Shear force in links, VL [kN]	
	maximum	permanent	maximum	permanent
1st storey	114.4	11.1	507.4	9.2
2nd storey	97.0	4.4	444.5	1.03
3rd storey	65.7	1.83	325.0	1.41

www.EngineeringEBooksPdf.com

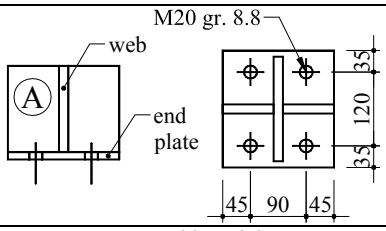
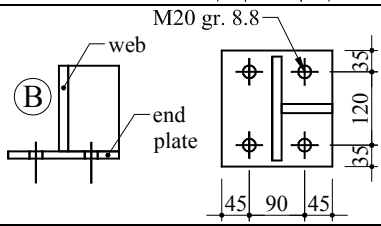
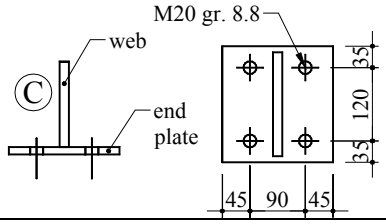
4. DUAL STEEL CONNECTIONS

When HSS is used in members designed to remain predominantly elastic, e.g. columns, or in end-plates of bolted beam to column joints, T-stub macro-components made of two steel grades are obtained. The performances of Dual-Steel bolted T-stub specimens were studied at the Politehnica University of Timisoara within a large experimental program.

The objective of the experimental program was to study the performance of welded and bolted end-plate beam-to-column joints realized with two different steel grades components. The experimental program consisted in tests on materials, weld details, T-stub components and beam to column joints. This section of the paper summarizes the investigations on T-stub components, only. Previous papers already presented the results and whole testing program [22], [23].

T-stubs are basic components of the component method used in EN 1993-1-8 [24] for evaluation of strength and stiffness of bolted end-plate beam to column joints. Both monotonic and alternating cyclic tests were performed on T-stub components obtained by welding S235 web plates to S235, S460 and S690 end-plates, using K beveled full-penetration welds (Table 8).

Table 8. T-stub characteristics

T-stub type	Label	Web	End-plate	Design failure mode
	TST-12A-S235	S235 t=15 mm	S235 t = 12 mm	2
	TST-20A-S235		S235 t = 20 mm	2 → 3
	TST-10A-S460		S460 t = 10 mm	2
	TST-16A-S460		S460 t = 16 mm	2 → 3
	TST-8A-S690		S690 t = 8 mm	2
	TST-12A-S690		S690 t = 12 mm	2 → 3
	TST-12B-S235	S235 t=15 mm	S235 t = 12 mm	1 / 2
	TST-20B-S235		S235 t = 20 mm	2 / 2 → 3
	TST-10B-S460		S460 t = 10 mm	1 / 2
	TST-16B-S460		S460 t = 16 mm	2 / 2 → 3
	TST-8B-S690		S690 t = 8 mm	1 / 2
	TST-12B-S690		S690 t = 12 mm	2 / 2 → 3
	TST-12C-S235	S235 t=15 mm	S235 t = 12 mm	1
	TST-20C-S235		S235 t = 20 mm	2
	TST-10C-S460		S460 t = 10 mm	1
	TST-16C-S460		S460 t = 16 mm	2
	TST-8C-S690		S690 t = 8 mm	1
	TST-12C-S690		S690 t = 12 mm	2

Notes:

1: One monotonic and two cyclic tests have been performed for each specimen type.

2. Failure modes according to EN 1993-1-8: 1) ductile, 2) semi-ductile, 3) brittle

On the purpose to obtain full strength rigid beam-to-column connections, outer stiffeners needs to be applied at the extended end-plate (Figure 17); consequently, double stiffened T-stub specimens are obtained (Type A in Table 8).

MAG welding was used, with G3Si1 (EN 440) electrodes for S235 to S235 welds, and ER 100S-

www.EngineeringEBooksPdf.com

G/AWS A5.28 (LNM Moniva) for S235 to S460 and S690 welds. T-stubs were connected using M20 gr. 8.8 bolts. EN 1993-1.8 was used to obtain the design strength of T-stubs and failure modes. Thickness of end-plates was determined so that the unstiffened T-stub (type C) would fail in mode 1 (end-plate) and mode 2 (combined failure through end-plate bending and bolt fracture). The same end-plate thickness was then used for the stiffened T-stubs (type B and A), see Table 8.

Table 9 shows the measured average values of yield stress f_y, tensile strength f_u and elongation at rupture, A. One observes the value of elongation for S460 is significantly large. Bolts were tested in tension as well, showing an average ultimate strength of 862.6 N/mm2. Loading was applied in displacement control under tension and force control under compression. Compressive force was chosen so as to prevent buckling of the specimen.

Table 9. Material properties

Nominal steel grade	f_y, N/mm^2	f_u, N/mm^2	A, %	Actual steel grade
S235	266	414	38	S235
S460	458	545	25	S460
S690	831	859	13	S690

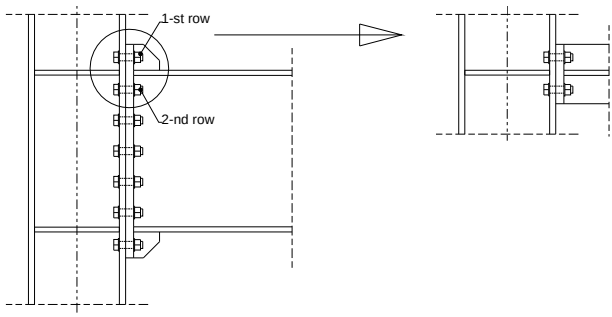
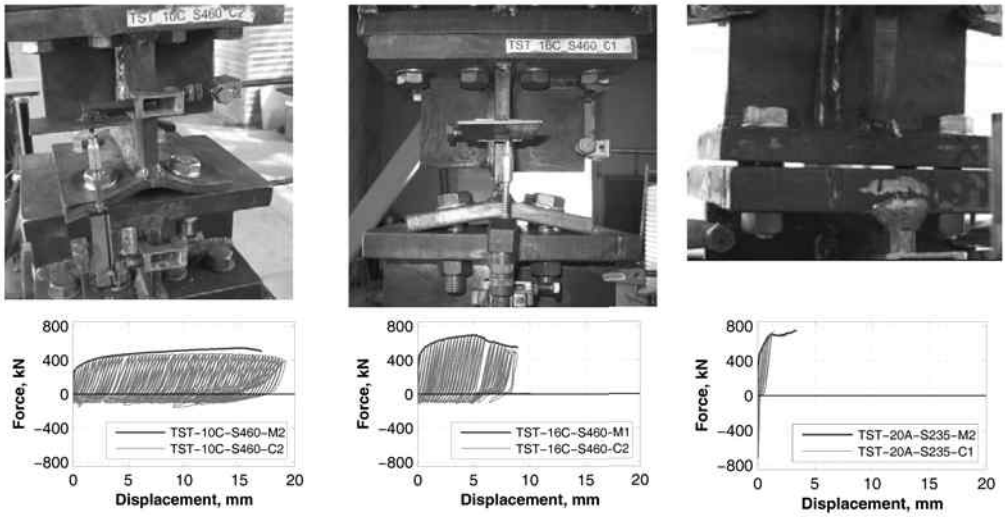


Figure 17. Assumption for A-type T-stub

For specimens of types B and C, it was not possible to have full reversible cycles due to the buckling. For stiffened T-stubs (eg. A or B), generally semi-ductile failure mode, 2, was obtained, except the case of thicker end-plate, even of S235 (MCS), when a brittle failure occurred. It seems the choice of thickness associated with steel grade is important in the conception of a proper connection, in order to obtain a good balance between strength, stiffness and ductility of components.

Figure 18 shows examples of the 3 types of observed failure modes, together with the corresponding force-displacement relationships of T-stub specimens. There were no significant differences in force values between failure modes of monotonic and cyclic specimens, both agreeing with analytical predictions by EN 1993-1-8. It is clear the ductile mode is the weaker one, while the brittle mode 3 is the stronger. Figure 19a and Figure 19b show the comparison between monotonic and cyclic tests in terms of ultimate displacements D_u and experimental vs. predicted monotonic yield force F_y, respectively. Under monotonic loading, ultimate displacement was smaller for specimens of thicker end-plates that failed in modes 2 and 3 involving bolt failure. Cyclic loading reduced significantly ultimate displacement of specimens with thinner end-plates that failed in mode 1. This behavior is attributed to low-cycle fatigue that generated cracks in the HAZ near the welds, along yield lines. On the other hand, cyclic loading did not affect much ultimate displacement for specimens with thicker end-plates that failed in modes 2 and 3, governed by bolt response. It is interesting to note that specimens realized from high-strength end plates (S460 and S690, with lower elongation at rupture), had a ductility comparable with the one of specimens realized from mild carbon steel (S235).

www.EngineeringEBooksPdf.com

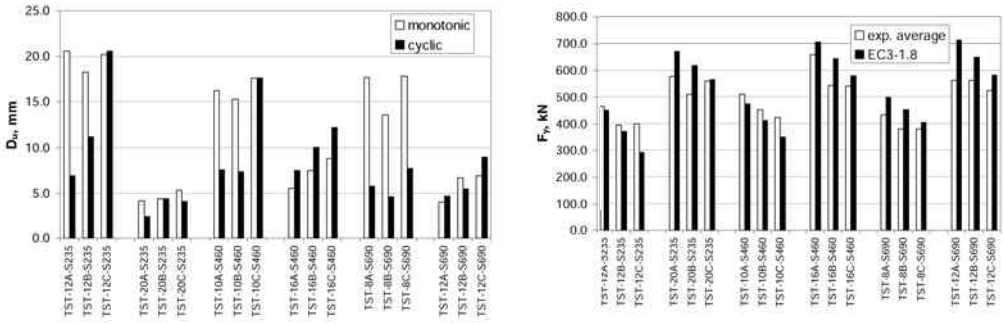


TST-10C-S460-C2 Failure mode 1 | TST-16C-S460-C2 Failure mode 2 | TST-20A-S235-C1 Failure mode 3

Figure 18. Examples of failure modes of T-stub specimens

In Table 10 and Figure 20 the interpretation of test results base on low-cycle approach is presented [25]. Based on these results, one concludes that, in general, no particular failure problems are met in case of Dual-Steel welded connections of the type used in extended end-plate bolted beam-to-column seismic resistant joints. If full strength Moment Resisting Joints are desired, they cannot be detailed and sized for failure Mode 1 of T-stubs, because it always leads to partial strength connections. Alternatively, the stronger Mode 3, the brittle one, is really dangerous, because the designed overstrength related to nominal yield strength of the MCS beam is often vanished by the real MCS yield strength of the material. So that still is need for connection ductility, even designed as full strength. Mode 2, when properly calibrated, enables to obtain both full strength and ductile beam to column joints. Playing with both steel grade and thickness of components, gives to obtaining beam to column joints with such properties.

One sees in Table 10 and Figure 20, this is, generally the case of TST-16A-S460, which is strong enough (Figure 19a) and has an acceptable energetic ductility (e.g. μ_E in Table 10). The paper presented in the Proceeding of SDSS 2010 Conference [26] proves that.



(a) (b)

Figure 19. Interpretation of results

www.EngineeringEBooksPdf.com

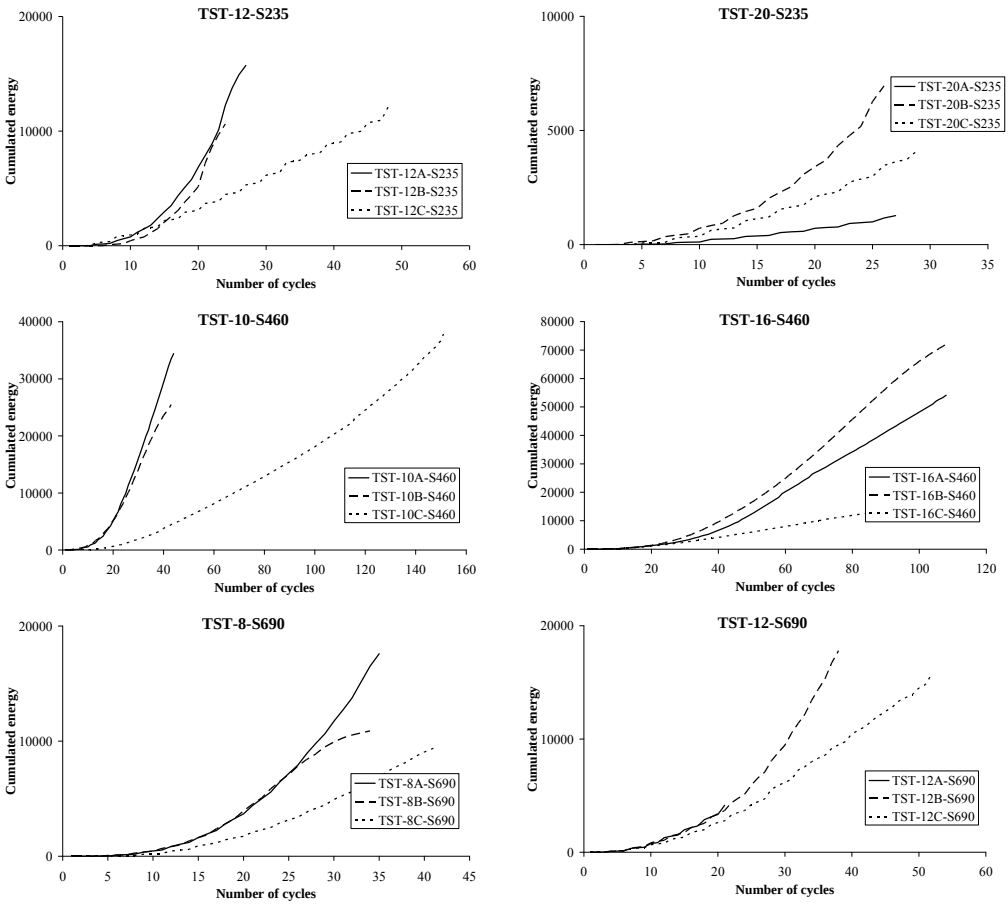


Figure 20. Cumulated energy

Table 10. Interpretation of cyclic tests in term of energy

Specimen	Nr. of cycles	$\Delta\sigma$ [N/mm^2]	$\Delta\sigma_C$ [N/mm^2]	$\mu_E=(E_u-E_y)/E_y$	Failure mode
TST-12A-S235	27	10367	247	670	1
TST-12B-S235	24	11146	255	523	1
TST-12C-S235	48	6060	175	583	1
TST-20A-S235	26	720	17	40	3
TST-20B-S235	26	4846	114	279	2→3
TST-20C-S235	28	2810	69	178	2
TST-10A-S460	45	12749	357	920	1
TST-10B-S460	43	10232	285	744	1
TST-10C-S460	151	10438	441	2435	1
TST-16A-S460	110	8296	315	1567	2

www.EngineeringEBooksPdf.com

Table 10. (Continued)

Specimen	Nr. of cycles	$\Delta\sigma$ [N/mm^2]	$\Delta\sigma_C$ [N/mm^2]	$\mu_E=(E_u-E_y)/E_y$	Failure mode
TST-16B-S460	106	12614	478	2439	2
TST-16C-S460	89	3530	126	491	2
TST-8A-S690	35	16306	423	456	1
TST-8B-S690	34	11782	303	340	1
TST-8C-S690	41	18867	516	673	1
TST-12A-S690	21	5141	113	70	3
TST-12B-S690	38	15912	425	481	2
TST-12C-S690	52	10832	321	469	2

5. CONCLUDING REMARKS

Dual-Steel frames enable for a better control of seismic response of multistory buildings. Ductile MCS members can be designed as fuses and replaceable components, while the HSS members, designed to remain predominantly elastic during earthquakes and to provide alternative load distribution paths during earthquake, might provide a beneficial recentering capacity of the entire structure to keep lower the residual drift. A Performance Based Design approach can be successfully applied in order to obtain such a type of behavior. Also, following the same principle, Dual-Steel connections can be shaped and sized to supply both necessary ductility and overstrength to cover better the seismic demands for MR joints. There are no technological difficulties when HSS components are welded to the MCS ones.

6. REFERENCES

[1] EN, 1998-1, 2004. Design provisions for earthquake resistance of structures - 1-1: General rules - Seismic actions and general requirements for structures, CEN, EN1998-1-1.

[2] AISC 341-05, 2005. Seismic provisions for structural steel buildings. *American Institute for Steel Construction*, 2005

[3] Dubina, D., Dinu, F., Stratan and Ciutina, A., "Analysis and design considerations regarding the project of Bucharest Tower International Steel Structure". *Proc. of ICMS 2006 Steel a new and traditional material for building*, Brasov, Romania, 2006, Taylor&Francis/Balkema, Leiden, The Nederlands, ISBN 10: 0 415 40817 2, Ed. D., Dubina, V. Ungureanu, 2006.

[4] Dubină, D., Dinu, F., Zaharia, R., Ungureanu, V. and D. Grecea, D., "Opportunity and Effectiveness of using High Strength Steel in Seismic Resistant Building Frames". *Proc. of ICMS 2006 Internat. Conf. "Steel, a new and traditional material for building"*, Poiana Brasov, Romania, September 20-22, 2006, Taylor&Francis/Balkema, Leiden, The Nederlands, ISBN 10: 0 415 40817 2, Ed. D., Dubina, V. Ungureanu, 2006.

[5] Dinu, F., Dubina, D. and Neagu, C., "A comparative analysis of performances of high strength steel dual frames of buckling restrained braces vs. dissipative shear walls". *Proc. of International Conference STESSA 2009: Behaviour of Steel Structures in Seismic Areas*, Philadelphia, 16-20 aug. 2009, CRC Press 2009, Ed. F.M. Mazzolani, J.M. Ricles, R. Sause, ISBN: 978-0-415-56326-0, 2009.

[6] EN1993-1-1: Design of Steel Structures. Part 1-1: General rules and rules for buildings, CEN, Brussels, 2003.

www.EngineeringEBooksPdf.com

[7] P100-1/2006: Cod de proiectare seismică P100: Partea I, P100-1/2006: Prevederi de proiectare pentru clădiri, 2006 (in Romanian).
[8] FEMA 356,. Prestandard and commentary for the seismic rehabilitation of buildings. *Federal Emergency Management Agency and American Society of Civil Engineers*, Washington DC, USA, 2000.
[9] Ricles J.M. & Popov, E.P. 1994. Inelastic link element for EBF seismic analysis, ASCE. Journal of Structural Engineering, 1994, Vol. 120, No. 2: 441-463.
[10] SAP2000, Version 9, 2005. Computers and Structures Inc. University Avenue, Berkeley, California 94704, USA, 2005.
[11] AISC 1999. Load and Resistance Factor Design Specification, American Institute of Steel Construction Inc., Chicago, 1999.
[12] Thorburn, L. J., Kulak, G. L., and Montgomery, C. J., "Analysis of steel plate shear walls", *Structural Engineering Rep. No. 107*, Dept. of Civil Engineering, Univ. of Alberta, Edmonton, Alberta, Canada, 1983.
[13] Driver, R. G., Kulak, G. L., Kennedy, D. J. L. and Elwi, A. E., "Seismic behavior of steel plate shear walls". *Structural Engineering Rep. No. 215*, Dept. of Civil Engineering, Univ. of Alberta, Edmonton, Alberta, Canada, 1999.
[14] Fajfar, P., "A non linear analysis method for performance based seismic design", *Earthquake Spectra*, vol.16, no. 3, pp. 573-592, August 2000.
[15] Stratan, A. and Dubina, D., "Bolted links for eccentrically braced steel frames", *Proc. of the Fifth Int. Workshop "Connections in Steel Structures V. Behaviour, Strength & Design*", June 3-5, 2004. Ed. F.S.K. Bijlaard, A.M. Gresnigt, G.J. van der Vegte. Delft University of Technology, Netherlands, 2004.
[16] Bordea, S., Stratan, A. and Dubina, D., "Performance based evaluation of a RC frame strengthened with BRB steel braces", *PROHITECH `09 International Conference*, 21-24 June, 2009, Rome, Italy, 2009.
[17] Dubina, D., Stratan, A. and Dinu, F., "Dual high-strength steel eccentrically braced frames with removable links". *Earthquake Engineering & Structural Dynamics*, Vol. 37, No. 15, p. 1703-1720, 2008.
[18] Balut, N. and Gioncu, V., "Suggestion for an improved 'dog-bone' solution", *STESSA 2003, Proc. of the Conf. on Behaviour of Steel Structures in Seismic Areas*, 9-12 June 2003, Naples, Italy, Mazzolani (ed.), A.A. Balkema Publishers, p. 129-134, 2003.
[19] Mansour, N., Christopoulos, C. and Tremblay, R., "Seismic design of EBF steel frames using replaceable nonlinear links", *STESSA 2006 – Mazzolani & Wada (eds),* Taylor & Francis Group, London, p. 745-750, 2006.
[20] Ghobarah, A. and Ramadan, T., "Bolted link-column joints in eccentrically braced frames", *Engineering Structures*, Vol.16 No.1: 33-41, 1994.
[21] Gasparini, D.A., and Vanmarcke, E.H., "Simulated Earthquake Motions Compatible with Prescribed Response Spectra", Department of Civil Engineering, *Research Report R76-4*, Massachusetts Institute of Technology, Cambridge, Massachusetts, 1976.
[22] Dubina, D., Stratan, A. Muntean, N. and Grecea, D. (2008a), "Dual-steel T-stub behavior under monotonic and cyclic loading", ECCS/AISC Workshop: Connections in Steel Structures VI, Chicago, Illinois, USA, June 23-55, 2008.
[23] Dubina, D., Stratan, A. Muntean, N. and Dinu, F., "Experimental program for evaluation of Moment Beam-to-Column Joints of High Strength Steel Components", *ECCS/AISC Workshop: Connections in Steel Structures VI*, Chicago, Illinois, USA, June 23-55, 2008.
[24] EN 1993-1.8. Design of steel structures. Part 1-8: Design of joints, European standard, 2003.

www.EngineeringEBooksPdf.com

[25] D. Dubina, D. Grecea, A. Stratan & N. Muntean, "Performance of dual-steel connections of high strength components under monotonic and cyclic loading", *Proc. of International Conference STESSA 2009: Behaviour of Steel Structures in Seismic Areas*, Philadelphia, 16-20 aug. 2009, CRC Press 2009, Ed. F.M. Mazzolani, J.M. Ricles, R. Sause, ISBN: 978-0-415-56326-0, 2009.

[26] Dubina, D., Grecea, D., Stratan, A. & Muntean, N., "Strength and ductility of bolted t-stub macro-components under monotonic and cyclic loading", *Proc. of SDSS'Rio 2010 Stability and Ductility of Steel Structures*, E. Batista, P. Vellasco, L. de Lima (Eds.), Rio de Janeiro, Brazil, September 8 - 10, 2010.

www.EngineeringEBooksPdf.com

SDSS'Rio 2010 STABILITY AND DUCTILITY OF STEEL STRUCTURES
E. Batista, P. Vellasco, L. de Lima (Eds.)
Rio de Janeiro, Brazil, September 8 - 10, 2010

ADVANCED STABILITY ANALYSIS OF REGULAR STIFFENED PLATES AND COMPLEX PLATED ELEMENTS

László G. Vigh and László Dunai

Budapest University of Technology and Economics, Department of Structural Engineering
e-mail: geri@vbt.bme.hu, ldunai@bme.epito.hu

Keywords: stiffened plate, buckling, imperfection, finite element model, FEM based design.

Abstract
In the paper research on advanced stability analysis of stiffened steel plates are presented. Regular panels are studied by laboratory and virtual tests and the buckling resistances are calculated and evaluated by conventional Eurocode method, by numerical buckling analyses of the plate elements under the actual stress conditions, and by material and geometrical nonlinear finite element analyses imperfections included, following the FEM based design recommendations. The stability analyses of complex plated elements are related to the design of a new Danube tied arch bridge. The non-conventional constructional solutions and complex loading conditions are studied by refined multi-level finite element models. The relative safeties of the different methods of the critical plated elements are determined. The paper highlights the practical problems of the advanced stability analysis: definition of critical point of the element, handling stress concentrations and definition of imperfections.

1 INTRODUCTION

Design methodology based on advanced finite element analysis deserves special attention in the new Eurocodes [1, 2] dealing with buckling analysis of plated structures. The code provides a base in design of special structures with giving the general alternative of using different level of numerical analyses or simulations instead of standardized formulae. In the current research of the authors – partially published in the paper – the design methods of stiffened plates are studied, with a special focus on the application of numerical methods.

In the first phase of the research regular multi-stiffened panels are studied by laboratory tests, with the detailed measurement of the geometric imperfections and residual stresses. In parallel with the experiments the buckling resistances are calculated and evaluated by three different ways: (i) conventional method of the Eurocode 3 for the separate orthotropic plates on the basis of the interaction of the plate and stiffener buckling, (ii) buckling analyses of the plate elements under the actual stress conditions, without separating the cross-section components; the stability resistance is derived on the bases of the critical load factor using the standardized method, and (iii) for model verification purposes, material and geometrical nonlinear finite element analyses with actual imperfections (geometrical imperfections and weld residual stresses) included, i.e. completing virtual experiments.

In the second phase the study is extended for the stability analyses of complex plated elements, related to the design of a new Danube tied arch bridge with a span of 307.8 meters. The non-conventional constructional solutions of the arch and stiffening beam box girders during the erection and the complex loading conditions are studied by refined multi-level finite element models. The relative safeties of the different methods of the critical plated elements in the bridge are determined. The practical problems of the advanced stability analysis raised by the definition of critical point of the element, handling stress concentrations and definition of imperfections are studied.

The experiences on the application of different design methods for practical problems are concluded.

www.EngineeringEBooksPdf.com

2 USE OF FINITE ELEMENT METHOD IN PLATE STABILITY ANALYSIS

The design and analysis of steel plated structures are specified in Eurocode 3 Part 1-5 (EC3-1-5, [1]). With respect to ultimate limit state analysis, governed by plate stability problems, the following levels can be distinguished (hereinafter called *Method*):

1 basic procedure (no use of numerical models),
2 partial application of numerical models in order to determine plate slenderness,
3 reduced stress method,
4 full numerical simulation.

In *Method 1*, the formulae given in the code are applied, as from the plate slenderness to the reduction factors due to buckling and ultimate capacities inclusive. The reduction factors in any case of stability phenomena are related to the element non-dimensional slenderness parameter $\bar{\lambda}_p$. Generally, it can be written as follows:

$$\bar{\lambda}_p = \sqrt{\frac{F_y}{F_{cr}}} \tag{1}$$

where $\bar{\lambda}_p$ is the non-dimensional slenderness; F_y stands for the ultimate load with no respect to stability problem; while F_{cr} is the critical load corresponding to the stability phenomenon under investigation.

Beside the formulations provided by EC3-1-5 for typical configurations, it is allowed to determine this non-dimensional slenderness by numerical analysis, i.e. through the calculation of critical load. In the above list this is referred as partial application of numerical model (*Method 2*).

The reduced stress method (*Method 3*) is the general version of *Method 2*, where the non-dimensional plate slenderness is determined as:

$$\bar{\lambda}_p = \sqrt{\frac{\alpha_{ult,k}}{\alpha_{cr}}} \tag{2}$$

where $\alpha_{ult,k}$ is the minimum load amplifier for the design loads to reach the characteristic value of the resistance of the most critical point, while α_{cr} is the load amplifier to reach the elastic critical load under complex stress field. Based on this, the reduction factors for each load type (longitudinal, transverse and shear stresses) are to be calculated according to the standard formulae, from which an interpolated value can be determined or, conservatively, the smallest value can be chosen. The outcome of this method is the stress limit for the complex stress field. It can be recognized that this method is in principle the same as the previous one, but works with the general stress field instead of loads. Thus, it can be more generally applied for any complex geometry and stress field. Shortcoming of the method is that limit state is assigned with the most critical point of the structure and thus exceeding the stress limit anywhere means failure of the structure. Additionally, determining the critical point and the governing stability modes could be difficult task.

Ultimate limit checks by non-linear simulation (*Method 4*) are supported by Annex C of EC3-1-5 that provides a general guidance on numerical analysis. It determines the geometrical, material models to be applied. For common structural elements, recommendations on initial (geometric and structural) imperfections are also given. The determined design load amplifier α_u shall cover the design model and analysis uncertainties:

$$\alpha_u \geq \alpha_1 \alpha_2 \tag{3}$$

where α_1 represents the numerical model uncertainties (should be evaluated by test verifications), while α_2 covers the design model uncertainties (γ_{M1} or γ_{M2} partial factors).

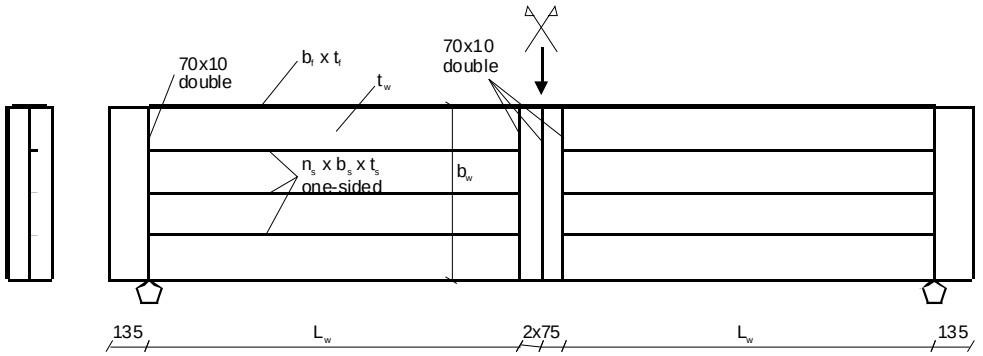
Note that EC3 Part 1-6 [2] dealing with shell structures discusses even more general use of FEM.

www.EngineeringEBooksPdf.com

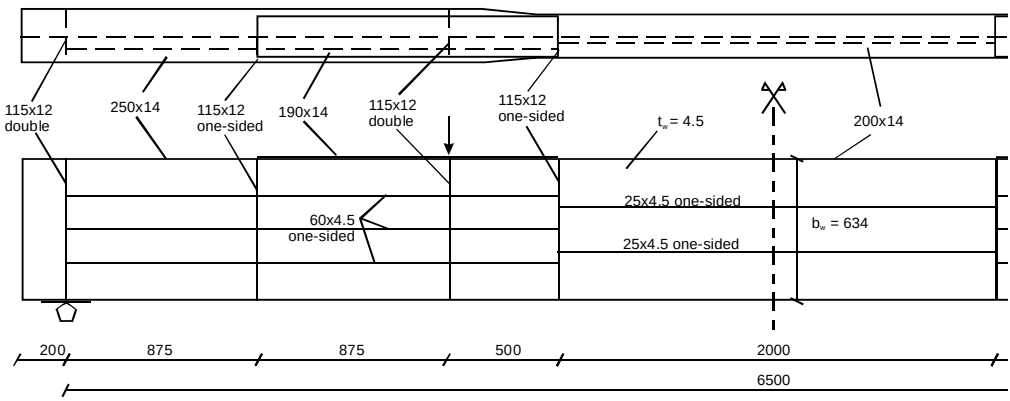
3 EXPERIMENTAL STUDIES ON MULTI-STIFFENED STEEL PLATE GIRDERS

3.1 Experimental program

To realize the ultimate resistance, an experimental study is conducted on conventionally welded plate girders with multi-stiffened web plate, as shown in Figure 1, [3]. The experimental program is summarized in Table 1. The series included one reference specimen with no stiffener and seven multi-stiffened girders. Flange-to-web joints of girders S8~S12 are prepared by automatic welding, while the longitudinal and vertical stiffeners are placed by manual welding. Except for case J1 where pure bending is obtained by 4-point-loading, the girders are subjected to 3-point-loading arrangement so dominant shear as well as interaction of shear and bending is analyzed. In the design the stiffener dimensions are determined so that overall buckling due to bending is avoided. Failures other than web buckling, namely lateral torsional buckling, flange buckling, etc. are excluded.



a) 3-point-loading arrangement



b) J1 girder: 4-point-loading arrangement

Figure 1: Test specimens.

www.EngineeringEBooksPdf.com

Table 1: Experimental program and results.

Case	L_w [mm]	b_w x t_w [mm]	b_f x t_f [mm]	n_s x b_s x t_s [-, mm]	*Imperfection* [mm] before stiffener production	*Imperfection* [mm] after stiffener production	P_{ult} [kN]	*Failure mode*
S0				---	---	12.7	555	S
S8			150x	3x20x4	8.1	11.2	665	S
S9	1275	600x4	(6+6)	3x25x5	12.4	7.2	727	S(+B)
S10				3x30x5	8.4	3.6	729	B(+S)
S12			200x10	3x30x5	4.9	2.1	968	S+B
J1			200x14		n.d.	2.5	392	B
J2	1902	634x4.5	260x22	2x25x4.5	n.d.	4.2	983	S
J3			200x12		n.d.	2.7	629	B(+S)

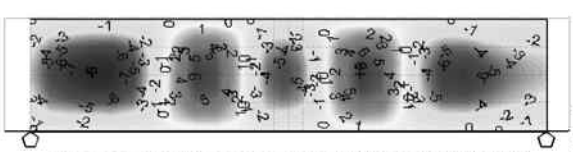
L_w – web panel length; b_w, t_w – web depth and thickness; b_f, t_f – flange width and thickness;
n_s – number of stiffeners in the web; b_s, t_s – stiffener width and thickness;
n.d. – no data; *S* – shear buckling; *B* – buckling due to bending

3.2 Imperfection measurements

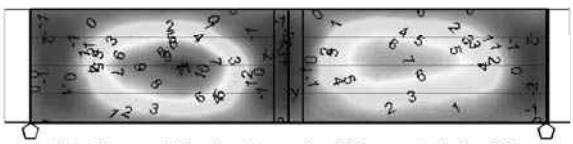
The stiffener production technology has major effect on the occurring imperfection and thus may have large influence on the ultimate behavior.

Geometric imperfections of the entire web plate of each test girder are mapped: with a frequency of 100 mm along the girder length, in each cross-section a continuous measurement is done along the web depth. Measurements before and after the welding of horizontal stiffeners of girders S8~S12 make the evaluation of technology effects available. Table 1 summarizes the results; Figure 2 illustrates the typical imperfection tendency. The stronger stiffener the higher change in shape and magnitude is observed after production. Note that – at this given production technology – the measured imperfections are typically higher than the equivalent geometric imperfection value given in EC3-1-5 (i.e. b_w / 200 = 3 mm). In the extreme case of the un-stiffened web, the actual imperfection is more than four times larger.

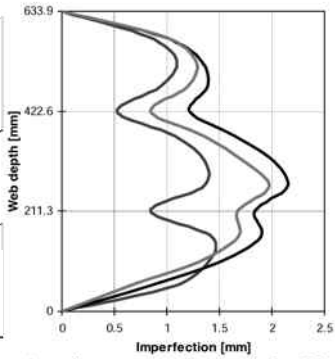
Residual stresses caused by welding are also measured by the so-called hole-drilling method. Figure 3 demonstrates the measured residual stresses along the depth of the web. The blue dashed and the continuous lines illustrate the distribution in un-stiffened plate (Dunai et al. [4]) and the stiffened plate [3] welded at the stiffeners, respectively. Well characterized effect of stiffener production can be observed; the difference between the state before and after welding is indicated by the red curve. Between the stiffeners the compressive residual stresses are increased, which is unfavorable with respect to local plate buckling. For further details on imperfection measurements and analysis of different welding technologies refer to [3, 4].



a) before welding horizontal stiffeners (girder S8)



b) after welding horizontal stiffeners (girder S8)



c) web cross-sections (girder J1)

Figure 2: Typical geometric imperfections.

www.EngineeringEBooksPdf.com

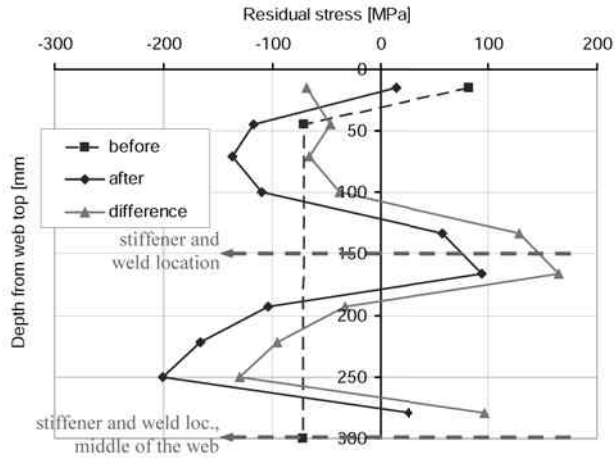


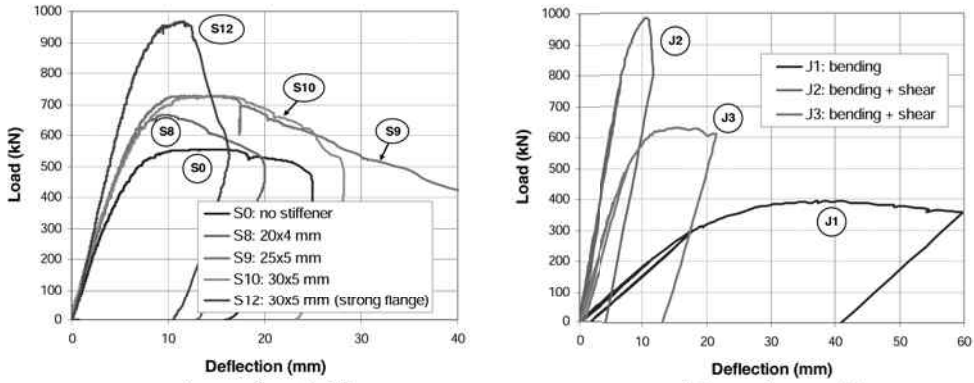
Figure 3: Residual stress distributions before and after welding of horizontal stiffeners.

3.3 Ultimate capacity

Figure 4 shows the obtained load-deflections diagrams of the tested eight girders, while typical failure modes are illustrated in Figure 5.

The results confirm the efficiency of small stiffeners in shear and bending capacity, thus the applicability of the conceived configuration. By increasing the stiffener size the ultimate capacity is efficiently improved, accompanying by a gradual change of failure mode of shear buckling to plate buckling due to bending. Negligible increase in the capacity value can be observed between S9 and S10 girders. This means that, from structural point of view, the optimal stiffener size is 25x5 mm for this girder geometry and loading: i.e. overall buckling due to bending is excluded and shear capacity reaches the bending resistance. For further discussion of the test results refer to [3].

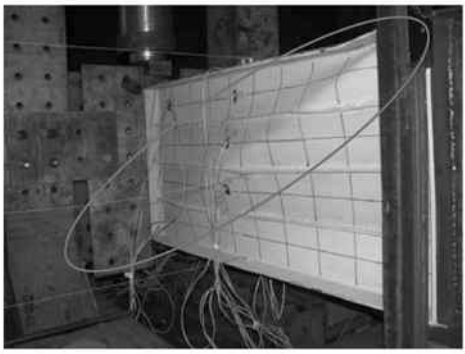
The test results are used for numerical model verifications, and are qualitatively as well as quantitatively compared to the theoretical, numerical and standard results, discussed in the following sections.



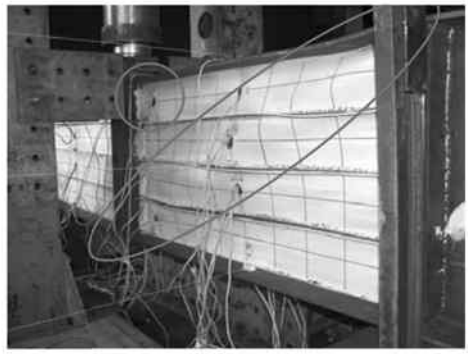
a) experiments 'S' b) experiments 'J'

Figure 4: Experimental load-deflection diagrams.

www.EngineeringEBooksPdf.com



a) S8: shear buckling



b) S12: interaction of shear and bending

Figure 5: Typical experimental failure modes.

4 STABILITY RESISTANCE CALCULATION FOR TEST GIRDERS

4.1 Standard Eurocode calculation

According to EC3-1-5, multi-stiffened (orthotropic) plates subjected to compression, bending and shear have to be analyzed with respect to the following failure modes:

- local plate buckling between stiffeners and plate buckling of stiffeners due to direct stresses,
- overall plate buckling due to axial stresses, plate-type behavior,
- overall plate buckling due to axial stresses, column-like behavior,
- overall and local plate buckling due to shear.

The local plate buckling is considered by the application of cross-section classification and effective width. For the overall buckling, the non-dimensional slenderness for plate-type and column-type behavior has to be separately determined, as follows:

$$\bar{\lambda}_p = \sqrt{\frac{\beta_{A,c} f_y}{\sigma_{cr,p}}}\ ,\ \bar{\lambda}_c = \sqrt{\frac{\beta_{A,c} f_y}{\sigma_{cr,c}}} \qquad (4, 5)$$

where $\bar{\lambda}_p$ and $\bar{\lambda}_c$ are the slendernesses for plate- and column-type behavior; $\sigma_{cr,p}$ and $\sigma_{cr,c}$ are the corresponding critical stresses; f_y is the yield stress. $\beta_{A,c}$ reflects the reduction in effective area due to local plate buckling. For plate-type behavior the plate buckling reduction factors (ρ) shall be then applied, while the column-like buckling is represented by the column buckling curves (reduction factor χ_c). The following interaction formula is applied to find the reduction factor ρ_c:

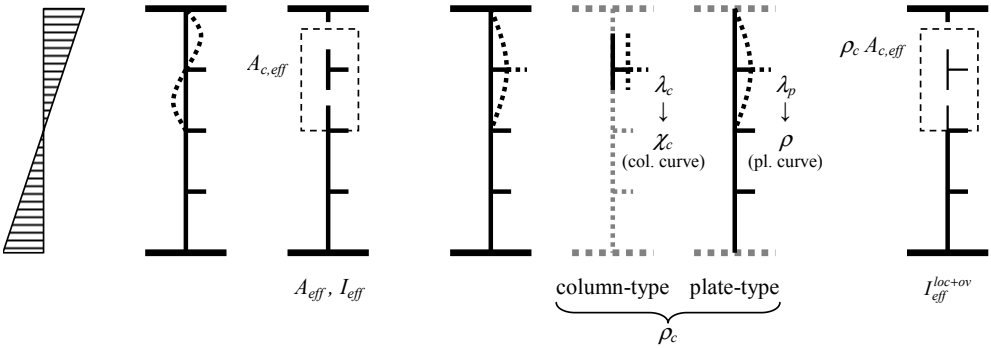
$$\rho_c = (\rho - \chi_c)\xi(2-\xi) + \chi_c \text{, where } \xi = \frac{\sigma_{cr,p}}{\sigma_{cr,c}} - 1, \quad but\ 0 \le \xi \le 1 \qquad (6, 7)$$

This reduction factor shall be applied for the compression parts of the plate except for the strips near-side the plate edges. The method is illustrated in Figure 6.

Shear buckling resistance is calculated on the basis of plate slenderness obtained from the elastic buckling stress. According to EC3-1-5 the stiffener effect is considered via an additional buckling coefficient term $k_{\tau st}$.

www.EngineeringEBooksPdf.com

$$k_\tau^{(ov)} = \begin{cases} 4.00 + \dfrac{5.34}{\alpha^2} + k_{st} & \alpha < 1 \\ 5.34 + \dfrac{4.00}{\alpha^2} + k_{st} & \alpha \geq 1 \end{cases} \tag{8}$$



a) local buckling b) overall buckling c) overall + local buckling

Figure 6: Stiffened plate girder subjected to bending – EC3-1-5 method.

4.2 Buckling coefficients of multi-stiffened plates

In the framework of parametric study invoking energy method, elastic buckling of plates stiffened with multiple stiffeners is analyzed in [3, 5]. Based on the results, buckling coefficients are formulated. Interaction of the different loads, as well as overall and local buckling is also investigated.

The author proposed modifications for the standard Eurocode calculations of critical loads in [3, 5]. On the one hand, the modifications aim to generalize the buckling coefficient formula for interaction of compression and bending. On the other hand, corrections of shear buckling coefficient is made to increase the accuracy and to consider interaction of local and overall shear buckling where relevant [3].

Note that the theoretical achievements and the conceived concept are also verified by numerical and experimental studies [3].

4.3 Calculation of tested girders with Methods 1 and 2

For the tested girders, ultimate capacities are calculated according to EC3-1-5. In the calculation, the λ_w plate slenderness for shear is determined either by the original formulas provided by EC3-1-5 (denoted as *orig.*) or by the help of the modified buckling coefficient formulas proposed by the authors (*mod.*). The plate slenderness λ_p for bending is calculated only by the proposed modifications. Actual material properties are applied; the yield stress of the web plate at specimens S0~S12: f_y^{web} = 479 MPa, at girders J1~J3: f_y^{web} = 380 MPa.

Completing the calculation, it is found that overall buckling is characterized by plate-type behavior (ξ = 1), and that – except for girder S8 – the reduction factor ρ_c = 1, meaning that overall buckling is not dominant. Consequently, the standard calculation also reflects that these small stiffeners efficiently impede the overall buckling due to bending. Comparing the standard results to the test values (Table 2), it is clear that the original EC3-1-5 procedure underestimates the shear resistance: the difference varies between -30% and -6%.

Application of the modified critical stress formulations (practically meaning *Method 2*) leads to better approximation of the shear resistance, as Table 2 and Figure 7 confirm. The difference between the original and the modified procedure is larger in case of three stiffeners (S8~S12), while it can be neglected in case of two stiffeners (J2~J3). Note that the deviation increases with stronger stiffener. It is

www.EngineeringEBooksPdf.com

also an important observation that the modified calculation gives the actual failure back: while the standard method indicates interaction failure for girder S10, the modified one results in bending failure that actually occurred in the test.

The accuracy of the formulas regarding overall plate buckling due to bending cannot be in general evaluated by the tested girders as this failure mode is mostly excluded. Further verification is carried out by the help of extended virtual experiments, as discussed in [3].

Table 2: Ultimate resistance of the tested girders – Comparison.

Case	λ_p [-]	λ_w [-] orig.	λ_w [-] mod.	P_{Rd} [kN]	P^*_{Rd}, P_{ult} [kN] orig.	mod.	FEM	test
S0	1.31	2.48		394	457		569	555
S8	1.01	1.99	1.83	479	544	577	677	665
S9	0.87	1.85	1.57	506	575	642	691	727
S10	0.83	1.72	1.38	531	604	667	718	729
S12				595	684	840	993	968
J1		---		234	339		411	392
J2	0.84	1.71	1.66	564	733	752	972	983
J3				464	587	598	631	629

λ_p – non-dimensional plate slenderness for direct stresses; λ_w – non-dimensional plate slenderness for shear stresses; P_{Rd} – design resistance according to EC3-1-5; P^*_{Rd} – resistance based on actual material properties; *orig.* – standard method; *mod.* – modified standard method; *FEM* – virtual experiments

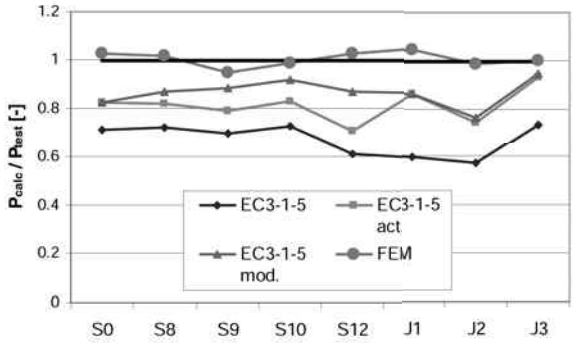


Figure 7: Comparison of the results.

4.3 Model development and verification – Virtual experimenting

For the further investigations, advanced finite element model is developed and numerical studies are carried out by the authors. Simultaneously to the real tests, virtual experiments – that is defined as full non-linear simulation representing the actual conditions (real imperfections, material, etc.) – are also executed. The virtual experimenting of the actual real tests on the steel girders supported the development and verification of the numerical model. In the second phase, additional parametric study – not detailed here – on the effect of different fabrication processes are also conducted by extended virtual experiments using the verified model [3].

The numerical analyses are completed by the ANSYS [6] finite element program system. In the numerical model, 4-node quadrilateral shell elements (designated as SHELL 181 in ANSYS) are applied (Figure 8), with a maximum side length of 20-50 mm, aligning to the residual stress shape.

Material and geometrical non-linearity is taken into account. Actual stress-strain relations of the steel material are set for the material non-linear behavior. The von Mises yield criterion is applied.

www.EngineeringEBooksPdf.com

Initial stresses caused by welding are considered in the models (Figure 2). The involved stress-distribution type represents the conventional manufacturing method: the usual values of 60% and 30% of the yield stress are applied to the tensile (at weld position, i.e. at the stiffeners) and compressive stresses, respectively. Geometrical imperfections are derived from the actual measurements discussed above.

In the analyses large displacements are considered. Displacement-controlled calculations are completed, i.e. loading is represented by gradually increasing displacements, better reflecting the experimental conditions. The analysis proceeds up to a certain set limit of displacement.

The iteration is completed on the bases of Newton-Raphson method. The convergence of the iterations is checked by the Euclidian norm of the unbalanced forces and moments; the applied convergence tolerance factor is 0.1%.

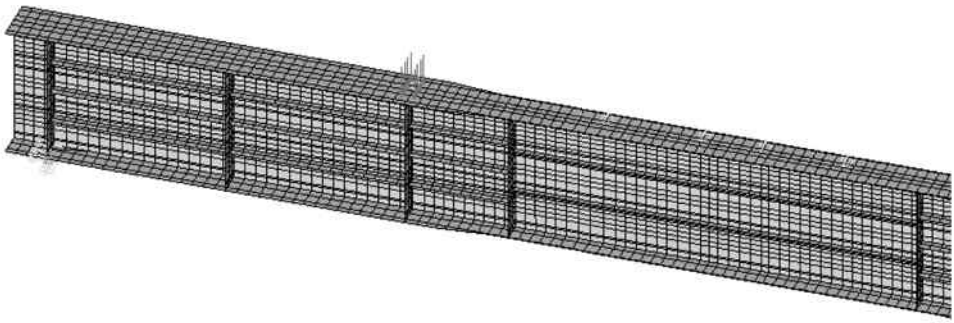


Figure 8: Finite element model of multi-stiffened plate girders.

Figure 9 shows the load-deflection curves obtained from the real as well as the virtual tests. The figure confirms that the simulation is in high accordance with the actual tests with respect to the overall behavior. As it is observed, the shape of the load-deflections curves coincide and the ultimate load capacities are close to the test results, which are also compared in Table 2 and Figure 7. The difference in ultimate loads is less than 5% in every case.

Comparison of failure modes similarly concludes that the model is reliable: the virtual experiment leads to the same failure as observed in the tests. An illustration is given in Figure 10.

As a consequence, the developed model well reflects the actual complex behavior of the multi-stiffened plate girders, thus it is applicable in further studies and design, too. By numerical simulation or virtual experimenting all the relevant details can be considered, and as the results prove, advanced numerical simulation may be rewarding due to the increased resistance.

Note that application of realistic imperfections has major importance in achieving accurate simulation, as the deformed shape may differ when the initial imperfection has different shape and magnitude from the actual one (e.g. as proposed by EC3-1-5, using buckling shape as imperfection, which may force one failure mode to dominate instead of occurring interaction modes). The imperfection sensitivity with these respects has not been studied yet; this task is involved in a separate research by Jakab et al. [7].

4.4 Effects of fabrication process

The research published in [3] involved further parametric studies on the effect of different fabrication processes, by extended virtual experiments using the verified numerical model. The analysis is extended to aluminum girders as well. Influence of different assumed initial imperfections resulted by different fabrication processes (e.g. MIG or FSW welding) and configurations is investigated. Based on the results, general conclusions are drawn on the applicability of the conceived configurations. Comparing to results obtained by the EC3-1-5 and EC9-1-1 standards, the standardized methods are also evaluated, and corrections are proposed.

www.EngineeringEBooksPdf.com

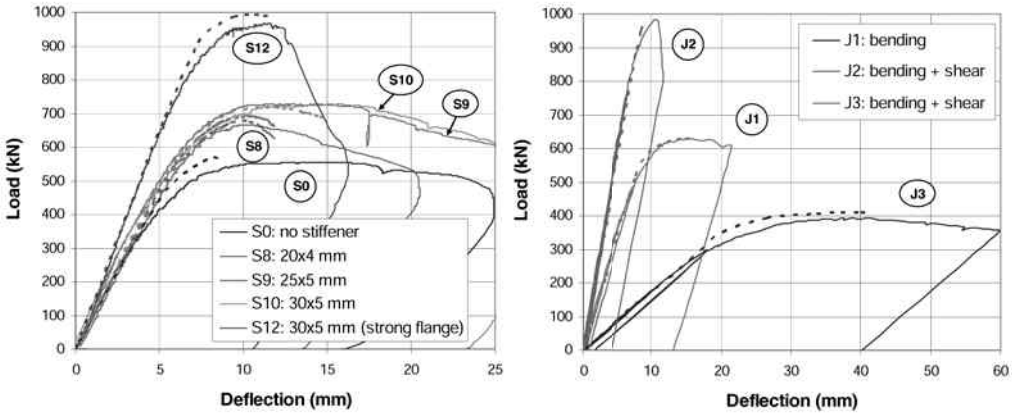
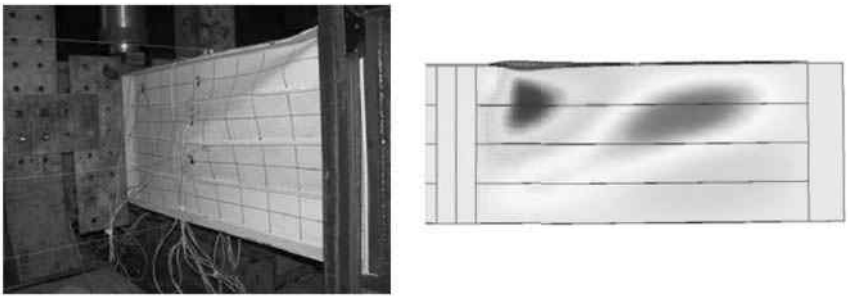


Figure 9: Comparison of test and FEM results – Load-deflection curves.



a) S8: shear buckling



b) S12: interaction of shear and bending

Figure 10: Comparison of test and FEM results – Failure modes.

www.EngineeringEBooksPdf.com

5 COMPLEX STIFFENED PLATE ELEMENTS OF A NEW DANUBE BRIDGE

A new Danube bridge is recently erected in Hungary: its main span is a basket handle shaped tied arch bridge, with a length of 307.8 m (Horváth et al. [8]). The height of the circular shaped arches is 48 m; the inside dimensions of the arch box cross-sections are 1960*3720 mm; the stiffening beams are parallelogram shaped box sections, with 2100 mm wide flanges and 3100 mm inner height. The walls of the arch and stiffening beam box sections are stiffened by open (flat and T-shape rib) longitudinal stiffeners; the thickness of the box sections varies from 20 to 50 mm.

The main bridge is assembled on a platform at the river bank and shipped to the final position. During the shipping operation, temporary supporting bars are installed near to the supports, to strengthen the structure over the barges. Figure 11 shows the erection of the bridge.



Figure 11: Erection of the arch bridge.

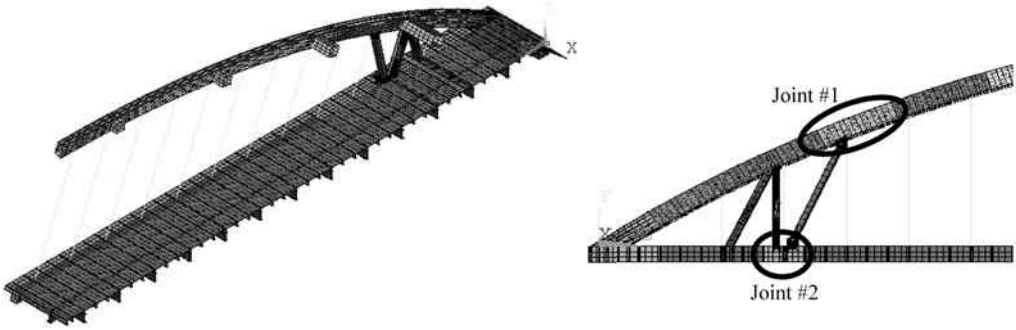


Figure 12: Global shell finite element model.

Global shell finite element model is developed for the investigation of the erection process, assuming double symmetry of the geometry, boundary conditions and loadings, as shown in Figure 12.

Six sub-models are developed in [9] to study in details the critical joints, owing refined meshes; their boundaries conform to the global model, from which the compatible displacements as the sub-model loads are derived. The structural details and the results of the stability analyses of two complex joints, marked in Figure 12, are illustrated in the following sections of the paper.

www.EngineeringEBooksPdf.com

The plate elements in the joints are classified according to the shapes and the stress field, as follows:

1. dominantly compressed stiffened plates (Joint #1, Figure 13),
2. stiffened plate subject to complex stress field (Joint #2, Figure 14/a),
3. irregular configuration and stress field (Joint #2, Figure 14/b,c).

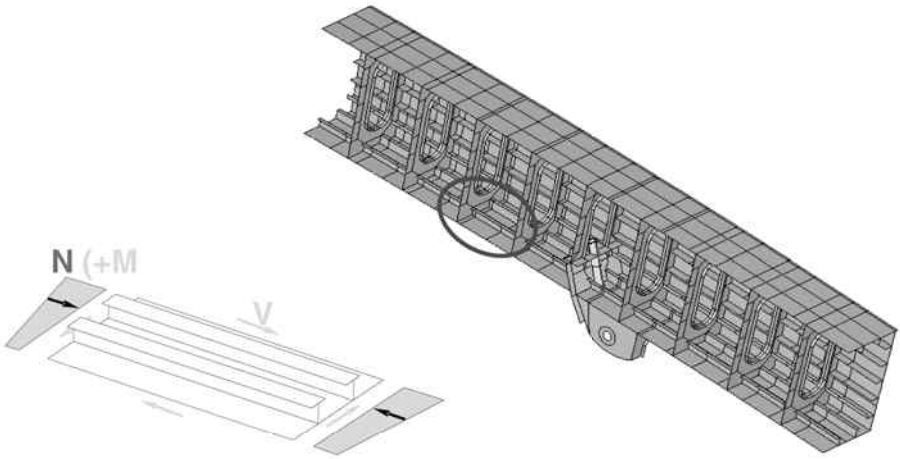
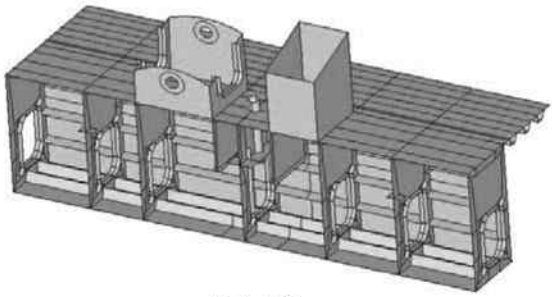
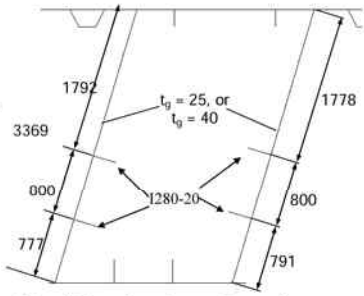


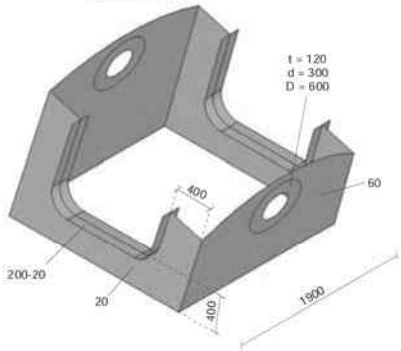
Figure 13: Longitudinally stiffened plate element in arch and supporting bar Joint #1.



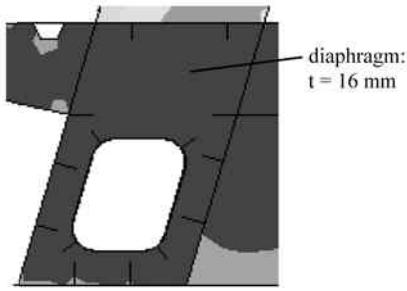
a) Joint #2



b) stiffened web configuration



c) gusset plates of pinned connection



d) typical diaphragm

Figure 14: Plate elements in stiffening beam and supporting bar Joint #2.

www.EngineeringEBooksPdf.com

6 STABILITY ANALYSES AND RESULTS

6.1 Longitudinally stiffened plates under compression

Beside the standard checks according to the relevant Hungarian codes, six of the critical stiffened panels subjected to pure compression are selected for detailed, advanced checking. Table 3 lists the geometry data of the investigated configurations; the yield stress of the material is f_y = 460 MPa.

Table 3. Investigated configurations and results of standard Method 1.

Case Nr.	t_p [mm]	b [m]	a [m]	stiffener	χ_c [-]	ρ [-]	ξ [-]	ρ_c [-]	ϕ [-]	ϕf_y [N/mm^2]
1	40	2	4.56	2 x 280-22	0.532	1.000	0.676	0.951	0.945	435
2	30	3.8	4.56	5 x 280-22	0.587	0.896	0.000	0.587	0.619	285
3	50	2	2.125	2 x T270-150-22	0.915	1.000	0.000	0.915	0.938	432
4	20	3.8	3.9	5 x 280-22	0.721	1.000	0.000	0.721	0.676	311
5	16	3.8	3.86	5 x 280-22	0.761	1.000	0.000	0.761	0.637	293
6	20	2	3.86	2 x 280-22	0.723	1.000	0.000	0.723	0.698	321

t_p – plate thickness; b – plate width; a – plate length between transverse stiffeners or diaphragms

6.1.1 Standard method (Method 1)

In accordance to EC3-1-5, resistance is calculated on the basis of effective cross-section calculation. For comparison reasons, the general reduction factor ϕ is introduced, standing for the ratio of the effective and gross area. Table 3 shows the obtained results. It can be observed that – except for the first case – column-like behavior is dominant ($\xi = 0$).

6.1.2 Method 2 and 3

In case of pure compression, *Method 2* (use of linear stability analysis) and *Method 3* (reduced stress method) lead to the same results. According to the method, critical stresses of the stiffened plate have to be evaluated by numerical analysis: bifurcation analysis is completed on FE models developed by ANSYS program. Three adjacent panels are modeled by shell elements as shown in Figure 15. Both the overall and local buckling shapes are determined. Typical buckling shapes are shown in Figure 16. The obtained overall buckling modes confirm that the plates are relatively short, which is also found by the standard analysis. As stated, overall buckling precedes local buckling in all the cases.

In Table 4, the calculated critical stresses for overall buckling are compared to the EC results. It is observed that the buckling stress formula given in EC3 1-5 is in good accordance with the FE calculations in case of compression. This also means that *Methods 1 and 2* do not lead to significant deviations in the ultimate load.

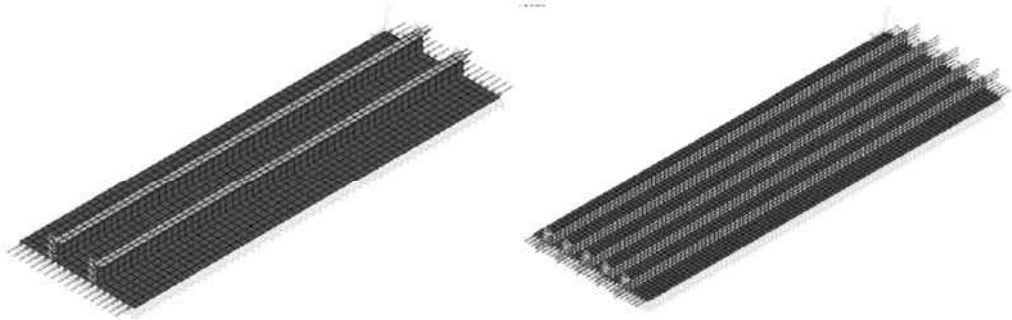
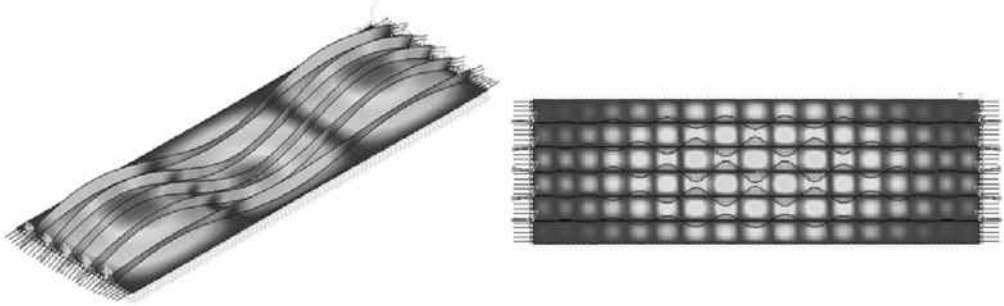


Figure 15: Numerical models of two typical stiffened panels.

www.EngineeringEBooksPdf.com



a) overall plate buckling b) local plate buckling

Figure 16: Plate buckling modes from linear stability analysis.

Table 4. Critical stresses for overall buckling.

Case	Critical stress [N/mm^2]		diff.
Nr.	EC3-1-5	FEM	[%]
1	868	931	7.3
2	578	588	1.7
3	3598	3560	-1.1
4	902	881	-2.3
5	995	955	-4.0
6	865	969	12.0

Table 5. Comparison of Methods 1 and 4.

Case	Ultimate load [N/mm^2]		diff.
Nr.	Method 1	Method 4	[%]
1	435	448	3.0
2	285	314	10.2
3	432	452	4.6
4	311	365	17.4
5	293	370	26.3
6	321	404	25.9

6.1.3 Non-linear simulation (Method 4)

The non-linear simulation is completed using the same geometrical model. Standardized material models and imperfections are applied. Figure 17 illustrates the material model: linearly elastic - perfectly plastic – with a fictive hardening to overcome numerical instability. The imperfections to be applied in the analysis are distinguished by the code with respect to the failure mode under investigation. In the studied case:

- "global" imperfection of longitudinal stiffener (Figure 17/a), with a magnitude of $e_{0w} = \min(a/400, b/400)$,
- local imperfection of plate panels or sub-panels (Figure 17/b), with a magnitude of $e_{0w} = \min(a/400, b/400)$,
- local imperfection of stiffener subject to twist (Figure 17/c), with a magnitude of $\phi_0 = 1/50$.

Generally, these imperfections should be combined, choosing a leading imperfection with full magnitude and the additional imperfections can be considered with magnitudes reduced to 70%. As in the studied case the local plate buckling between stiffeners is not dominant, its imperfection can be neglected. The overall buckling shapes typically includes the other two imperfections, thus, the buckling shapes may be applied as imperfections; however, it complicates the adaptation of the 70%-rule, since the magnitudes of the different imperfections included are linearly coupled. As reference, the magnitude is chosen as the global imperfection value satisfies the criterion. If the twist imperfection is considered as leading, the global imperfection becomes extremely large in certain cases. Note that the standard allows the usage of corresponding buckling shapes as imperfections in any case.

In the completed study the α_2 factor – representing the design model uncertainties equals to 1.0. The numerical model is verified by real experiments as discussed earlier. Based on the verification, the α_1 factor – representing the numerical model's uncertainties – also equals to 1.0.

www.EngineeringEBooksPdf.com

Figure 18 shows the load-deflection curves of typical cases. Ultimate capacity calculated by EC3-1-5 and results corresponding to large imperfection (i.e. choosing the twist imperfection as leading) are also indicated. As the figure confirms, the extremely large imperfection may lead to large differences in certain cases.

6.1.4 Comparison

As it is already stated, *Method 1 and 2* do not give significant differences because of the concurrent critical stresses. Hereafter, just *Method 1 and 4* are compared.

Table 5 lists the calculated ultimate loads. It can be observed that the difference between the standard method and full numerical analysis can exceed 25%. Note that as it is also found by [3], the differences can be even higher if actual strain hardening is also taken into account. It is observed that with increasing dominance of buckling the underestimation by the standard method (compared to FEM) is also increasing, thus, the larger the slenderness, the larger the safety. Needless to say, when failure occurs due to overall yielding, there is no difference in the results (Case 1 and 3).

However, the authors should emphasize that the imperfections proposed by EC3-1-5 are dependent only on the plate dimensions *a* and *b*, and independent from the fabrication process, stiffener geometry, etc., which would otherwise significantly influence the actual imperfections. In this way, it is queried whether the proposed imperfection magnitude is sufficient or not. Consequently, the conclusion of the above comparison can be drawn in two ways:

1 If the applied imperfections are assumed sufficient, the safety in the standard EC method can be relatively large.
2 If the applied imperfections are not sufficient, the FE analysis cannot be considered accurate, and the arising error is on the unsafe side.

Recall that the measurements discussed in Section 3 presume larger amplitude of imperfections than the ones currently applied in the code. Note that the analyses are completed with 2-4 times larger imperfections (leading twist imperfections) as well. Even with this extreme imperfection, the analyses – except for Case 2, where anyway overall yielding is dominant – give larger load capacity than *Method 1*.

It is also noted that with increasing slenderness the imperfection sensitivity is also increasing.

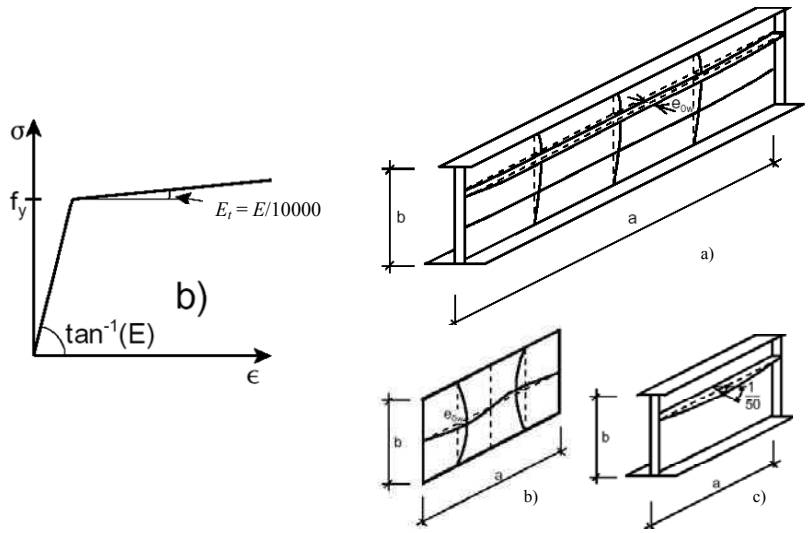
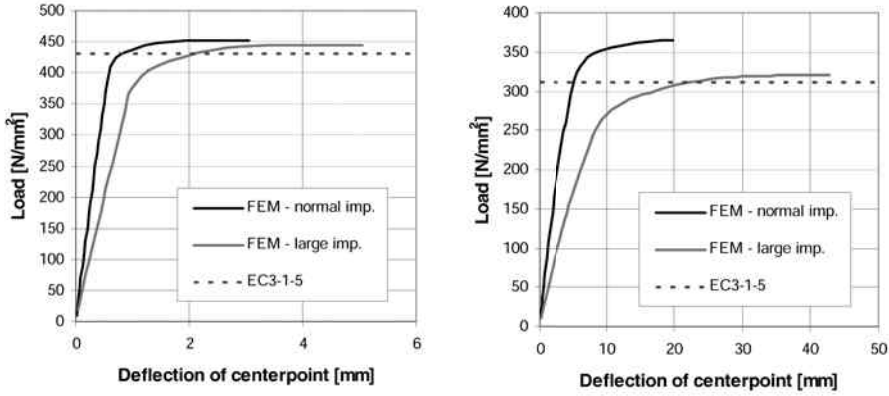


Figure 17: Applied material model and equivalent geometrical imperfections.

www.EngineeringEBooksPdf.com



a) Case #3 b) Case #4

Figure 18: Typical results of the non-linear simulation.

6.2 Complex plated elements

In the following sections, application of the reduced stress method is illustrated on complex plated elements subjected to complex stress field. Strength and stability check of more than a hundred of details is completed by the help of the shell-element sub-models mentioned in Section 5 [9]. Analysis of three representative details is briefly summarized hereafter.

Due to the complex stress field and/or the complex geometry, these details can hardly be handled by the basic standard method. In absence of prescribed equivalent geometrical imperfections, the use of *Method 4* is not practical either. As a reasonable alternative, the reduced stress method (*Method 3*) is applied, even though – as it is discussed in the following sections – it may be laborious and troublesome, too. The general outline of *Method 3* is tabulated in Table 6. Through the discussion of the representative examples, special attention is paid to the following aspects and problematic points that practically may arise:

- modeling of the plated element,
- definition of the critical point of the element and the strength load amplifier,
- determination of governing failure mode and choice of buckling reduction curve.

The shell-element sub-models allow accurate stress and linear stability analysis of the stiffened plated members, considering the complex interaction behavior of the adjacent elements.

6.2.1 Stiffened plates subject to complex stress field

During the erection of the bridge, simultaneous action of bending, shear and direct transverse loading applies in the longitudinally stiffened web plate in the vicinity of the temporary bars (Figure 14/a,b), causing the complex stress field shown in Figure 19. In this case, definition of the critical point of the element is relatively straightforward. Figure 20/a shows the buckling shape of the panel under investigation; the corresponding critical load amplifier: $\alpha_{cr} = 6.99$. The high value presumes that the element is not sensitive for buckling. Details of the calculation are given in Table 7.

Crucial point is the determination of the buckling reduction factor. The reduction factors related to the different failure modes (i.e. direct stresses, shear, etc.) are determined on the basis of the general slenderness parameter. Due to the complex stress field, various buckling curves are to be used even for this single case (Figure 21) and the choice is not straightforward. For simplification, Annex B of EC3-1-5 provides a general plate buckling curve (also indicated in Figure 21) that gives conservative, but

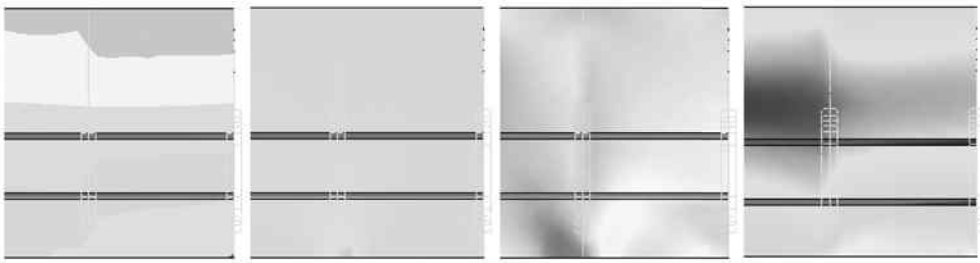
www.EngineeringEBooksPdf.com

reasonable approximations for the different load cases. Additional difficulty is that regarding the longitudinal and transverse buckling modes, one has to analyze the possibility of column-like or plate-type post-critical behavior. Equations 6 and 7 shall be used for the interpolation between the two behavior types. For this, determination of the column critical load amplifier $\alpha_{cr,c}$ (or $\sigma_{cr,c}$) would require a numerical model in which the corresponding longitudinal edges are relieved from adjacent elements. Following this rule would highly complicate the analysis, losing the benefits of such advanced modeling. Alternatively, it can be conservatively assumed that column-like buckling occurs.

Table 6: Outline of Method 3.

Step	Description		
1	strength load amplifier	$\alpha_{ult,k} = f_y / \sigma_{red}$ from linear elastic analysis	(9)
2	critical load amplifier	α_{cr} from linear elastic buckling analysis	
3	slenderness parameter	$\bar{\lambda}_p = \sqrt{\frac{\alpha_{ult,k}}{\alpha_{cr}}}$	(10)
4	buckling reduction factor	a) conservative approach: $\rho = \min(\rho_x, \rho_y, \chi_w)$ or	(11)
		b) interpolated values of ρ_x, ρ_y, χ_w	(12)
5	resistance check	$\frac{\rho \alpha_{ult,k}}{\gamma_{M1}} \geq 1.0$	(13)

σ_{red} – acting Von-Mises stress; $\alpha_{ult,k}$ – load amplifier to reach first yield; α_{cr} – load amplifier to reach elastic critical load; γ_{M1} – partial factor; ρ_x, ρ_y and χ_w are corresponding buckling reduction factors for longitudinal, transverse and shear stresses, respectively, taking into account column-like behavior if relevant



$\sigma_{x,max}$ = 214 MPa | $\sigma_{y,max}$ = 90 MPa | τ_{max} = 29 MPa | $\sigma_{red,max}$ = 187 MPa

a) longitudinal | b) transverse | c) shear | d) Von-Mises

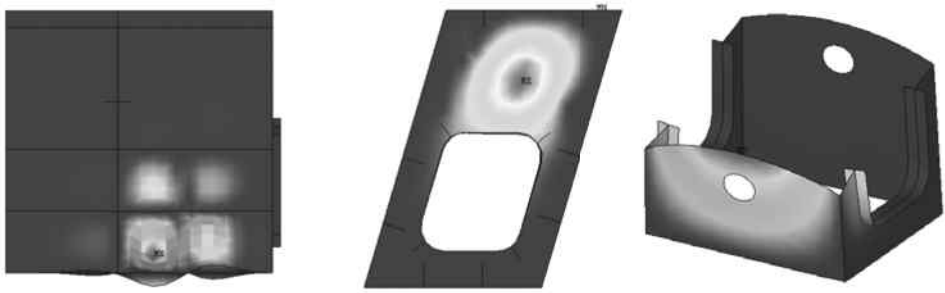
Figure 19: Stress components – Multi-stiffened web.

Table 7: Complex details – Results of Method 3.

Case	Description	σ_{red} [MPa]	$\alpha_{ult,k}$ [-]	α_{cr} [-]	λ_p [-]	ρ [-]	type of curve used	$\frac{\rho \alpha_{ult,k}}{\gamma_{M1}}$
1	web – load introduction	187	1.90	6.99	0.521	0.83	column	**1.58**
2	diaphragm	68	5.22	7.12	0.856	0.84	gen. plate	**4.38**
		316	1.12	7.57	0.385	0.91	column	**1.02**
3	pinned connection	100	3.55	7.57	0.685	0.73	column	**2.59**
		355	1.00	7.57	0.363	0.92	column	**0.92**

σ_{red} – acting Von-Mises stress; λ_p – non-dimensional general plate slenderness; ρ – general reduction factor; $\alpha_{ult,k}$ – load amplifier to reach first yield; α_{cr} – load amplifier to reach elastic critical load

www.EngineeringEBooksPdf.com



$\alpha_{cr} = 6.99$ $\alpha_{cr} = 7.12$ $\alpha_{cr} = 7.57$

a) multi-stiffened web b) diaphragm c) gusset plate stiffening bar

Figure 20: Plate elements in stiffening beam and supporting bar Joint #2 – Buckling shapes.

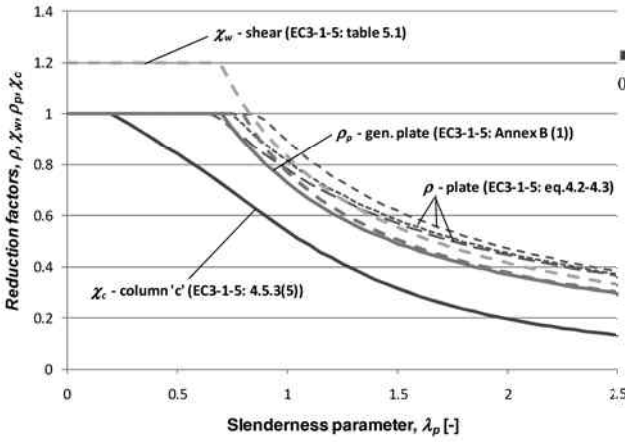


Figure 21: Different buckling curves (reduction factors).

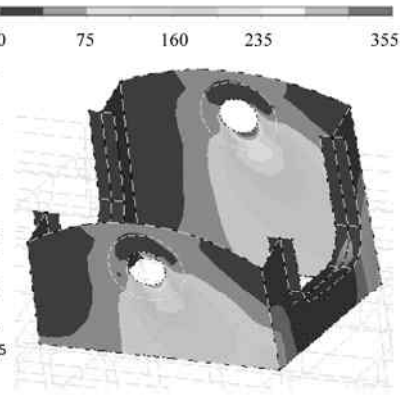


Figure 22: Von-Mises stress distribution in the gusset plates

6.2.2 Diaphragm

For the case of the typical 16-mm-thick diaphragm (Figure 14/d), critical stress for column-like buckling is easy to predict: it is certainly less than 20 MPa regarding any direction. Thus, it can be stated that plate-type behavior governs the failure (Figure 20/b shows the buckling mode). Table 7 lists the corresponding results.

6.2.3 Complex geometry elements – Gusset plate of pinned connection

The gusset plate of the pinned connection (Figure 14/c) is complex in terms of geometry as well as stress distribution (Figure 22). Definition of critical point of the element is complicated and as Table 7 confirms it may drastically change the outcomes with respect to strength as well as failure mode (how slender the element is). Rigorously taking the words of the code would mean one has to consider the peak stress arising in the vicinity of pin hole that reaches the yield stress. This would result in unsatisfactory element. However, this local plasticization does not characterize the overall behavior. Selecting more representative stress values leads to reasonable and satisfactory results (the uniform stress of 100 MPa reflects uniform bearing stress distribution).

www.EngineeringEBooksPdf.com

Determination of buckling reduction factor is also complicated by the fact that a type of distortional stability failure mode occurs with interaction of the gusset plate and the stiffening diaphragms (Figure 20/c). Conservatively, column buckling mode is considered; however, selecting more reasonable plate buckling curves would drastically change the results: for the relevant slenderness parameter one may find yielding instead of stability failure (i.e. reduction factor equals to 1.0).

6.2.4 Shortcomings of the advanced methods

As demonstrated, the general use of the *reduced stress method* for complex plated elements is complicated by the facts that:

1) Definition of critical point of the element is not straightforward:
   a) Finite element analysis may result in unrealistic peak stresses due to the mesh.
   b) Element stability behavior is not necessarily related to the peak stress (e.g. bearing stress distribution along perimeter of pin hole).
   c) The analysis does not necessarily reflect whether a certain buckling mode governs the failure.
2) Choice of appropriate buckling curve is not straightforward:
   a) High confidence is needed to estimate the actual failure mode and post-critical behavior.
   b) To combine plate-type and column-like behavior, one may have to analyze the same detail with different boundary conditions, which is not practical, especially when the element boundaries cannot be clearly defined.
3) The method may lead to extremely conservative results and thus uneconomic design, which may set back its use:
   a) The limit state is assigned with the most critical point of the structure and thus exceeding the stress limit anywhere means failure of the structure.
   b) Accordingly, conservatively selecting the worst cases (i.e. peak stress point and column buckling curve) may result in extremely underestimated capacity of the whole element or may presume certain failure (e.g. eligibility of the pinned connection cannot be confirmed).

The above problems could be overcome by using *full non-linear simulation* or virtual experimenting. However, such simulation requires careful detail modeling, relatively accurate estimations on material behavior and imperfections.

7 CONCLUSIONS

In the paper the stiffened plates are studied by experimental, standard based and advanced stability analyses. The investigations are related to regular test plate elements and complex plated elements of a bridge. The conclusions of the research can be drawn on different fields, as follows:

Buckling checking of regular stiffened plates:

- Based on experimental, numerical and theoretical studies buckling coefficients are of multi-stiffened plates are formulated and modifications are proposed for the standard Eurocode calculations of critical loads.
- The application of the modified critical stress formulations leads to better approximation of the shear resistance and it gives back the experimentally observed actual failure mode.

FEM based buckling checking:

- Geometrically and material nonlinear FE models are developed in parallel with experiments considering measured geometrical imperfections and residual stresses.
- The results of the analyses are in high accordance with the actual tests with respect to the ultimate behavior and capacities.
- By the virtual experimenting all the relevant details can be considered, and the results prove that FEM based design using advanced numerical simulation may be rewarding due to the increased resistance.

www.EngineeringEBooksPdf.com

Practical checking of irregular plates by FEM analysis:

- Different plate buckling design methods are applied to check the complex plate elements on a new Danube bridge in Hungary, under dominant compression stress, subjected to complex stress field and having irregular configuration and stress field.
- By comparison of the results it is concluded the difference between the standard method of the Eurocode and full numerical analysis can exceed 25% for dominantly compressed multi-stiffened elements.
- Practical shortcomings of using the reduced stress method of Eurocode standard for complex geometry and stress field on the basis of numerical calculation are observed due to the (i) uncertainties of definition the critical point of the element, (ii) choice of appropriate buckling curve.

The advanced stability analysis is refined for stiffened plates and extended for other type of structures (e.g. girders with trapezoidally corrugated webs) in the frame of ongoing research of the authors.

ACKNOWLEDGEMENT

The presented research is conducted under the partial financial support of the OTKA T049305 project of the Hungarian National Science Foundation.

REFERENCES

[1] *EN 1993-1-5:2005 Eurocode 3 – Design of steel structures – Part 1-5: Plated structural elements*, Final Draft, CEN, Brussels, 2005.

[2] *EN 1993-1-6:2005 Eurocode 3 – Design of steel structures – Part 1-6: Strength and stability of shell structures*, CEN, Brussels, 2005.

[3] Vigh, L.G., *Virtual and real test based analysis and design of non-conventional thin-walled metal structures*, PhD dissertation, Budapest University of Technology and Economics, 2006.

[4] Dunai, L., Jakab, G., Néző, J., Topping, B.H.V., "Experiments on welded plate girders: fabrication, imperfection and behaviour", *Proc. 1st International Conference on Advances in Experimental Structural Engineering (AESE '05)*, Vol. 1, pp. 51-58, Nagoya, Japan, 19-21 July, 2005.

[5] Vigh, L.G., "On the Eurocode buckling formulas of multi-stiffened metal plates", *Proc. of International Colloquium on Stability and Ductility of Steel Structures (SDSS 2006)*, Vol. 1, pp. 545-552, Lisbon, Portugal, 6-8 September, 2006.

[6] *ANSYS Structural Analysis Guide*, Online Documentation ANSYS Inc., 2005.

[7] Jakab, G., Szabó, G., Dunai, L., "Imperfection sensitivity of welded beams: experiment and simulation", *International Conference in Metal Structures: Steel – A New and Traditional Material For Building (ICMS 2006)*, pp. 173-182, Brasov, Romania, 20-22 September, 2006.

[8] Horváth, A., Dunai, L., Domanovszky, S., Pesti, Gy., "The Pentele Danube bridge in Dunaújváros, Hungary; design, research and construction", *Bauingenieur*, pp. 419-438, 2008.

[9] Dunai, L., Farkas, Gy., Szatmári, I., Joó, A., Tóth, A., Vigh, L.G., *Dunaújváros Danube Bridge – River Bridge – Additional static analyses 2* (in Hungarian), 7th research report, BME Department of Structural Engineering, Budapest, August 2006.

www.EngineeringEBooksPdf.com

SDSS'Rio 2010 STABILITY AND DUCTILITY OF STEEL STRUCTURES
E. Batista, P. Vellasco, L. de Lima (Eds.)
Rio de Janeiro, Brazil, September 8 - 10, 2010

DIRECT STRENGTH DESIGN OF COLD-FORMED SECTIONS FOR SHEAR AND COMBINED ACTIONS

Cao Hung Pham* and Gregory J Hancock*

* School of Civil Engineering, University of Sydney, Australia, 2006
e-mails: caohung.pham@sydney.edu.au, gregory.hancock@sydney.edu.au

Keywords: Design, Cold-Formed Steel, Direct Strength Method, Shear, Combined Actions

Abstract. *In order to extend the Direct Strength Method (DSM) of design of cold-formed sections to shear, and combined bending and shear, a research program has been performed recently at the University of Sydney. This includes evaluation and calibration of DSM design rules for shear and combined actions when applied to an extensive series of purlins tested at the University of Sydney, as well as shear only and combined bending and shear tests on channel sections. The paper summarises this research, as well as making proposals for shear, and combined actions. Two features researched are the effect of full section shear buckling (as opposed to web only shear buckling), and tension field action. Full section buckling is a feature of the DSM but requires software that can evaluate full sections for shear. Methods for doing this are summarised in the paper.*

1 INTRODUCTION

In both the Australian Standard and American Specification for the Design of Cold-Formed Steel Structures, which include the newly developed Direct Strength Method (DSM) of design, the method presented [Chapter 7 of AS/NZS 4600:2005 (Standards Australia [1]), Appendix 1 of the North American Specification (AISI [2])] is limited to pure compression and pure bending. The Direct Strength Method (Schafer and Peköz [3]) was formally adopted in the North American Design Specification in 2004 and in AS/NZS 4600:2005 as an alternative to the traditional Effective Width Method (EWM) in 2005. It uses elastic buckling solutions for the entire member cross section to give the direct strength rather than for elements in isolation.

The first advantage of the DSM is that it allows direct computation of the capacity of cold-formed thin walled members of complex section shape (eg. with intermediate stiffeners). Secondly, the interaction between local and overall modes, distortional and overall modes is easily taken into account. The DSM uses numerical solutions for elastic buckling and requires computer software such as THIN-WALL (CASE [4]) or CUFSM (Schafer and Ádány [5]) to evaluate elastic buckling stresses. There is no need to calculate cumbersome effective sections especially with intermediate stiffeners.

The development of the DSM for columns and beams, including the reliability of the method is well researched. In the review of the DSM of cold-formed steel member design, Schafer [6] noted that no formal provisions for shear currently exist for the DSM. However, as recommended in the AISI Direct Strength Design Guide [7], the existing provisions in the North American Design Specification and AS/NZS 4600:2005 could be suitably modified into the DSM format.

To investigate this proposition, vacuum rig tests on continuous lapped cold-formed purlins at the University of Sydney over a 10 year period, have been used to calibrate DSM design proposals for shear and combined bending and shear (Pham and Hancock [8]). The conclusions from this calibration are that the existing bending and shear equations in AS/NZS 4600:2005 in DSM format will provide reliable designs irrespective of whether the limiting design moment in the interaction equation is based on the lesser of the local buckling and distortional buckling moments (called Proposal 1) or the local buckling

www.EngineeringEBooksPdf.com

moment alone (called Proposal 2). To further investigate these proposals, additional tests on C-sections in predominantly shear, combined bending and shear, and bending alone have been performed at the University of Sydney (Pham and Hancock [9], [10])

The main objectives of this paper are:

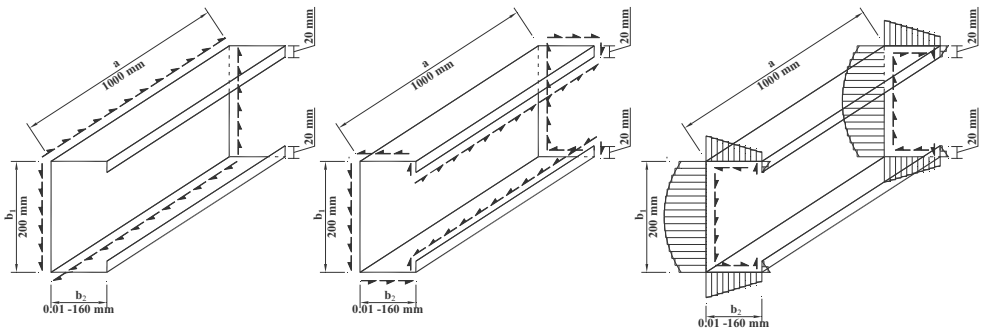
- To summarise analyses of full sections in shear, with and without intermediate stiffeners, with a view to providing elastic shear buckling loads V_{cr} which can be used as input to the Direct Strength Method of design of complete sections in shear.
- To summarise tests on high strength cold-formed lipped C-Sections (with and without intermediate stiffeners) in shear and combined bending and shear.
- To summarise proposals for extension of the Direct Strength Method to shear and combined bending and shear. The proposals are made both with and without Tension Field Action (TFA) and are compared with the test results on the lipped C-sections.

2 SHEAR BUCKLING OF FULL SECTIONS

The Spline Finite Strip Method (SFSM) is a development of the semi-analytical finite strip method originally derived by Cheung [11]. It uses spline functions in the longitudinal direction in place of the single half sine wave over the length of the section, and has been proven to be an efficient tool for analyzing structures with constant geometric properties in a particular direction, generally the longitudinal one. The advantage of the spline finite strip analysis is that it allows more complex types of loading and boundary conditions other than simple supports to be easily investigated and buckling in shear is also easily accounted for. Initially, the spline finite strip method was fully developed for the linear elastic structural analysis of folded plate structures by Fan and Cheung [12].

The SFSM was then extended to buckling and nonlinear analyses of flat plates and folded-plate structures by Lau and Hancock [13] and Kwon and Hancock [14, 15]. The spline finite strip method involves subdividing a thin-walled member into longitudinal strips where each strip is assumed to be free to deform both in its plane (membrane displacements) and out of its plane (flexural displacements). The functions used in the longitudinal direction are normally B3 splines. The ends of the section under study are normally free to deform longitudinally but are prevented from deforming in a cross-sectional plane.

For the shear buckling analyses described by Pham and Hancock [16], three different methods, which represent different ways of incorporating the shear stresses in the thin-walled section, are used in this analysis as shown in Fig. 1.



(a) Case A & Case B *(b) Case C* *(c) Case D*

Figure 1. Shear Flow Distributions in Lipped Channels

www.EngineeringEBooksPdf.com

These include pure shear in the web only (Cases A and B), pure shear in the web and the flanges (Case C) , and a shear distribution similar to that which occurs in practice allowing for section shear flow (Case D). For combined bending and shear, each method of the incorporation of the shear stress is combined with pure bending to produce the interaction relations. The stress states studied are not in equilibrium as shear can only be generated in a section by moment gradient. However, the studies allow the shear buckling, and combined bending and shear buckling to be isolated and investigated. Buckling modes from the SFSM described in Pham and Hancock [17] are shown in Fig. 2 for combined bending and shear where the shear is Case D in Fig. 1. They demonstrate a range of buckling modes including section twisting for sections with narrow flanges, flange distortional buckling and web shear buckling depending upon the width of the flanges.

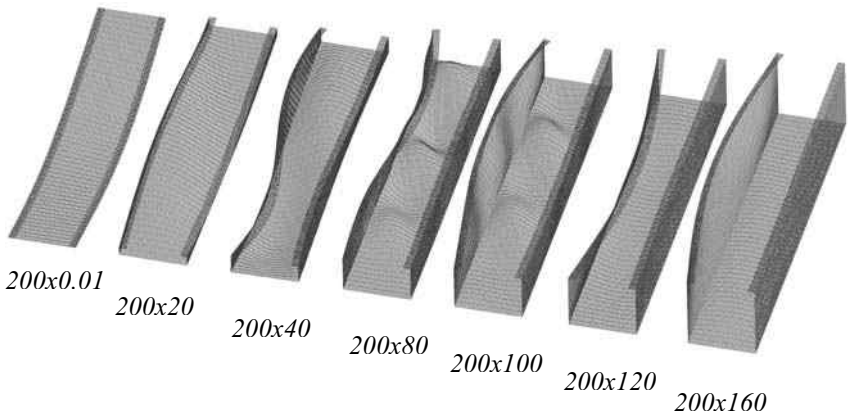


Figure 2. Buckling Mode Shapes of Lipped Channel Section under Combined Bending and Shear for *Case D*

The geometry of the lipped channel with an intermediate stiffener studied is shown in Fig. 3. The purpose of this study (Pham and Hancock [18]) was to determine the effect of an intermediate stiffener in the web on the shear buckling load of the section.

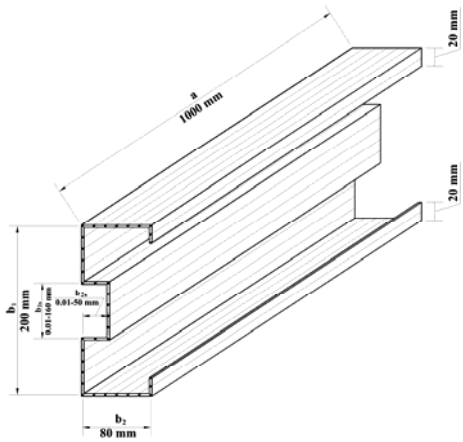


Figure 3. Lipped Channel Geometry with an Intermediate Stiffener

www.EngineeringEBooksPdf.com

The channel section consists of a web of width 200 mm (b_1), a flange of width 80 mm (b_2), a lip size of 20 mm, all with thickness of 2 mm. The stiffener is positioned at the longitudinal center line of the web and the main variables are the dimensions of the stiffener. The depth of stiffener (b_{1s}) increases from 0.01 mm to 160 mm whereas the width of the stiffener (b_{2s}) varies from 0.05 mm to 50 mm. The length of the member studied is 1000 mm. The aspect ratio of the web rectangular plate is therefore a/b_1 = 5. The buckling modes for the section in shear according to Case D in Fig. 1 with an intermediate stiffener of depth 50mm are shown in Fig. 4 as the height of the stiffener increases. Modes ranging from flange distortional buckling to local buckling in shear in the intermediate stiffener can be observed.

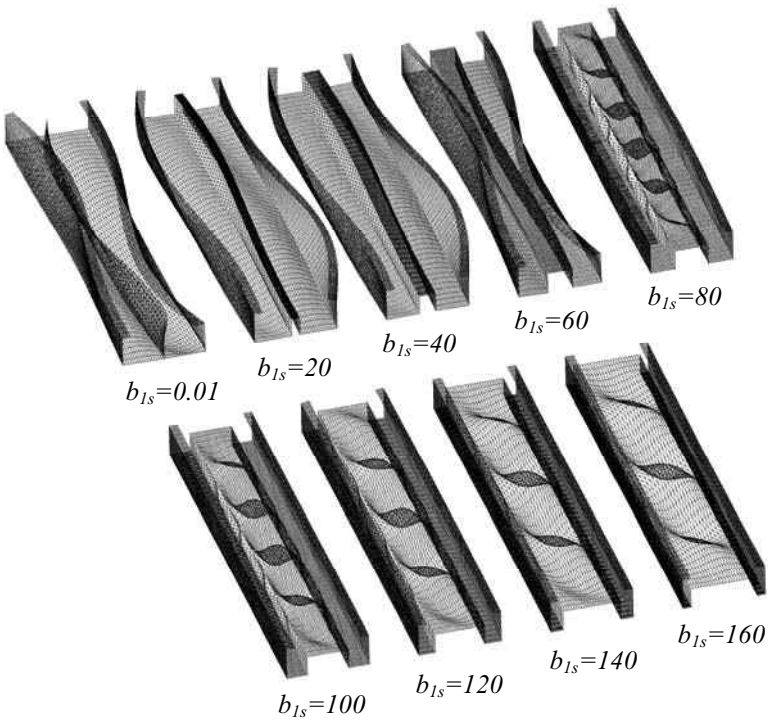


Figure 4. Buckling Mode Shapes of Lipped Channel Sections with an Intermediate Stiffener

3 EXPERIMENTS ON PLAIN C- LIPPED SECTIONS AND SUPACEE® SECTIONS IN SHEAR, AND COMBINED BENDING AND SHEAR

3.1 Experimental Rig and Tests Specimens

LaBoube and Yu [19] conducted a series of tests including a total of forty three beam specimens subjected primarily to shear stress. They found that, for shear, the exact critical buckling load for a beam webs is difficult to determine experimentally and the post-buckling strength of web elements due to tension field action increases as the h/t ratio of the web, the aspect ratio of the web, and the yielding point of the material increase. Moreover, the arrangement of connections has a significant effect on the ultimate shear capacity of the unreinforced webs. The current Effective Width Method for shear was calibrated against these tests.

www.EngineeringEBooksPdf.com

Another testing program was also performed at the University of Missouri-Rolla for the structural strength of beam webs subjected to combined bending and shear by LaBoube and Yu [20]. The results of twenty five beam tests indicated that the circular formula, originally developed for a separate individual sheet, would be conservative for beam webs with adequate transverse stiffeners, for which a diagonal tension field action can be developed. Based on these test results, the linear interaction equation was developed for beams webs with transverse stiffeners for combined bending and shear in the current Effective Width Method.

This paper summarises two series of tests on both high strength cold formed steel plain C- lipped sections and SupaCee® sections (Lysaght [21]) for the extension to the Direct Strength Method for shear, and combined bending and shear. The first experimental program comprised a total of sixty tests which included three test series conducted in the J. W. Roderick Laboratory for Materials and Structures at the University of Sydney. All tests were performed in the 2000 kN capacity DARTEC testing machine, using a servo-controlled hydraulic ram. Two different commercially available plain C- lipped channel sections of 150 mm and 200 mm depths as shown in Fig. 5 were chosen with three different thicknesses of 1.5 mm, 1.9 mm and 2.4 mm. The first series (*V*) is predominantly shear; and the second series (*MV*) is combined bending and shear. These series each consisted of twenty four tests and used the same test rig configuration. The third series is bending only (*M*) which used the common four point loading configuration. A total of twelve tests of this series were conducted. Although the tests described in LaBoube and Yu [20] contained straps at the loading points as described later, tests both with and without straps are included in the test program.

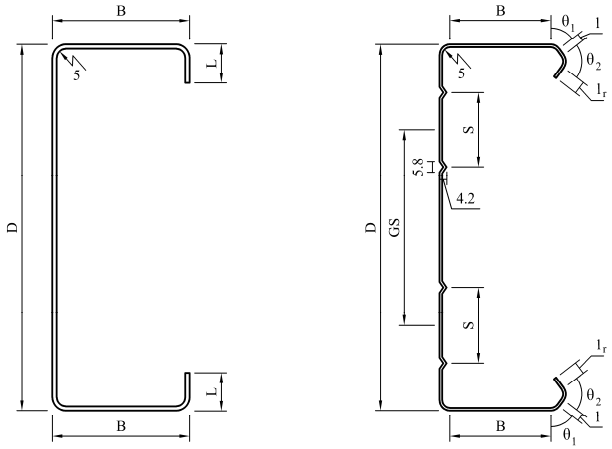


Figure 5. Dimensions of Plain and SupaCee® Channel Sections

The second series of test specimens was also performed at the University of Sydney including a total of thirty six tests of commercially available SupaCee® sections as shown in Fig. 5. Two different depths of 150 mm and 200 mm were chosen with three different thicknesses of 1.2 mm, 1.5 mm and 2.4 mm. Three test series, which were conducted identically to the first test program, also consisted of predominantly shear test (*V*), combined bending and shear test (*MV*) and bending only test (*M*). These test series each included twelve tests each and used the same test rig configurations with the first test program.

The basic design of the test rig was developed by LaBoube and Yu [19, 20]. A diagram of the test set-up is shown in Fig. 6 for both the *V* and *MV* series. The only difference between the *V* and *MV* tests is the ratio of shear span to depth where the shear span is the distance between the lines of bolts at the loading and support points. With the *V* series, the ratio of span to depth is 1:1 whereas that of *MV* series is 2:1.

www.EngineeringEBooksPdf.com

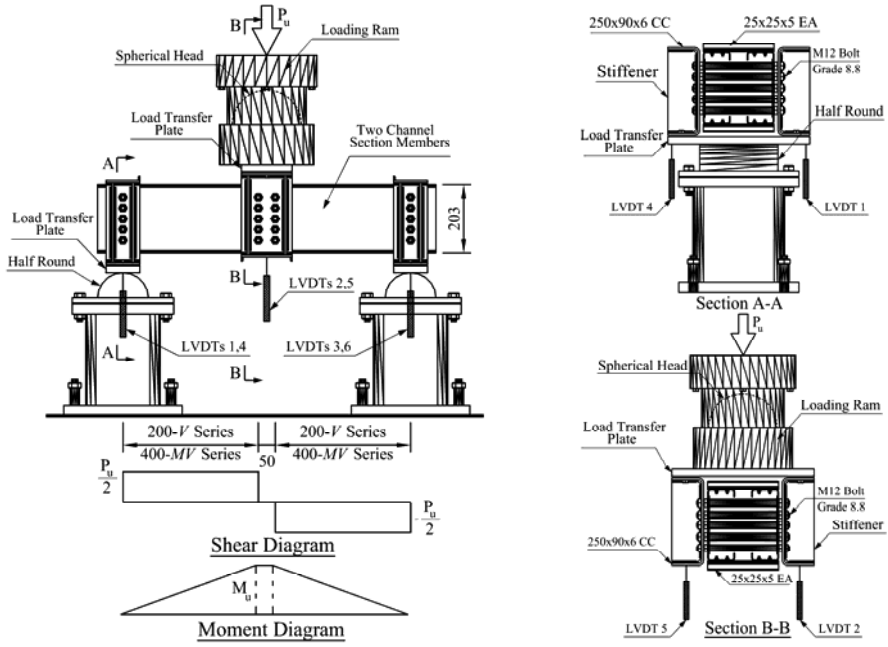


Figure 6. *V* and *MV* Test Series Configuration (Dimensions for 200 mm Deep Section)

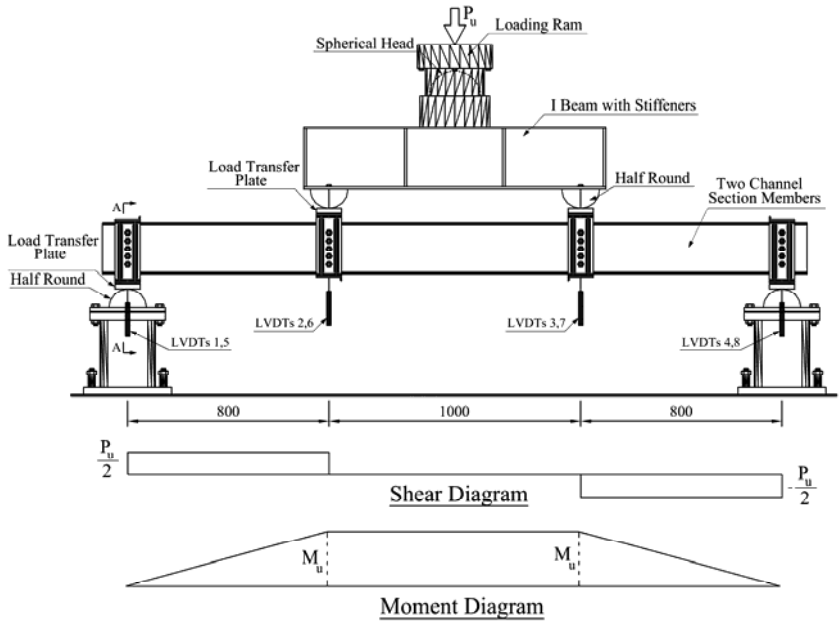


Figure 7. *M* Test Series Configuration (Dimensions for 200 mm Deep Section)

www.EngineeringEBooksPdf.com

The detailed test configuration of the bending only series is shown in Fig. 7. The four point bending arrangement provided a central region of uniform bending moment and zero shear force. At the two supports, the rig assembly is exactly the same as that of the predominantly shear test set-up. The difference is at the loading points which have a similar configuration to the support points. The channel section members were loaded symmetrically at two points via a centrally loaded spreader I beam with stiffeners. The distance between the two half rounds bolted to the I beam at the loading points was 1000 mm. These two half rounds bore upon two 20 mm thick load transfer plates. The half round ensured that the applied loads were vertical. The distance between the support and the adjacent loading point was 800 mm.

3.2 Plain Lipped C-Section Test Results

The full set of test results for the plain lipped C-Sections is given in the research report by Pham and Hancock [9]. The tests results are compared with existing design methods in AS/NZS 4600:2005 and with the tension field action included using the rules of AS 4100:1998 (Standards Australia, [22]). All slender section specimens in the *V* and *MV* Series were found to develop tension field action as the connection bolts at the loading and support points extended over the full depth of the section whether 150 mm (4 bolts) or 200 mm (5 bolts). The inclusion of straps attached to the flanges to prevent distortion at the loading and support points further enhanced the tension field action. They are compared with DSM design proposals in Section 4 following

3.3 SupaCee® Section Test Results

The full set of test results for the SupaCee® sections is given in the research report by Pham and Hancock [10]. The tests results are compared with existing design methods in AS/NZS 4600:2005 and with the tension field action included using the rules of AS 4100:1998 (Standards Australia, [22]). As for the plain lipped C-Sections, all slender section specimens in the *V* and *MV* Series were found to develop tension field action. The inclusion of straps attached to the flanges to prevent distortion at the loading and support points further enhanced the tension field action.

4 DIRECT STRENGTH METHOD (DSM) OF DESIGN

4.1 Introduction

In the paper “Direct Strength Design of Cold-Formed Purlins” (Pham and Hancock [8]), test results from eight different test series, which were implemented at the University of Sydney by using the vacuum testing rig or more than 10 years, have been utilized to extend DSM to purlins systems. These tests have covered a wide range of parameters including: single, double and triple spans; inwards and outwards loading; zero, one and two rows of bridging per span; screw fastened and concealed fixed sheeting systems; and cleat and flange bolting of purlins to rafters. The paper (Pham and Hancock [8]) has outlined two current approaches to the design of purlin systems using an extension to the Direct Strength Method (DSM) in Section 7 of AS/NZS 4600:2005 which are referred to herein as the C_b-factor and FELB approaches. The results are compared with the Effective Width Method (EWM) as well as the ones from purlins test results.

The paper has also made two proposals for the bending and shear failure mode for use in the DSM. Proposal 1 uses the lesser of the local buckling and distortional buckling section strengths in the combined bending and shear interaction equation, and Proposal 2 uses only the local buckling section strength in the interaction equation. All methods were calibrated and produced acceptable safety indices including those test cases where combined bending and shear dominated such as the triple spans under uplift loading with one and two rows of bridging. It therefore appears that Proposal 2 is an acceptable method for safe design even though it ignores the distortional buckling strength.

The main purpose of this section is to further refine the proposals for DSM based on tests which concentrated on shear, and combined bending and shear.

www.EngineeringEBooksPdf.com

4.2 DSM Design Rules for Flexure

The nominal section moment capacity at local buckling *(M_{sl})* is determined from Section 7.2.2.3 of AS/NZS 4600:2005 {Appendix 1, Section 1.2.2.2 of NAS [2]} as follows:

$$\text{For } \lambda_l \le 0.776 \ : \ M_{sl} = M_y \tag{1}$$

$$\text{For } \lambda_l > 0.776 \ : \ M_{sl} = \left[1 - 0.15\left(\frac{M_{ol}}{M_y}\right)^{0.4}\right]\left(\frac{M_{ol}}{M_y}\right)^{0.4} M_y \tag{2}$$

where λ_l is non-dimensional slenderness used to determine M_{sl}; $\lambda_l = \sqrt{M_y / M_{ol}}$; $M_y = Z_f f_y$,

M_{ol} is elastic local buckling moment of the section; $M_{ol} = Z_f f_{ol}$,

Z_f is section modulus about a horizontal axis of the full section,

f_{ol} is elastic local buckling stress of the section in bending.

The nominal section moment capacity at distortional buckling *(M_{sd})* is determined from Section 7.2.2.4 of AS/NZS 4600:2005 {Appendix 1, Section 1.2.2.3 of NAS [2]} as follows:

$$\text{For } \lambda_d \le 0.673 \ : \ M_{sd} = M_y \tag{3}$$

$$\text{For } \lambda_d > 0.673 \ : \ M_{sd} = \left[1 - 0.22\left(\frac{M_{od}}{M_y}\right)^{0.5}\right]\left(\frac{M_{od}}{M_y}\right)^{0.5} M_y \tag{4}$$

where λ_d is non-dimensional slenderness used to determine M_{sd}; $\lambda_l = \sqrt{M_y / M_{od}}$; $M_y = Z_f f_y$,

M_{od} is elastic distortional buckling moment of the section; $M_{od} = Z_f f_{od}$,

Z_f is section modulus about a horizontal axis of the full section,

f_{od} is elastic distortional buckling stress of the section in bending.

4.3 Proposed DSM Design Rules for Shear

The equations in Section 3.2.1 of the North American Specification [2] which are expressed in terms of a nominal shear stress F_v have been changed to DSM format by replacing stresses by loads as follows:

$$\text{For } \lambda_v \le 0.815 \ : \ V_v = V_y \tag{5}$$

$$\text{For } 0.815 < \lambda_v \le 1.231 \ : \ V_v = 0.815\sqrt{V_{cr} V_y} \tag{6}$$

$$\text{For } \lambda_v > 1.231 \ : \ V_v = V_{cr} \tag{7}$$

where $\lambda_v = \sqrt{V_y / V_{cr}}$, (8)

V_y is yield load of web $V_y = 0.6 A_w f_y$, (9)

V_{cr} is elastic shear buckling force of the web $V_{cr} = \dfrac{k_v \pi^2 E A_w}{12\left(1-\nu^2\right)\left(\dfrac{d_1}{t_w}\right)^2}$ (10)

d_1 is depth of the flat portion of the web measured along the plane of the web,

t_w is thickness of web, A_w is area of web $A_w = d_1 \times t_w$,

k_v is the shear buckling coefficient.

www.EngineeringEBooksPdf.com

To account for the shear buckling of the whole section rather than simply the web, the shear buckling coefficient k_v can be back-calculated from the shear buckling load V_{cr} of the whole section as computed in Section 2 using Eq. 10. In this way, the DSM philosophy of section rather than element buckling can now be incorporated in the nominal shear capacity. The value of the shear buckling coefficients (k_v) for the whole plain C- lipped sections and SupaCee® sections are now based on the elastic shear buckling studies as described in Section 2. Both lipped plain C- and SupaCee® channel sections with the thickness of 2 mm as shown in Fig. 5 are investigated. Two ratios of shear span (s) to depth (d_1) of 1:1 and 2:1 respectively are also considered. A shear distribution similar to that which occurs in practice allowing for section shear flow as shown in Fig. 1 Case D is used for modeling sections in pure shear resulting from a shear force parallel with the web. All edges of the end cross-section are simply supported.

The computed values of the shear buckling coefficients k_v for the plain channels increase from the theoretical value of a simply supported rectangular plate in shear of 9.34 for a Span:Panel Depth of 1:1 to 9.926 and 10.006 for the 150mm and 200 mm depth sections respectively. For the SupaCee® sections, the corresponding values are 12.204 and 11.709 as a result of the longitudinal intermediate stiffeners in the web.

The DSM nominal shear capacity (V_v) including Tension Field Action is proposed based on the local buckling (M_{sl}) equation (4) where M_{sl}, M_{ol} and M_y are replaced by V_v, V_{cr} and V_y respectively as follows:

$$V_v = \left[1 - 0.15\left(\frac{V_{cr}}{V_y}\right)^{0.4}\right]\left(\frac{V_{cr}}{V_y}\right)^{0.4} V_y \qquad (11)$$

Fig. 8 shows that all of the plain C- lipped and SupaCee® V-tests lie close to the proposed DSM nominal shear capacity with Tension Field Action given by Eq. 11. They lie well above the AISI in DSM format equations (see Eqs. 5 – 10) presumably because significant tension field action was developed. This may be a result of the bolts connecting the webs of the channels spanning the full depth of the section for both 150 mm and 200 mm tests. In tests where full tension field action is not developed, the results may lie below Eq. 11. Investigation of other test results such as those from LaBoube and Yu [19] will be required to confirm these design curves for all situations.

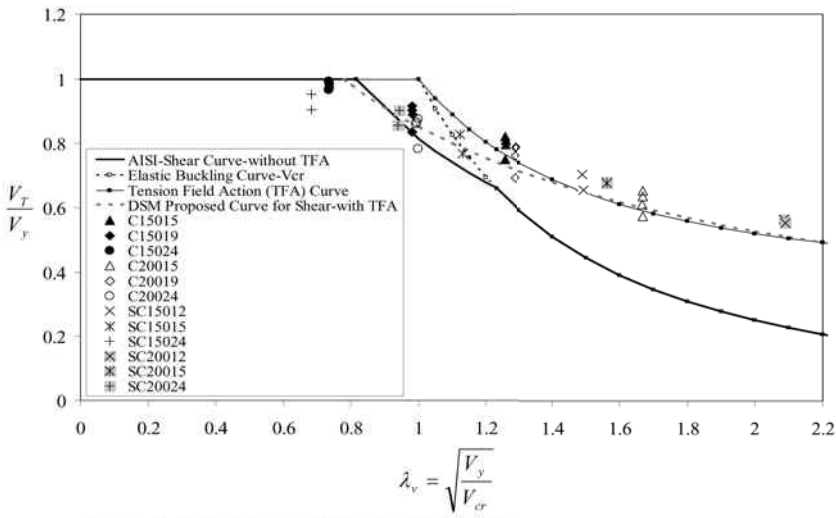


Figure 8. DSM Proposed Nominal Shear Curves and Shear Test Data

www.EngineeringEBooksPdf.com

4.3 Proposed DSM Design Rules for Combined Bending and Shear

In limit states design standards, the interaction is expressed in terms of bending moment and shear force so that the interaction formula for combined bending and shear of a section with an unstiffened web is given in Clause 3.3.5 of AS/NZS 4600:2005 {Section C 3.3.2 of AISI [2]}:

$$\left(\frac{M^*}{M_s}\right)^2 + \left(\frac{V^*}{V_v}\right)^2 = 1 \tag{12}$$

where M^* is bending action,
M_s is the bending section capacity in pure bending,
V^* is the shear action, and
V_v is the shear capacity in pure shear.

The equation for combined bending and shear with stiffened webs is also given in Clause 3.3.5 of AS/NZS 4600:2005 {Section C 3.3.2 of AISI [2]}:

$$0.6\left(\frac{M^*}{M_s}\right) + \frac{V^*}{V_v} = 1.3 \tag{13}$$

The choice of M_s, the bending section capacity, needs further investigation. As discussed earlier, it can be based on the lesser of M_{sl} from Eq. 2 and M_{sd} from Eq. 4 (called Proposal 1) or simply M_{sl} from Eq. 2 (called Proposal 2). Both proposals are investigated thoroughly in Pham and Hancock [9], [10]. A selection of the results is given here to demonstrate the differences with and without tension field action. Only the tests without the straps are included here as these always give lower values for the test loads and hence are a lower bound. Fig. 9 shows the full set of test data compared with Equations 12 and 13 when V_v is based on Eqs. 5 – 7 without tension field action, and Fig. 10 shows the same data and comparisons when V_v is based on Eq. 11 with tension field action. In each case, the upper figure is Proposal 2 where M_s is based on M_{sl} and the lower figure is Proposal 1 where M_s is based on the lesser of M_{sl} and M_{sd}.

It is clear from the graphs that the use of M_{sl} is acceptable in all cases provided the circular interaction equation (Eq. 12) is used for combined bending and shear. It is also clear that tension field action plays a large part in the tests so that the use of Eq. 11 which includes tension field action as shown in Fig. 8 produces more accurate estimates of the combined bending and shear strength.

5 CONCLUSION

The paper has presented proposals for the design of cold-formed steel sections by the Direct Strength method as in the North American Specification and Australian/ New Zealand Standard accounting for shear, and combined bending and shear. The proposals are compared with tests on C-sections in predominantly shear, combined bending and shear, and pure bending. One feature of the DSM is that the full section buckling including intermediate stiffeners under shear has been included rather than simple web buckling in shear. This proposal produces better correlation with the test data but requires special computer software such as the Spline Finite Strip Method (SFSM) to determine the shear buckling loads of full sections. The general conclusion is that the use of M_{sl} in the interaction equations for combined bending and shear is acceptable in all cases provided the circular interaction equation (Eq. 12) is used for combined bending and shear.

www.EngineeringEBooksPdf.com

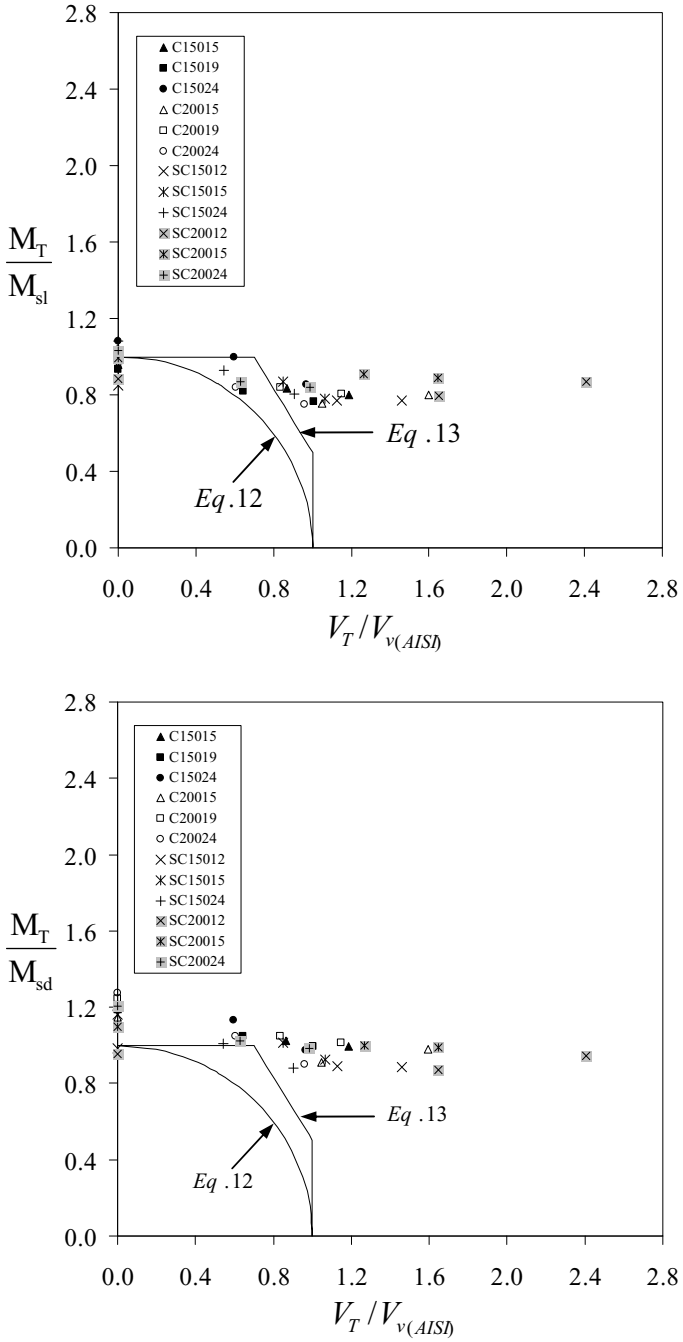


Figure 9. Comparison of Tests with Design Proposals for Combined Bending and Shear excluding TFA

www.EngineeringEBooksPdf.com

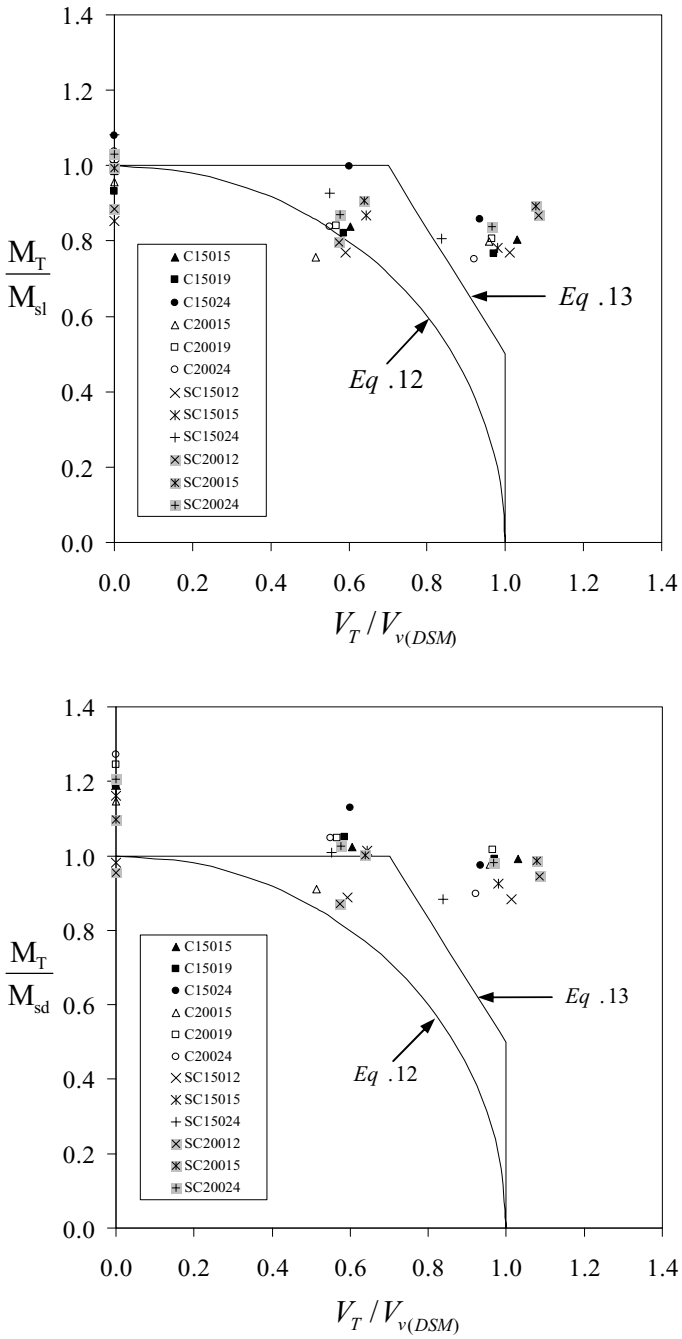


Figure 10. Comparison of Tests with Design Proposals for Combined Bending and Shear including TFA

www.EngineeringEBooksPdf.com

REFERENCES

[1] Standards Australia, "AS/NZS 4600:2005, Cold-Formed Steel Structures." Standards Australia/ Standards New Zealand, 2005.

[2] AISI, "North American Specification for the Design of Cold-Formed Steel Structural Members." 2007 Edition, AISI S100-2007, 2007.

[3] Schafer, B. W., and Peköz, T., "Direct Strength Prediction of Cold-Formed Steel Members using Numerical Elastic Buckling Solutions, Thin-Walled Structures, Research and Development." *Proceedings, Fourteenth International Specialty Conference on Cold-Formed Steel Structures*, St Louis, Missouri, U.S.A., 1998.

[4] CASE, "THIN-WALL – A Computer Program for Cross-Section Analysis and Finite Strip Buckling Analysis and Direct Strength Design of Thin-Walled Structures." Version 2.1, Centre for Advanced Structural Engineering, School of Civil Engineering, The University of Sydney, 2006.

[5] Schafer, B. W., and Ádány, S., "Buckling of Cold-Formed Steel Members using CUFSM, Conventional and Constrained finite strip methods." *Proceedings, Eighteen International Specialty Conference on Cold-Formed Steel Structures*, University of Missouri-Rolla, Orlando, Florida, U.S.A., pp. 39-54, 2006.

[6] Schafer, B. W., "Review: The Direct Strength Method of Cold-Formed Steel Member Design." *International Colloquium on Stability and Ductility of Steel Structures*, Lisbon, Portugal, 2006.

[7] AISI, "Direct Strength Method (DSM) Design Guide." American Iron and Steel Institute, Washington DC, 2006.

[8] Pham, C. H., and Hancock, G. J., "Direct Strength Design of Cold-Formed Purlins." *Journal of Structural Engineering*, American Society of Civil Engineers, Vol. 135, Issue 3, pp. 229-238, 2009.

[9] Pham, C. H., and Hancock, G. J. , "Experimental Investigation of High Strength Cold-Formed C-Section in Combined Bending and Shear.", *Research Report No R894*, School of Civil Engineering, The University of Sydney, NSW, Australia, April, 2009.

[10] Pham, C. H., and Hancock, G. J. , "Experimental Investigation of High Strength Cold-Formed SupaCee® Sections in Combined Bending and Shear.", *Research Report No R907*, School of Civil Engineering, The University of Sydney, NSW, Australia, December, 2009.

[11] Cheung, Y. K., "Finite Strip Method in Structural Analysis." *Pergamon Press, Inc.*, New York, N.Y., U.S.A, 1976.

[12] Fan, S. C., and Cheung, Y. K., "Spline Finite Strip in Structural Analysis." *Proceedings, the International Conference on Finite Element Method*, Shanghai, China, 1982.

[13] Lau, S. C. W. and Hancock, G. J., "Buckling of Thin Flat-Walled Structures by a Spline Finite Strip Method." *Thin-Walled Structures*, Vol. 4, pp 269-294, 1986.

[14] Kwon, Y. B. and Hancock, G. J., "Nonlinear Elastic Spline Finite Strip Analysis for Thin-Walled Sections." *Thin-Walled Structures*, Vol. 12, No. 4, pp 295-319, 1991.

[15] Kwon, Y. B. and Hancock, G. J. (1993). "Post-Buckling Analysis of Thin-Walled Channel Sections Undergoing Local and Distortional Buckling." *Computers and Structures*, Vol. 49, No. 3, pp 507-516.

[16] Pham, C. H., and Hancock, G. J., "Shear Buckling of Thin-Walled Channel Sections." *Journal of Constructional Steel Research*, Vol. 65, No. 3, pp. 578-585, 2009.

[17] Pham, C. H., and Hancock, G. J., "Buckling Studies of Thin-Walled Channel Sections under Combined Bending and Shear" *Proceedings, 19th International Specialty Conference on Cold-Formed Steel Structures,* St Louis, Missouri,, pp. 185-204, 2008.

www.EngineeringEBooksPdf.com

[18] Pham, C. H., and Hancock, G. J., "Shear Buckling of Thin-Walled Channel Sections with Intermediate Web Stiffener." *Proceedings of Sixth International Conference on Advances in Steel Structures*, Hong Kong, China, pp. 417 - 424, 2009.

[19] LaBoube, R. A., and Yu, W. W., "Structural Behavior of Beam Webs Subjected Primarily to Shear." *Final Report, Civil Engineering Study 78-2*, University of Missouri-Rolla, St Louis, Missouri, U.S.A, 1978.

[20] LaBoube, R. A., and Yu, W. W., "Cold-Formed Steel Web Elements under Combined Bending and Shear." *Proc., 4th Int. Specialty Conf. on Cold-Formed Steel Structures*, University of Missouri-Rolla, St Louis, Missouri, U.S.A, 1978.

[21] Lysaght, "NSW SupaCee® is trademark of Bluescope Steel Limited." *Bluescope Steel Limited trading as Bluescope Lysaght*, 2003.

[22] Standards Australia, "Steel Structures." *AS 4100:1998*, Standards Australia, 1998.

www.EngineeringEBooksPdf.com

SDSS'Rio 2010 STABILITY AND DUCTILITY OF STEEL STRUCTURES
E. Batista, P. Vellasco, L. de Lima (Eds.)
Rio de Janeiro, Brazil, September 8 - 10, 2010

MANUFACTURING SPECIFICATIONS FOR HOLLOW SECTIONS IN 2010

Jeffrey A. Packer*

* University of Toronto, Toronto, Canada
e-mail: jeffrey.packer@utoronto.ca

Keywords: Specifications, Standards, Tubes, Hollow Sections, Steel Structures.

Abstract. *The minimum mechanical and geometric property requirements, stipulated in contemporary manufacturing specifications for cold-formed and hot-finished structural hollow sections internationally, are reviewed and compared. Many of the key criteria are shown to have implications for the structural performance under static, impact and seismic loading conditions, as well as under hot-dip galvanizing. Considerable effort is currently being expended by an industry task force in North America to produce a new manufacturing standard for higher performance cold-formed hollow structural sections, to address current limitations of the product. Features of this resulting draft standard (termed ASTM A1xxx herein) are presented in the tables.*

1 CONTEMPORARY MANUFACTURING SPECIFICATIONS

The proportion of Hollow Structural Sections (HSS) within the structural steel market continues to grow, particularly within North America. Roughly 3 million tons of cold-formed HSS were produced in North America in 2008, compared to approximately 5.6 million tons of hot-formed steel I-sections (or "W-shapes") [1]. Beyond Europe, the most popular HSS material is that made to ASTM A500 [2], yet this product stills bears a warning regarding application to dynamically loaded structures. Despite this, the use of HSS to ASTM A500 is ubiquitous and the limitations of this structural section – and indeed many other hollow sections – are not well-appreciated. In the following, some of the key geometric and mechanical properties of prominent internationally-produced hollow sections are reviewed. Concern over the performance of hollow sections manufactured to some specifications has even caused certain jurisdictions (e.g. Singapore) to disapprove product produced to particular standards [3]. The outside dimensions of hollow sections are well-controlled with tight tolerances, so these are not discussed below.

1.1 ASTM A500 [2]

This is a cold-formed, electric-resistance-welded (ERW) product, currently restricted to perimeters of 1630 mm or less and wall thicknesses up to 16 mm, noted for its very liberal geometric production tolerances. A tolerance of -10% is permitted on wall thickness, with no tolerance on mass, weight or cross-sectional area (see table 1), resulting in tubes being produced routinely undersize. The American Institute of Steel Construction Specification [4] accounts for this practice by designating a "design wall thickness" of 0.93 times the nominal wall thickness for structural design in the U.S., whereas the Canadian Institute of Steel Construction [5] stipulates a "design wall thickness" of 0.90 times the nominal wall thickness for structural design in Canada. All section properties for each country are then calculated based on the respective design thickness. ASTM A500 tubing is also in use in many other countries worldwide without such design guidance, which – considering the much-diminished engineering properties relative to the expected values – may result in unsafe design situations.

Further confusion arises with minimum mechanical properties, since Grades B and C have different guaranteed yield strengths for circular hollow sections (CHS) and rectangular hollow sections (RHS), as

www.EngineeringEBooksPdf.com

indicated in table 1. Manufacturers in North America now commonly dual-certify their ASTM A500 product to both Grades B and C, producing to the higher grade and working to a "one product fits all" approach [6]. This makes it difficult to apply such material to seismic applications since the stipulated R_y value (to account for member expected over-strength) becomes very unreliable. Recognizing this problem, the latest Canadian steel structures standard [7] has stipulated that the product R_yF_y be taken as not less than 460 MPa (N/mm^2) for all HSS. The ASTM A500 standard has no provision for a Charpy V-notch toughness rating (table 1), further limiting its applicability to many dynamic loading situations. A large number of Charpy V-notch tests on A500 square HSS have, in fact, confirmed the inherent very low notch toughness level of this material, even in the longitudinal (or rolling) direction [8].

1.2 CAN/CSA G40.20-04/G40.21-04 [9]

This is another production specification for structural tubing in North America, governing part of the overall stock made in Canada. Although it is a cold-formed, ERW product and similar to ASTM A500, it has improved features that include (see table 1): (i) a single Grade 350W; (ii) strict geometric tolerances on thickness and mass/area, which result in hollow sections that are made to nominal cross-sectional properties and hence have a "design wall thickness" equal to the nominal wall thickness; (iii) the ability to specify a Charpy V-notch toughness requirement, by stipulating Grade 350WT and one of five toughness categories. The latter range from Category 1 of 27 Joules at 0^o C, to Category 4 of 27 Joules at -45^o C, and even a Category 5 "to be specified by purchaser". CAN/CSA G40.20/G40.21 is unique amongst cold-formed HSS production standards in that the cold-formed end product (Class C) can be heat-treated to form an alternative Class H product, by heating to 450^o C or higher followed by cooling in air [9]. This reduces the residual stresses in the cross-section and justifies the use of a column resistance curve for compression member design that is higher than that for Class C [7].

1.3 ASTM A501 [10]

This is an American specification for the manufacture of hot-formed HSS, but these products are not manufactured in the U.S. This specification was recently revived to facilitate the importation of hot-finished hollow sections from Europe, manufactured in accordance with EN10210 [11], [12]. Although it has no wall thickness tolerance there is a very tight mass/area tolerance, ensuring that sections are made to nominal cross-section properties (table 1). The higher-strength Grade B also automatically has a reasonable energy absorption capacity, for wall thicknesses greater than 8 mm (table 1).

1.4 ASTM A53 [13]

This is actually a pipe production specification, intended for mechanical and pressure applications. The product needs to satisfy a hydrostatic test and is only produced in circular shapes, but Grade B – produced by an ERW process – is used for structural purposes in many parts of the U.S. by adopting a "design wall thickness" of 0.93 times the nominal wall thickness, as for ASTM A500 [4]. Despite a low F_y/F_u ratio, which is favourable for seismic design, this material possesses a particularly low yield strength and – like ASTM A500 – is subject to slack geometric tolerances and does not have any notch toughness provision (table 1).

1.5 API 5L [14]

This specification for steel pipe, for pipeline transportation systems, covers a multitude of tube grades and sizes of which some are used for structural applications. PSL2 pipe is a common structural choice and Grade X52 is probably the most common choice for structural purposes. With a tight mass tolerance, a toughness requirement (table 1) and a diameter range from 10.3 to 2134 mm, this high-quality pipe material addresses a frequent need for either large diameter or thick-walled hollow sections. Other special features of PSL2 pipe are an upper bound on the yield strength (e.g., for X52 the minimum and maximum

www.EngineeringEBooksPdf.com

yield strengths are 360 and 530 MPa, respectively), and a maximum yield-to-tensile stress ratio of 0.93 in the as-delivered pipe (for D > 323.9 mm).

Table 1: Manufacturing standards for HSS and Pipe with minimum specified mechanical properties of common grades and influential dimensional tolerances on individual sections.

HSS or Pipe Specification		Grade	F_y (MPa)	F_u (MPa)	Toughness[b] (Joules @ °C)	Wall thickness Tolerance	Mass or Area tolerance
ASTM A500	CHS	B	290	400	–	-10%	–
		C	315	425			
	RHS	B	315	400			
		C	345	425			
ASTM A53		B	240	415	–	-12.5%	-10%
ASTM A501		B	345	483	27J @ -18°C for t>8mm	–	-3.5%
CSA-G40.20/G40.21		350W	350	450	5 Categories: 27J @ 0, -20, -30, -45°C, or as specified	-5%	-3.5%
API 5L		PSL 2 X52N	360	460	27J @ 0°C for D≤762mm	–10% for 5<t<15 -0.5mm, t<5	–3.5% for regular plain-end
EN10210		S355J2H	355 for t≤16 345 for 16<t≤40	470 for 3<t≤100	27J @ -20°C	–10% (more liberal for seamless)	-6%
EN10219		S355J2H	355 for t≤16 345 for 16<t≤40	470 for 3<t≤40	27J @ -20°C	–10%, t≤5 -0.5mm, t>5 for D≤406.4	-6%
AS/NZS 1163		C350L0	350	430	27J @ 0°C	–10% for D≤406.4	-4%
		C450L0	450	500			
SANS 657-1		355WA[c]	355[c]	450	On request	–9% for 3≤t≤4[d] –7.5% for 4<t≤5[d] –6.5% for 5<t≤6[d] –6.0% for t>6[d]	-10%
JIS G3475	CHS	STKN 490B	325 for t ≤40	490	27J @ 0°C for D≥400 if CHS, and t>12		
JIS-Approved	RHS	BCP325	325 for t<12 335 for 12≤t≤40				
ASTM A1xxx (For perimeters ≥ 317.5mm)		–	345	450	27J @ -18°C	-5%	–

Notes: a: Dimensions (of D, t and Perimeter) in mm.; b: Charpy V-notch impact test value for full-size (10 x 10 mm) longitudinal coupons; c: SANS 657-1 355 MPa yield strength grade launched in February 2010; d: After Amendment No.2 to SANS 657-1:2005.

www.EngineeringEBooksPdf.com

1.6 EN10210 [11], [12]

EN10210 is the current European specification for hot-finished (or "hot-formed") structural hollow sections, which are manufactured primarily in the U.K., Germany, France and Brazil. This material is fine-grained, has very low residual stresses, is available in a wide range of sizes and thicknesses, and the most common grade is S355J2H. Sections to this specification are typically made by cold-forming, using an ERW process, then re-heated to normalizing temperature and finished to final shape. The hot-finishing method produces smaller outside corner radii on square and rectangular hollow sections than with cold-formed RHS. These characteristics, and the properties shown in table 1, probably place this specification at the forefront of HSS manufacturing standards internationally. One concern arises, however, over the governing thickness tolerance of -6% (assuming constant HSS thickness), which has no "design thickness" compensation like for ASTM A500 [2]. Under-sizing of a hollow section (relative to expected or nominal size) can have a serious negative effect on the member capacity, member deflection and even connection strength, where the latter is proportional to t^{α} with $1 \leq \alpha \leq 2$ [15]. Very thick tubes to this specification – with low D/t, as used in bridges – are likely to be manufactured by the "seamless" process. This is apt to leave an unsmooth surface finish, which may raise concerns with the client.

1.7 EN10219 [16], [17]

EN10219 is the current European specification for cold-formed structural hollow sections, made primarily by the ERW process. The influential mechanical and geometric properties are very similar to EN10210 [11], [12], as indicated in table 1, except the wall thickness/mass tolerances result in a governing thickness tolerance of -6% (assuming constant HSS thickness) only up to 8.33 mm thickness; above that thickness the permissible under-sizing is less than 6% due to the -0.5mm tolerance controlling.

1.8 AS/NZS 1163 [18]

The latest Australasian standard for cold-formed ERW hollow sections has two popular grades, C350 and C450 (table 1), the potential for a Charpy V-notch toughness rating (sub-grading of L0 at 0^{o} C), and wall thickness/mass tolerances that are second only to CSA [9]. For Grade C450 there is a ductility concern, since the nominal F_y/F_u ratio of 0.9 is very high and it is accompanied by minimum elongations at failure of only 12% for CHS and 10% for RHS (for $t \leq 15$ mm). However, this standard is unique in that, while all HSS manufacturing standards require mechanical properties to be demonstrated just after production, AS/NZS 1163 also requires artificial "strain ageing" of the test pieces prior to tensile or impact testing. Ageing is achieved by heating to 150^{o} – 200^{o} C for at least 15 minutes, which raises the yield stress and decreases the ductility, thus somewhat ameliorating the above ductility characteristics.

1.9 SABS/SANS 657–1 [19]

The latest version of this South African standard, with Amendments 1 and 2 (2009), brings production tolerances close to EN10219-2 [17] except the wall thickness/mass tolerances for $t \leq 6$ mm are even more liberal (-9%t for $3.0 \leq t \leq 4.0$ mm; -7.5%t for $4.0 < t \leq 5.0$ mm; -6.5%t for $5.0 < t \leq 6.0$ mm). The sole grade for structural hollow sections (yield strength of 300 MPa) was relatively low, but a higher grade of 355 MPa has now been launched in February 2010. Whereas most cold-formed HSS manufacturing standards specify that the mechanical properties be determined from the finished product, this standard permits the properties to be determined from either the parent metal *or* the finished product. The former is typically chosen, giving South African hollow sections an inherent over-strength.

1.10 JIS G3475 [20]

Japan has a complex set of standards and approval bodies but steel CHS for building construction generally fall under the purview of the Japanese Industrial Standards. For structural members in which

www.EngineeringEBooksPdf.com

plastic deformation may occur – a common criterion for Japanese seismic design – Grades STKN490B and STKN400B have minimum yield strengths of 325 MPa and 235 MPa, respectively. Cold-formed square hollow sections (termed BCR and BCP materials, depending on the manufacturing process) are a very popular choice for building columns in Japan but standards for such are not established by JIS; instead, they are approved as structural members by the Ministry of Land, Infrastructure and Transport of Japan. For wall thicknesses of 12 mm and greater, both the circular and square hollow section standards provide an upper limit on the actual yield stress, an upper limit of 0.80 on the yield-to-tensile strength ratio in the as-delivered material (key for plastic deformation capacity), and a Charpy energy absorption rating. Table 1 gives further specification details for these materials.

2 CORNER CRACKING IN COLD-FORMED RHS

Cracking in the corners of cold-formed, square and rectangular hollow sections (RHS) has been reported and discussed for some time [21]. In the last decade the incidence has increased in North America and Asia, particularly during hot-dip galvanizing, where the problem has been generally attributed to Liquid Metal Embrittlement (LME) in association with very high residual stresses in the cold-formed RHS corners. Although this phenomenon is deemed a "rare but important issue" in Europe [22], the plethora of reports and studies published post-2000 substantiates this widespread problem (e.g. [23]). Complete structures made of galvanized RHS have even been condemned due to cracking, such as sign bridges in British Columbia, Canada, in 2006.

The occurrence of RHS corner cracking during hot-dip galvanizing seems to have become more prevalent since tin and bismuth were added to the zinc bath mixture by the dominant supplier, Teck Cominco, with the launch of a new coating system *BritePlus*™ that "enhances coating quality while producing a bright spangled appearance". Teck Cominco was blamed for causing this change in the ability to galvanize, but the interaction of three conditions determines the occurrence of LME [24]:

• A critical level of internal material stress (e.g. very high levels of residual stress due to severe cold working and welding) – see Section 2.1 below.

• A susceptible material (e.g. non-aluminium killed coil, high yield-to-ultimate stress ratio, pre-existing microcracks in the metal as a result of forming, adverse chemical composition) – see Section 2.2.

• Liquid metal, especially with the presence of impurities or additives.

Teck Cominco duly undertook some experimental research [25] into the galvanizing of contemporary RHS (127 x 76 x 9.5 mm), concluding that the dominant factor affecting cracking upon galvanizing was the RHS itself. Galvanizing bath chemistry did have a lesser effect, but only on already-susceptible RHS. The use of pre-galvanizing stress-relieving was also shown to be effective in retarding the incidence of cracking. However, experience in Canada has shown that corner cracking can still occur with CSA Class H RHS [9], which is stress-relieved to 450^{o}C (Section 1.2). The ASTM document catering to LME on galvanizing [26] advises that … "for heavy cold deformation exemplified by cold rolling … subcritical annealing temperatures from 650 to 705^{o}C should be employed". HSS manufacturers are aware of this potential cracking, but there is no definitive guidance on this issue from structural steel associations.

2.1 RHS production method

Corner cracking can be avoided by using hot-finished (or "hot-formed" and seamless) RHS, as these products have inherently better grain structure and superior mechanical properties compared to their cold-formed counterparts, but hot-finished RHS is either unavailable in much of the world or prohibitively expensive. With cold-formed RHS the tightness of the corner radii is critical. Kinstler [23] pointed out that … "the amount of cold work, as measured by the bending radius, is the most important single factor to consider when there is concern for brittle-type failure of steel galvanized after cold working".

In Europe, both the production standard EN10219 [17] and the structural steel design code Eurocode 3 contain requirements for corner radii of cold-formed RHS. Table 2 shows a composite of these recommendations which have been adopted by IIW [27] and are also now part of a draft international standard (ISO 14346). The IIW [27] data in table 2 are recommended outside corner radii for welding in

www.EngineeringEBooksPdf.com

the zones of cold-forming without heat treatment, but the recommendations apply equally to galvanizing as both represent criteria affected by the extreme corner residual stresses induced by cold-forming. The European codes logically specify minimum outside corner radii to avoid problems with welding or cracking in the corners, but table 2 shows that the current North American standards specify just maximum outside corner radii, due to an emphasis on achieving a reliably large "flat width" dimension. North American RHS section properties are calculated based on a standard outside corner radius of 2.0 times the "design wall thickness" and an inside corner radius equal to the "design wall thickness", for all wall thicknesses. As can be seen by the IIW [27] corner requirements, producing to an outside corner radius of around 2t – for thicker-walled sections – is inviting corner cracking problems, unless there is careful control of the steel chemistry.

Table 2: Manufacturing ranges for outside corner radii of cold-formed RHS.

Specification	RHS thickness, t (mm)	Outside or External Corner radius (r_o)	
		for fully Al-killed steel (Al ≥ 0.02%)	for fully Al-killed steel *and* C ≤ 0.18%, P ≤ 0.02% and S ≤ 0.012%
IIW [27] based on EC3 & EN 10219-2	2.5 ≤ t ≤ 6	≥ 2.0t	≥ 1.6t
	6 < t ≤ 10	≥ 2.5t	≥ 2.0t
	10 < t ≤ 12	≥ 3.0t	≥ 2.4t (up to t =12.5)
	12 < t ≤ 24	≥ 4.0t	–
ASTM A500	All t	≤ 3.0t	
CSA-G40.20/G40.21	t ≤ 3	≤ 6 mm	
	3 < t ≤ 4	≤ 8 mm	
	4 < t ≤ 5	≤ 15 mm	
	5 < t ≤ 6	≤ 18 mm	
	6 < t ≤ 8	≤ 21 to 24 mm	
	8 < t ≤ 10	≤ 27 to 30 mm	
	10 < t ≤ 13	≤ 36 to 39 mm	
	t > 13	≤ 3.0t	
AS/NZS 1163	All t, up to 50 x 50 mm	1.5t to 3.0t	
	All t, larger than 50 x 50	1.8t to 3.0t	
SANS 657-1	t ≤ 6	1.5t to 2.5t	
	6 < t ≤ 10	2.0t to 3.0t	
	t > 10	2.4t to 3.6t	
ASTM A1xxx (For perimeters ≥ 317.5mm)	t ≤ 10	1.6t to 3.0t	
	t > 10	2.4t to 3.6t	

Both the Australasian [18] and the South African [19] HSS production standards specify minimum corner radii (table 2), the former permitting a very small corner radii for thick-walled sections since the tolerance range is independent of thickness, but the latter is almost identical to EN 10219-2 [17]. Most standards acknowledge that the RHS sides need not be tangential to the corner arcs (i.e. the RHS corner sweeps out an angle less than 90^o). In such cases the outside corner radius requirement becomes an "external corner profile" requirement, with the latter applying to r_o, c_1 or c_2, where c_1 and c_2 are dimensions measured from the RHS outside of one flat wall to the end of the "flat" on the adjacent wall.

Tolerances for local surface imperfections (such as gouges or grooves) are usually provided in HSS standards, typically as a percentage of the wall thickness, with permissible repair procedures. However, micro-cracks in the corners of RHS – pre-existing in the coil material or produced during cold-forming of

www.EngineeringEBooksPdf.com

the RHS – are another issue that is not covered by HSS manufacturing specifications. The presence of micro-cracks in the corners may have a dramatic influence if the RHS is subsequently hot-dip galvanized.

2.2 Chemical composition of steel

Although all modern steels used for HSS are presumed to be fully-killed, the chemistry of the input material is vital to ensuring a quality product with the expected mechanical properties. The permitted amounts (by weight) of key chemical ingredients, by cast or heat analysis, for popular grades of prominent HSS specifications show many similarities, but the current ASTM specifications are notable for containing little prescription, particularly with regard to silicon (discussed below). The chemical compositions do not provide a sufficient recipe for achieving the desired mechanical properties in many cases, as a low carbon, micro-alloyed input steel is needed for "higher performance" HSS.

3 SUITABILITY OF COLD-FORMED RHS FOR GALVANIZING

This topic is generally avoided altogether in HSS manufacturing specifications, or blanket statements are given such as in EN10219 … "the products shall be suitable for hot dip galvanizing" [16]. Both the South African [19] and Australasian [18] standards discuss suitability for hot-dip galvanizing, if galvanizing is required by the purchaser, and AS/NZS even goes as far as recommending that a sample be hot-dip galvanized to determine its actual performance for a given bath and tube characteristics. The problem with such a purchaser-driven approach is that most HSS produced internationally is sold to stock-holders, so the end user or fabricator does not usually interact with the manufacturer at the time of production. The ASTM document catering to LME on galvanizing [26] states that … "a cold bending radius of three times the section thickness … will ordinarily ensure satisfactory properties in the final product". However, this cautious advice is a blanket provision, regardless of metallurgical content.

With hot-dip galvanizing, the piece is normally dipped in molten zinc at a temperature that can vary from 440 to 465^{o}C. The zinc temperature and immersion time do influence the thickness of the zinc coating obtained, but the most critical factor is the steel chemical composition and in particular the silicon content. The American Galvanizing Association recommends the following for good coatings:

• C < 0.25%; P < 0.04% and Mn < 1.35% • Si < 0.04% *or* 0.15% < Si < 0.22%.

The Silicon range above specifically avoids 0.04% < Si < 0.15%, a zone of high reactivity termed the "Sandelin effect". The Australasian HSS standard [18] also notes that caution should be exercised for 0.04% < Si ≤ 0.14%. Fully Al-killed steels are now commonplace so Si levels can now be easily manipulated, with low silicon content also helping to avoid corner cracking. A further qualification sometimes added to the silicon level is for (Si + 2.5P) ≤ 0.07 to 0.09 (the latter being cited in AS/NZS 1163 for use with low Si levels), but this does result in relatively thin zinc coatings, of around 80 μm.

REFERENCES

[1] Modern Steel Construction, *Outer Strength*, American Institute of Steel Construction, USA, 2009.

[2] ASTM International, *Standard Specification for Cold-Formed Welded and Seamless Carbon Steel Structural Tubing in Rounds and Shapes*, *ASTM A500/A500M–07*, USA, 2007.

[3] BCA, *Design Guide on Use of Alternative Steel Materials to BS 5950, BC1:2008*, Building and Construction Authority, Singapore, 2008.

[4] AISC, *Specification for Structural Steel Buildings, ANSI/AISC 360–10*, American Institute of Steel Construction, USA, 2010.

[5] CISC, *Handbook of Steel Construction, 9th. ed.*, Canadian Institute of Steel Construction, 2006.

[6] Packer, J.A., "Tubular brace member connections in braced steel frames", *Proc. of 11th. International Symposium and IIW International Conf. on Tubular Structures*, Québec City, Canada, 3-11, 2006.

[7] CSA, *Design of Steel Structures, S16–09*, Canadian Standards Association, 2009.

www.EngineeringEBooksPdf.com

[8] Kosteski, N., Packer, J.A., Puthli, R.S. "Notch toughness of internationally produced hollow structural sections", *ASCE Journal of Structural Engineering*, **131**(2), 279-286, 2005.

[9] CSA, *General Requirements for Rolled or Welded Structural Quality Steel/Structural Quality Steel, CAN/CSA G40.20–04/G40.21–04*, Canadian Standards Association, 2004.

[10] ASTM International, *Standard Specification for Hot-Formed Welded and Seamless Carbon Steel Structural Tubing*, *ASTM A501–07*, USA, 2007.

[11] CEN, *Hot Finished Structural Hollow Sections of Non-Alloy and Fine Grain Steels – Part 1: Technical Delivery Conditions, EN 10210–1:2006(E)*, European Committee for Standardization, 2006.

[12] CEN, *Hot Finished Structural Hollow Sections of Non-Alloy and Fine Grain Steels – Part 2: Tolerances, Dimensions and Sectional Properties, EN 10210–2:2006(E)*, European Committee for Standardization, 2006.

[13] ASTM International, *Standard Specification for Pipe, Steel, Black and Hot-Dipped, Zinc-Coated, Welded and Seamless*, *ASTM A53/A53M–07*, USA, 2007.

[14] API, *Specification for Line Pipe, ANSI/API Specification 5L and ISO 3183:2007, 44th. ed.,* American Petroleum Institute, USA, 2007.

[15] Packer, J.A., Wardenier, J., Zhao, X.L., van der Vegte, A., and Kurobane, Y., *Design Guide for Rectangular Hollow Section (RHS) Joints under Predominantly Static Loading, 2nd. ed.*, CIDECT, Geneva, Switzerland, 2009.

[16] CEN, *Cold Formed Welded Structural Hollow Sections of Non-Alloy and Fine Grain Steels – Part 1: Technical Delivery Conditions, EN 10219–1:2006(E)*, European Committee for Standardization, 2006.

[17] CEN, *Cold Formed Welded Structural Hollow Sections of Non-Alloy and Fine Grain Steels – Part 2: Tolerances, Dimensions and Sectional Properties, EN 10219–2:2006(E)*, European Committee for Standardization, 2006.

[18] Standards Australia/Standards New Zealand, *Cold-Formed Structural Steel Hollow Sections, AS/NZS 1163:2009*, Sydney, Australia, 2009.

[19] SABS, *Steel Tubes for Non-Pressure Purposes. Sections for Scaffolding, General Engineering and Structural Applications, SABS/SANS 657–1:2005*, South African Bureau of Standards, Pretoria, 2005.

[20] JIS, *Carbon Steel Tubes for Building Structures, JIS G3475*, Japanese Industrial Standards, 1996.

[21] Packer, J.A., "Overview of current international design guidance on hollow structural section connections", *Proc. of 3rd. International Offshore and Polar Engineering Conf.,* Singapore, **4**, 1-7, 1993.

[22] SCOSS, *Liquid Metal Assisted Cracking of Galvanized Steelwork, Topic Paper SC/T/04/02*, Standing Committee on Structural Safety, Institution of Structural Engineers, London, UK, 2004.

[23] Kinstler, T.J., *Current Knowledge of the Cracking of Steels during Galvanizing – A Synthesis of the Available Technical Literature and Collective Experience*, Report for American Institute of Steel Construction, GalvaScience LLC, Alabama, USA, 2005.

[24] BCSA, *Galvanizing Structural Steelwork – An Approach to the Management of Liquid Metal Assisted Cracking, BCSA and GA Publication No. 40/05*, British Constructional Steelwork Association and Galvanizers Association, UK, 2005.

[25] Poag, G. and Zervoudis, J., "Influence of various parameters on steel cracking during galvanizing", *AGA TechForum*, Kansas, USA, 2003.

[26] ASTM International, *Standard Specification for Safeguarding against Embrittlement of Hot-Dip Galvanized Structural Steel Products and Procedure for Detecting Embrittlement*, *ASTM A143/A143M–03*, USA, 2003.

[27] IIW, *Static Design Procedure for Welded Hollow Section Joints – Recommendations, IIW Doc. XV–1329–09*, International Institute of Welding, Paris, France, 2009.

www.EngineeringEBooksPdf.com

SDSS'Rio 2010 STABILITY AND DUCTILITY OF STEEL STRUCTURES
E. Batista, P. Vellasco, L. de Lima (Eds.)
Rio de Janeiro, Brazil, September 8 - 10, 2010

NUMERICAL STUDY ON STAINLESS STEEL BEAM-COLUMNS WITH TRANSVERSE LOADING

N. Lopes*, P. Vila Real* and L. Simões da Silva**

* LABEST – Department of Civil Engineering, University of Aveiro, Portugal
e-mails: nuno.lopes@ua.pt, pvreal@ua.pt

** ISISE – Department Civil Engineering, University of Coimbra, Portugal
e-mail: luisss@dec.uc.pt

Keywords: Stainless Steel, Beam-columns, Eurocode 3, Structures, Numerical.

Abstract. *In this work the accuracy and safety of the currently prescribed design rules in Eurocode 3 (EC3), for the resistance of stainless steel uniform beam-columns with transverse loading, are evaluated. This study was performed through numerical tests obtained using the methodology usually named by GMNIA (geometrically and materially non-linear imperfect analysis). This evaluation is carried out on members with Class 1 and Class 2 cross-sections subjected to axial compression and bending produced by in-plane transverse loading (concentrated and distributed loads perpendicular to the member axis on both the strong or weak axis). In these studies, the possibilities of occurring or not lateral-torsional buckling (LTB) are both analysed. The obtained numerical results are compared with the interaction curves obtained from Part 1-4 of EC3 and from other proposed design approaches for beam-columns.*

1 INTRODUCTION

Recent research studies [1, 2, 3] have been acknowledging the stainless steel important mechanical properties, contributing at the same time for the widespread and increase of structural applications with this type of steel. Nevertheless it is still recognized the necessity of a better characterization of its structural behaviour.

For stainless steel structural elements design subject to combined bending and axial compression, Part 1-4 of EC3 [4] has two notes saying that the national annexes may give other interaction formulae and others interaction factors, which suggests that the beam-columns formulae and the interaction factors were not well established for stainless steel members, at the time of the conversion from ENV to EN.

Regarding conventional carbon steel beam-column design, Part 1-1 of EC3, EN 1993-1-1 [5], introduced several changes in the design formulae for carbon steel beam-columns, when compared to the ENV version of EC3. Two new methods for the design of carbon steel beam-columns at room temperature are proposed in Part 1-1 of EC3 [5], which are the result of the work carried out by two working groups that followed different approaches [7], a French-Belgian team and an Austrian-German one. In this paper it will be checked if these two procedures can also be used with stainless steel members.

In recent research work [8], parametric studies of the behaviour of beam-columns in several stainless steel grades (austenitics, austenitic-ferritic and ferritics grades), with only end moments (uniform, triangular and bi-triangular bending moment diagrams) and an axial compression, were performed, resulting in the presentation of new proposals for the design of these structural elements. In these studies [8] it was evaluated the possibility of having, in parts 1-1 and 1-4 of the EN versions of EC3, the same approach for beam-columns design. This consideration of the two methods in Part 1-1 for stainless steel structural elements design is also studied in this paper.

www.EngineeringEBooksPdf.com

In addition, previous papers from the authors [9, 10], have presented new proposals for the flexural buckling of stainless steel columns and LTB of stainless steel beams, which are more accurate than the prescriptions in EC3 and safe when compared with the numerical results. These new proposals necessarily affect the behaviour of the interaction formulae for beam-columns and their influence were taken into account in the present paper.

In this work it is evaluated the accuracy and safety, on the resistance calculation of stainless steel beam-columns with and without LTB, subjected to transverse loads, of the: currently prescribed design rules in Part 1-4 of EC3; new carbon steel beam-column formulae at room temperature [4, 7], after being adapted to deal with stainless steel; and the recently proposed design expressions for stainless steel beam-columns with only end moments [8].

This evaluation is carried out by performing numerical simulations on Class1 and Class 2 stainless steel H-columns subjected to compression plus uniaxial bending. It is considered buckling in the two main cross-section axes and different bending moment diagrams (point load applied at the mid span and distributed load along the member length). HEA200 welded cross-sections were used of stainless steel grade 1.4301. The stainless steel mechanical properties used in this work can be found in Part 1-4 of EC3 [4]. An average of 5 beam lengths and 8 bending moment / axial load ratios were analyzed for each case.

In the numerical simulations, a sinusoidal lateral geometric imperfection was considered [11]. The adopted residual stresses follow the typical pattern for carbon steel welded sections [11, 12, 13], considered constant across the thickness of the web and flanges.

The numerical results were obtained with the finite element program SAFIR [14], a geometrical and material non linear finite element code, which has been adapted to be able to model stainless steel structures according the material properties defined in EN 1993-1-4.

The safety factor γ_{M1} in stainless steel structures at room temperature takes the value of 1.1 [4]. However in order to compare the actual interaction curves, in the studies presented in this paper, this factor was considered equal to 1.0, as already adopted in carbon steel design [5].

2 BEAM-COLUMN WITHOUT LTB

In this work, the possibility of the beam-columns not having LTB was first studied. It was only considered axial compression: with bending in the strong axis, assuming that the element is restrained about the z axis; and with bending in the weak axis, assuming that the element is restrained about the y axis.

2.1 EC3 proposal

Part 1-4 of EC3, gives the following expressions for the design of Class 1 and 2 stainless steel beam-columns subjected to axial compression and bending without LTB.

$$\frac{N_{Ed}}{N_{b,Rd,\min}} + k_y \frac{M_{y,Ed}}{W_{pl,y}\dfrac{f_y}{\gamma_{M1}}} + k_z \frac{M_{z,Ed}}{W_{pl,z}\dfrac{f_y}{\gamma_{M1}}} \le 1 \tag{1}$$

where

$$k_i = 1.0 + 2\left(\bar{\lambda}_i - 0.5\right)\frac{N_{Ed}}{N_{b,Rd,i}} \quad \text{but} \quad 1.2 \le k_i \le 1.2 + 2\frac{N_{Ed}}{N_{b,Rd,i}} \tag{2}$$

being i y or z axis

As it can be observed these formulae do not consider the influence of the shape of the bending moment diagram.

2.2 Adaptation of the carbon steel interaction curves

As mentioned before, the project team involved in the conversion from ENV to EN of Part 1-1 of EC3 has revised the interaction formulae for carbon steel beam-columns safety check [5]. Two new

www.EngineeringEBooksPdf.com

methods were incorporated: "Method 1" and "Method 2" reported in Annex A and Annex B of Part 1-1 of EC3, respectively. These two methods were adapted to take into account the reduction factor for flexural buckling of stainless steel columns [9].

According to EN 1993-1-1, the stability of beam-columns (of the classes 1 and 2), in the case of bending around the strong and weak axis, is checked in accordance with the following interaction formulae:

$$\frac{N_{Ed}}{\chi_y \frac{N_{Rk}}{\gamma_{M1}}} + k_{yy} \frac{M_{y,Ed} + \Delta M_{y,Ed}}{\frac{M_{y,Rk}}{\gamma_{M1}}} \leq 1 \quad \text{and} \quad \frac{N_{Ed}}{\chi_z \frac{N_{Rk}}{\gamma_{M1}}} + k_{zz} \frac{M_{z,Ed} + \Delta M_{z,Ed}}{\frac{M_{z,Rk}}{\gamma_{M1}}} \leq 1 \tag{3}$$

where k_{yy} and k_{zz} are the interaction factors.

2.2.1 Method 1

Without attempting to explain the background [7] of this proposal, the interaction factors are expressed through the relations, which use the equivalent moment factors:

$$c_{mi} = c_{mi,0} \tag{4}$$

$c_{mi,0}$ is respectively, for a mid span point load and for a uniformly distributed load:

$$c_{mi,0} = 1 - 0.18 \frac{N_{Ed}}{N_{cr,i}} \quad \text{and} \quad c_{mi,0} = 1 + 0.03 \frac{N_{Ed}}{N_{cr,i}} \tag{5}$$

The other coefficients not described here can be obtained in Annex A of Part 1-1 of EC3

2.2.2 Method 2

"Method 2" is described in Annex B of Part 1-1 of EC3. This approach proposes different interaction factors from "Method 1", using, for a mid span point load and for uniformly distributed load respectively

$$c_{mi} = 0.90 \quad \text{and} \quad c_{mi} = 0.95 \tag{6}$$

2.3 Formulation of a new proposal

Part 1-4 of EC3 [4] states that the safety evaluation of elements subjected to bending and axial compression should satisfy expression (1).

Based in the procedure in [15] for the determination of the carbon steel interaction curves at high temperatures, new formulae, for the stainless steel beam-columns safety evaluation, were developed [8], following the approaches included in the ENV version of Part 1-1 of the same EC3 [6] and adopted in Part 1-2 of EC3 [16]. In comparison with EC3 [4] the main changes appear in the determination of the interactions factors k_y and k_z.

$$k_i = 1 - \frac{\mu_i N_{Ed}}{\chi_i A \frac{f_y}{\gamma_{M1}}} \quad \text{with} \quad k_i \leq 1.5 \text{ and } k_i \geq \mu_y - 0.7 \tag{7}$$

To determine the values of μ_y and μ_z the following equations should be used

$$\mu_y = (0.97\beta_{M,y} - 2.11)\overline{\lambda}_y + 0.44\beta_{M,y} + 0.09 \quad \text{if } \overline{\lambda}_y \leq 0.3 \text{ then } \mu_y \leq 1.0 \text{ else } \mu_y \leq 0.9 \tag{8}$$

$$\mu_z = (1.09\beta_{M,z} - 2.32)\overline{\lambda}_z + 0.29\beta_{M,z} + 0.48 \quad \text{if } \overline{\lambda}_z \leq 0.3 \text{ then } \mu_z \leq 1.0 \text{ else } \mu_z \leq 0.9 \tag{9}$$

Finally the equivalent uniform moment factors $\beta_{M,y}$ and $\beta_{M,z}$ can be determined in function of the bending diagram shape as in [6] and [16], according to

$$\beta_M = \beta_{M,\Psi} + \frac{M_Q}{\Delta M}(\beta_{M,Q} - \beta_{M,\Psi}) \tag{10}$$

where $M_Q, \Delta M, \beta_{M,Q}$ and $\beta_{M,\Psi}$ can be found in part 1-2 of EC3 [16].

For a mid span point load and for uniformly distributed load its value is respectively

www.EngineeringEBooksPdf.com

$$\beta_{M,i} = \quad 4 \text{ and } \beta_{M,i} = 1.3 \tag{11}$$

2.4 Accuracy of the proposals

In this section the new proposals are evaluated by means of a direct comparison with numerical results. Due to space limitations only few results of the parametric study are shown.

The graphics from Figure 1 and Figure 2 were obtained for beam-columns with buckling about y and z axis, with uniaxial bending in the strong and weak axis respectively. Here, the length of 3 m corresponds to a non-dimensional slenderness values of $\overline{\lambda}_y = 0.37$ and $\overline{\lambda}_z = 0.62$, while the length of 7 m corresponds to $\overline{\lambda}_y = 0.87$ and $\overline{\lambda}_z = 1.45$.

The interaction curves in the graphics are obtained from: Part 1-4 of EC3 "EN 1993-1-4"; Part 1-4 of EC3 with a new proposal for columns [9] "EN 1993-1-4 mod"; Part 1-1 of EC3 for carbon steel beam-columns with a new proposal for columns [9] "Method 1"and "Method 2" and the interaction curves presented in the previous section [8] "New proposal".

The method which better approximates the numerical results from SAFIR is the "New proposal". "Method 1" and "Method 2" adapted from the formulae from Part 1-1 of EC3 for carbon steel and the new proposal for stainless steel columns also present good approximations. From these two methods, the one that has a better behaviour is "Method 1", but still not as good as the "New proposal". It can also be observed that the new proposal for columns [9] introduces a significant improvement in the interaction curves approximations to the numerical results.

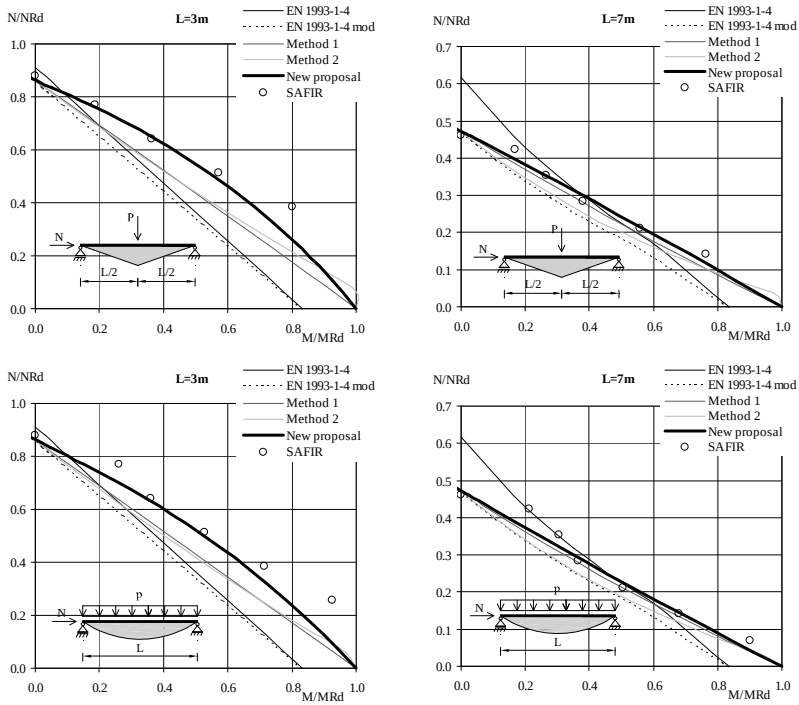


Figure 1: Different interaction curves, regarding compression and uniaxial bending about the strong axis.

www.EngineeringEBooksPdf.com

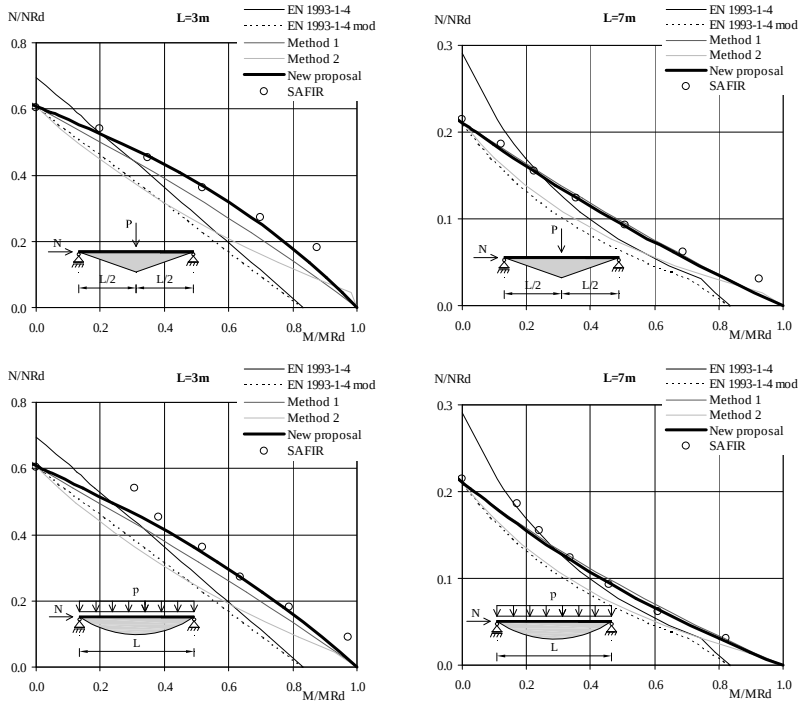


Figure 2: Different interaction curves, regarding compression and uniaxial bending about the weak axis.

3 BEAM-COLUMN WITH LTB

In this section it is presented the study made on stainless steel beam-columns with LTB. It was only considered axial compression with bending in the strong axis, assuming that the element is only restrained in the extremities by fork supports.

3.1 EC3 proposal

Part 1-4 of EC3, gives the following expressions for the design of Class 1 and 2 stainless steel beam-columns subjected to axial compression and bending, having the possibility of occurring LTB.

$$\frac{N_{Ed}}{\left(N_{b,Rd}\right)_{\min}} + k_{LT}\frac{M_{y,Ed}}{M_{b,Rd}} + k_z\frac{M_{z,Ed}}{W_{pl,z}\dfrac{f_y}{\gamma_{M1}}} \le 1 \tag{12}$$

where

$$k_{LT} = 0.1 \tag{13}$$

and k_z is given by expression (2).

3.2 Adaptation of the carbon steel interaction curves

As made before, it was studied the possibility of using the interaction curves recommended in Part 1-1 of EC3 [5], adapted to the stainless steel material properties. The two already described methods were also changed in order to account for the reduction factor for flexural buckling of stainless steel columns and the reduction factor for LTB of stainless beams.

www.EngineeringEBooksPdf.com

According to EN 1993-1-1, the stability of beam-columns with LTB (of the class 1 and 2), in the case of bending around the strong axis, is checked in accordance with the following interaction formulae:

$$\frac{N_{Ed}}{\chi_y \frac{N_{Rk}}{\gamma_{M1}}} + k_{yy} \frac{M_{y,Ed} + \Delta M_{y,Ed}}{\chi_{LT} \frac{M_{y,Rk}}{\gamma_{M1}}} \le 1 \text{ and } \frac{N_{Ed}}{\chi_z \frac{N_{Rk}}{\gamma_{M1}}} + k_{zy} \frac{M_{y,Ed} + \Delta M_{y,Ed}}{\chi_{LT} \frac{M_{y,Rk}}{\gamma_{M1}}} \le 1 \quad (14)$$

k_{yy} and k_{zy} are interaction factors different from the one prescribed for beam-columns without LTB.

3.2.1 Method 1

The procedure for the determination of the interaction factors for the "Method 1" is reported in Annex A of Part 1-1 of EC3, where:

$$c_{my} = c_{my,0} + \left(1 - c_{my,0}\right) \frac{\sqrt{\varepsilon_y}\, a_{LT}}{1 + \sqrt{\varepsilon_y}\, a_{LT}} \text{ and } c_{mLT} = c_{my}^2 \frac{a_{LT}}{\sqrt{\left(1 - \frac{N_{Ed}}{N_{cr,z}}\right)\left(1 - \frac{N_{Ed}}{N_{cr,T}}\right)}} \ge 1 \quad (15)$$

3.2.2 Method 2

"Method 2" is described in Annex B of Part 1-1 of EC3. According to this method, for a mid span point load and for uniformly distributed load respectively

$$c_{mLT} = c_{my} = 0.90 \text{ and } c_{mLT} = c_{my} = 0.95 \quad (16)$$

3.3 Formulation of a new proposal

In the reference [8] it is proposed that the safety evaluation of elements subjected to bending and axial compression with LTB should satisfy:

$$\frac{N_{Ed}}{\chi_z A \frac{f_y}{\gamma_{M1}}} + k_{LT} \frac{M_{y,Ed}}{\chi_{LT} W_{pl,y} \frac{f_y}{\gamma_{M1}}} + k_z \frac{M_{z,Ed}}{W_{pl,z} \frac{f_y}{\gamma_{M1}}} \le 1 \quad (17)$$

In these proposed interaction curves the interactions factors k_{LT} should be determined by

$$k_{LT} = 1 - \frac{\mu_{LT} N_{Ed}}{\chi_z A \frac{f_y}{\gamma_{M1}}} \quad \text{with} \quad k_{LT} \le 1 \text{ and } k_{LT} \ge \mu_{LT} - 0.7 \quad (18)$$

where

$$\mu_{LT} = \left(-0.07 \beta_{M,LT} - 0.07\right) \overline{\lambda}_z + 0.60 \beta_{M,LT} - 0.10$$
$$\text{if } \overline{\lambda}_y \le 0.3 \text{ then } \mu_y \le 1.0 \text{ else } \mu_y \le 0.9 \quad (19)$$

Finally, the equivalent uniform moment factor $\beta_{M,LT}$ can be determined in function of the bending diagram shape in the strong axis using expression (10), resulting in (for a mid span point load and for uniformly distributed load respectively, as in EC3 [16])

$$\beta_{M,LT} = \beta_{M,y} = 1.4 \text{ and } \beta_{M,LT} = \beta_{M,y} = 1.3 \quad (20)$$

3.4 Accuracy of the proposals

Again, direct comparisons with the numerical results are used to validate this new proposal. The graphics from Figure 3 were obtained for beam-columns with the possibility of occurring LTB, with bending in the strong axis. The length of 3 m corresponds to non-dimensional slenderness values of $\overline{\lambda}_z = 0.62$, while the length of 7 m corresponds to $\overline{\lambda}_z = 1.45$. The non-dimensional slenderness values for the LTB phenomena are given in the graphs. The interaction curves named "EN 1993-1-4 mod" in the graphs

www.EngineeringEBooksPdf.com

from Figure 6 were obtained from Part 1-4 of EC3 with the new proposal for columns [9] and with the new proposal for LTB [10].

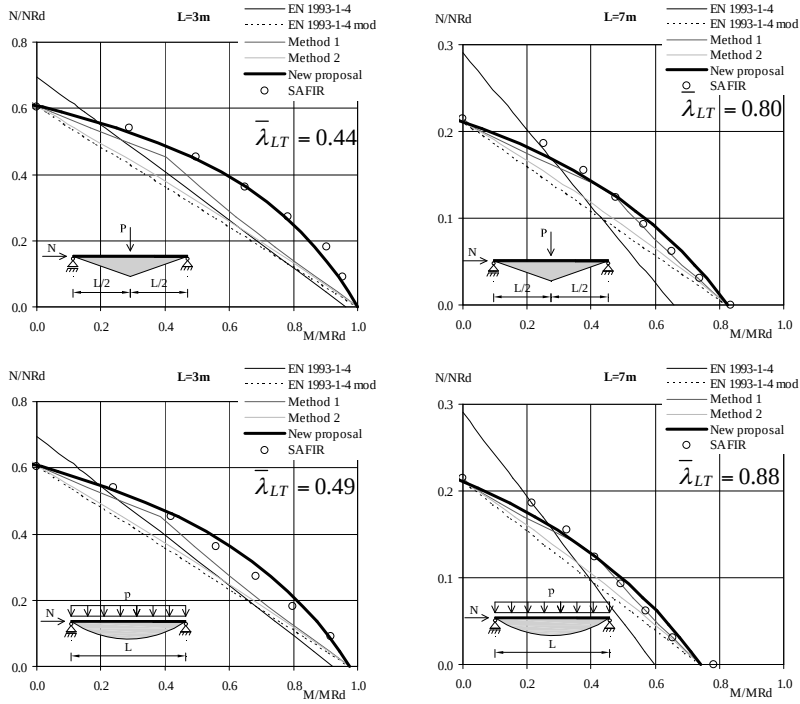


Figure 3: Comparison between different interaction curves for beam-columns with LTB.

Again, the method providing a better approximation to the numerical results is the “New proposal”. “Method 1” and “Method 2” also present safe approximations. From these two methods, the one that has a closer behaviour to the numerical results is “Method 1”.

It can also be observed that the new proposals, for columns [9] and for LTB of beams [10], introduce significant improvements in the interaction curves approximations when compared to the numerical results.

4 CONCLUSIONS

Different approaches for evaluating the safety of stainless steel elements subjected to axial compression and bending were presented and analysed. These approaches address the influence of global buckling phenomena (flexural buckling and LTB).

All the methods were tested with the new proposals, for columns [9] and for LTB [10], which introduced significant improvements in the interaction curves approximations when compared to the numerical results.

From the obtained results, it can be concluded that EC3 formulae for stainless steel beam-columns do not provide an accurate approximation to the real behaviour. Also, in order to use the new carbon steel interaction curves (Method 1 and Method 2) to stainless steel, additional modifications are needed.

The proposal that performed better is the one resulting from previous works by the authors [8], where new interaction curves, for the design of stainless steel beam-columns with and without LTB, were developed. This proposal has the advantage of being easier to use than Method 1 and Method 2. This

www.EngineeringEBooksPdf.com

paper only included two loading types (point load applied at the mid span and distributed load along the member length). However similar studies, on members with combined axial compression, end moments and transverse loads, have confirmed that it may be possible to use expression (10), from the ENV version of Part 1-1 of EC3 [6] and EN version of Part 1-2 of EC3 [16], for the calculation of the equivalent uniform moment factor β_M, since this proposal, follows this same approach and has shown to be accurate for other bending moment diagrams [8].

REFERENCES

[1] Estrada, I.; Real, E.; Mirambell, E., "General behaviour and effect of rigid and non–rigid end post in stainless steel plate girders loaded in shear. Part I: experimental study", *Journal of Constructional Steel Research*, Elsevier, Vol. 63, pp. 970–984, 2006.

[2] Gardner, L., "The use of stainless steel in structures", *Progress in Structural Engineering and Materials*, 7(2), pp. 45–55, 2005.

[3] Euro Inox and Steel Construction Institute, *Design Manual for Structural Stainless Steel*, 3rd edition, 2006.

[4] CEN, European Committee for Standardisation, *EN 1993-1-4, Eurocode 3: Design of steel Structures – Part 1-4: General rules – Supplementary Rules for Stainless steels*, Belgium, 2006.

[5] CEN, *EN 1993-1-1, Eurocode 3, Design of Steel Structures – Part 1-1: General rules and rules for buildings*, Belgium, 2005.

[6] CEN *ENV 1993-1-1 Eurocode 3: Design of Steel Structures - Part 1-1: General rules and rules for buildings*, Belgium, 1992.

[7] Boissonnade, N., Greiner, R., Jaspart, J. P., *Rules for Member Stability in EN1993-1-1 Background documentation and design guidelines*, ECCS TC 8 – Stability, 2006.

[8] Vila Real, P.; Lopes, N.; Simões da Silva, L. "Stainless steel beam-columns interaction curves with and without lateral torsional buckling", *proceedings of the ESMC2009 7th EUROMECH Solid Mechanics Conference*, Lisbon, Portugal, September of 2009.

[9] Lopes, N.; Vila Real, P.; Simões da Silva, L., "Numerical modelling of the Flexural buckling of axially loaded stainless steel members", *proceedings of the third International Conference on Steel and Composite Structures ICSCS07*, Manchester, United Kingdom, 2007.

[10] Lopes, N.; Vila Real, P.; Simões da Silva, L.; Mirambell, E., "Numerical modelling of the lateral-torsional buckling of Stainless steel I-beams: comparison with Eurocode 3", *proceedings of the Tenth International Conference on Enhancement and Promotion of Computational Methods in Engineering and science EPMESC X*, Sanya, China, 2006.

[11] Vila Real, P.; Lopes, N.; Simões da Silva, L.; Franssen, J.-M., "Lateral-torsional buckling of Stainless steel I-beams in case of fire", *Journal of Constructional Steel Res.*, ELSEVIER, 2008.

[12] Chen, W. F. and Lui, E. M., *Stability design of steel frames*, CRC Press, 1991.

[13] Gardner, L., Nethercot, D., "Numerical Modelling of Stainless Steel Structural Components - A consistent Approach", *Journal of Constr. Engineering*, ASCE, 2004.

[14] Franssen, J.-M., "SAFIR. A Thermal/Structural Program Modelling Structures under Fire", *Engineering Journal*, A.I.S.C., 2005.

[15] Talamona, D., *Flambement de poteaux métalliques sous charge excentrée, à haute température*, (in french); Ph.D. thesis, Université Blaise Pascal Ecole Doctorale Sciences pour l'Ingenieur de Clermont-Ferrand, 1995.

[16] CEN, *EN 1993-1-2, Eurocode 3, Design of Steel Structures – Part 1-2: General rules – Structural fire design*, Belgium, 2005.

www.EngineeringEBooksPdf.com

3. BRIDGES AND FOOTBRIDGES

www.EngineeringEBooksPdf.com

www.EngineeringEBooksPdf.com

SDSS'Rio 2010 STABILITY AND DUCTILITY OF STEEL STRUCTURES
E. Batista, P. Vellasco, L. de Lima (Eds.)
Rio de Janeiro, Brazil, September 8 - 10, 2010

IMPROVED CROSS FRAME CONNECTION DETAILS FOR STEEL BRIDGES WITH SKEWED SUPPORTS

Craig Quadrato*, Anthony Battistini*, Todd A. Helwig[**], Karl Frank[***], and Michael Engelhardt[****]

*Ph.D. Candidate, University of Texas at Austin
e-mails: craig.quadrato@us.army.mil, adb7@lehigh.edu

**Associate Professor University of Texas at Austin, Ph.D.
e-mail: thelwig@mail.utexas.edu

[***]Warren S. Bellows Centennial Professor in Civil Engineering University of Texas at Austin, Ph.D.
e-mail: karl.frank@hirschfeld.com

[****]Dewitt C. Greer Centennial Professor in Transportation Eng. University of Texas at Austin, Ph.D.
e-mail: mde@mail.utexas.edu

Keywords: Stability, Bracing, Skewed Abutments, Steel Girders, Warping Restraint.

Abstract. *Cross-frames are essential to straight steel girder bridge system stability during construction. However, due to fabrication complexities, these braces often make up a large percentage of the bridge cost and when they transmit live load forces, they can produce fatigue cracks at their connections to the girders. At the abutments of skewed bridges current detailing specifications require the cross frames to be parallel to the skew angle. Many jurisdictions currently use a bent plate to connect the skewed end cross frames to the girders. A Texas Department of Transportation sponsored research study is underway at The University of Texas to investigate the bent plate connection's impact on girder stability and develop alternative connection details for skewed steel bridge end cross frames. A connection candidate being investigated consists of using a round half-pipe stiffener to connect the girder to the cross frame. This paper investigates the pipe stiffener's impact on girder buckling strength.*

1 INTRODUCTION

A major skewed steel bridge issue is the differential deflections that occur along a contiguous line of intermediate cross frames as trucks pass over the bridge. When these differential deflections occur, the cross frames become part of the live load structural system and help carry the live loading between the girders. This in turn can lead to fatigue cracking at the girder to cross frame welds – especially near the skewed abutments where the differential deflections are the greatest.

One way to mitigate the differential deflections and associated fatigue cracking is to position the first intermediate cross frame line farther away from the skewed abutment. This will lessen the differential deflections along the first and subsequent cross frame lines. However, to ensure elastic stability during placement of the concrete slab over the longer unbraced length, a source of stability must be found to compensate for the longer unbraced girder length during concrete deck placement. One solution is to provide warping restraint to the girder flanges at the skewed end cross frame connection.

Current end cross-frame detailing specifications require the end cross frame to be placed parallel to the skewed support, and hence at an angle to the girders [1]. To provide access for welding during

www.EngineeringEBooksPdf.com

fabrication and erection, plates, bent to match the skew angle, are often used to connect the cross-frames to the girder. Such a connection provides little if any warping restraint. However, if a pipe, welded to the girder web and both flanges, is used to connect the end cross frames then significant warping restraint will be provided to the girders [2]. Such a connection is shown in Figure 1.

The attractiveness of the half-pipe stiffener detail lies in its fabrication and structural advantages. Besides offering warping restraint, the pipe stiffener connection accommodates any skew angle and can standardize the cross frame connection in any bridge orientation. Finally, the pipe stiffener offers the possibility of a more rigid connection increasing the end cross frame stiffness and its ability to prevent girder end twist during slab placement.

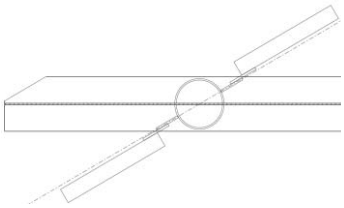


Figure 1: Pipe stiffener skewed end frame connection.

2 LABORATORY TESTING AND FINITE ELEMENT MODEL VALIDATION

Previous analytic studies have shown significant increases in buckling strength when warp restraining devices are used to connect a girder's top and bottom flange [3], [4]. During this study, laboratory tests were conducted to confirm these analytic results for a pipe stiffener. A finite element model was then created and validated with the laboratory results.

2.1 Laboratory Testing

A series of twin girder buckling tests were conducted at Ferguson Structural Engineering Laboratory at The University of Texas at Austin to confirm the analytical results in the literature. Pipe stiffened and plate stiffened 17m long W760x134 rolled girders were tested using a gravity load simulator to deliver a concentrated load at the mid-span of each girder. The ends of the girders were supported with a simple support and lateral restraints were used to prevent twist at the ends of the girders. A picture of a typical test is shown in Figure 2.

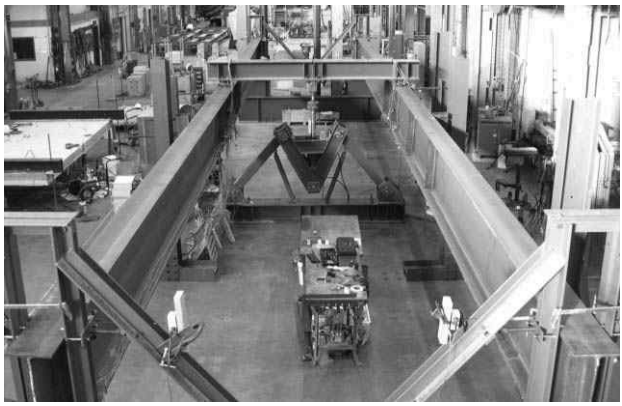


Figure 2: Plate stiffened twin girder buckling test.

www.EngineeringEBooksPdf.com

Comparisons for the results from the plate and pipe stiffened girders are shown in Figure 3. Shown in the figure are the results for the mid-span top flange lateral displacement of each girder type. From the figure it can be seen that the warping restraint provided by the pipe stiffener increases the buckling capacity of the girder by about 50%. This finding is consistent with the previously mentioned analytical results.

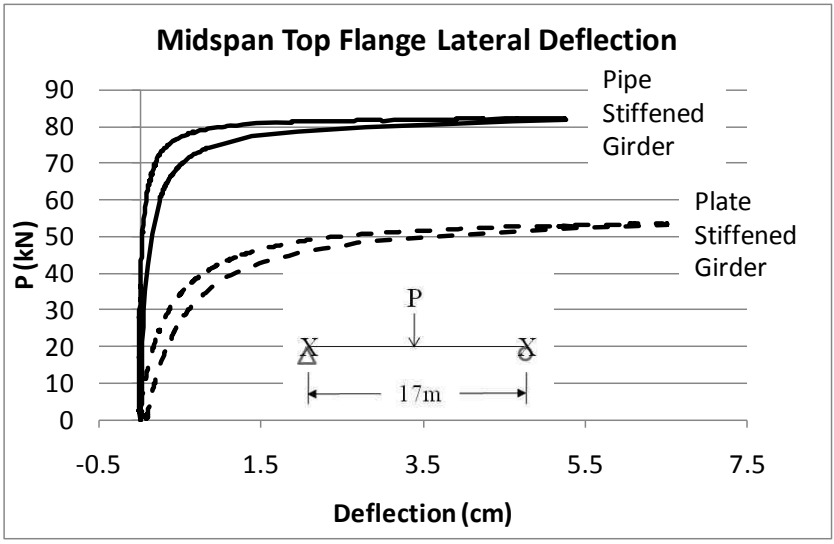


Figure 3: Pipe and plate stiffened girder buckling test laboratory results.

2.2 Finite Element Model Validation

In order to extend these results to other girder geometries, a finite element model of a pipe stiffened girder was created. The model was built in the three dimensional finite element modeling program ANSYS 11.0 using eight node shell elements. A picture of the pipe stiffened girder model is shown in Figure 4.



Figure 4: Pipe stiffened girder finite element model (elements shown).

A nonlinear geometric analysis of the model was run to compare with the laboratory results for the pipe stiffened girder. The analysis included the girder's initial imperfection and self weight. A graph of the results of the mid-span top flange lateral deflection comparison is shown in Figure 5. From the figure it can be seen that the model is conservative by about 2% at the maximum applied load. The main sources of conservatism are due to several assumptions made during modeling. First, it was assumed that

www.EngineeringEBooksPdf.com

the lateral stops at the end of the girder provide no warping restraint. Second, only a modest increase in the cross sectional torsional constant was made to account for the size of the W760x134 rolled shape fillet, while the fillet size at the girder ends were slightly larger than the average values given by the Steel Construction Manual [5]. Finally, the cross section geometry was assumed to be constant throughout its length. Despite these conservative assumptions and expected conservative result, the graph shows reasonable agreement between the specimen and model.

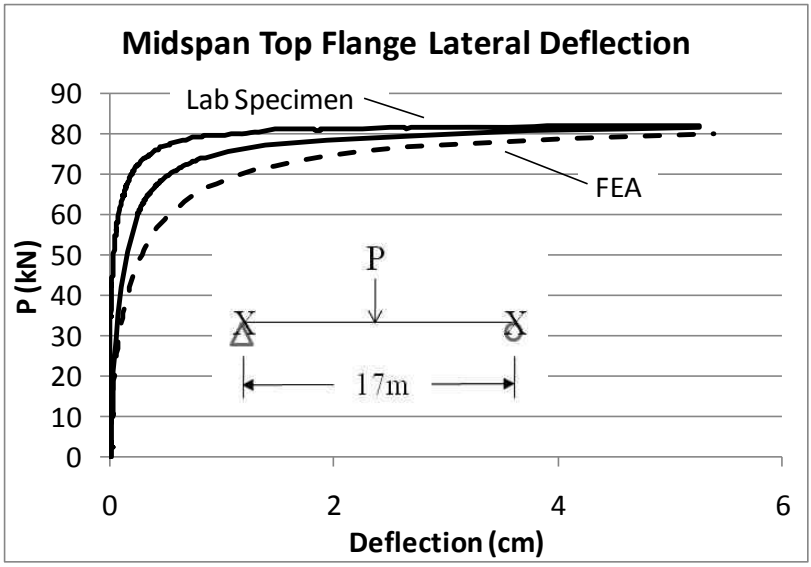


Figure 5: Lab specimen to FEA comparison for mid-span top flange lateral deflection

3 DESIGN EQUATION DEVELOPMENT

3.1 Background

The basic elastic buckling strength of bridge girder subject to uniform moment is defined by Equation 1 [6].

$$M_o = \pi / L_b \sqrt{EI_y GJ + \pi^2 E^2 C_w I_y / L_b^2} \tag{1}$$

where

E = Young's modulus
I_y = weak axis moment of inertia
L_b = unbraced length
G = shear modulus
J = torsion constant
C_w = warping constant
L_g = total girder length

www.EngineeringEBooksPdf.com

Two of the assumptions in Equation 1 are that the ends of the girder do not twist and are free to warp. However, due to flexible cross frame connections and skewed abutments neither of these assumptions is necessarily accurate at the end of skewed bridge girders. Previous research on the impact of end connections on girder twist has shown that most supports are much more torsionally stiff than the girder cross section, so any restraint provided by the end frame will more than adequately resist the loss of strength due to twist [7]-[9], and therefore the no-twist assumption can be used with little impact on the buckling strength of bridge girders.

However, as has been shown through the previously mentioned laboratory results and analytical studies, warping restraint can significantly improve the girder buckling strength. Typically warping restraint has been treated as an all or nothing proposition where accounting for its impact on buckling strength means either considering no warping restraint or infinite warping restraint [2]. But, the use of a closed pipe section to restrain warping by bracing one flange against the other does not provide such a clear boundary condition.

An accurate numeric integration technique to predict the buckling capacity of a girder with warping restraint provided by a pipe stiffener has been developed [3]; however, this highly iterative method does not lend itself to routine design practice. Additionally, while the impacts of warping restraint of adjacent girder sections on the critical sections have been researched and a simplified analysis procedure has been found [2], this technique does not apply to warping restraint provided to the end of girders. Fortunately, by relying on basic column buckling theory and the side-sway inhibited alignment chart [5], a simplified method can be used to aid in girder design where pipe stiffeners provide warping restraint to the girder ends.

3.2 Pipe Stiffener Design Methodology

An examination of Equation 1 shows that the terms under the radical define both components of the girder's resistance to lateral torsional buckling. The first term is the uniform (St. Venant) torsional resistance and the second term is the torsional warping resistance. Therefore, the warping resistance provided by a pipe stiffener could be incorporated into the second term as an effective torsional length factor (K_z) as shown in Equation 2. Such a method has previously been employed to calculate the impact of warping restraint provided by adjacent unbraced girder lengths [2].

$$M_o = C_b \pi / L_b \sqrt{EI_y GJ + \pi^2 E^2 C_w I_y / (K_z L_b)^2} \tag{2}$$

where

C_b = moment gradient coefficient
K_z = effective length factor for torsion

The critical parameter in determining K_z for a pipe stiffener lies in the relative rotational stiffness of the girder's compression flange about its strong axis ($2EI_f/L$ where I_f is the flange's strong axis moment of inertia) to the torsional stiffness of the pipe (GJ/L). If the torsional stiffness of the pipe is much greater than that of the girder flange then K_z will approach 0.5 (torsionally fixed). Likewise if the pipe's stiffness is much smaller than the flange's stiffness then K_z will approach 1.0 (torsionally free). This is analogous to a sidesway inhibited column where the torsional stiffness of the pipe is considered as the flexural stiffness of a girder framing into the end of a column. Approaching the problem in this way allows the sidesway inhibited alignment chart for columns to be used to select an appropriate K_z, where the relative rotational stiffness of the girder flange to the torsional stiffness of the pipe is used to calculate G_A or G_B at the girder's pipe stiffened end.

In order to use the alignment chart, the chart's assumption that the stiffening girders bend in single curvature in the formulation of the chart's G-value must be considered in terms of the pipe stiffener. If

www.EngineeringEBooksPdf.com

the pipe is much stiffer than the girder flanges, then as the flanges attempt to warp in opposite directions they will be rigidly held in position by the pipe. This condition would result in multiplying the assumed stiffening girder or analogous pipe stiffness by three in the equation for G used in the chart. As the torsional stiffness of the pipe drops relative to the flexural stiffness of the girder flanges, then this multiplier drops to one. Using this logic for pipe stiffeners G may be defined as in Equation 3.

$$G = \frac{\left(EI / L_b\right)_{flange}}{m\left(GJ / L\right)_{pipe}} \tag{3}$$

where

I = flange strong axis moment of inertia
m = pipe stiffness multiplier based on relative stiffness of pipe to flange ($1 \leq m \leq 3$)
L = pipe length

The difficulty in assessing the value of m comes from the indeterminate nature of the pipe boundary conditions. Since the boundary conditions depend on the relative torsional stiffness of the pipe to the flexural stiffness of the flange and in turn the flexural stiffness of the flange depends on the torsional stiffness of the pipe there is no simple solution to define m. Therefore, a parametric study using the 3-D finite element modeling program ANSYS and the previously described pipe stiffened girder model was used to establish values of m for corresponding ratios of the pipe torsional stiffness to the girder flange flexural stiffness.

3.3 Parametric Study to Determine m

The cross sections used in the parametric study to determine m are shown in Figure 6.

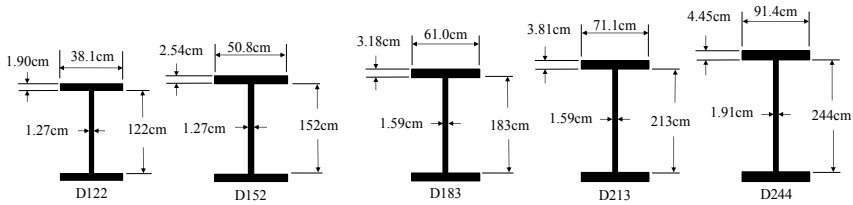


Figure 6: Cross sections used in parametric study.

Each cross section was analyzed via eigenvalue analysis with simple supports and no end twist using span to depth ratios of 10 to 40 in increments of 5. Uniform moment, mid-span concentrated load, and uniform loading were considered for each cross section and span to depth ratio. Each case was run with and without a pipe stiffener. Pipe diameters were varied from one half the flange width to two inches less than the flange width. All pipes used had a 1.27cm wall thickness. Based on the parametric studies, the values of m in Table 1 were selected.

Table 1: m values from parametric study.

m	$(GJ/L)_{pipe}/(EI/L_b)_{flange}$
1.0	< 4
1.5	4 - 6
3	> 6

www.EngineeringEBooksPdf.com

3.4 Analytic Equation Results

A comparison between the analytic solution given by Equation 2 and the finite element analysis for two of the cross sections, load cases, and pipe sizes are given in Figure 7 and Figure 8. The pipe stiffened girder critical loads have been normalized by the values for the critical loads for the non-pipe stiffened section and all span (L) to depth (D) ratios investigated are shown in the graphs.

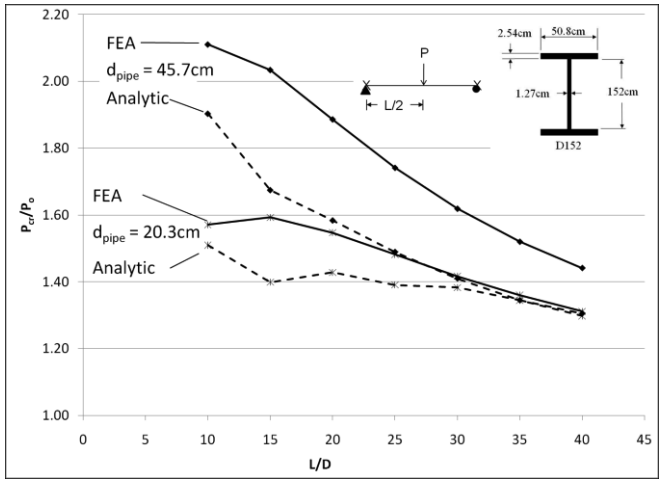


Figure 7: D152 analytic to FEA pipe stiffener comparison (point load).

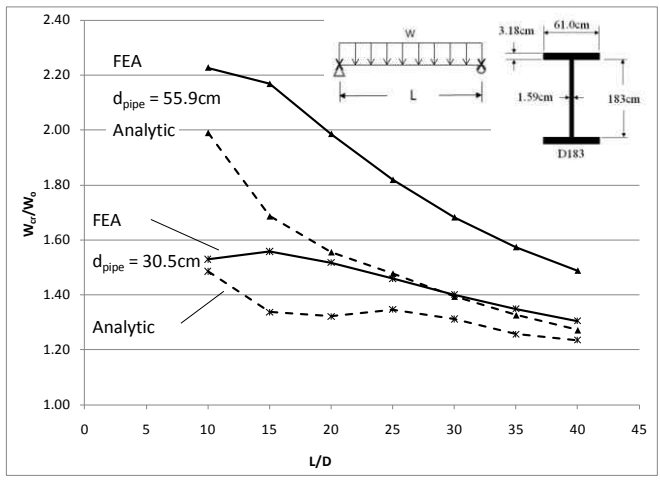


Figure 8: D183 analytic to FEA pipe stiffener comparison (distributed load).

From the graphs the increase in buckling capacity due to the pipe stiffener is evident. Additionally it can be seen that the analytic solution using Equation 2 is conservative with respect to the FEA solution. The majority of this conservatism comes from Equation 2 only accounting for the additional warping restraint provided by the pipe stiffeners. Additionally, the uniform (St. Venant) stiffness has also been increased and is not accounted for in Equation 2. It is conservative to neglect this effect and this leads to underestimating the FEA buckling strength by around 20% for the largest pipe diameters.

www.EngineeringEBooksPdf.com

4 CONCLUSION AND FUTURE WORK

The laboratory tests and finite element modeling results in this study confirm that the warping restraint provided by a pipe stiffener installed at the ends of simply supported girder substantially increases the girder's elastic buckling capacity. Therefore, a pipe stiffener cross frame connection is a good candidate to increase the unbraced length at the end spans of a skewed steel bridge and allow the first row of intermediate cross frames to be moved farther from the abutment. By doing so, the differential deflections along the cross frame lines will be decreased, therefore mitigating fatigue related cracking at the cross frame connections.

In addition to the warp restraint it provides, the half pipe stiffener allows a cross frame connection at almost any skew angle and can also serve as an integral bearing stiffener. Therefore it can be used to standardize connections for a wide variety of bridge skew angles. Additionally, in fatigue tests performed at Ferguson Structural Engineering Laboratory, the pipe stiffener performs at least as well as the plate stiffener. While this may not be a concern at the abutment, should the pipe stiffener be used in the negative moment region at an intermediate support, its connection to the tension flange will be exposed to fatigue.

Finally, a simplified method to calculate the increase in buckling capacity due to the warping restraint provided by the pipe stiffener has been proposed. This method, based on the no-sway alignment chart in the Steel Construction Manual [5], gives designers a simple and conservative tool to calculate the increase in unbraced length due to the pipe stiffener.

Further tests are underway at Ferguson Structural Laboratories to compare the commonly used bent plate connection and the pipe stiffener connections. These tests consist of a series of three girder tests with end and intermediate cross frames with 53° and 24° skew angles. These results will be used to quantify the stiffness of the two connections and further validate the finite element modeling of the connections and cross frames used in skewed steel bridges.

REFERENCES

[1] AASHTO/NSBA Steel Bridge Collaboration. *Guidelines for Design for Constructibility.* AASHTO, 2003.

[2] Structural Stability Research Council. *Guide to Stability Design Criteria for Metal Structrues.* Edited by T.V. Galambos. New York: John Wiley & Sons, 1988.

[3] Ojalvo, M., and R.S. Chambers. "Effects of Warping Restraints on I-Beam Buckling." *ASCE Journal of the Structural Division* 103, no. ST12 (1977): 2351-2360.

[4] Hunt, Fred A. "The Suppression of Warping in Thin-Walled Beams." *M.S. Thesis Submitted to The Ohio State University.* 1973.

[5] American Institute of Steel Construction. *Steel Construction Manual.* Chicago: American Institute of Steel Construction, 2005.

[6] Timoshenko, Stephen P., and James M. Gere. *Theory of Elastic Stability.* New York: McGraw-Hill, 1961.

[7] Schmidt, Lewis C. "Restraints Against Elastic Lateral Buckling." *Journal of the Engineering Mechanics Division*, December 1965: 1-10.

[8] Flint, A.R. "The Influence of Restraints on the Stability of Beams." *The Structural Engineer*, 1951: 235-246.

[9] Bose, B. "The Influence of Torsional Restraint Stiffness at Supports on the Buckling Strength of Beams." *The Structural Engineer*, December 1982: 69-75.

www.EngineeringEBooksPdf.com

SDSS'Rio 2010 STABILITY AND DUCTILITY OF STEEL STRUCTURES
E. Batista, P. Vellasco, L. de Lima (Eds.)
Rio de Janeiro, Brazil, September 8 - 10, 2010

FLANGE THICKNESS TRANSITIONS OF BRIDGE GIRDERS – BUCKLING BEHAVIOR IN GLOBAL BENDING

A. Lechner*, A. Taras* and R. Greiner*

* Institute for Steel Structures and Shell Structures, Graz University of Technology
Lessingstraße 25, A-8010 Graz, Austria
e-mails: lechner@TUGraz.at, taras@TUGraz.at, r.greiner@TUGraz.at

Keywords: Steel Bridges, Stability, Plate Girders, Local Buckling.

Abstract. *Flange thickness transitions constitute the most common constructional detail used to adapt the flexural resistance of bridge girders to variable bending moment distributions. The sudden change of stiffness distribution within the cross-section at these details causes additional local forces, stresses and deformations that cannot be properly taken into account by classical beam-theory calculations. Although these effects have been known in principle for some time, their correct inclusion in practical calculations has gained significance over the last years due to the use of thicker flange plates. The study presented in this paper focuses on the description of the realistic buckling behavior of bridge girder flanges at thickness transitions, whereby both linear and non-linear FEM calculations using shell elements are used and compared to the rather inaccurate predictions of the simple beam theory. One objective of this paper is also to give guidance to the designer concerned with the buckling strength of the girder flanges*.

1 INTRODUCTION

Flange thickness transitions and cover plates constitute two of the most common constructional details used to adapt the flexural resistance of bridge girders to variable bending moment distributions (Fig. 1). In the past, one or more additional cover plates have been added to flanges in riveted and welded constructions. Fig. 2 illustrates such constructional details used for welded girders, whereas flange thickness transitions can be provided by a variation in flange thickness only. The strengthening of the flange can be realized by flush upper edge, by centric arrangement or by flush lower edge, the latter allowing for an easier erection of laterally moved bridge girders.

Concerning the load carrying capacity of such flange thickness transitions, the buckling stability has to be verified with respect to the individual plate buckling slenderness of the two joined flanges. However eccentricity effects in connection with local imperfections, frequently caused by welding distorsion, need to be considered specifically. It has been observed that such local flange imperfections can be of considerable amount, see Fig. 2. Current codes for plate buckling, as Eurocode 3-1-5 [2], contain design provisions for plates with thickness transitions which recommend the use of transversal stiffeners for local restraint of these points.

In the present paper, the stability behavior will be investigated by means of linear buckling analyses (LBA) and geometrically materially nonlinear analyses including imperfections (GMNIA) using Abaqus [3], whereas in previous publications particularly the general stress state and the fatigue problem of flange thickness transitions have been addressed so far [5][6][7][8].

www.EngineeringEBooksPdf.com

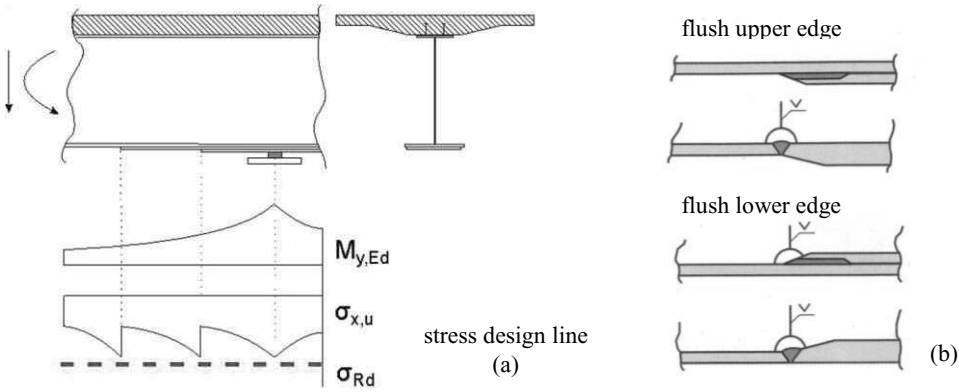


Figure 1: Overview of flange thickness transitions to adapt the flexural resistance of bridge girders in accordance with non-uniform bending moment distributions (a); constructional details with additional cover plates or with local variation in thickness of the flanges (b).



Figure 2: Geometrical imperfections in a large bridge girder, mainly caused by welding distorsion.

In Fig. 3 results of linear elastic analyses of a bridge girder with welded flange thickness transitions under uniform bending are shown. In the vicinity of the transition considerable additional shear in the web lower edge will be induced depending on the difference of axial force ΔN in the flanges due to the bending moment. The length of the decay of these forces is approximately the depth of the I-section. For the given case this would be 3500 mm. The results are plotted for three different flange configurations: flush upper edge (*fup*), *centric* and flush lower edge (*flo*). In case of *flo* the highest additional shear forces are induced, while *centric* causes the lowest effects.

A second effect should also be noted, i.e. the diagram of the axial flange forces which indicates a considerable increase of the flange force of the thinner flange when it approaches the point of the flange thickness transition. Since classical beam-theory disregards this effect totally, attention should be paid to it when considering the local flange buckling behavior in this region under compression.

www.EngineeringEBooksPdf.com

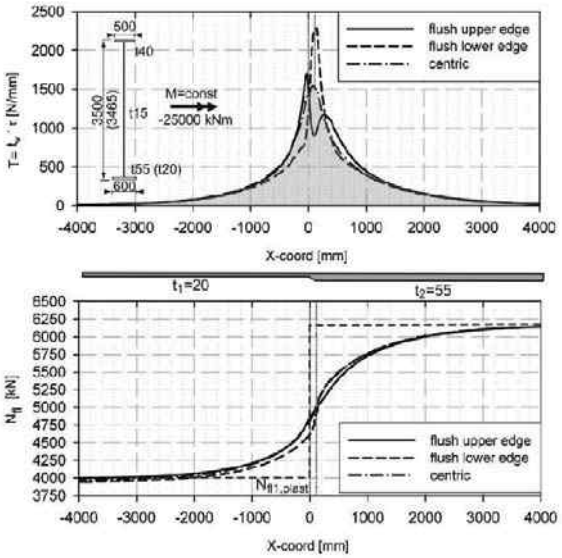


Figure 3: Elastic shear force distribution on web lower edge and axial force distribution in bottom flange.

2 ELASTIC CRITICAL BUCKLING BEHAVIOR

As a first step the local buckling behavior of the flange plate alone will be studied on basis of a three-sided supported plate with and without flange thickness transitions. The loading consists of a constant stress distribution σ_x across the width of the plate, acting in direction a. The numerical investigation has been carried out by using Abaqus [3] and the results have been compared to the analytical results from the classical Kirchhoff theory. (Approximately 8400 S4 – 4 node shell elements have been applied, shear effects were considered, 19 integration points were defined in thickness direction.)

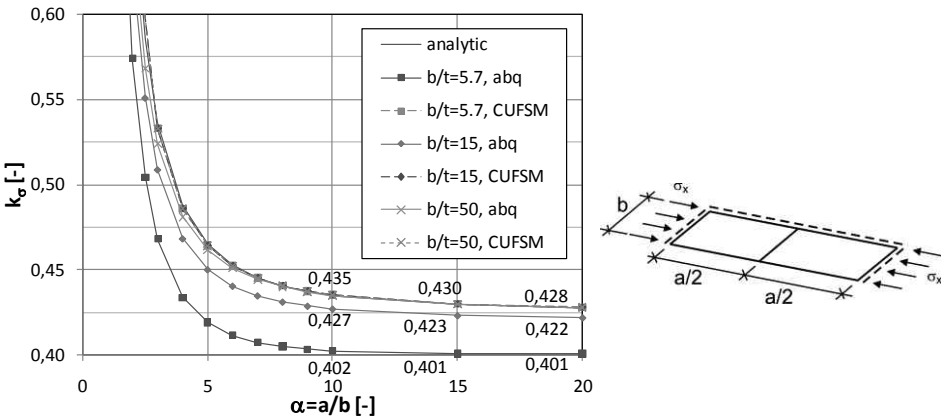


Figure 4: Plate buckling coefficients k_σ, comparison of FE-results with analytical solution and CUFSM.

www.EngineeringEBooksPdf.com

Three different width-to-thickness ratios have been studied; the parameters are b/t = 5.7, 15 and 50, E = 210000 N/mm^2, ν=0.3. The results are shown by k_σ-α-curves in Fig. 4. In the calculations of the plates with constant thickness it was observed that the solution from Abaqus for thicker shells (b/t = 5.7) was app. 6% lower than the analytical result and the result from the Finite Strip Method CUFSM [4], which is due to the consideration of shear effects in the Abaqus analysis. In contrary the results for thin shells are fully coincident.

Then, the flange thickness transition of the plate was investigated. It was modeled by a definition of variable shell-thickness in the transition zone. The transition zone was placed in the half length of a.

It was found that the elastic plate buckling behavior is enhanced considerably depending on the thickness-ratio of the two adjacent flanges t_1/t_2. The k_σ-value can be doubled or even more for shorter plates (Fig. 5). A closer consideration of the results shows that for cases of $t_1/t_2 \geq 1.5$ local buckling is developed only in the thinner plate, since at the thickness transition the thicker plate provides support conditions for the thinner one.

The influence of different flange configurations on the buckling coefficients k_σ was also investigated. The results were nearly coincident for *fup*, *flo* and *centric* – only for short plates with a/b < 5 the buckling coefficients increase by app. 3 % for eccentric configuration compared to *centric*.

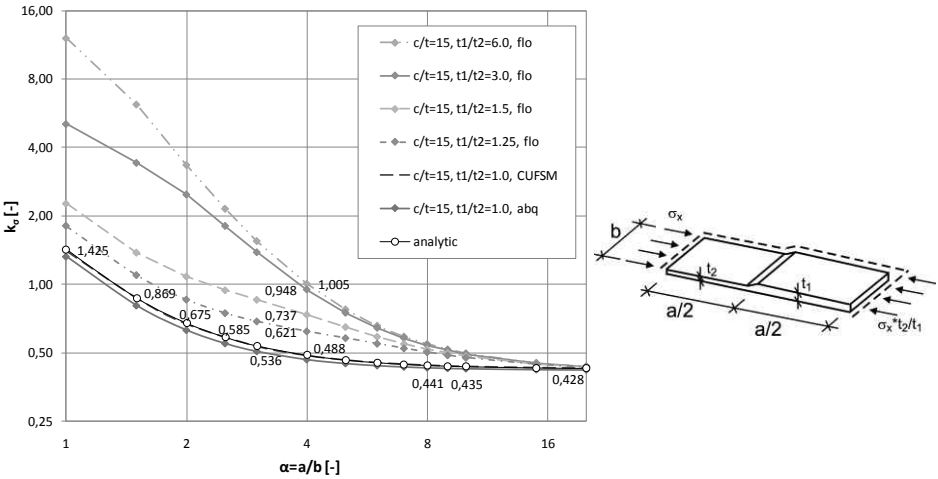


Figure 5: Plate buckling coefficients k_σ of plates with different flange thickness transitions t_1/t_2.

Moreover a supplemental buckling study on the I-sections of the girder with thickness transition in the compression flange was conducted. In this study only flange local buckling was allowed, while global buckling was excluded. Thereby the effects of the increase of the flange force of the thinner flange in the transition zone, which is shown in Fig. 3 above, have been investigated. The results were compared with the buckling results of the three-sided supported plate with thickness transition loaded by a constant axial force. It was found, that the recalculated buckling coefficients from the girder study were – with a variation of about +/- 8 % – close to those of the corresponding single plate with thickness transition.

3 NONLINEAR BUCKLING ANALYSES

3.1 Overview on numerical modeling

The focus of this investigation lies on the nonlinear analysis of girders with I-section with slender flanges in compression. Configurations with and without thickness transition (t_1/t_2) were considered. The nonlinear load carrying capacity of the girders was determined and compared with the results of the

www.EngineeringEBooksPdf.com

classical beam theory, i.e. neglecting local effects at the transition point. Thereby, the results of I-sections with constant flange thickness serve as base values for the investigation of the nonlinear behavior of the sections with thickness transitions. In this publication only a ratio of t_1/t_2=3.0 is published (sect. 3.3), although a larger number of ratios t_1/t_2 has been investigated.

In the Finite-Element model, S4 – 4 node shell elements have been applied as for the flat plate before (sect. 2). The web and the upper flange were modeled by S4 elements with similar element size. The web-flange connections were modeled by pin-connectors, whereby all rotational degrees of freedom remained uncoupled. Pure local buckling was allowed in the compression flange (bottom flange), which means that in particular global stability effects and restraining effects of the web-flange conjunction have been disregarded. Imperfections were only applied to the compression flange by geometrical and structural imperfections. According to Eurocode 3-1-5 [2] the geometrical imperfections of the flange plates were modeled pursuant to the fabrication tolerances with an amplitude of 80 % of its tolerance limits. The residual stresses σ_R were modeled by the yield stress $\sigma_R=f_y$ in the welding zone and by $\sigma_R=-0.2*f_y$ in the remaining flange area, being in self-equilibrium and following a trapezoidal distribution shown in Fig. 6 in the diagram and by the FE-contour plot *increment 0*. The examples presented in this numerical study are based on a flange width of the bottom flange B_{bf} = 600 mm (= compression flange), which leads to a geometrical imperfection of e_0 = 4.8 mm, which is 80 % of $B_{bf}/100 = B_{bf}/125$. In the cases of flanges of constant thickness, the geometrical imperfection is assumed to follow its 1st buckling eigenmode. However in all cases of flanges with thickness transitions, the geometrical imperfections were modeled as local flange undulations according to [1] with an amplitude of e_0 = 4.8 mm, based on a gauge length equal to the flange width B_{bf}. In general, the nonlinear investigations presented herein are based on a length of the flange plate of a = 6000 mm. So far, girders with I-section were loaded in pure bending, leading to constant axial forces in the flange plates in the classical beam theory model. The load introduction at the end of the girders was realized by rigid I-sections, which were pin-connected to the adjacent shell elements of the flanges and the web.

In order to investigate the buckling behavior of these compression flanges of girders with I-section and to compare it with the corresponding buckling behavior of a three-sided supported plate with equal geometry and material, the numerical simulations have been carried out for single plates as well. Its results are included in the diagrams of the following sections 3.2 and 3.3.

3.2 Results of I-sections with constant flange thickness

In Fig. 6 the load displacement diagrams for the girders of I-sections with constant flange thickness are shown for three different assumptions of the local imperfection (i.e. e_0 = 3.0 mm resp. 4.8 mm with or without σ_R). On the abscissa the total vertical displacement U3 of the outmost node of the compression flange at midsection is plotted, which comprises the deformations caused by the global bending of the girder and those by the local buckling of the flange plate itself. On the vertical axis the non-dimensional load-carrying capacity resulting from Abaqus is shown, though divided by the section capacity of the effective cross-section according to [2]. For the given example, the compression flange was classified as Class 4 with a buckling reduction factor of ρ = 0.817, while in the web buckling was prohibited. The results show, that for the nonlinear analysis including geometrical and structural imperfections the section hardly can achieve the section capacity defined by [2]. In Figure 7 this is shown in the left diagram by the illustration of the forces in the compression flange. Regardless of the deformation state the EC 3 capacity of $N/N_{pl,bf}$ = 0.817 cannot be achieved, this means that only due to web plastification the load factor of 1.09 at increment 120 can be explained. The result of the FE-analysis of the flange plate alone (*plate*) achieves a similar result by $N_{GMNIA}/N_{pl,bf} \cong 0.70$.

On the contrary, Fig. 6 and Fig. 8 show for the analysis without residual stresses that the numerical simulation easily can achieve the EC3 design limit. A maximum load factor of 1.074 can be attained already at small deformations. The investigation of the normal force in the flange shows a result of $N_{GMNIA}/N_{pl,bf} \cong 0.9$, which is significantly beyond the design limit of ρ = 0.817 (Fig 8, left diagram).

www.EngineeringEBooksPdf.com

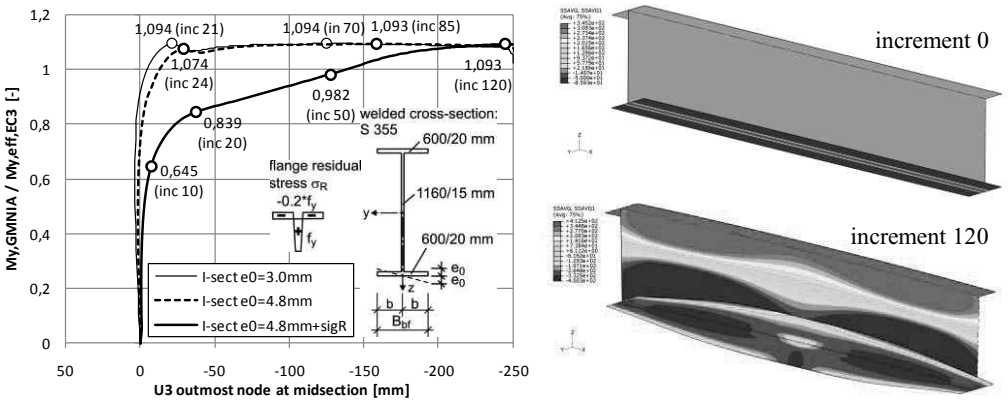


Figure 6: Load-displacement diagram for I-section with constant flange thickness and variation of buckling imperfections in bottom flange; GMNIA contour plots for increments 0 and 120, membrane stresses.

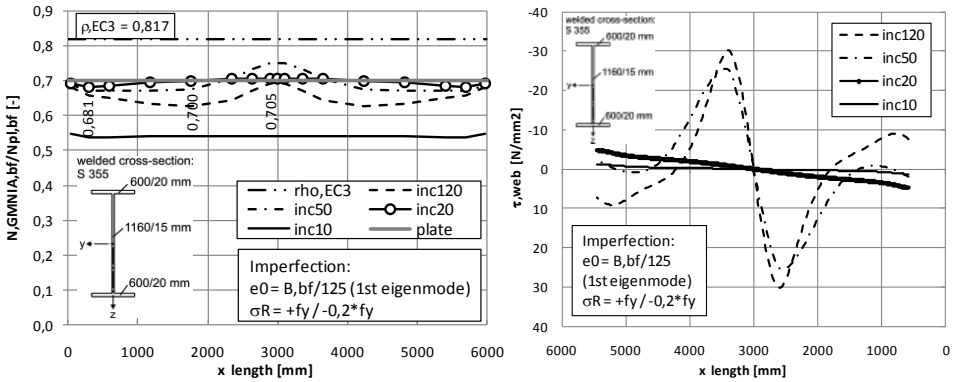


Figure 7: I-section with constant flange thickness, flange forces and shear stress at web bottom edge; with geometrical imperfections plus residual stresses.

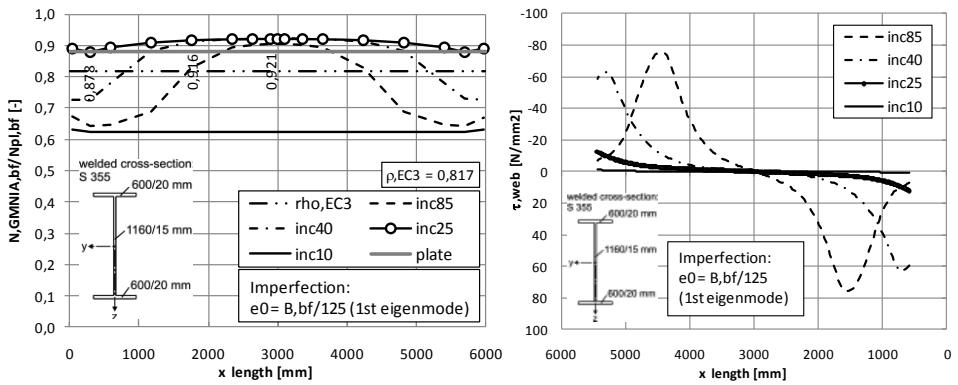


Figure 8: I-section with constant flange thickness, flange forces and shear stress at web bottom edge, with geometrical imperfections only.

www.EngineeringEBooksPdf.com

In addition, shear stress distributions in the bottom web edge are plotted in Fig. 7 and Fig. 8. It was found that during local buckling of the flange plate a rather significant redistribution of flange axial force into the web occurs. This leads to these nonlinear axial force distributions along the axis of the girders.

3.3 Results of I-sections with flange thickness transition $t_1/t_2 = 3.0$

In Fig. 9 the load displacement diagrams of the girders with I-section with flange thickness transitions of t_1/t_2 = 60/20 mm = 3.0 are shown for four different configurations: a) geometrical imperfection $B_{bf}/125$ and residual stress σ_R, b) geometrical imperfection $B_{bf}/125$ only, c) imperfection type a) plus vertical web stiffener, d) imperfection type b) plus vertical web stiffener at the transition point.

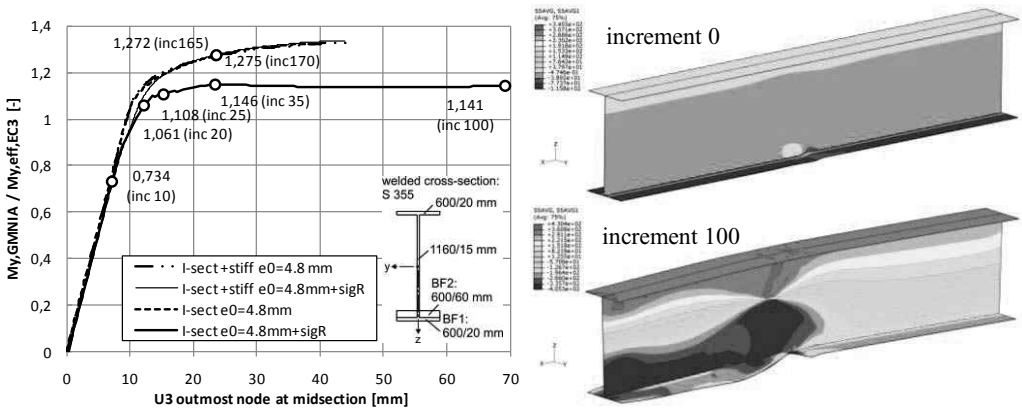


Figure 9: Load-displacement diagram for I-section, flange thickness transition t_1/t_2 = 3.00, variation of buckling imperfections on bottom flange; GMNIA contour plots for incr. 0 and 100, membrane stresses.

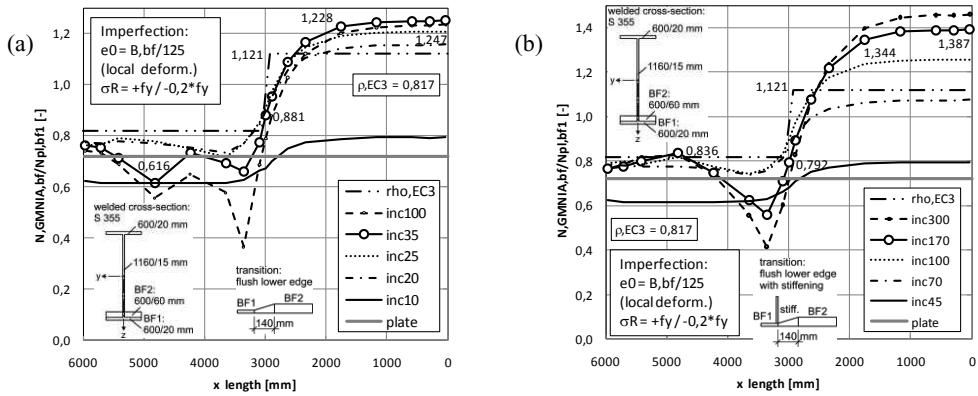


Figure 10: I-section with t_1/t_2 = 3.00, flange forces for configurations without (a) and with (b) vertical stiffener at the transition point.

By the comparison of these results with the results of the I-sections with constant flange thickness it turned out, that the nonlinear load-carrying capacity of the sections with thickness transitions is not as detrimental as expected. The GMNIA-analyses for all configurations with thickness transitions achieved more beneficial results compared to the corresponding girders with constant plate thickness. This can be seen in Fig. 9 in the left diagram by the nearly linear load-displacement path up to the nominal section capacity $M_{y,eff,EC3}$. In the GMNIA-contour plot *increment 100* it can be observed, although there is

www.EngineeringEBooksPdf.com

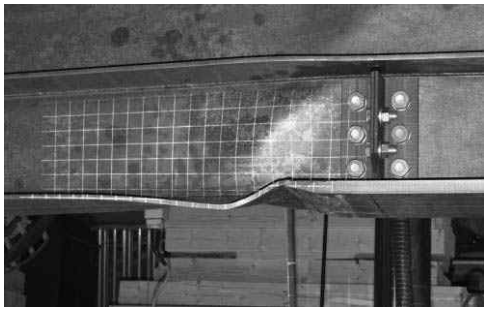
considerable flange eccentricity at the transition point, that a significant restraining effect of the thicker flange on the thinner flange plate appears. The configuration a) without web stiffener leads to a factor of 1.14 by Abaqus, which is considerably beyond the EC 3-limit of 1.0. For the configuration c) with web stiffener at the transition point a maximum load factor of app. 1.34 has been achieved. The axial force distributions for the compression flange shown in Fig. 10 also illustrate this positive behavior.

For comparison, the *plate*-solution that is shown in Fig. 10 achieves a factor of $N_{GMNIA}/N_{pl,bf} = 0.72$, which is even larger than the result of 0.70 for constant flange thickness (sect. 3.2). It may be concluded, that the restraining effects caused by the thicker flange are more beneficial than the detrimental effects due to flange eccentricity. Considering beneficial restraining effects of the web, which have not been investigated in this publication, the results would lead to an even more conservative behavior.

11 CONCLUSION

Concerning flanges with thickness transitions, the rules according to EN 1993-1-5 [2] define vertical stiffeners in the thinner flange close to the transition point (Fig. 11 (b)). Since this requirement could not be confirmed by this numerical study, further investigations in combination with laboratory experiments should be performed. At present, one experimental test was carried out at the Laboratory for Structural Testing (LKI) at Graz University of Technology (Fig. 11(a)). By the evaluation of this test, the need for additional stiffeners according to EN 1993-1-5 could not be approved as well. More detailed results on this test will be presented in subsequent publications.

(a)



(b) EN 1993-1-5

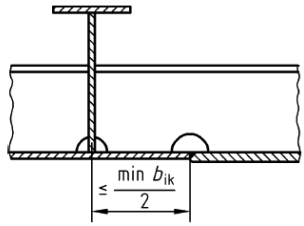


Figure 11: Laboratory test of I-section with flange thickness transition, LKI, Graz University of Technology (a); location of additional vertical stiffener according to EN 1993-1-5 (b).

REFERENCES

[1] EN 1090-2, *Execution of steel structures and aluminium structures – Part 2: Technical requirements for the execution of steel structures*, 2008.

[2] EN 1993-1-5, Eurocode *3, Design of Steel structures – Part 1.5. Plated structural elements*, 2007.

[3] ABAQUS v.6.7, Simulia, Providence, RI, USA, 2007.

[4] CUFSM v.3.12, Ben Schafer, JHU, Baltimore, USA, www.ce.jhu.edu/bschafer/cufsm, 2008.

[5] Stüssi, F., Dubas, P., *Grundlagen des Stahlbaues*, Springer Verlag, Heidelberg, Germany, 1971.

[6] Corfdir, P., Raoul, J., *Étude des contraintes au voisinage d'un raboutage de semelles d'épaisseurs différentes de poutres en I*, Construction Métallique, no 4-1990, 1990.

[7] Greiner, R., Taras, A., Unterweger, H., *Load-carrying behavior of flange-thickness transitions in welded steel girders*, Stahlbau 78, Heft 7, Ernst & Sohn Verlag, Germany, 2009.

[8] Lechner, A., Taras, A., *A numerical study of the fatigue proneness of flange thickness transitions in welded bridge girders*, Fatigue Design 2009, Cetim, Senlis, France, 2009.

www.EngineeringEBooksPdf.com

SDSS'Rio 2010 STABILITY AND DUCTILITY OF STEEL STRUCTURES
E. Batista, P. Vellasco, L. de Lima (Eds.)
Rio de Janeiro, Brazil, September 8 - 10, 2010

A VISCO-ELASTIC SANDWICH SOLUTION FOR ORTHOTROPIC DECKS OF STEEL BRIDGES

Ronaldo C. Battista*, Emerson F. dos Santos ** , Raimundo Vasconcelos * and Michèle S. Pfeil***

* Instituto COPPE
e-mails: battista@coc.ufrj.br, mpfeil@coc.ufrj.br

** Petrobrás
e-mail: emersonfigueiredo@petrobras.com.br

** * Universidade Federal do Amazonas
e-mail: vasconcelos@ufam.edu.br

Keywords: steel bridges, orthotropic deck, vehicle–structure dynamic interaction, viscoelastic material.

Abstract. *This paper presents and discusses alternatives to enhance the fatigue performance of lightweight and slender steel decks of box-girders bridges. Solutions were devised by adding to the steel deck a reinforced concrete slab in two different manners: (i) a sandwich structure in which a visco-elastic layer is inserted in between the steel plate and the concrete slab and (ii) a composite deck formed by the same concrete slab fixed with stud connectors to the steel deck plate. The performances of these composite orthotropic decks of bridge structures undergoing the effects of the dynamic interaction between vehicles, pavement and the structure itself are assessed by means of a computational tool specially developed to this end. It is shown that the sandwich deck displays lower peak displacement and stresses amplitudes than the composite deck counterpart and therefore can be adopted as a rational solution in the design of new bridges and also be employed in the rehabilitation of slender orthotropic decks of existing steel bridges.*

1 INTRODUCTION

To investigate the structural behaviour of typical slender orthotropic steel decks under dynamic action of heavy trucks traveling with constant velocities on rough surface of asphalt pavements and also to investigate the performance of two devised composite structural solutions in attenuating displacements and stresses amplitudes it was used as a case study a stretch of the slender ortrotropic steel deck of the central span of Rio-Niterói bridge, which crosses the Guanabara Bay at Rio de Janeiro, Brazil.

Figures 1 refer to several details of the orthotropic deck of the steel twin-box-girders of the Rio-Niteroi highway bridge which, before its rehabilitation in 2001 used to be, under stochastic traffic loading, frequently damaged by fatigue cracks in the welded joints and geometric details [1,2,3]. Cracks were first and more frequently observed in the welded details illustrated in Figs. 1.b, 1.c and 1.d: (i) the longitudinal welded connection between the deck plate and rib web; (ii) the transversal field-butt-welded connections of ribs and the welded splice plates; (iii) the welded connections between the ribs and the trapezoidal shape splice plates, and between these and the floorbeam web.

To enhance the fatigue performance of this and other orthotropic steel deck solutions were devised [2,3,4] by adding to the steel deck a reinforced concrete slab in two different manners as shown in Figure 2: (i) a sandwich structure in which a visco-elastic layer was inserted in between the steel plate and the concrete slab and (ii) a composite deck formed by the same concrete slab fixed with stud connectors to the steel deck plate. These two alternatives were tested on a prototype scale model [3] constructed in the

www.EngineeringEBooksPdf.com

Structures Laboratory of the Instituto COPPE/UFRJ (see Figure 3). While the composite deck displayed greater reductions in static stresses in relation to the unreinforced deck, the sandwich alternative showed greater modal damping factors.

Preliminary numerical studies served to show some important advantages of the sandwich alternative over the conventional counterpart. But because of the lack of technical understanding of the innovative sandwich solution and also because of the tight schedule to finish up the rehabilitation work the more conventional composite deck solution was adopted by the Rio-Niterói bridge administration. Experimental dynamic measurements for normal traffic loading on the composite deck made after its completion corroborated some important aspects of its structural behaviour which had been already pointed out in previous experimental and numerical studies [4].

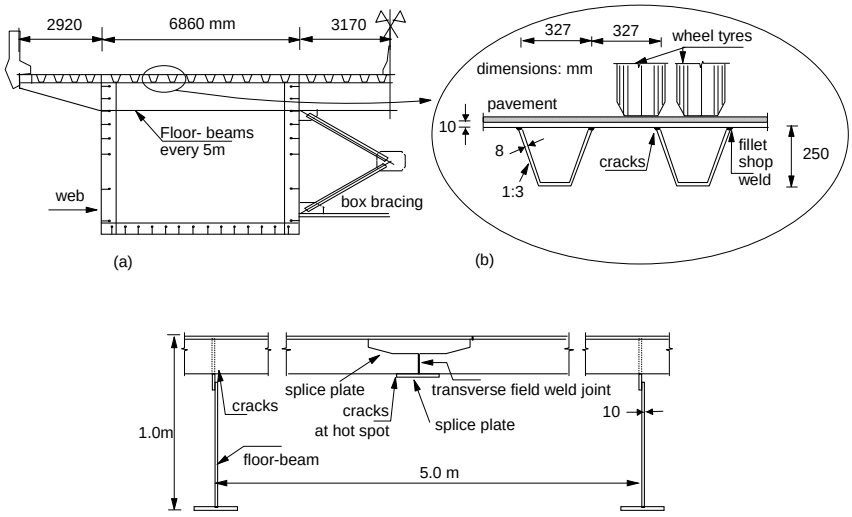


Figure 1: The orthotropic deck of the Rio-Niteroi bridge.

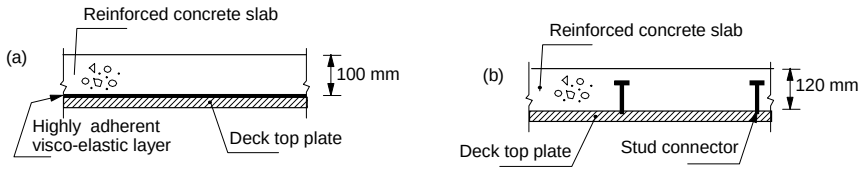


Figure 2: Alternative solutions to enhance the ultimate fatigue life of an orthotropic deck: (a) sandwich structure; (b) composite deck.

The performances of these composite orthotropic decks of bridge structures undergoing the effects of the dynamic interaction between vehicles, pavement and the structure itself were later assessed by means of a computational tool specially developed to this end [5,6,7]. In this tool, called CONTROLMADS, several finite elements are available, including a hexahedral element to represent visco-elastic components.

This paper presents and discusses the most relevant points of these studies and the main numerical results obtained for the two orthotropic deck alternatives under the action of a 3 axles heavy truck traveling with constant velocities. It is shown that the sandwich deck displays lower peak displacements and stresses amplitudes than the composite deck counterpart and therefore could have been adopted as a

www.EngineeringEBooksPdf.com

rational solution to the referred bridge's deck and may be employed in the design and worldwide rehabilitation of slender orthotropic steel bridge's decks.

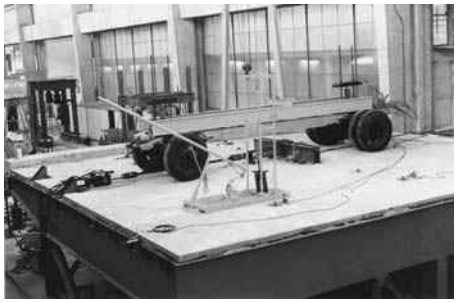


Figure 3: Upper view of the prototype scale model of the orthotropic deck at COPPE´s Laboratory of Structures; the deck already reinforced by a concrete slab on top of a visco-elastic layer.

2 ANALYTICAL – NUMERICAL MODEL FOR VEHICLE-BRIDGE INTERACTION

The equations of motion of the vehicle – bridge system were derived from equilibrium considerations applied to the free-body diagrams of the vehicle components and their connection to the bridge elements. Figure 4a shows the model of a 3 axles rigid vehicle traveling with constant velocity along the road surface of a bridge whose deck is represented by quadrilateral plane finite elements which combine flexural and membranes degrees of freedom. In this figure m_{pi} (i=1,6) correspond to the masses of the wheels – axle systems while m_v is the vehicle's body mass. In addition to the vertical displacement degree of freedom (DOF) assigned to each mass, rotation about the transverse axis (pitch) was provided to the vehicle's body mass, totalizing 8 DOF. All the springs and dampers are assumed to behave linearly. For a multi-leaf spring suspension type, each spring stiffness k_{vi} is to be obtained from the typical non-linear load x deflection behaviour [8] as an average values in the range of the corresponding wheel load.

The equations of motion of the vehicle-bridge system in matrix form are given by

$$\mathbf{M}\ddot{\mathbf{U}} + \mathbf{C}\dot{\mathbf{U}} + \mathbf{K}\mathbf{U} = \mathbf{F} \tag{1}$$

where **U** consists of the nodal displacement sub-vector $\mathbf{U}_e$ and the vehicle degrees of freedom; ***M***, ***C*** and ***K*** are respectively the mass, damping and stiffness matrices which include both bridge and vehicle characteristics and **F** is the nodal force vector. The damping matrix was considered proportional to mass and stiffness matrices (Rayleigh damping).

The interaction force on the i^{th} contact point between the bridge and the vehicle is written as:

$$F_i(x,t) = f_{epi} + f_{api} \tag{2}$$

where f_{epi} and f_{api} are respectively the elastic and damping forces, which depend on the relative motion of the corresponding mass m_{pi} to the bridge contact point. The relative displacement is given by:

$$u_{pi} - (u_{ri} + U_{ei}) \tag{3}$$

where u_{pi} is the i^{th} wheel vertical displacement, u_{ri} is the road surface roughness under the i^{th} wheel and U_{ei} is the bridge vertical displacement at the instantaneous point of contact to this wheel. The force at each contact point i (eq.2) is then rewritten as:

$$F_i(x,t) = k_{pi}\left(u_{pi} - (u_{ri} + U_{ei})\right) + c_{pi}\left(\dot{u}_{pi} - (\dot{u}_{ri} + \dot{U}_{ei})\right) \tag{4}$$

www.EngineeringEBooksPdf.com

where k_{pi} and c_{pi} are the stiffness and damping coefficients of the i^{th} axle-wheel system, $\dot{u}_{pi}$ and $\dot{U}_{ei}$ are the vertical velocities of the mass m_{pi} and the bridge contact point respectively, $\dot{u}_{ri} = (du_{ri}/dx)V(t)$ and $V(t)$ is the vehicle velocity.

Applying each contact force (eq.4) to the nodal force vector, the equation of motion corresponding to U_{ei} can be expressed as follows (displaying only the diagonal terms):

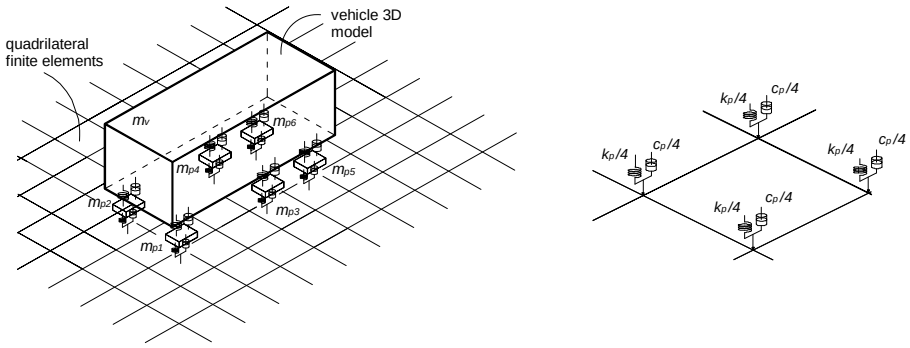
$$m_e\ddot{U}_{ei} + \ldots + (c_e + c_{pi})\dot{U}_{ei} + \ldots + (k_e + k_{pi})U_{ei} + \ldots - c_{pi}\dot{u}_{pi} - k_{pi}u_{pi} = -(m_v g + m_{pi} g) - c_{pi}\dot{u}_{ir} - k_{pi}u_{ir} \quad (5)$$

where m_e, c_e, k_e are respectively the mass, damping and stiffness coefficients corresponding to the structure. The coefficient matrices in eq. 1 change according to the vehicle position.

The coupled equations of motion of the vehicle and the bridge were solved in time domain by direct integration using Newmark scheme.

At the present stage the model considers that each interaction force (eq. 4) is uniformly distributed among the 4 nodal points of the shell element within which the point of contact is located (see Figure 3b).

The bridge surface profile was generated by applying the inverse discrete Fourier transform to a roughness spectrum as described by Honda *et al* [9]. The surface profile was assumed to be constant across the deck width. To take into account the tyres contact area, the value of u_{ri} in eq (2) is made equal to the average profile amplitude within the contact area, thus smoothing the original road profile.



(a) (b)

Figure 4: (a) Modeling of a 3 axles rigid vehicle traveling on a bridge deck modeled by quadrilateral plane finite shell elements; (b) detail of the contact points.

3 MODELING OF VISCO-ELASTIC MATERIALS

The visco-elastic layer in the sandwich solution was modeled by linear hexahedral elements shown in Figure 5, with 8 physical nodes and one fictitious node (dissipation node). The analytical model of the visco-elastic material follows the Golla Hughes Method (GHM) [10]. This method was proposed to circumvent the problem of frequency dependent properties of the visco-elastic materials in a time domain analysis. It consists in obtaining an equivalent dynamic system expressed in time domain involving visco-elastic materials modeled in Laplace domain. In this equivalent system additional degrees of freedom, called dissipation degrees of freedom are added to the mass, damping and stiffness matrices.

An important step in the GHM is the selection of the dissipation function *h(s)* and therefore the approximation of the complex modulus on Laplace domain. For the computational tool specially developed to deal with these materials [5,6] the dissipation function proposed by Biot [11] was used with two terms in the series resulting in the following expression:

$$h(s) = \frac{\alpha s^2 + \gamma s}{s^2 + \beta s + \delta} \quad (6)$$

where $(\alpha,\beta,\delta,\gamma)>0$. These parameters are selected in order to represent the variation with frequency of the modulus of elasticity and the loss factor of the visco-elastic material (VEM).

www.EngineeringEBooksPdf.com

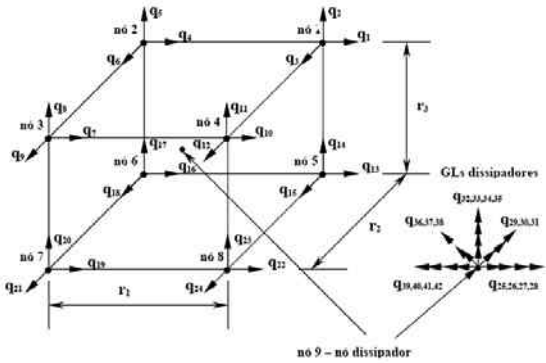


Figure 5: Linear hexahedral element with nodes and additional (dissipation) degrees of freedom for a VEM.

4 MODEL OF THE ORTHOTROPIC STEEL DECK

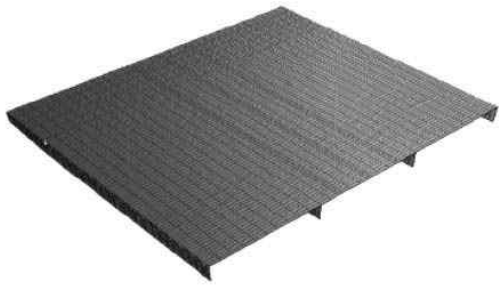
Figures 6 show the finite element model (FEM) of half cross section (see Fig.1a) of the actual steel orthotropic deck with three longitudinally stiffened panels spanning on four transverse floor-beams. Four node shell elements that combine separate membrane and plate bending behaviors were selected to model the deck plate, the trapezoidal stiffeners and the floor-beams' webs while the lower flange of the floor-beam and the central and lateral reinforced concrete barriers were represented by spatial frame elements. This model was initially calibrated in terms of experimental natural frequencies and associated vibration modes obtained from in *situ* measurements [1,2].

To model the concrete layer and the stud connectors in the actual composite deck (Figure 2b), shell elements and spatial frame elements were respectively added to the model of Fig.6. The shear connectors were considered embedded in the concrete layer and therefore, restrained to deform by bending and shear. The shell elements representing the concrete layer were disposed at its midplan and connected to the shell elements representing the steel plate by the stud elements and also by axially rigid elements to prevent the interpenetration of the concrete and steel layers. This second model was also calibrated in terms of experimental natural frequencies and vibration modes obtained from the 2002 measurements campaign [4].

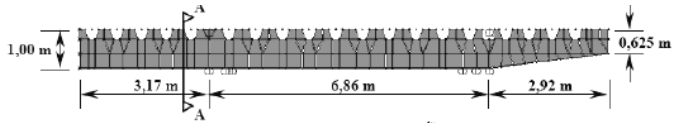
The sandwich solution model (Figure 2a) was developed by adding to the steel deck model (Figs. 6) hexahedral elements to represent the 5 mm thick visco-elastic layer and on its top shell elements to simulate the reinforced concrete slab. Table 1 presents a comparison between the theoretical vibration frequencies resulting from the numerical model and those obtained from experimental free vibration tests on the prototype scaled model of the sandwich deck shown in Figure 3. The description of the vibration mode shapes associated to these frequencies is also given in this table. Non-conformities between the bearing conditions of the prototype scale model and the boundary conditions simulated by the numerical FEM model are the main cause for the small differences between theoretical and experimental frequency values shown in Table 1.

www.EngineeringEBooksPdf.com

(a)



(b)

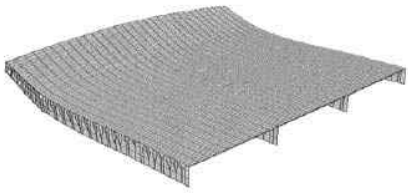


Figures 6: (a) FEM model of the three spans stretch of the orthotropic deck; (b) half deck cross section of the model showing a floor-beam.

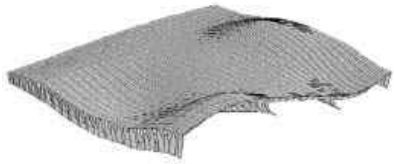
Figures 7 illustrate two vibration bending modes of the deck: one of the cantilevered deck panels (Fig.7a) and the other of the deck panels between webs of the box girders (Fig. 7b). In both alternative deck solutions, these modes appear associated to frequencies close to each other as given in Figure 7; the composite deck displaying the higher frequencies and thus the greater stiffness.

Table 1: Natural frequencies and vibration modes of the sandwich deck

Experimental (Hz ± 0.4Hz)	Numerical (Hz)	Mode shape
	12.6	Bending of cantilevered deck panel
14.4	15.7	Bending of cantilevered deck panel
24.8	25.0	Bending of deck between girder webs
	25.8	Bending of deck between girder webs
	27.8	Bending of deck between girder webs
30.3	27.9	Bending of deck between girder webs



(a) f= 12.6 Hz for the sandwich deck
f = 13.3 Hz for the composite deck



(b) f=27.9 Hz for the sandwich deck
f = 29.5 Hz for the composite deck

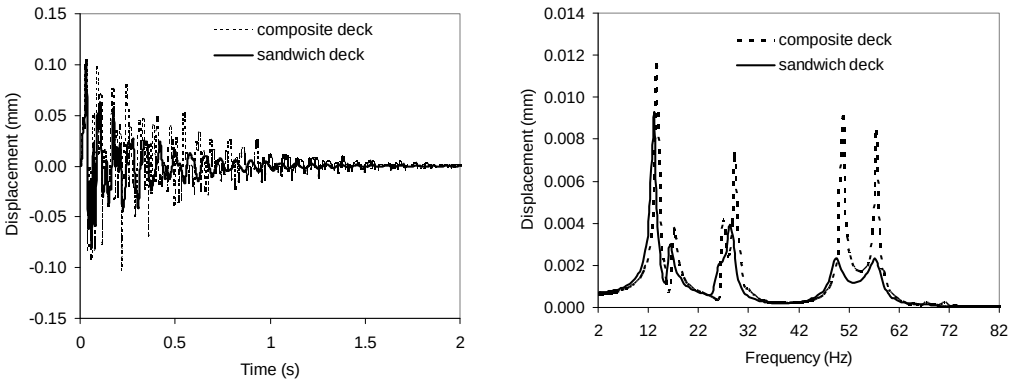
Figures 7: Typical free vibration modes of the deck. (a) bending of the cantilevered deck panels. (b) bending of deck panels between webs of the box girders.

www.EngineeringEBooksPdf.com

5 DYNAMIC DECK RESPONSES

5.1 Responses to impact loads

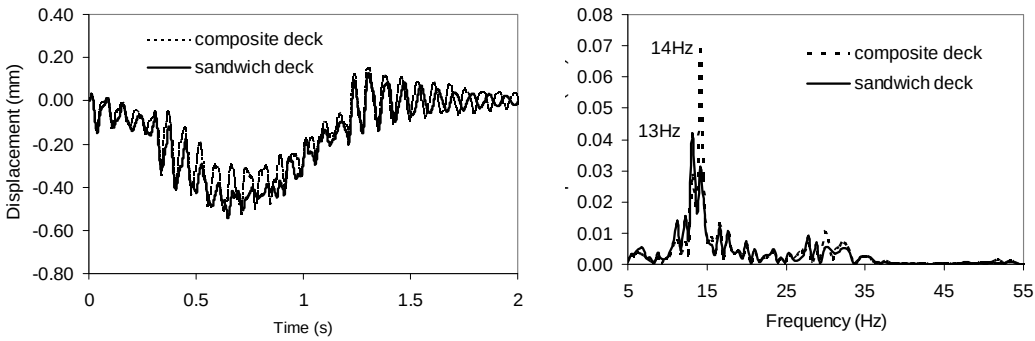
The structural performance of each of the two alternative solutions was first evaluated for an impact load function which consists of a series of triangular impulsive loads applied at 3.0 s time interval. This simplified load function was applied as preliminary approach to the effect of wheel loads produced by multi-axles truck passing on poorly maintained expansion joints. The time and frequency responses in terms of vertical displacement at the edge of the floor-beam cantilever due to the impact loads applied at midspan between webs of the box girder are shown respectively in Figure 9a and in Figure 9b. In Fig. 9a it can be seen that the sandwich deck displays lower amplitudes than the composite deck, and greater damping. These lower amplitudes occur for all excited modes as can be observed in Fig.9b.



(a) (b)

Figures 9: Vertical displacement responses at the edge of the floor-beam cantlever due to impact loads applied at midspan between box girder webs. (a) time domain; (b) frequency domain.

5.2 Responses to the passage of a three-axles truck



(b)

Figures 10. Vertical displacement responses at the edge of the cantilevered deck panel due to the three axles truck traveling along the slow lane with constant velocity equal to 60 km/h. (a) time domain; (b) frequency domain.

www.EngineeringEBooksPdf.com

With the analytical-numerical model for vehicle-structure interaction described in section 2 the two orthotropic deck alternative solutions were subjected to the passage of a 3 axles truck weighing 215 kN with constant velocity. In the structural analysis the concrete pavement was considered in bad condition.

The time and frequency responses in terms of vertical displacement at the tip of the cantilevered deck panel between two floor-beams due to the passage of the truck along the slow lane are shown respectively in Figure 10a and in Figure 10b. It is shown that the sandwich solution displays lower peak displacement amplitudes than the composite deck. These peak amplitudes are associated to the bending vibration mode involving the cantilevered deck panel (Fig. 7a).

6 CONCLUSIONS

The performance of two alternative solutions devised to enhance the structural dynamic behaviour and fatigue life of slender and lightweight orthotropic steel deck are investigated by means of a specially developed numerical model which includes layers of visco-elastic materials. An experimentally calibrated numerical model of an existing orthotropic deck is used for this purpose and the obtained results have shown that the sandwich deck displays lower peak displacements and stresses amplitudes than the composite deck counterpart and therefore can be adopted as a rational solution in the design of new bridges and also be employed in the rehabilitation of slender orthotropic decks of existing steel bridges.

REFERENCES

[1] Battista R.C., Pfeil M.S., Roitman N., Magluta C., " Global analysis of the structural behaviour of the central spans of Rio-Niterói Bridge", *PONTE SA Concessionaire of Rio Niterói Bridge – Contract Report COPPETEC ET150747*, Rio de Janeiro, 1997 (in Portuguese).

[2] Battista, R.C., Pfeil, M. S. "Strengthening fatigue-cracked steel bridge decks. *Proceedings of the Institution of Civil Engineers,* 157, 93 - 102, 2004.

[3] Battista R.C., BatistaE.M., Pfeil M.S., "Experimental tests on a prototype scale model of the slender steel orthotropic deck of Rio-Niteroi bridge ", *Ponte SA -Concessionaire of the Rio-Niteroi Bridge-Contract report COPPETEC ET-150771*, Rio de Janeiro, Brasil (in Portuguese), 1998.

[4] Battista, R.C., Pfeil, M.S., Carvalho, E.M.L., "Fatigue life estimates for a slender orthotropic steel deck", *Journal of Constructional Steel Research*, **64**(2), 134- , 2008.

[5] Barbosa F.S., "Computational modeling of structures with viscoelastic damping layers", D.Sc. thesis, COPPE – UFRJ, Rio de Janeiro, 2000 (in Portuguese).

[6] Vasconcelos, R.P., "Vibration dynamic control by viscoelastic devices", D.Sc. thesis, COPPE – UFRJ, Rio de Janeiro, 2003 (in Portuguese).

[7] Santos, E.F., "Analysis and mitigation of vibration in motorway bridges", D.Sc. thesis, COPPE – UFRJ, Rio de Janeiro, 2007 (in Portuguese).

[8] Gillepsie T.D., Karamihas S.M., Cebon D. et al, "Effects of heavy vehicle characteristics on pavement response and performance", The University of Michigan Transportation Research Institute, UMTRI92-2, 1992.

[9] Honda, H., Kajikawa, Y., Kobori, T., Spectra of Road Surface Roughness on Bridges. *J. Struct. Div. ASCE*, vol. 108, ST9, pp1956-66, 1982.

[10] Golla, D.F.; Hughes, .C.; "Dynamics of viscoelastic Structure", *Journal of Applied Mechanics*, 52, 897-906, 1985 .

[11] Biot M.A., "Variational Principles in irreversible thermodynamics with applications to viscoelasticity", Physical Review, vol. 97 n. 6, pp 1463-1469, 1955.

www.EngineeringEBooksPdf.com

SDSS'Rio 2010 STABILITY AND DUCTILITY OF STEEL STRUCTURES
E. Batista, P. Vellasco, L. de Lima (Eds.)
Rio de Janeiro, Brazil, September 8 - 10, 2010

ELEGANCE AND ECONOMY - A NEW VIADUCT OVER THE RIVER LLOBREGAT

Peter Tanner*, Juan L. Bellod* and David Sanz*

* Cesma Ingenieros, Madrid, Spain
e-mail: cesma@cesmaing.com

Keywords: Composite Bridge, Conceptual Design, Detailing, Stress Field Method, Patch Loading, Semi-probabilistic Finite Element Calculation.

Abstract *The viaduct over the River Llobregat at Puig Reig, Spain, illustrates how demanding conditioning factors can serve as inspiration for a satisfactory solution. The functional design adopted, characterized by the simplicity of its lines, was enhanced by the careful shaping of structural members and good detailing. This example shows that modern, technologically advanced bridge design can be compatible with a solution whose elegance meets even the most exacting aesthetic standards, with no need for inefficient members or adornments, at an affordable additional cost over the least expensive solution. The ideas underlying the conceptual design for the River Llobregat bridge, in particular with respect to the specific boundary conditions involved, are explained in the article, along with the actual layout, remarks about the design of structural details and the verification of structural safety during the incremental launching of the steel structure.*

1 INTRODUCTION

The new bridge over the River Llobregat forms part of a scheme to improve motorway C-16 in Catalonia, between Puig Reig and Berga, and shorten the driving time between Berga and Barcelona by more than half an hour. It spans the River Llobregat with a sizeable viaduct not far from the town of Puig Reig [1].

Many key aspects of a bridge project are governed by construction site-related and geometric, functional, constructional and economic constraints. The present case is no exception. But demanding boundary conditions often spur careful and indeed even innovative structural solutions for which specific design rules may be lacking. In these cases, structural safety and serviceability can not be achieved by simply applying codes and standards. Typical examples of such circumstances are structural detail design and finite element analysis-related structural safety. The approach adopted in the design of the River Llobregat bridge to solve both these problems is explained in detail in this paper.

2 BOUNDARY CONDITIONS

The total length of the viaduct on the widened motorway is over 550 m. Its ground plan layout is straight for most of its length, although as it nears the abutment on the Berga side it curves on a radius of 600 m at its sharpest. In elevation, the bridge slopes gently on a grade of 1,4%. Its single deck carries four lanes of traffic, two in each direction, plus four service lanes and the median, and has a total width of 23,8 m. Due to environmental restrictions, no temporary supports could be erected near the River Llobregat during construction, nor were heavy cranes allowed to access the area.

In most structures, economic constraints play a decisive role in the adoption of the final solution, and the Llobregat viaduct was no exception. Nevertheless, in view of the location of the bridge and its visibility from the nearby town, the owners also wanted a landmark structure with a simple and well-

www.EngineeringEBooksPdf.com

balanced design. All these constraints made it particularly important to strike an optimal balance between cost-effectiveness and aesthetics.

3 CONCEPTUAL DESIGN

3.1 Layout

The shape adopted for the bridge structure was informed by the above functional and site constraints. A continuous nine-span structure with a total length of 568 m was devised for the bridge deck. Topographic considerations led to the two end spans being 60 m long, while each of the seven inner spans is 64 m long. Despite the unfavourable outer to inner span ratio of 0,93 compared to other possible layouts with shorter bays, this solution was preferred to enhance the visual efficiency of the design since two of the most important determinants of elegant bridge design are transparency and slenderness: bridges are often regarded as elegant when characterized by the efficient use of construction materials in solutions with generous span lengths.

The composite deck consists of an open, 6 m wide steel box girder covered with a concrete slab. The steel section is 2,55 m high, for a slenderness ratio on the inner spans of 25. The impression of visual slenderness is heightened by the concrete slab, which cantilevers 8,9 m on each side of the steel box. The cantilevered slabs rest on a space truss consisting of longitudinal chords 3,5 m from the edge attached to horizontal ties and inclined diagonals, in turn connected laterally to the box girder (figure 1). From an elevation view, each set of two diagonals forms a “V”.



Figure 1: Partial view of the finished bridge (Photo: Paco Gómez).

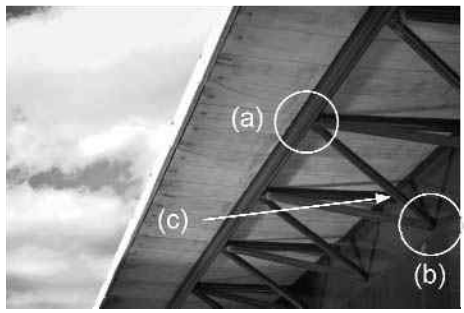


Figure 2: Connections between (a) longitudinal chord, diagonals and tie; (b) diagonals and box girder; (c) tie and box girder.

The diagonals, the horizontal ties running between the diagonals and connecting chord and diagonals both to the top of the box girder, as well as the joints between the diagonals and the bottom of the girder are all spaced at 8 m centres along the chord. Because of the slant on the diagonals and their layout, the trusses not only transmit loads from the cantilevers to the box girder, but form part of the overall resistance mechanism of the deck, reinforcing composite girder stiffness and strength. At the same time, the truss design is visually gratifying. Moreover, the layout adopted impacts the action effects on the truss members and joint behaviour, with the concomitant need for particular care in joint design.

Indeed, good detailing is essential to ensure appropriate member performance, including suitable load transfer mechanisms, fracture toughness, fatigue resistance and durability. Appropriate detailing may also facilitate bridge assembly and significantly affect its visual impact. Since the satisfactory structural behaviour of details and joints depends essentially on their conceptual design, this step is of cardinal importance and should be performed at an early stage in the design process, in keeping with the conceptual design of the system as a whole as well as of the structural members. In light of the importance of this consideration, the approach adopted for structural detail design is treated in section 4.

www.EngineeringEBooksPdf.com

3.2 Members

The box girder has a composite bottom flange in the area around the internal supports for greater hogging bending strength and system ductility. This is a particularly important issue, for system reliability is much greater in ductile than in brittle systems [2]. Failure mode is of utmost importance, moreover, because brittle structures may be very sensitive to the uncertain effects of actions and influences such as creep, shrinkage, temperature, differential settlements or earthquakes and may collapse suddenly under such circumstances, without prior warning.

The truss diagonals are made of 323 mm diameter hollow section profiles with wall thicknesses ranging from 16 mm to 22 mm, depending on the internal forces. The ties, positioned at right angles to the bridge centreline, are oval composite members whose top flange is connected to the deck slab. The longitudinal chords are also composite, oval-shaped, filled with concrete and connected to the slab, but have an open cross-section. The deck slab itself consists of 80 mm deep precast concrete slabs covered with cast-in-place concrete to the total depth, which varies from 180 mm at the edges to 340 mm over the longitudinal chords. The total slab depth over the 6 m wide box girder is 240 mm.

The concrete piers comprise two 1,3 m wide shafts spaced at 4,7 m centres and inter-connected by a convex concrete wall to form a single monolithic member 6 m wide. Pier depth is variable, tapering slightly to 1,4 m at the top. The piers owe their slender elegance to their height and these cross-sectional dimensions.

4 JOINT DESIGN

4.1 Overview

Further to the bridge layout, solutions had to be provided for three main types of connections (figure 2): longitudinal chord-diagonals-tie; diagonals-box girder; and tie-box girder. The steps involved in designing the structural details with respect to the connection between longitudinal chord, diagonals and tie are described in subsections 4.2 to 4.3. While the connection in question comprises a composite steel and concrete joint, the procedure adopted for its design was equivalent to the procedure used to design steel joints, such as the connection between the diagonals and the box girder.

4.2 Concept

By analogy to Eurocode 3 [3], the connection between longitudinal chord, diagonals and tie can be regarded to be a space KT joint (figure 2) in which the diagonals and tie are positioned on different planes. The longitudinal chord is continuous, while the brace members are arranged so that the diagonals overlap the tie. The ends of the diagonals are prepared for attachment to the curved surfaces formed by the oval chord and tie, without modifying their cross-sections. Forces are transferred from the diagonals to the tie and chord across full penetration butt welds via shear and normal stresses, respectively. Compression stress-induced side wall failure in the chord and tie is prevented by transverse stiffeners installed in both members, and the concrete fill in the chord. Situations such as punching shear failure in the chord or tie wall or brace failure in the event of load inversion in the diagonals upon integration of the slanted truss in the overall resistance mechanism of the deck were prevented by choosing a wall thickness in keeping with the material strength needed in each case. Similarly, the risk of lamellar tearing [4] in the chord and tie walls was mitigated by the choice of steel with suitable through thickness properties.

A specific problem was posed by the concurrence of two circumstances: the integration of the slanted truss in the overall resistance mechanism of the deck and the nature of the connections between longitudinal chord, diagonals and tie as composite steel and concrete joints. In this truss, the composite top chord is the so-called longitudinal chord. The introduction in the joints of this chord of the increment in the axial force, ΔN, due to the horizontal component (parallel to the bridge axis) of the internal forces in the diagonals generates a concentrated longitudinal shear force, V_E. Since the increment in the axial force, ΔN, is received by the steel section whereas the longitudinal chord is composite, the concentrated longitudinal shear force, V_E, is transmitted eccentrically (figure 3). This eccentricity, represented by the vertical distance between the centroid axis of the shear connection and the steel-concrete contact surface,

www.EngineeringEBooksPdf.com

e_z, induces a local bending moment which may in turn cause the concrete slab to separate upward from the steel structure. To prevent such mechanism, a vertical steel plate welded to the oval shape is embedded in the concrete slab. The transverse reinforcement in the slab is fitted into holes drilled in that vertical plate.

Under this arrangement, the aforementioned local bending moment is resisted by two forces, transmitted by contact pressure. One contact is between the reinforcement bars and the edges of the holes drilled in the vertical plate and the other between the concrete slab and the top flange included in the nodal region of the longitudinal chord (figure 3).

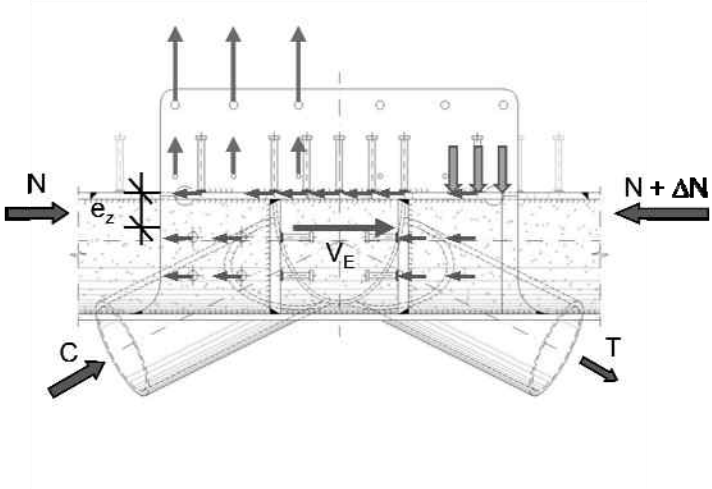


Figure 3: Device for the eccentric transfer of horizontal shear forces.

4.3 Practical design procedure

The methods for structural concrete design currently available do not enable engineers to map forces through a structure. This drawback is particularly troublesome when designing structural discontinuities such as joints and corners. Great strides have been made in reinforced concrete design in recent years in the wake of the introduction of the stress field method [5], with which consistent design models can be developed based on the lower bound theorem of the theory of plasticity. In the present case, the theorem was reformulated for use in composite structure detailing. A practical procedure has been followed in joint design as explained in a previous paper [6].

5 CONSTRUCTION

5.1 Assembly procedure

Once the abutments and the columns had been erected, the steel box girder was lifted into place with cranes in seven of the nine spans, starting at the abutment on the Berga side. Temporary supports were set as close as possible to each mid-span during this stage of construction to reduce bay lengths. The precast concrete slabs were then laid. Finally, concrete was cast in place and the temporary supports were removed (figure 4).

Since environmental legislation banned crane or heavy vehicle access to the banks of the River Llobregat, bridge construction had to proceed without such equipment. The solution chosen was incremental launching from the south abutment across the first two bays, which span the river. A launching nose was used (figure 5), to mitigate the action effects on these two spans and eliminate the risk of patch loading-induced instability (subsection 5.2).

www.EngineeringEBooksPdf.com

Since the steel box girder cantilevered 16,4 m over the centreline of pier 2 (figure 4) towards the southern abutment, the girder train was 107,6 m long. The 12,4 m length of the nose was established to ensure that during launching the action effects of greatest magnitude would be resisted by the cross section with the highest load-bearing capacity, designed to resist the hogging bending moments at the first pier in the final stage.



Figure 4: Stages of bridge girder construction.



Figure 5: Launching the steel structure across the first two spans.

The 120 m long structure (including the nose) that was to be launched was assembled on the embankment behind the south abutment. It rested on 7 pairs of provisional sliding bearings aligned with the two box girder webs and spaced at 20 m centres. An eighth pair of sliding bearings was positioned on top of the first pier. With this sliding bearing set-up, the structure could be launched with the precast concrete slabs for the first span already in place. This was doubly beneficial, for it lowered the risk of overturning and shortened the time needed to cast the *in situ* concrete.

The front end of the launching nose was fitted with jacks to restore the deflection in the cantilever upon arrival at the first pier. The friction transmitted by the sliding bearings over this highest pier during the launch generated a substantial overturning moment, which was countered by stabilizing the pier with a tension member attached to the abutment. This temporary member consisted of a truss-like structure with an intermediate support to ensure sufficient stiffness and strength (figure 5).

The reactions in the supports during the launch depended on many different factors (subsection 5.2.3). Moreover, the provisional sliding bearings used were not adjustable, nor could the support reactions be monitored during launching. The considerable uncertainties associated with these reactions called for especially thorough process analysis to ensure structural safety during the bridge launching operation.

5.2 Patch loading

5.2.1 Context

At the sliding bearings, sizeable forces were applied perpendicularly to the box girder flange along the plane of the web. The length across which these forces could be distributed was limited to the 1200 mm length of the bearings. During launching, these concentrated forces were transmitted across the flange to the slender web in an area with no transverse stiffeners, for these elements were spaced at 4 m, except in the hogging bending area around the pier, where that distance was shortened to 2 m. Web behaviour may be governed by yielding, buckling or crippling, depending on the steel structure geometry for given loading conditions and material strength. Web plate thickness, particularly important in this context, varied along the launched girder from 15 mm to 26 mm.

Resistance to transverse forces further depends on the internal forces and moments in the girder as a whole. Hogging bending moments generated by the cantilever, for instance, may reduce the ultimate transverse load. Such problems may be particularly relevant where box girders are concerned due to the possible negative interaction between compression flange and web instability. The recommendations set out in codes and standards ([7] and [8]) on resistance to transverse forces, however, refer primarily to rolled and welded I-

www.EngineeringEBooksPdf.com

girders. A practical procedure therefore had to be devised to verify structural safety in connection with the introduction of transverse forces in the box girder webs.

5.2.2 Verification procedure

The procedure adopted in the present design to verify the patch loading and overall bending moment interaction-related structural safety of the steel box girder during launching comprised the following steps:

1. Identification of the variations in the girder cross section, by segments.
2. Step-by-step computation of the action effects on the steel girder during the launching operation.
3. Using the results from step two, establishment, for each of the cross sections identified in step one, of the maximum reaction forces to be introduced in the box girder webs and the concomitant bending moments.
4. Computation of transverse force – bending moment interaction diagrams [9] to represent the strength of each of the segments identified in step one. This called for non-linear finite element analysis taking into consideration box girder segment and sliding bearing geometry, the geometric imperfections associated with girder manufacturing tolerances, and geometric and material non-linearity.
5. Verification of structural safety by representing the design value of the maximum action effects of reaction force – concomitant bending moment for each cross section analyzed on the respective design transverse force – bending moment interaction diagram.

Further information on the implementation of the above procedure, particularly with respect to the last two steps, is provided in item 5.2.3 below. By way of illustration, the results for one of the cross sections are provided.

5.2.3 Results

Five types of segments, defined by their cross sections, were identified on the girder. Most of the variation was related to the flange or web plate thickness or to the stiffener or diaphragm arrangement. Action effects in general and particularly the maximum effects on each of the aforementioned types of cross sections were calculated pursuant to elastic theory, including the launching operation in the model. All relevant parameters were taken into consideration: i.e., the exact girder and launching nose geometry, including precamber, the position of the sliding supports relative to the girder in each launching step, system stiffness including the nose, and the loads applied and their distribution.

Box girder capacity to resist transverse forces in conjunction with bending moments was computed with non-linear finite element models developed [10] for each segment type, using [11]. Cross section symmetry of each 12 m long segment was also taken into consideration (figure 6a). The sliding bearing was aligned with the web in the centre of the segment between two diaphragms, in an area with no transverse stiffeners.

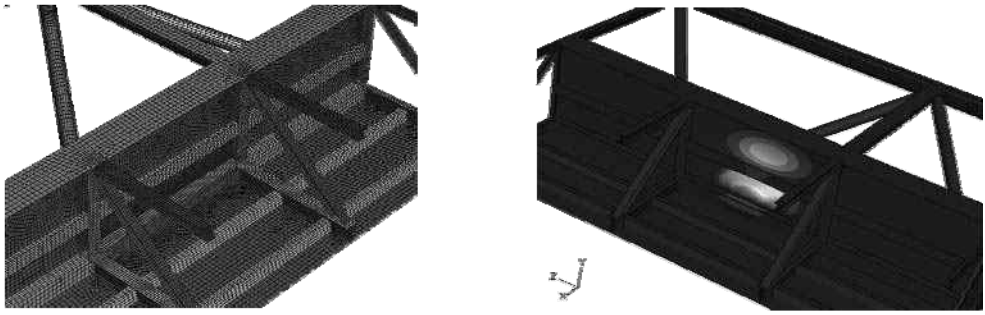


Figure 6: Non-linear finite element analysis to establish the patch load response; (a) mesh for one segment; (b) first failure mode [10].

www.EngineeringEBooksPdf.com

Different combinations of transverse forces and bending moments were entered into the model to establish the eigenvalues for plate buckling (figure 6b). The first three modes were then scaled to define the imperfections corresponding to manufacturing tolerances.

In the next step, model geometry was redefined by entering these equivalent imperfections for subsequent non-linear analysis. Transverse forces and bending moments were then entered into the modified model. The forces and moments were increased to failure values, taking geometric and material non-linearity into account. Following this procedure and varying the combination of applied forces and moments, the strength, in terms of a transverse force – bending moment interaction diagram, was found for each segment considered (figure 7).

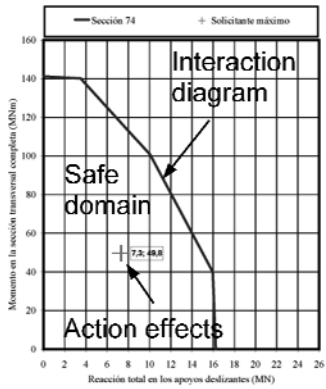


Figure 7: Use of a transverse force – bending moment interaction diagram to verify structural safety in a cross section.

To verify structural safety, the maximum reaction force to be introduced in the web of a given segment, in conjunction with the concomitant bending moment acting on the segment, was represented on the interaction diagram established to determine segment strength (figure 7). Reliability was checked with the design values for action effects and strength. In the absence of specific rules for conducting semi-probabilistic non-linear finite element analysis, these design values were established by applying the partial load and strength factors laid down in [7] to the nominal values computed for the action effects and strength, respectively. The structure was found to be reliable for, as figure 7 shows, the design value of the action effects lay within the safe domain of the design interaction diagram for strength.

6 CONCLUDING REMARKS

Throughout the design stage of the viaduct over the River Llobregat, special attention was paid to conceptual design to successfully translate the many conditioning factors into a reliable, functional, cost-effective, graceful and innovative structure. Such designs may, however, pose problems that lie outside the scope of existing design rules. Two typical examples are discussed in this paper, namely structural detail design and patch loading during incremental launching of the steel structure, in which structural safety could not be

www.EngineeringEBooksPdf.com

ensured by the mere compliance with codes and standards. The stress field method proved to be a very powerful tool for the efficient and reliable design of details and connections. Non-linear finite element analysis, in turn, was very useful for the explicit verification of both local and overall system stability: here the steel box girder during launching. Further studies are required, however, to develop a suitable design format for semi-probabilistic non-linear finite element analysis.

REFERENCES

[1] Tanner, P. and Bellod, J.L., "Modesty prevails: Llobregat river bridge in Spain", *Bridge Design and Engineering*, Issue 51, 30-31, 2008, ISSN 1359-7493.

[2] Tanner, P. and Bellod, J.L., "Increasing reliability of composite bridges by reducing steel. Ductility versus Brittleness", *Composite Bridges. State of the Art in Technology and Analysis*, Martínez Calzón (ed.), Colegio de Ingenieros de Caminos, Canales y Puertos, Madrid, 2002, ISBN 84-380-0221-8.

[3] EN 1993-1-8, *Eurocode 3: Design of steel structures – Part 1-8: Design of joints*, European Committee for Standardisation, Brussels, 2005.

[4] EN 1993-1-10, *Eurocode 3: Design of steel structures – Part 1-10: Material toughness and through-thickness properties*, European Committee for Standardisation, Brussels, 2005.

[5] Muttoni, A., Schwartz, J., Thürlimann, B., *Design of concrete structures with stress fields*, Birkhäuser, Basel-Boston-Berlin, 1997, ISBN 3-7643-5491-7.

[6] Tanner, P. and Bellod, J.L., "Salto del Carnero railway bridge, Saragossa, Spain", *Structural Engineering International*, Vol. 16, nº 3, 200-203, 2006, ISSN 1016-8664.

[7] RPX-95, *Recommendations for the design of composite bridges*, Ministry of Public Works, Madrid, 1996, ISBN 84-498-0223-8 (Spanish version).

[8] EN 1993-1-5, *Eurocode 3: Design of steel structures – Part 1-5: Plated structural elements*, European Committee for Standardisation, Brussels, 2006.

[9] Gillet, G., Bouchon, E., Bouvy, B., Le Faucheur, D., Sablon, J-Y., "Les études du viaduc de Verrières", *Bulletin Ouvrages d'Art*, Nº 38, Sétra, 2001.

[10] Principia, *Puente de Llobregat. Diagramas de interacción momento flector – reacción de apoyo*, Principia S.A., Madrid, 2007.

[11] Abaqus, *Standard Users' Manual*, Abaqus Inc., Providence, Rhode Island, 2006.

www.EngineeringEBooksPdf.com

SDSS'Rio 2010 STABILITY AND DUCTILITY OF STEEL STRUCTURES
E. Batista, P. Vellasco, L. de Lima (Eds.)
Rio de Janeiro, Brazil, September 8 - 10, 2010

DESIGN OF BEAM-TO-BEAM BUTT-PLATE JOINTS IN COMPOSITE BRIDGES

A. Lachal*, S.S. Kaing, S. Guezouli***

* LGCGM – Structural Engineering Research Group, INSA-Rennes, France
e-mails: Alain.Lachal@insa-rennes.fr, Samy.Guezouli@insa-rennes.fr

** Institut de Technologie du Cambodge (ITC), Phnom Penh, CAMBODIA
e-mail: ksserey@yahoo.fr

Keywords: Design method, Continuous joint, Composite bridge.

Abstract. *This paper presents an analytical design method for beam-to-beam butt-plate joints connected with studs to a concrete transverse deep beam for composite bridges. The proposed design method is an elastic model at the ultimate limit state, mainly based on the Eurocodes and also on the data obtained from experimental and numerical investigations carried out at the Laboratory of Structural Mechanics at INSA-Rennes.*

1 INTRODUCTION

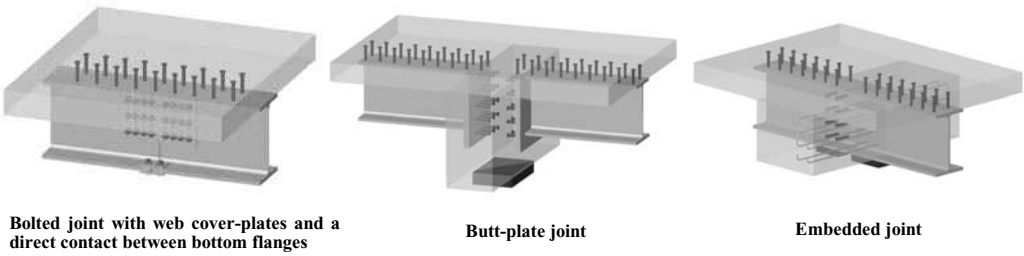


Figure 1: Beam-to-beam joint solutions

In order to promote new composite techniques for bridges of small and medium spans, innovative solutions have been investigated for the design and the fabrication of beam-to-beam joints. In Europe, several projects have been carried out on this subject the past ten years [1]. More recently, in France, taking benefit of a National Research Project (MIKTI), the Laboratory of Structural Mechanics at INSA in Rennes has undertaken research works to find new types of beam-to-beam joint ensuring the continuity of composite beam in bridges. New joint solutions have been selected (figure 1) with the aim to find economic solutions [2] using, if possible, standardized or ordinary prefabricated elements easily mounted on site by a same builder with a minimum of construction operations and without any sophisticated technology (as outdoor welding for example). Analytical methods have been developed for these new joints.

This paper presents the analytical design method of a beam-to-beam joint realised with butt-plates connected with studs to a reinforced concrete transverse deep beam (figure 1).

www.EngineeringEBooksPdf.com

2 EXPERIMENTAL AND NUMERICAL RESULTS

The specimen tested at the Laboratory of Structural Mechanics (INSA of Rennes) is presented in figure 2. A concrete block (which represents the concrete transverse beam) at mid-length of the specimen is supported on a bearing. The specimen is loaded at its two ends by two hydraulic actuators. On each

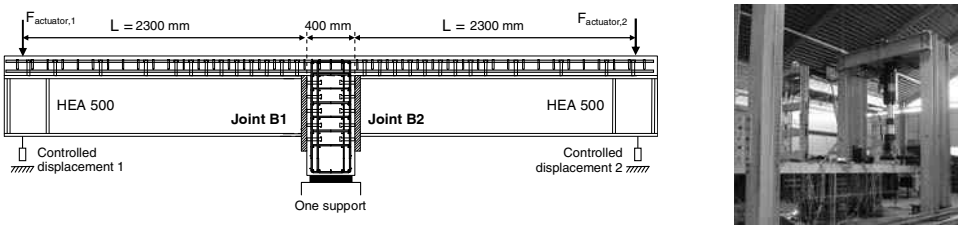


Figure 2: Tested specimen and experimental setup

side of the concrete block, end steel girders are connected by butt-plates whose dimensions are 600×500×45 and 24 studs (d = 22mm and h = 125mm) uniformly distributed on each butt-plate (4 lines and 6 rows of studs). On the right side (joint B2), the butt-plate was welded with the steel beam with a fillet weld and on the left side (joint B1) a full penetration butt weld was used. Main common details of the composite beam are HEA 500 (S355) steel cross-section (E_a = 200 000 MPa, $f_{y,a}$ (web) = 450 MPa, $f_{y,a}$ (flange) = 420 MPa), concrete slab (C45/50) whose dimensions are b_{eff}^{-} = 1600mm and h_a = 160mm with 1.26% percentage of longitudinal reinforcement (2 layers of 8 bars of 16mm diameter - S500), full shear connected (2 lines of 12 welded headed studs per span ; d = 22 mm, h = 125 mm, E_a = 200 000 MPa, f_y = 450 MPa). In the connected zone, the percentage of longitudinal reinforcement is increased to 2.67% (9 additional bars d_b = 16 mm - S500 of length b_{eff} + ℓ_{bd} = 2050mm) and the number of connectors is doubled (24 studs on the same length). The tested specimen has been equipped with 80 strain gauges and 40 transducers. The principal of experimental setup is indicated in Figure 2. Two types of loading procedure have been exerted: firstly a fatigue loading under a high range of bending moment to obtain significant information about the fatigue resistance of some details of the joint and the shear connection and secondly a monotonous increase of actuator loads towards the specimen collapse.

Figures 3 shows the moment-rotation curve where rotations are those defined between the cross-section at mid-joint and the beam cross-section immediately adjacent to the joint on each side. Rotations are deduced from inclinometers, beam deflections and relative linear displacements measured over the whole depth of the joint. Bending moments are calculated from the measured actuator loads multiplied by the appropriate lever arm L (figure 2).

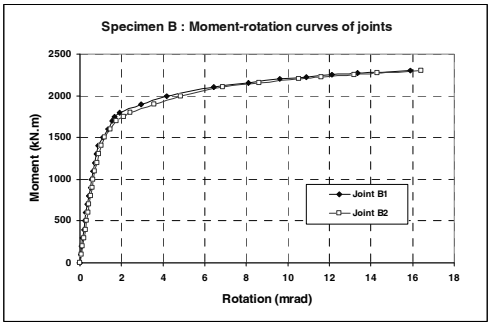


Figure 3: Moment-rotation curves

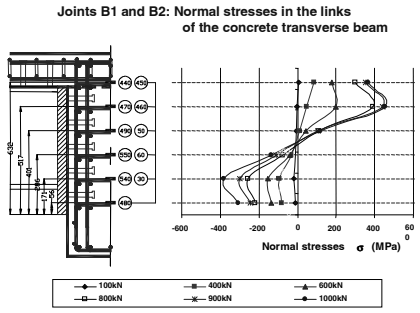


Figure 4: Normal stresses in the horizontal links on the width of the concrete block

www.EngineeringEBooksPdf.com

Main joint moment-rotation characteristics measured from the above curves for both joints B1 and B2 are: an initial rotational stiffness $S_{j,ini}^{exp}$ = 1986 kN.m/rad, a maximum exerted moment $M_{exerted}^{max}$ = 2300 kN.m and a rotational capacity greater than 16 mrad. Compared to the calculated initial rotational stiffness (under flexural bending) $S_{eq} = EI_2/\ell$ = 210000×140558×10^4/250 = 1180 kN.m/mrad and the elastic resistance moment $M_{el,b,R}$ = 1842 kN.m of an equivalent composite beam section having the same length of about 250 mm (as the one used to define the joint rotation); Joints B1 and B2 appear fully efficient in stiffness and strength.

Figure 4 gives the distribution of the normal stresses in the horizontal links on the width of the concrete block. Tensile stresses appear at the level of the two upper rows of studs; meanwhile maximum compression stresses are located just in front of the bottom flange of the girder. The neutral axis is situated near the mid-width of the web girder. Other experimental results deal with: stress distributions in several parts of the specimen: stud shanks, slab reinforcement, girder cross-sections…; slip measurements between the slab and the upper steel girder flange; fatigue of some details.

In addition, to reach information not accessible to measurement and to obtain a more accurate interpretation of the test results and a better understanding of some specific behaviour, a 3D finite element model based on CASTEM have been developed [3].

3 DESIGN METHOD OF THE JOINT

3.1 General design approach

The basic design principle adopted is to maintain a distribution of internal forces in the joint as equivalent as possible to the internal force distribution identified in the attached beam cross-section close to the joint. Insofar as such a joint is necessarily located on an intermediate support, only hogging bending moment transmitted by the joint has been considered here. In composite bridge, steel girder cross-sections are often in Class 3 so only elastic analysis has been developed in this study.

3.2 Internal forces transmitted to the joint

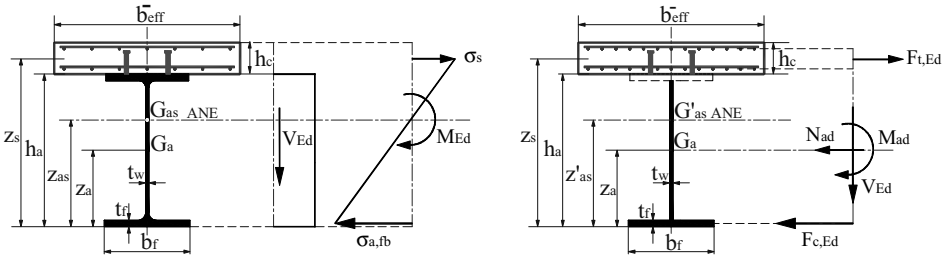


Figure 5: Internal forces transmitted by the composite cross-section to the joint

A shear force V_{Ed} and an hogging bending moment M_{Ed} are transmitted by the attached composite cross-section to the joint. Corresponding stress diagrams are represented in Figure 5. The position of the elastic neutral axis z_{as} of the composite cross-section is determined from the cross-sectional area A_a and the position of the centroid z_a of the steel cross-section and from the cross-sectional area A_s and the position of the centroid z_s of the reinforcement.

To allow the continuity of the composite beam, the joint has to transmit:

- the existing tensile force transmitted by the longitudinal reinforcing bars of the slab;
- the tensile normal force transmitted by the upper flange which is transferred to the longitudinal reinforcing bars (the reinforcement area will be increased and additional shear studs added on the steel beam flange near to the joint to allow the force transfer);
- the compressive normal force transmitted by the bottom flange to the joint;
- the shear force V_{Ed} transmitted by the intermediate zone of the joint located at the web level;

www.EngineeringEBooksPdf.com

- the remaining equilibrium forces (force and moment) transmitted by this intermediate zone.

The same position z_{as} of neutral axis is adopted so that the stress in the bottom steel flange is unchanged; consequently the tensile stress in the reinforcement is also unchanged if no slip is assumed at the steel-concrete interface. The new longitudinal reinforcement area A'_s is given by:

$$A'_s = \frac{A_a(z_{as} - z_a) + b_f t_f (h_a - t_f/2 - z_{as})}{z_s - z_{as}} \tag{1}$$

See notations in figure 5 (*the elastic modulus of steel reinforcement is considered equal to the one of structural steel and the area of radius under the upper tension flange of the steel section is neglected*).
So, the tensile normal force $F_t = A'_s \sigma_s$ in the longitudinal reinforcement and the compressive force is $F_c = b_f t_f \sigma_{a,fb}$ in the cross-sectional area of the bottom steel flange; where σ_s and $\sigma_{a,fb}$ are the stresses defined at the centroids of reinforcement and lower flange, respectively are easily determined (figure 5).
Additional internal forces N_{ad} and M_{ad} determined at the centroid G_a of the steel section (figure 5) are introduced to ensure the cross-section equilibrium.

3.3 Design of the additional reinforcement of the slab

The additional reinforcement area $A_{s,ad}$ is chosen immediately equal to or greater than $A'_s - A_s$. The corresponding additional bars are distributed over the effective width b_{eff}^- of the composite beam (see 5.4.1.2 of EN 1994-2 [4]) on a length $\ell_{s,ad} = 2(b_{eff}^- + \ell_{bd})$ where b_{eff}^- is related to the reinforcement on each side of the joint and ℓ_{bd} is the design anchorage length defined in 8.4 of EN 1992-1-1 [5]. According to $A_{s,ad}$ a new value of the position z'_{as} of the neutral axis is calculated (*slightly different from* z_{as}).

3.4 Design of the additional shear connection between the concrete slab and the steel girder

The number of additional shear studs to be distributed on a length approximately equal to b_{eff}^- on each side of the joint is given by: $n_{ad} \geq A_{s,ad}\sigma_s / P_{Rd}$ where P_{Rd} is the shear stud resistance given in 6.3.2.1 of EN 1994-1-1 [6]. The transverse steel reinforcement in the slab has to be checked again to take into account the increase of the longitudinal shear force near the joint so that any premature longitudinal shear failure and longitudinal splitting are prevented (EN 1994-2, 6.6.6 referring to EN 1992-1-1, 6.2.4).

4.6 Butt-plate design

The thickness t_p of the butt-plates is preliminary defined in order to assume the transmission of the compression forces $F_{c,Ed}$ from the bottom flanges to the concrete transverse deep beam:

$$F_{c,Ed} \leq f_{jd} b_{eff} \ell_{eff} \text{ ; where } b_{eff} = b_f + 2c \text{ and } \ell_{eff} = t_f + 2c \text{, with } c \leq t_p \sqrt{\frac{f_{yp}}{3 f_{jd} \gamma_{M_0}}} \text{ ; } \gamma_{M_0} = 1.0 \tag{2}$$

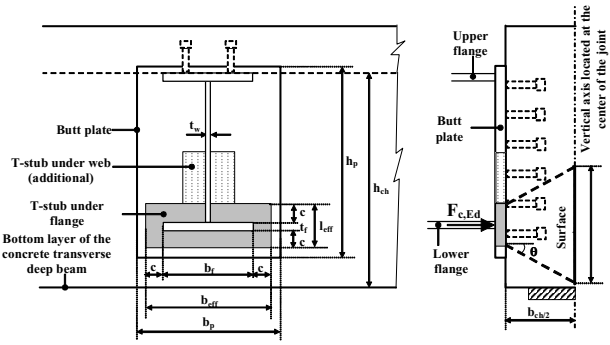


Figure 6: Butt-plate thickness design

www.EngineeringEBooksPdf.com

b_{eff}, b_f, c, ℓ_{eff}, are defined in figure 6. f_{yp} is the yield strength of the butt-plate and f_{jd} is the design bearing strength between the butt-plate and the concrete block. f_{jd} is determined from the design method proposed in EN 1993-1-8, 6.2.5 [7] for column bases loaded by normal force and bending moment. The width of the concrete transverse deep beam b_{ch} should be defined in order to allow a distribution of the compression force on the half-width $b_{ch}/2$ (figure 6) just to permit to put studs of the butt-plates in place keeping a sufficient gap between the opposite heads (a width b_{ch} equals about three times the shank height of the studs of the butt-plates would be sufficient to satisfy these conditions). In addition, the height h_{sc} of the transverse beam should be defined in order to allow the formation of compressive struts in the concrete of the bottom part of the transverse beam:

$$h_{sc} = h_a - \frac{t_f}{2} + \frac{\ell_{eff}}{2} + \frac{b_{ch}}{2} \tan\theta \;\; ; \;\; \text{with} \;\; 26{,}5° \le \theta \le 45° \tag{3}$$

The beam ends will be connected to the butt-plates by means of a fillet weld. Welds are designed by taking into account vertical shear V_{Ed} along with the additional forces N_{ad} and M_{ad} [7].

4.7 Butt-plate anchors design

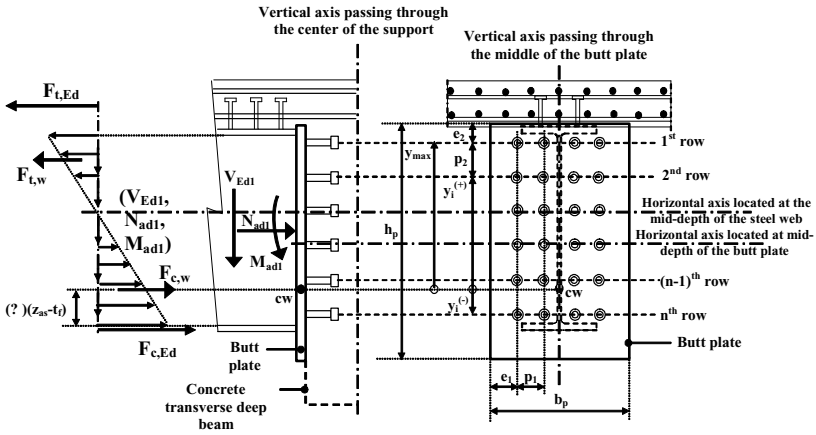


Figure 7: Butt-plate anchors design

Headed studs of the butt-plate should be placed on several rows and lines with respect to the spacing conditions set forth in Clauses 6.6.5.5 to 6.6.5.7 of EN1994-2 [4]. They are designed in order to transmit to the transverse concrete beam the vertical shear load V_{Ed} and the equilibrium forces N_{ad} and M_{ad} .

Calculation of the shear force inside the studs of the butt-plate takes into account the resistance contributed by friction $F_{f,Rd}$, within the compression zone, between the butt-plate and the transverse concrete beam. Moreover a uniform distribution in shear forces can be assumed between the $n_{con,w}$ connectors. The shear force $F(V_{Ed})$ transmitted by each connector is thus expressed as:

$$F(V_{Ed}) = (V_{Ed} - F_{f,Rd}) / n_{con,w} \ge 0 \; ; \quad \text{with:} \;\; F_{f,Rd} = C_{f,d} \left| F_{c,Ed} \right| \tag{4}$$

$C_{f,d}$ is the coefficient of friction between the butt-plate and the transverse concrete beam. A value of $C_{f,d}$ = 0.2 can be assigned, which corresponds to a contact between sand mortar and cement. For purpose of recall, $F_{c,Ed}$ is the compressive force contributed by the compression beam flange.

Following conclusions of ref. [8], specifications of ACI 318-08, appendix D [9], have been adopted to compute the strength of headed stud under tension (CCD method) or combined tension and shear.

The strength of a single stud or group of $n_{con,w}$ studs in tension is based on a two-stage verification:

www.EngineeringEBooksPdf.com

- as governed by the steel strength : $P_{ten,Rd}^{(1)} = n_{con,w} \cdot \frac{\pi d^2}{4} \cdot \frac{f_u}{\gamma_v}$ (N); (5)

where d (mm) is the shank stud diameter and f_u (N/mm^2) the ultimate tensile strength not be taken greater than the smaller of $1.9 f_y$ and 800 N/mm^2. The recommended value of the partial factor γ_v is 1.25 [6].

- as governed by the concrete breakout strength: $P_{ten,Rd}^{(2)} = 15.5 \frac{A_{Nc}}{A_{Nco}} (h_{sc} - k)^{1.5} \frac{\sqrt{f_{ck}}}{\gamma_v}$ (N); (6)

where h_{sc} is the depth embedment and k the height of the stud head. A_{Nc} is the projected concrete failure area of a single stud or group of studs that shall be approximated as the base of the rectilinear figure that results from projecting the failure surface outward $1.5(h_{sc} - k)$ from the centrelines of the stud, or in the case of a group of anchors, from a line through a row of adjacent studs (figure 8). A_{Nc} shall not exceed $n_{con,w,gr}\ A_{Nco}$ where $n_{con,w,gr}$ is the number of tensioned studs in the group. $A_{Nco} = 9(h_{sc} - k)^2$ is the projected concrete failure area of a single stud (Fig. 9) with an edge distance equal to or greater than $1.5(h_{sc}\text{-}k)$. Modification factors may be introduced in (13), (14) and (15) to take account of tension load eccentricity, edge effects and cracked or uncracked concrete [9].

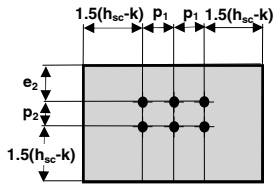


Figure 8: Projected area A_{Nc} for a group of studs

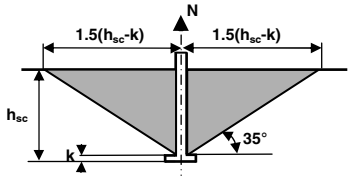


Figure 9: Section through failure cone (A_{Nco})

The general requirement for the strength design of butt-plate studs, including the interaction when studs or group of stud are subjected to both shear and axial loads may be given by the following general shear and tensile load interaction equation suggested with the reference [9]:

$$\left[\left(\frac{F(N_{ad}) + F(M_{ad})^{max}}{P_{ten,Rd}^*} \right)^{\frac{5}{3}} + \left(\frac{V_{Ed} - F_{f,Rd}}{n_{con,w} P_{Rd}^*} \right)^{\frac{5}{3}} \right] \leq 1{,}0 \quad (7)$$

where $F(N_{ad})$ and $F(M_{ad})^{max}$ are the normal forces due to N_{ad} and M_{ad} for the highest row of studs. $P^*_{ten,Rd}$ and P^*_{Rd} are the lowest strengths determined from appropriate failure modes. In order to take into account the potential risk of failure to a concrete block around studs, the strength of each group of connectors will be checked successively beginning with the highest row, followed by the group of two highest rows and so forth until the strength derived is greater than the previous value.

4.6 Design of the concrete transverse beam reinforcement

4.6.1 Stud reinforcement for shear

Transverse reinforcing bars placed close to the studs of the butt-plate have to transmit the resultant shear force ($V_{Ed} - F_{f,Rd}$) through a shear failure surface defined in a manner similar to that adopted to define the longitudinal shear strength of concrete flange (EN 1994-1-1, 6.6.6). The required total area of this transverse reinforcement is so determined.

www.EngineeringEBooksPdf.com

4.6.2 Supporting reinforcement

Supporting reinforcement serves to raise the previous resultant shear force ($V_{Ed} - F_{f,Rd}$) towards the upper part of the section; consequently a total area $A_{s,s}$ of the transverse reinforcing is determined.

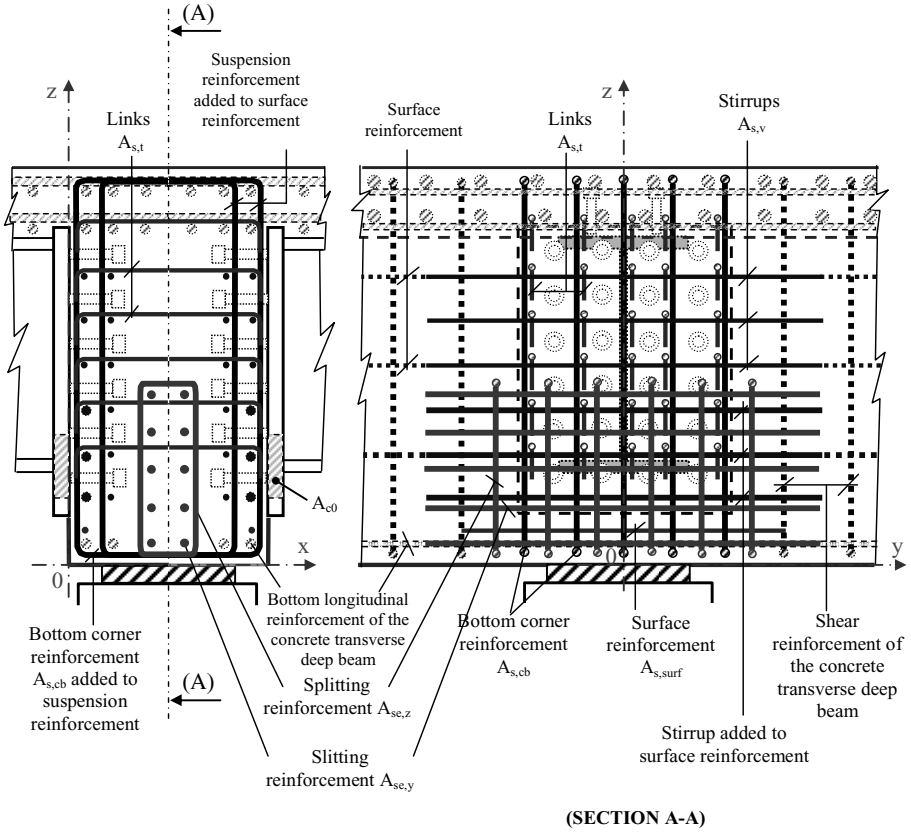


Figure 10: Reinforcement of the concrete block

4.6.3 Links (stud reinforcement for tension)

Links are introduced to improve the bonding of the both connected sides B1 and B2 through the concrete transverse beam thickness. The area of the links is defined on the basis of the maximum tensile force to be transmitted by the first stud row located in the upper part of the butt-plate.

4.6.4 Reinforcement in the compression zone of the concrete transverse beam

The compressive force transmitted by the bottom flange of the steel girder exerts a local effect of pressure onto a reduced contact surface area A_{c0} of the side surface of the concrete transverse beam. A reinforcement may be designed, which comprise both surface reinforcement $A_{s,suf}$ and splitting reinforcement $A_{se,y}$ and $A_{se,z}$ in both directions y and z, positioned beginning at a depth of 0.2 until reaching 0.8 of the half width $b_{ch}/2$ of the concrete transverse beam and distributed over lengths equal to $\ell_{\text{eff}} + b_{ch}\tan\theta$, in vertical z direction vertical, and $b_{eff} + b_{ch}\tan\theta + 2\ell_{bd}$, in horizontal y direction (figure 6).

www.EngineeringEBooksPdf.com

4.6.5 Reinforcement at the bottom corners

In order to prevent premature splitting or spalling of concrete of corners when exposed to the simultaneous action of compressive forces applied by the lower part of the butt-plates and the support reaction, it must be checked that the various reinforcements crossing the splitting failure plane are adequate in all directions of the plane (figure 6).

4.6.6 Example

Figure 10 shows the example of the reinforcement design adopted for the joint specimen tested at INSA Rennes Laboratory. Main characteristics of the specimen have been given in the previous § 2.

4.7 Fatigue resistance verification of the joint

According to Eurocode requirements, the fatigue resistance of various details as: longitudinal reinforcement, headed studs, welds, compressed concrete, and bottom flanges should be checked.

5 CONCLUSION

This paper provides useful guidance elements for the design of beam-to-beam butt-plate joints stud-connected to concrete transverse beams in composite bridges. Experimental and numerical results of researches conducted at the INSA-Rennes like Eurocode-based methods have been assigned priority for the design methods developed herein. Other standards were also applied whenever the topic examined was not covered by Eurocodes.

ACKNOWLEDGEMENTS

The authors would like to thank IREX, the “French Ministry of Ecology and Sustainable Development”, Arcelor-Mittal Research and SNCF-Engineering for their financial and technical support.

REFERENCES

[1] ECSC steel RTD programme, “Composite bridge design for small and medium spans”. *Final report*, 2002.

[2] Lachal, A. and Aribert, J.M., “National Research Project MIKTI”, Design of outstanding decks in the framework of small spans, Subject 1-B: Innovative techniques to connect continuous beams, specifications”, *Research report,* February 2002.

[3] Guezouli, S., Somja, H., Kaing, S.S., Lachal, A., “Numerical modelling of composite beam-to-beam joints, innovative solutions”. *Composite Construction VI*, Colorado 2008.

[4] EN 1994-2 – Eurocode 4, Design of composite steel and concrete structures, part 2“General rules and rules for bridges”. European committee standardisation, Brussels, February 2006.

[5] EN 1992-1-1 – Eurocode 2, Design of concrete structures, part 1-1, “General rules and rules for buildings”. European committee standardisation, Brussels, December 2004.

[6] EN 1994-1-1 – Eurocode 4, Design of composite steel and concrete structures, part 1-1 “General rules and rules for buildings”. European committee standardisation, Brussels, September 2004.

[7] EN 1993-1-8 – Eurocode 3, Design of steel structures, part 1-8 “Design of joints”. European committee standardisation, Brussels, April 2005.

[8] Saari, W.K., Hajjar, J.F., Schultz, A.E. and Shield, C.K., “Behavior of shear studs in steel frames with reinforced concrete infill walls”. *Journal of constructional steel research 60,* Elsevier Science Ltd., Oxford, 2004, p. 1453-1480.

[9] ACI 301-08, Appendix D, Building Code Requirements for Structural Concrete and Commentary, American Concrete Institute, Farmington Hills (MI), USA, 2008.

www.EngineeringEBooksPdf.com

4. CONNECTIONS

www.EngineeringEBooksPdf.com

www.EngineeringEBooksPdf.com

SDSS'Rio 2010 STABILITY AND DUCTILITY OF STEEL STRUCTURES
E. Batista, P. Vellasco, L. de Lima (Eds.)
Rio de Janeiro, Brazil, September 8 - 10, 2010

EXPERIMENTAL ANALYSIS OF COMPOSITE CONNECTIONS USING SLAB MADE BY PRECAST JOIST WITH LATTICE AND BRICKS

William Bessa*, Roberto M. Gonçalves*, Carlo A. Castiglioni and Luis Calado*****

* Escola de Engenharia de São Carlos, EESC – USP, São Carlos, Brazile-mails: willbessa@gmail.com, goncalve@sc.usp.br
** Politecnico di Milano, Milan, Italy
e-mail: castigli@stru.polimi.it

*** Instituto Superior Tecnico, Lisbon, Portugal
e-mail: calado@civil.ist.utl.pt

Keywords: Composite Connections, Precast Joist, FEM Modeling, Slab Cracking.

Abstract. *This research presents an experimental study of steel concrete composite connections with bottom and web angle. It was tested 4 full-scale specimens (2 single-sided and 2 double-sided composite connections), with 0,2% and 1% for the secondary steel ratio. The specimens were fabricated with precast concrete slabs with steel joist (predalles) and bricks infill, a constructive technique widely used in Brazil. The experimental studies of isolated specimens were a previous step for the typical floor composite connections analysis. The main objectives were to evaluate the concrete slab cracking on the behavior of composite connections (initial stiffness and resistant moment) and the secondary steel ratio increase. The experimental results were compared with numerical models, using FEM, with the goal of including the longitudinal and transversal steel bars, concrete slab, geometrical and material non linearity. Comparisons between numerical and experimental results showed satisfactory agreement and indicated the connection failure mode for the ultimate limit states.*

1 INTRODUCTION

The steel-concrete composite construction has increased in engineering practice, especially in composite frames for buildings that consist of steel concrete composite beams and steel columns. This type of composite frame has several structural and constructional advantages, such as good fire resistance and high strength, large stiffness and ductility, local and global buckling restraints on steel beams provided by concrete slabs, and reduced construction costs.

The stiffness and strength of steel frames can be significantly increased by a composite concrete slab in beams. This can be achieved by providing a few continuous reinforcing steel bars across the column lines and ensuring full or partial composite action through the use of shear connectors - Li et al. (1996) [1].

Design procedures for steel and composite connections have been modified during the last three decades in order to incorporate the semi-rigid connection behavior into the frame design process. The 3D numerical modeling of the real connections behavior leads to more reliable designs and economy in civil construction.

This paper presents an experimental study of steel concrete composite connections with bottom and web angle. It was tested 4 full-scale specimens (2 single-sided and 2 double-sided composite connections) with precast concrete slabs with steel joist (predalles) and bricks infill. The experimental results were compared with numerical models, using FEM, with the goal of including the concrete slab,

www.EngineeringEBooksPdf.com

shear connectors, longitudinal and transversal steel bars, material nonlinearities, geometrical discontinuities and large displacements.

2 EXPERIMENTAL PROGRAM

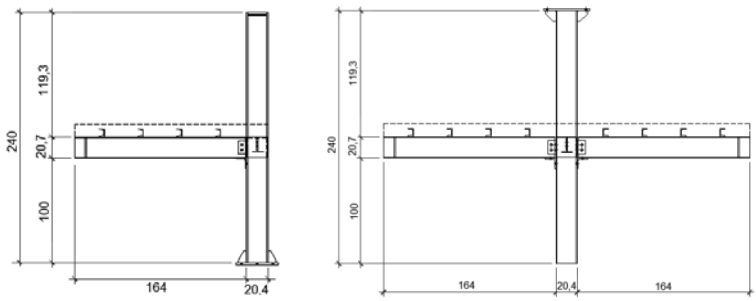
The experimental program was carried out by Bessa (2009) [2], at the São Carlos Engineering School of University of São Paulo (EESC-USP), for beam-to-column composite connections with bottom and web angle. It was tested 4 specimens (2 single-sided and 2 double-sided composite connections) with monotonic loading. It was considered specimens with 0,2% and 1% for the secondary steel ratio, and 1% for the longitudinal steel bars ratio.

The Table 1 shows the specimens tested with their respective main definitions: ***RSS = 1%*** and ***NRSS = 0,2%*** for the transversal steel bars ratio.

Table 1: Specimens tested.

Prototype	Connection	Longitudinal steel bars ratio	Transversal steel bars ratio
TNRSS	Simple sided	1%	0.2%
TRSS	Simple sided	1%	1%
CNRSS	Double sided	1%	0.2%
CRSS	Double sided	1%	1%

The Figure 1 illustrates the geometrical characteristics for the single sided and double sided specimens. The Table 2 indicates the connection components characteristics, with standard rolled steel beams and column, bolts with 19mm and 16mm (for column major and minor axis connections, respectively), angles (bottom and web) and shear connectors characteristics.



Single sided specimens (cm). Double sided specimens (cm).

Figure 1: Specimens geometrical characteristics.

Table 1: Specimens tested.

Element	Characteristics
Composite beam	W 350 x 13 kgf/m
Column	HP 200 x 53 kgf/m
Shear Connectors	U 75x50x7,5mm
Bolts – column major axis	ASTM A324 – ϕ19mm
Bolts - column minor axis	ASTM A324 – ϕ16mm
Bottom angle	L 4“ x 4“ x 5/16“
Web angle	L 3“ x 3“ x 1/2“
Steel longitudinal bars	8ϕ10mm
Steel transversal bars	Double sided

www.EngineeringEBooksPdf.com

The effective width of cross-section beam was done according with EUROCODE 4 (2004) [3]. The Figure 2 illustrates the composite beam section and steel bars detail in the pre-fabricated concrete slab for the simple-sided specimens (TNRSS and TRSS). The Table 3 indicates the main material properties.

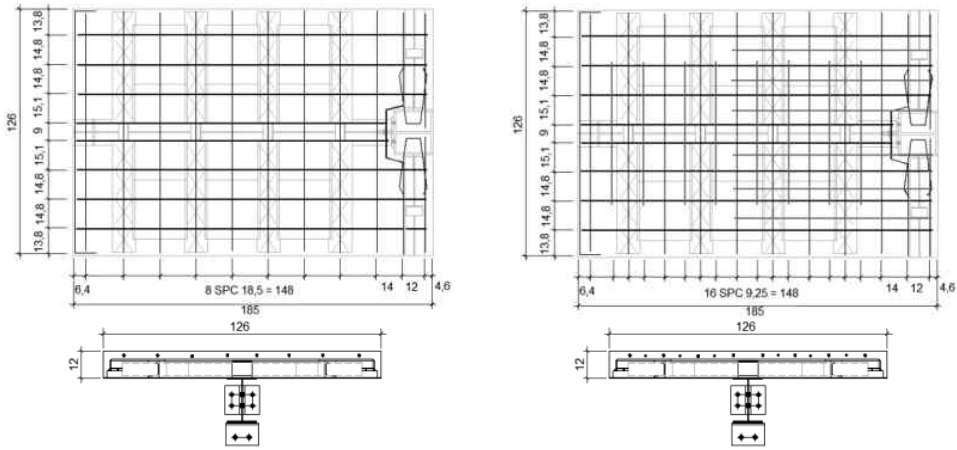


Figure 2: Steel bars details in the concrete slab and beam section.

Table 3: Material properties.

Element	f_y (kN/cm^2)	f_{max} (kN/cm^2)
Beam	36.41	45.12
Column	37.36	56.00
Bottom and web angle	39.70	47.80
Longitudinal steel bars	55.43	59.48
Concrete: f_{cm} = 18.9 MPa – TRSS and CRSS specimens		
f_{cm} = 39.2 MPa – TNRSS and CNRSS specimens		
where f_y = proportional limit stress and f_{max} = ultimate stress		

The same geometrical characteristics indicated in Table 2 and steel bars details illustrated in Figure 2 were adopted on the cruciform specimens (CNRSS and CRSS). The Figure 3 shows the general view of the TRSS and CRSS specimens.

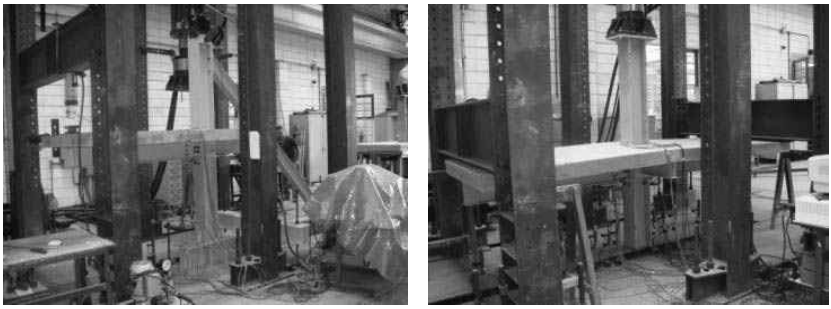
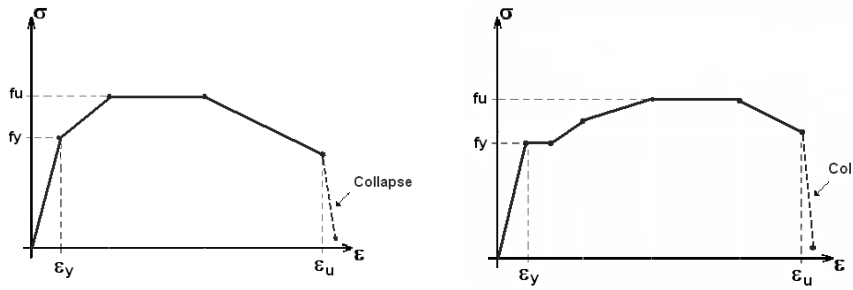


Figure 3: TRSS and CRSS specimens general view.

www.EngineeringEBooksPdf.com

3 NUMERICAL MODELING

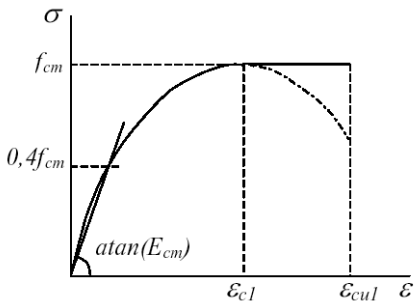
In the numerical modeling, the most important step to construct a representative model is the finite element choice and the non-linearity of the materials representation, with the respective stress-strain relationship. It was adopted the FEM methodology (ANSYS program), with multi-linear diagram for the stress-strain relationship – Maggi (2004) [4], according with the Figure 4 for the bolts and steel plates, which can be simulated the plastic stage and pos-plastic effects on the steel components.



Bolts Steel plates

Figure 4: Stress-strain relationship for the bolts and steel plates.

In the concrete slab, it was adopted the stress-strain relationship showed in Figure 5 for compressive stress, according to the EUROCODE 2 (2003) [5], and shortening strain as absolute value for tension strain-stress relationship.



f_{cm} = mean value of the measured cylinder compressive strength of concrete.

ε_{c1} = strain at peak stress.

ε_{cu1} = ultimate strain in the compression

Figure 5: Stress-strain relationship for the concrete slab.

A 3D finite element was adopted for the beam, column, bolts and concrete slab components. The solid element in ANSYS software was chosen with the objective of representing volumetric elements. A 2D plastic element was adopted for the steel bars and shear connectors. The geometrical discontinuities were represented by contact elements. These elements work only when there is compression in the contact. Besides, large displacements were used in the numerical modeling. The Figure 6 illustrates the general view for beam to column composite connections with bottom and web angle and concrete slab. The Figure 7 shows the bolt meshes detail used for these analyses.

The initial stiffness of the numerical models depends on the bolts pre-load, the elastic material properties and the geometrical characteristics. The loading was applied in two phases: first a negative gradient temperature was considered to simulate the bolts pre-loaded; in a second phase, a vertical load was applied at the end of beam. The constitutive models are independent of applied temperatures and, therefore, the application of the temperature does not influence the non-linear constitutive laws.

www.EngineeringEBooksPdf.com

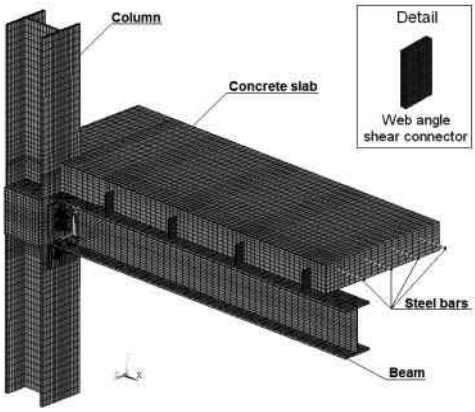


Figure 6: Complete numerical model.

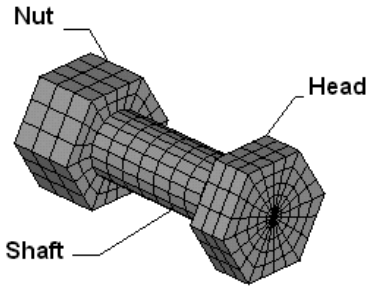


Figure 7: Bolt meshes detail.

4 RESULTS

The behavior of the beam-to-column connections crucially influences the overall frame response, which may be represented by moment-rotation (M-θ) relationship. The M-θ behaviors of numerical and experimental models are indicated in Figure 8 and Figure 9 for the single-sided and double-sided connections, respectively.

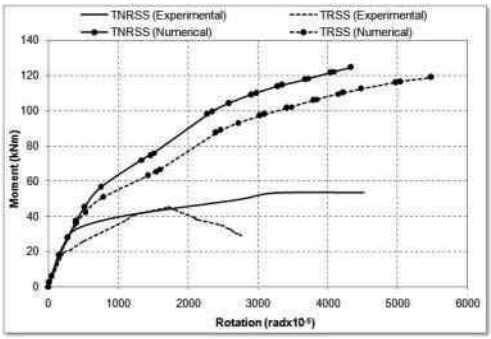


Figure 8: *M-θ* behavior for single sided connections.

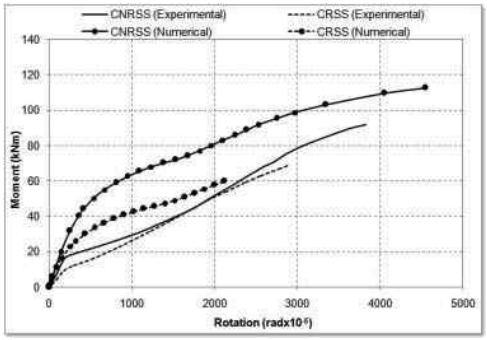


Figure 9: *M-θ* behavior for double sided connections.

Numerical initial stiffness showed a good agreement with experimental specimens, including similar results for connections with 0.2% and 1% for steel longitudinal bars ratio, with decrease of the resistant moment in the experimental specimens due to crack increasing in the slab concrete. The concrete slabs cracking next to the column are showed in the Figure 10 and Figure 11 for the TRSS and CRSS specimens, respectively.

Design value of the resistance moment of a composite section (M_{Rd}) and the initial stiffness are indicated in Table 4 for the analytical results (according to EUROCODE 3 (2005) [6]), numerical and experimental specimens. The resistance moment (M_{Rd}) corresponds to the connection maximum moment or the connection moment at the 20 rad.10^{-5} rotation.

www.EngineeringEBooksPdf.com




Figure 10: TRSS concrete slab cracking.




Figure 11: CRSS concrete slab cracking.

Table 4: General results.

Specimens	Parameter	Experimental (a)	Numerical (b)	Analytical (c)	(a)/(b)	(a)/(c)
TNRSS	M_{Rd} (kNm)	46.83	94.62	65.07	0.49	2.07
	$S_{j,ini}$ (kNm/rad)	10397.6	12143.8	12832.4	0.86	1.08
TRSS	M_{Rd} (kNm)	45.57	80.68	65.07	0.57	0.70
	$S_{j,ini}$ (kNm/rad)	8723.2	13686.79	12832.4	0.64	0.68
CNRSS	M_{Rd} (kNm)	51.81	80.04	65.07	0.65	0.08
	$S_{j,ini}$ (kNm/rad)	12835.2	14792.1	15295.1	0.87	0.48
CRSS	M_{Rd} (kNm)	50.93	59.17	65.07	0.86	0.78
	$S_{j,ini}$ (kNm/rad)	5456.5	13237.3	15295.1	0.41	0.37

According to the results, the single-sided and double-sided specimens presented reduced moment resistant due to cracking increasing in the concrete slab in the firsts steps loading. These effects can be imputed to the longitudinal steel bars anchorage no-efficiency in the isolated composite connections specimens.

On the other hand, the numerical modeling considers the effective longitudinal steel bars anchorage with, consequently, higher connection moment resistant compared with their respective specimens. The moment-rotation connection behavior can be predicted by [6], which proposed a simplified bi-linear or tri-linear design moment-rotation curve used in the frames analysis. The moment-rotation relationships are showed in the Figure 12 and Figure 13 for the single-sided and double-sided composite connections, respectively.

www.EngineeringEBooksPdf.com

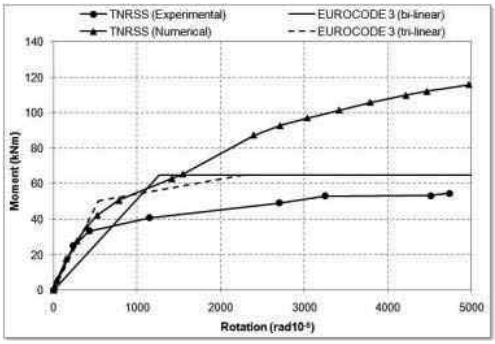


Figure 12: M-θ comparisons of single sided composite connections.

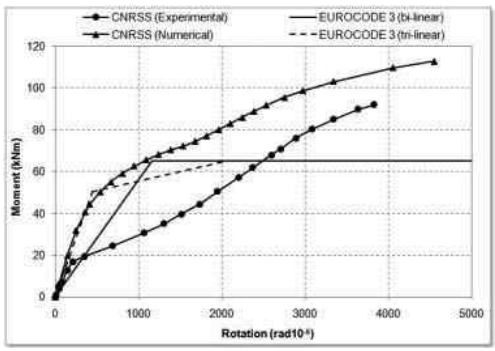


Figure 13: M-θ comparisons of double sided composite connections.

The Figure 14 illustrates the TRSS experimental prototype final displacement (numerical and experimental) at the 4.000.rad10^{-5} rotation.

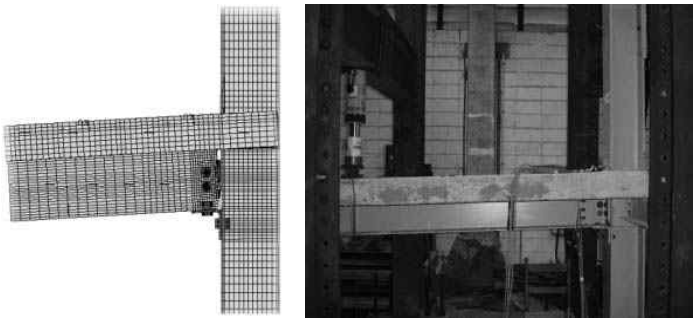


Figure 14: TRSS numerical and experimental specimen displacement at the 4.000.rad10^{-5} rotation.

www.EngineeringEBooksPdf.com

5 CONCLUSIONS

The experimental specimens of beam-to-column composite connections were described and compared with analytical results and numerical modeling. The single-sided and double-sided specimens were fabricated with precast concrete slabs with steel joist (predalles) and bricks infill.

Numerical modeling allows the development of the concrete slab cracking and local stress concentration in the concrete slab and, the interactions among concrete slab, shear connectors and longitudinal steel bars. The numerical and experimental results were compared with the analytical results; obtained by the Component Method, for the composite steel concrete connections and represented satisfactorily the plastic mechanism and the ultimate limit states.

The proposed details to the longitudinal steel bars anchorage were not effective to reduce the cracking mechanism in the isolated concrete slab specimens due to the no-beam continuity through to the column minor axis.

REFERENCES

[1] Li, T.Q; Moore, D.B; Nethercot, D.A; Choo, B.S. "The Experimental behavior of a full-scalle semi-rigidly connected composite frame: Overall considerations". *Journal of Constructional Steel Research,* **39**(3):167-91, 1996.

[2] Bessa, W. O. "Theoretical and Experimental Analysis of Beam-to-Column Composite Connections with Bottom and Web Angle – Typical Floor and Isolated Prototypes". Ph. D. Thesis, Engineering School of São Carlos, University of São Paulo, São Carlos, Brazil (in Portuguese), 2009.

[3] EUROCODE 4 prEN 1994-1-1. "Design of Steel and Concrete Structures: Part 1-1: General Rules for Buildings". European Committee for Standartization, Brussels (final Draft), 2004.

[4] Maggi, Y. I. "Analysis of the structural behavior of bolted beam-column extended end plate connections." *Ph. D. Thesis, Engineering School of São Carlos, University of São Paulo*, São Carlos, Brazil (in Portuguese), 2004.

[5] EUROCODE 2 prEN 1992-1. "Design of Concrete Structures: Part 1-1: General Rules and Rules for Buildings". European Committee for Standartization, Brussels (final Draft), 2003.

[6] EUROCODE 3. "Design of Steel Joints: Part 1-8: General Rules". European Committee for Standartization, Brussels, 2005.

[7] Leon, R.T. "Semi-Rigid Composite Construction." *Journal of Constructional Steel Research*, **25**: 99-120, 1990.

[8] Calado, L. and Castiglioni, C. A. "Steel beam-to-column connections under low-cyclic fatigue experimental and numerical research." Proceedings of XI Word Conference on Earthquake Engineering, Acapulco, Mexico, 1996.

[9] Wan, J.F and Li, G. Q. "Testing of semi-rigid steel-concrete composite frames subjected to vertical loads." *Engineering Structures*. In press, corrected proof, November, 2006.

[10] Ahmed, B. and Nethercot, D. A. "Prediction of initial stiffness and available rotation capacity of major-axis flush end-plate connections." *Journal of Constructional Steel Research*, **41(1)**: 31-60, 1997.

[11] Li, T.Q; Choo, B.S. and Nethercot, D. A. "Determination of rotation capacity requirements for the steel composite beams." *Journal of Constructional Steel Research*, **32**: 303-32, 1995.

www.EngineeringEBooksPdf.com

SDSS'Rio 2010 STABILITY AND DUCTILITY OF STEEL STRUCTURES
E. Batista, P. Vellasco, L. de Lima (Eds.)
Rio de Janeiro, Brazil, September 8 - 10, 2010

RESPONSE OF END-PLATE JOINTS UNDER COMBINED FORCES

N. Baldassino*, A. Bignardi* and R. Zandonini*

* Department of Mechanical and Structural Engineering, University of Trento
nadia.baldassino@ing.unitn.it , a_bignardi@tin.it, riccardo.zandonini@ing.unitn.it

Keywords: Robustness, Composite structures, Beam-to-column connection, Joint ductility, Load history

Abstract. *In recent years robustness assumed an important role in structural design, as the requirement to be fulfilled to prevent progressive collapse in case of accidental actions. Despite the strategies for robustness are well identified, at the moment the state of knowledge is far from being adequate for design needs. Studies have been carried on worldwide aiming at covering this gap. The senior authors were involved in a research project focused on the joint ductility as the key element to achieve a robust response of composite steel and concrete frames. This paper presents the results of a series of tests of beam-to-column steel bolted joints. The influence on the connection response of combined internal forces, of the load history and of the stiffness of the support was investigated. The main features of F.E. numerical models are also outlined, which were developed and calibrated against the experimental results as a tool for parametric analyses.*

1 INTRODUCTION

In the design process of civil and industrial buildings, the vulnerability against accidental actions has recently assumed a central role. The disasters caused by terrorist attacks, such as the collapse of the Twin Towers in 2001, have clearly pointed out the inadequacy of the traditional design approaches. They overlook the possible progressive collapse, consequent to the chain reactions activated by local damages caused by accidental actions. These critical situations call for a specific design methodology enabling verification of the safety of the structure as a whole in the statically modified condition.

The ability of a structure to withstand accidental actions without disproportionate consequences is defined as Structural Robustness. In non robust structures local damages can result in the partial or complete collapse of the structure [1], [2].

Studies of robustness started in the 60's triggered by the Ronan Point collapse in London. They allowed developing design strategies for checking robustness. Two different approaches characterised by different complexity were identified: the design against specific accidental actions and the design aimed at reducing the extent of a localised failure. The first strategy requires the design analysis of the structure against the actions associated to specific scenarios. The second strategy, which is less demanding, is based on structural design requirements to be satisfied for a minimum level of robustness to be achieved [3]. The difficulties in defining the possible design scenarios and the related loads, the complexity of the structural response and of the computational needs make difficult to transfer the general strategy into specific design rules and criteria. At this aim, a number of studies of different aspects of robustness have being carried on all around the world. The state of knowledge is actually far from being adequate for design needs.

The senior authors were involved in a research project on robustness funded by the ECSC (European Coal and Steel Community) [4]. The research, which comprises of both experimental and numerical studies, focused on the behaviour of composite steel and concrete framed structures. The experimental part of the study was designed in order to investigate the effects caused by the accidental loss of a column in a framed multi-storey office building. The reference frame was designed in accordance with the

www.EngineeringEBooksPdf.com

Eurocodes. The beam-to-column steel connections were bolted flush end-plate steel connections, while the flooring system used a solid concrete slab (Figure 1). The joint ductility was assumed as the key element of the design strategy to ensuring a robust response of the structure.

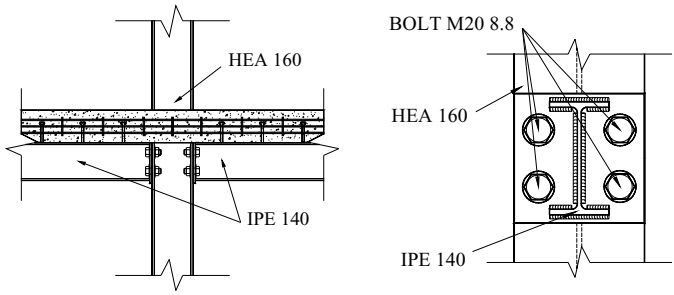


Figure 1: The investigated beam-to-column connection.

When a column is lost, a redistribution of the internal forces to the "undamaged" part of the structure occurs. This is an evolutionary phenomenon which is associated to the development of large displacements. In this context, a key role is played by the beams and the connections at the failed column. If the beams and the connections possess adequate resources in terms of resistance and ductility a catenary action can be activated allowing for the redistribution of the internal forces. Such redistribution implies the evolution of the internal forces in the beams and in the connections. At the end of the process the internal forces in the beam and the joint are substantially different from the initial ones with the axial force prevailing. Assuming the joint being the weakest component, a robust response implies that the joint possesses adequate resistance and ductility, allowing for large plastic displacements under different histories of axial force, shear force and bending moment. Fulfilment of such a requirement enables occurrence of the redistribution of the internal forces needed to reach the new equilibrium condition.

The experimental study was designed in order to investigate the behaviour of the structure at different levels. A 2-D full scale test on a sub-structure was complemented with tests on composite beam-to-column joint sub-assemblages, focused on the local performance of the joints under bending and axial force. In accordance with the philosophy of the component method, the research group of the University of Trento investigated the behaviour of the joints components in the field of large displacements when significant tensile forces build up in the floor system. The performance of both the concrete slab and the steel joint was investigated. The steel joint was analysed both at the full joint level and at the joint component level.

The tests on the joint were carried out on the full steel connection (beam and end-plate) on rigid support and on the complete steel joint (including beam and column stubs), so allowing investigation of the influence of the column's deformation on the connection response. The tests at the joint component level focus on the response of the tensile zone, which is the main source of joint deformability.

The evolution of internal actions experienced by the beam and the joint in case of the loss of a column is fairly complex, and difficult to be simulated when considering the connection in isolation. However, some interesting information on the response of the steel joint subject to combined forces (N, V, and M) can be obtained simulating a simpler load history. Therefore, tests were performed under different combination of N, V and M. Experimental results were used to develop and validate F.E. numerical models.

This paper reports the main results of the experimental study carried out on the full steel connection and joint. The key features of the numerical model are also outlined.

www.EngineeringEBooksPdf.com

2 THE EXPERIMENTAL STUDY

In framed structures the joints can play a fundamental role in ensuring a robust response. The redistribution of the internal forces and hence the activation of alternative load paths when local damage occurs requires an "adaptive capacity" of the joints to all the intermediate equilibrium configurations and up to the new and final one. The "robust design" of the joints requires checking the joint capacity to withstand the different combinations of internal actions and to sustain large displacements. The complexity of the load history and its dynamic nature further complicates joint design.

The experimental study investigated the joint performance when subject to load histories combining axial force (N), shear force (V) and bending moment (M). The loading history considered in the tests simulates in a simplified way the one a beam-to-column joint would experience in the case of sudden collapse of a column.

The specimens comprised of a beam stub made of a section IPE 140 of nominal length 950mm and a flush endplate steel connection of thickness 8mm. The end-plate was connected to two different 'supports' by means of four bolts M20 class 8.8 preloaded with a torque moment of 350Nm. The supports were either a rigid support or a column stub (HEB 160) with a length of 1000mm. This allowed investigating the influence of the column deformation on the joint response. The latter configuration will be referred to as the 'complete joint'.

For both test configurations the load was applied to the free end of the beam with an initial inclination angle (β) (Figure 2a). The nominal values of β were 0°, 11°, 20°. As soon as the load increases, a rotation of the beam occurs leading to a progressive alignment between the actuator and the beam. At collapse, it was expected the complete beam-actuator alignment if compatible with the deformation capacity of the connection/joint (Figure 2b). In this way tests under pure tension, β = 0°, and under different combinations of N, V and M were performed.

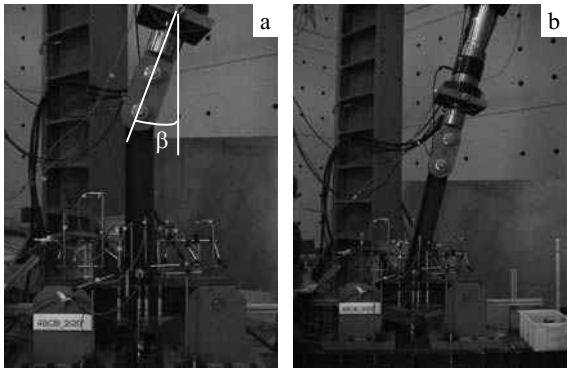


Figure 2: Test configuration for the complete joint.

A typical load history in terms of internal forces applied to the connection is plotted in Figure 3. The applied force's components (axial and shear forces) were computed with respect to the longitudinal axis of the beam in the deformed position; i.e., the force applied by the actuator was projected along the normal and the parallel directions with respect to the longitudinal beam axis. To this aim the inclination angles were measured by clinometers located on the beam web and on the actuator. The displacements of the flange at different points and of the bolts were also recorded. In the tests on the complete joint also the column deformation was measured.

In all the tests the load was applied by a hydraulic actuator in displacement control. The load history comprises of a pre-loading cycle followed by the application of the displacement at a speed of 0.015mm/s up to the collapse of the specimen.

www.EngineeringEBooksPdf.com

Tables 1 and 2 provide the values of the load and of the internal forces applied to the connection at collapse. They are related to the connection on rigid support and to the complete joint, respectively. The results show that at collapse a 'substantial' alignment between the beam and the actuator was achieved only in the case of full connection with an initial inclination angle of 11°. In the remaining tests a non negligible bending moment was still acting on the connection at failure.

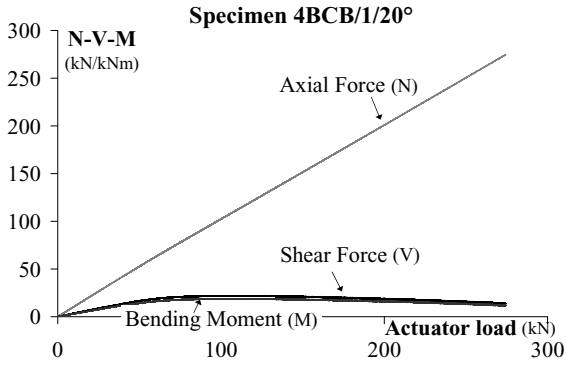


Figure 3: Internal forces at the connection vs. applied load.

Table 1: Internal forces and applied load at collapse: full connection on rigid support.

Specimen	Actuator initial angle Deg	Maximum load kN	Axial component kN	Shear component kN	Bending moment kNm
4BA/2	0°	533.840	533.840	0	0
4BB/3/11°	11°.10	453.480	453.480	-0.633	-0.537
4BB/4/11°	10°.98	441.560	441.556	1.950	1.658
4BB/1/20°	19°.51	293.640	293.299	14.139	11.998
4BB/2/20°	19°.34	307.960	307.823	9.168	7.782

Table 2: Internal forces and applied load at collapse: complete joint.

Specimen	Actuator initial angle deg	Maximum load kN	Axial component kN	Shear component kN	Bending moment kNm
4BCA/1	0°	375.520	375.520	0	0
4BCA/2	0°	382.160	382.160	0	0
4BCB/3/11°	11°.70	372.640	372.627	3.141	2.665
4BCB/4/11°	12°	383.520	383.418	8.828	7.496
4BCB/1/20°	20°	274.680	274.354	13.385	11.462
4BCB/2/20°	19°	319.880	319.831	5.583	4.745

As to the load ultimate capacity, the results in tables 1 and 2 indicate that:

- full connection on rigid support (Table 1): the connection's "loading" history affects remarkably the connection response, and the ultimate axial load capacity is significantly reduced with respect to the pure tensile condition: such a decrease is of 16% for an initial inclination angle of approximately 11°, and of 44% for an inclination angle of 20°;
- complete joint (Table 2): it appears that a moderate initial inclination of the applied load seems not to affect the joint response and performance. When the initial inclination angle increases, the influence of the joint's "loading" history becomes more important;

www.EngineeringEBooksPdf.com

- the type of support (rigid support vs. column, Table 1 vs. Table 2) remarkably affects the joint response and strength in case of tension tests and of moderate initial inclination angle. Assuming as a reference the case of connection on rigid support, the collapse load of the full joint reduces of an average of 29% and 16% in case of tension test and for an initial inclination angle of 11°, respectively.

A first appraisal of the severity of the load history applied to the connection/joint can be achieved by comparing the maximum value of the internal forces N, V and M developed in the tests to the plastic resistance of the beam V_{pl}, N_{pl}, M_{pl}. Test results showed maximum values of the ratios V/V_{pl}, N/N_{pl} and M/M_{pl} of 0.126, 0.623 and 0.609, respectively, in the case of the connection on rigid support and of 0.114, 0.527 and 0.553, respectively, in the case of the complete joint. These data indicate that tests were carried out under a 'prevailing' combination of axial force and bending moment, i.e, under loading condition similar to that developing in case of the collapse of a column. A further appraisal of the 'severity' of the loading history can be achieved by comparing the maximum bending moment applied in tests (M_{max}) with the ultimate bending moment of the joint (M_u). This one was evaluated in accordance with the simplified and conservative procedure proposed by the Eurocode 3 [5]. Tests results showed ratios M_{max}/M_u in the range 0.855-1.185 in the case of tests on rigid support, and 0.814-1.076 in the case of the tests on the complete joint. The figures greater than one may be justified by the conservativeness of the Eurocode 3 approach [5]. However, the results point out that the connection/joint in all tests was stressed under combined action at level close to its ultimate resistance.

The experimental response in all the tests was characterized by a remarkable inelastic deformation of the end-plate (Fig. 4a). Significant plastic deformation also occurred in the column flange in case of tests on the complete joints (Fig. 4b). Such inelastic deformation capacity has a key role in making the load alignment possible. A first appraisal of the joint deformation capacity as influenced by the load condition and history can be obtained by considering the average deformation of the joint zone at the maximum load. At this aim, the attention was focused on the displacement evaluated in correspondence of the axis of the beam (i.e., the geometrical centre of the connection), which are summarized in Table 3. In the case of the connection on rigid support the displacements are related to the sole end-plate, while for the complete joint the displacements take into account the contribution of both the end-plate and the column flange and web.

Table 3: Displacement in correspondence of the axis of the beam at the maximum load.

Connection on rigid support		Complete joint			
Specimen	Displacements mm	Specimen	Displacements		
			end-plate mm	web of the column mm	Total mm
-	-	4BCA/1	NA	NA	22.875
4BA/2	24.503	4BCA/2	14.225	8.880	23.105
4BB/3/11°	18.930	4BCB/3/11°	19.666	9.946	29.612
4BB/4/11°	16.419	4BCB/4/11°	19.986	9.009	28.995
4BB/1/20°	14.044	4BCB/1/20°	15.504	8.971	24.475
4BB/2/20°	15.257	4BCB/2/20°	15.895	7.074	22.969

NA: not available

In case of rigid support, the results indicate a substantial reduction of the end-plate deformation at collapse due to the presence of combined forces: the deformation capacity is reduced up to 40% for an initial inclination angle of 20°. In the case of the complete joint, it can be noted the non negligible contribution of the column to the total deformation of the joint, which represents on average the 34%. In addition, it can be observed the negligible influence of the load condition and history on the deformation of the column. The influence of the support condition can be appraised by comparing the displacement at failure of the connection and of the complete joint: in the cases of inclination angle of 11° and 20° the displacement of the complete joint is on average greater of about 65% and 62%, with respect to the case of rigid support. This is due, as expected, to the contribution of the column deformation. In the case of

www.EngineeringEBooksPdf.com

the tensile tests, the deformation is almost the same. These results should be analysed in conjunction with the maximum load reached in the tests (Table 1 and 2): the greater deformations showed by the complete joint are associated to lower collapse loads if compared with the corresponding connection on rigid support. In the case of tensile tests similar deformations are attained for a collapse load which differs of 30% on average.

Bolts were always subjected to significant bending and in all the tests the collapse was associated with the failure of the bolts (Fig. 4a-4b). However, for the specimens tested under a combination of axial and shear force cracks initiated just before failure at the toe of the weld between the beam stub and the end-plate in the more stressed zone in tension (Fig. 4c). The type of deformations observed, in the complete joints, for the end-plate and the column flange tends to increase such a bending, leading to a decrease, with respect to the connection tests on rigid support, of the ultimate loading capacity. This reduction is significant in particular for the case of pure tension. The influence of the bending of the bolts is neglected in the T-stub models usually adopted in design. The results seem hence to point out the need for deeper understanding of this issue.

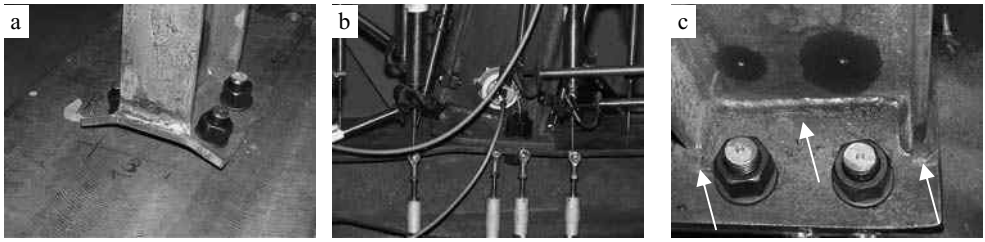


Figure 4: Deformation at collapse.

A contribution to the analysis of the 'collapse' mechanisms comes from the deformed shape of the connection at collapse. At this aim, the deformed shapes of the end-plate and of the column flange were obtained by means of a laser scanner. In order to investigate the potential collapse mechanism the data were analysed with the program Surfer [6]. In order to identify the regions of the plate characterised by strain concentration, the maximum local slope of the displacements' were computed (i.e., the 'yield lines'). The figures 5 and 6 show the slope contour maps of the end-plate associated with the tests on rigid support and on the complete joint. The figures 5a and 6a are associated to the tension tests, while the figures 5b-6b and 5c-6c are associated to tests with initial inclination angle of 11° and 20°, respectively.

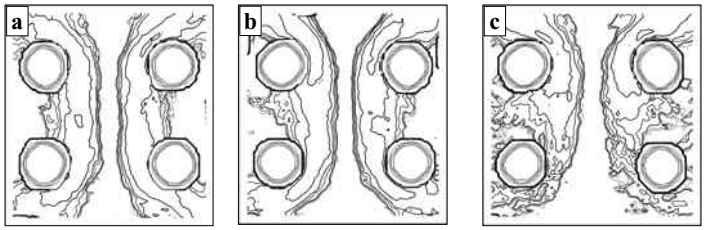


Figure 5: Slope contour map of the end-plate: connection on rigid support.

The slope contour lines identify in general a mechanism of collapse which involves two yield lines: one at the end plate-to-beam weld and a second 'connecting' the bolts. In no case, the mechanism does appear completely developed. In case of tests under combined actions the collapse mechanism still involves the bolts' area. However, the contour lines are less pronounced and get closer around the "compressed" bolt. In addition, contour lines appear in between the bolts. This effect becomes more

www.EngineeringEBooksPdf.com

evident in case of tests with an initial inclination angle of 20° (Fig. 5c and 6c). Besides, the mechanism of collapse indicated by the slope contour lines show spreading of plasticity also in between the bolts.

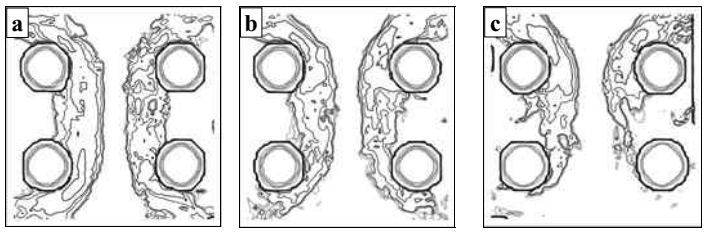


Figure 6: Slope contour map of the end-plate: complete joint.

3 THE NUMERICAL MODEL

In order to investigate in depth the complex behaviour of the connection F.E. models were developed and calibrated against the experimental results. At this aim the program ABAQUS ver. 6.8-1 [7] was adopted. The different support conditions (i.e, rigid support and column) and the different loading condition (i.e., tension tests and combined action) required the development of six F.E. models. The complexity of the models in terms of geometry and number of elements and the results of preliminary analyses suggested the use of brick linear elements type C3DR8 with reduced integration. The built up of the meshes was manually controlled allowing its refinement in correspondence of the zones of stress concentration, (i.e., the connection/joint, the bolts, the welds). The dimensions of the F.E. elements range between a minimum of 1mm, which is adopted in the connection area, to a maximum of 20mm, for the less stressed zones. The meshes comprise a minimum number of nodes of 98000 for the case of tensile tests on rigid support and a maximum of 229000 nodes in the case of the complete joints under combined action.

In order to reproduce the load history applied during the tests under combined action, for both the support conditions, the F.E. models comprise also of the actuator which was modelled as a rigid element.

Particular attention was devoted to model the contacts between the surfaces, such as the contacts between the end-plate and the support, between the bolt and the support, the nut and the washer. At this aim, a Coulomb like formulation was adopted in the form of 'finite sliding' which allows the sliding and the separation between the surfaces. The material properties were implements as true stress-true strain relationships evaluated on the basis of the results of 'ad hoc' tensile tests. The load is applied as a uniform pressure applied to the end of the beam for the case of tension tests and to the end of the rigid element which reproduce the actuator in the case of tests under combined action. Second order non linear analyses in large displacements were carried out. The load history comprised of two phases: in the first the bolts are preloaded, and in the following one the load is increased up to the collapse of the specimen. Unload to zero is then simulated so as to identify the residual plastic deformations.

For all the considered cases, the comparison between experimental and numerical results in terms of collapse load, displacements of the end-plate and of the column and residual plastic deformation shows a general good agreement. An example is shown in figure 7 which compares the slope contour maps for a complete joint with an initial inclination angle of 20° (test 4bcb/2/20°). The outcomes of the numerical analysis are on the left, while the experimental ones are on the right. The comparison proposed in figure 7 shows the good agreement of the results and points out the ability of the F.E. model in catching also the spread of plasticity in both the column flange and the end-plate.

The F.E. numerical models provide hence a useful tool for further studies of the effect of joint geometry, of mechanical properties of the steel as well as of the loading history. Preliminary analyses devoted to the investigation of the influence of the load history have been already performed. The results are at the moment under evaluation.

www.EngineeringEBooksPdf.com

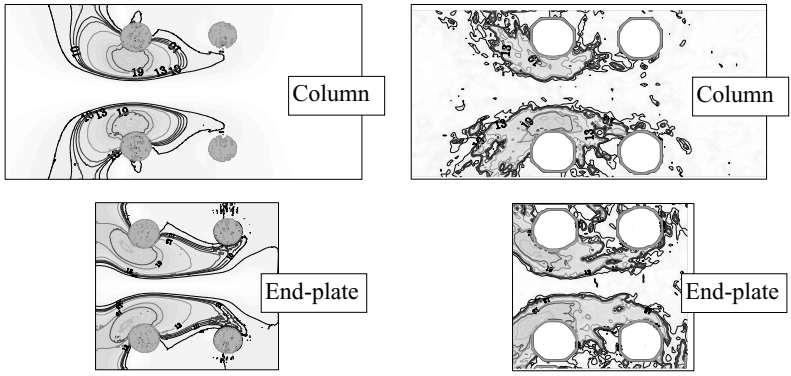


Figure 7: Slope contour lines for test on the complete joint with inclination angle of 20°.

4 CONCLUDING REMARKS

The paper presents and discusses the results of the experimental study of the performance of end-plate connections under combined forces. The tests were carried out on the sole connection on a rigid support and the complete joint, incorporating the column

Both series of tests confirmed the potential ductility of end-plate joints. However, the tests pointed out the negative influence of a loading history which combines shear, moment and axial force on both the ultimate load and deformation capacities. Besides, the importance of bolt bending is underlined. The main features of F.E. models calibrated against the experimental results were also presented. These models will provide a useful tool for extending the related knowledge via a parametric study of the effect of different geometries and mechanical properties as well as of the loading process.

ACKNOWLEDGEMENT

This research has been carried out with the financial support of the Research Fund for Coal and Steel of the European Community (Research project No. RFS-CR-04046).

REFERENCES

[1] Agarwal, J., England, J., Blockley, D., "Vulnerability Analysis of Structures", *Structural Engineering International,* IABSE, **16**(2), 124-128, 2006.

[2] Vlassis, A.G., Izzuddin, B.A., Elghazouli, A.Y., Nethercot, D.A., "Design Oriented Approach for Progressive Collapse Assessment of Steel Framed Buildings", *Structural Engineering International,* IABSE, **16**(2), 129-136, 2006.

[3] European Committee for Standardization, EN 1991-1-7, Eurocode 1 – Actions on Structures – Part 1-7: General Actions – Accidental actions, CEN, Brussels, July 2006.

[4] Kuhlmann, U., Rolle, L., Jaspart, J.P., Vassart, O., Weynand, K., Ziller, C., Busse, E., Lendering, M., Zandonini, R., Baldassino, N., Robust Structures by Joint Ductility, European Commission, Brussels, 2008.

[5] European Committee for Standardization, EN 1993-1-8, Eurocode 3 – Design of Steel Structures – Part 1-8: Design of Joints, CEN, Brussels, May 2005.

[6] Surfer® ver. 8, User Guide, Golden Software, Inc., Golden Colorado, USA.

[7] ABAQUS CAE v.6.8-1 documentation Dassaolt Systèmes Simulia Corp., Providence, RI, USA, 2008.

www.EngineeringEBooksPdf.com

SDSS'Rio 2010 STABILITY AND DUCTILITY OF STEEL STRUCTURES
E. Batista, P. Vellasco, L. de Lima (Eds.)
Rio de Janeiro, Brazil, September 8 - 10, 2010

INFLUENCE OF MEMBER COMPONENTS ON THE STRCUTURAL PERFORMANCE OF BEAM-TO-COLUMN JOINTS OF PITCHED ROOF PORTAL FRAMES WITH CLASS 3 AND 4 SECTIONS

I. Mircea Cristutiu*, Dan Dubina*

* "Politehnica" University of Timisoara-300224, Romania
e-mails: mircea.cristutiu@arh.upt.ro, dan.dubina@ct.upt.ro

Keywords: beam-to-column joints, pitched-roof portal frames, tapered-hunched members.

Abstract. *Pitched roof portal frames, largely used for industrial steel buildings are usually made of slender welded sections, characterized as low dissipative. Frame members are of variable cross-section in accordance with the stress and stiffness demand and Class 3 and/or Class 4 web section may be obtained. An extensive parametrical investigation on a significant number of beam-to-column joints for pitched roof portal frames with tapered column and hunched rafter is presented in order to establish their sensitivity in relation to the variation of different components of the joint. Different values are used for flange and web thickness in order to obtain sections of Class 3 and/or Class 4, or for the end plate (t_p=15 mm, 20 mm, 25 mm). Different steel grades are also used e.g. S235, S355 or S460. The sensitivity is analysed through main characteristics of the joint (i.e. moment capacity and stiffness). The parametric study is performed by FEM non-linear elastic-plastic analysis. The models are calibrated with experimental results. Final results concerning the joint characteristics will be compared with the results obtained through the Component method of EN 1993-1-8.*

1 INTRODUCTION

Modern industrial halls are made of steel pitched roof portal frames with slender sections of Class 3 and 4. The structural elements of the transverse frame have variable sections (e.g. tapered column and hunched rafters) in accordance with the stress and stiffness demand in component elements.

Since important axial compressive stresses develop in the rafter, an increased sensitivity to lateral-torsional instability characterizes the behavior of these members. If there are no lateral restrains, their lateral-torsional buckling strength is generally poor. However, the lateral restraining provided by the secondary structure and diaphragm effect of the envelope, significantly improve their response against buckling.

Due to the non-rectangular shape of the web of connected members, the knee joint detail is very specific. Usually bolted connection with extended end plate on the top or at the face of the column are used. Hereafter the case of the top connection will be examined.

A large parametrical investigation on a significant number of beam-to-column joints for pitched roof portal frames with tapered column and hunched rafter is presented in order to establish their sensitivity due to the variation of different components of the joint. Different grades of steel and thickness are used for the flange and in order to obtain sections of Class 3 and/or Class 4.

Moment capacity and stiffness of the joints are monitored by parametric study and advanced FEM non-linear elastic-plastic analysis is applied. The models are calibrated with experimental results. Final results concerning the joint characteristics are compared with results obtained through the component method of EN 1993-1-8.

www.EngineeringEBooksPdf.com

2 TESTING PROGRAM

2.1 Specimens for the testing program

In order to define realistic specimen configurations, a simple pitched-roof portal frame, as the one in Figure 1, was firstly designed: span 18 m, bay 6 m, height 5 m and roof angle $\alpha=8^0$. Common load cases in the Romanian design practice were taken into consideration i.e: dead load of roof cladding 0.25 kN/m^2 (γ_{ULS}=1.35); technological load 0.20 kN/m^2 (γ_{ULS}=1.35); snow load 2.0 kN/m^2 (γ_{ULS}=1.5). S355 steel frames were analyzed and designed according to the current EN 1993-1-1 rules. Finally a number of 3 frames were obtained with different cross-section classes. The thickness, width and height of the cross-section elements were changed to obtain approximately similar stiffness and stress distribution in the frame.

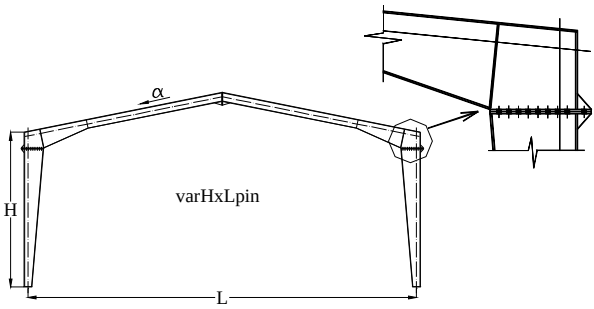


Fig. 1. Reference frame

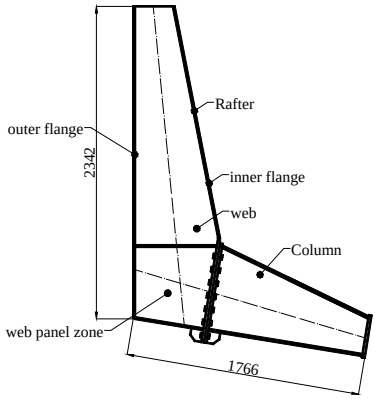


Fig. 2. Top rafter-to column joint

The three different joint configurations are: J2-3 (rafter and column of class 2 flanges and class 3 webs); J2-4 (rafter and column of class 2 flanges and class 4 webs); J3-4 (rafter and column of class 3 flanges and class 4 webs).

From design, the following joint dimensions and configurations were obtained (Table 1):

Table 1. Joint dimensions and characteristics

Joint	Column ($H*B*t_f*t_w$)	Rafter ($H*B*t_f*t_w$)
J2-3	650*240*15*8	650*200*12*8
J2-4	700*240*15*6	700*200*12*6
J3-4	700*280*12*6	700*230*10*6

where H = depth pf the section; B = width of the rafter; t_f = thickness of the flange; and t_w = thickness of the web.

Design of the joints was made using the component method in EN1993-1-8, adopted to account for significant axial force in the rafter [5]. M20-10.9 bolts and 20 mm end plates were used in all specimens.

A particular aspect of this type of joint is location of the zone of the web panel, working in shear at the end of the rafter that is bolted on the top of the column (Fig. 2).

2.2 Test set-up

Two specimens of each configuration were tested, one under monotonic and the other under cyclic loading. Figure 3 shows the loading scheme and test instrumentation.

www.EngineeringEBooksPdf.com

The tests have been conducted in displacement control procedure. Lateral restraints were applied at the points indicated in Figure 3, to avoid out of plane displacement due to inherent imperfection. Load was applied quasi-statically with a displacement velocity of 3.33 mm/min.

In order to identify the material behaviour tensile test was performed on the specimens, extracted from the tested joints. The results of the tensile tests lead to the conclusion that S275 steel grade was used by fabricator instead of S355. Therefore, from this moment on, S275 steel grade was considered.

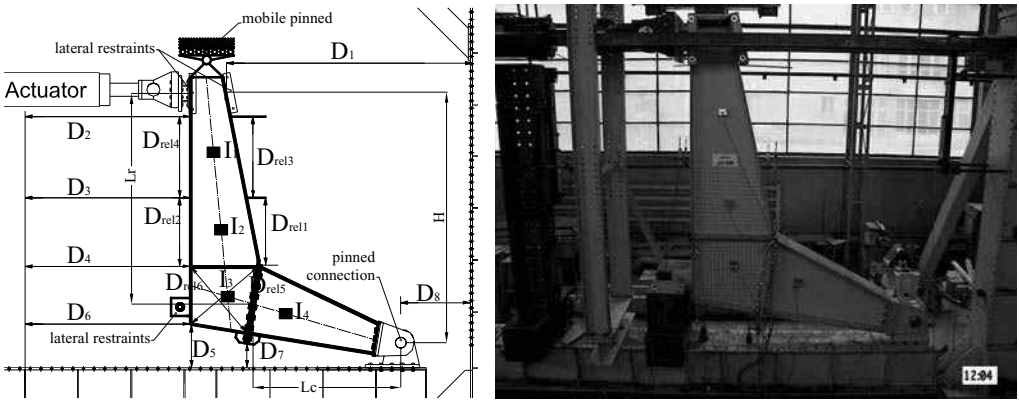


Figure 3. Loading scheme and instrumentation, where D_i = measured displacement; D_{reli} = measured relative displacement; I_i = inclinometers.

2.3 Results of the testing program

Comparative moment-rotation experimental curves for the tested specimens, under monotonic loading, are presented in Figure 4. As it can be seen, in all cases, the values of initial stiffness of the joints are very close. The failure mode is characterized by distortion of the compressed flange coupled with local buckling of the rafter web and is presented in Figure 5 for the 3 (three) different joint configurations [4].

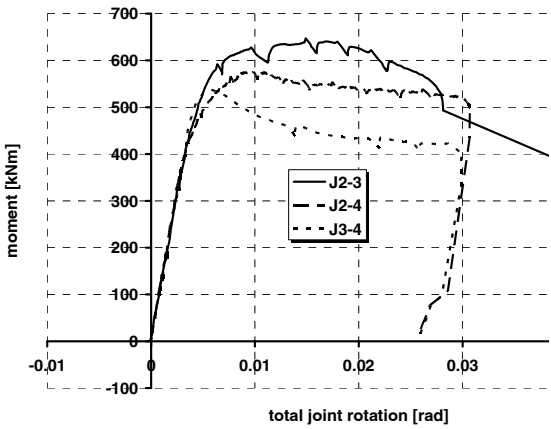


Figure 4. Comparative results from monotonic tests

www.EngineeringEBooksPdf.com



Figure 5a. Failure mode of specimen J2-3m – monotonic loading



Figure 5b. Failure mode of specimen J2-4m – monotonic loading

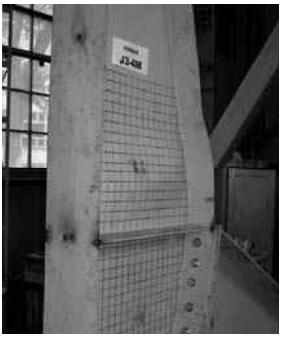


Figure 5c. Failure mode of specimen J3-4m – monotonic loading

3 NUMERICAL SIMULATION PROGRAM

3.1 FEM modeling

An advanced non-linear elastic plastic FEM model has been calibrated by using test results. With this purpose was applied Ansys computer program, using Shell 43 elements enabling for large strain plastic analysis. The initial geometrical imperfections were considered as the first eigen buckling mode of the connected elements. The material behavior was introduced by a bilinear elastic-perfectly plastic model, with a yielding limit of 275 N/mm^2. Between the end plates of the column and rafter, were used contact elements (Fig. 6a).

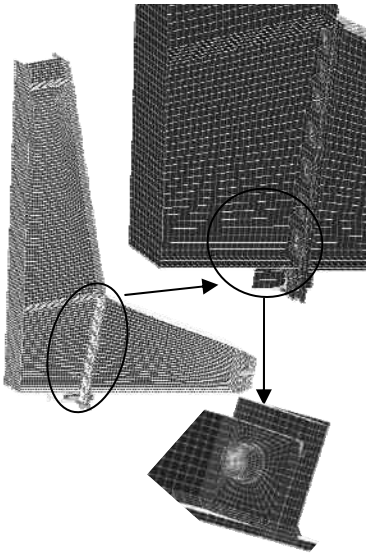


Figure 6a. FEM model

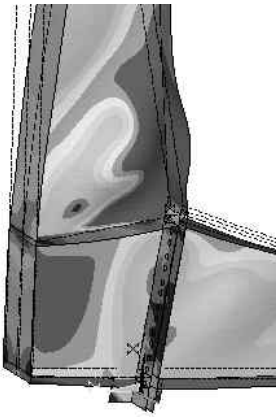


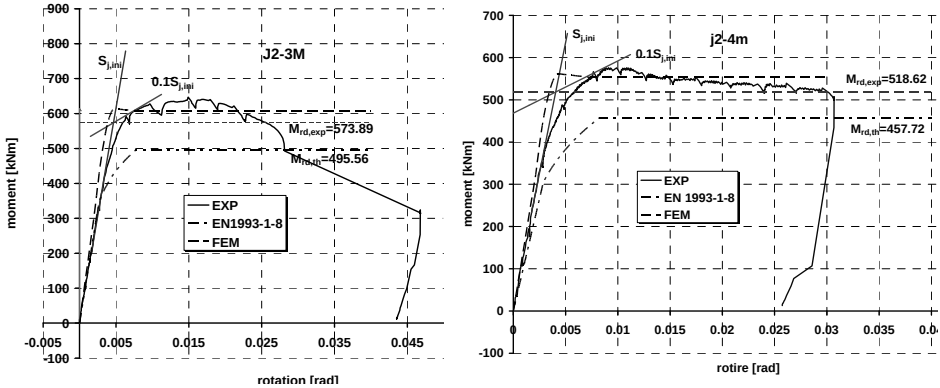
Figure 6b. Failure mode of the joint - FEM simulation



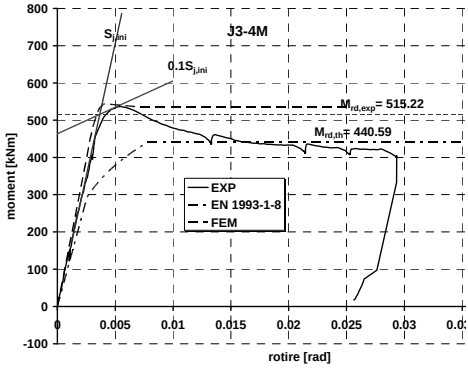
Figure 6c. Failure mode of the joint – experimental test

www.EngineeringEBooksPdf.com

The FEM analysis qualitatively shows the location of the stress concentration and the failure modes characterizing the different joint configurations. The same failure mode of the joint was identified with FEM simulation and in case of experimental tests (Fig. 5) i.e.: distortion of the compressed flange coupled with local buckling of the rafter web. A comparison between the moment-rotation curves of experimental tests, component method [5] and FEM is illustrated in Figure 7. From Figure 7 a good similarity between experimental curves and FEM simulation can be observed, regarding the capacity of the joint and its initial stiffness.



a) J2-3M b) J2-4M



c) J3-4M

Figure 7. Comparison between experimental curves, EN 1993-1-8 and FEM curves

3.2 Parametric study

It is very well known that experimental test, especially when dealing with big specimens, are time and labor consuming. An alternative to experimental test is represented by numerical simulations, where all the effects that might appear during a test should be taken into consideration.

Further on numerical simulation were made in order to determine the joint characteristic (moment and rotation capacity) and its behavior. The numerical simulations were made through nonlinear elastic-plastic analysis, using the same joint configurations as the ones for the experimental test (see Figs. 2, 3), but different steel grade, end plate thickness and different web thicknesses (6 or 8 mm) were used. The steel grades were S235, S355 and S460. Three different dimensions of the end plates were used i.e.: 15 mm, 20 mm and 25 mm, resulting finally a number of 36 analyzed cases. The dimensions of joint

www.EngineeringEBooksPdf.com

components used in the numerical simulation, for a chosen thickness of the end plate, are presented in Table 3.

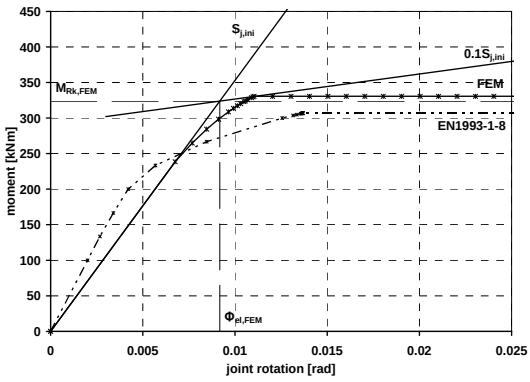
In the numerical analysis was used the same static scheme as for the experimental test (see Fig. 3).

Table 3. Main dimensions of the analysed joints

Steel grade	Joint name	Column			Rafter		
		Dimension H*b*t_f*t_w [mm]	Section class		Dimension H*b*t_f*t_w [mm]	Section class	
			flange	web		flange	web
S235	S235_650-1	650*240*15*8	2	3	650*200*12*8	2	3
	S235_650-2	650*240*15*6	2	3	650*200*12*6	2	3
	S235_700-1	700*240*15*8	2	3	700*200*12*8	2	3
	S235_700-2	700*240*15*6	2	4	700*200*12*6	2	4
S355	S355_650-1	650*240*15*8	2	3	650*200*12*8	2	3
	S355_650-2	650*240*15*6	2	3	650*200*12*6	2	3
	S355_700-1	700*240*15*8	2	3	700*200*12*8	2	3
	S355_700-2	700*240*15*6	2	4	700*200*12*6	2	4
S460	S460_650-1	650*240*15*8	2	3	650*200*12*8	2	3
	S460_650-2	650*240*15*6	2	3	650*200*12*6	2	3
	S460_700-1	700*240*15*8	2	3	700*200*12*8	2	3
	S460_700-2	700*240*15*6	2	4	700*200*12*6	2	4

3.2 Comparative analysis

Determination of the moment capacity of the considered connections was made according to the ECCS recommended procedure [6], as the one from Figure 8a. The obtained results via FEM and numerical analysis, expressed in terms of, moment capacity ($M_{Rk,FEM}$) and moment capacity ($M_{Rk,th}$) of the joint evaluated by means of component method, are presented in Figure 9 (a, b,c) for the three material types (i.e. S235, S355, S460). If the values of moment capacity obtained by FEM simulation, $M_{Rk,FEM}$, are taken as reference, one concludes that in almost all cases the results obtained with the component method are on the safe side.



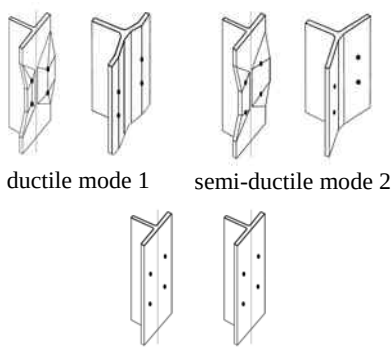
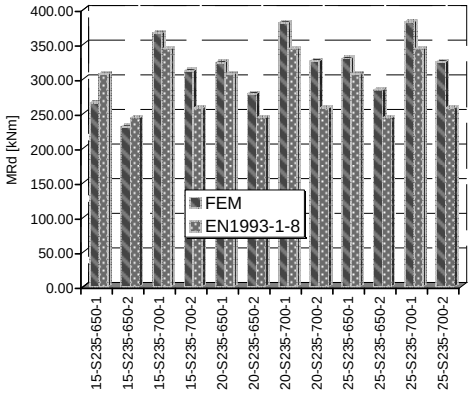
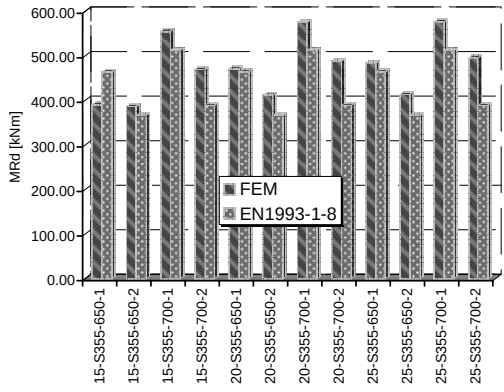


Figure 8. a) ECCS procedure for determining of $M_{Rk,FEM}$ and $\Phi_{el,FEM}$ (case of 20_S235_650-1); b) theoretical failure modes of actual components and equivalent T-stub [2]

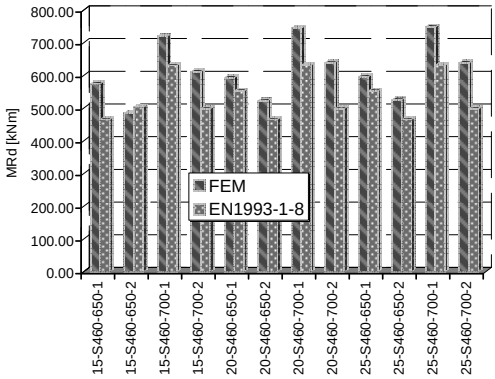
www.EngineeringEBooksPdf.com



a) S=235 N/mm^2



b) S=355 N/mm^2



c) S=460 N/mm^2

Figure 9. Comparative results $M_{Rk,FEM}$ and $M_{Rk,th}$ for different steel grades. a) S235; b) S355; c) S460

Comparative results between moment capacity evaluated with FEM ($M_{Rk,FEM}$) and the theoretical one ($M_{Rd,th}$) of the joints having a 20 mm thickness end plate, are illustrated in Figure 10.

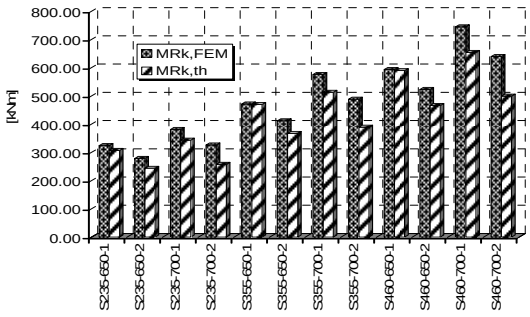


Figure 10. Comparative results (t_p=20 mm) $M_{Rk,FEM}$ and $M_{Rk,th}$

www.EngineeringEBooksPdf.com

4 CONCLUSIONS

A large number of rafter-to-column joints were analysed in order to determine the influence of the changing of one of the following parameters: steel grade, web thickness, end plate thickness and height of the cross-section, all joints are of full strength and perfectly rigid. Finite element models were calibrated with experimental test carried out at the CEMSIG [4] (http://cemsig.ct.upt.ro) research centre of the Politehnica University of Timisoara. The results obtained analytically were compared, thereafter, with the ones obtained via Component Method of EN1993-1-8 [2].

The same failure mode was obtained in all cases, i. e. distortion of the compressed flange coupled with local buckling of the rafter web (see Fig. 5), even changes in height of the cross-section and thickness of the web was performed. The ductile failure mode of type 1 (Figure 8b. [2]), with the plastic bending of end plate was recorded for the 15 mm thick end plate, while semi-ductile mode 2 and the brittle one mode 3, was recorded for 20 mm and 25 mm thick end plates, respectively. However the change of the end plate thickness from 20 to 25 mm in the procedure of EN1993-1-8, doesn't influence the final capacity of the joint. This might be explained by the identified failure mode that takes place in the connected elements. For this particular detail of the joint, case of the end plate extended towards interior for head-to-head welding preparation with the rafter flange, there must be paid attention for the variation of the thickness of the end plate. The obtained results confirmed the previous observation; lower moment capacity in case of lower thickness was obtained.

For the same steel grade, the height of the cross sections has the most significant influence on the moment capacity of the joint. The initial stiffness of the joint is not significantly influenced by the chosen parameters (steel grade, end plate thickness, and cross section height and web thickness). The difference in the moment capacity of the joint, between elements of class 3 and class 4, increases by increasing the steel grade.

REFERENCES

[1] EN 1993-1.1: Eurocode 3: Design of Steel Structures. Part 1.1: General rules and rules for buildings, may 2005, CEN, Brussels, Belgium;

[2] EN 1993-1.8: Eurocode 3: Design of Steel Structures. Part 1.8: Design of joints, may 2005, CEN, Brussels, Belgium;

[3] ECCS 1985 Recommended testing procedures for assessing the behaviour of structural elements under cyclic loads. European Convention for Constructional Steelwork (ECCS) 1985, Tchn. Comm. 1, TWG 13-Seismic design, No. 45;

[4] Cristuţiu I.M., Dubină D., Stratan A. şi Grecea D., - "Moment-rotation characteristics of bolted beam-to-column connections of pitched-roof portal frames with class 3 and 4 sections". *Proc. of Steel Structures in Seismic Area STESSA-2006*, F. Mazzolani and A. Wada (eds.), CRC Press, Taylor&Francis Group, 291-298, 2006

[5] Cerfontaine F. (2003), "Etude de l'interaction entre moment de flexion et effort normal dans les assemblages boulonnes" *PHd Thesis*. Universite de Liege, Faculte des Science Appliquees 2003.

[6] ECCS 1985 Recommended testing procedures for assessing the behavior of structural elements under cyclic loads. European Convention for Constructional Steelwork (ECCS) 1985, Tchn. Comm. 1, TWG 13-Seismic design, No. 45;

www.EngineeringEBooksPdf.com

SDSS'Rio 2010 STABILITY AND DUCTILITY OF STEEL STRUCTURES
E. Batista, P. Vellasco, L. de Lima (Eds.)
Rio de Janeiro, Brazil, September 8 - 10, 2010

APPLICATION OF EUROCODE 3 TO STEEL CONNECTIONS WITH FOUR BOLTS PER HORIZONTAL ROW

J.-F. Demonceau*, K. Weynand, J.-P. Jaspart*** and C. Müller******

* Department Argenco, University of Liège, Belgium – in post-doctoral training at RWTH Aachen University, Germany
e-mail: jfdemonceau@ulg.ac.be

** Feldmann + Weynand GmbH, Aachen, Germany
e-mail: k.weynand@fw-ing.de

*** Department Argenco, University of Liège, Belgium
e-mail: Jean-Pierre.Jaspart@ulg.ac.be

**** Institute for Steel and Light Weight Structures, RWTH Aachen University, Germany
e-mail: mul@stb.rwth-aachen.de

Keywords: Joints, Connections, 4 bolts per row, Component method.

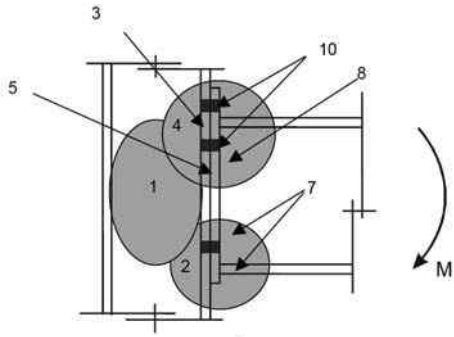
Abstract. *Eurocode 3 Part 1-8 provides detailed application rules for the design of bolted end-plate connections. Although these rules apply to connections with any number of bolt rows, they are limited to configurations with two bolts in each row. However, it is sometimes more economical to place four bolts in one row. This configuration is commonly met in different countries in Europe and, in particular, in Germany. The theoretical model on which the Eurocode 3 application rules are founded is general and can be potentially applied to connections with four bolts per row. However, specific design rules need to be developed. In the present paper, easy-to-apply analytical design rules aimed at predicting the mechanical properties of connections with four bolts per row and in full agreement with the Eurocode 3 approach are detailed. Validations through comparisons to experimental test results recently performed in the framework of a German national project are also presented.*

1 INTRODUCTION

The analytical model recommended in the Eurocodes to characterise the mechanical properties of a joint is founded on the "component method" which is, nowadays, a widely recognised procedure for the evaluation of the design properties of structural joints. This method applies to any type of steel or composite joints, whatever the geometrical configuration, the type of loading (axial force and/or bending moment, ...) and the type of member sections. This method considers any joint as a set of individual basic components. For the particular joint shown in Figure 1 (steel joint configuration with an extended end-plate connection subjected to hogging bending moments), the relevant components are given.

Each of these basic components possesses its own strength and stiffness either in tension, in compression or in shear (spring model – see Figure 1). The column web is subjected to coincident compression, tension and shear. The coexistence of several components within the same joint element can obviously lead to stress interactions that are likely to decrease the resistance of the individual basic components; such interactions are taken into account within the method.

www.EngineeringEBooksPdf.com



Zones	Components
Shear zone	1. Column web panel in shear
Compression zone	2. Column web in compression
	7. Beam flange and web in compression
Tension zone	3. Column flange in bending
	4. Column web in tension
	5. End-plate in bending
	8. Beam web in tension
	10. Bolts in tension

Figure 1: Steel joint with an extended end-plate connection subjected to hogging moments – Identification of the activate components – Spring model.

The application of the component method requires the following steps:

- identification of the active components in the joint being considered;
- evaluation of the stiffness and/or resistance characteristics for each individual basic component (specific characteristics - initial stiffness, design resistance, ... - or the whole load-deformation curve);
- assembly of all the constituent components and evaluation of the stiffness and/or resistance characteristics of the whole joint (specific characteristics - initial stiffness $S_{j,ini}$, design resistance $M_{j,Rd}$, ... - or the whole moment-rotation curve).

The assembly procedure consists in deriving the mechanical properties of the whole joint from those of all the individual constituent components. This requires a preliminary distribution of the forces acting on the joint into internal forces acting on the components in a way that satisfies equilibrium. In Eurocode 3 [1], an analytical assembly procedure is described for the evaluation of the initial stiffness $S_{j,ini}$ and the design moment resistance $M_{j,Rd}$ of steel joints. The application of the component method requires a sufficient knowledge of the behaviour of the basic components; as previously mentioned, most of the proposed design rules in the Eurocodes only cover joints with two bolts per row.

The components which are the most affected by the presence of four bolts instead of two are the components in bending, i.e. the "column flange in bending" and the "end-plate in bending". In the following paragraph, the characterization of these components with four bolts per row is investigated in details.

2 COMPONENTS IN BENDING WITH FOUR BOLTS PER ROW

2.1 T-stub model

The design rules for these components, as suggested in the Eurocodes, are founded on the "T-stub approach", firstly introduced by Zoetemeijer [2]. This approach consists in substituting to the tensile part of the connection by T-stub sections of appropriate effective length l_{eff}, connected by their flange onto a presumably infinitely rigid foundation and subjected to a uniformly distributed force acting in the web plate (Figure 2).

www.EngineeringEBooksPdf.com

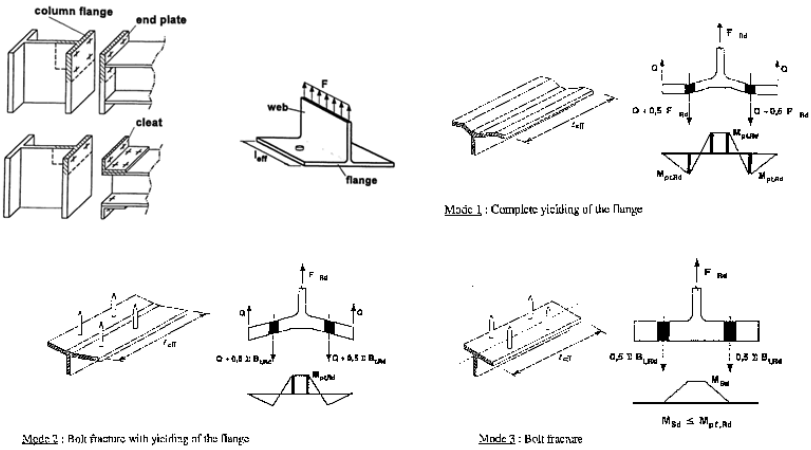


Figure 2: T-stub idealization and possible failure modes.

Through this approach, three different failure modes may be identified (Figure 2):

- Onset of a yield lines mechanism in the plate before the strength of the bolts is exhausted (Mode 1);
- Bolt fracture without prying forces, as a result of a very large stiffness of the plate (Mode 3) and;
- Mixed failure involving yield lines – but not a full plastic mechanism – in the plate and exhaustion of the bolt strength (Mode 2).

Within the Eurocodes, formulas to predict the design resistance of a T-stub flange with two bolts per row are given for each failure mode; the latter have been extended to T-stub configurations with four bolts per row (see Figure 3) in [3] and are reported in Table 1. Within this table, it can be observed that the formulas for Mode 1 and 3 remain unchanged; only the one related to Mode 2 is influenced by the "four bolts" and has to be adapted. This conclusion applies as long as the formulas are derived from a rigid-plastic theory; the latter may be fully justified for T-stubs with 2 bolts per row while it could possibly lead to unconservative results for T-stub with 4 bolts. For this reason, in [5], $F_{Rd,3}$ is limited to $0{,}9.\sum B_{t,Rd}$ according to [6] and [7]. Deeper investigations of this aspect are presently performed amongst the authors.

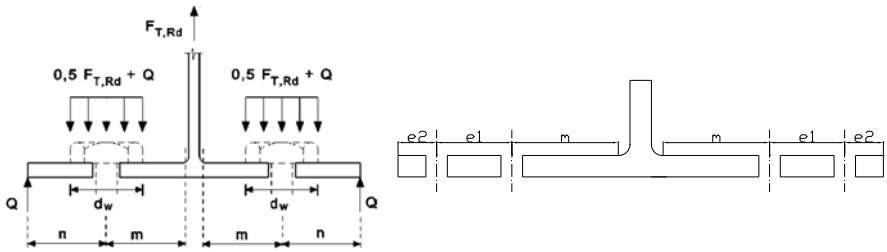


Figure 3: Definitions of the parameters for T-stubs with two or four bolts.

www.EngineeringEBooksPdf.com

Table 1: Formulas to predict the design resistance of T-stubs for each possible failure mode.

Failure modes	**T-stub with 2 bolts**	**T-stub with 4 bolts**
Mode 1	$F_{Rd,1} = \frac{(8n - 2e_w)M_{pl,1,Rd}}{2mn - e_w(m+n)}$	$F_{Rd,1} = \frac{(8n - 2e_w)M_{pl,1,Rd}}{2mn - e_w(m+n)}$
Mode 2	$F_{Rd,2} = \frac{2M_{pl,2,Rd} + n\sum B_{t,Rd}}{m+n}$	$F_{Rd,2} = \min(F_{Rd,2,p}; F_{Rd,2,np})$ with $F_{Rd,2,p} = \frac{2M_{pl,2,Rd} + \frac{\sum B_{t,Rd}}{2}.(\frac{n_1^2 + 2n_2^2 + 2n_1n_2}{n_1+n_2})}{(m+n_1+n_2)}$ and $F_{Rd,2,np} = \frac{2M_{pl,1,Rd} + \frac{\sum B_{t,Rd}}{2}.n_1}{(m+n_1)}$
Mode 3	$F_{Rd,3} = \sum B_{t,Rd}$	$F_{Rd,3} = \sum B_{t,Rd}$ (but limited in practice to $0{,}9\sum B_{t,Rd}$ ([6] & [7])

With:

- m defined in [1] (see Figure 3);
- $e_w = d_w/4$ (see Figure 3);
- $\Sigma B_{t,Rd}$ sum of the design resistances of the bolts connecting the T-stub to the rigid foundation;
- $M_{pl,1,Rd} = 0{,}25 l_{eff,1} t_f^2 f_y / \gamma_{M0}$;
- $M_{pl,2,Rd} = 0{,}25 l_{eff,2} t_f^2 f_y / \gamma_{M0}$;
- t_f the thickness of the T-stub flange;
- f_y the yield strength of the T-stub steel;
- $l_{eff,1}$ minimum effective length associated to circular or non-circular patterns (see next paragraph);
- $l_{eff,2}$ minimum effective length associated to non-circular patterns (see next paragraph)
- For T-stub with 2 bolts, n is defined in Figure 3 with $n \leq 1{,}25m$;
- For T-stub with 4 bolts, $n = e_1 + e_2$ (see Figure 3) with $n \leq 1{,}25m$, $n_1 = e_1$ and $n_2 = e_2$ with $n_2 \leq 1{,}25m + n_1$.

For the T-stub approach, the definition of accurate effective lengths is required; the values of the latter are mainly linked to the plastic mechanisms (made of plastic yield lines) which could developed within the considered component. Tables with analytical formulas to compute the latter are proposed in Eurocode 3 for an end-plate or a column flange with two bolts per row [1]. For the joint configuration with four bolts per row, the definition of such effective lengths was not available; it is the subject of the following paragraph.

2.2 Computation of the effective lengths for components in bending with four bolts per row

The presence of four bolts per row instead of two influences the development of the plastic yield lines within the components in bending. In Table 2, a summary of the analytical formulas to predict these effective lengths is given for outer bolt rows and inner bolt rows (see Figure 4), both for circular and non-circular yield patterns as defined in Eurocode 3 [1]; these formulas are based on the ones defined in [4]

www.EngineeringEBooksPdf.com

for joints with two bolts per row. The parameters which are used in the formulas presented here below are defined in Figure 4; the computation of m_x, m_1, m_2 and α has to be performed in agreement with the Eurocode recommendation [1].

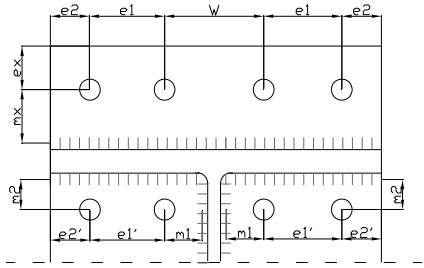
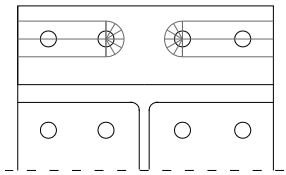


Figure 4: Definition of the parameters used in the computation of the effective lengths.

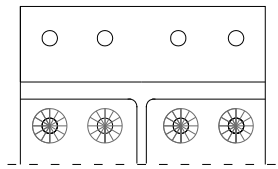
Table 2: Analytical formulas to predict the effective lengths for outer and inner bolt rows.

	Circular patterns	**Non-circular patterns**
	$l_{eff,c} = \min\left[l_{eff,I}; l_{eff,II}; l_{eff,III}; l_{eff,IV}\right]$	$l_{eff,nc} = \min\left[l_{eff,V}; l_{eff,VI}; l_{eff,VII}; l_{eff,VIII}; l_{eff,IX}\right]$
Outer bolt row	$l_{eff,I} = 4\pi m_x$	$l_{eff,V} = 2m_x + 0{,}625e_x + (e_1 + e_2)$
	$l_{eff,II} = \pi m_x + w + 2e_1$	$l_{eff,VI} = 4m_x + 1{,}25e_x + e_1$
	$l_{eff,III} = 2(\pi m_x + e_1)$	$l_{eff,VII} = 2m_x + 0{,}625e_x + e_1 + 0{,}5w$
	$l_{eff,IV} = \pi m_x + 2(e_1 + e_2)$	$l_{eff,VIII} = 0{,}5(2e_1 + 2e_2 + w)$
		$l_{eff,IX} = 8m_x + 2{,}5e_x$
Inner bolt row	$l_{eff,c} = l_{eff,X} = 4\pi m_1$	$l_{eff,nc} = l_{eff,XI} = \alpha m_1$

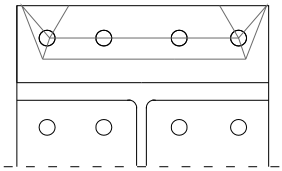
Some examples of possible yield patterns for the considered bolt rows are illustrated in Figure 5; all the possible yield patterns are described in details in [3].



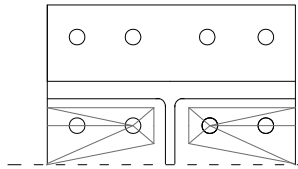
Outer bolt row – circular pattern



Inner bolt row – circular pattern



Outer bolt row – non-circular pattern



Inner bolt row – non-circular pattern

Figure 5. Examples of possible plastic yield patterns for outer and inner bolt rows with four bolts per row.

www.EngineeringEBooksPdf.com

It is important to notice that a fundamental difference exists in the definition of the equivalent T-stub for the outer and inner bolt rows:

- for an outer bolt row, the T-stub to be considered is a T-stub with two bolts (the T-stub web is the beam flange); the presence of four bolts within this row only influence the values of the effective lengths.
- for an inner bolt row, the T-stub to be considered is a T-stub with four bolts (the T-stub web is the beam web).

With the so-defined effective lengths and the resistance formulas presented in the previous paragraph, it is possible to apply the component method to connections with four bolts per row. This analytical model is validated in the following paragraph.

3 VALIDATION OF THE PROPOSED ANALYTICAL MODEL

Within the German national project AiF-Projekt 15059 [5], tests on connections with four bolts per row were performed at the University of Dortmund and the proposed analytical model was validated trough comparisons with these experimental results. This validation is briefly described here after.

3.1 Experimental tests performed in Dortmund

In total, 24 experimental tests on beam splices with end-plate connections with four bolts per row were performed at the University of Dortmund [5]. The tested specimens are illustrated in Figure 6. The parameters which were varied are (each configuration was tested twice):

- the number of bolt rows:
  - flush end-plate connection (Type A), i.e. without an outer bolt row and;
  - extended end-plate connection (Type B), i.e. with an outer bolt row.
- the thickness of the end-plate: 10 mm or 20 mm and;
- the width of the beam flange: 125 mm, 170 mm or 220 mm.

Table 3 summarizes the tested joint configurations with their associated name. The testing setup is presented in Figure 6. All the measurements performed during the experimental tests were made available by the University of Dortmund. These results were analysed in details and moment-rotation ($M - \phi$) curves of the joints were derived for each test. The latter were used to validate the analytical model.

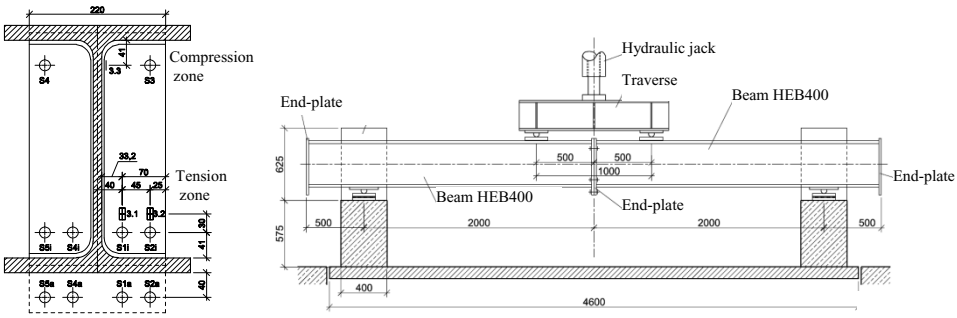


Figure 6: Tested connection configuration (with or without outer bolt row) and testing setup [5]

www.EngineeringEBooksPdf.com

Table 3. Experimental test campaign

	Flush end-plate (Type A)				**Extended end-plate (Type B)**			
	End-plate thickness				*End-plate thickness*			
Flange width	*10 mm*		*20 mm*		*10 mm*		*20 mm*	
220 mm	A01-1	A01-2	A04-1	A04-2	B01-1	B01-2	B04-1	B04-2
170 mm	A02-1	A02-2	A05-1	A05-2	B02-1	B02-2	B05-1	B05-2
125 mm	A03-1	A03-2	A06-1	A06-2	B03-1	B03-1	B06-1	B06-2

3.2 Analytical predictions vs. experimental results comparisons

The analytical predictions have been performed using the component method with the proposed modifications. The mechanical properties of the materials used in the analytical model are the actual ones, i.e. those obtained through coupon tests without safety coefficients. For the geometrical properties, the nominal ones have been used as the actual dimensions of the specimens (measured in Dortmund) were in very good agreement with the nominal ones. The analytical predictions have been compared to all the test results. Some comparisons are illustrated in Figure 7; the others are reported in [3].

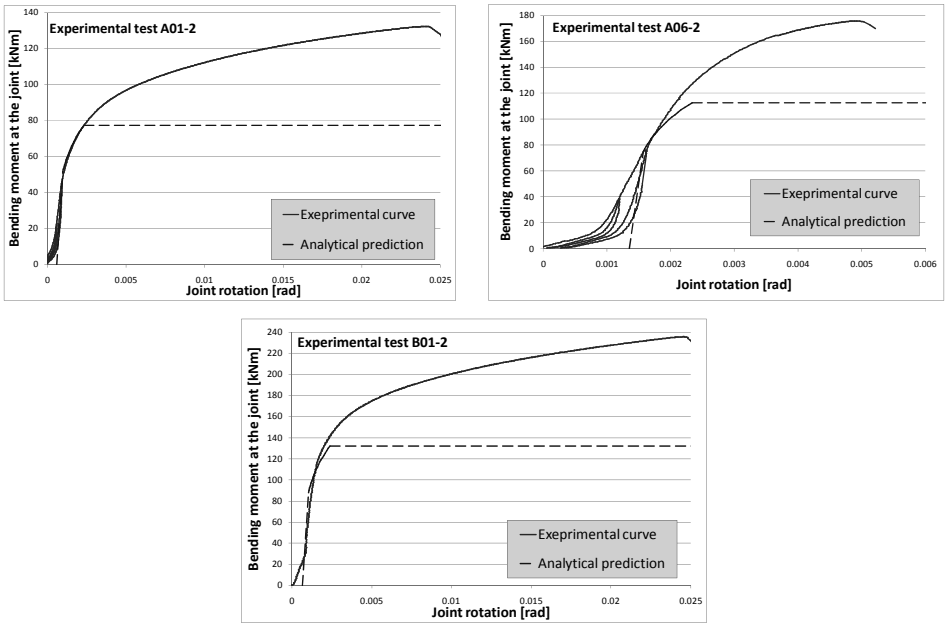


Figure 7. Examples of comparisons between analytical predictions and experimental results

Through the performed comparisons, it is observed that the analytical model gives an accurate prediction of the initial stiffness and the plastic resistance of the joints for most of the tested specimens. It is also the case for the other comparisons reported in [3]. The predicted resistant moments are close to the experimental ones (and always on the safe side) for all the tests and the computed initial stiffness are quite similar to the ones observed through the experimental curves. The curves representing the experimental behaviour of the tested joints show slip and settlements of the test setup. Obviously, for the comparison of analytical curves with the experimental curves these initial deformations must not be taken into account.

www.EngineeringEBooksPdf.com

4 CONCLUSIONS

Eurocode 3 Part 1-8 provides detailed application rules for the design of bolted end-plate connections; most of them are limited to configurations with two bolts only in each horizontal row. However, it is sometimes more economical to place four bolts in one row, for instance when wide flange H-sections are used. This configuration is commonly met in some different countries and, in particular, in Germany where this configuration is even standardized.

Within the present article, an analytical method able to predict the response of connections with four bolts per row and in full agreement with the rules recommended in the Eurocodes has been presented and validated. In particular, the effects of the presence of four bolts per row on the T-stub model have been described and new analytical formulas have been proposed (i) for the definition of the possible effective lengths and (ii) to predict the failure modes for T-stub with four bolts. The proposed analytical method has been validated through comparisons to experimental tests performed at the University of Dortmund. Through the performed comparisons, it was demonstrated that the analytical model is able to predict with a relatively good accuracy the resistant moment and the initial stiffness of connections with four bolts per row; in particular, the analytically predicted resistant moment is always on the safe side.

The proposed model based on the component method is universal and could be easily extended to other types of connections with four bolts per row than the ones considered in the presented study (connections with stiffeners between the bolts, connections with bolt rows which are close and in which group effects may develop, …).

ACKNOWLEDGEMENT

The AIF project 15059 [5] has been funded by the German Ministry for Economy and Technology (Bundesministerium für Wirtschaft und Technologie – BMWi).

REFERENCES

[1] EN 1993-1-8. Eurocode 3: Design of steel structures – Part 1-8: Design of joints. European committee for standardization, May 2005.

[2] Zoetemeijer P., “A design method for the tension side of statically loaded bolted beam-to-column connections”, Heron, Delft University, Vol. 20, n° 1, 1974.

[3] Demonceau J.-F., Weynand K., Jaspart J.-P., Müller C., “Analytical model to characterize bolted beam-to-column joints with four bolts per row”, Interim report to [5].

[4] Jaspart J.-P., “Contribution to recent advances in the field of steel joints. Column bases and further configurations for beam-to-column joints and beam splices”, Thèse d’agrégé de l’enseignement supérieur, Liège University, 1997.

[5] Ungermann D., Weynand K., Müller C., Oberegge O., et al.: AiF-Projekt 15059 N/2 “Entwicklung eines Bemessungsmodells für geschraubte, momententragfähige Kopfplattenverbindungen mit 4 Schrauben in einer Schraubenreihe auf der Grundlage der *EN 1993-1-8”*. Daft Final report, February 2010.

[6] Petersen, Ch.: “Stahlbau: Grundlagen der Berechnung und baulichen Ausbildung von Stahlbauten, Vieweg-Verlag, Braunschweig, 1993.

[7] Oberegge, O. et al.: Bemessungshilfen für profilorientiertes Konstruieren, Stahlbau-Verlagsgesellschaft, 3rd edition, Köln, 1997.

www.EngineeringEBooksPdf.com

SDSS'Rio 2010 STABILITY AND DUCTILITY OF STEEL STRUCTURES
E. Batista, P. Vellasco, L. de Lima (Eds.)
Rio de Janeiro, Brazil, September 8 - 10, 2010

A NEW HYBRID TESTING PROCEDURE FOR THE LOW CYCLE FATIGUE BEHAVIOR OF STRUCTURAL ELEMENTS AND CONNECTIONS

Carlo Andrea Castiglioni*, Alberto Drei* and Roberto Goncalves **

* Structural Engineering Department, Politecnico di Milano, Italy
e-mails: castigli@stru.polimi.it, drei@stru.polimi.it

** Escola São Carlos, Universidade de São Paulo, Brasil
e-mail: goncalve@sc.usp.br

Keywords: Low Cycle Fatigue, Testing Procedure, Cumulative Displacement, Collapse Load.

Abstract. *The current test recommendations adopted for the assessment of low cycle fatigue of steel building elements and detail are briefly described, and some disadvantage and incompleteness of these procedures are discussed, particularly in what regards the ultimate bearing capacity and the difficulty to represent the cumulative displacement behavior of elements and details in one direction. In order to overcome these problems, a new testing procedure is proposed, whose aim is to take explicitly into account the actual exercise load and its influence on the cyclic behaviour, particularly for the cumulative displacements, and on the effective collapse condition. The proposed cyclic test is a hybrid procedure where the sequence of reversed cycles have an initial force-controlled part, up to the applied vertical load, and a final displacement-controlled part.*

1 INTRODUCTION: TYPES OF CYCLING TESTING

To characterize or to model a structural element or a structural detail for which the expected load condition is characterized by a cyclic loading history with known or unknown amplitude as, for instance, for a structure in seismic area, a *Cyclic Test* is necessary.

Dynamic Tests with shaking machines or shaking tables simulate effectively dynamic loads or seismic events, but they are generally very expensive. *Pseudo-Dynamic Tests*, characterized by the application of variable step-by-step static forces in order to simulate the dynamic behaviour, provide a realistic seismic simulation using an equipment considerably less expensive than the shaking table, but are suitable only for structures that can be easily modelled with a few degrees of freedom (one or two storey frames, etc.) A *Quasi-Static Cyclic Test,* whose apparatus is the most common in research laboratories, is less suitable to simulate seismic load conditions, but it is simple and less expensive.

2 LOW CYCLE FATIGUE TESTING: STATE OF THE ART

In order to assess the state of the art on low cycle fatigue testing of structural elements, a research was done through the Internet, the Scopus search engine (web-based abstract and citation database provided by Elsevier) and through the proceedings of the World Conferences on Earthquake Engineering and other Conferences. The research, limited to the last 20 years, resulted in about 200 articles/papers found, the majority of them from European or North American universities, and a significant number from Japan. Two official procedures seem to be mainly used: the 1986 European ECCS-45 (European Convention For Constructional Steelwork "*Recommended Testing Procedure for Assessing the Behaviour of Structural Steel Elements under Cyclic Loads)* and the six years younger North-American ATC-24 (Applied

www.EngineeringEBooksPdf.com

Technology Council-24 *"Guidelines For Cyclic Seismic Testing of Components of Steel Structures")*. Moreover some recent papers adopt the new procedures from ANSI, mainly ANSI/AISC 341s1-05 appendix S of November 2005. There is also a more recent testing protocol, FEMA 461 (June 2007) *Interim Testing Protocols for Determining the Seismic Performance Characteristics of Structural and Non-structural Components.* Nevertheless many papers, especially from Japanese authors, don't indicate explicitly an official procedure, but apply loading histories defined in the paper, generally similar to the ECCS or ATC-24 protocols. The majority of the structural elements tested are beam-to-column connections. The other elements tested are heterogeneous, with particular relevance to the testing of composite columns and to the cyclic behavior of braces.

3 GEOMETRY OF SPECIMENS

To achieve an adequate knowledge of the cyclic structural behaviour of a steel structure by means of quasi static testing, the first step is to define the "minimum sub assemblage" that should be tested. For a framed steel structure, the minimum sub-assemblage is a two storey (two bays and two naves) spatial frame, with concrete slabs at each floor level. This specimen contains beams, columns, two, three and four ways beam-to-column joints and can be loaded vertically, to simulate gravity loads, and horizontally, to simulate earthquake loading. It is a complete specimen, but it can be tested only in special circumstances. A first simplification could be the testing of part of the sub-assemblage, a two bays, two storeys plane frame. As the most critical details, whose cyclic behavior should be investigated, are usually the beam-column joints, the next step toward a simplification is to consider a single node of the plane frame, with part of a column and part of a beam. This test setup is simple, it is the less expensive, but it is the less complete. The test configuration can be a horizontal T, with vertical column and horizontal beam, or an inverted T, with horizontal column and vertical beam (Fig. 3.1).

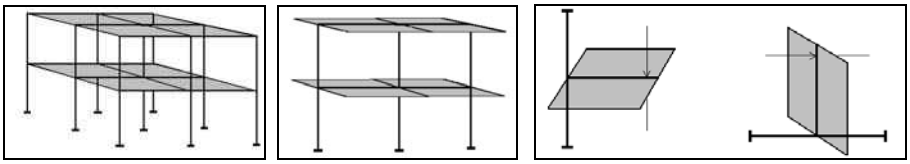


Figure 3.1: Spatial frame, Plane frame sub-assemblage and Testing setup outline for horizontal T and inverted T specimens.

The effects of the gravity loads acting in the real structure, in the usual testing procedures are generally neglected because it is difficult to apply them on the T specimen. The shear force and the bending moment due to gravity loads determines in a real node cyclically loaded a cumulative deformation in one direction. The current experimental recommendations fail to address the unsymmetrical displacement histories experienced by beam-to-column connections, as well as the governing phenomena.

4 ECCS-45 RECOMMENDATIONS

ECCS-45 recommendations were published in 1986, and no update followed that first edition. After the assessment, according to a proper definition, of the yielding loads F_y^+, F_y^- and the yielding displacements e_y^+, e_y^- in opposite directions, the protocol provides groups of three cycles with increasing imposed displacement in the $(2+2n)\ e_y^+ \div (2+2n)\ e_y^-$ interval with $n = 0,1,2,3,....$ up to the end of the test. The unsymmetrical demand on structural elements due to long duration actions which have no reversal in sign (e. g. gravity loads) can be taken into account performing the test with a partial reversal of displacements, that can be of various forms and must be properly justified. There is not any definition of collapse in the ECCS-45 recommendations. Regarding the end of the test, it is only specified that the test

www.EngineeringEBooksPdf.com

may be stopped at any level of displacement, decided with regard to specific code or research requirements. Nevertheless in order to compare the capacity of specimens, the adoption of a conventional collapse definition is needed, but there are different approaches concerning this subject. This fact is considered one of the main disadvantages of the ECCS procedure.

5 ATC-24 RECOMMENDATIONS

The *Applied Technology Council* (ATC) in 1992 published the ATC-24: *"Guidelines for Seismic Testing of Components of Steel Structures"*, specifically for experiments with slow cyclic load application. The recommended loading history to be applied, quite similar to ECCS-45, consists of stepwise increasing displacement cycles symmetric in peak displacements (Figure 5.1). At least six cycles are with a peak displacement less than δ_y (yielding displacement), then there are three groups of three cycles each, with displacement respectively δ_y, $\delta_y+\Delta$ and $\delta_y+2\Delta$. The experiment continues with groups of two cycles with peak displacement $\delta_y+3\Delta$, $\delta_y+4\Delta$ and so on until collapse.

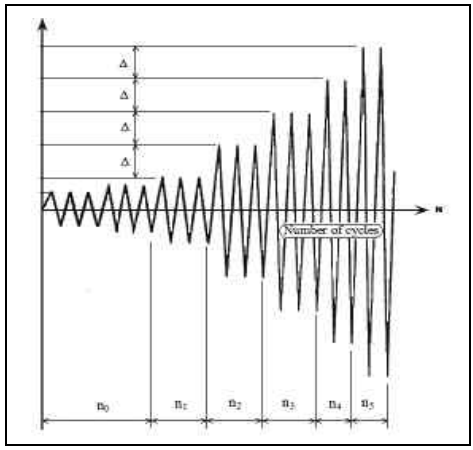


Figure 5.1: ATC-24 loading history

While ECCS-45 indicates only the recommended testing procedure, ATC-24 provides an additional commentary with general considerations justifying the proposed loading histories in term of seismic demand and seismic capacity of components. ATC-24 suggests the inter-storey drift as the most suitable parameter to represent the demand imposed by earthquakes to structural components. As a consequence, the increment Δ in peak deformation between load steps for the specimen should correspond to the deformation at an increase in storey drift equal to the yield displacement of the storey.

In defining failure, ATC-24 presents the same problem as ECCS. There is not a conventional definition of this phenomenon, nevertheless the parameter Q_{min}, required strength before failure, is specifically considered, defined as the minimum force at peak deformation that must be resisted according to a stipulated performance criterion.

6 AISC-341-05 AND FEMA-461 RECOMMENDATIONS

In AISC (American Institute of Steel Construction) *"Seismic Provisions for Structural Steel Buildings",* the recommendations for testing procedures are contained in Appendix S *"Qualifying Cyclic Tests of Beam-to-Column and Link-to-Column Connections"*. They are expressly for special (SMF) and intermediate moment frames (IMF), and for eccentrically braced frames (EBF). The latter 2005 edition supersedes the previous editions of 2002 and 1997. The recommendations are based on the results of the

www.EngineeringEBooksPdf.com

1997 FEMA-SAC project, established by FEMA (Federal Emergency Management Agency) in order to update the seismic design provisions, after the 1994 Northridge. The testing protocol is considered mainly a qualification oriented procedure. For beam-to-column connections the inter-storey drift angle θ *(inter-storey displacement divided by the storey height)* is directly assumed as the control parameter and defined in values imposed to the test specimen as specified below:

Θ (rad)	0.00375	0.005	0.0075	0.01	0.015	0.02	0.03	0.04	0.05
n of cycles	6	6	6	4	2	2	2	2	2

Loading continues then at increments of $\theta = 0.01$ *radian,* with two cycles of loading at each step. As this experimental tests are qualifying tests, there are specified requirements for strength and inter-storey drift angle θ. As an example, for SMF *the connection shall be capable of sustaining an inter-storey drift angle of at least 0.04 radian (paragraph 9.2a.)* Moreover, the test specimen must sustain the required values for at least one complete loading cycle.

FEMA 461 (June 2007) *Interim Testing Protocols for Determining the Seismic Performance Characteristics of Structural and Non-structural Components* – limiting our interest only to Quasi-Static tests carried out with displacement control – looks as a further recent upgrading of previous protocols, with more detailed and explicative considerations on the recommended loading histories.

The loading history consists of groups of two cycles with step-wise increasing deformation amplitudes, between a targeted smallest deformation amplitude Δo (a recommended value for Δo, in terms of story drift index, δ/h, is around 0.0015, when no data exists regarding what amplitude of deformation is likely to initiate damage) and the targeted maximum deformation amplitude Δm of the loading history. This is an estimated value of the imposed deformation at which the most severe damage level is expected to initiate. A recommended value for this amplitude, lacking other evidence, in terms of story drift index, δ/h, is 0.03. The number *n* of steps (or increments) in the loading history, is generally 10 or larger. For more details see FEMA 461.

7 PROPOSED INNOVATIVE CYCLIC PROCEDURE

The protocols described encompass only displacement controlled conditions, and fail to describe the unsymmetrical displacement histories experienced by real beam-to-column connections when subjected to earthquake motion. The new testing procedure, proposed in order to obviate these limitations, was extensively applied, up to now, only in an experimental campaign performed on steel racks, whose results are described in references [1], [2]. To simulate an experimental condition similar to the real behaviour of the node in the structure, a load corresponding to the shear force should be positioned at a proper distance L_s from the node, in order to produce both the same shear force and the same node rotation determined in reality by the gravity loads. The distance L_s is obtained by equalizing the rotation of the node of the specimen and the rotation of the node in the portal frame configuration.

7.1 Vertical load: L_s parameter

Let us consider a beam with length L, subjected to a uniform linear load p, connected to two columns by joints with rotational stiffness respectively K_1 and K_2. The elastic rotations and the bending moments are respectively θ_1 and $M_1 = pL^2/12$ on the left edge and θ_2 and $M_2 = -pL^2/12$ at the connection on the right. Hence from the equilibrium equation on each joint, introducing the beam stiffness $K_b = EI/L$ and solving with respect to the node rotations, we obtain:

$$\theta_1 = \frac{pL^2}{12}\frac{(6K_b + K_2)}{(4K_b + K_1)(4K_b + K_2) - 4K_b^2} \quad ; \quad \theta_2 = -\frac{pL^2}{12}\frac{(6K_b + K_1)}{(4K_b + K_1)(4K_b + K_2) - 4K_b^2}$$

To represent the situation of a T specimen subjected to a discrete load F on its extremity, let us have a cantilever of length Ls with a rotational elastic stiffness K_S at its connection. It is:

www.EngineeringEBooksPdf.com

$F = K_S\,\theta_S/L_S$ where F represents the force applied on the cantilever at a distance L_S, which causes a rotation θ_S in the joint of the beam. The stiffness of the joints in the real structure is generally the same: $K_1 = K_2 = K$, and the shear force at each connection of the beam with a distributed load p, is $F = pL/2$; comparing the node rotation θ_1 of the beam in the frame configuration to the rotation θ_S of the beam in the inverted T cantilever configuration an imposing that $K_S = K$, i. e. the T specimen and the real structure have the same joint stiffness, we obtain:

$L_s = \dfrac{L}{6}\dfrac{K}{(2K_b + K)}$; substituting again the beam stiffness $K_b = \dfrac{EI}{L}$ we can write:

$L_s = \dfrac{L}{6}\dfrac{KL}{(2EI + KL)}$ and inverting this relation $L = 3L_S + \sqrt{9L_S^2 + 12\dfrac{EI}{K}L_S}$

For a distributed load, L_S ranges from $L_S = 0$ for a supported beam ($K = 0$), to the limit value $L_S = L/6$ for a perfectly rigid joint $(K = \infty)$.

The values of L_S are generally small: considering the joint stiffness with respect to the beam stiffness, for values from $K = K_b$, to $K = 6K_b$, L_S is from about *5% L* to *12.5% L.* This result can be a limit to the application of the new procedure, due to the characteristics of the experimental setup.

7.2 Loading history of the proposed innovative procedure

The procedure is referred to cyclic tests, performed after two monotonic tests which identify yielding forces (F_y^+ ; F_y^-) and yielding displacements (d_y^+ ; d_y^-) in the two opposite directions of loading. These tests are generally necessary, because this new procedure is particularly suitable for elements and details with unsymmetrical behavior. The cyclic test is composed by a sequence of reversed cycles (repeated when in the post-elastic range) in which each cycle has an initial force-controlled part and a final displacement-controlled part. Gravitational load effects are expressed through F_g, which can be expressed as a fraction of the yielding force F_y. In what follows, the gravity force is considered to be positive.

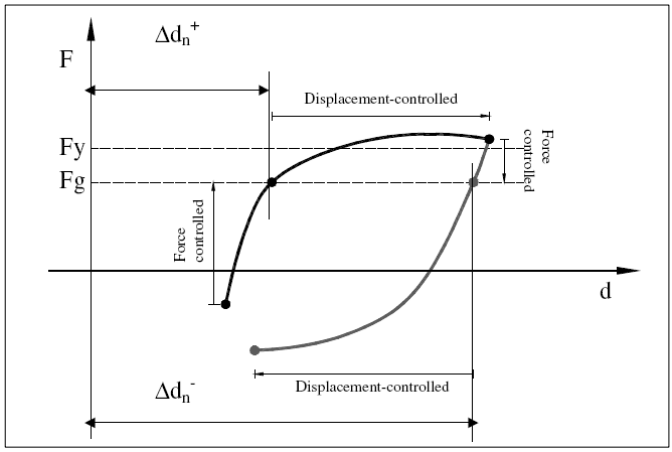


Figure 7.1: The two phases of the proposed new procedure

A typical positive cycle is composed of two parts (Figure 7.1):

- Application of the force correspondent to vertical (gravitational) load effects F_g on the beam-to-column connection (force-controlled part of the cycle), at distance L_s. The values of F_g can be assumed for example as 25%, 50%, 66% or 75% of the yield force F_y.

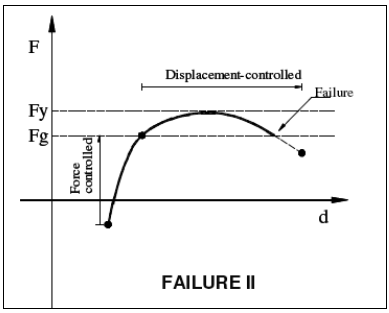
www.EngineeringEBooksPdf.com

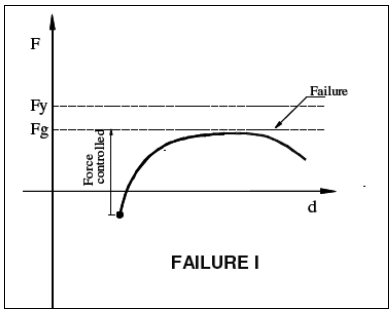
- Starting from the displacement at the end of the force-controlled part of the cycle Δd_n^+ the displacement controlled part of the cycle is imposed. The displacement amplitude applied is a multiple of the yielding displacement.

Also the following negative cycle is composed by two different parts:

- Force-controlled unloading until the attainment of the force F_g associated with the presence of the vertical (gravity) loads alone.
- Starting from the displacement Δd_n^- reached at the end of the force-controlled part of the cycle, the displacement-controlled part of the cycle is imposed to the specimen, until the intended displacement amplitude is reached.

The positive and negative cyclic displacements (in the post-elastic range) are derived from the following relation: $[(2 + n)d_y^+ + \Delta d_n^+] \div [(2 + n)d_y^- + \Delta d_n^-]$; with $(n = 0,1,2,3..)$





Figures 7.2 – 7.3: Type I and Type II failure I.

7.3 Failure for the proposed procedure

Failure is identified when in any of the positive or negative cycles one of the following situations occurs:

When the specimen fails to develop the force correspondent to the gravitational loads F_g in the force-controlled part of the positive cycle (Figure 7.2)

II. When the restoring force decreases to values below those corresponding to the gravitational loads F_g in the displacement-controlled part of the positive cycle (Figure 7.3).

7.4 Comments on the application of vertical loads

When L_s is small, depending on the experimental setup characteristics, it might not be possible to apply the hybrid procedure. If the parameter L_S is not too small and the test set up is adequate, the simplest procedure to obviate the small value of L_S, is to apply the gravity load F_g at the distance L_S and then performing the testing procedure with the variable force applied to a suitable distance, considering that the origin of the load-displacement diagram now corresponds to a fully pre-loaded an pre-deformed condition. The test begins now with the displacement controlled part, and is similar to the one proposed by ECCS-45 testing procedures, with a shifted origin.

7.5 Seismic bearing capacity representation

The effectiveness of the new testing procedure in representing the seismic bearing capacity of a structural element, can be suggested also by the following qualitative considerations.

For an elastic–perfectly plastic Single-Degree-of-Freedom element, subjected to an impulsive force large enough to cause a plastic excursion, the displacement behavior can be represented by the line OABCD in Figure 7.4. The energy absorbed by the element, is in part dissipated by the plastic deformation (AB), then the element oscillates between the positions A and B, with decreasing amplitude in time, due to the damping of the system. Neglecting this dynamic effect, it is possible to consider the cycle represented in Figure 7.4 as the result of two consecutive opposite impulsive forces, spaced in time,

www.EngineeringEBooksPdf.com

as in Figure 7.5. The second impulsive force determines the force-displacement relation of line CDEOA, with final damped oscillations between points A and E.

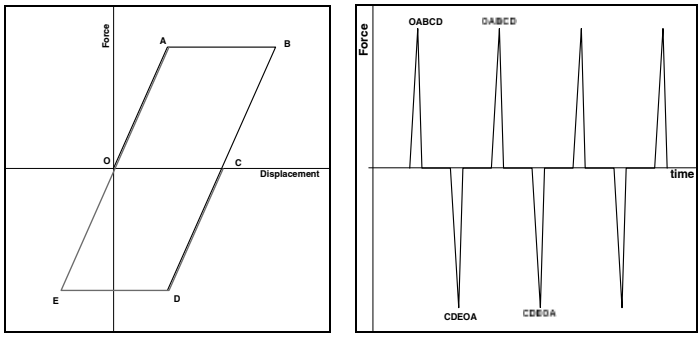


Figure 7.4 - 7.5: Time spaced opposite impulsive forces

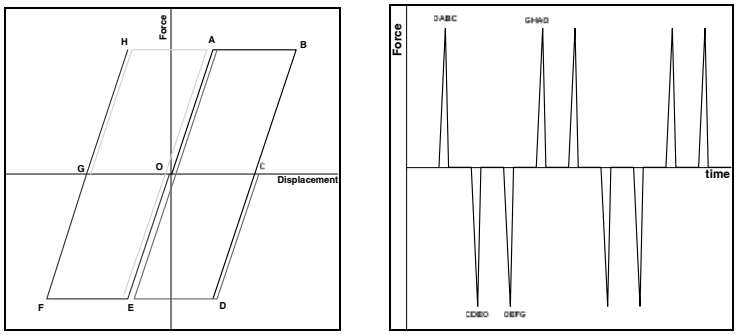


Figure 7.6 – 7.7: Equal displacement cycle obtained by four time spaced impulsive forces

From this point of view, an usual quasi-static testing cycle, performed between two opposite values of the displacement, as points C and G in figure 7.6, can be considered as the result of four consecutive impulsive forces, spaced in time, inverting their sign at every two impulses (Figure 7.7). The increasing plastic cycles, imposed in traditional quasi-static tests, can be obtained from the effect of groups of four increasing impulsive loads, spaced in time, with the same sign properties.

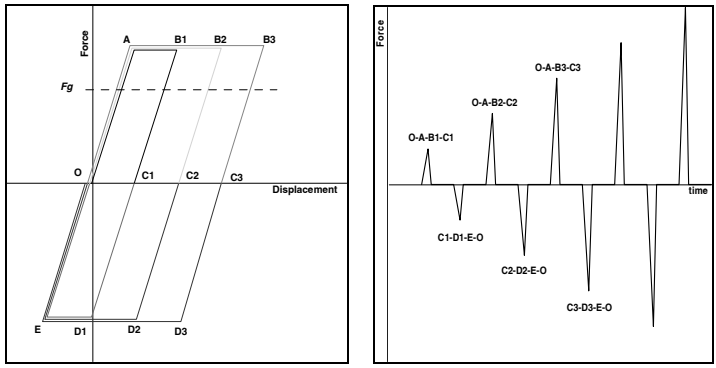


Figure 7.8 - 7.9: Force-displacement cycles from time spaced increasing impulsive forces

www.EngineeringEBooksPdf.com

As a seismic load can be seen as the application of a series of alternate impulsive forces, the seismic carrying capacity of a structural element may be better represented by a the quasi-static simulation of the effect of a group of alternate increasing impulsive forces spaced in time, as respectively in figures 7.8 and 7.9, than with equal amplitude increasing cycles.

The first impulse in plastic range can be considered to cause a total displacement of $2\ e_y$ (point B1) transferring the total energy $1.5\ F_y\ e_y$. The second impulse is equal to the previous one, but in the opposite direction, so the maximum displacement corresponds to point E. The third impulse can be set to cause a total displacement of $3e_y$ (point B2) transferring the total energy $2.5\ F_y\ e_y$, followed by an opposite similar impulse, reaching again point E. Subsequent couples of opposite impulses will cause total displacements of $4e_y$, $5e_y$, and so on, transferring the energy $3.5\ F_y\ e_y$, $4.5\ F_y\ e_y$. Of course the cycles can be repeated.

The result is a global behavior of the specimen with cumulated displacement in one direction. The loading cycles obtained (Figure 7.8) are similar to the new proposed testing procedure with no permanent loading, with displacement accumulation in one direction. Applying the new procedure, in the first cycle the force is applied with displacement control from point O up to the required displacement in point B1, then with force control the specimen is unloaded until point C1. The reverse load is applied with displacement control from C1 up to point E, imposing a displacement equal to OB1, and with force control the specimen is unloaded to point O. The subsequent cycle is performed with the same steps but a larger displacement, corresponding to point B2, and so on. To take into account the presence of permanent vertical loading, signifies only to limit the force control loading and unloading to the considered load F_g. Moreover it can be observed that, even if an impulsive force is applied before the completion of the effect of the previous one, that is during the elastic oscillation after the plastic displacement, the global aspect of the cycles obtained is similar, with different cumulative displacement in one direction.

8 CONCLUSION

This new procedure gives a significant improvement to the commonly adopted recommendations for low cycle fatigue testing. It has hybrid characteristics, as it is in part a force control procedure and in part a displacement control procedure for every inelastic cycle.

The global performance of the specimen is clearly defined with explicit reference to its requested carrying capacity F_g in usual service conditions, therefore in this sense the new experimental tests may be considered "complete": the performance of the specimen subjected to transversal reversal loads is investigated as far as it can resist the design gravity (dead and live) loads. The failure to resist these loads represents the collapse of the specimen. Accepting this point of view, the proposed new testing procedure could be the basis for new Low Cycle Fatigue testing recommendations, or for a new edition of ECCS recommendations, which takes into account the experiences accumulated in the last 25 years on this item.

REFERENCES

[1] SEISRACKS-Storage racks in seismic areas, Final Report, Report no. 5, *Research Programme of the Research Fund of Coal and Steel,* 2007

[2] Proença J., Calado L., Castiglioni C. A., Tristão G., "Cyclic testing on steel storage beam to upright sub assemblages and innovative testing cyclic procedure", *First European Conference on Earthquake Eng. and Seismology*, Genève, 2006

www.EngineeringEBooksPdf.com

SDSS'Rio 2010 STABILITY AND DUCTILITY OF STEEL STRUCTURES
E. Batista, P. Vellasco, L. de Lima (Eds.)
Rio de Janeiro, Brazil, September 8 - 10, 2010

PROPOSAL OF A THREE-DIMENSIONAL SEMI-RIGID COMPOSITE JOINT: TEST AND FINITE ELEMENT MODELS.

Beatriz Gil*, Rufino Goñi* and Eduarbo Bayo*

* Department of Structural Analysis and Design
University of Navarra, 31080 Pamplona (Navarra), Spain
e-mails: bgilr@unav.es ; rgonil@unav.es ; ebayo@unav.es

Keywords: semi-rigid composite joints, three-dimensional, experimental, test, finite element model.

Abstract. *In sway structures the stability has to be assured within the two main axes of the frames. By means of semi-rigid joints, the lateral stability of the structure may rely on the stiffness and ductility of the joints, thus avoiding bracing systems. This paper proposes new designs that include beams attached in a semi-rigid manner to both, the major and minor axes of the column. This new three-dimensional design for semi-rigid composite joints has been tested and the results are presented in this paper. The experimental program consists in two 3D semi-rigid composite joints under non-proportional loads and one façade joint. These tests provide information as to whether the joints satisfy the requirements of the EC3 in terms of ductility or not. Also the interactions in the proposed joint caused by loads in both directions are studied.*

1 INTRODUCTION AND OBJETIVES

Semi-rigid composite joints not only have the advantage of optimizing the use of the material, but also of providing lateral stiffness for sway frames. By means of semi-rigid joints, the lateral stability of the structure may rely on the stiffness and ductility of the joints, thus avoiding bracing systems. The stability of the structure has to be assured within the two main axes of the frames. The proposed design includes beams which are attached in a semi-rigid manner to both, the major and minor axes of the column. The design of the major axis connection is made with a bolted flush end plate and the central rebars of the slab passing through the column flanges, while that of the minor axis is built by means of an additional plate welded to the column flanges, instead of attaching it to the column web.

The behavior of semi-rigid 2D composite joints has been widely investigated and tested. However, the behavior and interaction in the 3D joints has been studied barely (Green et al. [1], Dabaon et al [2]). The Eurocodes (EC3 [3] and EC4 [4]) provide general rules for the design of joints but do not consider cases such as 3D joints and/or joints attached to the minor axis.

This paper presents the results of an experimental program consisting in one 3D semi-rigid composite internal joint under proportional loads, a similar one subjected to non-proportional loads and one façade joint. These tests provide information as to whether the joints satisfy the requirements of the EC3 and EC4 in terms of ductility and resistance. Also the interactions in the proposed joint caused by loads in both directions are studied. Simultaneously, finite element modeling with the same characteristics as the specimens is carried out and calibrated against the experimental results. This model will be used to develop a parametric study and obtain analytical methods for the design of this joint typology.

2 PROTOTYPES DESCRIPTION AND EXPERIMENTAL RESULTS

A design of three-dimensional semi-rigid composite joint, that is, a column with composite beams attached to both the strong and the weak axis, is proposed and tested. This design is based on those

www.EngineeringEBooksPdf.com

previously proposed by Gil and Bayo [5], [6] for 2D composite joints, and by Cabrero and Bayo [7], [8] for 3D steel only joints.

The experimental program consists on one test of a three-dimensional internal semi-rigid composite joint subjected to proportional loads (test E01), a second one consisting on a three-dimensional composite joint subjected to non-proportional loads (test E02), and a third one consisting on one three-dimensional composite joint with one beam on the major axis and two beams in the minor axis (test E03), that is, a joint on a external façade. In all of them, the design of the major axis connection is made with a bolted flush end plate and the central rebars of the slab passing through the column flanges [5], while that of the minor axis is built by means of additional plates welded to the column flanges, instead of attaching it to the column web [1, 7].

This design has been chosen instead of attaching the beam to the column web due to several advantages such as:

- The additional plates placed in the tension and compression area of the column flanges add stiffness and strength to the web, especially when it is subjected to non proportional loads.
- The joint is simpler to build than the same joint attached to the web.
- The joint becomes more resistant and ductile, avoiding possible instability of the column web.
- The gap between both plates attached to the minor axis the facilities the placing and tighting of the bolts.

The choice of geometry and materials has been made in accordance with Eurocode 2 [9], Eurocode 3 [3] and Eurocode 4 [4]. The sections, bolts, etc. of the three specimens are shown in the next table:

Table 1: Configuration of specimens

Test	Column	Slab	Axis	Viga	End Plate	Bolts	Rebars	L 1	L 2
E01	HEB 180	10 cm H30	Major	IPE 270	10 mm	T 16 (10.9)	6Ø16	1,2 m	1,2 m
			Minor	IPE 180	10 mm	T 12(10.9)	9 Ø12	1,2 m	1,2 m
E02	HEB 180	10 cm H30	Major	IPE 240	10 mm	T16 (10.9)	6Ø16	1,0 m	1,2 m
			Minor	IPE 200	10 mm	T 12(10.9)	9 Ø12	1,0 m	1,0 m
E03	HEB 180	10 cm H30	Major	IPE 240	10 mm	T16 (10.9)	6Ø16	1,0 m	1,2 m
			Minor	IPE 200	10 mm	T 12(10.9)	5 Ø12	1,0 m	1,0 m

3.1 TEST E01

The test configuration and loading pattern for the first specimen are shown in Figure 1. The specimen is placed face down and the load is applied to the top of the column. The end of each beam is supported on a load cell that measures the corresponding reaction in that support. Since the length of the beams in every axis is the same, the specimen is symmetric and the applied loads are proportional.

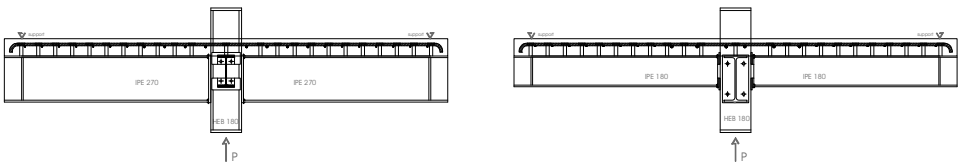


Figure 1: Tests configuration (E01)

Regarding the instrumentation, the load is introduced in the top of the column by means of two hydraulic jacks that feature 400 kN each. The reactions in the beams are measured with load cells with a limit of 200 kN. Two inclinometers are placed in the weak axis beams, close to the column; the third is placed in one of the strong axis beam and the fourth in the column web. A displacement transducer is used to measure the deflection at the bottom of the column and finally, strain gages are placed in the relevant components of the joint (plates, flanges, webs and rebars) in order to obtain qualitative information on the sequence of the yielding process. The load is applied in two stages. In the first one, the

www.EngineeringEBooksPdf.com

column is loaded progressively up to 200 kN and then is completely unloaded. In the second stage, the specimen is loaded progressively until failure.

Results: the tested joint shows a nonlinear behavior at early loading stages, as shown in the column load- deflection curve of Figure 2. This is due to the small tensile strength of the concrete whose cracks spread and grow with increased loading. The total load applied in the column is greater than 500 kN and the column deflection reaches almost 60 mm.

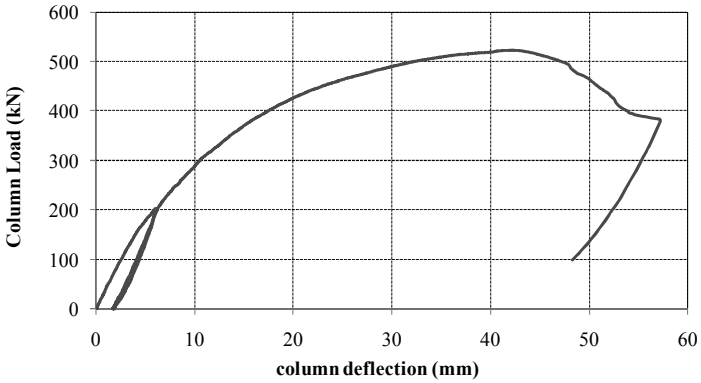


Figure 2: Applied load at the column vs deflection

Figure 3 shows the moment-rotation curve for a major axis joint and the minor axis one. It may be seen that the maximum moment in the major axis joint is around 150 kNm and the maximum rotation reached is 30 mrad. There are several steps at the end of the curve, due to the yielding of the components. The complete collapse of the joint is produced when suddenly a shear stud is broken due to the longitudinal shear. This shear is high due to the interaction of the loads in both directions. Prior to the stud failure, the additional plate in compression, the column web in compression and the rebars of the strong and weak axis had yielded. The minor axis joints reach a moment of around 40 kNm and a rotation capacity of 50 mrad, thus showing a quite ductile behavior.

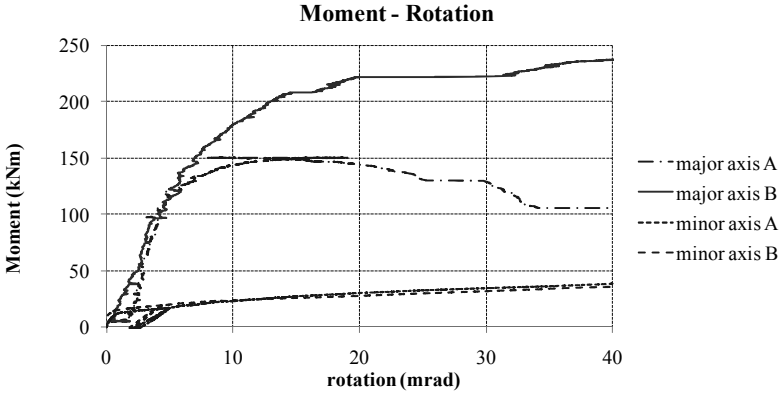


Figure 3: Moment-Rotation curves

When the specimen fails, there are two components in the minor axis that have yielded: the additional plate in compression and the reinforcement. The rest of the components in this axis remain in the elastic

www.EngineeringEBooksPdf.com

range. Regarding the response of the joint, it may be observed that the major axis joint shows almost the same initial stiffness in both sides, which is logical due to the symmetry of geometry and loads. The strength was also supposed to be same in both sides but this does not happen because of possible imperfections and asymmetries in the joint and/or the concrete slab. The difference between the moments in both sides is absorbed by torsion in the minor axis beams.

3.1 TEST E02

The test configuration and the loading pattern for the second specimen are shown in Figure 4. The column has pinned ends, and the joint is firmly attached to the floor and the ceiling, which absorb the vertical and horizontal reactions. A constant load of 20 kN is applied in both edges of the minor axis, and kept constant during the whole test. In the edges of the major axis, the load is applied by controlling the displacements. The displacement in one side is triple than the displacement on the other side in order to get different moments on both sides of the column. The purpose is to reproduce the case of frames subjected to lateral wind loads and to check the reliability of the joint.

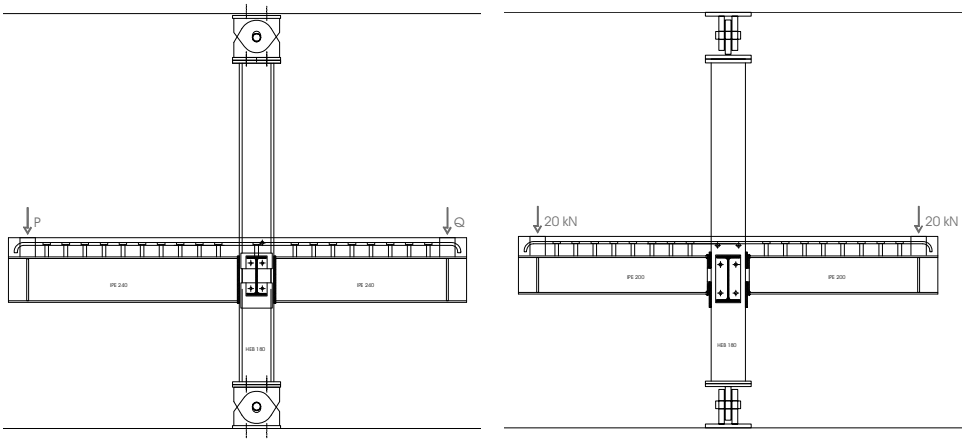


Figure 4: Test Configuration (E02)

The aim of this load pattern is to study the interaction of the web panel in shear with the rest of the components of the joint. Another aim is to analyze the benefits or drawbacks derived from the fact that the joint is loaded in both axes and, in the same way, the benefits or drawbacks derived from the additional plates in the minor axis of the proposed joint.

Results: the moment rotation curves for the major axis of the second tested joint (E02) are shown in Figure 5.

We distinguish the side with a larger moment (side A) than that with a lower moment (side B). Several facts resulting from the test are worth mentioning:

a) The sections at each connection do not remain plane after deformations. Thus, the connection rotation at the external plate level is different from that at the slab on the same vertical.
b) The stiffness of the connection is such that the side with the lower moment has a larger stiffness.
c) The converse is true for the resistance, that is, the more loaded connection has more resistance.

It may be seen how the major axis rotation in the more loaded side (A) reaches 80 mrad which satisfies the requirements of the Eurocode by a large margin. The major axis joint in the opposite side (B) reaches 30 mrad at the time of failure. This rotation is lower because, when the side A fails, the reinforcement, which is part of both joints, has already yielded (that is also the reason why the strength is lower). In any case it also satisfies the EC3 rotation requirements.

www.EngineeringEBooksPdf.com

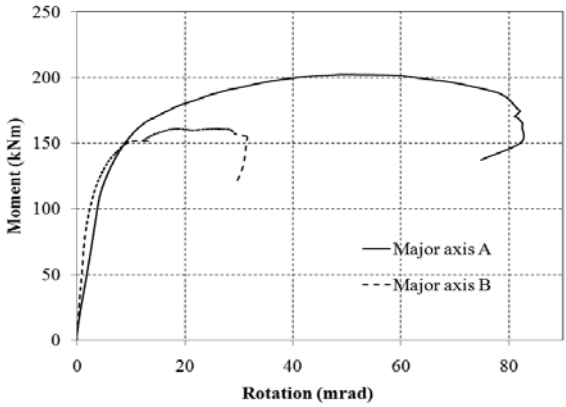


Figure 5: Moment-Rotation curve for the major axis joints (test E02)

The component yielding sequence is obtained by means of the strain gages placed on them and it is the following:

- The first component that yields is the reinforcement in both mayor and minor axis. Despite of the fact that the minor axis is not loaded until failure, the minor axis reinforcement yields because the mayor axis reinforcement pulls the minor axis one. This also induces an additional shear in perpendicular direction to the minor axis beam, at the interface between the steel beam and the concrete slab, so the shear studs bears more shear than if the structure were loaded in only one axis.
- The additional plates in the minor axis yield after the reinforcement, followed by the beam flange in compression.
- Finally, the flush end plate of the mayor axis joint yields.

The moment rotation curves for the minor axis are shown in the Figure 6. As the minor axis is only loaded up to 20 kN, the curve shows a linear behaviour and only the stiffness can be obtained.

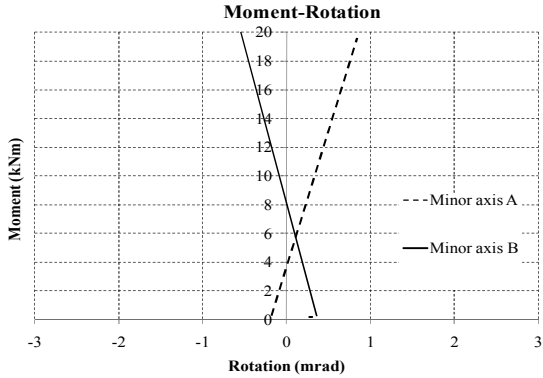


Figure 6: Moment-Rotation Curve for the minor axis joints (E02)

3.1 TEST E03

The third test has the same configuration and sections as in the previous one, except that this one lacks one of the major axis beams (Figure 7). The aim is to reproduce the case of joints attached to columns placed in the perimeter of the building (façade columns). The reinforcement is bent as shown in Figure 7, in order to guarantee the required anchorage length.

www.EngineeringEBooksPdf.com

The edges of the minor axis are loaded up to 50 kN and this load is kept during the whole test, meanwhile the major axis joint is loaded and unloaded in a first stage to get the initial stiffness, and then it is loaded until failure in the second stage.

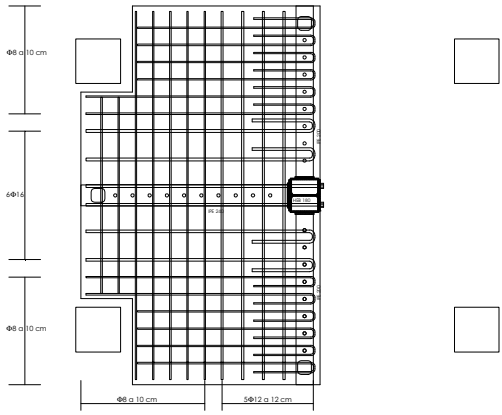


Figure 7. Test E03 configuration

4 FINITE ELEMENT MODEL

4.1 Geometry and Definition of the elements

A finite element model is developed by means of the ABAQUS program. The three-dimensional FE model (Figure 8) has the configuration and dimensions of the tested specimens.

The concrete slab, the slab reinforcement, the steel beams and column, the bolts and even the shear studs are modeled with 8-node solid elements with reduced integration (C3D8R). The reduced integration element has been chosen instead of incompatible modes (C3D8I) to avoid the shear locking that it is produced with the C3D8I element.

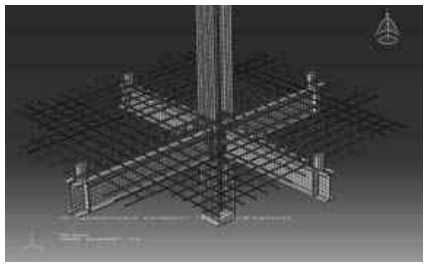


Figure 8. Finite element model.

4.2 Interactions, Boundary conditions, materials and analysis

The interactions between the different materials are modeled in the following way:

The reinforcement and the shear studs are embedded in the slab. This technique eliminates the translational degrees of freedom of the embedded nodes and makes them correspond with those of the host element. Solid elements have been chosen to capture the deformation of the connectors properly, and avoid the use of springs use (Queiroz et al. [10] and Dabaon et al. [2]). Surface to surface contact interactions are defined between the end plate and the column flange. The bolt head and the nut are tied to the plates to simplify their interaction.

www.EngineeringEBooksPdf.com

The materials chosen for the finite element model are the same as those in the specimen: S275 for structural sections and plates, B500SD for reinforcement, C30 for the concrete, and the shear studs with strength of 450 N/mm2. The real stress-strain curves are introduced.

A second order inelastic analysis is carried out using displacement control, which allows us to monitor possible drops in the load displacement and stress-strain curves. This method also allows us to reproduce the real conditions of the load pattern carried out in the tests.

4.3 Comparison with experimental results and model validation

Figures 10 and 11 show the load-deflection and moment rotation curves for the validation of the numerical model with the experimental results of the E01 and E02, respectively.

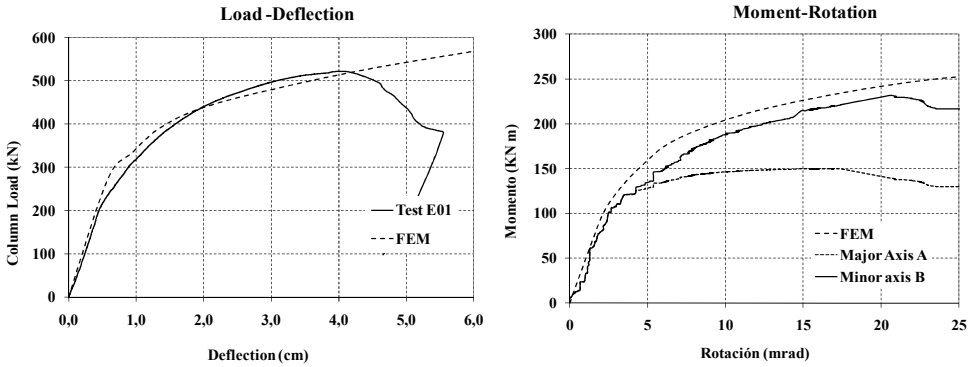


Figure 10: Validation of the FE model with the experimental results for E01

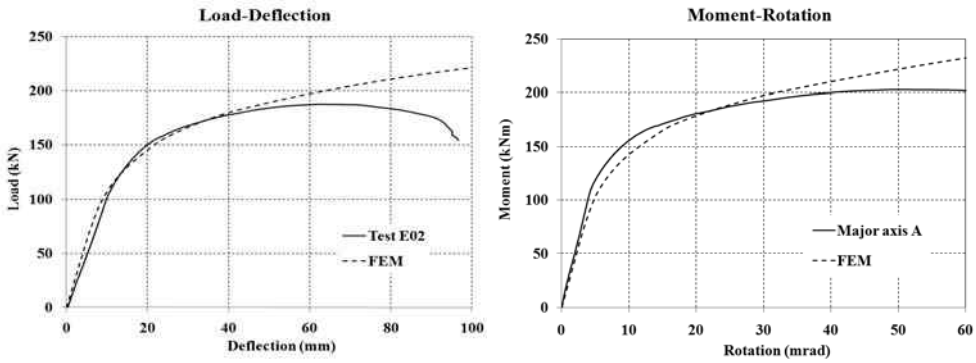


Figure 11: Validation of the FE model with the experimental results for E02

It may be seen how the stiffness and the strength in all the curves are captured accurately. However, the finite element model does not represent the rotation capacity due to the impossibility of the concrete model of the Abaqus program of capturing the concrete failure.

5 CONCLUSSIONS

A design for three-dimensional semi-rigid composite joints is proposed and tested. The purpose of this design is to give lateral stability in sway frames, that is, to bear not only vertical but also lateral wind loads. The strong axis connection of the proposed joint is carried out by means of a bolted flush end plate

www.EngineeringEBooksPdf.com

with the central rebars of the slab passing through the column flange. The weak axis connection is materialized by means of an additional plate welded to the column flanges, rather than attaching the beam to the column web. This design is tested under proportional and non-proportional loads.

The 3D joint shows a good behaviour in both axes. The additional plates of the minor axis affect the behavior of the whole joint, which is quite sensitive to their dimensions. It is recommended to enlarge the lower plate up to the lower major axis beam to add stiffness to the column web panel in shear and compression. The tested joints are quite ductile (over 30 mrad). However, when non proportional loads are applied, the side that bears the lowest load shows higher stiffness but lower strength due to the yielding of common components for both sides, such as the rebars.

Further work is need to assess the interaction between minor and major axis with non proportional loads. A parametric study is being carried with this aim, by means of finite element models calibrated with the experimental results.

6 ACKNOWLEDGEMENTS

The financial support provided by the Spanish Ministry of Education and Science through the grant # BIA2007-67906-C02-01 is greatly acknowledged.

REFERENCES

[1] Green, T. P., Leon, R. T. and Rassati, G. A., "Bidirectional Tests on Partially Restrained Composite Beam-to-Column Connections", *Journal of structural engineering*, Vol. 130, 320-327. 2004

[2] Dabaon, M. A., El-Boghdadi, M. H. and Kharoob, O. F., "Experimental and numerical model for space steel and composite semi-rigid joints", *Journal of Constructional Steel Research*, Vol. 65, 1864-1875. 2009

[3] CEN. "*Eurocode 3: Design of Steel Structures. Part 1.8: Design of Joints (prEN 1993-1-8:2003), stage 49 draft edition*". CEN. 2003

[4] CEN. "*Eurocode 4 : Design of Composite Steel and Concrete Structures. Part 1.1: General Rules and Rules for Buildings (prEN 1994-1-1:2003)*". CEN. 2004

[5] Gil, B. and Bayo, E., "An alternative design for internal and external semi-rigid composite joints. Part I: Experimental research", *Engineering Structures*, Vol. 30, 232-246. 2008

[6] Gil, B. and Bayo, E., "An alternative design for internal and external semi-rigid composite joints. Part II: Finite element modeling and analytical study", *Engineering Structures*, Vol. 30, 247-257. 2008

[7] Cabrero, J. M. and Bayo, E., "The semi-rigid behaviour of three-dimensional steel beam-to-column joints subjected to proportional loading. Part I. Experimental evaluation", *Journal of Constructional Steel Research*, Vol. 63, 1241-1253. 2007

[8] Cabrero, J. M. and Bayo, E., "The semi-rigid behaviour of three-dimensional steel beam-to-column joints subjected to proportional loading. Part II: Theoretical model and validation", *Journal of Constructional Steel Research*, Vol. 63, 1254-1267. 2007

[9] CEN. "*Eurocode 8 : Design of structures for earthquake resistance- Part 1: General rules, seismic actions and rules for buildings*". CEN. 2003

[10] Queiroz, G., Vellasco, P. C. G. and Nethercot, D. A., "Finite element modelling of composite beams with full and partial shear connection", *Journal of Constructional Steel Research*, Vol. 63, 505-521. 2007

www.EngineeringEBooksPdf.com

SDSS'Rio 2010 STABILITY AND DUCTILITY OF STEEL STRUCTURES
E. Batista, P. Vellasco, L. de Lima (Eds.)
Rio de Janeiro, Brazil, September 8 - 10, 2010

STRENGTH AND DUCTILITY OF BOLTED T-STUB MACRO-COMPONENTS UNDER MONOTONIC AND CYCLIC LOADING

Nicolae Muntean*, Daniel Grecea*, Adrian Dogariu* and Dan Dubina*

* Politehnica University Timisoara, Romania
e-mails: nicolae.muntean@ct.upt.ro, daniel.grecea@ct.upt.ro, adrian.dogariu@ct.upt.ro, dan.dubina@ct.upt.ro

Keywords: Strength, Ductility, Bolted T-stub, Macro-component, Monotonic and Cyclic loading.

Abstract. *In dissipative building frames, Mild Carbon Steel (MCS) is always used in members designed to undergo plastic deformations (e.g. beam and/or braces), while in truss members which have to remain predominantly elastic, such as columns, High Strength Steel (HSS) grade stub might be used [3]. In such a case within Moment Resisting (MR) Joints, T-stub macro-components made of two steel grades are obtained. Due to the fact, usually real yield strength in MCS beams is significantly higher than nominal value used in design, the T-stub macro-components, together with the column web panel become very important for strength and ductility of joints. However, web panel contribution is limited by EN 1998-1 at 30% from total plastic rotation capacity and, consequently, the main ductility demand goes for T-stub component. Bolted extended-end-plate full strength MR joints cannot be usually obtained without outer stiffeners or/and haunches. In such case it is difficult to obtain ductile failure modes for the relevant T-stub components. In order to observe and characterize this phenomenon, an extensive testing and numerical simulation program was undertaken at CEMSIG Centre. Present paper summarizes the main results of this investigation.*

1 INTRODUCTION

Seismic resistant building frames designed as dissipative structures must allow for plastic deformations to develop in specific members, whose behavior has to be predicted by proper design. Members designed to remain predominantly elastic during earthquake, such as columns, are responsible for robustness of the structure and prevention the collapse, being characterized by high strength demands. Consequently a framing solution obtained by combining High Strength Steel - HSS in non-dissipative members as columns provided with adequate over-strength, and Mild Carbon Steel – MCS in dissipative members, working as fuses, as beams, links or braces seems to be logical. The robustness of structures to severe seismic action is ensured by their global performance, in terms of ductility, stiffness and strength, e.g. the "plastic" members of MCS – (S235 to S355) will dissipate the seismic energy, while the "elastic" members (HSS - S460 to S690) by higher resistance of material and appropriate size of sections, will have the capacity to carry the supplementary stresses, following the redistribution of forces, after appearance of plastic hinges. Such a structure is termed Dual-Steels Structure – DS.

DS concept is extended to connections, too, on the same philosophy related to ductile and brittle components, in order to achieve both ductility and robustness criteria. In fact, when connect MCS beams to HSS columns will result a DS beam-to-column joint.

Starting from the above considerations, a large experimental research program was carried out at the "Politehnica" University of Timisoara, CEMSIG Research Centre (http://cemsig.ct.upt.ro) in order to study the performance of dual-steel configuration for beam-to-column joints under monotonic and cyclic loading. Joint specimens, T- stub and weld detail specimens have been tested [5], [6, [7].

When HSS is used in members designed to remain predominantly elastic, as columns or in end-plates

www.EngineeringEBooksPdf.com

of bolted joints, T-stub macro-components made of two steel grades are obtained. The performances of DS bolted T-stub specimens as strength and ductility under monotonic and cyclic loading are analyzed in present paper. Similar tests on MCS and DS bolted T-stubs, unstiffened and one-side stiffened were realized by [8], under monotonic loading and stiffener on the end-plate, and by [9], which applied cyclic loading on MCS unstiffened T-stubs.

According to seismic design provisions [2], Moment Resisting Frames (MRF) comprise full strength/rigid joints, which are demanding a minimum plastic rotation capacity ϕ_{pl}=0.035rad, and the overstrength of moment capacity of the joint of, at least 1.375 times the plastic bending moment of the beam, for partial resistant/semi-rigid joints the plastic rotation capacity $\phi_{pl}>\phi_{pl,necessary}$.

It is well-known that T-stub macro-component is falling down by 3 types of failure mode, named 1, 2 and 3 (see Table 4). After developing the experimental program and starting from previous considerations it was clear that failure mode 2 would be preferable in order to answer both criteria full strength and rotation capacity. Present paper is summarizing the results of this research, where starting from experimental results, authors are developing, starting from real joint configurations, some numerical studies in order to establish the borders for T-stub macro-component failure mode 2→1 and 2→3, and to verify their classification and behavior in between; after that we are going back to the joints to verify also their classification and behavior as failure mode in connection with the T-stub.

From the experimental program, a FEM model was settled for T-stub macro-component. Authors had the idea to start from some real rigid full-resistant joints, to settle the dimensions and steel grade of end plate in order to obtain the borders of type 2 failure mechanism, to make a numerical analysis on extracted T-stubs and compare the results with the theoretical ones and finally to come back to the joints and verify their behavior and failure mode.

2 TESTING PROGRAM

2.1 Summary of testing program

The objective of the whole experimental program was to study the performance of welded and bolted end-plate beam to column joints realized from two different steel grades. The experimental program consisted in tests on materials, welded components, T-stub components, and beam to column joints. This paragraph describes only the investigations performed and T-stub components. Previous papers by the same authors already summarized the results on materials, welded components, weld details and beam-to-column joints [5], [6], [7].

T-stubs are basic components of the component method used in EN 1993-1.8 [1] for evaluation of strength and stiffness of bolted end-plate beam to column joints. Both monotonic and alternating cyclic tests were performed on T-stub components obtained by welding S235 web plates to S235, S460 and S690 end-plates, using K beveled full-penetration welds (Table 1). MAG welding was used, with G3Si1 (EN 440) electrodes for S235 to S235 welds, and ER 100S-G/AWS A5.28 (LNM Moniva) for S235 to S460 and S690 welds. T-stubs were connected using M20 gr. 8.8 bolts. EN 1993-1.8 was used to obtain the design strength of T-stubs and failure modes. Thickness of end-plates was determined so that the unstiffened T-stub (type C) would fail in mode 1 (end-plate) and mode 2 (combined failure through end-plate bending and bolt fracture). The same end-plate thickness was then used for the stiffened T-stubs (type B and A), see Table 1.

2.2 Dual-steel bolted T-stubs: monotonic and cyclic loading performance

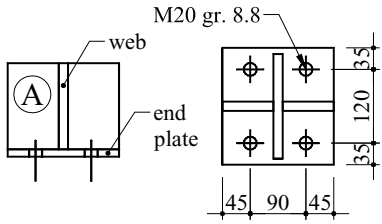
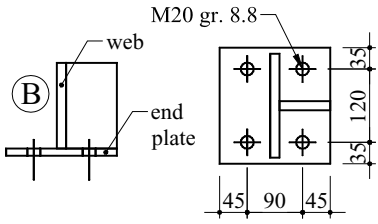
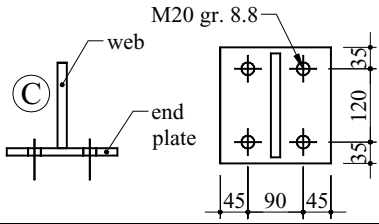
Flat materials used for T-stub and welds details were supplied by UNIONOCEL, Czech Republic. Table 2 shows the measured average values of yield stress f_y, tensile strength f_u and elongation at rupture A. It has to be recognized that the value of elongation for S460 is surprisingly large. Bolts were tested in tension as well, showing an average ultimate strength of 862.6 N/mm^2.

Loading was applied in displacement control under tension and force control under compression. Compressive force was chosen so as to prevent buckling of the specimen.

www.EngineeringEBooksPdf.com

For specimens of types B and C, it was not possible to have full reversible cycles due to the buckling. A good ductility was observed, in general; however, thicker end-plate specimens, even of S235, do not show the best ductility. It seems that the choice of thickness associated with steel grade is important in the conception of a proper connection, in order to obtain a good balance between strength, stiffness and ductility of components.

Table 1: T-stub characteristics

T-stub type	Label	Web	End-plate	Design failure mode
	TST-12A-S235	S235 t=15 mm	S235 t = 12 mm	2
	TST-20A-S235		S235 t = 20 mm	2 → 3
	TST-10A-S460		S460 t = 10 mm	2
	TST-16A-S460		S460 t = 16 mm	2 → 3
	TST-8A-S690		S690 t = 8 mm	2
	TST-12A-S690		S690 t = 12 mm	2 → 3
	TST-12B-S235	S235 t=15 mm	S235 t = 12 mm	1 / 2
	TST-20B-S235		S235 t = 20 mm	2 / 2 → 3
	TST-10B-S460		S460 t = 10 mm	1 / 2
	TST-16B-S460		S460 t = 16 mm	2 / 2 → 3
	TST-8B-S690		S690 t = 8 mm	1 / 2
	TST-12B-S690		S690 t = 12 mm	2 / 2 → 3
	TST-12C-S235	S235 t=15 mm	S235 t = 12 mm	1
	TST-20C-S235		S235 t = 20 mm	2
	TST-10C-S460		S460 t = 10 mm	1
	TST-16C-S460		S460 t = 16 mm	2
	TST-8C-S690		S690 t = 8 mm	1
	TST-12C-S690		S690 t = 12 mm	2

Note 1: One monotonic and two cyclic tests have been performed for each specimen type.
Note 2: Design failure mode 1 / 2 means failure mode 1 for unstiffened part and failure mode 2 for the stiffened one.

Table 2: Material properties

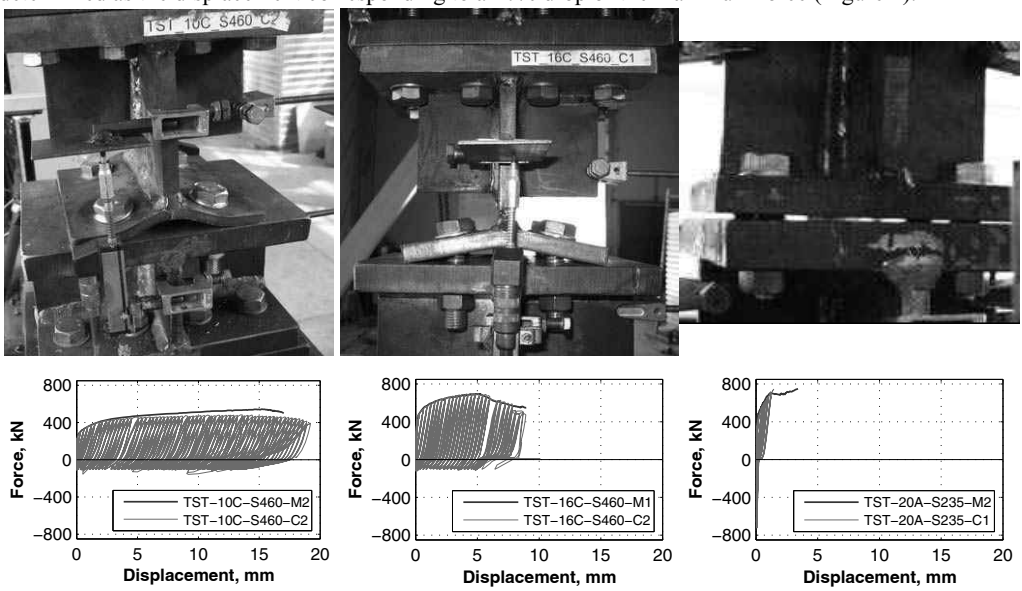
Nominal steel grade	f_y, N/mm^2	f_u, N/mm^2	A, %	Actual steel grade
S235	266	414	38	S235
S460	458	545	25	S460
S690	831	859	13	S690

Figure 1 shows examples with the 3 types of observed failure modes, together with the corresponding force-displacement relationships of T-stub specimens. There were no significant differences in force values between failure modes of monotonic and cyclic specimens, both generally agreeing with analytical predictions by EN 1993-1.8.

For the T-stub specimens, the following parameters were determined for each experimental test: initial stiffness K_{ini}, maximum force F_{max}, yield force F_y, and ultimate deformation, D_y. The initial

www.EngineeringEBooksPdf.com

stiffness was obtained by fitting a linear polynomial to the force-displacement curve between 0 and 25% of the maximum force. The yield force was determined at the intersection of the initial stiffness and tangent stiffness line, where the tangent stiffness was obtained by fitting a linear polynomial to force-displacement curve between 75% and 100% of the maximum force. The ultimate deformation was determined as the displacement corresponding to a 10% drop of the maximum force (Figure 2).



TST-10C-S460-C2
Failure mode 1

TST-16C-S460-C2
Failure mode 2

TST-20A-S235-C1
Failure mode 3

Figure 1: Examples of failure modes of T-stub specimens

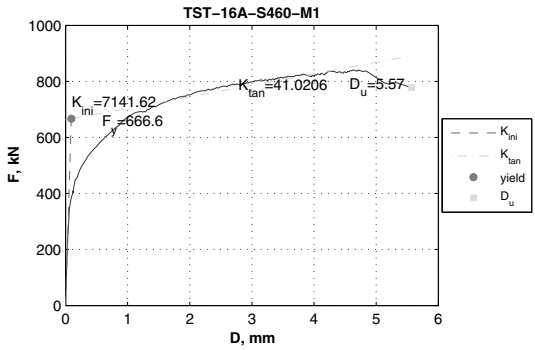


Figure 2: Experimental characteristics of T-stub specimens

Cyclic loading reduced the maximum force of the T-stub specimens, though the reduction was not significant. The ductility of the T-stub specimens was quantified through the ultimate displacement D_u. Under monotonic loading, ultimate displacement was smaller for specimens with thicker end-plates that failed in modes 2 and 3 involving bolt failure (Figure 3a). Cyclic loading reduced significantly ultimate displacement of specimens with thinner end-plates that failed in mode 1. This behavior is attributed to low-cycle fatigue that generated cracks in the HAZ near the welds, along yield lines. On the other hand,

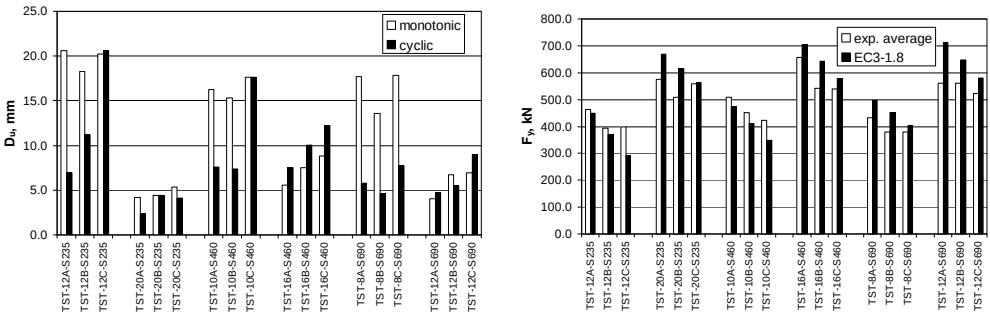
www.EngineeringEBooksPdf.com

cyclic loading did not affect much ultimate displacement for specimens with thicker end-plates that failed in modes 2 and 3, governed by bolt response. It is interesting to note that specimens realized from high-strength end plates (S460 and S690, with lower elongation at rupture), had a ductility comparable with the one of specimens realized from mild carbon steel (S235). The parameters governing the ductility of T-stubs were type of loading (mono-tonic / cyclic) and failure mode (end-plate or bolts).

A comparison between test and theoretical results was made (Table 3 and Figure 3). Theoretical characteristics were evaluated by component method from EN1993-1-8. It may be remarked that, with some exceptions, the procedure from EN1993-1-8, including specimens of type A is confirmed; the exceptions can be covered by safety coefficients.

Table 3: Interpretation of monotonic tests

Specimen	$F_{y,exp,average}$ [kN]	$F_{yEC3-1.8}$ [kN]	$F_{y,EC3}/F_{y,exp}$	$F_{max,exp}$ [kN]	$D_{u,exp}$ [mm]	$K_{ini,exp}$ [kN/mm^2]	Failure mode
TST-12A-S235	463.9	425.4	0.92	705.6	20.6	4709.4	1
TST-12B-S235	395.0	357.8	0.91	559.0	18.3	4097.9	1
TST-12C-S235	397.8	290.3	0.73	582.6	20.2	4352.2	1
TST-20A-S235	576.4	645.6	1.12	760.8	4.2	5312.4	3
TST-20B-S235	509.0	589.1	1.16	744.2	9.0	5561.8	2→3
TST-20C-S235	559.5	532.6	0.95	758.3	5.4	6737.8	2
TST-10A-S460	508.3	440.9	0.87	688.7	16.2	3703.6	1
TST-10B-S460	451.7	383.8	0.85	606.4	15.3	3063.3	1
TST-10C-S460	423.8	326.6	0.77	550.2	17.6	5916.5	1
TST-16A-S460	656.8	658.4	1.00	832.8	5.5	6242.1	2
TST-16B-S460	541.2	598.1	1.11	745.9	7.5	5114.8	2
TST-16C-S460	538.6	537.8	1.00	687.5	8.8	5436.1	2
TST-8A-S690	432.0	446.1	1.03	618.4	17.7	2756.1	1
TST-8B-S690	380.5	392.4	1.03	511.3	13.6	2392.7	1
TST-8C-S690	379.6	338.7	0.89	474.2	17.9	5262.6	1
TST-12A-S690	560.7	626.8	1.12	799.5	4.0	3005.0	3
TST-12B-S690	561.8	575.8	1.02	771.0	6.7	4431.4	2
TST-12A-S235	463.9	425.4	0.92	705.6	20.6	4709.4	1



(a) (b)

Figure 3: Interpretation of results

3 NUMERICAL ANALYSIS

During the experimental research, it was used for the end plate of T-stub macro-component, different steel grades as S355, S460 and S690. It is well known that the failure mode of a T-stub macro-component

www.EngineeringEBooksPdf.com

could be type 1, 2 or 3, which means ductile, semi-ductile and fragile (Table 4).

Table 4: Classification of joints according to T-stub failure mode

Failure mode	Ductility	Classification
Mode 1	Ductile	Partial-strength / Semi-rigid
Mode 2	Semi-ductile	Full strength / Rigid
Mode 3	Fragile	Full strength / Rigid

The numerical analysis started with two types of real rigid full-resistant joints from two multi-storey buildings of 21 and 16 stories, respectively, designed in two seismic loading circumstances, in Bucharest and Brasov (see Figure 4 and Table 5). The joint is not containing the beam component.

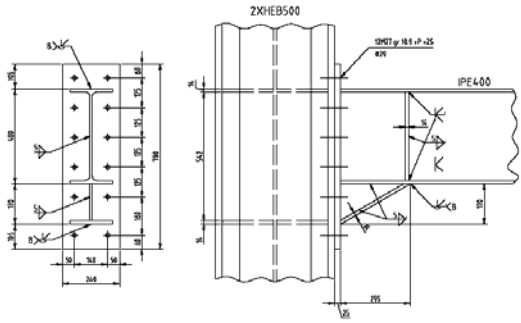


Figure 4: Brasov joint configuration

Table 5 Real joints configuration

Joint	Column	Beam	Haunch	Bolts
Bucharest	HEB 800	IPE 500	200x400	12 M24 gr 10.9
Brasov	HEB 500	IPE 400	170x300	12 M20 gr 10.9

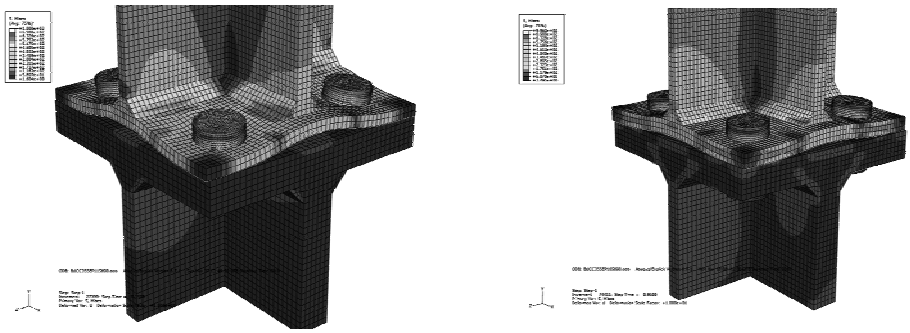
Table 6 Joint properties and classification

Joint	$M_{j,Rd}$ [kNm]	$M_{j,Rd}/M_{b,Rd}$	$S_{j,ini,Rd}$ [kNm]	EC3-1.8 Classification	T-stub failure mode (predicted)
BUC_EP15_S355	1027	1.320	804972	Rigid/full-strength	2→1
BUC_EP22_S355	1125	1.446	879040	Rigid/full-strength	2→3
BUC_EP14_S460	1056	1.357	766240	Rigid/full-strength	2→1
BUC_EP20_S460	1133	1.456	858772	Rigid/full-strength	2→3
BUC_EP11_S690	1038	1.334	603458	Rigid/full-strength	2→1
BUC_EP20_S460	1132	1.455	782508	Rigid/full-strength	2→3
BV_EP13_S355	553	1.192	448862	Rigid/full-strength	2→1
BV_EP20_S355	631	1.360	555632	Rigid/full-strength	2→3
BV_EP12_S460	567	1.222	412836	Rigid/full-strength	2→1
BV_EP16_S460	617	1.330	507110	Rigid/full-strength	2→3
BV_EP10_S690	571	1.230	323794	Rigid/full-strength	2→1
BV_EP12_S690	604	1.302	398500	Rigid/full-strength	2→3

Using different steel grades (S355, S460, S690) and thickness for the end-plate we obtained the failure modes of interest for our study, mode 2→1 and 2→3. The numerical analysis was performed with

www.EngineeringEBooksPdf.com

ABAQUS computer program [10]. These T-stubs configurations and classification are presented in Table 6. Figure 5 shows two examples of T-stubs behavior and failure modes obtained by numerical simulations for specimens derived from Bucharest joint, while Figure 6 describes the behavior curves for the T-subs corresponding to all the cases in Table 6.



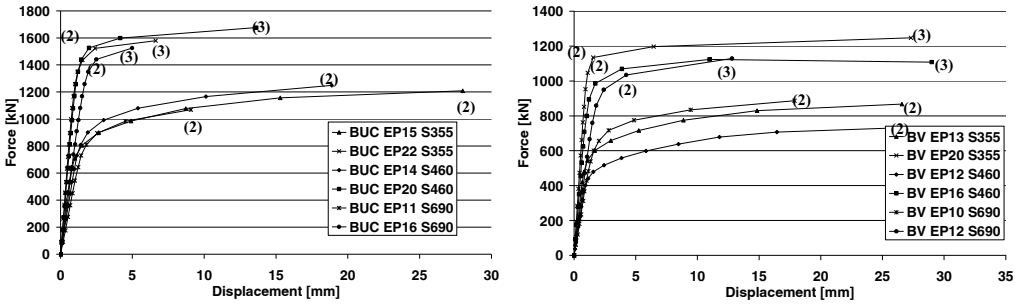
a) BUC_EP11_S690 (2→1) b) BUC_EP20_S460 (2→3)

Figure 5: T-stub behavior and failure mode according to numerical analysis

In failure mode (2), at the end, almost always, the bolt failure (3) might occur. In case of T-stubs designed for failure mode (2→1) (Figure 5.a), which are more ductile, first occurs the plasticization near the end-plate – beam flange junction, and starts the plasticization near the 1st and 2nd bolt rows, prior bolt fractures; in case of specimens of (2→3) failure mode (Figure 5.b), the second plasticization, usually does not occur, and bolt failure (3) arrives earlier.

In order to check the behavior of T-stubs in the MR joints, the response of two specimens of Table 6 has been simulated with ABAQUS, for monotonic loading only. The results, with a zoom of T-stub deformation mode are displayed in Figure 7.

Going back from the T-stub to the joints, we analyzed numerically also with ABAQUS, two types of joints from the same family, e.g. Bucharest, but with T-stub configuration from the 2 borders of failure mode (2→1) and (2→3). In Figure 7 there is evident that both are confirming the way that they were designed.

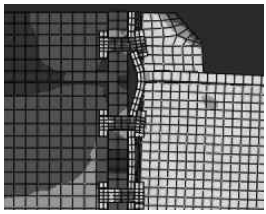


Bucharest Brasov

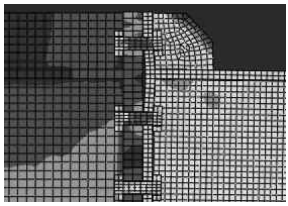
Figure 6: T-stub behavior according to numerical analysis

T-stub macro-component of the joint, which is falling down in mode 2 has sufficient rotation capacity and ductility (e.g. 40 mrad)to develop a plastic mechanism in joint if necessary, but only in mode (2→1) and not in mode (2→3), where the rotation capacity is quite poor like 15-20 mrad; on the hand, mode (2→3) is obviously stronger than mode (2→3).

www.EngineeringEBooksPdf.com



BUC_EP11_S690 (2→1)



BUC_EP16_S690 (2→3)

Figure 7: Joint behavior

4 CONCLUSIONS

Seismic provisions [1] impose both minimum over-strength (1.373 $M_{j,Rd}$) and ductility (35 mrad) for beam-to-column joints. Since the column web panel contribution is limited by design, in case of bolted extended and stiffened end-plate beam-to-column joints, the main source of ductility is the end-plate, providing that its plastic failure mechanism is governed by mode 2.

Present paper demonstrates the end-plate can be sized by design (thickness & steel grade)to supply the ductility requested by code provisions.

REFERENCES

[1] EN 1993-1.8. 2003. *Eurocode 3. Design of steel structures. Part 1-8: Design of joints*, European standard.

[2] EN 1998-1. 2004. *Eurocode 8. Design of structures for earthquake resistance. General rules, seismic actions and rules for buildings*, European standard

[3] Dubina, D. and Dinu, F., "High strength steel for seismic resistant building frames", *Proc. of 6th Int. Conf. Steel and Aluminium Structures – ICSAS'07*, R. G. Beale (ed.), Oxford Brooks Univ., 133-140, 2007.

[4] Dubina, D., Stratan, A. and Dinu, F., "High Strength Steel EB Frames with Low Strength Bolted Links", *Proc. of Int. Conf. on Advances in Steel Structures – ICASS 2007,* Liew J.Y.R., Choo Y.S.(eds.), Research Publishing, Singapore, 249-255, 2007.

[5] Dubina, D., Stratan, A. Muntean, N. and Grecea, D., "Dual-steel T-stub behaviour under monotonic and cyclic loading", *ECCS/AISC Workshop: Connections in Steel Structures VI*, Chicago, Illinois, USA, 23-55, 2008.

[6] Dubina, D., Stratan, A. Muntean, N. and Dinu, F., "Experimental program for evaluation of Moment Beam-to-Column Joints of High Strength Steel Components", *ECCS/AISC Workshop: Connections in Steel Structures VI*, Chicago, Illinois, USA, June 23-55, 2008.

[7] Dubina, D., Muntean, N., Stratan, A., Grecea, D. and Zaharia, R., "Testing program to evaluate behaviour of dual steel connections under monotonic and cyclic loading", *Proc. of 5th European Conference on Steel and Composite Structures - Eurosteel 2008*, 3-5 September, Graz, Austria, 609-614, 2008.

[8] Girao Coelho, A.M., Bijlaard, F.S.K., Gresnigt, N. and Simoes da Silva, L., "Experimental assessment of the behaviour of bolted T-stub connections made up of welded plates", Journal of Constructional Steel Research 60, 269-311, 2004.

[9] Piluso, V. and Rizzano, G., "Experimental analysis and modelling of bolted T-stubs under cyclic loads", Journal of Constructional Steel Research, 10.1016/j.jcsr.2007.12.009, 2007.

[10] ABAQUS Inc. "ABAQUS analysis user manual", version 6.6, 2006.

www.EngineeringEBooksPdf.com

SDSS'Rio 2010 STABILITY AND DUCTILITY OF STEEL STRUCTURES
E. Batista, P. Vellasco, L. de Lima (Eds.)
Rio de Janeiro, Brazil, September 8 - 10, 2010

PREDICTION OF THE CYCLIC BEHAVIOR OF MOMENT RESISTANT BEAM-TO-COLUMN JOINTS OF COMPOSITE STRUCTURAL ELEMENTS

Nauzika Kovács*, László Dunai* Luís Calado**

* Budapest University of Technology and Economics, Department of Structural Engineering, Hungary
e-mails: nauzika@vbt.bme.hu, ldunai@epito.bme.hu

** DECivil – Civil Engineering Department, IST Instituto Superior Técnico, Lisbon, Portugal
e-mail: calado@civil.ist.utl.pt

Keywords: beam-to-column joint, cyclic behavior, FE analyses, prediction model, parametric study, absorbed energy

Abstract. *An experimental program is performed on end-plate type joints (with different end-plates and bolts) of composite structural elements under cyclic loading. In parallel a numerical method is developed to predict the experimental cyclic behavior modes of the joints. The method is based on the monotonic joint behavior, assuming the knowledge of the typical hysteretic cycles. The method is applied in combination with verified finite element models to complete a parametric study. In this study the effect of the end-plate thickness and bolt size on the cyclic behavior is investigated. Finite element analyses are used to determine the monotonic force-displacement relationships. On this base the hysteretic behavior is derived by the developed prediction model, cycle by cycle, applying the ECCS recommendations for the cyclic loading history with the aim to evaluate the absorbed energy in order to determine the structural efficiency of the joints.*

1 INTRODUCTION

The focus of this research is on the beam-to-column connection zone of the dissipative structures, which are applied in seismic regions due to their ductile behavior and high strength. The seismic energy of the earthquake is absorbed by the plastic deformation in the joints and in the connecting elements. The current research studies this ductile plastic hysteretic force-displacement response of the end-pate type joints of the moment resisting frames by experimental tests and analytical investigations.

The end-plate type joints are widely used due to their simple production and erection procedure, however, the application of these joints, requires sophisticated design method due to their semi-rigid nature. Standard design method exists for the determination of the joint static behavior defining the moment resistance, initial stiffness and rotational capacity, but not considering the cyclic loading and the seismic response of the joints. The purpose of the current research is to complete analytical parametric studies on end-plate type joints of concrete in-filled composite members reflecting on the seismic behavior as the energy absorption capacity during the consecutive cycles. In the presented work the aim is to develop a method, which predicts the absorbed energy of the studied joint. First the monotonic joint model is developed by FE model and verified by experimental results as the base of the proposed semi-empirical method. By the combination of the finite element analysis and the developed cyclic prediction method, using the experimentally determined typical hysteretic diagrams, the experimental results are extended. The focus of the current research is on analyses of the bolt-failure and the end-plate type failure the studied joints. A parametric study is performed not exceeding the experimental global joint geometry with the aim to determine the absorbed energy capacity and to conclude the favorable end-plate and bolt geometry from seismic point of view.

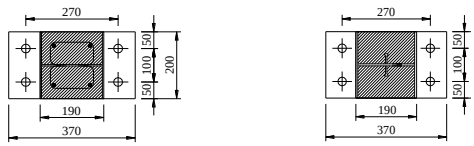
www.EngineeringEBooksPdf.com

2 EXPERIMENTAL PROGRAM

An experimental research program was carried out on 12 end-plate type bolted joints of concrete filled I-sections to investigate their response under cyclic bending. The test program was carried out as a cooperative effort between the Budapest University of Technology and Economics and the Technical University of Lisbon, where all the tests were conducted. In this systematic test program, the first six specimens were used to study basic behavior modes of the bolted end-plate type joints of composite members. Following these tests, six similar joints of composite members with slender cross-section were tested to study the beam interacting zone. The details of the experimental programs are presented in [1], here only short summary is given.

2.1 Test arrangement

The test arrangement is a cantilever type one, the specimens are subjected to cyclic loading, according to the ECCS standard-based loading history [2], in altering directions. The specimens are designed with H-shaped composite element (hot-rolled or welded) with concrete filling and reinforcement or headed studs between the flanges, as shown in figures 1a) and b).

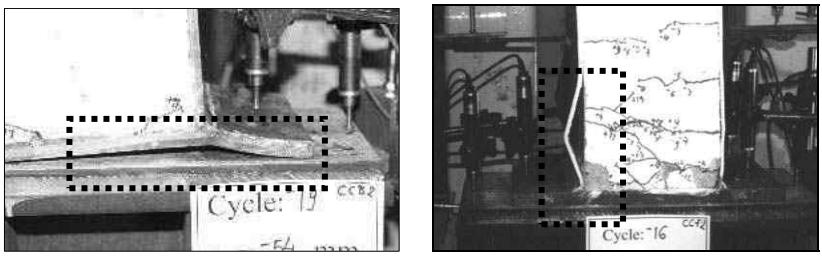


a) with reinforcement b) with headed studs

Figure 1: Composite specimens.

2.2 Test results

Two types of behavior are observed during the tests. When the resistance of the connecting members (beam) is relatively higher, the failure is occurred in the connection with residual plastic deformation and crack propagation of the end-plates and bolts, as shown in figure 2a). In case of stronger connecting elements (bolts, end-plate), the cyclic behavior is governed by the local plate buckling of the member interacting zone, as shown in figure 2b).



a) connecting element type b) local buckling type

Figure 2: Experimental behavior.

On the basis of the measured data the cyclic moment-rotation curves are determined. From the cyclic moment-rotation relationship the cyclic parameters (ductility, rigidity/resistance degradation and absorbed energy) are also evaluated. The cyclic behavior modes of the studied connection are classified by the governing phenomena: the bolt yielding and fracturing in tension (bolt-failure); the plate deforming in bending (plate-failure); the interaction between bolt and plate, and the local plate buckling-failure. In the further part of the paper only the connecting element type failure modes, (see figure 2a), are studied. The details of the experimental program and results can be found in [1].

www.EngineeringEBooksPdf.com

3 PREDICTION METHOD FOR THE CYCLIC BEHAVIOR

In parallel with the experimental research a semi-empirical method is developed to predict the hysteretic behavior of the joints. In the first step, the method defines the typical hysteretic cycle belongs to the behavior mode. In further steps, by applying the standard cyclic loading [2], the hysteretic diagram is built up by multi-linear hysteretic cycles. The degradation tendency during the consecutive cycles is expressed by performance coefficient, which is experimentally determined by the linearized degradation of the rigidity. The proposed method is able to approximate the cyclic response and the absorbed energy of the studied joints for each observed failure mode types. It is based on the knowledge of the behavior curve, which can be established by monotonic experimental test, by standard based design method or by finite element simulation. The prediction method is developed on both the force-displacement and moment-rotation relationship levels, in this paper the results of the predicted cyclic behavior is based on the monotonic force-displacement diagram evaluated by the FE model detailed in chapter 4. The details of the prediction method are presented in [3], here only a short summary is given.

3.1 Typical hysteretic cycle

An example of the typical cycle for end-plate type behavior is presented in figure 3. The linear polygonal approximation of the cycles achieves good coincidence, as shown in figure 3b). The tangents of the polygonal lines of the typical cycles are derived from experimental observations in the function of the initial rotational stiffness of the monotonic curve. The model uses performance coefficient to include the peculiarities of each behavior mode type, which are defined as representing parameters for the failure mode types and calculated form experimental results. The proposed method follows the cyclic behavior in stable plastic cycles (cycles between the yield limit and cycles with significant resistant degradation).

The approximation of the cycle starts from the (F_{1p}, Δ_{1p}), point of the monotonic curve, with the determination of the unloading path (from F_{1p} to $F = 0$) and the loading path of the negative direction (from $F = 0$ to $-F_{1p}$) by experimentally based performance coefficients, reaching the negative part of the monotonic curve. The unloading path, coming from $-F_{1p}$ is also determined by the performance coefficients. The loading path of the positive direction reaches the monotonic curve at the rotation level Δ_2, which is determined according to the applied loading history. The hysteretic curve can be calculated cycle by cycle using the above detailed process.

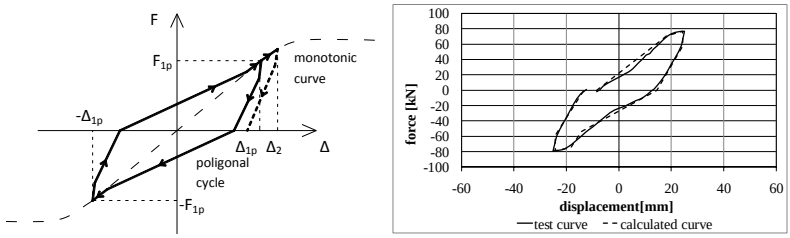
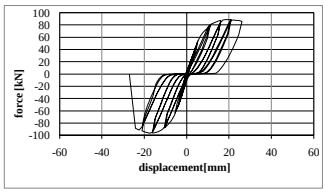


Figure 3: Typical hysteretic cycle.

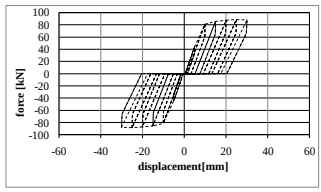
3.2 Predicted moment-rotation relationship

The developed prediction method is applied by using the FE model based monotonic curve to predict the cyclic response of the joints. From this monotonic curve the hysteretic diagram is calculated cycle by cycle applying the ECCS [2] loading history. The calculated hysteretic diagrams of the connecting element type failure modes, (see figure 2a), are presented in figure 4, which show good coincidences with the experimental curves.

www.EngineeringEBooksPdf.com

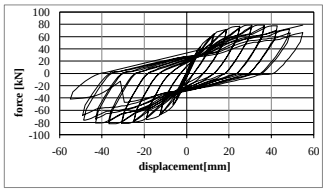


experimental

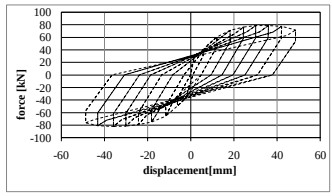


predicted

a) bolt-failure



experimental



predicted

b) plate-failure

Figure 4: Predicted and experimental hysteretic force-displacement curves.

The absorbed energy ratio of the consecutive hysteretic cycles is established from the predicted curves based and compared with the absorbed energy ratio of the corresponding experimental results. In case of the connecting element type failure the absorbed energy ratio is slightly overestimated by the prediction method, the difference between the predicted and the tested vales are between 1-18%. The details of the prediction method and results can be found in [3].

4 FINITE ELEMENT MODEL

In parallel with the prediction method an advanced finite element (FE) model has been developed using the ANSYS program, as shown in figure 5. The steel section is modeled by the 3D 8-node structural solid elements (SOLID185) having three degrees of freedom at each node. The concrete infill between the flanges of the I-section is modeled by 3D 8-node reinforced concrete solid element, which is capable of cracking in tension and crushing in compression, having three degrees of freedom at each node (SOLID65). The contact between the steel elements is modeled by contact pairs (CONTA174 and TARGE170) located on the surface of the 3D solid elements. Contact pairs are defined between the end-plate and the supporting plate; under the bolt head and nut, and surrounded the bolt shanks.

The material properties of the FE model are based on experimental material tests. For the steel I-section and bolts multilinear isotropic hardening material is used. In case of the studied joint geometry the failure occurred in the connecting element without significant damage of the composite beam, the cracking and crushing of the concrete material is avoided.

The support is defined by DOF constraints under the supporting plate at each node (see figure 5). In the FE analysis a displacement control is used to evaluate the monotonic force-displacement relationship of the specimens, which assumed to be the envelop curve of the experimental cyclic diagram.

The FE model is built up by input file using variables for all the geometry and material properties to prepare it for parametric analyses. The FE model is verified qualitatively by failure modes, as shown in figure 6, and quantitatively by the force-displacement relationship, as shown in figure 7.

The verified FE model is applicable for cyclic loading conditions and results in hysteretic force-displacement relationship, however it requires significant computation time. For this reason, it is decided to evaluate the monotonic force-displacement relationship and the prediction method is used for approximation of the hysteretic curve. A parametric study is performed with this method, as detailed in chapter 5.

www.EngineeringEBooksPdf.com

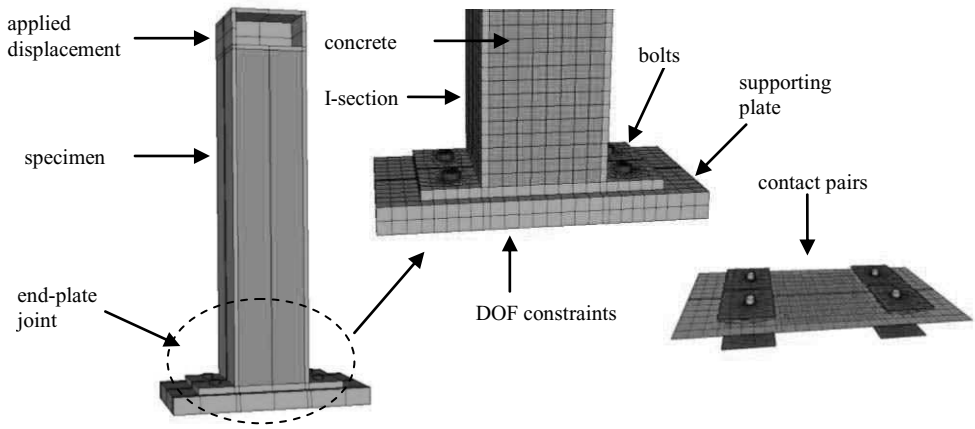
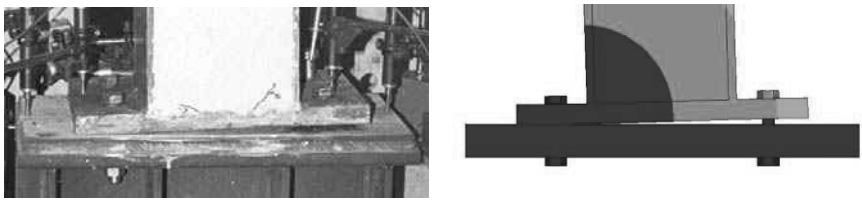


Figure 5: Details of the FE model.

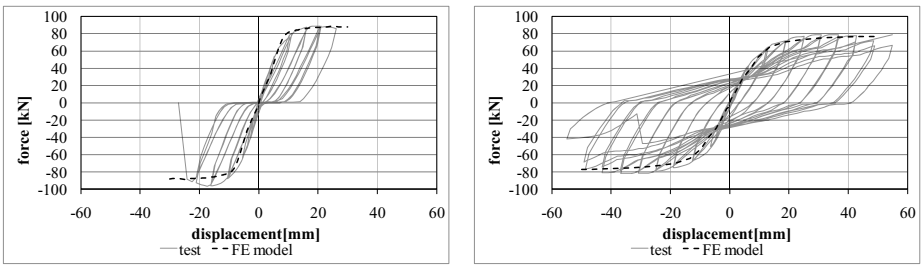


a) bolt-failure (specimen CCB1)



b) plate-failure (specimen CCB2)

Figure 6: Comparison of the failure modes.



a) bolt-failure b) plate-failure

Figure 7: Comparison of the force-displacement relationships.

www.EngineeringEBooksPdf.com

5 PARAMETRIC STUDY

The prediction method is applied in combination with verified finite element model to complete an extended parametric study. The parametric study examines bolted end-plate type connections remaining in the global geometry of the tested joint. Within this geometrical limitation the influence of the characterizing parameters – end-plate thickness, bolt size – is investigated on the resistance, initial stiffness and absorbed energy. It is assumed the section of the connecting composite member has resistance enough to avoid the local buckling failure of the member interacting zone.

In the presented parametric study the end-plate thickness is altering between 8-30 mm increased by 2mm, the bolts are between M10-M27, the grade of the steel, the bolt and the concrete materials are constant in each case and come from experimental material tests. The parametric study is performed on 84 specimens covering the whole parameter rage (end-plates t=8, 10, 12, 14, 16, 18, 20, 22, 24, 26, 28 and 30 mm; bolts M10, M12, M16, M20, M22, M24 and M27).

5.1 Monotonic force-displacement relationship

Finite element analyses are used to determine the monotonic force-displacement relationships of the joints for all the various parameters. Displacement control is used for each specimen and 30 mm maximal displacement is applied at the top of the specimen (see figure 5). The reaction forces occurred on the DOF constrains are detected and summarized in each load step and the monotonic (reaction) force-(applied) displacement curves are derived. As an example the monotonic relationship for bolt size M16 and end-plate thickness t=8-30 mm is shown in figure 8.

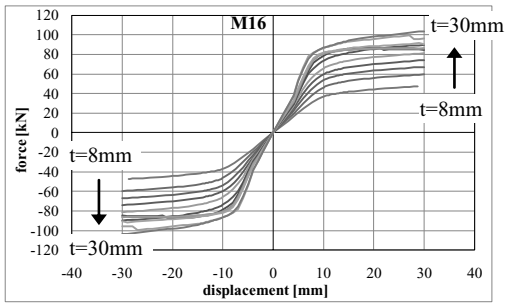


Figure 8: Monotonic force-displacement relationships.

The result of the monotonic FE analyses leads to the following input values of the prediction method: failure modes (bolt-failure or plate-failure), monotonic force-displacement curve, resistance, initial stiffness, yield limit. The failure modes of all the 84 specimens covering the parameter range are summarized in table 1.

Table 1: Failure modes.

end-plate thickness [mm]	8	10	12	14	16	18	20	22	24	26	28	30
M10	plate	plate	bolt	bolt	bolt	bolt	bolt	bolt	bolt	bolt	bolt	bolt
M12	plate	plate	plate	plate	bolt	bolt	bolt	bolt	bolt	bolt	bolt	bolt
M16	plate	plate	plate	plate	plate	plate	bolt	bolt	bolt	bolt	bolt	bolt
M20	plate	plate	plate	plate	plate	plate	plate	plate	bolt	bolt	bolt	bolt
M22	plate	plate	plate	plate	plate	plate	plate	plate	plate	plate	bolt	bolt
M24	plate	plate	plate	plate	plate	plate	plate	plate	plate	plate	bolt	bolt
M27	plate	plate	plate	plate	plate	plate	plate	plate	plate	plate	bolt	bolt

www.EngineeringEBooksPdf.com

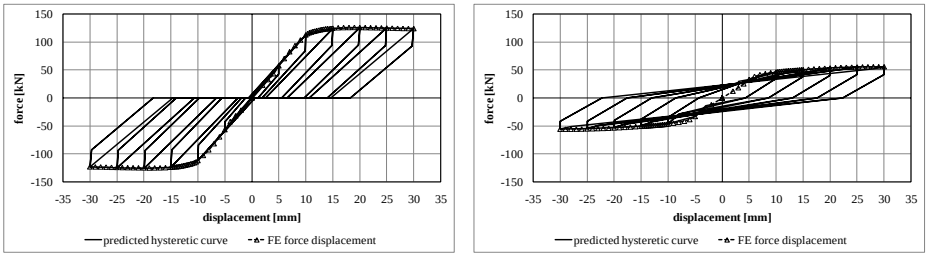
5.2 Predicted hysteretic curves and absorbed energy

On the basis of the monotonic curves the hysteretic behavior is derived by the developed prediction model, cycle by cycle, depending on the failure modes. The load history of table 2 is applied for each case, to have comparable results for each different parameter. At each displacement level two cycles are performed (e.g. cycle 1 and cycle 1 rep.).

Table 2: Cyclic load history.

Plastic cycle	1	1 rep.	2	2 rep.	3	3 rep.	4	4 rep.	5	5 rep.
Displacement [mm]	+10	+10	+15	+15	+20	+20	+25	+25	+30	+30
	-10	-10	-15	-15	-20	-20	-25	-25	-30	-30

The hysteretic diagrams are evaluated for all the 84 specimens using an automated algorithm. As an example the predicted hysteretic curves of the two different failure modes are presented in figure 9; from the wide parameter range the following values are chosen for presentation: t=26 mm, M20 for bolt failure and t=14 mm, M12 for plate failure.



a) bolt-failure (t=26 mm M20) b) plate-failure (t=14 mm M12)

Figure 9: Predicted hysteretic curves.

The predicted curves are performed with the aim to evaluate the absorbed energy of each specimen in the plastic cycles and to compare them to each other. In evaluation of the cyclic characteristics the calculation of the absorbed energy ratio is completed by recommendation of the ECCS [2]. The absorbed energy ratio can be calculated for each cycle as the ratio of the actual value and an ideal value, which could be measure in case of an ideal linear–perfectly plastic behavior. The absorbed energy ratio is approximately 0,6-0,7 for plate-failure specimens and 0,1-0,3 for bolt-failure specimens. For the comparison not the ratio, but the actual value of the absorbed energy, namely the area of the hemicycle of the force-displacement relationship is used with the unit [$kN \cdot mm$]. The absorbed energy is evaluated for each specimen in each cycle, an example the absorbed energy in cycle 4 and cycle 4 rep. are presented in figure 10. Similar tendencies of the absorbed energy of all the 84 specimens are observed in other plastic cycles.

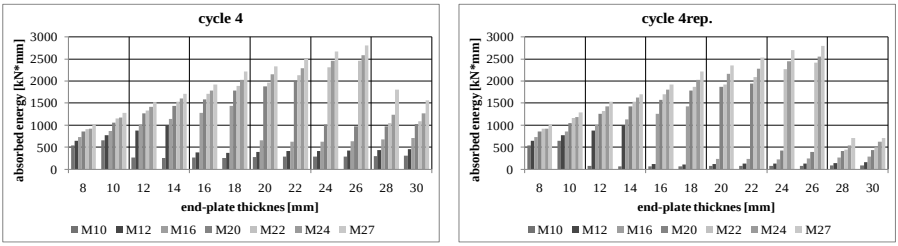


Figure 10: Absorbed energy.

www.EngineeringEBooksPdf.com

In figure 10 the failure modes of the specimens are visible through the absorbed energy. Relatively high absorbed energy in both the cycle and the repeated cycle show plate-failure. The relatively small absorbed energy, which drop down in the repeated cycle due to the rigid body type rotation of the specimen means bolt failure. From figure 10 the end-plate thickness (t) and bolt size (d) parameter pairs can be selected for the favorable plate type failure in accordance with the required absorbed energy. The parametric study covers the d/t=0,33÷3,38 parameter range. Bolt-failure with very limited absorbed energy observed when d/t≈0,33÷0,96. The favorable plate-failure occurs with large energy absorption capacity due to the excessive deformation of the end-plate in parameter range d/t≈0,85÷3,38. In generally (see figure 10) using one size larger bolts leads to approximately two or three times larger absorbed energy capacity, due to modifying the failure mode to plate failure. This increasing tendency is even more significant in the repeated cycle, in extreme case it is four times larger for plate-failure than for bolt-failure (see figure 10) and still increasing in further repeated cycles.

6 CONCLUDING REMARKS

The presented analytical study on end-plate type joint of composite members has a strong experimental background. The experimental tests were performed in cooperation between the Budapest University of Technology and Economics and the Technical University of Lisbon. Based on the experiences of the experimental tests an advanced finite element model is developed and used for parametric study to evaluate the monotonic behavior of the end-plate joints, not excluded the global geometrical range of the test. The FE model is capable to evaluate the cyclic response of the specimen, however, it takes long computation time. To cover a wide parameter range it is decided to evaluate the monotonic response by FE analyses in combination of the developed hysteretic prediction method.

The completed parametric study covers 84 specimens and based on the evaluated absorbed energy efficient joint details from cyclic point of view are determined.

The presented FE model runs from an input file and all the geometrical and material properties are defined by a variable. This means that parametric study altering other variable (e.g. bolt and steel grade, distance of the bolts, size of the end-plate etc.) after certain adjustment of the mesh is applicable and the monotonic force-displacement relationship is available. The method to predict the hysteretic curve uses automated algorithm to evaluate the predicted hysteretic curve.

In this paper only the connection type behavior is studied. From the results the d/t ratios leading to favorable absorbed energy are determined and can be used in design practice. The further step of the research is to improve the FE model to be able to take into consideration the local buckling type behavior of the composite member interacting zone.

ACKNOWLEDGEMENT

The research work was conducted under the financial support of the ongoing Portuguese – Hungarian Intergovernmental Science and Technology Cooperation Program ICCTI/OM TÉT.

REFERENCES

[1] Kovács, N., Calado, L. and Dunai, L., "Behaviour of bolted composite joints; Experimental study", *Journal of Constructional Steel Research*, 60(3-5) 725 738, 2004.

[2] ECCS, "Structural safety and loadings: recommended testing procedure for assessing the behaviour of structural steel elements under cyclic loads", *Technical Committee 1 TWG 1.3, - Seismic design, No. 45*, 1986.

[3] Kovács, N., Calado, L. and Dunai, L., "Experimental and analytical studies on the cyclic behaviour of end-plate joints of composite structural element", *Journal of Constructional Steel Research*, 64(2) 202 213, 2008.

www.EngineeringEBooksPdf.com

SDSS'Rio 2010 STABILITY AND DUCTILITY OF STEEL STRUCTURES
E. Batista, P. Vellasco, L. de Lima (Eds.)
Rio de Janeiro, Brazil, September 8 - 10, 2010

NUMERICAL MODELING OF JOINT DUCTILITY IN STEEL AND STEEL-CONCRETE COMPOSITE FRAMES

Leslaw Kwasniewski and Marian Gizejowski

Warsaw University of Technology
e-mails: l.kwasniewski@il.pw.edu.pl, m.gizejowski@ il.pw.edu.pl

Keywords: Joints, Progressive collapse, Robustness, Numerical modeling, Verification and Validation.

Abstract. *The paper presents a study on numerical modeling of typical joints in steel and composite steel-concrete frame structures for the purpose of the global progressive collapse analysis of multistory buildings. The difficulty in such analyses is to efficiently model the response of joints with consideration of all the aspects of structural detailing, like the postwelding properties of steel, the weld size effect, detailed bolt connection geometry including the bolt head, nut and washer, as well as to merge responses of two materials into one representation in case of composite joints. The problem is investigated using nonlinear dynamic computer simulations carried out using general purpose program LS-DYNA. The feasibility study is focused on identification of modeling parameters affecting the final results and on development of a plan for hierarchical verification and validation.*

1 INTRODUCTION

In progressive collapse analysis of structures, the primary objective is to limit structural damage and in this way save lives, prevent injury, and protect property. Different design approaches have been developed for reducing or eliminating disproportionate damage. There have been attempts to design stronger members to resist specific abnormal loads or to limit the total damage by effective redistribution of loads, i.e., alternate load paths [1]. For all approaches, the principal question for structural analysis is the extent of damage caused by a local failure initiated by an infrequent event. In the most common progressive collapse analysis, the usual loading procedure is the removal of one or more columns [1]. To find the extent of damage caused by a local component failure, the whole structure or a large portion of it has to be analyzed. Such analysis is rather complex as actual structural collapse itself is inseparably a nonlinear event in which structural elements are stressed beyond their elastic limit up to failure. There is also a need for global modeling, where large portions of a building are represented but at the same time capturing local effects is equally important. The possible load paths are dependent on the performance of localized plastic zones. To introduce plastic hinges in the analysis, generally two approaches can be applied. In the first, simplified approach, plastic hinges with the assumed characteristics in terms of moment–rotation relationships are introduced explicitly in the model. Such moment-rotation relationships are usually determined for planar bending only. Structural components such as beams and columns are usually represented by 3D beam elements in these models. The outcome of such analyses is strongly determined by the assumptions made.

The paper presents a study on more detailed numerical modeling of typical joints in steel and composite steel-concrete frame structures. The main objective of this research is to efficiently model beam-to-column joints for the purpose of the global progressive collapse analysis of multistory buildings. Structural joints, such as the considered here steel and composite steel-concrete joints are challenge for numerical modeling, especially when the full range of loading up to failure is considered. The difficulty is to efficiently model the response of joints with consideration of all the aspects of structural detailing, like

www.EngineeringEBooksPdf.com

the post-welding properties of steel, the weld size effect, detailed bolt connection geometry including the bolt head, nut and washer, as well as to merge responses of two materials into one representation in case of composite joints. For small specimens of structural joints, the most accurate approach is to model all the joint details and each material separately, for example, the bolt connectors and nuts as well as a concrete slab core with solid elements, while the slab profiled deck and other joint components with shell elements, and reinforcement bars with truss or beam elements. For large-scale models this strategy is infeasible today as it would result in a very large number of finite elements.

The problem is investigated using nonlinear dynamic computer simulations carried out using general purpose program LS-DYNA. Taking advantage of parallel processing on multiprocessor computers, detailed 3D models with different numbers of finite elements, interactions and other solution parameters have been developed for comparison among numerical and experimental results. Using transient nonlinear dynamic simulations selected connections are tested numerically for full range of loading up to failure. Typical plane bending and loading initiated by notional column removal is considered. The feasibility study is focused on identification of modeling parameters affecting the final results and on development of a plan for hierarchical verification and validation.

2 DETAILED NUMERICAL MODELING OF STEEL JOINTS

2.1 Solution methods

The review of published works on progressive collapse analysis (compare bibliography in [2]) shows that there is a broad variety of approaches and one can choose between linear and nonlinear, static and dynamic, and between 2D and 3D analyses. The nonlinear time history (dynamic) analysis is often recognized as giving most realistic results but at the same time, due to its high complexity, it is prone to incorrect assumptions and modeling errors.

Depending on how time is treated in the analysis, we can choose among dynamic, quasi-static, and strictly static approaches. The loss of stability is usually a dynamic process, and therefore should be directly traced using the most general, dynamic approach. Nonlinearity and discontinuity cause convergence problems that are less severe in the dynamic due to the stabilizing effect of the inertia forces [3].

A dynamic analysis with the finite element (FE) method applied for space discretization is usually conducted using implicit or explicit time integrators. Implicit dynamic analysis (using implicit time integrators) is dedicated for structural problems described by Belytschko *et al.* [3] as inertial problems where stress wave propagation and related effects are not important. For such problems, the response time is relatively long compared to the time required for a stress wave to traverse the structure. When the response time sought is short and the wave effects are important, the time step must be very small, and more appropriate solution methods are those based on the explicit time integration.

The explicit time integration scheme belongs to purely incremental methods and is applicable to formally dynamic problems. The incremental solution methods dominate incremental-iterative methods, especially for problems experiencing rough nonlinearities, which involve component failure or inequality constraints such as contact or friction [3]. In the explicit methods, the equations of motion are usually solved using the central difference method with very small time steps determined by the highest frequency of the linearized system [4]. The codes based on the explicit time integration are dedicated to dynamic transient problems and have proved to be especially effective when large deformations grow rapidly. Contrary to the implicit methods, the explicit time integration cycle is computationally much less expensive as there are no iterations and only one diagonal matrix needs to be inverted. However, the simulated period of time requires a much larger number of calculation cycles. With a time step of the order of microseconds, even a few seconds of a typical simulated event require millions of calculation cycles and substantial calculation time. The explicit method is simple, easy to implement, and very effective; it rarely aborts due to failure of the numerical algorithm, which quite often is the problem for implicit methods.

www.EngineeringEBooksPdf.com

2.2 Material properties

In steel and composite, steel–concrete, frame structures, working in the inelastic range, deformation is concentrated in plastic hinges and zones. The performance of the plastic hinges, usually localized at joints, depends strongly on the inelastic properties of the steel components [5]. The critical parameters are yield stress, ultimate stress, and ultimate strain. If the actual stress-strain relationships are measured through laboratory coupon tests, the input for a numerical model should be formulated as a true stress-strain curve, recalculated based on the directly measured engineering values and well known formulas [4]

$$\sigma_T = \sigma_E(1+\varepsilon_E), \tag{1}$$

$$\varepsilon_T = \ln(1+\varepsilon_E), \tag{2}$$

where subscripts $_T$ and $_E$ denote true and engineering values, respectively. If only nominal properties are known for the specific structural steel grade, simplified material models have to be applied, such as the elastic—ideally plastic or bilinear elastic—plastic model with hardening, recommended by Eurocode 3 [6]. Although progressive collapse is generally a dynamic event, happening in a matter of seconds, the strain rate effects seem to be not so important at least for the threat independent approach (but should be considered in the impact or explosion analyses).

Localized effects of the phase transformation and restrained shrinkage in post-welded steel components of joints are important for the failure assessment [7]. Welds of full penetration, the quality of which is guaranteed by non-destructive testing, are usually stronger-in-strength places than the surrounding parent material. The ductility requirement for welds is not important for the adequately selected weld consumable material, and failure of such connections may occur in the vicinity of welds, in the so-called heat affected zones (HAZ). Ductility and strength of steel in this region is controlled by the properties of different steel transformation phases such as hardened non-ductile martensite phase, then less hardened and more ductile bainite phase, and finally ductile pearlite phase of the parent material. Depending on the post-welding cooling process of steel from the austenite, different residual stress patterns and phase transformation components may exist in the region of HAZ and affect substantially the localized mechanical properties of steel, ability to plastic behavior and failure by cracks growth. Modeling of localized effects in the post-welded steel is not an easy task and usually neglected in bolted end-plate connections in which the ductility of high strength bolt material becomes the decisive failure criterion. The effect of residual stresses may be introduced by applying the concept of equivalent stress-strain diagram.

Concrete is at the same time a common construction material and the biggest challenge for numerical modeling. As a porous and brittle material, concrete shows a nonlinear compaction response, dramatically different strengths in tension and compression, and shear strength increased by mean stress [8]. Although in practice concrete is characterized by only one parameter, uniaxial unconfined compressive strength (f'_c), concrete's complex behavior under different stress states requires from a user determination of many parameters, stress-strain curves, and sometimes equations of state for pressure versus volume strain [4]. As such experimental data are usually not available, some of the new material models for concrete implemented in the commercial codes (e.g., LSDYNA) offer an option for automatic generation of all required input data. The internal generation is based on the well-worked laboratory experimental data for selected examples of standard concrete. The user is required only to provide unconfined compressive strength f'_c. The program provides generated parameters that can be modified and applied as the new input by a user who has additional information about the modeled concrete. Such an approach seems to be very convenient for users and sufficiently reliable for most engineering applications. This reliability is based here on the assumption that although there are many types of concrete standard materials with the same f'_c show similar properties for other stress states. In contrast to accuracy, which seems to be sufficient based on the single element tests [8], the main computational difficulty emerging here is the stability of the calculation, especially when the analysis is supposed to reach beyond the local material

www.EngineeringEBooksPdf.com

damage. To avoid numerical problems caused by extensive deformation, elements need to be erased in accordance with the prescribed failure criteria.

2.3 Space discretization

A modeling issue which should be considered here first is the space discretization allowing for adequate representation of component stiffness especially for connections where most of the inelastic deformation is concentrated. The space discretization for structural analysis is nowadays usually performed using finite elements (FE). Figure 1 shows two concepts for FE models of framed structures. In the first model (on the left) all components of the joint are modeled in very detailed way using solid elements. Such approach increases substantially a number of finite elements in the model but allows for capturing effects initiated by large structural deformations such as an inelastic bending of end plates or stress concentration in the vicinity of bolts. Due to large number of finite elements required, such models are infeasible for global modeling but can be used for partial verification of less detailed models such as one shown on the right in Figure 1. In this approach all beams and columns are represented by 3D FE models built of shell elements. The bolts are represented by 1D beam elements. Additionally, there is a global contact defined among all the steel components represented by shell elements, e.g., flush end plates and columns, and eventually shell elements representing floor slabs (not shown in Figure1). The contact is defined using an offset equal to half of the thickness for each interacting metal sheet.

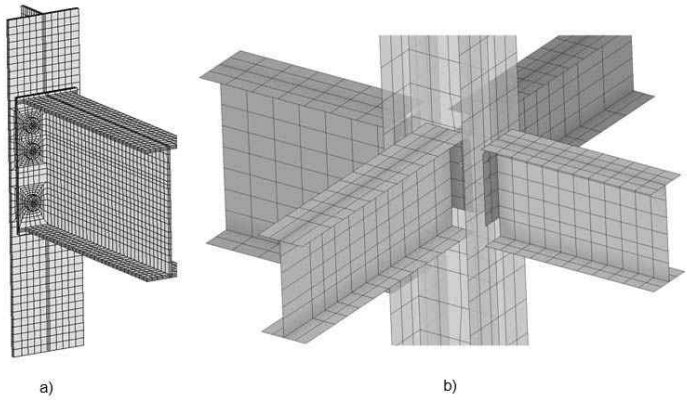


Figure 1: Modeling concepts for frame structure: a) 3D model built of solid elements, b) 3D model built of shell elements.

The model built of shell elements, shown in Figure 1 is a compromise between tendency of using detailed models and computational capabilities of today's computers.

3 VERIFICATION AND VALIDATION

The predictive capability of the nonlinear dynamic simulations is dependent on the inherent complexity of the method (e.g. contact and failure algorithms), taken assumptions (modeling simplifications) and uncertainties characterizing the input data (e.g. material parameters determining component failure). To improve the validity of the developed FE models and to identify the decisive model parameters a hierarchical verification and validation (V&V) procedure should be considered [9]. While verification uses analytical or highly accurate numerical solutions, validation is based on the comparison of computational results with experimental data. The hierarchy of the process means that the comparison is performed on different levels of complexity, for example from material characterization or element tests through subsystems to the full scale tests [9]. Many consider the V&V as a process which can never be completed as there are always some possible experiments left which could reduce errors of

www.EngineeringEBooksPdf.com

the solution and the available recourses are always limited. Practically the amount of experimental data which can be used for validation is always limited. A compromised solution is to replace some of the missing experimental data from the purposely designed validation tests (e.g. on joints) on the actual structure with numerical virtual tests using more detailed FE models of structural components. The emphasis should be put on the identification of the model parameters critical for the outcome of the computer simulations. This objective can be accomplished by showing the results for assumed bracket quantities of critical model parameters.

3.1 Mesh resolution

The main part of verification, which should precede validation, is the study on mesh resolution. Figure 2 shows as an example two of the FE meshes, called coarse and dense meshes, considered for an example beam to column connection. A 356x171x51UB (S355) beam is bolted on the flange of a column 305x305x137UC (S355) through an end plate (10 mm) with eight M20 grade 8.8 bolts. In this FE model the beam and the column, including flush plate are modeled using (first-order) shell elements, see Figure 1.

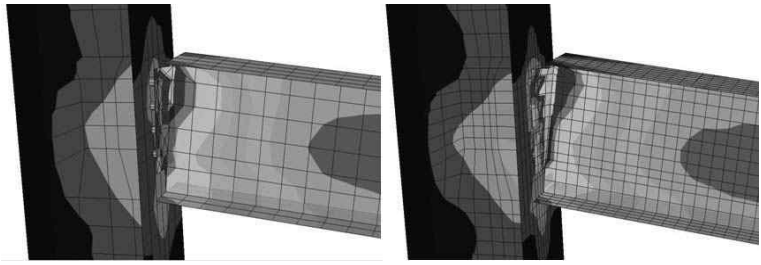


Figure 2: Study on mesh sensitivity for 3D FE model of joints: a) coarse mesh, b) dense mesh.

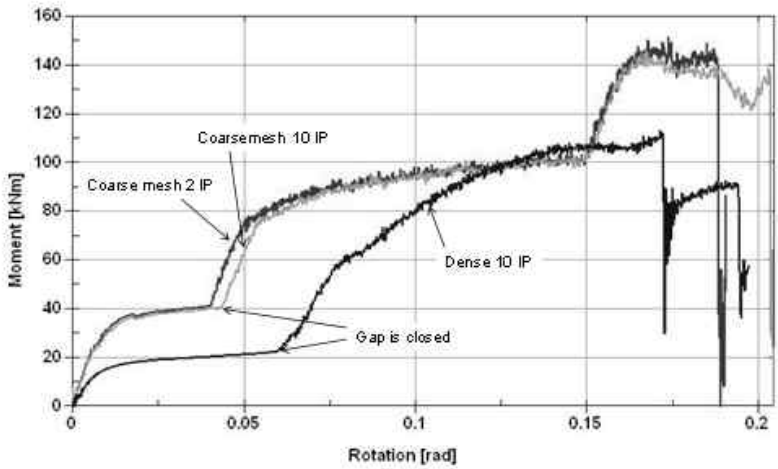


Figure 3. Comparison of moment-rotation curves for different FE models of beam to column joint.

Figure 3 presents comparison of calculated moment–rotation curves for typical tested joints with the same flush end-plate connections, i.e. in planar bending (with lateral movement restrained). The numerical results were obtained using dynamic analysis with explicit time integration. The curves shown

www.EngineeringEBooksPdf.com

in Figure 3 represent different mesh densities and different number of through thickness integration points (IP). Although the number of integration points has little effect on the results the finest mesh considered here gives twice smaller initial stiffness and 24% smaller approximation of the maximum bending moment in the reference to the coarse mesh. The initial stiffness of the connection is mostly determined by bending of the flush plate until the gap between the bottom beam's flange and the column's flange is closed and the visible in Figure 3 hardening phase begins. At the same time all models give similar approximation of the ultimate (failure) rotation. There is also clear difference between the results for coarse and dense FE meshes in terms of work done by loading as it shown in Figure 4.

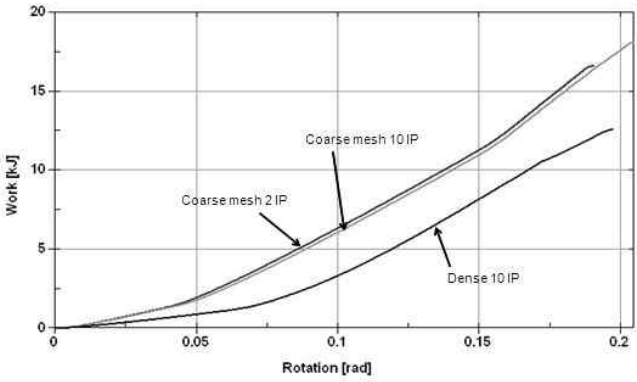


Figure 4. Comparison of work done by loading for different FE models of beam-to-column joint.

The dense mesh shown in Figure 2 might be inappropriate for global analyses as infeasible with available computational resources that are giving too small time steps and too large number of elements. This example illustrates a difficulty in finding good balance between the necessity of global analysis of large systems and requirements for the proper representation of some structural details, e.g., connections between components, to correctly capture the local effects, which in turn can determine the further solution.

3.2 Failure strain for structural steel and bolts

The empirical studies on beam-to-column joints indicate that the failure in the actual connections usually is initiated by rapture of fillet welds or failure of bolts (e.g. shear stripping of the threads), refer to [5]. In the FE models the material failure leading to the component disintegration is represented by deletion of a finite element from further calculations. For structural steel the most common failure criterion, determining an element deletion, is defined by a limit value of the effective plastic strain. Figure 5 shows comparison of three curves for the dense mesh and assumed different failure strains. Curve 1 was obtained for failure strain for bolts and structural steel ε_f =0.03, curve 2 for failure strains for bolts and flush plate increased by 20%, and curve 3 for bolt's failure strain increased by 43%.The coupon tests presented in [10] show high variation of the ultimate strains for the structural steel with the minimum magnitudes reaching almost half of the mean value.

Figs 6 and 7 present the results of the computer simulations for a major axis connection tested experimentally by Aribert *et al.* [5]. A HEA 360 (S355) beam is bolted on the flange of a column HEA 240 (S355) through a partial end plate (12 mm) with four M20 grade 8.8 bolts. This is a type of joint particularly convenient to use for a fast structure erection and although designed to transmit no bending moments, is actually able to carry a partial bending moment. Figure 6 shows the contours of effective Mises stress obtained for the used model with mesh density comparable to the dense mesh shown in Figure 2. The diagram shown in Figure 7 presents a comparison of several calculated moment-rotation curves with the experimental data provided in [5].

www.EngineeringEBooksPdf.com

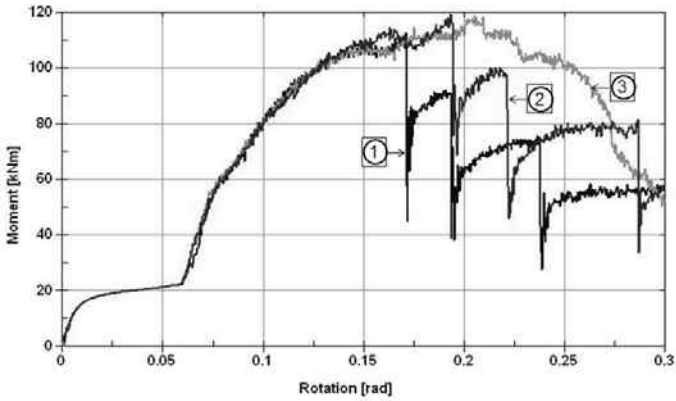


Figure 5. Comparison of moment rotation curves for different failure strains. Curve 1 – failure strain for bolts and structural steel ε_f =0.03, curve 2 – failure strains for bolts and flush plate increased by 20%, curve 3 – bolt's failure strain increased by 43%.

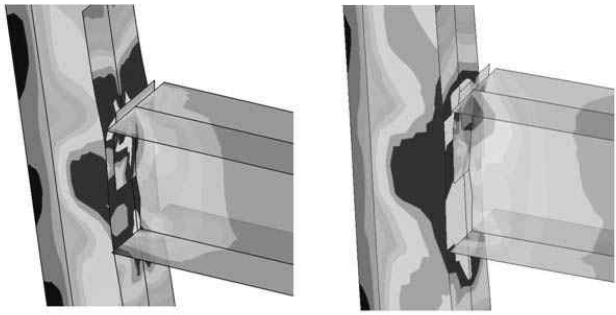


Figure 6. Contours of effective Huber-von-Mises stress calculated for maximum bending moments. Flush end-plate connection tested in [5] with different bolt's failure strain a) ε_f=0.02, b) ε_f=0.06.

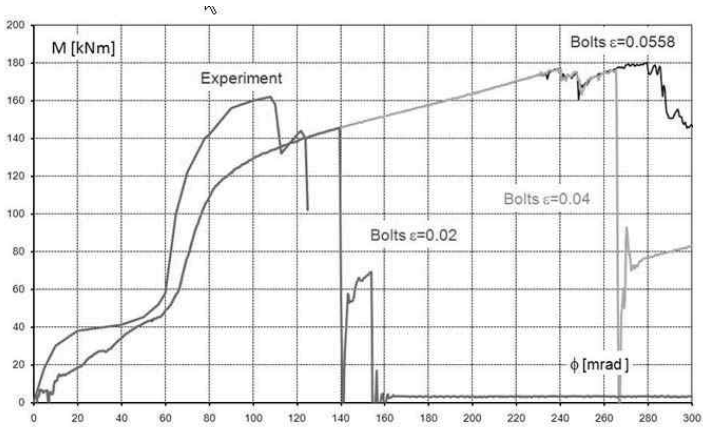


Figure 7. Comparison of experimental and numerical (coarse and fine meshes) moment-rotation curves.

www.EngineeringEBooksPdf.com

The calculated curves in Figure 7 were obtained for different magnitudes of failure strain for bolts. The failure of the actual tested connection was due to a shear rupture of the nut threads of two bolts before ultimate tensile force (and failure strain) for the bolts were reached. To capture this effect in the FE model it is necessary to reduce the bolt's failure strain ε_f and treat it as a modeling parameter rather than as material characteristics. The comparison of moment-rotation curves shows that the FE model underestimates the stiffness of the connation, especially initial stiffness related to bending of the partial-depth end-plate. However, the simplified FE model is able to capture the clear increase in moment resistance when a contact between compression beam flange and column flange occurs and the center of rotation moves to a new location, the same effect as reflected in Figure 3.

4 CONCLUSION

The validation procedure presented here shows that the bolt's failure strain is the main parameter determining the moment and rotation capacities for beam to column connections and in this way one of the main modeling parameters affecting global analyses. Overall the most important modeling parameters which can potentially influence the performance of a joint are mesh density, especially for the flush end plates, failure strain for bolts, and the contact algorithm. The beam-to-column joints are usually tested experimentally for planar bending with transverse movements constrained. However, during collapse of a framed structure more complex loading configurations, with biaxial bending and torsion, are usually also present. Additionally a structural as a collapse can cause locally reverse loading, the correct representation of unloading in the constitutive relationships defining material models is also important.

REFERENCES

[1] General Services Administration (GSA), "Progressive collapse analysis and design guidelines for new federal office buildings and major modernization projects", Washington (DC) Office of Chief Architect; 2000.

[2] Kwasniewski, L., "Nonlinear dynamic simulations of progressive collapse for a multistory building", *Engineering Structures*, In Press, Corrected Proof, Available online 13 January 2010.

[3] Belytschko, T., Liu, W.K., Moran, B., "Nonlinear Finite Elements for Continua and Structures", *John Wiley & Sons, LTD,* Chichester, England.

[4] Hallquist, J., "LS-DYNA keyword user's manual", *Livermore Software Technology Corporation*, 2006.

[5] Aribert, J-M., Braham, M., Lachal, A., "Testing of ''simple'' joints and their characterisation for structural analysis", *Journal of Constructional Steel Research,* **60**, 659–681, 2004.

[6] ENV 1993-1-1:1992." Eurocode 3. Design of steel structures. General rules and rules for buildings", 1993.

[7] Gizejowski, M.A., Salah, W., Barcewicz, W., "Finite element modelling of the behaviour of steel end-plate beam-to-column joints". *Archives of Civil Engineering*, **54**(4), 693-733, 2008.

[8] Schwer, L.E., "Simplified concrete modeling with *MAT_CONCRET_DAMAGE_REL3", *LS-DYNA Anwenderforum*, Bamberg, 2005.

[9] Kwasniewski, L., "On practical problems with verification and validation of computational models", *Archives of Civil Engineering*, **55**(3), 323-346, 2009.

[10] da Silva, L.S., Rebelo, C., Nethercot, D., Marquesa L., Simõesa, R., Vila Real, P.M.M., "Statistical evaluation of the lateral-torsional buckling resistance of steel Ibeams", Part 2: Variability of steel properties. *Journal of Constructional Steel Research,* **65**, 832-849, 2009.

www.EngineeringEBooksPdf.com

SDSS'Rio 2010 STABILITY AND DUCTILITY OF STEEL STRUCTURES
E. Batista, P. Vellasco, L. de Lima (Eds.)
Rio de Janeiro, Brazil, September 8 - 10, 2010

INFLUENCE OF CHORD AXIAL LOAD ON THE STIFFNESS AND RESISTANCE OF WELDED "T" JOINTS OF SHS MEMBERS

Rui M. M. P. de Matos*, Luís F. Costa-Neves* and Luciano R. O. de Lima**

* ISISE, Civil Engineering Department
University of Coimbra – Pólo II – Rua Luís Reis Santos, Coimbra
e-mails: ruimatos@dec.uc.pt, luís@dec.uc.pt

** Structural Engineering Department
Faculty of Engineering – State University of Rio de Janeiro
São Francisco Xavier, 524, sala 5016A. Maracanã. RJ – CEP 20550-900
e-mail: lucianolima@uerj.br

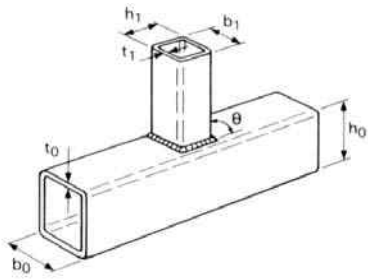
Keywords: Structural hollow sections, connections, Eurocode 3, resistance, stiffness.

Abstract. *The use of structural hollow sections is currently growing very fast, being of major importance an accuracy assessment of the analytical approaches available to these elements, namely their connections. These elements are mainly used in truss structures where the connected members are submitted to important axial forces.*
In this paper some results concerning Square Hollow Section (SHS) welded "T" joints will be presented. An emphasis is given to the effect of the chord axial loading on the connection resistance, to the ratio between membrane stiffness and initial stiffness, and also to the comparison between numerical and Eurocode 3 resistances.

1 INTRODUCTION

The use of structural hollow sections presents a constant growing in their use, namely in truss structures where members are loaded mainly in tension or in compression. The connections of these elements are a singularity with major importance, so its behavior should be carefully investigated.

This study is concerned to the so-called welded "T" joints of SHS members. The geometry and the main parameters of this particular typology of connections are presented in Figure 1. The main member of this connection is called chord (horizontal in the example) and the secondary is called brace (vertical in the example).



$$\beta = \frac{b_1}{b_0} \tag{1}$$

$$\mu_1 = \frac{b_1}{t_1} \tag{2}$$

$$\mu_0 = \frac{b_0}{t_0} \tag{3}$$

$$\gamma = \frac{b_0}{2t_0} \tag{4}$$

Figure 1: Welded "T" joint connection and geometrical parameters

www.EngineeringEBooksPdf.com

In this study different values of axial force will be applied in the chord, and four different geometries of connections (2 values of β and 2 values of γ) will be considered as well.

The numerical results obtained will be compared to the values provided by the EC3 approach to assess the accuracy of the analytical expressions that are the obvious tool to be used in current design.

These types of connections show the typical behavior represented in Figure 2: the force-displacement curve has an initial stiffness $S_{j,ini}$ and a post elastic membrane stiffness $S_{j,m}$. These connections do not present a clear yielding force level, and therefore some approaches were proposed in the past to estimate the yielding force based on displacement limits.

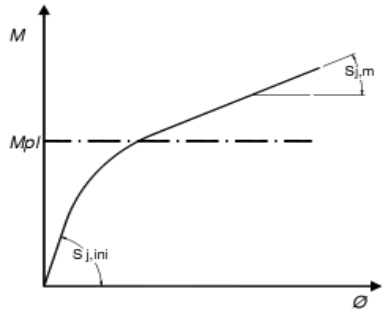


Figure 2: Typical behavior of the connection

2 EUROCODE 3 APPROACH

The part of Eurocode 3 dealing with connection design is the part 1.8. This document is based on the so-called component method, where the connections are modeled by some springs (components) placed in parallel and/or in series. For each component a resistance and a stiffness are obtained and are then used to derive the connection characteristics.

For this specific geometry of connection, the EC3-1-8 assumes a different approach that is based on the assumption that it is pinned and therefore the connection resistance is given by the resistance of the members individually.

The effect of the axial load in the chord is dealt with in EC3 in the expressions concerning the chord face failure for $\beta \leq 0{,}85$. These expressions are:

$$N_{i,Rd} = \frac{k_n f_{y0} t_0^2}{(1-\beta)\sin\theta_i}\left(\frac{2\eta}{\sin\theta_i} + 4\sqrt{1-\beta}\right) \Big/ \gamma_{M5} \tag{5}$$

$$k_n = 1{,}3 - \frac{0{,}4n}{\beta} \text{ but } k_n \leq 1 \text{ (compression)}; \; k_n = 1 \text{ (tension)} \tag{6}$$

3 NUMERICAL SIMULATION

This paper presents a parametric numerical study composed by 32 simulations. In this chapter the model and all the simulations performed will be described.

3.1 Numerical Model

The model was generated using shell elements (Shell181) of Ansys® [3] database. Also, account for the weld as well as the root radius of the chord was taken. Figure 3 shows this model.

www.EngineeringEBooksPdf.com

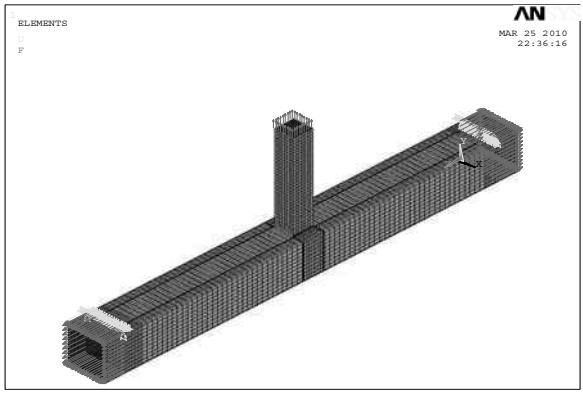


Figure 3: Numerical Model

As it can be depicted from Figure 3, the mesh is more refined near the supports and near the connection, where the high stress concentration is more likely to occur. The mesh is formed with regular elements and with low form factors to avoid numerical problems.

The material used for the members was S355 steel with an elastic modulus of 210 GPa and with an yielding stress of 355 MPa without strain hardening.

The chord load was applied in one load step and was kept constant, while the brace load was applied in some increasing sub steps up to the connection failure.

3.2 Model Validation

The numerical model was validated with the results obtained by Lie et al. [4]. The model was simulated with the same test layout used by the authors and adopting the same mechanical characteristics.

The test layout used by Lie et al. [4] is presented in Figure 4.

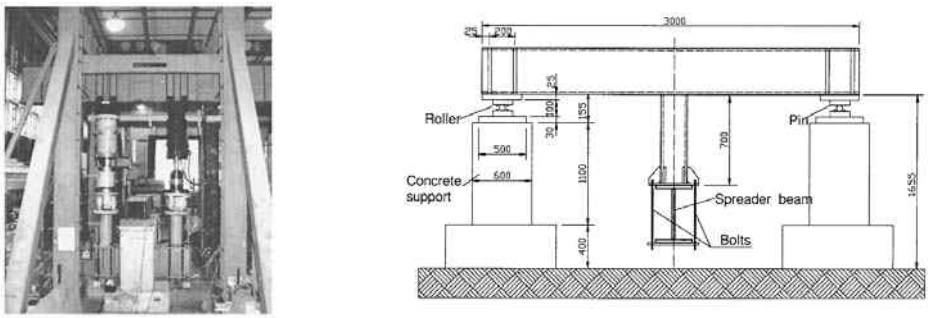


Figure 4: Test Layout [4]

In Figure 5 the comparison between the numerical and the experimental results expressed in terms of a force-displacement curve is presented. The numerical and the experimental results present a quite good agreement that shows that the numerical model is giving acceptable results.

www.EngineeringEBooksPdf.com

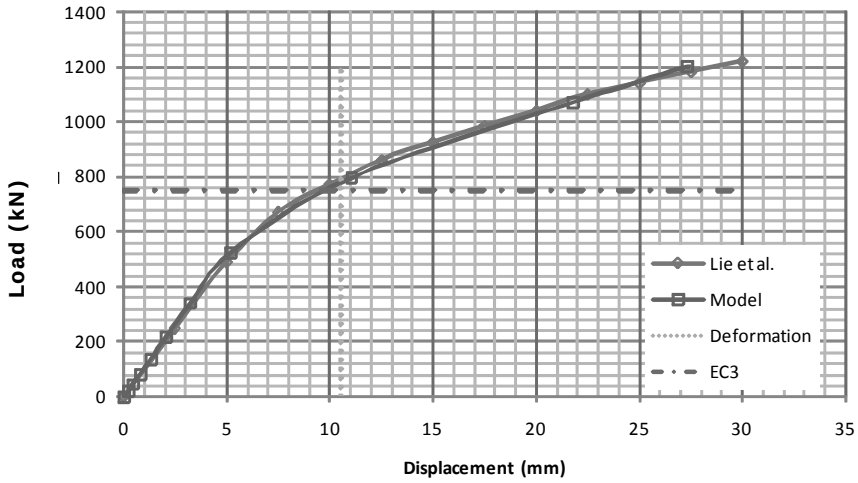


Figure 5: Numerical model validation

3.3 Numerical Model Tests

Table 1 shows the 32 numerical simulations performed. It is worth to stress that two chord geometries were used, by changing the thickness of this member, while two brace geometries were used (100 and 150 mm wide, to vary the parameter β). The tension load applied in the brace was increased up to failure, and eight different load levels in the chord were applied and kept constant during all the loading process. Null, tension and compression forces were used for a better assessment of the effect of this loading.

Table 1: Numerical simulations

Chord (mm)	Brace (mm)	Brace Force	Chord Force (N/N_{pl})
SHS 300x300xE E=8, 12	SHS 100x100x12 SHS 150x150x12	Tension	0 0,25 (Tension) 0,25 (Compression) 0,5 (Tension) 0,5 (Compression) 0,8 (Tension) 0,8 (Compression) 0,95 (Tension)

To compute the actual value of β for the connections, the brace width of the corresponding SHS plus $2x0{,}8xt_w$ (with t_w representing the weld width) was considered. In Table 2 the geometrical parameters of the connections studied are presented.

Table 2: Geometrical parameters

	E8 (γ =18,75)		E12 (γ =12,5)	
	t_w	β	t_w	β
M100	12	0,40	12	0,40
M150	12	0,56	12	0,56

www.EngineeringEBooksPdf.com

4 RESULTS

The numerical simulations performed in this study were used to derive the force-displacement curves corresponding to the described connections with varying chord axial load.

As referred, to obtain the connection yielding point some approximation method is needed, and in this case the method proposed by the International Institute of Welding (IIW) stating that the connection resistance is the force corresponding to a displacement of 3% b_0 (with b_0 presented in Figure 1) for ultimate limit state was used. As this study is performed with a chord of 300mm wide, the corresponding limit displacement is 9mm.

4.1 Force-displacement curves

Figure 6 shows the force-displacement curves obtained for the connection with a chord of 300x300x8 [mm] and a brace of 100x100x12 [mm].

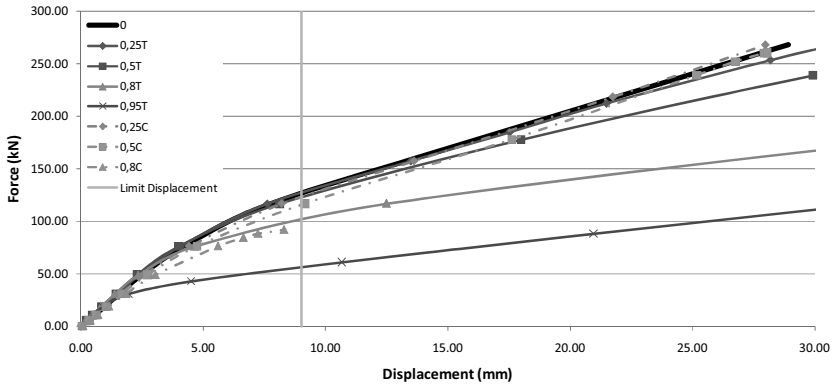


Figure 6: Force-displacement curve

In Figure 6 "T" corresponds to tension forces and "C" to compression forces in the chord, and the number corresponds to the value of the ratio N/N_{pl} in the chord.

It may be observed that these curves present the characteristic shape referred in Figure 2.

4.2 Eurocode 3 approach performance

A comparison of the ratio F/F_{pl} (where F is the numerical resistance and F_{pl} the corresponding value obtained with the EC3 approach) for two values of β is presented in Figure 7.

As it can be seen, the EC3 approach seems to be unsafe for high values of compression in the chord, while for tension this approach tends to be too conservative with the increase of the chord axial load.

4.3 Influence of chord axial load

Figure 8 plots the ratio F/F_{N0} (where F is the numerical resistance and F_{N0} is the numerical resistance of a connection without chord axial load) for two values β. It may be concluded that an increase of the chord axial load leads to a drop of the resistance of the connection both in tension and in compression. The resistance decrease in the tension range is slightly higher than the resistance decrease in the compression range.

www.EngineeringEBooksPdf.com

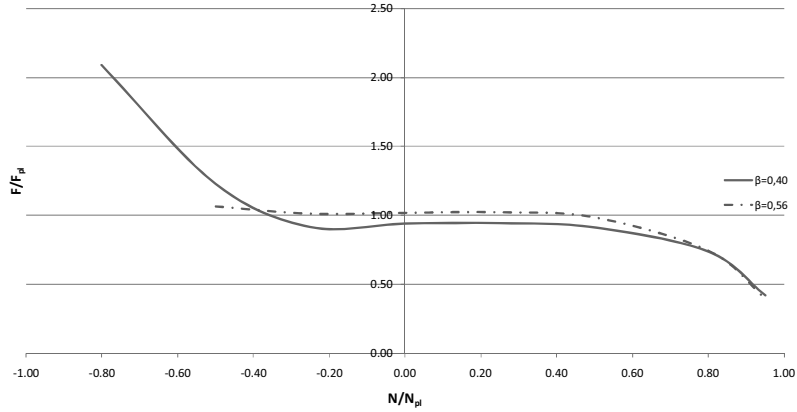


Figure 7: EC3 approach performance

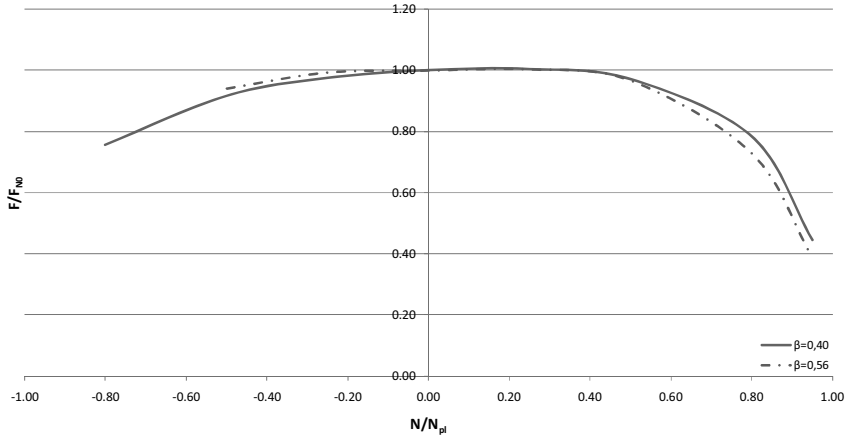


Figure 8: Influence of chord axial load

4.4 Relative importance of initial ($S_{j,ini}$) and membrane ($S_{j,m}$) stiffness

As described in Figure 2, this type of connection presents a behavior with a stiffness reserve after connection yielding called membrane stiffness - $S_{j,m}$. This section presents the variation of the ratio $S_{j,m}/S_{j,ini}$ for different values of the chord axial load. These results are plotted in Figure 9.

In Figure 9 E8M100 concerns a connection between a chord of 300x300x8 mm and a brace of 100x100x12 mm, while E12M100 represents a connection with a chord of 300x300x12 mm and a brace of 100x100x12 mm.

As it can be seen both curves present a similar same shape, but the connection with an higher value of γ (E8M100) presents higher values for this ratio when compared to the connection with a lower value of this parameter γ.

www.EngineeringEBooksPdf.com

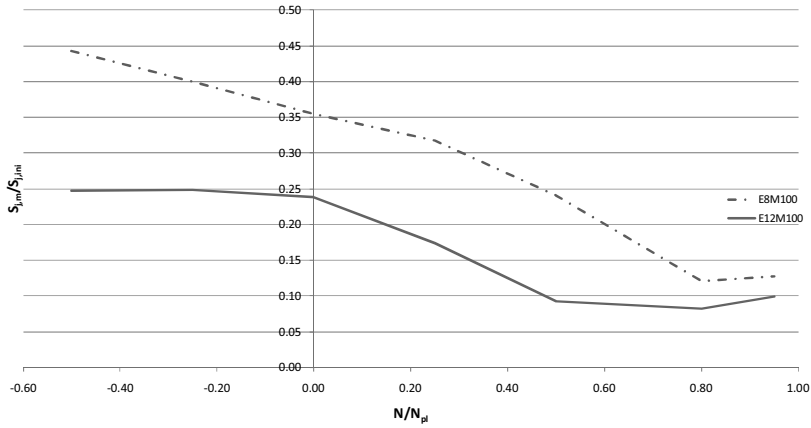


Figure 9: Ratio between membrane and initial stiffness for different levels of chord axial load

5 CONCLUSIONS

This study shows an evaluation of the Eurocode 3 approach performance for the prediction of the failure load in axially loaded braces in "T" connections, with an axially loaded chord. Also, the influence of the chord axial load level on the connection resistance and on the ratio between $S_{j,m}/S_{j,ini}$ were highlighted.

Concerning the EC3 approach performance it may be concluded, from Figure 7, that for higher compression values in the chord this approach seems to be too unsafe, while for higher values of chord tension forces the approach gives very conservative results.

This approach tends to reduce the connection resistance when chord compression forces are present, but this study suggests that this reduction should be even greater for larger values of the ratio N/N_{pl} in compression.

Both tension and compression forces applied in the chord reduces the connection resistance when compared with the case without chord axial load (Figure 8). The curves for both geometries presented a very similar shape and almost symmetrical in relation to the case without chord axial load.

Regarding the stiffness (initial and membrane), it can be concluded (Figure 9) that the curve relating the ratio between these stiffnesses with the variation of the chord axial load presents a similar shape for different values of γ, but this ratio increases with the increase of γ.

REFERENCES

[1] EUROCODE 3. EN 1993-1-1, Design of steel structures Part 1.1: General rules and rules for buildings, Brussels, CEN-European Committee for Standardisation, 2005.

[2] EUROCODE 3. EN 1993-1-8, Design of steel structures Part 1.8: Design of joints, Brussels, CEN-European Committee for Standardisation, 2005.

[3] Ansys 10.0 ®, ANSYS - Inc. Theory Reference, 2005.

[4] Lie S., Chiew S., Lee C. e Yang Z., "Static strength of cracked square hollow section T joints under axial loads. I: Experimental", Journal of Structural Engineering, vol. 132, nº 3, pp 368-377, 2006.

[5] Lima, L., Costa Neves, L., Silva, J., Vellasco, P., "Análise paramétrica de ligações "T" com perfis tubulares em aço através de um modelo de elementos finitos", Proceedings of the XXVI Iberian Latin-American Congress on Computational Methods in Engineering – CILAMCE, Brazilian

www.EngineeringEBooksPdf.com

Assoc. for Comp. Mechanics (ABMEC) & Latin-American Assoc. of Comp. Methods in Engineering (AMC), Guarapari, Espírito Santo, Brazil, 19th-21st October 2005, 2005.

[6] Lima, L., Costa Neves, L., Silva, J., Vellasco, P., Andrade, S., "Parametric Analysis of RHS T Joints Under Static Loading", CC2007 - 11th International Conference on Civil, Structural and Environmental Engineering Computing, Saint Julians, Procedings of the 9th International Conference on the Application of Artificial Intelligence to Civil, Structural and Environmental Engineering, Edimburg, Civil Comp Press v.1. pp 1-15, 2007.

[7] Matos, R., "Avaliação Paramétrica de Nós de Geometria "T" de Perfis Tubulares", MsC Thesis, University of Coimbra, 2008.

[8] Matos, R., Costa Neves, L., Lima, L., Silva, J., Vellasco, P., "Evaluation of the Resistance of RHS "T" Joints Under Axial Loading – a Parametric Study", CC2009 - 12th International Conference on Civil, Structural and Environmental Engineering Computing, Madeira, Civil Comp Press, Paper 1, 2009

[9] Matos, R., Costa Neves, L., Lima, L., Silva, J., Vellasco, P., "Influence of Chord Axial Load on the Resistance of RHS "T" Joints With Axially Loaded Braces – a Parametric Study", CC2009 - 12th International Conference on Civil, Structural and Environmental Engineering Computing, Madeira, Civil Comp Press, Paper 2, 2009

www.EngineeringEBooksPdf.com

SDSS'Rio 2010 STABILITY AND DUCTILITY OF STEEL STRUCTURES
E. Batista, P. Vellasco, L. de Lima (Eds.)
Rio de Janeiro, Brazil, September 8 - 10, 2010

EXPERIMENTAL STUDIES OF BEHAVIOUR OF COMPOSITE BEAM-COLUMN FLUSH END PLATE CONNECTIONS SUBJECTED TO SEISMIC LOADING

Olivia Mirza*and Brian Uy*

* University of Western Sydney, School of Engineering, Locked Bag 1797, Penrith South DC, Penrith 1797, New South Wales, Australia
e-mails: o.mirza@uws.edu.au, b.uy@uws.edu.au

Keywords: Composite steel-concrete beam, end plate connection, seismic loading.

Abstract. *Steel-concrete composite systems have seen extensive use in recent decades because of the benefits of combining the two construction materials. Reinforced concrete is inexpensive, massive and stiff, while steel members are strong, lightweight and easy to assemble. The object of this paper is to provide deeper insight into the nonlinear seismic response on the behaviour of composite structures and how they are influenced by various loading conditions. The results of the experimental study enable the authors herein to develop a new and improved shear connectors and beam-column connection for composite steel-concrete structures under seismic loading. The experimental results showed a notable strength and ductile behaviour. An optimised and economic shear connector and blind bolts was obtained. The failure patterns, failure mechanism, ductility and stiffness degradation are discussed. Furthermore, the finite element analyses are in good agreement with the experimental study.*

1 INTRODUCTION

This paper provides an experimental study and finite element analysis of a novel joint system used in steel frames to withstand seismic load at a 1 in 2500 year occurrence. Despite existing research being conducted with regards to the development of robustness of composite connections by [1], [2] and [3], it is still imperative to further investigate the performance characteristics of these new and innovative composite connections when subjected severe earthquake loads. Figure 1 illustrates the connection uses blind bolts through a steel tube filled with concrete. The main compressive loads are therefore transferred in this zone and the longitudinal reinforcement in the slab is thus used to carry the major tension force.

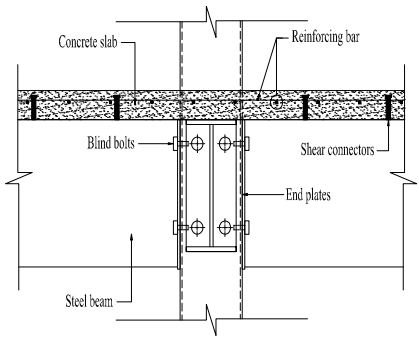


Figure 1: Typical connection detail.

www.EngineeringEBooksPdf.com

Gibson and McCue [4] stated that the ignorance of earthquakes, tsunamis, cyclones and tornadoes received awareness in engineering design after the destruction caused by the Meckering earthquake in 1968. The authors also discovered that most of the structural failures were attributed to an omission of earthquake loads during these building's early planning stages. According to [5], due to the abovementioned failures, seismic loads using a 1 in 500 year return period is commonly considered by engineers. One should bear in mind that these scales vary according to geographic locations. Recently, [6] clarified that there are multiple benefits that would exist if the 1 in 2500 year return period calculations were to be formalised. They include reduction in human casualties from tragic seismic disaster, increase in insurance confidence, increase in structural life expectancies and minimised economic and commercial impacts if the structures were to be subjected to earthquake. Therefore, rigorous experimental studies are being undertaken in this paper to look at how these proposed composite connections would actually behave in the unlikely event of a high consequence earthquake.

2 EXPERIMENTAL TEST SPECIMENS

The response of composite beam-column end plate connections would be critical to the seismic performance. Therefore, tests were conducted in an attempt to determine the feasibility of using such connection. The main aim of these tests was to study the behaviour of blind bolts. Figure 2 is an illustration of the layout and dimensions of the composite test specimen.

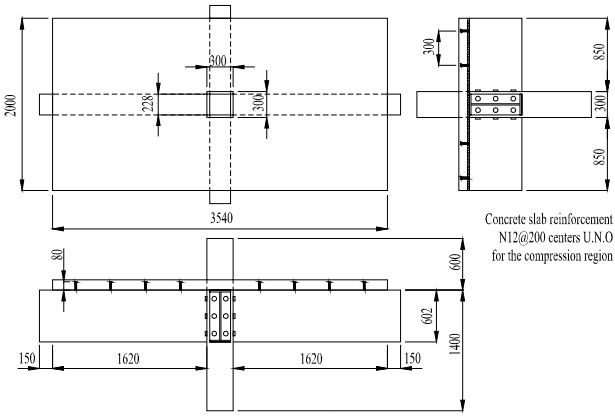


Figure 2: Detail of experiment specimens.

There were two experimental studies undertaken. The first specimen was subjected to monolithic static loading to determine the hogging moment magnitude. An initial load of 513 kN point load was applied to the specimen until the ultimate connection capacity was achieved. The specimen was loaded with a lever arm of 1620 mm. The second specimen was subjected to cyclic loading which is similar to earthquake loading. An initial load of 426 kN point load was applied to the specimen, and then reduced to 200 kN. The process was repeated for 30 cycles.

3 FINITE ELEMENT MODEL

3.1 Material properties

In general, constitutive laws are used to define the stress-strain characteristics of a material. The accuracy of the analysis is dependent on the constitutive laws used to define the mechanical behaviour. In materials such as concrete, structural steel and reinforcing steel, profiled steel sheeting and shear connectors, the constitutive laws are represented by the stress-strain relationships of the materials. In this

www.EngineeringEBooksPdf.com

paper, the mechanical behaviour at static and seismic loading is considered. For static loading, the material properties are according to [7], and for seismic loading, the concrete and steel material are according to [8].

3.2 Finite element type, mesh and boundary conditions

Three-dimensional solid elements were used to model the push off test specimens in order to achieve an accurate result from the finite element analysis. For both the concrete slab and the structural steel beam, a three-dimensional eight-node element (C3D8R) was used because it is a solid element and it was also used to improve the rate of convergence. A three-dimensional thirty-node quadratic brick element (C3D20R) for blind bolts and shear connectors was used because it is a second order element consisting of 20 nodes and these provide higher accuracy when compared with the first order elements. They capture stress concentrations more effectively and better for modelling geometric features. A four-node doubly curved thin shell element (S4R) was used for the profiled steel sheeting because it is the most appropriate type of element to model thin walled steel structures. The S4R element has six degrees of freedom per node and proved to give accurate solutions and also permits quadratic deformation over four nodal coordinates, membrane action and plain strain behaviour. Finally, a two-node linear three dimensional truss element (T3D2) for steel reinforcing was adopted where the axial direction is released using an option of equation provided in ABAQUS.

Figure 3 illustrates the finite element mesh used to represent a quarter model of the experimental specimen. The aim of this was to reduce the simulation cost and computational time. The generated mesh was designed to give an optimal accuracy where the fine mesh surrounds the blind bolts and shear connectors and a coarse mesh was used elsewhere.

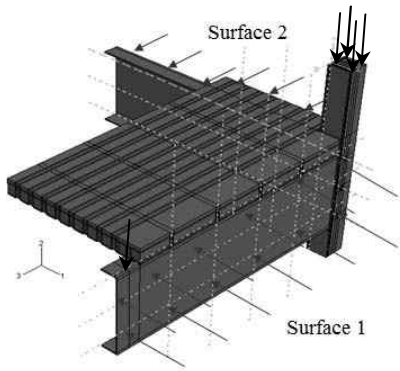


Figure 3: Finite element model layout.

All the nodes designated as Surface 1 are restricted to move in the y-direction while all the nodes in Surface 2, are restricted to move in the x-direction. For the application of load, uniform distributed axial load was applied to the centre of the reinforced concrete tubular column, whilst a concentrated load was applied at 150 mm from the tip of the end of structural steel beam. Both the loads were employed using the modified RIKS method which can be obtained through a series of iterations for each increment for a non-linear structure. The RIKS method was used for the nonlinear analysis to ensure that any unloading was captured.

www.EngineeringEBooksPdf.com

4 RESULTS AND DISCUSSIONS

4.1 Monolithic static loading

Figure 4 illustrates a peak load of 365 kN was measured. During the experimental procedure, when the load reached 168 kN, there were signs of concrete cracking. The concrete cracked 150 mm from the column face which is shown in figure 5. During the experiment, it was observed that the column surface and the end plate buckled which caused the connection to fail. As the end hydraulic loads progressed, the concrete cracks expanded, encouraging the deformation in the endplates to take place, shown in figure 6. Further load progress eventually caused the headed stud shear connectors to pull out from the structural steel beam and severe concrete cracking, as shown in figure 7. This noticeable deformation in the endplates was a result of the overall stiffness within the connection depleting, and because of the excessive end beam deflection.

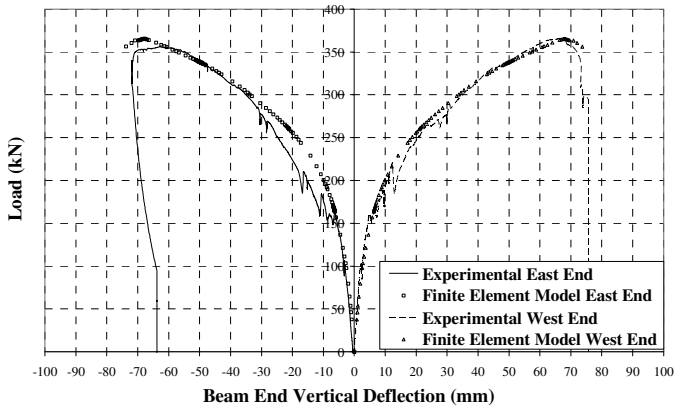


Figure 4: Load versus deflection for static loading.

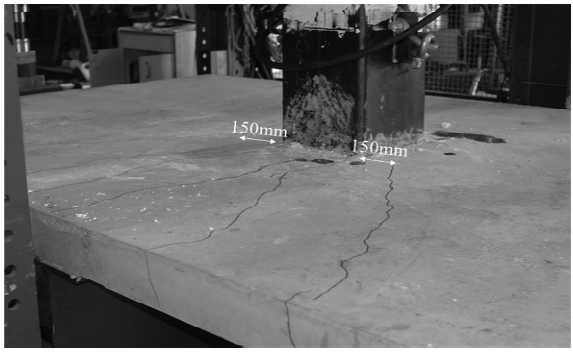


Figure 5: Concrete cracks at 150 mm from column face.

www.EngineeringEBooksPdf.com

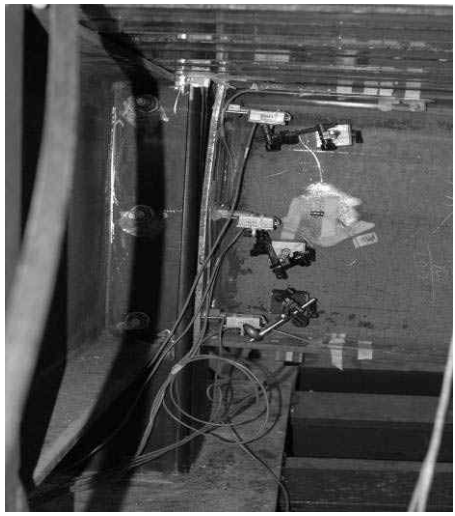


Figure 6: Blind bolts of the endplate displace 3 mm outwards.

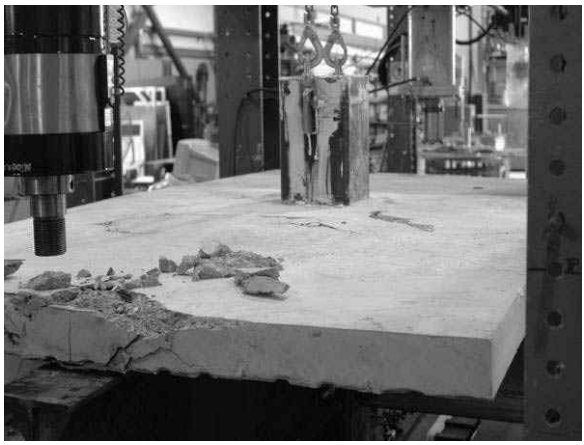


Figure 7: Shear connectors pull out and concrete failure.

Figure 4 proves that the finite element model is in good correlation with the experimental data. Initially, it was observed that the concrete element near the column face reached its cracking stress. This proved that the concrete started to crack near the column surface. With the continuation of the loading, it was observed that the end of concrete element started to crack followed by the headed stud shear connectors reaching their maximum stress, then pulling out from the structural steel element. Finally, the finite element illustrated that the column face and end plate exceed their yield stress and started to buckle which caused connections failure.

4.2 Seismic loading

Figure 8 illustrates that 140 kN peak load upward and 259 kN downward. During the first cycle, the upward load of 130 kN was reached. It was observed that the end of concrete slab started to crack shown in figure 9. When the downward load was applied in the first cycle, the load reached 225 kN. During the

www.EngineeringEBooksPdf.com

first cycle of downward load, it was observed that the thin wall of the column started to buckle which is shown in figure 10. When the process was repeated, for the upward load, the failure in the headed stud shear connectors was observed in the composite steel-concrete slab, as in figure 11. However, for the downward load, the buckling of the thin column wall became severe which caused the connection failure in the blind bolt area, as shown in figure 12. At the same time, it also can be observed that the profiled sheeting started to buckle and tear, as depicted in figure 12. Figure 8 also demonstrates that the finite element model is in good agreement with the experimental data. The failure showed in finite element is similar to the experimental study.

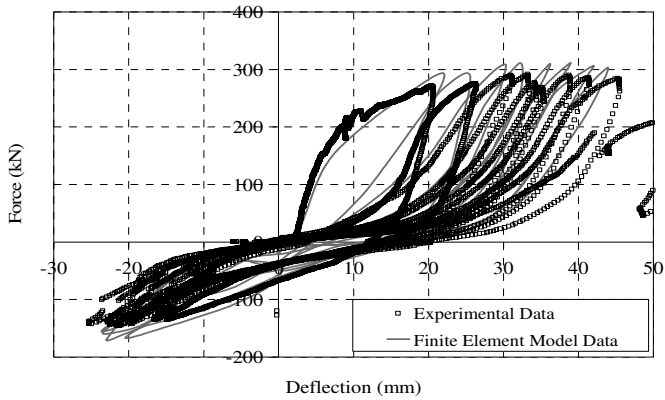


Figure 8: Load versus deflection for seismic loading.

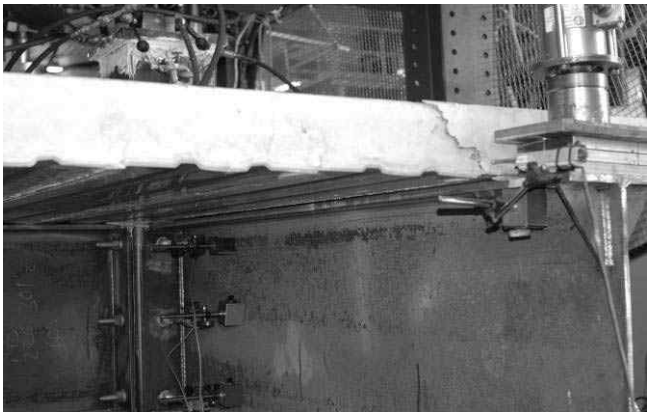


Figure 9: End concrete slab cracks.

www.EngineeringEBooksPdf.com

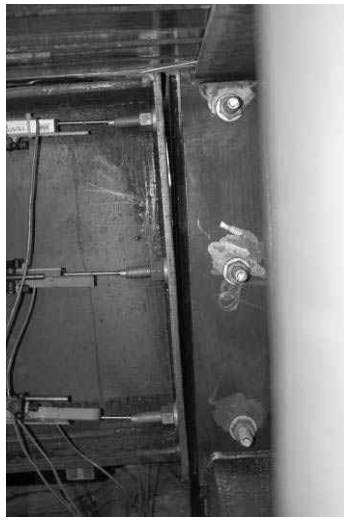


Figure 10: Column face and end plate buckle.

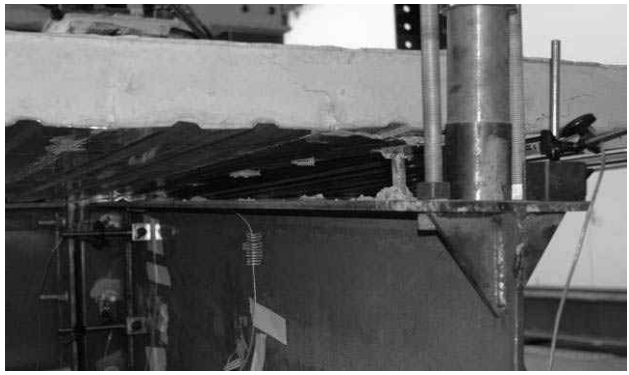


Figure 11: Headed stud shear connector failure.

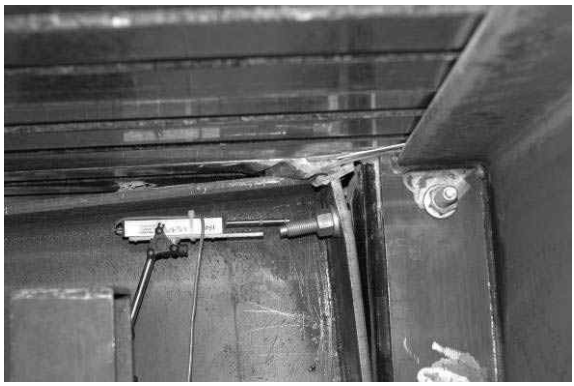


Figure 12: Severe buckle at column face and end plate.

www.EngineeringEBooksPdf.com

5 CONCLUSIONS

This paper discussed the behaviour of composite beam-column flush end plate connections subjected to low probability, high-consequences loading. It has been revealed that there is a need to cater for low probability, high-consequence earthquake loads such as those of a 1-in-2500 year return period to prevent further structural failures, catastrophic loss of lives, and economic blunders.

It has been asserted that medium-rise buildings are most likely to have an unenthusiastic behaviour towards an earthquake and that failure is most likely to occur at the connection of the structure. Hence the focus of this paper is the adequacy of standardising increased earthquake return periods within structural design connections. It is this earthquake return period that has been identified as being one of the main factors in governing the magnitude of an earthquake.

Given this fact, this paper has contributed to the broad spectrum of in-depth investigations that evaluate the practicalities of standardising earthquake return periods to 1-in-2500 years with the use of composite connections. The premature failure occurred in the cyclic test could be due to the low cycle fatigue. A reasonable accurate finite element model has been developed to investigate the behaviour of the shear connectors and end plate connections in composite steel-concrete beams. The comparison between the finite element models and experimental results are in good correlation.

ACKNOWLEDGEMENT

This project is supported by the Australian Research Council Linkage Grants Program, LP0669334 with industry partners Ajax Fasteners and Australian Tube Mills. The authors also would like to acknowledge the technical staff of University of Western Sydney for their involvement in experimental studies for this project.

REFERENCES

[1] Loh, H.Y., Uy, B. and Bradford, M.A., "The effects of partial shear connection in composite flush end plate joints Part I: Experimental study.", *Journal of Constructional Steel Research,* **4**(62), 379-390, 2006a.

[2] Loh, H.Y., Uy, B. and Bradford, M.A., "The effects of partial shear connection in composite flush end plate joints Part II: Analytical study and design appraisal", *Journal of Constructional Steel Research,* **4**(62), 391-412, 2006b.

[3] Wang, W.D., Han, L.H. and Uy, B., "Experimental behaviour of steel reduced beam section to concrete-filled circular hollow section column connections", *Journal of Constructional Steel Research,* **2**(64), 493-504, 2007.

[4] Gibson, G. and McCue, K., "Seismological contributions to earthquake loading codes.", *Proceeding of earthquake codes in the real world, AEES Australian Earthquake Engineering Society,* 2001.

[5] Wilson, J. and Lam, N., "Recent developements in the research and practice of earthquake engineering in Australia", *Australian Journal of Structural Engineering,* **1**(8), 13-27, 2007.

[6] Walker, G., "Earthquake insurance: An Australian perspective", *Australian Journal of Structural Engineering,* **1**(8), 38-49, 2008.

[7] Mirza, O. and Uy, B., "Behaviour of headed stud shear connectors for composite steel-concrete beams at elevated temperatures", *Journal of Constructional Steel Research,* **3**(65), 662-674, 2008.

[8] Kent, D.C. and Park, R., "Inelastic behavior of reinforced concrete members with cyclic loading", *Bullentine of the New Zealand Society for Earthquarke Engineering,* **1**(4), 108-125, 1971.

www.EngineeringEBooksPdf.com

SDSS'Rio 2010 STABILITY AND DUCTILITY OF STEEL STRUCTURES
E. Batista, P. Vellasco, L. de Lima (Eds.)
Rio de Janeiro, Brazil, September 8 - 10, 2010

MODELLING CONNECTIONS OF MOMENT RESISTING STEEL FRAMES FOR SEISMIC ANALYSIS

L. Mota*, A. T. da Silva*, C. Rebelo*, L. Simões da Silva* and L. de Lima**

* ISISE, Civil Engineering Department, University of Coimbra, Portugal
e-mails: laertes@dec.uc.pt, tenchini@dec.uc.pt, crebelo@dec.uc.pt, luisss@dec.uc.pt

** Structural Engineering Department
Faculty of Engineering – State University of Rio de Janeiro
São Francisco Xavier, 524, sala 5016A. Maracanã. RJ – CEP 20550-900

e-mail: lucianolima@uerj.br

Keywords: Steel structures; Beam-to-column joint, Seismic analysis, Hysteretic behaviour.

Abstract. *The seismic response of moment resisting steel frames depends on the behaviour of the beam-to-column connections, in particular when these are considered to be dissipative zones. This paper aims to contribute to a better understanding of modelling joints of steel moment resisting frames concerning their seismic behaviour. The modified Richard-Abbott constitutes a sophisticated model and is used here to reproduce the cyclic behaviour of the steel joints. A parametric study is carried out in order to evaluate the influence of stiffness degradation, strength degradation and hardening effect of the connections in global response of the structure. For the study case the maximum global displacements increase for higher hardening effect. This conclusion can be relevant because for moment resisting frames the horizontal displacement is usually the controlling design criterion in seismic design.*

1 INTRODUCTION

The competitiveness of steel and composite construction, especially in seismic areas, requires the presentation and consideration of solutions that clearly demonstrate added value concerning structural performance. The influence of the real behaviour of steel and composite joints on the seismic response of steel frames has long been recognized as a crucial aspect to ensure safe structural response [1]. The following questions are thus pertinent:

- How relevant is it to model the hysteretic behaviour of dissipative joints in the structural analysis?
- How sophisticated should the hysteretic model be?
- How relevant are the hysteretic parameters in the structural analysis?

This paper aims to contribute to a better understanding of modelling joints of steel moment resisting frames concerning their seismic behaviour. It is the main objective of this study to assess the influence of the hysteretic parameters of joint model in the global seismic response.

The recent publication of part 1-1 of Eurocode 8 [2] provides some rules for the design and detailing of joints subjected to seismic loading. In particular, for moment resisting frames, it is specifically allowed to use dissipative semi-rigid and/or partial strength connections, provided that all of the following requirements are verified:

a) the connections have a rotation capacity consistent with the global deformations;

b) members framing into the connections are demonstrated to be stable at the ultimate limit state;

c) the effect of connection deformation on global drift is taken into account using nonlinear static (pushover) global analysis or non-linear dynamic time history analysis.

www.EngineeringEBooksPdf.com

Additionally, the connection design should be such that the rotation capacity of the plastic hinge region is not less than 35 mrad for structures of high ductility class DCH and 25 mrad for structures of medium ductility class DCM with the behaviour coefficient q greater than 2 ($q > 2$). The rotation capacity of the plastic hinge region should be ensured under cyclic loading without degradation of strength and stiffness greater than 20%. This requirement is valid independently of the intended location of the dissipative zones. The column web panel shear deformation should not contribute for more than 30% of the plastic rotation capability. Finally, the adequacy of design should be supported by experimental evidence whereby strength and ductility of members and their connections under cyclic loading should be supported by experimental evidence, in order to conform to the specific requirements defined above. This applies to partial and full strength connections in or adjacent to dissipative zones.

It is clear that Eurocode 8 [2] opens the way for the application of analytical procedures to justify connection design options, while still requiring experimental evidence to support the various options. In contrast, North American practice, following the Kobe and Northridge earthquakes, was directed in a pragmatic way towards establishing standard joints that would be pre-qualified for seismic resistance [3]. This approach, although less versatile, would certainly be of interest for the European industry, especially if it could overcome uncertainties that would require experimental validation. Unfortunately, North American design practice and usual ranges of steel sections are clearly different from European design practice. Thus, the benefits of the SAC research programme [4] concerning pre-qualified moment resisting joints are not directly applicable.

2 STEEL JOINTS UNDER CYCLIC LOADING

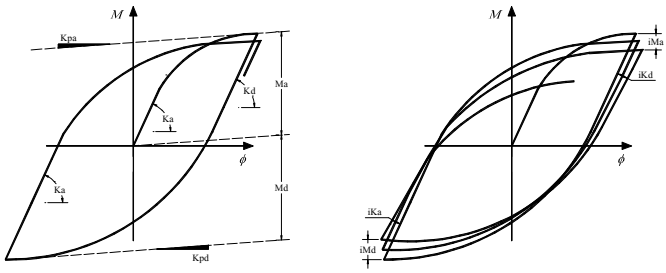
Predicting the behaviour of steel and composite joints is quite complex, because it combines several phenomena such as: material non-linearity (plasticity, strain-hardening), non-linear contact and slip, geometrical non-linearity (local instability), residual stress conditions and complicated geometrical configurations [5]. Although numerical approaches using non-linear finite elements could deal with all the complexities of joint behaviour, they require lengthy procedures and are very sensitive to the modeling and analysis options [6].

For static monotonic situations it is nowadays possible to accurately predict the moment-rotation response of a fairly wide range of joint configurations by applying the principles of the component method [7][8]. Under cyclic loading, the behaviour of steel joints is further complicated by successive static loading and unloading. The joint moment-rotation curve is characterized by hysteretic loops with progressive degradation of strength and stiffness that eventually lead to failure of the joint. This typical behavior is usually called oligocyclic fatigue, in close analogy with the behavior of steel under repeated cyclic loading stressed into the plastic range. A typical natural event that, for simplicity, is usually approximated by cyclic loading is an earthquake. Usually, seismic events provoke relatively high amplitudes of rotation in the joint area, so that steel repeatedly reaches the plastic range and the joint fails after a relatively small number of cycles.

2.1 Modified Richard-Abbott Model

For cyclic loading the usual approach is to develop multi-parameter mathematical expressions that are able to reproduce the range of hysteretic behaviors for a given group of steel joint typologies. The modified Richard-Abbott model, illustrated in Figure 1, constitutes such a sophisticated model that can adequately reproduce the cyclic behaviour of steel joints. Subsequently, the values of the parameters are calibrated to satisfactorily correlate to a range of section sizes for a given group of joint typologies [9].

www.EngineeringEBooksPdf.com



a) Degradation of stiffness b) Degradation of strength

Figure 1: Modified Richard-Abbott model

The structure system under cyclic actions may have its failure characterized by deterioration of mechanical properties. Cyclic action in inelastic range produces accumulation of plastic deformation, until ductility of system is locally exhausted and failure occurs due to fracture [9]. This can be taken into consideration for strength ($M_{o,red}$), stiffness ($K_{o,red}$) and hardening effect using the following expressions:

$$M_{o,red} = M_o\left(1 - i_M \times \frac{E_h}{M_y \times \phi_{u,0}}\right) \tag{1}$$

$$K_{o,red} = K_o\left(1 - i_k \times \frac{E_h}{K_0 \times \phi_{u,0}}\right) \tag{2}$$

$$\begin{aligned} M_{0,ini} &= M_0 && \text{if } \phi_{\max} \le \phi_y \\ M_{0,ini} &= M_0\left(1 + H \times \frac{\phi_{\max} - \phi_y}{\phi_y}\right) && \text{if } \phi_{\max} \ge \phi_y \end{aligned} \tag{3}$$

where $\phi_{u,0}$ is the corresponding ultimate value in the case of one single excursion from the origin (monotonic loading), ϕ_{max} is the maximum value of deformation reached in the loading history (in either positive or negative direction), ϕ_y is the conventional yielding value of deformation, E_h is the hysteretic energy accumulated in all previous experienced excursions, M_y represents the conventional yield resistance of the joint, M_0 and $M_{0,ini}$ are the initial and increased value of strength, respectively, K_0 the initial stiffness, i is an empirical parameter related to damage rate and H is an empirical coefficient defining the level of the isotropic hardening.

3 STUDY CASE

3.1 Methodology

The adopted methodology was the study of a predesigned plane frame, modeling the structural elements, beams and columns, in the linear elastic range connected by springs that simulate the structural links. The numerical calculation uses the Software *Seismostruct* [10], which includes the numerical implementation of the modified Richard-Abbott model, capable of simulating the generic cyclic behaviour of steel and composite connections [9].

Thus, the structural seismic performance is evaluated through non-linear dynamic analyses, verifying the variation of maximum horizontal displacements with height, the corresponding inter-storey drifts, maximum total base shear, maximum total support moment and maximum rotation measured in links.

www.EngineeringEBooksPdf.com

3.2 Structure description

The studied structural system is the steel frame with two bays and three storeys represented in Figure 2.

The choice of steel members, connection details and the geometry of the study frame is based on design of the Cardington Building [11,12], with an alternative choice of columns (HEA) and beams (IPE) to match the seismic design criteria and to correspond to southern European practice and simplifying the frame through reduction of the number of storeys and bays. Remark that all steel members are grade S355.

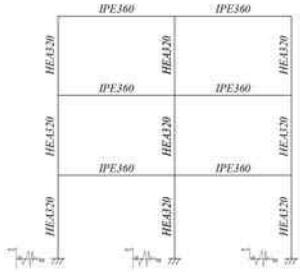


Figure 2: Structural system

3.3 Connection

The reference connection used in this structure, a double-extended beam-to-column steel connection with transverse stiffeners, was tested in laboratory by Nogueiro *et al* [13] and corresponds to the group J1 of the test program. Figure 3 illustrates it configuration as well as the evidenced experimental behaviour.

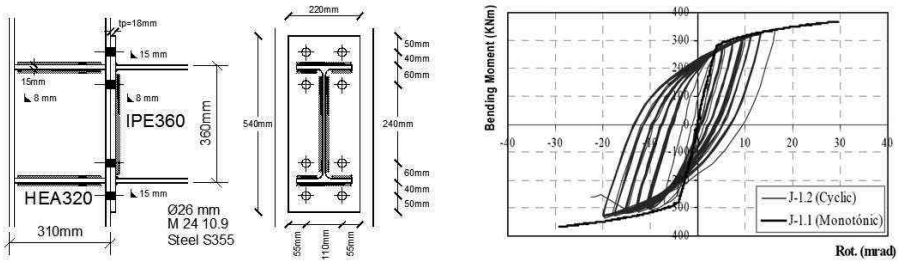


Figure 3: Joint J1; a) Geometry; b) Experimental hysteretic curve Bending moment-Rotation [13]

The connection presents semi-rigid behaviour with partial resistance. It is noted that the hysteretic response is very stable. No pinching or strength degradation is noted and only small stiffness degradation was observed. Table 1 reproduces the model parameters, obtained by numerical calibration with the experimental results. [9]

Table 1: Model parameters for joints J1

K_a KNm/rad	M_a KNm	K_{pa} KNm/rad	n_a	K_{ap} KNm/rad	M_{ap} KNm	K_{pap} KNm/rad	n_{ap}	t_{1a}	t_{2a}	C_a	i_{Ka}	i_{Ma}	H_a	E_{maxa} rad
69500	285	5500	1	0	0	0	0	0	0	0	2	0	0	0,1
K_d KNm/rad	M_d KNm	K_{pd} KNm/rad	nd	K_{dp} KNm/rad	M_{dp} KNm	K_{pdp} KNm/rad	n_{dp}	t_{1d}	t_{2d}	C_d	i_{Kd}	i_{Md}	H_d	E_{maxd} rad
69500	285	5500	1	0	0	0	0	0	0	0	2	0	0	0,1

www.EngineeringEBooksPdf.com

3.4 Non-linear dynamic analysis

For the evaluation of the seismic loading according to Eurocode 8 [2], soil type B and critical damping of 2% were selected. The chosen peak ground acceleration was 0.45g for a near-field earthquake. For the non-linear dynamic analyses, artificial accelerograms compatible with the target response spectrum and the chosen peak ground acceleration were generated using the software *Gosca* [14]. Figure 4 shows the selected artificial accelerogram.

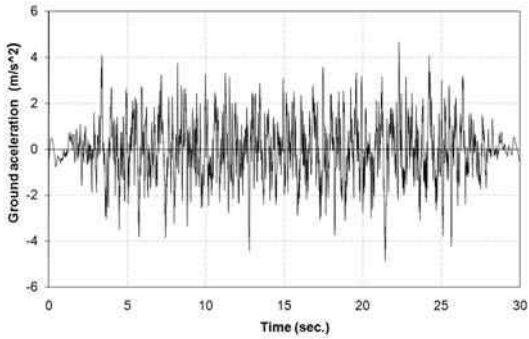


Figure 4: Artificial Accelerogram.

The time range for the system integration of non-linear motion equations considered in analysis was 7,32 x 10^{-3} seconds. Note that nonlinear dynamic analysis allows to incorporate the strength degradation and stiffness degradation of respective links in global behavior of the structures.

4 PARAMETRIC STUDY

A parametric study is carried out in order to evaluate the influence of stiffness degradation, strength degradation and hardening effect of the connection on the structural response of the moment resisting frame. Thus, the following empirical coefficients were varied for descending and ascending branch: i_K (calibration coefficient related to the stiffness damage rate), i_M (calibration coefficient related to the strength damage rate) and H_h (calibration coefficient that defines the level of isotropic hardening).

Table 2 lists the four frames that were used in analysis. Frame J1 is taken as reference and corresponds to the structure with reference joints J1. The other analyzed frames correspond to frames with joints similar to J1, but increasing each single empirical coefficient. The used value corresponds to the maximum value found in the parameters calibration performed by Nogueiro *et al* [9] for the Richard-Abbott mathematical model with a series of experimental tests results for double-extended beam-to-column steel joint subjected to cyclic loading.

Table 2: Analyzed parameters

Frames	Parameters		
	i_k	i_m	H
Frame_J1	2	0	0
Frame_i_K	60	0	0
Frame_i_M	2	0,05	0
Frame_H	2	0	0,02

www.EngineeringEBooksPdf.com

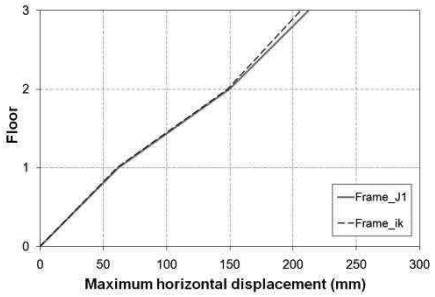
4.1 Results and discussion

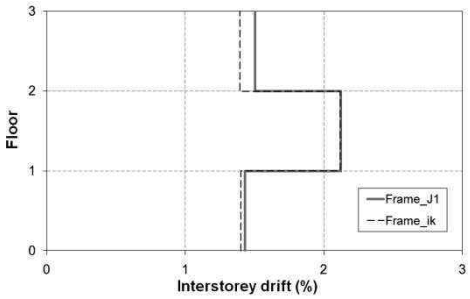
Figure 5 illustrates the maximum horizontal displacement and the corresponding interstorey drift for Frame_J1 and Frame_i_K. It is observed that up to the second floor the curves are similar, however, in the last floor the Frame_J1 presented larger displacement (212 mm) and interstorey drift. Comparing to Frame_J1, Frame_i_K presents a 3,8% smaller displacement (204 mm) and a 7,3% smaller interstorey drift.

As referred above, the parameter i_M was also analyzed, therefore Figure 6a and Figure 6b show the comparative curves of displacement and interstorey drift relatively to the reference frame (Frame_J1) and Frame_i_M. Analyzing these figures, it can be observed that the displacement in last floor of Frame_J1 presents an increase of 3,9%, but no variation was observed up to second floor. Frame_i_M presents larger interstorey drift between the first and second floor, but it presents smaller interstorey drift between second and third floor being the major variation for this case.

Finally, the Figure 7a and Figure 7b illustrate the curves of maximum horizontal displacement and interstorey drift, respectively, to Frame_J1 and Frame_H. In this case, increasing the value of parameter H, the Frame_H presented greater displacements in all floors and higher interstorey drift up to the second floor.

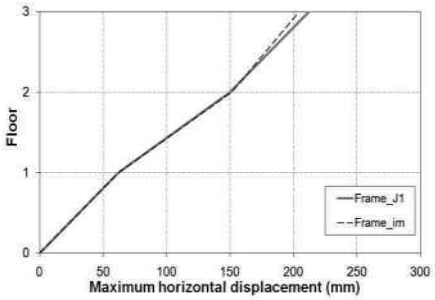
It was verified that for every analyzed frames the maximum roof displacement did not reach the reference value for Ultimate Limit State (2,5% of height = 320mm) [15].

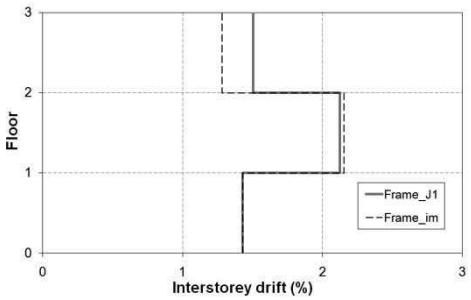




a) Maximum horizontal displacement b) Interstorey drift

Figure 5: Analysis of the parameter i_K

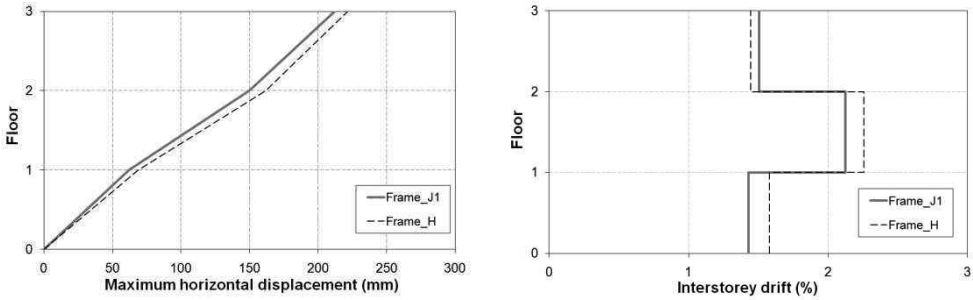




a) Maximum horizontal displacement b) Interstorey drift

Figure 6: Analysis of the parameter i_M

www.EngineeringEBooksPdf.com



a) Maximum horizontal displacement b) Interstorey drift

Figure 7: Analysis of the parameter H

The internal forces on the frame's base and maximum rotations observed in links were also analyzed. Table 3 lists the results obtained from the four analyses previously performed. It reveals that for increasing parameters i_K (Frame_i_K) and i_M (Frame_i_M) both moment and force decrease and for increasing H parameter total moment and shear force increase. The major difference presented (12,3%) was found in moment corresponding to Frame_H. It can also be observed that the total support moment is not sensitive to variations of the parameter i_M.

According to Table 3, the smaller maximum rotation is for reference frame (16,6 mrad) and the largest rotation (18,7 mrad) corresponds to Frame_H, as well as the maximum displacement. Remark that these rotations are not from the same link for each frame.

Table 3: Internal forces in base of frame and maximum rotations in links

Frames	Total support moment		Total support shear force		Maximum rotation in links	
	Maximum Value (kNm)	Δ (%)	Maximum Value (kN)	Δ (%)	Rot.(mrad)	Δ (%)
Frame_J1	1608,08		514,97		16,59	
Frame_i_K	1485,24	-7,64	457,24	-11,21	16,66	+0,38
Frame_i_M	1590,24	-1,11	505,80	-1,78	16,84	+1,49
Frame_H	1806,12	+12,32	564,88	+9,69	18,74	+12,94

5 CONCLUSION

The objective of this paper was to evaluate the influence of stiffness degradation, strength degradation and hardening effect of the connection on the seismic response of a three storey two bays moment resisting steel frame. It was evaluated the displacements, internal forces in base of frame and rotations in a selected link.

For the study case it can be concluded that the maximum global displacements increases for higher hardening effect and decreases for higher stiffness degradation and strength degradation. This conclusion can be relevant because for moment resisting frames the horizontal displacement is usually the controlling design criterion in seismic design. It can also be concluded that maximum rotation in links is not very sensitive to stiffness degradation and strength degradation.

Further studies will take into account variations of different seismic records and frame typologies.

www.EngineeringEBooksPdf.com

REFERENCES

[1] Mazzolani, F.M.; Piluso, V., *Theory and design of seismic resistant steel frames*, E & FN Spon London, 1996.

[2] CEN, *Eurocode 8: Design of Structures for earthquake resistance - Part 1: General rules, seismic actions and rules for buildings, EN-1998-1*, European Committee for Standardization, Brussels, 2004.

[3] FEMA Federal Emergency Management Agency. *Program to Reduce the Earthquake Hazards of Steel Moment Frame Structures. Seismic Evaluation and Upgrade Criteria for Existing Welded Moment Resisting Steel Frame Construction*. Sacramento, California, 1999.

[4] SAC Joint Venture. *Protocol for fabrication, inspection, tenting and documentation of beam-column connection tests and other experimental specimens*. Rep. No. SAC/BD-97/02, Sacramento, Calif, 1997

[5] Simões da Silva L, Santiago A, Vila Real P, "Post-limit stiffness evaluation of the ductility of steel joints". *Computers & Structures,* 80, 515-531, 2002.

[6] Simões da Silva, L., "Towards a consistent design approach for steel joints under generalized loading". *Journal of Constructional Steel Research*, 64(9), pp. 1059-1075 (2008), doi: 10.1016/j.jcsr.2008.02.017.

[7] CEN, *Eurocode 3: Design of Steel Structures, Part 1.8: Design of joints, EN-1993-1-8*, European Committee for Standardization, Brussels, 2005.

[8] Jaspart, J.P., "General Report: Session on Connections", *Journal of Constructional Steel Research*, Vol. 55, pp. 69-89, 2000.

[9] Nogueiro, P., Simões da Silva, L., Bento, R. and Simões, R., "Numerical implementation and calibration of a hysteretic model with pinching for the cyclic response of steel joints", *International Journal of Advanced Steel Construction,* 3(1), pp. 128-153, 2007.

[10] SeismoSoft, "SeismoStruct - A computer program for static and dynamic nonlinear analysis of framed structures", 2007 [online]. Available from URL: *www.seismosoft.com.*

[11] Simões da Silva, L., Gervásio, H., *Design of Steel Structures, Eurocode 3: Design of steel structures, Part 1-1 General rules and rules for buildings*, ECCS publication, 2010.

[12] British Steel plc, Swinden Technology Centre, "The behaviour of multi-storey steel framed buildings in fire", *European Joint Research Programme*, South Yorkshire, United Kingdom, 1999.

[13] Nogueiro, P., Simões da Silva, L., Bento, R. and Simões, R., "Experimental behaviour of standardised European end-plate beam-to-column steel joints under arbitrary cyclic loading", *Camotim, D. (ed.), Proceedings of SDSS'06 –International Colloquium on Stability and Ductility of Steel Structures*, Lisboa, Portugal, 6-8 September, 2006.

[14] Denoël, V., "Calcul sismique des ouvrages d'art" Travail de fin d'études de l'Université de Liège, GOSCA, 2001

[15] Grecea, D., Dinu, F., Dubina, D., "Performance Criteria for MR Steel Frames in Seismic Zones", *Lamas, A. (ed.), Proceedings of Third European Conference on Steel Structures*, Coimbra, Portugal, 19-20 September, pp. 1269-1278, 2002.

www.EngineeringEBooksPdf.com

SDSS'Rio 2010 STABILITY AND DUCTILITY OF STEEL STRUCTURES
E. Batista, P. Vellasco, L. de Lima (Eds.)
Rio de Janeiro, Brazil, September 8 - 10, 2010

INFLUENCE OF LOCAL PLASTIC BUCKLING OF A JOINT ON THE CARRYING CAPACITY OF THIN-WALLED TRUSSES

H. Pasternak*, G. Kubieniec* and V. Bachmann*

* Brandenburg University of Technology, Konrad-Wachsmann-Allee 2, 03046 Cottbus, Germany,
e-mails: Hartmut.Pasternak@tu-cottbus.de, Gabriel.Kubieniec@tu-cottbus.de,
Volkmar.Bachmann@tu-cottbus.de

Keywords: Trusses Joint, Carrying Capacity, Local Buckling.

Abstract. *The use of cold-formed structural members in steel structures increases rapidly and companies offer wider range of shapes of cross-sections possible to use in design practice. One of the biggest disadvantage of this type of the members in design is a lack of information of their real behaviour under load i.e. mainly about possible local buckling effects which can considerably decrease capacity of a whole compression member or even a whole structure. To illustrate this problem there were shown the results of experimental and numerical researches of a truss joint in which local plastic buckling of a wall of the compression member have decisive influence on its behaviour and carrying capacity.*

1 INTRODUCTION

The use of cold-formed structural members in steel structures increases rapidly and companies offer wider range of shapes of cross-sections possible to use in design practice. Those shapes assure not only a better usage of a material but also make steel structures lighter and more economical than those made from hot-rolled sections. Cold-formed structural members are normally used in applications like roof and wall systems of industrial, commercial and agricultural buildings, steel racks for supporting storage pallets, structural members for plane and space trusses, frameless stressed-skin structures, residential framing and steel floors and roof decks. They are usually manufactured by one of two processes i.e. roll forming and brake forming, which have influence on material properties of the latest one. One of the biggest disadvantage of this type of the members in design is a lack of information of their real behaviour under load i.e. mainly about possible local buckling effects which can considerably decrease capacity of a whole compression member or even a whole structure. The use of thinner material and cold-forming processes result in special design problems not normally encountered in hot-rolled construction. In addition, welding and bolting practises in thinner sections are also different, requiring design provisions unique to thin sheets. The thickness of individual plate elements of cold-formed sections are normally small compared to their widths, so local buckling may occur before section yielding. However, the presence of local buckling of an element does not necessarily mean that its load capacity has been reached [1]. To illustrate above mentioned problems, in the next chapters, there were shown the results of experimental and numerical researches of a truss and in particular its joint in which local plastic buckling of a wall of the compression member have decisive influence on its behaviour and carrying capacity. The elements of the truss were manufactured by roll forming.

www.EngineeringEBooksPdf.com

2 ANALYSED STRUCTURE

The object of investigation was the truss made from cold – formed sections (Fig 2 and Fig.3b) and in particular its joint (Fig. 3a). The truss consists of two types of cross sections i.e. Z and Sigma (Fig. 1a-c) which are produced by roll forming. Z profiles were made form steel S420 while Sigma from S355. The material properties of flat steel i.e. f_{yb} and f_u were determined on basis of tension tests of real elements. The influence of roll forming on material properties of cross sections i.e. yield strength of corners f_{yc}, was taken into consideration according to Karren's proposal [2]. The material properties of flat steel as well as those calculated for corners were set in Tab. 1. Z profiles are designed to be a compression and tension members of truss while sigma as bottom and top chords. In case of compressed ZV bar the Z profile was reinforced by two flat stiffeners (Fig 1b). All the elements are connected together in welded joint (Fig. 3a). The system of joining elements requires a special preparation (deformation) of ends of the members (Fig. 3c) and can cause unstable behaviour of walls of compressed member (local buckling). It forced to investigate the behaviour of joint as well as the determination of bending moment – rotation characteristic and its influence on capacity and rigidity of whole system (truss).

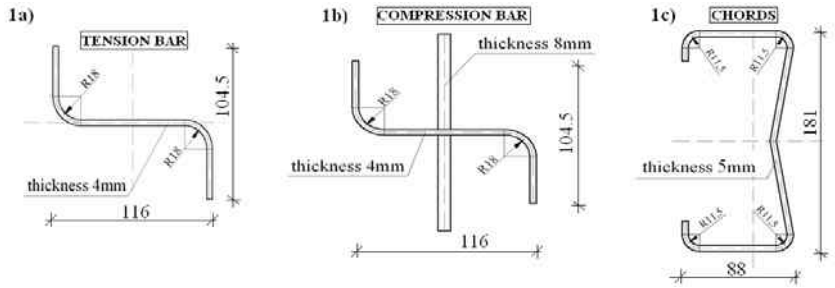


Figure 1: Cross-sections of truss members.

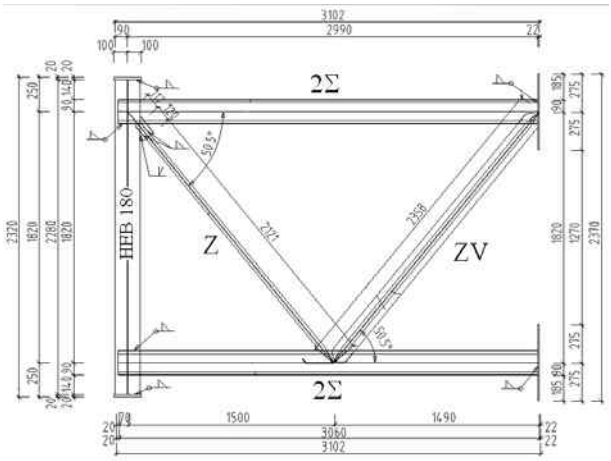


Figure 2: Geometry of truss made from cold-formed sections.

www.EngineeringEBooksPdf.com

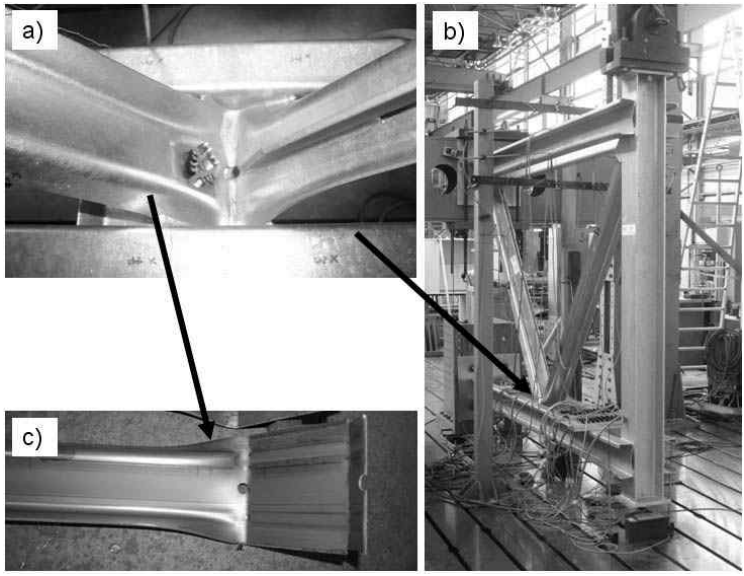


Figure 3: Welded truss joint (a), truss (b), and end of bar (c)

Table 1: Material properties of cross-sections

Section	f_{yb} [MPa]	f_u [MPa]	E [GPa]	f_{ya} [MPa]	f_{yc} [MPa]	A [cm^2]
Z	426	525	210	448	579	8
ZV	426	525	210	448	579	19.2
Σ	359	473	210	398	528	18.5

Z-tension bar, ZV-compression bar, Σ-chord, E- Young's modulus, f_{ya} f_{yb}, f_{yc}- average, basic and corner yield strength respectively, f_u- ultimate tensile strength, A- area of cross-section.

3 EXPERIMENTAL INVESTIGATION

3.1 Description

The experimental research was focused on describing the behaviour of the joint in particular local buckling of wall of compressed Z profile and associated additional effects. There were carried out three experiments in which the analysed structure was truss cutting containing joint (Fig. 4a). To produce required internal forces in particular elements of the truss cutting, special frame system was designed (Fig. 4b). The frame system consisted of three bars one horizontal and two diagonal made from C profiles connected together with use of bolts. The connections between particular elements of the frame were designed to be a "perfect" hinges to avoid problems with additional stiffness of whole system i.e. truss cutting + frame. During the experiments the measured quantities were vertical and horizontal displacement of joint (Fig. 5b and Fig. 8a) as well as load *P* and movements of supports *UR1* and *UR2* (Fig. 5a). The concentrated load *P* was realized by hydraulic press and was located directly above the end of compression bar *ZV*. The load position was thought to produce equal internal forces both in

www.EngineeringEBooksPdf.com

compression and tension bars. Moreover in every element there was applied appropriate layout of gauges to determine real stress states in cross-sections (Fig.6). On the basis of strain measurements the exact internal forces in individual members were calculated and compared at every load increment. Furthermore the visual inspection of welds was done before and during the experiments.

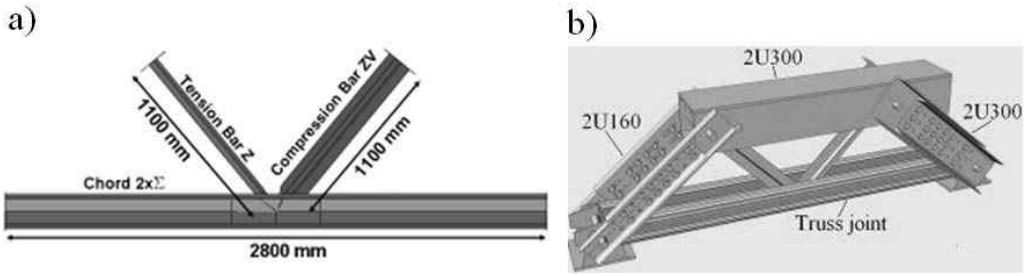


Figure 4: Dimensions of truss cutting containing joint (a) and frame system (b).

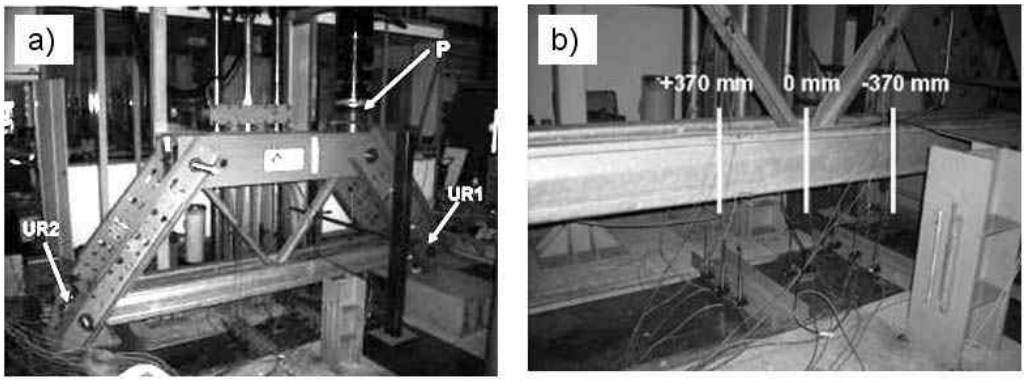


Figure 5: View of experimental area (a) and measurement system of vertical displacements of joint (b)

3.2 Results

As it was mentioned above the basic point of the research was to describe the phenomenon of local plastic buckling of the wall of compressed member. The shape of deformation of buckled wall was presented in Fig. 10. This effect appeared at external load P = 840 kN that corresponds to normal force in compression member N_{DD} = 285.15 kN (Tab.2). The normal force N_{DD} (calculated according to gauge measurements) amounted 84% of design capacity of cross-section N_{DDmax1} = 336 kN within the joint (cross section without stiffeners) and 35% of design capacity of cross-section in the middle of the bar N_{DDmax2} = 806 kN. The appropriate internal forces corresponding to selected external load levels were set in Tab. 2. On Fig. 6 there were presented tables containing values of normal stresses in individual measurement point for every cross-section. It can be seen that the normal stress distribution within cross-sections is nonlinear, that can be a result of existence of interaction between normal forces, bending and torsional moments. The excessive rotation of compression bar due to local buckling caused rotation of the rest of the members i.e. chord and tension element.

www.EngineeringEBooksPdf.com

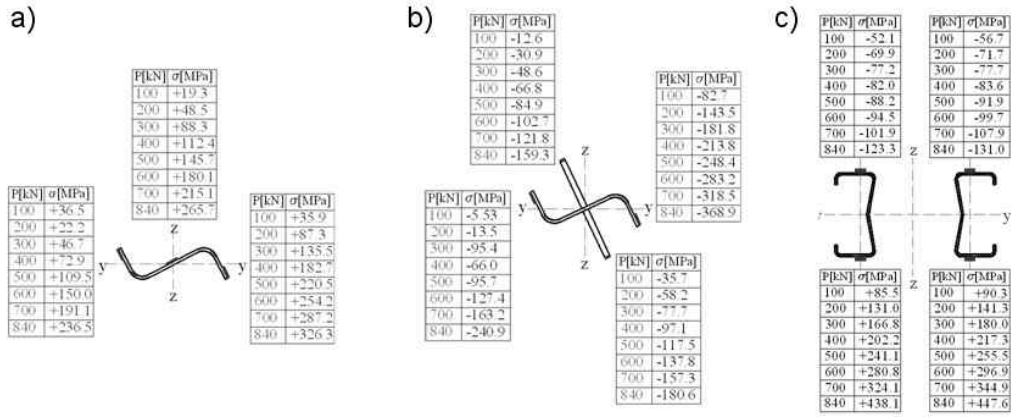


Figure 6: Layouts of gauges and stresses in tension bar (a), compression bar (b) and chord (c)

Table 2: Internal forces in individual members

P [kN]	N_{ZD} [kN]	N_{DD} [kN]	N_G [kN]
100	16.75	40.85	30.95
200	42.15	74.15	60.40
300	70.00	104.50	88.65
400	98.20	134.65	117.35
500	126.85	165.95	146.40
600	155.85	197.65	177.35
700	184.95	230.35	212.40
840	220.95	285.15	229.00

P-external load, N_{ZD}-tension force, N_{DD}-compression force, N_G-tension force chord (sigma profile)

3.2 Bending moment – rotation curve

To determine basic characteristic of joint i.e. bending moment-rotation curve, a system of measurement points of vertical displacements was applied. The layout of those points was presented on Fig. 7. On the basis of those measurements and with use of 4th order interpolating function, the deflection curve *u(x)* was build for selected load increments. Using well-known equations (1) and (2) representing dependences of bending moment and rotation on deflection, the values of these latest were determined. The bending moment-rotation curves were presented on Fig. 7b.

$$\varphi(x) = \frac{d}{dx} u(x) \tag{1}$$

$$M(x) = -EI \frac{d^2}{dx^2} u(x) \tag{2}$$

where: *u(x)*-deflection curve, *M(x)*-bending moment curve, *φ(x)*-rotation curve, *EI*-bending stiffness of chord.

www.EngineeringEBooksPdf.com

It can be seen that bending moment - rotation characteristic is linear in a large part of curve. The design moment resistance of a joint $M_{j,Rd}$ was estimated at value 58 kNm and corresponds to rotation of joint ϕ_{Rd} = 0.21 deg. The elastic range of behaviour of joint is characterized by two values i.e. bending moment $M_{j,Ed}$ = 36 kNm and rotation ϕ_{Ed} = 0.11 deg. The slope of the curve in this area described the initial stiffness of a joint $S_{j,ini}$ = 327 kNm/deg. EC-3 part 1.8 [3] allows to classify the joint by stiffness (p. 5.2.2) and by strength (p. 5.2.3). According to these points the joint was classified as a semi-rigid and partial strength. Taking into consideration method of classification of joints, which is contained in table 5.1 of EC-3 [3], the type of joint model was classified as a semi-continues model.

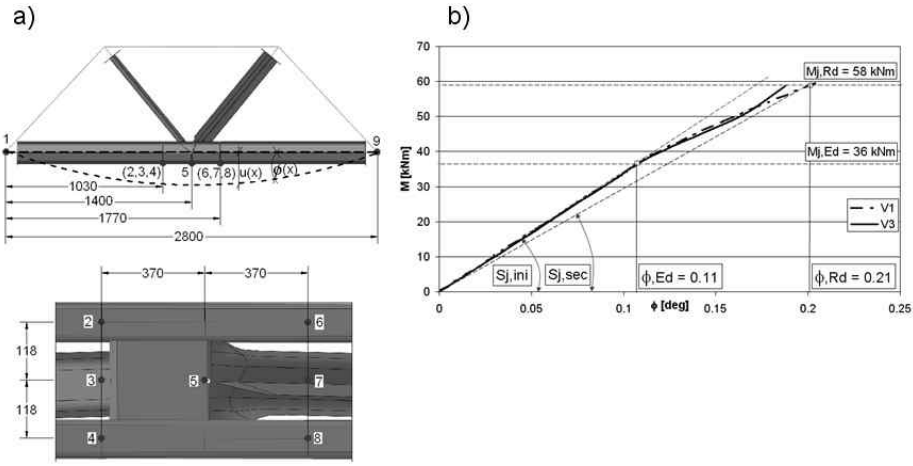


Figure 7: Measurement points for displacements (a), bending moment-rotation curve (b)

4 NUMERICAL MODEL

4.1 Global Analysis

Integral part of discussed study was a numerical model. The model was built and calibrated according to experimental research. The main structures i.e. truss cutting was modelled with use of 4-node shell finite elements (S4R) and the frame with beam elements (B2D3). In the nodes in which the beam elements were joined there were created hinges to assure correct behaviour of system consisting of frame and truss cutting. The discretized model was presented in Fig. 8. Assumptions taken during the numerical calculations were as follows: program and version: ABAQUS 6.8.2 [4]; bilinear material law for steel i.e. perfect elastic-plastic behaviour with a nominal slope of the yielding landing; geometrical imperfections and also residual stresses were not considered; materially non-linear analysis (MNA); both shell (S4R) and beam (B2D3) finite elements were used to discretize model; loads and boundary conditions were defined in appropriate coordinate systems; convergence criteria – force. The numerical solution stayed consistent with empirical results. All of the phenomena noticed in experiments appeared in FEM simulations i.e. local plastic buckling of wall of compressed element and its excessive

www.EngineeringEBooksPdf.com

rotation around the longitudinal axis (Fig. 9) as well as damage of welds along and across the joint. Moreover the capacity of whole system obtained in FEM calculation (P_{FEM}) stays in good adequacy with experimental one (P_{EXP}) i.e. P_{EXP} = 840 kN, and P_{FEM} = 835 kN. The experimental load-displacement curve included all geometrical imperfections caused by inaccuracy of the frame system. After a careful analysis of the numerically obtained results, the authors decided only to compare load capacities and not to include the experimental curve.

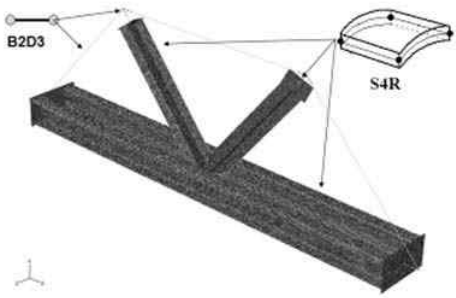


Figure 8: Numerical model of joint

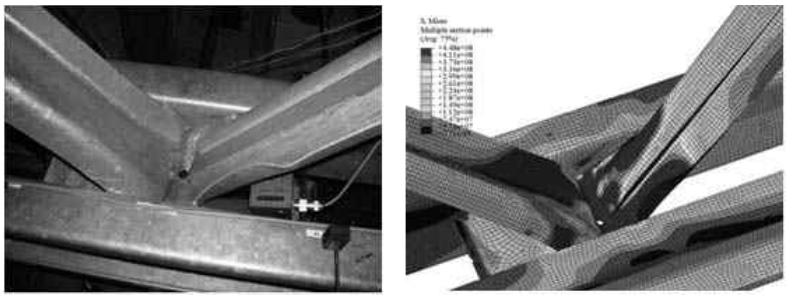


Figure 9: Comparison of results

4.2 Sub-modeling

As it was mentioned in previous chapters, the decisive influence on behaviour of joint and further on whole truss had local buckling of wall of compression element ZV. This phenomenon was investigated more precisely with use of sub-model consisted only of compression element (Fig.10a). The load was applied in appropriate local coordinate system. The boundary condition were designed to represent as accurate as possible the fillet welds joining individual element within the joint. The analysis showed that the compression bar was bale to carry normal compression force F_1 = 352 kN (Fig. 10b) which is 5% bigger than this calculated for cross section without stiffeners F_2 = 336 kN. The increase of this value can be explained by existence of small parts of cross-section of stiffeners inside the joint. It should be mentioned that the bar was not able to carry normal force calculated for cross section with stiffeners i.e. N_{DDmax2} = 806 kN (cf. previous chapter). The difference between numerical and experimental capacities of element i.e. F_1 = 352 kN and F_3 = 285 kN, respectively, can be explained by damage of welds that was observed during the experiment. This excessive rotation of all cross-sections which were included in the joint caused significant decrease of capacity of element.

www.EngineeringEBooksPdf.com

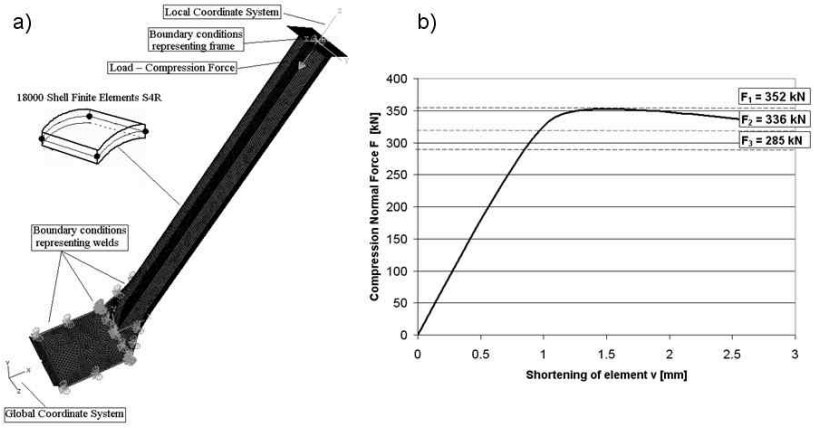


Figure 10: Compression bar: sub-model (a) and statical path of equilibrium of compression member (b)

5 CONCLUSIONS

The object of investigation was the truss made from cold – formed sections and in particular its joint. The experimental research was focused on describing the behaviour of the joint in particular local buckling of wall of compressed Z profile and associated additional effects. It can be seen that the normal stress distribution within the cross-sections is nonlinear, that can be a result of existence of interaction between normal forces, bending and torsional moments. The excessive rotation of compression bar due to local buckling caused rotation of the rest of the members i.e. chord and tension element. The basic characteristic of joint i.e. bending moment-rotation curve was built on the basis of measurements vertical displacements. It can be seen that bending moment - rotation characteristic is linear in a large part of curve. According to rules contained in EC-3 the joint was classified as a semi-rigid and partial strength. Moreover taking into consideration method of classification of joints, which is contained in table 5.1 of EC-3, the type of joint model was classified as a semi-continues model. Integral part of discussed study was a numerical model. The model was built and calibrated according to experimental research. The numerical solution stayed consistent with empirical results. All of the phenomena noticed in experiments appeared in FEM simulations i.e. local plastic buckling of wall of compressed element and its excessive rotation around the longitudinal axis as well as damage of welds along and across the joint. The decisive influence on behaviour of joint and further on whole truss had local buckling of wall of compression element ZV. This phenomenon was investigated more precisely with use of sub-model consisted only of compression element.

REFERENCES

[1]. Hancock, G.J.; Murray, T.M.; Ellifritt, D.S. 2001 *Cold-Formed Steel Structures to the AISI Specification,* New York-Basel. ISBN: 0-8247-9294-7.
[2]. Karren, K.W. 1967. Corner Properties of Cold-Formed Steel Shapes. *Journal of Structural Division, ASCE Proceedings, vol. 93.*
[3]. Eurocode 3: Design of Steel Structures, Part 1-8: Design of joints. European committee for standardisation (CEN) 2006.
[4]. Hibbit & Karlsson & Sorensen, Inc, 2001 : *Abaqus (standard) Reference Manuals ver. 6*.

www.EngineeringEBooksPdf.com

SDSS'Rio 2010 STABILITY AND DUCTILITY OF STEEL STRUCTURES
E. Batista, P. Vellasco, L. de Lima (Eds.)
Rio de Janeiro, Brazil, September 8 - 10, 2010

NUMERICAL ANALYSIS OF ENDPLATE BEAM-TO-COLUMN JOINTS UNDER BENDING AND AXIAL FORCE

Monique C. Rodrigues*, Luciano R. O. de Lima, Sebastião A. L. de Andrade*, Pedro C. G. da S. Vellasco** and José G. S. da Silva*****

* Civil Engineering Department, PUC-RIO, Brazil
e-mails: moniquecordeirorodrigues@gmail.com, andrade@puc-rio.br

** Structural Engineering Department, UERJ, Brazil
e-mail: lucianolima@uerj.br, vellasco@uerj.br

*** Mechanical Engineering Department, UERJ, Brazil
e-mail: jgss@uerj.br

Keywords: Steel Structural, Beam-to-Column Joints, Semi-Rigid Joints, Experimental Analysis, Component Method.

Abstract. *Steel beam-to-column joints are often subjected to a combination of bending and axial forces. Alternatively, significant axial forces can also be present at the joint in cases like: pitched-roof portal frames, sway frames or frames with partially constructed floors. Despite this fact, only very simplified design procedures are available for the analysis and design of beam-to-column joints under these actions. A single empirical limitation to the applied axial force of 5% of the beam plastic resistance under axial force is the only enforced provision present in the Eurocode 3 [1]. The main purpose of the present paper is to describe a numerical investigation developed to fully characterize the structural response of endplate beam-to-column joints subjected to bending and axial forces. Experimental results, carried out at the University of Coimbra, Portugal, were used to calibrate the finite element model. These analyses were focused on expanding the test results and enabling a complete understanding of the structural behaviour of this particular type of semi-rigid connections.*

1 INTRODUCTION

Steel beam-to-column joints are often subjected to a combination of bending and axial forces. Current specifications that take in account the steel semi-rigid joint behaviour do not consider the simultaneous presence of axial forces (tension and/or compression) acting in the joints. On the other hand, an empirical limitation of 5% of the beam plastic resistance is the only limitation suggested in Eurocode 3. In the cases where the axial force magnitude acting in the joint is less than this limit, its effects can be disregarded in the joint design. Despite this fact, the component method, proposed in the Eurocode 3, contemplate this situation since any component can be characterized, for any load type acting on the joint.

Although, the axial force transferred from the beam is usually low, it may, in some situations attain values that significantly reduce the joint flexural capacity. These conditions may be found in: Vierendeel girder systems (widely used in building construction because they take advantage of the member flexural and compression resistances eliminating the need for extra diagonal members); regular sway frames under significant horizontal loading (seismic or extreme wind); irregular frames (especially with incomplete floors) under gravity/horizontal loading; and pitched-roof frames.

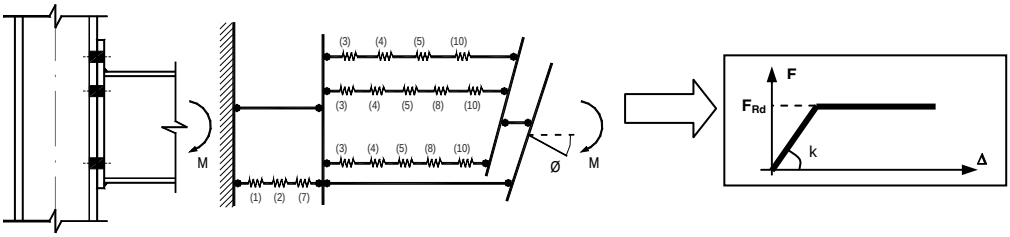
On the other hand, with the recent escalation of terrorist attacks on buildings, the study of progressive collapse of steel framed building has been highlighted. The component method, Eurocode 3 [1] consists of a simplified mechanical model composed of extensional springs and rigid links, whereby the joint is

www.EngineeringEBooksPdf.com

simulated by an appropriate choice of rigid and flexible components as presented in Figure 1. These components represent a specific part of a joint that, dependent on the type of loading, make an identified contribution to one or more of its structural properties. The joint design must define three basic properties: bending moment resistant, $M_{j,Rd}$; initial rotational stiffness, $S_{j,ini}$ and rotation capacity, ϕ_{Cd}.

The first step in a mechanical model development considering the component method for beam-to-column joints is the identification of the relevant components, which represent the existing deformation paths and possible ways of failure. The components are considered according to Eurocode 3 (2003).

The main objective of this paper is to present a numerical study of a flush endplate beam-column joints. The investigated joints were initially subjected only to bending moment and later joints subjected to bending moment and axial force simultaneously. The numerical results were calibrated against experimental results and to the Eurocode 3 provisions for FE01 test and Cerfontaine (2001) model to joints with bending moment and axial force.



(1) column web in shear
(2) column web in compression
(3) column web in tension
(4) column flange in bending
(5) endplate in bending
(7) beam flange in compression
(8) beam web in tension
(10) bolts in tension

Figure 1 – Mechanical Model – extended endplate joint (Lima et al, 2004)

2 NUMERICAL MODEL

The numerical model was based on tests carried out by Silva *et al.* (2003), for flush endplate beam-to-column joints. The adopted steel grade was S275. The beam was joined to the endplate (t_p = 8mm) with fillet welds (a_w = 8mm). The adopted full thread bolts were M20 (d= 19.05mm), cl. 10.9. Table 1 presents the numerical model material characteristics.

2.1 Model characteristics

The numerical simulation was performed with the finite element program ANSYS 11 package [4], using solid elements, SOLID 185, for the beam, column and bolts and shell elements, SHELL 181 for the transverse stiffeners adopted at the beam end near the load application point. In order to consider the contact between plates, contact elements TARGE 170 and CONTA 173, were used (endplate and column flange; bolt head and endplate; bolt shank and endplate hole and column flange; nut and column flange), with a 0.25 friction coefficient. Figure 1 illustrates the numerical model. Regarding the boundary conditions, the flange and column web were restricted in the x and y axis. The vertical displacement of the endplate was also prevented while the beam top flange was laterally restricted [5]. The model considered the whole length of the column following the strategy adopted in experimental programme. An elastic-plastic bilinear constitutive law was considered.

2.2 Algorithms and numerical strategies for nonlinear analysis

A full nonlinear analysis was performed for the developed numerical model. The geometrical and material non-linearities were considered using a Updated Lagrangean formulation and a Von Mises yield

www.EngineeringEBooksPdf.com

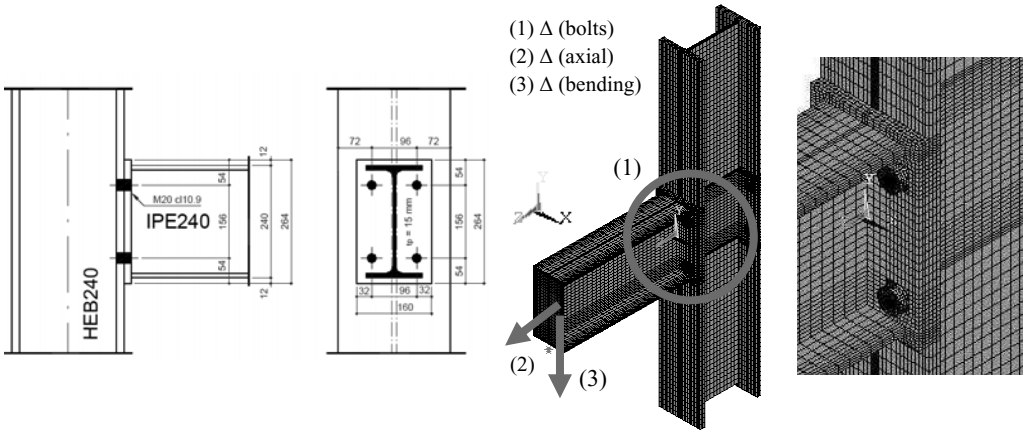
criterion associated to a bilinear stress-strain relationship and an isotropic hardening response. This procedure represents the full structural assessment of the analyzed joints, and may be summarized using the stress distributions contour plots and/or force-displacement curves for any joint node [5].

2.3 Cases studies

Table 2 presents a summary of studied cases and their respective loads where the axial force is a percentage of the beam plastic resistance (1084kN). The bending moment was applied at the beam bottom flange, the axial force along the beam cross-sectional area and the bolts pretension in the bolt head and nut. Overall loads are considered in terms of displacement application - see Figure 2.

Table 1 – Material mechanical properties (in MPa)

		f_y	f_u	E
PLATES	beam web	364.08	545.10	203714
	beam flange	340.68	537.89	215222
	column web	372.69	572.76	206936
	column flange	343.48	538.55	220792
	endplate	370.12	604.14	200248
BOLTS	M20	943.88	1222.40	210000
STIFFENER	t = 10 mm	1000		210000



(a) joint geometrical parameters (b) numerical model (c) detail

Figure 2 – Flush endplate joint specifications

Table 2 – Considered experimental tests (Silva *et al.*, 2003)

ID	Bending Moment kN.m	Axial Force Levels	
		($\%N_{pl,beam}$)	(kN)
FE1	72.2	-	-
FE3	77.2	-4%	-52.7
FE5	80.5	-20%	-265.0
FE6	72.3	-27%	-345.0
FE8	61.7	+10%	+130.6

www.EngineeringEBooksPdf.com

3 APLICATION OF COMPONENT METHOD

In order to compare the theoretical, experimental and numerical results, the FE01 joint was used considering the bending moment application only. The partial safety factors were considered equal to 1.0. Table 3 presents the individual values of resistance and stiffness coefficients of each component. It can be observed that the component that controls the joint design in tension zone is the endplate in bending (5) and in the compression region, the beam flange in compression (7).

Table 3 – Individual resistances - component method (Eurocode 3, 2003) - Test FE01

	Component		F_{Rd} (kN)	k/E (mm)
Components on the area in compression	(1)	column web in shear	494.8	8.43
	(2)	column web in compression	690.7	10.40
	(7)	beam flange in compression	444.3	∞
First bolt row (h=193.1mm)	(1)	column web in shear	642.6	8.43
	(2)	column web in compression	690.7	10.40
	(7)	beam flange in compression	542.3	∞
	(3)	column web in tension	533.3	7.03
	(4)	Column flange in bending	408.3	40.47
	(5)	endplate in bending	339.3	13.35
	(8)	beam web in tension	483.0	∞
	(10)	bolts in tension	441.0	7.76
Second bolt row (h=37.1mm)	(1)	column web in shear	303.2	8.43
	(2)	column web in compression	351.4	10.40
	(7)	beam flange in compression	203.0	∞
	(3)	column web in tension	533.3	7.03
	(4)	Column flange in bending	408.3	40.47
	(5)	endplate in bending	339.3	13.35
	(8)	beam web in tension	483.0	∞
	(10)	bolts in tension	441.0	7.76
$M_{j.Rd}$=339.3x0.193+203x0.037=73.05kN.m $S_{j.ini}$=11152.2kN.m/rad e $S_{j.ini}/\eta$=5576.1 kN.m/rad				

4 RESULTS AND DISCUSSION

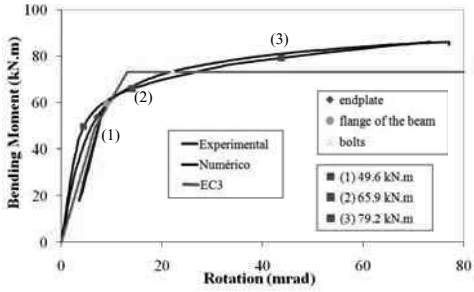
4.1 Joint only subjected to bending moment

Figure 3 presents the bending moment versus rotation curves for the FE01 joint (Luis *et al.,* 2003*)* where it is possible to observe that a good agreement between the numerical and experimental results was reached. This figure also presents, the progressive sequence of yielding of the experimental components obtained from the strain gauges results: endplate in bending, beam flange in compression and bolts in tension. In the numerical curve, it can be observed that from a bending moment level of 49.6kN.m, the initial stiffness is no longer linear, indicating that the beginning of the endplate in bending component yielding, Figure 3, confirming the results obtained from the experiments. From this figure it is also possible to observe that the beam flange in compression component yield at a 65.9 kN.m level, according to Von Mises criteria, Figure 4.

4.2 Joints subject to bending moment and axial force

This section presents the results for joints simultaneously subjected to bending moment and axial force. In order to reproduce the experimental test loading sequence, first the axial force was applied followed by the bending moment application. The individual and global bending moments *versus* rotation curves are presented in Figures 5 and 6, respectively.

www.EngineeringEBooksPdf.com



$M_{EXPj.Rd}$ = 72.20 kN.m

$M_{NUMj.Rd}$ = 70.04 kN.m

$M_{EC3j.Rd}$ = 73.05 kN.m

$S_{EXPj.ini}$ = 8564.0 kN.m/rad

$S_{NUMj.ini}$ = 9940.0 kN.m/rad

$S_{EC3j.ini}$ = 11152.2 kN.m/rad

Figure 3 – Moment versus rotation curve – Test FE01 – only for bending M

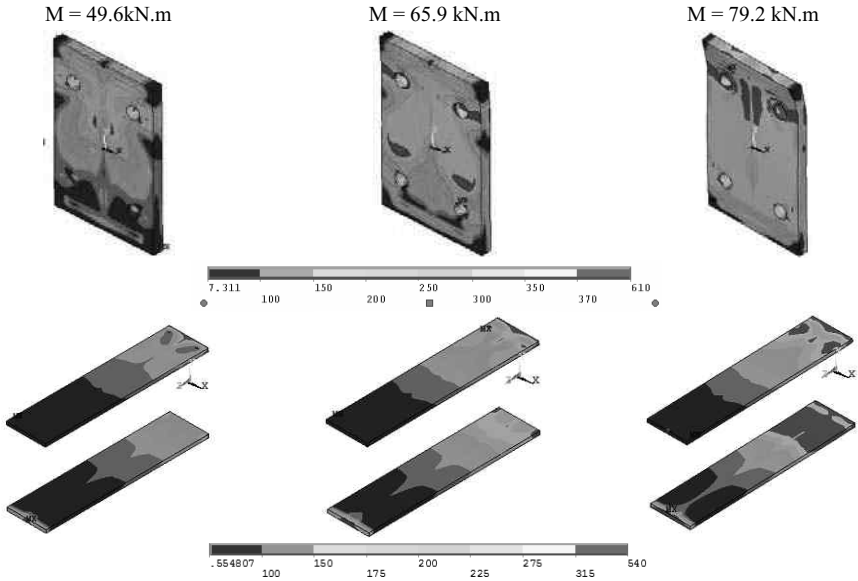
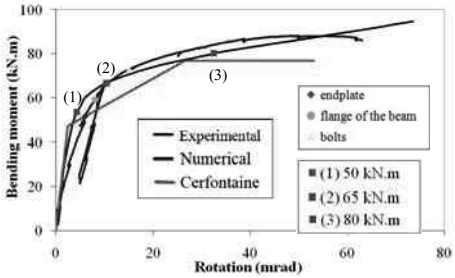


Figure 4 –Von Mises stress distribution – FE01 (in MPa)

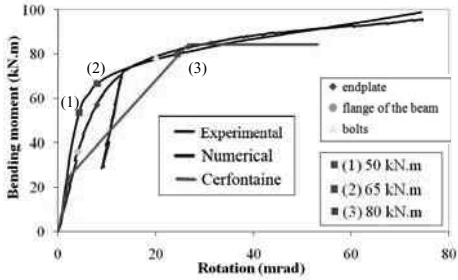
Figure 6 indicates that in all the numerical model bending moment *versus* rotation curves an increase of the compression axial force levels applied to the joint also led to an increase of the joint flexural resistance. The previous conclusion was also valid for the case with axial force corresponding to 20% of the beam plastic resistance, fact corroborated by the experiments, despite differences in the individual bending moment *versus* rotation curves. This is due to the fact that the components in the compression region, even with an increase of applied force, did not reach their resistance limits and, therefore, the components in tension were relieved by the compressive axial force. Small changes in initial stiffness of these curves were also observed. For tests with tension axial force, the bending moment resistance was reduced because the compression components reached the yielding for early bending moment levels.

The numerical initial stiffness presented values larger than their experimental counterparts but in terms of the bending moment resistance, the values were very similar. It could be verified that, increasing the joint axial forces, the endplate in bending component was not the controlling factor leading the joint design to be controlled by beam flange in compression component, fact that was also observed experimentally. Table 4 presents the values of bending moment resistance, $M_{j,Rd}$, and initial rotational stiffness, $S_{j,ini}$, for all the tests investigated.

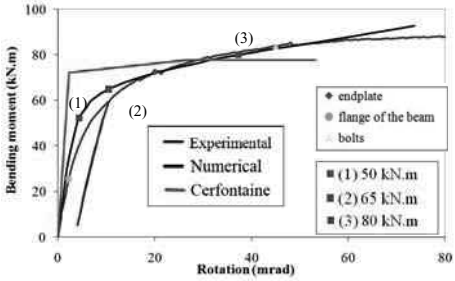
www.EngineeringEBooksPdf.com



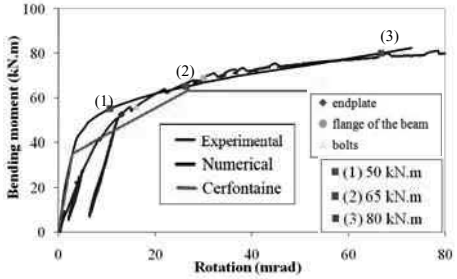
(a) Test FE03 – N= - 52.7kN



(b) Test FE05 – N= - 265.0kN



(c) Test FE06 – N= - 345.0 kN



(d) Test FE08 – N= + 130.6 kN

Figure 5 – Bending moment *versus* rotation curves

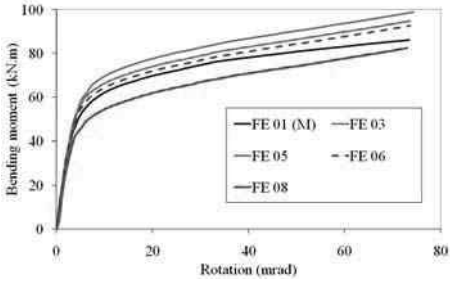


Figure 6 – Moment *versus* rotation curve – Numerical Model

Table 4 – Value of $M_{j.Rd}$ and $S_{j.ini}$

Test	$M_{j.Rd.ex}$ kN.m	$M_{j.Rd.num}$ kN.m	$\frac{M_{j.Rd.num}}{M_{j.Rd.ex}}$	$S_{j..ini.exp}$ kN.m/ rad	$S_{j..ini.num}$ kN.m/ rad	$\frac{S_{j..ini.num}}{S_{j..ini.exp}}$
FE1	72.20	70.04	0.97	8564	9940	1.16
FE3	77.20	70.20	0.91	9713	11128	1.14
FE5	80.50	75.20	0.93	10763	11351	1.05
FE6	72.30	69.10	0.96	9379	10800	1.15
FE8	61.70	57.50	0.93	7185	8474	1.18

Figures 7 and 8 present the Von Mises stress distribution for three different bending moment levels, i.e., 50 kN.m, 65kN.m and 80 kN.m, respectively. Once again, comparing the results, it could be observed that increasing the applied axial force, the beam flange in compression component reached the yielding before.

www.EngineeringEBooksPdf.com

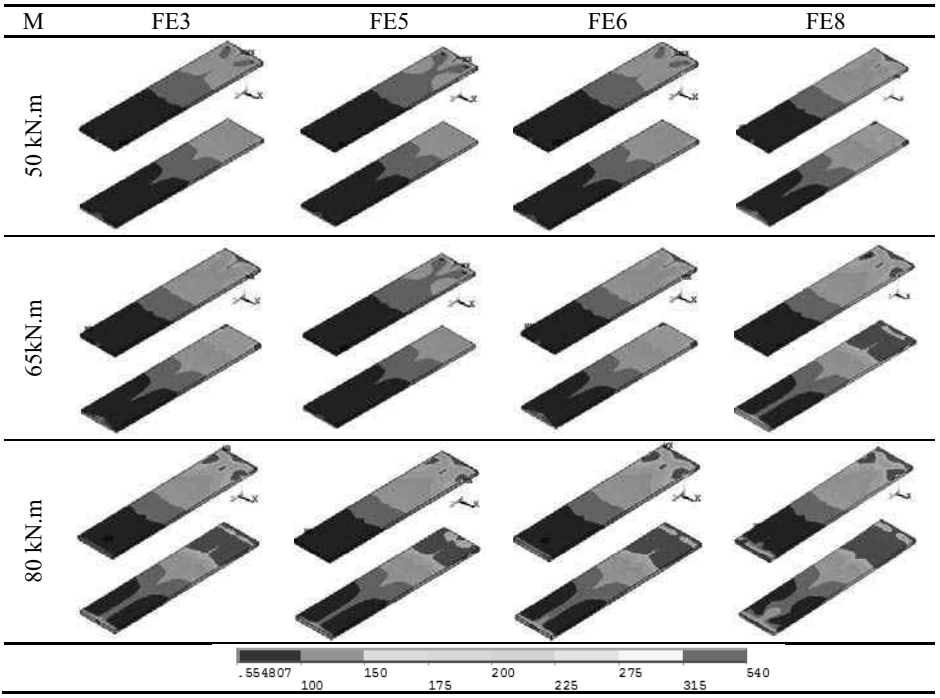


Figure 7 –Von Mises stress distribution – bottom beam flange (in MPa)

In FE06 test a compressive axial load magnitude corresponding to 27% of the beam plastic resistance was applied but the joint bending resistance was less than its correspondent to the FE05 test. This was due to the fact that in the FE06 test, the compressive axial load level led to an early yielding of the beam flange in compression component. Comparing the results for the individual bending moment *versus* rotation curves presented in Figure 5, it could be observed that for the numerical and experimental results related to FE03, FE05 and FE08 tests, the values obtained from the use of Cerfontaine model represent a lower bound for the bending moment resistance. Alternatively in FE06 test, the Cerfontaine model use led to an unsafe prediction.

5 CONCLUSION

The present paper aimed to evaluate the structural response of beam-to-column joints subjected to bending moments and compressive axial forces. The adopted methodology first considered the available component method introduced in the Eurocode 3 (2003). Afterwards, a numerical model based on finite element simulations was developed, using Ansys 11.0 package [3], considering a full nonlinear analysis (material and geometric) followed by the application of the Cerfontaine model (2001). The numerical model calibration was performed against experimental evidence in terms of bending moment versus rotation curves and stress distribution patterns. A numerical and experimental results comparison indicated a good agreement in terms of bending moment resistance, initial stiffness and component yielding sequence. For the studied cases, the presence of a compressive axial force in the joint led to an approximate 10% increase in the joint bending moment resistance, i.e., from M_{jRd}=80,5kN.m to $M_{j,Rd}$=72,2kN.m for the FE01 joint [2] where only bending moments were applied to the joint. On the

www.EngineeringEBooksPdf.com

other hand, when tensile axial force was applied to the joint, a reduction of 15% was verified in the joint bending moment resistance.

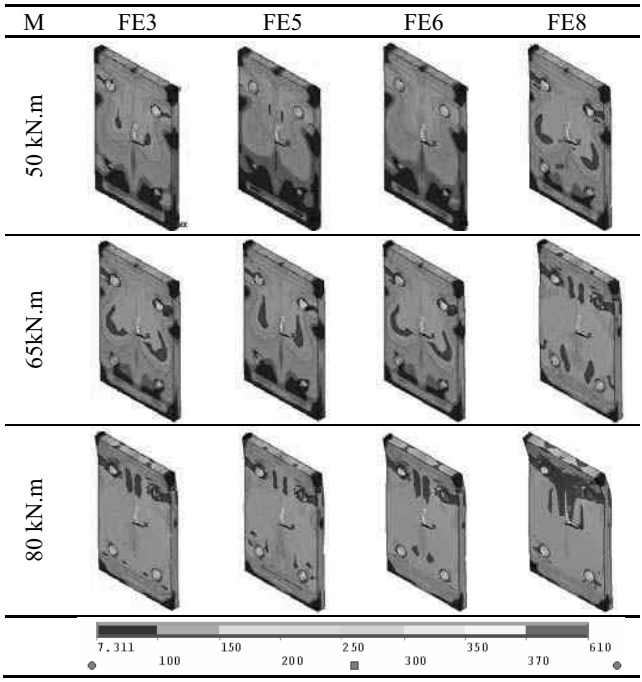


Figure 8 – Distribution of the Von Mises stress - endplate (in MPa)

6. ACKNOWLEDGMENTS

The authors gratefully acknowledge the Brazilian National and State Science Support Agencies: CAPES, CNPq and FAPERJ for the financial support granted to this research program.

REFERENCES

[1] Ansys. Inc. Theory Reference (version 11). 2008.

[2] Bursi. O. and Jaspart. J. P.. 1997. Calibration of a Finite Element Model for Isolated Bolted End-Plate Steel Connections. Journal of Constructional Steel Researchers. vol. 44. nº 3. pp. 225-262.

[3] Cerfontaine, F, 2001. Etude analytique de l'interaction entre moment de flexion et effort normal dans les assemblages boulonnés. In: Construction Méttalique, nº 4, p. 1-25.

[4] Eurocode 3. prEN 1993-1.8. 2003. Design of steel structures – Part 1.8: Design of joints ("final draft"). CEN. European Committee for Standardisation. Brussels.

[5] Rodrigues. M.C.. 2009. Numerical Modeling of Beam-Column Joints in Steel under Bending Moment and Axial Force. 178f. Dissertation - Civil Engineering Department. UERJ. Rio de Janeiro. 2009.

[6] Silva, L. S. da, Lima, L. R. O. de, Vellasco, P. C. G. da S. and Andrade, S. A. L. de, 2004. Behaviour of Flush Endplate Beam-to-Column Joints Under Bending and Axial Force. International Journal of Steel and Composite Structures, vol. 4, nº 2, pp. 77-94.

www.EngineeringEBooksPdf.com

SDSS'Rio 2010 STABILITY AND DUCTILITY OF STEEL STRUCTURES
E. Batista, P. Vellasco, L. de Lima (Eds.)
Rio de Janeiro, Brazil, September 8 - 10, 2010

LOSS OF PRELOAD IN BOLTED CONNECTIONS DUE TO EMBEDDING AND SELF LOOSENING

Roland Friede, Jörg Lange

Institut for Steel Structures and Material Mechanics, Technische Universität Darmstadt, Germany
friede@stahlbau.tu-darmstadt.de, lange@stahlbau.tu-darmstadt.de

Keywords: slip joint, bolted connection, preload, embedding, self loosening

Abstract. *At the Technische Universität Darmstadt, Germany, a research project analyzes the effect of embedding and self loosening of bolted connection. Therefore tests on single bolted lap joints were performed. The amount of static embedding proved to depend mainly on the coating system. If there was a cyclic displacement in the joint, even uncoated connections lost up to 40 % of the preload. Self loosening tests showed the importance of several parameters, especially the clamping length and the amount of displacement. The paper presents the tests and the results.*

1 INTRODUCTION

Bolted connections are more or less preloaded. Especially when the stiffness of the connection is important or a cyclic load can lead to a fatigue problem, it is necessary to fasten the connection with a special amount of preload. But there are some effects that can lead to a decrease of the preload during the lifetime of the construction. The two most important effects are (a) embedding and (b) self loosening.

To protect connections against the loss of preload, several antiloosening devices are on the market. Recent results showed that unfortunately almost all of them were malfunctioning. Due to that in 2003 all German regulations for these elements were withdrawn [1]. At the moment a research project is running at the Technische Universität Darmstadt, Germany, to analyze the mechanism of embedding and self loosening. The aim is, to find a constructive way to protect bolted connections. Therefore several tests to identify the important parameters were realized. Within this paper the tests and the main results are presented.

2 LOSS OF PRELOAD

After the fastening the preload of bolted connection can be reduced due to embedding and self loosening. Embedding is the result of yield processes in the microstructure of the connecting surfaces. The height of the embedding depends on time, pressure, temperature, material, number of surfaces and the implemented load. In standard steel connections especially the coating system has a large influence. Within different tests the amount of embedding has been earlier assessed for static loads and different coating systems [2]. The reduction of the preload due to embedding depends on the construction. Especially the resilience of the bolt and the clamped material is important. If the bolt and the plates are stiff, embedding leads to a higher loss of preload [3]. When the loss of preload exceeds a tolerable value, the bolts have to be refastened.

Self loosening in lap joints can take place when a cyclic slippage in transverse direction takes place. In this situation the loosening moment in the thread can exceed the holding moment due to friction. The height of the critical slippage can be calculated by equation (1). The equation bases on a model of a beam clamped on both sides (see Fig. 1) [3].

www.EngineeringEBooksPdf.com

$$a_{ult} \leq \frac{F_v \cdot l_k^3 \cdot \mu}{12 \cdot EI} \tag{1}$$

If the slippage is below the critical slippage the deformed bolt can follow the displacement. Long and bending flexible bolts have got an advantage. To avoid self loosening there are several possibilities [4]:

- Enlarge the clamping length
- Increase the preload
- Raise the friction
- Use long and thin bolts
- Reduce the displacement, e.g. by using fitting bolts
- Use efficient securing devices

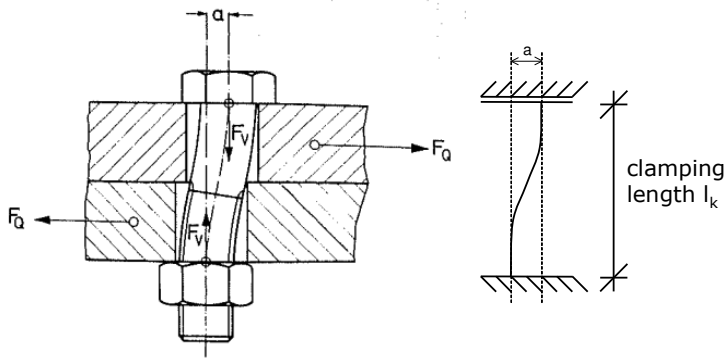


Figure 1: Lap joint with transversal deformation [3] / mechanical model

A dynamic test to assess the self loosening effect was developed by Junker in 1966 [5]. With that test it is possible to analyze the locking characteristics of fasteners under transverse loading conditions. In that test a bolted shear connection is moved by an eccentric rotating engine. Due to an elastic centerpiece the deformation controlled load is transformed into a mixture of deformation and force. The Junker test is standardized by the German code DIN 65151 [6]. With the Junker test it is not possible to affirm a secure connection but to compare different connections and safety devices. For test specimens hardened surfaces are used generally.

3 RESEARCH PROJECT

At the Technische Universität Darmstadt, Germany, a research project to assess the effects of embedding and self loosening of bolted connections is conducted. The aim is, to create new data about these effects and to find possibilities for designing secure constructions. During the project several tests were run which are presented in the following chapters.

3.1 Embedding tests

Within these tests [7] the embedding of bolted connections with different coating systems was assessed. Therefore static and cyclic tests were run on single bolted connections with bolts M20 10.9. For the test specimens (plate thickness 25 mm, overlapping area 100x100 mm, S235, ø22 mm) different coating systems were used. Table 1 shows the five different coating systems. The systems 0, 1 and 2 are supposed to have a hard surface, the systems 3 and 4 have a soft surface.

www.EngineeringEBooksPdf.com

Table 1: Coating system of embedding tests

System Number	Coating (thickness)	
System 0	Uncoated	
System 1 (150 µm)	Primer	Epoxy-zinc (70 µm)
	Cover	Epoxy-iron mica + polyurethane (80 µm)
System 2 (230 µm)	Primer	Epoxy-zinc (70 µm)
	Intermediate	Epoxy-iron mica + polyurethane (80 µm)
	Cover	Epoxy-iron mica + polyurethane (80 µm)
System 3 (80 µm)	Coating	Alkyd (80 µm)
System 4 (160 µm)	Coating	Alkyd (80 +80 µm)

In a first step the connections were fully fastened ($M_A = 450$ Nm, $F_P \sim 160$ kN). The preload was measured over the elongation with a micrometer. This method was tested and calibrated in advance. It showed that the preload is reduced after the fastening very quick. After about one day the preload stays constantly, the static embedding came to a halt. At the test specimens with the system 3 and 4 the soft coating is literally squeezed out of the contact surfaces (see Fig. 2).

In a second step the two plates were fixed in a testing machine and a cyclic deformation between the plates was applied (see Fig. 2). In these tests self loosening was avoided by a weld spot. The preload was measured over the load cycles.

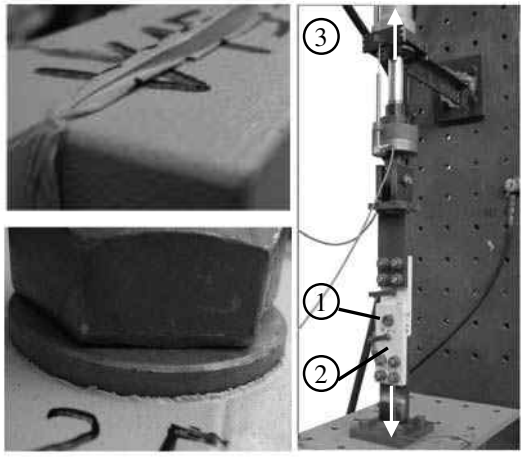


Figure 2: Static test, coating squeezed out (left),
cyclic test with bolt (1), plates (2) and cylinder (3) (right) [7]

www.EngineeringEBooksPdf.com

The results of these tests (step one and two) are given in Fig. 3. For the four different coating systems the mean values of three tests are shown. On the left side are the results of the static step. It can be seen that in every test at first a declination of the preload takes place which goes over to a constant value. The static embedding is between 8 and 80 % of the initial preload. On the right side the results continue with the load cycles of the second step. The preload is reduced because of the slippage in the contact pairs. The static and cyclic embedding leads to a total loss of preload of about 45 to 95 %.

The results show that embedding can have a big influence on the preload. The amount of static embedding depends on the coating system, in uncoated connections the preload is reduced too. The slippage in the connection leads to an additional loss of preload that is even severe for uncoated systems. Slippage in the connection has to be avoided or additional procedures have to be foreseen. These could be e.g.: use long and thin bolts, use additional elastic devices, use thin and hard or even better no coating, use material with hardened surface, increase the preload.

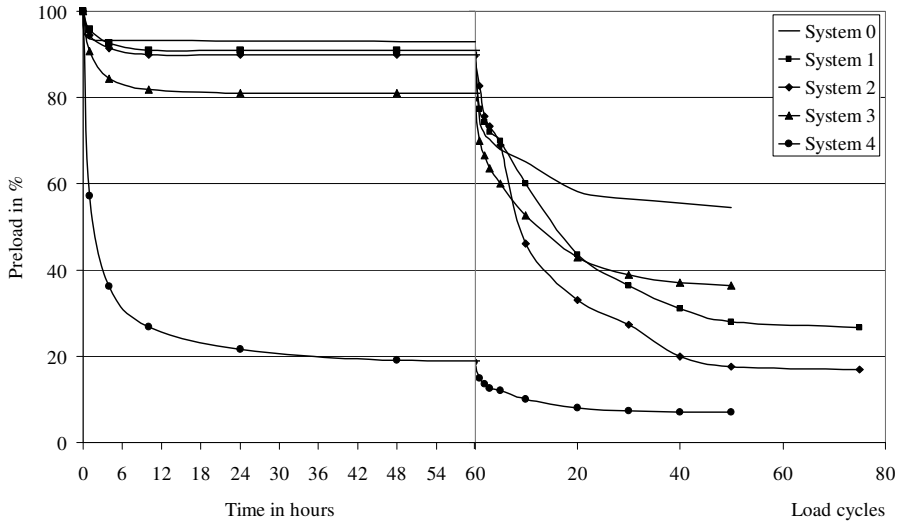


Figure 3: Results of the embedding tests: static test (left), cyclic test (right)

3.2 Self loosening tests

A new test was developed to assess self loosening. The idea was to analyze the effect under realistic conditions. Compared to the Junker test, standard material with a not-hardened surface was used. Within these tests (see also [8] and [9]) different parameters like the clamping length, the amount of the slippage and the effect of coating were assessed. The tests were run with single bolted lap joints with plates (plate thickness 20-60 mm, overlapping area 220x200 mm, S235, Δø2 mm) and bolts M16 to M24 (strength grade of 8.8 and 10.9). The tests were run displacement controlled with a slippage between ±0.3 and ±2 mm and a frequency of 0.2 to 0.4 Hz. The force in the bolts was measured via strain gauges implemented in the bolt shank. Fig. 4 shows a sketch and a picture of the experimental setup.

www.EngineeringEBooksPdf.com

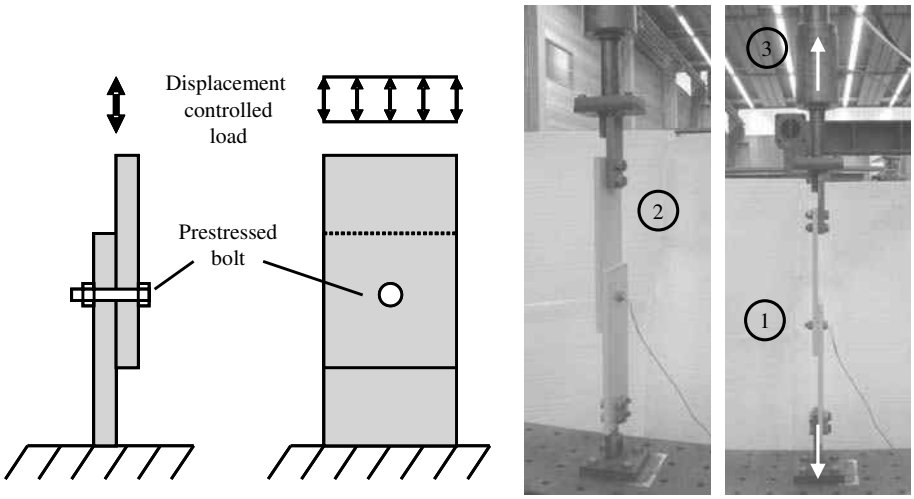


Figure 4: Sketch of the self loosening tests; experimental setup - bolt (1), plates (2), cylinder (3)

Some of the results are presented in diagrams below. The curves are means of at least two tests. The loss of preload can be traced back on a combination of embedding and self loosening. The figures show the number of load/displacement cycles on the horizontal axis and the relative preload on the vertical axis.

In Fig. 5 the results of tests with varying clamping length are shown. A clamping length under 90 mm led to a complete loss of the preload within 200 cycles, a number that is far away from being associated with a fatigue problem. But even a clamping length above 90 mm led to a significant loss of the preload. During the tests with a clamping length of 90 or higher, no slippage of the bolt/nut was measured. Self loosening did not occur.

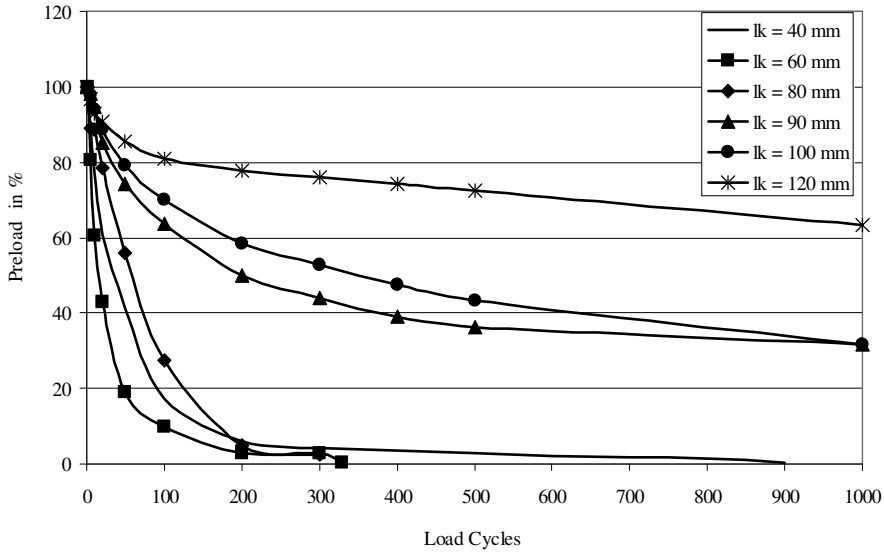


Figure 5: Self loosening of bolts M20 10.9 with different clamping length l_k

www.EngineeringEBooksPdf.com

In figure 6 results of self loosening tests with a different displacement between the plates are shown. Smaller displacements led to a minor declination of the preload. In the tests with bolts M20 10.9 a displacement of 0.3 led to a constant preload on a high level. The tests with a higher displacement led to slippage of the bolt/nut and self loosening.

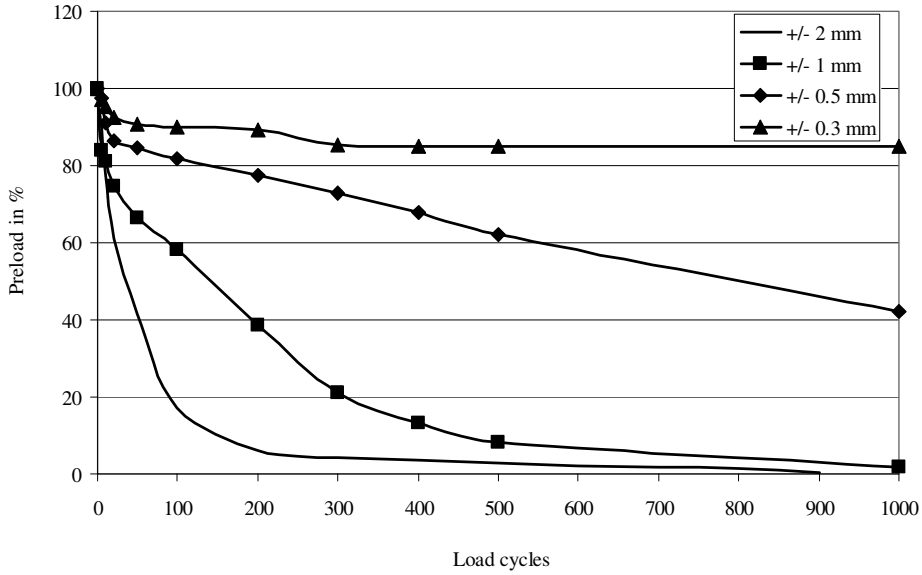


Figure 6: Self loosening of bolts M20 10.9 l_k = 40 mm with different displacements

The parameters tested can be divided into three groups (see table 3): positive influence (slow down the loss of preload), negative influence and no influence.

Table 3: Influence on the self loosening of the tested parameters

Positive influence:	Enlargement of the clamping length Reduction of the slippage Using of the securing device NORD-LOCK
No influence:	Additional axial force Fastening with the combined method (combination of torque and rotation controlled) Producing the clamping length with additional non fixed plates compared to the same clamping length in one peace Bolt diameter
Negative influence	Additional coating 8.8

www.EngineeringEBooksPdf.com

4 CONCLUSION

Every bolted connection is more or less preloaded. After the fastening the preload can be reduced due to embedding and self loosening. At the Technische Universität Darmstadt, Germany, the effects were assessed.

A first test series assessed the effect of embedding. Static and cyclic tests with single lap joint connections with bolts M20 10.9 were run. The result was that embedding under static load leads to a loss of the preload, in the tests between 8 and 80 % of the starting preload. The coating system has got a major influence. Therefore it is necessary to choose an adequate coating system. Hard coatings, like epoxy-zinc and epoxy-iron mica + polyurethane systems, led to good results. Soft coatings, like alkyd, are pushed out of the connection and led to a higher loss of preload. The thickness must be limited. The results are comparable to earlier tests [2]. Under cyclic loads the reduction of preload grows. Even in uncoated connections the preload is reduced to 55 % of the initial preload. This is a result of abrasion in the contact pairs. In the coated connection the reduction amplifies. In the worst case the preload is gone.

The loss of preload hast to be taken into account during the design process. To secure the connection slippage has to be avoided or an adequate construction is necessary (e.g. use long and thin bolts, use additional elastic devices, use thin or even better no coating, use material with hardened surface, increase the preload, refasten during frequent maintenance).

In a second test series the effect of self loosening was assessed. Therefore single lap joint connections with bolts M16 to M24 8.8 and 10.9 under cyclic loads were assessed. The results are that self loosening can be avoided under the following circumstances:

- Reduce the slippage in the lap joint ($\leq$ 0.3 mm for bolts M20)
- Enlarge the bolt length above the clamping length to diameter ratio of five ($l_k/d > 5$)
- Achieve form fit between the bolt and the nut by additional securing elements or adhesives

Nevertheless the preload will be reduced due to static and cyclic embedding. Additional there is always a risk of fatigue failure when a slippage in the lap joint leads to bending of the bolt. The only enduring protection from self loosening is to avoid the slippage in the joint.

A comparison of the test results with the critical slip showed that eq. 1 leads to conservative results. To improve the calculation of the critical slip it is possible to take the flexibility of the clamped ending of the beam model into account [10]. That leads to eq. 2. For bolts M20 the stiffness C_φ = 1250 kNm/rad fits quite well to the test results.

$$a_{grenz} \leq F_V \cdot \mu \left[\frac{l_k^3}{12 \cdot EI} + \frac{l_k^2}{2 \cdot C_\varphi} \right] \tag{2}$$

Embedding and self loosening reduce the preload and can lead to the complete failure of the bolt. During the design process the reduction of preload in bolted connections has to be taken into account. Although a lot of test results are available, in some cases it is still very difficult to foresee and prevent the reduction of preload with economic solutions. Therefore it is, beside a good design, necessary to develop worst case scenarios and to monitor critical connections frequently.

www.EngineeringEBooksPdf.com

REFERENCES

[1] Esser J., Hellwig G., „Konsequenzen für die Normung – Wirkungslose Schraubensicherungen“, *DIN-Mitteilungen*, 2004/04

[2] Katzung W., Pfeiffer H. and Schneider A., “Zum Vorspannkraftabfall in planmäßig vorgespannten Schraubenverbindungen mit beschichteten Kontaktflächen”, *Stahlbau* **65** (9), 307-311, 1996.

[3] Blume D., Illgner K.H., *Schrauben Vademekum*, Bauer & Schaurte Karcher, Neuss, 1988.

[4] Strelow D., “Sicherungen von Schraubenverbindungen”. *Merkblatt 302 – Stahl Informations-zentrum*, Düsseldorf, 1983.

[5] Junker D., Strelow D., „Untersuchungen über die Mechanik des selbsttätigen Lösens und die zweckmäßige Sicherung von Schraubenverbindungen I-III“ *Draht-Welt* **52**, 103-114, 175-82, 317-335, 1966

[6] DIN 65151 „*Aerospace series – Dynamic testing of the locking characteristics of fasteners under transversal loading conditions (vibration test), 2002/08*

[7] Proff S., *Untersuchung des Setzverhaltens von hochfest vorgespannten Schraubenverbindungen unter zyklischer Beanspruchung*. Studienarbeit am IFSW TU Darmstadt, 2007.

[8] Friede R., Lange J., *Self loosening of prestressed bolts*, Nordic Steel construction conference 2009, Malmö.

[9] Osmani B., *Durchführung und Auswertung von Versuchen zum selbsttätigen Losdrehen und Lockern von HV-Schrauben*. Master-Thesis am IFSW TU Darmstadt, 2010.

[10] Klöcker M., Hufschmidt K. „Einflussgrößen auf das selbsttätige Losdrehen von Schraubenverbindungen und praxisgerechte Prüfung“, *DVM-Tag 2004 Schraubenverbindungen*, Berlin 2004

www.EngineeringEBooksPdf.com

PLASTIC RESISTANCE OF L-STUBS JOINTS SUBJECTED TO TENSILE FORCES

M.Couchaux*,, I.Ryan* and M.Hjiaj****

* CTICM, Saint-Aubin, France
e-mails: mcouchaux@cticm.com, iryan@cticm.com

** INSA of Rennes, Rennes, France
e-mail: Mohammed.Hjiaj@insa-rennes.fr

Keywords: plastic, contact, bolted, tensile.

Abstract. *The tensile parts of tubular bolted flange joints can be treated as L-stubs or T-stubs. It has been shown that contact has a significant effect on the elastic behavior of these joints. In the present paper, the effects of contact between flange plates are modeled via a mechanical model. Taking into account the behavior of the flange in the contact area and bolt bending, a model is developed to predict the resistance of L-stub joints. The comparison of analytical results with 3D finite element elasto-plastic analyses indicates that the proposed model provides good predictions. Effects of contact, and therefore of the prying force, are particularly important in the case of relatively thin flanges.*

1 INTRODUCTION

T-stubs and L-stubs (see Figure 1) are commonly used to model the tensile part of many types of bolted joint ([2]-[7]) both in the elastic and in the plastic range of behavior. L-stubs are commonly used to model the tension part of ring flange joints. The pertinence of this approach has been validated by Seidel [4]. The effects of prying force are particularly important for this type of joints as it can increase significantly the value of the bolt force and thus modify the plastic or ultimate resistance of this type of joint.

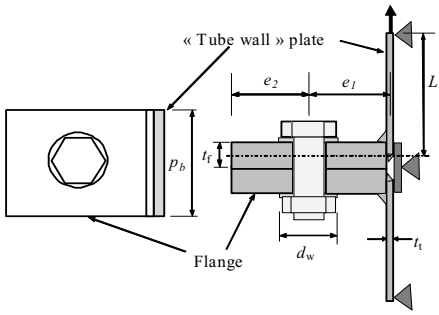


Figure 1: Geometry and main dimensions of an L-stub joint

Prying force is the resultant of contact pressures between the two opposite flanges. For some time now, the prying force has been represented by a concentrated force acting at or near the flange plate edges of T-stubs [5] or L-stubs ([2], [4]). Senda et al [3] postulated a linear distribution of contact pressure. However it was shown in [7] that the contact pressure distribution may depend on the length of the

www.EngineeringEBooksPdf.com

contact area and may not be unique in shape. Couchaux et al [7] proposed to model the flange in contact with the opposite ones via a mechanical model. This model has been applied in the elastic range and the results were in good agreement with numerical ones. Due to contact phenomena the prying force can be significantly increased particularly for thinner flanges. When the plastic resistance of a joint is attained, global plastic deformations are not usually very large so that the distribution of contact pressure can be fairly accurately obtained via an elastic analysis. Following the usual practice of considering plastic resistance models to evaluate the capacity of joints, the authors propose to determine the resistance of L-stub joints while considering the effects of contact. The contact distribution is evaluated for an elastic behavior of the flange just prior to the formation of a plastic mechanism in the flange or yielding of the bolt. As a more accurate determination of the contact area is not easy, a simplified formulation is provided. The results obtained by both models are satisfactorily compared to those obtained by non-linear elasto-plastic 3D finite element analyses.

2 ANALYTICAL MODEL

2.1 General hypothesis

The following four failure modes are considered for the L-stub joint: bending mechanism collapse of the flange, failure of the bolts with contact over a part of the flange width, failure of the bolts with full separation of the flange and finally rupture of the tube wall. Thus, the position of the prying force is important for the first and the second failure modes. The bolt is assumed to apply two equal punctual forces, each at a distance e_w (see Figure 2) from the bolt axis. In conjunction with its axial tensile load a plastic bending moment is usually rapidly attained on the tube wall, noting that in general the tube-wall thickness t_t is much less than that of the flange t_f (here we consider that $t_t < t_f$). The plastic tube-wall bending moment, as a function of the applied axial tensile load $F_{T,pl,MN}$, at the junction with the flange is given by:

$$M_{pl,t,MN} = M_{pl,t}\left[1-\left(\frac{F_{T,pl,t,MN}}{F_{T,pl,t}}\right)^2\right] \quad (1)$$

where:

$M_{pl,t} = \frac{l_{eff} t_t^2}{4} f_{y,t}$, $F_{T,pl,t} = l_{eff} t_t f_{y,t}$ with $f_{y,t}$: Yield strength of the tube wall steel.

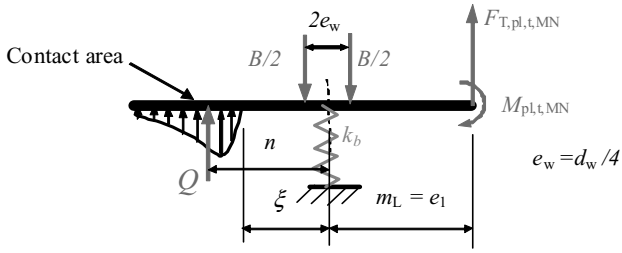


Figure 2: L-stub contact/prying forces just prior to Mode 1 or 2 failures

The behavior of steel is assumed to be elastic perfectly plastic. The flange is modeled by beam elements while the half-length bolt is modeled as a linear elastic axial spring connected to rigid supports at each end, that at the head or nut side being to the center of a rigid bar of width $2e_w$ resting on the flange. The area extending from the bolt to the free edge is considered as a potential contact area. In this model, the behavior of the flange "beam" in the contact area is considered via the mechanical model described in [7]. In the non-contact area of the flange, the Bernoulli beam theory is adopted so the elastic stiffness is $I_f = t_t^3 l_{eff}/12$ where l_{eff} is similar to that defined in EN1993-1-8 [5]. The elastic axial stiffness

www.EngineeringEBooksPdf.com

of the half-length bolt is $k_b = 2EA_s/L_b$, where L_b is similar to that defined in EN1993-1-8 [5]. The absence of a bolt hole in the flange plate is considered to compensate for the effect of any bending in the bolt.

2.2 Behavior in the contact area

The mechanical model, developed in [7] for a beam in contact with an infinitely rigid foundation, is applied to the case of a flange in the contact area. The contact pressure is assumed to be constant across the width of the beam (i.e. effective length of the L flange). Loading and boundary conditions of the flange on the contact area are shown in Figure 3.

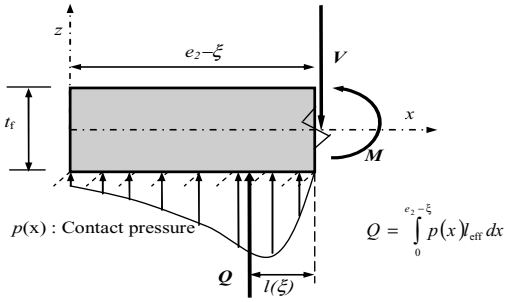


Figure 3: Boundary conditions in the contact area

Considering the boundary conditions and the mechanical model, Couchaux et al [7] obtained the relation between shear force V and bending moment M. The exact solution being quite involved, the following simplified relation has been proposed:

$$l(\xi) = \frac{M}{V} = \frac{1}{\left\{1+\left(\frac{e_2-\xi}{1{,}11\cdot t_f}\right)^6\right\}^{\frac{1}{6}}} \frac{2(e_2-\xi)}{3} \tag{2}$$

2.3 Evaluation of the separation length

In the non contact area, the flange is loaded by the tube wall and the bolt. Furthermore, when the separation length from the bolt axis, ξ, is less than the edge distance e_2, the flange is fully clamped at its junction with the contact area. The expression for the flange deflection at the bolt axis, δ_B, is then:

$$\delta_B = F_{T,pl,t,MN}\frac{\xi^2}{EI_f}\left(m_L/2+\xi/3\right) - B\frac{\xi^3}{3EI_f} - M_{t,pl,MN}\frac{\xi^2}{2EI_f} \tag{3}$$

The contribution of bolt force is simplified here by considering the action of a unique bolt force equal to B at a distance ξ from the fully clamped section. Since the flange deflection δ_B and the bolt elongation are equal, we obtain the following expression:

$$B\left[\frac{1}{k_b}+\frac{\xi^3}{3EI_f}\right] = F_{T,pl,t,MN}\frac{\xi^2}{EI_f}\left(m_L/2+\xi/3\right) - M_{t,pl,MN}\frac{\xi^2}{2EI_f} \tag{4}$$

Global equilibrium considerations also lead to the following expression for the bolt force:

$$B = \frac{F_{T,pl,t,MN}\left(m_L+n\right) - M_{t,pl,MN}}{n} \tag{5}$$

where: $n = \xi + l(\xi)$.

The separation length ξ, which depends on the relative stiffness of the bolt and the flange and also on the relative resistances of the joint and the tube wall, is comprised between the values e_w and e_2.

www.EngineeringEBooksPdf.com

2.4 Failure mode 1: yielding of the flange

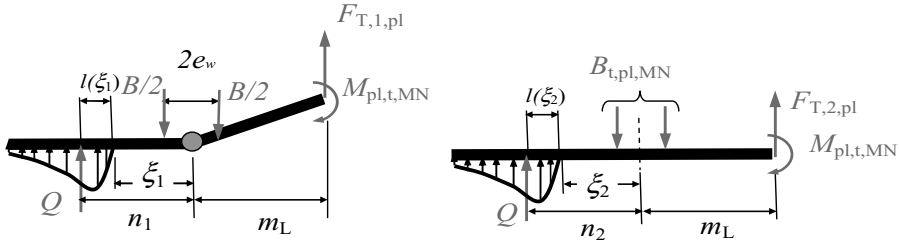
Due to the interaction between tensile force and bending moment in the tube wall (given by (1)), the tensile force which leads to the formation of a plastic bending moment in the flange at the bolt line is:

$$F_{T,1,pl} = F_{T,1,pl,(0)}\, g(f_1) \tag{6}$$

where:

$$F_{T,1,pl,(0)} = \frac{2n_1 M_{pl,f} + M_{pl,t}(2n_1 - e_w)}{2n_1 m_L - e_w(m_L + n_1)},\quad M_{pl,f} = l_{eff}\frac{t_f^2 f_{y,f}}{4}, l_{eff,1} = \min(l_{eff}; p_b - d),$$

$$g(f_1) = \left[\frac{\sqrt{1+4f_1}-1}{2f_1}\right],\quad f_1 = \left(\frac{F_{T,1,pl,(0)}}{F_{T,pl,t}}\right)^2 \frac{1}{1+\left(\frac{t_f}{t_t}\right)^2 \frac{2n_1}{2n_1 - e_w}}.$$



Mode 1: *Yielding of the flange* **Mode 2:** *Failure of the bolt*

Figure 4: Failure modes 1 and 2

Substituting (5) and (6) into (4), we get an equation from which the separation length ξ_1 can be obtained using an iterative procedure. The separation length depends both on the bolt and flange elastic stiffness and also on the plastic resistances of the flange and of the tube wall. The joint resistance corresponding to mode 1 is a plastic failure mechanism which can now be obtained from expression (6).

2.5 Failure mode 2: Failure of the bolt with prying action

2.5.1 Effect of bolt bending on the tensile resistance of the bolt

Experimental evidence shows that bolt bending is fairly significant both in the elastic and the elasto-plastic ranges of behavior. However, most of the existing analytical models for bolted joints don't consider this aspect explicitly. In the following, a simple evaluation of the effect of bending moment on the resistance of bolt is presented. The interaction between bending moment and tensile force in the bolt at the plastic limit can be approximated by the expression:

$$\frac{M_{pl,b,MN}}{M_{pl,b}} + \left(\frac{B_{t,pl,MN}}{B_{t,pl}}\right)^2 = 1 \tag{7}$$

where:

$$B_{t,pl} = A_s f_{yb},\quad M_{pl,b} = \frac{4R_s^3}{3} f_{yb},\quad R_s = \sqrt{\frac{A_s}{\pi}} \approx 0{,}45\, d.$$

In most cases when failure of bolts occurs before flange or tube wall, the prying force is often at or very close to the flange edge. If the flange curvature is neglected, we have (see Figure 5):

$$\theta_B \approx \frac{\delta_B}{e_2} \tag{8}$$

Considering the bolt as a cantilever beam subjected to a tensile force $B_{t,pl,MN}$ and bending moment $M_{pl,b,MN}$ we get:

$$B_{t,pl,MN} = \frac{2EA_s}{L_b}\delta_B \tag{9.1}$$

www.EngineeringEBooksPdf.com

$$M_{\text{pl,b,MN}} = \frac{2EI_s}{L_b}\theta_B \tag{9.2}$$

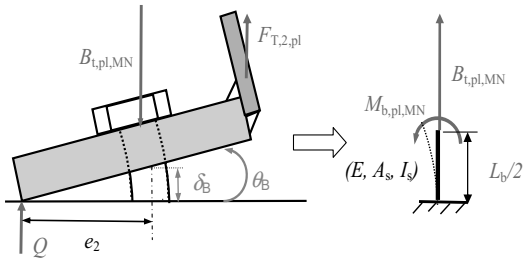


Figure 5: A Deformation of a L-stub when bolt yields first

Introducing (8), (9.1) and (9.2) in (7) we get:

$$B_{\text{t,pl,MN}} = B_{\text{t,pl}} \frac{\sqrt{4+\alpha^2}-\alpha}{2} \approx B_{\text{t,pl}}\left[1-0,48\ \alpha\right] \tag{10}$$

where:

$$\alpha = \frac{3\pi R_s}{16e_2} \approx 0,27\frac{d}{e_2}.$$

If the usual lower limit is adopted for e_2 , i.e. e_2= 1,2d_0 ≈1,32d where d_0 is the bolt hole diameter, one obtains $B_{\text{t,pl,MN}}$=0,9$B_{\text{t,pl}}$, which seems to justify the use of the 0,90 factor on the bolt axial design resistance given in many standards and to explain how bolt bending can be neglected.

2.5.2 Joint resistance involving bolt failure with prying

Due to the interaction between tensile force and bending moment in the tube wall (given by (1)), the tensile force (see Figure 4) which leads to the failure of the bolt is:

$$F_{\text{T,2,pl}} = F_{\text{T,2,pl,(0)}}\ g\left(f_2\right) \tag{11}$$

where:

$$F_{\text{T,2,pl,(0)}} = \frac{M_{\text{pl,t}} + n_2 B_{\text{t,pl,MN}}}{m_{\text{L}} + n_2},\quad g\left(f_2\right) = \left[\frac{\sqrt{1+4f_2}-1}{2f_2}\right],\ f_2 = \left(\frac{F_{\text{T,2,pl,(0)}}}{F_{\text{T,pl,t}}}\right)^2 \frac{1}{1+\dfrac{n_2 B_{\text{t,pl,MN}}}{M_{\text{pl,t}}}}.$$

Substituting (11) into (4), we obtain an equation from which the separation length ξ_2 can be determined by iteration. As for the mode 1, the separation length depends on the bolt and flange elastic stiffness and also on the resistances of the bolt and the tube wall. The joint resistance corresponding to mode 2 is by bolt failure which can now be obtained from expression (11).

2.6 Failure mode 3: Failure of the bolt without prying action

If flanges fully separate, rotations will be less than those assumed in § 2.5.1 and there is no prying action. Therefore the joint resistance will be equal to that of the bolt in tension which can safely be taken as:

$$F_{\text{T,3,pl}} = B_{\text{t,pl,MN}} \tag{12}$$

www.EngineeringEBooksPdf.com

2.7 Failure mode 4: Rupture of the tube wall

As the axial load applied to the tube-wall increases and tends towards the axial plastic resistance of the tube wall, yielding progresses across the wall section to such an extent that the associated tube-wall moment tends towards zero at the junction with the flange. Therefore the joint resistance corresponding to rupture of the tube wall can be given as:

$$F_{\mathrm{T},4,\mathrm{pl}} = F_{\mathrm{T},\mathrm{pl},\mathrm{t}} = l_{\mathrm{eff}} t_{\mathrm{t}} f_{\mathrm{y,t}}$$

2.8 Plastic resistance of L-stubs

The tensile resistance of L-stub joint is taken as the smallest of the values for the four failure modes:

$$F_{\mathrm{T,pl}} = \min\left(F_{\mathrm{T},1,\mathrm{pl}};\ F_{\mathrm{T},2,\mathrm{pl}};\ F_{\mathrm{T},3,\mathrm{pl}};\ F_{\mathrm{T},4,\mathrm{pl}}\right) \tag{13}$$

3 SIMPLIFIED MODEL

For the analytical model proposed above for the determination of the separation length, required for failure modes 1 and 2, an incremental resolution method is needed. To overcome this inconvenience a simplified expression has been developed to provide the separation length and which gives good results in the elastic range of behavior [8] and is shown here to be acceptable in the plastic range as well. The simplified expression for the distance n from the bolt axis to the prying force is:

$$n = \min\left(\left(2e_2 + \xi\right)/3;\ \left(\xi + 0{,}74 t_{\mathrm{f}}\right)\right) \tag{14}$$

where the separation length is:

$$\xi = e_2 . \min\left(1; \sqrt{\frac{\alpha_{\mathrm{R},0}}{\alpha_{\mathrm{R}}}}\right) \geq e_{\mathrm{w}},\ \text{with}\ \alpha_{\mathrm{R}} = 4\left(\frac{m_{\mathrm{L}}}{t_{\mathrm{f}}}\right)^3 \frac{A_{\mathrm{s}}}{L_{\mathrm{b}} l_{\mathrm{eff}}},\ \alpha_{\mathrm{R},0} = \frac{e_2/m_{\mathrm{L}} + 1}{\left(e_2/m_{\mathrm{L}}\right)^3}.$$

The formula (14) for n can be used to determine both lengths n_1 (i.e. for failure mode 1) and n_2 (i.e. for failure mode 2). To account simply for the reduction of the plastic bending moment in the tube wall as its axial load increases, the joint resistance are calculated via (6) and (11) for mode 1 with $M_{\mathrm{pl,t,MN}} = 0{,}5 M_{\mathrm{pl,t}}$ and for mode 2 with $M_{\mathrm{pl,t,MN}} = 0$.

4 COMPARISONS WITH NUMERICAL RESULTS

4.1 Finite element model and interpretation

The model is using the Finite element code ANSYS V11.0 and is quite similar to that used by Seidel [4] and Couchaux et al [7]. Joints are generated with three dimensional elements, which are hexahedral. A bolt of diameter d of a constant bolt cross-section, which is equal to the tensile stress as defined for EN1993-1-8 [5]. Only a quarter of the flange to flange joint needs to be modeled due to symmetry.

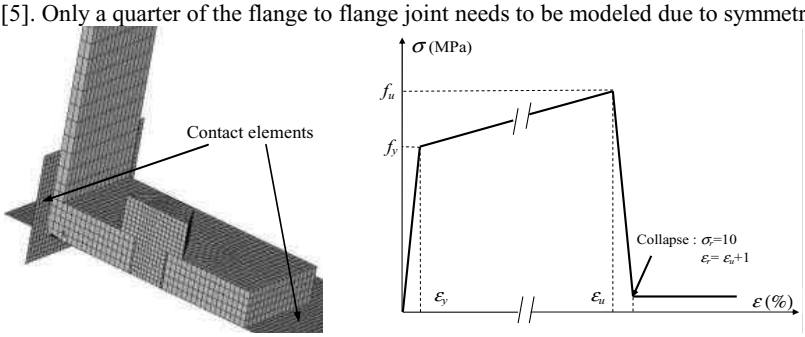


Figure 6: Meshing and behavior of steel considered in the model

www.EngineeringEBooksPdf.com

Two types of contact elements are also used: a) Flexible contact elements between the flange and the bolt and b) Rigid contact element between one flange and two plane of symmetry. The first rigid plane is horizontal and models the fictitious flange. The second rigid plan is vertical and models the resistance to tube dilation provided by a circular flange (see Figure 1 and 6). An isotropic Coulomb friction law (μ = 0,25) is used to reproduce sliding/sticking conditions between the flange and the bolt. Friction is neglected between the two flanges because of the symmetry.

A vertical displacement is applied at the end of the tube wall. The stress-strain relationship for the steel (flange, tube and bolts) is assumed to be multi-linear (see Figure 6). Large deformations are also considered. As soon as the deformation level reaches ε_u, the stress drops to 10 MPa in order to model the failure of the element. This phenomena leads either to a drop-off of the force applied to the joint or to the termination of the calculation. This latter state is assumed to be the ultimate state for the joint. The criterion of the yielding surface is that by Von-Mises. Finally, the ECCS method [1] is used to determine the plastic resistance from the numerical results as presented by the force-displacement curves.

4.2 Comparison of the FEM model results with those by the analytical models

A limited parametric study has been carried out to confront results of the analytical and the simplified models with those by the FEM model. All the joints studied have the dimensions presented in Figure 7. The thickness of the flange, t_f, which is comprised between 8 and 35 mm is the only variable parameter considered for the present study. The mechanical characteristics of steels for bolts, flanges and tube walls used are given in Table 1.

Table 1 Mechanical characteristics of steel

Elements	f_y	f_u	ε_u
-	*MPa*	*MPa*	*%*
Bolt M20 class 10.9	900	1050	5
Flange/Tube wall S355	355	480×1,5	30

The ratio of the joint resistance to the bolt resistance calculated by the analytical, simplified and numerical models are presented in Figure 7. When greater than 18mm, the flange thickness has almost no influence on the resistance of the joints considered because failure is by mode 2. The mode 2 failure involves significant prying forces in L-stubs leading to yielding/failure of the bolt. For lower flange thickness values, the joint resistance decreases with the thickness since it depends on the flange yielding only. The results obtained via the analytical and simplified models are in good agreement with those obtained by the numerical one. The simplified model usually underestimates the joint resistance. In the cases studied, the tube-wall failure mode is never attained.

www.EngineeringEBooksPdf.com

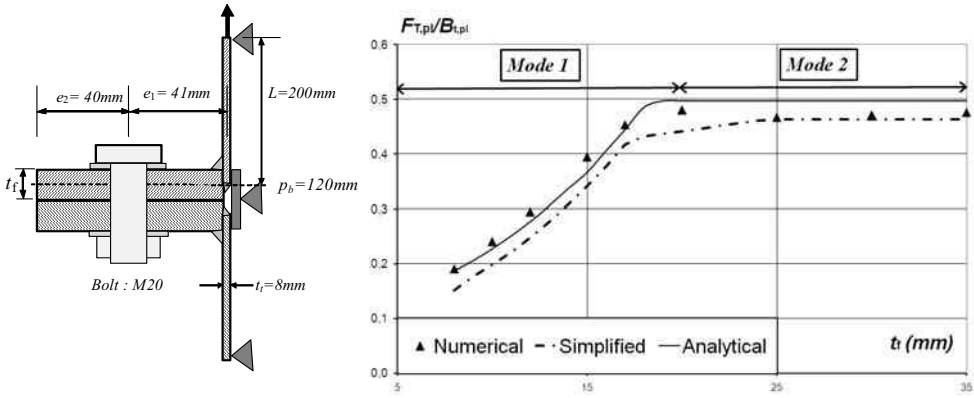


Figure 7: Joint configuration and ratio of joint resistance to the bolt resistance

5 SUMMARY

In the present paper an analytical model is proposed for calculating the plastic resistance of L-stubs joints subjected to tensile force by considering four failure modes not much unlike those described by EN1993-1-8 for T-stubs. The effects of contact between the two opposite flanges, which often leads to a significant additional prying force in the bolt, and bolt bending are also considered explicitly. Contact effects and particularly the position of the prying force can be determined considering an elastic behavior of the joint just prior to the formation of the failure mechanism.

REFERENCES

[1] ECCS, Recommended testing procedures for assessing the behaviour of structural elements under cyclic loads, European Convention for Constructional Steelwork, Technical Committee 1, TWG 13 – Seismic Design, No.45, 1986.

[2] Petersen, Ch., Stahlbau (Steel Construction), Braunschweig: Vieweg-Verlag, 1988.

[3] Senda, H., Suzuki, T., Ogawa, T., Inelastic behaviour of bolted T-stub connections, *Journal of structural and construction engineering, Transaction of AIJ,* ***476***, 159-168, 1996 (in Japanese).

[4] Seidel, M., Zur Bemessung geschraubter Ringflanschverbindungen von Windenergieanlangen, Institut für Stahlbau, Dissertation, Heft 20, Universität Hannover, 2001.

[5] Eurocode 3, Design of steel structures – Part 1 – 8: Designs of joints, 2005.

[6] Lemonis, M.E., Gantes, C.J., Incremental modelling of T-stub connections, *Journal of Mechanics of materials and structures*, **1**(7), 1135-1157, 2006.

[7] Couchaux, M., Hjiaj, M., Ryan, I., Bureau, A., Effect of contact on the elastic behaviour of bolted flange connections, *11th Nordic Steel Construction Conference*, Malmö, Sweden, 2009.

[8] Couchaux, M., Behaviour of bolted circular flange joints, PhD Thesis, INSA of Rennes, 2010 (in preparation in French).

www.EngineeringEBooksPdf.com

SDSS'Rio 2010 STABILITY AND DUCTILITY OF STEEL STRUCTURES
E. Batista, P. Vellasco, L. De Lima (Eds.)
Rio de Janeiro, Brazil, September 8 - 10, 2010

COMPOSITE BEAM MODELLING AT REAL SCALE INCLUDING BEAM-TO-BEAM JOINT

S. Guezouli*and A. Lachal*

* National Institute of applied Sciences (INSA) – Rennes – France
e-mails: samy.guezouli@insa-rennes.fr, alain.lachal@insa-rennes.fr

Keywords: Composite Bridge, Continuous Beam, Composite Joint, F.E.M.

Abstract. *This paper deals with the influence of a particular type of beam-to-beam joint on global and local behavior of a continuous composite beam of bridge. The F.E. code "Pontmixte" developed at INSA of Rennes has been already presented and used for various applications in previous papers. The model used by this code permits to include easily a particular finite element representing a joint that enforces the continuity of the composite continuous beam. End-plates welded at the ends of the steel beams are connected with studs to a transverse concrete transverse beam laying on an intermediate support represent the beam-to-beam joint. After a fast description of a 3D model developed with the F.E. code "CASTEM" concerning only the joint, a Moment-Rotation curve will be obtained and computed in "Pontmixte" for numerical simulations. Comparing the results of the original continuous beam (without joint) against the ones obtained with the same beam including the joint at one of the intermediate supports, the performance of a such type of beam-to-beam joint as well as the performance of the specific finite element computed in "Pontmixte" are clearly identified provided some remarks pointed out in the conclusion.*

1 INTRODUCTION

The understanding of the beam-to-beam joint behavior for composite bridges is of a big importance. The French national research calls MIKTI highlighted some joint solutions fundamentally different ones to others. For the first solution, the steel girders are connected with cover-plates and high strength bolts. This solution, generally located near the cross-section of zero bending moment, remains well-known for steel constructions [1] and it is not in need of more numerical modeling investigation so simplified 1D and 2D models could give sufficient information. For the second solution, both ends of steel girders are embedded in a concrete block resisting over the pier. Each steel girder lies directly over its own support in order to avoid a shear force transfer through the mid-cross-section of the embedding. This type of joint is necessarily located at intermediate support and could be investigated by a 3D numerical model similar to the one presented in this paper and concerning the third solution. For the solution under investigation, the steel girders are equipped with butt-plates welded at their ends. These are connected with shear studs to a transverse beam lying on an intermediate pier (Fig.1).

The finite element code Castem [2] is used to propose a 3D model for this type of joint in order to study the influence on the joint behavior of some parameters such as the friction coefficient between the butt-plate and the transverse beam as well as the butt-plate thickness and the connection degree. These future understandings will leads to propose an accurate design method of such joint solution. The behavior of the joint, represented by a moment-rotation curve of the composite cross-section, will be computed in the program Pontmixte [3] considering a specific finite element. The main objective of this work is to propose a first approach taking into account this type of joint to study a continuous composite beam at real scale.

www.EngineeringEBooksPdf.com

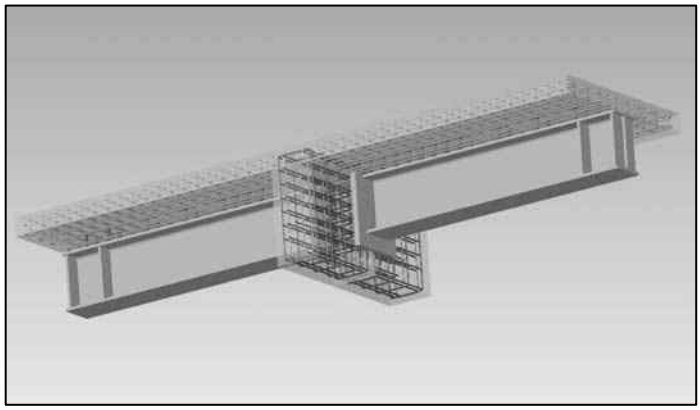


Figure 1: Beam-to-beam joint under investigation.

2 EXPERIMENTAL TEST AND 3-D F.E. MODEL

Geometrical details of the experimental test are given in figure 2. The steel girder is an HEA 500 rolled section in steel grade S355. The width of the slab is 1600 mm and the thickness is 160 mm. The strength class C45/55 is used for the concrete. Several details are given in a companion paper presented by A. Lachal and al. In SDSS'Rio2010. It is pointed out that the rotation ϕ of the joint is calculated as the difference between the rotation θ_1 at the attached beam cross-section and the rotation θ_2 at the axis support cross-section. This detail is considered for experimental as well as for numerical values of the joint rotation.

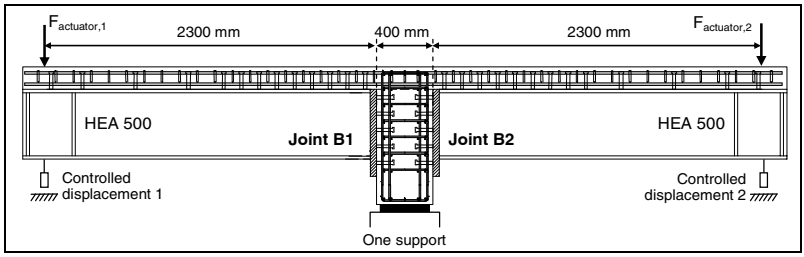


Figure 2: Geometrical details.

The 3-D finite element model developed on Castem uses principally cube finites elements with 8 nodes. The concrete slab including reinforcing bars and vertical shear studs uses 22140 elements, the steel girder, the stiffeners and the butt-plates 4974 elements, the transverse beam with horizontal shear studs 5576 elements and a small transversal steel girder used to applied the load 246 elements. The model uses the symmetry and contains 32936 finite elements. Figure 3 shows the top and the side views of the mesh (the concrete was removed for best clearance).

The mechanical properties are summarized as follows:

- For the concrete slab, perfect-plastic Drüker-Prager behavior model is used (Fig.4) with Mazars damage model. This isotropic scalar model is well-adapted to monotonic loading and depends on some parameters that are easily identified. The initial cracking of the slab due to the cyclic pre-loading of the

www.EngineeringEBooksPdf.com

specimen test is taken into account by an exponent variation of its Young's modulus (Fig.5) from the plane of symmetry ($E^c/100$) till the end cross-section (E^c = 35200 MPa) with the parameters C_1 = 0.019 and C_2 = 1.853.

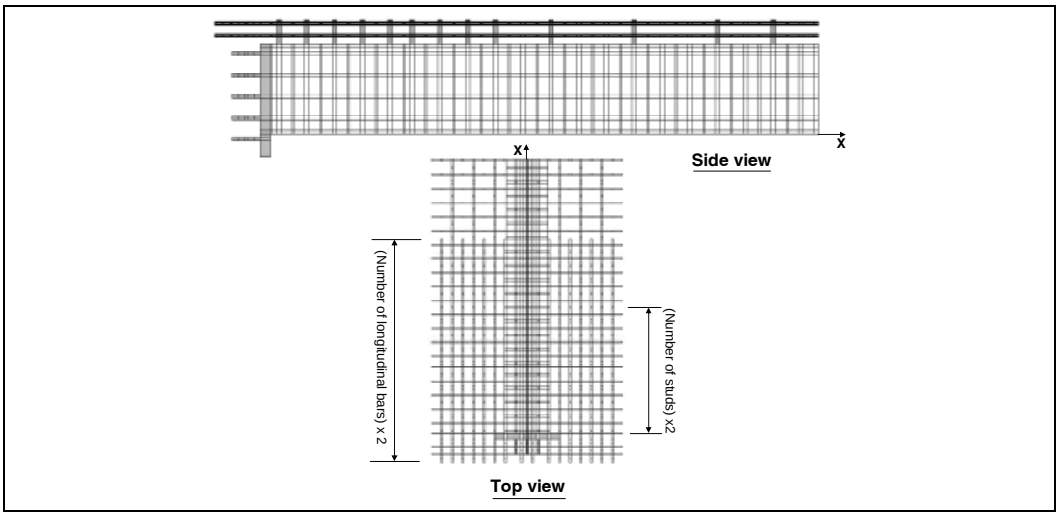


Figure 3: The 3D-model mesh – Top and side views.

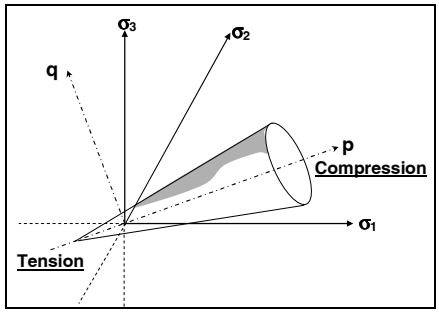


Figure 4: Drüker-Prager behavior model.

- The transverse beam is supposed to be a homogenized material. In order to take into account the reinforcing bars that are not included in the model, the Young's modulus is considered equal to $1{,}3E^c$. As-well-as the slab, this material behavior is perfect-plastic Drücker-Prager with 45MPa for yield compression and 7MPa in tension.

- The adherence between the upper flange of the girder and the slab is neglected, only the studs insure the transfer of the shear forces at the interface. For this material, also a perfect-plastic Drücker-Prager model is adopted with a compression resistance equal to 4,5MPa and a tension resistance equal to 0MPa; the Young's modulus is equal to E^c. Oppositely, the friction between the butt-plate and the transverse beam have a significant importance mechanically and also numerically and could not be neglected. Numerically, if no material is provided at the interface, the contact could cause the divergence of the iterative process. Mechanically, perfect-plastic Drücker-Prager model with 45MPa in compression and 0MPa in tension could be adopted but in future developments, specific contact elements have to be used.

www.EngineeringEBooksPdf.com

The Young's modulus is equal to $1{,}3E^c$ to provide the concrete cracking of the transverse beam during the contact with the butt-plate.

- Mechanical characteristics of steel materials (girder, stiffeners, reinforcing bars, butt-plate and studs) are given on table 1. Their behavior model is elastic-plastic with kinematic hardening (Figs.6) (f_y is the elastic limit stress and f_u the ultimate limit stress).

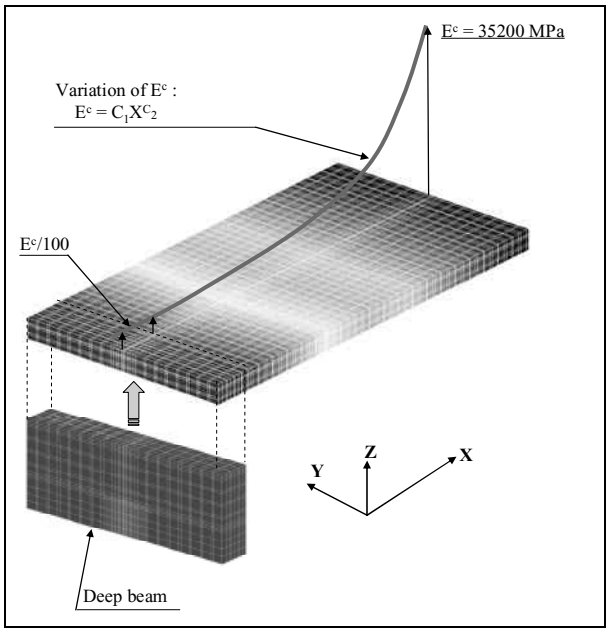


Figure 5: Young's modulus variation of the concrete slab.

Table 1 – Mechanical characteristics.

Material	Girder – Stiffeners – Butt-plate	Reinforcing bars	Studs
E (MPa)	200000	200000	200000
f_y (MPa)	430	585	350
f_u (MPa)	525	680	580

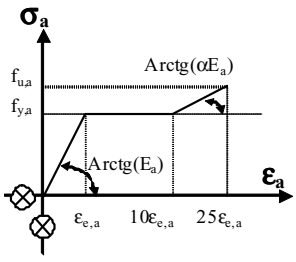


Figure 6.a: Girder–stiffeners–butt-plate.

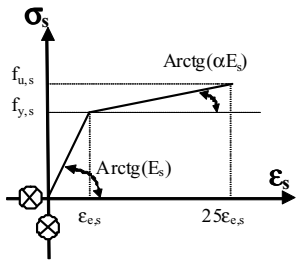


Figure 6.b: Bars.

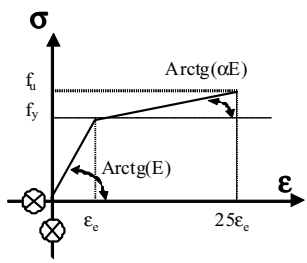


Figure 6.c: Studs.

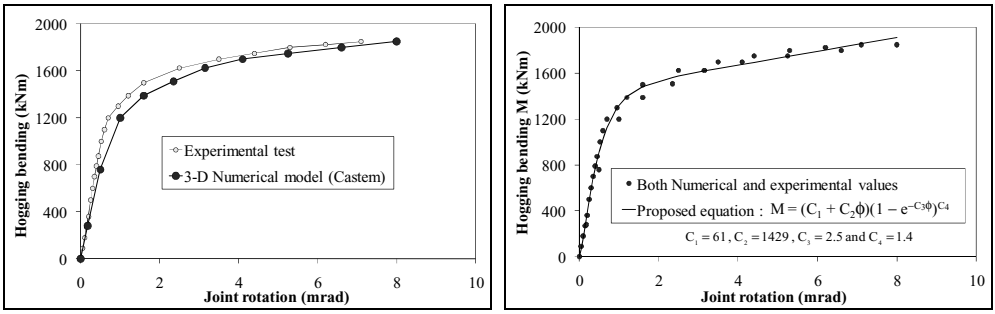
www.EngineeringEBooksPdf.com

The model as-well-as the specimen test is loaded until cracking of one of the constitutive materials. The test was stopped for a load equal to 900 kN. Figures 7 show the butt-plate deformation at this stage of loading comparing the model and the experimental test.



Figures 7: The 3D-model and the experimental test at end-loading.

The Moment-Rotation (M-ϕ) curve of the joint is compared between the 3D model and the experimental test in figure 8.a. The initial stiffness of the numerical (M-ϕ) curve appears lower than the one of the experimental test and for the same rotation, the resistance is also lower in the numerical curve. This is mostly due to the assumption of the Young's modulus variation of the slab taking into account its initial cracking. The considered value of $E^c/100$ at the joint cross-section could be greater and the curves should be closer than the ones given in figure 8.a. Nevertheless, using all the points coming from the numerical and the experimental results, a non-linear regression with multiple parameters leads to the proposed equation given in figure 8.b. This equation depends on 4 parameters C_1 to C_4 (given in figure 8.b). The values of these parameters depend on the geometrical and the mechanical properties of the tested model. This equation has an oblique asymptote that remains available until a rotation of 8×10^{-3} rad. and clearly leads to a horizontal asymptote and then decreases for higher values of rotations. Finally, this model will be computed in the program "Pontmixte".



Figures 8: Comparison between experimental and numerical results (a) and proposed equation (b).

3 COMPUTING THE PROPOSED MODEL IN "PONTMIXTE"

The finite element computed in "Pontmixte" could be defined as a fiber composite beam element with 2D integration (Fig.9). The slab is reinforced by longitudinal bars about 1% of its area. Supposing that the joint is located at the node (i) of a regular composite finite element, a virtual finite element representing the joint (i_1-i_2) is used. This element has no dimension and will change the stiffness of the finite element (i-j) at the node (i) considering new variations K_a, K_c and K_ϕ. The connection between the classical composite finite element and the one including the joint is shown in figure 10 with different degrees of freedom.

www.EngineeringEBooksPdf.com

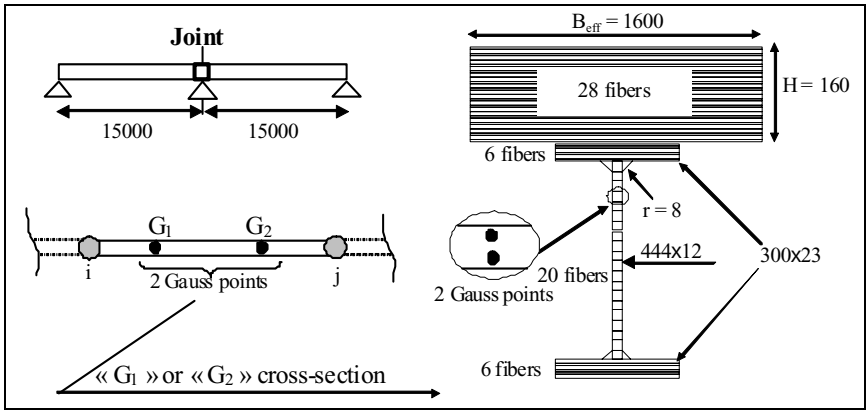


Figure 9: Fiber model computed in « Pontmixte ».

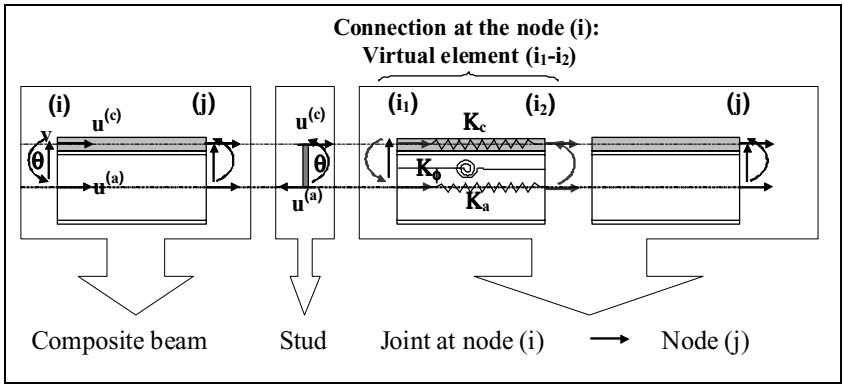


Figure 10: The joint F.E.

Figure 11 shows how the composite beam element could include the changes in the stiffness matrix to take into account the joint at the node (i) for example. Now, what values should be taken for K_a, K_c and K_ϕ during the iterative process?. For the beginning (iteration 0), we propose to take following classical values: $K_a = (EA)_a / L$, $K_c = (EA)_c / L$ and $K_\phi = (EI)_a / L$. It is noted that:

$(EA)_a$: product of young's modulus and area of the steel girder,
$(EA)_c$: product of young's modulus and area of the concrete slab,
$(EI)_a$: product of young's modulus and inertia of the steel girder.

For the iteration $I \geq 1$, the value of K_ϕ at the iteration (I) is obtained from the one at iteration (I-1) using the curve (M-ϕ) of the proposed model (Fig.8.b). It is pointed out that the rotation ϕ in the proposed formulae corresponds to the difference between θ_{i1} and θ_{i2} of the virtual finite element. In order to use simple formulae for K_a and K_c, the hypothesis done is:

$$\frac{K_\phi^{(I)}}{K_\phi^{(I-1)}} = \frac{K_a^{(I)}}{K_a^{(I-1)}} = \frac{K_c^{(I)}}{K_c^{(I-1)}} \qquad (1)$$

www.EngineeringEBooksPdf.com

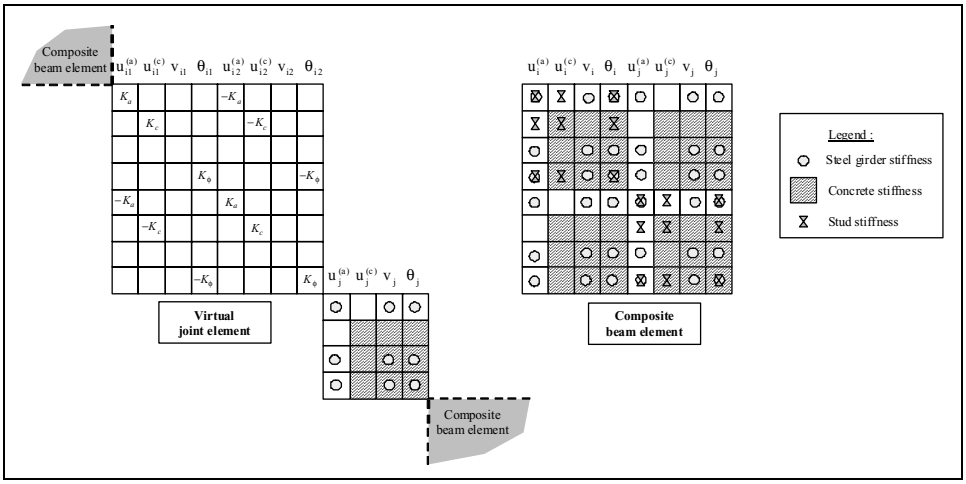


Figure 11: The stiffness matrix scheme.

4 THE RESULTS

The beam under investigation has 2 spans of 15m length and the mechanical characteristics of the materials are the same than those given on table 1. The slab is fully connected to the girder and the load is uniformly distributed all along the beam (Fig.12). The transverse beam is located on the intermediate support and the butt-plates are at 200mm on both sides of the axis of the support. The nodes concerned by the virtual joint elements are at these butt-plate cross-sections.

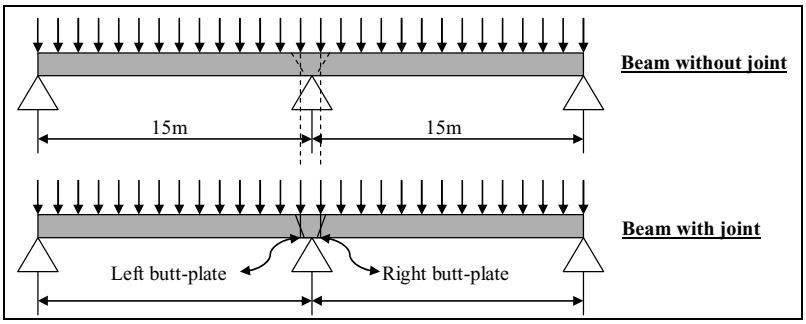


Figure 12: Beam under investigation – with and without joint.

The discontinuity of the continuous beam needs a correction because there are no studs on 400mm depth of the transverse beam. A previous design of the joint based on an analytical elastic method comparing a panel with or without joint leaded to consider twice number of longitudinal bars and studs on 15% length of span left and right the intermediate support [4]. It appears in figure 13, that this correction is over estimated, the beam without joint is less resistant than the one with joint. On the same figure, the comparison between the computed 3-D model and the numerical curves is satisfactory. In figure 14, the cross-section rotations are plotted all along the beam at the end step loading (arriving to 95%$M_{pl.Rd}$). The joint influence is not only local but it changes the rotations as well as the deflections (Fig.15) of all the other cross-sections along the beam and leads to a new equilibrium of the internal forces.

www.EngineeringEBooksPdf.com

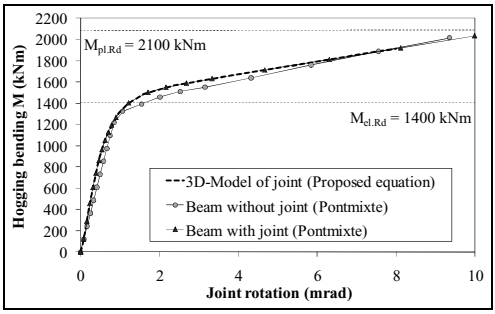


Figure 13: Influence of the joint on (M-ϕ) curve.

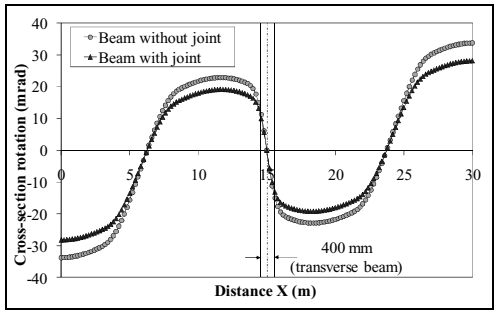


Figure 14: Influence of the joint on (θ-X) curve.

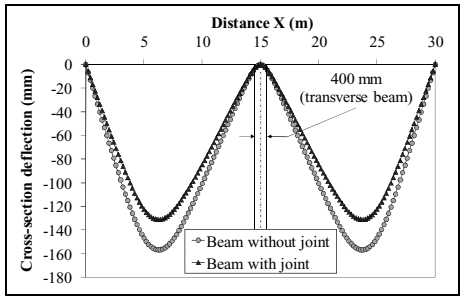


Figure 15: Influence of the joint on deflection curve.

5 CONCLUSION

This work shows that it is possible without computing difficulty to take into account beam-to-beam joints in the non linear calculation of a composite continuous beam at real scale. The additional reinforcing (bars and studs) considered to correct the discontinuity on the pear has a special importance; the proposed model should lead by numerical simulations to a design method more accuracy than the one used for this example. This work depends on many parameters such as the butt-plate thickness, the friction between the butt-plate and the concrete of the transverse beam and the connection degree that should be taken into account in future 3D model.

REFERENCES

[1] Shanmugam, N.E. and Wan Mohtar, W.H.M., "Experimental and finite element studies on tapered steel plate girders", *Proc. of the 3rd International Conference on Steel and Composite Structures (ICSCS07)*, Manchester, UK, pp. 165-170, 2007.

[2] Cast3M, *un code de calcul pour l'analyse de structures par la méthode des éléments finis (E.F) et la modélisation en mécanique des fluides*. CEA, Sarclay, 2003.

[3] Guezouli, S. & Yabuki, T.," "Pontmixte" a User Friendly Program for Continuous Beams of Composite Bridges", *Proc. of SDSS2006 International Colloquium on Stability and Ductility of Steel Structures*, D. Camotim, N. Silvestre and P.B. Dinis (eds.), IST Press, Lisbon, 853-860, 2006.

[4] CEN (European Committee for Standardisation), prEN (2003) – Part 2. *Design of composite steel and concrete structures – Rules for bridges*. Stage 34 draft revised, Brussels, August 2003.

www.EngineeringEBooksPdf.com

SDSS'Rio 2010 STABILITY AND DUCTILITY OF STEEL STRUCTURES
E. Batista, P. Vellasco, L. de Lima (Eds.)
Rio de Janeiro, Brazil, September 8 - 10, 2010

RESISTANCE OF LASER MADE T RHS JOINTS UNDER COMPRESSION LOAD

Jerzy K. Szlendak*

*Department of Civil Engineering, Bialystok Technical University
ul. Wiejska 45E, 15-351 Bialystok, Poland
e-mail: szlendak@stal-projekt.com.pl

Keywords: static behaviour, T RHS branch-chord lock laser made joints, full scale tests, preliminary design model, axial loaded joints resistance.

Abstract. *Research on simple laser made T RHS joints is presented. Up to now, it is no experimental evidence of such joint behaviour. Natural scale tests of three connections are described. Dimension of rectangular chord section was 100 x 100 x 3 mm. Geometry and material properties of the tested connections are given. The problem of tolerances in preparing the branch-chord lock is undertaken. For each specimen axial-deflection curves are presented. Yield line local push mechanism on front wall chord section is used to the theoretical estimation of the failure load. However, because the slenderness of the chord wall is high the membrane action of the chord loaded wall and buckling of the side walls of chord significantly influence the behaviour and resistance of joints. Preliminary design model for calculation and a prediction of joints resistance is proposed. The comparison between theoretical and experimental results is shown. Finally, some conclusions are given.*

1 INTRODUCTION

The laser technology, figure 1, is used to create such contact area between the chord and branch RHS member which could transfer the joint local stresses only by squash and shear. The socket has been developed in the shape, figure 2, which make possible transfer not only normal but also moment

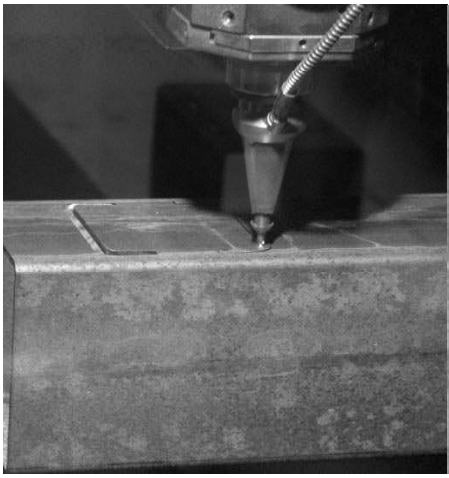


Figure 1: Laser cut of chord lock



Figure 2: Laser cut of chord and branch locks & elements

www.EngineeringEBooksPdf.com

load from branch to the chord, [1]. Any typical welds are used what is a new idea for such type plug & play type joints. In the paper first three experimental results of T RHS joints resistance are presented. The design formula from other research study [2] and EC-3 [3] for RHS T welded joints is tested to be used to predict the theoretical resistance of laser made non-welded joints.

2 TEST RIG, TEST SPECIMENS AND MEASUREMENTS

Test rig is shown in figure 3 and 4. Three T RHS laser made joints in natural scale were tested here up to failure. In several steps the branch was loaded up to the reach the failure load. After each loading step, the joint was unloaded to measure the permanent deformations of the tested specimen. Typical type of joint failure was the inelastic deformation of the loaded flange, figure 5, and finally the local shear of the connecting "gusset" plate, figure 6. In Table 1 the geometry of the specimens, mechanical properties, and failure load are given. The mechanical properties are the medium value from two tension coupons tests. LVDT gauges were used to measure the displacements, see figure 3.

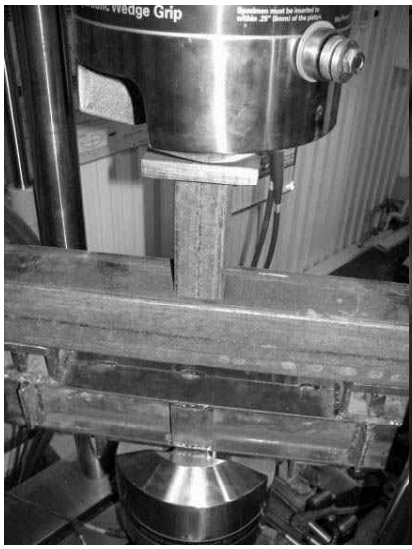


Figure 3: View of specimen in the test rig

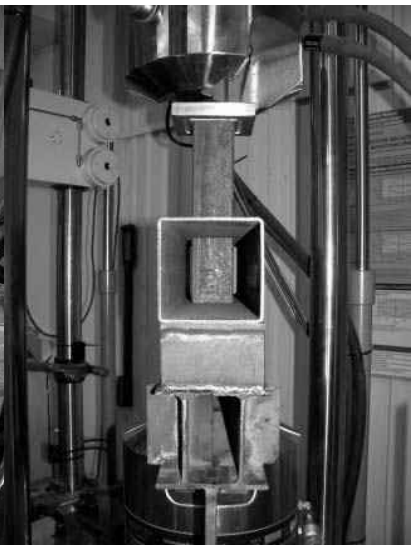


Figure 4: Section of specimen in the test rig

Table 1: Geometrical dimensions and mechanical properties.

Geometrical dimensions					Yield stress	Parameters			Ultimate load
No specimen	RHS chord boxho mm	RHS branch bnxhn mm	chord wall thick t_0 mm	branch wall thick t_n mm	chord f_{y0} MPa	β	η	λ_0	Experimental failure load N_{exp} kN
WTL1	100x100	40x40	3,0	3,0	334	0,40	0,40	33,3	21,2
WTL2	100x100	60x60	3,0	3,0	343	0,60	0,60	33,3	31,5
WTL3	100x100	80x80	3,0	3,0	335	0,80	0,80	33,3	35,3

www.EngineeringEBooksPdf.com



Figure 5: View of chord face failure WTL1

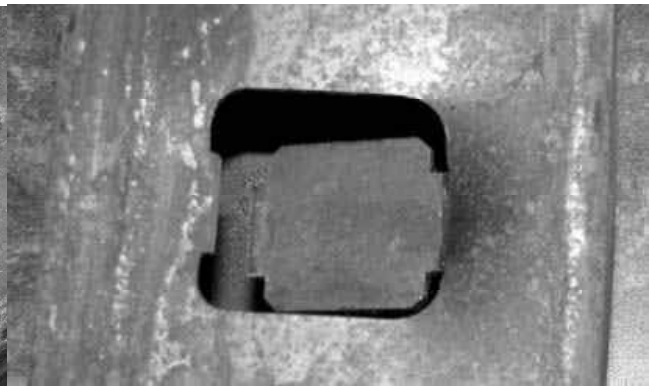


Figure 6: View of chord face failure WTL1 (shear failure)

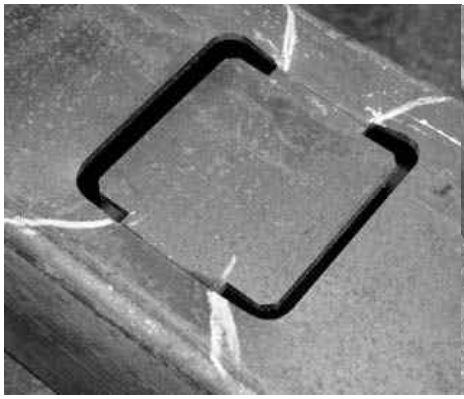


Figure 7: View of chord face failure WTL2

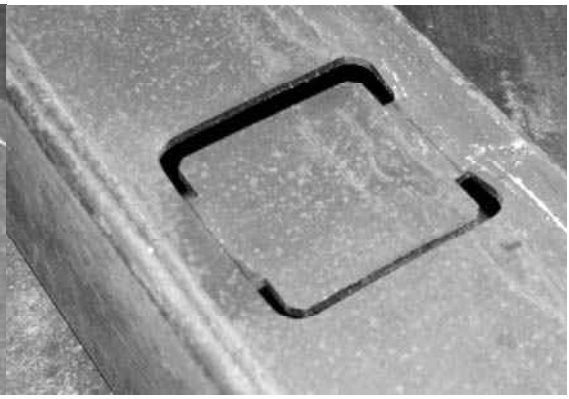


Figure 8: View of chord face failure WTL2



Figure 9: View of chord webs failure WTL3



Figure 10: View of chord face and webs failure WTL3

www.EngineeringEBooksPdf.com



Figure 11: Longitudinal section of WTL1

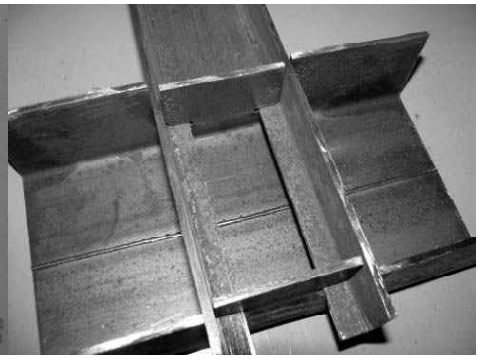


Figure 12: Longitudinal section of WTL1

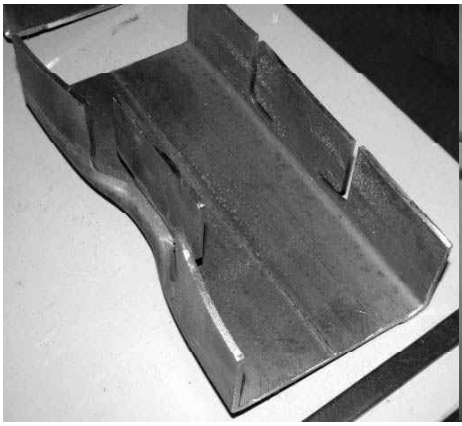


Figure 13: Longitudinal section of WTL3 (horizontal)



Figure 14: Longitudinal section of WTL3 (vertical)



Figure 15: Section of WTL2

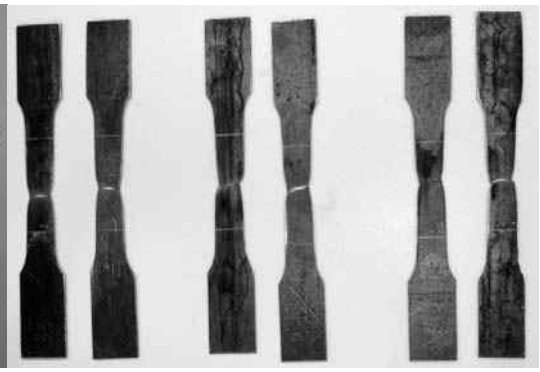


Figure 16: Tensile samples for tests of material properties

Registrations of the results were made permanently during the full loading and unloading process, up to failure. After each loading step the joint was unloaded to measure the permanent deformations.

www.EngineeringEBooksPdf.com

3 THEORETICAL ESTIMATION OF THE JOINTS RESISTANCE

For prediction the theoretical strength of joints, from the observations which were done during experimental tests, the following assumptions are adopted:

1. Yield line mechanism, which is created on the face wall of chord, is decisive. Erasing inelastic deformations leads finally to situation that flange or flange and webs of chord failed.
2. Inner zone the joint is almost absolutely stiff, figure 6, 8, 11, 14. So, for the simplicity could be assumed that this part of joint is compact.
3. Local shear of the connecting "gusset" plates, figure 6, is analysed separately.

Eurocode 3, gives the formula to predict the welded T RHS joint resistance:

$$N_{1,Rd} = \frac{f_{y0} t_o^{\,2}}{(1-\beta)}\left(2\beta + 4\sqrt{1-\beta}\right) \qquad (1)$$

In Table 2 the theoretical predictions (1) and the experimental strength of three tested joints are presented. Typical mode of failure was very large deflections of loaded face of chord section, figures 11, 12, 13 and 15. In case the WTL3 joint ($\beta = 0{,}8$) the significant webs failure has been observed, where membrane action increase the strength of the joint, see figure 19.

Table 2: Comparison between theoretical and experimental strength of joints.

No specimen	Theoretical prediction (1) $N_{1,Rd}$ kN	Experimental strength N_{exp} kN	N_{exp} / $N_{1,Rd}$	Mode of failure
WTL1	19,53	21,18	1,08	face wall deflection larger then $3t_0$ (9mm)
WTL2	28,78	31,49	1,09	face wall deflection larger then $3t_0$ (9mm)
WTL3	51,09	35,31 (51,67)	0,69 (1,01)	face wall deflection larger then $3t_0$ (9mm) and webs failure (maximum load)

4 COMPARISONS OF EXPERIMENTAL RESULTS AND THEORETICAL ESTIMATIONS

In figures 17, 18 and 19 the axial force - deflection curves (N - δ) for each tested joints are presented. They are shown not only loading but also unloading curves registered by LVDT gauges. Unloading curves gives possibility to obtain the end of its elastic behaviour and show how arising the joints permanent deformations. Joint failure limit deformation was adopted from welded joint and it has been assumed $3t_0$. Theoretical prediction of joints resistance obtained from formula (1) and shear failure load for the connecting "gusset" plates, figure 6, are also given. As could be observed theoretical prediction (1) rather good estimate the real joint strength for the joints with parameter $\beta = 0{,}4$ and $\beta = 0{,}6$. However when $\beta = 0{,}8$ this prediction is too optimistic compared with joint failure limit deformation $3t_0$. Permanent deformations of loaded face of chord arise very quickly on the loading path;

www.EngineeringEBooksPdf.com

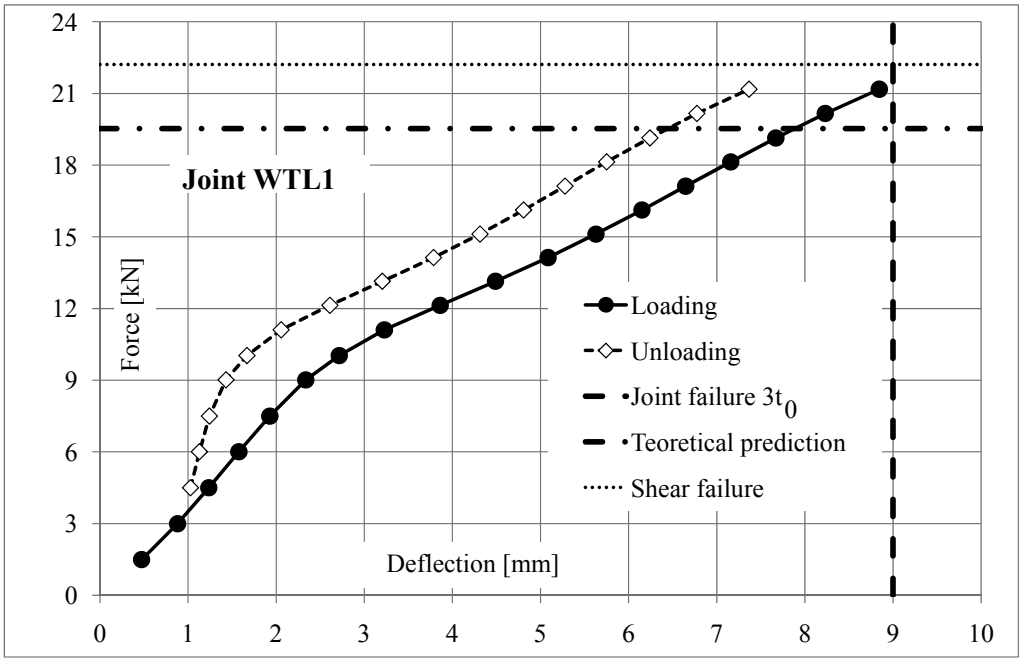


Figure 17: Axial force-deflection diagram for WTL1 joint ($\beta = 0,4$)

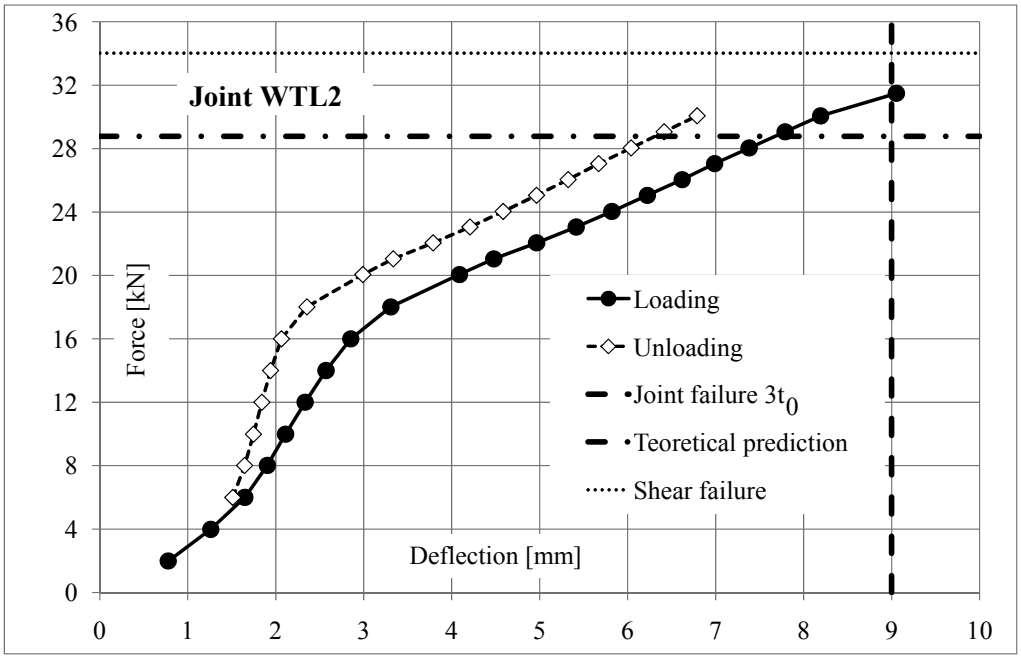


Figure 18: Axial force-deflection diagram for WTL2 joint ($\beta = 0,6$)

www.EngineeringEBooksPdf.com

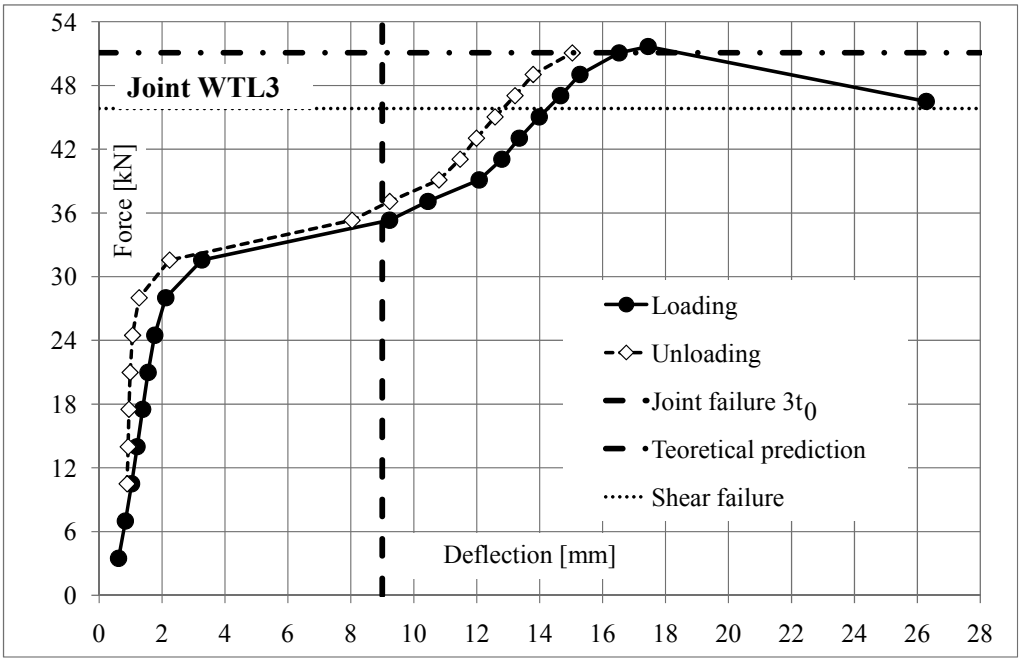


Figure 19: Axial force-deflection diagram for WTL3 joint ($\beta = 0{,}8$)

see figures 17, 18 and 19. So, the reduction coefficient for the theoretical prediction (1) ought to be adopted if next experimental data confirms that observation.

5 CONCLUSION

In order to keep a competitive position the costs of manufacturing steel connections need to be reduced as much as possible. Author starts to research one of the types of "plug and play" joints. Laser has been used to cut the proper locks. From the first experiments, which results are presented in this paper the preliminary conclusions could be given:

1. For the joints where the branch is smaller than the chord member ($\beta \leq 0{,}8$) the design formula use in Eurocode 3 [3] for the welded joints could be used to T RHS branch-chord lock laser made joints
2. Shape and dimensions of the lock should be such design then it to be at least as strong as the face plate of chord.
3. For the presented lock shear of face plate has not be decisive.
4. Permanent deformations of the loaded face of chord arise very quick

Further experimental and theoretical studies are going on.

ACKNOWLEDGEMENTS

The author gratefully acknowledge the financial support of this research by *The National Centre for Research and Development (NCBiR)* research project N R04 0008 06 , *PR/WBiIŚ/1/09/NCBR*, Poland. Special thanks Mr P. Oponowicz (PhD student) for his co-operation.

www.EngineeringEBooksPdf.com

REFERENCES

[1] Szlendak J.K., “RHS trusses and frames completed without welding with branch-chord clock laser made joints”, *The National Centre for Research and Development (NCBiR)* research project N R04 0008 06, *PR/WBiIŚ/1/09/NCBR*, Poland, 2009.

[2] Szlendak J.K., “Design models of welded beam-column joints in steel structures with rectangular hollow sections”. DSc thesis, Bialystok Technical University Press, Bialystok, Poland, 2007 (in Polish).

[3] EN 1993-1-8:2006, Eurocode 3: Design of Steel Structures *Part 1-8: Design of Joints*, 2006.

www.EngineeringEBooksPdf.com

SDSS'Rio 2010 STABILITY AND DUCTILITY OF STEEL STRUCTURES
E. Batista, P. Vellasco, L. de Lima (Eds.)
Rio de Janeiro, Brazil, September 8 - 10, 2010

COLD-FORMED STEEL AND CONCRETE COMPOSITE BEAMS: STUDY OF BEAM-TO-COLUMN CONNECTION AND REGION OF HOGGING BENDING

Mairal, R.* and Malite, M.*

*School of Engineering of São Carlos, University of São Paulo
E-mails: ramairal@hotmail.com.br, mamalite@sc.usp.br

Keywords: Composite Beams, Composite Connections, Cold-formed.

Abstract. *In Brazil, the cold-formed steel structure has been widely used justified by the large availability of steel sheets in the market (thin sheets) and the search for more competitive structural solutions. Thus as steel and concrete composite structures applied in small constructions, the traditional hot-rolled is replaced by cold-formed members in beams and columns. Even though the composite beams system is known in the hot-rolled and welded shapes field, the structural behavior of the cold-formed steel still needs more accurate investigation. A theoretical and experimental study about cold-formed steel and concrete composite beams was developed, focusing on the beam-to-column connection and the structural behavior on the region of hogging bending. For the experimental program two beam-column connections were analyzed to obtain the moment-rotation curves, the failure modes and check the application of the existent theoretical models.*

1 INTRODUCTION

It is denominated a composite steel-concrete system the one that has a steel (hot-rolled, welded or cold-formed) which works together with the concrete, forming a composed beam, composite column, composite slab or composite connections. The use of composite structures is much diffused internationally, in Brazil this type of structure is gaining space and popularity. Although the use of composite systems has always been restricted to hot-rolled and welded shapes steel, there is a tendency to the use of composite systems with cold-formed steel mainly in small buildings (up to 5 floors).

The behavior of the composite beams in cold-formed steel has particularities in regard to the composite in hot-rolled and welded shapes some researches on the structural behavior of the composite beams in the region at the positive moment were done, though a few studies talk about the region of hogging bending and the connections (beam-to-column connection or beam-to-beam). Both subjects are strongly jointed, since the continuance effect in the supports depends on the structural behavior of beam-to-beam or beam-to-column connection.

This paper aimed to evaluate the behavior of a beam-to-column connection, using double U lipped channels cold-formed steel to compose the beams and using seat angle and web angles to the connections, for the column it was used a HP hot-rolled steel. It is a type of connection analyzed by Leon et al. (1996) [1], but replacing the hot-rolled steel by cold-formed steel.

www.EngineeringEBooksPdf.com

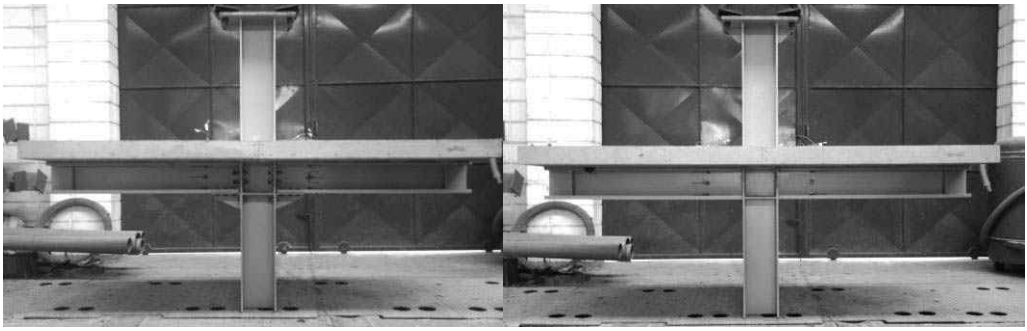
2 CLASSIFICATION OF THE COMPOSITE CONNECTIONS

Leon et al. (1996) [1] nominate the composite connections as an especial case of PR type connection as PR-CC (*partially restrained composite connection*), being made by a simple steel connection or semi-rigid, having its stiffness and resistance moment substantially increased. Considering the hogging bending, the reinforcement steel in the concrete slab to form the top portion of the moment resisting mechanism while the bottom portion is constituted in general by a steel seat angle and steel web angle providing the shear resistance.

3 EXPERIMENTAL PROGRAM

3.1 Models Description

In the experimental program two composite connection were analyzed (Figure 1): model 1 with steel seat angle and web angle to connect the beam to the column, which is detailed in Figure 2 and Figure 3, and model 2 with the same dimensions as model 1, but with a beam welded directly to the column. This model served as a reference since there is total continuance from the connection beam. Both models have a concrete slab (thickness = 100 mm; wide = 850 mm). The detailing of the main reinforcement slab is presented in Figure 4.



a) model 1 b) model 2

Figure 1 – General view of the models

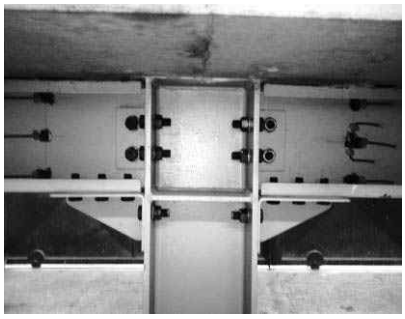


Figure 2 – Connection of the model 1

The channel shear connectors were made of a cold-formed steel (U 75x40x3.00) with 130 mm of length welded to the beam, and in an enough amount so there was complete interaction between the beam and the slab.

www.EngineeringEBooksPdf.com

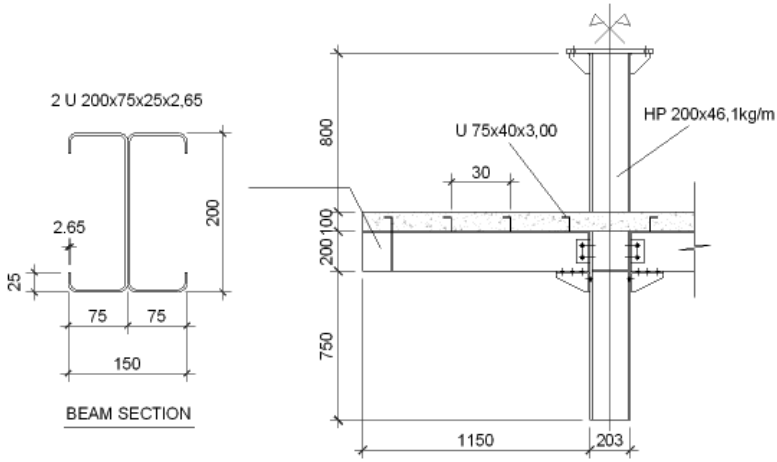


Figure 3 – General drawing of model 1

The beam was making in a way that all the elements had their effective width equal to its own width (compact section).

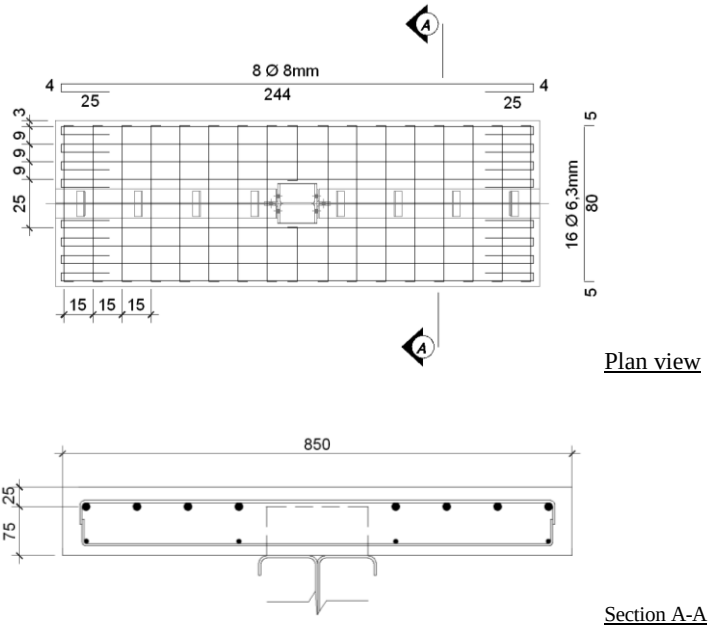


Figure 4 – Detailing of the reinforcement of the slab

3.2 Instrumentation and loading application

The instrumentation used is indicated in Figure 5, and was part of the strain-gages, displacement transducers in the beams and on the column to evaluate the relative rotation as well as the inclinometers put on the top part of the slab.

www.EngineeringEBooksPdf.com

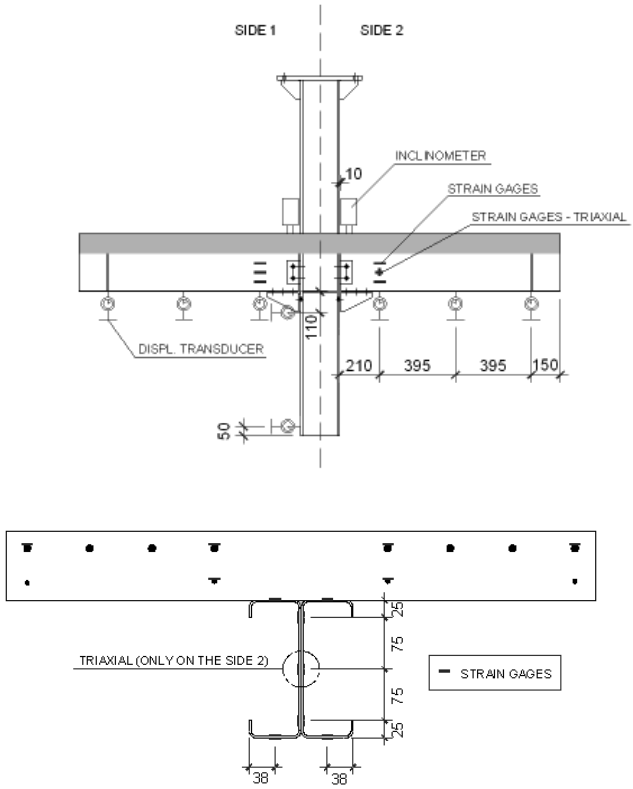


Figure 5 – Typical instrumentation of the models

The force was applied positioning a frame reaction on the model's extremities, to 1000 mm from the column face, and a third frame in the center of the model with hydraulic actuator, which applied an upward generating that way other two downward vertical forces on the extremities and consequently a hogging bending (negative moment) on the beams (see Figure 6).

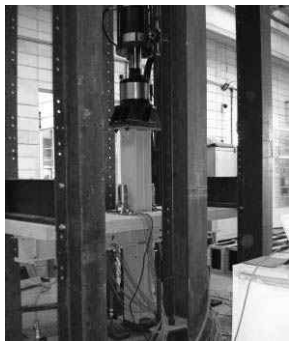


Figure 6 – Force application device

www.EngineeringEBooksPdf.com

4 EXPERIMENTAL RESULTS

The values obtained from mechanical properties of the beams and reinforcement slab are presented in table 1.

Table 1: Mechanical Properties of the steel

Steel	f_y (MPa)	f_u (MPa)	Elongation (%)
Beams	275	385	36
Reinforcement	613	718	-

The maximum force applied by the hydraulic actuator (F_{max}) and corresponding hogging bending ultimate strength (M_{max}) for each model are presented in table 2.

Table 2: Values of F_{max} and M_{max}

Model	F_{max} (kN)	M_{max} (kN.cm)
model 1	133.5	6,675
model 2	132.1	6,605

The average of the strain obtained by the strain-gages for 25%, 50% and 90% of F_{max} is presented in Figure 7. For model 2 these values were deleted in this paper but they can be found in Mairal & Malite (2010) [2]

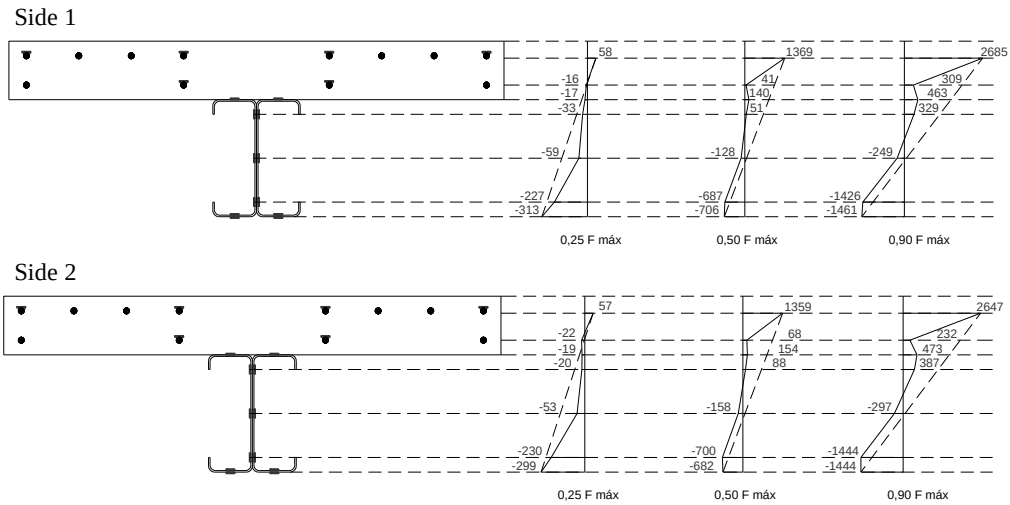
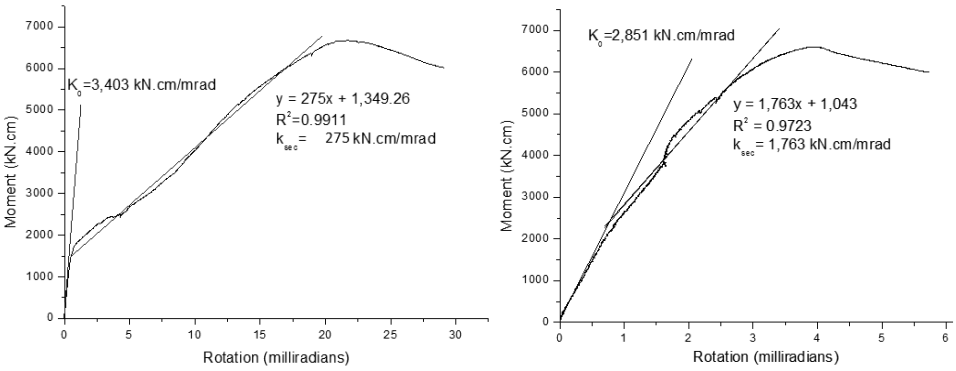


Figure 7 – Strains in model 1 (x 10^6) – average values

www.EngineeringEBooksPdf.com

Figure 8 shows the Moment-Rotation curve (M-θ) for models 1 and 2.

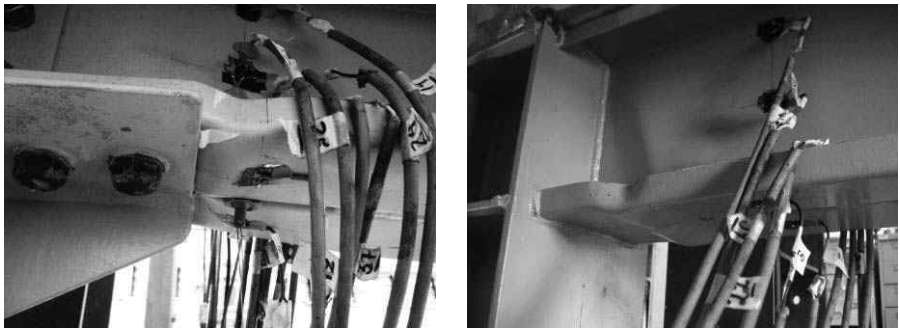


a) model 1 b) model 2

Figure 8 – Average M-θ curve

The beginning of the cracking process for model 1 occurred for an approximated moment of 1,750 kN.cm now for model 2 this process started at 500 kN.cm.

In both models, the failure mode was characterized by the formation of plastic mechanism on the beams closed to the connection (see Figure 9), simultaneously to the beginning of the yield stress of some slab reinforcements.



a) model 1 b) model 2

Figure 9 – Mechanism of failure observed in the models

5 ANALYTICAL RESULTS

The composite connection was estimated according to ABNT NBR 8800 (2008) [3] (method of components) and according to Leon et al. (1996) [1]. The hogging bending ultimate strength of the composite beam was calculated admitting the steel section and concrete in the cross section are fully plastic (plastic stress distribution method), procedure adopted for hot-rolled and welded steel shapes with compact section, and also admitting a linear distribution of strains across the section (elastic method) recommended by ABNT NBR 14762 (2009) [4].

The value of the shear connector stiffness used in the method of components was obtained through push-out tests accomplished by David (2007) [5].

www.EngineeringEBooksPdf.com

5.1 – Composite Beam (negative moment)

The value of the hogging bending ultimate strength according to the plastic method was $M_{R,pl.}$ = 7,380 kN.cm and for the strength compatibility method was $M_{R,el.}$ = 4,939 kN.cm.

5.2 – Composite Connection

By the method of components (NBR 8800) it was obtained an secant stiffness k_{sec} = 432 kN.cm/mrad, a hogging bending ultimate strength of the connection M_{max} = 6,654 kN.cm and the rotation capacity θ_u = 24 mrad. According to Leon et al. (1996) an initial stiffness k_i = 3,391 kN.cm/mrad, secant stiffness of k_{sec} = 2,196 kN.cm/mrad, hogging bending ultimate strength of M_{max} = 8,750 kN.cm and the rotation capacity of the connection θ_u = 23.6 mrad. The graphic moment-rotation according to Leon et al. is presented in Figure 10.

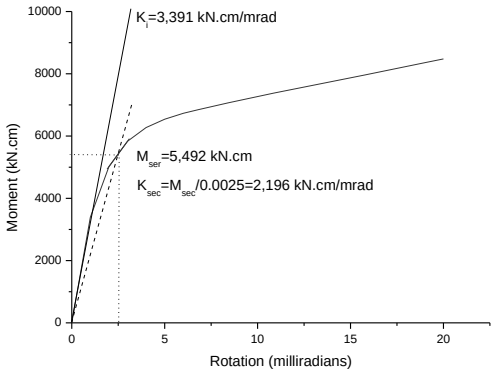


Figure 10 –M-θ curve obtained according to Leon et al. (1996)

6 ANALYSIS OF RESULTS

For the plastic method the value of M_{max} resisted by the composite beam (hogging bending) was 9% superior to the M_{max} experimentally obtained by model 1, and by the strength compatibility method was 26% inferior.

Figure 11 presents moment-rotation curve from models 1 and 2, and Leon et al. (1996).

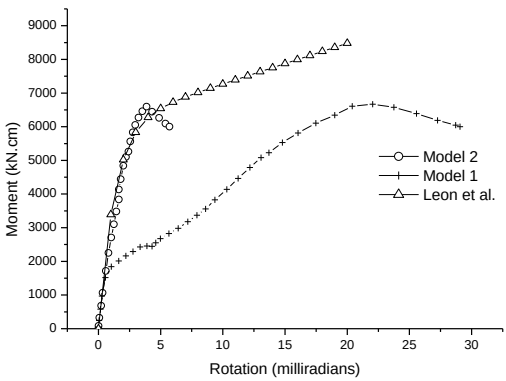


Figure 11 – Comparison of the M-θ Curves (model 1, model 2 and Leon et al.)

www.EngineeringEBooksPdf.com

Table 3 presents the comparison of the initial stiffness (k_i), secant stiffness (k_{sec}), ultimate strength (M_{max}) and rotation capacity (θ_u) from theoretical and experimental results for model 1.

Table 3: Theoretical and experimental results for model 1

Model	K_i (kN.cm/mrad)	K_{sec} (kN.cm/mrad)	M_{max} (kN.cm)	θ_u (mrad)
Theoretical - NBR 8800 (method of components)	-	432	6,654	24
Theoretical – Leon et al.	3,391	2,197	8,750	23.6
Experimental - Model 1	3,403	275	6,675*	21.5

* Failure mode in the composite beam

7 CONCLUSION

In the case of composite beam the ultimate strength (M_{max}) experimentally obtained presented an intermediate value to the ones obtained by the plastic and elastic method, having its value closer to the plastic method as can be seen in item 5.1. Seeing that the failure mechanism occurred in the beam thus it was not possible to evaluate experimentally the ultimate strength of the connection and can be classified as fully strength connection (FS) when they are capable of transferring the full moment capacity of the beam. From a point of view on the stiffness the connection might be classified as semi-rigid (PR – Partially Restrained).

The moment-rotation curve of model 1 presented an abrupt change of stiffness after the beginning of the process of cracking of the concrete slab, presenting a behavior different of model 2. The rotation capacity of model 1 was about 6 times superior to model 2 as can be seen in Figure 10, showing more ductility of this type of connection when compared to the rigid connection (model 2).

The method of the components in this case estimate relative well the secant stiffness and rotation capacity presenting a much closer value than the experimental one, although have not taken into account the stiffness of the web angle. By Leon et al. procedure it is well estimated the initial stiffness and the rotation capacity, but the value of the secant stiffness is much larger than the experimental one.

REFERENCES

[1] Leon, R.T.; Hoffman, J.J.; Staeger, T., *"Partially restrained composite connections"* AISC Steel Design Guide Series, 8. Chicago, USA, 1996.

[2] Mairal, R.; Malite, M., "Cold-formed steel and concrete composite beams: study of beam-to-column connection and region of hogging bending" (in Portuguese) - School of Engineering of Sao Carlos – University of Sao Paulo – Final Report, 2010.

[3] Brazilian Code, *"Design of steel and composite structures for buildings"* (in Portuguese), ABNT NBR 8800, 2008.

[4] Brazilian Code, *"Design of cold-formed steel structures"* (in Portuguese), ABNT NBR 14762 – Draft 2009.

[5] David, D. L.; Malite, M. *"Theoretical and experimental analysis of shear connectors and composite beams constituted of cold-formed steel beams and floor system with lattice girder beams*" Doctoral thesis (in Portuguese), School of Engineering of Sao Carlos – University of Sao Paulo, 2007.

www.EngineeringEBooksPdf.com

SDSS'Rio 2010 STABILITY AND DUCTILITY OF STEEL STRUCTURES
E. Batista, P. Vellasco, L. de Lima (Eds.)
Rio de Janeiro, Brazil, September 8 - 10, 2010

SHEAR BOLTED CONNECTIONS: NUMERICAL MODEL FOR A DUCTILE COMPONENT, THE PLATE-BOLT IN BEARING

J. Henriques*, L. Ly, J.-P. Jaspart** and L. Simões da Silva***

* ISISE, Departamento de Engenharia Civil, Faculdade Ciências e Tecnologia, Universidade de Coimbra
e-mails: jagh@dec.uc.pt, luisss@dec.uc.pt

** MS^{2}F, ArGEnCo, Faculté de Sciences Appliquées, Université de Liège
e-mail: dplam.ly@ulg.ac.be, Jean-Pierre.Jaspart@ulg.ac.be

Keywords: Shear, Connection, Component, Bearing, Plastic.

Abstract. *In order to achieve a full plastic distribution of forces in a shear bolted connection, ductility is required to the steel plate and to the plate-bolt contact zone in the firstly loaded bolt rows. Knowing that bolts present a brittle behavior, deformation capacity has to be obtained from ductile components as the plate-bolt in bearing. In the present paper a numerical model is proposed to evaluate the plate-bolt in bearing component. The main objective is not only to achieve it elastically but to obtain a good approximation of the post-elastic response. The proposed model has been successfully validated by experimental tests on shear bolted connections performed at the Delft University of Technology and at the University of Ljubljana. The EC3 Part 1.8 [1] approach, to evaluate resistance and initial stiffness of the plate–bolt in bearing component, is included in the comparison and discussion of results.*

1 INTRODUCTION

In shear bolted connections forces are transferred from one plate to another (others) by plate-to-bolt contact. Neglecting the small friction developed between plates and the negligible bending of the bolt, four sources of resistance and deformation modes should be considered: bearing of the plate and/or bolt; shear in the plates; tension in the plates; shear in the bolt shanks. In these types of connections, the load to be transferred between the plates is distributed non-uniformly amongst the bolt-rows (Figure 1). In [2], Ju *et al* showed that in the nonlinear range the maximum load achieved by the connection is almost linearly proportional to the number of bolts in the connection. According to [1], a full plastic distribution of forces can be assumed as long as the connection length is limited. Pietrapetrosa *el al* [3] studied fitted bolted connections and showed that, inside the limits given by the code and by practical guidance, sufficient ductility to achieve a full plastic distribution of internal forces is available. On the other hand, Wald *et al* [4] verified that if imperfections (misalignment of bolts) are considered, failure could be first attained in the extreme bolts and therefore a full plastic resistance was not reached. The presence of imperfections requires therefore higher deformation capacity from the connection components. Knowing that the bolt has a brittle behavior, ductility has to be obtained from the plate-bolt in bearing component in order to achieve a full plastic resistance, as observed in [5]

In EC3 Part 1.8 [1] the bearing resistance and the bearing stiffness may be determined using the proposed design functions. However, these functions are mainly directed to mild steel and to connections with normal round holes. So, in this paper, the calibration of a numerical model to study the plate-bolt in bearing component, which can be later used to extend the actual knowledge to new common practices (connections with High Strength Steel, oversized or slotted holes, etc), is presented. Tests made on shear bolted connections at the University of Ljubljana and at the Delft University of Technology are used to

www.EngineeringEBooksPdf.com

validate the numerical model. In the absence of experimental work which addressed only the phenomenon of bearing, the validation of the numerical model is done using experimental work on bolted shear connections. The use of this type of tests influences the numerical model as bearing is not isolated, so that other phenomena have to be taken into account.

The 3D finite element model is compared with the experiments in terms of stiffness, strength and ductility allowing evaluating and commenting the reliability of the developed model. Additionally, a comparison with EC3 Part 1.8 [1] recommendations is presented.

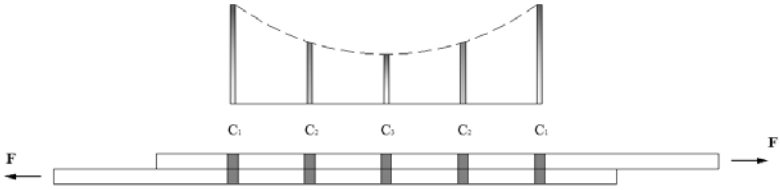


Figure 1 – Elastic distribution of forces in shear bolted connections.

2 CODE APPROACH

The plate-bolt in bearing is a complex component as its behavior is influenced by phenomena such as: shear forces developed in the plate, net section deformability, contact problems (bolt/plate), friction and confinement between plates. So, many different parameters as bolt and hole diameter (d and d_0), plate thickness (t), edge and end distances (e_2 and e_1), spacing (p_1 and p_2), bolt and plate material (grade) should be taken into account. Using reduction factors, the design bearing resistance defined in EC3 Part 1.8 [1] considers all the referred geometrical and material parameters and is expressed as:

$$F_{b,Rd} = \frac{\alpha_b k_1 f_u dt}{\gamma_{M2}} \tag{1}$$

where: the reduction factors α_b and k_1 introduce the additional influence of geometric and material properties, as defined in EC3 Part 1.8 [1].

The initial stiffness for the plate-bolt in bearing component may be obtained from EC3 Part 1.8 [1] stiffness coefficient.

$$S_{p,b} = 12 k_b k_t d f_u \tag{2}$$

where: the factors k_b and k_t take into account the geometrical properties as expressed in EC3 Part 1.8 [1].

The ultimate deformation of plate/bolt in bearing is based on the mechanical properties of mild steel; an expression has been derived from experimental tests by Jaspart [6]. No recommendation is found in the EC3 Part 1.8 [1].

$$\delta_{u,p} = 11 \frac{F_{b,Rd}}{S_{p,b}} \tag{3}$$

3 EXPERIMENTAL DATA

In the Delft University of Technology [8] and in the University of Ljubljana [9], shear bolted connections, with one and two bolts, made of high strength steel (S690) were tested. In the present paper only one bolt joints are used for numerical validation. Figure 2 illustrates the specimens general configuration. Table 1 and Table 2 present the relevant data of the used specimens.

www.EngineeringEBooksPdf.com

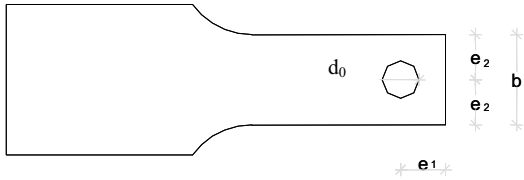


Figure 2 – Specimens configuration.

Table 1 – Data for the specimens tested at Delft University.

Test ID	Plate							Bolt		
	e_1/d_0	e_2/d_0	b [mm]	t [mm]	A_{gross} [mm]	A_{net} [mm]	Class	d [mm]	d_0 [mm]	Class
A1210	1,2	1,0	52	10	520	260	S690	24	26	10.9
A1212	1,2	1,2	62,4	10	624	364	S690	24	26	10.9
A1215	1,2	1,5	78	10	780	520	S690	24	26	10.9
A2020	2,0	2,0	104	10	1040	780	S690	24	26	10.9

Table 2 – Data of the specimens tested at Ljubljana University.

Test ID	Plate							Bolt		
	e_1/d_0	e_2/d_0	b [mm]	t [mm]	A_{gross} [mm]	A_{net} [mm]	Class	d [mm]	d_0 [mm]	Class
B110	1,2	1,5	90	10	900	600	S690	27	30	10.9
B113	2,5	1,5	90	10	900	600	S690	27	30	10.9
B117	1,5	1,5	90	10	900	600	S690	27	30	10.9

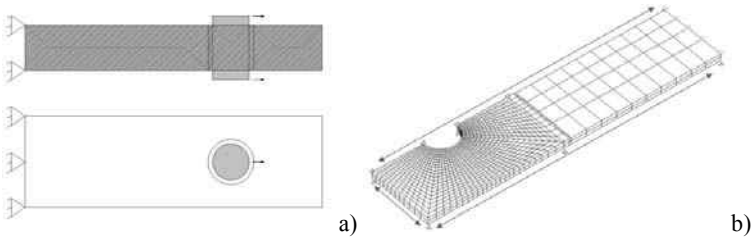
4 NUMERICAL MODEL

4.1 General description

The numerical tool used is LAGAMINE [7] which is a software developed at ArGenCo Department at the University of Liège. The basic model to study the bearing component consists in a plate with a hole which is pushed in the longitudinal direction by a rigid element (bolt). The plate is fixed in the opposite end direction. Figure 3-a) shows an illustration of the idealized basic model. Because in the experiments double overlap bolted connections were tested, numerical results had to be extrapolated for comparison. Profiting from the symmetry of the problem, only half of the width and of the thickness has been modeled and additional boundary conditions are considered accordingly. Because of the concentration of stresses expected around the hole, especially in the bearing zone, the mesh refinement is higher in this region, as illustrated in Figure 3-b).

The plate is modeled using the 3D volume elements (BLW3D) available in LAGAMINE [7]. This is a 8 node element with 1 Gauss integration point. For the bolt, two different modeling have been analyzed. Initially, the bolt has been modeled as a rigid element, no deformation being considered. Subsequently, a deformable bolt is assumed and the same volume elements and symmetry simplifications have been used. To model the contact, the plane elements (CIF3D), available for three-dimensional mechanical contact problems, have been used. The CFI3D is composed by 4 nodes and 4 Gauss integration points.

www.EngineeringEBooksPdf.com



a) b)

Figure 3 – Idealized model.

4.2 Constitutive law

In order to simulate ductility the usual characterization of the steel behavior has a limited field of application and therefore a more accurate characterization is required. The usual (nominal) stress-strain (σ_n-ε_n) curve is derived considering conservation of the cross-section which is reflected in non-negligible false stress when relevant plastic deformations begin. The standard procedure of uniaxial tension tests disregards the updating of the cross-section. Consequently, the true stress (σ_t) can be obtained applying a correction on the nominal value (F_i/A_0). Regarding the strain, logarithmic strain is known as the true strain (ε_t), and has been used here. Thus, the true stress and the true strain may be determined as follows.

$$\sigma_t = \frac{F_i}{A_0\left(\frac{1}{\sqrt{\left(1+\varepsilon_{n,x}^{p}\right)}} - \upsilon\varepsilon_{n,x}^{e}\right)^2} \tag{4}$$

$$\varepsilon_t = \ln\left(1+\varepsilon_n\right) \tag{5}$$

where: F_i is the force applied at each load step; A_0 is the initial cross-section; $\varepsilon^p_{n,x}$ and $\varepsilon^e_{n,x}$ are the nominal plastic and elastic strains in the longitudinal direction; υ is the Poisson's ratio.

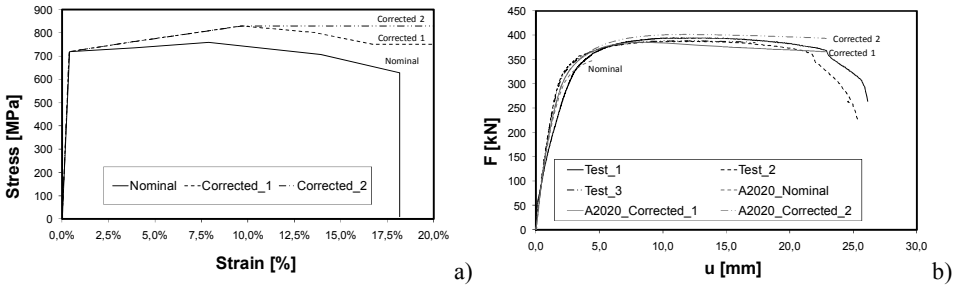
The presented formulae are only applicable up to the beginning of necking. With necking the element loses its uniformity and a local striction begins. Consequently, in the nominal stress-strain curve, a decrease of the stress is observed; however this loss of capacity is not real. With Kato (1990) [10] mathematical expression, the constitutive law can be corrected beyond necking. However, this requires a correct determination of the strain, which is often not possible with standard procedure of material characterization tests.

4.3 Calibration of the numerical model

- Constitutive law: In Figure 4-a) are represented the three analyzed models: nominal; correction neglecting the necking phenomenon; and correction considering a plateau. In Figure 4-b), using the test specimen A2020 the obtained results are presented. Clearly, the nominal stress-strain curve is insufficient to reproduce the complete force-deformation curve observed in the tests. As reported, the use of the true stress and the true train gives a good approximation to experimental results. The neglect of the necking effect can be seen through the cure A2020 corrected-1 with a small loss of load capacity, compared to experimental results; and then using correction with plateau after necking allows obtaining better results.
- Bolt model: Two types of bolt modeling have been analyzed: rigid bolt; and deformable bolt. Figure 5-a) compares the obtained force-deformation curves. No significant variation is noticed. Figure 5-b) illustrates the stress distribution for the points represented in the curve. Again, no relevant difference is noticed.

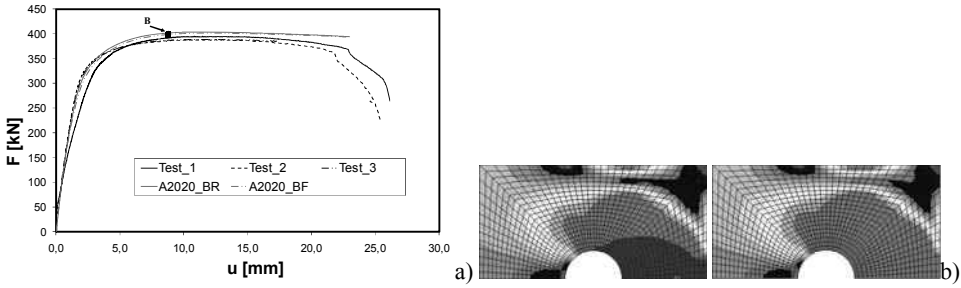
www.EngineeringEBooksPdf.com

- Confinement effect: Three models have been analyzed: i) confinement modeled by constraining, at the top surface, part of the nodes (adjacent to bolt-plate contact) in the transversal direction; ii) confinement considered by modeling part of the outer plate; iii) model without confinement. In Figure 6 the comparison with experimental results clearly shows that the confinement should be considered. Comparing the two types of confinement it can be verified that modeling the outer plate provides relatively higher resistance. However, this modeling implies the calibration of the friction coefficient.
- Friction coefficient: In all the models presented so far the usual value of 0.3 has been considered. In the literature, some values have been found for an approximate value of the friction coefficient to use for contact surfaces clamped by bolts; the values presented for contact surfaces steel on steel vary from 0.15 to 0.25. In Figure 7, the comparison between the different values taken for the friction coefficient is shown. The results show that the value of 0.20 fits better when compared to experimental results.



a) b)

Figure 4 – a) Different constitutive laws analyzed; b) Comparison of the constitutive laws influence.



a) b)

Figure 5 – a) Comparison between the rigid and the flexible bolt modeling; b) left – stress distribution for rigid bolt modeling and right – stress distribution for flexible bolt modeling for load step represented by point B.

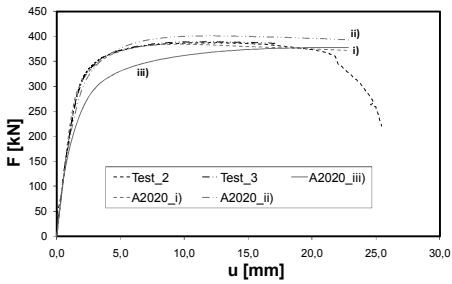


Figure 6 – Comparison of the models to study the confinement effect.

www.EngineeringEBooksPdf.com

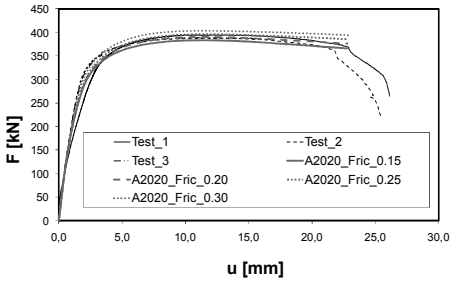


Figure 7 – Comparison of results using different friction coefficient.

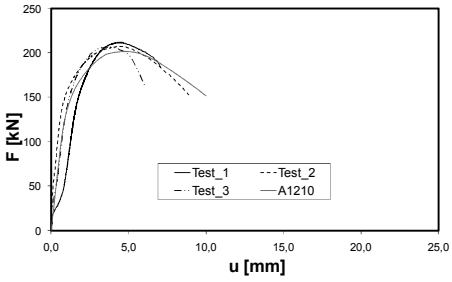
Finally, as a conclusion of the parametric study, the numerical calculations presented hereafter consider: constitutive law corrected and necking effect considered assuming a plateau; bolt is modeled as rigid; outer plate is modeled in order to introduce the confinement effect; and the friction coefficient has been taken equal to 0.2.

5 ANALYSIS OF RESULTS

5.1 Comparison with experimental tests

In this paper, only two specimens are used to compare results. Additional results may be found in [11]. Figure 8-a) presents the load-displacement curves for test specimen A1210 and the corresponding numerical model. This specimen failed by net-cross section failure. From the load displacement curves one can observe that the numerical model has a good accuracy. Initial stiffness and resistance are well approximated. In Figure 8-b) and c) the test failure pattern and final deformation of the numerical model may be compared. The numerical model achieved a correct deformation shape when compared with the experimental failure configuration.

Figure 9-a) presents the load displacement curves for test specimen B113 and for the corresponding numerical model. This specimen presented a bearing failure. In Figure 9-b) and c), test failure pattern and final deformation of the numerical model are illustrated. Good approximation is observed between the numerical calculation and the experimental tests.



a)



b)



c)

Figure 8 – Comparison of results for A1210 specimen: a) load-displacement curve; b) test failure configuration; c) numerical model final deformed configuration.

www.EngineeringEBooksPdf.com

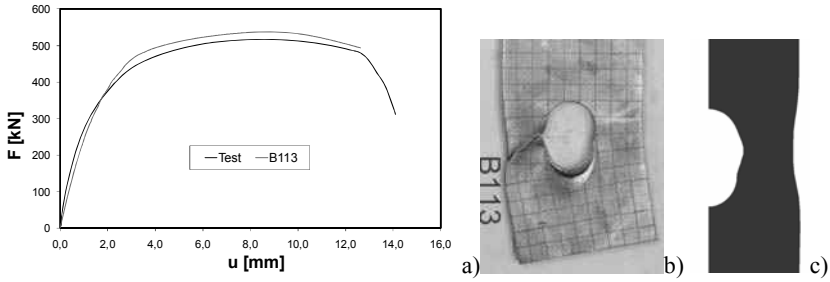


Figure 9 – Comparison of results for B113 specimen: a) load-displacement curve; b) test failure configuration; c) numerical model final configuration.

5.2 Comparison with code approach

For comparison, specimens A1212 and A1215 are used. More results may be found in [11]. Results are presented in Figure 10 and Figure 11. For comparison of resistance and initial stiffness, the used numerical calculations correspond to the pure bearing behavior of the tested plate, no extrapolation is therefore required and no confinement was considered. In order to compare the ultimate deformation using equation (3) with experimental results, an extrapolation to double overlap connections is done.

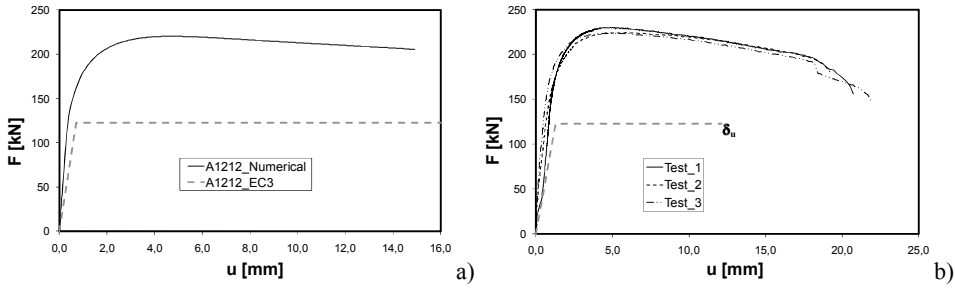


Figure 10 – Comparison of results using A1212 specimen: a) numerical model vs EC3 Part 1.8 [1] approach; b) ultimate deformation according to (3) vs experimental tests.

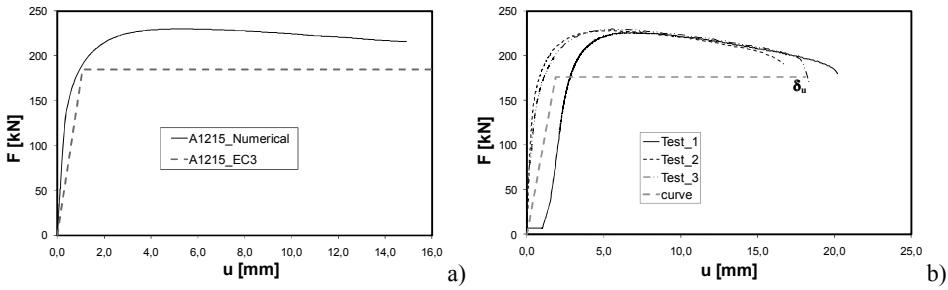


Figure 11 – Comparison of results using A1215 specimen: a) numerical model vs EC3 Part 1.8 [1] approach; b) ultimate deformation according to (3) vs experimental tests.

In terms of resistance, the code evaluation for specimen A1212 is not in line with the numerical model; there is a difference of up to 44%. This difference is justified by two aspects: first, a lower value of ultimate resistance (f_u) is assumed by the code for calculation according to (1) when compared with the real one; secondly, and most relevant, the reduction factors defined by the Eurocode are not appropriate

www.EngineeringEBooksPdf.com

for High Strength Steel. Parameter e_2 penalizes excessively the bearing resistance. For the models A1215, the deviation in the results (resistance) is much lower, about 20%. Here, the lower ultimate resistance of the steel used by code approach should be the main explanation. For the initial stiffness, all models present more a less the same differences. Finally, the estimation of the ultimate deformation (δ_u) using expression (3) presents, for model A1215, very close results in comparison to experiments. On the other hand, great difference is noticed for model A1212 which should be justified by the fact that expression (3) is based on the resistance determined by the code approach; and this was shown not to be appropriate when dealing with low edge distances in plates made of High Strength Steel.

6 CONCLUSIONS

In the present paper a numerical model to evaluate the plate/bolt in bearing component has been proposed. The experimental tests used for validation considered double overlap connections. Consequently, phenomena which are not directly related to the bearing deformation have been introduced in the model, as confinement and friction effects. The model was successfully validated by the experiments. Net-section failure was also simulated with success. Therefore, the suitability of the numerical model is assured. EC 3 part 1.8 [1] approach has been compared with the numerical simulation; it has been observed that in the case of High Strength steel some improvement should be brought to the expressions enabling to determine the resistance and the initial stiffness. The influence of edge distance as predicted by the code for mild steel has a limited application to HSS.

REFERENCES

[1] CEN European Committee for Standardization, *Eurocode 3: Design of steel structures – Part 1-8: Design of joints*, EN 1993-1-8, Brussels, Belgium, 2005.

[2] Ju S.-H, Fan C.-Y. and Wu G. H., *Three-dimensional finite elements of steel bolted connections*, Engineering Structures 26, 403-413, 2003.

[3] Pietrapertosa C., Piraprez E. and Jaspart J.P., *Ductility requirements in shear bolted connections*, ECCS/AISC Workshop: Connections in steel structures V: Behaviour, Strength and Design, Amsterdam, The Netherlands, June 3-4, pp. 335-345, 2004.

[4] Wald F., Sokol Z., Moal M., Mazura V. and Muzeau J. P. , *Stiffness of cover plate connections with slotted holes*, Eurosteel: Third European conference on Steel Structures, Coimbra, Portugal, pp. 1007-1016, 2002.

[5] Henriques J., Jaspart J.-P. and Simões da Silva L., *Ductility requirements for the design of bolted shear connections*, AISC ECCS Workshop, Chicago, 2008.

[6] Jaspart J.-P., *Étude de la semi-rigidité des nœuds poutre-colonne et son influence sur la resistance des ossatures en acier*, Doctor Thesis, Department MSM, University Liège, Belgium, 1991.

[7] LAGAMINE code, Finite Element Software, ArGEnCO Department, Liège University, Belgium.

[8] Freitas S. T., *Experimental research project on bolted connections in bearing for high strength steel*, Final report of the framework of the Socrates-Erasmus program, June 2005.

[9] Moze P., Beg, D. and Lopatic J., *Ductility and Strength of bolted connections made of high strength steel*, International conference in metal structures "Steel – A new and traditional material for buildings", Poiana Brasov, Romania, Sptember 20-22, pp. 323-330, 2006.

[10] Kato B., *Tension testing of metallic structural materials for determining stress-strain relations under monotonic and uniaxial tensile loading*, Rilem draft recommendation, TC 83 – CUS Fundamental Mechanical Properties of Metals, 1990, 23, 35-46, 1990.

[11] Henriques J., *Ductility requirements in shear bolted connections*, Master Thesis, Civil Engineering Department, University of Coimbra, Portugal, 2008.

www.EngineeringEBooksPdf.com

5. DYNAMIC BEHAVIOR AND ANALYSIS

www.EngineeringEBooksPdf.com

www.EngineeringEBooksPdf.com

SDSS'Rio 2010 STABILITY AND DUCTILITY OF STEEL STRUCTURES
E. Batista, P. Vellasco, L. de Lima (Eds.)
Rio de Janeiro, Brazil, September 8 - 10, 2010

CONSIDERATIONS ON THE DESIGN, ANALYSIS AND PERFORMANCES OF ECCENTRICALLY BRACED COMPOSITE FRAMES UNDER SEISMIC ACTION

Hervé Degée*, Nicolas Lebrun* and André Plumier*

* University of Liège, Department Argenco
e-mails: H.Degee@ulg.ac.be, Nicolas.Lebrun@ulg.ac.be, A.Plumier@ulg.ac.be

Keywords: Composite structures, eccentrically braced frames, seismic link.

Abstract. *Eccentrically braced frame (EBF) is a typical configuration for steel structures in seismic areas. In these structures, plastic deformations are localized in specific portions (so-called "seismic links") of the beams or of the bracing system. Cyclic deformations in these links are due to bending or shear force according to the length of the link. Eccentric configurations using seismic links can also be used for composite structures in which beams are realized with a steel profile connected to a collaborating connected concrete slab. This paper investigates different aspects of the design and performance of eccentrically braced composite frames.*

1 INTRODUCTION

Eccentrically braced frame (EBF) is a typical configuration for steel structures in seismic areas where it has proved its high efficiency (Ref. 3). EBFs combine the advantages of braced structure (i.e. significant lateral stiffness reducing therefore the sensitivity to second order effects and the damages to non structural elements) with high energy dissipation capability. A typical EBF consists of a beam, one or two braces and columns. Its configuration is similar to traditional braced frames with the exception that at least one end of each brace must be eccentrically connected to the frame. The eccentric connection introduces bending and shear forces in beam elements adjacent to the brace. The short segment of the frame where these forces are concentrated is the seismic link. Figure 1 shows four possible eccentric configurations suggested by Eurocode 8 (Ref. 1). Eccentric configurations using seismic links can also be used for composite structures in which beams are realized with a steel profile connected to a collaborating connected concrete slab.

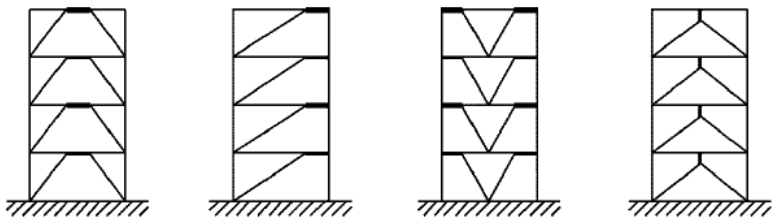


Figure 1: Typical EBF configurations.

The considerations and results summarized in the present paper are elaborated in the context of the European Research program OPUS funded by RFCS (Ref. 2) having the full title "Optimizing the seismic performance of steel and steel-concrete structures by standardizing material quality control". To make it short, the final objective of this research program is to assess the consequences of the variability of

www.EngineeringEBooksPdf.com

material properties on the efficiency of the capacity design of steel and steel-concrete composite structures. In this context, each partner of the research focuses on one specific structural type. University of Liège is dealing with composite braced frames (concentric and eccentric).

2 DESIGN OF CASE-STUDIES

2.1 Global geometry

In such a way to be able to assess influence of material variability, a set of case-studies has been prepared. More precisely, 2 buildings have been designed assuming that the seismic resistance is ensured in one direction by classical concentric bracings (X-bracings) and in the other direction by eccentric bracings. In the following, the focus of the paper is put exclusively on eccentric bracings. For more information, it is possible to refer to Ref. 2. Figure 2 shows the global geometry of the building (similar for both case-studies). Beams are designed as composite assuming a perfect collaboration of the concrete slab with the steel beams. Table 1 summarizes the main design assumptions considered for the two case studies: the first one corresponds to a situation of rather high seismicity, while the second corresponds to a situation of moderate seismicity. Two specific design choices are briefly commented in the following sections.

Table 1: Design conditions.

	Case-study 1	Case-study 2
Steel (profiles)	S355	S275
Concrete (slabs)	C30/37	C25/30
PGA	0.25g	0.1g
Spectrum type (Eurocode 8)	Type I	Type II
Soil type	B	C
q-factor	4	2

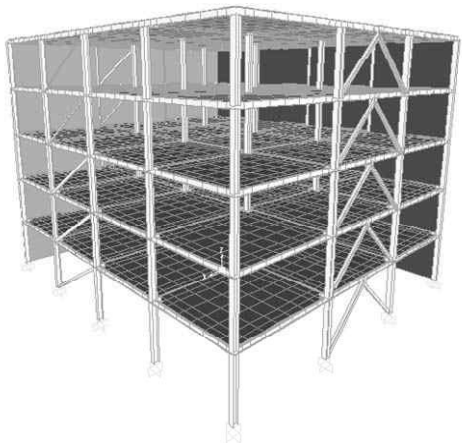


Figure 2: Global structural model.

2.2 Location of the seismic link

The first choice to be made when designing eccentrically braced frames is the location of seismic links, or in other words the appropriate choice between the four configurations proposed by Figure 1.

www.EngineeringEBooksPdf.com

Classical solutions are configurations 1 to 3 with seismic links in the beam. However it must be noticed that in these situations, braces must be capacity-designed, which means that normal forces in the braces are conditioned by the resistance of the beam in order to guarantee that plastic hinges develop in the expected seismic links. In the case of composite structures using a configuration with seismic links in the beam, composite resistance of the beam is in general such that capacity design rules can lead to very important cross-sections of braces and that more economical solutions can be developed by using the fourth configuration, namely with vertical seismic link. This one has the advantages to reduce overdesign of braces and to guarantee without difficulties that beams (composite) are capacity-designed with respect to vertical link (pure steel). In case-studies developed in this paper, it has been chosen to use short vertical links in which energy is dissipated by shear yielding of the link's web. This solution is very flexible in that sense that vertical links are exclusively designed to withstand seismic forces and can thus be easily optimized, which is not so obvious in the case of seismic links in beams that are also conditioned by gravity load and where optimization capacities are reduced.

2.3 Beam-column connections

Another important aspect of the design is the identification of the primary seismic structure, i.e. the part of the structure that withstands seismic forces. When using eccentric bracings (and more generally when using whatever kind of bracings), it is expected that the primary structure is the bracing system. In the case of composite structures, this is only possible if concrete slabs are disconnected around the columns. If not so, stiffness of the composite frame is such that the structure is actually behaving as a combined moment resisting frame/braced frame. This results in the fact that, in the present case-studies, composite effect is exclusively considered in beams under gravity loads.

2.4 Final design

Final design is summarized in table 2, where profiles used for the bracing system are listed. Additional information is also given in table 3:

- θ factor (see definition in Eurocode 8) measuring the sensitivity to second order effects.
- overstrength of the seismic links (i.e. ratio between the actual resistance of the link and internal forces obtained from spectral analysis).

Table 2: Cross-sections of the bracing system

		Case-study 1	Case-study 2
Seismic link	1st storey	HE 450 B	HE 300 B
	2nd storey	HE 450 B	HE 300 B
	3rd storey	HE 400 B	HE 240 B
	4th storey	HE 340 B	HE 200 B
	5th storey	HE 280 B	HE 140 B
Diagonal braces	1st storey	HE 240 B	UPE 220
	2nd storey	HE 240 B	UPE 220
	3rd storey	HE 240 B	UPE180
	4th storey	HE 240 B	UPE 140
	5th storey	HE 240 B	UPE 80

Some comments can be made:

- Values of the θ factor are very low, evidencing the high lateral stiffness of the frames;
- Over-strengths are reasonably moderate, even in the case of moderate seismic action (case-study 2);
- Homogeneity requirement of Eurocode 8 is easily fulfilled (variation of the over-strength all over the building lower than 25%). This requirement is much easier to fulfill in eccentric bracings than in concentric bracings where additional requirements on upper and lower limit in brace's slenderness can often be in contradiction with homogeneity condition.

www.EngineeringEBooksPdf.com

Table 3: θ-factors – Overstrength factors.

		Case-study 1	Case-study 2
θ factor	1st storey	0.05	0.06
	2nd storey	0.06	0.07
	3rd storey	0.05	0.06
	4th storey	0.05	0.05
	5th storey	0.04	0.04
Over-strength	1st storey	1.87	2.06
	2nd storey	1.80	2.01
	3rd storey	1.84	1.97
	4th storey	1.75	2.06
	5th storey	2.03	2.43

3 MODELLING

The second part of the study is the assessment of the seismic performances of the designed structures considering nominal values of the material properties. This is made using appropriate numerical simulations.

However, the choice of using short seismic links in which yielding is mainly associated with shear behavior implies that classical beam elements cannot be used directly. Indeed these elements are able to model correctly the bending behavior but they need to be adapted to account properly for shear yielding. The solution used here is presented in figure 3. It consists in adding a horizontal non linear spring at the junction of the beam and of the link. Properties of this spring are calibrated versus a non linear simulation of the link using shell finite elements.

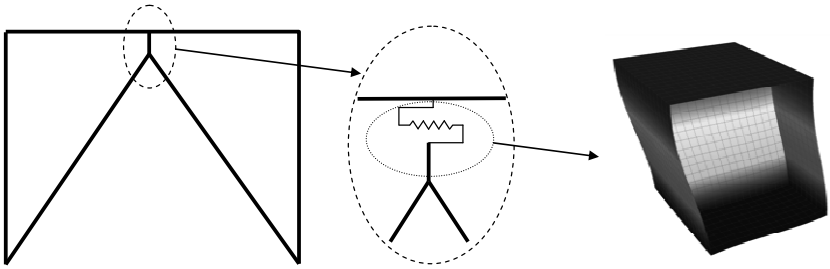


Figure 3: Numerical model.

4 NUMERICAL ASSESSMENT

4.1 Pushover analysis

The first assessment is made by using classical pushover analyses. A typical curve obtained for case-study 1 is given in figure 4. The slight difference between the load level corresponding to first yielding and the maximum of the pushover curve translates the good homogeneity of the overstrength ratio in the seismic links of the 5 storeys leading to a quasi-simultaneous yielding of the 5 links.

4.2 Incremental dynamic analysis

A more refined assessment is then made using incremental dynamic analysis. To this purpose, 7 accelerograms compatible with the reference elastic spectrum are generated. The structures are then analyzed using dynamic time-history analysis with increasing multiplier applied to the accelerograms

www.EngineeringEBooksPdf.com

(from 50% of the design PGA to 15 times the design PGA). Maximum values of specific characteristics are recorded for each acceleration level. Figure 5-a shows for example the evolution of the maximum top displacement for increasing value of the PGA for the first case-study. Figure 5-b compares then the couples "maximum top displacement/maximum base shear" obtained from dynamic analyses (plain lines) with similar curve obtained from static pushover (dash line).

Some comments can be drawn from there:

- Pushover curve can be seen as a reasonable lower bound of dynamic incremental curves;
- Curves from figure 5-a are typical of what can be used for Ballio-Setti assessment of q-factors. However due to the very low sensitivity of eccentrically braced structures, it can be seen that dynamic instability still don't occur even for a PGA equal to 15 times the design PGA.
- Significant yielding characterized by a strong bend in "base shear/top displacement" curves occurs at a PGA level of about 2 times the PGA. This is in good agreement with the overstrength values computed on the design examples and listed in table 3.

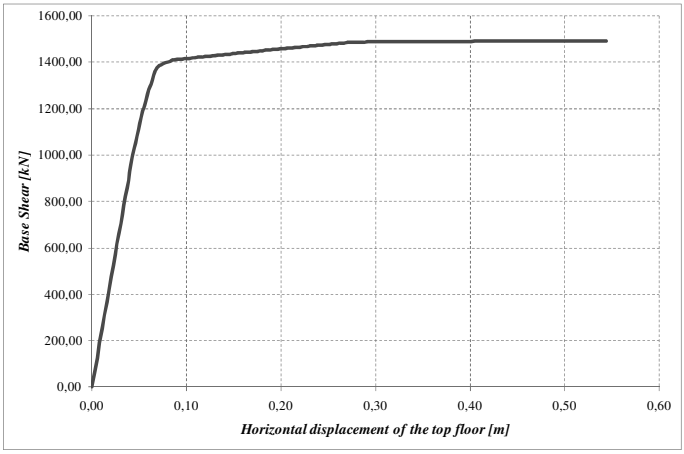
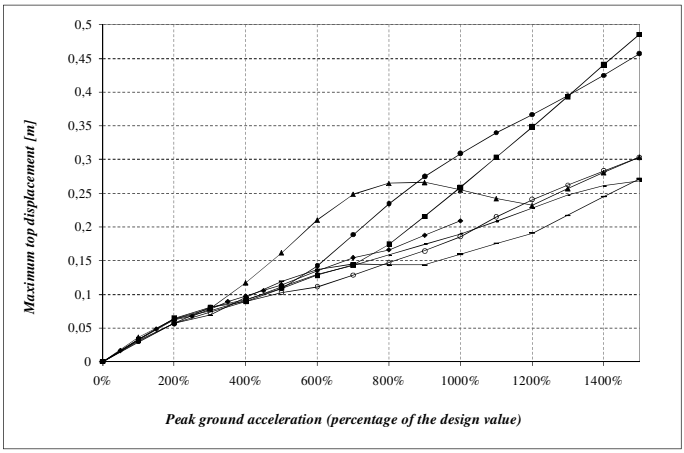


Figure 4: Pushover curve.



www.EngineeringEBooksPdf.com

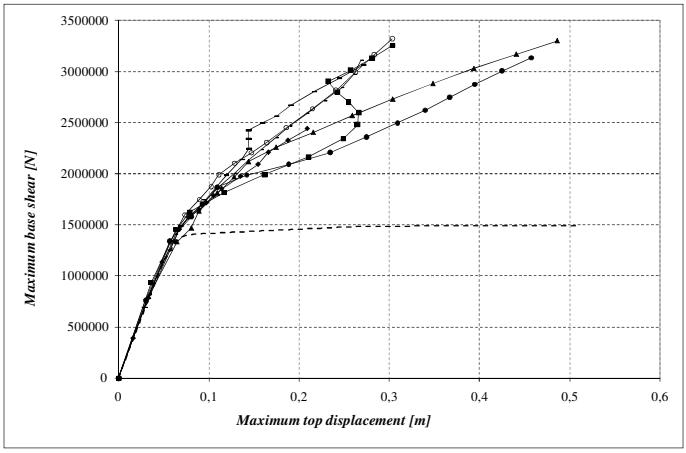


Figure 5: Incremental Dynamic Analyses (IDA) curves.

Additional interesting information can also be drawn from these results regarding actual values of the behavior factor q. To this purpose, it is assumed that collapse of the structure is obtained when rotation θ of the seismic link exceeds a given value. In the present study, values recommended by FEMA 356 (Ref. 4) are considered. For short links, governed by shear, 2 limit states are defined:

- Life safety: $\theta > 0.11$ rad
- Collapse prevention: $\theta > 0.14$ rad

On this base, it is possible for each dynamic incremental curve to define the multiplier of the reference PGA that leads to overcoming the rotation limit. An estimate of the behavior factor is then given by this particular value of the load multiplier. Values obtained for case-study 1 are given in table 4. In this table, no value corresponds to situation in which the limit value of the rotation is still not obtained even with a load multiplier of 15.

It can be seen that, in average, the estimated actual behavior factor is higher than the one considered for the design (q = 4, see table 1) whatever the safety level chosen.

Table 4: Estimated q-factor (case-study 1).

	Life Safety	Collapse prevention
Acc. 1	5.4	6.9
Acc. 2	3.5	3.8
Acc. 3	6.2	6.9
Acc. 4	4.6	4.6
Acc. 5	6.2	-
Acc. 6	-	-
Acc. 7	5.4	6.9
Average	**5.2**	**5.8**

www.EngineeringEBooksPdf.com

5 STATISTICAL ASSESSMENT

The final aim of the research work summarized in this paper is to assess the influence of the variability of the material properties. To this purpose, the following methodology is defined:

- On the base of statistical data provided by steel suppliers, generation of sets of material properties that follow these statistical curves;
- Execution of dynamic analysis for each material sample. For each of the 7 reference accelerograms, the load multiplier corresponds to the FEMA 'collapse prevention' limit state obtained in section 4 using nominal material properties;
- For each analysis, record of the interesting parameters defining the structural behavior (link rotation, normal forces in braces, interstorey drifts, top displacement…).
- Statistical treatment of these results.

Examples of statistical distributions obtained for case-study 1 and for 100 material samples are given in figure 6 for the link rotation and for the normal force in braces. Even if these results are not fully statistically reliable, some preliminary conclusions can be drawn:

- Rotation demand obtained with actual material properties is always smaller than estimated on the base of nominal properties.
- Demand in terms of internal forces in braces is much lower than obtained by application of the capacity design rules of Eurocode (in this particular case, the design normal force is equal to 1612 kN).

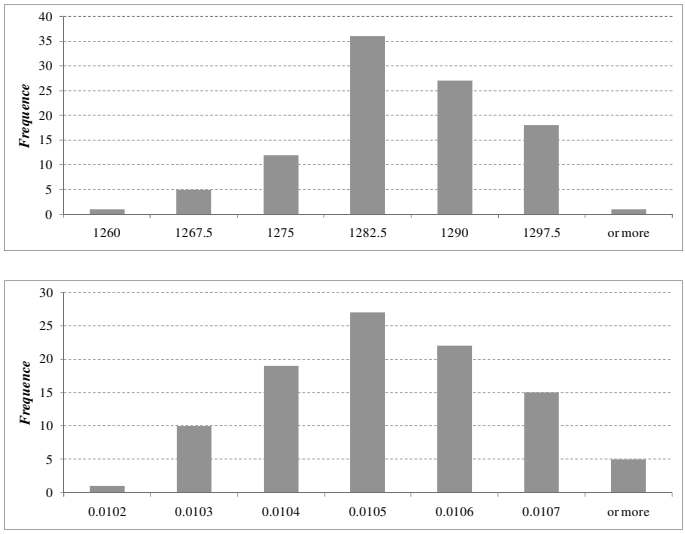


Figure 6: Example of statistical results – Normal forces in braces at 1st storey [kN] (top) – Rotation demand in seismic link at 1st storey [rad] (bottom).

6 PERSPECTIVES

Further developments of this research are still in progress. In particular, the number of material samples is enlarged in order to make the results more reliable. Similar work is also performed on concentric bracings.

www.EngineeringEBooksPdf.com

The main outcomes will deal with assessment and possible recalibration of overstrength coefficients proposed by the codes in the capacity design procedures, in order to make them fit better with actual statistical distribution of steel properties.

7 ACKNOWLEDGEMENTS

Acknowledgement is made to the European Commission Research Fund for Coal and Steel for the funding of the research project RFSR-CT-2007-00039 "OPUS – Optimizing the seismic performance of steel and steel-concrete structures by standardizing material quality control". H. Degée also acknowledges the support received from the Belgian Found for Scientific Research (F.R.S.-FNRS).

REFERENCES

[1] EN1998-1:2004, Eurocode 8 : Design of structures for earth-quake resistance, Part 1: General rules, seismic actions and rules for buildings, *European Committee for Standardization*, Brussels, 2005.

[2] Optimizing the seismic performance of steel and steel-concrete structures by standardizing material quality control (OPUS). A. Osta et al. *Mid-term technical report, RFCS, Steel RTD, RFSR-PR-06056*, 2009.

[3] Becker,R., Ishler, M.. Seismic design practice for eccentrically braced frames. *Structural Steel Educational Council*, 1996.

[4] FEMA 356. Prestandard and Commentary for the seismic rehabilitation of buildings, 2000.

www.EngineeringEBooksPdf.com

SDSS'Rio 2010 STABILITY AND DUCTILITY OF STEEL STRUCTURES
E. Batista, P. Vellasco, L. de Lima (Eds.)
Rio de Janeiro, Brazil, September 8 - 10, 2010

EFFECT OF THE LOADING MODELLING, HUMAN HEEL IMPACT AND STRUCTURAL DAMPING ON THE DYNAMIC RESPONSE OF FOOTBRIGES

José Guilherme S. da Silva[1], Francisco J. da C. P. Soeiro[1], Pedro C. G. da S. Vellasco[2], Luciano R. O. de Lima[2] and Nelson L. de A. Lima[3],

[1] State University of Rio de Janeiro, UERJ
Mechanical Engineering Department
e-mail: jgss@uerj.br, soeiro@uerj.br

[2] State University of Rio de Janeiro, UERJ
Structural Engineering Department
e-mail: vellasco@uerj.br, lucianolima@uerj.br

[3] State University of Rio de Janeiro, UERJ
Civil Engineering Post-Graduate Programme
e-mail: nelson_lima@hotmail.com

Keywords: Structural Dynamics, Human Comfort, Composite Footbridges, Computational Modelling.

Abstract. *The demands imposed by daring architectural projects led to design and construction of light pedestrian footbridges with large spans. This trend generated very slender structural footbridges and consequently changed the serviceability and ultimate limit states associated to their design. In the particular case of pedestrian footbridges this phenomenon occurs when the fundamental frequency is equal or near the existing loading frequencies or some of its multiples. The present investigation was carried out based on a more realistic loading model developed to incorporate the dynamical effects induced by people walking when the dynamical response of pedestrian footbridges is investigated. In this particular loading model the movement of legs that cause an ascent and descending of the effective mass of the human body, at each step, was considered while the position of the dynamical loading is changed according with the individual position. This fact implies that the generated time function has a space and time description. The investigated structural model was based on several footbridges, with main spans varying from 10m to 35m. The structural system was made of a composite (steel-concrete) solution built with an "I" steel beam section and a reinforced concrete deck. The proposed computational model, developed for the composite slab dynamic analysis, adopted the usual mesh refinement techniques present in finite element method simulations. The footbridges dynamic response was investigated and the peak accelerations were obtained and compared to results recommended by design standards to take into account human comfort evaluations.*

1 INTRODUCTION

In the last few years footbridges have been constructed with daring structures that consider the experience and knowledge of structural engineers by using newly developed materials and technologies boosted by the ever-growing investigations on this field. It widely known that the main objective of the structural engineer is related to the design of slight structures whose conception requires a substantial amount of theoretical knowledge associated to structural design and construction processes. This fact have generated very slender pedestrian footbridges and consequently changed the serviceability and ultimate limit states associated to their design [1] - [3].

www.EngineeringEBooksPdf.com

In the particular case of footbridges this phenomenon precisely occurs when the structural fundamental frequency is equal or near of the existing loading frequencies, or is similar to some of its multiples. Another important aspect that still deserves further investigation is related to the modelling of the harmonic dynamical loads induced by pedestrians walking.

The present investigation was carried out based on a more realistic loading model developed to incorporate the dynamical effects induced by people walking in the footbridges dynamical response [1], [2]. In this particular loading model, the leg motion of that causes a human body effective mass ascent and descending movement at each step was considered. The position of the dynamical loading also changed according to the individual position and the generated time function, corresponding to the excitation induced by people walking, have a space and time description [1], [2].

The investigated structural model was based on several footbridges, with main spans varying from 10m to 35m. A composite (steel/concrete) solution made of an "I" steel profile and a reinforced concrete slab was the adopted structural system. The proposed computational model, developed for the composite slab dynamic analysis, adopted the usual mesh refinement techniques present in finite element method simulations [4].

In this paper, the developed analysis methodology is described and discussed. Based on an extensive parametric study, the footbridges dynamic response was obtained in terms of peak accelerations and compared to the limiting values proposed by several authors and design codes [3], [5] In specific design situations, the obtained results have shown that the code recommendations could lead to unsafe values based on the adoption of excessively simplified load models [3]. Hence, it was detected that this type of structure can reach high vibration levels, compromising the footbridge user's comfort and especially its safety.

2 MODELLING OF THE DYNAMIC ACTIONS INDUCED BY PEOPLE WALKNG

In this paper a loading model were developed in order to incorporate the dynamical effects induced by people walking in the dynamical response of pedestrian footbridges. The mathematical model behind this strategy was proposed by [1], [2], as well as a numerical approach to evaluate the floor structure reaction, as illustrated in Figure 1.

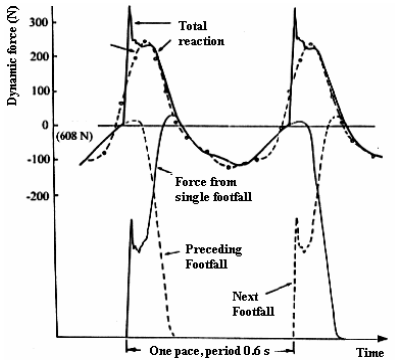


Figure 1: Footfall force and reaction on the floor structure [2].

It must be emphasized that the geometry of the human body walking is an organized motion of legs that cause an ascent and descending of the body effective mass at each step. The human body mass accelerations are associated to floor reactions, and it is approximately periodic to the step frequency. The two feet produce this type of loading, as function of the static parcel associated to the individual weight and three or four load harmonic components. These harmonic appear due to the interaction between the increasing load represented by one foot and the simultaneous unloading of the other foot.

www.EngineeringEBooksPdf.com

In this particular model the position of the dynamical loading changes according to the individual position, while the generated time function has a space and time description. However, the study of several other parameters related to this type of modelling like the step distance and step frequency, as illustrated in Table 1 became necessary to fully represent the investigated problem.

Table 1: Human walking characteristics.

Activity	Velocity	Step Distance	Step Frequency
Slow Walking	1.1	0.6	1.7
Normal Walking	1.5	0.75	2.0
Fast Walking	2.2	1.0	2.3

The pedestrian motion on the footbridge was modelled based on the Equation (1) to (4) and four harmonics were used to generate the dynamical forces, Table 2. Like in the previous model, the third harmonic with a 1.79Hz step frequency, as shown in Table 2, was the walking load resonant harmonic (3 x 1.79Hz = 5.37Hz), Figure 2. In this situation, the finite element mesh has to be very refined and the contact time related to the dynamical load application on the structure depends on the step distance and frequency, Table 2.

$$F(t)=\begin{cases}\left(\dfrac{f_{mi}\,F_m-P}{0.04T_p}\right)t+P & if\ \ 0\le t<0.04T_p\\[2ex] f_{mi}\,F_m\left[\dfrac{C_1\left(t-0.04T_p\right)}{0.02T_p}+1\right] & if\ \ 0.04T_p\le t<0.06T_p\\[2ex] F_m & if\ \ 0.06T_p\le t<0.15T_p\\[2ex] P+\displaystyle\sum_{i=1}^{nh}P\alpha\,sen\left[2\pi i\,f_c\left(t+0.1T_p\right)+\varphi_i\right] & if\ \ 0.15T_p\le t<0.90T_p\\[2ex] 10\left(P-C_2\right)\left(\dfrac{t}{T_p}-1\right)+P & if\ \ 0.90T_p\le t<T_p\end{cases} \tag{1}$$

$$F_m=P\left(1+\sum_{i=1}^{nh}\alpha_i\right) \tag{2}$$

$$C_1=\left(\frac{1}{f_{mi}}-1\right) \tag{3}$$

$$C_2=\begin{cases}P\left(1-\alpha_2\right) & if\ \ nh=3\\ P\left(1-\alpha_2+\alpha_4\right) & if\ \ nh=4\end{cases} \tag{4}$$

www.EngineeringEBooksPdf.com

Where:

F_m : maximum value of the Fourier series, given by Equation (4);
f_{mi} : heel-impact factor;
T_p : step period;
C_1 : Equation (5) coefficients;
C_2 : Equation (6) coefficients.

Table 2: Forcing frequencies (f_s), dynamic coefficients (α_i) and phase angles (Φ_i).

Harmonic	Human Walking		
	f_s (Hz)	α_i	Φ_i
1	1.6 - 2.2	0.5	0
2	3.2 - 4.4	0.2	$\pi/2$
3	4.8 - 6.6	0.1	π
4	6.4 - 8.8	0.05	$3\pi/2$

According to [2], the proposed mathematical function, Equations (1) to (4), used to represent the dynamical actions produced by people walking on floor slabs is not a Fourier series simply because the equation also incorporates in its formulation the heel impact effect.

This mathematical model was evaluated considering four harmonics, see Tables 1 and 2, and also incorporated the transient effect due to the human heel impact. The load model used a heel impact factor equal to 1.12 (f_{mi} = 1.12) [2]. However, it must be emphasized that this value can vary substantially from person-to-person. An increase of the dynamic load due to the human heel impact could be observed when a comparison to an analysis that did not consider this effect is made. Figure 2 illustrates the dynamical load function for an individual walking at 5.37Hz (3 x 1.79Hz = 5.37Hz), based on Equations (1) to (4).

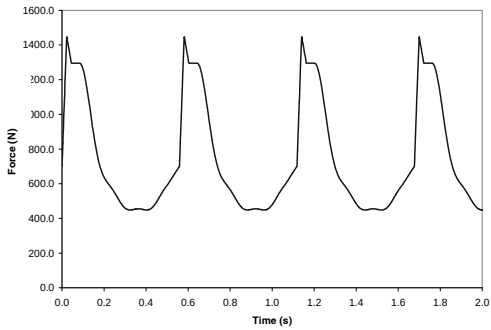


Figure 2: Dynamic loading function for a single human walking at 5.37Hz (3 x 1.79Hz = 5.37Hz) [1].

The following strategy was adopted: a 0.65m step distance corresponding to the third harmonic with a 1.79Hz step frequency, as shown in Table 2. The step period is equal to 1/f = 1/1.79Hz = 0.558s, corresponding to a distance of 0.65m. This way, the modelling considered six forces to model one human step where each of the loads P1, P2, P3, P4, P5 and P6 were applied to the structure during 0.558/5 = 0.1116s, corresponding the contact time of each dynamical load [1], see Figure 3.

However, the dynamical forces were not simultaneously applied. The first applied load would be P1, according with Equation (2), by 0.1116s, and at the end of this period of time, the load P1 becomes zero and the load P2 is then applied for 0.1116s. This process successively occurs until all dynamical loads are applied along the structure, as presented in Figure 3. It should be emphasised that all the dynamical actions associated to the time function will be correctly applied to the structural system [1].

www.EngineeringEBooksPdf.com

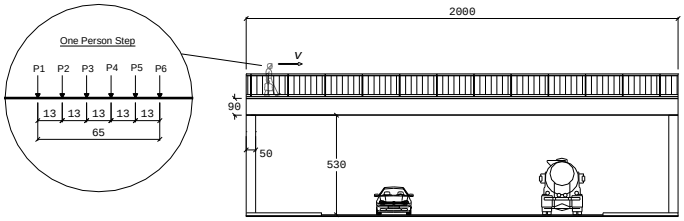


Figure 3: People walking on the footbridge (dimensions in cm).

3 STRUCTURAL SYSTEM AND COMPUTATIONAL MODELLING

The outdoor footbridge studied in this paper is simply supported by columns at its extremities, spanning from 10m to 35m by 2.5m, currently used for pedestrian crossing. The structural system was made of composite girders and a 100mm thick concrete slab, as presented in Figure 4.

The steel sections used were welded wide flanges (WWF) made with a 300MPa yield stress steel grade. A 2.05x105 MPa Young's modulus was adopted for the steel beams. The concrete slab has a 30MPa specified compression strength and a 3.84x104MPa Young's Modulus. Table 3 depicts the geometrical characteristics of all the steel sections used in the structural model. It is also assumed that an individual human weight was equal to 700N (0.7kN) [3]. In this investigation a damping ratio, ξ, equal to 0.005, 0.0075 and 0.01 (ξ = 0.5%, 0.75% and 1%) was adopted in all the structural systems [3], based on the Rayleigh proportional damping formulation [1].

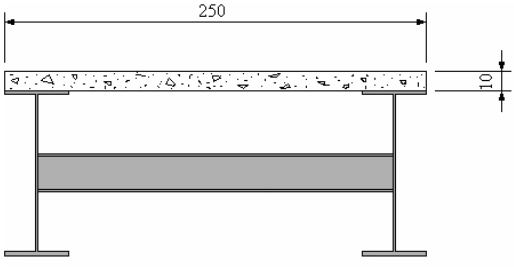


Figure 4: Footbridges cross section (dimensions in cm).

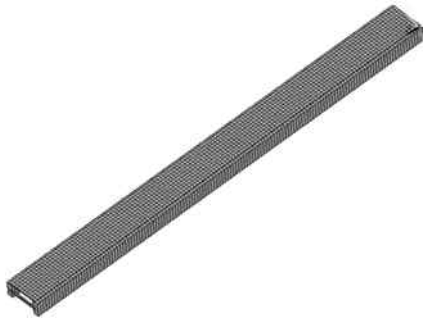


Figure 5: Footbridge finite element model.

Table 3: Geometrical characteristics of the beam steel sections.

Main Span (m)	Beams	Height (mm)	Flange Width (mm)	Top Flange Thickness (mm)	Bottom Flange Thickness (mm)	Web Thickness (mm)
10.0	400x58	400	200	12.5	12.5	6.3
12.5	500x73	500	250	12.5	12.5	6.3
15.0	550x100	550	250	19.0	19.0	6.3
17.5	600x140	600	300	22.4	22.4	8.0
20.0	700x154	700	320	22.4	22.4	8.0
22.5	800x173	800	320	25.0	25.0	8.0
25.0	900x191	900	350	25.0	25.0	8.0
27.5	1000x201	1000	400	22.4	22.4	8.0
30.0	1100x235	1100	400	25.0	25.0	9.5
32.5	1200x244	1200	450	22.4	22.4	9.5
35.0	1200x307	1200	450	31.5	31.5	9.5

www.EngineeringEBooksPdf.com

The proposed computational model, developed for the composite slab dynamic analysis, adopted the usual mesh refinement techniques present in finite element method simulations implemented in the ANSYS program [4]. In this computational model, floor steel girders are represented by three-dimensional beam elements, where flexural and torsion effects are considered. The concrete slab is represented by shell finite elements, as presented in Figure 5. The computational model considered a full interaction between steel and concrete simulating a composite (steel-concrete) structural system.

4 DYNAMIC ANALYSIS

For practical purposes, a linear time-domain analysis was performed throughout this study. This section presents the evaluation of the structural systems vibrations levels when submitted to dynamic excitations coming from human walking. The outdoor footbridges dynamic responses were determined through an analysis of its natural frequencies, displacements and accelerations. The results of the dynamic analysis were obtained from an extensive numerical analysis, based on the finite element method using the ANSYS program [4]. These values were compared with the results supplied by current criteria for structural design [3], [5]. This comparison was performed to evaluate a possible occurrence of unwanted excessive vibration levels and human discomfort.

4.1 Natural Frequencies and Vibration Modes

The footbridges natural frequencies were determined with the aid of the finite element method simulations [4], as illustrated in Table 4. These results were compared to those obtained according to the design criteria [3] and were used to evaluate only the footbridges fundamental frequencies.

When the footbridges freely vibrate in a particular mode, it moves up and down with a certain configuration or mode shape. Each footbridge natural frequency has an associated mode shape. It was observed in all investigated structural models that flexural effects were predominant in the fundamental mode vibrations. However it is important to observe that torsional effects are present starting from the second vibration mode, see Figure 6. Figure 6 also illustrates the mode shapes corresponding to the first six natural frequencies of the pedestrian footbridge with the main span equal to 20m.

The numerical results for the footbridges fundamental frequency, with the main span varying from 10m to 35m, were in accordance to the literature values [3]. It could be clearly observed, as expected, that as the structural span is increased the footbridge fundamental frequency decreases, see Table 4. This fact also serves to demonstrate that the developed models are coherent to the theory.

Table 4: Footbridges natural frequencies.

Main Span	Natural Frequencies f_{0i} (Hz)						AISC*	Differences
	f_{01}	f_{02}	f_{03}	f_{04}	f_{05}	f_{06}	f_{01} (Hz)	(%)
10.0	9.04	19.52	30.58	53.31	53.76	62.87	8.58	5.14
12.5	7.72	17.83	26.66	46.31	46.88	50.53	7.23	6.26
15.0	6.63	16.19	22.85	36.76	39.87	45.98	6.03	9.03
17.5	5.91	15.07	20.07	29.98	35.32	42.12	5.23	11.55
20.0	5.37	14.60	18.23	24.87	32.95	39.16	4.74	11.87
22.5	4.99	14.11	16.83	21.28	30.87	36.73	4.35	12.66
25.0	4.65	13.51	15.63	18.79	28.96	34.50	4.04	13.13
27.5	4.31	12.61	14.45	17.11	27.04	32.17	3.74	13.17
30.0	4.11	11.47	13.59	16.19	24.86	30.52	3.52	14.48
32.5	3.84	10.36	12.67	15.51	22.99	28.58	3.28	14.55
35.0	3.55	9.45	11.53	14.68	21.07	26.21	2.96	15.41

*AISC: [3]

www.EngineeringEBooksPdf.com

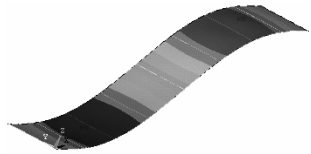
Table 4 indicated that the difference between the footbridge fundamental frequency evaluated by the developed model or by the AISC recommendations [3] is proportional to the footbridge span. Considering that the finite element model (FEM) was developed to determine accurate results and the AISC equations [3] are in fact based on simplified models, associated to a single degree of freedom system (SDOF), it is reasonable to accept that the numerical results determined in the present study are closer to the actual value.



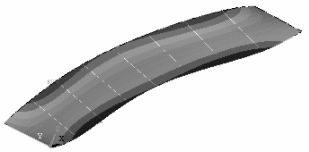
(a) Mode shape associated to the 1st natural frequency: f_{01}=5.37Hz.



(b) Mode shape associated to the 2nd natural frequency: f_{02}=14.60Hz



(c) Mode shape associated to the 3rd natural frequency: f_{03}=18.23Hz.



(d) Mode shape associated to the 4th natural frequency: f_{04}=24.87Hz.



(e) Mode shape associated to the 5th natural frequency: f_{05}=32.95Hz.



(f) Mode shape associated to the 6th natural frequency: f_{06}=39.16Hz.

Figure 6. Footbridge vibration modes. Main span equal to 20m.

4.2 Peak Accelerations

The present analysis proceeded with the evaluation of the footbridges performance in terms of vibration serviceability due to dynamic forces induced by people walking. The first step of this investigation concerned in the determination of the footbridge peak accelerations. These peak accelerations were compared to the limits recommended by design criteria and codes [3], [5], see Table 5.

Table 5: Outdoor footbridges peak accelerations at resonance.

Main Span (m)	Heel Impact Coefficient (f_{mi})	Structural Damping (ξ)		
		0.50%	0.75%	1.00%
10.0	1.12	1.060	1.010	0.967
12.5		1.660	1.580	1.510
15.0		0.934	0.892	0.851
17.5		1.670	1.590	1.520
20.0		0.969	0.926	0.883
22.5		1.200	1.140	1.090
25.0		0.481	0.460	0.439
27.5		1.390	1.330	1.270
30.0		0.675	0.645	0.615
32.5		1.570	1.500	1.430
35.0		0.559	0.531	0.509
Limit acceleration: a_{lim} = 0.490 m/s^2 [3], [5]				

www.EngineeringEBooksPdf.com

The peak accelerations values have shown that for all analyzed outdoor footbridges the peak accelerations were higher than those proposed by the design criteria and code recommendations [3], [5], violating human comfort criteria, see Table 5. This fact emphasizes that when the position of the dynamical loading corresponding to the excitation induced by people walking was changed and at the same time the human heel effect was incorporated in the analysis there is a substantial increase in the structure dynamical response and that the structural models indicated possible problems related to human comfort for the load model, see Table 5.

It must be emphasized that the footbridges structural damping and heel impact coefficients considered in this investigation are in accordance to current design recommendations [3], [5]. The obtained results have shown that when the structural damping, ξ, decrease the peak accelerations values increase and when the heel impact coefficient, f_{mi}, increase the peak accelerations values also increase. Such fact is relevant, because the limit states related to excessive vibrations were violated and the human comfort was compromised when the transient effect due to the human heel impact was considered in the analysis, Table 5.

5 FINAL REMARKS

This paper considered the investigation of the dynamic behaviour, in terms of vibration serviceability limit states, of several outdoor composite (steel-concrete) footbridges. The developed loading model incorporated a more realistic load where the dynamic action position changed according to the individual position on the structural model. Another important point is related to the fact that the generated time function has a space and time description and the load model also considered the human heel impact effect. On the other hand, the AISC recommendations only considered a single harmonic applied at the pedestrian footbridge midspan, without varying the load position.

The outdoor footbridges dynamic responses in terms of peak accelerations were obtained and compared to the limit values proposed by current design code recommendations. The obtained results in this investigation have shown that when the position of the dynamical loading was changed according to the individual position and, at the same time the human heel effect was incorporated in the analysis, the peak accelerations were higher than current design code recommendations limit values.

6 ACKNOWLEDGEMENTS

The authors gratefully acknowledge the financial support provided by the Brazilian National and State Scientific and Technological Supporting Agencies: CNPq, CAPES and FAPERJ.

REFERENCES

[1] Lima, N.L. de A., “Efeito da modelagem do carregamento, do impacto do calcanhar humano e do amortecimento estrutural na resposta dinâmica de passarelas mistas”, MSc Dissertation (In Portuguese), Civil Engineering Post-Graduate Programme, State University of Rio de Janeiro, UERJ, Rio de Janeiro, RJ, Brazil, 138 pgs, 2007.

[2] Varela, W.D., “Modelo teórico-experimental para análises de vibrações induzidas por pessoas caminhando sobre lajes de edifícios”, PhD Thesis (In Portuguese), Federal University of Rio de Janeiro, Civil Engineering Department, COPPE/UFRJ, Rio de Janeiro, Brazil, 309 pgs, 2004.

[3] Murray, T.M., Allen, D.E., Ungar. E.E., “Floor vibrations due to human activity”, Steel Design Guide Series, American Institute of Steel Construction, AISC, 70 pgs, 2003.

[4] ANSYS, Swanson Analysis Systems”, Inc., P.O. Box 65, Johnson Road, Houston, PA, 15342-0065, Version 10.0, Basic analysis procedures, 2nd Edition, 2003.

[5] International Standards Organisation/ISO 2631-2, “Evaluation of human exposure to whole-body vibration. Part 2: Continuous and shock-induced vibration in buildings (1-80Hz)”, 1989.

www.EngineeringEBooksPdf.com

SDSS'Rio 2010 STABILITY AND DUCTILITY OF STEEL STRUCTURES
E. Batista, P. Vellasco, L. de Lima (Eds.)
Rio de Janeiro, Brazil, September 8 - 10, 2010

STRUCTURAL DAMAGE ASSESSMENT USING THE DIFFERENTIAL EVOLUTION AND THE ANT COLONY OPTIMIZATION TECHNIQUES

Genasil F. dos Santos[1], José Guilherme S. da Silva[2], Francisco J. da C. P. Soeiro[2]

[1] State University of Rio de Janeiro, UERJ
Civil Engineering Post-Graduate Programme, PGECIV
e-mail: genasil@yahoo.com.br

[2] State University of Rio de Janeiro, UERJ
Mechanical Engineering Department, MECAN
e-mail: jgss@uerj.br, soeiro@uerj.br

Keywords: structural damage assessment, system identification techniques, inverse problems, differential evolution optimization technique, ant colony optimization technique.

Abstract. *Structural systems in a variety of applications including aerospace vehicles, automobiles and engineering structures such as tall buildings, bridges and offshore platforms, accumulate damage during their service life. The approach used in this investigation is one where the structural properties of the analytical model are varied to minimize the difference between the analytically predicted and empirically measured response. This is an inverse problem where the structural parameters are identified. In this work a reduced number of vibration modes and nodal displacements were used as the measured response. For the damage assessment problem a finite element model of the structural system is available and the model of the damaged structure will be identified. Damage will be represented by a reduction in the elastic stiffness properties of the system. In this investigation, the Differential Evolution (DE) and the Ant Colony Optimization (ACO) were applied to simple truss structures with different levels of damage.*

1 INTRODUCTION

In a typical load bearing structure, degradation of structural properties due to damage manifests itself as a change in the static and dynamic response. A correlation of the measured response with that obtained from an analytical model of the undamaged structure, allows for the possibility of determining a modified model that predicts the altered response. This inverse problem is solved using a system identification technique [1].

In this paper the output error approach of system identification is used to determine changes in the structural parameters that result from structural damage. Damage is represented by reduction in the elastic properties of the element. The net changes in these quantities due to damage are lumped into a single coefficient d_i for each element that is used to multiply the stiffness matrix of that particular element. These coefficients d_i constitute the design variables for the resulting optimization problem.

Static displacements and eigenmodes are used as measured data for the inverse problem of damage detection. Reduced sets of eigenmodes and static displacements are used [2-3]. The approach of considering one design variable d_i for each element in the structure usually results in a large dimensionality problem.

These results in a very nonconvex design space, probably with several local minima, where Gradient-based nonlinear methods for function minimization may have difficulties to find the global optimum. In this work two global optimization methods, the Differential Evolution and the Ant Colony Optimization which are two heuristic population based methods were used for function minimization.

www.EngineeringEBooksPdf.com

2 STRUCTURAL DAMAGE ASSESSMENT

In a finite element formulation, structural characteristics are defined in terms of the stiffness, damping, and mass matrices [K], [C] and [M], respectively. The governing equation of equilibrium for a dynamical system involves each of these matrices, and can be written using Equation (1). In Equation (1), x is the displacement vector and P(t) is the vector of applied loads. The static load-deflection relation only involves the system stiffness matrix, as presented in Equation (2).

$$[M]\ddot{x}+[C]\dot{x}+[K]x=P(t) \tag{1}$$

$$[K]x=P \tag{2}$$

The analytical model describing the eigenvalue problem for an undamped system can be stated in terms of the system matrices defined above, the i-th eigenvalue ω_i^2, and the corresponding eigenmode Y_i as follows:

$$\left([K]-\omega_i^2[M]\right)Y_i=0 \tag{3}$$

It is clear from these equations that a change in the system matrices results in a different structural system response and this difference can be related to changes in specific elements of the system matrices. Since internal structural damage typically does not result in a loss of material, it will assume the mass matrix to be constant.

The stiffness matrix can be expressed as a function of the thickness (t), the length (L), the cross-sectional area (A), the Young's modulus (E), and the flexural and torsional stiffness (EI) and (GJ), respectively. The stiffness matrix of the truss element modified to include the damage coefficient is given by Equation (5), where C = cos α and S = sin α. The truss element is shown in Figure 1. The numerical approach was applied to simple steel truss structures, see Figure 2, with different levels of damage.

$$[K]=[K(t,L,A,E,EI,GJ)] \tag{4}$$

In this paper, changes in these quantities are lumped into a damage coefficient d_i, which is used to multiply the stiffness matrix of a particular element. The coefficients d_i constitute the design variables for the damage assessment problem and vary from 0 (undamaged element) to 1 (completely damaged element). The values of the coefficients d_i give the location and the extent of damage in the structure.

$$K_i^{(.)}=\frac{(1-d_i)E_iA_i}{L_i}\begin{bmatrix} C^2 & CS & -C^2 & -CS \\ CS & S^2 & -CS & -S^2 \\ -C^2 & -CS & C^2 & CS \\ -CS & -S^2 & CS & S^2 \end{bmatrix} \tag{5}$$

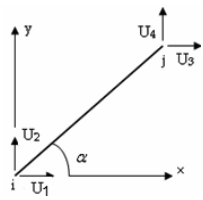
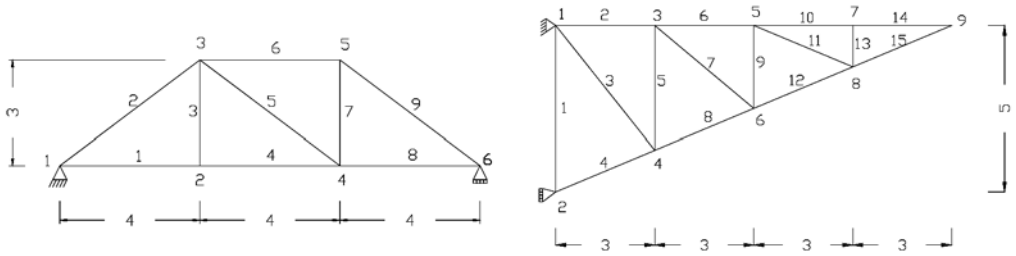


Figure 1: Truss element.

www.EngineeringEBooksPdf.com



a) Nine bar truss. b) Fifteen bar truss.

Figure 2: Investigated steel truss structures (dimensions in meters).

If the measured and analytically determined static displacements or vibration modes are denoted by Y_m and Y_a, respectively, the optimization problem can be formulated as determining the vector of design variables d_i that minimize the scalar objective function representing the difference between the analytical and experimental response, as presented in Equation (6), where i represents the degree of freedom and j denotes a static loading condition or a particular vibration mode.

$$F = \sum_{ij} \left\| Y_m^{ij} - Y_a^{ij} \right\|^2 \tag{6}$$

One important advantage of this approach is that the complete set of modes or displacements is not needed since the objective function involves only the difference between components of those vectors. Some of the components may be neglected according to its importance in the behaviour of the structure. In this paper, for damage assessment purposes, only the vertical displacements were used. They are dominant and easier to measure. The other components are relatively small and neglecting them in the objective function does not affect the process of damage detection. The approach still works and becomes more realistic since in large structures only few dominant displacements can be obtained accurately. Also in the cases where eigenmodes were used for damage assessment purpose, only the first four modes and the respective eigenvalues (natural frequencies) were used in the objective function.

The objective function presented in Equation (6) was minimized with two global optimization techniques: Differential Evolution (DE) and the Ant Colony Optimization (ACO). These methods are described briefly in the next section.

3 OPTIMIZATION TECHNIQUES

3.1 Differential Evolution (DE)

The Differential Evolution (DE) was proposed by Storn and Price [4] as an algorithm to solve global optimization problems of continuous variables. The main idea behind DE is how possible solutions taken from the population of individuals are set, recombined and chosen to evolve the population to the next generation. In a population of individuals, a fixed number of vectors are randomly initialized, and then evolved over the optimization task to explore the design space and hopefully to locate the optimum of the objective function. At each iteration, new vectors are generated by the combination of vectors randomly chosen from the current population.

This operation is called “mutation” and a mutant population is created. The outcoming vectors are then mixed with a predetermined target vector. This operation is called “crossover” or “recombination” and produces a “trial vector”. Finally, the “trial vector” is accepted for the next generation if it yields a reduction in the value of the objective function. This last operation is referred to as “selection”.

www.EngineeringEBooksPdf.com

As can be seen, the basic algorithm preserves some common aspects of the traditional simple Genetic Algorithm (GA), specially the nomenclature of selection, crossover and mutation. A population of individuals can be expressed as a matrix given by Equation (7), where *i* is the number of individuals of the population and *j* is the number of design variables.

$$P = \begin{bmatrix} x_{11} & x_{12} & \dots & x_{1j} \\ x_{12} & x_{22} & \dots & x_{2j} \\ \dots & \dots & \dots & \dots \\ x_{i1} & x_{i2} & \dots & x_{ij} \end{bmatrix} \tag{7}$$

As described before, the “mutation” operator adds the weighted difference between two individuals to a third individual (base vector). There are several ways to mutate a variable and the equation below shows a possible mutation scheme, among others.

$$v_i = x_{r1} + F\left(x_{r2} - x_{r3}\right) \tag{8}$$

In Equation (8), $\mathbf{v_i}$ is the mutant vector, x_{r1}, x_{r2} and x_{r3} are random integer indexes and mutually different, F is a real constant factor which controls the amplification of the differential variation and x_{best} is the best individual of the current population. The next operation is “crossover”. Each mutant vector is combined with a target vector $\mathbf{x_i}$. This operation is performed by swapping the contents of the mutant vector with the correspondent component of the target vector based on a crossover probability (CR). The resulting vector is denominated “trial vector”.

At the sequence of the DE algorithm, the selection operator decides whether or not the new vector $\mathbf{x_{trial}}$ should become a member of the next generation. This is decided by the objective function value of all new individuals $f(\mathbf{x_{trial}})$ which are compared with the one of the target vector $f(\mathbf{x_{target}})$. If there is an improvement, $\mathbf{x_{trial}}$ is selected to be part of the next generation, otherwise, $\mathbf{x_{target}}$ is kept. According to Storn and Price [5] it is recommended that the population has a size of 10 times the number of design variables, the crossover probability, CR, usually is chosen in the range [0,1] and the weight factor F is usually chosen in the interval [0,2]. In this paper CR was set as 0.8 and F was set as 0.9.

3.2 Ant Colony Optimization (ACO)

The Ant Colony Optimization method was proposed by Dorigo [6]. The native ants are capable of finding the shortest path from a food source to the nest without using visual cues. Also, they are capable of adapting to changes in the environment, for example finding a new shortest path once the old one is no longer feasible due to a new obstacle.

It is well-known that the main means used by ants to form and maintain the line is a pheromone trail. Ants deposit a certain amount of pheromone while walking, and each ant probabilistically prefers to follow a direction rich in pheromone rather than a poorer one. This elementary behaviour of real ants can be used to explain how they can find the shortest path which reconnects a broken line after the sudden appearance of an unexpected obstacle has interrupted the initial path.

In fact, once the obstacle has appeared, those ants which are just in front of the obstacle cannot continue to follow the pheromone trail and therefore they have to choose between turning right or left. In this situation one can expect half the ants to choose to turn right and the other half to turn left.

It is interesting to note that those ants which choose, by chance, the shorter path around the obstacle will more rapidly reconstitute the interrupted pheromone trail compared to those which choose the longer path. Hence, the shorter path will receive a higher amount of pheromone in the time unit and this will in turn cause a higher number of ants to choose the shorter path. Due to this positive feedback process, very soon all the ants will choose the shorter path.

www.EngineeringEBooksPdf.com

The ACO was developed initially for combinatorial optimization only. Particularly good results were obtained in the solution of the Problem of the Traveling Salesman [7]. The damage assessment problem deals with continuous variables. In this work an extension of the ACO algorithm applied to continuous variables is used [8-9]. A population of ants can be expressed in a matrix, where the rows represent the number of design variables in the problem. Each ant is referred as an individual and has numerical values associated with it. The path of each ant is related to the value of the objective function.

The pheromone trail corresponds to an amount of pheromone laid on the path by each ant. For the i-th dimension of the design space the pheromone trail, τ_i, is given by Equation (9), where x_i^* is the i-th coordinate of the best point found by the optimization task within the design space until the current iteration, σ_i is an index related to the aggregation of the population around the current minimum for the i-th coordinate of the design space and is given by Equation (10), where **z** is a vector corresponding to the i-th column of the population matrix and $\bar{\mathbf{z}}$ is the mean value of the vector **z**.

$$\tau_i(x) = e^{-\frac{\left(x - x_i^*\right)^2}{2\left(\sigma_i\right)^2}} \tag{9}$$

$$\sigma_i = \sqrt{\frac{1}{n_{pop} - 1}\sum_{j=1}^{n_{pop}}\left(z_j - \bar{z}\right)} \tag{10}$$

The updating process of the values of each design variable for all individuals is based on the probability distribution given by Equation (9). Also it can be seen that the concentration of pheromone increases in the area of the candidate to the optimum. This approach (also called as positive update) reinforces the probability of the choices that lead to good solutions. However, for avoiding premature convergence, negative update procedures are not discarded.

A simple method to perform negative update is by dissolving certain the amount of pheromone in the path. The idea of this scheme is to decrease the amount of pheromone by changing the current standard deviation (see Equation 10) for each variable. The dissolving rate affects the exploration capabilities, and consequently, the convergence of the algorithm. In the examples presented in this paper the same parameters were used in the ACO algorithm. In this investigation, the population size and the number of iterations considered for each example were equal to ten times the number of design variables.

4 DISCUSSION OF RESULTS

The methods described in the previous section were implemented using the MATLAB Code obtained from [10-11]. A finite element program [12] was used for response analysis. In this work the experimental results were synthetic which means that they were obtained from the analytical model (finite element model) considering the parameters corresponding to the damaged structure. Also noise that occurs in the experimental process was not considered. The flow between the various processors was controlled by a MATLAB main program.

This technique was applied to the steel trusses, see Figure 2 (a) and (b) for damage detection. For all the members in both structures the cross-sectional area is 12 cm² and the Young's Modulus 207 GPa. For the nine bar truss, Figure 2(a), the first four eigenmodes were used as experimental results for each damage simulation. For the fifteen bar truss, Figure 2(b) the measured response were the vertical static displacements obtained with the application of four vertical static loads of 10 kN on nodes 3, 5, 7 and 9.

The two optimizations techniques (DE and ACO) were used in the process of damage detection. Different levels of damage were simulated, from 10% until 90%, in both structures. Tables 1 and 2 show the results comparing both numeric techniques. In the nine bar truss, Figure 2(a), member 4 was damaged whereas in the fifteen bar truss, Figure 2(b), member 2 was damaged.

www.EngineeringEBooksPdf.com

Table 1: Results for the nine bar steel truss.

Element	10% damage		30% damage		50% damage		70% damage		90% damage	
	DE	ACO	DE	ACO	DE	ACO	DE	ACO	DE	ACO
1	0.0005	0.0000	0.0003	0.0000	0.0000	0.0000	0.0010	0.0000	0.0028	0.0013
2	0.0000	0.0000	0.0000	0.0000	0.0005	0.0000	0.0000	0.0000	0.0087	0.0001
3	0.0009	0.0003	0.0012	0.0002	0.0003	0.0001	0.0001	0	0.0062	0.0005
4	0.1008	0.0998	0.3002	0.2997	0.4958	0.5000	0.7010	0.7000	0.9018	0.8999
5	0.0001	0.0000	0.0000	0.0000	0.0001	0.0000	0.0007	0.0000	0.0006	0.0000
6	0.0001	0.0000	0.0006	0.0002	0.0000	0.0001	0.0035	0.0002	0.0030	0.0008
7	0.0001	0.0001	0.0002	0.0002	0.0093	0.0000	0.0005	0.0001	0.0035	0.0000
8	0.0001	0.0004	0.0000	0.0003	0.0009	0.0002	0.0001	0.0001	0.0028	0.0003
9	0.0001	0.0000	0.0000	0.0000	0.0007	0.0000	0.0002	0.0000	0.0004	0.0001
Objective Function	7.7E-15	1.3E-5	2.9E-15	3.5E-6	8.8E-13	1.4-E5	4.0E-14	3.2E-6	4.5E-13	7.3E-4

Table 2: Results for the fifteen bar steel truss.

Element	10% damage		30% damage		50% damage		70% damage		90% damage	
	DE	ACO	DE	ACO	DE	ACO	DE	ACO	DE	ACO
1	0.0007	0.0000	0.0002	0.0000	0.0002	0.0000	0.0005	0.0000	0.0067	0.0000
2	0.0945	0.0939	0.2994	0.2859	0.4993	0.5055	0.6981	0.6892	0.8998	0.8999
3	0.0087	0.0026	0.0004	0.0259	0.0004	0.0000	0.0091	0.0329	0.0091	0.0285
4	0.0006	0.0000	0.0000	0.0213	0.0001	0.0000	0.0137	0.0200	0.0007	0.0040
5	0.0005	0.0000	0.0001	0.0000	0.0008	0.0000	0.0000	0.0000	0.0016	0.0010
6	0.0002	0.0326	0.0006	0.0416	0.0002	0.0422	0.0006	0.0418	0.0184	0.0154
7	0.0037	0.0013	0.0000	0.0199	0.0002	0.0152	0.0003	0.0263	0.0000	0.0086
8	0.0149	0.0000	0.0019	0.0000	0.0262	0.0000	0.0470	0.0003	0.0029	0.0019
9	0.0001	0.0000	0.0001	0.0000	0.0002	0.0000	0.0044	0.0000	0.0002	0.0010
10	0.0000	0.0001	0.0000	0.0000	0.0005	0.0000	0.0013	0.0000	0.0042	0.0004
11	0.0103	0.0002	0.0001	0.1313	0.0000	0.0055	0.0163	0.2449	0.0185	0.0109
12	0.0004	0.0000	0.0000	0.0000	0.0000	0.0000	0.0027	0.0000	0.0003	0.0001
13	0.0000	0.0000	0.0000	0.0000	0.0000	0.0000	0.0014	0.0000	0.0000	0.0001
14	0.0007	0.0000	0.0000	0.0000	0.0010	0.0000	0.0000	0.0001	0.0000	0.0002
15	0.0001	0.0000	0.0000	0.0233	0.0001	0.0006	0.0067	0.1018	0.0095	0.0000
Objective Function	2.2E-11	1.3E-8	8.3E-13	8.3E-9	6.1E-12	1.2E-8	3.1E-10	7.7E-9	4.1E-10	1.2E-8

It must be emphasized that in general, both methods performed very well. The location and level of damaged in all cases were detected correctly. The Differential Evolution was more efficient. The results were more accurate with less computational effort. In some cases the Ant Colony Optimization detected damage in good members as occurred in member 11 of the fifteen bar truss for some cases of damage.

5 CONCLUSIONS

The paper presented an approach for damage detection using a system identification technique that results in a nonlinear optimization problem. Two global optimization methods were used: Differential Evolution (DE) and Ant Colony Optimization (ACO). Reduced set of eigenmodes and static displacements were used as experimental data in the identification procedure. The methods were applied to simple steel truss structures with different levels of damage and presented promising results. Both optimization techniques performed well identifying the location and extent of damage very clearly. The Differential Evolution method was more efficient presenting more accurate results with less computational effort. An extension of this work is to study the application of the present approach to large truss structures and to other types of structures such as beams, plates and shells.

www.EngineeringEBooksPdf.com

6 ACKNOWLEDGEMENTS

The authors gratefully acknowledge the financial support provided by the Brazilian National and State Scientific and Technological Supporting Agencies: CNPq, CAPES and FAPERJ.

REFERENCES

[1] Hajela, P. and Soeiro, F. J. C. P., "Recent Developments in Damage Detection Based on System Identification Methods", Structural Optimization, 1990.

[2] Hajela, P. and Soeiro, F. J. C. P., "Structural Damage Detection Based on Static and Modal Analysis", AIAA Journal, 1990.

[3] Soeiro, F. J. C. P. and Hajela, P., "Locating Damage in a Truss Structure Using Identification Techniques: an Experimental Investigation", Journal of the Brazilian Society of Mechanical Sciences, 1992.

[4] Storn, R. and Price, K., "Differential Evolution - a Simple and Efficient Heuristic for Global Optimization over Continuous Spaces", Journal of Global Optimization, Kluwer Academic Publishers, 1997.

[5] Storn, R., Price, K. and Lampinen, J., "Differential Evolution - A Practical Approach to Global Optimization", Springer-Verlag, Natural Computing Series, Berlin Heidelberg, 2005.

[6] Dorigo, M., "Optimization, Learning and Natural Algorithms", PhD thesis, Politecnico di Milano, Italy, 1992,

[7] Dorigo, M. and Gambardella, L. M., "Ant Colony System: A Cooperative Learning Approach to the Traveling Salesman Problem", IEEE Transactions on Evolutionary Computation, 1997.

[8] Pourtakdoust, S. H. and Nobahari, H., "An Extension of Ant Colony System to Continuous Optimization Problems", Lecture Notes in Computer Science, 2004.

[9] Socha, K., "ACO for Continuous and Mixed-Variable Optimization", Lecture Notes in Computer Science, 2004.

[10] Storn, R. and Price, K., "Differential Evolution (DE) for Continuous Function Optimization", http://www.icsi.berkeley.edu/~storn/code.html, 2009.

[11] Viana, F.A.C., "Simple Optimization Toolbox", <http://fchegury.googlepages.com/>, University of Florida, 2008.

[12] Kwon, Y. W. and Bang, H. C., "The Finite Element Method Using MATLAB", 2nd Ed. CRC Press, Boca Raton, Fl., 2000.

www.EngineeringEBooksPdf.com

www.EngineeringEBooksPdf.com

SDSS'Rio 2010 STABILITY AND DUCTILITY OF STEEL STRUCTURES
E. Batista, P. Vellasco, L. de Lima (Eds.)
Rio de Janeiro, Brazil, September 8 - 10, 2010

FREE AND FORCED NONLINEAR VIBRATION OF STEEL FRAMES WITH SEMI-RIGID CONNECTIONS

Andréa R.D. Silva*, Ricardo A.M. Silveira*, Alexandre S. Galvão and Paulo B. Gonçalves*****

* Department of Civil Engineering, School of Mines, Federal University of Ouro Preto
e-mails: andreadiassilva@yahoo.com.br, ricardo@em.ufop.br

** Fluminense Federal University, Campus of Volta Redonda
e-mail: asgalvao@vm.uff.br

*** Department of Civil Engineering, Pontifical Catholic University of Rio de Janeiro
e-mail: paulo@puc-rio.br

Keywords: Structural stability, Nonlinear vibration, Pre-loaded structures, Semi-rigid connections.

Abstract. *The increasing slenderness of structural frames makes them more susceptible to vibration and buckling problems. The present work studies the free and forced nonlinear vibrations of steel frames with semi-rigid connections. Special attention is given to the influence of static pre-load on the natural frequencies and mode shapes, nonlinear frequency-amplitude relations, and resonance curves. These results are obtained using a nonlinear finite element program for static and dynamic analysis of steel frames. Two structural systems with important practical applications are analyzed, namely: a shallow arch and a pitched-roof steel frame. The results show the importance of the static pre-load and the stiffness of the semi-rigid connection on the buckling and vibration characteristics of these structures.*

1 INTRODUCTION

During the last ten years, studies and research have concentrated on the vibration problems of structures subjected to dynamic loads. This has brought significant advance in the civil construction industry, where new techniques and materials have been either developed or improved. Maybe the largest contributor to this advance is the use of more precise numerical computational tools, whose models permit realistic simulation and resolution of structural problems. Today, with all these advances, it is possible to design more streamline and flexible buildings. However, this makes them more susceptible to the effects of dynamic actions, creating ever-growing problems. This can be observed in the technical literature where failures involving from localized damage to total structural collapse are described. There are also cases of vibration-related discomfort experienced by users, even when there is no structural damage. Because of this, nonlinear dynamic analysis of slender steel structures is ever more relevant.

In most reports on linear and nonlinear structural vibrations, it is assumed that the system is free of loading and that a dynamic load is suddenly applied for a given time duration. This may lead to erroneous results when slender structures susceptible to buckling are investigated. Simitses [1] discussed the effects of static preloading on the dynamic stability of structures. The effect of static pre-load on the structure's dynamics has also been studied by Wu and Thompson [2], and Zeinoddini et al. [3], among others. The interplay between buckling and vibration has been the subject of some previous papers [3-6]. These studies show that compressive stress states decrease the structure's natural frequencies and may even change the mode shapes associated with the lowest natural frequencies [5]. They also decrease the effective stiffness and consequently increase the vibration amplitudes, which may weaken or even damage the structure. Finally, shifting the natural frequencies to a lower frequency range may increase resonance

www.EngineeringEBooksPdf.com

problems due to environmental loads. Solutions to these vibration problems usually require the use of costly control systems or changes in the structural design [7].

Transient linear and nonlinear analysis of beams and frames with semi-rigid connections, as well as the study of vibratory problems associated with these structural systems, can also be found in publications by Chan and Chui [8], Sophianopoulos [9] and Sekulovic et al. [10].

The aim of the present work is to conduct, using the nonlinear finite element program CS-ASA (Computational System for Advanced Structural Analysis, Silva [11]), a dynamic analysis of steel frames and to study the influence of second-order effects generated by large displacements and rotations, connection flexibility, and pre-stress states on the nonlinear response of slender steel structures.

2 THE FREE VIBRATION PROBLEM

The geometric nonlinear finite element formulation for frames with rigid connections implemented in the CS-ASA is based on work by Yang and Kuo [12]. The consideration of semi-rigid connections is based on the formulations proposed by Chan and Chui [8] and Sekulovic et al. [10].

In the finite element method context, the equilibrium of any structural system can be expressed as:

$$\mathbf{F}_i(\mathbf{U}) = \lambda \mathbf{F}_r \tag{1}$$

where $\mathbf{F}_i$ is the internal forces vector, function of the generalized displacement vector $\mathbf{U}$, λ is a load factor, and $\mathbf{F}_r$ is a fixed reference vector defining the direction and distribution of the applied loads.

To obtain the nonlinear equilibrium path of a structure, an incremental technique for the response is used to solve the equation system (1). This procedure basically consists of calculating a sequence of incremental displacements, $\Delta\mathbf{U}_i$, that correspond to a sequence of given load increments, $\Delta\lambda_i$. However, as $\mathbf{F}_i$ is a nonlinear function of $\mathbf{U}$, the estimated solution for the problem (predicted solution: $\Delta\lambda^0$, $\Delta\mathbf{U}^0$) for each load step normally does not satisfy (1). Consequently, a residual force vector $\mathbf{g}$ is defined. If this residual force vector does not satisfy the convergence criteria, a new estimate for $\mathbf{U}$ is obtained.

The vibration frequency analysis is crucial in the stability analysis of structural systems with strongly nonlinear equilibrium paths, and the dynamic stability criterion can be used to define the type of the equilibrium configuration. So, the vibration frequencies and the corresponding modes of vibration in a structure can be obtained by solving the following eigenvalue problem:

$$(\mathbf{K} - \omega^2\mathbf{M})\boldsymbol{\phi} = \mathbf{0} \tag{2}$$

where $\mathbf{K}$ is the tangent stiffness matrix of the structural system, $\mathbf{M}$ is the mass matrix, ω is the natural frequency, and $\boldsymbol{\phi}$ is the vibration mode vector. The influence of static preloading and semi-rigid connections on structural system vibration modes and natural frequencies is studied here. The static preloading effect is related with the presence of axial force on bars and its inclusion is made considering the geometric stiffness matrix as part of $\mathbf{K}$ in (2); the semi-rigid connections influence is included evaluating the joint stiffness at the assumed load level and consequently changing the linear stiffness matrix. However, as the geometric nonlinearity and the connection flexibility effects are considered, the solution to the equation (2) cannot be obtained directly. Table 1 illustrates the step-by-step numerical procedures for solving the static nonlinear problem and, subsequently, calculating the natural frequencies and vibration modes of the loaded structure. This algorithm illustrates that for each load step the equation (2) is solved considering the structural stiffness change due the initial stress (preloading).

3 NONLINEAR TRANSIENT ANALYSIS

The nonlinear time response of the structure can be obtained by solving the following set of discrete equations of motion:

$$\mathbf{M}\ddot{\mathbf{U}} + \mathbf{C}\dot{\mathbf{U}} + \mathbf{F}_i(\mathbf{U}) = \lambda(t)\mathbf{F}_r \tag{3}$$

www.EngineeringEBooksPdf.com

Table 1: Numerical strategy for free vibration analysis of pre-loaded frames.

1. Input the material and geometric properties of the frame
2. Obtain the reference force vector $\mathbf{F}_r$
3. Displacement and load parameter in the actual equilibrium configuration: ${}^t\mathbf{U}$ and ${}^t\lambda$
4. INCREMENTAL TANGENT SOLUTION: $\Delta\lambda^0$ and $\Delta\mathbf{U}^0$
  4a. Calculate the tangent stiffness matrix **K**
  4b. Solve: $\delta\mathbf{U}_r = \mathbf{K}^{-1}\mathbf{F}_r$
  4c. Define $\Delta\lambda^0$ with a determined strategy for the load increment [11]
  4d. Calculate: $\Delta\mathbf{U}^0 = \Delta\lambda^0\delta\mathbf{U}_r$
  4e. Update the variables in the new equilibrium configuration $t + \Delta t$:
    ${}^{(t+\Delta t)}\lambda = {}^t\lambda + \Delta\lambda^0$ and ${}^{(t+\Delta t)}\mathbf{U} = {}^t\mathbf{U} + \Delta\mathbf{U}^0$
5. NEWTON-RAPHSON ITERATION: k = 1, 2,3,...
  5a. Calculate the internal forces vector: ${}^{(t+\Delta t)}\mathbf{F}_i^{(k-1)} = {}^t\mathbf{F}_i + \mathbf{K}\Delta\mathbf{U}^{(k-1)}$
  5b. Calculate the unbalanced forces vector: $\mathbf{g}^{(k-1)} = {}^{(t+\Delta t)}\lambda^{(k-1)}\mathbf{F}_r - {}^{(t+\Delta t)}\mathbf{F}_i^{(k-1)}$
  5c. Verify the convergence: $\|\mathbf{g}^{(k-1)}\| / \left({}^{(t+\Delta t)}\lambda^{(k-1)}\mathbf{F}_r\right) \le \xi$, with ξ being the tolerance factor.
    YES: *Stop the iteration cycle and go to item 5h*
  5d. Obtain $\delta\lambda^k$ using an iteration strategy [11]
  5e. Determine $\delta\mathbf{U}^k = \delta\mathbf{U}_g^k + \delta\lambda^k\,\delta\mathbf{U}_r^k$, with $\delta\mathbf{U}_g^k = -\mathbf{K}^{-1(k-1)}\mathbf{g}^{(k-1)}$ and $\delta\mathbf{U}_r^k = \mathbf{K}^{-1(k-1)}\mathbf{F}_r$
  5f. Update the load parameters, λ, and the nodal displacement vector, **U**:
    a) *Increments*: $\Delta\lambda^k = \Delta\lambda^{(k-1)} + \delta\lambda^k$ and $\Delta\mathbf{U}^k = \Delta\mathbf{U}^{(k-1)} + \delta\mathbf{U}^k$
    b) *Totals*: ${}^{(t+\Delta t)}\lambda^k = {}^t\lambda + \Delta\lambda^k$ and ${}^{(t+\Delta t)}\mathbf{U}^k = {}^t\mathbf{U} + \Delta\mathbf{U}^k$
  5g. Return to step 5
  5h. Determine the natural frequencies and the associated vibrations modes:
    a) Update the tangent stiffness matrix **K** and the mass matrix **M**
    b) Decompose **M** by the the Cholesky method: $\mathbf{M} = \mathbf{S}^T\mathbf{S}$ and obtain $\mathbf{A} = (\mathbf{S}^{-1})^T\mathbf{K}\mathbf{S}^{-1}$
    c) Solve the eigenvalue problem $\mathbf{AX} = \lambda\mathbf{X}$ by using the Jacobi Method, obtaining the eigenvalues (ω^2) and the eigenvectors (vibration modes)
6. CONSIDER NEW LOAD INCREMENT AND RETURN TO STEP 4

where **M** and **C** are the mass and viscous damping matrices, respectively, and $\mathbf{F}_i$ is the internal force vector that depends on the displacement vector **U** of the system, $\dot{\mathbf{U}}$ and $\ddot{\mathbf{U}}$ are the velocity and acceleration vectors, respectively, and $\lambda(t)\mathbf{F}_r$ is the external excitation vector.

The solution of the nonlinear dynamic system (3) can be obtained through a time integration algorithm together with adaptive strategies for the automatic increment of the time step. The numerical methodology used here is presented in table 2. Details of the nonlinear dynamic formulation as well as the computational program are found in Silva [11].

3.1 Nonlinear Vibration Analysis

The nonlinear frequency-amplitude relation provides fundamental information on the nonlinear vibration analysis of any structural system, and it gives a good indication of the type (hardening or softening) and degree of nonlinearity of the system. Here the methodology proposed by Nandakumar and Chatterjee [13] is used to obtain this relation using the finite element method. First, the nonlinear equations of motion are numerically integrated (table 2), and the time response of the slightly damped system is obtained for a chosen node. Then, the maximum amplitude and corresponding period between two consecutive positive peaks are computed at each cycle. Consider two successive peaks at times $t_{(i)}$ and $t_{(i+1)}$ (see figure 1). Let their average value be d_{1m} and let the trough between these two positive peaks be d_2. Then, the amplitude can be defined by:

www.EngineeringEBooksPdf.com

$$d_i = 1/2\left(d_{1m(i)} + \left|d_{2(i)}\right|\right) \tag{4}$$

and the frequency as $f_i = 1/T_i$, with $T_i = t_{(i+1)} - t_{(i)}$. The resulting amplitude and frequency values are plotted to give the frequency-amplitude relation. To obtain the peak amplitudes with the necessary accuracy, a small time step must be imposed in the integration process. In addition, a large number of elements are necessary to describe accurately the large amplitude response of the structure.

Table 2: Numerical strategy for nonlinear transient analysis.

1. Input the material and geometric properties of the frame, and obtain the force vector $\mathbf{F}_r$

2. Start the initial displacement, velocity and acceleration vectors, ${}^0\mathbf{U}$, ${}^0\dot{\mathbf{U}}$ and ${}^0\ddot{\mathbf{U}}$

3. FOR EACH TIME STEP $t + \Delta t$

3a. Derive the tangent stiffness, mass and damping matrices: **K**, **M**, and **C**

3b. Using Newmark parameters β and γ, calculate the constants:

$a_0 = 1/\left(\beta\Delta t^2\right)$; $a_1 = \gamma/\left(\beta\Delta t\right)$; $a_2 = 1/\left(\beta\Delta t\right)$; $a_3 = 1/\left(2\beta\right) - 1$; $a_4 = \gamma/\beta - 1$;

$a_5 = \Delta t\left(\gamma/\left(2\beta\right) - 1\right)$; $a_6 = a_0$; $a_7 = -a_2$; $a_8 = -a_3$; $a_9 = \Delta t\left(1 - \gamma\right)$; $a_{10} = \alpha\Delta t$

3c. Form the effective stiffness matrix: $\hat{\mathbf{K}} = \mathbf{K} + a_0\mathbf{M} + a_1\mathbf{C}$

3d. Calculate: $\hat{\mathbf{F}} = {}^{(t+\Delta t)}\lambda\mathbf{F}_r + \mathbf{M}\left(a_2\,{}^t\dot{\mathbf{U}} + a_3\,{}^t\ddot{\mathbf{U}}\right) + \mathbf{C}\left(a_4\,{}^t\dot{\mathbf{U}} + a_5\,{}^t\ddot{\mathbf{U}}\right) - {}^t\mathbf{F}_i$

3e. Solve for displacement increments: $\hat{\mathbf{K}}\Delta\mathbf{U} = \hat{\mathbf{F}}$

4. NEWTON-RAPHSON ITERATION: k = 1, 2,3,...

4a. Evaluate the approximation of the acceleration, velocities and displacements:

${}^{(t+\Delta t)}\ddot{\mathbf{U}}^k = a_0\Delta\mathbf{U}^k - a_2\,{}^t\dot{\mathbf{U}} - a_3\,{}^t\ddot{\mathbf{U}}$; ${}^{(t+\Delta t)}\dot{\mathbf{U}}^k = a_1\Delta\mathbf{U}^k - a_4\,{}^t\dot{\mathbf{U}} - a_5\,{}^t\ddot{\mathbf{U}}$; ${}^{(t+\Delta t)}\mathbf{U}^k = {}^t\mathbf{U} + \Delta\mathbf{U}^k$

4b. Update the geometry of the frame

4c. Evaluate the internal forces vector: ${}^{(t+\Delta t)}\mathbf{F}_i^k = {}^t\mathbf{F}_i + \mathbf{K}\Delta\mathbf{U}^k$

4d. Form: ${}^{(t+\Delta t)}\mathbf{R}^{(k+1)} = {}^{(t+\Delta t)}\lambda\mathbf{F}_r - \left(\mathbf{M}\,{}^{(t+\Delta t)}\ddot{\mathbf{U}}^k + \mathbf{C}\,{}^{(t+\Delta t)}\dot{\mathbf{U}}^k + {}^{(t+\Delta t)}\mathbf{F}_i^k\right)$

4e. Solve for the corrected displacement increments $\hat{\mathbf{K}}\delta\mathbf{U}^{(k+1)} = {}^{(t+\Delta t)}\mathbf{R}^{(k+1)}$

4f. Evaluate the corrected displacement increments: $\Delta\mathbf{U}^{(k+1)} = \Delta\mathbf{U}^k + \delta\mathbf{U}^{(k+1)}$

4g. Check the convergence of the iteration process:

$\left\|\Delta\mathbf{U}^{(k+1)}\right\| / \left\|{}^t\mathbf{U} + \Delta\mathbf{U}^{(k+1)}\right\| \le \xi$, where ξ is a tolerance factor **NO**: Go to 4

4h. Calculate the acceleration, velocities and displacements at time $t + \Delta t$

${}^{(t+\Delta t)}\ddot{\mathbf{U}}^{(k+1)} = a_0\Delta\mathbf{U}^{(k+1)} - a_2\,{}^t\dot{\mathbf{U}} - a_3\,{}^t\ddot{\mathbf{U}}$; ${}^{(t+\Delta t)}\dot{\mathbf{U}}^{(k+1)} = a_1\Delta\mathbf{U}^{(k+1)} - a_4\,{}^t\dot{\mathbf{U}} - a_5\,{}^t\ddot{\mathbf{U}}$

${}^{(t+\Delta t)}\mathbf{U}^{(k+1)} = {}^t\mathbf{U} + \Delta\mathbf{U}^{(k+1)}$

5. FOR THE NEXT TIME STEP

5a. Evaluate the internal forces vector: ${}^{(t+\Delta t)}\mathbf{F}_i^{(k+1)} = {}^t\mathbf{F}_i + \mathbf{K}\Delta\mathbf{U}^{(k+1)}$

5b. Select a new time step Δt (adaptative strategy)

3.2 Resonance Analysis

Low-dimensional numerical models employ relatively easy techniques for obtaining nonlinear resonance curves. In contrast, it is computationally difficult to obtain these curves for structural systems with a large number of degrees of freedom. Here, a simple repetitive procedure coupled with the integration method is implemented, which consists in giving constant excitation-frequency increments $\Delta\Omega$ and, for each incremental step, integrate the differential equations of motion during N harmonic excitation cycles. The response of the initial cycles associated with the short transient response is

www.EngineeringEBooksPdf.com

dismissed, and the maximum amplitude of the steady-state solution is plotted as a function of the forcing frequency. Of course, this brute force method is unable to obtain unstable branches of resonance curves or all co-existing stable solutions.

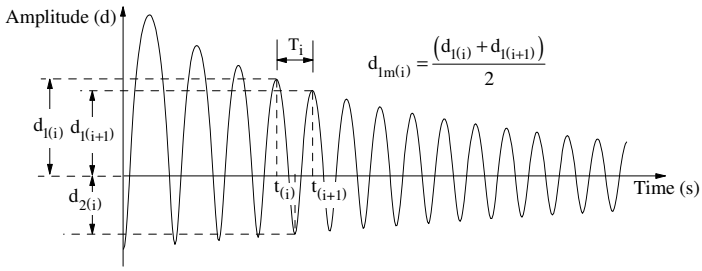


Figure 1: Procedure for obtaining the displacements d_i and the frequency f_i.

4 NUMERICAL EXAMPLES

4.1 Shallow arch

Slender arches are structures that may present, depending on the support conditions and the type and intensity of loading, a highly nonlinear structural behavior. The dynamic response of these arches has been extensively analyzed due to their practical applications. This subsection analyzes the sinusoidal arch under vertical distributed load P presented in figure 2 [14].

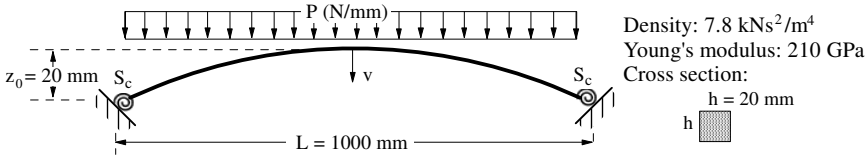


Figure 2: Arch with semi-rigid joints: geometry and loading.

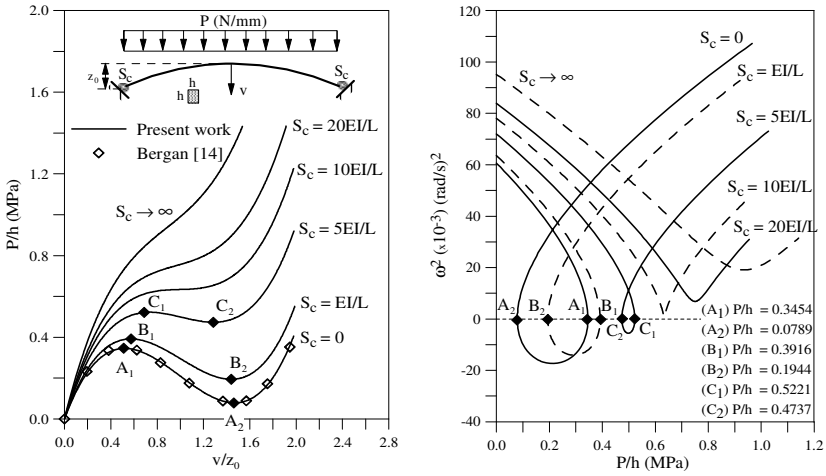
Figure 3a shows the arch equilibrium paths for different support rotation stiffness S_c. For more flexible connections the presence of two limits points in the equilibrium path is observed which disappears as the stiffness of the supports increase. The curve obtained for the simply supported arch, $S_c = 0$, is compared with the analytical solution provided by Bergan [14].

Figure 3b shows the nonlinear relation between the load P and the lowest natural frequency considering increasing support stiffness. The curves show not only the influence of static pre-loading in the natural frequencies, but also indicate, in accordance with the dynamic instability criterion, the stable and unstable equilibrium configurations along of the equilibrium paths. Based on this criterion, the unstable parts ($\omega^2 < 0$) are located between the points A_1, A_2, B_1, B_2, C_1 and C_2.

Figure 4a illustrates the nonlinear relation between the frequency and the free vibration amplitude of the arch. To obtain such a response, a damping rate equal to 0.01 and a constant time step equal to 10^{-5} is considered. Three different support conditions are studied: pinned ($S_c = 0$), perfectly rigid ($S_c \to \infty$) and semi-rigid ($S_c = 10\ EI/L$). In all three situations, the arch displays initially hardening behavior, i.e., the frequency increases with increasing vibration amplitudes. However, for large vibration amplitudes a softening behavior is observed which is more pronounced for the pinned arch. The natural frequencies, in Hz, for each arch (rigid, semi-rigid and pinned) is indicated by a dashed line. The dynamic response of the pinned arch under a uniformly distributed harmonic excitation, $P = A_p \sin(\Omega t)$, is investigated next. Figure 4b shows the variation of the maximum and minimum amplitude of the steady-state response, v/z_0, as a function of the forcing frequency parameter Ω/ω_a ($\omega_a = 238.4$ rad/s) for different amplitudes of the

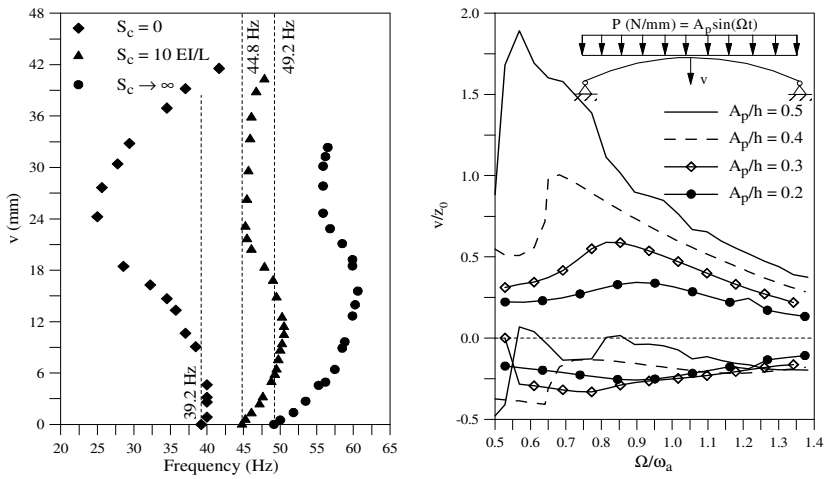
www.EngineeringEBooksPdf.com

harmonic excitation, A_p/h. When the excitation magnitude increases, the resonance peaks move sharply to the lower frequency range, indicating a strong softening behavior in agreement with the frequency-amplitude relation shown in figure 4a. This behavior is also compatible with the type of nonlinearity observed in the system's static solution. As is typical of nonlinear systems, the resonance curve begins to bend at $A_p/h = 0.4$ in a region of low frequencies, which produces more than one permanent solution for the same frequency value. When the magnitude of excitation reaches $A_p/h = 0.5$, the amplitude increases considerably in the low frequency region up to the point where the arch loses stability and inverts its concavity.



(a) Nonlinear equilibrium paths (b) Natural frequency-load relation

Figure 3: Static analysis and influence of static pre-load on the lowest natural frequency.



(a) Frequency-amplitude relation (b) Resonance curves

Figure 4: Nonlinear vibration and resonance analysis for selected values of the connection stiffness S_c.

4.2 Pitched-roof steel frame

The numerical strategy developed is now applied to the analysis of a pitched-roof frame with beam-column flexible joints, as shown in figure 5. Twenty finite elements are used here to model the structure.

www.EngineeringEBooksPdf.com

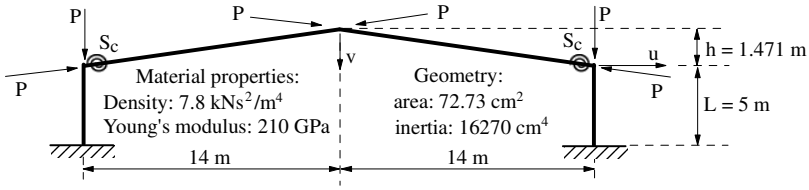
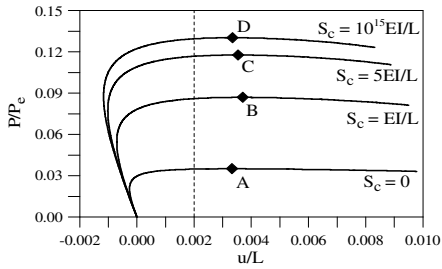
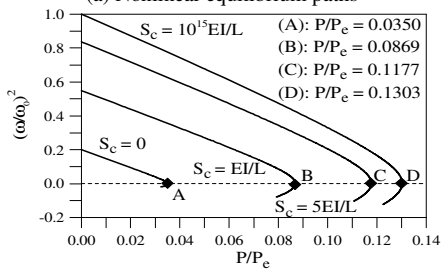


Figure 5: Pitched-roof frame: geometry and loading.

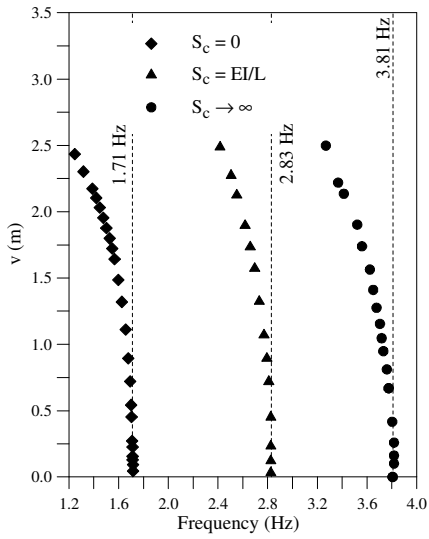
Figure 6a shows the nonlinear equilibrium paths for increasing values of the joint stiffness S_c. The nonlinear relation between the load and the natural frequencies for different values of joint stiffness is given in figure 6b. The applied load is non-dimensionalized by the Euler load $P_e = \pi^2 EI/L^2$, and the frequencies are non-dimensionalized by the lowest free vibration frequency of the unloaded frame with rigid connections, $\omega_0 = 23.912$ rad/s. The non-linear paths display a limit load (points *A*, *B*, *C* and *D)* as shown in figure 6a. Figure 6b shows the variation of the lowest natural frequency with the applied load. The almost linear relation between the square of the frequency of the pre-loaded structure and the applied load can be used to evaluate the buckling load through at least two experimental values of the lowest frequency for two small load levels. Finally, figure 6c shows the frequency-amplitude relation of the pitched-roof for three selected values of the beam-column joints stiffness. The relation is almost linear for small-to-medium amplitude oscillations and of the softening type when very large vibration amplitudes occur, which is outside the range of practical applications.



(a) Nonlinear equilibrium paths



(b) Natural frequency-load relation



(c) Nonlinear frequency-amplitude relation

Figure 6: Static and vibration analysis of the pitched-roof steel frame.

5 CONCLUSION

The results presented in this paper indicate that the precise evaluation of the connection stiffness, a key point in the design of steel structures, is essential for the calculation of critical conditions. This is particularly important for practical application where damage usually occurs at the connections, decreasing their stiffness and radically changing the nonlinear behavior of the frame. The results also

www.EngineeringEBooksPdf.com

indicate that the loss of stiffness of a connection during the service life of the structure may significantly affect the structural behavior under both static and dynamic loads. This is in agreement with the literature describing structural failures due to support deterioration. In some cases, a slow decrease in the joint stiffness S_c value can change the overall stiffness of the structure and its dynamic characteristics, and this can only be detected and quantified by detailed nonlinear behavior analyses of the structure. Finally, the results also showed the influence of the static pre-loading on the natural frequencies and the nonlinear frequency-amplitude relation of the analyzed structural systems.

Acknowledgment

The authors wish express their gratitude to CAPES, CNPq, FAPEMIG and FAPERJ for the financial support received in the development of this research.

REFERENCES

[1] Simitses, G.J., "Effect of static preloading on the dynamic stability of structures", *AIAA Journal*, **21**(8), 1174-1180, 1983.

[2] Wu, T.X. and Thompson, D.J., "The effects of local preload on the foundation stiffness and vertical vibration of railway track", *Journal of Sound and Vibration*, **219**(5), 881-904, 1999.

[3] Zeinoddini, M., Harding, J.E., Parke, G.A.R., "Dynamic behaviour of axially pre-loaded tubular steel members of offshore structures subjected to impact damage", *Ocean Engineering*, **26**(10), 963-978, 1999.

[4] Gonçalves, P.B., "Axisymmetric vibrations of imperfect shallow spherical caps under pressure loading", *Journal of Sound and Vibration*, **174**(2), 249-260, 1994.

[5] Nieh, K.Y., Huang, C.S., Tseng, Y.P., "An analytical solution for in-plane free vibration and stability of loaded elliptic arches", *Computers & Structures*, **81**(13), 311-1327, 2003.

[6] Xu, R. and Wu, Y-F., "Free vibration and buckling of composite beams with interlayer slip by two-dimensional theory", *Journal of Sound and Vibration*, **313**(3-5), 875-890, 2008.

[7] Soong, T.T. and Dargush, G.F., *Passive Energy Dissipation Systems in Structural Engineering*, John Wiley & Sons, Chichester, 1997.

[8] Chan, S.L. and Chui, P.P.T., *Nonlinear Static and Cyclic Analysis of Steel Frames with Semi-Rigid Connections*, Elsevier, Kidlington, UK, 2000.

[9] Sophianopoulos, D.S., "The effect of joint flexibility on the free elastic vibration characteristics of steel plane frames", *Journal of Constructional Steel Research*, **59**(8), 995-1008, 2003.

[10] Sekulovic, M., Salatic, R., Nefovska, M., "Dynamic analysis of steel flexible connections", *Computers & Structures*, **80**, 935–955, 2002.

[11] Silva, A.R.D., *Computational System for Advanced Static and Dynamic Analysis of Steel Structures*, D.Sc. Thesis, PROPEC/Deciv/UFOP, Ouro Preto, Brazil, 2009 (in Portuguese).

[12] Yang, Y.B. and Kuo, S.B., *Theory and Analysis of Nonlinear Framed Structures*, Prentice Hall, 1994.

[13] Nandakumar, K. and Chatterjee, A., "Resonance, parameter estimation, and modal interactions in a strongly nonlinear benchtop oscillator", *Nonlinear Dynamics*, **40**, 149-167, 2005.

[14] Bergan, P.G., "Solution algorithms for nonlinear structural problems", *Computers & Structures*, **12**, 497-509, 1980.

www.EngineeringEBooksPdf.com

SDSS'Rio 2010 STABILITY AND DUCTILITY OF STEEL STRUCTURES
E. Batista, P. Vellasco, L. de Lima (Eds.)
Rio de Janeiro, Brazil, September 8 - 10, 2010

STATIC AND DYNAMIC BEHAVIOR OF LENS-TYPE SHEAR PANEL DAMPERS FOR HIGHWAY BRIDGE BEARING

Tatsumasa Takaku, Feng Chen*,

Takashi Harada, Masayuki Ishiyama, Nobuhiro Yamazaki,**

Tetsuhiko Aoki*, and Yuhshi Fukumoto******

* Toko Engineering Consultants, Ltd., Tokyo, Japan. e-mails: takakus@tokoc.co.jp

** Nippon Chuzo Co., Ltd, Kawasaki, Japan. e-mail: n_yamazaki@nipponchuzo.co.jp,

*** Aichi Institute of Technology, Toyota, Japan. e-mail: aoki@aitech.ac.jp

**** Osaka University, Osaka, Japan. e-mail: yushi@mx3.mesh.ne.jp

Keywords: Shear Panel Damper, Low-yield Steel, Seismic Design, Dynamic Test, Bridge Bearing

Abstract. *This paper describes a lens-type shear panel damper newly developed for highway bridge bearing. It has the form of concave lens shape made of low-yield steel LY 100. Both low yield strength and high ductility are the major requirements for damping devices. Response by static and dynamic shear tests results in rectangular shape of load-displacement hysteretic loops with high quality damping. Failure at the ultimate state highly depends on the cumulative deformation capacity of panel. Damage and life cycles can be estimated by Miner's rule. The analytical estimates agree well with the test findings. Large deformation of steel with high speed strain rate generates a lot of heat leading to high temperature of 300~400 ℃ on surface. Earthquake energy is converted to both strain and heat energies which results in large energy dissipation.*

1 INTRODUCTION

The writers have investigated the performance of shear panel dampers made of low-yield steel LY 100 for bridge bearings, and static and dynamic tests have been conducted on a half size model of prototype to examine the fundamental properties of the damper [1]-[3]. This paper includes a seismic design methodology for the lens-type shear damper under several seismic excitations of Level 2 earthquakes specified in the code [4]. Random loading tests have been conducted to evaluate the structural and functional performance of the damper under the design level earthquakes and to determine the safety margin against collapse under exceedingly big earthquakes. For fracture evaluation, two types of prediction analysis, damage index method and damage pass method, are proposed.

2 DAMPERS, SPECIMENS AND TEST SETUP

2.1 Lens-type shear panel damper and half size model (Fig. 1)

Fig. 1 illustrates the panel details of a half size model of prototype for test use. In general, a damper system is composed of several components and the failure mechanism is rather complicated. The proposed shear panel consists of a single plate element only, and the failure mode is limited inside of the panel. In order to get a better damping performance, the panel details are modified according to the test results.

www.EngineeringEBooksPdf.com

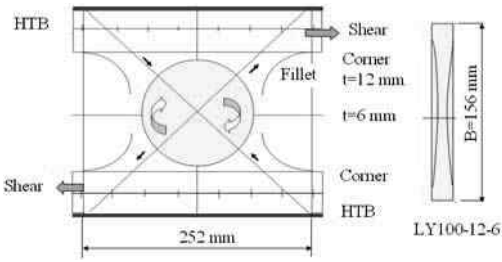


Fig. 1: Lens- type shear panel damper: Panel shape and connection

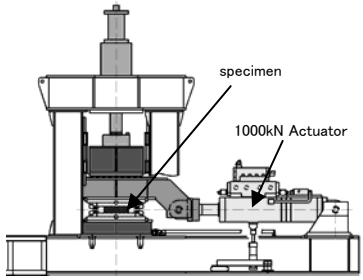


Fig. 2: Test setup

2.2 Specimens and test setup (Fig. 2, Table 1, and Table 2)

Measured and nominal properties of the low-yield steel of JFE-LY100 are listed in Tables 1 and 2. Test setup is shown in Fig. 2. Cyclic lateral load is applied to the upper setup beam. The max. capacity of an actuator is 250 mm in stroke, 1200mm/s in velocity and 1000KN in load. Friction type HTB and a shear key with small clearance of 0.5mm between sole plates, allowing small rotation, are used to connect the lower and upper setup beams.

Table 1 Measured mechanical properties of LY100-12-6

Yield stress(0.2%strain) σy	80 N/mm2
yield displacement(shear strain 3.2%) δy	5 mm
yield shear stress τy=σy/√3	46.2 N/mm2
yield strenght Qy (at lens center,t=6mm)	66.1 KN
yield strenght Qy (at panel edge,t=12mm)	86.5 KN
Max.shear Qmax (at base with fillet)	245 KN
Qmax/Qy	2.80～2.87
δmax/δy	8～10
δ max	40～50 mm

Table 2 Mechanical properties of low yield steel (JFE LY100, nominal) LY100-12-6

Steel grade	LY-100
Yield strength	80～120 N/mm^2
Tensile strength	200～300 N/mm^2
Yield ratio	<60%
Elongation	>50%
Charpy value (at 0℃)	>27 J
Panel size、B/t	156x156x12mm,13
Concave lens (diameter, t)	130mm、t=6～12mm
Fillets	R=4t=48mm

3 STATIC AND DYNAMIC LOADING TESTS

3.1 Static tests: Gradually increased loading (δy to 10δy, shear strain 3.2% to 32%, and Table 4)

The increment of shear displacement in each cycle was ±δy, where δy=5mm was the shear yield displacement corresponding to the 0.2% offset yield shear stress of LY100 (Table 1).The displacement cycles were imposed until collapse at the final stage. One cycle was equivalent to shear strain of 3.2%. In the static loading tests, 10δy which was equivalent to the shear strain of 32% were recorded at the final stage, where severe cracking damage with large out-of plane twisted deformation was observed. The specimens left residual deformation after tests.

3.2 Sinusoidal loading tests: Harmonic motion of Sine wave with constant amplitudes.

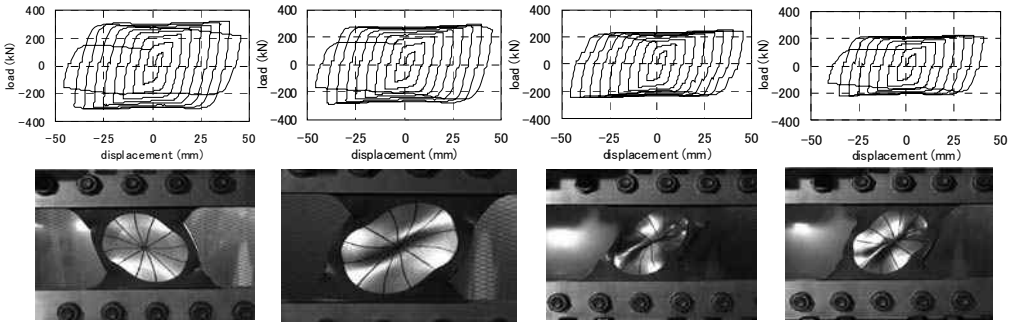
Six kinds of amplitudes (5, 10, 20, 30, 35, and 40mm) and four kinds of velocity (slow and time periods of 0.5, 1.0, and 2.0 sec) were combined as test parameters. Slow speed was equivalent to static loading.

4 FUNDAMENTALS OF LENS-TYPE SHEAR PANEL: STATIC AND DYNAMIC TEST RESULTS

www.EngineeringEBooksPdf.com

4.1 Lens behavior-1: Concave depth and failure modes (Fig. 3), "Lens makes for flexibility"

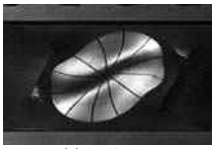
In general when the steel plate thickness increases, strength increases as well, but ductility reduces. Lens-type shear panel makes the best use of this property by changing the lens thickness and controlled failure modes. It is so designed to combine thicker edge around and thinner concave that allow low strength and high ductility with use of LY100. Failure modes highly depend on the concave depth. When the concave depth becomes deep, failure moves from the lens edge and fillet corners to the lens center where the cross sectional area becomes smallest in the panel. Fig. 3 shows the static test results for various lens shapes. In the static tests of LY100-12-8, LY100-12-6(Fig.2), and LY100-12-4, the maximum displacements count up to 8δy, 9δy, and 10δy in proportion to the concave deepness. On the contrary, LY100-12-3 shows different behavior. It collapsed at the edge around and center at the same time for the maximum displacement of 8δ y . Early crack initiation at the lens center due to the alternate tension field was observed. This phenomenon was clearly observed in the dynamic test. Taking safety margin into consideration, LY100-12-6 was recommended to be the best use for shear panel dampers.



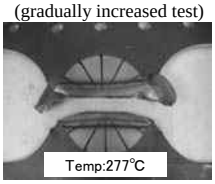
(a) LY100-12-8 (b) LY100-12-6 (c) LY100-12-4 (d) LY100-12-3

Fig. 3: Lens behavior-1: Concave depth and failure modes

4.2 Lens behavior-2: Fillets and failure modes (Fig. 4),"Too large fillet cut lens center"

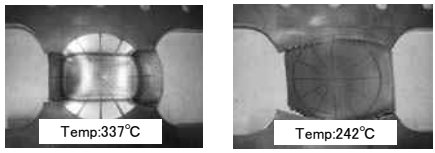


(a) static test
(gradually increased test)

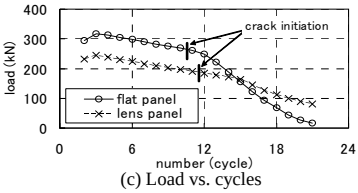


(b) dynamic test
(sinusoidal test ,amplitude 20mm)

Fig. 4: Lens behavior-2: fillet and failure modes (R=6.5t=78mm)



(a) Lens panel (b) Flat panel



(c) Load vs. cycles

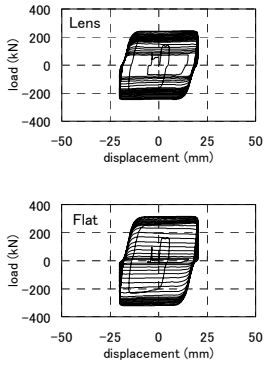


Fig.5: Lens behavior-3: load versus loading cycles for lens and flat panels (Sinusoidal test for amplitude=20mm and T=1sec)

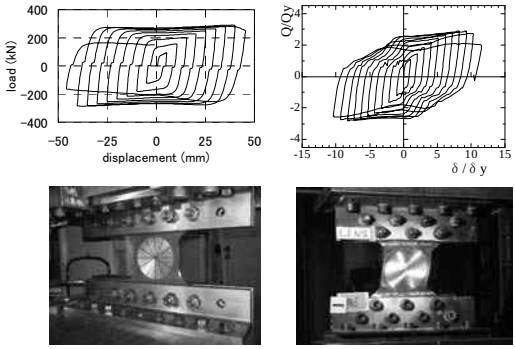
Fillet at the panel corner plays an important role to reduce the local stress concentration and consequently, to control the failure mode of cracking. When fillet is too large in size, cracking initiates

www.EngineeringEBooksPdf.com

at the lens center. In design sense, it is preferable to fail at the four corners instead of lens center for better ductility. Fig. 4 shows for R=6.5t case. In the static tests, peak shears for R=4t and R=6.5t are 291KN and 330KN, respectively where cracks initiate at the same panel corners. In the dynamic test, both cases show different failure modes. In the case of R=4t, cracks stay at the corners. While, for R=6.5t cracks initiate at the center. In the case of R=4t (Fig.5(a)), wider plastic zone and higher temperature up(377℃) are recognized than for R=6.5t, which means the panel for R=4t has better ductility.

4.3 Lens behavior-3: Lens panel and flat panel (Fig. 5),"Flat panel is fragile in dynamics"

Fig. 5 shows the dynamic test results; failure modes of LY100-12-6 (lens) and LY100-12-12 (flat) for the constant amplitude of ±20mm.In the static test, both show similar failure mode. In proportion to the cross sectional area, the shear force recorded 245KN and 315KN, respectively. In contrast to the static test, the dynamic test results provided different type of behavior definitely. In the case of LY100-12-6, the plastic zones accompanied with heat radiation spread out widely in the radial direction from center to outside, with high temperature of 337℃ on the surface. In the case of LY100-12-12, the plastic zone is limited to a narrow band with less temperature of 242℃. Fig. 5 shows the load versus repeated cycle. After 12 cycles, significant crack damage at the edges causes sudden drops of deterioration. Passage of crack propagation left irregularity like gear notch.



(a) Single array (b) Double array

Fig. 6: Panel connection: Use HTB (friction type)

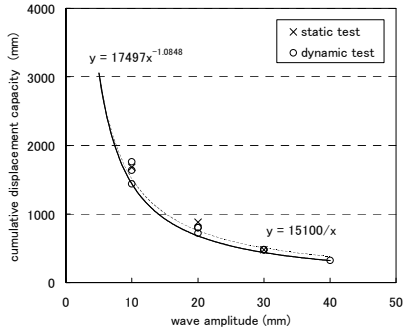


Fig. 8: Cumulative displacement capacity versus wave amplitude

4.4 Panel connections: Use friction type HTB (Fig. 6),"Boundary changes ductility"

Major requirements for specimen connections are as follows:

1. It should transfer seismic lateral forces to shear panel damper tightly with strong enough rigidity so that damping effect is performed completely.
2. Panel edges should be so tightly fixed that it resists both against moment and shear. It is recommended to set double array HTB rather than single arrangement. Single array HTB allows slight rotation due to moment which results in semi-rigid connection.
3. At the ultimate state of failure, the cracking in the tension state is more critical than buckling in compression. Friction type HTB is available to reduce the stress concentration with less local constraints. Large deformation causes big thickness changes in the 3-dimensional directions so that it causes cracking at the constraint points such as welding deposits.

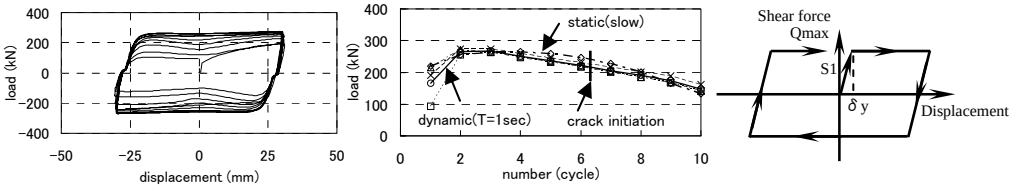
Fig. 6 shows the panel behavior connected by single (Case A) and double (Case B) array HTB. In Cases A and B, Qmax /Qy=2.8~2.87 and 2.8~2.90, and δmax/δy=9 and 10, respectively. Note that the boundary changes both strength and ductility. Since the specimen size is limited to small due to the

www.EngineeringEBooksPdf.com

available capacity of loading frame and actuator, a half size model with single array HTB, Case B, was tested at the Aichi Institute of Technology.

4.5 Analytical model: Bilinear model with rectangular shape by static and dynamic tests (Fig. 7)

Fig. 7 shows the typical load-displacement hysteretic curves for 30mm constant amplitude under the sinusoidal tests (two cases of slow and T=1sec).The peak load gradually decreases with cycles and the cracking starts at 6 cycles. Fig. 7 also shows an assumed analytical model, a bilinear model of rectangular shape, where two parameters of Qmax and S1 are defined. The maximum loads, Qmax and Qpeak are determined; Qmax for analytical model denotes the average value of resistance shears, and Qpeak for design use is the highest value among them. Qpeak /Qmax is about 1.13～1.18, both in the static and dynamic tests. S1 is determined from the unloading gradients. The values of Qmax, Qpeak, Qpeak/Qmax and S1 are determined as 245K, 282KN, 1.15 and 140KN/mm, respectively.



Sinusoidal test (sine wave, amplitude 30mm, slow and T=1sec)

Fig. 7: Analytical model: bilinear model with rectangular shape (Q_{max}, S1)

5 CUMULATIVE DISPLACEMENT CAPACITY (CDC) AND HEAT TRANSFER

5.1 Sinusoidal test results: CDC and damage index (Fig. 8 and Table 3)

Table 3 sine test results, cumulative displacement capacity and damage index $1/N_f$

amplitude x(mm)	period T(sec)	velocity v (mm/s)	num.of cycles to failure C_f	modified cf* d/4x	limit disp. (test results) d(mm)	deformed capacity x*d(mm2)	critical disp. (Cdc) y=15100/x	num.of cycles to failure N_f=15100/4x^2	damage index $1/N_f$
5	1	31	170	168	3360	16800	3020	151	0.0066
10	2	31	38	36	1440	14400	1510	37.8	0.0265
10	1	63	46	44	1760	17600	1510	37.8	0.0265
10	0.5	126	43	41	1640	16400	1510	37.8	0.0265
15	1	94	17	15	900	13500	1007	16.8	0.0596
20	2	63	12	10	800	16000	755	9.4	0.1060
20	1	126	12	10	800	16000	755	9.4	0.1060
20	0.5	251	11	9	720	14400	755	9.4	0.1060
30	2	94	6	4	480	14400	503	4.2	0.2384
30	1	188	6	4	480	14400	503	4.2	0.2384
30	0.5	377	6	4	480	14400	503	4.2	0.2384
40	1	251	4	2	320	12800	378	2.4	0.4238
Specified(averaged) values for design									
18.875	1			10.6	800	15100	800	10.6	0.094

The displacement capacity which has strong relation to the strain energy capacity depends greatly on the strain rate and seismic magnitude (EQ), the stress states and intensity (panel shape), and the fracture toughness (LY100).As a performance indicator, the cumulative displacement capacity Cdc is used for their evaluation.Table-3 summarizes the 12 case test results which deal with CDC and the number of cycles to failure N_f versus constant wave amplitude x (5, 10, 15, 20, 30, and 40 mm). The relationship between the cumulative displacement capacity (y and Cdc) to the wave amplitude (x) is shown in Fig. 8.

$$y = 17497x^{-1.0848} \quad (1)$$

www.EngineeringEBooksPdf.com

$$xy = 15100 \tag{2}$$

Eq.(1) is derived from the test data through regression analysis, and Eq.(2) is a simplified hyperbola of Eq.(1) showing x times y is equal to constant which characterizes lens identity. Based on Miner's rule, N_f and damage accumulated in each cycle D_f are given by Eqs.(3),and(4), respectively.

$$N_f = 15100/4x^2 \tag{3}$$

$$D_f = 1/N_f \tag{4}$$

Miner's rule gives the design criteria to failure by Eq. (5).

$$D_1 = \sum\left(1/N_f\right) < 1 \tag{5}$$

For example, in Table 3, when a damper is subjected to a harmonic motion with a specified amplitude x=18.875mm, its survival number of cycles N_f and the damage index D_f are 10.6 and 0.094, respectively.

By using the analytical data of traveled pass D_{tp}, the damage pass D_{tp}* is defined by Eq.(6).

$$Dtp^* = \sum(\text{damage pass coefficient e})\cdot(\text{response amplitude x}) = \sum\left(4x^2/18.875\right) \tag{6}$$

where e=x/18.875and Cdc=800mm. Safety of D_2 can be evaluated by Eq.(7).

$$D_2 = \sum\left(Dtp^*/800\right) < 1 \tag{7}$$

CDC can be evaluated by the two methods: 1) Damage index method by Eq. (3), (4), and (5),and 2) Damage pass method by Eq.(6) and (7). Both results give the same answer exactly, because they stand on the same base of Eq.(2). Damage index method has an advantage to evaluate the damage state without determination of cumulative damage pass limit (Cdc). A trial simulation is shown in Table 4.

Table 4 Gradually increased displacement tests: cumulative displacement and design limit

	amplitude	Trav. pass	damage index method				damage pass method		
loading	x(mm)	Σ(4x)	N_f=15100/4x^2	1/N_f	D_1=Σ(1/N_f)	e=x/18.875	e* x	Q=Σ(4e*x)	D_2=Q/800
δy	5	20	151.0	0.007	0.007	0.265	1.32	5.3	0.007
2δy	10	60	37.8	0.026	0.033	0.530	5.30	26.5	0.033
3δy	15	120	16.8	0.060	0.093	0.795	11.92	74.2	0.093
4δy	20	200	9.4	0.106	0.199	1.060	21.19	158.9	0.199
5δy	25	300	6.0	0.166	0.364	1.325	33.11	291.4	0.364
6δy	30	420	4.2	0.238	0.603	1.589	47.68	482.1	0.603
7δy	35	560	3.1	0.325	0.927	1.854	64.90	741.7	0.927
8δy	40	720	2.4	0.424	1.351	2.119	84.77	1080.8	1.351
9δy	45	900	1.9	0.536	1.887	2.384	107.28	1509.9	1.887
design limit	35	900			D_1<1			800	D_2<1

5.2 Gradually increased displacement tests and evaluation of CDC: design criteria (Table 4)

Table 4 shows the test results for gradually increased displacement history and evaluation of CDC by damage index method and damage pass method. At 7δy, the cumulative damage D_1=Σ(1/N_f) becomes 0.927, that is, the D_1 value is close to 1 indicating almost failure. In the static test, the max. displacement counts up to 9δy with traveled pass 900mm. In the dynamic test, the estimated max. displacement is reduced to 7δy, where the damaged traveled pass is 741mm, that is, a little below the cumulative displacement limit value of 800mm. Design criterion can be safely proposed that D_s (static max. displacement), D_d (dynamic max. displacement), D_{tp}*(damage pass), can be determined less than 45mm (9δ y), 35mm (7δy), 800mm, respectively.

5.3 Energy Dissipation by heat transfer: "High speed strain rate generates heat"(Figs. 4, 5,and 9)

Large displacement with high speed strain rate generates heat in steel. However, mechanism of heat generation system of steel caused by high strain rate has not been solved yet theoretically in the study. Observations and comments are described as follows:

www.EngineeringEBooksPdf.com

1. Heat was generated only in the dynamic test, not in the static test. Slight temperature up was observed in the dynamic random test.

2. Between time period of 0.5 and 2.0 sec., no remarkable difference of heat-up temperature was observed, keeping 300~400℃ on the panel surface.

3. Plastic zone and heat radiation spread out widely in the radial direction from lens center to outward.

4. Cracking delay was observed: It seems that expansion due to heat reduces the stress concentration. Heat transfer contributes to the energy dissipation, and consequently good ductility is expected.

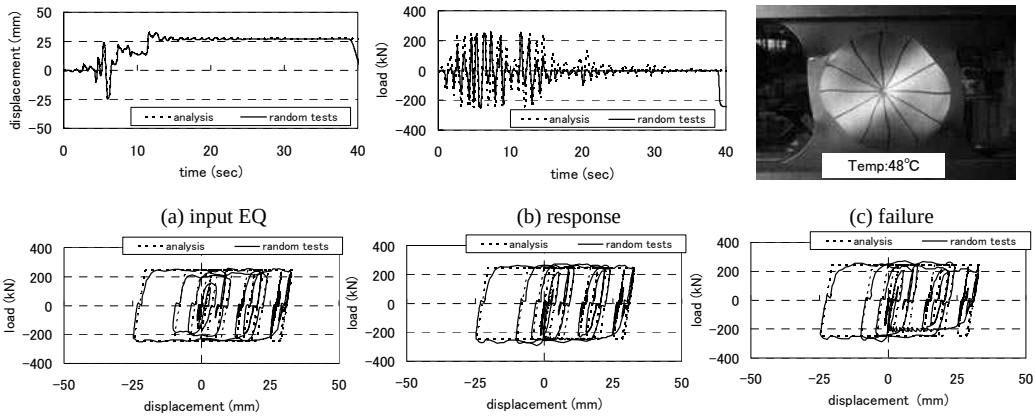
5. In random loading, recorded temperature up is limited to 40~50℃,which means that the seismic behavior is close to the static one when subjected to actual earthquakes.

6 RANDOM LOADING AND TEST RESULTS: SAFTY MARGIN AND LIFE CYCLE

6.1 Random loading tests: Test program (EQ, amplification factor, and damper model)

A full scale bridge model and one-degree-of-freedom model with dampers are used for the dynamic analysis, and their responses are provided to the random loading test as displacement control data. Three types of Level 2 specified earthquakes (EQ2-2-1, EQ2-2-2, EQ2-2-3)[4] and their amplification factors (1.0 and 1.2) are combined as test parameters. As damper models, stiff (S) and regular(R) models with different stiffness are considered (Table 5).In total, 8 cases (E1~E8) are considered.

6.2 Random test results: Comparison with analysis (Qmax and Qpeak) (Fig. 9 and Table 5)



(a) input EQ (b) response (c) failure

(d) 1st EQ(initial) (e) 2nd~4th EQ(intermediate) (f) 5th EQ(final)

Fig. 9 Repeated random loading test results for Level-2, EQ2-2-1,and s=1.2

Time-history of displacement and resistance (Q_{peak} and Q_{max})

Fig. 9 shows the test results which explain time-history of displacement and shear resistance of damper.

1. Displacement time-history: Loading is applied to the damper by the displacement control, and input to actuator should be equivalent to output records.

2. Resistance time-history for Q_{max} and Q_{peak}: Damper stiffness model is based on the hysteretic curves in the static tests, and analytical model assumed a rectangle shape shown in Fig. 7. In a half size model, Q_{max} and Q_{peak} are determined as 245KN and 282KN,Q_{peak}/Q_{max}=1.15, for damper S-model. Response time-history verifies that the damper shear resistance is always below Q_{peak} keeping in safe region.

6.3 Random test results: strength (safety margin) and endurance (life cycle)

www.EngineeringEBooksPdf.com

Table 5 shows the test results for the repeated random loading. Combined 8 cases with Level 2 EQ (EQ2-2-1, EQ2-2-2, and EQ2-2-3) and amplification factors (1.0and1.2) are described. In each case, the tests result is compared with the prediction. In test, max./min. displacement and the number of cycles to failure, c1and c2, are counted, where c1and c2 are the observed cycles to crack initiation and to failure at the final state, respectively. Average (life) cycle cf=(c1+c2)/2 is used for comparison with the prediction. Both damage index and damage pass methods are used for the predicted data. The predicted N_f can explain well the test data of life cycles cf. As design criteria, it is proposed that the N_f value should be greater than 3, which means a damper can survive at least in three times of Level 2 earthquake. In fact, big earthquakes are always accompanied by aftershocks in a few days without repair time. Shear panels connected by HTB are so designed as to repair easily in a short time once damages are found.

Table-5 Random loading test results and comparison with failure prediction

Case	damper	random loading	ampl.factor	test results: response and cf			prediction by Dtp* and N_f		
	model	level-2 EQ	s	cf	max.disp. (mm)	travel.pass (mm)	Dtp*	800/Dtp*	N_f
E1	R	EQ2-2-1	1	4.5	33.6	325.1	183	4.37	4.37
E2	R	EQ2-2-2	1	5.5	22.9	321.5	160	4.99	4.99
E3	R	EQ2-2-3	1	5.5	14.8	235.3	123.9	6.46	6.46
E4	R	EQ2-2-1	1.2	3	40.3	390.1	263.3	3.04	3.04
E5	R	EQ2-2-2	1.2	4.5	27.5	386	229.3	3.49	3.49
E6	R	EQ2-2-3	1.2	4.5	17.8	265.2	177.1	4.52	4.52
E7	S	EQ2-2-1	1.2	4.5	33.1	332.6	182.9	4.37	4.37
E8	S	EQ2-2-1	1	6	27.6	272.6	124.8	6.41	6.41
estimate1	S	EQ2-2-1	1.2		33.1	327.1	179.7	4.45	4.45
estimate2	S	EQ2-2-1	1.46		40.3	398.0	266.0	3.01	3.01

damper model: R(regular)model;Qmax=225KN,S1=134KN/mm,S(stiff)model ; Qmax=245KN,S1=140KN/mm,Dtp*:damage pass
s:amlification factor, estimate: scaled by a parameter (s)on the basis of E8(s=1)

6.4 Influence of amplification factor s to dynamic response: D_{tp}* and N_f are scaled by s^2

Displacements and traveled pass are simply scaled by s. On the other hand, damage pass D_{tp}* and N_f are scaled by s^2.Table-5 shows the estimated response values. N_f is easily estimated by the parameter s.

7 CONCLUSIONS

1. Shear panel damper is developed as a part of function-separated bearing system to serve for lateral seismic loads, and it provides easy maintenance and urgent repair works once being damaged.

2. As a shear panel, the concave lens shape +low-yield steel LY100 gives the most effective way to satisfy the requirements of low strength and high ductility with large energy dissipation.

3. Large deformation of low-yield steel with high speed strain rate provides new findings in this study: Two items are crucial needed for further study : 1) cumulative deformation capacity, and 2) energy dissipation by heat transfer.

REFERENCES

[1] Aoki,T.,Liu,Y.,Takaku,T.,Uenoya,M.,&Fukumoto,Y.,2007. Experimental investigation of tapered shear type seismic devices for bridge bearings.*Proc.,8th Pacific Structural Steel Conference (PSSC)*,New Zealand, March 2007.1,111-117.

[2] Aoki,T., Liu,Y.,Takaku,T.,&Fukumoto,Y.,2008.A new type of shear panel dampers for highway bridge bearings. *EUROSTEEL2008*, 3-5, September 2008, Graz, Austria.

[3] Aoki,T., Dang.J., Zhang.C., Takaku,T.,& Fukumoto,Y., Dynamic shear tests of low-yield steel panel dampers for bridge bearing. *Proc., of 6thInternational Conference of STESSA* 2009,16-20 August 2009, Philadelphia, USA.

[4] Japan Road Association: *Specification for Highway Bridges*, *Part 5, Seismic Design* 2000.

www.EngineeringEBooksPdf.com

SDSS'Rio 2010 STABILITY AND DUCTILITY OF STEEL STRUCTURES
E. Batista, P. Vellasco, L. de Lima (Eds.)
Rio de Janeiro, Brazil, September 8 - 10, 2010

ELASTO-PLASTIC BUCKLING BEHAVIOR OF H-SHAPED BEAM WITH LARGE DEPTH-THICKNESS RATIO UNDER CYCLIC LOADING

Tao WANG*, Kikuo IKARASHI*

* Department of Architecture and building Engineering, Tokyo Institute of Technology
e-mails: wanntao2@gmail1.com, ikarasahi@arch.titech.ac.jp

Keywords: Coupled Buckling, Vertical Buckling, Plate Slenderness ratio, Plastic Deformation Capacity.

Abstract. *Plastic deformation capacity of thin-walled structure is not only affected by the plate slenderness ratio but also by the other dimensional parameters such as aspect ratio, sectional area. This paper presents an experimental study on H-shaped Beams subjected to cyclic loading in large range of deformation with large depth-thickness ratios which are over or comparable with the limited values of those restricted in the current standards (Ref. [1] and [2]). The geometric parameters are relevantly identified to evaluate the plastic deformation ratio, and the new divisional rank for plastic deformation capacity of H-shaped beam is proposed.*

1 INTRODUCTION

According to the standards for steel structures in many countries, plate slenderness ratio (width-thickness ratio or depth-thickness ratio) is assumed to be of major parameter to estimate the plastic deformation capacity of thin-walled steel structures. Up to now many experimental and analytical researches have been reported aimed to reveal the relationship between plastic deformation capacity and plate slenderness ratio. These results have now been incorporated in all sorts of standard and recommendations of steel structures. Consequently, plate slenderness ratio is rigidly restrained in order to prevent the elastic buckling[1]. In Japan, the division for plate slenderness ratio of H-shaped beam is provided with respect to the plastic deformation capacity as a general provision which is only applicable in a limited region where the depth-thickness ratio is relatively small[2].

It is commonly known that coupled local buckling may dominate the H-shaped beam's behavior when the depth-thickness ratio is large. On the other hand, recent studies subjected to H-shaped Beam with large depth-thickness ratio had shown the practical use of thin plate as the earthquake-resisting element even though the plate slenderness ratio is over the limited value in some cases[2-5]. However, no standardized method is currently available for estimating the plastic deformation capacity of such beams. This paper is intended to develop an easy method to estimate the plastic deformation capacity of H-shaped beam with large depth-thickness ratio, and aims at revealing the post buckling behavior under the cyclic loading situation by contrast with those under the monotonic loading situation.

2 CYCLIC LOADING TEST

Figure 1 is the loading model subjected to the local buckling test where the lateral direction was cramped in the test arrangement so as to prevent the overall buckling. Specimens used for testing were SS400 grade, H-shaped welded steel beams. The dimension and cross-section constants for each specimen (H-D-2b-t_w-t_f), given a number is listed in Table 1, in which seven types of plates with different thickness are adopted. They are the same sort of material but a little different from each other based on the tension test due to their different thickness. The mechanical property of each plate is listed in Table 2.

www.EngineeringEBooksPdf.com

Table 1: Specimens list

specimen	section(nominal value)	(surveyed value)		l
	H-D-2b-t_w-t_f	d/t_w	b/t_f	
No.1	H-350-175-3.2-12	105	7.4	1400
No.2	H-350-175-4.5-12	76	7.5	
No.3	H-350-175-4.5-16	73	5.6	
No.4	H-350-175-4.5-19	71	4.7	
No.5	H-350-175-6-9	59	10.2	
No.6	H-350-175-6-12	57	7.5	
No.7	H-350-175-6-16	56	5.6	
No.8	H-350-175-912	38	7.5	
No.9	H-350-175-4.5-12	76	7.5	1050
No.10	H-350-175-6-12	58	7.5	

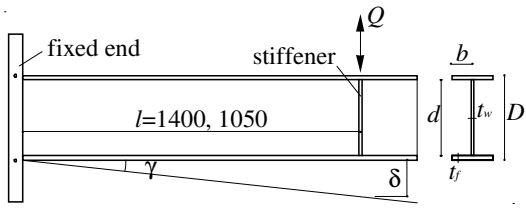


Figure 1: Loading model

Table 2: Material property

t (mm) thickness	σ_y (N/mm^2) yield stress	σ_u (N/mm^2) tensile stress	E (kN/mm^2) Yong's modulus	ε_u (%) Max strain	*Elng.* (%) fracture strain	*Y.R.* (%) yield ratio
3.2	281	424	206	19.8	29.4	66.3
4.5	267	417	205	20.9	27.8	64.0
6.0	332	433	205	17.7	29.4	76.7
9.0	291	439	206	15.0	30.4	66.3
12	306	479	205	13.0	32.6	63.9
16	266	412	209	12.3	31.8	64.6
19	257	410	206	11.8	33.1	62.7

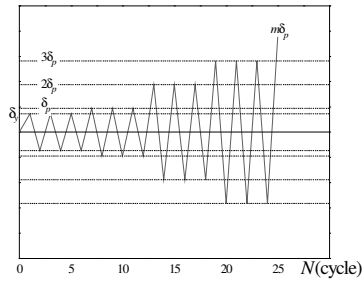
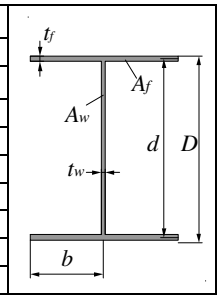


Figure 2: Loading program

Table 3: Parameter definition

marks	meaning
l	Length of beam
λ_w=l/d	Aspect ratio of web
λ_f =l/b	Aspect ratio of flange
A_w= dt_w	Sectional area of web
A_f=2bt_f	Sectional area of flange
d /t_w	Web depth-thickness ratio
b/t_f	Flange width-thickness ratio
β	Bending incline (β=1)
σ_{wy}, σ_{fy}	Yield stress of web, flange



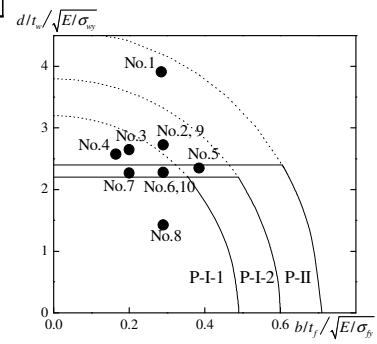


Figure 3: Plate slenderness ratio

Cyclic loading program of this test is shown in Figure 2, in which δ_y and δ_p are the displacement related with M_y And M_p given by:

$$\delta_y = \frac{M_y l^2}{3EI} + \frac{M_y}{GA_w} \tag{1}$$

$$\delta_p = \frac{M_p l^2}{3EI} + \frac{M_p}{GA_w} \tag{2}$$

In which EI and GA_w are flexural rigidity and shear rigidity. The other geometric parameters and marks used in this study are defined in Table 3. M_y And M_p denote the bending moment at the end plate on the yielded condition which can be represented by,

$$M_y = Q_y \cdot l = \frac{1}{6}\sigma_{wy} \cdot t_w (d - t_f)^2 + 2\sigma_{fy} \cdot bdt_f \tag{3}$$

www.EngineeringEBooksPdf.com

$$M_p = Q_p \cdot l = \frac{1}{4}\sigma_{wy} \cdot t_w (d - t_f)^2 + 2\sigma_{fy} \cdot bdt_f \tag{4}$$

According to the Standard for Limit State Design of Steel Structures of Japan[2], the divisional curves with three ranks for width -thickness ratio and depth-thickness ratio are shown in Figure 3. The relationship between width-thickness ratio and depth-thickness ratio about each specimen is also shown by plots in the same figure.

3 EXPERIMENTAL RESULTS AND COMPARISON

3.1 Hysteresis Curve and Post Buckling Behavior

Figure 4 show the hysteresis curves of three of the specimens with different typical behaviors for No.3, No.5 and No.7 respectively. The horizontal axis and vertical axis show the dimensionless numbers for the displacement (δ) and load(Q). In the elastic region the relationship between δ and Q is defined as,

$$Q / Q_{ps} = \delta / {}_E\delta_{ps} \tag{5}$$

According to Ref.[6], Q_{ps} can be represented by,

$$\frac{Q_{ps}}{{}_wQ_p} = \begin{cases} 1 - \left[\dfrac{\sqrt{\dfrac{{}_wM_p^2}{M_p^2} - 4sb\left(1 - sb - \dfrac{{}_wM_p}{M_p}\right)} - \dfrac{{}_wM_p}{M_p}}{2sb} \right]^2 & sb > 1 - \dfrac{{}_wM_p}{M_p} \\ 1 & otherwise \end{cases} \tag{6}$$

Where, Q_{ps} denotes the yield shear load taking account of bending effect. ${}_wQ_p$ is the yield load on pure shear condition, ${}_wM_p$ denotes the full plastic moment born on web, sb denotes the ratio of shear to bending on the yield condition. They are given by,

$${}_wQ_p = A_w\sigma_{wy} / \sqrt{3} \tag{7}$$

$${}_wM_p = \frac{1}{4}t_w d^2 \sigma_{wy} \tag{8}$$

$$sb = \frac{\lambda_w / \beta}{(0.25 + A_f / A_w)\sqrt{3}} \tag{9}$$

Each hysteresis curve in Figure 4 exhibits a stable behavior until the local buckling happens. For each specimen, the load drops down immediately the local buckling happens, and a fracture is observed several cycles later, then the beam collapses in the end. As the photos of collapsed beams shown in Figure 5, the buckling modes can be divided into three typical types: (a) shows web buckling type (W.type); (b) shows coupled buckling type (C.type); (c) shows vertical buckling type (V.type). The mode of flange buckling type is not discussed due to large depth-thickness ratio of web used in this test.

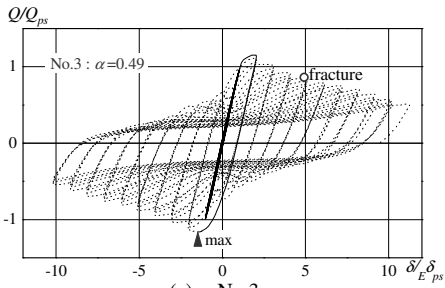
Compared with the other two types, it can be observed from the Figure 4(c) that the degradation incline of V.type is extremely sharp. Vertical buckling may be induced by web local buckling when flanges are not strong enough to sustain the buckled web. As a consequence, the bending rigidity of beam quickly falls down once the buckled web makes a dent in flange. The vertical buckling does not happen even though web bucking dominates in case of Figure 4(a) because the bending burden on flange is relatively small or α(Eq.(10)) is large, hence the vertical buckling is prevented. On the other hand, the

www.EngineeringEBooksPdf.com

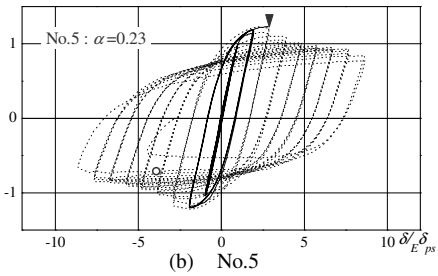
vertical buckling does not happen in case of Figure 4(b) because the depth-thickness ratio of web is relatively small or $(d/t_w)/(b/t_f)$ is small. As a discussion result, the degradation incline of non-V.type is about -7% of the elastic incline; the necessary conditions for non-V.type are about α>0.5 or $(d/t_w)/(b/t_f)$<6 (approx).

Where, α is the ratio of shear to bending stress, equal to 0 for pure bending, can be expressed by,

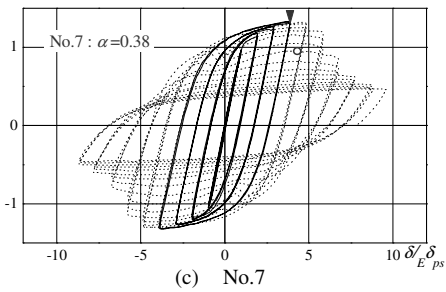
$$\alpha = \left(\frac{1}{6} + \frac{A_f}{A_w}\right)\beta / \lambda_w \tag{10}$$



(a) No.3



(b) No.5

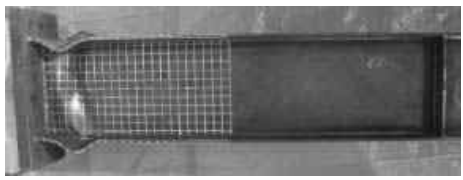


(c) No.7

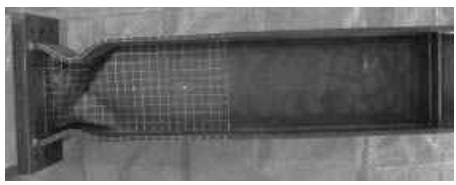
Figure 4: Load- displacement hysterisis curve



(a) No.3, Web buckling type (W.type)



(b) No.5, Coupled buckling type (C.type)



(c) No.7, Vertical buckling type (V.type)

Figure 5: Buckling mode

3.2 Skeleton curve and restriction on plate slenderness ratio

According to Ref.[7], the skeleton curve can be defined as shown in Figure 6 on the right side transformed from hysteresis curve on the left side by joining the renewed points before reaching the maximum load. After the maximum load, the skeleton curve is treated as wrapping line.

Based on the rule defined in Figure 6, all hysteresis curves of the specimens (appendix Figure A) are transformed into the skeleton curves (Figure 7). The maximum load of No.2 and No.3 shown in Figure 7

www.EngineeringEBooksPdf.com

are over the plastic shear load Q_{ps} even though their depth-thickness ratios are lager than the limited values, indicating that the restriction for depth-thickness ratio in Ref. [1] and [2] is conservative.

According to Ref.[5], improved method for restriction of width (depth)-thickness ratio had been proposed. The restriction curve is expressed as follows:

$$\left(\frac{BTW}{BTW0}\right)^3+\left[4.63-125\left(\frac{\sqrt{E/\sigma_{wy}}}{BTW0}\right)^3\right]\left(\frac{BTF}{\sqrt{E/\sigma_{fy}}}\right)^3=1 \tag{11}$$

Where, α is given as Eq. (10), $BTW0$ is given by Eq. (12) below:

$$\frac{BTW0}{\sqrt{E/\sigma_{wy}}}=\begin{cases}4.9 & \alpha<1/6\\ 5.75-5.1\alpha & 1/6\le\alpha\le1/2\\ 3.2 & \alpha>1/2\end{cases} \tag{12}$$

BTW and *BTF* are the restrictive value of depth and width-thickness ratio. They are proposed by taking account of the effect of plate slenderness ratio and the other geometric parameters comprising plate sectional area and aspect ratio based on the calculation of buckling strength.

As a sample shown in Figure 8 where the rectangular plots are the value on restriction curves obtained from Eq. (11), circle plots are the real width (depth)-thickness ratio of each beam, the ratio of the value at circle plots to rectangular plots on each situation can be represented by,

$$WF=\frac{d/t_w}{BTW}=\frac{b/t_f}{BTF} \tag{13}$$

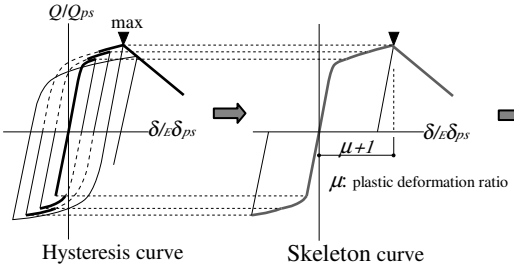


Figure 6: Definition of skeleton curve

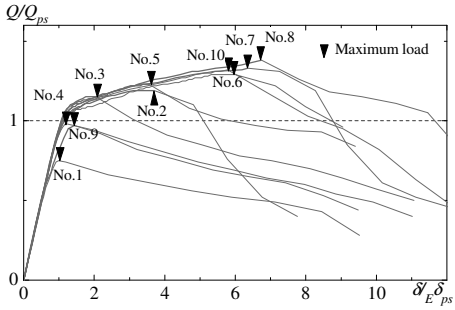


Figure 7: Skeleton curves (all specimens)

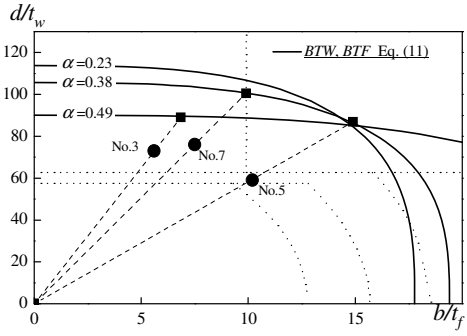


Figure 8: Restriction curve (Eq. (11))

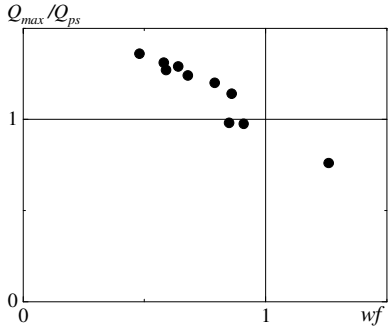


Figure 9: Maximum load and *wf*

www.EngineeringEBooksPdf.com

Where, *WF* is referred to as normalized plate slenderness ratio.
Substituting form Eq. (11) into Eq. (13), *WF* is given by,

$$WF = \left[\frac{(d/t_w)^3}{BTW0^3} + \frac{4.63(b/t_f)^3}{(E/\sigma_{fy})^{3/2}} - \frac{125(b/t_f)^3}{BTW0^3} \right]^{1/3} \tag{14}$$

Figure 9 shows the relationship between *WF* and maximum load Q_{max}. It can be observed from the figure that $Q_{max} > Q_{ps}$ when *WF*<1. Therefore, the normalized plate slenderness ratio *WF* defined in Eq.(14) can be regarded as a parameter to restrict the beam dimension to prevent elastic local buckling.

4 PLASTIC DEFORMATION RATIO AND NORMALIZED SLENDERNESS RATIO

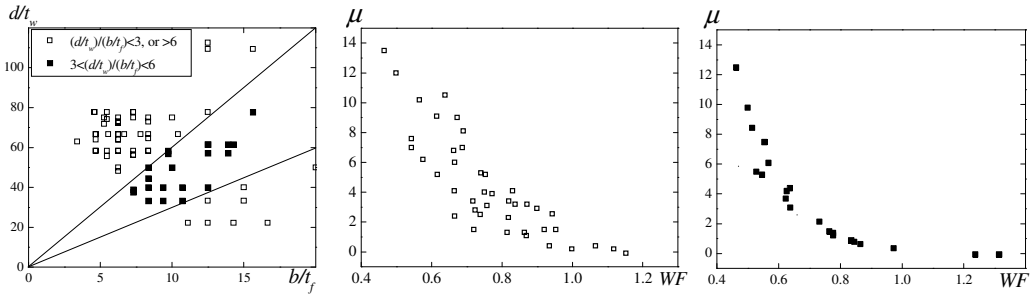
In Figure 6, μ denotes the plastic deformation ratio at the point of maximum load, it is a parameter defined to evaluate the plastic deformation capacity in this study. As shown in Figure 3, the divisional curve of P-I-1 is to ensure μ>4, P-I-2 is to ensure μ>2, P-II is to ensure μ>0 and $Q_{max} > Q_{ps}$.

Figure 10(b) and (c) show the relationship between *WF* and μ obtained from a number of FEM analysis subjected to monotonic loading where the same models as Figure 1 was adopted. The width-thickness and depth-thickness ratio about each beam is shown in Figure 10(a). The aspect ratio of web of each beam is set at $2<\lambda_w=l/d<12$. According to the buckling modes, the results are roughly divided into two parts in Figure 10(a). Figure 10(b) shows the plots in case of $(d/t_w)/(b/t_f)$ <3, or $(d/t_w)/(b/t_f)$>6 where a large part of their buckling modes are single buckling modes or non-C.type buckling modes. Figure 10(c) shows the plots in case of $3<(d/t_w)/(b/t_f)<6$ which are assumed to be the coupled buckling modes. According to the plots showing the relationship between *WF* and μ in both Figure 10(b) and (c), μ tends to become larger as *WF* becomes smaller. Therefore, *WF* can be reasonably regarded as a major parameter to estimate the plastic deformation ratio.

As described earlier (Chapter 3.1), the load falls down immediately after the buckling, such phenomenon is independent to the buckling style in case of cyclic loading situation. But the load does not fall down immediately after the single buckling in case of monotonic loading situation. Consequently, there is some dispersion in the Figure 10(b). But the dispersion in Figure 10(c) is small due to its coupled buckling modes.

To minimize the dispersion and evaluate the plastic deformation capacity safely, the normalized slenderness ratio *WF* expressed by Eq. (14) is modified as *wf* given by

$$wf = \sqrt{\frac{(d/t_w)^2}{BTW0^2} + \left(\frac{5\sigma_{fy}}{E} - \frac{36}{BTW0^2} \cdot \frac{\sigma_{fy}}{\sigma_{wy}} \right) (b/t_f)^2} \tag{15}$$



(a): Object of depth and width-thickness ratio (b): $(d/t_w)/(b/t_f)$ <3 or >6 (c): $3<(d/t_w)/(b/t_f)<6$

Figure 10: Plastic deformation capacity and *wf*

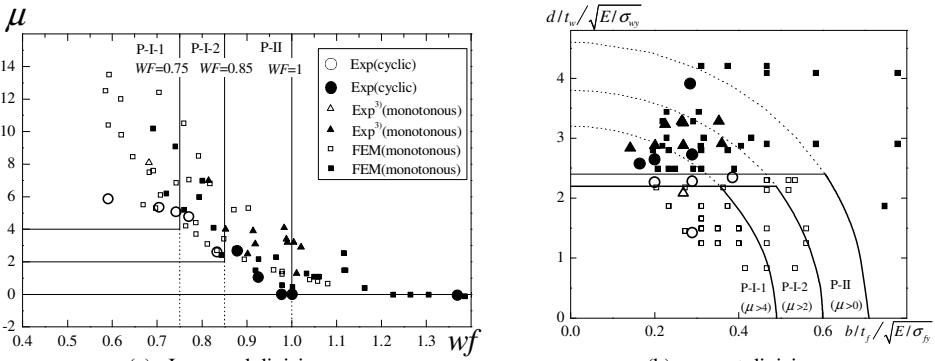
www.EngineeringEBooksPdf.com

Where, α is given as Eq. (10), $BTW0$ is given as Eq. (16).

$$\frac{BTW0}{\sqrt{E/\sigma_{wy}}}=\begin{cases}4.4 & \alpha<1/6\\ 5.18-4.6\alpha & 1/6\le\alpha\le1/2\\ 2.9 & \alpha>1/2\end{cases} \tag{16}$$

Figure 11(a) shows the relationship between μ and wf (Eq. (15)). Each black plot denotes the case when plate slenderness ratio is over the restricted value as shown in Figure 11(b). According to the position of these black plots in Figure 11(a), the restriction can be alleviated in case of wf<1. The circle plots denoting the results under cyclic loading in this test are smaller than the other cases. They are distributed in the lower limit. To estimate the plastic deformation capacity reasonably, the lower limit of μ must be adopted due to the disadvantageous loading situation. According to the result shown in Figure 11, the divisional rank for plastic deformation capacity is proposed as follows:

Rank P-I-1(μ>4): wf<0.75;
Rank P-I-2(μ>2): wf<0.85;
Rank P-II (μ>0): wf<1.



(a): Improved division (b): current division

Figure 11: Division for plastic deformation capacity

5 CONCLUSIONS

This paper presents an experimental study of the local buckling behavior subjected to H-shaped beam. The current standards for steel structures (ref.[1] and [2]) are shown to be generally conservative. According to the hysteresis curve of each specimen, the vertical buckling induced by web local buckling was found to be the major effect on the deterioration. The approximation of the necessary conditions for non-vertical buckling type was given. Compared with experiment and a number of numerical analysis under monotonic loading situation, the plastic deformation ratio of the beams under cyclic loading is relatively small in case of beam with non-C.type buckling modes. The geometrical parameters such as aspect ratio, sectional area as well as the plate slenderness ratio are identified to evaluate the plastic deformation ratio. Improved division for plastic deformation capacity is proposed using normalized plate slenderness ratio.

REFERENCES:

[1] Architectural institute of Japan, “Design Standard for Steel Structures”, 2005.

[2] Architectural institute of Japan “Standard for Limit State Design of Steel Structures”, 2002.

[3] Toshiro SUZUKI, Kikuo IKARASHI and Yasuhiro TSUNEKI, “A Study on Collapse Mode and Plastic Deformation Capacity of H-Shaped Steel Beams under Shear Bending”, *Journal of Structural and Construction Engineering, Arch, inst. of Japan,* No.547, 185-191, 2001 .9

www.EngineeringEBooksPdf.com

[4] Kikuo IKARASHI and Tao WANG, "A Method for Evaluation of Elastic Buckling Strength of H-Shaped Steel Member under Bending-Shear and Axial Force", *Journal of Structural and Construction Engineering, Arch, inst. of Japan,* No.613, 137-146, 2007.3

[5] Kikuo IKARASHI and Tao WANG, "Evaluation of Width-Thickness Ratio Limitation of H-Shaped Beam Members Based on Coupled Buckling Analysis", *Journal of Structural and Construction Engineering, Arch, inst. of Japan,* No.629, 1177-1184, 2008.7

[6] Japan Society of Civil Engineers, "Guidelines for Stability Design Steel Structures", 2005.

[7] Architectural institute of Japan, "Evaluation Procedures for Performance -Based Seismic Design of Buildings -Calculation of Response and Limit Strength, Energy Balance -Based Seismic Resistant Design, Time History Response Analysis- ", 2009.2

APPENDIX:

Table A: Test result

Specimen	No.1	No.2	No.3	No.4	No.5	No.6	No.7	No.8	No.9	No.10
α	0.51	0.38	0.49	0.57	0.23	0.30	0.38	0.21	0.50	0.40
WF	1.37	0.88	0.93	0.98	0.83	0.74	0.7	0.59	1	0.77
μ	0	2.67	1.05	0	2.55	5.07	5.45	5.86	0	4.78
Buckling mode	W	V	W	W	C	V	V	C	W	C

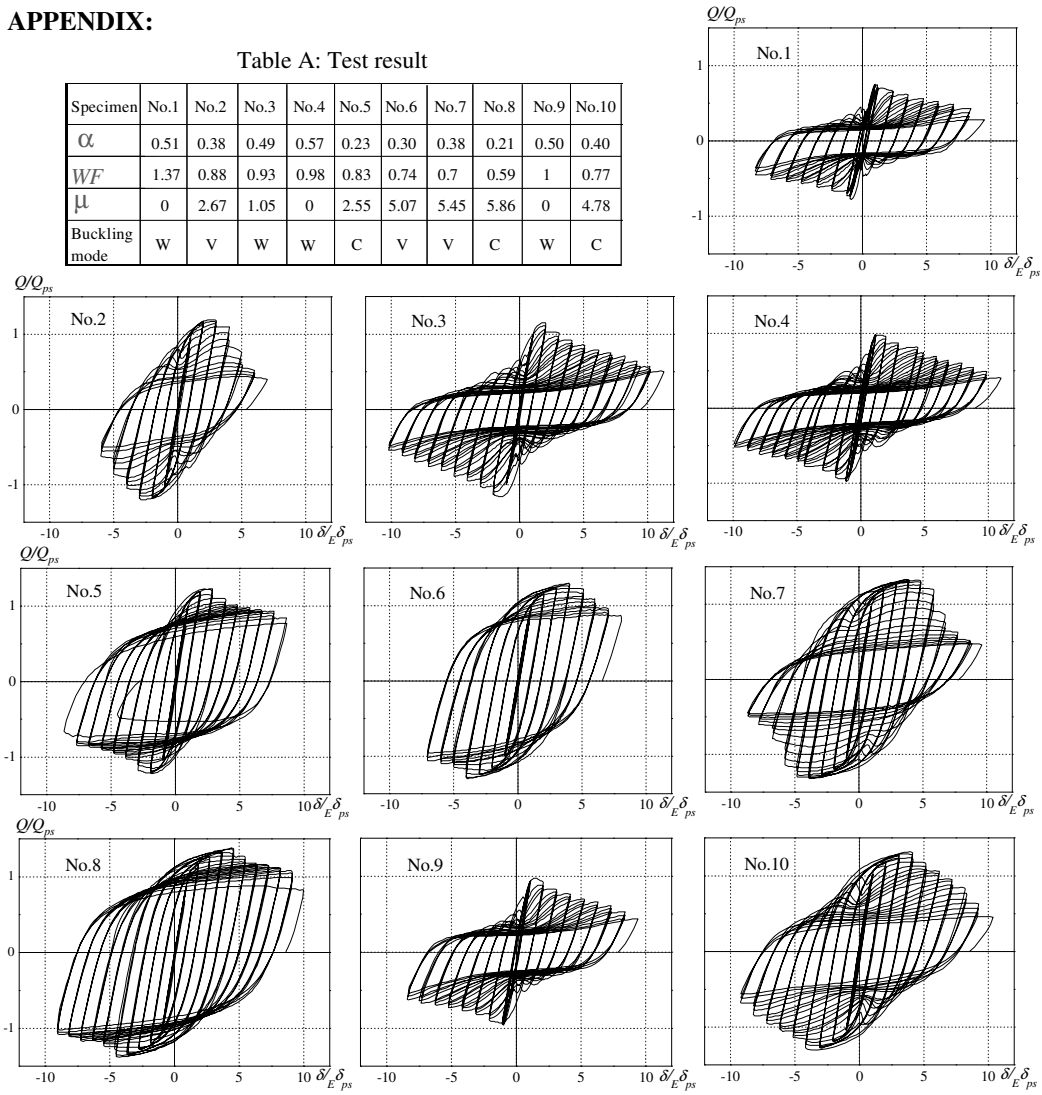


Figure A: Hysteresis curves (all specimens)

www.EngineeringEBooksPdf.com

SDSS'Rio 2010 STABILITY AND DUCTILITY OF STEEL STRUCTURES
E. Batista, P. Vellasco, L. de Lima (Eds.)
Rio de Janeiro, Brazil, September 8 - 10, 2010

ANALYTICAL STUDIES OF A FULL-SCALE STEEL BUILDING SHAKEN TO COLLAPSE

Keh-Chyuan Tsai*, Yi-Jer Yu and Yuan-Tao Weng*****

* Professor, Dept. of Civil Engineering, National Taiwan University, Taiwan
e-mails: kctsai@ntu.edu.tw
** Assistant Research fellow, National Center for Research on Earthquake Engineering, Taiwan
e-mail: yjyu@ncree.org
** Associated Research fellow, National Center for Research on Earthquake Engineering, Taiwan
e-mail: ytweng@ncree.org

Keywords: Nonlinear analysis, Structural dynamics, Collapse analysis.

Abstract. *This paper describes the numerical simulations for earthquake engineering research. The applications of a general-purpose structural analysis computer program PISA3D, developed in Taiwan National Center for Research on Earthquake Engineering (NCREE), on the seismic frames are introduced. In this paper, a four-story building is used as a case study to investigate modeling techniques for nonlinear structural response and collapse analyses. This paper presents several numerical models in detail. The models for the simulation of steel hollow structural column buckling are discussed. A column model incorporating the fibered beam-column element using the cyclic buckling fibers proposed in this study can satisfactorily simulate the degrading force versus deformation relationships found in the ABAQUS column model subjected to the local buckling. A frame model incorporating the same type of fibered column element could predict the collapse time of the test building.*

1 INTRODUCTION

In September 2007, the world's largest 3-directional earthquake simulation table, E-Defense shaking table was utilized for tests of a full-scale four-story steel building shaken to collapse. Before the tests were executed, a blind prediction contest was held [1]. Three groups of researchers from the Taiwan National Center for Research on Earthquake Engineering (NCREE) participated in the blind contest [2]. One team used a general purpose nonlinear structural analysis program PISA3D, and submitted the 3-D and 2-D predictions. This PISA3D/NCREE team was awarded second place in the 2-D analysis research category. In this paper, this four-story building is used as a case study to investigate modeling techniques for nonlinear structural responses and collapse analysis. This paper presents several numerical models in detail. The models for the simulation of steel hollow structural column buckling are discussed. A basic model incorporating the bilinear plastic hinge column elements was constructed first. Then the refinements were carried out by replacing the 1st-story columns in the basic model with the nonlinear degrading column elements. Two types of degrading column are considered including the fiber and hinge models, with and without the effects of axial-flexural interaction, respectively. Based on these nonlinear response analyses, it is illustrated that the collapse responses of the building can be estimated satisfactorily by incorporating degrading fibered columns.

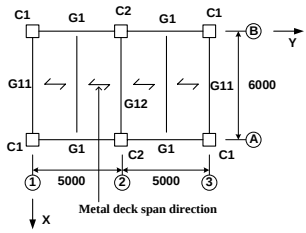
The photo of the full-scale four-story steel building is shown in Fig. 1. The contestants were required to predict the key maximum experimental responses of the specimen under the three-directional incipient-collapse level shaking as well as the specimen's collapse time under the collapse level earthquake [2]. The floor framing plan and the elevations are shown in Figures 2a and 2b, respectively. The longitudinal and transverse directions of the building are defined as Y and X directions, respectively.

www.EngineeringEBooksPdf.com

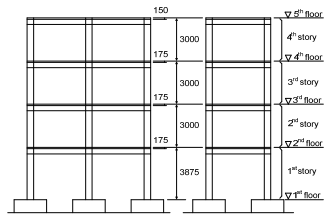
The structural configuration consists of two-bays of 5m each in the Y direction and one-bay of 6m in the X direction. Each story height is 3.5m except the first story is 3.875m high. The thickness of the concrete slab is 175mm for the 1st, 2nd and 3rd floor and 150mm for the 4th floor. The 75mm deep metal deck was spanning in the Y direction. Wide flange sections are used for beams, and rectangular hollow structural sections (HSS) for columns. The steel material is SN400B for the frame beams and BCR295 for the columns. The building was designed following the current Japanese specifications and practices [3].



Figure 1: Collapse of the four-story steel building.



(a) Floor framing plan



(b) Frame elevations

Figure 2: Floor framing plan and elevations (mm).

The building specimen was subjected to 3-directional ground motions recorded during the 1995 Kobe earthquake at the Takatori train station. The test consisted of repeated applications of the records with progressively increasing scale factors. The Takatori motion scaled by 0.6 was designated as the incipient-collapse level motion, and the full scale Takatori motion was designated as the collapse level motion. For the purposes of discussion, the incipient-collapse level and collapse level excitations are defined as EQ-I and EQ-C, respectively.

2 PISA3D

The Platform for Inelastic Structural Analysis of 3-D Systems (PISA3D) [4] is developed in the Dept. of Civil Engineering of National Taiwan University and maintained in NCREE. It is an object-oriented general-purpose computational platform for nonlinear structural analyses. The PISA3D incorporates the object-oriented concept and the Design Patterns to construct the software framework, making it easy to maintain and extend. PISA3D provides a rather large variety of nonlinear materials and elements. PISA3D users could build 3-D analytical models and perform nonlinear analyses to investigate the responses of structures under the combined load effects. Users can download the program for free from http://pisa.ncree.org.tw. In this paper, PISA3D is adopted to present the response simulations of the frame specimen.

3 BASIC MODEL

In the basic model, the frame mass is considered as a lump mass located at the top elevation of the concrete slab of each floor. However, the location of the mass is eccentric due to the asymmetric configuration of the exterior walls. The Newmark method of constant average acceleration scheme (β=1/4) is used for the time integration. The Rayleigh damping ratio of 2% for the first and second modes is adopted for the 3D model. The modeling techniques of the basic model are described below.

3.1 Fibered beam model

All the frame beam members are considered as the steel and concrete full-composite beam in the basic model. The beam model adopted fibered beam-column element to represent the composite floor beam. The fibered beam-column element in the PISA3D is flexibility-based. The element formulation

www.EngineeringEBooksPdf.com

relies on force interpolation functions that strictly satisfy the equilibrium of the bending moments and the axial force along the element [5]. The steel beam consists of 13 fibers using the bilinear material model and the yield strength provided by the contest organizers. The stress versus strain relationship of the concrete provided by the organizer was used for concrete fibers. Five integration points along the fibered beam-column element were chosen to integrate the element responses.

3.2 Panel zone joint

From the beam-to-column subassembly tests [6] conducted by the organizer, shear deformations were evident in the panel zone. Thus, in the basic model, the panel zone deformations were specifically included by introducing zero-length joint elements while the member rigid end offset feature for the joining beam and column ends were incorporated into the analytical model. In the present study, rotational stiffness, *K* and yield capacity, *My* for all panel zone joint elements were calculated using the following two equations [7]:

s

$$K = \frac{G d_b d_c t_j}{\left(1 - \frac{d_b}{H}\right)} \tag{1}$$

$$M_y = \frac{0.55 F_y t_j d_b d_c}{\left(1 - \frac{d_b}{H}\right)} \tag{2}$$

where d_b, d_c are the beam and column depth, respectively. The t_j and H are the thickness of the panel zone and the story height, respectively.

3.3 Hinge model for the column

In the basic model, hinge-model beam-column element was adopted for all the column members. This beam-column element is a lumped-plasticity model. It has an elastic component that is series-connected by one shear and one flexural plastic hinges at each end. All the nonlinear deformations can only take place in these hinges. The bilinear material property was adopted. The plastic section modulus and the steel yield strength provided by the organizers were used. No axial-flexural interaction is considered in this model. The material strain hardening ratio was assumed to be 0.02.

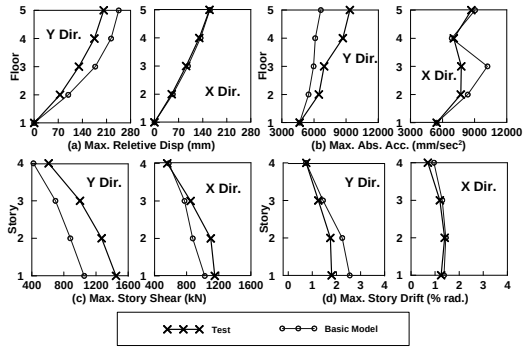


Figure 3: Absolute maximum responses of basic model subjected to the EQ-I.

3.4 Comparisons between the basic model simulation and test results

Figures 3a to 3d show the absolute peak responses of the basic model under the EQ-I. It is evident that the displacement-related responses (maximum floor displacements and story drift) in the X direction are very close to the test results. Figures 3a shows that the maximum floor displacements computed from the basic model were larger than the test results. The basic model underestimated the story shear

www.EngineeringEBooksPdf.com

responses (Figure 3c). For some unknown reasons, this under-prediction on story shear has been found common in most teams participated in the blind contest [8].

From Fig. 3a, it can be found that the analytical Y-direction displacement responses were somewhat greater than those in the X direction. This finding agrees with the observed test responses. Under the EQ-C, the test frame did collapse primarily along the Y direction [3]. Figure 4 shows the first story drift time history responses in the Y direction of the basic model under the EQ-C. It can be found that the collapse drift ratio of 0.13-radian defined by the contest organizers was never reached in the response history analysis using this basic model. Further studies are necessary.

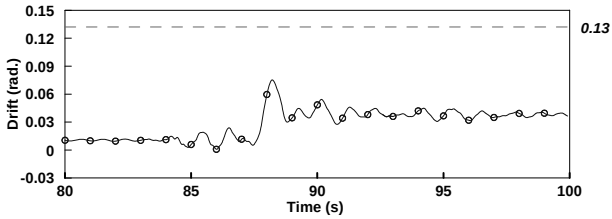


Figure 4: First story drift time histories in the Y direction under the EQ-C for the basic model.



Figure 5: Local buckling of the first-story column at the end of the tests.

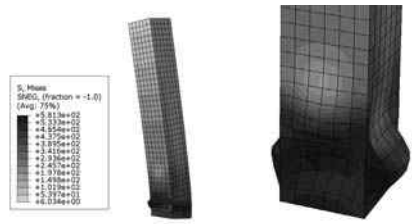


Figure 6: Local buckling of the ABAQUS column model.

4 REFINE THE COLUMNS USING PARALLEL MATERIAL HINGE MODEL

When the specimen was subjected to the EQ-C, local buckling occurred at both the bottom and top ends of several first story columns [3]. Figure 5 shows the bottom column end local buckling of the 1st-story column specimen at the intersection of Frame Lines A and 2 (Figure 2a). This local buckling led the building into a side-sway collapse mechanism in the first story [3]. Recall in the basic model that the column strength degradation due to the local buckling was not specifically considered as all column elements were represented using bilinear material. This should be helpful in explaining why the basic model failed to predict the collapse of the specimen.

In order to refine the column properties in the frame model, an independent ABAQUS [9] finite element (FE) column model was constructed to study the local buckling response. This column analytical model is 1938 mm high (one half of the 1st-story column of the specimen) and the cross section is HSS300×300×9 mm, identical to the column members in the test frame. The column bottom end is fixed but the top end is free. The FE model was constructed using the 4-node, quadrilateral, stress/displacement shell elements with the reduced integration and a large-strain formulation (S4R). The bilinear steel material model was adopted for a total of 936 shell elements. This FE column model was subjected to a constant axial load of 257 kN (observed from the gravity load in the bottom corner column in the basic model) and cyclic increasing lateral displacements in one direction only.

Figure 6 shows the local buckling response of the ABAQUS column model when the column top end reached 0.04 radians lateral drift. Figure 7 shows the ABAQUS column base moment versus top end lateral drift relationships. It is evident that the HSS300×300×9 mm column strength degradation is rather pronounced

www.EngineeringEBooksPdf.com

when the lateral drifts are greater than 0.02 radians. In order to refine the column element properties in the frame model, the "Parallel" material model in PISA3D was adopted in this study. The construction of the hinge-buckling-column "HBC" model utilized two material properties and the feature of parallel material to simulate the cyclic local buckling response of the column. In the present study, the parallel material property as shown in Fig. 8c is a result of combining the degrade material given in Fig. 8a with the hardening material illustrated in Fig. 8b. The cyclic responses of a PISA3D "HBC" model for the 1938 mm high HSS300×300×9 mm column using the Parallel material are also plotted in Fig. 7. It can be found from comparing the ABAQUS and PISA3D results that the column's cyclic strength degradation due to the local buckling can be better simulated from using the HBC model than the bilinear hinge column model. The effects of axial loads on the accuracy of the HBC models will be discussed later.

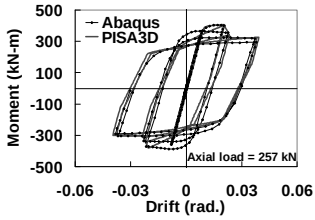


Figure 7: Comparing the HBC cyclic column lateral force versus deformation responses with the ABAQUS FE results.



(a) Degrade Material (b) Hardening Material (c) Parallel Material

Figure 8: Parallel material model in PISA3D (a) + (b) = (c)

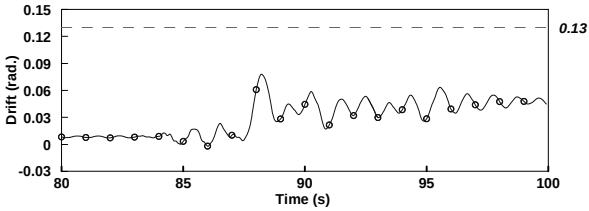


Figure 9: First story drift time histories in the Y direction under the EQ-C for the HBC model.

From the findings stated above, the refined HBC model was constructed and studied by replacing the 1st-story columns in the basic model with HBC model columns. The responses of the refined HBC frame model were very similar to the basic model. Figure 9 shows the first story drift time history response of the refined HBC model under the EQ-C. It can be found that the 0.13-radian drift was still not reached in the refined HBC frame model. The basic and the refined models introduced so far never considered the effects of interactions among the varying axial loads and bi-axial bending moments in columns as hinge models were adopted. Using the fiber model for column, the axial-flexural interactions can be conveniently incorporated into the frame model. In this approach, the compressive stress degradation characteristic has been implemented into the buckle-material fiber model in order to capture the local buckling responses of the column.

5 REFINE THE COLUMNS USING BUCKLE MATERIAL FIBER MODEL

The Buckle material in PISA3D adopted the cyclic response rules proposed by Maison and Popov [10] as shown in Fig. 10. Users can specify the stress and strain values at the control points to adjust the

www.EngineeringEBooksPdf.com

hysteresis responses. The "FBC" column model adopted fibered beam-column element with a cross section consisting of 44 fibers using the Buckle material model given in Fig. 10. Five integration points were used. In this study, the degradation characteristics in the cyclic responses obtained from the afore-mentioned ABAQUS FE column analysis was used to calibrate the parameters of the FBC column model. Two levels of column axial loads (257 and 515 kN for corner column and center column, respectively) were chosen. Figure 11 shows that at both two different axial force levels, the FBC column model can satisfactorily simulate the cyclic degrading responses of the ABAQUS FE model. It can be found that under the 515 kN constant axial load, the cyclic degradation of the ABAQUS FE model is severer than in the case of 257 kN axial load. This phenomenon has been well captured by using the same set of degrading parameters in the two FBC models. Based on this finding, a more refined frame model was constructed.

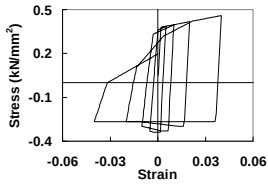


Figure 10: The stress versus strain relationship of each fiber in the FBC model.

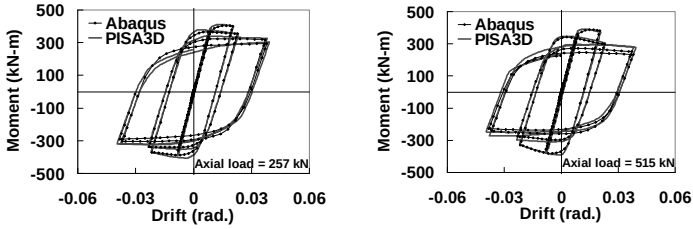


Figure 11: Comparing the FBC cyclic column lateral force versus deformation responses with the ABAQUS FE results for two levels of column axial loads.

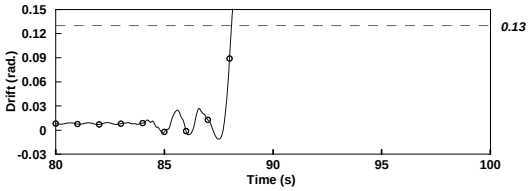
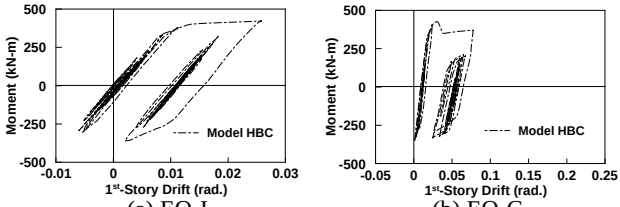


Figure 12: First story drift time histories in the Y direction under the EQ-C for the FBC model.

The refined "FBC" frame model was constructed by replacing the 1st-story columns of the basic model with the FBC-model columns. Figure 12 shows the 1st-story drift time histories under the EQ-C for the FBC frame model. It can be found in the figure that this model reached the 0.13-radian collapse criterion and the time of the occurrence was very close to the test results [11]. Figures 13 and 14 show the "HBC" and "FBC" center column base moment (toward the longitudinal direction of the frame collapse) versus 1st story drift relationships for two levels of excitations, respectively. Under the EQ-I, the strength degradation was not yet developed in Model HBC as shown in Fig. 13a. However, it is evident that the strength deterioration in Fig. 14a (representing the column buckling) has occurred in Model FBC during the EQ-I. As a result, the column base responses of the two models are very different during the EQ-C as evidenced in Figs. 13b and 14b. The reduced strength as observed in the beginning of the FBC model in Fig. 14b was very similar to the response reported in the reference [3]. The strength deterioration was not reached in Model HBC during the EQ-I (Figure 13a) and its initial strength in the beginning of EQ-C (Figure 13b) was higher than that in FBC frame model. These results seem to fail HBC frame model to

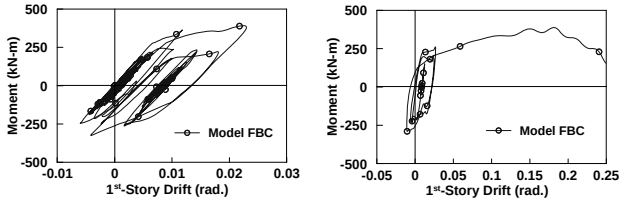
www.EngineeringEBooksPdf.com

predict the collapse responses. The FBC frame model incorporating the effects of interactions among the varying axial loads and bi-axial bending moments in columns have captured the collapse of the building specimen. This should suggest that the collapse of the test frame, or the accuracy of analytical collapse simulation, is strongly governed by the severe local buckling of the columns in the first story. The cyclic column axial and bi-axial flexural interactions are critical in developing the local buckling of the columns. The proper column analytical model using reasonable degrading rules is important for the collapse simulation.



(a) EQ-I (b) EQ-C

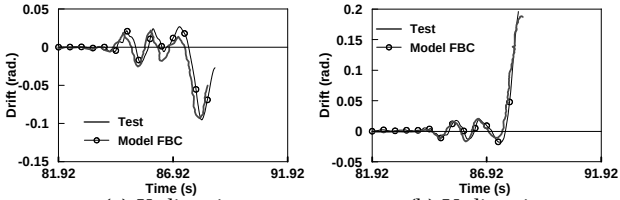
Figure 13: Column bottom end moment versus 1st-story drift relationships in Model HBC.



(a) EQ-I (b) EQ-C

Figure 14: Column bottom end moment versus 1st-story drift relationships in Model FBC.

Figure 15 compares the X and Y directions' 1st-story drift time histories of Model FBC and test results [11] under the EQ-C. In the both directions, the analytical results show good correspondence with the test responses. In addition, the time instant at which the inter-story drift of the analytical model reached 0.13 radians appears very close to that measured from the test (Figure 15b). It is illustrated that the refined FBC analytical model made in this study can satisfactorily simulate the collapse of the specimen.



(a) X-direction (b) Y-direction

Figure 15: First-story drift time histories under the EQ-C.

6 SUMMARY AND CONCLUSIONS

Based on the analytical and experimental studies, summaries and conclusions can be made as follows:

1. The basic frame model using bilinear hinge-model column elements failed to predict the frame collapse time. The key reason is that the column strength degradation due to the local buckling has not been considered.
2. Under the EQ-I, the strength degradation was not yet developed in the HBC frame model but was evident in the FBC frame model. The reduced strength as observed in the beginning of the FBC model was very similar to the response of the test specimen. This strength deterioration was not reached in the

www.EngineeringEBooksPdf.com

HBC frame model during EQ-I and its initial strength in the beginning of EQ-C was higher than that in the FBC frame model. These results seem to fail the HBC frame model to predict the collapse responses.
3. The ABAQUS column local buckling responses can be represented using the PISA3D fiber-model column with Buckle Material. The proposed FBC column model can conveniently incorporate the combined cyclic strength degrading effects among the varying axial loads and bi-axial bending moments. The collapse of the test frame is strongly governed by the severe local buckling of the columns in the first story. The collapse time can be predicted in the FBC frame model using this column model element. This suggests that the analytical force versus deformation relationships of the first story columns strongly affects the frame collapse prediction. The column analytical model with proper degrading rules is important for the collapse simulation.

ACKNOWLEDGEMENTS

The authors greatly appreciate the E-Defense for conducting the tests, the blind prediction contest, and sharing the test results. This interesting test and the valuable experimental data have stimulated the interests of many researchers and engineers in studying the analytical modeling techniques for steel structures under earthquake ground motions.

REFERENCES

[1] HEERC, Hyogo Earthquake Engineering Research Center. *Blind Analysis Contest Application Site*. Web page: http://www.blind-analysis.jp/index_e.html. 2007.

[2] Ohsaki M., Kasai K., Hikino T., and Matsuoka Y. “Overview of 2007 E-Defense blind analysis contest results”, *Proceeding of 14th World Conference on Earthquake Engineering*, Beijing, China. 2008.

[3] Suita K., Yamada S., Tada M., Kasai K., Matsuoka Y., and Shimada Y. “Collapse experiment on 4-story steel moment frame: Part 2 Detail of collapse behavior”, *Proceeding of 14th World Conference on Earthquake Engineering*, Beijing, China. 2008.

[4] Lin B.Z., Chuang M.C., and Tsai K.C. “Object-oriented development and application of a nonlinear structural analysis framework”, *Advances in Engineering Software* 2009; 40:66-82.

[5] Spacone E., Filippou F.C., Taucer F.F. “Fibre beam-column model for non-linear analysis of R/C frames: part 1. formulation”, *Earthquake engineering and structural dynamics* 1996; Vol. 25. 711-725.

[6] Shimada Y., Kishiki S., Yamada S., Matsuoka Y., and Suita K. “Panel zone performance in a weak panel-type moment frame consisting of a composite beam and a square hollow section column”, *Proceedings of 6th International Conference on Behavior of Steel Structures in Seismic Areas*, Philadelphia, Pennsylvania, USA. 2009.

[7] Tsai K.C. and Popov E.P. “Seismic panel zone design effect on elastic story drift in steel frames”, *Journal of Structural Engineering* 1990; 116(12), pp. 3285-3301.

[8] Hikino T., Ohsaki M., Kasai K., and Nakashima M. “Simulation of E-Defense full-scale shake-table test results of moment-resisting steel frame”, *Proceedings of 6th International Conference on Behavior of Steel Structures in Seismic Areas*, Philadelphia, Pennsylvania, USA. 2009.

[9] ABAQUS. ABAQUS analysis user’s manual. *ABAQUS Inc*., Version 6.6. 2006.

[10] Maison B.F., and Popov E.P. “Cyclic response prediction for braced steel frames”, *Journal of the Structural Division* 1980; Vol. 106, No. 7, p.1401–p.1416.

[11] Tada M., Tamai H., Ohgami K., Kuwahara S., and Horimoto A. “Analytical simulation utilizing collaborative structural analysis system”, *Proceeding of 14th World Conference on Earthquake Engineering*, Beijing, China. 2008.

www.EngineeringEBooksPdf.com

SDSS'Rio 2010 STABILITY AND DUCTILITY OF STEEL STRUCTURES
E. Batista, P. Vellasco, L. de Lima (Eds.)
Rio de Janeiro, Brazil, September 8 - 10, 2010

ROBUSTNESS OF STEEL AND COMPOSITE BUILDINGS UNDER IMPACT LOADING

Ludivine Comeliau, Jean-François Demonceau and Jean-Pierre Jaspart

Liège University, ArGEnCo Department
e-mails: ludivine.comeliau@ulg.ac.be, jfdemonceau@ulg.ac.be, jean-pierre.jaspart@ulg.ac.be

Keywords: Robustness, Building frames, Column impact, Dynamic effects.

Abstract. *In case of a vehicle impact against a building frame, one or more columns may be damaged or even fully destroyed. In such an exceptional event, the risk of progressive collapse of the whole structure has to be mitigated. Several approaches potentially exist to face this problem. In the present study, the so-called* alternative load path method *is followed. In two recent PhD studies at Liège University, a complete analytical procedure was developed permitting the prediction of the structural response of steel or composite plane frames further to the loss of a column. For sake of simplicity, these first works were based on the assumption of static behaviour. More recently, complementary research was carried out with the objective to address the dynamic effects. As a result, an original procedure for the appraisal of the structural robustness of plane building frames was proposed. The present paper presents this work.*

1 INTRODUCTION

The loss of a column in a building frame may be associated with different types of exceptional events: explosion, impact of a vehicle, fire... Amongst these actions, some induce negligible dynamic effects; then a "static" response can be assumed. However, in many other circumstances, the column is removed relatively quickly, which induces significant dynamic amplifications that need to be taken into account.

Investigations were conducted at Liège University in the last few years regarding the static behaviour of two-dimensional building frames suffering the loss of a column further to an unspecified accidental event. These studies are detailed in two PhD theses: the thesis of Demonceau [1] and the thesis of Luu [2]. They resulted in the development of simplified analytical methods for the prediction of the structural response assuming static behaviour. The dynamic response of building frames further to the loss of a column was more recently investigated by Comeliau [3]. In particular, the behaviour of a simplified substructure was studied. In this paper, researches conducted in [3] are summarized and the main results are reflected.

2 GLOBAL APPROACH AND PREVIOUS RESEARCHES

The approach followed in [1] and [2] to study the static response of a structure losing a column is based on a decomposition of the latter in two parts: the directly affected part, which is made up of the beams and columns above the lost column; and the indirectly affected part, which consists of the rest of the frame (Figure 1).

The evolution of the vertical displacement Δ_A at the top of the failing column versus the axial load N_{lo} that it supports is represented by a curve as illustrated in Figure 2. The behaviour can be divided in three main phases. The first one corresponds to the application of the "normal" loads on the structure. It goes from point (1) (unloaded, $\Delta_A = 0$) to point (2) (conventional loading, $\Delta_A \ll$). The structure is assumed to remain elastic during this phase. At point (2), the exceptional event occurs; then the column "AB" is progressively removed: the compression it sustains starts to decrease. During phase 2, the directly

www.EngineeringEBooksPdf.com

affected part goes from a fully elastic behaviour to a plastic mechanism. The first plastic hinge appears at point (3) while the complete plastic mechanism is formed at (4). After point (4), rapidly increases and second order effects become important. In particular, significant catenary actions develop in the bottom beams of the directly affected part, which makes the system stiffness increase and the deformation rate decrease. If the frame exhibits sufficient robustness, a final stable state is obtained at (5), when .

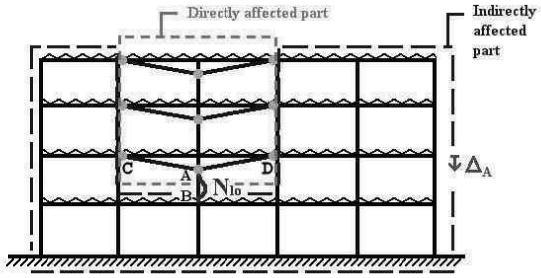


Figure 1: Directly and indirectly affected parts of a building frame / Plastic mechanism caused by the loss of a column

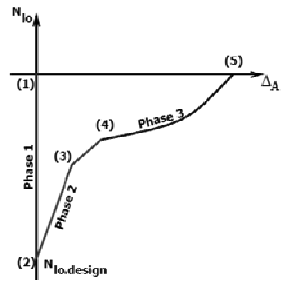


Figure 2: Evolution of the displacement versus the axial load

Obviously, it is only possible to reach a final stable state, corresponding to point (5), if no failure occurs prematurely, would it be in the directly affected part or in the rest of the structure; i.e. it is necessary that: (i) the loads transferred from the directly affected part to the indirectly affected part do not induce the collapse of elements in the latter, (ii) the compression supported by the upper beams of the directly affected part due to an "arch effect" do not lead to their buckling, (iii) the different structural elements of the directly affected part exhibit sufficient resistance and ductility to reach the displacement . In some cases, the column may be completely removed ( ) before reaching phase 3.

The response of the structure at phases 1 and 2 was investigated in [2] while phase 3 was studied in [1]. During this last phase, the global plastic mechanism is formed in the directly affected part and large displacements are observed. As a consequence, second order effects become significant. In particular, tension loads develop in the bottom beams of the directly affected part. It was shown that the membrane forces developing in the two beams overhanging directly the lost column ("CA" and "AD" in Figure 1) are significantly more important than the ones developing in the other beams. That is why it was decided to investigate the behaviour of this single storey and thus to extract from the frame a simplified substructure consisting of this double-beam and its beam-to-column joints (Figure 3). The influence of the indirectly affected part is characterised by an elastic horizontal spring having a stiffness K and a resistance . Analytical methods aiming to estimate the value of these parameters K and were developed in [2]. The ability of such a substructure to simulate with sufficient accuracy the behaviour of the directly affected part was validated by numerical tests [1]. Finally, an analytical approach was developed to predict the response of the frame during phase 3 [1], on the basis of the "substructure approach". So, the static curve (,) can be entirely derived from the combination of the developments detailed in [1] and [2], which provides a global analytical procedure. However, it is only valid as long as a static response of the frame is observed.

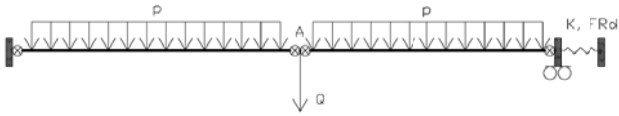


Figure 3: Double-beam simplified substructure

www.EngineeringEBooksPdf.com

3 DYNAMIC BEHAVIOUR OF A SUBSTRUCTURE

3.1 Description of the considered substructure and loading

The dynamic behaviour of a simplified substructure such as described above was investigated under the following hypothesis: steel structures are considered, the behaviour law is admitted to be independent of the strain rate and a quasi-static elastic-perfectly plastic law is assumed (infinite ductility), the stiffness K of the lateral spring remains constant, the beam-to-column joints are perfectly rigid and fully resistant.

A uniformly distributed load p is applied on the double-beam. Initially, the central support is present and sustains a force N_0 ($N_0 = p.l_0$, l_0 being the initial length of each beam). Then, the latter is progressively removed, which is simulated by the application of a force P equal and opposite to N_0 in the middle of the system. The complete loss of the support takes a time t_r and a linear decrease of the force it sustains is assumed. In static conditions, it had been shown in [1] that the uniformly distributed load p could be neglected as far as the behaviour in phase 3 was investigated, i.e. for P greater than P_{pl}, which is the force corresponding the plastic plateau in the static curve (development of a beam mechanism). The validity of this assertion for dynamic situations was studied [3]. Many numerical dynamic tests were made on a substructure in order to compare the maximum displacement obtained in the two loading situations (Figure 4) for the same loading parameters P and t_r. It was observed that the difference is limited provided the force P is great enough (above the static plastic plateau). That is the reason why the behaviour of the substructure under the simplified loading situation was mainly investigated. Moreover, it was shown that the introduction of damping in the system does not induce a significant decrease of the maximum displacement [3]. As a consequence, undamped systems were considered; this constitutes a conservative approach.

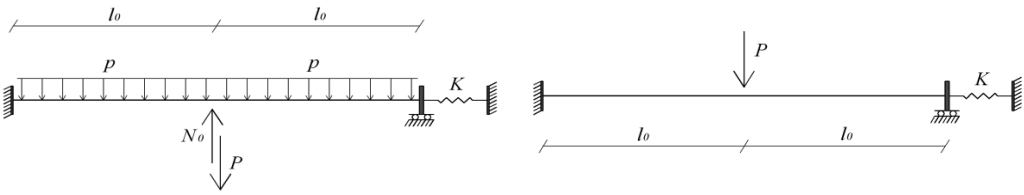


Figure 4: Considered system with realistic and simplified loadings

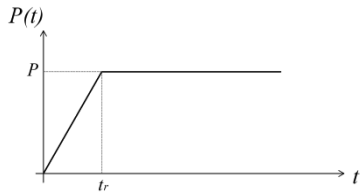


Figure 5: Time evolution of the applied force P(t)

3.2 Influence of different parameters on the dynamic behaviour

To investigate the dynamic response of the substructure, a simplified loading is considered, consisting of a single concentrated load applied in the middle of the system. Obviously, as well as in static, the level of the load P and the geometrical and mechanical characteristics of the structure have an influence on its behaviour. In case of dynamic loadings, the application rate of P, characterised by the rise time t_r (Figure 5), is also important. Besides, mass and damping properties are essential factors on which the dynamic response depends.

As mentioned above, the studied systems are undamped ones. As far as mass influence is concerned, a change in mass has first the effect of modifying the principal natural period of the system. Numerical tests proved that the dynamic response of a given structure is actually governed by two parameters: P and

www.EngineeringEBooksPdf.com

t_r/T, where T is the period of the principal eigenmode in elastic domain [3]. Thus, if the mass of the system is modified but the rise time of the load is adapted so that the ratio t_r/T is kept constant, then the maximum displacement remains unchanged. Furthermore, the time evolution of the displacement remains the same provided it is expressed as a function of a non-dimensional time t/T (or t/t_r).

In [3], the behaviour of the substructure according to the loading parameters P and t_r (or t_r/T) was investigated through numerical dynamic analyses. All the results presented below are related to the following particular substructure:

- beams: $l_0 = 6{,}5\ m$, IPE 450, S235, $m = 3000\ kg/m$ ($T = 0{,}31\ sec$);
- spring: stiffness $K = 10000\ kN/m$, resistance $F_{Rd} \gg$

Performing dynamic analyses for different loading conditions (P, t_r) and registering the maximum displacement u_{max} obtained for each one, curves giving u_{max} as a function of the applied force P were established, for different values of t_r (constant along one curve). These curves are drawn in Figure 6; only dynamic loadings leading to u_{max} smaller than the displacement corresponding to the complete yielding of the beams in tension are considered. On this graph, the upper curve is the static one, while the lower curve is the so-called pseudo-static one, which gives the maximum displacement reached if P is applied instantaneously ($t_r = 0$). Such a curve can easily be established provided only the nonlinear static curve is known, following a procedure developed at London Imperial College [4]. Obviously, the maximum displacement corresponding to a force P will always be situated between the static displacement ($t_r \to \infty$) and the displacement caused by the sudden application of the load ($t_r = 0$). As a consequence, every (P, u_{max}) curve will lie between the static and the pseudo-static ones all along, for any value of t_r. As a general rule, for a given value of P, u_{max} tends to decrease when t_r increases.

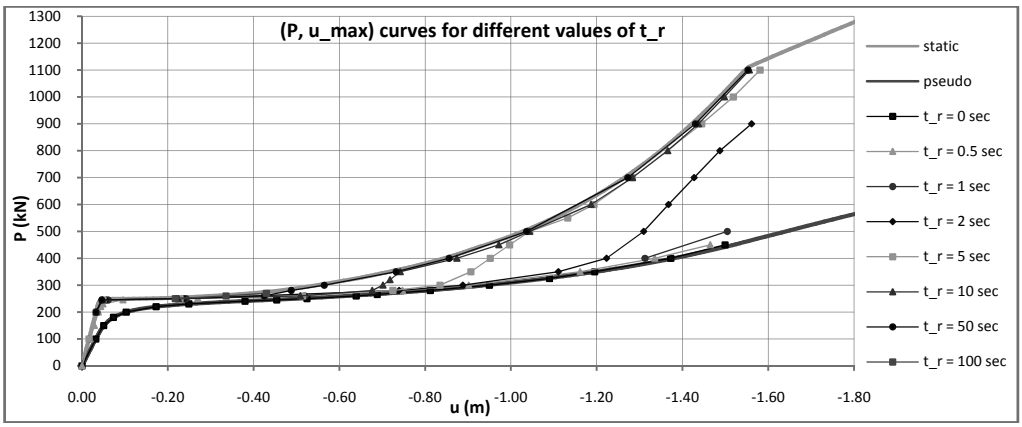


Figure 6: Maximum dynamic displacement according to the value of the load and its rise time

Different types of behaviour can already be highlighted from Figure 6. For loads $P > P_{pl}$, two types of response are observed according to the loading parameters P and t_r. For the first type, the maximum dynamic displacement is greater than the static displacement while, for the second one, u_{max} is very close to u_{stat}. Examples of both response types are presented below. For each of them, the dynamic curve representing the time evolution of the displacement $u_{dyn}(t)$ is compared to the static curve $u_{stat}(t)$, which represents the evolution of the displacement, dynamic amplification being neglected. Accordingly, $u_{stat}(t^*)$ is the static displacement associated with the value of the applied load $P(t^*)$ at the time t^*.

A response of type 1 (Figure 7) is met when the system yields and gets beyond the static displacement corresponding to the final load P. Then, it finally oscillates around a value of the displacement greater than this static displacement. If a behaviour of type 2 occurs (Figure 8), then, when the plastic mechanism forms and the displacement suddenly increases, the latter however remains smaller than the static displacement corresponding to the final force P. Next, the dynamic curve $u_{dyn}(t)$ oscillates around a

www.EngineeringEBooksPdf.com

more or less constant value whilst the applied load continues to rise. Once the force $P(t)$ has increased enough so that the associated static displacement meets the dynamic displacement, the latter starts to increase again, oscillating around the static curve. Eventually, the maximum dynamic displacement is close to $u_{stat}(P)$.

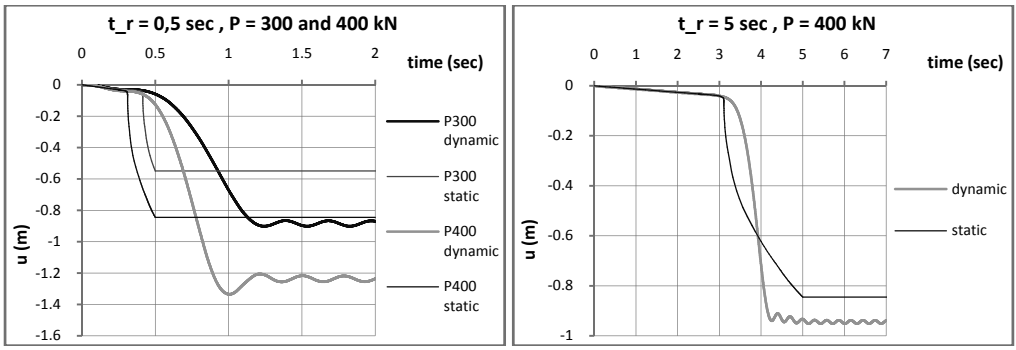


Figure 7: Examples of the time evolution of the displacement for a response of type 1

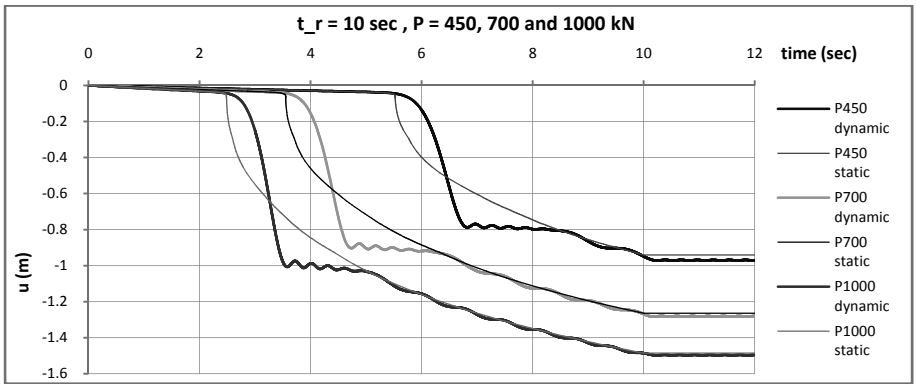


Figure 8: Examples of the time evolution of the displacement for a response of type 2

The time evolution of the displacement for both response types can be explained as follows. When the plastic mechanism forms, the displacement rapidly increases and a distinct change in the slope of the curve $u_{dyn}(t)$ is observed. However, due to its inertia, the system gets on the move progressively and the displacement remains at the beginning below the static displacement $u_{stat}(t)$ corresponding to the applied load $P(t)$. The system starts to accelerate and the dynamic displacement gets closer to the static one. Then it exceeds the latter and, the displacement of the system becoming higher than the static displacement associated with the force $P(t)$ applied at the considered time, the velocity begins to decrease. The reduction of the velocity to zero, which corresponds to the first maximum of the dynamic displacement curve and a "stabilisation" of the system, may occur for a displacement smaller or greater than the static displacement associated with the final load; that is what distinguishes the two behaviour types. Then, there is a sort of plateau in the curve $u_{dyn}(t)$. In the first case (type 1), this plateau is infinite. In the second case (type 2), it carries on until the applied force $P(t)$ has sufficiently increased so that the corresponding static displacement is equal to the dynamic displacement. Next, the dynamic curve oscillates around the static one to finally stabilize around a value of the displacement close to $u_{stat}(P)$.

As far as internal forces are concerned, the axial load in the beams remains very small before the appearance of the three plastic hinges. When the moment in the middle and at the extremities of the

www.EngineeringEBooksPdf.com

double-beam reaches the plastic value M_{pl}, the mechanism forms and the displacement rapidly increases, which induces the development of significant membrane forces in the beams. As a consequence, the moment acting in the plastic hinges decreases to respect the M-N plastic interaction relation. At the end, oscillations of M and N are observed while the displacement is oscillating around a constant value. The amplitude of the oscillations of the tension force is limited as the amplitude of the variations of the displacement is also small. On the other hand, the moment varies more importantly, in phase with the oscillations of u. There corresponds a succession of elastic "unloadings-loadings" that can be observed on the M-N interaction diagram as well as on the M-u and N-u curves [3]. Moreover, it is interesting to note that the maximum axial load in the beams, which is obtained when u_{max} is reached, is the same as the tension force that would develop if this displacement was reached statically. Accordingly, this membrane force can be deduced from the sole knowledge of u_{max} and the static response.

3.3 Simplified approach to estimate the maximum dynamic displacement

The objective was to develop a simplified method to estimate the maximum displacement reached for given loading conditions (P, t_r/T) with $P > P_{pl}$. Then, it would be possible to predict the required deformation capacity of the structural members as well as the tension force they should resist. In view of the aspect of the (P, u_{max}) curves (see Figure 6), the idea was to approach the latter, beyond the plastic plateau, by approximate curves established as follows [3]: section 1 ≡ horizontal at the level of P_{pl}; section 2 ≡ pseudo-static curve; section 3 ≡ vertical between the pseudo-static and the static curve, at the abscissa $u = u_{trans}$ at which the actual (P, u_{max}) curve joins the static curve; section 4 ≡ static curve. An example of such a curve is presented in Figure 9 ("correct" approximate curve). For too low values of the ratio t_r/T, the dynamic curve does not join the static one and sections 3 and 4 cannot be defined. It is also possible that section 2 does not exist.

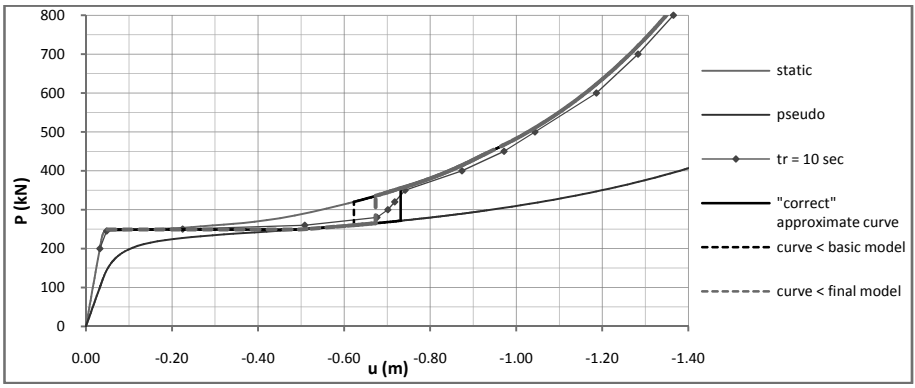


Figure 9: Example of an approximate dynamic curve $(P, u_{max})_{appr}$

To be able to draw such an approximate curve, the value of u_{trans} is still to determine. The point (P_{trans}, u_{trans}) at which the dynamic curve (P,u_{max}) associated with a given value of t_r/T joins the static curve corresponds to a transition between the two types of response previously described. Indeed, we have $u_{max} > u_{stat}$ for $P < P_{trans}$ (type 1) and $u_{max} \approx u_{stat}$ for $P > P_{trans}$ (type 2). As explained before, the behaviour type is governed by the value of the displacement ($u_{plateau}$) when the velocity is reduced to zero for the first time after the formation of the plastic mechanism. In fact, type 1 corresponds to $u_{plateau} > u_{stat}(P)$ while type 2 is associated with $u_{plateau} < u_{stat}(P)$.

As a consequence, if $u_{plateau}$ could be evaluated for a given loading, then the approximate dynamic curve $(P, u_{max})_{appr}$ corresponding to a fixed value of t_r (or t_r/T) could be established following this procedure: (i) determination of the displacement $u_{plateau}$ for different values of P and comparison with the static displacement $u_{stat}(P)$; (ii) identification of the force for which $u_{plateau} = u_{stat}(P)$: this value

www.EngineeringEBooksPdf.com

of the load is P_{trans}; (iii) deduction of $u_{trans} = u_{stat}(P_{trans})$ from the static curve; (iv) drawing of the complete curve $(P, u_{max})_{appr}$. In order to carry out the first stage of this procedure, a simplified model was developed to estimate $u_{plateau}$ [3]. The latter is described below.

At first, a basic simplified model was developed under the following assumptions. It is a rigid-plastic model, in which the beams are considered to be infinitely rigid and thus keeping a constant length $l = l_0$. The plastic hinges developing at their extremities are submitted to a moment $M = M_{pl}$ admitted constant, interaction with the axial load being neglected. Finally, moderate displacements are supposed, which means that:

- $\theta \approx \frac{u}{l}$ $(\approx \sin\theta \approx \mathrm{tg}\,\theta)$
- $\cos\theta \approx 1 - \frac{\theta^2}{2} \approx 1 - \frac{u^2}{2l^2}$

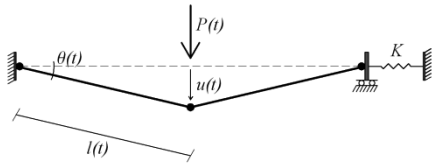


Figure 10: Considered system and main definitions

An energy equation was written, consisting in expressing that the work done by the external force $P(t)$ is equal to the sum of the kinetic energy, the work of the plastic hinges and the energy stocked in the lateral spring:

$$E_{kinetic} + E_{hinges} + E_{spring} = W_e \iff \frac{1}{2}M_g.\dot{u}^2 + 4.\int M(\theta).d\theta + \int F_K(\delta_K).d\delta_K = \int P(u).du \qquad (1)$$

$$\iff M_g.\ddot{u}(t) + \frac{4.M_{pl}}{l} + \frac{2K}{l^2}\cdot u(t)^3 = P(t) = P.\frac{t}{t_r} \qquad (2)$$

Where $M_g = 1/3 \cdot m \cdot 2l_0 = 1/3 \cdot M_{tot}$ is the generalised mass of the system, δ_K is the elongation of the horizontal spring and F_K the force it sustains.

This equation is only valid until the first maximum of the displacement is reached, which is $u_{plateau}$, and provided it occurs before the applied load become constant, so that it is expressed as $P(t) = P.t/t_r$. However, these restrictions are of no consequence here. Indeed, what we are interested in is the determination of $u_{plateau}$ and what happens after is no concern. Moreover, as the final objective is the determination of P_{trans}, only responses relatively close to the intermediate situation between the two behaviour types are interesting; and, in such cases, the plateau always starts at a time $t_{plateau} < t_r$. In order to resolve the previous equation, initial conditions have to be defined. In the considered rigid-plastic system, the displacement and the velocity are both zero until the plastic mechanism is formed. So the equation is resolved from the time t_{pl}, with the initial conditions: $u_0 = u(t_{pl}) = 0$ and $\dot{u}_0 = \dot{u}(t_{pl}) = 0$.

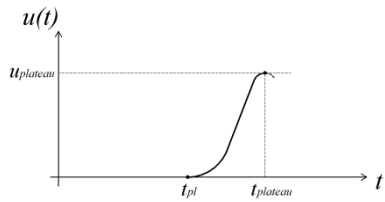


Figure 11: Typical response of the system defined on the basis of the model

Unfortunately, this equation has no analytical solution and had to be numerically resolved. Moreover, it was observed that the use of this basic model leads to underestimate $u_{plateau}$, and then the value of u_{trans} (see the corresponding curve on the graph of Figure 9). That can be explained by the fact that different aspects neglected in the development of the basic model would induce greater displacements if

www.EngineeringEBooksPdf.com

taken into account. Eventually, the final model was developed from equation (1) but considering the M-N plastic interaction ($M_{pl}(N) = M_{pl}(u) < M_{pl}$) and the elongation of the beams ($l(N) = l(u) > l_0$). Then, the last approximate curve of Figure 9 was drawn using this final model and following the previously described procedure. It is observed that the developed simplified method still leads to underestimate the extreme dynamic displacement for values of the force P close to P_{trans}. For the considered example, the maximum unsafe error is about 8%.

4 CONCLUSION AND PERSPECTIVES

Within the present paper, part of the research carried out in [3] is reflected. As an introduction, a general approach developed at Liège University to study the behaviour of building frames further to the loss of a column was first presented, as well as previous works performed on the static response of such frames ([1] and [2]). In particular, the possibility to define a substructure able to reproduce the global response of a frame when membrane effects develop further to a column loss was illustrated.

Then, some investigations conducted in [3] were introduced. The latter are mainly dedicated to the study of the dynamic response of the previously defined substructure further to the loss of its central support. The time evolution of the displacement, yielding and internal forces was studied in detail through numerical simulations; the influence of different properties of the structure (mainly its first period T) and of its loading conditions (the value of the load P initially sustained by the central support and the duration t_r of its removal) was highlighted. Finally, a simplified method was proposed to quantify the maximum dynamic displacement u_{max} suffered by a substructure under a given loading ($P, t_r/T$).

Of course, it would be interesting to refer to these developments in the case of an actual building frame; in the same way as, in static conditions, such a simplified substructure is able to reproduce the response of the whole frame. The dynamic behaviour of building frames further to the loss of a column was studied [3]. Qualitatively, it showed many similarities with the response of a substructure in terms of displacement, yielding and internal forces. However, the ability of the extracted substructure to reflect the dynamic behaviour of the whole frame should be investigated in more depth.

A second perspective concerns the improvement of the simplified model. Indeed, the proposed procedure aiming to predict the maximum dynamic displacement may lead to underestimate the latter. This method was validated for few study cases, with maximum unsafe errors of about 10%, which is reasonable. However, the number of tests is too small to draw general conclusions. Besides, the equation of the model has no analytical solution and has to be numerically solved. As the objective at Liège University is to come at the end with easy-to-apply simplified analytical methods, it would be interesting to establish an approximate solution of the model equation, having an analytical expression.

In conclusion, the presented investigations constitute a first step for the implementation of the dynamic effects within the general concept developed in Liège and already validated in static. Further studies are planned in a near future.

REFERENCES

[1] J.F. Demonceau. “Steel and composite building frames: sway response under conventional loading and development of membrane effects in beams further to an exceptional action”. PhD thesis presented at Liège University. Belgium, 2008.

[2] H.N.N. Luu. “Structural response of steel and composite building frames further to an impact leading to the loss of a column”. PhD thesis presented at Liège University. Belgium, 2008.

[3] L. Comeliau. “Effets du comportement dynamique des structures de bâtiments en acier suite à la ruine accidentelle d’une colonne portante”. Travail de fin d’études, Université de Liège. Belgique, 2009. http://hdl.handle.net/2268/32284

[4] A.G. Vlassis. “Progressive collapse assessment of tall buildings”. Thesis submitted in fulfilment of the requirements for the degree of Doctor of Philosophy of the University of London and the Diploma of Imperial College London. UK, April 2007.

www.EngineeringEBooksPdf.com

SDSS'Rio 2010 STABILITY AND DUCTILITY OF STEEL STRUCTURES
E. Batista, P. Vellasco, L. de Lima (Eds.)
Rio de Janeiro, Brazil, September 8 - 10, 2010

DESIGN OF STEEL FRAMES OF DISSIPATIVE SHEAR WALLS

C. Neagu*, F. Dinu*, and D. Dubina***

* The "Politehnica" University of Timisoara, 1 Ioan Curea, 300224 Timisoara, Romania
e-mails: calin.neagu@ct.upt.ro, florea.dinu@ct.upt.ro, dan.dubina@ct.upt.ro
** Romanian Academy, Timisoara Branch, 24 Mihai Viteazul, 300223 Timisoara, Romania

Keywords: Steel shear wall, Seismic design, Experimental, Monotonic, Cyclic, q factor.

Abstract. *This paper presents the results of an experimental program carried out on two story frame models of dissipative shear walls. Rigid and semi-rigid beam-to column joint are considered. The experimental investigation is accompanied by a numerical simulation program in order to validate and extend the conclusions of the experimental study to real multi-story frames. Values of behavior factor q obtained from experimental tests are proposed.*

1 INTRODUCTION

Steel plate shear walls SPSW have been used as lateral force resisting systems since 80's, but the design specifications were rather incomplete or absent. Numerous research programs and also seismic experiences have confirmed their effectiveness. A major role on their development can be attributed to the introduction of design rules in the code provisions, e.g. AISC 2005 [1]. In Europe, the application of SPSW system is limited, partly due to the lack of design provisions in seismic code EN 1998-1 [2], particularly there are no recommendations for behavior and overstrength factors q and Ω, respectively. An additional problem refers to the prediction of the strength and stiffness capacity of the SPSW structures. Design practice requires simple models and conventional analysis software that are available and relatively simple to use. One of the models used to represent the behavior of SPSW is the strip model, developed by Thorburn et al. [3]. Thus, in order to model the steel shear walls, the steel plates are replaced by a series of truss members - strips, parallel to tension fields. A minimum of ten strips per panel are required to adequately represent the tension field action developed in the plate.

In the recent years, many researchers studied the behavior of SPSW and their viability as seismic force resisting systems. Choi & Park [4] and Habashi & Alinia [5] studied experimentally the interaction between the infill panels and the boundary elements. In another experimental program, Choi & Park [6] studied the ductility and energy dissipation capacity of various SPSW typologies, and compared them with other types of bracing. In their study, Ghomi & Gholhaki [7] investigated the influence of beam-to-column connections on the ductility of SPSW. Based on the results of the cyclic test, Li et al. [8] proposed a capacity design principle for boundary elements.

In order to address the issues presented above with regards to the performances of SPSW systems, a parametric study on different structural configurations was performed, on the aim to evaluate the demands in terms of strength and ductility [9]. Acceptance criteria and performance parameters (eg. behavior factor q) were taken according to [1]. Based on these results, an experimental program on steel plate shear wall systems has been developed at the Steel Structures Laboratory from the Politehnica University of Timisoara. The test results shown very good agreement with the parameters and acceptance criteria used in design. The paper summarizes the experimental results and gives some preliminary indications regarding the selection of behavior factor q.

www.EngineeringEBooksPdf.com

2 EXPERIMENTAL PROGRAM

2.1 Analysis and design of steel plate shear wall structure

Previous studies of the authors [9] focused on the comparative analysis of the seismic performances of conventional centric and eccentric braced systems and new systems using buckling restrained braces and dissipative Steel Plate Shear Walls. Structures were investigated using pushover analysis. The parameters that were assessed in order to evaluate the seismic performance of the structural systems were story drift and plastic deformations in dissipative members. Particular attention was paid to the potential values to be used in design of overstrength factor Ω and to the global plastic mechanism at failure. Dual systems of SPSW have shown they are very effective both in terms of stiffness and ductility. Therefore, post-elastic behaviour of SPSW systems confirms the behavior factor q proposed in AISC 2005, which is similar to that used for high dissipative moment resisting frames or eccentrically braced frames.

Encouraged by the results of the numerical investigations, a test program was developed. In order to test realistic structural configurations, test specimens were extracted from a 6 story steel frame building (Figure 1.a). The 6 story structure was designed according to EN1993-1 [10], EN1998-1 and P100-1/2006 [11]. The steel materials were S235 grade for infill panels and S355 grade for frame members. A 4 kN/m^2 dead load on the typical floor and 3.5kN/m^2 for the roof were considered, while the live load amounts 2.0kN/m^2. Structure is located in a high seismic area, which is characterized by a design peak ground acceleration of 0.24g at a returning period of 100 years and soft soil conditions, with T_c=1.6sec. For serviceability check, acceleration amounts 0.12g and allowable inter-story drift is 0.008 of the storey height. For collapse prevention, acceleration amounts 0.36g. EN1998-1 does not provide any recommendations regarding the q factor for SPSW systems. For these structural systems, AISC 2005 provisions were taken as guidance. According to the later code, the behavior factor q for SPSW is similar to that of high dissipative moment resisting frames. Concluding, the design was based on a q factor equal to 6. Two-story specimens were extracted from the structure. Due to the limitations in testing capacity, the specimens were half-scale representative of the actual building (Figure 1.b).

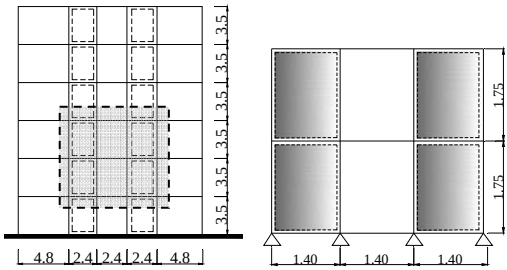


Figure 1. Six story model used for extracting the test specimens a) and two story half-scale specimen b).

2.2 Analysis and design of half-scale models

The two story specimens, extracted from the structure were half-scaled. In order to evaluate to contribution of the frame to the strength and stiffness of the structure, two types of beam-to-column connection were used. The first one is a flush end plate bolted connection and the second one is an extended end plate bolted connection. According to EC3 classification [12], flush end plate connection is semi-rigid and *weak* partial strength ($M_{j,\,Rd}$=0.4$M_{b,Rd}$) (further refereed as *semi-rigid*) and extended end plate connection is rigid and *strong* partial strength, with a capacity almost equal to that of the connected beam ($M_{j,Rd}$ = 0.9$M_{b,Rd}$) (further refereed as *rigid*). The infill panels were bolt connected to the boundary members using fish plates. To reduce the number of bolts, an edge plate was welded to the infill panels to increase the bearing resistance. Nonlinear pushover analyses were conducted on each model in order to evaluate the behavior and the characteristic parameters, like yield strength and yield displacements, ultimate capacity and dissipation capacity. The shear walls were modeled by 10 inclined pin-ended strips,

www.EngineeringEBooksPdf.com

oriented at angle α [13]. Beams and columns were modelled with plastic hinges located at both ends. Pushover analyses have shown the ultimate capacity of structure with rigid beam-to-column connections is 10% above that of the structure with semi-rigid connections, while the stiffness is not much improved. A total of 5 specimens were designed and fabricated (see Table 1). The frames measured 3500 mm high and 4200 mm wide between member centerlines (Figure 2). The slenderness ratio h/t_w of shear walls amounted 595 for 2 mm panels and 397 for 3 mm panels. The two actuators used for the tests have 360mm stroke and 1000 kN capacity and 360mm stroke and 500 kN capacity, respectively.

Table 1. Design of specimens.

Specimen	Infill panel	Column	Beam	Connection	Load type
SR-M-T2	2mm	HEB240 (HEB180)	HEA180	Semirigid	Monotonic
SR-C-T2				Semirigid	Cyclic
R-M-T2				Rigid	Monotonic
R-C-T2				Rigid	Cyclic
SR-C-T3	3mm			Semirigid	Cyclic

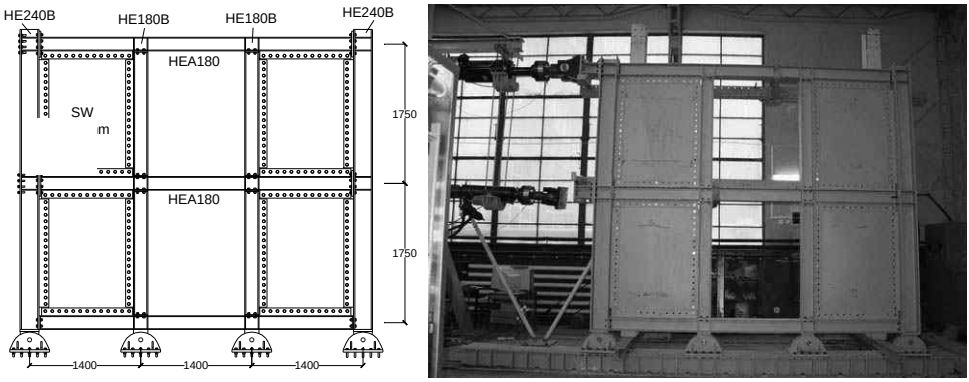


Figure 2. Typical half-scaled test specimen: designed (left) and testing set-up (right).

Table 2 and Table 3 show the measured average values of yield stress f_y, tensile strength f_u and elongation at rupture A_u. It can be observed that there are important differences between nominal and actual material characteristics. The material overstrength is larger for hot rolled sections than for plates. Thus, for hot rolled sections the maximum yield strength scattering amounts 105 N/mm^2, while for plates amounts 80 N/mm^2. The connection of the steel panels to the beams and columns used bolts. The connection was designed to develop expected shear strength of the steel panels. Extended end plate bolted connections were used for rigid beam-to-column connections while for semi-rigid ones flush end plate bolted connections.

Table 2. Mechanical properties of rolled profiles.

Profiles	Nominal steel, ordered (EN 10025-2/2004)	Element	Tests			Actual steel grade (supplied)
			f_y, N/mm^2	f_u, N/mm^2	A_u, %	
HEB240	S335	Flange	457	609	40	S460
		Web	458	609	31	
HEB180	S355	Flange	360	515	44	S355
		Web	408	540	40	
HEA180	S355	Flange	419	558	32	S420

Table 3. Mechanical properties of flat steel (panels).

www.EngineeringEBooksPdf.com

Element	Thickness, mm	Nominal steel, ordered	f_y, N/mm^2	f_u, N/mm^2	A_u, %	Actual steel grade
Plate	2	S235	305	429	24	S275
Plate	3	S235	313	413	25	S275

All specimens were tested monotonically and cyclically using ECCS procedure [14]. According to this procedure, first a monotonic test is done in order to evaluate the force-displacement curve that is used to evaluate the yield displacement. Yield displacement D_y and yield force F_y are obtained by intersecting the initial stiffness α_y and a tangent at the curve *F - D* with a slope of 10% of the initial stiffness. Yield displacement D_y is then used to calibrate the cyclic load history. This contains four elastic cycles ($\pm 0.25D_y$, $\pm 0.5D_y$, $\pm 0.75D_y$ and ± 1.0Dy), followed by groups of 3 cycles of amplitudes multiple of $2D_y$ ($3\times 2D_y$, 3×4Dd$_y$, $3\times 6D_y$, …). Based on experimental results, the evaluation of yield displacement was adjusted to take into account the specific behavior of SPSW. Thus, the slope of initial stiffness was corrected and amounted 20% of the initial stiffness.

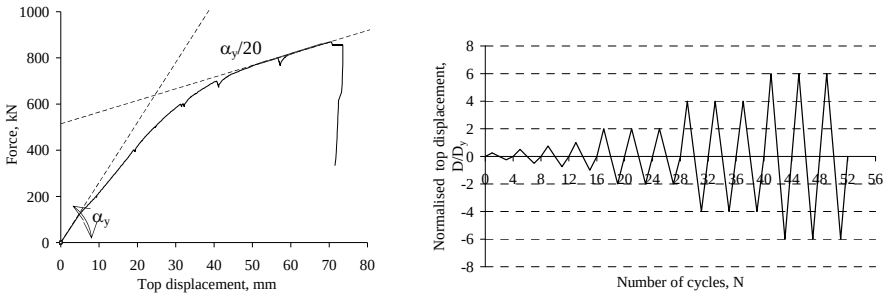


Figure 3. ECCS cyclic loading protocol.

2.3 Experimental results

2.3.1 Monotonic tests

The first test was done on the semi-rigid structure with 2mm panels SR-M-T2. The loading scheme twisted the top beam and also the left hand side column. Due to safety reasons, the test was stopped before reaching the failure of the specimen. An attempt was made to correct the problem but the frame structure was affected and therefore the test was ceased. For the R-M-T2, the out-of-plane restraint was improved and there were no impediments to conclude the test. The specimen exhibited desirable and stable behavior, as shown in Figure 4.



Figure 4. Damage to the specimen R-M-T2.

www.EngineeringEBooksPdf.com

Some local fractures were initiated at the corners of the panels at interstory drifts of approximately 2%. There were no damages of the beam-to-column connections before plastic deformations took place in panels. Local plastic deformations started to initiate at the beam flange in compression for drifts larger than 2%. The test was stopped at a top displacement of 240mm as force started to drop. The plastic rotation for the maximum capacity amounted 0.03rad. Results of the monotonic test were compared with the results of the pushover test. The strip model used in the pushover test did not describe accurately the behavior of the specimens. When the strip area was reduced by 10%, the accuracy of the model was very much improved (Figure 5). This reduction of the panel area conservatively reduces the strength and stiffness of the structure. The model permits the evaluation of the initial stiffness and ultimate capacity of the SPSW structure.

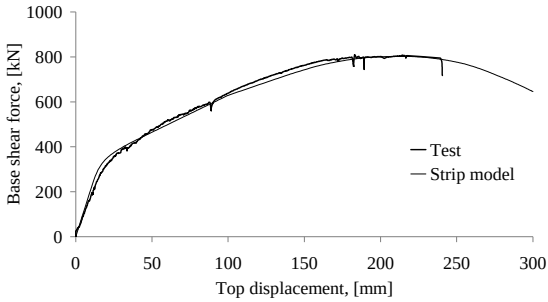


Figure 5. Comparison of experimental results for rigid specimen with 2mm thick panel and numerical results using the strip model.

2.3.2 Cyclic tests

All specimens exhibited stable behavior up to cycles of 4% interstory drift. Very little pinching were recorded in the hysteresis loops for large drifts and semi-rigid specimens, only. Panels yield at approximately 0.006 of the story height for semi-rigid specimens and 0.008 of the story height for rigid specimen. Some local fractures were initiated at the corners of the panels at drifts of approximately 2%. Local plastic deformations were observed at the beam flange in compression for rigid connections. Bolted connections between infill panels and the fish plates shown small slippages but no plastic deformations either in plates or bolts. This enabled a very easy dismantling of the steel panels after the test. Associated with a small residual drift (for rigid structure), this can assure an easy intervention after a moderate earthquake to replace the damaged panels.

Figure 6 plots the hysteresis of rigid and semi-rigid specimens and Figure 7 plots the envelopes of the hysteresis (results from each third cycle were considered). Contribution of rigid connections on the ultimate capacity of the specimens is larger than in the monotonic tests. As the initial stiffness is mainly attributed to the panels, differences between rigid and semi-rigid specimens in terms of stiffness are not as important as differences in terms of strength.

An important objective of the experimental program was the evaluation of the behavior factor q. The q factor can be expressed as a product of the ductility factor q_μ, that accounts for the ductility of the structure and the overstrength factor q_s, that accounts for the reserve in strength of the structure (due to structural redundancy, material overstrength, member oversize due to design, other non seismic load combinations and serviceability requirements). The overstrength may vary significantly and is affected by the contribution of gravity loads, material overstrength, etc. Therefore, in order to calibrate the behavior factor q, it is more important to focus on the ductility component, which can be taken equal to the displacement ductility factor μ [15]. The displacement ductility factor q_μ is therefore defined as the ratio of the ultimate displacement D_u and the yield displacement D_y. The parameter D_u corresponds to a reduction of the load carrying capacity of 10% compared to the maximum one. The yield displacement D_y can be considered the one corresponding to the modification of the elastic stiffness. Based on the

www.EngineeringEBooksPdf.com

observation of the hysteresis curves, the ultimate displacements D_u for SR-C-T2 and SR-C-T3 were corrected to take into account the slippage during the load reversal. Table 4 presents the q_μ factor values for the specimens. Comparing these values, it may be seen the specimens have similar ductility factors q_μ, with values ranging between 4.9 and 5.2. These values show SPSW structures have a good ductility and can provide q factors similar to those corresponding to other dissipative structure, like for example high dissipative moment resisting frames, which have ductility factors q_μ equals to 5 (see [2]).

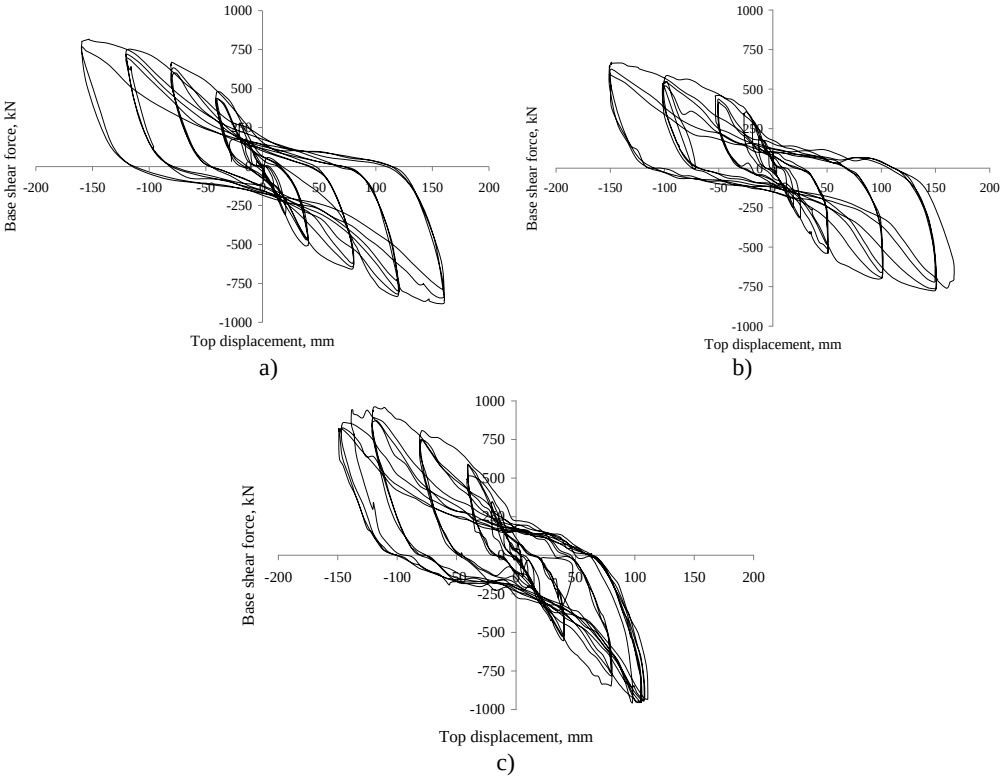


Figure 6. Hysteresis curves: a) R-C-T2 specimen; b) SR-C-T2 specimen; c) SR-C-T3 specimen

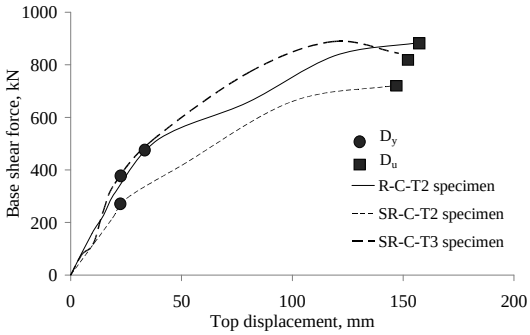


Figure 7. Envelope curves of the hysteresis.

www.EngineeringEBooksPdf.com

Table 4. q factor values for rigid and semi-rigid specimens.

Structure	D_y [mm]	D_u [mm]	q_μ	q_μ^*
R-C-T2	32	157	4.9	4.9
SR-C-T2	23	148 (114)	6.4	4.9
SR-C-T3	23	150 (120)	6.5	5.2
Average values			5.9	5.0
* *corrections due to slippage at the load reversal*				

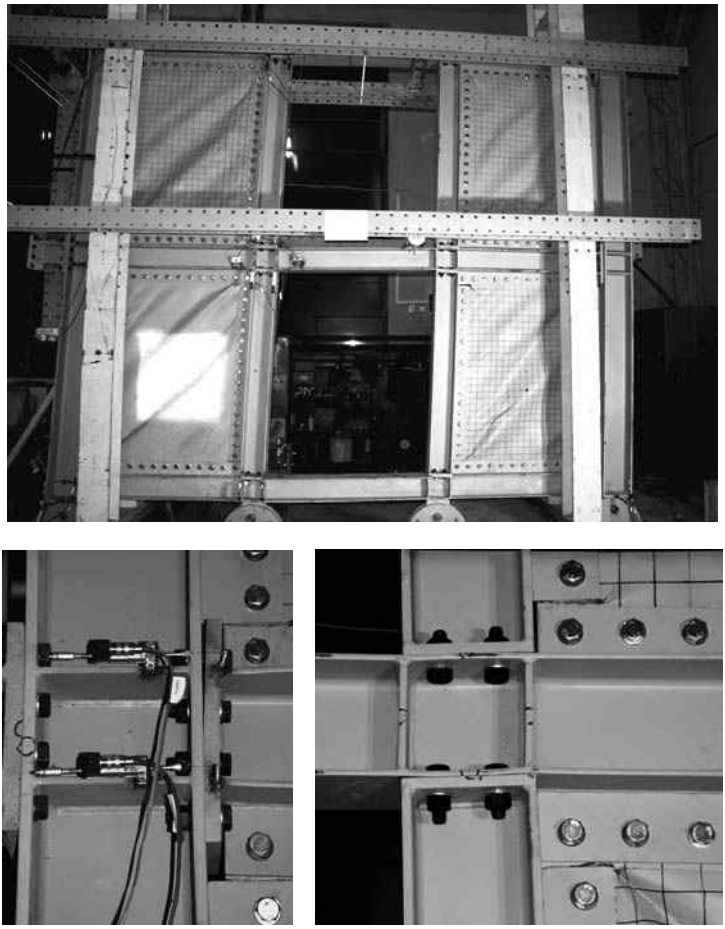


Figure 8. General view and details of the R-C-T2 specimen

3 CONCLUSIONS

The paper investigated the performances of the dual SPSW structures. Due to the limitations of the testing capacity, the models were half-scaled. A total of 5 specimens were designed and fabricated, which included specimens with semi-rigid and rigid connections. Specimens were tested monotonically and cyclically. The results of the tests have confirmed the conclusions of the previous numerical studies

www.EngineeringEBooksPdf.com

developed by the authors, on the performances of dual SPSW structures. The strip model developed by Thorburn et al. [3] was used for the preliminary analysis of the models. Based on the experimental results, this model was modified by correcting the area of the strips by a factor of 0.9. Rigid connections increased the yield resistance and the ultimate capacity of the structures. The initial stiffness is also improved when rigid beam-to-column connections are adopted. Behavior factor q amounts in average 5, considering the contribution of the ductility, only. These values indicate SPSW structures exhibit a dissipative behavior, similar to other dissipative structures, like for example moment resisting frames. However, further investigations are needed to calibrate the behavior factors q for SPSW structures.

REFERENCES

[1] AISC 341-05, Seismic provisions for structural steel buildings. *American Institute for Steel Construction*, 2005

[2] EN 1998-1: Design provisions for earthquake resistance of structures - 1-1: General rules - Seismic actions and general requirements for structures, CEN, EN1998-1-1, October 1994.

[3] Thorburn, L. J., Kulak, G. L. and Montgomery, C. J., "Analysis of steel plate shear walls". *Structural Engineering Rep. No. 107*, Dept. of Civil Engineering, Univ. of Alberta, Edmonton, Alberta, Canada, 1983.

[4] Choi, I.-R. and Park, H.-G., "Steel plate shear walls with different infill plate designs". *Journal of structural engineering*, Vol. 135, No.7, 2009.

[5] Habashi, H.R. and Alinia, M.M., "Characteristics of the wall frame interaction in steel plate shear walls". *Journal of Constructional Steel Research,* Vol. 66, Issue 2, 2010.

[6] Choi, I.-R. and Park, H.-G., "Ductility and energy dissipation capacity of shear-dominated steel plate walls". *Journal of structural engineering*, Vol. 134, No. 9, 2008.

[7] Sabouri-Ghomi, S. and Gholhaki, M., "Ductility of thin steel plate shear walls". *Asian Journal of civil (Building and housing),* Vol. 9, No. 2, 2008.

[8] Li, C.-H., Tsai, K.-C. and Lin, C.-H., "Cyclic performance of full-scale two-storey narrow steel plate". *Conference STESSA 2009: Behavior of Steel Structures in Seismic Areas*, Philadelphia, 16-20 aug. 2009, CRC Press 2009, Ed. F.M. Mazzolani, J.M. Ricles, R. Sause, ISBN: 978-0-415-56326-0.

[9] Dinu, F., Dubina, D. and Neagu, C., "A comparative analysis of performances of high strength steel dual frames of buckling restrained braces vs. dissipative shear walls". *Proc. of International Conference STESSA 2009: Behaviour of Steel Structures in Seismic Areas*, Philadelphia, 16-20 aug. 2009, CRC Press 2009, Ed. F.M. Mazzolani, J.M. Ricles, R. Sause, ISBN: 978-0-415-56326-0.

[10] EN1993-1-1: Design of Steel Structures. Part 1-1: General rules and rules for buildings, CEN, Brussels, 2003.

[11] P100-1/2006: Cod de proiectare seismică P100: Partea I, P100-1/2006: Prevederi de proiectare pentru clădiri, 2006 (in Romanian).

[12] EN1993-1-8: Design of Steel Structures. Part 1-8: Design of joints, CEN, Brussels, 2003.

[13] Driver, R. G., Kulak, G. L., Kennedy, D. J. L. and Elwi, A. E., "Seismic behavior of steel plate shear walls". *Structural Engineering Rep*. No. 215, Dept. of Civil Engineering, Univ. of Alberta, Edmonton, Alberta, Canada, 1997.

[14] ECCS, "Recommended Testing Procedures for Assessing the Behaviour of Structural Elements under Cyclic Loads". *European Convention for Constructional Steelwork*, Technical Committee 1, TWG 1.3 – Seismic Design, No.45, 1985.

[15] Newmark, N.M. and Hall, W.J., "Earthquake spectra and design". *Earthquake Engineering Research Institute*, California, 1982.

www.EngineeringEBooksPdf.com

SDSS'Rio 2010 STABILITY AND DUCTILITY OF STEEL STRUCTURES
E. Batista, P. Vellasco, L. de Lima (Eds.)
Rio de Janeiro, Brazil, September 8 - 10, 2010

EFFECTS OF WIND ON A 3 DIMENSIONAL STEEL STRUCTURE FOR THE CENTRAL CORRIDOR ROOF (CENTRAL SPINE) AT TCS CAMPUS AT SIRUSERI, CHENNAI (INDIA) - A CASE STUDY

T. S. Gururaj* and Nagaraja M. Thontalapura**

* Founder President, Potential Service Consultants Pvt. Ltd., Bangalore, India
e-mail: gururaj@potentialconsultants.com

** Vice President (Civil/Structural), CPG Consultants India Pvt. Ltd., Bangalore, India
e-mail: tmnagaraja@yahoo.com; tmnagaraja@cpgcorp.com.sg

Keywords: analysis, steel, wind, central spine

Abstract. *With the advent of high speed computers, 3D structural modeling and analysis have evolved to new heights. Equally exceptional user friendly finite element software tools have made the modeling exercise a lot easier than ever before. This paper will provide a case study on the evolution of the structural system for one of the modern architectural marvels of India. The authors, who were deeply involved in the various stages from concept to construction, will discuss in particular, the analysis and design of the central spine which resembles a* ***"Giant Wasp"*** *(as called by the concept architect). This paper will also discuss the structural system suitably provided for the huge cantilevers at the ends representing the tail, huge cantilevers at the sides representing wings, tall curved portals representing the legs and the pyramid shaped lattice girders representing the body of so called giant wasp. Also discussed in this paper, will be the behavior of the central spine structure due to wind.*

1 INTRODUCTION

The proposed techno park at Siruseri, Chennai, India is spread over a plot area of approximately 70 acres. It has 6 engineering blocks, customer care center, General services block, Training and library block and other facilities as in figure 1.

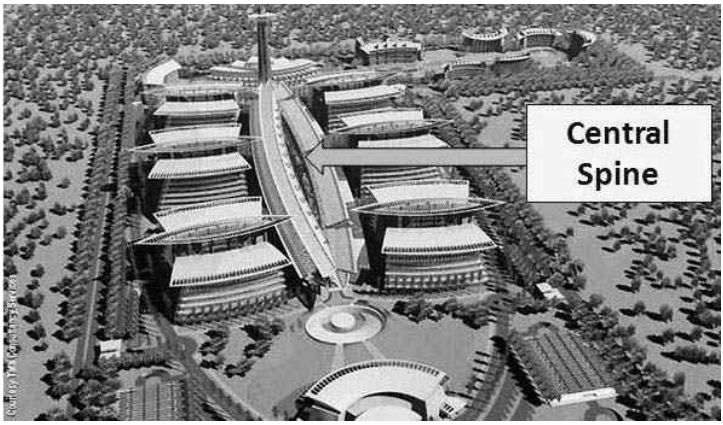


Figure 1: TCS campus showing central spine

www.EngineeringEBooksPdf.com

This paper will discuss about the central corridor roof between the engineering blocks which is also known as the central spine. The central spine serves as the shelter for people movement. This also houses the landscape which consists of water body and other facilities. This is spread over a length of 400 m. The architectural concept is such that 2 giant wasps each of 8 pairs of legs and long tails are facing each other. The formation of the entire structure is by means of 3 dimensional curves. In both the side elevations it is symmetrical about vertical axis (refer figure 2). In top plan, it is symmetrical about both vertical and horizontal axes as in figure 2.

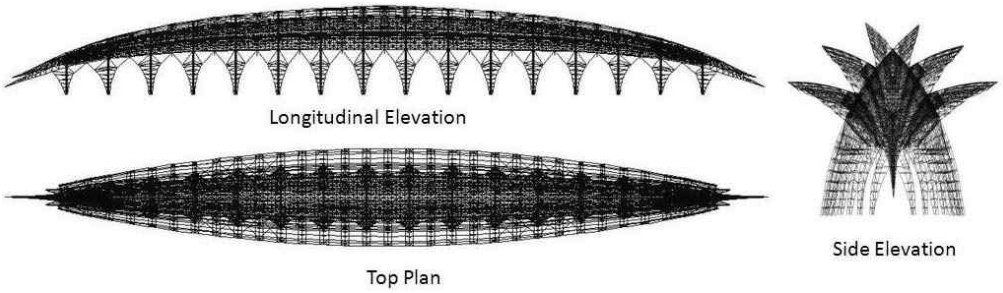


Figure 2: Views of central spine

1.1 Project team

Architect: Carlos Ott architects (Uruguay, South America); Resident architect: CRN architects (Chennai, India); Engineering Services: Potential Service Consultants (Bangalore, India); Review and Project Management Consultants: TCE Consulting Engineers (Bangalore, India)

2 STRUCTURAL SYSTEM

2.1 Main portals and arch bracings

Main portals are formed by intersecting gothic arches as in figure 3. They are the main supporting elements of the central spine in the vertical direction. They are made of two outer pipes and one inner pipe as in figure 3. These 3 pipes are connected by triangulated web members. They are further connected to the arch bracing members which are provided along the elevation. The outer and inner pipes form cantilever trusses called wings to support the purlins on them.

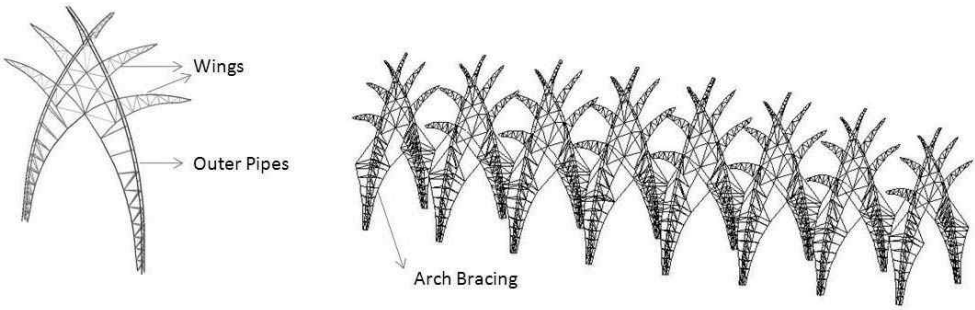


Figure 3: Main portals with arch bracing

www.EngineeringEBooksPdf.com

2.2 Middle wings

To reduce the span of purlins a truss system known as middle wings (figure 4.) which are quite similar to the top part of main portals, are introduced in between the 2 portals. By this, the span of purlins is reduced to around 11 m which is reasonable. The middle wings are supported by the lattice and box girders running between the 2 main portals.

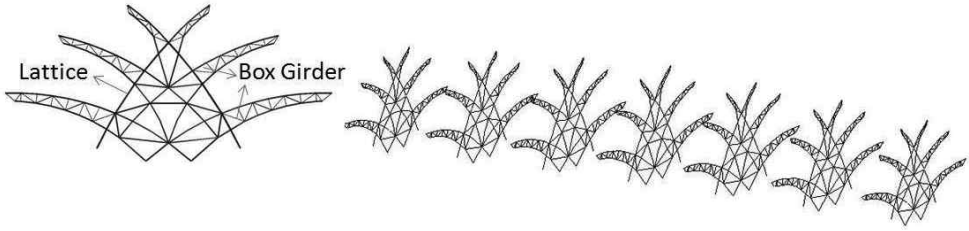


Figure 4: Middle wings

2.3 Lattice girder and Tail

The lattice girder as shown in figure 5 connects the main portals in the longitudinal direction. Between 2 consecutive main portals, at the centre it supports the middle wing. The lattice girder is connected at the bottom exactly at the centre to the arch bracing in each span. It is extended from the base of top wing to the bottom wing forming a curved pyramid. Tail is the continuation of lattice girder at both ends converging at a point. Space frame method is used to form this structure as in figure 6. It is an open structure without any roof covering making it very obvious so that it looks like the tail of the "Giant Wasp". The cantilever is about 35 m from the last portal. It is tied back to the 2nd portal to control the deflection in the vertical direction and horizontal "X" bracings are provided at the bottom to control deflection due to wind.

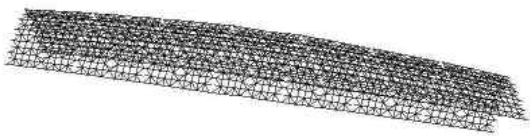


Figure 5: Lattice girder

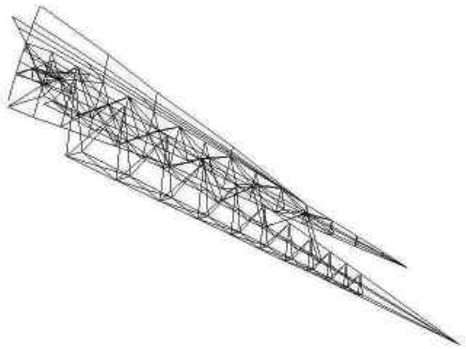


Figure 6: Tail of central spine

2.4 Foundation

The two legs of each portal consisting of five pipes (including the arch bracing) are connected to a base plate with required stiffeners. Base plate is further connected to the podium column capital by means of cast-in holding down bolts.

www.EngineeringEBooksPdf.com

3 ANALYSIS AND DESIGN DATA

3.1 Loads

Dead loads and imposed loads have included the weight of all structural and architectural components on the basis of the unit weights as mentioned in the table 1. Wind loads are based on the code provisions mentioned in IS 875 [1]. The wind speed is calculated using the parameters in table 2.

Table 1: Dead loads and imposed loads [1]

Material	Weight
Unit weight of steel	78.5 kN/cum
Sheeting Weight	0.12 kN/sq.m
Louver Weight	0.4 kN/sq.m
Roof Sheeting area	0.4 kN/sq.m

Table 2: Wind load parameters [1]

Parameter	Value
Basic wind speed, Vb	50 mps
Risk Coefficient, K1	1.0
Terrain factor, K2	1.13
Topography factor, K3	1.0

3.2 Temperature loads and expansion joints

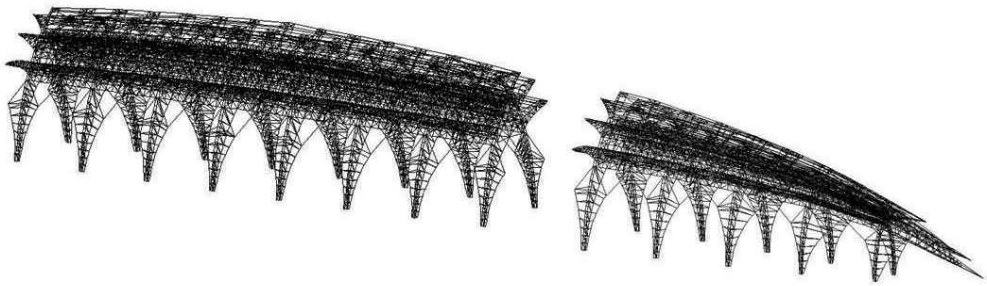


Figure 7: Central spine divided into central and tail part with expansion joint

Elongation due to differential temperatures is of importance in long steel buildings. It can be taken care by either providing expansion joints at an appropriate spacing or designing structural members for the additional moments caused by the temperature. Expansion gap between two structures shall be sufficient to accommodate temperature and shrinkage for effects due to wind. Expansion joints are provided at 2 locations along the length, breaking the whole structure into 3 parts known as Central part(1. no.) and Tail part (2. no.). Central part will have 7 spans. The final configuration of the whole structure is as shown in the figure 7.

3.3 Materials used

Structural steel confirming to IS: 2062 with minimum yield strength of 310 N/sq.mm is used for all structural members. For expansion joints approved Teflon sheet is provided.

4 WIND PRESSURE COMPUTATIONS

4.1 Configuration

Figure 8 shows the configuration of the central spine (CS) structure. There are sixteen bays of geometrically similar configuration of diminishing size from centre to ends. Each bay is around 21 m long. At the middle, the width is 35 m and height is 55 m, at the ends the width is 12 m and 18 m height.

www.EngineeringEBooksPdf.com

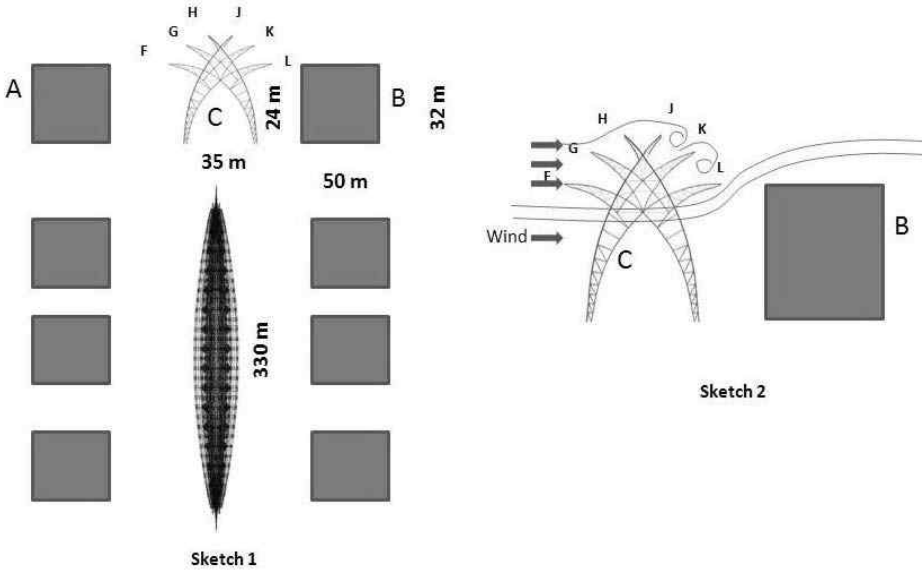


Figure 8: Configuration of central spine influencing wind pressure

The bays are open in the bottom, for example up to a height of 24 m at the centre, above which CS supports six wings symmetrically by the framework, which also supports Louvers (water barrier made of overlapping plates) at the roots of the wings with a porosity of 20%. The Louvers extend below F & L.

4.2 Types of wind loads

The following cases have been considered to analyze the structure:
Case 1: Wind from empty position of A to B
Case 2: Wind from the direction of B to A, with A absent

4.3 Wind loads with CS and building B only, wind from position A to B

As shown in sketch 2 of figure 8, the part of the wind below the point C will move on to B, gets diverted upwards and impacts to rear wing L. But wings K & L are partially shielded by F, G, H and their loads will be less than those values on G & H. Somewhat similar phenomenon occurs on the bottom of F, where the Louvers below F block the flow partially, creating a positive pressure. The Louvers between F & G and G & H also create positive pressure (or makes negative pressure, less so). The nearest configuration in the Indian wind code IS 875-1987 is Table 8 [1] for the wings F, G and H, J, K and L all with $\varphi = 1$. By considering shielding effect and the pressure build ups, the overall pressure coefficients with directions for all the wings and the Louvers are as in figure 9. The configurations of Table 13[1] and Table 14[1] can be used as guidance with $\theta = 0^0$. These are used for the analysis of the entire structure. The local pressure coefficients listed in table 3 are used for designing the purlins.

Table 3: Local pressure coefficients (Positive upwards)

Wing	Front 10% of length	Middle	Rear
F / L	1.5 / 2.6	0.8 / 1.6	-0.9 / -0.9
G / K	2.6 / 1.3	1.4 / 0.7	1.0 / 0.5
H / J	2.0 / 1.3	2.0 / 1.3	2.0 / 1.3

www.EngineeringEBooksPdf.com

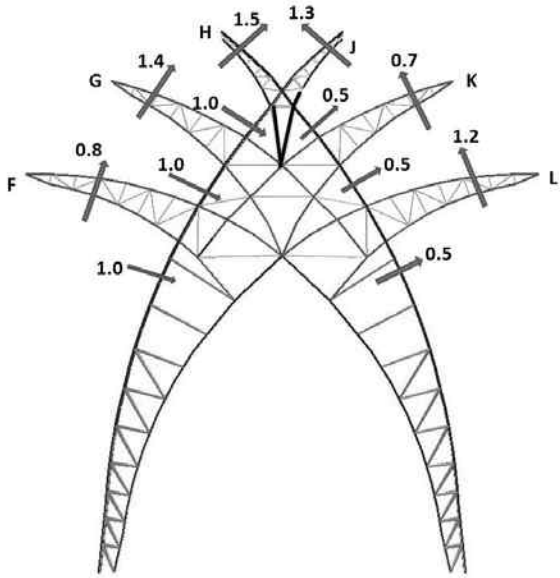


Figure 9: Overall wind pressure coefficients on portals

4.4 Wind loads with CS and building B only, wind from position B to A

Here, the bottom of wing L is above the building B & hence the flow will be similar to that as wing F with wind from A to B. Loads on K & J will be similar to those on G & H of the earlier case. However since F, G and H are fully shielded by L, K and J their loads will be half of the previous values including those on Louvers.

5 STRUCTURAL ANALYSIS AND DESIGN

Table 4: Sample results of analysis and design

BEAM RESULTS For Combination 25 (Units: Kn, Kn*meter)

Dl+ll+wly3 no sheet

Bm.	Node	Axial	V2	V3	MT	M2	M3
28411	6661	416.9	-14.5	-2.7	-3.6	18.2	-56.0
	6649	-413.9	15.0	3.6	3.6	1.3	-36.4
Maximum		416.9	15.0	3.6	3.6	18.2	-56.0
Beam no.		28411					

DESIGN	EQUATION	FACTORS	VALUES	RESULT
V2 Shear (6.4.2)	V/[Av*τva] <1.00 τva=0.4*fy	Av = 41.48	V = 14.95 τva = 124.00	0.03
M3 Moment (6.2.1)	$\frac{M}{Ze*0.66*fy} < 1.0$	Z = 593.21 Ze = 593.21	M = 55.96	0.46
V3 Shear (6.4.2)	V/[Av*τva] <1.00 τva=0.4*fy	Av = 41.48	V = 3.56 τva = 124.00	0.01
M2 Moment (6.2.5)	$\frac{M}{Ze*0.66*fy} < 1.0$	Z = 593.21 Ze = 593.21	M = 18.20	0.15
Deflection	$\frac{defl.}{L/325} < 1.00$		defl = 0.00365	0.19
Axial Force (5.1.1)	$\frac{P}{Ae*\sigma ac} < 1.00$	(kL/r)x =51 (kL/r)y =51 fcc = 758.91	P = 416.93 Ag = 69.13 σac = 155.45 Ae = 69.13	0.39
Combined Stresses Local-compr. (7.1.1-b)	$\frac{\sigma a}{0.6fy} + \frac{\sigma bx}{0.66fy} + \frac{\sigma by}{0.66fy} < 1.00$ at L = 0.00		σa = 60.31 σbx = 94.33 σby = 30.68	0.94

www.EngineeringEBooksPdf.com

The structural analysis is carried out by creating a 3 dimensional space frame model using the commercially available software STRAP VER.11.5 for the load combinations as per IS 800 standards. Line elements are used in the finite element model with rigid nodes. Triangular surfaces were created to idealize the curved surface and pressure loads were applied perpendicular to the surface in the required direction. This method has helped in reducing the time that would have been spent for member load computation and its application on each member. In total, including both central and tail part, the structural model contains about 10,400 nodes, 36,700 members and 61,600 degrees of freedom.

Design of structural steel members is done using elastic method as per IS: 800 [2] with relevant allowable stresses. Each member is designed for combined stresses due to axial force, shear force and moments. Sample output for the analysis and design are shown in table 4.

6 CONCLUSIONS

It is observed that the load combinations involving the wind loads computed using the pressure coefficients shown in figure 9 govern the design of members of the central spine structure. Since the structure is very light, the earthquake forces do not have any influence on the design. For academic purpose, the load combinations including earthquake, wind loads on members, live and dead loads are studied. The deflected shapes of the main portals with some governing load combinations are shown in figures 10 and 11.

The pipe sizes used for the main portals are 350 mm diameter with thicknesses varying from 22 mm to 16 mm. For the other elements almost all available pipe sizes are used considering the most economical sizes and durability. The joints are connected by full strength butt welds. The thickness of base plate worked out to be between 70 to 80 mm for various portals by suitably providing the stiffener plates. Overall structural steel consumption is around 3000 Tons with a roof sheeting area of around 25,000 square meters. The central spine structure under construction is shown in figure 12.

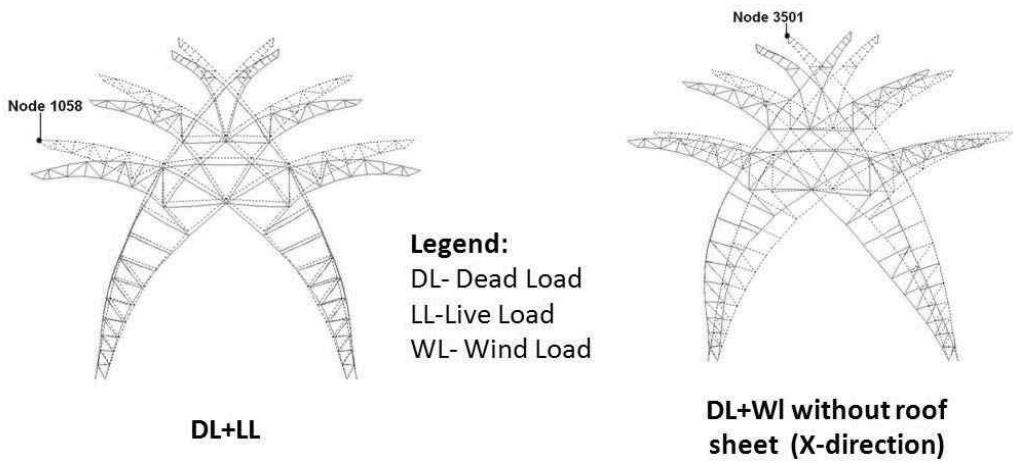


Figure 10: Deflected shapes for DL, LL and WL

www.EngineeringEBooksPdf.com

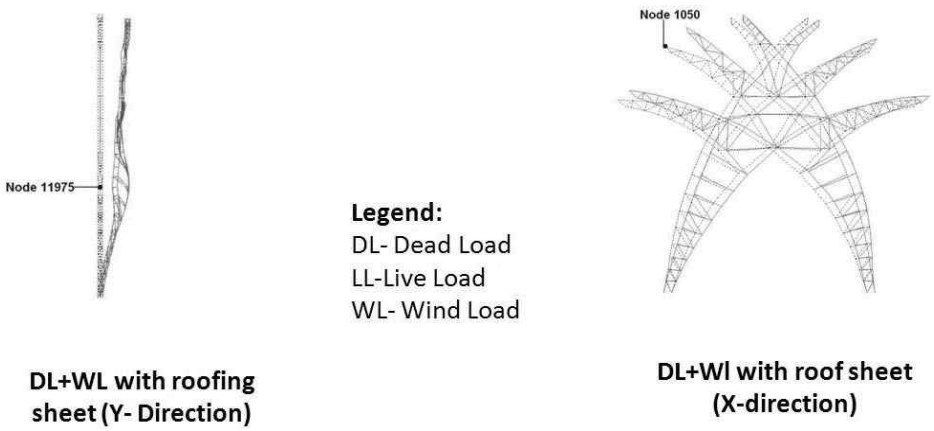


Figure 11: Deflected shapes due to DL and WL



Figure 12: Central Spine under construction

7 ACKNOWLEDGEMENTS

The authors would like to thank structural engineers Mr. B. N. Sridhara, Mr. Sajeev Thomas and Prof. G. N. V. Rao, Department of Aerospace engineering, Indian Institute of Science, Bangalore for their support and cooperation during the design stage. Authors are also thankful to the project team and clients Tata Consultancy Services Ltd for their cooperation in preparing this paper.

8 REFERENCES

[1] IS: 875 (Part 1, 2 and 3) – 1987, *Indian Standard- code of practice for design loads (other than Earthquake) for buildings and structures,* Bureau of Indian Standards, New Delhi, 1989

[2] IS: 800 – 1984, *Indian Standard- code of practice for steel design,* Bureau of Indian Standards, New Delhi, 2002

www.EngineeringEBooksPdf.com

SDSS'Rio 2010 STABILITY AND DUCTILITY OF STEEL STRUCTURES
E. Batista, P. Vellasco, L. de Lima (Eds.)
Rio de Janeiro, Brazil, September 8 - 10, 2010

INFLUENCE OF SYSTEM UNCERTAINTIES ON STRUCTURAL DAMAGE IDENTIFICATION THROUGH AMBIENT VIBRATIONS OF STEEL STRUCTURES

Leandro Fadel Miguel*, Letícia Fadel Miguel*, Jorge D. Riera*, Marta G. Amani and Raúl O. Curadelli****

*Federal University of Rio Grande do Sul, Porto Alegre, Brazil
e-mails: leandro.miguel@ufrgs.br, letffm@ufrgs.br, jorge.riera@ufrgs.br

** Universidad Nacional de Cuyo, Mendoza, Argentina
e-mail: amanimg@yahoo.com, ocuradelli@yahoo.com

Keywords: Identification, Damage Detection, Structural Monitoring, Ambient Vibrations.

Abstract. *The practical difficulties presented by forced vibration testing of large steel structures, such as tall buildings, transmission lines or bridges, led to an increased interest in structural monitoring through ambient vibrations, which usually allows the proper identification of modal properties, natural frequencies, damping and modes of vibration. Changes in these modal properties constitute an indication of structural damage, which may then be assessed on the basis of experimental evidence. The authors proposed an approach to determine the so-called damage damping and stiffness matrices, which are essential to identify the location and intensity of damage. No restrictions were introduced on the damping matrix of the system. The approach requires ambient vibration data of all relevant coordinates used in the structural model, which are processed employing the SSI method. In practice, the identification method is seriously hampered by ambient factors such as temperature or humidity. In general those effects must be filtered out in other to obtain a reliable diagnosis of damage, approach that demands long term monitoring. In this paper, an alternative approach is explored, based on the introduction of error damping and stiffness matrices. Data on both matrices is generated on the basis of observed variations of structural member stiffness and damping caused by ambient factors. The influence of this uncertainty on the identified spectral properties is assessed by simulation.*

1 INTRODUCTION

In recent contributions the authors examined experimental evidence concerning the influence of ambient factors on the spectral properties of dynamic systems [1], [2], [3]. Proposed procedures to eliminate those effects from vibration measurements aimed at damage detection in structural systems [4] demand extensive monitoring to cover the range of expected variations of ambient conditions. These requirements may render them either too expensive or simply unfeasible due to technical or logistic reasons. Moreover, the issue introduced by noise in the system matrices, which should be distinguished from noise in the vibration recording system, is largely ignored. Empirical or semi-empirical results of those contributions are briefly described for completeness in next section.

In this paper, however, the authors follow an entirely different approach. Changes in the system matrices are assumed to belong in one of two types: *reversible and irreversible*. The first are due to so-called ambient factors, which include temperature, humidity, and other effects, while the second constitute evidence of *damage*. In the absence of damage, which is the topic of the present study, the components of the mass, damping and stiffness matrices of the system *must necessarily be stationary random processes*. It follows that the components of the error matrices, defined as the difference between

www.EngineeringEBooksPdf.com

the system matrices at any arbitrary time and the reference matrices that describe the condition of the system in its initial state must be random variables with zero mean. Hence, the effect of the so-called *error matrices* on the system spectral properties is assessed first. These matrices are generated by multiplying all components of the reference matrices by uncorrelated normally distributed random coefficients with zero mean and prescribed standard deviation.

2 INFLUENCE OF AMBIENT FACTORS ON SPECTRAL PROPERTIES OF STRUCTURAL SYSTEMS

In previous papers [5], the authors examine available experimental evidence on the influence of ambient factors on steel and concrete structures. In [1] it was shown that, in a limited number of samples of concrete structures, the *expected value* η of the ratio between observed natural frequencies of structural systems at a mean temperature different from the reference temperature and the frequencies measured at the reference temperature may be estimated by the equation:

$$\eta = 1 - 0{,}002\,\Delta T - 0{,}0003\,\Delta h \tag{1}$$

In which ΔT denotes the temperature difference (positive value indicates temperature increase) and Δh the change in atmospheric humidity. Similarly, the expected value ξ of the ratio between the critical damping ratio affected by ambient factors and the damping ratio measured at reference conditions is given by:

$$\xi = 1 + 0{,}018\,\Delta T - 0{,}0049\,\Delta h \tag{2}$$

On the other hand, the following expression was obtained for steel structures [3]:

$$\eta = 1 - 0{,}00051\,\Delta T \tag{3}$$

By means of simple models of struts, Riera et al (2008) estimate that the maximum values for the temperature coefficients in Eq. (1) span between 0.005 (elements subjected to tensile force) and 0.015 (compressed elements). In case of steel structures (Eq. 3) these limits are 0.0084 and 0.0028, respectively.

In the same study, in order to assess the influence of temperature on natural frequencies, an artificial neural networks was constructed and it perform in the same way: the network input is a ΔT value which means changes in temperature (˚C) from reference values (increase is positive) and the output provides a correction factor that should be multiplied by the measured natural frequency. The linear regression equation (Eq. 3) and results obtained with the ANN for the training and validating subsets are shown in Figure 1.

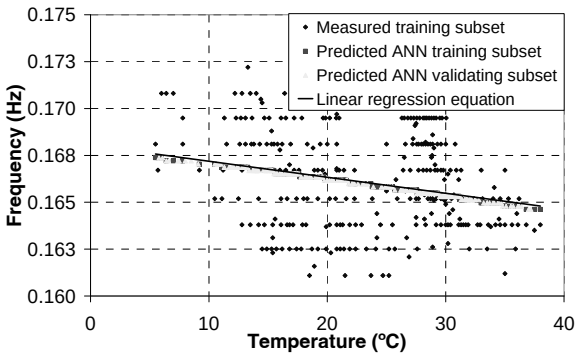


Figure 1: Linear regression equation and ANN results.

www.EngineeringEBooksPdf.com

If the equation for the frequency change is thus of the form:

$$\eta = 1 - c\,\Delta T \tag{4}$$

It may be expected that the stiffness affected by ambient factors and the reference stiffness will be related by $\eta^{½}$. If this ratio is denoted as β, then it follows that:

$$\beta = 1 - ½\,c\,\Delta T \tag{5}$$

Consequently, Eq.(5) estimates the expected value of the ratio between stiffness coefficients in the structure affected by ambient factors and stiffness coefficients in the structure in the reference condition, in which the spectral properties were experimentally determined. Note that ΔT denotes the mean temperature change between both conditions, while the temperature as well as the slenderness and axial loads in individual members vary throughout the structure. In this context, it is proposed herein that the ratio between corresponding stiffness coefficients K_{ij} is a random variable β_{ij} with mean given by Eq. (5) and variance to be later defined. In the simulation analysis, the stiffness matrix affected by ambient factors is obtained by multiplying the coefficients K_{ij} of the reference matrix by a set of uncorrelated random numbers β_{ij}.

On the other hand, if C_r and M_r are the generalized damping and stiffness coefficients of the r^{th} mode the structure, then under certain conditions and proportional viscous damping the following equation holds:

$$Cr / Mr = 2\,\zeta r\,\omega r \tag{6}$$

In which ζ_r and ω_r denote the critical damping ratio and the frequency of mode r. A similar equation may be written for the matrix of the system affected by ambient factors. Assuming that the mass matrix remains constant, the mean ratio γ between the coefficients of the modified and reference damping matrices can be shown to be of the form:

$$Cr / Cro = (\zeta r / \zeta ro)\,(\omega r / \omega ro) \tag{7}$$

The left-hand side of Eq.(7) may be identified as γ while the ratios between parenthesis in the right-hand side are ξ and η, respectively, leading to:

$$\gamma = \eta\,\xi \tag{8}$$

For concrete structures, substitution of Eqs. (2) and (4) in Eq. (7) leads to:

$$\gamma = 1 + 0.016\,\Delta T \tag{9}$$

Using the same arguments, the coefficients of the damping matrix after and before the introduction of ambient factors are related by a random variable γ_{ij} with mean given by Eq.(8).

3 INFLUENCE OF ERROR MATRICES ON SPECTRAL PROPERTIES OF STRUCTURAL SYSTEMS

3.1 Effect of changes in the stiffness matrix

Some theoretical results will be recalled first: if the stiffness matrix of a linear system without damping is multiplied by a constant factor, the eigenvectors, i.e. the vibration modes, do not change, but the natural frequencies should be multiplied by the square root of the factor. This would be equivalent to considering an error stiffness matrix that is proportional to the original matrix.

The influence on the mean spectral properties introduced by stationary random changes in the stiffness matrix due to ambient factors will be assessed first by simulation, considering for such purpose the typical steel truss structure shown in Figure 2. This plane Warren truss consists of 37 nodes and 71 steel bars, which have a cross section of $2\times10^{-3}m^2$. Young's modulus of the material is $2\times10^{11}N/m^2$ and

www.EngineeringEBooksPdf.com

its mass density 7.86×103kg/m^3. The height of the truss is 9m while the total length is 168m. The supports of the structure are modeled as two hinged supports at nodes 1 and 37 and as a roller support at node 19. The pinned end allows nodes to rotate freely with all three translations restricted.

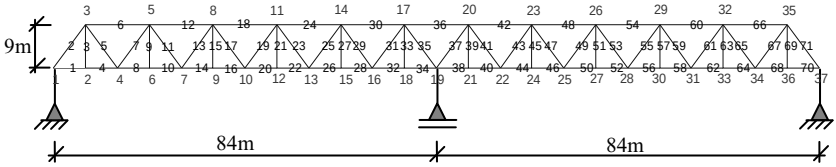


Figure 2: Continuous Warren truss adopted for simulation study.

Stiffness matrices affected by noise were generated by multiplying all components of the reference stiffness matrix by uncorrelated normally distributed random coefficients with zero mean and coefficients of variation (CV) equal to 0.01, 0.03, 0.05 and 0.10. For each CV, 100 disturbed simulated stiffness matrices were generated. The natural frequencies for the first seven modes were next determined for each simulated sample and the corresponding mean calculated next (Table 1).

Table 1: Natural frequencies comparison (Hz).

Original	*CV = 0.01*		*CV = 0.03*		*CV = 0.05*		*CV = 0.10*	
	Mean	Difference (%)	Mean	Difference (%)	Mean	Difference (%)	Mean	Difference (%)
3.14377	3.1440	-0.01	3.1419	0.06	3.1388	0.16	3.1243	0.62
4.74475	4.7449	0.00	4.7417	0.07	4.7373	0.16	4.7151	0.62
8.63623	8.6357	0.01	8.6292	0.08	8.6255	0.12	8.6023	0.39
11.7569	11.7573	0.00	11.7487	0.07	11.7281	0.24	11.6536	0.88
11.9576	11.9584	-0.01	11.9549	0.02	11.9476	0.08	11.9270	0.26
18.6109	18.6103	0.00	18.5934	0.09	18.5808	0.16	18.5277	0.45
20.6468	20.6454	0.01	20.6247	0.11	20.6125	0.17	20.5373	0.53

It may be seen that a trend to observe *smaller* frequencies that steadily decrease with the coefficient of variation of the fluctuating components of the stiffness matrix is perceptible for all modes, approaching 0.5% for a CV of around 10%. *Since frequency changes of this order would already be indicative of damage, it is clear that the effect cannot be disregarded* and that further studies are needed, first to quantify it in different structural systems and then to filter it out in damage identification procedures.

3.2 Influence of changes in the damping matrix

Changes in damping can be quite relevant in the detection of damage in structural systems [2]. Thus, the influence of ambient factors on critical damping ratios, introduced by random changes in the damping matrix, will be assessed by means of numerical simulation. For this purpose, the three bays 10-stories high steel frame shown in Figure 3, considered earlier [6], was studied. The structure was designed in accordance with the provisions of the Uniform Building Code. The total mass per floor is 47 t and damping matrix is assumed to be proportional to a combination of the mass and the stiffness matrices (Rayleigh damping). The modal damping ratio in each mode is shown in Table 2. Frame and member dimensions are also indicated in Figure 3.

The noisy damping matrices were generated by multiplying all components of the original damping matrix by uncorrelated normally distributed random coefficients with zero mean and coefficients of variation (CV) equal to 0.1 and 0.15. These values were adopted because for CVs lower than about 0.15, the damping matrices with random noise continue being approximately proportional, and thus, there is no difficult to obtain the modal damping ratios as in the original damping matrix. For each CV, 1000 simulated noisy damping matrices were generated. The modal damping ratios for the first seven modes

www.EngineeringEBooksPdf.com

were next determined for each simulated sample. The mean values of the modal damping ratios for each mode obtained from the simulated damping matrices affected by random noise are compared in Table 2 with the modal damping ratios for the modes of the original structure. Table 2 also presents the corresponding coefficients of variation of the population of simulated structures. *The results show slight changes in the modal damping of the first three modes, which increase with the CV of the noise terms.*

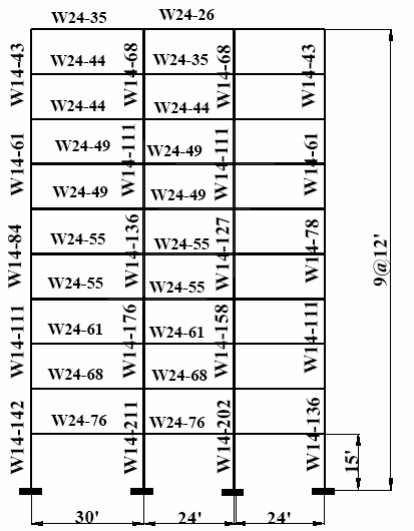


Figure 3: Three bays 10-stories high steel frame adopted in simulation study.

Table 1: Modal damping ratios comparison.

ξ_0	*CV = 0.10*		*CV = 0.15*	
	$\xi_{0.1}$	Difference (%)	$\xi_{0.15}$	Difference (%)
0.0100	0.0103	-3.28	0.0105	-4.83
0.0051	0.0056	-7.97	0.0055	-7.42
0.0049	0.0052	-6.15	0.00488	1.15
0.0056	0.0057	-1.89	0.0056	-1.45
0.0068	0.0069	-1.10	0.0069	-1.10
0.0082	0.0083	-0.84	0.0082	0.00
0.0100	0.0100	0.00	0.0100	0.00

For higher values of the CV the proportionality property of the damping matrices including noise is no longer an acceptable assumption and the assessment of the influence of noise becomes more difficult.

4 CONCLUSION

In this paper, the effect of so-called *error matrices* on the spectral properties of structural systems is examined. The study aims at providing data to assess the range of application and general validity of empirical expression obtained earlier by the authors. The error matrices were generated herein by multiplying all components of the reference matrices by uncorrelated normally distributed random coefficients with zero mean and prescribed standard deviation.

www.EngineeringEBooksPdf.com

The influence on the natural frequencies due to random changes in the stiffness matrix due, for instance, to ambient factors, was assessed first, considering for such purpose a typical steel Warren truss. A trend to lower frequencies that steadily decrease with the CV of the fluctuating components of the stiffness matrix is perceptible for all modes, approaching 0.5% for a CV of around 10%. Since frequency changes of this order would already be indicative of damage, it is clear that the effect cannot continue being disregarded in efforts to detect and quantify damage through ambient vibrations.

The influence of ambient factors introduced by random changes in the damping matrix was assessed in a three bays 10-stories high steel frame. Slight changes in the modal damping of the first modes, which increase with the CV of the noise terms were detected.

These results are considered as an intial step in efforts to reduce uncertainties in procedures proposed to detect and quantify damage in steel structures through ambient vibration monitoring.

REFERENCES

[1] Amani, M.G., Curadelli, R.O., Riera, J.D., Ambrosini, R.D. “Influencia de Factores Ambientales en las Propiedades Espectrales de Estructuras de Hormigón”. *XXXIII Jornadas Sudamericanas de Ingeniería Estructural*, Santiago, Chile, 2008.

[2] Curadelli, R.O., Riera, J.D., Ambrosini, R.D., Amani, M.G. “Damage detection by means of structural damage identification”. *Engineering Structures*, 30, 3497-3504, 2008

[3] Fadel Miguel, L.F., Riera, J.D., Miguel, L.F.F. “Influência de Fatores Ambientais nas Propriedades Espectrais de Estruturas Metálicas”. *XXXIII Jornadas Sudamericanas de Ingeniería Estructural*, Santiago, Chile, 2008.

[4] Alampalli, S. “Effects of Testing, Analysis, Damage and Environment on Modal Parameters”. *Mechanical Systems And Signal Processing*, 14(1), 63-74, 2000.

[5] Amani, M.G., Riera, J.D., Curadelli, R.O. “Procedures for Structural Damage Identification through Ambient Vibrations”. *Proceedings of 4th World Conference on Structural Control and Monitoring*, San Diego, CA, USA, 2006.

[6] Bertero V, Mahin S, Herrera R. “A seismic design implications of near-fault San Fernando earthquake records”. *Earthquake Engineering and Structural Dynamics*, 6, 31–42. 1978.

www.EngineeringEBooksPdf.com

SDSS'Rio 2010 STABILITY AND DUCTILITY OF STEEL STRUCTURES
E. Batista, P. Vellasco, L. de Lima (Eds.)
Rio de Janeiro, Brazil, September 8 - 10, 2010

NON-LINEAR DYNAMIC ANALYSIS OF STAYED STEEL COLUMNS

Ricardo R. de Araujo*, José G. S. da Silva*, Pedro C. G. da S. Vellasco*, Sebastião A. L. de Andrade, Luciano R. O. de Lima* and Luis A. P. Simões da Silva*****

* Structural & Mechanical Engineering Departments, State University of Rio de Janeiro - UERJ, Brazil
e-mails: rraraujo@eng.uerj.br, jgss@uerj.br, vellasco@uerj.br, lucianolima@uerj.br

** Civil Engineering Department, Pontifical Catholic University of Rio de Janeiro - PUC-Rio, Brazil
e-mail: andrade@puc-rio.br

*** Civil Engineering Department, University of Coimbra, Portugal
e-mail: luisss@dec.uc.pt

Keywords: pre-stressed steel columns, experimental analysis, steel structures, computational modelling, non-linear analysis.

Abstract. *This work describes non-linear finite element simulations made on stayed system subjected to sudden impact loads. The study aimed to determine the influence of the prestress forces magnitude and its response with and without damping effects. Various cases where the load magnitude varied from 10% up to 100% of the stayed column load bearing capacity were investigated. The performed analyses enabled an evaluation of the structural system amplification factor to be later compared to allowing horizontal deflection limits usually adopted in steel design standards.*

1 INTRODUCTION

Prestressed stayed steel columns are excellent structural systems for situations where loads have to be supported with an easy and fast erection and assembly. Its structural conception and high slender shape enable it to become a light, economic and efficient structural system [1]. Although, this structural solution dates back from the 1960's [2-9], especially when subjected to dynamic actions, is not fully understood.

This motivated a detailed study of the structural system non-linear dynamic behaviour by means of ANSYS [10] simulations when submitted to sudden loads. The current non-linear dynamic finite element analysis was performed on twelve meter length pre-stressed steel columns . These structural elements load bearing capacity was substantially increased by the additional restriction provided by the tie forces that are transferred to the main columns by means of horizontal tubes, perpendicularly welded to the column midpoint [11][16].

The parametric study main variables were the pre-stressed element shape/area (cable or reinforced bar) and the adopted element pre-stress force. These two variables substantially altered the dynamic response and proved to be key elements for a better understanding of the structural system dynamic response [12].

The load was introduced to the system by means of a concentrated load positioned at the top of the column through a rectangular pulse with five seconds to simulate a sudden impact load situation. The investigation was centred on varying the magnitude of the applied load from 10% up to 80% the stayed column capacity with and without prestress forces while considering or not the structural dampening.

www.EngineeringEBooksPdf.com

2 NUMERICAL MODELLING

The same model used in a previous static analysis [12], was adopted with the aid of the ANSYS program. The prestressed stayed steel column model was divided into three parts: the central tubular column, the secondary cross bars and the tie cables. Twelve one meter length element were used in the central column while the secondary cross bars were simulated with two 300 mm elements. These dimensions delimitate a 10% inclination angle for the column ties, each modelled by a single element.

Two different materials were used in the analysis. The first type, used in the main column and secondary cross bars, possessed a 205000MPa Young´s modulus, a 20500MPa tangential modulus, a 0.3 Poisson ratio, a 380 MPa yield stress and 7850 kg/m^3 of density. The second type, used in the tie cables, possessed a 100000MPa Young´s modulus, a 10000MPa tangential modulus, a 0.3 Poisson ratio, a 750 MPa yield stress and 9100 kg/m^3 of density.

The main tubular column and secondary cross bars were modelled by PIPE20 elements while the ties were simulated with LINK10 (specified with a tension only option) elements. The geometrical characteristics are: the main column has a external diameter and thickness of 89.3 mm and 3.2 mm; the secondary cross bars have external diameter and thickness of 42.6 mm and 3 mm; and the stays have 6.35 mm diameter. An 8 mm amplitude sinusoidal initial imperfection was introduced in the numerical model to be compatible with the tests measured imperfections [13-17].

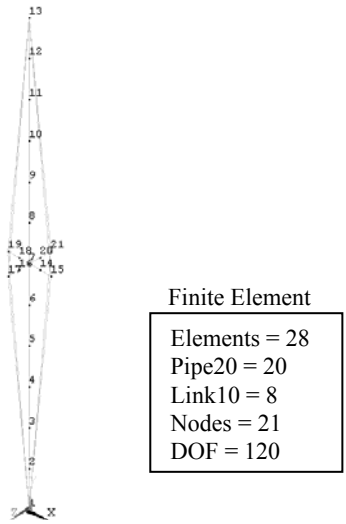


Figure 1: Finite element model used to represent the prestressed stayed steel column.

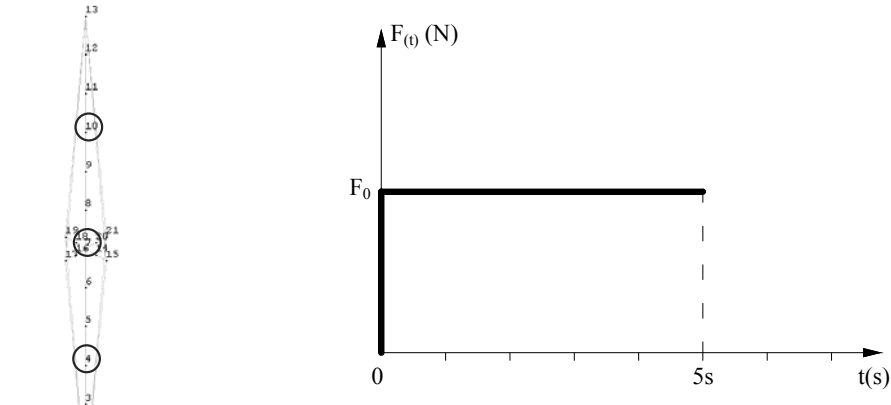
3 DYNAMIC ANALYSIS

The prestressed stayed steel column was modelled with cables and bars as stays. In this case only cables were modelled. The non-linear dynamic analysis considered a rectangular pulse to represent an impact load case, applied on the top of the structural system, in order to simulate a sudden load. In this analysis the time of the dynamic loading application was considered equal to five seconds.

The investigation was centred on varying the magnitude of the applied dynamic load from 10% up to 80% of the stayed column capacity with and without prestress forces while considering or not the structural damping. The time step used in this investigation was equal to 0.001s ($\Delta t = 10^{-3}$ s). The analysis enable the determination of the amplification factors for the studied prestressed stayed steel columns using cables as stays.

www.EngineeringEBooksPdf.com

Three nodes were chosen in the main column at 1/4, 1/2 and 3/4 span to enable a comparison to the recommendations present in the Brazilian Standard [18] and Eurocode [19]. Lateral displacements were evaluated at and compared to the suggested limit of L/500 (24 mm - Brazilian Standard [18]) and L/300 (40 mm - Eurocode [19]), where L is the main column length (12 m).



(a) Nodes Location (b) Impact loading

Figure 2: Prestressed stayed steel column: nodes location and impact loading.

3.1 Structural damping

In this investigation, the structural damping was considered according to the Rayleigh proportional damping formulation [20]. The bridge structure damping matrix is defined by the parameters α and β, determined in function of the damping modal coefficient. According to this formulation [20], the structural system damping matrix [C] is proportional to the mass and stiffness matrix, as shown in Equation (1):

$$[C] = \alpha [M] + \beta [K] \tag{1}$$

The expression above can be rewrite in terms of the modal damping coefficient and the natural frequency, leading to the Equation (2):

$$\xi_i = \frac{\alpha}{2\omega_i} + \frac{\beta\omega_i}{2} \tag{2}$$

Where ξ_i is the modal damping coefficient and ω_i is the natural frequency associated to the mode shape "i". Isolating the parameters α and β of the Equation (2) for two natural frequencies, ω_{01} and ω_{02}, adopted according to the relevance of the corresponding vibration mode for the structural system dynamical response, it can be written:

$$\alpha = 2\xi_1\omega_{01} - \beta\omega_{01}\omega_{01} \tag{3}$$

$$\beta = \frac{2(\xi_2\omega_{02} - \xi_1\omega_{01})}{\omega_{02}\omega_{02} - \omega_{01}\omega_{01}} \tag{3}$$

www.EngineeringEBooksPdf.com

With two values of natural frequencies is possible to evaluate the parameters α and β de-scribed before, see Equations (3) and (4). The reference frequencies ω_{01} and ω_{02} are generally taken as the extreme frequencies of the structure spectrum. In this paper, the frequency ω_{01} adopted will be the structure fundamental frequency (2.80 Hz: without prestress and 2.71 Hz: with prestress [12]) and the frequency ω_{02} considered will be the system tenth natural frequency (39.23 Hz: without prestress and 38.58 Hz: with prestress [12]). The modal damping coefficient adopted in this investigation is equal to 0.005 (ξ=0.5%) [1].

3.2 Dynamic amplification factor

With these values the numeric study proceeded with the non-linear dynamic analysis to determine the sudden load amplification factors for the two investigated cases. The following tables can be better understood with the knowledge of the following adopted abbreviations: P_{cr} is the critical load of the structural system with and without prestress forces; Δ is the axial displacement at the top of the structural system; Δ_e is the static displacement; Δ_d is the dynamic displacement and DAF is the dynamic amplification factor.

Table 1 depicts the dynamic amplification factors (DAF) for the structural system without prestress forces and also presents the translational horizontal (Axis X) and vertical (Axis Y) displacements at node 7, see Figure 2, for the applied sudden loads, see Figure 2.

It should be stressed that the displacement at node 7, see Figure 2, exceeds the L/500 (24 mm) limit suggested by the Brazilian Standard [18] for all the cases where the sudden impact load was higher or equal to 60% of the system critical load and exceeds the L/300 (40 mm) limit suggested by the Eurocode [19] for all the cases where the sudden impact load was higher or equal to 80% of the system critical load.

Table 1: Dynamic amplification factors for structural systems without prestress forces.

Without Prestress forces						
P_{cr} 21086,8 N	Axis X (mm)		Axis Y (mm)		DAF - X	DAF - Y
	Δ_e	Δ_d	Δ_e	Δ_d	Δ_d/Δ_e	Δ_d/Δ_e
P_{cr} 10%	1.17	2.17	0.074	0.13	1.86	1.82
P_{cr} 20%	2.58	4.83	0.15	0.27	1.87	1.80
P_{cr} 30%	4.33	8.15	0.22	0.40	1.88	1.79
P_{cr} 40%	6.55	12.40	0.30	0.54	1.89	1.77
P_{cr} 50%	9.47	18.04	0.39	0.67	1.90	1.73
P_{cr} 60%	13.50	25.89	0.48	0.80	1.92	1.69
P_{cr} 70%	19.44	37.53	0.58	0.94	1.93	1.61
P_{cr} 80%	29.17	56.89	0.73	1.07	1.95	1.47

Figures 3 and 4 presents the structural system non-linear dynamic response for the cases where a sudden load magnitude of 10% and 60% of the system critical load was applied to the column top, respectively.

www.EngineeringEBooksPdf.com

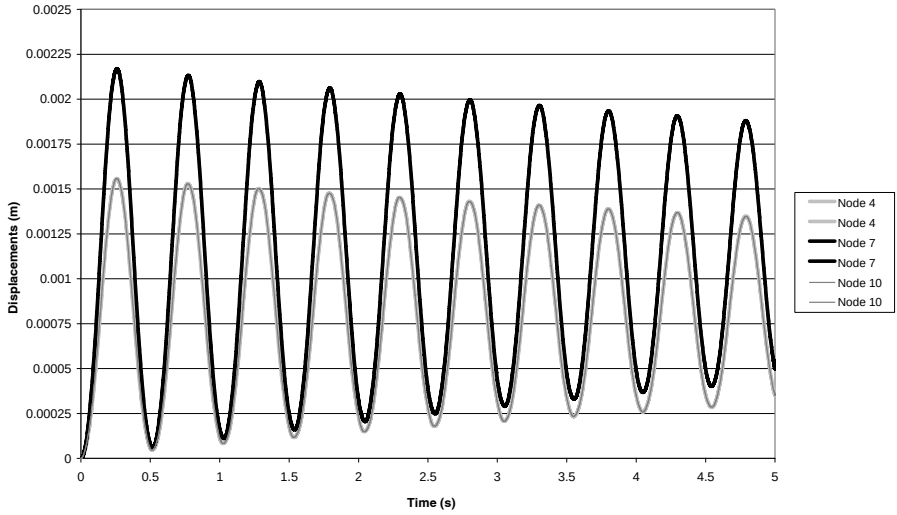


Figure 3: Displacements related to a 10% P_{cr} force applied to a structural system without prestress forces.

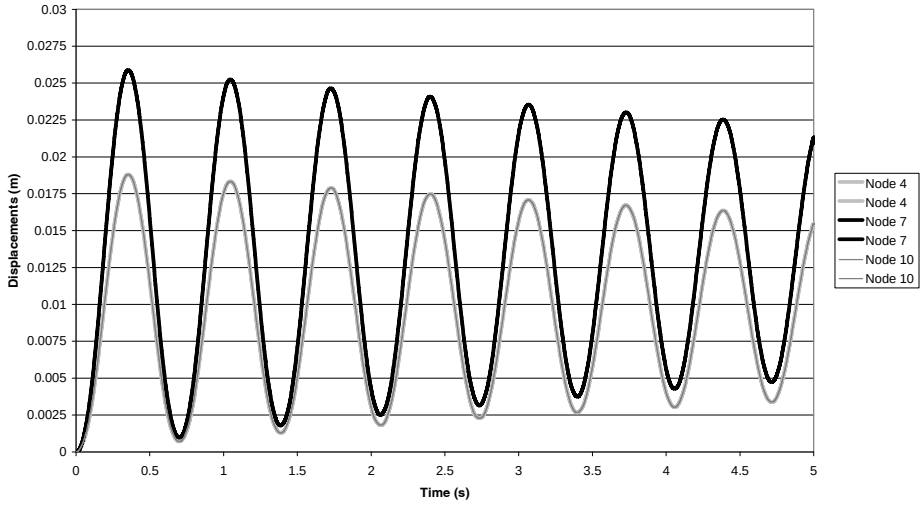


Figure 4: Displacements related to a 60% P_{cr} force applied to a structural system without prestress forces.

Table 2 depicts the dynamic amplification factors (DAF) for the structural system without prestress forces and also presents the translational horizontal (Axis X) and vertical (Axis Y) displacements at node 7, see Figure 2, for the applied sudden loads, see Figure 2.

It should be stressed that the displacement at node 7, see Figure 2, exceeds the L/500 (24 mm) limit suggested by the Brazilian Standard [18] for all the cases where the sudden impact load was higher or equal to 70% of the system critical load and exceeds the L/300 (40 mm) limit suggested by the Eurocode

www.EngineeringEBooksPdf.com

[19] for all the cases where the sudden impact load was higher or equal to 80% of the system critical load.

Table 2: Dynamic amplification factors for structural systems with prestress forces.

With Prestress Forces						
P_{cr} 21086,8 N	Axis X (mm)		Axis Y (mm)		DAF - X	DAF - Y
	Δ_e	Δ_d	Δ_e	Δ_d	Δ_d/Δ_e	Δ_d/Δ_e
P_{cr} 10%	1.15	2.39	0.42	0.78	2.08	1.85
P_{cr} 20%	2.11	4.26	0.52	0.96	2.02	1.85
P_{cr} 30%	3.30	6.65	0.63	1.15	2.01	1.84
P_{cr} 40%	4.83	9.70	0.73	1.34	2.01	1.84
P_{cr} 50%	6.86	13.69	0.84	1.53	1.99	1.83
P_{cr} 60%	9.70	19.20	0.95	1.72	1.98	1.81
P_{cr} 70%	13.93	27.58	1.07	1.91	1.98	1.78
P_{cr} 80%	20.94	41.32	1.21	2.09	1.97	1.73

Figures 5 and 6 presents the structural system non-linear dynamic response for the cases where a sudden load magnitude of 10% and 70% of the system critical load was applied to the column top, respectively.

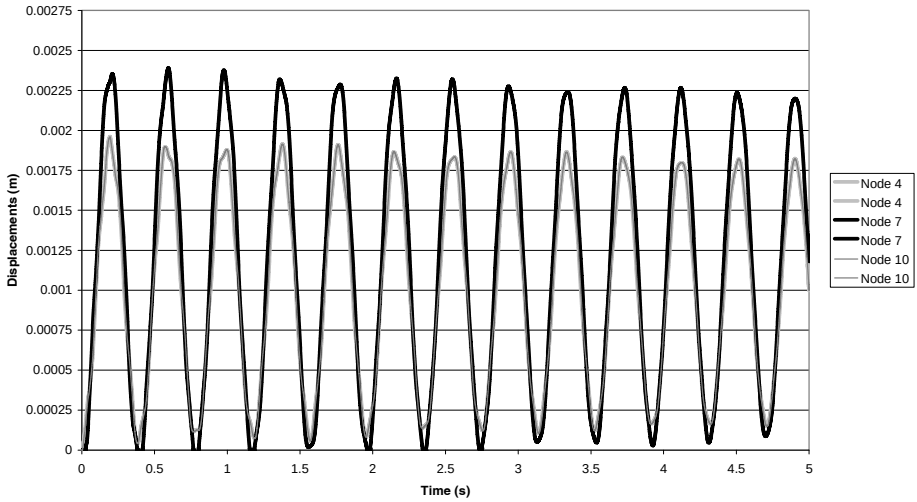


Figure 5: Displacements related to a 10% P_{cr} force applied to a structural system with prestress forces.

www.EngineeringEBooksPdf.com

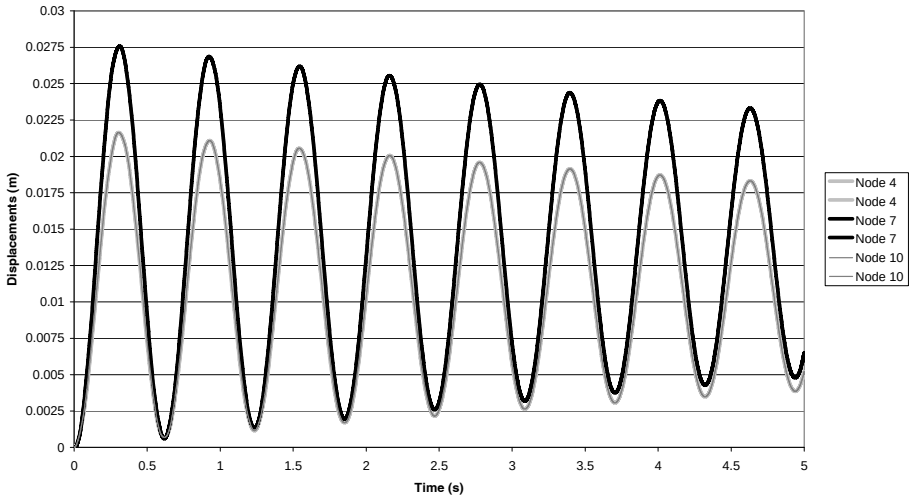


Figure 6: Displacements related to a 70% P_{cr} force applied to a structural system with prestress forces.

4 FINAL REMARKS

The current non-linear dynamic finite element analysis was performed on twelve meter length pre-stressed steel columns. These structural elements load bearing capacity was substantially increased by the additional restriction provided by the tie forces that are transferred to the main columns by means of horizontal tubes, perpendicularly welded to the column midpoint. The parametric study main variables were the prestressed element shape/area (cable or reinforced bar) and the adopted element pre-stress force. These two variables substantially altered the non-linear dynamic response and proved to be key elements for a better understanding of the structural system dynamic response.

Along the present investigation it was observed that a magnitude over 60% of structural system critical load without prestress forces and a magnitude over 70% of the structural system critical load with prestress forces led to horizontal displacements values that exceeded the limit suggested by the Brazilian Standard (horizontal displacements: L/500 = 24 mm). On the other hand, in the Eurocode this limit (horizontal displacements: L/300 = 40 mm) increases to 80% of structural system critical load with and without prestress forces. Another important outcome of the present investigation was that the stay prestress force magnitude directly influences the model displacements results altering the above mentioned limits.

5 ACKNOWLEDGEMENTS

The authors gratefully acknowledge the financial support provided by the Brazilian National and State Scientific and Technological Supporting Agencies: CNPq, CAPES and FAPERJ.

REFERENCES

[1] Araujo, R. R. ; Andrade, S ; Vellasco, P ; Silva, J ; Lima, L . *Experimental and numerical assessment of stayed steel columns*. Journal of Constructional Steel Research, v. 64, p. 1020-1029, 2008

[2] Voevodin, A. A.; *Ustoichivost predvaritelno-napryazhennoy shprengelnoy stoiki (Stability of a Prestressed Trussed Column)*, Trudy NIIR, Rússia, 1970.

www.EngineeringEBooksPdf.com

[3] Belenya, E.; *Prestressed load-bearing metal structures*, English Translation, MIR Publishers Moscow, 1977.

[4] Hafez, H. H.; Temple, M. C.; Ellis, J. S.; *Pretensioning of single-cross-arm stayed columns*, Journal of the Structural Division, ASCE, 108(7), 1623-1640, 1982.

[5] Wong, K. C.; Temple, M. C.; *Stayed column with initial imperfection*, Journal of the Structural Division, ASCE, 105(2), 359-375, 1979.

[6] Chan, S.; Shu, G.; Lü, Z.; *Stability analysis and parametric study of pre-stressed stayed columns*, Engineering Structures, Elsevier, 24, 115-124, 2002.

[7] Saito, D.; Wadee, M. A.; *Post-buckling behaviour of prestressed steel stayed columns*, Engineering Structures, Elsevier, 30, 1224-1239, 2008.

[8] Saito, D.; Wadee, M. A.; *Buckling behaviour of prestressed steel stayed columns with imperfections and stress limitation*, Engineering Structures, Elsevier, 31, 1-15, 2009.

[9] Saito, D.; Wadee, M. A.; *Numerical studies of interactive buckling in prestressed steel stayed columns*, Engineering Structures, Elsevier, 31, 432-443, 2009.

[10] ANSYS. Basic Analysis Procedures Guide, Release 11 (www.ansys.com).

[11] Araujo, R. R. de; *Estudo Teórico-Experimental de Colunas de Aço Estaiadas e Protendidas*. Rio de Janeiro, 2005. 128p. MSc Dissertaion, PUC-Rio (in portuguese).

[12] Araujo, R. R. ; Andrade, S. A. L. ; Vellasco, P. C. G. S. ; Silva, J. G. S. . *Dynamic Response of Pre-Stressed Steel Columns*. In: Eleventh International Conference on Civil, Structural and Environmental Engineering Computing, 2007, St. Julians. St. Julianss, 2007.

[13] Araujo, R. R. ; Andrade, S. A. L. ; Vellasco, P. C. G. S. ; Silva, J. G. S. ; Lima, L. R. O. . *Structural Response of Pre-Stressed Stayed Steel Columns*. Proceedings of the International Colloquia on Stability and Ductility of Steel Structures - SDSS'06. Lisboa : IST Press, 2006. v. 1. p. 241-248.

[14] Araujo, R. R. ; Andrade, S. A. L. ; Vellasco, P. C. G. S. ; Silva, L. Simões da . *Avaliação estrutural de colunas de aço estaiadas pré-esforçadas. In: VI Congresso de Construção Metálica e Mista*, 2007, Porto. VI Congresso de Construção Metálica e Mista. Coimbra - Portugal, 2007. v. 1. p. II-671-II-678 (in portuguese).

[15] Araujo, R. R. ; Silva, L. Simões da ; Andrade, S. A. L. ; Vellasco, P. C. G. S. ; Silva, J. G. S. ; Lima, L. R. O. . *Experimental Analysis of Prestressed Stayed Steel Columns*. In: Eurosteel 2008 - Fifth European Conference on Steel and Composite Structures, 2008, Grazz. Proceedings of the Fifth European Conference on Steel and Composite Structures. Brussels : ECCS European convention for Constructional Steelwork, 2008. v. B. p. 1605-1610.

[16] Araujo, R. R. de; *Comportamento Estrutural de Colunas de Aço Estaiadas e Protendidas*. Rio de Janeiro, 2009. 301p. DSc Thesis, PUC-Rio (in portuguese).

[17] Araujo, R. R. ; Silva, L. Simões da ; Andrade, S. A. L. ; Vellasco, P. C. G. S. ; Silva, J. G. S. ; Lima, L. R. O. *Structural Evaluation of Steel Columns With Reinforced Bar Stays*. In: 7th EUROMECH Solid Mechanics Conference, 2009, LISBOA. Proceedings of the 7th EUROMECH Solid Mechanics Conference. LISBOA : Editora do LNEC, 2009. v. 1. p. 1-10.

[18] ABNT NBR 8800. *Projeto de Estruturas de Aço e Estruturas Mistas de Aço e Concreto de edifícios*. Associação Brasileira de Normas Técnicas. Brasil, 2008. 237 p.

[19] EUROCODE 3. EN 1993, *Design of steel structures Part 1-1: General rules and rules for buildings*, Brussels, CEN-European Committee for Standardisation; 2005.

[20] Clough, R.W. and Penzien, J. *Dynamics of Structures*, McGraw-Hill, 634 pages, 1993.

www.EngineeringEBooksPdf.com

6. FIRE ENGINEERING

www.EngineeringEBooksPdf.com

www.EngineeringEBooksPdf.com

SDSSRio 2010 STABILITY AND DUCTILITY OF STEEL STRUCTURES
E. Batista, P. Vellasco, L. de Lima (Eds.)
Rio de Janeiro, Brazil, September 8 - 10, 2010

INTERACTION DIAGRAMS FOR DESIGN OF CONCRETE-FILLED TUBULAR COLUMNS UNDER FIRE

Rodrigo B. Caldas*, João Batista M. Sousa Jr. and Ricardo H. Fakury***

* Universidade Federal de Minas Gerais
e-mail: caldas@dees.ufmg.br, fakury@dees.ufmg.br

** Universidade Federal de Ouro Preto
e-mail: joao@em.ufop.br

Keywords: Design Strength, Composite Columns, Fire.

Abstract. *This work presents a procedure for the design of concrete-filled hollow columns under fire action, employing cross-section strength interaction diagrams. Fire action induces thermal strains and modifies the stress-strain relationships for steel, concrete and reinforcement bars. Strength interaction diagrams are tools that relate ultimate values of bending moments and axial force in the cross section. A previously developed algorithm is used for the construction of diagrams, obtained by a stepwise variation of the deformed configuration, under assumptions of conventional ultimate strain values for concrete and steel. The moment magnification factor is used to approximate the second order effects in the column. The procedure is compared with European Committee for Standardization rules for calibration of eccentricities to be used in the calculations.*

1 INTRODUCTION

Axial force-bending moment diagrams are useful and popular tools for ambient temperature design of composite beam-column cross sections. A procedure for the construction of such diagrams for arbitrarily shaped steel-concrete composite sections under generic temperature distribution, such as that present in a fire, was developed by Caldas [1]. This author obtained these diagrams for RC sections and compared the results to experimental values. The results showed that the procedure is able to take into account the influence of thermal strains, the ultimate concrete strain variation with temperature and different fire exposure boundary conditions (1, 2, 3 or 4 faces of rectangular sections).

This paper applies the developed procedure [1, 2, 3, 4] to the design of slender concrete filled circular hollow section columns under fire action. The results are then compared to the analytical method adopted by the European Committee for Standardization, EN 1994-1-2:2005 [5].

2 COLUMN DESIGN

2.1 Resistance of cross section (interaction diagrams)

Under fire action, the thermal strains and the degradation of the mechanical properties of the materials pose challenging difficulties to the limit state analysis of beam-column cross sections. Generic temperature distributions result in unexpected variations of the interaction diagrams. In order to define these limit states it is necessary to establish ultimate strain values for concrete and steel. For concrete, the ultimate compressive strain is conventionally assumed as the value correspondent to the peak stress of the Eurocode 2, EN 1992-1-2:2004 [6], temperature-dependent uniaxial stress-strain relation (figure 1). Concrete tensile stress is not taken into account.

www.EngineeringEBooksPdf.com

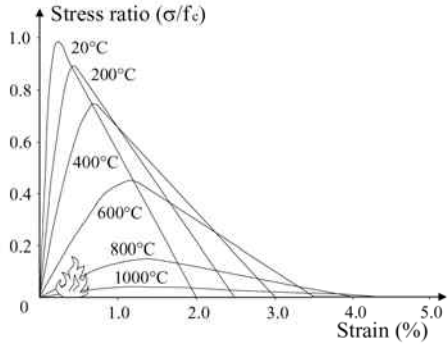


Figure 1: Stress-strain relationships of concrete at elevated temperature [6].

With regard to the steel properties, the ultimate strain value for the hollow section steel and the reinforcement bars is assumed as 1%. The steel stress-strain relation is the bilinear relation with 0.2% reduction factor.

Mechanical or stress-inducing strains are given by

$$\varepsilon(x,y)=\varepsilon_o+k_x y-k_y x-\varepsilon_{th} \quad \text{or} \quad \varepsilon(\xi,\eta)=\varepsilon_o+k_o\eta-\varepsilon_{th}\,, \tag{1}$$

where $_{th}$ is the thermal strain, and the section curvatures are expressed in the coordinate systems shown in figure 2. In this system k_x and k_y are the curvatures about x and y axes, k_o is the curvature about ξ axis and ε_o the centroidal strain.

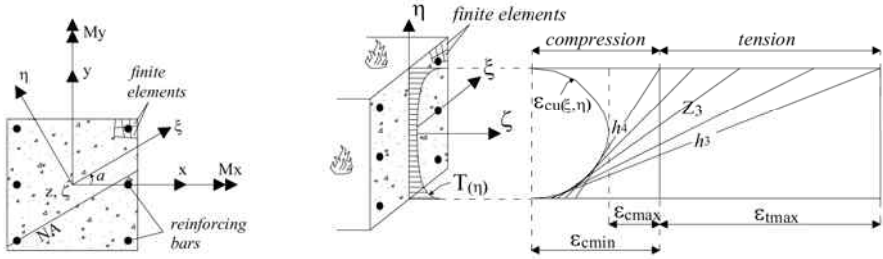


Figure 2: Coordinate systems (NA is the neutral axis) and ultimate configurations.

In the present formulation, an ultimate limit state is conventionally assumed when (x, y) in any point of the cross section reaches its temperature-dependent limit value. If the thermal strains $_{th}$ and the ultimate concrete compressive strains depend on the temperature field $T(x, y)$, it is possible to evaluate these values for the grid of points that was employed, for instance, in the thermal analysis of the section. This allows one to obtain points of the surface $_{cu}(\xi,$) that represent the ultimate compressive concrete strain (figure 2) and therefore have an approximation of this surface. If the plane deformed section touches this surface at any point, an ultimate state is reached and the correspondent axial force and bending moments are points of the interaction diagram for the cross section, under the given temperature profile.

For a fixed value of the neutral axis angle one may then define an arbitrary continuous variable that traces the evolution of the deformed configuration of the section such that every consecutive point lies on the ultimate limit state surface [1, 2].

www.EngineeringEBooksPdf.com

Using the same grid (or mesh) that was employed in the thermal analysis the axial force and bending moments are evaluated by numerical integration:

$$N_z = \sum_{i=1}^{n} (\sigma(\varepsilon) A)_i \ , \quad M_x = \sum_{i=1}^{n} (\sigma(\varepsilon) y A)_i \quad \text{and} \quad M_y = \sum_{i=1}^{n} (\sigma(\varepsilon) x A)_i \ . \tag{2}$$

2.2 Verification of column length

From the *N-M* interaction curve (or alternatively the N-M_x-M_y interaction surface), a procedure for the verification of columns was developed [1] and adapted in the present work for concrete-filled circular hollow sections. Second order effects along the member are taken into account by the amplification factor

$$\delta = \frac{1}{1 - N / N_{fi,e}} \ , \tag{3}$$

where the buckling load under fire action is evaluated as

$$N_{fi,e} = \frac{\pi^2 EI_{fi}}{\ell^2} \ . \tag{4}$$

The temperature dependent section stiffness EI_{fi} is evaluated by numerical integration, using the section grid, considering an averaged temperature on each mesh element,

$$EI_{fi} = 0{,}8EI_a + 0{,}8EI_s + 0{,}5EI_c \ , \tag{5}$$

where subscripts c, a and s refer to concrete, profile steel and reinforcement, respectively. The characteristic value for the concrete secant modulus under fire action is taken as the relation between the peak stress and its correspondent strain for the specified temperature (figure 1). In order to apply the procedure it is necessary to impose an eccentricity on the axial load. Several values of this eccentricity were tested, namely, $e_{min} = 0.015+0.03d$, where d is the section outer diameter, /150, /200, /250, /300, /400, /500 and /1000.

3 EUROCODE 4 ANALYTICAL METHOD

According to the analytical method of EN 1994-1-2:2005 [5], the axial resistent force of composite columns subjected to fire is given by

$$N_{fi,Rd} = \chi_{fi} N_{fi,p\ell,Rd} \ , \tag{6}$$

where $N_{fi,p\ell,Rd}$ is the plastic axial force under fire conditions and χ_{fi} is the reduction factor related to buckling curve *c*.

The composite column effective flexural stiffness is given by

$$EI_{fi} = \varphi EI_a + \varphi EI_s + \varphi EI_c \ , \tag{7}$$

where is a reduction coefficient depending on the effect of thermal stress, taken as 0.80 in this case. The temperature field in the cross section is required in order to employ the proposed method. In the present work a finite difference scheme, assuming radial symmetry of the temperature distribution in terms of polar coordinates and described in [7] was employed to obtain the temperatures.

www.EngineeringEBooksPdf.com

4 COLUMN ANALYSIS

Employing interaction diagrams and the procedure presented in section 2.2, the load carrying capacity of a group of concrete-filled hollow circular columns was compared to the values obtained by the the Eurocode 4 analytical method [5]. The latter was assumed as a reference value, due to the fact that it has been calibrated by experimental results.

Steel and concrete material properties were taken from [5], considering 4% moisture (in weight) and upper limit thermal conductivity. The hollow section profiles have yield strength of 350 MPa and 200000 MPa elastic modulus. Concrete characteristic compressive strength is 40 MPa and the reinforcement steel has yield strength of 500 MPa and 210000 MPa elastic modulus. Concrete cover was 35 mm. The buckling length of the columns was taken as 2 m, representing columns of intermediate floors with 4 m between lateral restraints in ambient condition.

The colums are identified by (diameter)x(thickness)-(number of reinforcement bars)x(reinforcement bar diameter).

Figure 3 exemplifies the procedure employing the interaction diagram for an eccentricity of /200 for the 219.1x8.2-0 column.

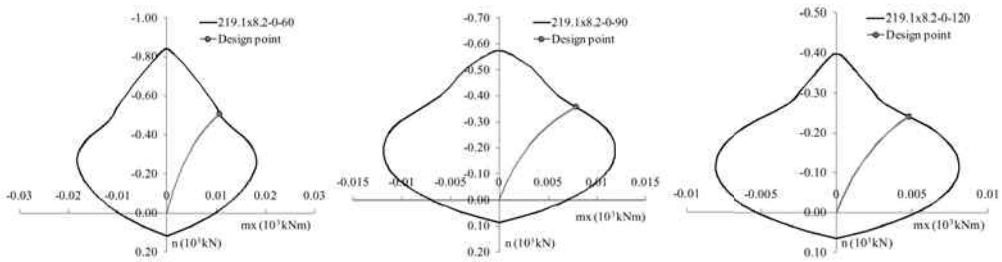


Figure 3: Interaction diagrams for 219.1x8.2-0 columns for 60, 90 and 120 min fire exposure.

Figure 4 displays the graphic results for the column design loads obtained employing the interaction diagrams for ambient and elevated temperature (zero, 30, 60, 90 and 120 minutes of standard fire exposure) and different eccentricity values along with the Eurocode ($N_{Rd,fi,Eurocode}$) analytical method results. It may be observed that the eccentricities e_{min} and /150 lead to the smallest values for column resistance. The value e_{min} was employed by Caldas [1] in the analysis of reinforced concrete columns under fire action and is prescribed by the american [8] and brazilian [9] design codes under ambient temperature. The utilization of these values is therefore discouraged. The values of eccentricity between /200 and /1000 gave the closest results to the analytical Eurocode method. The former led to results on the safe side, with the largest error happening for the 30-minute fire exposure, but decreasing for superior times.

It may be noted that the influence of the eccentricity value is less pronounced when the column slenderness increases, as well as for higher exposure times. This behaviour is evident with the 219.1x8.2-0 column where the curves converge to the Eurocode curve for larger times. In contrast, the 355.6x9.5-8x20 column displays a different behaviour with a strong dependency on the eccentricity for the complete range of exposure times. The behaviour of the columns with and without reinforcement are similar.

Table 1 displays the relationship between points from the interaction diagram and values obtained according to EN 1994-1-2:2005 [5]. N_{max} is the axial compressive resistant force with zero moment which is compared to the axial plastic resistant load $N_{fi,p\ ,Eurocode}$ [5]. M_{max} is the maximum moment from the interaction diagram which is compared with the maximum plastic moment $M_{fi,p\ ,max,Eurocode}$ from EN 1994-1-1:2004 [10].

www.EngineeringEBooksPdf.com

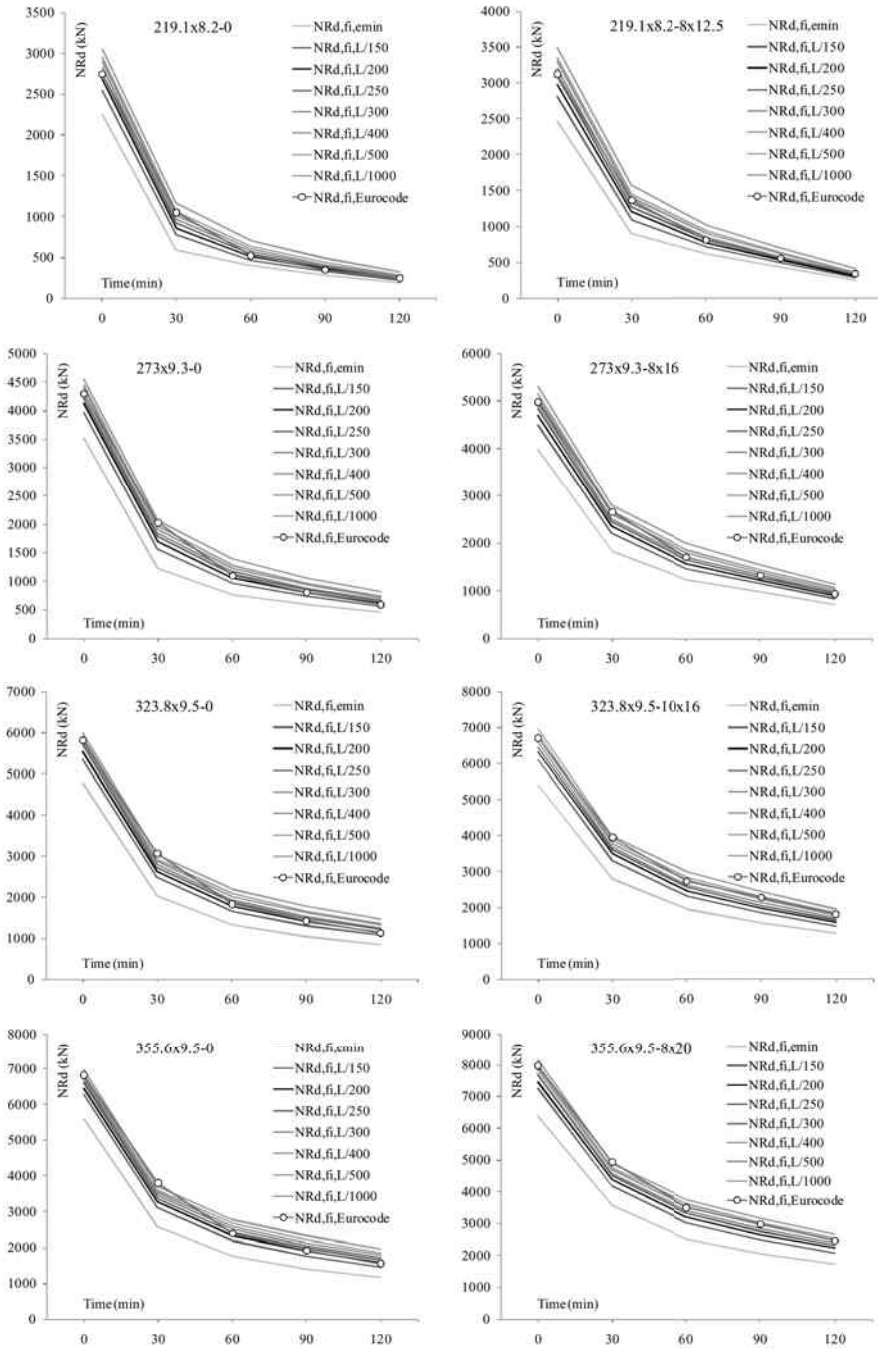


Figura 4: Assessment of column resistance under fire for different eccentricities and comparison with Eurocode.

www.EngineeringEBooksPdf.com

Table 1: Comparison of interaction diagram solution with EN 1994-1-2:2005 [5].

Column identification	$\frac{N_{max}}{N_{fi,p,Eurocode}}$	$\frac{M_{max}}{M_{fi,p,max,Eurocode}}$	$\frac{M_{N=0}}{M_{fi,p,Eurocode}}$	$\frac{N_{fi,e}}{N_{fi,e,Eurocode}}$
219.1x8.2-0-0	1.00	0.87	0.92	0.93
219.1x8.2-0-30	0.80			0.87
219.1x8.2-0-60	0.94			0.91
219.1x8.2-0-90	0.94			0.95
219.1x8.2-0-120	0.96			0.96
219.1x8.2-8x12.5-0	1.00	0.84	0.87	0.94
219.1x8.2-8x12.5-30	0.83			0.90
219.1x8.2-8x12.5-60	0.86			0.93
219.1x8.2-8x12.5-90	0.83			0.91
219.1x8.2-8x12.5-120	0.82			0.93
273x9.3-0-0	1.00	0.87	0.93	0.93
273x9.3-0-30	0.82			0.87
273x9.3-0-60	0.95			0.87
273x9.3-0-90	0.95			0.90
273x9.3-0-120	0.94			0.93
273x9.3-8x16-0	1.00	0.84	0.87	0.93
273x9.3-8x16-30	0.86			0.90
273x9.3-8x16-60	0.89			0.92
273x9.3-8x16-90	0.86			0.95
273x9.3-8x16-120	0.86			0.95
323.8x9.5-0-0	1.00	0.87	0.93	0.92
323.8x9.5-0-30	0.84			0.85
323.8x9.5-0-60	0.95			0.83
323.8x9.5-0-90	0.95			0.86
323.8x9.5-0-120	0.95			0.88
323.8x9.5-10x16-0	1.00	0.84	0.88	0.92
323.8x9.5-10x16-30	0.87			0.89
323.8x9.5-10x16-60	0.90			0.89
323.8x9.5-10x16-90	0.86			0.91
323.8x9.5-10x16-120	0.86			0.88
355.6x9.5-0-0	1.00	0.86	0.93	0.91
355.6x9.5-0-30	0.86			0.84
355.6x9.5-0-60	0.95			0.81
355.6x9.5-0-90	0.96			0.83
355.6x9.5-0-120	0.95			0.84
355.6x9.5-8x20-0	1.00	0.84	0.88	0.92
355.6x9.5-8x20-30	0.88			0.88
355.6x9.5-8x20-60	0.91			0.89
355.6x9.5-8x20-90	0.88			0.92
355.6x9.5-8x20-120	0.88			0.93
Minimum =	0.80	0.84	0.87	0.81
Maximum =	1.00	0.87	0.93	0.96

$M_{N=0}$ is the moment from the interaction diagram for which the normal force is zero. This value is compared to the plastic moment $M_{fi,p,Eurocode}$ [10]. These values were obtained for ambient temperature. Also presented are the elastic buckling loads $N_{fi,e}$ calculated according to Section 2.2, and according to EN 1994-1-2:2005 [5].

The relation $N_{max} / N_{fi,p,Eurocode}$ presents a minimum value of 0.80 suggesting that complete section plastification does not occur according to the interaction diagram procedure. This is related to the ultimate concrete strain variation with respect to the temperature variation along the radius (figure 1). For ambient temperature this relation is equal to 1.00 as the ultimate concrete strain is constant.

www.EngineeringEBooksPdf.com

The values of $M_{max} / M_{fi,p,max,Eurocode}$ attain a minimum of 0.84, which is coherent with the 0.80 coefficient employed by the brazilian code ABNT NBR 8800:2008 [11]. For the relation $M_{N=0} / M_{fi,p,Eurocode}$ the minimum value is 0.87, which agrees well with the value 0.90 prescribed by ABNT NBR 8800:2008 [11] and EN 1994-1-1:2004 [10]. Caldas *et al.* [12] provide an explanation for these coefficients.

The relation between the elastic buckling loads varies between 0.81 and 0.96 due to the differences in the evaluation of the effective stiffness in Section 2.2 and EN 1994-1-2:2005 [5], Section 3. The effective stiffness was chosen to be evaluated acccording to Section 2.2 in order to have a unified procedure for reinforced concrete columns [1] and composite columns, with the only difference being the eccentricity to be employed.

5 CONCLUSION

The authors of this paper, previous developed a procedure for the construction of interaction diagrams for generic concrete and steel cross sections subjected to arbitrary temperature distributions [1, 2, 3, 4]. The consideration of initial imperfection and 2nd order local effects allows the diagrams to be used in the analysis of slender columns under fire. In this work the procedure was applied to the analysis of hollow circular concrete filled columns and different eccentricities were analyzed and compared with results obtained from the Eurocode 4, EN 1994-1-2:2005 [5].

The eccentricities e_{min} and /150 produce excessively conservative results and are not recommended for the analyzed columns, and eccentricities smaller than /200 led to unsafe results, always compared with the Eurocode. Therefore the authors recommend the proposed design method of Section 2.2 with the value of /200 for the eccentricity.

The comparison of the points from the interaction diagram with the EN 1994-1-2:2005 [5] lead to interesting results. The relation $N_{max} / N_{fi,p,Eurocode}$ presents a minimum value of 0.80 suggesting that complete section plastification does not occur according to the interaction diagram procedure. The relations $M_{max} / M_{fi,p,max,Eurocode}$ and $M_{N=0} / M_{fi,p,Eurocode}$ present minimum values that agree well with the brazilian [11] and european [10] design codes for composite columns under ambient temperature.

Acknowledgements

The authors wish to thank for the support from Vallourec & Mannesmann Tubes (V&M Brasil), CNPq and FAPEMIG.

REFERENCES

[1] Caldas, R.B. È*Numerical analysis of steel, concrete and composite structures under fire*Š, PhD thesis (in Portuguese), DEES, Universidade Federal de Minas Gerais, 2008.

[2] Caldas, R.B., Sousa Jr., J.B.M., Fakury, R.H. È Interaction diagrams for reinforced concrete sections subjected to fireŠ, submitted to *Engineering Structures*.

[3] Sousa Jr., J.B.M., Caldas, R.B., Fakury, R.H. È Interaction diagrams for concrete-filled tubular sections under fireŠ, *Proc. of Tubular Structures XII,* Shen, Chen and Zhao (eds.), Taylor and Francis Group, London, 635-639, 2009.

[4] Caldas, R.B., Fakury, R.H., Sousa Jr., J.B.M. È Análise de seções transversais de concreto armado em situação de incêndioŠ (*in Portuguese)*, *Proc. of 49° Congresso Brasileiro do Concreto*, 2007.

[5] *European Committee for Standardization*. Eurocode 4: Design of Composite Steel and Concrete Structures, Part 1-2: General Rules, Structural Fire Design, EN 1994-1-2:2005.

[6] *European Committee for Standardization*. Eurocode 2: Design of Concrete Structures, Part 1.2: General Rules, Structural Fire Design. EN 1992-1-2:2004

www.EngineeringEBooksPdf.com

[7] Caldas, R.B., Fakury, R.H., Sousa Jr., J.B.M. Araújo, A.H.M. ÈCapacidade resistente à compressão de pilares tubulares circulares de aço preenchidos com concreto em situação de incêndioŠ, *Proc. of 30° CILAMCE, Congresso Ibero-Latino-Americano de Métodos Numéricos em Engenharia*, 2009.

[8] *American Concrete Institute*. Building Code Requirements for Structural Concrete. ACI 318, 2005.

[9] *Associação Brasileira de Normas Técnicas* (*Brazilian Association of Technical Standards*). Design of Structural Concrete. ABNT NBR 6118:2007.

[10] European Committee for Standardization. Eurocode 4: Design of Composite Steel and Concrete Structures, Part 1.1: General Rules and Rules for Buildings. EN 1994-1-1:2004.

[11] *Associação Brasileira de Normas Técnicas* (*Brazilian Association of Technical Standards*). Design of Steel and Composite Structures for Buildings. ABNT NBR 8800:2008.

[12] Caldas, R.B., Fakury, R.H., Sousa Jr., J.B.M. ÈBases do dimensionamento de pilares mistos de aço e concreto segundo o projeto de revisão da NBR 8800Š, *Revista da Escola de Minas*, **60**(2), 271-276.

www.EngineeringEBooksPdf.com

SDSS'Rio 2010 STABILITY AND DUCTILITY OF STEEL STRUCTURES
E. Batista, P. Vellasco, L. de Lima (Eds.)
Rio de Janeiro, Brazil, September 8 - 10, 2010

DUCTILITY OF SIMPLE STEEL CONNECTIONS IN FIRE

J. Buick Davison*, Ian W. Burgess*, Roger J. Plank **, Hongxia Yu*, Ying Hu******

* Department of Civil and Structural Engineering, University of Sheffield
e-mails: j.davison@sheffield.ac.uk, ian.burgess@sheffield.ac.uk
** Formerly, School of Architecture, University of Sheffield, e-mail: r.j.plank@sheffield.ac.uk
*** Tsinghua University, China, e-mail: yuhx@mail.tsinghua.edu.cn
**** MACE, University of Manchester, email: ying.hu@manchester.ac.uk

Keywords: Ductility, Robustness, Tying, Fire, Connections

Abstract. *This paper summarises the findings of a recently-completed large series of experiments to investigate the resistance of simple connections to combinations of shear, bending and tension forces at temperatures up to 650°C. A total of 64 isothermal tests was conducted on double-angle web cleat, fin plate, partial depth endplate and flush endplate connections to study their ability to resist large tensile forces whilst undergoing large rotations. The tests highlight the importance of considering the ductility of connections as well as their strength, and also reveal that their mode of failure may change with increasing temperature. High-temperature performance of bolts and welds is shown to be of particular importance.*

1 INTRODUCTION

In braced steel frames, the beam to column connections may be designed to function as nominal pins under gravity loads. However, if subjected to fire the connections may be required to resist not only vertical shear forces, but also significant axial loads, and to undergo large rotations. These conditions demand that connections possess good ductility. In the past, experimental investigations of the performance of simple connections in fire have been concerned with moment-rotation characteristics, and have largely neglected to consider the effect of co-existing axial forces. This paper summarises the findings of a recently-completed large series of experiments to investigate the resistance of simple connections to combinations of shear, bending and tension forces at temperatures up to 650°C. A total of 64 isothermal tests was conducted on double-angle web cleat, fin plate, partial depth endplate and flush endplate connections to study their ability to resist large tensile forces whilst undergoing large rotations.

2 TEST ARRANGEMENT

2.1 Furnace and test set up

Experiments were conducted in a $1m^3$ electric furnace illustrated in Figure 1. Each specimen consisted of a stub beam bolted to a short length of column. The column was suspended from a ring frame via a threaded rod passing through the top of the furnace and secured to an inclined support projecting into the furnace. The stub beam was supported by its connection to the column and was loaded at its remote end by a pin-connected bar passing into the furnace. A triangulated system of pin-connected bars was devised to allow the vertical displacement of a screw jack to apply an inclined tying force to the beam [1]. By adjusting the lengths of the bars, the applied force could be applied at different angles relative to the beam axis (nominally 35, 45 or 55°) resulting in changes in the shear:tensile force ratio. Tests were conducted isothermally at 20, 450, 550 and 650°C.

www.EngineeringEBooksPdf.com

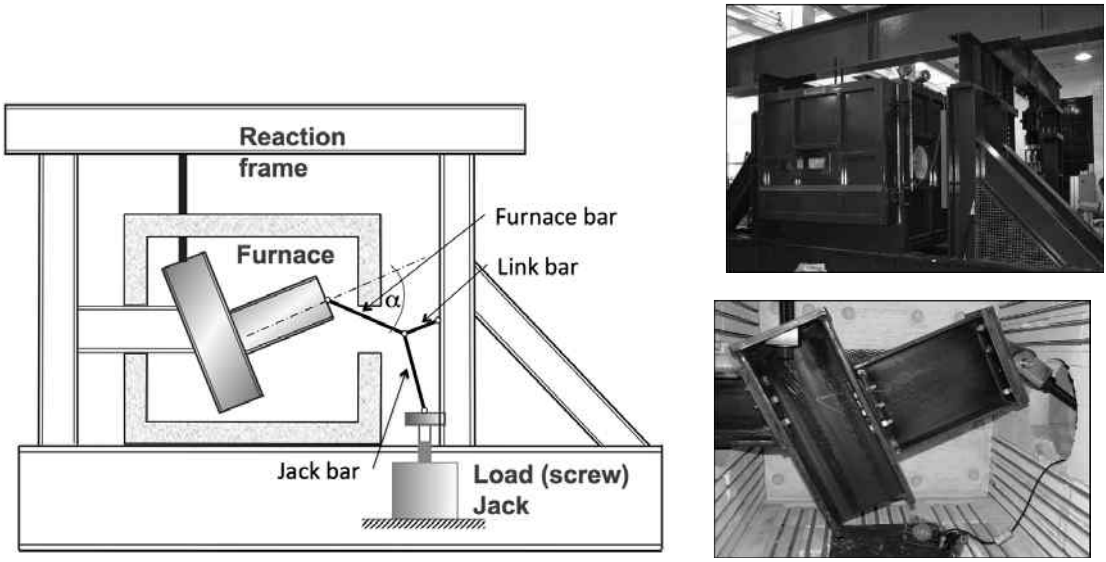


Figure 1: Sketch of test arrangement, photograph of furnace and a typical specimen.

2.2 Specimens and material properties

All test specimens used S355 254UC89 columns and S275 306x165UB40 beams. Connections were generally in accordance with UK design recommendations and used S275 fittings (plates and angles) with M20 8.8 fully threaded bolts. The test programme examined "simple connections" (i.e. connections designed to take vertical shear loads not moments) and included fin plates, web angles, partial depth endplates and flush endplates.

2.3 Instrumentation

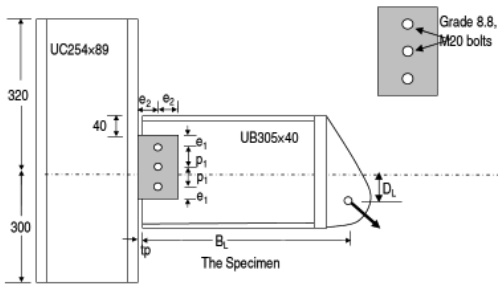
The applied force transmitted through the furnace bar was calculated by resolving the system of forces measured in the strain gauged link and jack bar; the angles between all the bars were recorded using digital images. Deformation of the specimen within the heated furnace was recorded with digital images taken through a 100x200mm observation hole in the front. Targets placed on the column and beams enabled rotations and displacements to be calculated [2].

3 FIN PLATES

Fourteen fin plate connections were tested as shown in figure 2 and summarised in table 1. α refers to the angle between the axis of the stub beam and the furnace bar (see figure 1), with the subscripts *n, i.* and *e* denoting the *nominal* angle, the actual *initial* set-up angle and the final angle at the *end* of the test, which altered due to the deformation of the specimen. The specimen geometry denotes the number of bolt rows, bolt-grade and bolt diameter. In all cases the fin plate was 200mm deep, 100mm wide and 8mm thick in S275 steel with bolts at 60mm vertical pitch. It is clear from table 1 that the failure of fin plate connections is generally governed by the behaviour of the bolts in shear (see figure 3). At elevated temperatures the reduction in overall resistance is closely related to the degradation of bolt strength, which due to the heat treatment undergone in the manufacturing process of bolts, is proportionally greater than that of the steel fin plate. Substituting higher grade bolts (10.9) moved the failure into the beam web

www.EngineeringEBooksPdf.com

which failed in block shear, as shown in figure 3, but only at ambient temperature – at higher temperatures bolt failure remained critical.



Bolt diameter d	20
Bolt hole diameter d_0	22
End distance e_1	40
Edge distance e_2	50
Bolt spacing p_1	60
Fin plate thickness t_p	10
Lever arm B_L	490
Vertical off set D_L	51.7

Figure 2: Fin plate test details.

Table 1: Fin plate test results.

Test	Specimen geometry	°C	α_n	α_i	α_e	Force (kN)	Rotation (Degree)	Failure mode
1	3-8.8-20	20	55	53.9	32.4	145.95	8.107	Bolt shear
2	3-8.8-20	450	55	51.5	41.4	70.5	6.093	Bolt shear
3	3-8.8-20	550	55	53.4	42.7	34.8	6.558	Bolt shear
4	3-8.8-20	650	55	53.1	44.0	18.0	6.255	Bolt shear
5	3-8.8-20	20	35	33.8	34.1	185.1	7.805	Bolt shear
6	3-8.8-20	450	35	39.0	33.5	84.5	6.237	Bolt shear
7	3-8.8-20	550	35	40.9	31.5	37.5	7.121	Bolt shear
8	3-8.8-20	650	35	40.5	30.6	19.3	7.367	Bolt shear
9	3*2-8.8-20	550	35	41.6	32.2	81.1	6.853	Bolt shear
10	3*2-8.8-20	550	55	56.0	46.6	67.0	4.782	Bolt shear
11	3-10.9-20	20	35	36.5	29.8	213.0	10.62	Beam web
12	3-10.9-20	550	35	40.9	23.9	56.8	11.50	Bolt shear
13	3-8.8-24	20	35	37.4	29.7	203.1	8.339	Beam web
14	3-8.8-24	550	35	42.1	29.1	74.0	7.855	Bolt shear
14	3-8.8-24	550	35	42.1	29.1	74.0	7.855	Bolt shear

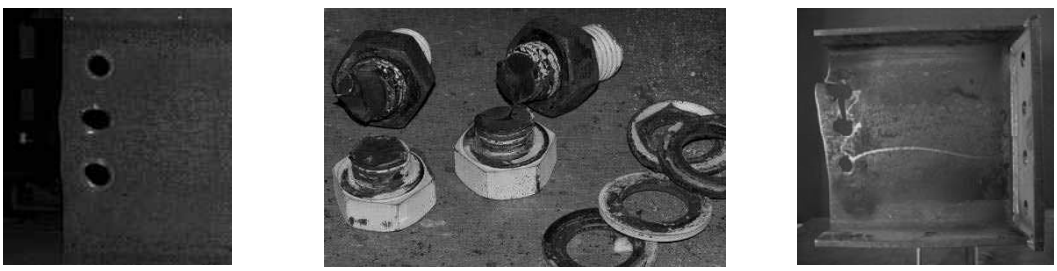


Figure 3: Deformation of beam web and bolt shear (test 12); beam web block shear (test 11)

www.EngineeringEBooksPdf.com

As part of the investigation a component based model of the fin plate connection was developed [1]. The behaviour of each bolt row was simulated by three springs arranged in series representing the bearing in the fin plate, bearing on the beam web and shear of the bolt. A parallel spring was used to represent friction at the fin plate/beam web interface. Each spring was represented by a non-liner force-displacement curve including modifications to allow for changes in temperature. Figure 4 shows a comparison of the force-rotation behaviour for connections loaded at 55° at ambient and high temperature (650°C) to illustrate how well the model works. In the simple model, bolts in shear may be assumed to have infinite ductility at their maximum capacity (thus allowing all bolts to reach their peak) or be capable of retaining their peak shear resistance only up to a displacement of ½ the bolt diameter. The circle on the figures denotes the maximum load if the latter assumption is made.

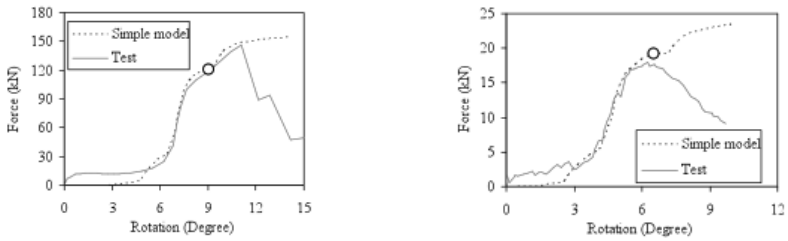
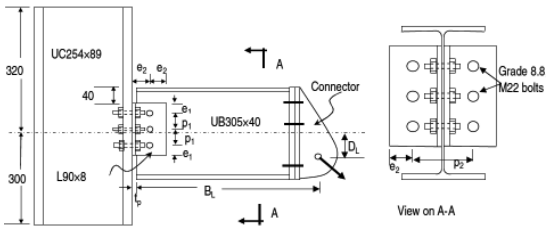


Figure 4: Comparison of simple component model with test results (tests 1 and 4).

4 WEB ANGLES

Web angles (or cleats) were once very popular in the UK but have tended to be less widely used recently as steelwork contractors prefer to fabricate endplate type connections. However, these connections were included the experimental study as they are potentially very ductile. Figure 5 shows details of the test arrangement and table 2 presents the key test results.



Bolt diameter d	20
Bolt hole diameter d_0	22
End distance e_1	60
Edge distance e_2	50
Bolt spacing p_1	60
Bolt spacing p_2	103
Lever arm B_L	490
Vertical off set D_L	51.7

Figure 5: Web angle test details.

The failure mode changed with increasing temperature but not with change of loading angle. For example, at room temperature all tests failed by the column bolt heads first punching through the angle leg and then a block shear fracture of the cleat (see left hand image in figure 6). At 450 and 550°C, the web angles fractured at the heel; at 650°C, the failure mode was double shear of the beam web bolts (right hand images in figure 6). Web angles showed good rotational capacity and developed useful amounts of deformation under tensile forces [3].

www.EngineeringEBooksPdf.com

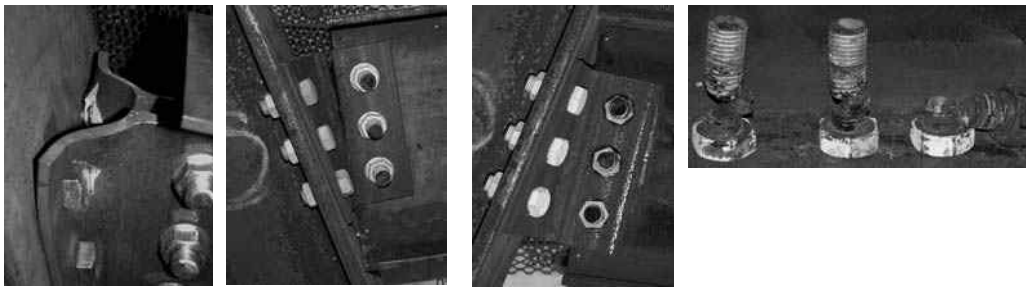


Figure 6: typical failure modes at 20°C, 450-500°C, and 650°C

Table 2: Web angle test results.

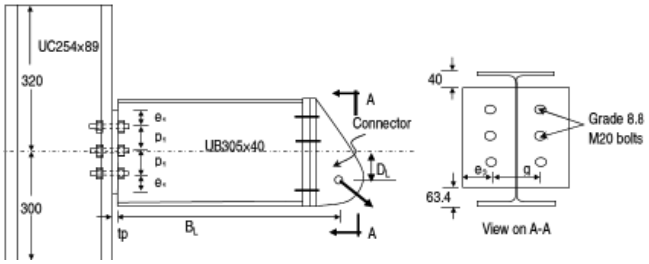
Test	Specimen geometry	°C	α_n	α_i	α_e	Force (kN)	Rotation (Degree)	Failure mode
1	3-8.8-20	20	55	55.0	34.4	186.34	16.57	Punching shear
2	3-8.8-20	450	55	55.8	43.5	93.74	9.39	Angle fracture
3	3-8.8-20	550	55	56.0	42.2	52.91	10.52	Angle fracture
4	3-8.8-20	650	55	56.5	34.4	25.70	14.15	Bolt shear
5	3-8.8-20	20	45	45.7	32.0	212.54	17.12	Punching shear
6	3-8.8-20	450	45	46.7	37.3	99.42	10.29	Angle fracture
7	3-8.8-20	550	45	47.0	36.8	56.35	11.53	Angle fracture
8	3-8.8-20	650	45	48.1	34.5	28.18	15.94	Bolt shear
9	3-8.8-20	20	35	37.4	21.2	243.17	16.71	Punching shear
10	3-8.8-20	450	35	41.1	29.1	112.85	10.75	Angle fracture
11	3-8.8-20	550	35	41.4	26.6	61.21	12.56	Angle fracture
12	3-8.8-20	650	35	40.9	21.6	31.57	14.86	Bolt shear
13	3*2-8.8-20	550	35	40.2	27.2	85.01	10.95	Angle fracture
14	3*2-8.8-20	550	55	55.7	41.0	66.78	9.19	Angle fracture
14	3-8.8-24	550	35	42.1	29.1	74.0	7.855	Bolt shear

A component model was developed for the web angle connection, the derivation of which is fully described in [4]. The four components modeled by non-linear springs are: column bolts in tension, web angles in bending, beam web bolts in shear and the beam web in bearing. Further work (not reported here) has been conducted to examine the performance of web angles using stainless steel either for the bolts or for the angles. These have shown improvements in high temperature performance.

5 PARTIAL DEPTH ENDPLATES

Partial depth endplates are widely used in the UK. They are simple to fabricate, have good rotational ductility and give good resistance to vertical shear. Their performance in resisting tying forces is quite limited and where resistance to significant tension forces is required designers may opt for a flush endplate instead. A series of 12 tests was conducted to investigate this connection's performance under shear and tension at elevated temperatures – details are shown in figure 7 and table 3 below. All tests failed in a similar manner i.e. fracture of the endplates close to the toe of the weld, as shown for example in the multiple images of test 4 shown in figure 8.

www.EngineeringEBooksPdf.com



Bolt diameter d	20
Bolt hole diameter d_0	22
End distance e_1	40
Edge distance e_2	30
Bolt spacing p_1	60
End plate thickness t_p	10
Gauge distance g	90
Lever arm B_L	490
Vertical off set D_L	51.7

Figure 7: Partial depth endplate test details.

Table 3: Partial depth endplate test results.

Test	t_p (mm)	Bolt rows	°C	α_n	α_i	α_e	Force (kN)	Rotation (Degree)	Failure mode
1	10	3	20	35	35	43.5	192.0	8.6	Plate fracture
2	10	3	450	35	35	38.7	90.4	4.2	Plate fracture
3	10	3	550	35	35	40.2	68.5	3.9	Plate fracture
4	10	3	650	35	35	39.6	32.6	3.6	Plate fracture
5	10	3	20	45	45	51.1	150.0	8.8	Plate fracture
6	10	3	450	45	45	48.6	64.5	3.5	Plate fracture
7	10	3	550	45	45	47.9	44.1	3.2	Plate fracture
8	10	3	650	45	45	48.6	28.5	3.8	Plate fracture
9	10	3	20	55	55	56.1	179.3	11.2	Plate fracture
10	10	3	450	55	55	55.9	55.6	4.8	Plate fracture
11	10	3	550	55	55	55.1	36.3	3.9	Plate fracture
12	10	3	650	55	55	55.7	22.1	4.5	Plate fracture

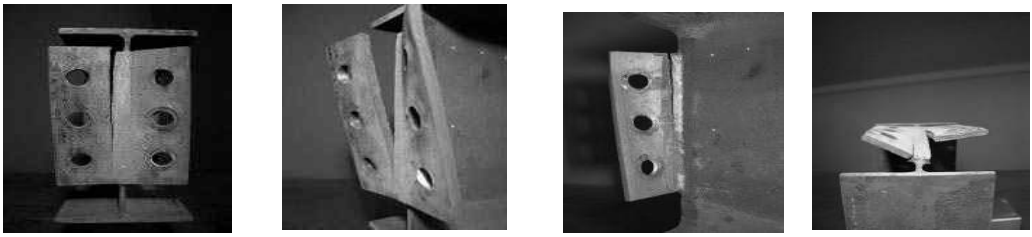


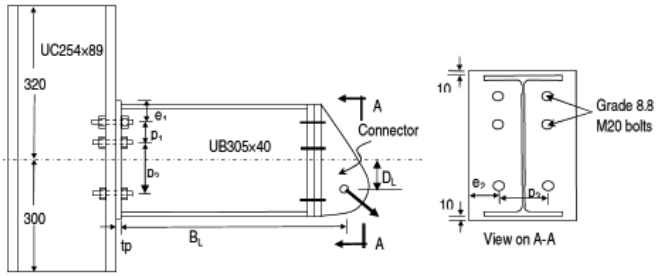
Figure 8: Partial depth endplate (test 4) failure mode.

For this connection type, modeling the behaviour, either by FEA or through a component model, required understanding the failure of the plate. Hu *et al.* [5] reported the development of an ABAQUS model incorporating cohesive elements to represent the behaviour of the plate in the HAZ adjacent to the toe of the weld connecting the endplate to the beam web. The cohesive elements were used to model a fracture as a separation across a surface using a traction-separation constitutive law. Thus tearing through the plate could be modelled. Later, Hu used the test data and FE model to construct a simpler component model building on earlier work by Spyrou [6] and Sarraj [7] but incorporating a new component to simulate the weld behaviour as reported in [8].

www.EngineeringEBooksPdf.com

6 FLUSH ENDPLATES

Flush endplates, as shown in figure 9, are often used as 'simple' connections i.e. designed for vertical shear loads, even though they are capable of taking reasonable amounts of moment and are more accurately categorized as partial-strength semi-rigid connections [9]. Flush endplates are popular because they are easy to fabricate, provide some rotational stiffness, which is useful for temporary stability during the erection phase, and they can resist significant tying forces.



Bolt diameter d	20
Bolt hole diameter d_0	22
End distance e_1	40
Edge distance e_2	55
Bolt spacing p_1	70
Bolt spacing p_2	133.4
Bolt spacing p_3	90
End plate thickness t_p	10
Lever arm B_L	490
Vertical off set D_L	51.7

Figure 9: Flush endplate test details.

The test programme outlined in table 4 shows that the connection is relatively stiff compared with the other connection types investigated. The mode of failure is dependent on the test temperature – at room temperature the critical failure mode was plate fracture close to the weld but under fire conditions the bolts became critical. The ductility of the bolts at high temperature contributes to the rotational capacity of the joint. The use of a thicker endplate increases peak resistance but at the expense of ductility [10,11].

Table 4: Flush endplate test results.

Test	t_p (mm)	Bolt rows	°C	α_n	α_i	α_e	Force (kN)	Rotation (Degree)	Failure mode
1	10	3	20	35			DNF		
2	10	3	450	35	40.5	35.1	180.9	6.1	Plate fracture
3	10	3	550	35	41.2	30.7	105.9	2.2	Bolt fracture
4	10	3	650	35	43.3	32.5	43.6	3.4	Bolt fracture
5	10	3	20	45			DNF		
6	10	3	450	45	46.3	43.7	164.6	6.4	Plate fracture
7	10	3	550	45	44.7	43.1	81.8	1.4	Bolt fracture
8	10	3	650	45	46.6	38.9	36.0	4.9	Bolt fracture
9	10	3	20	55	54.7	43.8	259.0	4.4	Plate fracture
10	10	3	450	55	55.7	46.7	182.5	5.6	Plate fracture
11	10	3	550	55	55.4	47.2	87.8	2.2	Bolt fracture
12	10	3	650	55	55.4	48.1	39.2	3.1	Bolt fracture
13	8	3	20	35	37.8	27.2	258.1	5.3	Plate fracture
14	8	3	550	35	41.8	33.3	101.0	7.5	Bolt fracture
15	15	3	550	35	42.2	37.0	124.6	2.5	Bolt fracture
16	10	2	20	35	36.5	32.8	303.0	6.6	Bolt fracture
17	10	2	550	35	41.7	39.5	79.9	2.6	Bolt fracture

www.EngineeringEBooksPdf.com

7 DISCUSSION

In the event of a fire in a steel framed structure, thermal expansion of the steel, reduction of material strength and stiffness, and the subsequent regaining of strength and stiffness as the distorted frame cools and contracts, places great demands on the ductility of the beam to column connections. In braced frames, it is desirable to minimise fabrication costs by using relatively simple connections designed to resist vertical shear. However, in fire these simple connections are subjected to significant axial force and enforced rotation. Their ability to maintain integrity of the structure is clearly very important but at the present time it is not possible to guarantee satisfactory performance due to the complexity of the actions (both structural and thermal) during a fire event and the inability of present structural analysis tools to properly account for connection behaviour under extreme conditions. The test programme reported here has provided an insight into the likely response of simple connections to combined shear and axial forces at elevated temperatures. Furthermore, the development of component-based models for each connection type offers the opportunity to incorporate simple yet realistic connection behaviour into structural fire analysis programs. These in turn will permit designers to devise the best connection arrangements for use in structural fire engineering of steel frames.

Acknowledgment: The authors gratefully acknowledge the support of the Engineering and Physical Sciences Research Council of the United Kingdom under Grant EP/C510984/1. Corus Ltd provided the steel sections.

REFERENCES

[1] Yu, H.X., Burgess, I.W. Davison, J.B., and Plank, R.J., “Experimental Investigation of the Behaviour of Fin Plate Connections in Fire”, *J. Construct. Steel Research*, **65**, 723–736, 2009.

[2] Spyrou, S. and Davison, J.B., “Displacement Measurement in Studies of Steel T-Stub Connections”, *J. Construct. Steel Research*, **57**(6), 649-661, 2001.

[3] Yu, H.X., Burgess, I.W. Davison, J.B., and Plank, R.J., “Tying Capacity of Web Cleat Connections in Fire. Part 1: Test and Finite Element Simulation”, *Engineering Structures*, **31**(3), 651-663, 2009.

[4] Yu, H.X., Burgess, I.W. Davison, J.B., and Plank, R.J., “Tying Capacity of Web Cleat Connections in Fire. Part 2: Development of Component-Based Model”, *Engineering Structures*, **31**(3), 697-708, 2009.

[5] Hu, Y., Burgess, I.W., Davison, J.B. and Plank, R.J., “Modelling of Flexible End Plate Connections in Fire Using Cohesive Elements”, *Proc. Structures in Fire Workshop*, Singapore, 127-138, 2008.

[6] Spyrou, S., Davison, J.B., Burgess, I.W. and Plank, R.J., “Experimental and Analytical Investigation of the "Tension Zone" Component within a Steel Joint at Elevated Temperatures”, *J. Construct.Steel Research*, **60**(6), 867-896, 2004.

[7] Sarraj, M., *The Behaviour of Steel Fin Plate Connections in Fire*, PhD thesis, University of Sheffield, 2007.

[8] Hu, Y., Davison, J.B., Burgess, I.W. and Plank, R.J., “Component Modelling of Flexible End-plate Connections in Fire”, *International Journal of Steel Structures*, **9**, 29-38, 2009.

[9] Eurocode 3: Design of steel structures – Part 1-8: Design of joints, CEN, 2005.

[10] Yu, H.X., Burgess, I.W., Davison, J.B. and Plank, R.J., “Experimental Investigation of the Behaviour of Flush Endplate Connections in Fire”, submitted to ASCE.

[11] Yu, H.X., Burgess, I.W., Davison, J.B. and Plank, R.J., “Development of a Yield-Line Model for Endplate Connections in Fire”, *J. Construct. Steel Research*, **65**(6), 1279-1289, 2009.

www.EngineeringEBooksPdf.com

SDSS'Rio 2010 STABILITY AND DUCTILITY OF STEEL STRUCTURES
E. Batista, P. Vellasco, L. de Lima (Eds.)
Rio de Janeiro, Brazil, September 8 - 10, 2010

METHODOLOGY FOR RELIABILITY-BASED DESIGN OF STEEL MEMBERS EXPOSED TO FIRE

Shahid Iqbal and Ronald S. Harichandran

Dept. of Civil and Envir. Engineering, Michigan State University, East Lansing 48824-1226, USA
e-mails: iqbalsha@msu.edu, harichan@egr.msu.edu

Keywords: Reliability-Based Design, Steel Members, Fire Design, Statistics, Random Parameters

Abstract. *A general reliability-based methodology is proposed for developing capacity reduction and fire load factors for the load and resistance factor design (LRFD) of steel members exposed to fire. The effect of active fire protection systems (e.g., sprinklers, smoke and heat detectors, fire brigade, etc.) in reducing the probability of occurrence of a severe fire is included. The design parameters that significantly affect the fire design of steel members are chosen as random variables, and their statistics, obtained from the literature and the analysis of raw data, are provided.*

1 INTRODUCTION

Performance-based codes allow use of engineering approaches for fire design of steel members instead of prescriptive approaches that are commonly used. For example, Appendix 4 of the 2005 AISC Specifications (referred to hereafter as "AISC Specifications") [1] now allows steel members to be designed against fire using room temperature design specifications and reduced material properties. A similar approach for design of steel members is included in Eurocode 3 [2]. Using this engineering approach, the verification of design for strength during fire requires that the load effects are less than the capacity of the structure. This leads to satisfying the design equation

$$W_{n,f} \leq \phi_f R_{n,f} \tag{1}$$

where $W_{n,f}$ is the load effect at the time of fire, $R_{n,f}$ is the nominal capacity at the time of fire, and ϕ_f is the capacity reduction factor. The AISC Specifications [1] allow using the same capacity reduction factors for fire design as those used for room temperature design. For example, ϕ_f = 0.9 is suggested for beams. Most other codes suggest that a capacity reduction factor of 1.0 be used (e.g., in the Eurocode 3 [2], the partial safety factor is 1.0 for fire design). This recommendation is based on arguments that the probability of fire occurrence and the strength falling below the design value simultaneously is very small, and that fire design is based on the most likely expected strength [3]. Also, it is expected that live loads under fire conditions are likely to be smaller than those at room temperature conditions and hence there will be enough reserve strength available [3]. However, limited work has been done to develop capacity reduction factors based on reliability analysis [4].

Fire safety is attained through two components: (1) active fire protection systems such as automatic sprinklers which help in controlling and suppressing the fire; and (2) passive fire protection systems such as structural and non-structural components of a building which control the spread of fire and prevent or delay the collapse of compartments. The AISC Specifications suggest that while calculating the steel and fire temperatures for fire design, due consideration should be given to the effectiveness of all active fire protection systems (sprinklers, smoke and heat detectors, etc.). The Commentary to the AISC Specifications [5] states that the fire load may be reduced by up to 60 percent if a sprinkler system is installed in the building. Automatic sprinklers reduce the probability of occurrence of a severe fire. The reduction in fire load should be based on proper reliability analysis that includes the effect of sprinklers

www.EngineeringEBooksPdf.com

on the occurrence of a severe fire, and correspondingly on the probability of failure of structural steel members. Recently, a study was conducted in Europe through a research project of the European Coal and Steel Community (ECSC) (hereinafter referred to as the ECSC study) to develop fire load factors by taking into account the variability of the fire load and the effect of active fire protection systems [6]. However, the fire load factors were obtained using simplified assumptions and the study did not account for variability in other parameters. It is not apparent whether rigorous reliability analysis would yield results similar to those of the ECSC study.

A general reliability-based methodology is presented in this paper for developing capacity reduction and fire load factors for the load and resistance factor design (LRFD) of steel members exposed to fire. In addition, the uncertainties of design parameters that significantly affect the fire design are characterized. As an illustration, the statistics of the random variables and model errors derived in this study are used in the companion paper [7] for deriving capacity reduction and fire load factors for steel columns exposed to fire.

To better understand the performance functions, the engineering approach for designing steel members subjected to fire conditions is described next.

2 ENGINEERING APPROACH FOR DESIGN OF STEEL MEMBERS EXPOSED TO FIRE

In the engineering approach, the nominal capacity of steel members exposed to fire, $R_{n,f}$, is a function of fabrication parameters, F_i, and reduced material properties, $k_j(T_s)M_j$, and may be expressed as

$$R_{n,f} = f_R\left(F_1,.....F_l, k_1(T_s)M_1,.....k_k(T_s)M_k\right) \tag{2}$$

where the F_i are dimensional and sectional properties (e.g., depth of section, cross-sectional area, etc.), and M_j are the material properties at room temperature (e.g., yield strength, etc.). $k_j(T_s)$ are factors that account for reduction in strength and stiffness of steel at elevated temperature, and their values at different steel temperatures are specified in the AISC Specifications.

According to the AISC Specifications, the design action (applied axial force, bending moment or shear force, etc.) is determined from the load combination given by

$$w_u = 1.2\,D + 0.5\,L + 0.2\,S + T \tag{3}$$

where, D, L and S are nominal dead, live and snow loads, respectively, and T includes loads induced by the fire itself, especially due to restraint from the surrounding structure preventing thermal expansions.

At elevated temperatures, the strength and stiffness of steel reduces significantly, and if unprotected, steel members fail within a short time. Therefore, steel members are generally protected by insulation to slow down the rise of the steel temperature. The required thickness of insulation can be determined using an iterative procedure, and the fire temperature in the compartment and the steel temperature of the member required for this procedure can be estimated as described in the next section.

3 FIRE AND STEEL TEMPERATURES

The variation of fire temperature, T_f, with time can be estimated using a suitable mathematical model from the literature. In this study, the Eurocode parametric fire model modified by Feasey and Buchanan [8] is used to estimate the fire temperature under real fire scenarios.

Once the fire temperature variation with time is known, the temperature of steel members can be estimated through thermal analysis. Most design specifications such as the Eurocode 3 and AISC Specifications, allow the steel temperature to be calculated using simple thermal analysis methods such as the lumped heat capacity method. The lumped heat capacity method assumes that the steel section is a lumped mass at uniform temperature. The heat balance differential equation for protected steel members can be written as [3]

www.EngineeringEBooksPdf.com

$$\frac{dT}{dt} = \left(\frac{F}{V}\right)\left(\frac{k_i}{d_i \rho_s c_s}\right)\left\{\frac{\rho_s c_s}{\rho_s c_s + 0.5(F/V) d_i \rho_i c_i}\right\}(T_f - T_s) \quad (4)$$

where dT/dt = rate of change of steel temperature, F = surface area of unit length of the member (m^2) ,V = volume of steel per unit length of the member (m^3), ρ_s = density of steel (kg/m^3), c_s = specific heat of steel (J/kg.K), ρ_i = density of insulation (kg/m^3), c_i = specific heat of insulation (J/kg.K), d_i = thickness of insulation (m), k_i = thermal conductivity of insulation (W/m.K), T_s = steel temperature (°C), and T_f = fire temperature (°C).

Equation (4) can be written in finite difference form and the steel temperature can then be calculated at any time using a finite difference method that can be implemented in a spreadsheet. However, for incorporation into performance functions used in reliability analysis, a closed-form expression for calculating the maximum steel temperature is convenient. The closed-form solution of equation (4) was developed by Iqbal and Harichandran [9].

4 METHODOLOGY TO DEVELOP CAPACITY REDUCTION AND FIRE LOAD FACTORS

Capacity reduction and fire load factors can be developed by performing the following steps:

1. Obtain statistical parameters such as the mean, coefficient of variation (COV) and distributions of design parameters (e.g., yield strength of steel, cross-sectional area of steel, fire load, opening factor, etc.).
2. Select an appropriate performance function (design equation) for the structural member.
3. Characterize model errors (i.e., the professional factor) to account for the differences in the capacity calculated from the design equation and that measured in fire tests.
4. Select a target reliability index, β_t, which reflects the target probability of failure and is a relative measure of safety.
5. Calculate the capacity reduction and fire load factor through reliability analysis.

In the succeeding paragraphs, the above steps are elaborated in the context of steel members exposed to fire.

4.1 Statistics of random parameters

The parameters that significantly affect the fire design of steel members were chosen as random variables, and their means, COV, and distribution types are summarized in table 1. We analyzed raw experimental data to obtain the statistics of all parameters in table 1 except for the dead load, arbitrary-point-in-time live load and fire load. The statistics of the dead and arbitrary-point-in-time live loads were reported by Ellingwood [10] and Ravindra and Galambos [11], and the statistics of the fire load were taken from a survey of U.S. office buildings by Culver [12].

Bruls et al. [13] studied the variation of thermal conductivity of insulation at different temperatures. Although, thermal conductivity varies with temperature, they concluded that since the failure of structural steel members generally occurs at a temperature of 400 to 600°C, the thermal conductivity corresponding to a critical temperature of 500°C can be used in design. In this study, a statistical analysis of thermal conductivity of gypsum board material in the temperature range of 400-600°C was performed to obtain the statistics shown in table 1.

4.2 Performance function for reliability analysis

Ellingwood [10] showed that the probability of coincidence of a fire with maximum values of live load, roof live load, snow, wind, or earthquake loads is negligible, and a structure is likely to be loaded to only a fraction of the design load when a fire occurs. Therefore, it is appropriate to use the combination of dead and arbitrary-point-in-time live load for reliability analysis under fire conditions. The load effect W_f for reliability analysis may then be calculated as

$$W_f = E(c_D AD + c_L BL_{apt}) \quad (5)$$

www.EngineeringEBooksPdf.com

where c_D and c_L = deterministic influence coefficients that transform the load intensities to load effects (e.g., moment, shear, and axial force), A and B = random variables reflecting the uncertainties in the transformation of loads into load effects, E = a random variable representing the uncertainties in structural analysis, and D and L_{apt} = random variables representing dead and arbitrary-point-in-time live load. The statistics of D and L_{apt} are given in table 1. The statistics of parameters A, B and E are: (1) mean of A = 1.0, COV of A = 0.04; (2) mean of B = 1.0, COV of B = 0.20; and (3) mean of E = 1.0, COV of E = 0.05 [11].

The actual capacity of steel members under fire can be obtained by modifying the nominal capacity given by equation (2) to

$$R_f = P.f_R\left(f_1F_1,.....f_lF_l,k_1(t_sT_s)m_1M_1,.....k_k(t_sT_s)m_kM_k\right) \quad (6)$$

Table 1: Mean, COV and distributions of fire design parameters

Variable	Mean	COV	Distribution
Arbitrary-point-in-time live load, L_{apt}	0.24*nominal	variable	Gamma
Dead load, D	1.05*nominal	0.100	normal
Fire load, q_f	564 MJ/m^2	0.62	Gumbel
Ratio of floor area to total area, A_f/A_t	0.192	0.23	lognormal
Opening factor, F_v	1*nominal	0.05	normal
Thermal conductivity of normal weight concrete (NWC), k	1.747 W/m.K	0.171	normal
Specific heat of NWC, c_p	856 J/kg.K	0.062	normal
Density of NWC, ρ	2258 kg/m^3	0.069	normal
Thermal conductivity of lightweight concrete (LWC), k	0.372 W/m.K	0.199	Gumbel
Specific heat of LWC, c_p	826 J/kg.K	0.062	Gumbel
Density of LWC, ρ	1344 kg/m^3	0.069	normal
Thermal absorptivity of NWC, b_{NWC}	1830 Ws$^{0.5}$/m^2 K	0. 094	normal
Thermal absorptivity of LWC, b_{LWC}	640 Ws$^{0.5}$/m^2 K	0. 107	normal
Thermal absorptivity of gypsum board, b_g	423.5 Ws$^{0.5}$/m^2 K	0.09	normal
Thermal absorptivity of a compartment having a 50/50 mix of NWC and gypsum board as boundaries, b_{mix}	1127 Ws$^{0.5}$/m^2 K	0.10	normal
Thickness of fire protection materials, d_i			
(1) spray applied materials	nominal+1/16 inch	0.20	lognormal
(2) gypsum board systems	nominal	0.05	normal
Density of fire protection materials, D_i			
(1) spray applied materials	307 kg/m^3	0.29	normal
(2) gypsum board systems	745 kg/m^3	0.07	lognormal
Thermal conductivity of fire protection materials, k_i, at temperature of 400-600°C			
(1) spray applied materials	0.187 W/m. K	0.24	lognormal
(2) gypsum board systems	0.159 W/m. K	0.28	lognormal

Note: The COV of the arbitrary-point-in-time live load depends on the tributary area [11] and is given as:
$0.82[1-0.00113(A_T-56)]$ for $56 \le A_T \le 336$ square feet
$0.56[1-0.0001865(A_T-336)]$ for $A_T > 336$ square feet

www.EngineeringEBooksPdf.com

where P, f_i, m_j, and t_s are the following non-dimensional random variables:

P = "Professional factor" reflecting uncertainties in the assumptions used to determine the capacity from design equations. These uncertainties may result from using approximations in place of exact theoretical formulas and from assumptions such as perfect elasto-plastic behavior and a uniform temperature across the section.

f_i = Random variable that characterizes the uncertainties in "fabrication."

m_j = Random variable that characterizes uncertainties in "material properties."

t_s = Random correction factor that accounts for differences between the steel temperature obtained from models and that measured in actual tests.

Using equations (5) and (6), the limit state equation for reliability analysis under fire conditions may be written as

$$g(\mathbf{X}) = R_f - W_f \tag{7}$$

where $\mathbf{X}$ denotes a vector containing all the random variables. The probability of failure, p_F, of a steel element under fire is $p_F = \mathrm{P}[g(X) < 0]$.

It is assumed that the random variables f_i and m_j are the same as those used for developing LRFD specifications for ambient temperature conditions and their statistics are available in the literature. The statistics of P are specific to each design equation, cannot be generalized, and can be obtained from a comparison between the predicted capacity and test results. The statistics of t_s are characterized below.

4.3 Model Error for Steel and Fire Temperatures

The maximum temperature of steel sections estimated using equation (4) differs from that measured in actual fire tests. To account for the differences in calculated and measured steel temperatures, the model error was characterized as described below, both for steel beams (three sided exposures) and steel columns (four sided exposure).

The experimental temperature of steel elements has been reported by many researchers but most tests were carried out under standard fires instead of real fires, and thus cannot be used to estimate the error arising from the fire models. Kirby et al. [14] carried out a series of nine real fire tests and recorded the temperature of protected and unprotected steel elements. The tests were performed for a range of fire loads (380 – 760 MJ/m^2 of floor area), for different opening conditions (F_v = 0.0029 – 0.062 m$^{1/2}$), and various types of materials were used as compartment boundaries in order to represent many possible real fire scenarios. Foster et al. [15] reported the temperature of four protected steel columns. In this test the fire load was 720 MJ/m^2 of the floor area and the opening factor was 0.043 m$^{1/2}$.

The model error for the temperature of steel beams, t_{sb}, was characterized using the test data reported by Kirby et al. (1994) [14], and the model error for the temperature of steel columns, t_{sc}, was characterized using the test data reported by Kirby et al. [14] and Foster et al. [15]. t_{sb} has a mean of 0.98 and COV of 0.11, and t_{sc} has a mean of 1.05 and COV of 0.13. Both, t_{sb} and t_{sc} were best described by the Gumbel distribution.

4.4 Probability of failure and target reliability index

CIB W 14 [16] suggests that the rare occurrence of a severe fire should be taken into account while developing safety factors for fire design. The presence of active fire protection systems such as automatic sprinklers, fire brigade, etc., reduce the probability of occurrence of a severe fire and hence reduce the probability of failure. Safety factors depend on the selected target reliability index, β_t, which is related to the target probability of failure. Therefore, the reduced probability of failure under fire can be accounted for by using a reduced target reliability index.

A detailed methodology for calculating β_t by incorporating the effect of active fire protection systems was presented in the ECSC study [6]. The ECSC study also suggests appropriate values for the effectiveness of different active fire protection systems in reducing the probability of occurrence of a

www.EngineeringEBooksPdf.com

severe fire. Using the methodology described in the ECSC study, β_t was estimated for typical fire compartments in U.S. office buildings (ranging in floor areas from 25-500 m^2). It was found that it is reasonable to use β_t values ranging from zero to 2.0 for developing capacity reduction and fire load factors. Since the probability of occurrence of a severe fire varies depending on the presence of active fire protection systems, β_t also varies for different design situations.

4.5 Determination of capacity reduction and fire load factors

4.5.1 Partial safety factors for each design parameter

For a normally distributed random design parameter, X, the partial safety factor resulting from the first-order reliability method (FORM) is given by [17]

$$\phi_X = \frac{m_X}{X_n}(1 + \alpha_X \beta_t V_X) \tag{8}$$

where m_X, V_X, X_n, and α_X are the mean, COV, nominal value of X, and the direction cosine of the "design point," respectively. For non-normal random parameters (e.g., a lognormal distribution), the partial safety factor can be determined from equation (8) using the mean and standard deviation of the "equivalent normal variable" at the design point [17].

All the parameters in equation (8) are known from previous steps except the direction cosine of the design point which is obtained through reliability analysis.

4.5.2 Combination of partial safety factors into single capacity reduction factor

For convenience in design, the variability of all design parameters except for the fire load is accounted for through a combined capacity reduction factor instead of using a separate partial safety factor for each design parameter. The partial safety factors obtained through equation (8) for each individual design parameter except the fire load can be combined into a single capacity reduction factor. The fire load is a major parameter in fire design, and uncertainty associated with it has a significant effect on the safety of the design. Therefore, the variability of the fire load on overall safety is accounted for through the specific partial safety factor on the fire load. As mentioned in the introduction, the AISC specifications recommend that the fire load be reduced by 60% if a reliable sprinkler system is installed. This recommendation also motivated use of a separate safety factor for the fire load. This fire load factor is to be applied to the fire load used in describing the design fire (or time-fire temperature curve).

4.5.3 Optimal capacity reduction and fire load factors

The capacity reduction and the fire load factors will vary for each design situation. For ease of design, it is desirable to have a single optimal capacity reduction factor applicable to all design situations. In addition, for fire design of steel members, the AISC Specifications recommend using dead and live load factors of 1.2 and 0.5, respectively. Therefore, the optimization procedure described in NBS 577 [17], and summarized below can be used to develop optimal capacity reduction and fire load factors corresponding to dead and live load factors of 1.2 and 0.5, respectively.

The nominal capacity for each design situation based on the FORM is

$$R_n^{II} = \frac{1}{\phi_{f,i}^{II}} \sum_i \gamma_i^{II} Q_{n,i} \tag{9}$$

where γ_i^{II} and $\phi_{f,i}^{II}$ are the load and resistance factors for each design situation, and $Q_{n,i}$ are the nominal values of dead and live loads. The nominal capacity corresponding to the recommended dead and live load factors is

$$R_n^{I} = \frac{1}{\phi_f} \sum_i \gamma_i Q_{n,i} \tag{10}$$

www.EngineeringEBooksPdf.com

where the γ_i are 1.2 and 0.5 for dead and live load, respectively. ϕ_f is the optimal capacity reduction factor, and its value in equation (11) can be selected by minimizing the objective function

$$\varepsilon(\phi_f) = \sum \left[R_{n,j}^{II} - R_{n,j}^{I} \right]^2 p_j \tag{11}$$

where p_j is the weight assigned to the jth design situation. In this study, each design situation was assigned the same weight.

5 CONCLUSION

A general reliability-based methodology is proposed for developing capacity reduction and fire load factors for the design of steel members exposed to fire. Statistics of a variety of parameters important for the design of steel members under fire were obtained from experimental data reported in the literature. Model errors associated with the thermal models were also characterized based on experimental data. It was found that uncertainty associated with the fire design parameters is much higher than that associated with room temperature design parameters. The capacity reduction and fire load factors correspond to a preselected target reliability index that accounts for the effect of active fire protection systems (e.g., sprinklers, smoke and heat detectors, etc.) in reducing the probability of occurrence of a severe fire.

REFERENCES

[1] AISC. “Load and resistance factor design specifications for structural steel buildings”, American Institute of Steel Construction, Inc., Chicago, Illinois, 2005.

[2] EN. “Eurocode 3: Design of steel structures- Part 1-2: General rules-Structural fire design”, BS EN 1993-1-2, 2005.

[3] Buchanan, A. H. *Structural Design for Fire Safety*, John Wiley & Sons Ltd., New York, 2001.

[4] Magnusson, S. E. and Pettersson, O. “Rational design methodology for fire exposed load bearing structures”. *Fire Safety Journal*, **3**(4), 227-241, 1981.

[5] AISC. “Commentary on the load and resistance factor design specifications for structural steel buildings”, American Institute of Steel Construction, Inc., Chicago, Illinois, 2005.

[6] European Coal and Steel Community (ECSC). “Natural fire safety concept, valorization project”, Product-Structural Dept. ARBED-Research Centre L-4009 ESCH/ALZETTE, Luxembourg, 2001.

[7] Iqbal, S. and Harichandran, R. S. “Capacity reduction and fire load factors for steel columns exposed to fire”, *Proc. of SDSS’Rio 2010 Stability and Ductility of Steel Structures*, Rio de Janeiro, Brazil, 2010.

[8] Feasey, R. and Buchanan, A. “Post-flashover fires for structural design.” *Fire Safety Journal*, **37**(1), 83-105, 2002.

[9] Iqbal, S. and Harichandran, R. S. “Reliability-based design specifications for simply supported steel beams exposed to fire”, *Proc. of 10th International Conference on Structural Safety and Reliability*, Osaka, Japan, 2009.

[10] Ellingwood, B. R. “Load combination requirements for fire-resistant structural design”. *Journal of Fire Protection Engineering*, **15**(1), 43-61, 2005.

[11] Ravindra, M. K. and Galambos, T. V. “Load and resistance factor design for steel”. *Journal of the Structural Division*, **104**(ST9), 1337-1353, 1978.

[12] Culver, C. G. “Survey results for fire loads and live loads in office buildings”, National Bureau of Standards, 1976.

www.EngineeringEBooksPdf.com

[13] Bruls, A., Cajot , L. G. and Franssen, J. M. “Characterization of an insulating material with regard to ECCS recommendations for the fire safety of steel structures”. *Journal of Constructional Steel Research*, **9**(2), 111-135, 1988.

[14] Kirby, B. R., Wainman, D. E., Tomlinson, L. N., Kay, T. R. and Peacock, B. N. “Natural fires in large scale compartments—A British steel technical, fire research station collaborative project”, British Steel Technical, 1994.

[15] Foster, S., Chladna, M., Hsieh, C., Burgess, I. and Plank, R. “Thermal and structural behaviour of a full-scale composite building subject to a severe compartment fire”. *Fire Safety Journal*, **42**(3), 183-199, 2007.

[16] CIB W14. “Design guide for structural fire safety”. *Fire Safety Journal*, **10**(2), 81-137, 1986.

[17] Ellingwood, B. Galambos, T. V., MacGregor, J. G. and Cornell, C. A. “NBS special publication 577: Development of a probability based load criterion for American National Standard A58”, National Bureau of Standards, Ernest Ambler, 1980.

www.EngineeringEBooksPdf.com

SDSS'Rio 2010 STABILITY AND DUCTILITY OF STEEL STRUCTURES
E. Batista, P. Vellasco, L. de Lima (Eds.)
Rio de Janeiro, Brazil, September 8 - 10, 2010

CAPACITY REDUCTION AND FIRE LOAD FACTORS FOR STEEL COLUMNS EXPOSED TO FIRE

Shahid Iqbal and Ronald S. Harichandran

Dept. of Civil and Envir. Engineering, Michigan State University, East Lansing 48824-1226, USA
e-mails: iqbalsha@msu.edu, harichan@egr.msu.edu

Keywords: Reliability-Based Design, Steel Columns, Fire Design, Safety Factors

Abstract. *Capacity reduction and fire load factors are developed for load and resistance factor design of axially loaded steel column exposed to fire. Fire load, opening factor, ratio of floor area to the total area of compartment boundaries, thermal inertia of compartment boundaries, thickness, density and thermal conductivity of insulation, yield strength and modulus of elasticity of steel, cross-sectional area and radius of gyration of steel, dead load, and live load are taken as random variables. The chosen statistics of the live load, fire load and ratio of floor area to the total area of compartment boundaries are representative of typical office buildings in the U.S. The effect of active fire protection systems such as sprinklers in reducing the probability of occurrence of a severe fire is accounted for. It is found that the capacity reduction and fire load factors are not constant for all design situations as suggested in design specifications, and vary depending on the presence of active fire protection systems in a building.*

1 INTRODUCTION

Until recently, steel columns exposed to fire were designed using prescriptive approaches that do not account for actual loading conditions and real fire scenarios. Performance-based codes which allow more rational engineering approaches for the fire design of steel members are being promoted. For example, Appendix 4 of the 2005 AISC Specifications (referred to hereafter as "AISC Specifications") [1] now allows steel columns to be designed against fire using room temperature design specifications and reduced material properties. The AISC Specifications [1] suggest using a capacity reduction factor ϕ_f = 0.9 for fire design. Most other codes suggest that a capacity reduction factor of 1.0 be used (e.g., in the Eurocode 3 [2], the partial safety factor is 1.0 for fire design). The Commentary to the AISC Specifications [3] states that the fire load should be reduced by up to 60%, if a reliable automatic sprinkler system is installed in the building. However, no substantial work has been done to develop capacity reduction and fire load factors based on rigorous reliability analysis. The companion paper by Iqbal and Harichandran [4] describes a general methodology for reliability-based design of steel members exposed to fire. This paper presents specific capacity reduction and fire load factors for load and resistance factor design (LRFD) of axially loaded steel columns exposed to fire.

2 APPROACH FOR DESIGN OF STEEL COLUMNS EXPOSED TO FIRE

In the AISC specifications [1], the required axial capacity for fire design is determined from the load combination given by

$$P_u = 1.2P_D + 0.5P_L + 0.2P_S + P_T \tag{1}$$

where P_D,P_L and P_S are nominal dead, live and snow loads, respectively, and P_T includes loads induced by the fire itself, especially due to restraint from the surrounding structures preventing thermal expansion.

www.EngineeringEBooksPdf.com

Takagi and Deierlein [5] compared the AISC and Eurocode 3 design specifications with finite element simulations for columns exposed to fire. They reported that the AISC Specifications are unconservative at elevated temperatures, particularly for slenderness ratios between 40 and 100 and temperatures above 500°C. For instance, at 500°C the nominal strengths predicted by the AISC specifications are up to 60% larger than strengths predicted by simulations. On the other hand, the Eurocode 3 column strength equations were within 20% of the simulated results. We used the equations proposed by Takagi and Deierlein [5] in this study, which have a format similar to those in the AISC Specifications and predict strengths similar to the Eurocode 3 [3] columns strength equations (see figure 6 of reference [5]):

$$P_{n,f} = \{0.42^{\sqrt{\frac{k_y(T_s)F_y}{F_e(T_s)}}}\} A_s k_y(T_s) F_y \tag{2}$$

where

$$F_e(T_s) = \frac{\pi^2 k_E(T_s) E_s}{\left(\frac{KL}{r}\right)^2} \tag{3}$$

$P_{n,f}$ = nominal axial capacity of column under fire, A_s = cross-sectional area, KL = effective length, r = radius of gyration about the buckling axis, $k_y(T_s)F_y$ = reduced yield strength, $k_E(T_s)E_s$ = reduced elastic modulus, and F_y and E_s are the yield strength and elastic modulus of steel at room temperature, respectively. $k_y(T_s)$ and $k_E(T_s)$ are the yield strength and elastic modulus reduction factors, respectively, and their values at different temperatures are given in the AISC Specifications and Eurocode 3.

From equations (2) and (3) it is obvious that the capacity of steel columns at elevated temperatures depends on the steel temperature, T_s, that can be estimated as described in the companion paper by Iqbal and Harichandran [4].

3 DEVELOPMENT OF CAPACITY REDUCTION AND FIRE LOAD FACTORS

3.1 Statistics of random parameters

The statistics (mean, coefficient of variation, and the distribution type) of fire parameters that significantly affect the fire design of steel columns are provided in the companion paper by Iqbal and Harichandran [4]. The other parameters that affect the design of steel columns are the same as those used for developing LRFD specifications for ambient temperature conditions and their statistics are given in table 1. The statistics of all the parameters in table 1 were reported by Schmidt and Bartlett [6], and the distributions were assumed to be normal.

Table 1: Mean and COV of room temperature design parameters

	Characterizes variation in	Mean	COV
m_1	Yield strength, F_y	1.03*nominal	0.063
m_2	Modulus of elasticity, E_s	1.04*nominal	0.045
f_1	Cross-sectional area , A_s	1.03*nominal	0.031
f_2	Radius of gyration, r_y	1.00*nominal	0.016

3.2 Performance function for reliability analysis

The applied axial load, W_f, for the reliability analysis of steel columns exposed to fire can be determined as described in the companion paper by Iqbal and Harichandran [4].

The actual capacity of steel columns under fire can be obtained by modifying the nominal capacity given in equations (2) and (3) to

www.EngineeringEBooksPdf.com

$$P_f = P\{0.42^{\sqrt{\frac{k_y(t_sT_s)m_1F_y}{F_e(T_s)}}}\} f_1 A_s k_y(t_sT_s) m_1 F_y \quad (4)$$

$$F_e(T_s) = \frac{\pi^2 k_E(t_sT_s) m_2 E_s}{\left(\frac{KL}{f_2 r}\right)^2} \quad (5)$$

where P, f_i, m_i, and t_s are non-dimensional random variables as defined in the companion paper by Iqbal and Harichandran [4]. The statistics of f_i and m_i are given in table 2 and that of t_s were reported in the companion paper by Iqbal and Harichandran [4]. The statistics of P are described in the next sub-section.

The limit state equation for reliability analysis under fire conditions may be written as

$$g(\mathbf{X}) = P_f - W_f \quad (6)$$

where $\boldsymbol{X}$ denotes a vector containing all the random design parameters. The probability of failure, p_F , of a steel column under fire is $p_F = P[g(\boldsymbol{X}) < 0]$.

3.3 Professional factor (model error) for axial capacity of columns

To account for differences between axial capacity of columns measured in the laboratory and that predicted by equation (2), the professional factor, P, was characterized using the test results presented by Janss and Minne [7] and Franssen et al. [8]. Janss and Minne [7] reported results for eighteen columns with slenderness ratio between 25 and 102 for which the yield strength was measured. Franssen et al. [8] reported test results for twenty one fire tests with slenderness ratio between 20 and 140. The nominal capacity of these tested columns was calculated using equations (2) and (3). P (ratio of measured axial capacity to nominal capacity) has a mean of 1.10 and a COV of 0.18, and is best described by the normal distribution.

4 RELIABILITY ANALYSES

Twenty steel columns with slenderness ratios ranging from 25 to 200 and axial load capacities ranging from 133 kN (30 kips) to 10,675 kN (2400 kips) were selected for the reliability study. Columns with smaller capacity are representative of those in upper stories and those with higher capacity are representative of those in lower stories of typical office buildings. Live to dead load ratios ranging from 0.5 to 5.0 were considered. The AISC design specifications were used to first design the columns for ambient temperature conditions. The same columns were then designed for fire exposure using the engineering approach described in section 2 and the required thickness of insulation was determined. As suggested in most codes, a capacity reduction factor of 1.0 was used to design for fire. The columns were assumed to be protected by gypsum board insulation, which is generally the case in the U.S. Load ratios (ratio of applied load under fire to room temperature nominal capacity) ranging from 0.35 to 0.66 were considered.

The FERUM (Finite Element Reliability Using Matlab) software [9] was used to perform the reliability analysis. FERUM is a general purpose structural reliability software written using Matlab. It can be used to perform reliability analysis using different methods, including the first order reliability method (FORM). The output for FORM analysis for a particular design situation includes the reliability index, the probability of failure, the values of all design parameters at the failure/design point, and the direction cosines of the design point for each design parameter.

FORM analysis was performed for each design situation (each of the 20 columns) using the performance function given in equation (6). Using the direction cosines obtained from the reliability analysis, the partial safety factors, ϕ_i, for each design parameter were obtained as described in the companion paper by Iqbal and Harichandran [4]. These individual partial safety factors, except for the fire load, were then combined into a single capacity reduction factor through

www.EngineeringEBooksPdf.com

$$\phi_f = \frac{\left\{0.42^{\sqrt{\frac{k_y(\phi_1 T_s)\phi_2 F_y}{F_{e\phi}(T_s)}}}\right\}\phi_3 A_s k_y(\phi_1 T_s)\phi_2 F_y}{P_{n,f}} \tag{7}$$

where

$$F_{e\phi}(T_s) = \frac{\pi^2 k_E(\phi_1 T_s)\phi_4 E_s}{\left(\frac{KL}{\phi_5 r}\right)^2} \tag{8}$$

where, ϕ_i are the partial safety factors for each design parameter. Thus, 20 different capacity reduction factors (one for each column) were obtained. Thereafter, a single optimized capacity reduction factor was obtained using the optimization procedure described in the companion paper by Iqbal and Harichandran [4]. Since the capacity reduction factors were obtained for target reliability index (β_t) values, ranging from 0 to 2, this procedure was repeated for each β_t. A similar procedure was used to obtain the fire load factors corresponding to each value of β_t.

4 RESULTS

4.1 Capacity reduction and fire load factors

The plot of the optimized capacity reduction factor, ϕ_f, vs. β_t is shown in figure 1. The value of ϕ_f is given by

$$\phi_f = \begin{cases} 1.0 & \text{for } \beta_t \le 1.25 \\ 1.25 - 0.2\beta_t & \text{for } 1.25 \le \beta_t \le 2.0 \end{cases} \tag{9}$$

Most codes suggest that ϕ_f = 1.0 be used (e.g., in the Eurocode 3, the partial safety factor γ_M is 1.0 for fire design). The AISC specifications [1] use ϕ_f = 0.9 for fire design of steel columns. Results obtained in this study indicate that the nominal capacity need not be reduced (i.e. ϕ_f = 1.0) if β_t is less than 1.25, which in turns depends on the effectiveness of active fire protection systems in reducing the probability of occurrence of a severe fire. Since most office buildings in the U.S. are required to have automatic sprinklers, β_t is not likely to exceed 1.25. Therefore, using ϕ_f = 1.0 is reasonable for most design situations.

The plot of the fire load factor, γ_q, vs. β_t is also shown in figure 1. The nominal value of the fire load was taken as the 90th percentile [10]. The value of γ_q is given by

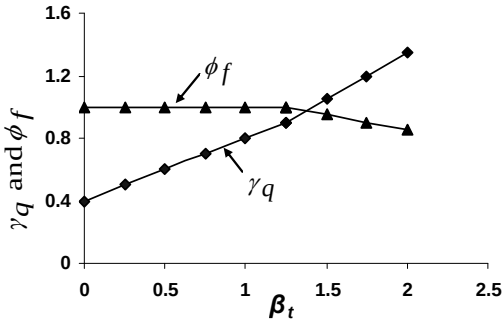


Figure 1: Capacity reduction and fire load factors vs. target reliability index

www.EngineeringEBooksPdf.com

$$\gamma_q = \begin{cases} 0.4 + 0.4\beta_t & \text{for } \beta_t \le 1.25 \\ 0.15 + 0.6\beta_t & \text{for } 1.25 \le \beta_t \le 2.0 \end{cases} \quad (10)$$

When β_t is less than 1.42, γ_q given by equation (10) is less than 1.0 indicating that the fire load can be reduced as suggested in the Commentary to the AISC Specifications [2] and the ECSC study [11].

4.2 Validity of capacity reduction and fire load factors for multiple fire scenarios

The capacity reduction and fire load factors shown in figure 1 were developed for a fire compartment assumed to be constructed of lightweight concrete blocks having a thermal absorptivity, b = 640 $Ws^{0.5}/m^2K$, and having an opening factor, F_v = 0.02 $m^{1/2}$.

In reality, the compartments may be constructed using different bounding materials such as gypsum board, lightweight concrete blocks, etc., having different values of b. Kirby et al. [12] studied the equivalency between standard and realistic fire scenarios by carrying out nine real fire tests. Different types and combinations of lining materials were used as bounding material in these tests, and the value of b ranged from 350-755 $Ws^{0.5}/m^2K$. The statistics of b shown in table 1 in the companion paper by Iqbal and Harichandran [4] effectively cover the range of b values used by Kirby et al. [12], and values of 423, 640 and 1127 $Ws^{0.5}/m^2K$ were used in this study to obtain multiple fire scenarios. Similarly, the ventilation conditions in different compartments may vary considerably. Opening factors of 0.04 $m^{1/2}$, 0.08 $m^{1/2}$ and 0.12 $m^{1/2}$ are typical low, medium and high values in actual building compartments [13] and were used in this study to obtain multiple fire scenarios.

Nine fire scenarios obtained from different combinations of the three opening factors and the three thermal absorptivity values were selected for validating the capacity reduction and fire load factors derived above. For these nine fire scenarios, five columns were designed for fire conditions using the capacity reduction and fire load factors shown in figure 1. The steel sections used for these columns, and their room and elevated temperature capacities are given in table 2. For all columns, a live to dead load ratio of 2.0 was assumed. Each column was designed for β_t values of 0, 0.5, 1.0, 1.5 and 2.0 for all nine fire scenarios. Thus, for each β_t value we had 45 design situations yielding a total of 225 design situations. Reliability analysis was then performed and the computed reliability index values, β, for all five columns are compared with the β_t values in figure 2.

The β values compare quite well with the β_t values, indicating that the derived capacity reduction and fire load factors work well for all design situations considered. The β values are conservative for β_t values less than about 1.5. For β_t values less than 1.5 (see figure 1), the ϕ_f found from reliability analysis was greater than 1.0, and the nominal capacity could be increased. However, since ϕ_f is generally always taken to be less than or equal to 1.0 in LRFD specifications, we restrained the ϕ_f for fire design to also not exceed 1.0. Because of this inherent conservatism, the β values are higher than the β_t values.

Table 2: Properties of columns used for validation

Parameter	W10x19	W10x30	W18x65	W14x90	W12x190
H (m)	3.66	3.66	3.66	3.66	3.66
P_n (KN)	231	876	2497	5276	10751
$P_{n,f}$ (KN)	104	394	1124	2375	4837
Load ratio	0.45	0.45	0.45	0.45	0.45

Note: H is the height of column, and P_n and $P_{n,f}$ are nominal capacities at room temperature and under fire, respectively.

www.EngineeringEBooksPdf.com

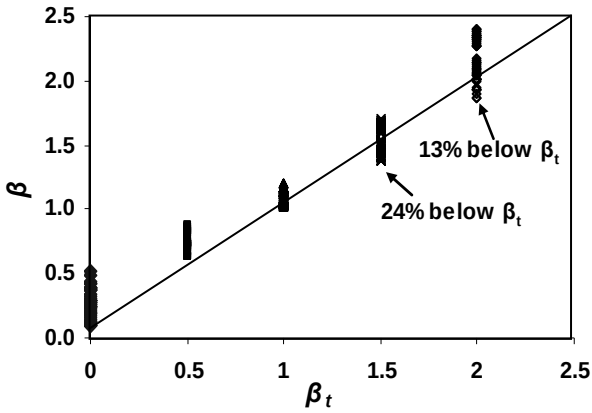


Figure 2: Computed and target reliability index values for different fire scenarios

5 CONCLUSION

Capacity reduction and fire load factors are developed for steel columns in U.S. office buildings exposed to fire. The effect of active fire protection systems (e.g., sprinklers, smoke and heat detectors, fire brigade, etc.) in reducing the probability of occurrence of a severe fire is included by adjusting the target reliability index appropriately.

From detailed reliability analyses, it is found that the capacity reduction and fire load factors should not be constant for all design situations as suggested in design specifications, but should vary depending on the presence of active fire protection systems in a building and the compartment size.

As suggested in the AISC Specifications and Eurocode provisions, the fire load factor should be reduced for typical fire compartment sizes when active fire protection systems are present.

REFERENCES

[1] AISC. “Load and resistance factor design specifications for structural steel buildings”, American Institute of Steel Construction, Inc., Chicago, Illinois, 2005.

[2] EN. “Eurocode 3: Design of steel structures- Part 1-2: General rules-Structural fire design”, BS EN 1993-1-2, 2005.

[3] AISC. “Commentary on the load and resistance factor design specifications for structural steel buildings”, American Institute of Steel Construction, Inc., Chicago, Illinois, 2005.

[4] Iqbal, S. and Harichandran, R. S. “Methodolgy for reliability-based design of steel members exposed to fire”, *Proc. of the SDSS’Rio 2010 Stability and Ductility of Steel Structures*, Rio de Janeiro, Brazil, 2010.

[5] Takagi, J. and Deierlein, G. G. “Strength design criteria for steel members at elevated temperatures”. *Journal of Constructional Steel Research*, **63**(8), 1036-1050, 2007.

[6] Schmidt, B. J. and Bartlett, F. M. “Review of resistance factors for steel: data collection”. *Canadian Journal of Civil Engineering*, **29**(1), 98-108, 2002.

[7] Janss, J. and Minne, R. “Buckling of steel columns in fire conditions”. *Fire Safety Journal*, **4**(4), 227-235, 1981.

www.EngineeringEBooksPdf.com

[8] Franssen, J. M., Talamona, D., Kruppa, J. and Cajot, L. G. “Stability of steel columns in case of fire: experimental evaluation”. *Journal of Structural Engineering*, **124**(2),158-163,1988.

[9] Der Kiureghian, A., Haukaas, T. and Fujimura, K. “Structural reliability software at the University of California, Berkeley”. *Structural Safety*, **28**(1-2), 44-67, 2006.

[10] Buchanan, A. H. *Structural Design for Fire Safety*, John Wiley & Sons Ltd., New York, 2001.

[11] European Coal and Steel Community (ECSC). “Natural fire safety concept, valorization project”, Product-Structural Dept. ARBED-Research Centre L-4009 ESCH/ALZETTE, Luxembourg, 2001.

[12] Kirby, B. R., Wainman, D. E., Tomlinson, L. N., Kay, T. R. and Peacock, B. N. “Natural fires in large scale compartments - a British Steel technical, fire research station collaborative project”, British Steel, Rotherham, 1994.

[13] Beck, V. R. “The prediction of probability of failure of structural steel elements under fire conditions”. *Transactions of the Institution of Engineers Australia*, **27**(1), 111-118, 1985.

www.EngineeringEBooksPdf.com

www.EngineeringEBooksPdf.com

SDSS'Rio 2010 STABILITY AND DUCTILITY OF STEEL STRUCTURES
E. Batista, P. Vellasco, L. de Lima (Eds.)
Rio de Janeiro, Brazil, September 8 - 10, 2010

STABILITY OF STEEL COLUMNS SUBJECTED TO FIRE

Markus Knobloch*, Diego Somaini*, Jacqueline Pauli* and Mario Fontana*

* ETH Zürich, Institute of Structural Engineering – Steel, Timber and Composite Structures,
8093 Zurich, Switzerland
e-mails: knobloch@ibk.baug.ethz.ch, somaini@ibk.baug.ethz.ch,
pauli@ibk.baug.ethz.ch, fontana@ibk.baug.ethz.ch

Keywords: Fire, Structural design, Cross-sectional capacity, Flexural buckling.

Abstract. *The stability behavior of steel columns subjected to fire is strongly influenced by the distinct nonlinear stress-strain relationship of steel at elevated temperatures. The smaller proportional strain compared to ambient temperature and the very large strains required to reach so-called effective yield strength have a marked effect on the cross-sectional capacity and the overall flexural buckling behavior. The paper presents electrical furnace tests on stub columns in pure compression and slender columns in concentric and eccentric compression. The results show the influence of the nonlinear material behavior, the strain rate and thermal creep effects on the structural behavior of steel columns in fire.*

1 INTRODUCTION

Under fire conditions, unprotected steel members heat up quickly, primarily because of their high surface area-to-volume ratio and the good thermal conductivity of steel. At elevated temperatures, the strength and stiffness of steel decrease rapidly, and the almost linear elastic-perfectly plastic stress-strain relationship becomes distinctly nonlinear (e.g. [1]). As a result, the proportional limit is reached for smaller strains than at ambient temperature and large strains are required to reach so-called effective yield strength, both strongly influencing the stability behavior of steel columns in fire. Due to the smaller strains at proportional limit, the influence of plastification on the buckling behavior has to be considered up to larger buckling slenderness ratios than at ambient temperature. And even compact cross sections suitable for plastic design at ambient temperature develop local buckling at large strains required to reach so-called yield strength at elevated temperatures [2]. Therefore, the column strength in fire is limited due to both the critical buckling load considering overall flexural buckling in the plastic range and the cross-sectional capacity at elevated temperatures considering local buckling effects for compact sections.

The buckling behavior of concentrically and eccentrically loaded slender steel columns in fire is studied by Talamona et al. [3]. Based on their finite element results and a comparison to fire tests, Franssen et al. [4] develops a design model for steel columns whose stability failure mode is in the plane of the loading based on the Perry-Robertson principle, later adopted by EN 1993-1-2 [5]. Toh et al. [6] proposes a model for buckling strength in fire based on the Rankine approach. Simplified models usually base on ambient temperature design considering temperature-dependent reduction factors. Therefore, the models do not explicitly consider the nonlinear stress-strain relationship of steel at elevated temperatures and disregard local buckling effects of compact and semi-compact sections. These models are easy to use but have difficulty to precisely describe the structural behavior of steel columns subjected to fire.

A comprehensive analytical, experimental and numerical study analyzing the cross-sectional capacity of steel sections in axial compression and bending as well as the overall structural behavior of steel members at elevated temperatures in fire has been carried out at ETH Zürich. This paper analyses the critical buckling load of steel columns in fire and presents furnace test results on the cross-sectional capacity and slender column strength at elevated temperatures.

www.EngineeringEBooksPdf.com

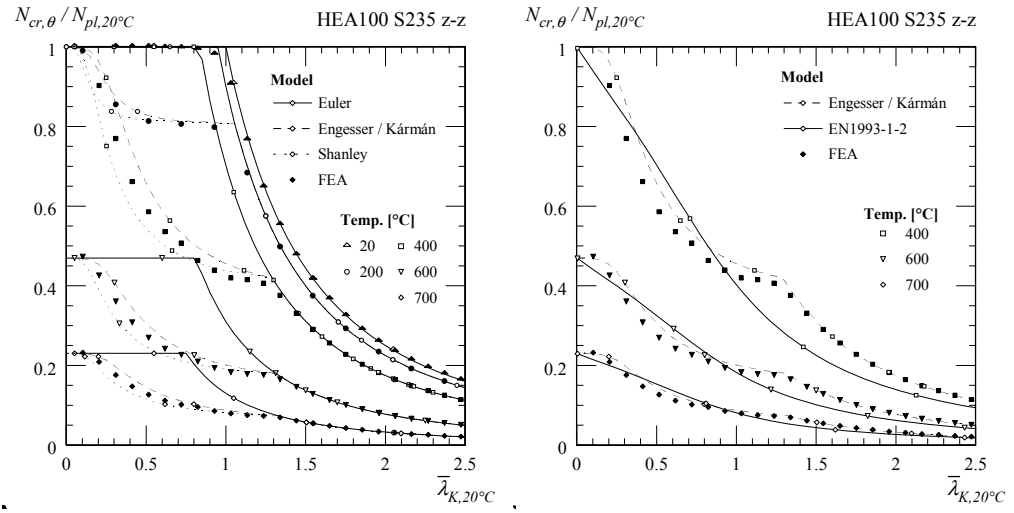


Figure 1: Critical buckling loads as a function of non-dimensional slenderness ratio at different temperatures according to Euler, Engesser/Kármán [8, 9], Shanley [7] and numerical simulations for a HEA 100 (S235) profile (left); Buckling strength calculated according to EN 1993-1-2 [5] at different temperatures compared to Engesser/Kármán and FEM results for a HEA 100 (S235) profile (right).

2 CRITICAL BUCKLING LOAD AT ELEVATED TEMPERATURE

The Euler formula for calculating the critical buckling load N_{cr} is fundamental for commonly used design models and is based on perfect linear elastic material behavior. Euler's formula leads to suitable results for the critical buckling load of slender steel columns at elevated temperatures (with uniform temperature distribution) which develop overall buckling at strains smaller than proportional strain ($\varepsilon_{Buckling} \leq \varepsilon_{p,fi}$). However, using Euler's formula for stocky and medium slender steel columns which develop buckling at larger strains ($\varepsilon_{Buckling} > \varepsilon_{p,fi}$) does not lead to suitable predictions of the critical buckling load due to the influence of the distinctly nonlinear stress-strain relationship of steel at elevated temperatures. Shanley [7], Engesser and Kármán [8,9] develop analytical models to determine the critical buckling load of cast iron columns that exhibit nonlinear material behavior as well. Their analytical models can easily be adapted for determining the critical buckling load of steel columns at elevated temperatures. Shanley's formula uses the tangent modulus and is a lower bound for the critical buckling load. Engesser's and Kármán's formula, however, substitutes the Young's modulus with their buckling modulus leading to an upper bound of the critical load. Figure 1 (left) shows the critical load $N_{cr,\theta}$ for buckling about the weak axis at elevated temperatures, given normalized to the plastic cross-sectional capacity at ambient temperature $N_{pl,20°C}$, for a HEA 100 steel column according to Euler's (continuous line), Shanley's (dotted line) and Engesser/Kármán's model (dashed line) considering temperature-dependent stress-strain relationships according to EN 1993-1-2 [5]. Additionally, the results of a numerical parametric study using the finite element approach (dots) are given. The numerical results are calculated with Abaqus, Rel. 6.8 using beam-elements (denoted as B31OS of the element library) and very small geometric imperfections (e_0 = L/50'000). The analytical and numerical results confirm that the critical buckling load of stocky and medium slender columns is strongly affected by the nonlinear material behaviour. Figure 1 (right) compares the Engesser's/Kármán's model and the FEM results to the buckling strengths according to EN 1993-1-2 [5] (continuous line). For medium slender columns the buckling strengths according to EN 1993-1-2 are larger than the critical buckling load at elevated temperatures.

www.EngineeringEBooksPdf.com

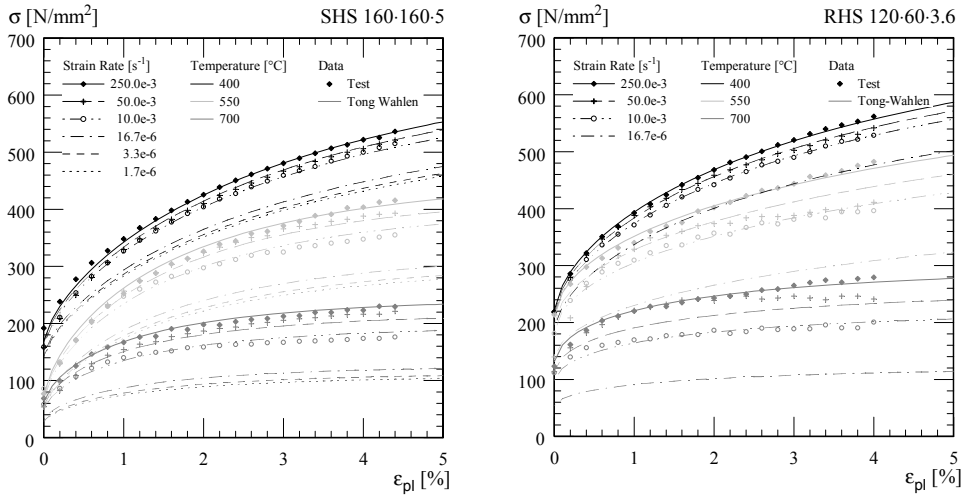


Figure 2: Stress-strain behaviour for 400, 550 and 700°C and different strain rates of the tested specimens cut from the SHS 160·160·5 (left) and RHS 120·60·3.6 (right) profile (dots) and calculated with the Tong-Wahlen model (lines).

3 EXPERIMENTAL INVESTIGATIONS

3.1 Material properties

Standard tensile material coupon tests at ambient and dilatometer compression tests at elevated temperatures were carried out at ETH Zürich to determine the basic engineering stress-strain behavior of the furnace test specimens. Material coupons were cut from the flat parts of the hot finished square and rectangular hollow sections (SHS 160·160·5 and RHS 120·60·3.6; steel grade S355) used for the structural furnace tests. Figure 2 shows the elevated temperature test results of the dilatometer tests performed on the SHS (left) and RHS (right) specimens. The nominal stress σ is given as a function of the plastic strain ε_{pl} for different temperatures and strain rates (dots). The nominal stress decreased with increasing temperature. For equal temperatures, the nominal stress decreased with decreasing strain rates indicating the strong influence of thermal creep effects on the stress-strain behavior. Only tests at high strain rates could be performed using the dilatometer. The Tong-Wahlen Model [10] was therefore used to determine the relationships between nominal stress and plastic strain at slower strain rates used for the structural furnace tests (see Figure 2, lines). Detailed test results are given in [11].

3.2 Stub column tests

A series of 11 stub column electric furnace tests on hot finished square (SHS 160·160·5) and rectangular (RHS 120·60·3.6) hollow sections (steel grade S355) at ambient and elevated temperatures under pure axial compression was performed at ETH Zürich. Wall thickness measurements were taken for each specimen. The average thicknesses were 5.3 mm for the SHS profiles and 3.8 mm for the RHS profiles leading to actual width-to-thickness ratios of 27 and 28. The length of the specimens was three times the nominal height of the cross section. End plates (270·270·20 mm) were welded to the ends of the specimens. Initial geometric imperfection measurements were taken using a three-dimensional video extensometer leading to maximal out-of-plane deflections between -0.3 and 0.3 mm.

The stub column electrical furnace tests were performed using a vertical reaction frame. Figure 3 shows the test setup which consists of the electric furnace with four heating zones (a), an hydraulic load jack (compression capacity 3 MN) at the bottom (b) and the reaction frame (c). Full axial load-end

www.EngineeringEBooksPdf.com

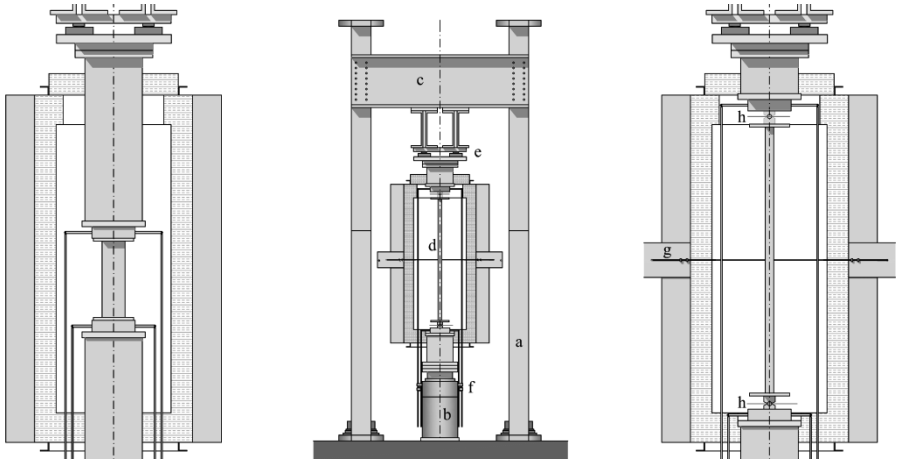


Figure 3: Setup of the stub and slender column tests; (a) electric furnace; (b) hydraulic load jack; (c) reaction frame; (d) test specimen; (e) load cells; (f) LVDT vertical; (g) LVDT horizontal; (h) roller bearing.

shortening histories were recorded, including the post-ultimate range. Two LVDTs (f) below the furnace determined the average end shortening of the stub columns recording the relative displacement at mid-heights of the parallel plates above and below the specimen. Four load cells (e) placed outside the furnace to protect them from heating measured the axial load. Three thermocouples glued on the specimen took the temperature measurement at the bottom, top and mid-height of one stub column surface.

Applying the steady-state method, the specimens were first uniformly heated to the temperatures of 400°C, 550°C and 700°C with a heating rate of 5°C/min (furnace air temperature). During the heating a very low constant axial pre-load of approximately 5kN was applied to the specimens. The thermal elongation during the heating was not restrained. After reaching the target temperatures, the axial load was applied to the stub columns with longitudinal strain rates of $16.7 \cdot 10^{-6}$, $3.3 \cdot 10^{-6}$ and $1.7 \cdot 10^{-6}$ s^{-1} (corresponding to 0.1 %/min, 0.02 %/min or 0.01 %/min) during the entire test. The different strain rates were used to analyze the influence of the thermal creep on the cross-sectional capacity at elevated temperatures.

Figure 4 shows the axial load-end shortening curves of the SHS (left) and RHS (right) test specimens. The main results of the stub column tests are summarized in Table 1. The ultimate loads at 400°C, 550°C and 700°C were reduced to 65%, 38% and 11% of the resistance at ambient temperature for the SHS profiles and to 84%, 53% and 15% for the RHS profiles. In addition, the axial load-end shortening behavior became more ductile and the load decreased less in the post-ultimate range with increasing

Table 1: Stub column test results - Measured area, ultimate load and strain at ultimate load.

Specimen	Temperature θ, [°C]	Strain rate $\dot{\varepsilon}$, [10^{-6} s^{-1}]	Area A, [mm^2]	Ultimate Load F_u, [kN]	Strain at F_u $\varepsilon_{tot,u}$, [%]	$F_u/N_{c,fi,2.0}$ [-]
SHS160_Stub_20C	20	16.7	3282	1225	0.36	1.01
SHS160_Stub_400C	400	16.7	3276	795	0.67	0.72
SHS160_Stub_550C	550	16.7	3276	468	0.64	0.61
SHS160_Stub_550Cs	550	3.3	3276	403	0.80	0.56
SHS160_Stub_550Css	550	1.7	3278	364	0.65	0.52
SHS160_Stub_700C	700	16.7	3288	138	0.72	0.46
SHS160_Stub_700Cs	700	3.3	3269	88	0.96	0.31
RHS120_Stub_20C	20	16.7	1311	483	0.48	0.96
RHS120_Stub_400C	400	16.7	1300	408	0.73	0.85
RHS120_Stub_550C	550	16.7	1303	257	0.81	0.79
RHS120_Stub_700C	700	16.7	1312	74	0.69	0.58

www.EngineeringEBooksPdf.com

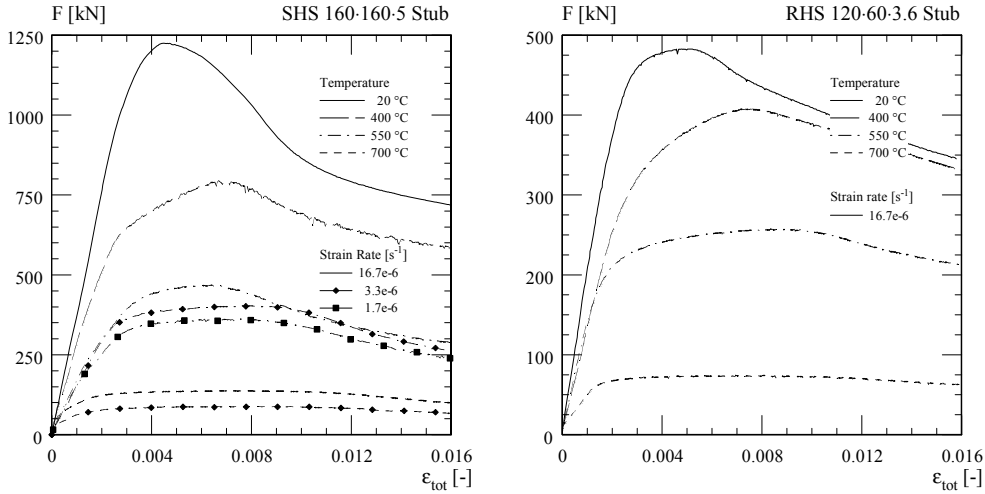


Figure 4: Axial load-end shortening curves of the SHS 160·160·5 (left) and the RHS 120·60·3.6 (right) stub column tests as a function of strain rate and temperature.

temperature. The strain rate markedly influenced the load-end shortening behavior and the ultimate load of the stub columns at 550° and 700°C. The ultimate loads determined with a strain rate of 0.02 %/min were approximately 14% (550°C) and 36% (700°C) lower than the resistance of the stub columns with a strain rate of 0.1 %/min. The ultimate load of the stub column at 550°C was additionally reduced by approximately 10% by reducing the strain rate from 0.02 %/min to 0.01 %/min. Table 1 additionally compares the ultimate loads F_u to the temperature-dependent cross-sectional resistance $N_{c,fi,2.0}$ calculated as the product of the actual area A and the actual stress reached at 2% strain $f_{2.0,\theta}$ considering the appropriate strain rate of each stub column test. The cross-sectional resistance $N_{c,fi,2.0}$ is not reached in the tests due to local buckling effects.

3.3 Slender column tests

A series of 16 slender column electric furnace tests (including 4 ambient temperature tests) under concentric and eccentric axial compression was performed at ETH Zürich on the same cross sections (from the same charges) used for the stub column tests. The lenght of the specimens was 1844 mm, the effective length of the test setup 1990 mm. End plates (270·270·20 mm) were welded to the ends of the specimens. The non-dimensional slenderness ratios about the weak axis at ambient temperature considering nominal values were 0.41 for the SHS and 1.05 for the RHS. Overall initial geometric imperfection measurements were taken along the central line of each face of the columns (see Table 2). The initial geometric imperfections were small and varied between approximately l/1´200 and l/10´000.

Steady-state slender column electrical furnace tests were performed using the same test setup and procedure used for the stub column tests, again leading to full axial load-end shortening histories. Horizontal displacement measurements were taken at mid-height on both sides of the column (see Figure 3g). Simply supported boundary conditions (about the weak axis of the cross sections) were realized using high-temperature resistant roller bearings (h). On the RHS profiles concentric and eccentric (10 and 50 mm) load tests were carried out. Tests using different strain rates (identical to the rates for the stub columns) to experimentally analyze the thermal creep effect were performed for the SHS profiles.

Figure 5 shows the axial load-end shortening curves of the SHS (left) and RHS (right) test specimens. The main results of the slender column tests are summarized in Table 2. The bending moment about the weak axis corresponding to the ultimate axial load F_u is calculated as the product of F_u and the

www.EngineeringEBooksPdf.com

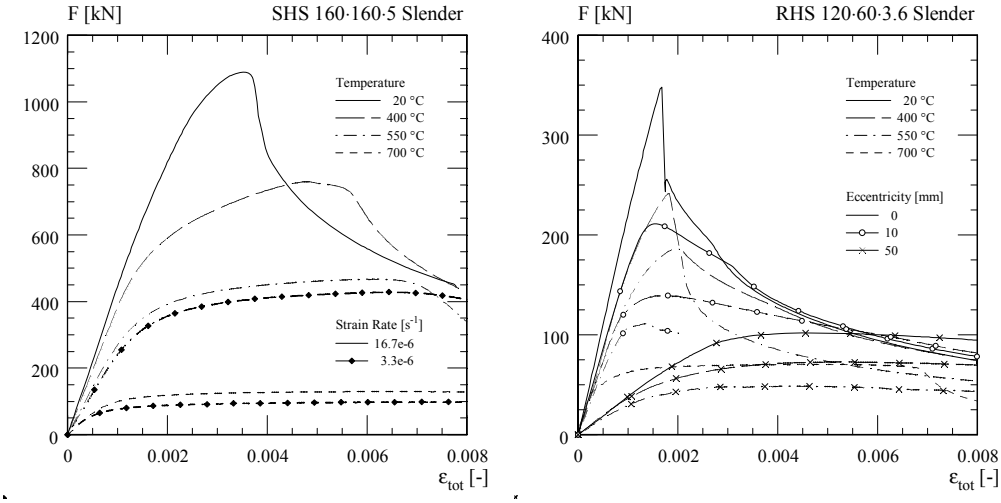


Figure 5: Axial load-end shortening curves of the SHS 160·160·5 slender column tests for different strain rates (left) and the RHS 120·60·3.6 slender column tests for different load eccentricities (right) as a function of temperature.

eccentricity e_1 ($M_{z,u,I}$) or the sum of the overall initial geometric imperfection about the weak axis $e_{0,z}$, eccentricity e_1 and deflection at ultimate load w_u ($M_{z,u,II}$). Due to the very small overall geometric imperfections (in addition to the relatively small overall slenderness), the SHS columns did not fail due to column buckling, but showed a failure mode governed by local buckling. The strain rate had again a marked effect on the ultimate load of the SHS profiles (see Figure 5 left). However, the thermal creep effect was less pronounced than for the stub column tests. The buckling strengths of the concentrically loaded RHS profiles at elevated temperatures were reduced to 70% (400°C), 53% (550°C) and 20% (700°C) of the strengths at ambient temperature.

Table 2: Slender column test results - Measured imperfections, ultimate load and strain and deflection at ultimate load, calculated bending moments at ultimate load

Specimen (SL: Slender)	Measured imperfection			Slender column tests				At ultimate load			
	strong axis	weak axis		Temperature	Eccentricity	Strain rate	Ultimate load	Strain	Deflection	Bending Moment	
	$e_{0,y}$ [mm]	$e_{0,z}$ [mm]	$l/e_{0,z}$ [-]	T [°C]	e_1 [mm]	$\dot{\varepsilon}$ [10^{-6} s^{-1}]	F_u [kN]	$\varepsilon_{tot,u}$ [%]	w_u [mm]	$M_{z,u,I}$ [kNm]	$M_{z,u,II}$ [kNm]
RHS160_SL_20C	0.30	0.61	3023	20	0	16.7	1089	0.35	0.4	0	1.1
RHS160_SL_400C	0.64	1.14	1618	400	0	16.7	760	0.48	6.0	0	5.4
RHS160_SL_550C	0.34	0.41	4498	550	0	16.7	467	0.62	1.2	0	0.7
RHS160_SL_550Cs	0.14	0.49	3763	550	0	3.3	428	0.64	4.8	0	2.3
RHS160_SL_700C	0.49	1.50	1229	700	0	16.7	130	0.61	6.5	0	0.9
RHS160_SL_700Cs	1.39	1.39	1327	700	0	3.3	98	0.70	0.7	0	0.2
RHS120_SL_20C	0.30	0.45	4098	20	0	16.7	348	0.17	4.0	0.0	1.5
RHS120_SL_20C_e10	1.29	0.36	5122	20	10	16.7	211	0.16	16.1	2.2	5.6
RHS120_SL_20C_e50	0.62	0.23	8017	20	50	16.7	102	0.47	32.6	5.1	8.4
RHS120_SL_400C	0.13	0.34	5424	400	0	16.7	242	0.18	5.0	0.0	1.3
RHS120_SL_400C_e10	0.35	0.41	4498	400	10	16.7	139	0.18	20.0	1.5	4.2
RHS120_SL_400C_e50	0.67	0.39	4728	400	50	16.7	73	0.51	35.1	3.7	6.2
RHS120_SL_550C	0.03	0.70	2634	550	0	16.7	186	0.20	5.7	0.0	1.2
RHS120_SL_550C_e10	0.66	0.19	9705	550	10	16.7	111	0.13	13.2	1.1	2.6
RHS120_SL_550C_e50	0.25	1.04	1773	550	50	16.7	49	0.43	29.0	2.5	3.9
RHS120_SL_700C	0.36	0.10	18440	700	0	16.7	71	0.41	1.4	0.0	0.1

www.EngineeringEBooksPdf.com

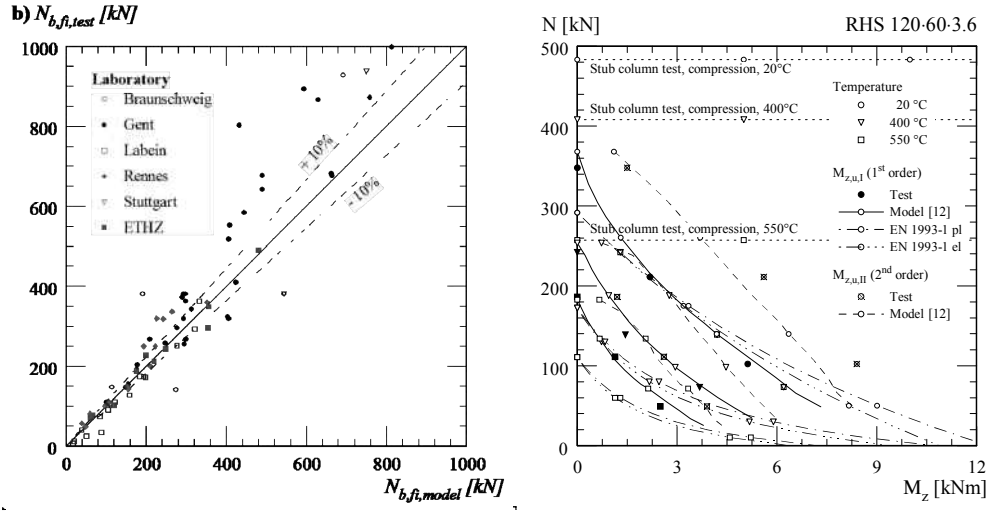


Figure 6: Comparison between slender column test results [13] and results according to the analytical model [12] (left); N-M interaction curves of the slender column tests performed at ETH and according to the analytical model [12] and the European fire design model [5] (right).

4 COMPARISON OF SLENDER COLUMN TESTS AND ANALYTICAL MODELS

Simple European fire design models [5] for steel beam-columns adapt the ambient temperature design M-N interaction formulae considering a so-called European buckling curve for the fire design situation and temperature-dependent reduction factors for the Young's modulus and yield strength at 2% strain. A novel simplified analytical model for calculating the buckling strength of steel columns in fire is proposed in [12]. The model checks equilibrium for the external loads of second order acting on the deflected column and the column internal resistance forces. Using a strain-based formulation, the model facilitates to explicitly consider nonlinear material behavior, geometric imperfections and residual stresses.

Figure 6 (left) compares column strengths in fire according to the simplified analytical model [12] with results of independent full scale furnace tests [13] and the RHS slender column tests of ETH Zürich presented in the previous section. The model [12] considers the geometry, steel temperature at failure and the material properties of the test specimens if reported [13]. The comparison shows a generally good agreement between analytical prediction and tests results. However, partially missing data about the test specimens (e.g. stress-strain relationship at failure temperature and test conditions), replaced by nominal values leads to a rather large scatter. A better congruence is found for tests performed at ETH.

Figure 6 (right) shows the M-N interaction curves of the RHS 120·60·3.6 profile. The slender column furnace test results (dots), the stub column furnace test results (being an upper limit for the strengths in axial compression), the M-N interaction curves according to the European design models (dash-dotted lines) and the simplified analytical model according to [12] (continuous and dashed lines) are given. Using European buckling curves with actual geometry values and material properties lead to conservative results for the buckling strengths both at ambient and elevated temperatures. The very small geometric imperfections seem to be a reason for the higher strengths reached experimentally, in particular for the ambient temperature test. The simplified analytical model considers the actual imperfection values as well as the nonlinear material behavior resulting in accurate results for the M-N interaction compared to the test results for the interaction curves considering bending moments $M_{z,u,I}$. Slightly different deflections at ultimate axial load between the simplified analytical prediction and the test measures lead to somewhat less accurate results of the analytical model for calculating the bending moment $M_{z,u,II}$.

www.EngineeringEBooksPdf.com

5 CONCLUSIONS

The structural stability behavior of steel columns in fire has been analytically and experimentally analyzed and the cross-sectional capacity and overall flexural buckling behavior of square and rectangular hollow sections at elevated temperatures have been determined. The experimental program comprised material tests at elevated temperatures, stub column furnace tests in pure axial compression and slender column buckling furnace tests in concentric and eccentric compression at different temperatures and strain rates. Results, including full axial load-end shortening curves have been presented. The strain rate markedly influenced the stress-strain behavior and the local and global buckling behavior. The influence of the nonlinear stress-strain relationship of steel at elevated temperatures on cross-sectional capacity, critical buckling load and overall buckling strength need to be considered for more slenderness ratios at elevated than at ambient temperatures. The stub column results show that the use of the actual area and the temperature-dependent stress at 2% strain leads to unconservative results for the cross-sectional capacity in pure compression. Further experimental and numerical studies on the cross-sectional capacity and the overall flexural buckling strengths of square and rectangular hollow sections subjected to concentric and eccentric compression will be presented on the conference.

ACKNOWLEDGEMENTS

The authors gratefully acknowledge the Swiss National Science Foundation for funding the project No. 200021-117906.

REFERENCES

[1] Twilt, L., “Stress-strain relationships of structural steel at elevated temperatures: Analysis of various options & European proposal”, TNO-report BI-91-015, ECSC project SA 112 – Part F, TNO, Delft, 1991

[2] Knobloch, M., Fontana, M. and Frangi, A., “On the interaction of global and local buckling of square hollow sections in fire”, K. Rasmussen and T. Wilkinson (ed.), Proceedings of the Fifth International Conference on Coupled Instabilities in Metal Structures CIMS2008, Sydney, Australia, 23-25 June 2008, pp. 587-594.

[3] Talamona, D., Franssen, J.M., Schleich, J.B. and Kruppa, J., “Stability of steel columns in case of fire: Numerical modeling“, Journal of Structural Engineering, 123(6), 713-720, 1997

[4] Franssen, J.M., Talamona, D., Kruppa, J. and Cajot, L.G., “Stability of steel columns in fire: Experimental Evaluation”, Journal of Structural Engineering, 124(2), 158-163, 1998

[5] EN1993-1-2, “Design of Steel Structures, Part 1-2: General Rules, Structural Fire Design”, Brussels, 2005.

[6] Toh, W.S., Tan, K.H., Fung, T.C., „Compressive resistance of steel columns in fire: Rankine approach“, Journal of Structural Engineering, 126(3), 398-405, 2000

[7] Shanley, F.R., “Inelastic column theory”, Journal Aeron, 14, 1947

[8] Engesser, F., „Knickfragen“, Schweiz. Bauzeitung, 25, 1895

[9] Kármán v., T., „Untersuchungen über die Knickfestigkeit“, Forschungshefte, VDI, H.81, 1910

[10] Hochholdinger, B., Grass, H., Lipp, A., Wahlen, A. and Hora, P., “Determination of flow curves by stack compression tests and inverse analysis for the simulation of press hardening”, Numisheet - 7th International Conference and Workshop on Numerical Simulation of 3D Sheet Metal Forming Process, Interlaken, Switzerland, 2008

[11] Pauli, J., Knobloch, M. and Fontana, M., “Stub column tests on square and rectangular hollow steel sections at elevated temperatures”, Proceedings of the Fourth International Conference on Structural Engineering, Mechanics and Computation, Cape Town, South Africa, 2010

[12] Somaini, D., Knobloch, M. and Fontana, M., “Simplified analytical model for centrically and eccentrically loaded steel columns in fire”, Proceedings of the Fourth International Conference on Structural Engineering, Mechanics and Computation, Cape Town, South Africa, 2010

[13] Schleich J.B., Cajot, L.G., Pierre, M. and Warszta, F., “Buckling curves in case of fire, Final Report, Part 1”, Esch/Alzette: PROFIL ARBED

www.EngineeringEBooksPdf.com

SDSS'Rio 2010 STABILITY AND DUCTILITY OF STEEL STRUCTURES
E. Batista, P. Vellasco, L. de Lima (Eds.)
Rio de Janeiro, Brazil, September 8 - 10, 2010

FIRE BEHAVIOR OF CONCRETE FILLED CIRCULAR HOLLOW SECTION COLUMNS WITH MASSIVE STEEL CORE

Martin Neuenschwander, Markus Knobloch and Mario Fontana

ETH Zürich, Institute of Structural Engineering –
Steel, Timber and Composite Structures, 8093 Zürich, Switzerland
e-mails: neuenschwander@ibk.baug.ethz.ch, knobloch@ibk.baug.ethz.ch, fontana@ibk.baug.ethz.ch

Keywords: Fire resistance; Steel-concrete composite; Concrete-filled steel CHS columns; Buckling

Abstract. *The paper analyses the structural fire behavior of centrically loaded concrete-filled steel CHS with a massive steel core. A numerical model for a geometrically and temperature-dependent materially nonlinear analysis of the imperfect structure is presented. A comprehensive numerical study shows the influence of the thermal expansion as well as the bonding behavior between steel and concrete on the structural fire behavior.*

1 INTRODUCTION

Concrete-filled circular hollow steel section columns (CHS) with a massive steel core have an attractive slender appearance due to their typical high slenderness ratio of the column. They can be used for heavily loaded columns and/or for minimizing the size of the column. Subjected to fire conditions the steel tube is directly exposed to the fire and heats up quickly. The concrete inside the tube slows down the heating of the steel core. At elevated temperatures the strength and stiffness of steel and concrete decreases. The reduced strength and stiffness have a marked influence on both the cross-sectional capacity and the slender column strength of steel concrete composite sections. The load-carrying behavior of concrete-filled CHS with massive steel cores at ambient temperatures is recently studied experimentally and numerically by Hanswille/Lippes [1]. Fire resistance tests of centrically and eccentrically loaded concrete-filled hollow steel section columns with both plain and reinforced concrete (without steel cores) were performed by [2-6], for example. The use of reinforced concrete improves the fire resistance significantly [7]. Numerical studies on the fire behavior of concrete-filled hollow steel section columns are presented in [8,9]. The fire behavior of concrete-filled CHS with massive steel core has not been comprehensively analyzed so far. Hence, it is necessary to obtain basic data on the structural behavior of these columns and to develop a fire design model.

2 NUMERICAL MODEL

2.1 Finite element method model

A finite element model was developed using ABAQUS/Standard, Rel. 6.8 to analyze the load-carrying behavior of concrete-filled hollow steel tube columns with massive steel cores. The columns were modeled with linear three-dimensional continuum elements with a reduced integration scheme (C3D8R elements of the ABAQUS element library) for the entire section. The longitudinal axis coincided with the x-direction and the cross-sectional plane with the yz-plane. The radial symmetry of the temperature fields and the circular shape of the cross section allowed modeling only one half of the column with the xz-plane being a symmetry plane. The overall initial geometric imperfection was assumed to have a sinusoidal shape with amplitude of $L/1000$ at midspan of the column. The columns were free to rotate about the y-axis at both ends while all other rotational degrees of freedom were

www.EngineeringEBooksPdf.com

constrained. All translational movements were constrained at both ends except that the columns were free to move in the x-direction at the upper end. These boundary conditions were applied to the reference nodes of rigid surfaces forming rigid end plates (perfect load-distributing plates). All nodes of the cross sections at the upper and lower end of the columns were tied to the respective rigid surfaces; hence had to follow the movement of the reference nodes. A point load could be applied either centrically or eccentrically at the upper end of the column.

The load-carrying behavior of the composite columns in fire was numerically analyzed using three different finite element models: *model 1* considered friction between steel and concrete, and *model 2* considered perfect bonding. *Model 1* and *2* considered the influence of compatibility stresses caused by partly constrained thermal strains on the load-carrying behavior. A third model, *model 3*, considered a bonding behavior with friction equal to model 1 and did not consider thermal expansion. The interfaces between the steel and the concrete were defined by a surface-to-surface discretization. This modeling technique allowed varying the mesh density according to the geometry and the material properties assigned. It was possible to either simulate perfect bonding by tying the surfaces together or to attribute mechanical properties in the normal and the tangential direction of the interface. Both cases were implemented in two independent models: *model 1* and *3* considered friction between both materials with a friction coefficient of $\mu_f = 0.6$ and *model 2* assumed perfect bonding. The initial position of the surfaces relative to each other was adjusted to avoid overclosures due to non-matching meshes of the different parts forming the interface. The contact constraints were enforced by means of a linear penalty stiffness method in conjunction with an augmented Lagrange iteration scheme for the model without perfect bonding (*model 1*): In this case the contact state of the surfaces was first established in a Newton iteration. Secondly, the contact pressure was augmented for those nodes that were overclosed for more than a certain penetration tolerance and the contact was solved again iteratively until these overclosures were dissolved [10]. Using this advanced modeling technique the contact resolution was more precise potentially helping to obtain a converged global solution. Additionally, a more precise contact could be achieved by using an iteration which did not stop until no severe discontinuities occurred anymore to overcome convergence difficulties related, most probably, to the distribution of redundant contact pressure forces when the interface opened.

The common metal plasticity model of ABAQUS was used for the material behavior of the steel tube and the steel core. Nominal yield strengths of 235 N/mm^2 for the tube and 355 N/mm^2 for the core at ambient temperature were considered. The influence of the temperature on the constitutive behavior was considered by the stress-strain relationships according to EN 1993-1-2 [11] including strain hardening. The ABAQUS concrete damaged plasticity model was applied for the concrete as a nominal stress model (i.e. without considering material damage by specifying evolution laws for the damage variables in tension or compression). Hardening and post-failure behavior in compression were modeled according to the temperature-dependent stress-strain relationships of EN 1992-1-2 [12]. The cylinder compression strength at ambient temperature was 25 N/mm^2. The tension stiffening was accounted for by means of the fracture energy approach considering a temperature-independent value of $G_f = 0.14$ *N/mm*. ABAQUS default values of the model parameters defining the shape of the yield surface were employed and assumed also to be independent of the temperature. An angle of dilation of $\psi = 15°$ was considered. Additionally the viscoplastic regularization technique was used with $\mu = 0.1$ for the viscosity parameter to overcome convergence problems related to the constitutive equations of the concrete model and its non associated character as well as the softening in the compression zone [11]. Residual stresses of the massive steel core were considered according to the distribution proposed by [1].

Fire test data on concrete-filled steel section columns with massive core are very rare. The load-carrying tests with different load eccentricities at ambient temperature given in [1] were used for validating the numerical model. The ratio between the numerical and the experimental results for the almost centrically loaded composite columns was $P_{FEA}/P_{Exp} = 0.943$. The finite element method model presented above was found to be suitable for predicting the resistance of slender composite columns with massive steel core. Details of the validation will be given at the conference.

www.EngineeringEBooksPdf.com

2.2 Calculating procedure

Composite columns in fire are subjected to both a mechanical pre-loading and a thermal action – often considered with the standard ISO time temperature curve [13]. The fire resistance time is the duration of fire exposure until column failure occurs and depends on the mechanical pre-loading and the thermal action. It was the aim of the study to determine the mechanical maximum pre-loading to reach a fire resistance of 30, 60 and 90 minutes standard ISO fire exposure. The maximum pre-loading for *model 1* and *2* (the pre-loading of *model 3* was considered equal to *model 1*) was determined iteratively since the *P–Δ* effect has a marked effect on the load-carrying capacity N_K of slender composite columns. Each iteration consisted of three calculation steps (Fig. 1): First, a static stress analysis was carried out at ambient temperature and the column was loaded successively up to the pre-loading P_0 which was estimated as a function of the column strength at ambient temperature. Secondly, the pre-calculated temperature fields (calculated in a separate and independent heat transfer analysis) were applied for consecutive time increments up to the desired fire resistance time within a static (thermal) stress analysis step. Temperature-dependent material properties for steel and concrete according to [11] and [12] including thermal expansion (for *model 1* and *2*) were considered. Finally, the column was mechanically loaded until failure occurred to determine the load reserve *ΔP* at elevated temperatures. Subsequently the pre-loading of the column had to be updated for the next iteration. The pre-loading consisted of the sum of the pre-loading and a fraction of the load reserve, both of them of the previous iteration. Considering a too large fraction of the load-reserve led to a premature failure of the column during the thermal loading since the *P-Δ* effect was more pronounced due to the higher load (Fig. 1 dashed line). The iteration process was continued until the load reserve was smaller than a limit of 2% of the sum of the pre-load of the current iteration and the load-reserve of the current iteration.

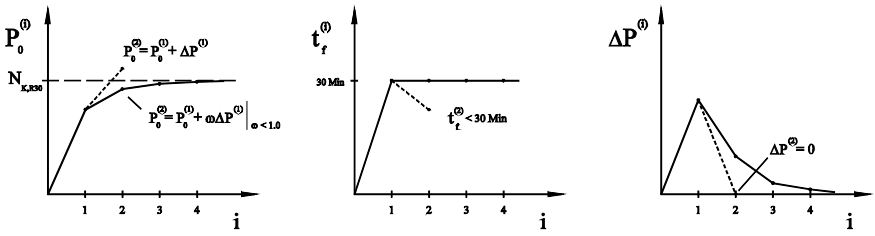


Figure 1: Iteration scheme (a) mechanical pre-loading, (b) thermal loading, (c) load reserve

3 RESULTS

3.1 Load-carrying behavior

The fundamental load-carrying behavior of concrete-filled CHS columns with massive steel core subjected to fire was numerically analyzed with the finite element model considering a frictional interface (*model 1* and *3*). The pre-loading corresponding to a given fire resistance time was determined according to the calculation procedure described in the previous section. Figure 2 (left) shows the applied axial load N_{res}, the temperature of five distinct points over the cross section θ_i (indices of the temperature refer to the position, Fig. 2 bottom right), the midspan deflection considering initial geometric imperfection $w_{tot} = w_0+w$ (indices of the displacements refer to the models used), and the end shortening u as a function of the fire exposure time t. The results are given for a composite column with an outer diameter of 273 mm and a thickness of 5 mm of the steel tube (steel grade S235), a diameter of 180 mm of the massive core (steel grade S355) and unreinforced concrete (nominal cylinder compression strength of 25 N/mm^2 at ambient temperature) as an example. A fire resistance of 30 min and an effective length of the column of 4 m were used for the calculations presented in Fig. 2.

www.EngineeringEBooksPdf.com

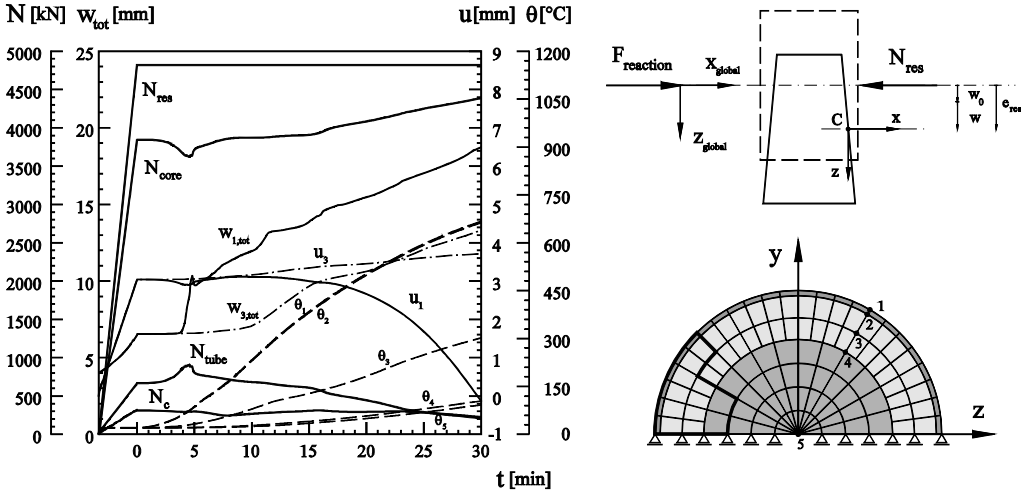


Figure 2: Axial load-time, temperature-time and deflection-time curves (left); Slice of column including axial load N, deflection w and global and local coordinates (top right) cross section with element mesh (bottom right)

Figure 2 (left) additionally shows the parts of the applied load N_{res} carried by the steel tube N_{tube}, the concrete N_c , and the steel core N_{core} in the cross section at midspan of the column. The nodal forces and the actual coordinates were used for calculating the resulting forces of every part of the cross section (tube, core and concrete) including their eccentricities relative to the centroid of the cross section. Figure 2 (top right) shows an deformed part of the column, the local coordinate system used to measure the eccentricity (without rotation for simplicity) and its relation to the global coordinate system of the model. The eccentricities e of the resulting forces of the different parts of the cross section and the corresponding moments M are given in Fig. 3 (left). Figure 3 (right) shows the averaged normal stresses in the steel core $\sigma_{i,core}$ and the steel tube $\sigma_{i,tube}$ (indices of the stresses refer to the model used) as well as stresses in the inner $\sigma_{i,inner}$ and outer parts of the concrete $\sigma_{i,outer}$. The stresses were calculated from the elements highlighted in Fig. 2 (bottom right, black line) located at midspan of the column on the compression side. Hoop compatibility compression stresses arose and enabled slightly higher stresses in the steel tube than the uniaxial yield strength.

The load-carrying behavior of concrete-filled CHS columns with steel core in fire is mainly influenced by (a) a reduction of the material properties of steel and concrete with increasing temperature, in particular a decrease of steel's stiffness and proportional limit for temperatures above 100°C and the yield strength above 400°C and (b) compatibility stresses due to partially constrained thermal strains which arose from transient temperature gradients over the cross section. The development of the midspan deflection w_{tot} during the fire exposure can be grouped into four stages (Fig. 2 left): (1) from the start of the fire exposure until approximately 4 minutes, when the deflection remained almost constant for *model 1* (with thermal expansion) and *3* (without thermal expansion); (2) from 4 to 10 minutes, when a marked increase in the deflection was observed for the model considering thermal strains (*model 1*) whereas the deflection remained almost constant for the model disregarding the thermal expansion (*model 3*); (3) from 10 to 16 minutes, when the deflection of *model 3* increased for the first time and, thus, marked the effect of the temperature-dependent reduction of the stiffness and the proportional limit, and (4) after 16 minutes, when the thermal strains had almost no influence on the midspan deflection and the curves for both models were nearly parallel.

www.EngineeringEBooksPdf.com

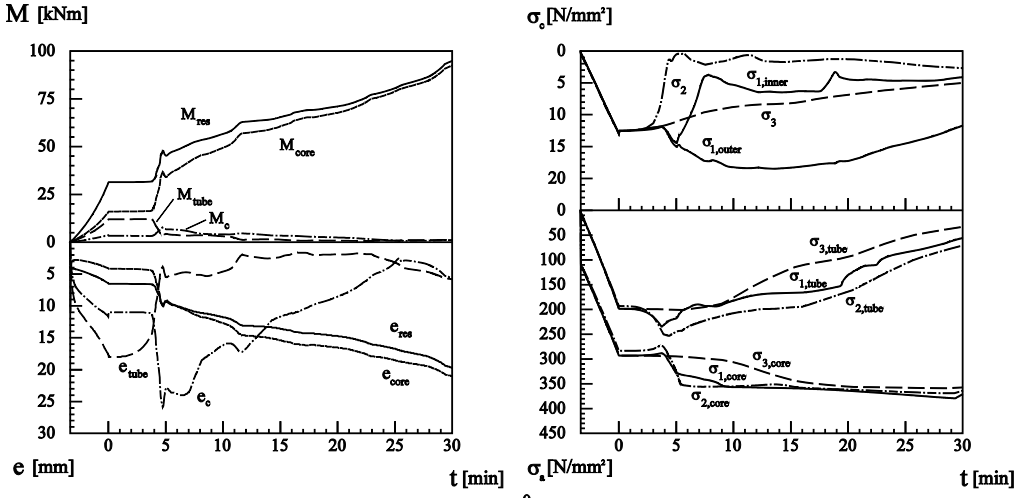


Figure 3: Bending moments (top) and eccentricities (bottom) of the different parts of the cross section at midspan (left) and stress development for the different FEM models (right) (top: concrete, bottom: steel tube and steel core).

At stage 1 the steel tube was heated up leading to thermal strains, which were constrained partially by the inner parts of the column which were still at ambient temperature. Therefore compatibility stresses arose: (a) tension stresses in the inner cooler part resulting in a marked decrease of the compression force in the steel core and in the concrete (Fig. 2 left); and (b) compression stresses in the outer part leading to an increase of the compression force in the steel tube. Using perfect bonding (*model 2*) led to higher compatibility stresses as a result of the constrained thermal strains since stress-relieving slip could not developed. These compatibility stresses led to higher compression stresses in the steel tube and a larger decrease of the concrete compression stresses (Fig. 3 right).

At the beginning of stage 2 the yield strength was reached on the compression side in the steel tube causing a localized loss of stiffness leading to a loss of bending stiffness and consequently to the increase of the deflection. The bending moment was redistributed from the steel tube to the concrete and the steel core (Fig. 3 left). The associated stress distribution of the cross section before (top) and after (bottom) the increase of the deflection is given in Figure 6 (right). The stresses of the steel tube are given in the front and the stresses of the core in the back. The concrete stresses are hidden behind the tube stresses since their magnitude is much smaller. The compression zone is located on the right side.

After approximately 10 minutes of fire exposure the end shortening of the *model 1* began to decrease and deviate from the end shortening of *model 3* (Fig. 2 left). The thermal strains now developed less constrained and the compatibility stresses less influenced the behavior of the composite column. The stresses of the inner part of the concrete started growing again (Fig. 3 right). At the beginning of stage 3 (after 10 minutes) the steel tube reached a temperature of about 200°C. The bending moment was mainly redistributed to the core.

Stage 4 was characterized by the completion of the redistribution of the moment to the steel core and the reduction of the strength of the steel tube which reached a temperature of 400°C after approximately 16 minutes. The compression force was mainly distributed to the steel core. After approximately 25 minutes the concrete reached a temperature of about 250°C and the strength decreased. The failure of the composite column was governed by a plastic failure and local buckling of the steel tube, when the core was still at a temperature of approximately 100°C.

www.EngineeringEBooksPdf.com

The comparison between the results of model 1 and 3 (Fig. 2 and 3) shows the strong influence of the compatibility stresses caused by partly constrained thermal strains on the structural behavior of the composite columns during the first and second stage (start to approximately 10 minutes of fire exposure). The bonding behavior between steel and concrete mainly affects the load-carrying behavior during the second stage. Perfection bonding leads to higher compatibility stresses and higher compression stresses in the tube and a larger decrease of the concrete compression stresses (Fig. 3 right).

3.2 Parametric study

Due to large difference in calculation time and small differences in the results, in particular for the fire resistance, the simpler model considering perfect bonding (*model 2*) was used for conducting a comprehensive parametric study. The cross-sectional properties were identical to the analysis of the load-carrying behavior. The behavior of concrete-filled CHS columns with different lengths and fire exposure durations was analyzed and the results comprised the axial load N, the deflection at midspan w, and the temperature at different points of the cross section θ_i , as a function of the fire exposure time t.

Figure 4 shows the results for a column with an effective length of 4 m as an example. The pre-loading for the column with a fire resistance of 30 minutes (Fig. 4 left) was about the double of the pre-loading of the column with a fire resistance of 90 minutes (Fig. 4 right) leading to a larger midspan deflection caused by the mechanical pre-loading. The higher pre-loading also led to a larger increase of the deflection induced by the partial yielding of the steel tube. The lower pre-loading resulted in a later partial yielding of the steel tube since more compression stresses as a result of constrained thermal strains could be carried. Hence the tube had a higher temperature and exceeded 100°C when the increase of the deflection occurred which in this case was not only triggered by compatibility stresses but also by temperature-dependent stiffness reduction. The deflection at midspan after 30 and 90 minutes respectively was almost similar in magnitude (Fig. 4).

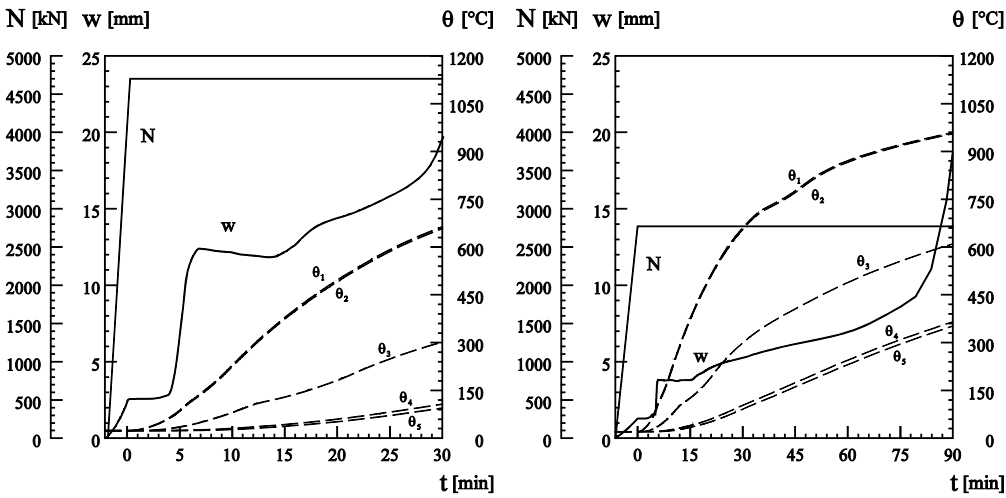


Figure 4: Axial load N, midspan deflection w and temperature θ_i of the composite column with an effective length of 4’000 mm and a fire resistance of 30 (left) and 90 minutes (right).

Figure 5 shows the results for a slender column with an effective length of 8 m as an example. It can be observed that the increase of the deflection was less abrupt compared to the shorter column of 4 m (Fig. 4). Due to the higher slenderness ratio the initial deflections caused by the pre-loading were larger than for the shorter column leading to considerable bending stresses over the cross section. Since the stresses were mainly because of bending the normal stress gradient over the cross section was steeper and

www.EngineeringEBooksPdf.com

the yielding zone could not spread as quickly as for the shorter column. The end deflection of the slender columns differed markedly for the two fire resistance times (Fig. 5).

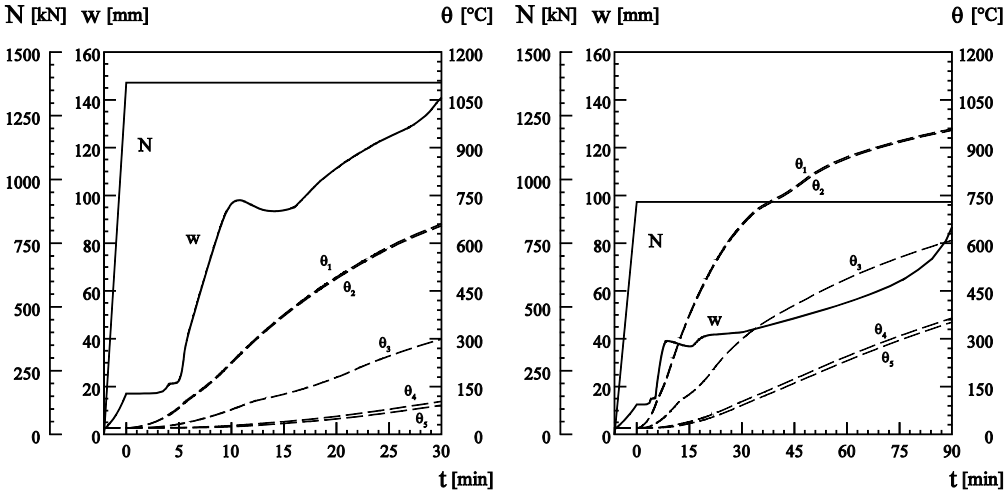


Figure 5: Axial load N, midspan deflection w and temperature θ_i of the composite column with an effective length of 8'000 mm and a fire resistance of 30 (left) and 90 minutes (right).

3.3 Buckling strength

The results of the parametric study were used to develop curves for the ultimate buckling strength. Figure 6 (left) shows the curves for ambient temperature and for fire resistance times of 30, 60 and 90 minutes. The results are given for a concrete-filled CHS column with steel core with an outer diameter of 273 mm and a thickness of 5 mm of the steel tube (steel grade S235), a diameter of 180 mm of the massive core (steel grade S355) and plain concrete (nominal cylinder compression strength of 25 N/mm^2 at ambient temperature) as an example.

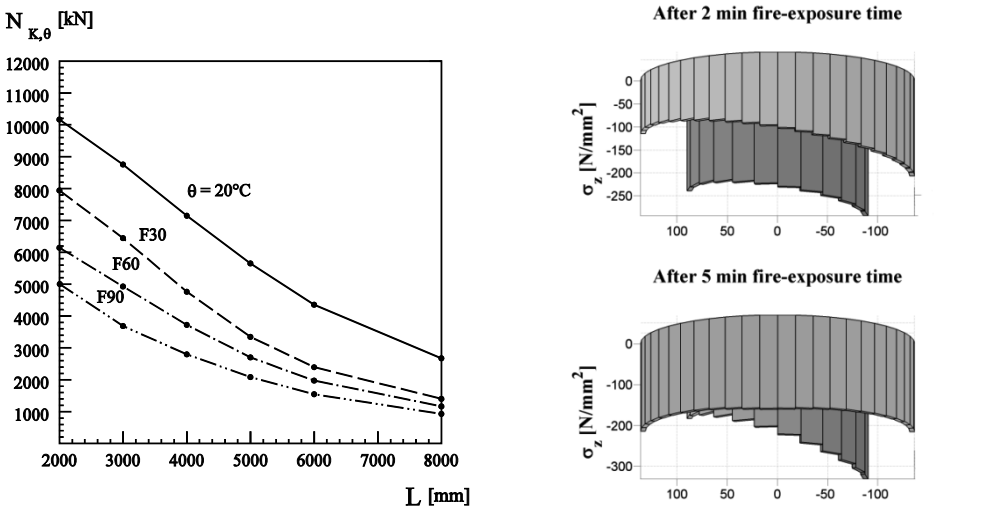


Figure 6: Curves for the buckling strength (left) and stress distributions over cross section (right).

www.EngineeringEBooksPdf.com

4 CONCLUSIONS

The structural fire behavior of concrete-filled circular hollow section columns with massive steel core has been numerically analyzed. A finite element model considering temperature-dependent material properties for concrete and steel as well as the bonding behavior between steel and concrete was proposed and applied to columns with different sections and buckling lengths. Results, including temperature-, end shortening-, deflection- and stress-fire exposure time curves, have been presented. The compatibility stresses caused by partly constrained thermal strains and the bonding behavior between steel and concrete have a strong effect on the fundamental load-carrying behavior and the fire resistance of the composite columns. The results of a parametric study have been used for developing curves for the ultimate column buckling strengths for various fire resistances. The finite element model developed in this study may be used for further analyzing the fundamental structural behavior of composite columns in fire and determining their fire resistances. Further analytical and numerical studies on the fire behavior of centrically and eccentrically loaded concrete-filled CHS columns with steel core are underway and will be presented on the conference.

REFERENCES

[1] Hanswille G. and Lippes M., Einsatz von hochfesten Stählen und Betonen bei Hohlprofil-Verbundstützen, *Stahlbau*, **77**(4), 296-307, 2008.

[2] Grandjean et al., Determination de la durée au feu des profils creux remplis de béton. Rapport final, Commission des Communautés Européennes, Rechereche Technique Acier, Luxembourg, 1981.

[3] Kordina K. and Klingsch W., Fire resistance of composite columns of concrete filled hollow sections. Research report. CIDECT 15 C1/C2-83/27, Germany, 1983.

[4] Lie T.T. and Caron SE, Fire resistance of circular hollow steel columns filled with siliceous aggregate concrete. Test results, internal report no. 570, Ottawa: Institute of Research in Construction, National Research Council of Canada, 1988.

[5] Lie T.T., Chabot M. and Irwin R.J., Fire resistance of circular hollow steel sections filled with bar-reinforced concrete, Internal Report No. 636, Institute for Research in Construction, National Research Council of Canada, Ottawa 1992.

[6] Myllymäki J., Lie T.T. and Chabot M., Fire resistance tests of square hollow steel columns filled with reinforced concrete, Internal Report No. 673, Institute for Research in Construction, National Research Council of Canada, Ottawa 1994.

[7] Kodur V.K.R. and Lie T.T., Fire resistance of circular steel columns filled with fibre-reinforced concrete, ASCE, *Journal of Structural Engineering*, Vol **122**, No. 7, 776-782, 1996.

[8] Ding, J., Wang Y.C., Realistic modelling of thermal and structural behaviour of unprotected concrete filled tubular columns in fire, *Journal of Constructional Steel Research*, **64**(10), 1086-1102, 2008.

[9] Zha X.X., FE analysis of fire resistance of concrete filled CHS columns, *Journal of Constructional Steel Research*, **59**(6), 769-779, 2003.

[10] Zienkiewicz O.C. and Taylor R.L., The Finite Element Method for Solid and Structural Mechanics, Sixth Edition, Elsevier Ltd., London, 2006.

[11] EN 1993-1-2. Eurocode 3: Design of steel structures – Part 1-2: General rules – Structural fire design, Brussels, 2006.

[12] EN 1992-1-2. Eurocode 2: Design of concrete structures – Part 1-2: General rules – Structural fire design, Brussels, 2006.

[13] ISO 834. Fire-resistance tests - Elements of building construction - Part 1: General requirements, 1999.

www.EngineeringEBooksPdf.com

SDSS'Rio 2010 STABILITY AND DUCTILITY OF STEEL STRUCTURES
E. Batista, P. Vellasco, L. de Lima (Eds.)
Rio de Janeiro, Brazil, September 8 - 10, 2010

BUCKLING OF CONCRETE FILLED STEEL HOLLOW COLUMNS IN CASE OF FIRE

Tiago A. C. Pires*; João P. C. Rodrigues* and J. Jéfferson Rêgo Silva**

* Faculty of Sciences and Technology of the University of Coimbra. Portugal.
e-mails: tacpires@yahoo.com.br; jpaulocr@dec.uc.pt

**Federal University of Pernambuco. Recife, Brazil.
e-mail: jjrs@ufpe.br

Keywords: fire, resistance, composite, steel, concrete, columns, buckling

Abstract. *The use of concrete filled steel hollow sections (CSHS) in building construction has increased in the last decade. This type of columns has several advantages linked to their high load bearing capacity and good fire performance. However, when the columns are inserted in a building structure, the effect of the restraining to their thermal elongation, change significantly their fire behavior. The high restraining forces developed during the fire, associated to the degradation of the mechanical properties, will lead to their buckling sooner than they are isolated. In order to study these phenomena a series of fire resistance tests on CSHS columns was carried out in University of Coimbra. Several parameters expected to have influence in the fire resistance of these columns were studied: the slenderness of the column, the load level, the stiffness of the surrounding structure, the percentage of steel reinforcement and the thickness of the concrete layer inside the column. This paper presents some results of the fire resistance tests and analyzes the different buckling phenomena observed in the tested columns.*

1 INTRODUCTION

The use of concrete filled steel hollow sections (CSHS) in construction is increasing due to many advantages such us the high load-bearing capacity, possibility of use small cross-sections, short construction times, avoid the use of formworks in casting and enhanced fire performance.

The behavior in fire situation of CSHS columns has been studied by several authors for years [1, 2], but the majority of these studies do not consider the restraining to their thermal elongation. The behavior of CSHS columns inserted in a building structure and subjected to fire is different from when isolated. Thermal restraint promoted by the surrounding structure plays a key role in the stability of the column. There are many ways in which the column can interact with the surrounding structure, including the restraining to its thermal elongation, change of the column bending stiffness relative to the adjacent structure, and increasing of P-δ effect due to its lateral deformation. The surrounding structure induces additional axial forces and moments on the column those varies with temperature and are dependent of the degree of axial and rotational thermal restraint [3, 4].

In 2000, Rodrigues [5] published the results of a series of 168 fire resistance tests on compressed steel elements with restrained thermal elongation. Parameters such us the slenderness of the surrounding structure, eccentricity of the load, type of end supports and restraining stiffness, were tested. It was showed that for the case of pin-ended elements with centered loading as higher is the stiffness of the surrounding structure smaller is the critical temperature. The buckling of the elements with centered loading occurred suddenly while the ones with eccentric loading occurred in a very gentle way.

In 1999, Valente & Neves [6] presented a numerical research using the FEM program FINEFIRE, to analyze the influence of axial and rotational restraint on the critical temperature of steel columns. It is

www.EngineeringEBooksPdf.com

showed that the increasing on axial restraint diminishes, in general, while the rotational restraint increases the critical temperature of steel columns.

In 1999, Kodur presented the results of a series of 75 fire resistance tests in CSHS columns [1]. The results suggested that the fire resistance of CSHS columns is between 60 and 120min. Reinforced concrete and steel fiber reinforced concrete CSHS columns presented more than 180min of fire resistance. The failure mode of these columns was global buckling especially for the cross sections with diameter smaller than 203mm.

The major conclusions of the studies carried out on the area are that the load level, the cross-sectional dimensions, the effective length of the column, the slenderness ratio, the degree of concrete filling of the column, the type of filling (i.e. filled with concrete, reinforced concrete or fiber reinforced concrete) had a significantly influence in the fire resistance.

However, the influence of other parameters, such as the strength of the concrete and steel, the type of aggregate and the load eccentricity had a moderated influence, while the steel reinforcement ratios, the thickness of the steel tube's wall and the axis distance of reinforcing bars to this wall had a small influence on the fire resistance.

In order to study the influence of several parameters that may affect the behavior of CSHS columns subjected to fire, a set of fire resistance tests have been performed in the Laboratory of Testing Materials and Structures of the University of Coimbra. Parameters such as the slenderness of the column, the load level, the stiffness of the surrounding structure, the percentage of steel reinforcement and the thickness of the concrete layer inside the column, were tested. In this paper several results of these tests are presented and the main failure modes of the columns discussed.

2 EXPERIMENTAL PROGRAM

2.1 Test set-up

Figure 1 presents a general view of the test set-up built in the Laboratory of Testing Materials and Structures of the University of Coimbra for studying the behavior in case of fire of building columns with restrained thermal elongation.

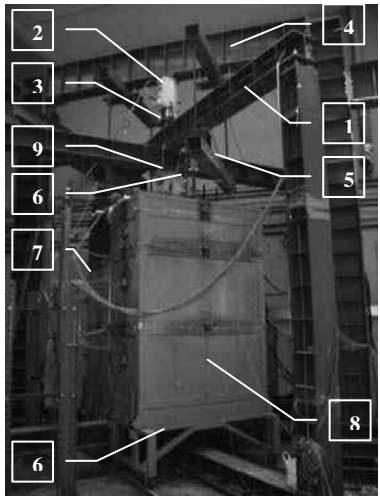


Figure 1. Test set-up

The system comprised a 3D restraining steel frame of variable stiffness (1) with the function of simulating the stiffness of the surrounding structure to the column subjected to fire. Several values of the

www.EngineeringEBooksPdf.com

stiffness of the surrounding structure were tested however in this paper will be presented only the results for 13kN/mm.

This restraining frame was composed by four columns, two upper beams and two lower beams, arranged orthogonally. The beams of this frame were made of steel profiles HEB300, grade S355. The connections between them were done by four M24 bolts, grade 8.8, except the connections between the columns and the upper beams that were used M27 threaded rods, grade 8.8.

The columns were subjected to a constant compressive load during the test that tried to simulate the serviceability load of the column when inserted in a real building structure. This load was a percentage of the design value of buckling load at room temperature calculated according to [7]. The threaded rods that connect the columns of the 3D restraining frame to its upper beams were initially completely loosened during the application of this load. This allowed the complete transfer of the load to the testing columns.

This load was applied by a hydraulic jack of 3MN (2) and controlled by a load cell (3) placed between the upper beam of the 3D restraining frame and the head of the piston of the hydraulic jack. The hydraulic jack was fixed in a 2D reaction frame (4), in which was also mounted a safety structure (5) to prevent damages in the experimental setup in case of sudden collapse of the column.

The axial displacements of the testing columns were measured by seven linear variable displacement transducers (LVDT), three in the top plate and four in the base plate (6). Their location is presented in figure 2.

Six cable LVDT (7) were used to measure the columns lateral deformation, in three different sections (S1, S2, and S3) and two orthogonal directions (figure 2).

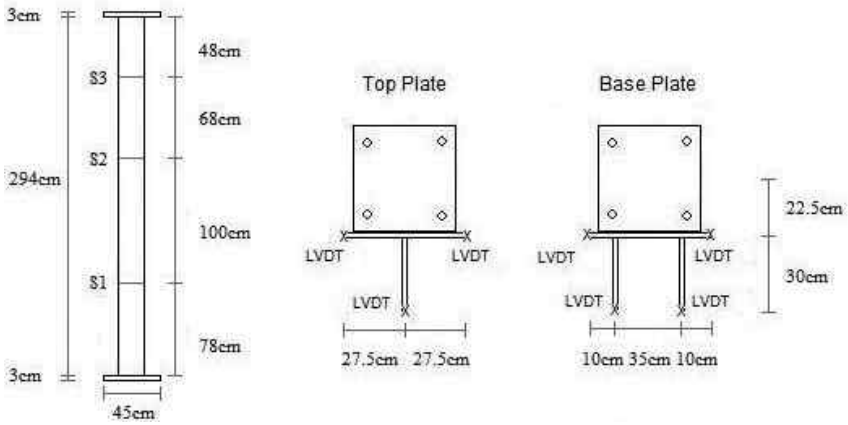


Figure 2. Position of LVDT in the testing columns

The thermal action was applied by a modular electric furnace (8) composed by two modules of 1m height and one module of 0.5m height, placed on top of each others, forming a chamber around the column of about 1.5m x 1.5m x 2.5m. There were three thermocouples type K, at middle height of each module, to measure the furnace temperatures.

A special device was built to measure the restraining forces generated by the testing column during the heating process (9). It consists of a hollow and stiff cylinder of high strength steel rigidly connected to an upper beam of the 3D restraining frame. On top of the testing column a massive steel cylinder was rigidly connected that entered into the hollow steel cylinder. The lateral surface of the massive cylinder was Teflon (PTFE) lined in order to avoid the friction between the cylinders.

The restraining forces were measured by a load cell of 3MN placed inside the hollow steel cylinder that was compressed by the massive cylinder due to the thermal elongation of the testing column during the fire resistance test.

www.EngineeringEBooksPdf.com

2.2 Specimens

The steel profiles used in the fabrication of the columns had external diameter of 219.1mm and 168.3mm, both with 6mm of thickness and steel grade S355.

The concrete was class C20/25 [8] filling all the cross-section or forming a ring of 50mm for the greater column sections and 40mm for the smaller column sections around the tube internal wall.

The longitudinal reinforcement of the concrete had diameter of 12mm for the greater column sections and 10mm for the smaller column sections and steel grade A400. The stirrups used had 6mm diameter spaced each other 200mm. The concrete covering of the reinforcing bars was 30mm.

The temperatures in the columns were measured by thermocouples type K placed in five cross-sections along the height (S1 to S5) as showed in figure 3.

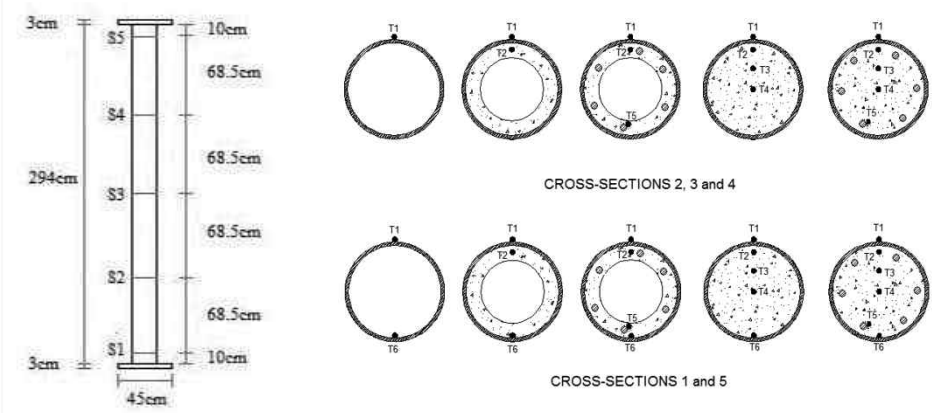


Figure 3. Position of thermocouples on test columns

2.3 Test plan

Table 1 presents part of the test plan already concluded and the correspondent failure modes of the test columns. The values of the serviceability load applied to the columns were 70 or 30% of the design value of the buckling load at room temperature ($N_{b,rd}$) [7].

The thermal action applied was the ISO 834.

Table 1: test plan and failure modes.

Column refer.	degree of concrete filling	cross-section (mm)	slenderness	reinforced concrete	$N_{b,rd}$ (kN)	Failure mode
A01	total	168.3	86.2	No	816 (70%)	global buckling
A03	total	168.3	86.2	No	350 (30%)	global buckling
A09	ring (40 mm)	168.3	78.5	No	775 (70%)	global/local buckling
A11	ring (40 mm)	168.3	78.5	No	332 (30%)	crushing
A13	--	168.3	63.1	--	589 (70%)	global/local buckling
A14	--	168.3	63.1	--	252 (30%)	global buckling
A15	total	219.1	66.2	No	1355 (70%)	global buckling
A17	total	219.1	66.2	Yes	1482 (70%)	global buckling
A18	total	219.1	66.2	No	581 (30%)	global buckling
A20	total	219.1	66.2	Yes	635 (30%)	global buckling

www.EngineeringEBooksPdf.com

Table 1: test plan and failure modes (cont.).

Column refer.	degree of concrete filling	cross-section (mm)	slenderness	reinforced concrete	$N_{b,rd}$ (kN)	Failure mode
A21	ring (50 mm)	219.1	59.5	No	1239 (70%)	global buckling
A23	ring (50 mm)	219.1	59.5	Yes	1269 (70%)	global/local buckling
A24	ring (50 mm)	219.1	59.5	No	531 (30%)	global buckling
A26	ring (50 mm)	219.1	59.5	Yes	544 (30%)	crushing
A31	--	219.1	48.1	--	874 (70%)	global/local buckling
A32	--	219.1	48.1	--	375 (30%)	global buckling

3 RESULTS

3.1 Restraining forces

Figure 4 presents some results of the development of the restraining forces on the test columns in function of the mean steel temperature. The restraining forces, due to the restraining to thermal elongation, start to increase up to a maximum and then decrease due to the degradation of the mechanical properties. The test was ended when the restraining forces reached again the initial applied load. The deformed shape of the columns presented in figures of the next section corresponds, more or less, to that instant.

Concerning the type of failure of the columns it can be observed that A13 and A31 presented a sudden buckling. The restraining forces diminished quite suddenly probably due to the inexistence of concrete inside the tube. The columns with concrete inside presented a more gentle way of failure. The degree of concrete filling of the columns didn't lead to great changes in the mode of failure.

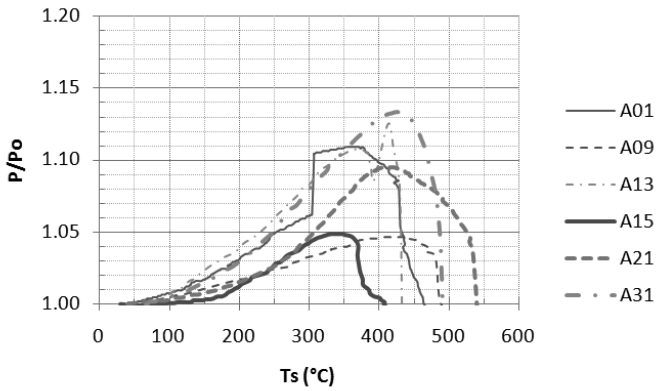


Figure 4. Restraining forces in function of the columns mean steel temperature

3.2 Failure modes

In general the failure mode of the columns was global buckling, in the major part of the cases, however local buckling also occurred in some cases (figure 6 - A09 and A13). The global buckling observed had a double curvature like a slight "s". As expected the failure mode is more clear in columns whose the applied load level was 70% $N_{b,rd}$ (figures 6 and 8).

www.EngineeringEBooksPdf.com

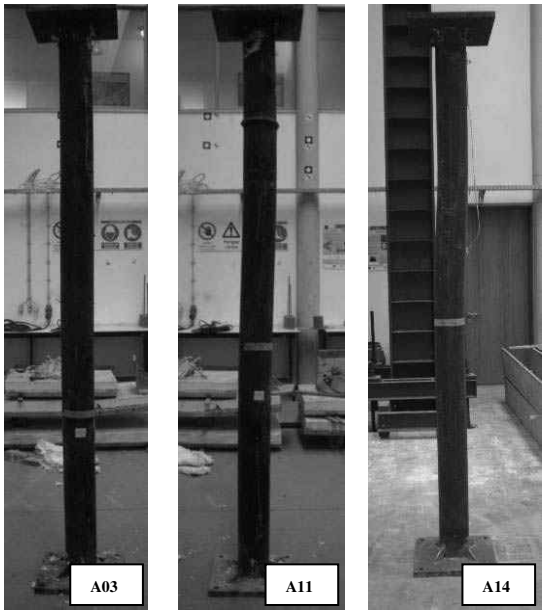


Figure 5. Columns totally filled with concrete (on left), with ring of concrete inside of 40mm (on center) and without concrete (on right), tube dia. = 168.3mm and load level =30% $N_{b,rd}$

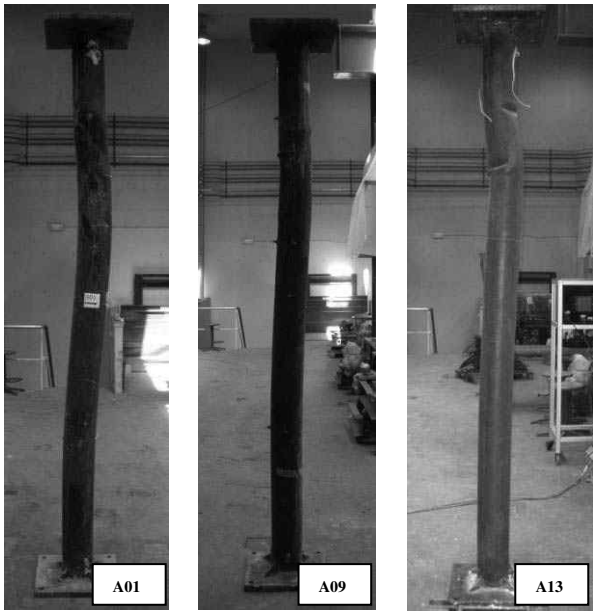


Figure 6. Columns totally filled by concrete (on left), with ring of concrete inside of 40mm (on center) and without concrete (on right), tube dia. = 168.3mm and load level=70% $N_{b,rd}$

www.EngineeringEBooksPdf.com

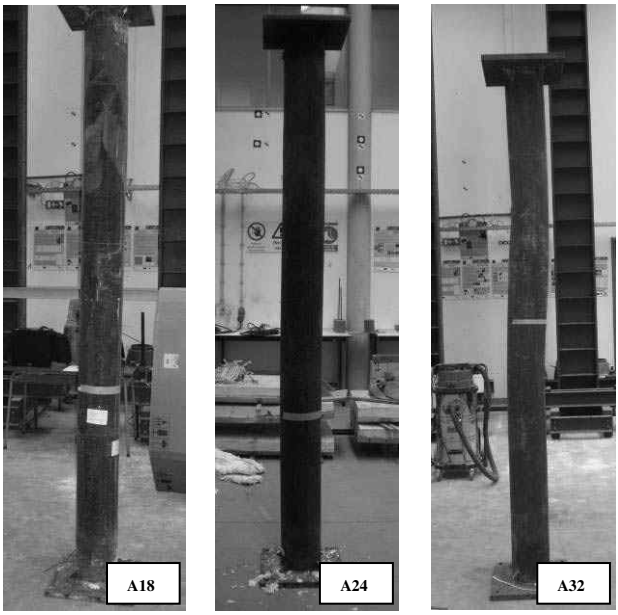


Figure 7. Columns totally filled by concrete (on left), with ring of concrete inside of 40mm (on center) and without concrete (on right)), tube dia. = 219.1mm and load level=30% $N_{b,rd}$

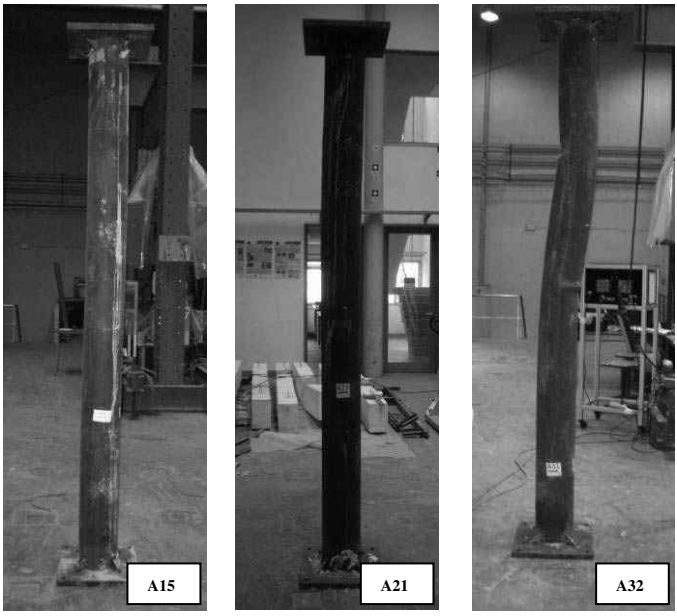


Figure 8. Columns totally filled by concrete (on left), with ring of concrete inside of 40mm (on center) and without concrete (on right)), tube dia. = 219.1mm and load level = 70% $N_{b,rd}$

www.EngineeringEBooksPdf.com

Some columns presented failure by crushing (figure 5 – A11). For the load level of 70% $N_{b,rd}$ was not observed any failure by crushing.

The deformed shape of the columns was softer in the concrete filled columns than in bare steel columns. The concrete core remains colder than the steel profile in the fire event, avoiding local buckling and reducing the final deformed shape of the column. In this way the concrete inside the column enhances its behavior when subjected to fire. The local buckling was more evident in bare steel columns than in columns filled with concrete (figures 6 and 8).

The increase in columns cross-section reduced the slenderness of the column and the columns deformation shape after tests.

CONCLUSIONS

This paper reported the behavior of steel hollow columns, completely or partially filled with concrete, subjected to fire. They were presented the different modes of failure of these columns. Based on the results the following suggestions may be addressed.

- The load level of 70% $N_{b,rd}$ is too high for fire design of steel hollow columns and is advisable the use of a lower load level.
- The concrete inside the hollow column, especially when completely filing, it improves the fire behavior and reduces the possibility of local buckling.
- The reduction in the slenderness of the column enhances the behavior of the columns under fire.

This experimental study is part of a major research program that it is being carried out at the University of Coimbra. Others results and parameters that influence the fire resistance is also being investigated and will be presented in future.

REFERENCES

[1] Kodur V.K.R. “Performance-based fire resistance design of concrete-filled steel columns”. *Journal of Constructional Steel Research*, **51**, 21-36, 1999.

[2] Han L.H., Yang, Y.F., Xu, L. “An experimental study and calculation on the fire resistance of concrete-filled SHS and RHS columns”. *Journal of Constructional Steel Research*, **59**, 427-452, 2003.

[3] Ali F.A., Shepherd A., Randall M., Simms I.W., O’Connor D.J., Burgess I. “The effect of axial restraint on the fire resistance of steel columns”. *Journal of Constructional Steel Research,* **46** (1-3), paper nº 117, 305-306, 1998.

[4] Neves I.C., Valente J.C., Rodrigues J.P.C. “Thermal restraint and fire resistance of columns”. *Fire Safety Journal*, **37**, 753-771, 2002.

[5] Rodrigues J.P.C., Neves I.C., Valente J.C. “Experimental research on the critical temperature of compressed steel elements with restrained thermal elongation”. *Fire Safety Journal*, **35**, 77-98, 2000.

[6] Valente J.C. & Neves I.C. “Fire resistance of steel columns with elastically restrained axial elongation and bending”. *Journal of Structural Steel Research,* **52** (3), 310-331, 1999.

[7] EN 1994-1-1: Design of composite steel and concrete structures. part 1-1: general rules and rules for buildings”. *European Committee for Standardization*, 2005.

[8] NP EN 206-1:2007 - “Concrete Part 1: Specification, performance, production and conformity”, 2007, p. 84.

[9] EN 1994-1-2: Design of composite steel and concrete structures. part 1-2: general rules – structural fire design”. *European Committee for Standardization*, 2005.

[10] .Lie T.T. and Kodur V.K.R. “Fire resistance of steel columns filled with bar-reinforced concrete”. Journal of Structural Engineering, 122 (1), 30-36, 1996.

www.EngineeringEBooksPdf.com

SDSS'Rio 2010 STABILITY AND DUCTILITY OF STEEL STRUCTURES
E. Batista, P. Vellasco, L. de Lima (Eds.)
Rio de Janeiro, Brazil, September 8 - 10, 2010

BUCKLING OF STEEL AND COMPOSITE STEEL AND CONCRETE COLUMNS IN CASE OF FIRE

Antonio M. Correia* and João Paulo C. Rodrigues **

* Superior School of Technology and Management of Oliveira do Hospital, Portugal
e-mail: antonio.correia@estgoh.ipc.pt

** Faculty of Sciences and Technology of University of Coimbra, Portugal
e-mail: jpaulocr@dec.uc.pt

Keywords: fire, resistance, buckling, steel, concrete, columns, walls.

Abstract. *Bare steel columns are known to have a very low fire resistance. The high thermal conductivity and the sudden decrease of the steel yield stress and Young Modulus in function of the temperature are responsible for this behaviour. The purpose of this study is to compare different modes of failure of building steel columns. The buckling of the columns is strongly influenced by the contact with other elements such as brick walls. Three types of situations were compared: steel columns embedded on brick walls, bare steel columns and composite columns made of partially encased steel sections. The deformed shapes of the columns are analyzed in this work.*

1 INTRODUCTION

The behavior of a steel and composite steel and concrete structure is strongly influenced by the high temperatures attained in the structural elements in case of fire. In columns the axial forces will increase up to a maximum and then reduce with their buckling. This increasing of axial forces result from the axial restraint imposed by the surrounding structure to the column subjected to fire and the decreasing from the degradation of the mechanical properties of steel and concrete with the temperature. This phenomenon has been studied for years, both experimentally and numerically, by several authors [4, 5].

Buckling can be substantially different when the column is completely engulfed in fire or embedded on a building wall. In the last case the high thermal gradients along the cross-section is responsible for high thermal stresses causing thermal bowing. An inversion of bending moments along the height of the column lead to lateral displacements moving the column from one to the other side.

In the Laboratory of Testing Structures and Materials of the University of Coimbra, Portugal, a large number of fire resistance tests were conducted in steel and composite steel and concrete columns, with restrained thermal elongation, embedded or not on brick walls [1, 2, and 3].

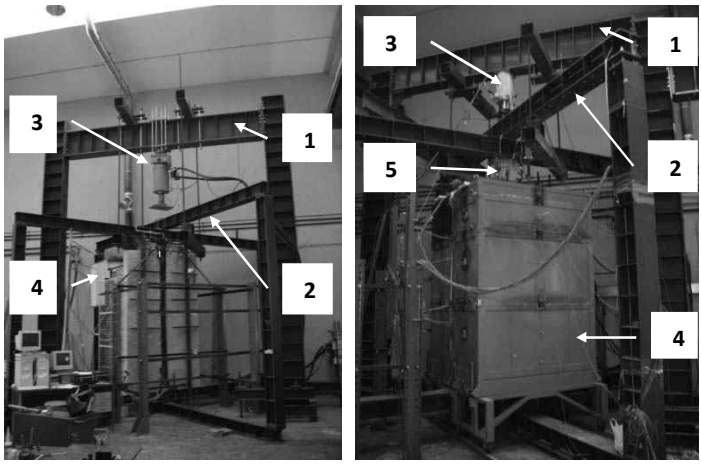
2 EXPERIMENTAL PROGRAMME

Figure 1 presents the test set-up, which were especially constructed in the Laboratory of Testing Materials and Structures of the University of Coimbra, for fire resistance tests on building columns embedded on brick walls (a) and isolated (b), both with restrained thermal elongation.

This system comprised a 3D restraining steel frame of variable stiffness (2) with the function of simulating the stiffness of the surrounding structure to the column subjected to fire. The use of a three-

www.EngineeringEBooksPdf.com

dimensional frame allowed to take into account not only the axial stiffness but also the rotational stiffness, such as observed in a real structure. The restraining frame was composed by four columns, two upper beams and two lower beams, placed orthogonally. The beams of this frame were HEB 300 steel profiles, grade S355, in the test set-up for isolated columns (fig. 1(b)), and HEA200 in the test set-up for columns embedded on brick walls (fig. 1(a)). The connections between the structural elements of the restraining frame were performed with four M24 bolts, grade 8.8, except the connections between columns and the upper beams (2) where threaded rods M27, grade 8.8, were used. The stiffness of this restraining frame was varied from one to other test by changing the position of its columns.
In tests the columns were subjected to a constant compressive load that tried to simulate the serviceability load of the column when inserted in a real building. This load was 70% and 30% of the design value of buckling resistance at room temperature calculated according to Eurocodes 3 and 4 parts 1.1. [6, 7].



a) b)

Figure 1: Experimental set-up a) columns embedded on walls b) isolated columns

This load was applied by a hydraulic jack of 3MN and was controlled by a load cell of 1MN placed between the upper beam of the 3D restraining frame and the hydraulic jack. The hydraulic jack was placed in a 2D restraining frame (1), in which was also placed a safety structure to prevent sudden collapse of the specimen.
In the test set-up for testing bare columns (fig. 1b), the thermal action was applied by a modular electric furnace (4). This furnace is composed by two modules of 1m and one module of 0.5m height, placed on top of each others, forming a chamber around the column of about 1.5m x 1.5m x 2.5m. In the testing set-up for columns embedded on walls, the thermal action was applied by a gas fired furnace, 2 meters height and 1 meter wide (4) (fig. 1a). Both furnaces followed approximately the standard ISO 834 fire curve.
A special device was built to measure the restraining forces generated in the testing column during the fire resistance test (5). It consists of a hollow and stiff steel cylinder, rigidly connected to an upper beam above the specimen. On top of the specimen was rigidly connected a massive steel cylinder that entered into the hollow cylinder. The massive cylinder was Teflon lined in order to prevent friction with the hollow cylinder. Inside the hollow cylinder there was a compression load cell of 3 MN to measure the restraining forces.

www.EngineeringEBooksPdf.com

2.1 Steel columns embedded on brick walls

In this series, fourteen tests were performed, testing different orientations of the steel profile, with the web perpendicular and parallel to the wall surface, different thicknesses of the wall, two steel cross-sections, HEA200 and HEA160 (table 1). Eight tests were performed without loading. The tests with loading were performed with an applied load of 70% of the design value of the buckling load at ambient temperature, $N_{Rd,20}$. The thick wall was approximately of the same width of the steel profile width. The thin wall was approximately 75% wide of the steel profile width (table 1).

Table 1 – Test plan for steel columns embedded on walls

Test Number	Steel Profile	Orientation of web to furnace	Wall width (mm)	Load (kN)	Stiffness (kN/mm)	Type of buckling
E01	HEA 160	parallel	140	704 (70% $N_{Rd,20}$)	7	Bending
E02	HEA 160	perpendicular	140	704 (70% $N_{Rd,20}$)	7	Bending
E03	HEA 200	parallel	180	-	7	-
E04	HEA 200	perpendicular	180	-	7	-
E05	HEA 160	parallel	140	-	7	-
E06	HEA 160	perpendicular	140	-	7	-
E07	HEA 160	parallel	140	621 (70% $N_{Rd,20}$)	7	Bending
E08	HEA 200	parallel	140	-	7	-
E09	HEA 200	perpendicular	140	-	7	-
E10	HEA 160	parallel	100	-	7	-
E11	HEA 160	perpendicular	100	-	7	-
E12	HEA 160	parallel	100	621 (70% $N_{Rd,20}$)	7	Bending
E13	HEA 160	perpendicular	100	704 (70% $N_{Rd,20}$)	7	Bending
E14	HEA 160	parallel	100	1088 (70% $N_{Rd,20}$)	7	Bending

2.2 Steel bare columns

Table 2 describes the second series of fourteen tests, referring to isolated steel bare columns, totally engulfed in fire that resulted in a quite uniform heating within the cross section.

Table 2 – Test plan for isolated steel bare columns

Test Number	Steel Profile	Load (kN)	Stiffness (kN/mm)	Eccentricity	Type of buckling
E15	HEA 200	1000 (70% $N_{Rd,20}$)	13	Centered	local+global
E16	HEA 200	224 (70% $N_{Rd,20}$)	13	Two axis	local+global
E17	HEA 200	570 (70% $N_{Rd,20}$)	13	One axis	local+global
E18	HEA 160	621 (70% $N_{Rd,20}$)	13	Centered	global
E19	HEA 200	428 (30% $N_{Rd,20}$)	13	Centered	local+global
E20	HEA 160	266 (30% $N_{Rd,20}$)	13	Centered	global
E21	HEA 160	621 (70% $N_{Rd,20}$)	45	Centered	global
E22	HEA 160	266 (30% $N_{Rd,20}$)	45	Centered	global
E23	HEA 200	1000(70% $N_{Rd,20}$)	45	Centered	local+global
E24	HEA 200	266 (30% $N_{Rd,20}$)	45	Centered	local+global
E25	HEA 200	428 (30% $N_{Rd,20}$)	128	Centered	local+global
E26	HEA 160	266 (30% $N_{Rd,20}$)	128	Centered	global
E27	HEA 200	1000 (70% $N_{Rd,20}$)	128	Centered	local+global
E28	HEA 160	621 (70% $N_{Rd,20}$)	128	Centered	global

www.EngineeringEBooksPdf.com

Two different profile cross-sections, HEA200 and HEA160, leading two different slenderness, 50.6 and 63.3, two different load levels, 70% and 30% of $N_{Rd,20}$, and three different stiffness of the surrounding structure, 13, 45 and 128 kN/mm, were tested. The two other tests, E16 and E17 were performed only for HEA200, with the lower stiffness of the surrounding structure, 13kN/mm, but with eccentric loading: E16 with eccentricities of 0.2m in two directions and E17 with one eccentricity of 0.2m in one direction.

2.3 Composite steel and concrete columns

Table 3 describes the third series of twelve tests on partially encased H steel sections. The profiles cross-sections were HEA200 and HEA160, the load levels were 30 and 70% of $N_{Rd,20}$ [8, 9] and the stiffness of surrounding structure were 13, 45 and 128 kN/mm. Concrete C25/30 was used between flanges and the longitudinal reinforcement steel and the stirrups were A500. In this series no tests with eccentric loading were performed.

Table 3 – Test plan for composite steel and concrete columns

Test Number	Steel Profile	Load (kN)	Stiffness (kN/mm)	Reinforcement	Type of buckling
E29	HEA 160	261(30% $N_{Rd,20}$)	128	4 bars – 16mm + stirrups 6mm //0.15m	global
E30	HEA 160	610(70% $N_{Rd,20}$)	128	4 bars – 16mm + stirrups 6mm //0.15m	global
E31	HEA 200	508(30% $N_{Rd,20}$)	128	4 bars – 20mm + stirrups 8mm //0.15m	global
E32	HEA 200	1185(70% $N_{Rd,20}$)	128	4 bars – 20mm + stirrups 8mm //0.15m	global
E33	HEA 160	261(30% $N_{Rd,20}$)	45	4 bars – 16mm + stirrups 6mm //0.15m	global
E34	HEA 160	610(70% $N_{Rd,20}$)	45	4 bars – 16mm + stirrups 6mm //0.15m	global
E35	HEA 200	508(30% $N_{Rd,20}$)	45	4 bars – 20mm + stirrups 8mm //0.15m	global
E36	HEA 200	1185(70% $N_{Rd,20}$)	45	4 bars – 20mm + stirrups 8mm //0.15m	global
E37	HEA 160	261(30% $N_{Rd,20}$)	13	4 bars – 16mm + stirrups 6mm //0.15m	global
E38	HEA 160	610 (70% $N_{Rd,20}$)	13	4 bars – 16mm + stirrups 6mm //0.15m	global
E39	HEA 200	508(30% $N_{Rd,20}$)	13	4 bars – 20mm + stirrups 8mm //0.15m	global
E40	HEA 200	1185(70% $N_{Rd,20}$)	13	4 bars – 20mm + stirrups 8mm //0.15m	global

3 RESULTS

3.1 Steel columns embedded on walls

The steel columns embedded on walls had a differential heating characterized by greater temperatures on the exposed side, leading to huge thermal gradients within the cross-section. This difference of temperatures leads to a greater thermal expansion of the heated zone of the steel profile.

www.EngineeringEBooksPdf.com

Due to the restraining prevented by the surrounding structure the thermal elongation was transformed in stresses, which being greater on the hot side, lead to bending moments, and the columns trends to bend instead of buckle.

The thermal bowing is a phenomenon in which the differential thermal action leads to an inversion of the deflection if the structural element, from one to the other side. This was observed in test E02, as showed in figures 2a) and 2b). This column has suffered at first, a deflection towards the side of the fire, and afterwards a deflection towards the opposite side, outside of the fire.

This is most likely to happen in steel columns with the web perpendicular to the wall surface, but it can also occur in case of the steel profile placed with the web parallel to the wall surface, as long as the upper beams are strong enough to withstand the applied load.

The differential heating provoked a redistribution of bending moments, moving from one to the other side, following the lateral displacements of the column.



a) b)

Figure 2: Column E02 after test - web perpendicular to wall – wall thickness 140mm - HEA 160



a) b)

Figure 3: Column E13 after test - web perpendicular to wall – wall thickness 100mm - HEA 160

In figures 3a) and 3b), is observed column E13 after test. A HEA160, with the web perpendicular to the wall surface, is tested. The wall is 100mm thick, about 65% the column width. In this case, the

www.EngineeringEBooksPdf.com

thermal gradient through the columns cross-section was not as strong as in test E02, leading to buckling in the plane of the wall. The wall plays an important role in preventing the sudden failure of the column.

Figure 4 presents the evolution of restraining forces versus mean temperature of the steel columns, for tests E07 and test E12. It is observed that the decreasing of restraining forces after the maximum is quite gentle meaning with this failure by bending. Also, it was concluded that the thicker walls provide a greater insulation to the steel profile, giving as result a lower increase of the restraining forces and higher fire resistance.

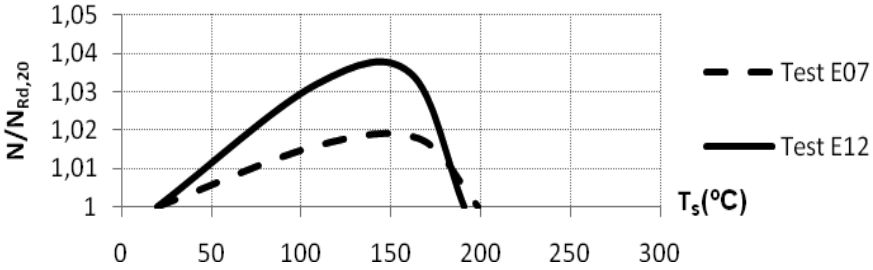
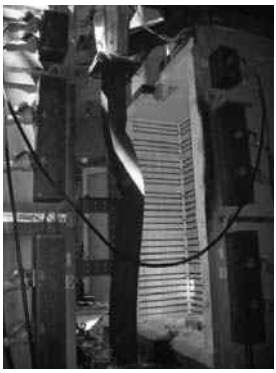


Figure 4: Restraining forces on columns embedded on walls in function columns mean steel temperature

3.2 Steel bare columns





a) local buckling b) global buckling

Figure 5: Column E15 after test



Figure 6: Column E18 after test

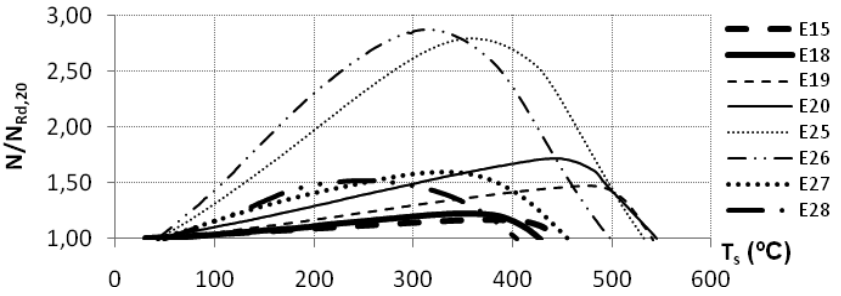


Figure 7: Restraining forces in bare steel columns in function of columns mean steel temperature

www.EngineeringEBooksPdf.com

Despite of the detrimental effect caused by the contact with the walls, leading to bending moments to develop in the cross section of the columns, the uniform heating in bare steel columns leads to a faster heating of the cross section.

The buckling modes observed in the steel bare columns were global and local buckling for columns HEA200 (fig. 5a) and 5b)) and only global buckling for columns HEA160 (fig. 6). The columns presented in figures 5 and 6 were tested with the load level of 70% and stiffness of the surrounding structure of 13 kN/mm.

Figure 7 presents the evolution of restraining forces in bare steel columns in function of columns mean steel temperature. It can be observed that the lower load levels and higher the stiffness of surrounding structure, the higher the restraining forces. The restraining forces decrease in the major part of the cases not so sudden meaning global buckling of the columns.

3.3 Composite steel and concrete columns

In composite steel and concrete columns regardless the load level, type of cross section, and stiffness of surrounding structure, was only observed global buckling however with detachment of the concrete between flanges (fig. 8a)).



a) b) c)

Figure 8: Column of test E38 after test

As it can be seen in figure 8b), the concrete between flanges prevented the buckling of these. The failure of some composite columns was observed with the detachment of the stirrups from the web allowing the concrete to move away as a block (fig. 8c)).

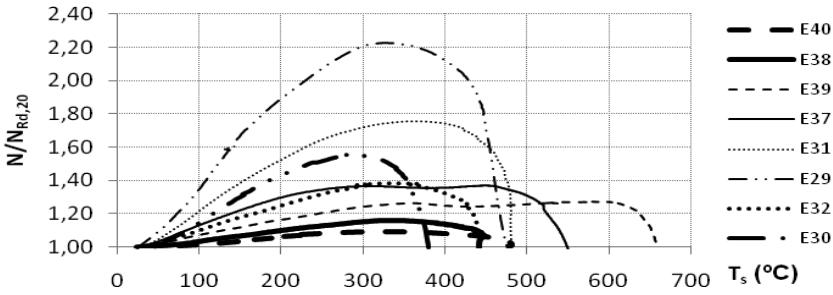


Figure 9: Restraining forces on composite columns in function of columns mean steel temperature

www.EngineeringEBooksPdf.com

Figure 9 presents the evolution of restraining forces in the composite steel concrete columns in function of mean steel temperature. The conclusions are the same as for the steel columns. The lower the load level and the higher the stiffness of the surrounding structure the higher the restraining forces. A more pronounced descending of the restraining forces is observed in this case that could be associated to the detachment of the concrete between flanges.

4 CONCLUSIONS

The main conclusions regarding steel columns are related to thermal bowing. Columns in contact with walls under a fire event are submitted to a huge thermal gradient which is responsible for an inversion of displacements and bending moments from the heated to the unheated side of the column. The columns in this case bend instead of buckle. The walls have a favorable effect in preventing local buckling of column flanges and in case of columns with the web perpendicular to the wall, prevent buckling around minor axis, providing an increase on fire resistance.

Steel bare columns failed by buckling around minor axis. Local buckling was observed only in columns HEA200.

Composite steel-concrete columns were found to be very effective in resisting to fire. Besides having a higher load-bearing resistance, the concrete between flanges is effective in preventing local buckling and providing thermal insulation.

The load level has a great influence in the deflections in the instant of collapse. Higher load level leads to higher deflections for both types of columns.

REFERENCES

[1] Correia, A. M, Rodrigues, J. P. C, Silva, V. P. "Studies on the fire behaviour of steel columns embedded on walls", *Proc. of 11th Interflam*. London. 2007.

[2] Correia, A. M., Rodrigues, J. P., Silva, V. P., "Experimental Research on the Fire Behaviour of Steel Columns Embedded on Walls", Proc. of International Conference Applications of Structural Fire Engineering, Prague, Czech Republic, 2009.

[3] Correia, A. M., Rodrigues, J. P., Silva, V. P., Laim, L., "Section factor and steel columns embedded in walls", Proc. of 11th Nordic Steel Construction Conference, Malmö, Sweden, 2009.

[4] Neves, I. C., Valente J. C., Rodrigues J.P.C., "Thermal restraint and fire resistance of columns" Fire Safety Journal", vol. 37, England, 753-771, 2002.

[5] Rodrigues J. P.C., Neves I.C., Valente J.C. "Experimental Research on the critical temperature of compressed steel elements with restrained thermal elongation", vol. 35, England, 77-98, 2000.

[6] EN1993-1-1:2005. "Design of steel structures – part 1-1: General Rules and rules for buildings", CEN, Brussels.

[7] EN1993-1-2:2005. "Design of steel structures – part 1-2: General Rules – Structural fire design", CEN, Brussels.

[8] EN1994-1-1:2005. "Design of composite steel and concrete structures – part 1-1: General Rules and rules for buildings", CEN, Brussels.

[9] EN1994-1-2:2004. "Design of composite steel and concrete structures – part 1-2: General Rules – Structural fire design", CEN, Brussels.

www.EngineeringEBooksPdf.com

SDSS'Rio 2010 STABILITY AND DUCTILITY OF STEEL STRUCTURES
E. Batista, P. Vellasco, L. de Lima (Eds.)
Rio de Janeiro, Brazil, September 8 - 10, 2010

A COUPLED FLUID-THERMAL-MECHANICAL ANALYSIS OF COMPOSITE STRUCTURES UNDER FIRE CONDITIONS

Julio Cesar Gonçalves da Silva and Alexandre Landesmann

Civil Engineering Program, Federal University of Rio de Janeiro (COPPE/UFRJ)
POB 68.506, Rio de Janeiro/RJ, 21945-970, Brazil
e-mails: jcsilva@coc.ufrj.br, alandes@coc.ufrj.br

Keywords: Fire-design Analysis, Steel-Concrete Structures, Computational Fluid Dynamics.

Abstract. *This paper presents a numerical investigation on a unidirectional procedure joining fluid and thermo-mechanical modeling for assessing composite steel-concrete structures exposed to fire. The first stage of the analysis consists of an evaluation of fire dynamics, which is carried out utilizing a 3D Computational Fluid Dynamics (CFD) model. The temperature variation of fire-exposed members is performed in the second-phase, accounting for the fire elapsed time, obtained CFD heat fluxes and temperature-dependent thermal properties of materials. Finally, the structural behavior is evaluated by a FE-based approach including stress–strain-temperature relationships for steel and concrete, as covered by parts 1.2 of Eurocodes. A real case study is analyzed utilizing the proposed CFD-FEM approach. Obtained results indicate that joined 3D fluid-thermal-mechanical models can be incorporated into the current fire-design analysis, representing a more realistic and economical fire-design verifications.*

1 INTRODUCTION

Fire design is used to assure that a structure designed for normal room temperatures can also resist the additional effects induced by fire, for a *fire resistance time*. Simple calculation models are given in some design codes, *e.g.* parts 1.2 of Eurocodes [1,2]. However, these rules are restricted to a first-order small deflections theory, in which resistance is limited to the plastic or buckling capacity. Therefore, members will have a relatively low survival in fire and would require expensive fire protection. Under fire conditions, large deflections may be tolerated when considerable additional load carrying capacity is designed to avoid structural collapse. In this condition, the structural behavior is mainly governed by the change of geometry, where the behavior of beams will vary from bending to catenary action, and the beneficial tensile membrane action can develop in structural floor slabs. In recent years, a number of researchers have developed and applied complex numerical *FE*-based modeling to simulate the structural behavior of steel, concrete and composite structures in fire conditions [3,4,5]. On the other hand, dedicated fire CFD (*Computational Fluid Dynamics*) codes have also been widely available (*e.g.*, SMARTFIRE® and NIST-FDS®) and largely used for fire field modeling, making it more accessible to the fire engineer with limited CFD experience, to simulate the actual fire dynamics and scenarios. CFD model solves numerically the *Navier-Stokes* equations, which are based on the assumption of low speed, thermally-driven flow with a special emphasis on smoke and heat transport from fires [6]. Conversely, very few works are dedicated to the investigation of the development of actual fires in real buildings (works of [7,8] deserve to be specially mentioned). The differences in numerical techniques, spatial and temporal length scales, and the complexity of the computer codes make the development of an efficient coupled analysis of fire–structure interactions not an easy task.

In this context, this paper presents a one-way coupling procedure that has been developed based on the CFD code SMARTFIRE and the FEM code VULCAN, making it possible to perform an accurate global analysis of buildings under fire conditions [9]. The proposed approach for integrating the CFD and solid-phase (thermal and structural response) models are divided in 3-phase steps (1, 2, and 3, respectively denoted as *Fluid*, *Thermo*

www.EngineeringEBooksPdf.com

and *Mechanical*), which are described in the following sections of this paper. Calculations are considered to be independently, *i.e.*, with a loosely coupling. In this approach, the CFD-fluid results (*phase 1*), *i.e.*, gas temperatures, velocities, chemical species, etc. - within the fluid domain of a building geometry in the presence of a given fire source [10], are used to perform the thermal response (*phase 2*) of exposed members, and finally adopted in the calculation of the associated mechanical response structural elements (*phase 3*). The advantage of the one-way coupling include: (*i*) computational efficiency - a single CFD simulation to be used for many subsequent structural analysis calculations and (*ii*) it allows the CFD and structural modeling to be performed independently by experts in their respective disciplines [7]. Two-way coupling should be used in more elaborate treatments where the predicted response of the structure is coupled back to the CFD codes.

2 NUMERICAL SIMULATION

2.1 CFD Simulation (phase 1)

CFD is the analysis of systems involving fluid flow, heat transfer and associate phenomena such as chemical reactions by means of a computer-based simulation [6]. CFD requires the subdivision of the domain into a number of *smaller*, non-overlapping sub-domains, as shown in Fig.1(a), generating thus a mesh (or grid) of cells (elements or control volumes) covering the whole domain. Furthermore, CFD models calculate changes in each cell by using the fundamental equations of fluid dynamics[6]. They consist generally of a set of three-dimensional, time-dependent and nonlinear partial differential equations expressing the: (*i*) conservation of mass, (*ii*) momentum and (*iii*) energy.

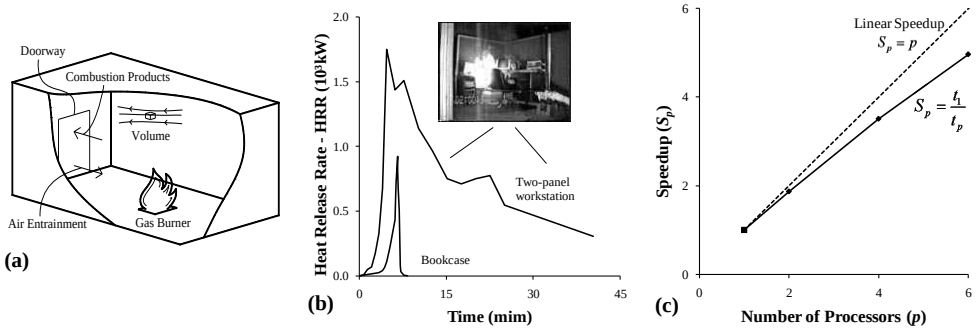


Figure 1: (a) Infinitesimal fluid element approach [6] and (b) HRR curves (Heat Release Rate) used in the present CFD analysis, (c) Speedup (S_p) curve of computational job compared to the *linear speedup*.

2.1.1 Heat Release Rate (HRR)

Calculations of fire behavior in buildings are not possible unless the Heat Release Rate (HRR) of the fire is known [11]. This is the rate at which the combustion reactions produce heat. It is thought to be the most important variable in fire hazard, as well as, an essential characteristic that describes quantitatively the fire development [12]. In practice, the HRR is directly obtained through an experimental measuring program, by means of open-burning HRR calorimeters. In the present paper, two main modular furniture units are implemented on the CFD analysis model: (*i*) a 3-shelf wood *bookcase* with files and (*ii*) *a two-panel workstation* (office worker cubicles). The corresponding adopted experimental HRR curves for each fire object are shown in Fig.1(b). The bookcase contained about 480 kg of a paper fuel load in shelving units totaling 1.67 m^2 of the floor area [11]. This amount corresponds to a fire of approximately 1 MW lasting about 7 minutes. It should be noted that, in most bookcase storage furniture, the fire hazard is created by the contents, not by the furniture item itself. Office workstations have been tested in several projects at NIST (more details at NIST website: *http://fire.nist.gov/fire/fires/fires.html*). As observed in Fig.1(b), quite severe fire conditions can be generated by this kind of furniture combination. As presented, fires of nearly 1.7 MW were recorded from the burning of a single person's workstation. For the present implementation (Fig.1b) a complete workstation with a combustible mass of about 750 kg is considered.

www.EngineeringEBooksPdf.com

2.1.2 Parallel implementation of CFD codes

The excessive computational resource, required to perform reliable CFD fire simulations, has been considered to be a significant drawback preventing the widespread use of fire-field modeling [13]. In this context, parallel processing has the potential to meet this computational demand at a reasonable processing cost, instead of increasing computational power of single PCs [14]. In the present work, the parallel performance of the CFD-based fire modeling code has been implemented on a homogeneous network (1Gbps) of 6 PENTIUM 4HT (2.4 Ghz, 512Kb, 1Gb RAM, 400 Mhz). This network configuration was tested with a single fire modeling scenario consisting of approximately 67,000 cells. A systematic partitioning of the problem domain into a number of identical sub-domains was carried out. Each sub-domain is computed on a separate processor and runs its own CFD code. At the boundary of the domain partitions each sub-domain needs to communicate with its neighboring sub-domain to exchange necessary data. Fig.1(c) presents the relative speedup of the proposed computational job compared to the speed of a *linear speedup* test (where: p is the number of processors, t_1 is the execution time of the serial algorithm, t_p is the execution time of the parallel algorithm with p processors). As observed (Fig.1c), the increase in speed could dramatically reduce the spent time, or increase the amount of work that can be achieved by the fire engineer. The proposed case required approximately 8h and 46min to run in a single processor, while, this job was completed within 1h 46min with 6 parallel processors. Although, the performed test is related to a simplified case studied [10], the obtained results indicate that the CFD parallel implementation can be assumed to efficiently solve large fire field modeling problems. Moreover, this can be achieved on non-specialized PC equipment which may typically exist in many fire safety engineering offices [13].

2.2 FEM Thermal (phase 2)

The distribution of temperature in a structure is of great importance, not only because of the degradation in material properties in heated zones but also for secondary effects caused by thermal elongation. Coupling between fire dynamics and structural analysis in building fires (*i.e.* between *phases 1* and *3*), is largely due to radiative heat transfer from combustion products to structural elements [7]. Based on this assumption, the present thermal analysis approach states that the radiant heat flux φ incident upon the surface of the element is related to the local gas temperature T (*e.g.*, from CFD) by the formula $\varphi = erT^4$ (e is the emissivity and r is the Stefan–Boltzmann constant $5.67 \cdot 10^{-8}$ W/m^{2}K^4). Therefore, given a spatially surrounding temperature and a ''time–temperature curve'' the thermal environment of the enclosure is specified and attention can be directed to calculate the temperature in the structural elements (*phase 2*). Hence, in order to obtain the members' temperature evolutions as a function of the elapsed fire duration, two approaches were employed: (*i*) a simplified transient temperature equation [2], and (*ii*) a 2D nonlinear heat transfer finite model incorporated in the code SAFIR [15]. For the applications presented in this paper, temperature evolution obtained by both approaches resulted in very close results; however, FEM results were preferred as they seemed to be more accurate.

2.3 FEM Structural (phase 3)

The FEM analysis model reported in this paper – to simulate the 3D structural behavior of reinforced concrete slabs and composite steel-concrete beam-column members exposed to fire – was incorporated within the numerical software VULCAN [3], developed at the University of Sheffield (UK). The beam-column element used in this paper [4] is a three-noded line element with each node having six degrees of freedom in local coordinates, as indicated in Fig.2(a). It is assumed (Fig.2a,b) that the nodes of these different types of element (slabs, beam and shear connectors) are defined in a common reference plane coinciding with the mid-surface of the concrete slab element, whose location is fixed throughout the analysis, as given by Fig.2(b) [5]. Moreover, the following assumptions are established [5]: (*i*) the member is straight and prismatic, (*ii*) plane cross-sections remain plane under flexural deformations and there is no slip between different materials, (*iii*) the twist (θ', as given in Fig.2a) of the beam member is relatively small and there is no distortion of the cross-section, (*iv*) in the present simulations, temperature distribution is assumed to be constant over the member cross-section, (*v*) the interaction of steel beams and concrete slabs within a composite floor is represented by linking two-noded shear-connector elements of zero length, with three translational and two rotational degrees of freedom at each node.

www.EngineeringEBooksPdf.com

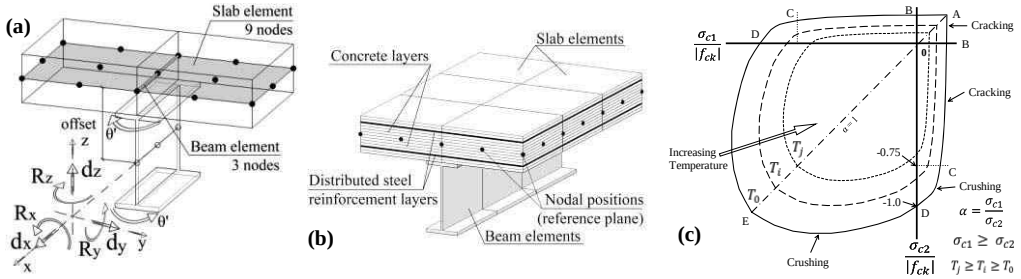


Figure 2: (a) Nodal degrees of freedom in local coordinates for (b) composite beam and slab elements [4,5], (c) concrete failure envelopes at elevated temperatures [3].

In the present simulations, concrete floor slabs are modeled as layers of finite plate elements (Fig.2b). The elements used are the quadrilateral nine-noded higher-order isoparametric elements [16]. The plate elements are subdivided into several layers representing concrete and distributed reinforcing steel as shown in Fig.2(b). The main assumptions of the layered approach can be summarized as follows [3]: (*i*) the slab elements are considered to consist of plain concrete and reinforcing steel layers - there is no slip between layers, (*ii*) each layer can have a different but uniform temperature, (*iii*) the initial material properties of each layer may be different and the stress–strain relationships may change independently for each layer, (*iv*) the reinforcing steel bars in either of the orthogonal mesh directions are modeled by an equivalent, smeared, steel layer with stiffness only in the direction of the reinforcement, (*v*) concrete layers are in a state of plane stress and considered to be orthotropic after cracking.

The mechanical properties of materials (concrete and steel, including reinforcement bars) are assumed to be temperature dependent in accordance to EC4-p1.2 [2] definitions, as treated by Fig.3(a,b) for concrete and Fig.3(c) for steel, respectively. The concrete model is assumed to be isotropic, homogeneous and elastic before cracking or crushing occurs [3]. Nevertheless, in order to account for fire design conditions, the compressive f_{ck} and tensile characteristic strengths f_{tk} of concrete are modified as a function of the temperature [2] (being denoted respectively as $f_{ck,T}$ and $f_{tk,T}$). The adopted uniaxial stress–strain relationships for concrete at elevated temperature are given by Fig. 3(a,b), respectively for compressive and tensile strengths. When concrete is subjected to tension, a linear elastic behavior is assumed up to its ultimate tensile capacity (f_{tk}). The uniaxial tensile and compressive strengths are considered to be related by $f_{tk} = 0.3321\sqrt{f_{ck}}$ in MPa. Beyond this point, the tensile stress decreases gradually with increasing tensile strain. As observed in Fig. 3(b), the bilinear curve [17] has been used to model tensile strain softening, where the following parameters have been addressed [18]: $\varepsilon_{cr}=f_{tk}/E_c$ $\varepsilon_{cu}=\alpha_1 \cdot \varepsilon_{cr}$, and $\alpha_1=10$ to 25, the value of 15 is adopted herein. The proposed model does not consider spalling, the concrete cross-section being assumed to remain intact. When subjected to compression, the nonlinear stress–strain relationship is applied as recommended by EC4-p1.2 [2]. In the present approach, after crushing concrete is assumed to lose all stiffness [3].

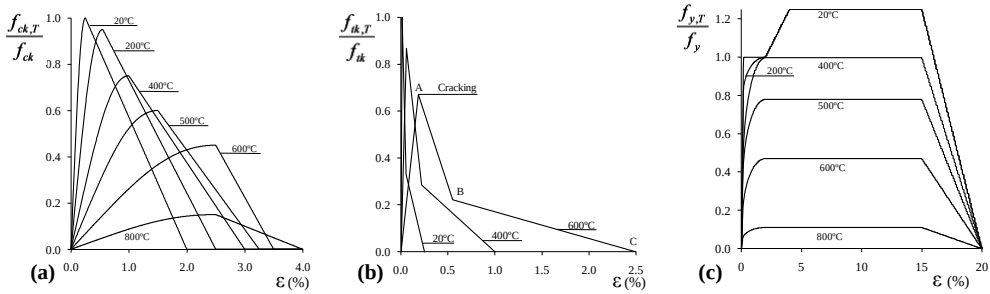


Figure 3: Stress–strain relationships for materials at elevated temperatures [2]: concrete under (a) compression and (b) tension, (c) steel (compression and tension).

www.EngineeringEBooksPdf.com

The reinforcement is modeled using a modified layered orthotropic slab element, where a perfect bond between steel and concrete layers is assumed [3]. The stress–strain curve of reinforcing steel at elevated temperatures, originally proposed by EC4-p1.2 [2], is considered as given in Fig.3(c). The calculation of effective-stiffness factors is based on the theory of elastic beam bending and is determined by the dimensions of the cross section of the composite slab. The details of this modified layered procedure have been described by Huang *et al.* [3]. The biaxial strength envelope formulation of concrete [18] was adopted in this paper, *i.e.* VULCAN *FE*-procedure, as given by Fig.2(c) [3]. In this approach, compressive and tensile stresses are denoted to be negative and positive, respectively. The principal directions are chosen so that $|\sigma_{c1}| \geq |\sigma_{c2}|$, as indicated in Fig.2(c). The initiation of cracking or crushing at any location occurs when the concrete principal stresses reach one of the failure boundaries. After cracking a smeared model is adopted [3] in which a crack at any *Gauss point* is identified either in the biaxial tension region (*segment AB*) or in the combined tension–compression region (*segment BC*), as shown in Fig.2(c). After the initiation of cracking in a single direction, the concrete is treated as an orthotropic material with principal axes, normal and parallel to the crack direction. The concrete parallel to the crack is capable of resisting both tensile and compressive stresses [3].

3 NUMERICAL APPLICATIONS

In order to show how a coupled model works, such as the structure of the small office, given by Fig.4, is verified for fire conditions, assuming two distinct temperature evolutions: (*i*) CFD performed analysis and (*ii*) standard ISO-834 fire design curve [1]. The general layout of the simulated area is given in Fig.4(a), where the correspondent fire objects are presented in Fig.4(b). These fire objects are represented by the HRR curves, previously given in Fig.1(b).

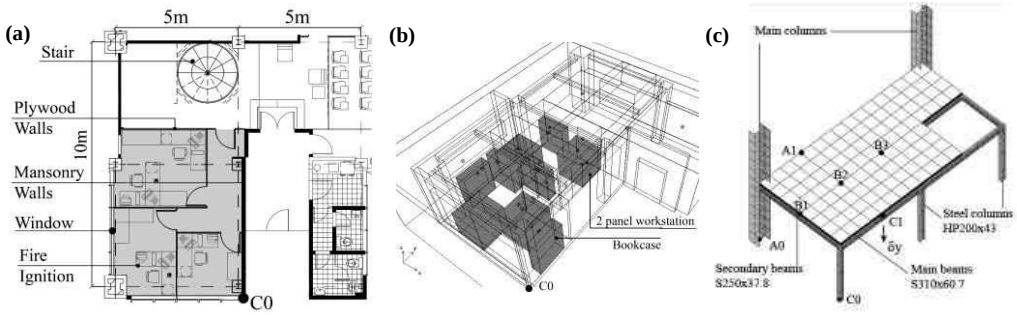


Figure 4: (a) Layout for the fire compartment region and the (b) respective indication of the proposed fire objects for CFD analysis, (c) proposed measure points for CFD gas temperature evaluation.

As indicated in Fig.4(a), the fire compartment measured 10m x 5 m in plan and 3.20 m in height and contained standard wooden doors of dimension 0.70 m x 2.10m. The walls of the compartment were also specified in Fig.4(a), made of masonry blocks with a thickness of 0.15m and double 9mm plywood walls, which were considered as combustible material. The initial air temperature was assumed to be 20°C and the fire ignition was postulated on a 2-panel workstation, as pointed out in Fig.4(a). The gas temperatures variation was collected from the CFD model on the several points indicated in Fig.4(c). The structural arrange for the floor is indicated in Fig.4(c), being composed of 5 secondary beams (*S250x37.8*) and 4 main beams (*S310x60.7*), where 3 one-way spanning slab are also specified in Fig.4(c). Each slab panel is meshed into 32 shell-elements. It consists of two steel reinforcement layers, representing the main and the secondary reinforcement directions of the slab. The bottom layer meshes with a total reinforcement distributed steel area of *2.5* cm^2/m^2 are modeled (a general view of the FEM model will be given in Fig.7). The reinforcement was considered as a *0.25 mm* thick smeared steel layer and a *15 mm thick* concrete cover. The elastic *moduli* were assumed to be E_s=210 kN/mm^2 and E_c=18 kN/mm^2, respectively for steel and concrete at room

www.EngineeringEBooksPdf.com

temperature. Material constitutive properties assumed the EC4-p1.2 [2] model as previously indicated in Fig.3, with correspondent compressive strength of 21 N/mm^2 (f_{ck}), and yield strength of 500 N/mm^2 and 250 N/mm^2 (f_y), related to reinforcement and structural (profiles) steels at room temperature respectively. Due to the original non-composite structural design, a superimposed uniform fire combination loading [1,2] of 5.77 kN/m^2 is incrementally increased and applied to the slabs, which corresponds to a linear distributed load of 14.42 kN/m to be postulated for beams.

The variation of the 400^{o}C isotherm for different fire times is presented in Fig.5. Accordingly, in a very early stage of the fire development (4.8 min), it is possible to identify a heat exchanging between the compartment and the exterior, due to the breakage of the glass in the left-hand window. After this point, due to the new ventilation condition caused by the opening of the window, the fire dynamics become more severe, and the fire continues to spread over the defined area, consuming most of the proposed furniture (fire objects) and plywood walls. At approximately 5.6 min, the 400^{o}C isotherm reaches the stair opening, providing additional air exchange, with the upper floor. This fire will develop up to the maximum temperature in about 7 minutes and will continue to consume all possible fuel up to nearly 13 minutes, after which the cooling down phase will take place.

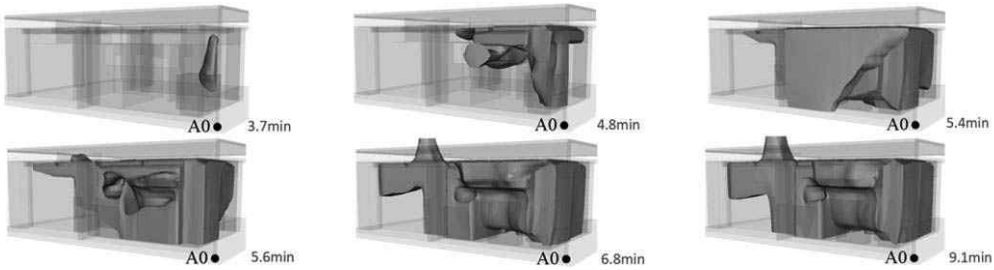


Figure 5: 400^{o}C isotherm surface on the fire compartment for different fire time.

The members' temperature variations as a function of the fire elapsed time are illustrated in Fig.6. CFD gas temperature results are compared to standard ISO-834 curve [1] in Fig6(c). The mean temperatures for steel member profile (primary and secondary) beams are compared in Fig6(a). The maximum observed temperature reaches nearly 1,000^{o}C, when the gas temperature is almost equal to that of the steel profile. The temperature variation across the thickness of the solid slab is presented in Fig.6(b), also assuming a ISO-834 fire curve. For the CFD model simulation, the flashover is assumed to occur at about 3 minutes (Fig.6c). After this point, temperatures rapidly increase to reach 1,000^{o}C at a fire elapsed time of nearly 7 minutes.

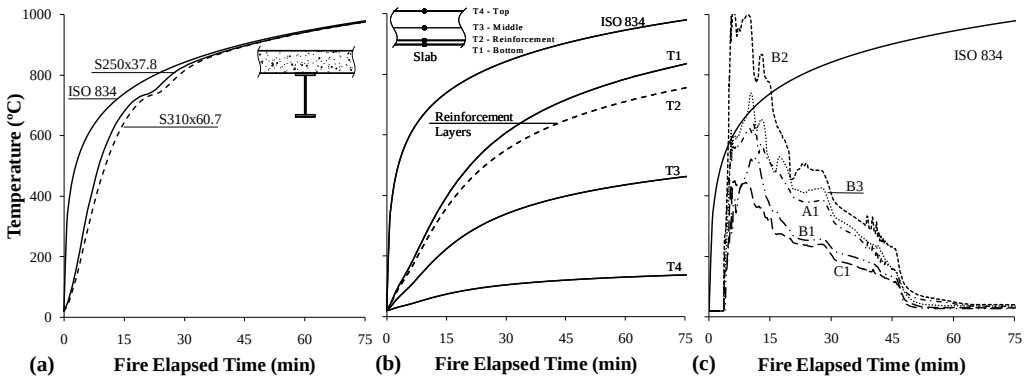


Figure 6: Variation of temperatures as a function of the fire time: (a) mean temperatures of structural elements, (b) idem across the slab element, (c) gas temperature variation (CFD and ISO-834 curves).

www.EngineeringEBooksPdf.com

Based on the performed gas-temperature variation (Fig.6), the structural behavior the proposed small office are compared as indicated in Fig.7(a,b). A general view of the deformed configuration for CFD Fire conditions and ISO-834 fire curve at 15 minutes of fire elapsed time is given in Fig.7(c). The structural behavior associated to CFD results (Fig.7a) is implicitly assumed to be more realistic than the results given in the ISO-834 curve (Fig.7b). Since the CFD curves presented a limited heat release, the related vertical (gravitational) displacements for distinct points, along the secondary and main beams, are consequently low when compared to the related ISO-834 curve[1]. In this, structural elements are subjected to an initial external loading, which remains constant, followed by a progressive temperature increase. The performed analysis accounts for: (*i*) the variation of the steel or concrete stress-strain curve, (*ii*) the thermal strains caused by temperature rise and (*iii*) the continuous presence of the external fire combination loading. The proposed results also implicitly accounts for the contribution of catenary and the tensile membrane actions, on beams and slabs, respectively. Theses effects can significantly improve the load-carrying capacity of members subjected to fire. Hence, practical exploration of catenary action in beam may involve optimization of restraint stiffness that would give acceptable lateral deflections yet not place too much burden on the adjacent structure [20].

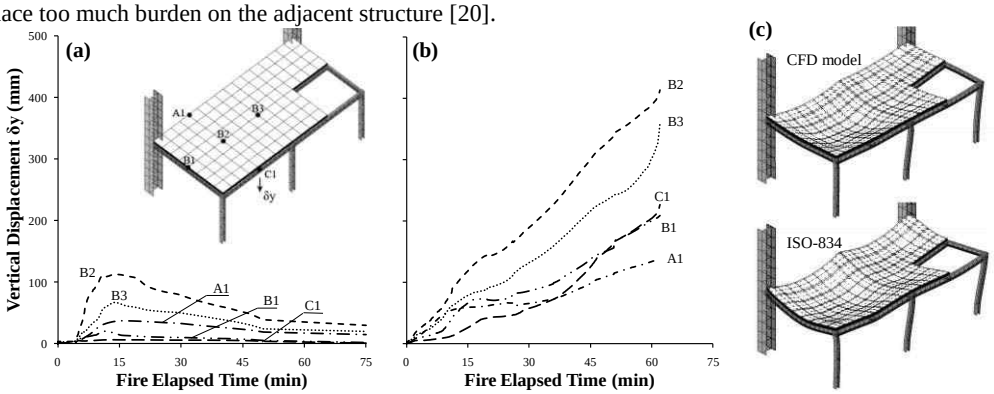


Figure 7: Structural behavior of the proposed small office for different fire conditions. Variation of vertical displacement as a function of the fire elapsed time for (a) CFD and (b) standard ISO-834, (c) general configuration of deformed configuration model for 15 minutes.

4 CONCLUDING REMARKS

A one-way coupling approach was presented in this paper, which can perform numerical simulations, integrating three phases of fire design processes: *Fluid*, *Thermo* and *Mechanical*. Essential attributes for the proposed coupling procedure, as well as, significant characteristics of each step of the integrated analysis were also investigated. With regards to the CFD models, a parallel implementation, allowing efficient solutions of large fire field modeling problems indicating that this procedure can be performed on a regular basis. The member temperature evolution was examined by a heat-transfer *FE*-based model and simplified code recommendations, accounting for thermal-dependent properties of materials. In this verification, temperature results due to radiative heat transfer of combustion products were considered for structural elements. Structural behavior were verified by means of second-order inelastic models, accounting for catenary and tensile membrane actions, representing significant additional structural survival for members exposed to fire. The obtained results indicate that coupled 3D fluid-thermal-mechanical models, similar to those presented herein, can be incorporated into current fire-design analyses, providing a more realistic and economical fire-design verifications.

ACKNOWLEDGMENT

The writers gratefully acknowledge the support of the *CBCA - Brazilian Center of the Steel Construction*.

www.EngineeringEBooksPdf.com

REFERENCES

[1] Comité Européen de Normalisation, CEN. *Eurocode 1 - Actions on Structures - Part 1-2: General Actions - Actions on structures exposed to fire*. Brussels, 2002.

[2] Comité Européen de Normalisation, CEN. *Eurocode 4 - Design of composite steel and concrete structures - Part 1-2: General Rules - Structural Fire Design*. Brussels, 2004.

[3] Huang, Z., Burgess, I.W. and Plank, R.J., "Modeling Membrane Action of Concrete Slabs in Composite Buildings in Fire. I: Theoretical Development". *Journal of Structural Engineering*. **129**(8), 2003.

[4] Huang, Z., Burgess, I.W. and Plank, R.J., "3D Modelling of Beam-Columns with General Cross-Section in Fire", *Proceedings of Structures in Fire*, Otawa, 2004.

[5] Huang, Z., Burgess, I.W. and Plank, R.J., "Fire resistance of composite floors subject to compartment fires". *Journal of Constructional Steel Research*. **60**(2), 339-360, 2004.

[6] Yeoh, G.H. and Yuen, K.K., *Computacional Fluid Dymanics in Fire Engineering*, Elsevier, 2009.

[7] Kumar, S., Miles, S., Welch, S., Vassart, O., Zhao, B., Lemaire, A.D. *et al*., "FIRESTRUC - Integrating advanced three-dimensional modelling methodologies for predicting thermo-mechanical behavior of steel and composite structures subjected to natural fires", *RFS Research Programme of the Research Fund for Coal and Steel*, 2006.

[8] Prasad, K. and Hamins, A., "Fire Structure Interface and the Thermal Response of the World Trade Center Towers", *Proceedings of Structures in Fire*, Aveiro, 499-509, 2006.

[9] Silva, J.C. and Landesmann, A., "Application of a 3D Fluid-Thermal-Mechanical Model for Performance-based Analysis of Composite Structures under Fire", *Proceedings of Structural Stability Research Conference*, Orlando, 2010.

[10] Silva, J.C. and Landesmann A., "Application of CFD model to compartment fire dynamics analysis", *Proceedings of Iberian-Latin-American Congress on Computational Methods in Engineering*, Rio de Janeiro, Brazil, 2009 (in portuguese).

[11] National Fire Protection Association, NFPA. *Handbook of Fire Protection Engineering*. Quincy, Massachusetts, 2002.

[12] Babrauskas, V. and Peacock, R.D., "Heat Release Rate: The Single Most Important Variable in Fire Hazard". *Fire Safety Journal*. **18**(3), 255-272, 1992.

[13] Grandison, A.J., Galea, E.R., Patel, M.K. and Ewer, J., "The Development od Parallel Implementation for a CFD based fire field model utilising conventional office based PCs". *Journal of Applied Fire Science*. **12**(2), 137-157, 2003-2004.

[14] Hoffmann, N., Berhane, D. and Galea, E.R., "Large-Scale Fire Field Modelling - the Route to General Use via Parallel Processing", *Proceedings of INTERFLAM '93*, Oxford, 1993.

[15] Franssen, J.M., Kodur, V.K.R. and Mason, J., *User's manual for SAFIR 20001 a computer program for analysis of structures submitted to the fire*, 2000.

[16] Bathe, K.-J., *Finite element procedures*. Englewood, Prentice-Hall, 1996.

[17] Rots, J.G., Kuster, G.M.A. and Blaauwendraad, J., "The need for fracture mechanics options in finite element models for concrete structures", *Proceedings of International Conference on Computer Aided Analysis and Design of Concrete Structures*, Pineridge Press, Part 1, 19-32, 1984.

[18] Barzegar-Jamshidi, F., "Non-linear finite element analysis of reinforced concrete under short term monotonic loading". PhD Thesis. Urbana-Champaign, University of Illinois at Urbana-Champaign, 1987.

[19] Bailey, C.G. e Toh, W.S., "Behaviour of concrete floor slabs at ambient and elevated temperatures". *Fire Safety Journal* **42**(6-7), 425-436, 2007.

[20] Yin, Y.Z. and Wang, Y.C., "A numerical study of large deflection behaviour of restrained steel beams at elevated temperatures". *Journal of Constructional Steel Research* **60**(7), 1029-1047, 2004.

www.EngineeringEBooksPdf.com

SDSS'Rio 2010 STABILITY AND DUCTILITY OF STEEL STRUCTURES
E. Batista, P. Vellasco, L. de Lima (Eds.)
Rio de Janeiro, Brazil, September 8 - 10, 2010

BEHAVIOUR OF COMPOSITE FLOOR BEAM WITH WEB OPENINGS AT HIGH TEMPERATURES

V.Y. Bernice Wong*, Ian W. Burgess* and Roger J. Plank**

* Department of Civil and Structural Engineering, The University of Sheffield, Sheffield S1 3JD, UK
e-mails: v.wong@sheffield.ac.uk, ian.burgess@ sheffield.ac.uk

** School of Architectural Studies, The University of Sheffield, Sheffield S10 2TN, UK
e-mail: r.j.plank@ sheffield.ac.uk

Keywords: Composite Beam, Web Opening, Finite Element Modelling, Structural Fire Engineering

Abstract. *A simplified analytical model for composite cellular floor beam, based on currently available design methods, has been completed. This has been used in an initial study of loaded composite cellular floor beams at normal and elevated temperatures. The approach predicts the capacity and failure type of a composite member by applying design criteria for each of the different possible failure modes at successive cross-sections of the member. A finite element investigation into the behaviour, including local instabilities, of cellular composite members subjected to elevated temperatures has also been conducted, considering material and geometrical non-linearities. These studies have been validated by modelling recent full-scale furnace tests on composite cellular beams. Close comparisons are observed between finite element, experimental results and the predictions of the simplified analytical model.*

1 INTRODUCTION

Composite cellular floor beams are currently widely used in multi-storey building construction, especially to achieve long spans at the same time as providing passage for service ducts, hence reducing overall building height. The downstand composite beams make use of their full structural depth, maximising the lever arm between the compressed concrete flange and the steel section which acts essentially in tension. The optimisation of this structural form, however, raises questions about potential failure modes, particularly at elevated temperatures.

In practice, web-openings in a beam result in unusual stress distributions within the web, and unique beam failure modes. A web opening produces an additional local ("Vierendeel") bending across the opening due to high shear forces acting on the beam. This can result in the formation of four plastic hinges at the "corners" of the opening. Equally, the shear forces transferred across the web-posts between openings can result in local buckling of these web-posts. The loss of strength and stiffness of structural steel in the fire situation depends on its temperature; the elastic modulus of steel reduces rapidly in comparison to its strength, which results in more rapid reduction of capacities based on buckling than those based on strength. Hence the buckling capacity of web-posts reduces more rapidly with temperature than those based on other failure types. Therefore web-post buckling tends in general to be the critical mode of failure in fire, even for beams with low web slenderness (d/t) ratios.

In this paper, a simplified analytical model representing composite cellular floor beam in case of fire is described. This has been used in an initial study of loaded composite cellular floor beams at normal and elevated temperatures. A finite element model taking into consideration the material and geometrical non-linearities has also been developed to investigate the behaviour of cellular composite members subjected to elevated temperatures. These studies have been validated by modelling recent full-scale furnace tests on composite cellular beams.

www.EngineeringEBooksPdf.com

2 ANALYTICAL MODEL

Based on the available design guides [1] - [6] for ambient temperatures, an analytically-based model has been developed for determining the critical temperatures of composite cellular floor beams in fire, taking into account shear force transfer by Vierendeel action across the openings and the forces generated in web-posts. The high-temperature limiting cases of the composite beam are assessed by applying the material properties appropriate to elevated temperature to the ambient-temperature equations.

2.1 Resistance to Vierendeel bending

Transfer of shear across a web opening results in the eventual formation of plastic hinges at the four "corners" of the opening, which are assumed to be sited at the corners of the inscribed square in the case of a circular opening. For a composite beam, the composite action developed between the top-tee section and the concrete slab increases the resistance to Vierendeel bending at one of these hinges.

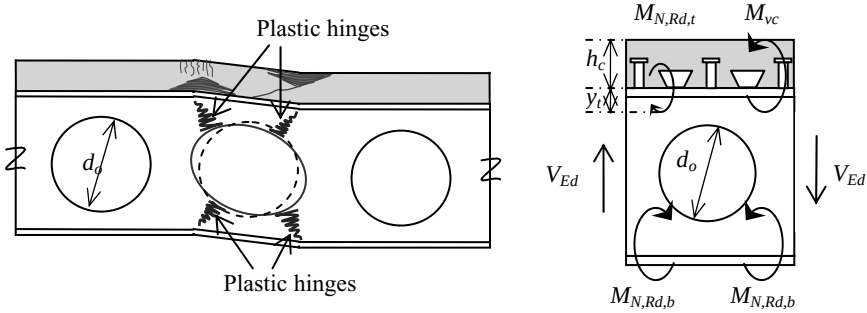


Figure 1: Vierendeel mechanism (a) Mode of failure; (b) Vierendeel bending around web opening.

In fire, the total Vierendeel resistance ($M_{v,Rd,fi}$) provided by the local plastic bending resistances at the four corners is defined as:

$$M_{v,Rd,fi} = M_{N,Rd,t,fi} + 2M_{N,Rd,b,fi} + M_{vc,fi} \tag{1}$$

$M_{N,Rd,t,fi}$ and $M_{N,,Rd,b,fi}$ are the plastic bending resistances of the top-tee and bottom-tee of the perforated section. The latter are reduced due to coincident tensile forces, according to the following approximate equation:

$$M_{N,Rd,fi} = M_{Rd,fi}\left[1 - \left(\frac{N_{Ed,fi}}{N_{Rd,fi}}\right)^2\right] \tag{2}$$

where:

$M_{Rd,fi}$ is the local bending resistance of the tee section. Plastic resistance should be used for Class 1 and 2 sections; elastic section properties are used for Class 3 and 4 sections.
$N_{ED,fi}$ is the axial compression or tension force due to global moment action
$N_{Rd,fi}$ is the resistance of the tee sections

www.EngineeringEBooksPdf.com

$M_{vc,fi}$ is the bending resistance due to local composite action between the top-tee section and the concrete slab. This may be approximated by:

$$M_{vc,fi} = n_s P_{Rd,fi}(h_c - \frac{x_c}{2} + y_t) \quad (3)$$

where:

n_s is the number of shear connectors provided above the opening
$P_{Rd,fi}$ is the design shear resistance of a shear connector at high temperatures
h_c is the overall depth of the concrete slab
x_c is the thickness of concrete in the compressive zone
y_t is the distance of the neutral axis of the steel top-tee section from the top of the flange

The applied Vierendeel moment for a circular web opening is calculated by $V_{ED}(0.5d_o)$; where V_{Ed} is the design shear force at a distance x from the support acting over an effective length of $0.5d_o$, where d_o is the diameter of the circular opening.

2.2 Web-post buckling resistance

For cellular beams with narrow web-posts between closely spaced openings web-post buckling is often critical, and therefore it is necessary to select an opening size with a suitable web-post width. The SCI guidance [7] - [8] recommends that the web-post width for beams with circular web openings should not be less than 130mm or $0.3d_o$, whichever is the greater. In cellular beam design, each web-post is checked for resistance to local buckling as an equivalent 'strut', by considering a compression force acting over its minimum width S_o (Figure 2).

At high temperature, the shear resistance of the web reduces at a faster rate than bending resistance of the beam, and thus the web is more influenced by local buckling. In fire, the capacity of a web-post ($V_{h,buck,fi}$) is defined as:

$$V_{h,buck,fi} = \chi_{fi} f_{y,fi} S_o t_w \quad (4)$$

where:

$f_{y,fi}$ is the design yield strength of the perforated section at high temperature
t_w is the thickness of the web-post

The value of χ_{fi} is calculated following the principles of EN1993-1-2 [9], and is defined as:

$$\chi_{fi} = \frac{1}{\phi_{fi} + \sqrt{\phi_{fi}^2 - \overline{\lambda}_{fi}^2}} \quad \text{but } \chi_{fi} \le 1.0 \quad (5)$$

with

$$\phi_{fi} = 0.5[1 + \alpha(\overline{\lambda}_{fi} - 0.2) + \overline{\lambda}_{fi}^2] \quad (6)$$

and

$$\overline{\lambda}_{fi} = \sqrt{\frac{f_{y,fi}}{f_{E,fi}}} \quad (7)$$

The imperfection factor α is taken as 0.49 for $d/t \le 85$ and 0.76 for $d/t > 85$.

www.EngineeringEBooksPdf.com

The buckling stress ($f_{E,fi}$) acting across the web-post and the slenderness (λ_{fi}) of the web-post are defined as:

$$f_{E,fi} = \frac{\pi^2 E_{fi}}{\lambda_{fi}^2} \tag{8}$$

$$\lambda_{fi} = \frac{\sqrt{12} l_{e,fi}}{t_w} \tag{9}$$

in which $l_{e,fi}$ is the web-post's effective length at elevated temperature.

For a circular web opening, $l_{e,fi}$ is given by:

$$l_{e,fi} = 0.9 l_e \quad \text{for } d/t \le 85 \tag{10}$$

$$l_{e,fi} = 1.2 l_e \quad \text{for } d/t > 85 \tag{11}$$

l_e is the web-post effective length at ambient temperature, which is calculated from:

$$l_e = 0.5\sqrt{S_o^2 + d_o^2} \tag{12}$$

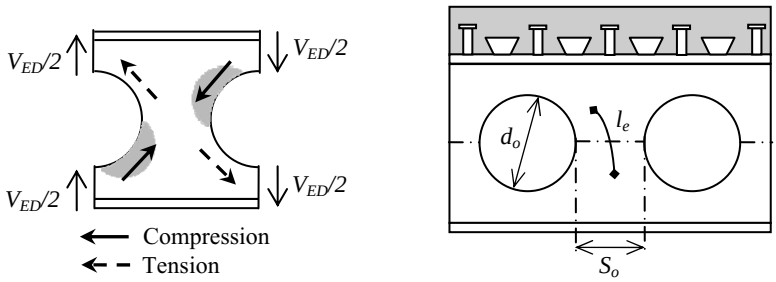


Figure 2: Web-post buckling (a) assumed forces; (b) web-post geometry

The applied vertical compressive force (V_t) acting across the web-post is calculated by $V_{ED}/2$; where V_{Ed} is the design shear force at the distance from the support to the centre of the web-post.

www.EngineeringEBooksPdf.com

3 ANALYTICAL MODEL VALIDATION

Results obtained from the proposed analytical model were validated by comparison with available experimental test results and finite element modelling.

3.1 Fire tests

Nadjai et al. conducted fire tests [10] on composite cellular floor beams heated using an ISO 834 standard fire curve (Figure 3). Table 1, and Figures 4 and 5 summarise the test specimens used.

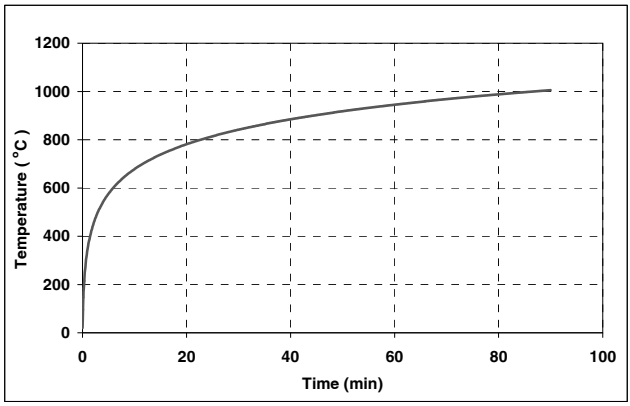


Figure 3: ISO 834 standard temperature-time curve

Type	Cellular beam (S355)				
	Beam Size	Opening	Web-post width	Spacing	Applied Load
A	Symmetric beam (575x140x39kg/m) Top-tee: UB 406x140x39kg/m Bottom-tee: UB 406x140x39kg/m	8 x 375mm	125mm	500mm	2 x 54kN
B	Asymmetric beam (630x140/152x46kg/m) Top-tee: UB 406x140x39kg/m Bottom-tee: UB 457x152x52kg/m	6 x 450mm	180mm	630mm	1 x 126kN
150mm thick x 1200mm wide concrete slab of strength 35N/mm^2 A142 reinforcement mesh of yield strength 460N/mm^2 Shear connectors of 19mm diameter x 120mm height, equally distributed at 150mm spacing					

Table 1: Sectional details of composite cellular beam tests

www.EngineeringEBooksPdf.com

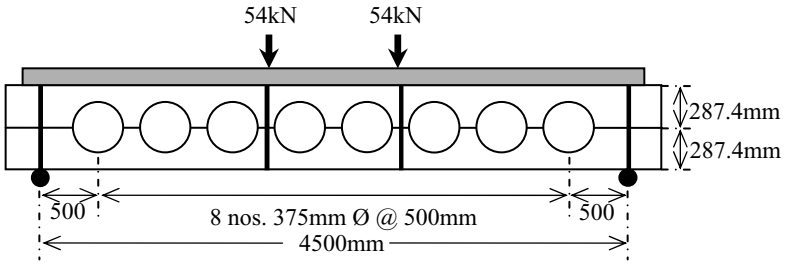


Figure 4: Geometric detail of symmetric composite cellular beam test (Type A)

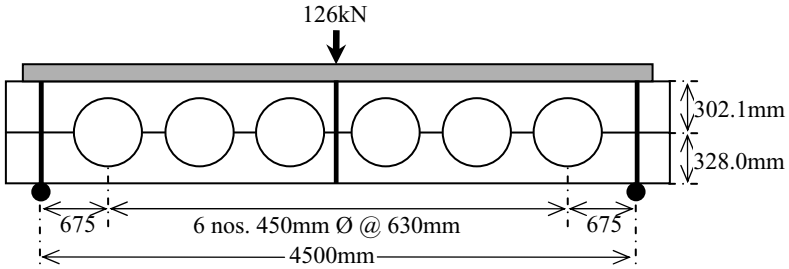
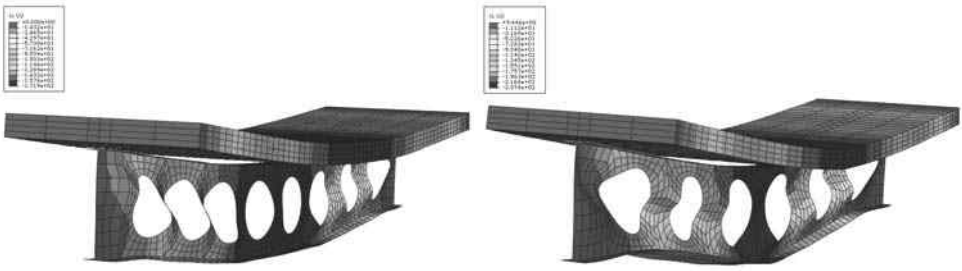


Figure 5: Geometric detail of asymmetric composite cellular beam test (Type B)

3.2 Finite element (FE) modelling

The commercial FE package ABAQUS [11] was used to carry out the simulation work. A three-dimensional eight-noded solid element and four-noded quadrilateral shell elements with reduced integration were used to represent the concrete slab and cellular steel beam respectively. Reinforcing mesh in the solid slab element was defined as a layer of steel of equivalent area in each direction. Full interaction between the concrete slab and the steel beam was assumed, due to the high density of shear connectors which was used in the test. Full composite action between the concrete slab and the cellular steel beam was achieved by using a tying constraint to tie their surfaces together. The support and loading conditions in the FE models simulated the experimental conditions, restraining the appropriate degrees of freedom. Figure 5 illustrates the type of failure mode predicted by the FE modelling for beams of Types A and B.



(a) (b)

Figure 5: FE simulation (a) beam Type A web-post buckling; (b) beam Type B web-post buckling

www.EngineeringEBooksPdf.com

3.3 Results and discussion

A summary of the results obtained from the analytical model, FE modelling and experiment are shown in Figures 6 and 7. The structural behaviour of the composite perforated sections observed from the experiments is clearly in good agreement with the finite element results in terms both of failure modes and overall behaviour. Web-post buckling is clearly observed in beams of both Types A and B. Figures 6 and 7 compare between the FE simulation and experiment in terms of the mid-span displacements and the beam bottom-flange temperature. The critical temperatures generated by the proposed analytical model have also been shown. Critical temperatures calculated from the simplified analytical model were 703ºC and 668ºC for beams of Type A and Type B respectively. These are slightly conservative predictions which are appropriate for use in design.

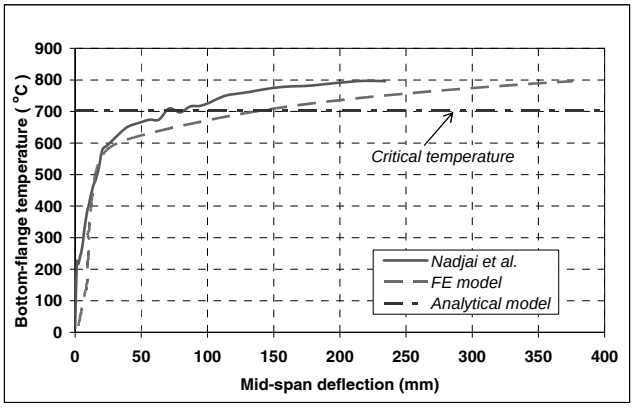


Figure 6: Comparison of mid-span deflection behaviour and critical temperature for Beam Type A

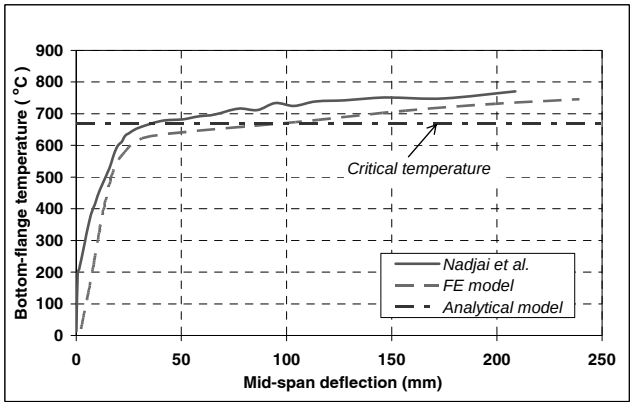


Figure 7: Comparison of mid-span deflection behaviour and critical temperature for Beam Type B

www.EngineeringEBooksPdf.com

4 CONCLUSION

A simplified analytical model for the fire resistance of cellular beams based on available design guides has been presented. This has been validated by comparison with results obtained from available experimental fire tests and finite element modelling. The final failure conditions of the composite cellular beams predicted by the analytical model agree well with the experimental observations and FE simulations. The FE model can be utilised to investigate the high-temperature behaviour of composite cellular beams in far more detail than is possible by testing alone. The use of the proposed simplified analytical model has been shown to have lead to conservative predictions, and to be in reasonable agreement with both the FE and the furnace tests in terms of critical bottom-flange temperatures.

ACKNOWLEDGEMENTS

The authors gratefully acknowledge the support from the Engineering and Physical Sciences Research Council of the United Kingdom for providing funding for this research work under Grant EP/F001711/1.

REFERENCES

[1] Lawson, R.M. “Design for openings in the webs of composite beams”, SCI/CIRIA publication P068, 1987.

[2] Ward, J.K. “Design for composite and non-composite cellular beams”, SCI publication P100, 1999

[3] Chung, K.F. and Lawson, R.M. “Simplified design of composite beams with large web openings to Eurocode 4”. *Journal of Constructional Steel Research*, **59**, pp135-163, 2001.

[4] Liu, T.C.H., Chung, K.F. “Steel beams with large web openings of various shapes and sizes: finite element investigation”. *Journal of Constructional Steel Research*, **59**, pp1159-1176, 2003.

[5] Chung, K.F., Liu, T.C.H. and Ko, A.C.H. “Steel beams with large web openings of various shapes and sizes: an empirical design method using a generalised moment-shear interaction curve”. *Journal of Constructional Steel Research*, **59**, pp1177-1200, 2003.

[6] Lawson, R.M., Lim, J., Hicks, S.J. and Simms, W.I. “Design of composite asymmetric cellular beams and beams with web openings”. *Journal of Constructional Steel Research*, **62,** pp614-629, 2006

[7] Steel Construction Institute, “Guidance on the use of intumescent coatings for the fire protection of beams with web openings”, Publication RT1085 Version 04, 2007.

[8] Steel Construction Institute, “Guidance on the fire protection of beams with web openings”, Publication RT1187 Version 01, 2008.

[9] CEN, Brussels, BS EN 1993-1-2: 2005, “Eurocode 3: Design of steel structures. Part 1-2: General rules – Structural fire design”. 2005.

[10] Nadjai, A., Bailey, C.G., Bake, S.M., Ali, F., Talamona, D., Allam, A. “Behaviour of composite floor cellular steel beams at elevated temperatures”. *International Congress on Fire Safety in Tall Buildings, Spain*, pp359-371. 2006

[11] Pawtucket, R.I. “ABAQUS user’s manual version 6.2”, Hibbitt, Karlsson and Sorensen Inc. 2001.

www.EngineeringEBooksPdf.com

SDSS'Rio 2010 STABILITY AND DUCTILITY OF STEEL STRUCTURES
E. Batista, P. Vellasco, L. de Lima (Eds.)
Rio de Janeiro, Brazil, September 8 - 10, 2010

TO SHEAR RESISTANCE OF CASTELLATED BEAM EXPOSED TO FIRE

F. Wald, A. Pelouchová, J. Chlouba and M. Strejček

Czech Technical University in Prague
e-mails: wald@fsv.cvut.cz, alena.pelochova@fsv.cvut.cz,
jiri.chlouba@fsv.cvut.cz; mical.strejcek@fsv.cvut.cz

Keywords: Fire design, Fire test, Castellated beam, Shear resistance.

Abstract. *The paper presents the comparison of the fire design of the unprotected castellated composite beam to the results of the fire test on administrative building. The transfer of heat into the structure shows a good conservative prediction of the test on real structure. The shear failure modes of the simplified mechanical prediction of the behaviour at elevated temperature are well visible on the load deformation curve as well as on relative deformation of the beam web close to its support.*

1 INTRODUCTION

The main goal of the fire test on a floor of an administrative building was the overall behaviour of the structure, which may not be observed on the separate tests on individual elements. A new building was erected in front of the Czech Technical University in Prague educational centre Joseph gallery in Mokrsko in Central Bohemia. The experiment followed the seven large fire tests in Cardington laboratory on steel frame conducted between 1998 and 2003, see [1]. The structure was design complex to allow a simple as well as advanced modelling of today modern buildings. Except of the three types of flooring systems were tested six wall structures with mineral wool. On one half of the floor was used the composite slab supported by the fire unprotected composite pretty castellated beams with large openings ArcellorMittal Angelina^{TM}, see Figure 1. The experimental structure represents a part of a floor of administrative building of size 18 x 12 m with height 2,68 m, see [2].



Figure 1: Thermocouples located at the midspan on the castellated beams and its connections

www.EngineeringEBooksPdf.com

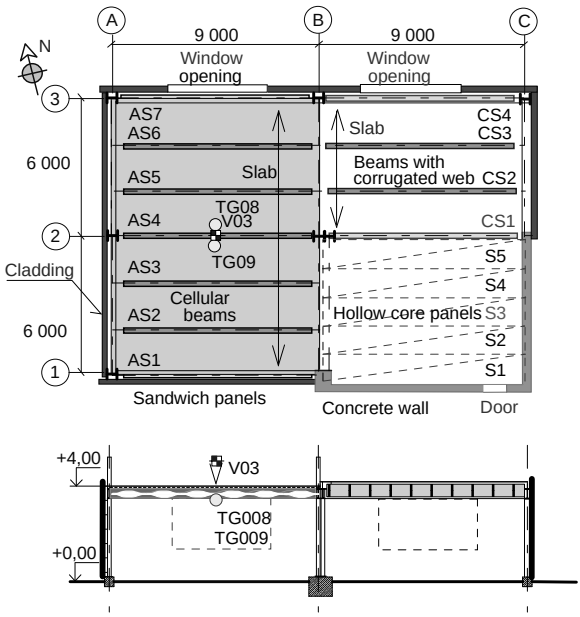


Figure 2: Structure of experimental building for fire test

The composite slab on the castellated beams was designed with a span 9 to 12 m and on beams with corrugated webs with a span 9 to 6 m. The deck was a simple trapezoidal composite slab of thickness 60 mm with the height over the rib 120 mm with sheeting CF60 (Cofraplus 0,75 mm) and concrete of measured cubic strength 34 N/mm^3 in 28 days reinforced by a smooth mesh ø 5 mm 100/100 mm; with strength 500 MPa and coverage 20 mm. The castellated beams with sinusoidal shape openings were made from profile IPE 270 and its web height was 395 mm. The beam has the parameters A_{net} = 3769,5 mm^2 A_{gross} = 5419,5 mm^2; $I_{y,net}$ = 128,8 · 10^6 mm^4; $I_{y,gross}$ = 137,4 · 10^6 mm^4. The connections were design as simple with header plate connection partially encased in the concrete slab.

The test was observed apart from other by more then 300 thermocouples, twenty deflectometers, six flux density meters, two meteorological stations, ten video, and four thermo imagine cameras. The gas temperature round the castellated beam was measured by thermocouples TG08 and TG09 at the level of lower flange, see Figure 1. Round the experimental building was erected the structure from scaffold. The vertical deformations were measured from the twins of timber formwork beams, which were fixed on linear scaffolds and on bridged truss girders 1,5 m above the building floor.

The mechanical load was designed for typical administrative building, where the variable action in Czech Republic reached usually from 2,5 to 3,5 kN/m^2. The dead load of the composite slab and beams reached 2,6 kN/m^2. The load was created by bags. The load represents the variable load at ambient temperature 3,0 kN/m^2 and added permanent load 1,0 kN/m^2 in characteristic values. Mechanical load 3,0 kN/m^2 was represented by 78 sand bags; each bag had approximately 900 kg. These sand bags were put on wooden pallets and uniformly distributed on the composite slab and pre-stressed panels.

Two window openings in the front wall with dimension 2.43 x 4.0 m provided air supply into the fire compartment. Fire load was made of rough battens from soft pine wood, total volume of 15 m^3. The usual characteristic value of the fire load for administrative building is 420 MJ/m^2, by the experiment the fire load reached 515 MJ/m^2.

The aim of this paper is to show the accuracy of simplified modelling of the shear behaviour of the composite castellated beam. The prediction of the beam AS4 located between the columns A2 and B2 is presented.

www.EngineeringEBooksPdf.com

2 HEAT TRANSFER INTO THE CASTELLATED BEAM

In fire, the temperature distribution across a composite member is non-uniform, since the web and bottom flange have thin cross-sections and a greater exposed perimeter than the top flange. The deterioration of the material properties of the web may therefore become an important effect on the overall performance of the member in the event of fire. The former fire resistance studies has been focussed to intumescent protection, see [3], as well as temperature developments in unprotected steel, see [4].

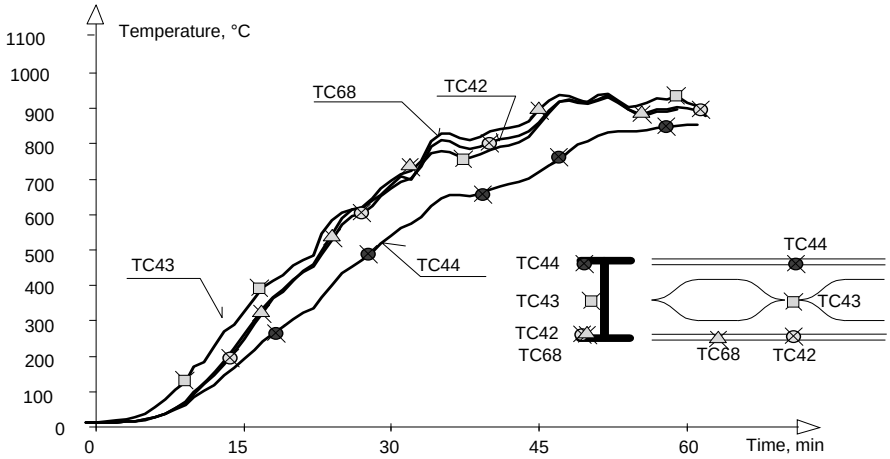


Figure 3 Temperatures measured at the midspan on the castellated beam AS4

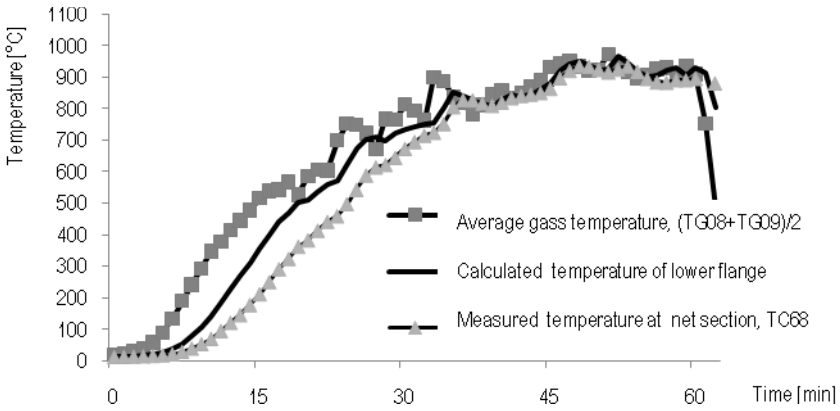


Figure 4: Calculated and measured temperature of the beam lower flange

In the described test was measured the gas temperature round the castellated beam by thermocouples TG08 and TG09 at the level of lower flange. The average gas temperature round the castellated beam was calculated from thermocouples as an average TG08 a TG09, see Figure 3. The step by step procedure according to EN 1993-1-2, see [5] was used to predict the parts of the structure temperature. For the lower flange was calculated the section factor $A_p/V = 232{,}1\ \mathrm{m}^{-1}$, for the beam web 303,0 m^{-1}, for the upper flange exposed from the three sides 156,6 m^{-1} and for the net section of the beam 178,3 m^{-1}. The comparison of this simple prediction to the measured values is shown at Figures 4 and 5.

www.EngineeringEBooksPdf.com

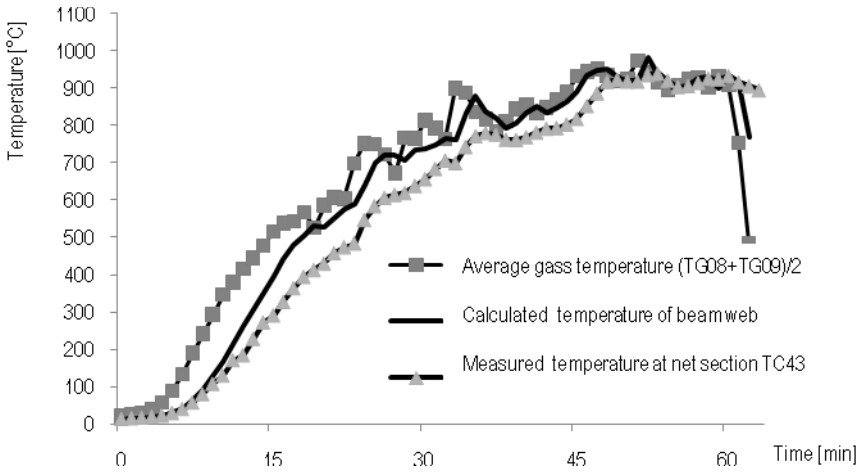


Figure 5: Calculated and measured temperature of the beam web

3 BEAM RESISTANCE

Several investigations into the castellated beams structural behaviour have supported the widespread use of as structural members in steel to concrete composite frames. First studies at ambient temperature concentrated on in plane response in the elastic range and later plastic one as well. Extensive measurements were made of the stress distributions across the cross-section, and these were compared with the predictions of various theoretical studies employing a Vierendeel analogy, finite difference techniques, and a complex variable analytical method. As a result of various series of tests a number of different failure modes have been observed, see [6]. The main failure modes are a Vierendeel collapse mechanism in which plastic hinges form at the section touching the four re-entrant corners of a castellation, buckling of a web-post, and web weld failure. Several prediction of collapse mechanisms have been proposed, see [7], and the lateral buckling of the web-posts has been analysed. Only limited investigations of composite floors using castellated steel beams at ambient temperature have been conducted, see [8]. The beams have been used widely in roof and composite construction without having been rigorously investigated under fire conditions. A composite concrete floor-slab has the effect of significantly increasing the flexural resistance of a steel section. Investigation of the behaviour of composite beams with isolated web openings in otherwise solid webs has shown that the slab significantly increases the shear-carrying capacity beyond that of the steel beam alone. This is due to the enhanced flexural and shear capacity of the upper part of the beam across an opening, although an unsupported webpost is more susceptible to buckling, see [9] and [4]. The simplified model for evaluation of the fire resistance of the beams was developed based on FE modelling approved by two fire tests, see [10].

In the fire test in Mokrsko 2008 were examined beams with large web openings which are sensitive to the shear resistance of the web and flanges. The advanced FE model was prepared to predict the behaviour before and after the fire test au University of Sheffield, see [2]. In the simplified calculation were utilised for the internal forces distribution by the Vierendeel analogy and the adequate failure modes were observed, see [11].

www.EngineeringEBooksPdf.com

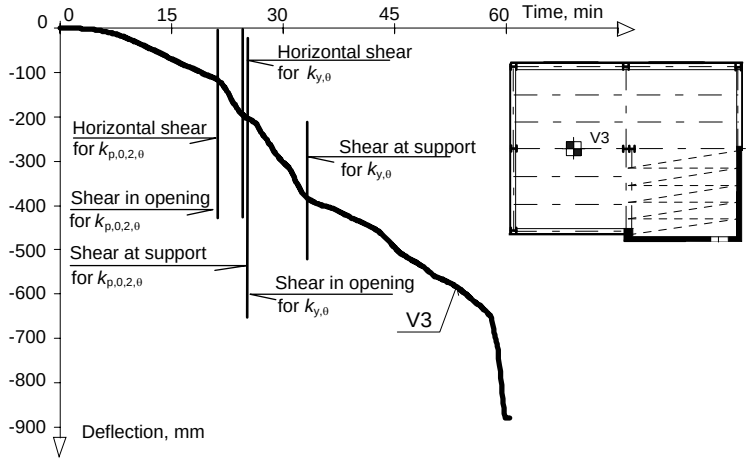


Figure 6: Measured deflection of the castellated beam AS4 with reached shear resistances

The beam was exposed a uniform action $f = 6{,}8 + 2{,}6 = 9{,}4$ kN/m, which creates a bending moment $M = f \cdot l^2/2 = 9{,}4 \cdot 9^2/2 = 95{,}175$ kNm and acting shear force $V = f \cdot l/2 = 9{,}4 \cdot 9/2 = 42{,}3$ kNm. In evaluation of the shear resistance was assumed the shear area at beam support as $395 \cdot 6{,}6 = 2607$ mm^2; the area of the web in opening $0{,}9\ (2 \cdot 72{,}5 \cdot 6{,}6) = 861{,}3$ mm^2; the minimal horizontal shear area is $0{,}9 \cdot 250 \cdot 6{,}6 = 1485$ mm^2. The critical temperature of the shear resistance in support $V_{max} = 42{,}3$ kN may be calculated from the reduction factor of the effective yield stress $k_{y,\theta}$ from $42{,}3 = k_{y,\theta} \cdot 0{,}6 \cdot 235$ $2607/10^3$ which is $k_{y,\theta} = 0{,}1151$. Thus the critical temperature is 795,7 °C. The beam web reached this steel temperature in 34 min. From the reduction factor of proportional limit for steel at elevated temperature $k_{p,0.2,\theta}$ the temperature of steel 661,8 °C is derived, which was reached in 25 min.

For the shear resistance in the beam web opening $V_{max} = 36{,}2$ kN may be the reduction factor of the effective yield stress calculated from $36{,}19 = k_{y,\theta} \cdot 0{,}6 \cdot 235$ $861{,}3/10^3$ and $k_{y,\theta} = 0{,}2980$. The adequate beam web temperature 673,7 °C will be reached in 25 min. For the effective yield stress it is $k_{p,0.2,\theta}$ it is web temperature 544,5 °C in 21 min.

From the horizontal shear resistance V_h, which is $V_{max} = 54{,}8$ kN may be derived for $54{,}8 = k_{y,\theta} \cdot 0{,}6 \cdot 235$ $1484/10^3$ the factor $k_{y,\theta} = 0{,}2620$ and the temperature 686,8 °C, which is reached on 24 min. The proportional limit $k_{p,0.2,\theta} = 0{,}2620$. The reached values of degradation of the beam are shown on Figure 6. No beam weld failure was observed on collapsed structure.

Close to connections was the beam instrumented with strain gauges for high temperatures to assume the shear stress across the web during the fire test. The application of the free-filament high-temperature strain gauges, which are sandwiched between two thin ceramics cement layers, allow to measure up to a temperature of 1150 °C. The accuracy of the measurement is 3 % till the 5000 μm, which limits the positioning of the strain gauges. Two strain gauges were applied in the middle third of the web height of castellated beam, see Figure 7. The stress at elevated temperature σ_θ was derived from the measured strain using Young´s modulus of elasticity at elevated temperature $E_{a,\theta} = k_{E\theta}\, E$ and the corresponding temperature recorded by the thermocouples

$$\sigma_\theta = \min\,(k_{E,\theta}\, E\, \varepsilon_\theta;\, k_{y,\theta}\, f_y) \tag{1}$$

where $k_{E,\theta}$ is the reduction factor for the slope of the linear elastic range at the steel temperature, see [5], E is the elastic modulus of steel; ε_θ is the strain at elevated temperature; $k_{y,\theta}$ is the reduction factor for the yield strength of steel at the steel temperature, see [5]; f_y is the yield strength at ambient temperature, 355 MPa. Figure 8 documents the strain development the predicted loss of the shear resistance.

www.EngineeringEBooksPdf.com

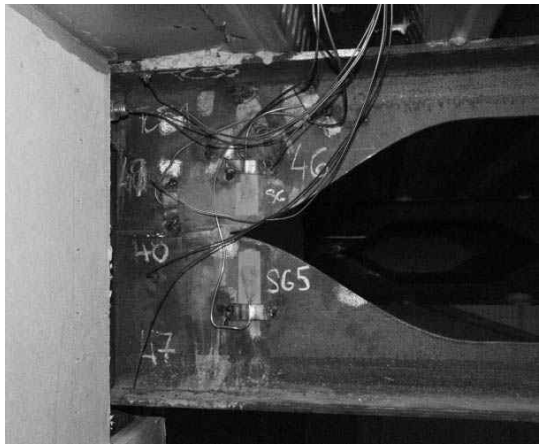


Figure 7: Strain gauges on the web of the castellated beam

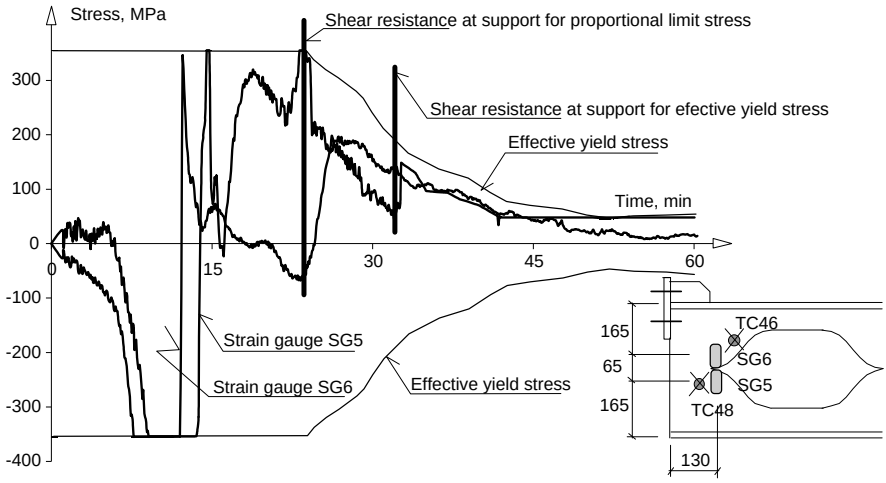


Figure 8: The measured stresses on the web of the castellated beam and predicted shear resistance

4 CONCLUSION

The fire test approved a good fire resistance of composite slab with unprotected castellated beams, which is higher compare to the separate composite beam resistance, see Figure 9. The slab resistance, designed for R60, was reached at 62 min and the beam shear resistance in 21 min.

The experimental data confirms a reasonable accuracy of prediction just by a simple model, even though the stresses of beam in structure are highly influenced be elements elongation/shortening.

ACKNOWLEDGEMENT

This outcome has been achieved with the financial support of the Ministry of Education, Youth and Sports of the Czech Republic, project No. MSM 6840770005.

www.EngineeringEBooksPdf.com



Figure 9: The deformed beams in the 35 min of the fire test

REFERENCES

[1] Wald, F., Simoes da Silva, L., Moore D.B., Lennon, T., Chladna, M., Santiago, A., Beneš, M., Borges, L., „Experimental behaviour of a steel structure under natural fire", *Fire Safety Journal*, **41**, 509-522, 2006.

[2] Kallerová P. a Wald F., *Fire test on experimental building in Mokrsko*, CTU in Prague, Prague. 2009, ISBN 978-80-01-04146-8, URL: fire.fsv.cvut.cz/firetest_Mokrsko

[3] Bailey CG. "Indicative fire tests to investigate the behavior of cellular beams protected with intumescent coatings" *Fire Safety Journal*, **39**, 689-709, 2004.

[4] Nadjaia, A., Vassart O., Ali F., Talamonab, D., Allamb A, Hawes, M., Performance of cellular composite floor beams at elevated temperatures, *Fire Safety Journal*, **42**, 489-497, 2007.

[5] EN 1993-1-2, *Eurocode 3: Design of steel structures* - Part 1-2: General rules - *Structural fire design*, CEN, 2005.

[6] Kerdal D., Nethercot D.A. "Failure modes for castellated beams" *Journal of Constructional Steel Research*, **4**, 295–315, 1984.

[7] RT1006 version 02 "Fire design of cellular beams with slender web posts. Ascot: SCI; 2004.

[8] Megharief, J. and Redwood R., "Behaviour of Composite Castellated Beams" *Journal of Constructional Steel Research*, **46**, 199-200, 1998.

[9] Bitar, D., Demarco, T., Martin, P.O., *Steel and non-composite cellular beams-novel approach for design based on experimental studies and numerical investigations*. Proceedings. EUROSTEEL, Coimbra 2005.

[10] Nadjaia, A., Goodfellow, N., Vassart, O., Ali, F., Choi, S., *Simple calculation method of cellular composite floor beams at elevated temperatures*, in Structures in fire, Singapore, 2008, 551-559, ISBN 978-981-08-0767-2.

[11] Pelouchová A., *Evaluation of fire resistance of castellated beams at Mokrsko fire test*, part IV of Diploma theses, CTU in Prague, Prague 2010.

www.EngineeringEBooksPdf.com

www.EngineeringEBooksPdf.com

SDSS'Rio 2010 STABILITY AND DUCTILITY OF STEEL STRUCTURES
E. Batista, P. Vellasco, L. de Lima (Eds.)
Rio de Janeiro, Brazil, September 8 - 10, 2010

NUMERICAL ANALYSIS OF STEEL COLUMNS CONSIDERING THE WALLS ON FIRE CONDITION

Jonas B. Dorr*, Jorge M. Neto* and Maximiliano Malite*

* Engineering School of Sao Carlos of the University of Sao Paulo, Brazil
emails: jonasbdorr@gmail.com, jmunaiar@sc.usp.br, mamalite@sc.usp.br

Keywords: Steel column, thermal gradient, masonry, thermal analysis, thermo-structural analysis, numerical analysis.

Abstract. *Steel columns are structural elements widely used in multi-storey buildings, industrial, commercial warehouse, among others. However, the reduction of stiffness and strength of steel in response to a temperature raise imposes the need to predict the critical time of exposure of the structure in fire, looking for safety and economic design structures. The presence of walls introduces change in gradient temperature at the steel cross section. In those circumstances, this paper aims to present a numerical study of steel columns with open section of type I, whereas the compartment of the environment in fire. The buckling of the compressed element will be marked by a reduction factor obtained using the relationship between the buckling load in a fire situation, characterized by asymptotic displacement, and buckling load identified at room temperature.*

1 INTRODUCTION

Fire is one of the natural phenomenon which, if it is not properly considered in the design of structures, can cause devastating consequences. Among the main materials used in the structures of the buildings it can be mentioned the steel structural, which has severe behavior changes on fire condition. The behavior of steel structures on fire condition, including the composite structure, for a long time it has been seen as dominated by the effects of the resistance loss from the material caused by the temperature rise, and large deformation through the load imposed to a weakened structure. To overcome this disadvantage it can be considered the application of fire protection to ensure that the steel can be exposed to fire for more time so it can reach similar temperatures to those that would be reached without the use of this protection. However, this procedure involves costs that, generally, make the steel structures less competitive related to the use of other structural material.

Regarding to the requirements of fire resistance from steel and composite structures elements on a fire condition, most of the standards and main normative codes of the world are still based on isolated elements in furnace experiments. This is because of the difficulty, both economic and technical, to perform experiments with complex structures, which would represent better the real structures behavior. The current international standards show simplified procedures to determine the critical time of fire resistance of steel structure. However, these simplifications are restricted to few cases and show approximated results; usually those results are not what really happen. In this way the numerical models in finite elements help to explain, in a more coherent way, the structural behavior of these elements on fire condition.

In this research [1] performed at the University of Sao Paulo was made structural numerical analysis at room temperature and thermo-structural analysis using the finite element method with the computational package Ansys [2], whose intent was to show the structural materials behave under high temperatures considering many situations and configurations, checking if the standards requirements provide with safe this behavior. However, on that study, due to uncertainties relative to the analysis

www.EngineeringEBooksPdf.com

procedure when using different types of elements simultaneously, it was used only the finite element type SOLID, with 8-nodes, for the modeling of steel cross section and compartment walls, but this element requires large computational effort. The aim of this paper is to demonstrate these numerical models now performed with finite element type SHELL, more appropriate for modeling of structures in thin walls, like steel cross sections. The advantage of using the element SHELL, whose geometry has only 4 nodes, is to allow large displacements, and also to allow coarse mesh for the numerical models of finite element, still obtaining very similar results to those achieved by the SOLID elements. This way this element requires much lower computational effort than that required by the SOLID element. The processing time is about 10 to 20 times lower.

2 NUMERICAL MODELING ASPECTS

Numerical models are built on this paper using the Ansys package, which provides to the researcher necessaries tools to obtain the results interesting to the thermal, structural and thermo-structural analysis. With this code is possible to consider the three primary modes of heat transfer: *conduction*, *convection* and *radiation*. The analysis of interest will be a *transient thermal analysis* type, which considers the evolution of the temperature over the time, allowing to determine the distribution of the temperature in the model at any instant. After made this thermal analysis for the definition of the thermal gradient in the cross section of the columns for each layout among columns and walls, simulating fire compartment, it will be realized thermo-structural analysis where it will apply a constant load with the thermal gradient in the cross section being varied along the time according to the previous analysis. A prior analysis at room temperature is going to be used to determine the ultimate load of the resistant capacity of the column so ratios of this will be used at each thermo-structural analysis.

2.1 About the thermal analysis

Thermal analysis is realized previously to obtain the thermal gradient in the cross section for determined time, since t = 0 to 150 minutes, with intervals of whole minutes. Consideration of masonry occurs in that first analysis and has, as main function, the heat exchange with the steel cross section and to isolate the fire environment, allowing the heat loss on the opposite side of the masonry and the steel. Masonry does not have structural function, being eliminated from the next analysis (thermo-structural). Because of a better coupling of the wall to the steel cross section. The masonry, differently from the steel cross sections, was modeled with SOLID.

The *heat flow* by convection is produced by the difference of the density among the gas from the fire environment. For the numerical model it will be used the value for the heat transfer coefficient by convection α_c equals 25 W/m².ºC, according to item 8.5.1.1.2 from Brazilian standard [3].

Radiation is the process where the heat flows like waves. Among the parameters to be considered in the numerical models proposed in this paper regard to the radiation will be attributed: emissivity coefficient with a value of 0.5 (at first), Stefan-Boltzmann constant with a value equals to 5.67×10^{-8} W/m².K^4, both according to the Brazilian standard [3] and configuration factor with a value equals 1.0 according to [4].

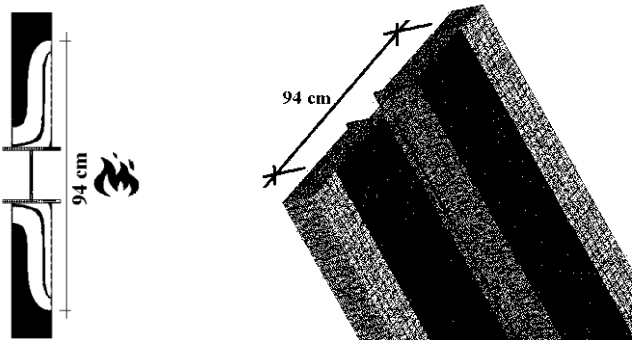
For the emissivity, the European standard [5] in its section 2.2, suggests the value 0.7, but emphasizes that is necessary to consider the *shadow effect*. However, for reasons of comparison to previous results and processing times, the value of 0.5 will be used in this paper. Furthermore, future works will use the value 0.7 coefficient and will consider the heat loss on the other side of the fire compartment with radiation and convection coefficients according to [5], also the axial restraint.

The application of the thermal effect was considered using the surface element SURF152, both for convection and radiation, being one element for each effect. Each element has only one degree of freedom per node, in this case, corresponding to the temperature. For gases heating from compartment fire was used the standard fire curve ISO 834-1:1999 and described in Equation 1, where ºC is the temperature of the gases and *t* represents the time in minutes [6]. The area considered for application of the thermal effect was 94 cm, as it is shown in Figure 1, being according to the strategy used in the experimental and numerical models [7].

www.EngineeringEBooksPdf.com

$$\theta_g = 345 \log_{10}(8t + 1) + 20°C \quad (1)$$

The mechanical and physical properties of steel as function of temperature were used according to [5]. The thermal properties adopted for the masonry (compartment), according to the computational code Ozone v2.0 [8] were: density equals 1600 kg/m^3, specific heat equals 840 J/g.K and thermal conductivity equal to 0.7 W/m.K.



(a) (b)

Figure 1: (a) Thermal gradient in the whole cross section and masonry and (b) part exposed to fire.

Efficiency tests were made with three meshes with different densities of finite elements for the model with 2 walls reaching the flanges. The numbers of elements used in each mesh are shown in Table 1, as well as the number of nodes and the approximate dimensions of the elements.

Table 1: Dimensional details of the elements and nodes for each mesh.

	ref1	**ref2**	**ref3**
Elements of the column (shell)	2040	8160	18360
Nodes	2135	8349	18643
Width x Height (mm x mm)	17x53	8.5x26.5	5.6x17.6
Elements of the end plate (shell)	240	960	2160
Elements of the masonry (solid)	3840	7680	11520
Width x height x thickness (mm x mm x mm)	31.3x26.5x8.8	62.5x53.0x17.5	20.8x17. 7x5.8

2.2 About the analysis thermo-structural

For the numerical model of the structural analysis were adopted the following mechanical properties at room temperature: yield strength equals 275 MPa and elasticity modulus equals 210,000 MPa. In the structural analysis made with the code Ansys, considering high temperature, was adopted the constitutive relation proposed by Eurocode 3 [5], that takes into account the penalty of the yield strength and elasticity modulus with the temperature.

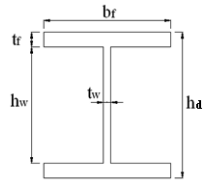
The mesh density of referring to the models in thermal analysis, eigenvalue and thermo-structural must be identical, allowing the thermal gradients in the cross section from thermal analysis and global imperfection from eigenvalue analysis to be transferred correctly to thermo-structural analysis. Also were tested the 3 meshes density described above and their differences will be explained later.

Just like [1], the thermo-structural analysis was performed under open cross section, from type I laminate subjected to the effects of geometric imperfections of the global kind. The cross section used in the models was UC 203 x 203 x 46 (English series). Their geometrical characteristics are shown in Table

www.EngineeringEBooksPdf.com

2. The local and distortional buckling modes, have not been considered because it is a cross section where the local slenderness is not predominant.

Table 2: Cross section UC 203 x 203 x 46.

Dimension	Value (mm)	Figure
h_w	181.2	
h_d	203.2	
t_w	7.2	
b_f	203.6	
t_f	11.0	
L	3170.0	

The columns were considerate with both extremity pin-ended, according to Figure 3, considering end plate with 20 mm of thickness, whose elasticity modulus was considered 1000 times higher than that adopted for the cross section (at room temperature), in order to avoid local effects.

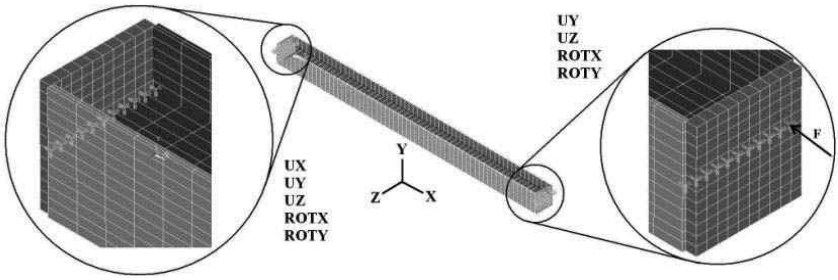
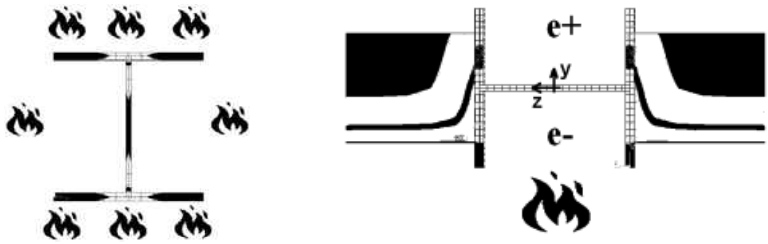


Figure 3: Detail of the column extremity, application of axial force and degrees of freedom restricted.

Thermo-structural analysis is performed by applying a static load lower and proportional to the buckling load at room temperature considering the global geometric imperfection obtained through eigenvalue analysis, according to [9]. After that, the thermal gradient is applied as a body load with the results of transient thermal analysis. The critical time is evaluated at the instant when the column loses the stability due to the temperature elevation. This procedure was performed both with the single column with thermal action on all sides, as shown in Figure 4a, also with the masonry at the flanges from Figure 4b and Figure 4c, in this case the thermal action was applied only in one of the sides.



(a) (b)

Figure 4: (a) Single column with thermal effects on all sides; (b) configuration of the walls reaching the flanges and way of initial global imperfection positive and negative.

www.EngineeringEBooksPdf.com

3 RESULTS

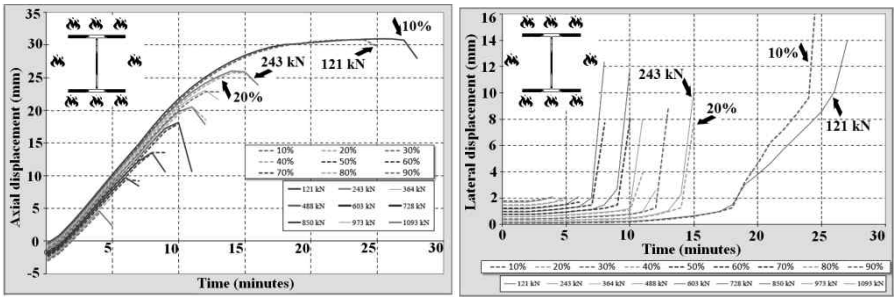
In this section will be presented the results obtained through the thermal analysis and thermo-structural analysis, those models were compared with other researchers for their validation.

3.1 Thermal models

The results of thermal model built with walls in contact with the flanges were compared with results from the other researchers [7] and showed good agreement when using the same emissivity values and heat loss like the reference. Thermo-structural models compared with [1] using the results of the thermal analysis with 0.5 emissivity coefficient, adiabatic model and standard fire curve ISO834-1:1999 in order to make the comparison possible.

3.2 Thermo-structural model with single column

The results of the axial displacement at the top and the lateral displacement at midspan presented good concordance with those shown in [1]. Figure 5 shows with solid curve the previous results with SOLID elements and, with dashed curve, the results with SHELL elements from this paper. It was identified significant differences at the processing time from both finite elements used: for SHELL elements the thermo-structural analysis took 1.1 to 2.8 hours depending on the ratios of the buckling load applied, while for those SOLID elements the time of the processing took about 24 hours to complete the analysis.



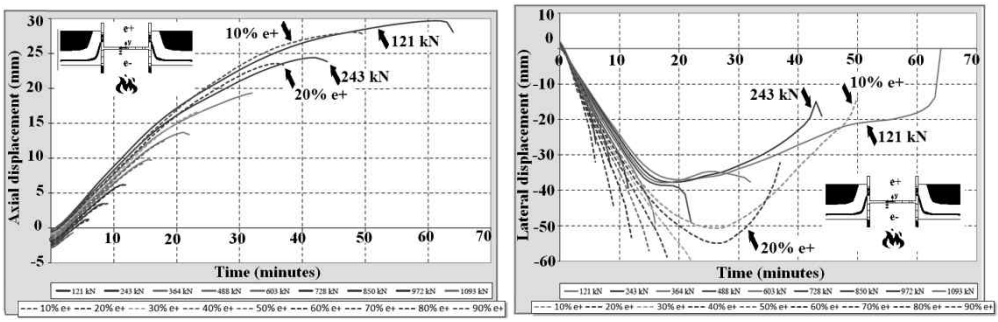
(a) (b)

Figure 5: Results from (a) axial displacement at the top and (b) lateral displacement at midspan for single column without walls and heat source in all directions by comparing SOLID elements, with solid curve, and SHELL elements, with dashed curve.

3.3 Thermo-structural models with masonry reaching the flanges of the cross section

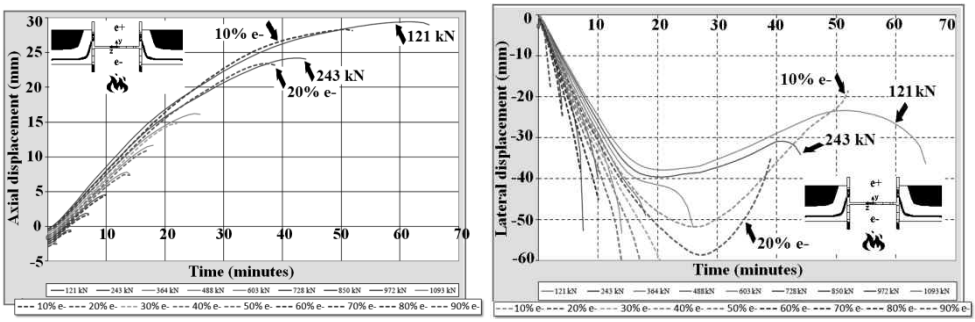
For the model with masonry reaching the flanges the processing time was longer than that identified to the single column. This is because the walls keep the fire in only one room, in a way that the thermal action occurs only in one side of the steel cross section. Such aspect, also with the fact that they change the thermal gradient of the cross section, stealing steel heat, makes the average temperature of the columns becomes less than those identified for the single columns without walls. With the lower average temperature will be necessary a larger number of loading steps to lose stability, in other words, minutes of fire. Beside this, the thermal gradient will develop an element bowing, increasing the lateral displacement at midspan related to the single column. The results obtained in this research, compared with the results of [1], are shown in Figure 6a, with the axial displacement at the top of the column, and in Figure 6b the lateral displacement at midspan of them. The Figure 7a and Figure 7b show the axial and lateral displacement, respectively, considering the global initial imperfection negative, as already shown in Figure 4. In all figures below, the solid curve are with SOLID elements [1], while the dashed curves represent the results of the SHELL element used in this paper.

www.EngineeringEBooksPdf.com



(a) (b)

Figure 6: Global initial geometric imperfection positive related to the heat source with (a) axial displacement at the top; and (b) lateral displacement at midspan comparing SOLID elements, solid curves, with SHELL elements, dashed curves.



(a) (b)

Figure 7: Global initial geometric imperfection negative related to the heat source with (a) axial displacement at the top; and (b) lateral displacement at midspan.

It is noticed good concordance between the model built in SHELL and the one built in SOLID for the axial displacement. The lateral displacement at midspan, however, was larger for all the cases with the element SHELL. It is believed that this is due to the fact that these elements allow larger displacement and because it has rotation degrees of freedom, not present in the SOLID element.

The critical times for this model were slightly lower, this is because the largest displacement at midspan increases the distance between the load action line and the longitudinal column axis, increasing and concentrating the internal efforts. The processing time for the mesh named *ref2* took about 6 to 12 times less time to complete the process related to the model in SOLID, that took 2 to 3 days.

In the three meshes tested the processing times were calculated and placed in chart form in Figure 8. Meshes *ref2* and *ref3* had results close to each other and also close from the reference curves, in SOLID element. The results of mesh *ref1* were slightly below of the reference curve. Noticing the big difference in the processing time and the good quality of the results, it was chosen the mesh named *ref2*.

www.EngineeringEBooksPdf.com

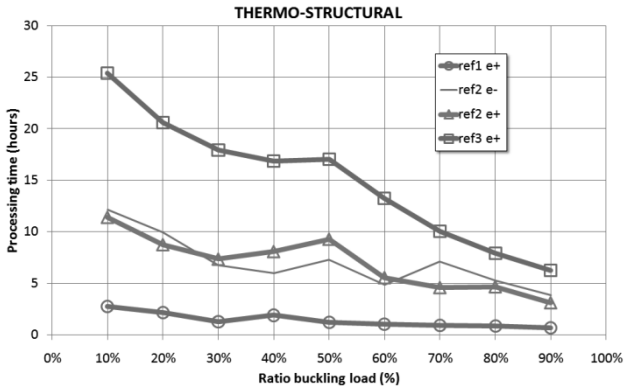


Figure 8: Tested meshes and processing times.

Because each load step receives small increments and each substep requires numerical convergence, the final time of processing becomes higher always when the buckling load ratio gets lower, in other words, reaches a higher critical time. The critical time will be equal to that load step where the numerical convergence is lost, what means, the internal efforts no longer balance with the external loads applied. In the search for numerical convergence can happen high distortions in the elements resulting in shapes often incoherent with reality, while some other times can demonstrate local or global buckling as it is supposed to happen in a real situation. Figure 9 shows some of these shapes from the elements, but remembering that this occurs in the loss of convergence, being a numerical answer many times incoherent. The quality of the results is not affected, because what is interesting for us is the behavior of the structural element until the load step of the convergence loss, such as the minute of exposure to the fire where it occurs.

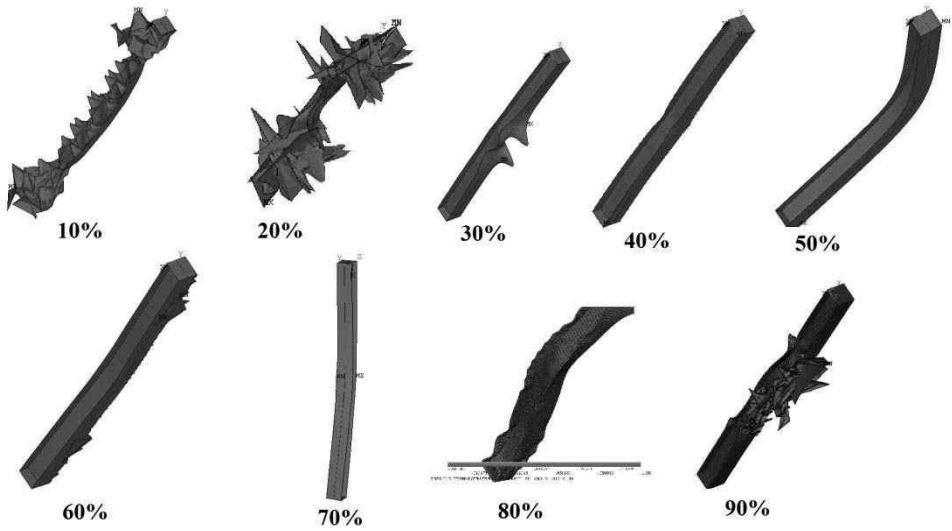


Figure 9: Structural element buckling during the numerical convergence loss from the models with walls reaching flanges for each buckling load ratio.

www.EngineeringEBooksPdf.com

4 FURTHER WORKS

Further works following in this same research line will study the heat incidence of the fire by radiation with emissivity 0.7, and also will consider heat loss in the unexposed side and the axial restraint.

5 CONCLUSION

It can be concluded that the element SHELL is more appropriate to represent thin structures like steel cross sections in both analysis at room temperature and in thermo-structural analysis. These elements seem to be adequate in thermal analysis and make possible the transference of the thermal gradient in the cross section obtained previously for the thermo-structural analysis.

Since the methodology used in the model developed in SHELL was similar to that applied to the SOLID model, it is possible to say that the results of the *displacement x time* show coherence. This way, it is observable that the models studied in this paper have great efficiency because they need less processing time, i.e., they have a lower computational cost. Because of this the model enable the realization of a large number of analysis in short time.

For thermal analysis, the transfer of nodal temperatures, following the numeric strategy adopted, shown coherence even in the SOLID x SHELL interface, or it is same them say, in the contact between the cross section and the masonry.

Finally, it is necessary to remember that the numerical analysis presented in this paper still represents one preliminary phase of the study, other compartment walls layouts will be studied. For further studies will be performed new tests trying to turn the strategy even more comprehensive and closer to real situations.

REFERENCES

[1] Kimura, E.F.A., "Coupled thermal and structural analysis of steel columns under fire condition (in portuguese)", *Dissertation (MSc.), Engineering School of Sao Carlos of the University of Sao Paulo*, São Carlos, 2009.

[2] ANSYS INC. Ansys – Documentation.

[3] Associação Brasileira de Normas Técnicas (ABNT), "NBR 14323 – Steel structure design in building on fire condition – Procedures (in portuguese)", Rio de Janeiro, 1999.

[4] Regobello, R., "Numerical analysis of steel and composite steel-concrete cross sections and structural elements in fire situation (in portuguese)", *Dissertation (MSc.), Engineering School of Sao Carlos of the University of Sao Paulo,* São Carlos, 2007.

[5] Eurocode 3, EN 1993-1-2, "Design of steel structures, Part 1.2: General rules – structural fire design", *European Community (EC)*, Brussels, 2005.

[6] International Standard. "Fire-resistance tests – elements of building construction – Part 1: General requirements", *ISO 834-1:1999*, 1999.

[7] Silva, V.P., Correia, A.M., Rodrigues, J.P.C, "Simulation on fire behaviour of steel columns embedded on walls (in portuguese)", *XXXIII Jornadas Sudamericanas de Ingenieria Estructural*, Maio 2008, Santiago, Chile, 2008.

[8] Cadorin J.F., Franssen J.M., Pintea D., "The design fire tool OZONE, V 2.0 – theoretical description and validation on experimental fire tests", *1st draft, Université Liège*, Liège, 2001.

[9] Almeida, S. J. C de, "Numerical analysis of compressed cold formed steel members considering initial geometric imperfection (in portuguese)", *Dissertation (MSc.), Engineering School of Sao Carlos of the University of Sao Paulo*, São Carlos, 2007.

www.EngineeringEBooksPdf.com

SDSS'Rio 2010 STABILITY AND DUCTILITY OF STEEL STRUCTURES
E. Batista, P. Vellasco, L. de Lima (Eds.)
Rio de Janeiro, Brazil, September 8 - 10, 2010

ON THE STRENGTH AND DSM DESIGN OF COLD-FORMED STEEL COLUMNS FAILING DISTORTIONALLY UNDER FIRE CONDITIONS

Alexandre Landesmann* and Dinar Camotim**

* Civil Engineering Program, COPPE, Federal University of Rio de Janeiro, Brazil, alandes@coc.ufr.br

** Department of Civil Engineering and Architecture, ICIST-IST, TU Lisbon, Portugal, dcamotim@civil.is.utl.pt

Keywords: Cold-formed steel column, Lipped channels, Rack-sections, Direct strength method, Fire design.

Abstract. *This paper reports the results of an ongoing shell finite element investigation on the distortional post-buckling behaviour, ultimate strength and design of pinned and fixed cold-formed steel lipped channel and rack-section columns subjected to various (uniform) temperature distributions caused by fire conditions. The columns are axially compressed up to failure, making it possible to assess the influence of the temperature on their ultimate strength. The steel material behaviour at elevated temperatures is described by the model prescribed in Eurocode 3 for cold-formed steel. The failure load data gathered are then used to carry out a preliminary assessment on the applicability of the Direct Strength Method (DSM) to estimate the load-carrying capacity of pinned and fixed lipped channel and rack-section columns failing distortionally under fire conditions.*

1 INTRODUCTION

The use of cold-formed steel profiles in industrial or residential buildings has grown steadily in the last few years, mainly due to their high structural efficiency (strength-to-weight ratio), fabrication versatility and increasingly low production and erection costs. Therefore, it is important to assess the structural response of such profiles under high temperatures, namely those caused by fire − this has already been extensively done for hot-rolled (mostly) and welded steel members. However, the research effort devoted to cold-formed steel members under fire is still relatively scarce, as attested by the fairly small number of existing publications – the works of Kaitila [1], Chen & Young [2,3], Feng *et al.* [4] and Ranawaka & Mahendran [5] deserve a special mention. Moreover, only the last of these studies addresses members failing in distortional modes. Thus, the aim of this work is to report the available results of an ongoing shell finite element investigation on the post-buckling behaviour, ultimate strength and design of axially compressed pinned (simply supported) and fixed cold-formed steel lipped channel and rack-section columns failing distortionally at elevated temperatures caused by fire conditions. Since there are no specific rules available to predict the ultimate load of such cold-formed steel columns, ultimate load data concerning columns made from various steel grades (covering a wide distortional slenderness range) are obtained and then used to make a preliminary assessment on the applicability of the Direct Strength Method (DSM [6]) to perform this task for pinned and fixed lipped channel and rack-section columns.

2 NUMERICAL ANALYSIS

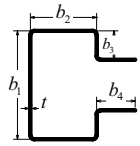
2.1 Column geometry and buckling behavior

The cold-formed steel lipped channel and rack-section columns analysed in this work exhibit the cross-section dimensions and elastic constants displayed in table 1. These cross-section dimensions make it possible to select column lengths ensuring distortional critical buckling modes for both simply supported (locally and globally pinned end sections that may warp freely) and fixed (locally and globally fixed end sections prevented from warping) columns. The buckling analyses required to identify the above column geometries were carried out in the code *GBTUL* [7], based on a recently developed *Generalised Beam Theory* (GBT) formulation [8].

www.EngineeringEBooksPdf.com

Table 1. Column cross-section dimensions and elastic constants

Column	b_1 (mm)	b_2 (mm)	b_3 (mm)	b_4 (mm)	t (mm)	E (GPa)	ν
Rack	134.7	80.8	24.2	47.1	2.3	210	0.3
Lipped C	130	100	12.5	--	2.0	205	0.3



The curves depicted in figures 1(a)-(b) provide the variation of the elastic critical buckling stress σ_{cr}, normalised with respect to the critical (distortional) buckling at room temperature ($\sigma_{cr.D.20}$), with the column length L (logarithmic scale) and temperature T, for pinned and fixed rack-section and lipped-channel columns – 4 temperatures are considered: *20/100ºC* ("room temperature"), *500ºC*, *600ºC* and *800ºC*. Also shown are the critical (distortional) buckling mode shapes of the four column sets analysed. One readily observes that, within each set, (i) a given buckling curve is obtainable through a "vertical translation" of the top one, with a magnitude that depends exclusively on the Young's modulus erosion due to the rising temperature (Poisson's ratio ν is deemed temperature-independent and equal to *0.3*), and that (ii) the critical distortional stress ($\sigma_{cr.D.T}$) corresponds to the same length (L_D) for each column set. Table 2 indicates the values of L_D and $\sigma_{cr.D.20}$ concerning the four column sets dealt with in this work.

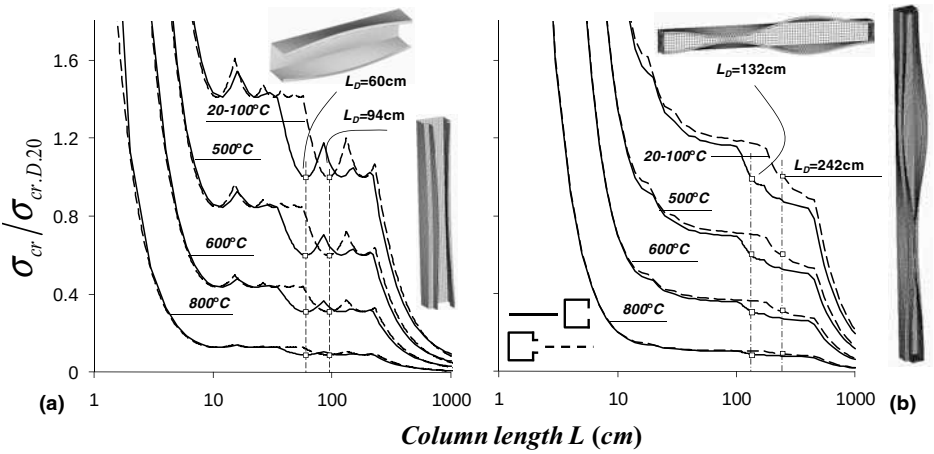


Figure 1: Variation of the buckling curve ($\sigma_{cr}/\sigma_{cr.D.20}$ vs. L) with T for (a) pinned and (b) fixed rack-section and lipped channel columns.

Table 2. Column lengths and critical stresses

Cross-section	Rack		Lipped Channel	
End sections	Pinned	Fixed	Pinned	Fixed
L_D (cm)	94	242	60	132
$\sigma_{cr.D.20}$ (MPa)	210.4	253.7	155.4	191.5

2.2 Shell finite element post-buckling analyses

The column post-buckling analyses were carried out in the code ANSYS [9] and employing a shell finite element model previously validated by the authors [10] that involves column discretisations into fine SHELL181 (ANSYS nomenclature) element meshes – thin-shell four-node elements with six d.o.f. per node. A parametric study was carried out with the aim of assessing how the (elevated) temperature influences the post-buckling and ultimate strength behaviour of pinned and fixed lipped channel and rack-section columns buckling in distortional

www.EngineeringEBooksPdf.com

modes. The analyses (i) were performed by means of an incremental-iterative technique combining Newton-Raphson's method with an arc-length control strategy and (ii) simulate the response of columns subjected to a uniform temperature distribution (they are deemed engulfed in flames and, thus, share the temperature of the surrounding air [11, 12]) and subsequently axially compressed up to and beyond failure – *steady state* analyses providing *failure loads*. At this stage, it is worth noting that the authors [10, 12] have recently shown that the failure loads yielded by the *steady state* analyses match the more realistic *failure temperatures* obtained through the "corresponding" *transient* analyses (axially compressed columns heated up to failure), which means that the column (distortional) failure under fire conditions can be fully investigated by resorting only to failure loads.

The columns analysed contained initial geometrical imperfections with a critical-mode (distortional) shape and amplitude equal to *10%* of the wall thickness t – due to the column distortional post-buckling asymmetry (*e.g.*, [13]), these initial imperfections involve outward (lipped channel columns) and inward (rack-section columns) flange-lip motions, which are those leading to lower post-buckling strengths. These columns were made of different steel grades, whose constitutive relations were assumed to vary with the temperature according to the model prescribed in Eurocode 3 (Part 1.2) [14].

The column end sections were either (locally and globally) *pinned* or *fixed* (torsional rotations prevented in both cases) – the latter condition was modelled by means of rigid end-plates attached to the cross-section centroids and only allowed to exhibit axial translations. Finally, the axial compression was applied by means of either (i) two sets of concentrated forces acting on the both end section nodes (pinned columns) or (ii) two point loads acting on the end-plate points corresponding to the cross-section centroids (fixed columns) – these loadings were applied in small increments, making use of the ANSYS automatic load stepping procedure.

2.3 Column post-buckling behaviour and ultimate strength

Figure 2 shows geometrically and materially non-linear equilibrium paths ($\sigma/\sigma_{cr.D.20}$ vs. v/t, where σ is the applied stress and v is the maximum vertical displacement along the flange-stiffener longitudinal edges) concerning pinned and fixed lipped channel and rack-section columns made of two steel grades (*S355* and *S700*) and subjected to four uniform temperatures (*20/100ºC-300ºC-500ºC-700ºC*). The circles located on the curves indicate the ultimate stress ratios $\sigma_u/\sigma_{cr.D.20}$. The observation of these sets of post-buckling results prompts the following remarks (some of which were already partially addressed in [10, 15]):

(i) Obviously, the ultimate stress decreases as the temperature T rises, both for the pinned and fixed columns.

(ii) The post-critical strengths of the fixed columns are considerably higher than those exhibited by the pinned columns – for T=*700ºC*, this difference is less perceptible due to the low $\sigma/\sigma_{cr.D.20}$ values.

(iii) For all the pinned columns, the collapse occurs either (iii_1) immediately after the onset of yielding and at relatively small deformation levels (*S355*) or (iii_2) following a well pronounced equilibrium path plateau, *i.e.*, is preceded by a fair amount of ductility (*S700*).

(iv) For all the fixed lipped channel columns, the collapse occurs for fairly high deformation levels. Nevertheless, failure is not preceded by a visible equilibrium path plateau (*i.e.*, there is a well defined maximum stress value) –

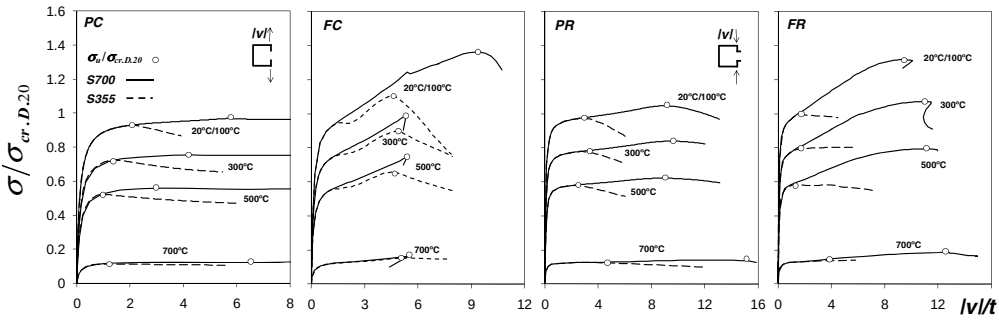


Figure 2: Distortional post-buckling equilibrium paths of pinned (P) and fixed (F) lipped channel (C) and rack-section (R) columns made of *S355* and *S700* steels and subjected to temperatures *20/100-300-500-700* ºC.

www.EngineeringEBooksPdf.com

the *S355* columns exhibit a small snap-through phenomenon following the onset of yielding[1].

(v) In the case of the fixed rack-section columns, there is a marked difference between the collapse behaviours of those made of *S355* and *S700* steel. While the latter behave like their lipped channel counterparts, the former fail immediately after the onset of yielding (*i.e.*, do not exhibit the snap-through phenomenon mentioned above).

(vi) There is no clear trend concerning the variation of the deformation level at collapse with the temperature.

3 COLUMN DSM DESIGN

This section presents a preliminary assessment of the applicability of the Direct Strength Method (DSM), already included the North American Specification for cold-formed steel structures [6], to predict the ultimate strength of pinned and fixed lipped channel and rack-section columns failing distortionally at room and elevated temperatures. At *room temperature*, the nominal ultimate load of cold-formed steel columns experiencing distortional collapses is given by the DSM equation (curve)

$$P_{n.D} = \begin{cases} P_y & \text{for } \bar{\lambda}_D \le 0.561 \\ \left[1 - 0.25\left(\dfrac{P_{cr.D}}{P_y}\right)^{0.6}\right]\left(\dfrac{P_{cr.D}}{P_y}\right)^{0.6} P_y & \text{for } \bar{\lambda}_D > 0.561 \end{cases} \quad (1)$$

where (i) P_y and $P_{cr.D}$ are the column squash and distortional critical buckling loads, and (ii) $\bar{\lambda}_D = \sqrt{P_{cr.D} / P_y}$ is the column distortional slenderness. Figures 3(a)-(b) compare the ultimate loads predicted by the above DSM curve with (i) numerical values obtained in this work and (ii) experimental values reported by Ranawaka [16], for pinned (fig. 3(a)) and fixed (fig. 3(b)) rack-section and lipped-channel columns. While the numerical values deal with (i) both end support conditions and (ii) several yield stresses[2], making it possible to cover wide distortional slenderness ranges (the minimum and maximum values achieved were *0.77* and *2.89*), the experimental values concern only a few fixed columns, namely one lipped channel column pair and three rack-section column pairs[3]. The observation of the columns ultimate strength results prompts the following (preliminary) remarks:

(i) First of all, one readily notices that the ultimate load estimates provided by the DSM distortional curve for the pinned columns with moderate-to-high slenderness considerably overestimate the numerical values yielded by the ANSYS analyses – indeed, safe (and fairly accurate) predictions only occur in a low slenderness range. This confirms earlier findings by authors [10, 15], which performed similar numerical analyses for other pinned (simply supported) lipped channel and rack-section columns failing in distortional modes.

(ii) Concerning the fixed columns, the first remark is that the DSM distortional curve estimates either match almost perfectly or slightly underestimate (particularly the stockier columns) the ultimate loads of the *8* columns tested by Ranawaka [16]. As for the numerical ultimate loads provided by the ANSYS analyses, they are also quite close to the DSM distortional curve predictions, even if there is a slight overestimation in the high slenderness range (both for the lipped channel and rack-section columns).

(iii) There is no significant difference between the "quality" of the DSM distortional curve estimates concerning the lipped channel and rack-section columns. Indeed, the ratios between the DSM predictions and the numerical

[1] It is worth noting that numerically difficulties prevented reaching a well defined clear ultimate load/stress in the fixed lipped channel columns at elevated temperatures (the equilibrium path descending branch appears very abruptly). This also explains why, at *700* ºC, the S355 and S700 fixed lipped channel columns exhibit identical ultimate loads/stresses (the latter is certainly underestimated).

[2] The following room temperature yield stresses were considered: (i) σ_y*=150-235-355-600-700-1000 MPa* (pinned lipped channel columns), (ii) σ_y*=150-250-355-550-700-1200 MPa* (pinned rack-section columns), (iii) σ_y*=250-355-550-700-1000-1600 MPa* (fixed lipped channel columns) and (iv) σ_y*=250-355-550-700-1000-1200 MPa* (fixed rack-section columns).

[3] Results concerning the following column dimensions and room temperature yield stresses were reported in [16]: (i) b_1*=30, b_2=30, b_3=5, t=0.60 mm*, σ_y*=315-675 MPa* and *L*=20 *cm* (lipped channel columns) and (i) b_1*=40, b_2=30, b_3=5, b_4=10, t=0.60-0.80-0.95 mm*, σ_y*=250-550 MPa* and *L=22-24-28 cm* (rack-section columns).

www.EngineeringEBooksPdf.com

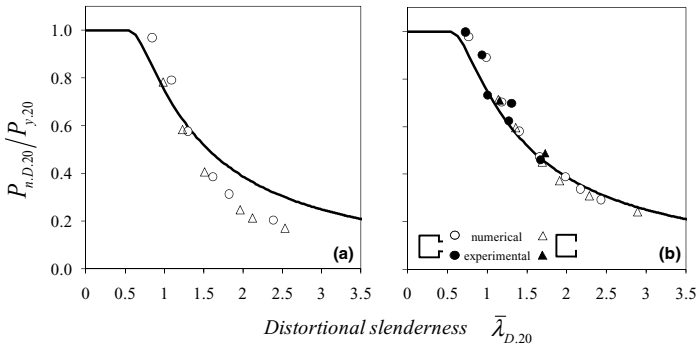


Figure 3: Comparison between the DSM distortional curve predictions and the numerical (obtained in this work) and experimental (reported in [16]) ultimate loads for (a) pinned and (b) fixed columns at room temperature.

ultimate loads for both column geometries differ by less than *5%*. The lipped channel ultimate load ratios are generally (slightly) smaller, most likely due to the higher flange-to-web width ratio (*0.77* against *0.60*) – note that a higher ratio corresponds to a "weaker" flange, thus leading to a lower post-critical strength.

(iv) At this stage, note that the calibration and validation of the DSM distortional curve involved almost exclusively fixed columns (*e.g.*, Schafer [17]), since it is extremely difficult to test pinned columns failing in distortional modes – in particular, it is virtually impossible to ensure that the column end sections are able to warp freely.

(v) In view of the above facts, it seems fair to conclude that there are significant differences in the distortional post-critical strengths of pinned and fixed columns, which are not adequately reflected in the corresponding (distortional) critical buckling stresses[4].

Taking into consideration the above assessment of the performance of the DSM distortional curve to predict the ultimate strength of lipped channel and rack-section columns at room temperature, the suitability of this DSM approach to estimate column (distortional) ultimate loads at elevated temperatures is addressed next. Accordingly, the methodology followed in this work, which was already (partially) explored by other researchers [2, 3, 5] (and also by the authors [10, 15]), consists of modifying equation (1) to account for the influence of the temperature on $P_{cr.D}$ and P_y – this influence is felt through the values of the Young's modulus and yield stress, which are reduced as the temperature increases due to the fire conditions. In other words, one replaces $P_{cr.D}$ and P_y (or σ_y) by $P_{cr.D.T}$ and $P_{y.T}$ (or $\sigma_{y.T}$) – note that $\bar{\lambda}_D$ also varies with T.

Figure 4 concerns pinned columns and shows a comparison between the ultimate loads predicted by the modified DSM curve and the numerical values obtained in this work. It includes *8* plots, each corresponding to a different temperature ranging from *20/100* ºC (room temperature – results already presented in fig. 3(a) and included here for comparison) to *800* ºC. The yield stress variation considered makes it possible to cover a wide slenderness range: from *0.98* to *3.4*, for the lipped channel columns, and from *0.84* to *3.2*, for rack-section columns. Keeping in mind that it has been shown that the available DSM distortional curve consistently overestimates the ultimate loads of the pinned columns with moderate or high slenderness values, at room temperature, the observation of the sets of results presented in figure 4 leads to the following comments, concerning the applicability of the modified DSM approach to predict column (distortional) ultimate loads at elevated temperatures:

(i) Regardless of the temperature, the modified DSM curve ultimate strength predictions generally overestimate the numerical ultimate loads ($P_{u.D.T}$) considerably – there are only a few exceptions, all concerning stocky columns at room temperature (mostly), *T=200 ºC* and *T=300 ºC*. As for the amount of overestimation, it (i_1) increases with T up to *400 ºC* and (i_2) remains practically constant from then on (*i.e.*, for *T≥400 ºC*).

[4] In the context of lipped channel and rack-section columns affected by local/distortional/global mode interaction, Dinis & Camotim [18-20] showed that there are marked differences between the post-buckling behaviour and strength of pinned (simply supported) and fixed columns.

www.EngineeringEBooksPdf.com

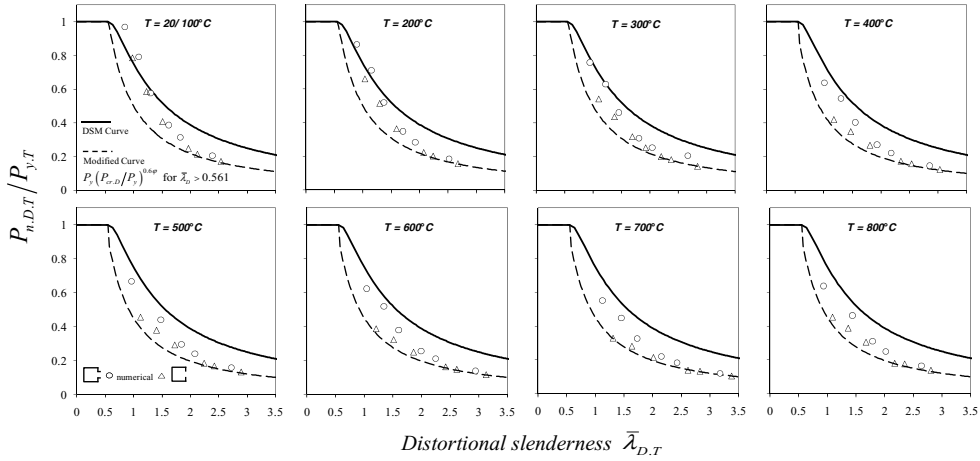


Figure 4: Comparison between the modified DSM distortional curve estimates and the numerical ultimate loads for pinned columns at temperatures *20/100-200-300-400-500-600-700-800* ºC.

(ii) Nevertheless, it may be said that the various sets of $P_{u,D,T}/P_{y,T}$ values remain fairly "aligned" with a Winter-type curve, which suggests that it s possible to further modify equation (1) in order to achieve a better correlation with the numerical column ultimate loads determined in this work. Just for the sake of illustration, each plot in figure 4 includes also a very simple/crude exponential curve (dashed line), that does not clearly underestimate any of the numerical values (while remaining as close to all of them as possible) and was obtained by adopting the following modification of equation (1): (ii_1) eliminate the term with the *0.25* coefficient and (ii_2) multiply the power of the remaining term (*0.6*) by a slightly temperature-dependent parameter φ – one has either $\varphi=0.5$ (if $T\leq300$ ºC) or $\varphi=0.45$ (if $T>300$ ºC).

(iii) The fact that the φ values given in the previous item are much smaller than *1.0* stems from the combined influence of (iii_1) the temperature effects and (iii_2) the "inherent lack of safety" of DSM design curve predictions for pinned columns. Moreover, since those φ values are governed by the slender column estimates, it is just logical that the modified curves considerably underestimate the numerical ultimate loads of the columns with low and intermediate slenderness values (more so for the lower temperatures).

(iv) Finally, note that the lipped channel column $P_{u,D,T}/P_{y,T}$ values are also slightly smaller than the rack-section ones for elevated temperatures. The differences become more pronounced for $T\geq300$ ºC and high slenderness values.

Figure 5 display similar results for fixed columns, but now the ultimate loads predicted by the modified DSM curve are compared with both numerical (obtained in this work) and experimental (reported in [16]) values. The latter concern *8* column geometries and four temperatures (*20/100-200-500-800* ºC) and it should be noted that these *32* columns do not exhibit the same material behaviour as the remaining ones – indeed; they follow an experimentally obtained stress-strain law [16], and not the model prescribed in EC3-1.2 that was adopted to obtain the numerical ultimate loads. As before, plots corresponding to *8* different temperatures are presented and the yield stress variation considered now enables covering the following slenderness ranges: *1.13* to *3.56* (lipped channel columns) and *0.77* and *2.9* (rack-section columns). Recalling that the available DSM distortional curve provides fairly accurate ultimate load estimates for fixed columns at room temperature, the observation of the results displayed in figure 5 prompt the following remarks on the suitability of the modified DSM approach to predict column (distortional) ultimate loads at elevated temperatures:

(i) Again regardless of the temperature, most of the modified DSM curve ultimate strength predictions now slightly overestimate the numerical ultimate loads ($P_{u,D,T}$) – the few exceptions still concern stocky columns at room temperature (mostly), *T=200 ºC* and *T=300 ºC*. As for the pinned columns, the amount of overestimation, (i_1) increases with *T* up to *400 ºC* and (i_2) remains practically constant for $T\geq400$ *ºC*.

www.EngineeringEBooksPdf.com

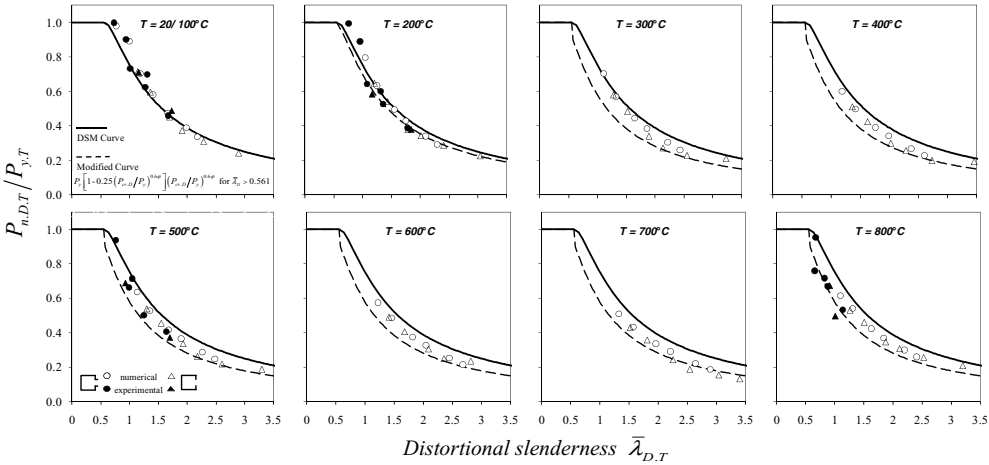


Figure 5. Comparison between the modified DSM distortional curve estimates and the experimental (reported in [16]) and numerical ultimate loads for fixed columns at temperatures *20/100-200-300-400-500-600-700-800* ºC.

(ii) Concerning the experimental $P_{u,D,T}/P_{y,T}$ values, the DSM curve estimates (ii_1) slightly underestimate them at room temperature, (iv_2) slightly overestimate them at T=200 ºC and (iv_3) fairly overestimate them at T=500 ºC and T=800 ºC – in these last two cases, the experimental ultimate loads are below the numerical ones.

(iii) As before, each plot in figure 5 includes an exponential curve (dashed line) that does not significantly underestimate any of the *numerical* values but remains as close to all of them as possible – one has now φ=*1.0* (room temperature), φ=*0.9* (T=*200* ºC) and φ=*0.7* ($T \geq$*300* ºC). Note that these φ values are much closer to *1.0* than those obtained for the pinned columns, due to the fact that they stem from the sole influence of the temperature effects (there is no "inherent lack of safety" of DSM design curve predictions for fixed columns).

(iv) Only *2* out of all experimental $P_{u,D,T}/P_{y,T}$ values fall below the dashed lines – they both concern T=800 ºC.

(iv) Once more, the numerical lipped channel column $P_{u,D,T}/P_{y,T}$ values are slightly smaller than the rack-section ones, with the differences being again more pronounced for $T \geq$*300* ºC and high slenderness values.

Obviously, further research is required in order to confirm the preliminary assessment presented here – in particular, it is indispensable to obtain additional numerical and experimental columns ultimate loads at elevated temperatures, involving different cross-sections and temperature-dependent steel material behaviours. Then, it will be possible to progress towards developing new DSM design curves to predict the distortional failure of (pinned and fixed) columns subjected to elevated temperatures, namely those caused by fire conditions – on the basis of the available results, it seems that such curves should be mildly dependent on the temperature.

4 CONCLUDING REMARKS

This paper reported the available results of an ongoing shell finite element investigation on the distortional strength and design of pinned and fixed cold-formed steel lipped channel and rack-section columns at elevated temperatures. The variation of the material behaviour with the temperature followed the EC3-1.2 model for cold-formed steel, and the geometrically and physically non-linear shell finite element analyses were carried out in the code ANSYS. Then, the suitability of modified DSM design curves to predict the ultimate strength of columns subjected to elevated temperatures and failing in distortional modes was addressed. A preliminary assessment was presented, on the basis of the comparison between the above DSM curves estimates and numerical (pinned and fixed column ultimate loads analysed in this work) and experimental (fixed column tests reported in [16]) ultimate loads. Although a fairly large amount of research work is required before this preliminary assessment can be confirmed, it seems that an efficient DSM design will have to be based on new curves mildly dependent on the temperature.

www.EngineeringEBooksPdf.com

REFERENCES

[1] Kaitila O., "Imperfection sensitivity analysis of lipped channel columns at high temperatures", *Journal of Constructional Steel Research*, **58**(3), 333-351, 2002.

[2] Chen J., Young B., "Cold-formed steel lipped channel columns at elevated temperatures", *Engineering Structures*, **29**(10), 2445-2456, 2007.

[3] Chen J., Young B., "Design of high strength steel columns at elevated temperatures", *Journal of Constructional Steel Research*, **64**(6), 689-703, 2008.

[4] Feng M., Wang Y.C., Davies J.M., "Structural behaviour of cold-formed thin-walled short steel channel columns at elevated temperatures − Part 1: experiments," *Thin-Walled Structures*, **41**(6), 543-570, 2003.

[5] Ranawaka T., Mahendran M. "Distortional buckling tests of cold-formed steel compression members at elevated temperatures", *Journal of Constructional Steel Research*, **65**(2), 249-259, 2009.

[6] American Iron and Steel Institute (AISI), *Appendix I of the North American Specification (NAS) for the Design of Cold-formed Steel Structural Members: Design of Cold-Formed Steel Structural Members with the Direct Strength Method,* Washington DC, 2007.

[7] Bebiano R., Pina P., Silvestre N., Camotim D., *GBTUL 1.0β – Buckling and Vibration Analysis of Thin-Walled Members*, DECivil/IST, Technical University of Lisbon, 2008. (http://www.civil.ist.utl.pt/gbt)

[8] Bebiano R., Silvestre N., Camotim D.:, "GBTUL − A code for the buckling analysis of cold-formed steel members", *Proceedings of 19th International Specialty Conference on Recent Research and Developments in Cold-Formed Steel Design and Construction* (St. Louis, 14-15/10),R. LaBoube, W.W. Yu (eds.), 61-79, 2008.

[9] Swanson Analysis Systems (SAS): *ANSYS Reference Manual* (version 8.1), 2004.

[10] Landesmann A., Camotim D., "Distortional failure and design of cold-formed steel lipped channel columns under fire conditions", *Proceedings of SSRC Annual Stability Conference*, (Orlando, 12-15/5), 505-532, 2010.

[11] Landesmann A., Camotim D., Batista E.M., "On the distortional buckling, post-buckling and strength of cold-formed steel lipped channel columns subjected to elevated temperatures", *Proceedings of International Conference on Applications of Structural Fire Engineering* (Prague, 19-20/2), F. Wald, P. Kallerová, J. Chlouba (eds.), A8-A13, 2009.

[12] Landesmann A., Camotim D., "On the distortional buckling, post-buckling and strength of cold-formed steel lipped channel columns under fire conditions", *submitted for publication*, 2010.

[13] Prola L.C., Camotim D., "On the distortional post-buckling behavior of cold-formed lipped channel steel columns", *Proceedings of SSRC Annual Stability Conference* (Seattle, 24-27/4), 571-590, 2002.

[14] Comité Européen de Normalisation (CEN), *Eurocode 3: Design of Steel Structures – Part 1-2: General Rules – Structural Fire Design*, Brussels, 2005.

[15] Landesmann A., Camotim D., "Distortional failure and design of cold-formed steel rack-section columns under fire conditions", *Proceedings of 4th International Conference on Steel & Composite Structures* (Sydney, 21-23/7), B. Uy *et al.* (eds.), 287-289, 2010. (full paper in CD-ROM Proceedings)

[16] Ranawaka T., *Distortional Buckling Behaviour of Cold-Formed Steel Compression Members at Elevated Temperatures*. Ph.D. Thesis, Queensland University of Technology, Brisbane, 2006.

[17] Schafer B.W., "Review: the Direct Strength Method of cold-formed steel member design", *Journal of Constructional Steel Research*, **64**(7-8), 766-88, 2008.

[18] Dinis P.B., Camotim D., "Local/distortional/global buckling mode interaction in cold-formed steel lipped channel columns", *Proceedings of SSRC Annual Stability Conference* (Phoenix, 1-4/4), 295-323. 2009.

[19] Dinis P.B., Camotim D., Batista E.M., Santos E., "Local/distortional/global mode coupling in fixed lipped channel columns: behaviour and strength", *Proceedings of Sixth International Conference on Advances in Steel Structures* (Hong Kong, 16-18/12), S.L. Chan (ed.), 19-34 (vol. I), 2009.

[20] Dinis P.B., Camotim D., "Local/distortional/global buckling mode interaction in cold-formed steel rack-section columns", *Proceedings of SSRC Annual Stability Conference* (Orlando, 12-15/5), 481-504, 2010.

www.EngineeringEBooksPdf.com

AUTHOR INDEX

www.EngineeringEBooksPdf.com

www.EngineeringEBooksPdf.com

A. K. Abu 21
H. Ahmed 813
R. Alsafadie 547
M. G. Amani 417
S. A. L. de Andrade 279, 423, 879
T. Aoki 369
P. Arasaratnam 571
A. H. M. de Araújo 1177
R. R. de Araujo 423
V. Bachmann 271
N. Baldassino 183
A. M. Barszcz 611
C. Basaglia 33, 913
E. M. Batista 1061, 1151
J.-M. Battini 547
R. C. Battista 149
A. Battistini 133
E. Bayo 215
R. G. Beale 813, 905
R. Bebiano 33
A. Bedynek 747
D. Beg 787
J. L. Bellod 157
W. Bessa 175
L. M. Bezerra 539, 1169
A. Bignardi 183
F. S. K. Bijlaard 619
R. Bjorhovde 9
J. Bonada 1125
B. Braun 731
I. W. Burgess 21, 441, 505
A. Caballero 1051
L. Calado 175, 231
R. B. Caldas 433
D. Camotim 33, 529, 913, 1061, 1141, 1151
M. Casafont 1093, 1125
C. A. Castiglioni 175, 207
R. Chacon 739
B. Chen 755
F. Chen 369
J. Chlouba 513
A. M. G. Coelho 619
L. Comeliau 393
A. M. Correia 489
C. Costa 855
R. S. Costa 871
M.Couchaux 295
A. Crisan 937
I. M. Cristutiu 191, 649
R. B. Cruise 697
M. Cudejko 847
R. O. Curadelli 417
M.-E. Dasiou 921
J. B. Davison 441
H. Degée 337
J. F. Demonceau 199, 393
P. B. Dinis 1061, 1141
F. Dinu 401
A. Dogariu 223
J. B. Dorr 521
A. Drei 207
D. Dubina 59, 191, 223, 401, 929, 937
L. Dunai 81, 231
P. N. Dung 1101
J. Durodola 813
M. Engelhardt 133
R. H. Fakury 433
M. Fontana 465, 473
A. Formisano 945
K. Frank 133
A. M. S. Freitas 953
C. A. S. Freitas 1169
M. S. R. Freitas 953
R. Friede 287
M. Friedrich 721
Y. Fukumoto 369
A. S. Galvão 361
T. Gao 1017
L. Gardner 555, 657, 665
B. Gil 215
M. A. Gizejowski 239, 611, 839
M. H. R. Godley 905

www.EngineeringEBooksPdf.com

P. B. Gonçalves 361, 797
R. M. Gonçalves 175, 207
R. Gonçalves 33
R. Goñi 215
D. Grecea 223
R. Greiner 141, 595
G. de C. Grigoletti 961, 1133
S. Guezouli 165, 303
T. S. Gururaj 409
L.-H. Han 887
G. J. Hancock 101, 969, 1025
T. Harada 369
R. S. Harichandran 449, 457
T. A. Helwig 133, 1161
J. Henriques 327
M. Hjiaj 295, 547
J.C.D. Hoenderkamp 579
Y. Hu 441
K. Ikarashi 377, 1043
A. Insausti 555
S. Iqbal 449, 457
M. Ishiyama 369
I. Iturrioz 961, 1133
M. Jakomin 805
J.-P. Jaspart 199, 327, 393
G. A Jimenez 713
N. de O. P. Junior 1177
S. S. Kaing 165
J. Kala 779
Z. Kala 779
S. Käpplein 1009, 1033
M. Karmazínová 895, 985
K. Kathage 1001, 1009
W. A. S. Khalil 611, 839
A. Khelil 1085
J. R. Kissell 641
M. Knobloch 465, 473
Z. Kolakowski 1193
F. Kosel 805
N. Kovács 231
A. Kozlowski 1185
H. Krüger 1001
T. Kubiak 1193
G. Kubieniec 271
U. Kuhlmann 681, 731
L. Kwasniewski 239
A. Lachal 165, 303
A. Landesmann 497, 529
R. Landolfo 945, 1109
J. Lange 287, 563
A. C. C. Lavall 673, 871
N. Lebrun 337
A. Lechner 141
X. A. Lignos 921
L. R. O. de Lima 247, 263, 279, 345, 423, 855
N. L. de A. Lima 345
J. Lindner 1077
N. Lopes 123
G. Di Lorenzo 945, 1109
L. Ly 327
J. Machacek 847
E. Magnucka-Blandzi 977
K. Magnucki 977
R. Mairal 319
M. Malite 319, 521
O. Mammana 1109
R. Mania 1193
L. A. C. da Mata 863
R. M. M. P. de Matos 247
F. M. Mazzolani 945
J. J. Melcher 779, 895, 985
H. Merle 563
G. P. Mezzomo 961, 1133
K. K.-Michalska 1193
L. F. Miguel 417
E. Mirambell 739, 747
O. Mirza 255
T. Misiek 1001, 993, 1009
C. D. Moen 1017
C. Müller 199
N. Muntean 223
Z. Nagy 649, 929

www.EngineeringEBooksPdf.com

C. Neagu 401
J. M. Neto 521
M. Neuenschwander 473
L. F. da C. Neves 247, 855, 879
J. Noguera 1125
L. Nunes 929
C. G. Oliveira 863
P. Osterrieder 721
J. A. Packer 115
A. M. Paradowska 697
H. Pasternak 271
M. M. Pastor 1093, 1125
J. Pauli 465
T. Peköz 1093
A. Pelouchová 513
S. S. Pereira 863
P. Pernes 929
M. S. Pfeil 149, 863
C. H. Pham 101, 969, 1025
T. A. C. Pires 481
R. J. Plank 441, 505
A. Plumier 337, 1101
F. Portioli 1109
Z. N. del Prado 797
Z. M. C. Pravia 961
C. Quadrato 133
G. Queiroz 863
E. Real 739, 747
P. V. Real 123
C. Rebelo 263
J. A. V. Requena 1177
S. Richter 721
J. D. Riera 417
F. C. Rodrigues 863, 871
J. P. C. Rodrigues 481, 489
M. C. Rodrigues 279
L. Roelle 681
F. Roure 1093, 1125
I. Ryan 295
H. Saal 763, 993
S. R. Sajja 905
E. F. dos Santos 149
E. S. Santos 1151
G. F. dos Santos 353
D. Sanz 157
L. Di Sarno 831
B. W. Schafer 1069, 1117
F. Seidel 1077
M. S. Seif 1117
N. Shimizu 1043
A. R. D. Silva 361
A. T. da Silva 263
J. C. G. da Silva 497
J. G. S. da Silva 279, 345, 353, 423
J. J. R. Silva 481
L. S. da Silva 123, 263, 327, 423
R. G. L. da Silva 673
R. S. Y. C. Silva 539, 1169
R. A. M. Silveira 361
N. Silvestre 33, 657, 1061, 1141
P. D. Simão 619
F. Sinur 787
K. S. Sivakumaran 571, 755
M. Škaloud 3, 771, 779
H.H. Snijder 579
F. J. da C. P. Soeiro 345, 353
D. Somaini 465
F. T. Souza 953
J. B. M. Sousa Jr. 433
R. C. Spoorenberg 579
M. Strejček 513
R. Stroetmann 587
J. Szalai 689
J. K. Szlendak 311
J. Swiniarski 1193
M. Tait 571
T. Takaku 369
J. M. S.-Talero 1051
P. Tanner 157
Z. Tao 887
A. Taras 141, 595
G. Terracciano 945

www.EngineeringEBooksPdf.com

M. Theofanous 665
N. M. Thontalapura 409
K.-C. Tsai 385
T. Ummenhofer 1001, 1033
V. Ungureanu 929, 937
H. Unterweger 603
B. Uy 255, 887
R. Vasconcelos 149
I. Vayas 921
P. C. G. da S. Vellasco 279, 345, 423, 879
J. da C. Vianna 879
L. C. M. Vieira Jr. 1069
R. C. Vieira 1177
L. G. Vigh 81, 705
M. Volz 763
F. Wald 513
T. Wang 377
Y.-T. Weng 385
K. Weynand 199
A. Wojnar 1185
V. Y. B. Wong 505
R. Wongjeeraphat 1161
N. Yamazaki 369
H. Yu 441
Y.-J. Yu 385
R. Zandonini 183
J. Zhang 635
J. Zielnica 821
R. D. Ziemian 641
L. Ziemianski 1185
T. Zirakian 627, 635
M. Zörnerová 771

www.EngineeringEBooksPdf.com